

Advanced Monte Carlo for Radiation Physics, Particle Transport Simulation and Applications

Springer

Berlin

Heidelberg

New York

Barcelona

Hong Kong

London

Milan

Paris

Tokyo

Physics and Astronomy



ONLINE LIBRARY

<http://www.springer.de/phys/>

A.Kling F. Barão
M.Nakagawa L.Távora P.Vaz (Eds.)

Advanced Monte Carlo for Radiation Physics, Particle Transport Simulation and Applications

Proceedings of the Monte Carlo 2000 Conference,
Lisbon, 23–26 October 2000

With 548 Figures and CD-ROM



Springer

Dr. Andreas Kling
Instituto Tecnológico e Nuclear
Estrada Nacional no. 10
2686-953 Sacavém, Portugal
e-mail: akling@itn.pt

Prof. Luis Távora
Departamento da Física
Universidade de Coimbra
3004-516 Coimbra, Portugal
e-mail: lmtavora@saturno.fus.uc.pt

Prof. Fernando J. C. Barão
Laboratório de Instrumentação
e Partículas
Av. Elias Garcia, 14-1º
Rovisco Pais
1000-149 Lisboa, Portugal
e-mail: barao@lip.pt

Prof. Pedro Vaz
Departamento de Física
IST
Av. Rovisco Pais
1049-001 Lisboa, Portugal
e-mail: pedrovaz@itn.pt

Prof. Masayuki Nakagawa
Department of Nuclear Energy System
JAERI
Tokai-mura, Naka-gun
319-1195 Ibaraki-ken, Japan
e-mail: nakagawa@mike.tokai.jaeri.go.jp

Library of Congress Cataloging-in-Publication Data

Monte Carlo 2000 Conference (2000: Lisbon, Portugal)

Advanced Monte Carlo for radiation physics, particle transport simulation, and applications: proceedings of the Monte Carlo 2000 Conference, Lisbon, 32–26 October 2000 / Andreas Kling ... [et al.], eds.
p. cm. Includes bibliographical references and index.

ISBN 3-540-41795-8 (alk. paper)

1. Radiation—Statistical methods—Congresses. 2. Monte Carlo method—Congresses. 3. Neutron transport theory—Congresses. I. Kling, Andreas, 1961– II. Title

QC474.M66 2000 539.7'22'01519282—dc21 2001042697

ISBN 3-540-41795-8 Springer-Verlag Berlin Heidelberg New York

This work is subject to copyright. All rights are reserved, whether the whole or part of the material is concerned, specifically the rights of translation, reprinting, reuse of illustrations, recitation, broadcasting, reproduction on microfilm or in any other way, and storage in data banks. Duplication of this publication or parts thereof is permitted only under the provisions of the German Copyright Law of September 9, 1965, in its current version, and permission for use must always be obtained from Springer-Verlag. Violations are liable for prosecution under the German Copyright Law.

Springer-Verlag Berlin Heidelberg New York
a member of BertelsmannSpringer Science+Business Media GmbH

<http://www.springer.de>

© Springer-Verlag Berlin Heidelberg 2001

Printed in Germany

The use of general descriptive names, registered names, trademarks, etc. in this publication does not imply, even in the absence of a specific statement, that such names are exempt from the relevant protective laws and regulations and therefore free for general use.

Typesetting: Camera-ready by the authors/editor

Cover design: design and production GmbH, Heidelberg

Printed on acid-free paper SPIN 10794596 54/3141/x0 – 5 4 3 2 1 0

Preface

During recent years, substantial and significant developments have occurred which are related to the advent of powerful processors and computing architectures as well as to the large-scale implementation of modern information technologies and networked systems. The combination of these factors has gradually strengthened the usage of the Monte Carlo methods and techniques in “traditional” domains and applications, with an increasing complexity of the systems being described. At the same time, several multi-disciplinary projects have emerged during the last decade which require the study of high-intensity accelerator and target systems for multiple applications in different domains.

The Monte Carlo method and its applications have been frequently addressed at several major conferences, congresses, meetings and workshops organized in recent years on topics related to radiation shielding, radiation physics, medical physics, high-energy physics etc. These events included at least one session fully dedicated to the Monte Carlo method, with a strong emphasis normally given to its “applications” related to the principal topics and areas of interest.

Considering these factors, a group of people spread over the five continents ascertained during the summer of 1999 that the time had come for organizing a conference purely devoted to Monte Carlo issues and methods in radiation physics problems and applications. The charm, mild climate and geographic location of Lisbon, combined with the nationality of the people who proposed setting up the organizational structure of such a conference determined the place of the conference.

The international conference “Monte Carlo 2000 – Advanced Monte Carlo for Radiation Physics, Particle Transport Simulation and Applications” (MC2000) was held in Lisbon, Portugal, at the Congress Centre of IST (Instituto Superior Tecnico, the Lisbon School of Engineering), during 23–26 October 2000. At MC2000 all sessions were dedicated to Monte Carlo issues. The conference was organized around the three main categories of Monte Carlo simulations, involving, respectively, electron–photon, neutron–gamma and hadronic codes. The following issues were addressed:

- Theory and methods;
- Physics and modelling issues;
- Algorithm developments;
- Computational science;
- Basic data;

- Analysis of experiments and measurements;
- Benchmarks;
- Status of general-purpose codes;
- Tools (graphics and analysis);
- Applications.

Speakers invited to the plenary sessions addressed topics such as:

- Past, present and future of Monte Carlo for radiation physics and particle transport simulation;
- Open problems, “hot” topics, needs and requirements, overview of developments and “state-of-the-art” on selected topics;
- Prospects for Monte Carlo simulations in the 21st century.

The organization of MC2000 would not have been possible without the support at all levels of:

- Several Portuguese institutions led by ITN (Nuclear and Technological Institute, Lisbon), LIP (“Laboratório de Instrumentação e Partículas”, Lisbon), “Centro de Instrumentação da Universidade de Coimbra” and other institutions also contributed significantly to the organization.
- International organizations and foreign institutions, namely the OECD Nuclear Energy Agency, the Radiation Safety Information Computational Center (RSICC, Oak Ridge, Tennessee, USA), the International Atomic Energy Agency (IAEA), the American Nuclear Society, and the Atomic Energy Society of Japan.

Organizing the conference took many thousands of man-hours of work, performed at several levels. I would like to acknowledge:

- the coordination role of the General Chairman, Masayuki Nakagawa (JAERI);
- the three co-chairs of the Scientific Committee, respectively Alex Bielaiew (U. Michigan), Gregg McKinney (LANL) and Richard Prael (LANL), for their outstanding work in shaping and setting up the scientific programme of the conference and coordinating the programme of the sessions;
- the members of the International Advisory and Scientific Programme Committees for their contributions, comments, suggestions, paper-reviewing work, etc.;
- the session co-chairs for their skills in conducting the busy sessions;
- the participants to the conference and the authors of the submitted papers for their interest and their contributions which made MC2000 a high-level scientific event.

Last, but not least, I will explicitly mention the members of the Local Organizing Committee, namely Fernando Barão, Andreas Kling, Maria Fernanda da Silva and Luis Távora for the organizational work, whose quality was noted by the participants. A special thanks is due to Ms. Filomena Baptista and Ms. Luisa Oliveira from the Local Secretariat for their remarkable work.

During the closing session of the conference, a discussion took place during which participants tried to assess the needs and pertinence of future Monte Carlo conferences. Although the majority of the participants felt that a further conference should definitely be organized, no consensus could be established on its date and place. In this respect, and reporting on developments which occurred after the conference, we are glad to inform you that Bernadette Kirk (RIAS, ORNL) has stated her intention to organize such a conference during 2005.

About this proceedings: it includes over 200 papers, processed by the five editors. A special acknowledgement is due to Andreas Kling, Editor-in-Chief, for his gigantic and skilful work compiling, handling and solving the difficult L^AT_EX-related problems.

Lisbon, February 2001

Pedro Vaz,
MC2000 Technical Program Coordinator

General Chairman:

M. Nakagawa (JAERI, Japan)

Co-chairs:

A. Bielajew (U. Michigan, USA)

G. McKinney (LANL, USA)

R. Prael (LANL, USA)

P. Vaz (IST, Portugal and
OECD/NEA)

– Technical Program Coordinator

Organizing Committee:

C. Abreu (U. Algarve, Portugal)

F. Barão (IST and LIP, Portugal)

A. Kling (ITN and CFNUL, Portugal)

M.F. da Silva (ITN and CFNUL,
Portugal)

L. Távora (U. Coimbra, Portugal)

P. Vaz (IST, Portugal and OECD/NEA)

Conference Secretariat:

L. Oliveira (ITN, Portugal)

F. Baptista (ITN)

N. Antunes (LIP, Portugal)

International Advisory Committee:

U. Amaldi (CERN and TERA, Italy)

P. Andreo (IAEA)

A. Bielajew (U. Michigan, USA)

T. Gabriel (ORNL, USA)

J. Hubbell (NIST, USA)

B. Kirk (RSICC, USA)

I. Lux (HAEA, Hungary)

G. McKinney (LANL, USA)

A. Nahum (ICR, UK)

M. Nakagawa (JAERI, Japan)

T. Nakamura (Tohoku Univ., Japan)

L. Pape (CERN)

D. Rogers (NRCC, Canada)

E. Sartori (OECD/NEA)

S. Seltzer (NIST, USA)

N. Smith (AEAT, UK)

J. Soares (ITN and CFNUL, Portugal)

K. Ueki (NTD, Japan)

P. Vaz (IST, Portugal and OECD/NEA)

L. Waters (LANL, USA)

S. Zaritsky (Kurchatov Inst., Russia)

Scientific Program Committee:

C. Abreu (U. Algarve, Portugal)	V. Korobeinikov (IPPE, Russia)
F. Barão (IST and LIP, Portugal)	M.C. Lopes (CROC, Portugal)
J. Barthe (CEA, France)	C. Ma (Stanford Univ., USA)
F. Brown (LANL, USA)	A. Maio (FCUL, Portugal)
T. Booth (LANL, USA)	L. Maiorov (Kurchatov Inst., Russia)
K. Burn (ENEA, Italy)	N. Mokhov (FNAL, USA)
B. Cabral (FCUL, Portugal)	T. Mori (JAERI, Japan)
J.L. Chartier (CEA, France)	A. Nahum (ICR, UK)
C. Conde (U. Coimbra, Portugal)	Y. Namito (KEK, Japan)
N. Cramer (ORNL, USA)	L. Petrie (ORNL, USA)
D. Cullen (LLNL, USA)	B. Petrovic (Westinghouse, USA)
M.B. Emmett (ORNL, USA)	M. Pimenta (IST, Portugal)
A. Fassò (SLAC, USA)	M. Ricard (IGR, France)
A. Ferrari (CERN)	F. Salvat (U. Barcelona, Spain)
D. Filges (FZJ, Germany)	F. Sánchez-Doblado (U. Sevilla, Spain)
B. Grosswendt (PTB, Germany)	B. Siebert (PTB, Germany)
G. Guldrini (ENEA, Italy)	M. Silari (CERN)
A. Haghighat (PSU, USA)	M.F. da Silva (ITN and CFNUL, Portugal)
C. Hartmann-Siantar (LLNL, USA)	L. Távora (U. Coimbra, Portugal)
H. Hirayama (KEK, Japan)	J.N. Urbano (U. Coimbra, Portugal)
G. Hughes (LANL, USA)	G. Valdez (SNL, USA)
A. Kling (ITN and CFNUL, Portugal)	
R. Konsek (SNL, USA)	

Supporting Organizations:

ITN – Instituto Tecnológico e Nuclear
LIP – Laboratório de Instrumentação e Física de Partículas
IST – Instituto Superior Técnico (Physics Department)
Cinst-UC – Centro de Instrumentação, Universidade de Coimbra
CFNUL – Centro de Física Nuclear da Universidade de Lisboa
FCUL – Faculdade de Ciências da Universidade de Lisboa (Physics Department)
UALG – Universidade do Algarve (Physics Department)
SPF – Sociedade Portuguesa de Física
CROC – Centro Regional de Oncologia de Coimbra do IPOFG
FCT – Fundação para a Ciência e Tecnologia
FCG – Fundação Calouste Gulbenkian
FLAD – Fundação Luso-Americana para Desenvolvimento
CGD – Caixa Geral de Depósitos
CML – Camara Municipal de Lisboa
EDP – Museu da EDP/ Central Tejo
OECD/NEA – OECD Nuclear Energy Agency
IAEA – International Atomic Energy Agency
RSICC – Radiation Safety Information Computational Center (USA)
AESJ – Atomic Energy Society of Japan
ANS – American Nuclear Society

Contents

Plenary Talks

Some Random Thoughts on Monte Carlo Electron and Photon Transport <i>A.F. Bielajew</i>	1
Remarkable Moments in the History of Neutron Transport Monte Carlo Methods <i>I. Lux</i>	7
Hadronic Monte Carlo Transport: A <i>Very</i> Personal View <i>R.E. Prael</i>	17
Highlights of Hadronic Sessions, Speculations and Perspective Views <i>D. Filges, W. Gudowski</i>	21

Session Electron–Gamma I: Electron Interaction Physics / Electron Transport Mechanics

Analog Electron Physics. Interaction Cross-Sections <i>F. Salvat, J.M. Fernández-Varea, S. Seguí</i>	27
Modelling the Generalized Oscillator Strength for Low-Energy Electron or Positron Inelastic Scattering <i>D. Liljequist, J.M. Fernández-Varea, F. Salvat</i>	33
Low-Energy Electron Scattering in Solids – a Monte Carlo Approach <i>H.-J. Fitting, J.-Ch. Kuhr</i>	39
Monte Carlo Simulation of Few-keV Positrons Penetrating in Solids <i>M. Dapor, A. Miotello</i>	43
A “Transport” Condensed History Method <i>E.W. Larsen, D.R. Tolar, Jr.</i>	49

**Session Electron–Gamma II: Photon Interaction
Physics / Applications I**

A Half Century of Monte Carlo, from Slide Rule and Mechanical Desk Calculator to the Laptop Supercomputer <i>J.H. Hubbell, S.M. Seltzer</i>	55
Comparison of EGS4 and Measurements Regarding K-X ray and Bremsstrahlung Photons <i>Y. Namito, H. Hirayama</i>	63
EGS4 Modelling of Coherent Scattering in the Biological Context <i>A. Taïbi, A. Tartari, M. Gambaccini</i>	69
Implementation of the Anomalous Dispersion of Rayleigh Scattered Photons in EGS4 Code <i>C. Baraldi, E. Casnati, G. Di Domenico, A. Tartari</i>	75
Backscattering from Gold Irradiated with 15–40 keV Photons <i>N. Nariyama</i>	81
Monte Carlo Polarimetric Efficiency Simulations for a Single Monolithic CdTe Thick Matrix <i>R.M. Curado da Silva, M. Hage-Ali, E. Caroli, P. Siffert, J.B. Stephen</i>	87
Simulations for X-Ray Synchrotron Beams Using the EGS4 Code System in Medical Applications <i>I. Orion, F.A. Dilmanian, Z. Zhong, A.B. Rosenfeld, A. Henn, I. Sagi, L. Peña</i>	93
<hr/> Session Electron–Gamma III: Applications II <hr/>	
Applications of Monte Carlo Code to a Study of Gamma-Ray Buildup Factors, Skyshine and Duct Streaming <i>H. Hirayama</i>	99
Simulation of X-ray Spectra Generated by Kilovolt-Electron Bombardment <i>J.M. Fernández-Varea, X. Llovet, E. Acosta, E. Benedito, F. Salvat</i>	105
Particle Transport in Inhomogeneous Media <i>J. Tickner</i>	111
Fast Simulation of X-ray Transition Radiation in the GEANT4 Toolkit <i>V.M. Grichine</i>	117

Optimization of a Tunable Quasi-Monochromatic X-ray Source for Cell Irradiations <i>W. Neubert, W. Enghardt, U. Lehnert, E. Müller, B. Naumann, A. Panteleeva, J. Pawelke</i>	123
<hr/>	
Session Electron–Gamma IV: Status of General Purpose Codes	
<hr/>	
Electron Photon Shower Simulation in TRIPOLI-4 Monte Carlo Code <i>Y. Peneliau</i>	129
The EGSnrc System, a Status Report <i>I. Kawrakow, D.W.O. Rogers</i>	135
Status of MARS Electromagnetic Physics <i>O.E. Krivosheev, N.V. Mokhov</i>	141
Status of PENELOPE <i>J. Sempau, J.M. Fernández-Varea, F. Salvat, E. Benedito, M. Dingfelder, H. Oulad ben Tahar, X. Llovet, E. Acosta, A. Sánchez-Reyes, J. Asenjo</i>	147
Geant4 Electromagnetic Physics <i>S. Chauvie, V. Grichine, P. Gumplinger, V. Ivanchenko, R. Kokoulin, S. Magni, M. Maire, P. Nieminen, M.G. Pia, A. Rybin, L. Urban (on behalf of the Geant4 Collaboration)</i>	153
Electron–Photon Transport in FLUKA: Status <i>A. Fassò, A. Ferrari, P.R. Sala</i>	159
<hr/>	
Session Electron–Gamma V: Generation of Random Numbers, Variance Reduction	
<hr/>	
Random, Quasirandom and Hybrid Methods for Transport Problems <i>J. Spanier</i>	165
On the Use of Antithetic Variates <i>M.S. Milgram</i>	175
Adjoint Monte Carlo Simulation of Fixed-Energy Secondary Radiation <i>N.M. Borisov, M.P. Panin</i>	181
Symmetry-Based Variance Reduction Applied to ^{60}Co Teletherapy Unit Monte Carlo Simulations <i>D. Sheikh-Bagheri</i>	187

Importance Biasing Quality Criterion Based on Contribution Response Theory	
<i>N.M. Borisov, M.P. Panin</i>	193
Calculations of Electron Deep Penetration Using the Method of Trajectory Rotation	
<i>V. Moskvín, L. Papiež, T. Tabata, I.J. Das</i>	199
<hr/>	
Session Electron–Gamma VI: Application in Medical Physics, Dose Calculation	
<hr/>	
The Impact of Monte Carlo Dose Calculations on Intensity-Modulated Radiation Therapy	
<i>J.V. Siebers, P.J. Keall, R. Mohan</i>	205
PC-Based Process Distribution to Solve Iterative Monte Carlo Simulations in Physical Dosimetry	
<i>A. Leal, F. Sánchez-Doblado, M. Perucha, M. Rincón, R. Arrans, C. Bernal, E. Carrasco</i>	211
Inverse Treatment Planning for Radiation Therapy Based on Fast Monte Carlo Dose Calculation	
<i>M. Fippel, M. Alber, M. Birkner, W. Laub, F. Nüsslin, I. Kawrakow</i> ...	217
Macro Monte Carlo: Clinical Implementation in a Distributed Computing Environment	
<i>H. Neuenschwander, W. Volken, D. Frei, C. Cris, E. Born, R. Mini</i> ...	223
VMC⁺⁺, Electron and Photon Monte Carlo Calculations Optimized for Radiation Treatment Planning	
<i>I. Kawrakow</i>	229
<hr/>	
Session Electron–Gamma VII: Microdosimetry, Track Structure, Radiobiological Modeling	
<hr/>	
The Track Structure of Photons, Electrons and α-Particles from the Point of View of the Formation of Ionization Clusters	
<i>B. Grosswendt</i>	237
Track Structure in Molecular Radiation Biology	
<i>H. Nikjoo, S. Uehara, I.K. Khvostunov, F.A. Cucinotta</i>	251
Analogue Monte Carlo to Model Radiation-Induced DNA Damage	
<i>M. Terrissol, J.M. Vrigneaud</i>	261

Basic Data for Track Structure Simulations: Electron Interaction Cross-Sections in Liquid Water	
<i>M. Dingfelder, W. Friedland</i>	267
Inelastic Cross-Sections for Use in Monte Carlo Track Structure Codes	
<i>D. Emfietzoglou</i>	273
Modelling Ultrasoft X-ray Effects on DNA	
<i>M. Terrissol, J.M. Vrigneaud</i>	279
Radiobiological Modeling in Voxel Constructs	
<i>R.D. Stewart, R.J. Traub</i>	285
<hr/>	
Session Electron–Gamma VIII: Monte Carlo in Radiotherapy Dosimetry, Monte Carlo Simulation of Medical Accelerators	
<hr/>	
Monte Carlo Techniques for Primary Standards of Ionizing Radiation and for Dosimetry Protocols	
<i>D.W.O. Rogers</i>	291
Absorbed Dose Conversion Factors for Megavoltage Photon Beams	
<i>R. Nutbrown, S. Duane, D. Shipley, R. Thomas</i>	299
Is the Spencer–Attix Cavity Equation Applicable for Solid-State Detectors Irradiated in Megavoltage Electron Beams?	
<i>P.N. Mobit, G.A. Sandison</i>	305
Monte Carlo Simulation of Electron Beams for Radiotherapy – EGS4, MCNP4b and GEANT3 Intercomparison	
<i>A. Trindade, P. Rodrigues, C. Alves, A. Chaves, M.C. Lopes, C. Oliveira, L. Peralta</i>	311
Evaluation of a 50-MV Photon Therapy Beam from a Racetrack Microtron Using MCNP4B Monte Carlo Code	
<i>I. Gudowska, B. Sorcini, R. Svensson</i>	317
Energy Spectra and Dose Distributions of a Medical Linear Electron Accelerator Simulated with BEAM/EGS4 and MCNP	
<i>D. Albers, F. Cremers, I. Eggers, M. Todorovic, R. Schmidt</i>	323
Monte Carlo Simulation of an Arc Therapy Treatment by Means of a PC Distribution Model	
<i>A. Leal, F. Sánchez-Doblado, M. Perucha, M. Rincón, R. Arráns, C. Bernal, E. Carrasco</i>	329

Session Electron–Gamma IX: Applications III

Analysis of the Influence of the Radial Displacement of the Source in the Simulation of Ge-Detector Calibration Using MCNP Code	
<i>J. Ródenas, A. Martinavarro, V. Rius</i>	333
Monte Carlo Simulations of Photon Field Characteristics for In Situ Gamma Spectrometry Applications	
<i>J. Kluson</i>	339
Visual Monte Carlo and Its Application to Internal and External Dosimetry	
<i>J.G. Hunt, F.C. da Silva, D. de Souza-Santos, I. Malatova, S. Foltanova, B.M. Dantas, A. Azeredo, M. Isakson</i>	345
Monte Carlo Simulation of Mammography X-ray Units: a Comparison Between Different Electron Extensions of the EGS4 Code System	
<i>M. Marziani, M. Gambaccini, L.M.N. Távora, A. Taibi</i>	351

Session Electron–Gamma X: Applications IV

The Use of MCNP in Flash Radiographic Applications at AWE	
<i>S. Quillin, I. Crotch, S. McAlpin, J. O'Malley</i>	357
Comparison of Monte Carlo Simulation and Measurement of Electron Reflection from Solids	
<i>V. Starý</i>	369
Low-Energy Electron Response of CsI(Tl) and BGO	
<i>A. Martínez-Dávalos, J.M. López-Robles</i>	377
Monte Carlo Estimate to Improve Photon Energy Spectrum Reconstruction	
<i>S. Sawchuk</i>	383
Monte Carlo Simulations on Rough and Porous Alumina	
<i>L. Sorbier, E. Rosenberg, C. Merlet</i>	389
Simulation of the Response Function of an Amorphous Silicon Flat-Panel Array	
<i>F. Cremers, C. Kausch, D. Albers, M. Todorovic, R. Schmidt</i>	395
Space Applications of the Geant4 Simulation Toolkit	
<i>E. Daly, H. Evans, F. Lei, F. Longo, S. Magni, R. Nartallo, P. Nieminen, M.G. Pia, P.R. Truscott</i>	401

Session Electron–Gamma P: Miscellaneous Topics

**Introduction of the Muonic and Cerenkov Effects
in the EGS4 Code**
E. Duverger, A. Mishev, R.I. Gschwind, L. Makovicka, J. Stamenov 407

**Spectrum Shape Analysis Applied to Radioactive Waste
Gamma-Ray Spectroscopy**
B. Perot, J.-L. Artaud, B. Chaballier, J. Misraki, P. Chany 413

**Assessment of a Compton Suppression Spectrometer
for the Measurement of Medium- and High-Level
Radioactive Waste Packages**
J.-L. Artaud, B. Perot, B. Chaballier, H. Toubon 419

**The Degradation of the Energy of Primary Photons Described
through the Entropy**
A.D. Oliveira, J.J. Pedroso de Lima 425

**Monte Carlo Simulation of the Conversion Electron Scattering
in Targets for the Synthesis of Superheavy Elements**
A. Špalek, O. Dragoun 431

Monte Carlo Simulations on a 9-node PC Cluster
J. Gouriou 437

**Application of Numerical Phantoms and MCNP Calculation
for In Vivo Calibration**
D. Franck, N.M. Borisov, L. Laval 443

**Use of Monte Carlo Method
in Support of Medical Applications of Radiation**
N. Cerullo, G. Curzio, G. Daquino, A. Mariani 449

**Intra-Operative Radiation Therapy Optimization
Using the Monte Carlo Method**
M. Rosetti, M. Benassi, V. Bruzzaniti, A. Bufacchi, M. D'Andrea 455

**Coupling Photon Monte Carlo Simulation and CAD Software.
Application to X-ray Nondestructive Evaluation**
J. Tabary, A. Glière 461

**Dose Rate Calculations from Radioactive Vascular Stents:
DPK Versus Exact MC Approach**
S. Gorodkov, A. Möslang, P. Vladimirov 467

Dosimetric Study of a Low-Dose-Rate Brachytherapy Source
M. Rodríguez-Villafuerte, S. Arzamendi, R. Díaz-Perches 473

Electron Transport Simulation in the Range 1 keV–4 MeV for the Purpose of High-Resolution Dosimetric Application <i>V. Cobut, L. Cirioni, J.P. Patau</i>	479
Shield Optimization for X-rays Using the Monte Carlo Method Combined with Analytical Calculation <i>Zhang Dian-hui, Huang Liu-xing, Niu Sheng-li</i>	483
MCNP Analytical Models of a Calibration Head Phantom for Bone-Seeker Nuclides In Vivo Measurements <i>G. Gualdrini, P. Ferrari, P. Battisti, P. De Felice, L. Pierotti</i>	489
Monte Carlo Studies of the Portuguese Gamma Irradiation Facility. The Irradiator Geometry and Its Influence on Process Parameters <i>C. Oliveira, L. Ferreira, J. Salgado</i>	497
Multiple Scattering in GEANT4. A Comparison with Molière Theory and L3 Detector Data <i>P. Arce, M. Maire, L. Urbán, M. Wadhwa</i>	503
On the Use of CAD Geometry for Monte Carlo Particle Transport <i>H. Tsige-Tamirat</i>	511
Analysis of the Simulation of Ge-Detector Calibration for Environmental Radioactive Samples in a Marinelli Beaker Source Using the Monte Carlo Method <i>J. Ródenas, J. Ortiz, L. Ballesteros, V. Serradell</i>	517
Simulation of a ^{32}P Sourcewire and a $^{90}\text{Sr}/^{90}\text{Y}$ Sourcetrain Using MCNP4b and EGS4 <i>M. Todorovic, F. Cremers, D. Albers, R. Schmidt</i>	523
Monte Carlo Simulations for the Estimation of Dose Rates During Handling of Spent Fuel at the Portuguese Research Reactor <i>A. Kling, J.G. Marques, A.J.G. Ramalho</i>	529
Photoelectron Collection Efficiency in Rare Gases: A Monte Carlo Study <i>P.J.B.M. Rachinhas, J.A.M. Lopes, T.H.V.T. Dias, F.P. Santos, C.A.N. Conde, A.D. Stauffer</i>	535
Medical Applications of the Geant4 Toolkit <i>S. Agostinelli, S. Chauvie, F. Foppiano, S. Garelli, F. Marchetto, M.G. Pia, P. Nieminen, V. Rolando, A. Solano</i>	543

Effect of Voxel Size on Monte Carlo Dose Calculations for Radiotherapy Treatment Planning <i>G. Mora, T. Pawlicki, A. Maio, C.-M. Ma</i>	549
Monte Carlo Physical Dosimetry for Small Photon Beams <i>M. Perucha, F. Sánchez-Doblado, M. Rincón, A. Leal, L. Núñez, R. Arráns, E. Carrasco, J.A. Sánchez-Calzado, L. Errazquin</i>	555
Monte Carlo Dose Distributions for Radiosurgery <i>M. Perucha, F. Sánchez-Doblado, A. Leal, M. Rincón, L. Núñez, R. Arráns, E. Carrasco, B. Sánchez-Nieto, J.A. Sánchez-Calzado, L. Errazquin</i>	561
Monte Carlo Conformal Treatment Planning as an Independent Assessment <i>M. Rincón, F. Sánchez-Doblado, A. Leal, M. Perucha, R. Arráns, J.C. Medrano, E. Carrasco, J.A. Sánchez-Calzado, L. Errazquin</i>	565
Modelling of Multiple Scattering Distributions by Mixture Models <i>R. Frühwirth, M. Regler</i>	571
Radiative Transport in Multiple Scattering Media <i>E.J.N. Pereira, J.M.G. Martinho, M.N. Berberan-Santos</i>	577
Markov Chain Monte Carlo Methods in Radiotherapy Treatment Planning <i>R.P. Hugtenburg</i>	583
<hr/> Session Neutron–Gamma I: Theory and Methods <hr/>	
Research Themes of Broad Transport Applicability <i>J. Spanier</i>	589
Response Decomposition with Monte Carlo Correlated Coupling <i>T. Ueki, J.E. Hoogenboom, J.L. Kloosterman</i>	597
The Geometrical Sensitivity Option in MCBEND <i>T. Shuttleworth</i>	603
An Alternative Monte Carlo Method for the k-Eigenfunction? <i>T.E. Booth</i>	609
Continuous Energy Adjoint Monte Carlo for Coupled Neutron–Photon Transport <i>J.E. Hoogenboom</i>	613
Application of A³MCNPTM to Radiation Shielding Problems <i>A. Haghighat, J.C. Wagner</i>	619

Session Neutron–Gamma II: Code Status

Status of JAERI's Monte Carlo Code MVP for Neutron and Photon Transport Problems	
<i>T. Mori, K. Okumura, Y. Nagaya</i>	625
Current Status of the Oak Ridge Monte Carlo Codes: MORSE/SAS4 and KENO	
<i>M.B. Emmett, D.F. Hollenbach</i>	631
The Current Status and Future Plans for the Monte Carlo Codes MONK and MCBEND	
<i>N. Smith, T. Shuttleworth, M. Grimstone, L. Hutton, M. Armishaw, A. Bird, N. France, S. Connolly</i>	637
MCNP Capabilities at the Dawn of the 21st Century: Neutron–Gamma Applications	
<i>E.C. Selcow, G.W. McKinney, T.E. Booth, J.F. Briesmeister, L.J. Cox, R.A. Forster, J.S. Hendricks, R.D. Mosteller, R.E. Prael, A. Sood, S.W. White</i>	643
TRIPOLI-3: A Neutron/Photon Monte Carlo Transport Code	
<i>J.C. Nimal, T. Vergnaud</i>	651

Session Neutron–Gamma III: Physics and Data

Modern Nuclear Data for Monte Carlo Codes	
<i>R.C. Little, S.C. Frankle, M.C. White, R.E. MacFarlane, Ch.J. Werner, J.M. Campbell</i>	657
The MCNP Code in Planning and Interpretation of Thermal Neutron Pulsed Experiments	
<i>J. Dąbrowska, K. Drozdowicz, U. Woźnicka</i>	663
Modelling Detector Responses to Neutrons Using MCNP	
<i>J. Tickner</i>	669
Simulation of Thermal Neutron Transport Processes Directly from the Evaluated Nuclear Data Files	
<i>P.A. Androsenko, M.R. Malkov</i>	675
Influence of the Photoneutrons on the Kinetics of the Beryllium Reflected Core of the Budapest Research Reactor	
<i>G. Hordósy, A. Keresztúri, P. Vértes, Cs. Hegedűs</i>	681

Session Neutron–Gamma IV: Algorithms and Computational Science

Variance Reduction with Multiple Responses

K.W. Burn, G. Gualdrini, E. Nava 687

Use of a Hybrid Monte Carlo Technique for Power Shape Calculations

L. Hutton, N.R. Smith 697

Eigenvalue Uncertainty Evaluation in MC Calculations, Using Time Series Methodologies

O. Jacquet, R. Chajari, X. Bay, A. Nouri, L. Carraro 703

Development and Comparison of Monte Carlo Techniques Implemented in the MORET4 Code for the Calculation of Loosely Coupled Systems

J. Miss, O. Jacquet, A. Nouri 711

Session Neutron–Gamma V: Experiments and Measurements

Sensitivity Analysis and Uncertainty Assessment in Applied Monte Carlo Particle Transport

B.R.L. Siebert 719

Sensitivity and Uncertainty Analysis for Nuclear Criticality Safety Using KENO in the SCALE Code System

B.T. Rearden 725

Monte Carlo Characterisation of the Radiation Field in the Thermal Column of the Portuguese Research Reactor

A. Fernandes, A. Vieira, I.C. Gonçalves, A. Ramalho 731

Fission Rate Analysis of a Fast Reactor Fuel Performance Test Using MCNP

T. Sekine, T. Aoyama 737

Benchmarking Monte Carlo Codes for Criticality Safety Using Subcritical Measurements

T. Valentine 743

Session Neutron–Gamma VI: Applications

Review of Industrial and Medical Applications that Utilize Coupled Neutron–Photon Monte Carlo Transport

T. Goorley 749

MCNP Calculations for the Shielding Design of a Beam Tube to Be Installed at the Portuguese Research Reactor <i>I.F. Gonçalves, A.G. Ramalho, I.C. Gonçalves, J. Salgado</i>	755
Monte Carlo Applications in Fusion Neutronics <i>U. Fischer</i>	761
MCNP Simulation of Void Reactivity in a Simplified CANDU Core Sub-region <i>F. Rahnema, S. Mosher, M. Pitts, P. Akhtar, D. Serghiuta</i>	767
Monte Carlo Simulation of Natural Gamma Ray Spectrometry for Underwater Surfaces <i>M. Maučec, P.H.G.M. Hendriks, R.J. de Meijer</i>	773
Monte Carlo Modelling of the Belgian Materials Testing Reactor BR2: Present Status <i>B. Verboomen, A. Beeckmans de West-Meerbeeck, Th. Aoust, Ch. De Raedt</i>	779
<hr/> Session Neutron–Gamma VII: Benchmarks <hr/>	
Benchmark for a 3D Monte Carlo Boiling Water Reactor Fluence Computational Package – MF3D <i>S. Sitaraman, R.-T. Chiang, K. Asano, K. Koyabu</i>	785
Intercomparison of Monte Carlo and S_N Sensitivity Calculations for a 14 MeV Neutron Benchmark <i>U. Fischer, I. Kodeli, C. Konno, R.L. Perel</i>	791
Comparison of Snyder Head Phantom Models Used for Neutron Capture Therapy Benchmark Monte Carlo Dosimetry Calculations <i>T. Goorley, W.S. Kiger III, R. Zamenhof</i>	797
Monte Carlo Modeling of Fast Sub-critical Assembly with MOX Fuel for Research of Accelerator-Driven Systems <i>A. Polanski, V. Barashenkov, I. Puzynin, I. Rakhno, A. Sissakian</i>	803
Evaluation of CRISTO II Storage Arrays Benchmark with TRIPOLI-4.2 Criticality Calculations <i>Y.K. Lee</i>	809
<hr/> Session Neutron–Gamma VIII: Graphics and Analysis <hr/>	
Current State of Monte Carlo Visualization Tools <i>R. Schwarz, L. Carter</i>	815

Conceptual Designing of a Reduced Moderation Pressurized Water Reactor by Use of MVP and MVP-BURN <i>T. Kugo</i>	821
The Role of Graphical Supporting Tools for Monte Carlo Analysis <i>M. Armishaw, A. Bird, H. Crofts, N. Smith</i>	827
Simulating Variable Source Problems via Post Processing of Individual Particle Tallies <i>D.L. Bleuel, R.J. Donahue, B.A. Ludewigt, J. Vujic</i>	833
MCNP Modelling of HTGR Pebble-Type Fuel <i>Z. Karriem, C. Stoker, F. Reitsma</i>	841
<hr/> Session Neutron–Gamma P: Miscellaneous Topics <hr/>	
Universal Approach for ADS Blanket Calculations Using the Monte Carlo Method <i>V.V. Korobeinikov</i>	847
Monte Carlo Depletion Analysis of a PWR Integral Fuel Burnable Absorber by MCNAP <i>H.J. Shim, C.S. Jang, C.H. Kim</i>	851
Application of Biasing Optimization Techniques to Monte Carlo Shielding Analysis of a Transport Cask <i>S. Mitake, O. Sato, H. Tsunoda</i>	859
Improvement and Benchmarking of the New Shutdown Dose Estimation Method by Monte Carlo Code <i>L. Petrizzi, H. Iida, D. Valenza, P. Batistoni</i>	865
Monte Carlo Simulation of Neutron and Photon Transport with Direct Utilization of Information from Evaluated Nuclear Data Files <i>P.A. Androsenko, D.L. Joloudov, A.V. Kompaniyets</i>	871
Application of MCNP-Based Software Package MF3D for BWR Radiation Damage Computations <i>R-T. Chiang, S. Sitaraman, K. Asano, K. Koyabu</i>	877
Why Do We Need TARGET? <i>D. Schlegel, S. Guldbakke</i>	881
Noise Method for Monitoring the Subcriticality in Accelerator-Driven Systems <i>Y. Rugama, J.L. Muñoz-Cobo, T.E. Valentine</i>	887

Sediment-Density Dependency of Natural Gamma Ray Spectra in a Borehole Geometry <i>P.H.G.M. Hendriks, M. Maučec, R.J. de Meijer</i>	893
Some Experimental and Monte Carlo Investigations of the Plastic Scintillators for the Current Mode Measurements at Pulsed Neutron Sources <i>A. Rogov, Yu. Pepyolyshev, M. Carta, A. d'Angelo</i>	899
Feasibility Study of Non-Radioactive Tracers for Monitoring Injected Water in Oil Reservoirs <i>H. Sawamura, K. Nishimura, H. Mituishi, T. Muta, J.S. Schweitzer</i>	905
Neutronics and Shielding Analysis of an Ignitor <i>S. Rollet, M. Rapisarda</i>	911
Monte Carlo Calculations for Neutron and Gamma Radiation Fields on a Fast Neutron Irradiation Device <i>A. Vieira, A. Ramalho, I.C. Gonçalves, A. Fernandes, N. Barradas, J.G. Marques, J. Prata, Ch. Chaussy</i>	919
Shielding Assessment of the MYRRHA Accelerator-Driven System Using the MCNP Code <i>M. Coeck, Th. Aoust, F. Vermeersch, A. Abderrahim</i>	925
Numerical Tests for the Problem of U–Pu Fuel Burnup in Fuel Rod and Polycell Models Using the MCNP Code <i>V.G. Muratov, A.V. Lopatkin</i>	931
<hr/> Session Hadronic I: Hadron Code Review <hr/>	
The HERMES Monte Carlo Program System: a Versatile Tool for Spallation Physics and Detector Applications <i>D. Filges, R.-D. Neef, H. Schaal, G. Sterzenbach</i>	937
MARS Code Status <i>N.V. Mokhov, O.E. Krivosheev</i>	943
Present Status of Nucleon–Meson Transport Code NMTC/JAERI <i>H. Takada, S. Meigo, K. Niita</i>	949
FLUKA: Status and Prospects for Hadronic Applications <i>A. Fassò, A. Ferrari, P.R. Sala, J. Ranft</i>	955

Status of the MCNPX Transport Code

*H.G. Hughes, M.B. Chadwick, R.K. Corzine, H.W. Egdorf, F.X. Gallmeier,
R.C. Little, R.E. MacFarlane, S.G. Mashnik, E.J. Pitcher, R.E. Prael,
A.J. Sierk, E.C. Snow, L.S. Waters, M.C. White, P.G. Young* 961

**Session Hadronic II: Physics Model Calculations
and Data Compilation**

Physics Models and Nuclear Data Evaluations for Enhanced Monte Carlo Transport

M.B. Chadwick, H.G. Hughes, R.C. Little, E.J. Pitcher, P.G. Young . . . 967

Development of Heavy Ion Transport Monte Carlo Code

H. Iwase, T. Kurosawa, T. Nakamura, N. Yoshizawa, J. Funabiki 973

**Baryon Stopping in High-Energy Collisions
in the DPMJET-III Model**

J. Ranft, R. Engel, S. Roesler 979

Session Hadronic III: Applications I

Muons and Neutrinos at High-Energy Accelerators

N. Mokhov, S. Striganov, A. Van Ginneken 985

Utilization of Monte Carlo Calculations in Radiation Transport Analyses to Support the Design of the U.S. Spallation Neutron Source (SNS)

J.O. Johnson 991

**Deep Penetration Monte Carlo Calculations
for the European Spallation Source ESS**

I. Koprivnikar, E. Schachinger 997

**Validation of MC Models of Spallation Reactions
in Thin and Thick Targets in the GeV Range**

*F. Goldenbaum, M. Enke, D. Filges, J. Galin, C.-M. Herbach, D. Hilscher,
U. Jahnke, A. Letourneau, B. Lott, R.-D. Neef, K. Nünighoff, N. Paul,
A. Péghaire, L. Pienkowski, H. Schaal, U. Schröder, G. Sterzenbach,
A. Tietze, V. Tishchenko, J. Toke, M. Wohlmuther* 1003

**Design and Effects of the Proton Window
of the Spallation Neutron Source**

F.C. Difilippo 1009

Application of the EA-MC Code Package to the Design of Accelerator-Driven Systems	
<i>Y. Kadi</i>	1015

Session Hadronic IV: Physics Models for Monte Carlo Codes

Hadronic Collisions: Physics, Models and Event Generators	
<i>J. Ranft</i>	1021

Modelling Hadronic Interactions	
<i>J.P. Wellisch</i>	1027

The Monte Carlo Event Generator DPMJET-III	
<i>S. Roesler, R. Engel, J. Ranft</i>	1033

Object-Oriented Approach to Preequilibrium and Equilibrium Decays in Geant4	
<i>V. Lara</i>	1039

The GEM Code – the Generalized Evaporation Model and the Fission Model	
<i>S. Furihata</i>	1045

Session Hadronic V: Applications II

Application of Monte Carlo to Proton Beam Radiation Therapy	
<i>J.V. Siebers</i>	1051

Monte Carlo Analysis of Correlation of Displacement Damage Due to Neutrons, Protons, Electrons and Gamma Ray in Microelectronic Devices	
<i>Huang Liu Xing, Chen Shi Bin, Chen Yu Sheng</i>	1057

Monte Carlo Simulations of Neutral Gas and Fast Ion Dynamics in GDT Experiments	
<i>K. Noack</i>	1063

Treatment Planning for Carbon Ion Radiotherapy	
<i>M. Krämer, O. Jäkel, T. Haberer, G. Kraft, D. Schardt, D. Scholz, U. Weber</i>	1069

Neutron Shielding Calculations for a 230-MeV Proton Therapy Facility	
<i>U. Titt, W.D. Newhauser, X. Yan, D.T. Dexheimer</i>	1075

**Coupling MCNP-DSP and LAHET Monte Carlo Codes
for Designing Subcriticality Monitors for Accelerator-Driven
Systems**

T. Valentine, Y. Rugama, J.L. Muñoz-Cobo, R. Perez 1081

Session Hadronic VI: Experiments and Benchmarks

**Shielding Benchmark Experiments Through Concrete and Iron
with High-Energy Proton and Heavy Ion Accelerators**

*T. Nakamura, M. Sasaki, T. Nunomiya, N. Nakao, E. Kim, T. Kurosawa,
S. Taniguchi, H. Iwase, Y. Uwamino, T. Shibata, S. Ito, A. Fukumura,
D.R. Perry, P. Wright* 1085

**New Method and Data on Residue Production in Spallation
by ^{208}Pb on Protons for the Design of Spallation Sources**

*T. Enqvist, W. Wlazło, J. Benlliure, F. Rejmund, P. Armbruster,
M. Bernas, A. Boudard, S. Czajkowski, R. Legrain, S. Leray, B. Mustapha,
M. Pravikoff, K.-H. Schmidt, C. Stéphan, J. Taieb, L. Tassan-Got,
C. Volant* 1097

Determination of Stopping Power of Ions in Matter

N.P. Barradas, C. Jeynes, R.P. Webb, E. Wendler 1105

**Comparison of Spallation Neutron and Residual Nuclide
Production Data with Different Intra-Nuclear Cascade Models**

S. Leray, A. Boudard, J. Cugnon, R. Legrain, C. Volant 1111

Session Hadronic VII: Monte Carlo Methods and Theory

Design of Tracking and Generic Processes in Geant4

*M. Asai, K. Amako, J. Apostolakis, H. Kurasige, T. Sasaki,
J.-P. Wellisch* 1117

**Multigroup Boltzmann–Fokker–Planck Approach
for Ion Transport in Amorphous Media**

N.D. Keen, A.K. Prinja, G.D. Dunham 1123

**A Stochastic Model of Multiple Scattering of Charged Particles:
Process, Transport Equation and Solutions**

L. Papież, V. Tulovsky, V. Moskvina 1129

Session Hadronic P: Miscellaneous Topics

PICA3, an Updated Code of Photo-nuclear Cascade Evaporation Code PICA95, and Its Benchmark Experiments <i>T. Sato, K. Shin, S. Ban, T.A. Gabriel, C.Y. Fu, H.S. Lee</i>	1139
Monte Carlo Simulation as an Aid to Alpha-Particle Spectrometry <i>A. Martín Sánchez, A. Fernández Timón, C.J. Bland</i>	1145
Measurements and Calculations of Secondary Particle Yields from 100–800 MeV/Nucleon Heavy Ions <i>T. Kurosawa, T. Nakamura, H. Iwase, H. Sato, N. Nakao, Y. Uwamino, A. Fukumura</i>	1151
Development of an Extended Range Bonner Sphere Spectrometer <i>C. Birattari, P. Cappellaro, A. Mitaroff, M. Silari</i>	1157
Influence of the FLUKA Geometrical Model on the ADS Demonstration Facility Criticality Calculations <i>P. Neuhold</i>	1163
Simulation of Nucleus–Nucleus Interactions in the Framework of the FRITIOF Model <i>A. Polanski, A.S. Galoyan, V.V. Uzhinskii</i>	1169
Monte Carlo Simulation of the Neutron Time-of-Flight Facility at CERN <i>V. Vlachoudis, C. Borcea, S. Buono, P. Cennini, A. Ferrari, Y. Kadi, V. Lacoste, E. Radermacher</i>	1175
Systematic Uncertainties on the Determination of the top Mass at the LHC from Soft Fragmentation Effects <i>M. David, A. Maio, A. de Angelis, A. Gomes</i>	1181
Author Index	1187

Some Random Thoughts on Monte Carlo Electron and Photon Transport

A.F. Bielajew

Department of Nuclear Engineering and Radiological Sciences, The University of
Michigan, 2355 Bonisteel Boulevard, Ann Arbor, MI 48109-2104, U. S. A.

Cherished colleagues, Ladies and Gentlemen, General Chairman Dr. Nakagawa,
General Secretary Dr. Vaz, fellow Co-Chairmen, Drs. McKinney and Prael:

A Tribute to Two Gentlemen

I would like to preface my presentation with some very personal remarks, a tribute to two gentlemen. Both of them have exerted enormous impact on our field. Either of them ought to be giving this plenary session lecture. They were both enthusiastically invited, but neither could be here due to health reasons. I am sure that you would all join me in wishing them well.

Martin J. Berger

Martin is the acknowledged grandfather of our subfield, Monte Carlo electron and photon transport. Indeed, it was his founding publication [1], *Monte Carlo calculation of the penetration and diffusion of fast charged particles* that laid the groundwork for our speciality. Indeed, as a neophyte to this field, I devoured that paper and the references therein. If it is possible to love someone from reading his publication, then I did so with Martin. This founding paper, almost 40 years after its publication, is still referred to frequently, and many of the ideas within it are still being pursued. After I finished working through this paper my future research path became clarified. My few meagre accomplishments in the Monte Carlo realm were simply follow-ups and clarifications on Martin's early work. Martin's pioneering effort is known as the Condensed History Method. This method made practical the Monte Carlo simulation of electron tracks, which involve up to about a million or so discrete interactions, by condensing the interactions into a manageable number of virtual events. Without Martin's brilliant innovation, the myriad of applications we will learn about this week would not have been possible.

Martin along with Steve Seltzer distributed a coded realization of many of Martin's ideas in a Monte Carlo code called ETRAN [2]. ETRAN's electron transport physics still underpins the widely-used ITS and MCNP Monte Carlo codes, two of the workhorses of the Monte Carlo industry.

Martin also served for 12 years as Chief of the Radiation Theory Section of the National Bureau of Standards, now known as the National Institute for Standards and Technology. The list of names of the scientists involved in that

group reads like a *Who's who* of the radiation sciences, Fano, Hubbell, Seltzer and Spencer, to name a few. I also learned that Martin had a strong disdain for administrative paperwork, refusing to process it until an administrator presented himself or herself in his office and threw a tantrum. Around my lab, we frequently “Bergerize” paperwork so as not to distract ourselves from our research!

At the date of his official retirement in 1991, Martin had 115 publications to his credit. However, retirement has not slowed his productivity. A colleague who had the privilege of serving with him in a committee reported to me that Martin still works with the “energy of a teenager”. Regrettably, Martin does not travel as much as we all would like.

Walter R. (Ralph) Nelson

Ralph Nelson once confided in me that had he known of Martin’s work, that he probably would not have gone on to produce the Electron Gamma Shower (EGS) code [3,4]. However, we are fortunate that the EGS code was written, as the intercomparisons between EGS, ITS and MCNP have led to a very robust system of codes, constantly cross checked among each other and with experimental data. The EGS code has been cited in about 1200 publications, a citation frequency that is only bested by papers that lead their authors to a coveted trip to Stockholm, if those papers concern a fundamental physics question. Although Ralph is best known for as the guiding force behind EGS, he is also widely known in Health Physics circles as the first to characterize the production of radioactivity in soil and groundwater generated by a high-energy accelerator. His pioneering studies of wide-angle muons has also earned him membership in the elite “missed the charmed quark” club (so named by James Bjorken) whose experiments showed signals of the existence of the charmed quark before its identification in the definitive experiments by Sam Ting of MIT and Burt Richter of SLAC. Ralph’s service to the community has been outstanding, authoring one book on Radiation Dosimetry [5] as well as editing two books that have become standard references in our field [6,7]. These latter two books are associated with workshops that Ralph organized at the Ettore Majorana Center in Erice, Sicily.

What Is Monte Carlo?

The Monte Carlo method, in its modern genesis, was pioneered by Stan Ulam and John(ny) von Neumann for the post WWII development of thermonuclear weapons. The Monte Carlo method has enjoyed more than 50 years of development with the neutron-gamma transport methods having achieved a reasonable state of maturity. Despite its development as a weapons design tool, it is a wonderful (and happy) irony that the results of the Monte Carlo method have never been employed in conflict. Rather, scientists have exploited Monte Carlo methods for positive public benefit in health and related sectors. For example, modern radiotherapy dose-planning are all dependent to some degree on Monte Carlo calculations.

The Monte Carlo method is a numerical solution to a problem that models objects interacting with other objects or their environment based upon the most essential and simple object-object or object-environment relationships. Hence, the Monte Carlo method is intuitively very simple. The solution is determined by random sampling of these relationships and iterating until the result converges. Hence, the method tends to exploit modern computers to maximum advantage and readily absorbs all the computer power that one may have at one's disposal. There are many applications of the Monte Carlo method and one can find examples in the entertainment industry, social science, traffic flow, population growth, game/decision theory, mathematics, finance, genetics, radiation sciences, radiation measurement, radiotherapy, radiation dosimetry ...

The algorithms in the Monte Carlo method are simple. Consequently, the debugging effort is minimized compared to other methods. The algorithms must include:

- cross section preparation—tables of interactions and relationships
- ray tracing through geometries
- sampling from probability distributions
- tallying, scoring, accumulation of results
- interface to human interpretation

The Monte Carlo method is in principle as accurate as the uncertainties in the cross sections, so long as the ray tracing, sampling and accumulations are faithful. The method is *microscopic*: Geometries, boundaries and sources do not alter the fundamental structure of the algorithms. As one builds an application from simpler realizations, the increase in difficulty in obtaining a solution increases less than linearly with the complexity of the application. Often the Monte Carlo method is the fastest and most efficient realization of a macroscopic result from a microscopic model.

How Does One Do Monte Carlo?

- Clearly identify the problem. This is a lot harder than one might think!
- Employ a graduate student, someone good with computers, mathematics, logic and physics, willing to work for 5–7 years for next to nothing!
- Purchase a modest amount of computing power—a personal computer will do for a start.
- Read all the online documentation and other free material.
- Send the student to Monte Carlo courses.
- Expect meaningful results starting in about 2 years.
- Gear up for production by purchasing only as much computing power as you need.
- Expect 3–4 publications and a thesis after 1 *mlogs* (*mlogs* \equiv mean life of a graduate student)

Why Is Monte Carlo so Appealing?

Monte Carlo:

- Is powerful, general, versatile
- Is hi-tech, computerphilic, nerdy, geek-friendly, youth-oriented
- Is exact, to within one's knowledge of the cross sections and faithfulness of the transport routines
- Is intuitive
- Is fun (very visual)
- Requires a lot of time—computer time and personal time
- Is an increasingly indispensable intermediary between ideas (theory) and applications (experiments). It is a laboratory for the theorist and a theory for the experimentalist.
- Is one easily identifiable area where a graduate student can quickly achieve technical superiority to his or her professor!

Where Have We Been?

Within the narrow focus of $e^{\pm}\gamma$ Monte Carlo:

In the past we have been concerned with:

- The reliability of electron transport methods. *These are now reaching a high degree of refinement and robustness.*
- The accuracy of cross sections. *There is still work to be done for $E < Z[\text{keV}]$.*
- Computer speed and throughput. *Fortunately, Moore's law will still hold true for the near future.*
- Random numbers. *Pseudo-random number generation appears to be in good shape but quasi-random numbers have not been fully exploited in radiation transport problems.*

A testament to the reliability and utility of current-day transport methods is that very few papers in this conference are devoted to methods development.

Where Are We now?

We are now in a golden age of applications! Current use will continue to exploit known transport methods with more and more creativity on a broader range of applications.

Where Are We Going?

Before answering this questions, let's make the observations that:

- The 19th Century was the century of Chemistry.

- The 20th Century was the century of Physics.
- The 21st Century will be the century of Biology.

How do the physicists, the computational scientists, the Monte Carloists among us, adapt to this reality? In Biology, adaptation is the key to survival. Here is a naive and very personal suggestion.

Recall the definition: *The Monte Carlo method is a numerical solution to a problem that models objects interacting with other objects or their environment based upon the most essential and simple object-object or object-environment relationships.* Why not model biological systems in microscopic detail?

$e^\pm\gamma$ Monte Carlo has benefited from excellent knowledge of the laws of nature derived from Quantum Electrodynamics, arguably the most successful physical theory. The situation is a lot less rosy in Biology and so we may have to be creative.

A Draft Research Agenda for the Near and Far Future

- We still need to do some basic physics. *We need cross section data in biological materials down to 10 eV or so.*
- We need bigger, faster computers. *There are 10^{13} – 10^{15} atoms in a cell. There are 10^{13} – 10^{15} cells in the human body. A first principles approach to modelling an entire cell is not yet in reach. However, it will be in the next decade or two.*
- We need to communicate the exquisitely accurate particle fluences, ionization and excitation densities to molecular transport codes.
- We need to do LOTS of experiments.
- We have to understand how cells respond to radiation.
- There is a lot of basic biology that needs to get done, bolstered by information provided by physicists, computational scientists and Monte Carloists.
- We need to get physicists, chemists and biologists to *speak the same language*.
- We may have to *invent* this new language.
- We have to form new kinds of tri-partisan research institutions and organizations.
- Physicists have to learn a lot more biology and chemistry.

Conclusions

- The Monte Carlo technique in the $e^\pm\gamma$ sector has come a long way and has become very refined.
- While tools development is ongoing, applications are increasing in number and diversifying.
- Our biggest successes in the future will come from support to the life sciences, in particular, providing basic support to understanding the response of living cells to radiation.
- There are many more applications in Biology that we may address, but we have to redefine ourselves somewhat.

Acknowledgements

I would like to acknowledge Ms. Sandra Bogarde and Dr. John Hubbell of NIST for their assistance in assembling some of the material related to Martin Berger. I also acknowledge Dr. Ralph Nelson for generously providing some personal material to assist this presentation. I would like to thank Dr. David Rogers of the National Research Council of Canada and Prof. Francesc Salvat of the University of Barcelona for personal insights into Martin's personality and work habits. I would like to thank Dr. Pedro Vaz for encouraging me to write up this transcript of my plenary session address. Finally, I would like to thank Prof. Jim Duderstadt, President Emeritus of the University of Michigan for his thoughts on the major basic scientific endeavors of the last two and the next century. To my knowledge, this idea was first presented by Jim at one of my department's colloquia on Feb. 18, 2000.

References

1. M.J. Berger: *Methods in Comput. Phys.* **1**, 135 (1963)
2. S.M. Seltzer: 'An overview of ETRAN Monte Carlo methods'. In: *Monte Carlo Transport of Electrons and Photons*, ed. by T.M. Jenkins, W.R. Nelson, A. Rindi, A.E. Nahum, D.W.O. Rogers, (Plenum Press, New York 1989) pp. 153–182
3. R.L. Ford, W.R. Nelson: *The EGS code system – Version 3*. Stanford Linear Accelerator Center Report SLAC-210 (1978)
4. W.R. Nelson, H. Hirayama, D.W.O. Rogers: *The EGS4 Code System*. Report SLAC-265, Stanford Linear Accelerator Center, Stanford, Calif (1985)
5. K.R. Kase, W. R. Nelson: *Concepts of Radiation Dosimetry* (Pergamon, 1978)
6. W.R. Nelson, T.M. Jenkins (Eds.): *Computer Techniques in Radiation Transport and Dosimetry* (Plenum Press, New York 1980)
7. T.M. Jenkins, W.R. Nelson, A. Rindi (Eds.): *Monte Carlo transport of electrons and photons below 50 MeV* (Plenum Press, New York 1989)

Remarkable Moments in the History of Neutron Transport Monte Carlo Methods

I. Lux

Hungarian Atomic Energy Authority, H-1539 Budapest 115, P.O.Box 676

Ladies and Gentlemen, Dear Colleagues,

It is my utmost pleasure to talk to the acknowledged audience of this outstanding conference. Forgive me if I begin my talk with something personal. Quite a time ago, when I have made my first steps in the wonderland of Monte Carlo I have often dreamed about visiting the two capitals of this art: Novosibirsk in Russia and Los Alamos in the USA. I had the opportunity to see quite a few places in the World but somehow neither of these two. Now we all have gathered in Lisbon and you brought here in your head and in your papers all what is worth of knowing in this field of science, while strange enough, Lisbon is almost exactly in the midpoint between Novosibirsk and Los Alamos¹. I would like to call to your attention the symbolic meaning of this.

During the limited time at my disposal I am not going to tell you anything new. Instead I will try to highlight a few results from the past of the neutron and photon transport Monte Carlo methods which have caused me a great pleasure for their ingenuity and wittiness and which certainly merit to be remembered even when tricky methods are not needed anymore.

1 Sampling from Probability Distributions

As most likely many of you, when starting to deal with random numbers, I have also spent quite a time to derive new algorithms for sampling various specific distributions. My boss at that time kept telling me: *“Do not get involved too much unless you want to get stuck in it forever!”* True enough I have worked with the matter quite a lot, nonetheless nothing of what I happened to find out was as ingenious as the two methods below, that I have selected to quote to you. Both relate to the selection from the normal distribution.

1.1 Using the Central Limit Theorem (c.f. e.g. [1])

Let $\eta = \xi_1 + \xi_2 + \dots + \xi_n - n/2$ [where the ξ_i 's are random numbers uniformly distributed over $[0,1]$, in brief $\xi_i: U(0,1)$] then η is a sample from $N(0, n/12)$ with a good approximation if n is large enough. For practical purposes $n = 12$ is reasonable, which then yields a sample from a standard normal distribution.

¹ Approximate co-ordinates: Novosibirsk: 55°N/85°E, Lisbon 38°N/9°W, Los Alamos 28°N/103°W

1.2 Using a Second Dimension [2]

Let x and y both $N(0,1)$. Then their common density function, i.e. the density function of the point $Q(x, y)$ in the Descartes co-ordinates system is:

$$p_Q(x, y) = (1/2\pi) \exp[-(x^2 + y^2)]. \quad (1)$$

Changing the co-ordinates system to polar co-ordinates: $Q(r, \varphi)$, the transformed density function reads:

$$p_Q(r, \varphi) = r p_Q(x, y) = (1/2\pi) r e^{-r^2} \quad (2)$$

which is the product of the isotropic density function of φ over $[0, 2\pi]$ and of the directly integrable and invertible density function of r . Thus, if ξ_1 and ξ_2 are uniform random numbers, then

$$\Theta = 2\pi\xi_1 \quad \text{and} \quad \rho = (-2 \ln \xi_2)^{1/2} \quad (3)$$

are representations of the random polar co-ordinates, while

$$\eta_1 = \rho \cos \Theta \quad \text{and} \quad \eta_2 = \rho \sin \Theta \quad (4)$$

are two samples from the standard normal distribution. Beautiful, isn't it?

2 Economizing with Random Numbers

In the time of the powerful computers and of the brute force methods, it may seem strange that there were times when people - sober and clear in mind - spent time and effort just to spare the generation of a few random numbers per history. But this is true, this is history and even this is the case at some places also now.

An outstandingly simple example of the re-use of second-hand random numbers is the following:

Let $\xi: U(0,1)$ and let it be used to select an interval from among $0 < c_1 < c_2 < \dots < c_k < \dots < c_N$. (This of course corresponds to a selection from among N independent discrete events). Assume that the k -th interval is selected ($c_{k-1} \leq \xi < c_k$), then

$$\xi_1 = (\xi - c_{k-1}) / (c_k - c_{k-1}) : U(0, 1), \quad (5)$$

and independent from ξ . This simple rule has prevented a tremendous amount of random numbers from having been generated and made an almost equally large number of montecarlists happy.

3 Generating Random Walks

The very essence of transport Monte Carlo is the generation of the particles' histories. Efficient techniques have been developed suprisingly fast and very little has been added to this art since the early age of Monte Carlo.

3.1 The Most Common Techniques

Although commonplace, I really do have to talk about these methods for their absolutely simple beauty. Let me first of all mention the well-known *survival biasing*, i.e. the procedure that replaces any absorption by weight reduction. This is the simplest nonanalogue game, which at the same time realizes the physical nonsense of splitting up non-divisible particles. On the other hand this is about the only method which can be proven to reduce variance in full generality.

Survival biasing was introduced in order to prevent absorption-caused early termination of histories. However, it generated immediately the problem of how to terminate a history at all? (OK, escape is always a way out, but not so effective in deep-penetration problems). This is when *Russian roulette* has been introduced, a “get lost or get larger” game in which the expected statistical weight of a particle remains unchanged. The third tool in this arsenal is *splitting*, which is used to slice up particles with too high statistical weights in order to reduce the variance of the score.

These tools are often used together, they are strongly believed to increase efficiency and many Monte Carlo practitioners are convinced that they possess the omnipotent recipe for an optimum selection of the related parameters. There are methods, there are approximate analytical derivations (may I also offer some in [3]), but no valid, exact method of using these techniques in an optimum way has ever been derived. Nonetheless they are present in every code and work excellent via rules of thumb.

3.2 Exponential Transformation and Its Relatives

For problems where deep penetration into matter is to be examined, in conventional Monte Carlo methods it is difficult to generate sufficient number of sufficiently penetrating histories in a reasonable time frame. In one-dimensional cases it is quite obvious that artificially decreasing the cross section of the material in the preferred (inward) direction and increasing it in the opposite (outward) direction would force the particle penetrate. This can be done by the transformation

$$\Sigma^* = \Sigma - b\mu, \quad (6)$$

where b is a suitable constant and μ is the directional cosine of the flight relative to the preferred direction. Obviously, this simple trick may have dramatic effects on the histories generated.

Because of the exponential feature of the transition kernel, such a transformation results in multiplication factors in the integral form of the transport equation. These factors can either be included into the (biased) collision kernel and into the quantity to be determined, or can multiply the statistical weight of the particle.

In the simplest (homogeneous) case the transition kernel has the form

$$T(\mathbf{r}, \mathbf{r}'; \mathbf{E}) = \Sigma \exp(-\Sigma x), \quad \text{where } \mathbf{r}' = \mathbf{r} + \omega \mathbf{x}, \mathbf{E} = (E, \omega), \text{ and } \mathbf{n} \cdot \omega = \mu, \quad (7)$$

\mathbf{n} being the directional unit vector of the preferred direction. Introducing the transition kernel with the transformed cross section we have:

$$T = T^*(T/T^*) = T^*(\mathbf{r}, \mathbf{r}'; \mathbf{E}) [(\Sigma/\Sigma^*) \exp(-b\mu)]. \quad (8)$$

The factor after T^* is the one to be included into the biased collision kernel and also into the modified estimated quantity, or, alternatively, to be accounted for in the statistical weight.

The first version of this method has been proposed as early as 1949 [3]. In a more general formulation of this transformation it can be seen [4], that path-stretching and exponential transformation are closely related and are both special forms of the general importance sampling procedure.

3.3 Restart of Particles at Geometrical Boundaries

The exponential distribution of the free flights has further remarkable consequences. Authors of such Monte Carlo codes, which are meant to describe complicated geometrical forms, are most happy with the fact that when generating the next collision site of a particle, there is no need to calculate all boundary crossings along a free flight direction. Instead you determine the point where the particle would leave the actual material and - if the actual free flight extends over this boundary - just select a new flight from this point with the cross section of the composition just to enter. To illustrate that for a two-layer case, let the thickness of the first layer be x_1 and the cross sections of the layers be Σ_1 , Σ_2 , respectively. Then the density function of a free flight x is

$$T(x) = \Sigma(x) \exp \left[- \int \Sigma(x') dx' \right] = \begin{cases} \Sigma_1 \exp(-\Sigma_1 x) & \text{if } x < x_1, \\ \Sigma_2 \exp[-\Sigma_1 x_1 - \Sigma_2(x - x_1)] & \text{otherwise.} \end{cases} \quad (9)$$

The second expression is rewritten in the form

$$\Sigma_2 \exp[-\Sigma_1 x_1 - \Sigma_2(x - x_1)] = [\exp(-\Sigma_1 x_1)] \Sigma_2 \exp[-\Sigma_2(x - x_1)], \quad (10)$$

where the first term is the probability of reaching the layer-boundary in one flight, whereas the second term is the conditional density function of the flight in the second layer - obviously identical in form with the unconditional density for a flight just started from the boundary. In case of radioactive decay this feature is characterized by stating that “*decaying particles do not age*”. We may as well state that “*Monte Carlo particles do not get tired*”.

4 Estimators

The third trap in constructing Monte Carlo games is the selection (or, for more ingenious players, the invention) of the estimators to be used. (Just to remind, the first two traps where you can get stuck even for a lifetime are: generating random numbers and constructing efficiency increasing nonanalogue games). For the sake of simplicity let us assume that the quantity to be estimated is some kind of reaction rate in a given volume. An obviously unbiased estimator of this quantity is the so-called collision-estimator, which scores the probability of the given reaction at every collision. The unbiasedness of any other estimator is less obvious and considerable effort has been invested in the exact derivation of more effective unbiased estimators (let me only refer to the ingenious but most artificial derivation of the track-length estimator in [5]). Some of the results in this direction are mentioned below.

4.1 Partially Unbiased Estimators

In full generality, any estimator is unbiased if for a well defined set of histories, the expected score provided by the estimator is equal to the quantity to be estimated. Let us assume that we have one such unbiased - reference - estimator (e.g. the collision estimator in the special case here). Then a less demanding condition for another unbiased estimator is that the expected score in any history be the same as the one resulting from the reference estimator. Even less generally, any estimator yielding the same expected score as the reference unbiased estimator in a free flight followed by a collision event is also unbiased. Such estimators have been called partially unbiased [3]. In the simplest case, when the estimator does not depend on the collision process but only on the free flight, the condition for partially unbiased estimators reads:

$$\int T(P, P') f(P, P') dP' = \int T(P, P') f_{ref}(P, P') dP', \quad (11)$$

where $T(P, P')$ is the transition kernel, $f(P, P')$ is any unbiased estimator and $f_{ref}(P, P')$ is the reference unbiased estimator. $P(\mathbf{r}, \omega, E)$ is a point in the phase space and $P'(\mathbf{r} + t\omega, \omega, E)$ is a possible next collision point. The condition obviously requires the equality of the expected scores over a free flight started from P . Inserting the specific exponential form of the transition estimators into this condition, the unbiasedness of the track-length estimator (as well as of almost every widely used estimator) can be easily seen [4].

4.2 Generation of Estimators by Transformation

The condition of partial unbiasedness in (11) gives the way of proving the unbiased feature, but gives no direct clue as how to generate new estimators. This latter can nevertheless be done with a relative ease by using transformations on

the reference unbiased estimator. Such transformations were first proposed in [6] and have then been generalized in [4]. The transformations have the form:

$$f(P, P') = \int dP_1 [T(P, P_1)X(P, P_1, P')f_{ref}(P, P')] / \int dP_2 T(P, P_2)X(P, P_1, P_2) \quad (12)$$

where X is an arbitrary function for which the integrals in the transformation exist. Multiplication by T and integration show the partially unbiased feature of the transformed estimator $f(P, P')$. It is also shown in [4], that any partially unbiased estimator can be obtained by this transformation from any reference estimator. All of the commonly used estimators as well as some strange ones are also derived.

5 Moment Equations

Now the forth (and perhaps last) grade where a Monte Carlo practitioner (and moreover a theorist) may get lost forever is the wonderland of variance reduction and efficiency increasing techniques. It is almost hopeless to estimate the composite effect of the random number generation, estimator selection and random walk biasing on the variance of the estimated quantity (and even less on the efficiency of the simulation). Many players call it *“more an art than a science”*.

An extremely useful tool in such investigations has been offered by the score-moment equations first proposed by Amster and Djomehri in [7]. The moment equations are coupled integral equations and describe the relationship among the various expected score-moments in terms of the quantities governing the simulation. Thus the expected score $M_1(P)$ due to a particle started from a point P in an analog game satisfies the equation

$$M_1(P) = \int T(P, P')f(P, P')dP' + \int dP'T(P, P') \int dP''C(P', P'')M_1(P'') \quad (13)$$

where P , P' and P'' are the phase-space points of the particle [as in (11)] at which it starts a free flight, enters a collision and leaves a collision, respectively, C is the collision kernel and the other quantities have been defined earlier. This equation expresses the fact that the expected score is composed by the contribution expected from the first flight started from P , and by the score expected after performing a successful flight and collision. The second moment $M_2(P)$ of the score due to the same particle is governed by the following equation:

$$\begin{aligned} M_2(P) = & \int T(P, P')f^2(P, P')dP' \\ & + 2 \int dP'T(P, P')f(P, P') \int dP''C(P', P'')M_1(P'') \\ & + \int dP'T(P, P') \int dP''C(P', P'')M_2(P''), \end{aligned} \quad (14)$$

This equation - among many others - also expresses the effect of the estimator on the second moment (variance).

5.1 Weight Generation Rules

The moment equations have soon been generalized to nonanalogue games [3]. Let an asterisk denote the respective nonanalogue quantities, then the first moment of the score in a nananalogue game corresponding to the analog one in (13) satisfies the equation

$$WM_1^*(P) = \int T^*(P, P')W'f^*(P, P')dP' + \int dP'T^*(P, P') \int dP''C^*(P', P'')W''M_1^*(P''), \quad (15)$$

where W , W' and W'' are the statistical weights of the particle at the phase-space points P , P' and P'' respectively. The generalized first moment equation allowed a very simple formulation of such rules that govern the selection of the statistical weight of a particle in a particular nonanalogue game. Obviously, if

$$W' = WT(P, P')/T^*(P, P'), \quad \text{and} \quad W'' = W'C(P', P'')/C^*(P', P''), \quad (16)$$

whereas $f^*(P, P')$ is a partially unbiased estimators, then (15) becomes identical to (13) and the nonanalogue first moment equals to the analog one. One of the outstanding beauties of the moment equation approach is this extremely simple formulation of the unbiased nonanalogue games.

5.2 Zero Variance Games

It might first sound either a joke or a cheat if someone when gambling talks about the certainty of his/her winning. Zero variance nonanalogue games are something like this, a random estimation procedure with a fixed result. The nonexistence of such a bird did not prevent the theorists from treating the case and they did it rightly. Approximations to a hypothetical zero variance game may substantially reduce the variance.

The first such schemes assumed a (hypothetically zero variance) contribution to the estimate at the last flight of any particle. Collisionwise estimators were first proposed in [8], whereas zero variance schemes were first treated in the moment-equation formalism in [9]. A general treatment is given in [4].

The simplest form of the nonanalogue second moment equation [corresponding to (14)] reads

$$W^2M_2^*(P) = \int T^*(P, P')(W')^2f^2(P, P')dP' + 2 \int dP'T^*(P, P')W'f(P, P') \int dP''C^*(P', P'')W''M_1^*(P'') + \int dP'T^*(P, P') \int dP''C^*(P, P'')(W'')^2M_2^*(P''). \quad (17)$$

Making use of the weight generation rules in (16) and introducing the notation

$$M(P) = M_2^*(P)/M_1(P), \quad (18)$$

a little algebra yields the following equation

$$\begin{aligned} M(P) = & \int T(P, P') A(P, P') f(P, P') dP' \\ & + \int dP' T(P, P') A(P, P') \int dP'' C(P', P'') M_1(P'') \\ & + \int dP' T(P, P') B(P, P') \int dP'' C(P', P'') \\ & \cdot [R(P', P'') M(P'') - M_1(P'')], \end{aligned} \quad (19)$$

where,

$$\begin{aligned} A(P, P') = & T(P, P') [f(P, P') \\ & + \int dP'' C(P', P'') M_1(P'')] / T^*(P, P') M_1(P), \end{aligned} \quad (20)$$

$$B(P', P'') = T(P, P') \int dP'' C(P', P'') M_1(P'') / T^*(P, P') M_1(P), \quad (21)$$

and

$$R(P', P'') = C(P', P'') M_1(P'') / C^*(P', P'') \int dQ C(P', Q) M_1(Q). \quad (22)$$

Now, choosing the following expressions for the nonanalogue transition and collision kernels, respectively:

$$T^*(P, P') = T(P, P') [f(P, P') + \int dP'' C(P', P'') M_1(P'')] / M_1(P), \quad (23)$$

$$C^*(P', P'') = C(P', P'') M_1(P'') / \int dQ C(P', Q) M_1(Q), \quad (24)$$

it is seen from (20) and (21) that $A(P, P') \equiv R(P, P') \equiv 1$, whereas, in view of (13), the first two terms on the rhs. of (19) sum up to $M_1(P)$. Thus, subtracting $M_1(P)$ from both sides of (19), we have:

$$\begin{aligned} M(P) - M_1(P) = & \int dP' T(P, P') B(P, P') \int dP'' C(P', P'') \\ & \cdot [M(P'') - M_1(P'')]. \end{aligned} \quad (25)$$

It is easily seen that for the properties of the integral kernel in (25), the only solution to this equation is $M(P) \equiv M_1(P)$, and therefore, from (18)

$$M_2^*(P) \equiv [M_1(P)]^2, \quad (26)$$

i.e. the variance of the estimate is zero. Obviously both kernels in (23) and (24) are expressed in terms of the expected score $M_1(P)$, and therefore they can not be applied directly in realistic problems. Nevertheless, in certain cases using a rough estimate of the final result may substantially improve the efficiency of the game. And yet we have not mentioned the inherent beauty of the derivation above, which makes almost any result justified even if otherwise useless.

Let us note that the nonanalogue kernels in (23) and (24) emphasise flights and flight directions, respectively, from where higher contribution to the score are expected, i.e. the zero variance game is the ultimate solution in importance sampling. It can also be easily seen, that in case of the simplest collision estimator $f(P, P') = f(P')$ the nonanalogue transition kernel in (23) reduces to

$$T^*(P, P') = T(P, P')\psi^*(P')/M_1(P), \quad (27)$$

where Ψ^* is the adjoint collision density.

The nonanalogue second moment equations have been extensively used for the analysis of the variance and efficiency of various realistic scenarios. I only wish to refer to [4] and to the references therein.

I am convinced that many other remarkable moments of the Monte Carlo history would merit to be mentioned in such a presentation. I admit, I may have been subjective (but I guess this was expected by the organizers). I apologize if I have left unmentioned results that are important for some of you, but time is what we have fought against all through our lives, this is what Monte Carlo theory is about. And time has defeated us once more.

References

1. J.M. Hammersley, D.C. Handscomb: *Monte Carlo Methods* (Chapman and Hall, London, 1979)
2. G.E.P. Box, M.E. Muller: Ann. Math. Statist. **29**, 610 (1958)
3. H. Kahn: *Modification of the Monte Carlo Method*, Rand Report P-132 (Rand Corporation, Santa Monica 1949)
4. I. Lux, L. Koblinger: *Monte Carlo Particle Transport Methods: Neutron and Photon Calculations* (CRC Press, Boca Raton 1991)
5. J. Spanier, E.M. Gelbard: *Monte Carlo Principles and Neutron Transport Problems* (Addison-Wesley, Reading Massachusetts 1969)
6. L.D. Maiorov, A.D. Frank-Kamenietzky: *Relative Efficiencies of Various Monte Carlo Estimators*, IAE-1791 Report, Kurchatov Institute of Atomic Energy, Moscow (1969) (in Russian)
7. H.J. Amster, M.J. Djomehri: Nucl.Sci.Eng. **60**, 131 (1976)
8. S.M. Ermakov: *Monte Carlo Methods and Related Problems* (Nauka, Moscow, 1971), (in Russian); *Monte Carlo Methods und verwandte Fragen* (Oldenburg Verlag, München, 1975)
9. S.R. Dwivedi: Nucl. Sci. Eng. **80**, 172 (1982)

Hadronic Monte Carlo Transport: A *Very* Personal View

R.E. Prael

Los Alamos National Laboratory, Diagnostic Applications Group, X-5, P.O. Box
1663, MS F663, Los Alamos, NM 87545, USA

1 Introduction

Much to the disappointment of many, our distinguished speaker for the initial plenary session has been unable to attend our conference. I was prevailed upon by the conference organization to present a talk which, as prescribed, will be of a historical nature, but as the title describes, will also be a *very personal view*. Perhaps the opinions expressed will find sympathy with my associates around the world who have devoted their efforts to and found some satisfaction with providing the code tools for radiation transport to a large, and occasional anxious, community of users.

2 How LANL (and I) Got into the Business

The original request was made in 1979 by Gary Russell (now LANSCE) to adapt the ORNL code HETC [1] to use MCNP tracking and to interface with MCNP [2] for neutron transport. The primary motivation was neutron source target and facility design which, over the years, became the LANSCE facility. It was felt to be advantageous to have a locally supported computational capability closely associated with the experimental program and with in-house experience with the MCNP code.

Our “peer group” in this area was the International Collaboration on Advanced Neutron Sources (ICANS), the members of which were primarily using HETC and developing local versions of that code. The “LANL version of HETC” featured MCNP geometry, a secondary neutron interface file for input to MCNP and new output editing capabilities developed for local application. That was the first of three adaptations of MCNP geometry coding for use with HETC/LAHET over the years – a laborious procedure which was a major motivation for actually merging the codes into MCNPX [3].

US Air Force funding in the mid-1980’s allowed some collaboration (2 of us!) on model development (including the multistage preequilibrium exciton model) and the construction of the LAHET Code System [4] that was eventually released. With Yair Yariv in residence at LANL, the ISABEL physics package was included in LAHET. (Our sponsors insisted on a name change – LAHET rather than the “LANL version of HETC”).

Detector design for the ill-fated SSC project led Avigdor Gavron and Laurie Waters to make the first extension of LAHET to high energies. Just as important,

a new peer group came about, leading to frequent interaction with Alfredo Ferrari (FLUKA code) and Nikolai Mokhov (MARS code).

3 Beg, Borrow and Bargain ... or How to Provide Code Without Funding or Manpower

Until the Accelerator Production of Tritium (APT) project arrived (and the MCNPX development program), the LANL code development effort was strictly a low-budget operation and much dependent on the good will of others. Over the years, new capabilities came about by the procedure of

- “Dear Tony (Gabriel), can I have your code?”
- “Dear Detlef (Filges), could you send me ...”
- “Dear Alfredo (Ferrari), may I please use your ...”
- “Dear Nikolai (Mokhov), ...”

However, some of the features developed for LAHET have also found their way around the world, in many cases to be improved, so perhaps we have also given something back to the international community.

With that history in mind, this talk provides an opportunity to offer some thanks to those who, among many, directly and indirectly contributed to the LANL effort to establish a general Monte Carlo radiation transport capability:

- Tony Gabriel, Tut and Fran Alsmiller (ORNL)
- Tony Armstrong (SAIC)
- Yair Yariv (SOREQ)
- Detlef Filges and associates (Fz-Jülich)
- Francis Atchison (PSI)
- Alfredo Ferrari and Paola Sala (CERN)
- Nikolai Mokhov (FNAL)

4 Growing Codes

High-energy transport codes of the world have evolved downward in energy toward our conventional neutron transport capability. Our medium energy codes have been extended upward in energy, but have always been closely linked to neutron codes (MORSE, MCNP, etc.). Merging medium- and high-energy capabilities directly into MCNP in effect is growing the code upward from thermal energies. During the SSC period, applications included liquid hydrogen moderators and cryogenic magnets, so that the computational range under consideration involved over 17 decades in energy!

The manner in which code development has evolved does produce “culture clashes.” Monte Carlo code development for particle physics and accelerator applications is largely characterized as simulation and is inherently analog. Our neutron transport codes use Monte Carlo for a solution of the integral transport

equation and are filled with variance reduction methods. The methods that have evolved tend to be nonanalogue and it may be hard to reverse that process. In addition, the physics content is fixed in the form of massive data libraries. Unfolding these features to perform, for example, a pulse height tally from a neutron source becomes a very difficult task in MCNP (or MCNPX).

A consequence of merging philosophies as well as code is that many details must be treated that do not have a simple representation in the coding being adapted; an example is producing trackable recoil protons from nucleon elastic scattering when using library data for ^1H . Although adding a new procedure to create the protons is simple enough, doing the job was overlooked and has produced many questions from health physics users of MCNPX. Getting the energy deposition tally correct in this case requires more effort. In general, trying to estimate energy deposition correctly in MCNPX is always going to be hard since the contributions are so diverse and the logic so complex. It is a positive development that nuclear engineering students with MCNP experience are now doing research on accelerator applications and may be expected to be major contributors to code development efforts in the future.

5 We Don't Need No . . . Muons!

The above title is a reflection of the fact that many things will not be included in a code until a demanding user appears. At LANL, we have never had a “customer” with an interest in detailed muon transport, so the code capability in this regard has never evolved beyond the limited treatment included in the original HETC code.

However, if a request arrives with *real funding*, then priorities get radically revised. Otherwise, so many features that make a “complete” radiation transport code just wait, and wait, and wait, even when the modeling can be “borrowed” from FLUKA or MARS or another friendly source.

6 Merging Code at LANL

As suggested above, the effort to merge the LANL Monte Carlo radiation transport codes is long overdue. Retrofitting LAHET to include newer MCNP features is very nonproductive. The APT program (L. Waters) and proton radiography have provided the means and motivation to proceed with the code merger. A single code is more easily modernized and can take better advantage of computer science development. Improved structure to “compartmentalize” physics code packages will encourage model developers to test new physics and features in a transport code environment. One may hope that the MCNPX effort (MCNP + LAHET + new physics) will become “institutionalized” in the general framework of the ongoing MCNP program.

One may look to the GEANT collaboration over the years and find much to be admired:

- a continuous “center of development”;
- a widespread network of contributors;
- a structure that accommodates imported code packages, physics or otherwise.

The continuing MCNP effort shares some of these features, and code modernization and code merger based on MCNP are evolving others. Perhaps conferences such as this one will stimulate increased interaction between the GEANT collaboration and LANL code development.

7 Conclusion: Regrets and Rewards

There has been no general support for radiation transport across the complex of US Department of Energy laboratories and consequently very little US model development in recent years. Historically, code development work follows project funding, so desired features for our codes only become available after most project design and development is done. It is really satisfying to be able to provide calculation support when the proposal is being written!

Being able to provide code support for LANL efforts in space science has been very rewarding, but so much more could be done with a real project commitment and perhaps even a funded collaboration with NASA. Knowledgeable users and applications for our codes abound in the fields of medical accelerators and radiation dosimetry; examples in this field were presented at this conference as tutorials by with Jeff Siebers (VCU) and Wayne Newhauser (MGH). It is a regret that we do not have a charter to support these fields. On the other hand, it is a rewarding experience to be able to encourage and support CEM2K development by Stepan Mashnik at LANL.

It is a privilege to participate in the MC2000 conference this week, where model developers, code developers and users in design and experimental areas may interact and communicate. New collaborations, formal and informal, will be initiated. It is my hope that the methods we develop and the codes we produce will be applied far beyond our customary fields in accelerator applications.

References

1. Radiation Shielding Information Center: *HETC: Monte Carlo High-Energy Nucleon-Meson Transport Code*, ORNL/RSIC report CCC-179 (1972)
2. J.F. Briesmeister, Editor: *MCNPTM – A General Monte Carlo N-Particle Transport Code, Version 4C*, LANL Report LA-13709-M (2000)
3. H.G. Hughes et. al.: *MCNPX – The LAHET/MCNP Code Merger*, LANL Report LA-UR-89-3014 (1997)
4. R.E. Prael, H. Lichtenstein: *User Guide to LCS: The LAHET Code System*, LANL Report LA-UR-89-3014 (1989)

Highlights of Hadronic Sessions, Speculations and Perspective Views

D. Filges¹ and W. Gudowski²

¹ Forschungszentrum Jülich, Institut für Kernphysik, 52425 Jülich, Germany

² Nuclear and Reactor Physics Royal Institute of Technology, 10044 Stockholm, Sweden

One of **the most important highlights** is reported progress in High Energy Transport (HET) code development. Particularly, we have noticed progress in following codes:

- Hermes code system – D. Filges, R.-D. Neef, H. Schaal and G. Sterzenbach, “The HERMES Monte Carlo Program Systems a Versatile Tool for Spallation Physics and Detectors”
- Fluka code – A. Fassò, A. Ferrari, J. Ranft and P. Sala, “FLUKA: Status and Perspectives for Hadronic Applications”
- MCNPX code – H.G. Hughes, “Status of the MCNPX Transport Code”
- Mars code system – N. Mokhov and O. Krivosheev, “MARS Code Status”
- NMTC/JAERI code – H. Takada, S. Meigo and K. Niita, “Present Status of Nucleon-Meson Transport Code NMTC/JAERI.
- GEANT 4 platform – M. Asai, “Generic Design of Physics Processes in Geant 4”
- EA-MC code, coupling HET physics of Fluka with new low-energy M-C transport routines including burn-up possibilities – Y. Kadi, “The EA-MC Monte Carlo Code Package - A New Approach to the Design of Accelerator-Driven Systems”
- and MCNP code widely used in coupling with HET for neutron-gamma-electron transport at energies below 20 MeV – E.C. Selcow, G.W. McKinney, “MCNP Capabilities at the Dawn of the 21st Century: Neutron-gamma Applications”.

Moreover a remarkable development of Hadronic Event Generators has been reported:

- Hadronic Event Generator covering a wide range of energies from 10^{12} down to ~ 10 GeV is now available and reasonably validated – S. Roesler, R. Engel and J. Ranft, “The Monte Carlo Event Generator DPMJET-III”
- GEM code based on the generalized evaporation model and the RAL fission model reproducing successfully the cross sections for fission fragment production as well as ^7Be and ^9Li productions – S. Furihata, “The GEM code - The Generalized Evaporation Model and the Fission Model”
- FRITJOF model is being upgraded – A. Polanski, A.S. Galoyan and V.V. Uzhinski, “Simulation of Nucleus-Nucleus Interactions in the Framework of the FRITJOF Model”

Some very important nuclear data experiments have been reported, particularly a very elegant GSI-experiment in inverse kinematic, giving spallation product data of an unprecedented quality – J. Benlliure, P. Armbruster et al., “New Data and Monte Carlo Simulations on Residue Production in Spallation Reactions Relevant for the Design of Neutron Sources”

Presentations on this conference identified clearly driving forces for high energy transport code development:

- High Energy Physics
- Neutrino physics (front end for neutrino experiments i.e. μ^+ for neutrino production + neutrino physics itself)
- Spallation neutron sources
- Radioactive beams
- Accelerator-driven Systems (for transmutation and energy production)
- Medical Applications (proton and “heavy ion” therapy)
- Space related research – cosmology, material damages, shielding and dose calculations
- Nuclear data – experiments and evaluations

Strongest drivers for M-C code development appear to be:

- Spallation Neutron Sources - for High Energy Transport (spallation target optimization, shielding problems) and N-G transport (for optimization of neutron scattering facilities and for shielding):
 - Spallation Neutron Source (SNS) in USA is already under construction and requires some of the crucial design decisions to be taken now (if not already taken). The main parameters of this spallation neutron source are: Proton energy - 1 GeV, power 2-4 MW, short and long neutron pulses are foreseen.
 - European Spallation Source (ESS), requires in very few years (2-3 years) a full-scale design should/must be ready (a lot of interesting work done with HERMES). The main parameters of ESS are: Proton energy - 1.33 GeV, power 5 MW.
 - KEK/JAERI multipurpose facility requires a lot of design and “fine-tuning” work in the range of 50 GeV down to neutron scattering energies, stimulates development of M-C codes in Japan. The main parameters are: Proton energy - 3 GeV (out of 50 GeV designed for high energy/neutrino physics), power - 1-5 MW.
- Accelerator-driven systems (including APT)
 - Already stimulated MCNPX, Fluka and MC-EA development
 - Stimulates further integration of HET with low energy N-G transport
 - Drives development of Monte-Carlo towards burnup codes (MC-AE, MCB) + hybrid code systems
 - Need better radiation damage codes

- Medical applications
 - Use so far existing M-C codes for design/development work, and non MC for treatment planning
 - Need dedicated, very fast codes with some specific features, however we doubt if really few-second performance is really necessary
 - Should definitely become a common project of hadron/medical MC community

With some concern we have noticed on this conference some under-represented major research activities of importance for Monte Carlo:

- High Energy Physics, even if code developments address HEP needs (Fluka, GEANT, MCNPX, Mars, hadron event generator development) there was virtually no feedback from HEP community. We did not hear much neither about CALOR, PSI-HETC/O5R, SHIELD codes
- More detailed presentations of some Hadronic Event Generators were missing, e.g. Cugnon INC model, GEMINI evaporation model, CEM of Mashnik etc.
- Data cross section calculation and evaluation were inadequately represented, not much about ALICE or GNASH codes. We would like to hear much more about NJOY development.
- Radioactive Beams and heavy ion transport (with an exception of the presentation of H. Iwase et al., “Development of Heavy Ion Transport Monte Carlo Code”)
- Accelerator-driven systems – only very few specific presentations

We are strongly convinced that free exchange of Monte Carlo source codes would contribute to a further development of their applications in high-energy physics. In Table 1 we summarize availability of most of the Monte Carlo codes.

We can conclude that M-C makes NO BIG SENSE without good models and good input data. That is why we would like to put some attention on:

- Good session on some data aspects (HAD VI). There are some good news:
 - Experimental spallation product data of very good quality are available now, should contribute to improvement of physical models
 - Nuclear cross section data library for over 40 isotopes, for neutrons and protons up to 150 MeV is available and growing
 - Photonuclear reaction data and simulation capabilities are being available now in some codes
- Data evaluation processes are very IMPORTANT for MC. We were missing NJOY presentation. NJOY being a major “front-end” data generator for M-C should continuously improve ACER processing.
- New validation and data experiments should make stronger impact on MC community

- JAERI/KEK – ASTE experiments
- FZK/HMI/GANIL – NESSI experiments
- CEA-Saclay – data from Saturne
- GSI/CEA – inverse kinematic experiments
- NTOF project in CERN in collaboration with many institutes in the frame of the 5th Framework Program in Europe
- HINDAS – European project in the 5th Framework Program in Europe
- New interesting validation experiments related to Accelerator-Driven Systems are under way or under preparations:
 - Subcritical experiment MUSE – CEA/Cadarache in the 5th Framework Program in Europe
 - Subcritical experiment in Minsk – the International Science and Technology Centre (ISTC) funded project.
 - 1 MW Pb/Bi spallation target experiment at LANL – collaboration between IPPE (Obninsk), LANL (Los Alamos), RIT (Stockholm), CEA (Cadarache) with the funding of the International Science and Technology Centre.
 - 1 MW Pb/Bi spallation target experiment at PSI – MEGAPIE project in collaboration with CEA, FZK, JAERI.

Materials and radiation damage research should benefit more from Monte-Carlo:

- MC is a very good tool for radiation damage simulations, however presented papers did not go beyond DPA, H and He production rate estimates. There is no reliable way to estimate life-time of key-components of the spallation

Table 1. Availability of Monte Carlo codes

Code	Availability of Monte Carlo codes		
	Free	Limited (binaries)	Restricted/commercial
FLUKA		×	
HERMES	×		
MARS	×		
MCNP and MCNPX	×		
EA-MC			×
NMTC/JAERI-JAM	?	?	?
DPMJET-III	×		
TIERCE			×
MCBEND/MONK			×
TRIPOLI-3	×		
MVP	?	?	?
A3MCNP	×		
MCU	?	?	?
MCB (MC burnup)	×		
SCALE V	×		

target and exposed structural materials. Radiation transport MC should join efforts with solid state M-C.

Some general observations

- In spite of development of MC methods and increased computer performance, coupling of deterministic methods and MC seems to be necessary, particularly in realistic shielding calculations and dose estimations in small volumes
- We noticed interesting ideas and solutions enhancing Monte Carlo performance through coupling of deterministic codes and advanced MC variance reduction techniques.

Observations and concerns

- There are 2 divergent paths in the MC code development for radiation transport applications:
 - Creation of a “platform” (frame) linking different codes, including MC-deterministic mix, through an inter-code communication standard and very advanced visualisation routines. Examples: Hermes and GEANT
 - Developing of a single code covering very broad particle transport problems. Examples: FLUKA, MARS and MCNPX.
 - This diversity can stimulate and fertilize MC development but it still remains a question for MC community: IS IT THE BEST WAY TO GO IN THE XXI CENTURY
 - We believe that the community of MC code users should be carefully consulted !

In our opinion development of HET codes should aims at:

- Implementing of better physics
- Precise validation processes
- Modularity of the routines
- User friendly interfaces including:
 - Extensive use of graphical interfaces (GUI)
 - Development of the common system utilities for input/output analysis

Some observations:

- European groups are using a whole mix of hadronic transport codes: Fluka, Hermes, MCNPX, Lahet, Mars, Dubna-CE etc.
- It seems that American and Japanese groups are relying mostly on “locally” developed codes (often with adopted features from other codes).

What should we think about before the next M-C Conference?

- Split to EG, NG and HADRONIC sessions is obsolete, leads sometimes to collisions (e.g. FLUKA code was presented at the same time on 2 different sessions covering separately high and low energy physics ...)

- Codes/code systems should be presented coherently on plenary sessions
- Split to parallel sessions should be more TOPIC oriented
- Broader participation of MC related communities should be ensured (broaden expertise of a Programme Committee)
- An effort should be launch to try to standardize HET code platform for the best of the users. Working Group under NEA/OECD umbrella?

Concerns:

- Almost no discussions on Hadronic Sessions!
 - Probably due to very tight schedule (or discouraging chairmen?)
- It must be improved on the next conference

Analog Electron Physics. Interaction Cross-Sections

F. Salvat¹, J.M. Fernández-Varea¹, and S. Seguí²

¹ Facultat de Física (ECM), Universitat de Barcelona. Societat Catalana de Física (IEC). Diagonal 647, E-08028 Barcelona, Spain

² Facultad de Matemática, Astronomía y Física, Universidad Nacional de Córdoba. Medina Allende y Haya de la Torre, 5000 Córdoba, Argentina

1 Introduction

The aim of the present communication is to describe briefly the physics of electron interactions in matter and its implementation in general-purpose Monte Carlo (MC) simulation codes. We shall limit ourselves to moderately high energies, say above 1 keV. At these energies, simulations can be performed on the basis of a trajectory model in which electrons are assumed to undergo discrete interactions with individual atoms (or molecules) of the medium. Between each pair of successive interactions, an electron moves freely, i.e. following a straight trajectory. The medium is considered as a dense isotropic gas, which implies that the length of each free flight is a random variable following the familiar exponential distribution. It is worth recalling that this simple picture overlooks coherent scattering effects (interference between waves scattered at different sites) which may become important at low energies, when the electron wavelength is of the order of the interatomic distances. In the energy range of interest here, the validity of the trajectory model can be justified by the same arguments that explain the production of cloud chamber tracks (see e.g. [1] p. 335). Within the trajectory model, all the information needed to simulate electron transport is contained in the atomic (or molecular) differential cross sections (DCS) for the various interaction mechanisms, namely, elastic scattering, inelastic scattering and bremsstrahlung emission. For a comprehensive tabulation of total (integrated) cross sections, see [2].

2 Interaction Cross Sections

The development of accurate methods for the calculation of DCSs for interactions with atoms is one of the most active fields in theoretical atomic physics. The so-called multichannel methods, which represent the state of the art for elastic and inelastic scattering theory, yield results in close agreement with experimental data. However, these calculations require formidable amounts of numerical work and results are available only for a limited number of cases. For simulation purposes, it is necessary to rely on simpler approximations of wider applicability.

A practical approach, which seems to meet the accuracy requirements of transport calculations of high-energy electrons ($E > 1$ keV), combines independent-particle atomic models (e.g. Hartree–Fock–Slater self-consistent wave functions) with first-order perturbation theory (Born approximation with plane or distorted waves).

2.1 Elastic Scattering

Elastic DCSs can be calculated by means of the static-field approximation and the partial-wave method. The target atom is considered as a frozen charge distribution and the motion of the projectile electron in the field $V(r)$ of the atom is described by the Dirac equation, i.e. the wave function representing the incident and scattered beams is a Dirac distorted plane wave. The atomic DCS per unit solid angle takes the form

$$\frac{d\sigma_{\text{el}}}{d\Omega} = |f(\theta)|^2 + |g(\theta)|^2, \quad (1)$$

where $f(\theta)$ and $g(\theta)$ are the direct and spin-flip scattering amplitudes, which are determined by the asymptotic behaviour of the wave function. Programs to calculate elastic DCSs have been elaborated by various authors; some of them are available from the Computer Physics Communications program library. With the aid of certain factorization methods, elastic DCSs can be computed for electron energies up to a few hundred MeV [3]. These calculations provide a consistent picture of the screening of the nuclear charge by the atomic electrons and of the effect of the finite size of the nucleus.

Projectiles with energies of a few keV or less move relatively slowly and can polarize the atomic charge cloud. This polarization effect, which modifies the free-atom DCS at small angles, is usually disregarded in MC simulations. In the case of electron scattering, exchange between the projectile and the target electrons also influences the DCS at low energies. This effect can be approximately described by adding a local contribution to the scattering field (see e.g. [4] and references therein).

The static-field approximation can be extended to molecules (and clusters). The simplest method consists of computing the molecular scattering amplitude by adding the scattering amplitudes from all the atoms in a molecule and averaging over molecular orientations. This method is not exact, because it neglects distortions of the atomic charge distributions caused by molecular binding, but is more accurate than the usual independent-atom approximation (in which the molecular DCS is obtained by adding the atomic DCSs). Comparisons of results from both calculations indicate that molecular binding effects (e.g. in water) are negligible for energies larger than ~ 1 keV [5].

2.2 Inelastic Scattering

Inelastic collisions of a projectile with initial energy E and momentum $\hbar\mathbf{k}$ cause transitions of the target atom from its initial (ground) state to an excited final

state, which may be bound (excitation) or free (ionization). The DCS depends on the energy loss W and the angular deflection $\Omega = (\theta, \phi)$ of the projectile *and* on the final state of the target. In radiation transport theory, we normally use the double-differential DCS, obtained by summing over degenerate final atomic states, which completely describes the effect of the interactions on the projectile (at the expense of hiding information about the effect on the target).

Inelastic DCSs can be obtained from the plane-wave Born approximation (PWBA), i.e. considering the interaction between the projectile and the target atom as a perturbation to first order and describing the initial and final states of the projectile as *plane waves*. The standard references on this subject are the review articles of Fano [6] and Inokuti [7]. The DCS is conveniently expressed in terms of W and the “recoil” energy Q (the kinetic energy of an electron with a momentum equal to the momentum transfer): it can be cast in the form

$$\frac{d^2\sigma_{\text{in}}}{dW dQ} = \frac{2\pi e^4}{m_e v^2} \left(\frac{1}{WQ(1 + Q/2m_e c^2)} + C_{\text{tr}} \right) \frac{df(Q, W)}{dW}, \quad (2)$$

where the term C_{tr} accounts for the transverse part of the interaction (exchange of virtual photons) and the last factor is the atomic generalized oscillator strength (GOS). For free atoms, we can adopt an independent-particle model and compute the GOS from first principles (see e.g. [8] and references therein). In the case of condensed materials, the GOS is related to the complex dielectric function of the medium,

$$\frac{df(Q, W)}{dW} \propto \text{Im} \left(\frac{-1}{\varepsilon(Q, W)} \right). \quad (3)$$

The dielectric properties of the condensed medium also affect the transverse interaction, giving rise to the so-called density effect correction for relativistic projectiles. In the case of electron collisions, exchange effects can be approximately accounted for by means of the Ochkur correction [9]. A consequence of the simplicity of the PWBA is the well-known Bethe formula for the stopping power of fast projectiles, which depends only on the mean ionization energy I (an integral property of the GOS for $Q = 0$).

The PWBA yields a realistic description of the interactions for projectiles with speeds much larger than the typical atomic electron velocities. More accurate approximations are needed to study, e.g., the ionization of inner shells by electrons with energies near the ionization threshold. A suitable alternative is to use the distorted-wave Born approximation (DWBA), in which the initial and final projectile wave functions include the distortion caused by the atomic field [10]. A further advantage of the DWBA is that it allows the description of exchange effects in a consistent way. In Fig. 1, we compare total cross sections for ionization of the K shell of Cr by electron impact calculated from the PWBA (with various corrections) and from the DWBA with experimental data from various authors. It is clear that the PWBA fails near the threshold and that application of exchange and Coulomb corrections lead to better agreement with

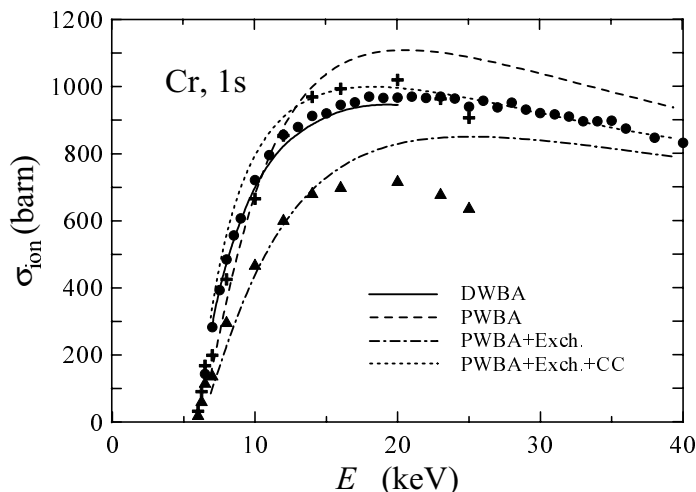


Fig. 1. Ionization cross section of the K shell of Cr by electron impact as a function of the projectile energy

experiment. Differences between the corrected PWBA and the DWBA decrease as the energy of the projectile increases.

DWBA computations are intrinsically difficult and, moreover, the volume of numerical data necessary to describe the multi-variate DCS is virtually impossible to handle in a MC simulation. For general-purpose MC codes, even the PWBA is too complicated for practical use. A convenient simplification (with only a small cost in accuracy) is provided by the optical-data models in which the GOS is approximated as a superposition of “oscillators” with relatively simple dispersion relations and weights determined from experimental or theoretical optical ($Q = 0$) oscillator strengths [11]. Except for near-threshold ionization, these models provide a satisfactory global description of inelastic interactions.

2.3 Bremsstrahlung Emission

The most accurate method to compute the atomic DCS for ordinary bremsstrahlung (i.e. emission of photons by electrons decelerated by the static field of the target atom) is provided by the DWBA (see e.g. [12]). The DCS depends on the energy W and direction Ω_γ of the emitted photon and on the angular deflection Ω of the projectile. Integration over Ω yields the double differential DCS, $d^2\sigma/(dW d\Omega_\gamma)$, which has been tabulated by Pratt and co-workers [13]. In practical MC simulation, it is usual to disregard the correlation between the photon energy and the direction of emission and to factorize this DCS in the form

$$\frac{d^2\sigma}{dW d\Omega_\gamma} = \sigma_{\text{br}} p(W) p(\Omega_\gamma), \quad (4)$$

where σ_{br} is the total cross section, $p(W)$ is the energy spectrum [13] (which varies roughly as W^{-1}) and $p(\Omega_\gamma)$ is the average angular distribution of emitted photons. It should be noted that this factorization also implies the neglect of any deflection of the projectile trajectory in radiative events. A comprehensive review of ordinary bremsstrahlung theory, including emission in the field of atomic electrons, has been given by Seltzer and Berger [14].

Recent studies (see e.g. [15]) show that polarization bremsstrahlung (i.e. the emission of photons as a result of the polarization of the target by the projectile electron) makes a significant contribution to the spectrum from atoms, which increases as the emitted photon energy W decreases below the characteristic x-ray energies of the target atom. This contribution is usually disregarded in MC simulations. In fact, it is not clear whether there is polarization bremsstrahlung in condensed media.

3 Implementation in MC Codes

Analog (detailed, step by step) simulation is feasible under restricted circumstances (relatively low energies, thin targets, ...) and offers a direct method to validate the adopted DCSs by comparison with available experimental data. For high-energy electrons (say, above a few hundred keV), the number of interactions suffered by an electron along its trajectory is too large for detailed simulation; the usual practice is to use “condensed” (class I) simulation methods, in which the global effect of multiple interactions is described by means of approximate multiple scattering theories [16]. Alternatively, one can use “mixed” (class II) schemes in which hard (catastrophic) interactions, with energy loss or angular deflection above given thresholds, are simulated individually. For a given set of DCSs, class II schemes are intrinsically more accurate than class I simulations. The difficulty in using accurate (i.e. numerical) DCSs in a general-purpose code is that the size of the required database (covering e.g. the energy range from 1 keV to 1 GeV) may be exceedingly large.

Recently, we have developed a simple scheme that allows mixed simulation of electron elastic scattering in a wide range of energies [3]. The method is based on a change of variables proposed by Kawrakow and Bielajew [17] that absorbs most of the energy dependence of the DCS and allows a substantial reduction of the database size.

Inelastic scattering and bremsstrahlung emission pose more severe problems for detailed and mixed simulation. The associated DCSs depend on multiple variables and this complicates the storage of information as well as the corresponding random sampling. In the case of bremsstrahlung, the factorization given by (4) has been adopted in most of the available MC codes. The intrinsic angular distribution $p(\Omega_\gamma)$ of emitted photons can be estimated from theory. The total cross section σ_{br} and the energy spectrum $p(W)$ obtained from DWBA calculations can be directly stored in memory. The simulation of each hard radiative event then reduces to the generation of two independent random variables, the energy loss and the polar scattering angle. This method works well for thick samples,

since the angular distribution of emitted photons is dominated by the spread of the electron beam. For thin samples, however, the correlation between photon energy and direction of emission can be important and simulations should be based on the double differential DCS.

In the case of inelastic scattering, the energy loss W and the angular deflection Ω are strongly correlated and we are forced to sample them from the double differential DCS given by (2). This procedure is feasible in limited energy ranges, but it would become too slow for a general-purpose code. The optical-data models provide a practical method to overcome this difficulty. The trick is to do the sampling in two steps; first one samples the active oscillator and then W and Ω are sampled from the DCS of that oscillator. This method has been used in various detailed low-energy codes and can be easily adapted to class II simulation.

The approach described here seems to be satisfactory for most high-energy applications. However, for electrons with energies below 1 keV more sophisticated theoretical methods may be needed to compute the cross sections. Furthermore, coherent scattering effects may invalidate the trajectory model. The generation of secondary radiation, not only knock-on electrons (delta-rays) but also Auger electrons and characteristic x-rays that are emitted after inner-shell impact ionization, is another important feature that needs careful consideration in low-energy simulations.

References

1. L.I. Schiff: *Quantum Mechanics*, 3rd edn. (McGraw-Hill Kogakusha, Tokyo 1968)
2. S.T. Perkins, D.E. Cullen, S.M. Seltzer: *Tables and Graphs of Electron-Interaction Cross Sections from 10 eV to 100 GeV Derived from the LLNL Evaluated Electron Data Library (EEDL), $Z = 1-100$* (Lawrence Livermore National Laboratory 1991) UCRL-50400 vol. 31
3. E. Benedito, J.M. Fernández-Varea, F. Salvat: Nucl. Instrum. Meth. B (submitted)
4. F. Salvat, R. Mayol, J.D. Martínez: J. Phys. B: At. Mol. Phys. **20**, 6597 (1987)
5. F. Salvat: Radiat. Phys. Chem. **53**, 247 (1998)
6. U. Fano: Ann. Rev. Nucl. Sci. **13**, 1 (1963)
7. M. Inokuti: Rev. Mod. Phys. **43**, 297 (1971)
8. C.E. Theodosiou: Phys. Rev. A **16**, 2232 (1977)
9. V.I. Ochkur: Soviet Phys. JETP **18**, 503 (1964) and **20**, 1175 (1965)
10. D.H. Sampson: Phys. Rev. A **34**, 986 (1986)
11. S. Tanuma, C.J. Powell, D.R. Penn: Surf. Interf. Anal. **17**, 911 (1991)
12. H.K. Tseng: J. Phys. B: At. Mol. Opt. Phys. **30**, L327 (1997)
13. L. Kissel, C.A. Quarles, R.H. Pratt: At. Data Nucl. Data Tables **28**, 381 (1983)
14. S.M. Seltzer, M.J. Berger: Nucl. Instrum. Meth. B **12**, 95 (1985)
15. N.B. Avdonina, R.H. Pratt: J. Phys. B: At. Mol. Opt. Phys. **32**, 4261 (1999)
16. M.J. Berger, *Methods in Computational Physics*, ed. by B. Alder, S. Fernbach and M. Rotenberg (Academic Press, New York 1963), vol. 1, p. 135
17. I. Kawrakow, A.F. Bielajew: Nucl. Instrum. Meth. B **134**, 325 (1998)

Modelling the Generalized Oscillator Strength for Low-Energy Electron or Positron Inelastic Scattering

D. Liljequist¹, J.M. Fernández-Varea², and F. Salvat²

¹ Department of Physics, Stockholm University. Box 6730, S-113 85 Stockholm, Sweden

² Facultat de Física (ECM), Universitat de Barcelona. Societat Catalana de Física (IEC). Diagonal 647, E-08028 Barcelona, Spain

1 Introduction

Modelling the generalized oscillator strength (GOS) has shown itself to be a convenient way of treating inelastic scattering of electrons and positrons in Monte Carlo simulations [1–3]. In the Born approximation, the non-relativistic inelastic differential cross section for a positron or an electron colliding with an atom may be written as [4]

$$\frac{d^2\sigma}{dQ dW} = \frac{2\pi e^4}{mv^2} \frac{1}{WQ} \frac{df(Q, W)}{dW}. \quad (1)$$

Here, e and m are the electron charge and mass, respectively, v the velocity of the incident particle, W is the energy loss of the particle in the collision, and Q the “recoil energy”, defined by $Q \equiv q^2/2m$, where $\mathbf{q} = \hbar\mathbf{k}$ is the momentum transfer; q is by kinematics related to the scattering angle θ .

The quantity $df(Q, W)/dW$ is the GOS or, to be more precise, the GOS density. It is subject to the Bethe sum rule

$$\int_0^\infty \frac{df(Q, W)}{dW} dW = Z, \quad (2)$$

where Z is the number of electrons in the target atom. For zero momentum transfer, the GOS becomes the “optical” oscillator strength (OOS) $df(W)/dW = df(0, W)/dW$ that describes optically allowed atomic transitions, and the Bethe sum rule becomes the well-known f sum rule for the OOS.

Within linear response theory, the stopping of charged particles is connected to the optical (dielectric) properties of the penetrated material. The relation between the GOS and the dielectric function ε is given by

$$\frac{df(Q, W)}{dW} = \frac{2W}{\pi\Omega_p^2} Z \operatorname{Im} \left[\frac{-1}{\varepsilon(k, \omega)} \right]. \quad (3)$$

Here, $W = \hbar\omega$ where ω is frequency, and Ω_p is a convenient constant (it is the plasmon energy that would be obtained if all electrons in the target material were free). Equation (3) actually indicates how the GOS is modified to include the

screening and collective excitations that occur in condensed matter (see e.g. [3]). For $Q = 0$, (3) gives the relationship between the OOS as defined here and the dielectric function $\varepsilon(\omega)$, which can be obtained from tabulated optical data [5], including photoelectric absorption data [6]. OOSs calculated from optical data have been used extensively in the so-called optical-data models which, during recent years, have been developed for the Monte Carlo simulation of electron or positron inelastic scattering in condensed matter [7,3].

The OOS has to be “extended” into the $Q > 0$ region to obtain a model of the full GOS, in such a way as to satisfy the Bethe sum rule for every Q . Different physically motivated models have been used for this [8–10], and have been discussed and compared elsewhere [11]. The OOS itself is sufficient for the calculation of low loss energy spectra at small scattering angles $\theta < \theta_{\max}$, by the formula

$$\left[\frac{d\sigma}{dW} \right]_{\theta < \theta_{\max}} = \frac{2\pi e^4}{mv^2} \frac{1}{W} \frac{df(W)}{dW} \ln \left[1 + \left(\frac{mv^2 \theta_{\max}}{W} \right)^2 \right]. \quad (4)$$

Our present work is a first step towards a twofold aim. The first is to model, consistently, a division of the total OOS obtained from optical data, into contributions due to the excitation of electrons in valence bands and in separate inner shells, so as to be able to incorporate the generation of secondary electrons and characteristic secondary radiation into high-precision optical-data Monte Carlo simulations. The second, related aim is to find improved, yet simple OOS models, which will be applied where optical data are cumbersome or not easily available. The degree of detail required depends on the context; as well-known, very simple models are sometimes quite sufficient [1,2].

2 *Ab initio* GOS and OOS Calculations

Methods for the *ab initio* relativistic calculations of the atomic GOSs and OOSs have recently been developed, and will be described in more detail elsewhere [12]. Some results are used in the present paper. Briefly, a self-consistent atomic potential is obtained by the Dirac–Hartree–Slater method. Within the single-active-electron approximation, the GOS is then calculated from matrix elements of the form $\langle \psi_f | E^{i\mathbf{k} \cdot \mathbf{r}} | \psi_i \rangle$, where ψ_i and ψ_f are the initial and final states of the target electron, respectively.

In the limit $k \rightarrow 0$ one has the OOS. The calculation is implicitly performed for a free atom. The results for the contribution to the OOS from inner-shell excitations should also be applicable, to a good approximation, to condensed matter, apart from features that depend critically on the final-state density (near the Fermi level). The absence of band structure and collective interactions means that the contribution to the OOS from valence electron excitations in condensed matter cannot be calculated.

3 Modelling the OOS

When modelling the OOS – as a prerequisite step to modelling the full GOS – a basic requirement is that the f sum rule is always satisfied. The model has to be compatible with the accepted value for the mean ionization potential, I ; this gives the equation

$$Z \ln I = \int_0^\infty \frac{df(W)}{dW} \ln W dW . \quad (5)$$

We may now think of the OOS as split into n contributions $df_j(W)/dW$, $j = 1, \dots, n$, each with its total (integrated) oscillator strength f_j and its partial mean ionization potential (PMIP) I_j [8], calculated by an equation analogous to (5), i.e. replacing Z by f_j , I by I_j and $df(W)/dW$ by $df_j(W)/dW$. Each term in the sum might for example (but not necessarily) represent excitations from a particular atomic shell. We then get the relation

$$Z \ln I = \sum_{j=1}^n f_j \ln I_j , \quad (6)$$

where $\sum_{j=1}^n f_j = Z$, in accordance with the f sum rule.

We now assume that we have a knowledge of the integrated oscillator strength f_v and the PMIP I_v required for a particular contribution to the OOS, e.g. the contribution $df_v(W)/dW$ due to excitation of the valence electrons (exemplified below). Let φ be an arbitrary function, chosen to give the *shape* of $df_v(W)/dW$, i.e.

$$\frac{df_v(W)}{dW} = c \varphi(bW) , \quad (7)$$

where b and c are scaling factors. Inserting this into the integrals by which f_v and I_v are defined, we obtain

$$\ln b = \frac{\int_0^\infty \varphi(x) \ln x dx}{\int_0^\infty \varphi(x) dx} - \ln I_v \quad (8)$$

and

$$c = \frac{bf_v}{\int_0^\infty \varphi(x) dx} . \quad (9)$$

Thus, the required scaling factors are easily calculated. This “scaling procedure” has been found to be quite effective.

4 OOS Density in Cu and Al

The OOS for solid Cu, calculated from optical data [10], is plotted in Fig. 1. On a logarithmic scale, the presently calculated total OOS for a free atom (not shown to avoid cluttering the figure) agrees surprisingly well with the solid-state OOS, down to $W \approx 15$ eV. In the range $W = 10$ –60 eV, the calculated atomic OOS is smooth, while there is a “ripple” on the solid Cu OOS (see Fig. 1). This “ripple”

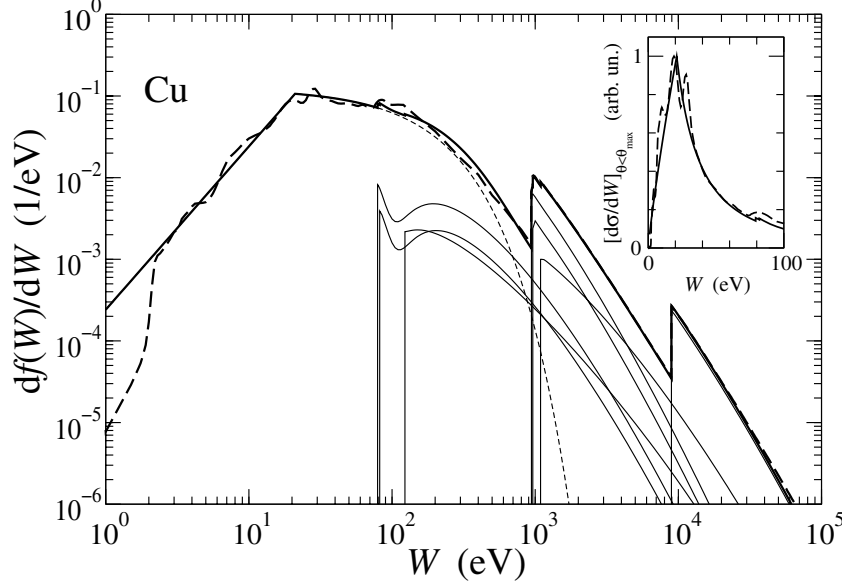


Fig. 1. OOS of metallic Cu. *Thin continuous curves*: calculated atomic inner-shell OOSs. *Thin dashed curve*: valence OOS model (10) after scaling. *Full curve*: sum of the previous, i.e. total presently modelled OOS. *Dashed curve*: total OOS from optical data [10]. Inset figure: low loss spectrum (4) (in arbitrary units), for 60 keV electrons and $\theta_{\max} = 0.1$ rad, calculated from the total presently modelled OOS (*full curve*) and from the optical data OOS (*dashed curve*)

is in fact the details of the characteristic low loss spectrum which, calculated by (4), is shown in the inset in Fig. 1.

For modelling the solid Cu OOS, calculated free-atom OOSs were used for the 1s, 2s, 2p, 3s and 3p subshells, while the contribution from the valence electrons was, by guidance from the optical data, modelled by

$$\varphi(x) = x^2 \Theta(1 - x) + \exp[-(x - 1)/a] \Theta(x - 1). \quad (10)$$

Here, a is a dimensionless shape parameter and Θ is the step function, i.e. $\Theta(y) = 0$ for $y < 0$ and $\Theta(y) = 1$ for $y > 0$. The result for $a = 7.0$ is plotted in Fig. 1. The scaling procedure ensures that the f sum rule is satisfied and the required value $I = 322$ eV obtained. The low loss spectrum obtained by (4) from the model (10) is shown in the inset in Fig. 1.

The present result shows that (10) can be used as a simple and fairly realistic model for the valence contribution to the OOS of solid Cu, consistent with the f sum rule and the mean ionization potential. Low loss spectra of similar shape are seen e.g. in transition metals [13] and water [14], so we expect that the model (10) should also be useful in such cases.

In the case of Al, the use of a Drude model for the plasmon is natural. The OOS of metallic Al, calculated from optical data [10], is shown in Fig. 2, together

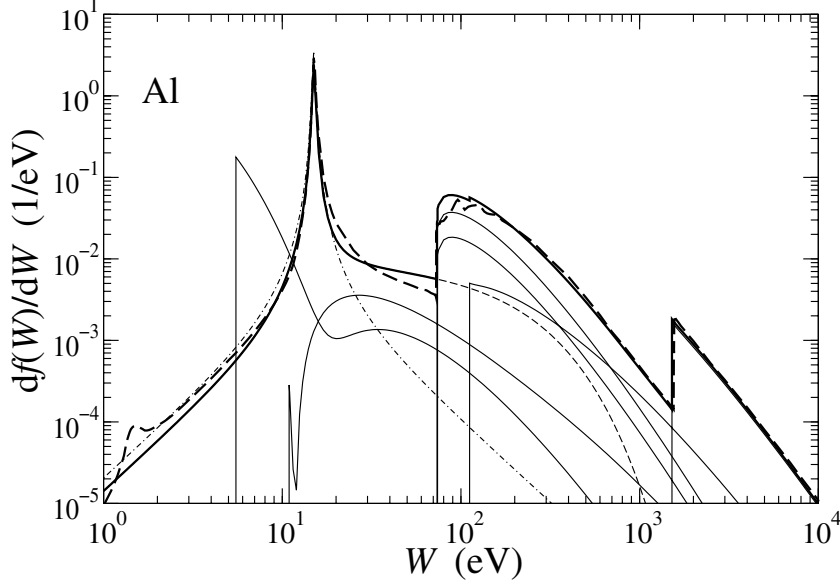


Fig. 2. OOS of metallic Al. *Thin continuous curves:* calculated atomic OOSs. *Dot-dashed curve:* the Drude-peak OOS (11). *Full curve:* sum of calculated inner-shell OOSs and the valence model (12) after scaling. *Dashed curve:* total OOS from optical data [10]

with the different contributions to the free-atom OOS as presently calculated. A contribution with the shape of a Drude peak, i.e.

$$\frac{df(W)}{dW} = f_p \frac{2}{\pi} \frac{W^2 \Gamma}{(W_p^2 - W^2)^2 + W^2 \Gamma^2} \quad (11)$$

is also indicated in Fig. 2, with oscillator strength $f_p = 3.0$, width $\Gamma = 0.54$ eV [15] and $W_p = 15$ eV. This Drude model agrees fairly well with the optical data plasmon peak, but one should note that on the high-energy side, the optical data OOS rather tends to follow the slope of the free-atom valence (3s, 3p) contribution. Moreover, the value $I = 166$ eV for Al, together with the presently calculated atomic inner-shell oscillator strengths and PMIPs, shows by means of the f sum rule and (6), that the valence electron oscillator strength should be about 3.3 and the valence PMIP about 33 eV, while the calculated PMIP of the Drude peak is $\approx W_p$. Thus, the optical data OOS and calculated inner-shell OOSs are apparently not compatible with a valence contribution represented by a simple Drude peak at the plasmon energy. The following model was tried:

$$\varphi(x) = \frac{x^2 g}{(1 - x^2)^2 + x^2 g^2} + a_1 \exp[-(x - 1)/a_2] \Theta(x - 1). \quad (12)$$

The first term is a Drude peak. The parameter g is a reduced width, which is given a value $g = 0.54/15 = 0.036$ that agrees with the optical data plasmon

peak. The second term, with shape parameters a_1 and a_2 , models another contribution to the valence OOS. The position of the Drude peak is very sensitive to a_1 and a_2 under the scaling procedure, so there is limited freedom in choosing these parameters. The total calculated OOS indicated in Fig. 2 – the sum of calculated inner-shell OOS contributions and the model (12) – is found with $a_1 \approx 0.09$ and $a_2 \approx 10.5$; this makes the second term, after scaling, somewhat similar in shape to the free-atom 3s contribution.

Contributions to the OOS of Al have been discussed in detail, e.g. by Shiles et al. [15]. Although our results have yet to be analyzed in the light of [15], they tentatively suggest that the valence contribution can be approximately described as a Drude-shaped plasmon peak, plus an additional contribution involving energy transfers W well above the plasmon energy. The combination of *ab initio* calculated inner-shell OOS and optical data has been used to deduce this.

5 Acknowledgements

This work is part of a research supported by the European Community – Access to Research Infrastructure action of the Improving Human Potential Programme, through the Centre de Supercomputació de Catalunya (CESCA) and the Centre Europeu de Paral·lelisme de Barcelona (CEPBA).

References

1. D. Liljequist: J. Appl. Phys. **57**, 657 (1985)
2. J. Baró, J. Sempau, J.M. Fernández-Varea, F. Salvat: Nucl. Instrum. Meth. B **100**, 31 (1995)
3. J.M. Fernández-Varea, D. Liljequist, S. Csillag, R. Rätty, F. Salvat: Nucl. Instrum. Meth. B **108**, 35 (1996)
4. M. Inokuti: Rev. Mod. Phys. **43**, 297 (1971)
5. D. Palik (editor): *Handbook of Optical Constants of Solids* (Academic, New York 1985)
6. B.L. Henke, E.M. Gullikson, J.C. Davis: At. Data Nucl. Data Tables **54**, 181 (1993)
7. K.O. Jensen, A.B. Walker: Surf. Sci. **292**, 83 (1993)
8. D. Liljequist: J. Phys. D: Appl. Phys. **16**, 1567 (1983)
9. J.C. Ashley: J. Appl. Phys. **69**, 674 (1991)
10. J.M. Fernández-Varea, R. Mayol, D. Liljequist, F. Salvat: J. Phys.: Condens. Matter **5**, 3593 (1993)
11. J.M. Fernández-Varea, R. Mayol, F. Salvat, D. Liljequist: J. Phys.: Condens. Matter **4**, 2879 (1992)
12. S. Segui, J.M. Fernández-Varea, E. Acosta, F. Salvat: to be published
13. D.L. Misell, A.J. Atkins: Phil. Mag. **27**, 95 (1973)
14. M. Dingfelder, D. Hantke, M. Inokuti, H.G. Paretzke: Rad. Phys. Chem. **53**, 1 (1998)
15. E. Shiles, T. Sasaki, M. Inokuti, D.Y. Smith: Phys. Rev. B **22**, 1612 (1980)

Low-Energy Electron Scattering in Solids – a Monte Carlo Approach

H.-J. Fitting and J.-Ch. Kuhr

Physics Department, Rostock University, Universitätsplatz 3, D-18051 Rostock,
Germany

Abstract. This special Monte-Carlo program for low energy electron-solid interaction is based on elastic Mott cross sections and momentum-dependent energy loss functions $\text{Im}[-1/\varepsilon(\mathbf{q}, \omega)]$ in full dispersion $\Delta E(\mathbf{q})$, including electron-electron scattering, volume and surface plasmon excitation, core ionization. Respective secondary electron creation and cascade processes have been included. The electron energy range extends from several keV down to energies $\sim 10\text{eV}$. The calculation is aimed mainly to low energy electron microscopy and electron spectroscopy.

1 Introduction

Low energy electron scattering in the sub-keV range shows certain peculiarities caused by relativistic effects like the elastic Mott scattering, by possible high momentum transfers in inelastic collisions, by resonant interactions in band transitions and plasmon generation as well as by excitation of surface modes like surface plasmons and phonons. E.g., the depth z_0 up to which electrons can couple to surface plasmons amounts to several Angstroms and is comparable with the inelastic mean free path λ_{in} of slow electrons in solids. From that it may be deduced that surface plasmons will strongly affect the surface near secondary electron generation and transport as well as the straggling of low energy primary electrons. Basic information on the physical principles, the MC performance and a series of results is already given in [1,2].

2 MC Direct Access Program

As a part of the MC code presented here, we have developed a numerical algorithm which allows *direct* access to the inverse transformation of a given probability function. The method has been termed “method of direct access to the inverse transformation”. Every time when a random number is generated, the algorithm finds the corresponding scattering value (e. g. scattering angle, energy loss, free flight step length) directly by looking up a multidimensional table, which has been calculated and stored in element-specific files prior to the run. This means that we do not have to perform numerical integrations or elaborate computations of cross sections during run time. As a consequence, the required CPU time for picking up the individual scattering data of an electron trajectory is independent of the mathematical complexity of the underlying model.

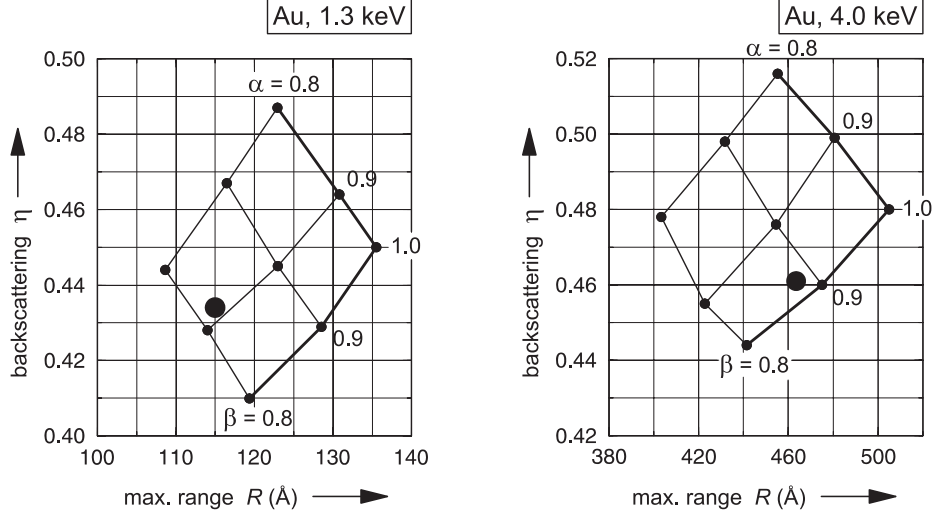


Fig. 1. Verification of the elastic and inelastic scattering mean free path by a MC-calculated network within the backscattering-maximum range plane: (η) - R ; α is the weight of the theoretical elastic mean free path; β the weight of the inelastic mean free path; \bullet actual experimental values of Bronshtein and Freiman [3] as well as Fitting [4]

3 MC Quality Check

In [1] we propose and recommend a general validity and quality test of MC programs by means of a combined backscattering (η) -maximum range (R) check performed in a related (η) - R plane, see Fig. 1. Both integral scattering quantities are experimentally well fixed and allow to approach the actual elastic-inelastic scattering relation.

By multiplication with energy independent weighting factors α and β the elastic and inelastic mean free paths $\lambda_{\text{el}} \propto 1/\sigma_{\text{el}}$ and $\lambda_{\text{in}} \propto 1/\sigma_{\text{in}}$ have been varied in a systematic way,

$$\lambda'_{\text{el}}(E) = \alpha \cdot \lambda_{\text{el}}(E)_{\text{theory}} \quad (1)$$

$$\lambda'_{\text{in}}(E) = \beta \cdot \lambda_{\text{in}}(E)_{\text{theory}} \quad (2)$$

Thus, the combination $\alpha = \beta = 1$ corresponds to the case “theory as given”, but the factors $\alpha < 1$ and $\beta < 1$ do increase the coupling strengths and the cross sections. In both subfigures of Fig. 1 the measured (η) - R pairs are indicated by the large full circle so that the difference between simulation and experiment becomes visible. In order to fit the simulated data to the experiment, we get for the elastic mean free path values $0.88 < \alpha < 0.98$ and for the inelastic mean free path $0.82 < \beta < 0.88$. Thus, the theoretical inelastic coupling strength should be

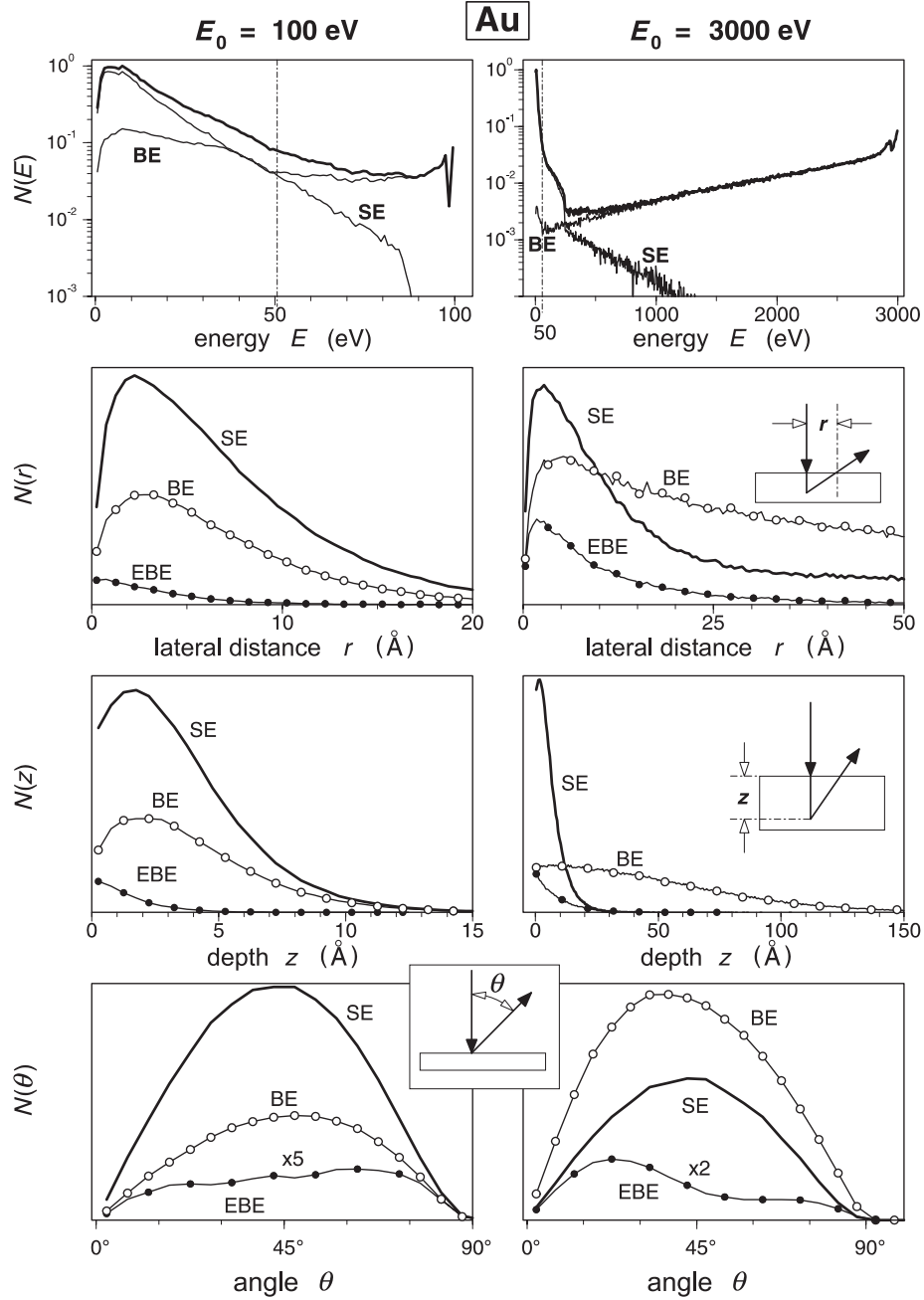


Fig. 2. Full energy distributions (above), spatial (middle), and angular (below) distributions of backscattered electrons from a Au surface (normal incidence with initial energies $E_0 = 100$ and 3000 eV)

increased slightly, whereas the elastic scattering with $\alpha \leq 1$ for 4 keV electrons in gold seems to be described in good quality.

We would like to stress once more that the η -R procedure proposed is recommended first not only for fitting the theory to the experiment but also for a general proof of the validity of a given MC program. This check allows a comparison of different MC programs and presents a criterion for their quality.

4 Backscattering Electron Spectroscopy

Typical reflection energy loss spectroscopy (REELS) experiments are chosen to demonstrate the usefulness of the present low energy MC program. In Fig. 2 (upper part) the overall energy distribution of 100 eV and 3000 eV electrons backscattered from gold are shown separated in backscattered primary electrons BE and true secondary electrons (SE) loosen from the target material. We see that both partial distributions are mixed and the common criterion with a discrimination $E_{SE} < 50$ eV and $E_{BE} \geq 50$ eV becomes invalid for low initial energies, e.g. $E_0 = 100$ eV. Obviously the SE function is overestimated due to prevailing scattering of BE into SE energy regions.

In Fig. 2 (lower part) angular distributions of backscattered (BE), elastically backscattered (EBE) and secondary (SE) electrons are given. SE and BE show typical cosine distributions with respect to the polar angle Θ , but the EBE reflect anisotropic effects of the elastic PWM Mott cross section, especially effective for low energies.

Lateral $N(R)$ and depth $N(z)$ distributions of backscattered (BE), elastically backscattered (EBE) and secondary (SE) electrons are presented in the middle part of Fig. 2. They demonstrate in a convincing manner that the lateral and depth resolution at higher energies can be improved with SE down to about 20 Å, and to a much less extent with BE. On the other hand, at low energies of about 100 eV the spatial resolution of BE and SE is nearly equal, (10 to 20 Å), whereas the EBE resolution is better than 5 Å. This shows the main advantage of low-voltage scanning electron microscopy LV-SEM where, in principle, nanostructures should become resolvable.

Moreover, the results suggest applications in spectroscopic electron microscopy as a mode of analytical microscopy.

References

1. J.-Ch. Kuhr, H.-J. Fitting: phys. stat. sol.(a) **172**, 433 (1999)
2. J.-Ch. Kuhr, H.-J. Fitting: J. Electron Spectr. & Rel.Phén. **105**, 257 (1999)
3. I.M. Bronshtein, B.S. Fraiman: *Vtorichnaya Elektronnaya Emissiya* (Izd. Nauka, Moscow 1969)
4. H.-J. Fitting: phys. stat. sol.(a) **26**, 525 (1974)

Monte Carlo Simulation of Few-keV Positrons Penetrating in Solids

M. Dapor and A. Miotello

Instituto Nazionale per la Fisica della Materia Dipartimento di Fisica dell'Università
di Trento I-38050 Povo, Trento, Italy

Abstract. The initial depth distributions, in selected materials, of thermalized positrons having initial incident energies in the range 1-10 keV, are simulated by a Monte Carlo code utilizing the Relativistic Partial Wave Expansion Method for the calculation of the differential elastic scattering cross section and the Ashley method for calculating stopping power and inelastic mean free path.

1 Introduction

The Monte Carlo method is a very powerful and reliable procedure to study keV electrons and positrons penetrating in solids. In recent years the interest of many experimental papers has been focused on the energy range 1-10 keV of the primary colliding particles: indeed, this range is relevant for very useful techniques in materials analysis such as the Auger electron spectroscopy and the positron annihilation spectroscopy.

The aim of this work is mainly focused to simulate the depth distribution of the incident positrons.

The stopping profile is related to the fraction of particles transmitted below the surface into the bulk: such a fraction is lower than the fraction of positrons (or electrons) transmitted through a thin film because of the backscattering process from the substrate. The usual method to experimentally evaluate the depth distribution, *i.e.* the calculation of the derivative (changed of sign) with respect to the film thickness of the measured transmitted fraction through unsupported thin films [1], neglects the effects of the backscattering from the substrate [2,3]. The Monte Carlo simulation allows, on the other hand, to directly calculate the depth distribution without any necessity to use the fraction of the particles transmitted through unsupported thin films. In this sense the Monte Carlo stopping profiles are of fundamental importance for the accurate evaluation of the initial distributions of the trapped particle necessary for solving the diffusion equation as appropriate for the positron annihilation technique.

2 The Monte Carlo Scheme

Let's consider a positron stream with energy E_0 incident on a homogeneous target in the $+z$ direction. Each particle can be both elastically scattered and/or undergo inelastic interactions by losing energy essentially by collisions with the

atomic electrons and by plasmon excitations. In our Monte Carlo scheme the incident particles are assumed to lose energy with continuity inside the solid, the energy loss processes being all incorporated in the stopping power. The choice of the stopping power (Bethe formula or dielectric function approach [4]) depends on the primary energy: if it is higher than ~ 10 keV the Bethe formula may be used. For energies lower than 10 keV the dielectric function approach for the numerical evaluation of stopping power and inelastic mean free path becomes necessary [4]. The differential elastic scattering cross section for the description of the elastic collisions is numerically computed by the relativistic partial wave expansion method [5,6]. Details of the Monte Carlo codes realized by our group for different energy ranges and materials (elemental and oxides) may be found in our recent papers [7–10].

3 Results and Discussion

We present in Fig. 1 and in Fig. 2 our results concerning the depth profiles of positrons implanted in Al and in Cu respectively. The primary energies considered were 3.0, 5.0, 7.0 and 10.0 keV. The presented stopping profiles were given as $R \cdot P(z, E_0)$ where R is the range and z the depth inside the solid measured from the surface. Note that, for any given and fixed primary energy E_0 , the integration of $P(z, E_0)$ from $z = 0$ to $z = R$ gives the absorption coefficient. The calculated implanted profiles are in agreement with the experimental data of Mills and Wilson [1]. Each curve of implantation was obtained by simulating 10^6 positron trajectories. We also performed similar calculations for carbon, silver, and gold. Starting from the implantation profiles it is possible to calculate the backscattering coefficient r and the range R as a function of the primary energy and of the atomic number. Our results concerning the backscattering coefficients and the ranges are presented in the Tab. 1 and in Tab. 2, respectively. For comparison, we also reported the backscattering coefficients obtained by Coleman et al. [11] both by Monte Carlo method (Tab. 3) and by experiment (Tab. 4). In Tab. 5 we give the experimental values of the range obtained by Mills and Wilson by measuring the transmission of positrons through thin films.

4 Conclusion

We have presented selected examples of backscattering coefficients and ranges of positrons colliding with different solids as calculated with a Monte Carlo code described here and in our previous papers. The reported results compare very well with data both calculated and experimentally obtained by other groups. The calculated stopping profiles of positrons are the essential first step to solve the transport equation utilized with the positron annihilation technique in order to study, for example, defects in solids.

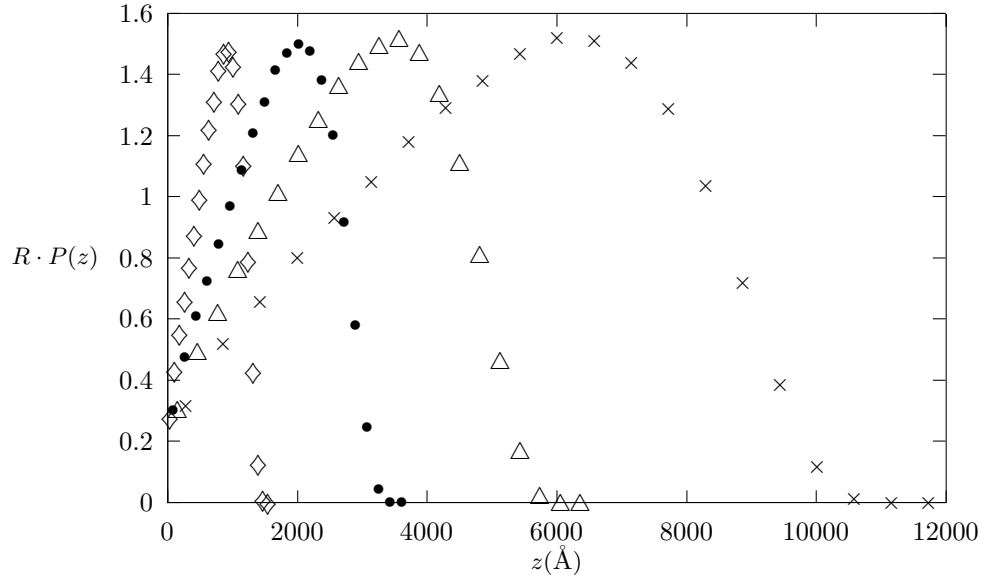


Fig. 1. Stopping profiles for positrons in Al. The primary energies are: 3 keV (\diamond), 5 keV (\bullet), 7 keV (\triangle), 10 keV (\times)

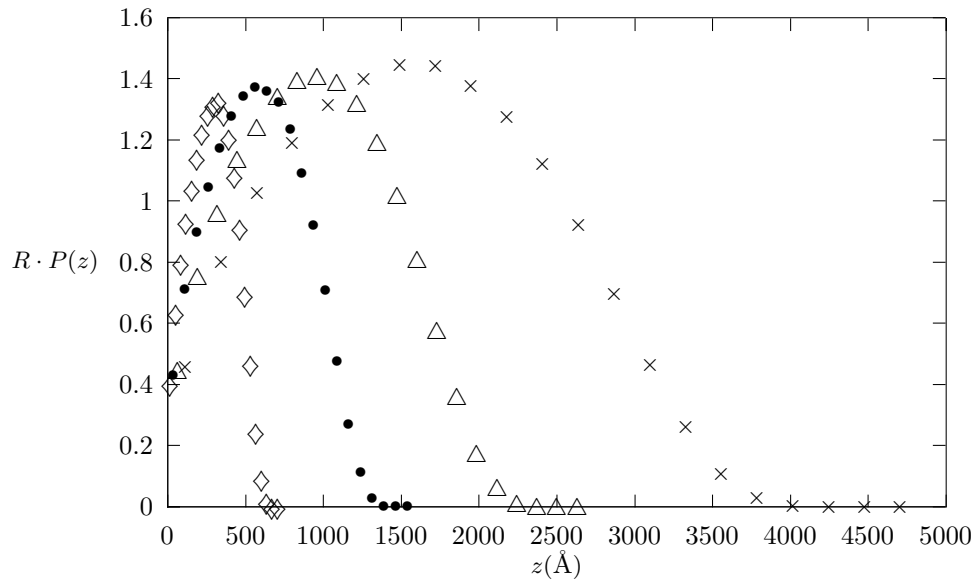


Fig. 2. Stopping profiles for positrons in Cu. The primary energies are: 3 keV (\diamond), 5 keV (\bullet), 7 keV (\triangle), 10 keV (\times)

Table 1. Positron backscattering coefficients. Present Monte Carlo results

$E_0(\text{keV})$	C	Al	Cu	Ag	Au
3.0	0.0674	0.109	0.196	0.186	0.228
5.0	0.0639	0.113	0.212	0.207	0.261
7.0	0.0631	0.116	0.221	0.224	0.285
10.0	0.0629	0.120	0.233	0.246	0.309

Table 2. Maximum range of positrons (\AA). Present Monte Carlo results

$E_0(\text{keV})$	C	Al	Cu	Ag	Au
3.0	1684	1479	644	574	455
5.0	3991	3435	1396	1189	963
7.0	7153	5798	2386	2039	1535
10.0	13390	10655	4042	3496	2551

Table 3. Positron backscattering coefficients. Coleman et al. Monte Carlo results

$E_0(\text{keV})$	Be	Al	Cu	Ag	Au
3.0	0.038	0.115	0.194	0.182	0.242
5.0	0.037	0.126	0.205	0.216	0.290
7.0	0.040	0.125	0.231	0.236	0.316
10.0	0.036	0.128	0.235	0.245	0.340

Table 4. Positron backscattering coefficients. Coleman et al. experimental results

$E_0(\text{keV})$	Al	Cu	Ag	Au
3.0	0.086	0.177	0.168	0.186
5.0	0.112	0.205	0.227	0.232
7.0	0.122	0.226	0.243	0.273
10.0	0.123	0.229	0.277	0.294

Table 5. Maximum range of positrons (\AA). Mills and Wilson experimental results

$E_0(\text{keV})$	Al	Cu
3.1	2150	691
5.0	3650	1246

References

1. A.P. Mills Jr., R.J. Wilson: Phys. Rev. A **26**, 490 (1982)
2. V.E. Cosslett, R.N. Thomas: Brit. J. Appl. Phys. **16**, 779 (1965)
3. M. Dapor: Phys. Rev. B **43**, 10118 (1991)
4. J.C. Ashley: J. Electron. Spectrosc. Relat. Phenom. **46**, 199 (1988)
5. F. Salvat, R. Mayol: Computer Physics Communications **74**, 358 (1993)
6. M. Dapor: J. Appl. Phys. **79**, 8406 (1996)

7. M. Dapor: Phys. Rev. B **46**, 618 (1992)
8. A. Miotello, M. Dapor: Phys. Rev. B **56**, 2241 (1997)
9. M. Dapor, A. Miotello: Eur. Phys. J. Appl. Phys. **5**, 143 (1999)
10. M. Dapor, A. Miotello, D. Zari: Phys. Rev. B **61**, 5979 (2000)
11. P.G. Coleman, L. Albrecht, K.O. Jensen, A.B. Walker: J. Phys.: Condens. Matter **4**, 10311 (1992)

A “Transport” Condensed History Method

E.W. Larsen¹ and D.R. Tolar, Jr.²

¹ Department of Nuclear Engineering and Radiological Sciences, University of Michigan, 2355 Bonisteel Boulevard, Ann Arbor, Michigan 48109-2104, U. S. A.

² Lawrence Livermore National Laboratory, P.O. Box 808, L-95, Livermore, California 94551, U.S.A.

“Condensed history” methods [1–4] are Monte Carlo electron transport simulation algorithms in which the cumulative effects of multiple electron collisions are approximated in a single “step” of (user-specified) path length s_0 . This “step,” often chosen to be many mean free paths, is the distance that each Monte Carlo electron travels between “collisions”. Many current condensed history methods utilize a splitting routine over the range $0 \leq s \leq s_0$. For example, the PENELOPE method [3] splits each step into two substeps; one with length ξs_0 and one with length $(1 - \xi)s_0$, where ξ is a random number from $0 < \xi < 1$. A simpler method was proposed earlier by Berger [1], who suggested that the two substeps should have equal length $s_0/2$. Because condensed history methods approximate the physical transport process, solutions of condensed history simulations contain both statistical errors and a truncation error – which is presumably proportional to some power of the path length s_0 . Also, because condensed history schemes are not equivalent to transport schemes, they contain features that lead to difficulties in some practical calculations. Most notably, it is not always easy to move condensed history Monte Carlo particles accurately across a material interface. For example, as a Monte Carlo particle approaches an interface, the PRESTA method in EGS2 considers a sequence of smaller steps, until the particle is almost traveling in an analog mode [4]. After the particle passes through the interface, the steps are gradually increased back to s_0 .

In this paper we describe a new condensed history algorithm that *is* a transport process. That is, the proposed new method constitutes an exact Monte Carlo simulation of a “stretched” Boltzmann equation. This “stretched” equation permits a larger mean free path – which is user-specified – and a larger scattering angle than the physical transport equation. Thus, because Monte Carlo particles can experience many fewer interactions than physical electrons, the stretched Boltzmann equation may be simulated more efficiently than the original Boltzmann equation. This shortening of particle histories is, of course, the main goal of standard condensed history methods. However, because the method proposed here is the Monte Carlo simulation of a Boltzmann equation, it can be directly implemented in an analog Monte Carlo transport code. Moreover, the difficulties associated with moving conventional condensed history particles across material interfaces are absent in the new method – which treats such interfaces exactly as they are treated in standard analog codes.

To derive a suitable “stretched” transport equation, we consider the original linear Boltzmann equation with continuous slowing down energy dependence. After converting energy loss to path length s , we obtain:

$$\frac{\partial}{\partial s} \psi(\underline{r}, \underline{\Omega}, s) + \underline{\Omega} \cdot \underline{\nabla} \psi(\underline{r}, \underline{\Omega}, s) + L \psi(\underline{r}, \underline{\Omega}, s) = 0 \quad , \quad (1)$$

where, assuming $\Sigma_a = 0$, L is the collision-minus-scattering operator. Using well-known identities, L may be written as:

$$L \psi(\underline{\Omega}) \equiv \sum_{n=0}^{\infty} \left(\frac{2n+1}{4\pi} \right) (\Sigma_{s0} - \Sigma_{sn}) \int_{4\pi} P_n(\underline{\Omega} \cdot \underline{\Omega}') \psi(\underline{\Omega}') d\Omega' \quad , \quad (2)$$

where $P_n(\mu_0)$ are the Legendre polynomials and the mean free path is Σ_{s0}^{-1} .

Now we rewrite (1) as

$$\frac{\partial}{\partial s} \psi(\underline{r}, \underline{\Omega}, s) + \underline{\Omega} \cdot \underline{\nabla} \psi(\underline{r}, \underline{\Omega}, s) + \frac{1}{s_0} \psi(\underline{r}, \underline{\Omega}, s) = \frac{1}{s_0} (1 - s_0 L) \psi(\underline{r}, \underline{\Omega}, s) \quad , \quad (3)$$

where s_0 is a user-specified constant. Next, assuming $s_1 \approx s_0$, we introduce the approximation

$$(1 - s_0 L) \psi(\underline{\Omega}) \approx e^{-s_1 L} \psi(\underline{\Omega}) = \int_{4\pi} G(\underline{\Omega} \cdot \underline{\Omega}', s_1) \psi(\underline{\Omega}') d\Omega' \quad , \quad (4)$$

where

$$G(\mu_0, s_1) = \sum_{n=0}^{\infty} \left(\frac{2n+1}{4\pi} \right) e^{-(\Sigma_{s0} - \Sigma_{sn})s_1} P_n(\mu_0) \quad (5)$$

is the Goudsmit-Saunderson distribution function [5] for $\mu_0 = \underline{\Omega} \cdot \underline{\Omega}'$, the cosine of the angular deflection of a particle after traveling a path length s_1 . Equations (3) and (4) yield

$$\frac{\partial}{\partial s} \psi(\underline{r}, \underline{\Omega}, s) + \underline{\Omega} \cdot \underline{\nabla} \psi(\underline{r}, \underline{\Omega}, s) + \frac{1}{s_0} \psi(\underline{r}, \underline{\Omega}, s) = \frac{1}{s_0} \int_{4\pi} G(\underline{\Omega} \cdot \underline{\Omega}', s_1) \psi(\underline{r}, \underline{\Omega}', s) d\Omega' \quad (6)$$

Like (1), (6) is a linear Boltzmann equation. However, the mean free path in (1) is Σ_{s0}^{-1} , while the mean free path in (6) is s_0 . If s_0 is significantly greater than Σ_{s0}^{-1} , and if $s_1 \approx s_0$ can be well-chosen, then (i) Monte Carlo simulations of (6) should be much less expensive than those of (1), and (ii) the solution of (6) should well-approximate the solution of (1).

Perhaps the simplest choice of s_1 is $s_1 = s_0$. Then, in (6), particles travel a mean distance s_0 between collisions, and when these particles scatter, their new direction of flight is sampled from the Goudsmit-Saunderson distribution for particles that have *exactly* traveled the distance s_0 . The choice $s_1 = s_0$ forms

the basis of Fillipone’s SMART scattering matrix method [6] for deterministic electron transport simulations.

However, a different choice of s_1 may be preferable. Equation (6) can be written in the form

$$\frac{\partial}{\partial s} \psi(\underline{r}, \underline{\Omega}, s) + \underline{\Omega} \cdot \underline{\nabla} \psi(\underline{r}, \underline{\Omega}, s) + M \psi(\underline{r}, \underline{\Omega}, s) = 0 \quad , \quad (7)$$

where M is the “stretched” collision-minus-scattering operator

$$M \psi(\Omega) \equiv \sum_{n=0}^{\infty} \left(\frac{2n+1}{4\pi} \right) \left[\frac{1 - e^{-(\Sigma_{s0} - \Sigma_{sn})s_1}}{s_0} \right] \int_{4\pi} P_n(\underline{\Omega} \cdot \underline{\Omega}') \psi(\underline{\Omega}') d\Omega' \quad . \quad (8)$$

Comparison of (2) and (8) shows that the $n = 0$ terms in the sums on the right sides of these equations are both equal to zero. This confirms that both scattering operators conserve particles. However, the $n = 1$ terms are equal if and only if

$$\Sigma_{tr} = \frac{1 - e^{-\Sigma_{tr}s_1}}{s_0} \quad , \quad (9)$$

with $\Sigma_{tr} = \Sigma_{s0} - \Sigma_{s1}$ = transport cross section. If we require (9) to be satisfied, then (6) preserves the physically-correct scattering power. This requirement is met if s_1 is defined in terms of s_0 and Σ_{tr} by

$$s_1 = \frac{1}{\Sigma_{tr}} \ln \left(\frac{1}{1 - \Sigma_{tr}s_0} \right) \quad . \quad (10)$$

Alternatively, s_0 may be defined in terms of s_1 and Σ_{tr} by

$$s_0 = \frac{1 - e^{-\Sigma_{tr}s_1}}{\Sigma_{tr}} \quad . \quad (11)$$

Either way, to obtain a finite, positive value of s_1 , s_0 must satisfy

$$0 < s_0 < \Sigma_{tr}^{-1} \quad . \quad (12)$$

This is not a serious constraint, as one would rarely wish to choose a mean free path for the stretched Boltzmann equation to be as large as a transport mean free path. It is quite easily shown that s_1 [as defined by (10)] satisfies $s_1 > s_0$, with $s_1 \approx s_0$ for s_0 small. Physically, $s_1 > s_0$ because when a real electron travels a net distance s_0 from its point of origin, the true path length it has traveled exceeds s_0 , due to small angular deflections that cause the path of the electron to deviate slightly from a straight line.

The “Transport Condensed History” (TCH) method proposed in this paper consists of replacing (1) by (5) and (6), with s_0 and s_1 related by (11). [In our simulations, we chose s_1 and then used (11) to determine s_0 .]

The requirement that (9) be satisfied implies that the collision-minus-scattering operators L [(2)] and M [(8)] have the same zero-th and first Legendre

moments. This has a most significant consequence: according to a theory developed by Lewis [7], it follows that for an infinite homogeneous medium, the solutions of the two transport equations (1) and (8), with the same initial conditions at $s = 0$, have *identical* space-angle moments of orders 0 and 1. In other words, if ψ_L is the solution of (1) and ψ_M is the solution of (7), then one has for all $s > 0$

$$\begin{aligned} & \int dx dy dz \int d\Omega x^{n_1} y^{n_2} z^{n_3} \Omega_x^{n_4} \Omega_y^{n_5} \Omega_z^{n_6} \psi_M(\underline{r}, \underline{\Omega}, s) \\ &= \int dx dy dz \int d\Omega x^{n_1} y^{n_2} z^{n_3} \Omega_x^{n_4} \Omega_y^{n_5} \Omega_z^{n_6} \psi_L(\underline{r}, \underline{\Omega}, s) \quad , \end{aligned} \quad (13)$$

where n_1, n_2, n_3, n_4, n_5 and n_6 are any non-negative integers satisfying

$$0 \leq n_1 + n_2 + n_3 + n_4 + n_5 + n_6 \leq 1 \quad . \quad (14)$$

In (14) the integrations over x, y and z are over all space, and the integration over Ω is over the entire unit sphere. Thus, ψ_M preserves certain important properties of the exact solution for all $s > 0$.

To test the TCH method, we consider a monoenergetic 12.5 keV electron pencil beam in an infinite medium of aluminum. The continuous slowing down approximation is employed with multigroup cross sections obtained from the EPICSHOW code [8]. Scattering events, which are modeled using the Screened Rutherford kernel, are the only interactions considered. As the electrons slow down to various energies, the mean position and the standard deviation about this mean are calculated. The results are obtained using three different methods: (i) analog Monte Carlo, (ii) transport condensed history, and (iii) PENELOPE condensed history. For the condensed history codes, s_1 is selected as 1/2 the path length required for the electron to lose the energy of one group. One million particles histories are used.

The mean depth \bar{z} , the standard deviation about this mean σ_z , and the rms value of the radial deflection σ_r for several energies are shown in Tab. 1. Because the zeroth and first angular moments of the Boltzmann equation are preserved, transport condensed history exactly (within statistical error) matches the analog Monte Carlo results for \bar{z} [7]. PENELOPE generally overestimates the mean depth by 4%. As neither transport nor PENELOPE preserve higher-order moments, the predictions for σ_z are about 5% too high. Surprisingly, PENELOPE predicts σ_r within 1%, especially at lower energies. For transport condensed history, these results are only within about 3%. In this problem, the time required to generate the analog Monte Carlo results is roughly ten times greater than the run-times for the other two methods.

To summarize, we have developed a new condensed history method for electron transport that is a true Boltzmann transport process. This TCH method can be implemented in any analog Monte Carlo code with no change in logic. It should be more efficient than present condensed history schemes near material

Table 1. Mean Depth and Standard Deviations for a 12.5 keV Electron Beam (amc = analog Monte Carlo, tch = transport condensed history, pen= PENELOPE condensed history)

Final Energy (keV)	Solution Method	\bar{z} (μm)	σ_z (μm)	σ_r (μm)
10.0	amc	43.56	15.53	29.11
10.0	tch	43.57	17.63	27.88
10.0	pen	45.43	18.46	26.43
8.0	amc	57.82	29.87	51.70
8.0	tch	57.83	32.50	50.07
8.0	pen	59.91	32.47	50.48
6.0	amc	63.01	40.45	66.69
6.0	tch	63.02	42.95	65.09
6.0	pen	65.23	42.86	66.11
3.0	amc	64.47	47.42	75.94
3.0	tch	64.46	49.68	74.45
3.0	pen	66.58	49.73	75.72
1.0	amc	64.51	48.38	77.16
1.0	tch	64.51	50.60	75.70
1.0	pen	66.74	50.65	76.92
0.1	amc	64.51	48.42	77.21
0.1	tch	64.51	50.63	75.76
0.1	pen	66.74	50.79	77.03

boundaries and interfaces because the expense of shrinking or expanding the step sizes [4] is unnecessary.

In future work, we plan to test the TCH method in heterogeneous media and to develop more advanced TCH methods whose scattering operators preserve higher angular moments of the Boltzmann scattering operator. The advantages of doing this become increasingly significant, the more moments that are preserved. In the TCH method outlined in this paper, M is defined such that its first two Legendre moments agree with the first two Legendre moments of L . If an alternate definition of M can be given whose first three Legendre moments agree with those of L , then Lewis’ results [7] show that (13) and (14) again hold – but with the right side of (13) replaced by $2!$ In other words, all space-angle moments of the exact solution up to order two would be preserved, for all $s > 0$. This means that the mean spatial displacements *and* all standard deviations around these displacements would be preserved. Again, for any such scheme, the underlying governing equation would be a “stretched” transport equation, which could be implemented in any analog Monte Carlo code, and which would present no new coding difficulties at material boundaries.

In conclusion, we believe that this general approach has much to offer, and we plan to work on the extensions and improvements described above. Results of such work will be discussed in future publications.

References

1. M.J. Berger: Methods in Computational Physics **1**, 135 (1963)
2. E.W. Larsen: Ann. Nucl. Energy **19**, 701 (1992)
3. J. Baro, J. Sempau, J.M. Fernandez-Varea, F. Salvat: Nucl. Instr. and Meth. **B100**, 31 (1995)
4. A.F. Bielajew: Nucl. Instr. and Meth. **B18**, 165 (1987)
5. S. Goudsmit, J.L. Saunderson: Phys. Rev. **57**, 24 (1940)
6. W.L. Filippone: J. Sci. Eng. **99**, 232 (1988)
7. H.W. Lewis: Phys. Rev. **78**, 526 (1950)
8. D.E. Cullen, *EPICSHOW (Version 97-1)*, Lawrence Livermore National Laboratory, (1997)

A Half Century of Monte Carlo, from Slide Rule and Mechanical Desk Calculator to the Laptop Supercomputer

J.H. Hubbell¹ and S.M. Seltzer²

¹ 11830 Rocking Horse Road, Rockville, MD 20852 USA; all correspondence to:
National Institute of Standards and Technology, Mail Stop 8463, Gaithersburg, MD
20899-8463

² National Institute of Standards and Technology, Mail Stop 8460, Gaithersburg, MD
20899-8460

Abstract. Some early examples of Monte Carlo simulations of radiation transport, prior to the general availability of automatic electronic computers, are recalled. In particular, some results and details are presented of a gamma ray albedo calculation in the early 1950s by Hayward and Hubbell using mechanical desk calculators (+, −, ×, ÷ only), in which 67 trajectories were determined using the RAND book of random numbers, with three random numbers at each collision being used to determine (1) the Compton scatter energy loss (and thus the deflection angle), (2) the azimuthal angle and (3) the path length since the previous collision. Successive angles were compounded in three dimensions using a two-dimensional grid with a rotating arm with a slider on it, the device being dubbed an “Ouija Board”. Survival probabilities along each path segment were determined analytically according to photoelectric absorption exponential attenuation in each of five materials, using a slide rule. For the five substances, H₂O, Al, Cu, Sn and Pb, useful number and energy albedo values were obtained for 1 MeV photons incident at 0° (normal), 45° and 80° angles of incidence. Advances in the Monte Carlo method following this and other early-1950s computations, up to the present time with high-speed all-function automatic computers, are briefly reviewed. A brief review of advances in the input cross section data, particularly for photon interactions, over that same period, is included.

1 Introduction

The aim of this paper is two-fold: (1) to review some of the historical roots and foundation upon which today’s Monte Carlo computations rest, particularly for photon transport applications, and (2) to summarize the status of the photon interaction cross section data upon which these computations depend.

The use of stochastic methods in obtaining numerical solutions for a variety of problems goes back considerably more than a half-century, at least as far as Buffon [1] and his needle-tossing experiment to determine the value of π . As described and illustrated by McCracken [2], Buffon proposed that if a needle is randomly tossed onto a grid of parallel lines separated by twice the length of the needle, landing with equal probability of pointing in any direction, the fraction of needle-landings which intersect a grid-line, is $1/\pi$ for a large number of tosses. McCracken [2] also described how this experiment could be performed using two

Monte-Carlo type wheels, seen now in the form of the “Wheel of Fortune” in a popular television quiz program. One wheel would be divided into segments of the distance twice the length of Buffon’s needle, and the other wheel would be divided into segments of the 360° of possible orientations of the tossed needle. From each pair of randomly obtained numbers, the crossing or non-crossing of a grid line by the needle can be determined. This is more cumbersome than just tossing the needle, but opens the door to programming into an automatic computer.

The earliest applications of the Monte Carlo method to radiation transport problems were primarily for predicting the neutron fluxes associated with the nuclear reactors designed and brought on line in the 1940’s, reflected in the work of Kahn [3,4]. One of the first automatic computers, the ENIAC, was used by Mayer as early as 1949 for neutron transport Monte Carlo calculations as reported at a 1949 symposium on the Monte Carlo method [5].

2 Applications of Monte Carlo to Photon Transport Problems: Some Early Highlights

The earliest application of the Monte Carlo method to photon (gamma-ray) transport problems, of which this author is aware, appears to be a study by Spencer [6] of the effects of polarization on multiple (successive) Compton scatterers. Two sets of 20 case histories involving a total of 150 collisions were generated, identical except one included polarization, the other did not. A small cumulative effect of the polarization was noted. The later examination of this question by Spencer and Wolff [7] using instead the Boltzmann equation and diffusion theory, confirmed a 1 % to 2 % enhancement of the spectral density in the 200 keV to 400 keV secondaries at depths of 8 to 16 mean-free-paths, for 1.277 MeV photons incident on a water scattering medium.

During this same period Wilson [8,9] used a mechanical spin-able cylinder, engraved with lines representing interaction probabilities, to apply the Monte Carlo method to cosmic-ray electron-photon shower studies in the energy range 20 MeV to 500 MeV. Other landmarks in the early evolution of Monte Carlo application to radiation transport problems can be found in the historical account by McCracken [2] already mentioned, also in the excellent reviews by Halton [10], Raeside [11] and Nahum [12]. The most extensive bibliography is provided by Halton [10] who even includes an alphabetical author index to the 251 references cited.

In 1952 there was a party in the home of Ugo Fano, Chief of the Radiation Theory Section at the National Bureau of Standards, the occasion being the completion of the photon cross section tables of Gladys White (Grodstein) [13] covering the energy range 10 keV to 100 MeV for 19 elements $1 \leq Z \leq 92$ plus air, NaI(Tl), water and concrete. For the elements, besides the total cross section and mass attenuation coefficient, the component cross sections for photoeffect, pair (and triplet) production, and scattering (coherent and incoherent combined) cross sections were separately listed.

Using this new tool [13], two other members of Fano's group, Hayward and Hubbell [14,15] used the Monte Carlo method to study the dependence of gamma-ray backscattering (or albedo) on the angle of incidence and on the Z of the target material, to complement an experimental study, also by Hayward and Hubbell [16,17], of these dependencies. The other new tool, put to use in this Monte Carlo simulation, was a preprint of the RAND [18] book of random numbers. Although, as mentioned above, automatic electronic computers such as the ENIAC and at NBS the SEAC were coming on line, programming these machines in octal arithmetic and other complicating factors was non-trivial, and it was decided that useful results could be obtained without recourse to them.

Thus, the devices used by Hayward and Hubbell [14,15] consisted of Marchant and Monroe electrically-powered desk calculators limited to the functions $+$, $-$, \times , and \div , a two-foot long slide rule for exponential functions, and a third device, for compounding deflection and azimuthal angles in three-dimensional space, we dubbed the "ouija board". The "ouija board" employed a stereographic projection of a sphere on a plane circle such that the orthogonality between parallels and meridians is preserved. and the parallels meet the periphery of the circle at equal intervals. The moving part of the device was a transparent plastic arm pivoted at the center of the equator with a radius scribed on it, and a sliding indicator moved radially along it. Each parallel represented a deflection angle θ and each meridian an azimuthal angle ϕ . The sliding indicator was set so that the intersection of the lines on it and on the rotatable arm fell on the point in the grid of the projection corresponding to the deflection and azimuthal coordinates Θ_n and $\Delta\Phi_n$ for the n^{th} collision. Then the rotating part was swung counterclockwise through the angle θ_{n-1} and the new θ_n and $\Delta\phi_n$ were read from the point defined by the new position of the intersecting scribe marks, with the new ϕ_n the summation up to n over $\Delta\Phi_i$. Instead of the "ouija board" we could have used trigonometric tables, but the look-ups and interpolations would have been much more time-consuming.

The calculation was carried out for a point monodirectional source of 1 MeV photons incident on a semi-infinite medium, the surface of which could be mathematically rotated for exit-photon scoring. The medium was first treated as a pure Compton scatterer, disregarding the photoeffect so that the initial calculation would be applicable to all elements. The photoeffect was included analytically afterwards by calculating the survival probability, using the slide rule and its exponential scale, after each collision in each of the five materials: water, aluminum, copper, tin, and lead.

Three random numbers, each between zero and one, were used to determine the properties of each n^{th} Compton collision. The first, R_λ , gave the energy loss suffered by the photon which in turn determined the deflection angle Θ_n . The second random number, $R_{\Delta\phi}$, determined an azimuthal direction $\Delta\Phi_n$ equally probable over the range $\pm 180^\circ$, the sign being determined according to whether the last digit of the random number was even or odd. A third set of random numbers, R_{KN} , was used to determine the path length between collisions $\Delta\ell_i =$

$(-\ln R_{\text{KN}})/\mu_{\text{KN}}(E_i)$ where $\mu_{\text{KN}}(E_i)$ is the integrated Compton scattering cross section at the photon energy E_i in the i^{th} segment.

For each of the five materials studied, survival probabilities S_n were determined using the photoeffect cross sections provided by White [13]. The case histories were followed until the photon energy was less than 30 keV, beyond which S_n usually fell below 0.1 % for water and was much smaller for the higher Z materials. After the computation procedure was established and became routine, it was found that one entire case history could be computed by one person in one day. 67 such case histories (trajectories) were computed, over a period of two or three months.

The surface of the medium was introduced mathematically, and the escape of photons from this surface was determined, with the survival probability at the point of intersection of the surface, for angles of incidence of 0° (normal incidence), 45° and 80° . Both the number albedo and the energy albedo were determined. Also, the approximate number of collisions required to reduce the survival probability to 10 % was found to be 9 collisions in water, decreasing with increasing Z to 2 collisions in Pb, and to reduce to 1 % was 15 collisions in water compared to 3 collisions in Pb.

While this Monte Carlo hand calculation was in progress, various groups were programming similar computational schemes for automatic electronic computers, which could reduce the time required for one history from one day to about half a minute. One of these efforts was by Beach and Theus [19] in which 635 histories were generated using the NAREC (Naval Research Electronic Computer), reported at a Monte Carlo symposium at the University of Florida in Gainesville in 1954. At the same 1954 conference, Berger [20] reported photon transport results obtained from 200 histories computed on the National Bureau of Standards SEAC (Standards Electronic Automatic Computer). More extensive results from this NBS effort, providing reflection, transmission, buildup factor, energy spectra and angular distributions, for incident photons of (0.66, 1.0, 4.0, 10) MeV energies, were published by Berger [21] and by Berger and Doggett [22].

Following these pioneering works, steady progress and refinements have been made in the Monte Carlo application to photon (and electron) transport problems, from the above examples in the 1940's and 1950's, up through the modern codes such as EGS4 [23] and ETRAN [24] the status of which will be discussed by others who are more knowledgeable, at this conference.

3 Status of Photon Interaction Data for Use in Monte Carlo Applications

For a more detailed account of the current status of photon cross section data, reference can be made to two recent review articles [25,26]. Some comments are offered as follows on the individual cross sections needed as input to Monte Carlo photon transport computations: (a) atomic photoeffect, (b) incoherent (Compton) and coherent (Rayleigh) scattering, and (c) pair and triplet production. Currently, photonuclear absorption is omitted from compilations of photon

cross section and attenuation coefficient data, and is ignored in transport computations, although at the peak of the giant dipole resonance between 5 MeV and 40 MeV the photonuclear process can contribute between 2 % (high- Z elements) and 6 % (low- Z elements) to the total cross section, and can produce radioactivities in the target material.

3.1 Atomic Photoeffect

Current photon cross section and attenuation coefficient compilations such as XCOM [27], EPDL [28], and that from Hubbell and Seltzer [29], also the energy-transfer and energy-absorption coefficient computations by Seltzer [30], still depend heavily on the relativistic Hartree-Slater computations of Scofield [31]. There are some minor problems with this data set just above many of the absorption edges, due to limitations of the theoretical model in these regions. New theoretical values by Chantler [32], computed within a consistent Dirac-Hartree-Fock framework, offer some hope of improving the data base in the near-edge regions, but some further evaluation and revision of this data set is still in progress.

3.2 Incoherent (Compton) and Coherent (Rayleigh) Scattering

For incoherent scattering, current cross section compilations still rely heavily on the nonrelativistic Hartree-Fock (except configuration-interaction for $Z = 2$ to 6) compilation drawn from a variety of available sources by Hubbell et al. [33]. A recent relativistic systematic computation by Kahane [34] is available, but the differences from the Hubbell et al. [33] set are small, and less than the uncertainties in available measurements. S-matrix [35] alternative theories and the effects of Compton profile considerations [36,37] are also being investigated, but have yet to find their way into general-use compilations.

For coherent scattering, besides the mostly-nonrelativistic Hartree-Fock compilation assembled by Hubbell et al. [33], relativistic Hartree-Fock [38] and relativistic Hartree-Fock-Slater modified atomic form factors [39] are available. Since this scattering process is most probable in the forward directions, and because the scattered photon suffers negligible energy loss, the choice of model for many photon transport problems is somewhat optional, with the Hubbell-Øverbø [38] relativistic HF values frequently being preferred. In addition to the atomic form factor presentation of coherent (elastic) scattering data, an S-matrix computation [40] and tabulation, differential in scattering angles 0° to 180° for a set of photon energies 50 keV to 1500 keV, for all elements $13 \leq Z \leq 104$ has been provided by Chatterjee and Roy [41].

Harking back to the early work on polarization effects on photon transport by Spencer [6] and Spencer and Wolff [7], there is current interest in polarization consideration, for example by Fernandez et al. [42] and by Namito et al. [36], and is being incorporated, at least as an option, in EGS4 and other Monte Carlo codes.

3.3 Pair and Triplet Production

For the cross sections for electron-positron pair production in the field atomic nuclei and in the field of an atomic electron (triplet production), the main data source is still the computation and tabulation by Hubbell et al. [43]. In this computation, the screening input for nuclear-field pair production was the relativistic HF atomic form factor results of Hubbell and Øverbø [38], and for the triplet computations the non-relativistic HF incoherent scattering function tabulation by Hubbell et al. [33] was used.

4 Summary

Some highlights of the introduction of the Monte Carlo method to photon transport computations in the late 1940's and early 1950's have been recounted, particularly a hand computation of 67 case histories, each history requiring a man-day to complete, in the transition period when automatic electronic computers were entering the scene. The fodder for Monte Carlo photon transport computations, either by hand or by modern laptop super computers, are the basic interaction cross sections, and some comments on the current status of this fodder have been offered, including mention of some work yet to be done.

References

1. G.-L. Leclerc de Buffon: *Essai d'arithmtic morale* (1977)
2. D.D. McCracken: Sci. Am. **192**, 90 (1955)
3. H. Kahn: 'Stochastic (Monte Carlo) attenuation analysis'. In *RAND Report* (1949) p. 88
4. H. Kahn: Nucleonics **6**, 27 (1950), Nucleonics **37**, 60
5. M. Mayer: 'Report on a Monte Carlo calculation performed with the ENIAC'. In *Monte Carlo Method*, ed. by A.S. Householder, G.E. Forsythe and H.H. Germond, (U.S. Nat. Bur. Standards Applied Math. Series, No. 12) pp. 307-20
6. L.V. Spencer: *Polarization of multiply scattered gamma rays*, National Bureau of Standards Interim Report on Contract with the U.S. Office of Naval Research (unpublished)
7. L.V. Spencer, C. Wolff: Phys. Rev. **90**, 510 (1953)
8. R.R. Wilson: Phys. Rev. **79**, 204 (1950)
9. R.R. Wilson: Phys. Rev. **86**, 261 (1952)
10. J.H. Halton: SIAM Rev. **12**, 1 (1970)
11. D.E. Raeside: Phys. Med. Biol. **21**, 181 (1976)
12. A.E. Nahum: 'Overview of photon and electron Monte Carlo'. In *Monte Carlo Transport of Electrons and Photons*, ed. by T.M. Jenkins, W.R. Nelson and A. Rindi (Plenum, New York 1988) pp. 3-20
13. G.R. White (Grodstein): *X-ray attenuation coefficients from 10 keV to 100 MeV*, National Bureau of Standards Report 1003 (1952)
14. E. Hayward, J.H. Hubbell: *The albedo of various materials for 1 MeV photons*, National Bureau of Standards Report 2768 (1953)
15. E. Hayward, J.H. Hubbell: Phys. Rev. **93**, 955 (1954)

16. E. Hayward, J.H. Hubbell: *An experiment on gamma-ray backscattering*, National Bureau of Standards Report 2264 (1953)
17. E. Hayward, J.H. Hubbell: J. Appl. Phys. **25**, 506 (1954)
18. RAND Corporation: *A Million Random Digits with 100,000 Normal Deviates* (The Free Press, New York 1955)
19. L.A. Beach, R.B. Theus: 'Stochastic calculations of gamma ray diffusion'. In *Symposium on Monte Carlo Methods*, ed. by H.A. Meyer (Wiley, New York 1956) pp. 103–122
20. M.J. Berger: 'An application of the Monte Carlo method to a problem in gamma ray diffusion'. In *Symposium on Monte Carlo Methods*, ed. by H.A. Meyer (Wiley, New York, 1956) pp. 89–102
21. M.J. Berger: J. Res. Nat. Bur. Standards **55**, 343 (1955)
22. M.J. Berger, J. Doggett : J. Res. Nat. Bur. Standards **56**, 89 (1956).
23. W.R. Nelson, H. Hirayama, D.W.O. Rogers: *The EGS4 code system*, Stanford Linear Accelerator Center Report SLAC-265 (1985)
24. S.M. Seltzer: Int. J. Appl. Radiat. Isotopes **42**, 917 (1985)
25. J.H. Hubbell: Phys. Med. Biol. **44**, R1 (1999)
26. J.H. Hubbell: X-Ray Spectrom. **28**, 215 (1999)
27. M.J. Berger, J.H. Hubbell: *XCOM: Photon cross sections on a personal computer*, National Bureau of Standards Internal Report 87-3597 (current database updated to 1999, available from the authors on PC disk, also available from site: <http://physics.nist.gov/PhysRefData/Xcom/Text/XCOM.html>)
28. D.E. Cullen, J.H. Hubbell, L. Kissel: *EPDL97: the evaluated photon data library, '97 version*, UCRL-50400, Vol. 6, Rev. 5 (1997)
29. J.H. Hubbell, S.M. Seltzer: *Tables of X-ray mass attenuation coefficients and mass energy-absorption coefficients 1 keV to 20 MeV for elements Z = 1 to 92 and 48 additional substances of dosimetric interest*, National Institute of Standards and Technology Internal Report NISTIR 5632 (1995) (available from site: <http://physics.nist.gov/PhysRefData/XrayMassCoef/cover.html>)
30. S.M. Seltzer: Rad. Res. **136**, 147 (1993)
31. J.H. Scofield: *Theoretical photoionization cross sections from 1 to 1500 keV*, Lawrence Livermore Laboratory Report UCRL-51326 (1973)
32. C.T. Chantler: J. Phys. Chem. Ref. Data **24**, 71 (1995)
33. J.H. Hubbell, W.J. Veigele, E.A. Briggs, R.T. Brown, D.T. Cromer R.J. Howerton: J. Phys. Chem. Ref. Data **4**, 471 (1975). Erratum in J. Phys. Chem. Ref. Data **6**, 615 (1977)
34. S. Kahane: At. Data & Nucl. Data Tables **68**, 323 (1998)
35. R.H. Pratt, L. Kissel, P.M. Bergstrom: 'New relativistic S-matrix results for scattering - beyond the usual anomalous factors/beyond impulse approximation'. In *Resonant Anomalous X-Ray Scattering. Theory and Applications*, ed. by G. Materlik, C.J. Sparks and K. Fischer (Elsevier, 1994) pp. 9-33
36. Y. Namito, H. Hirayama, S. Ban: Radiat. Phys. Chem. **53**, 283 (1998)
37. J.H. Hubbell: *An examination and assessment of available incoherent scattering S-matrix theory, also Compton profile information, and their impact on photon attenuation coefficient compilations*, National Institute of Standards and Technology Internal Report 6385 (1999)
38. J.H. Hubbell, I. Øverbø: J. Phys. Chem. Ref. Data **8**, 69 (1979)
39. D. Schaupp, M. Schumacher, F. Smend, P. Rullhusen, J.H. Hubbell: J. Phys. Chem. Ref. Data **12**, 467 (1983)
40. S.C. Roy, L. Kissel, R.H. Pratt: Radiat. Phys. Chem. **54**, 3 (1999)

41. B.K. Chatterjee, S.C. Roy: J. Phys. Chem. Ref. Data **27**, 1011 (1998)
42. J.E. Fernandez, J.H. Hubbell, A.L. Hanson, L.V. Spencer: Radiat. Phys. Chem. **41**, 579 (1993)
43. J.H. Hubbell, H.A. Gimm, I. Øverbø: J. Phys. Chem. Ref. Data **9**, 1023 (1980)

Comparison of EGS4 and Measurements Regarding K-X ray and Bremsstrahlung Photons

Y. Namito and H. Hirayama

KEK, Japan

Abstract. In 1999, we implemented a function to calculate electron impact ionization (EII) into the EGS4 code. This modification is updated so that it is ready to be integrated into the EGS5 code. We performed various comparisons between the modified code and the measurements regarding K-X ray and bremsstrahlung photons to verify the validity of the code. As a K-shell EII cross section, Gryziński's relativistic cross section was mainly used, as this cross section gave the best agreement between the calculation and the measurement. The deviation of the calculated and the measured K-X ray intensity was 15% in average.

1 Introduction

Calculating the energy spectra and angular distribution of photons induced by interactions between a keV-MeV electron beam and a target is one of the important problems in a field where a general-purpose electron-photon transport code can be applied. For example, a simulation of the widely used X ray generator is closely related to this kind of calculation.

When an electron beam is incident on a sample, a K-X ray is generated via two channels:

1. Bremsstrahlung photon is absorbed by atoms (photoelectric effect)
2. Electron collides with K shell electron and a vacancy is created in K shell. This is called as EII.

In the original EGS4 code [1], only channel 1) was considered. In 1999, we implemented channel 2) to EGS4 code. [2]

Recently we updated this improved program so that it is ready to be built up for EGS5. [3,4] Here, the following modifications were applied to the EII K-X calculation.

1. Fluorescence yield was updated from [5,6] to [7,8].
2. Possible underestimation of K_β is now avoided by means of improvement of piecewise linear fitting named "Local extrapolation method" [9] and increasing the number of photon energy intervals.
3. The number of energies of K-X rays is increased from 4 to 10.
4. EII of any element in compound and mixture is treated.

Items 1-3 were due to the change in the treatment of photoelectric effect related phenomena in EGS4 code [10].

Comparison of the EGS4 code and measurements regarding K-X rays and bremsstrahlung induced by interactions between an electron beam and samples were performed to verify the validity of the improvement of the code.

Several authors studied this field. Távara and Morton also introduced EII into EGS4 code and simulated Placious's experiment [11]. Fernández-Varea et al simulated X-ray spectra due to electron beam which was measured by Acosta et al. [12]. These measurement are mentioned in the next section.

2 Method

We simulated following three measurements.

1. Dick et al performed a systematic measurement of K-X ray when electron beam of 10, 20, 40, 100, 200, 500, 1500 and 3000 keV hits target(Al, Ti, Cu, Ag and Au) normally [13]. K-X ray yield per incident electron was measured at $\theta = 120^\circ$ and 180° .
2. Acosta et al measured photon spectra emitted from a Cu target at $\theta = 130^\circ$ using Si detector when an electron beam of 20 keV incident normally on the target [15].
3. Placious measured bremsstrahlung photons and K-X rays from Sn targets at $\theta = 70^\circ$ and 140° for the normal incidence of 100 keV electrons [15,16].

EGS4 calculations with and without the improvement to treat EII were performed. As a K-shell EII cross section, Gryziński's relativistic cross section [17] was used. All the comparisons were done in absolute, i.e. no normalization between the measurement and the calculation were done.

To simulate Acosta's experiment, a two stage calculation was done. In the first stage, photons emerging from the target to $\theta=135-145^\circ$ were scored (A). In the second stage, we calculated energy deposition in Si detector using "A" as a source. All the absorbing layers in Si detector were considered.

3 Comparison of Calculation and Measurement

3.1 K-X ray Yield

The calculated and measured K-X ray yields are shown in Fig. 1. The statistical error in the calculation is within 3% for EGS4+EII, 10% and 5% for EGS4 of Al and other targets, respectively. The geometric average of the ratio of the calculated K-X ray yield to the measured one is shown for each target in Table 1. Here, a result of EGS4+EII calculation using Casnati's EII cross section [18,19] is also shown, whose agreement with measurement is worse comparing to the calculation using Gryziński's cross section.

The EGS4 calculation apparently becomes underestimated with decreasing Z of the target. C/M is only 0.0027 for Al, but C/M is 0.85 for Au. The degree of

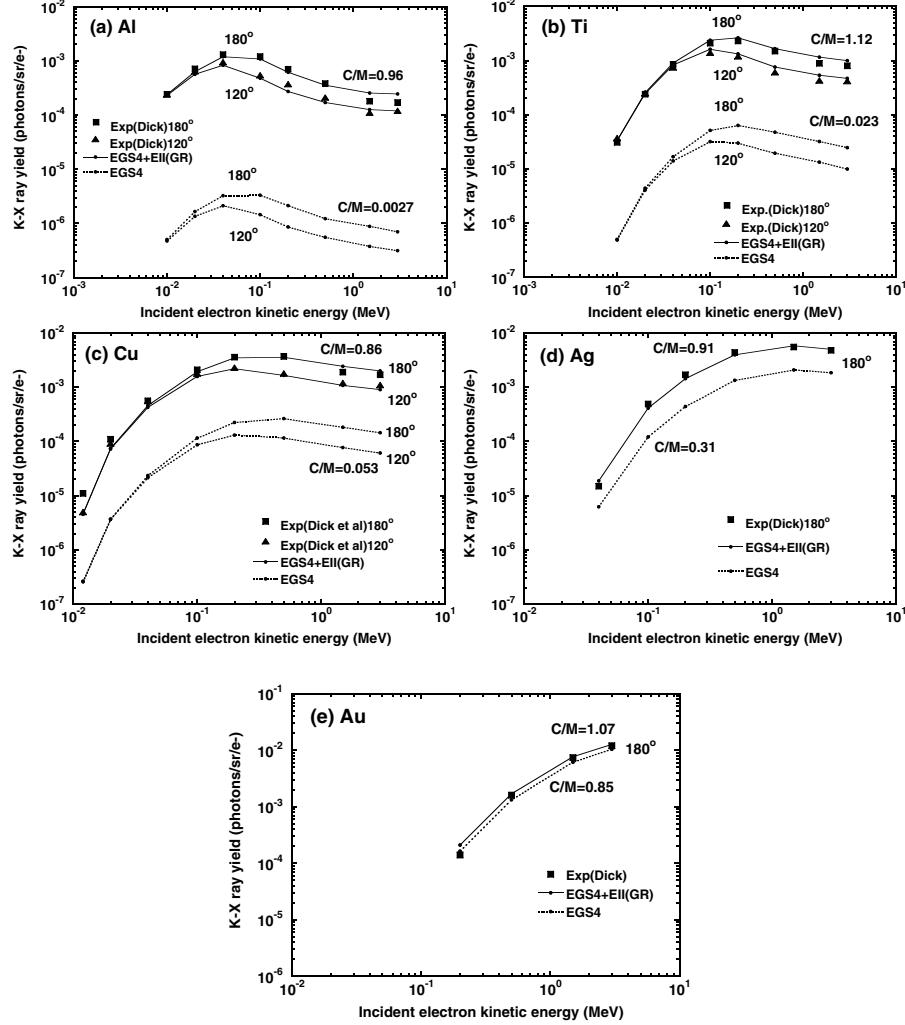


Fig. 1. Comparison of the K-X ray yield. The measured values by Dick et al. are indicated by filled boxes ($\theta = 180^\circ$) and filled triangles ($\theta = 120^\circ$). EGS4: EGS4 calculation without EII; EGS4+EI: EGS4 calculation with EII using Gryziński's cross section. (a) Al (b) Ti (c) Cu (d) Ag (e) Au

underestimation depends weakly on the electron incident energy and the scoring angle.

For Al, Ti, Cu and Ag samples, the dominant contribution of K-X ray is EII. For Au sample, the dominant contribution of K-X ray is the photoelectric effect of bremsstrahlung photons.

Table 1. Geometric average of C/M of K-X ray yields. Gr and Ca means the calculation result using Gryziński's and Casnati's cross sections, respectively

Target	Al	Ti	Cu	Ag	Au	Av
EGS4	0.0027	0.023	0.053	0.31	0.85	0.061
EGS4+EII(Gr)	0.96	1.12	0.86	0.91	1.07	0.98
EGS4+EII(Ca)	1.16	1.40	1.18	1.11	1.16	1.21

3.2 Photon Spectra from a Cu Target

The calculated and measured photon spectra from a Cu target are shown in Fig. 2. C/M=0.92, 0.83 and 0.85 for energy intervals of 1-7.6 (low energy bremsstrahlung), 7.6-9.2 (K-X) and 9.2-20 keV (high energy bremsstrahlung) when EII is considered in a calculation. When EII is ignored, C/M=0.07 in K-X region. Gauss smearing of FWHM=1.6 keV was applied to the EGS4 result to simulate the energy resolution of the Si detector.

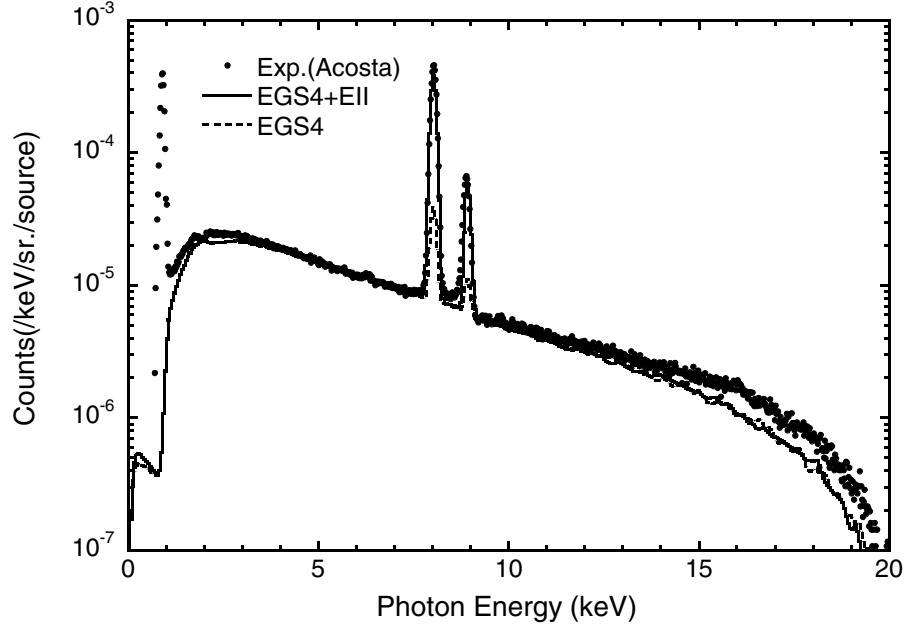


Fig. 2. Spectra of the bremsstrahlung and K-X rays from a Cu target toward $\theta = 130^\circ$. A 20 keV electron beam is normally incident on the target. The closed circle indicates a measurement using a Si detector by Acosta et al. The solid and dashed lines indicates the EGS4 calculation with EII using Gryziński's cross section and without EII

3.3 Photon Spectra from a Sn Target

The calculated and measured photon spectra from Sn target are shown in Fig. 3. $C/M=0.74$ and 0.88 at $\theta = 70^\circ$ and $\theta = 110^\circ$, respectively for energy intervals of 10.0-36.0 keV (K-X) when EII is considered in a calculation. When EII is ignored, $C/M=0.52$ and 0.67 at $\theta = 70^\circ$ and $\theta = 110^\circ$, respectively for energy region of 10.0-36.0 keV.

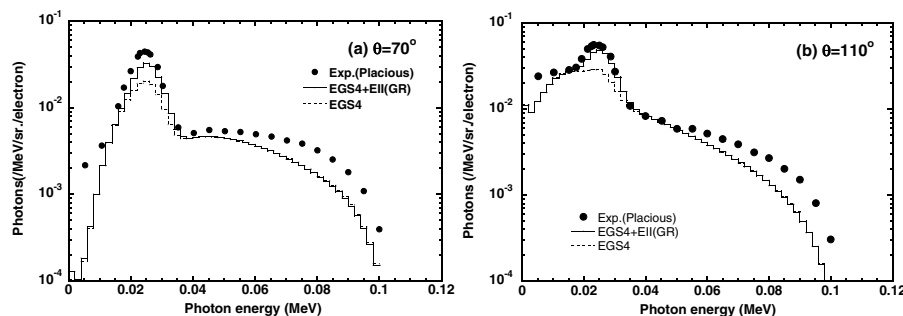


Fig. 3. Spectra of the bremsstrahlung and K-X rays from a Sn target toward (a) $\theta = 70^\circ$ and (b) $\theta = 120^\circ$, respectively. A 100 keV electron beam is normally incident on the target. The closed circle indicates a measurement using an NaI detector by Placious. The solid and dashed lines indicates the EGS4 calculation with EII using Gryziński's cross section and without EII

As NaI detector was used in this measurement, energy resolution is poor comparing to Acosta's measurement. Then, large amount of bremsstrahlung photons contributed to the counts in the K-X ray energy region. Gauss smearing of $\text{FWHM}=8$ keV was applied to the EGS4 result to simulate energy resolution of the NaI detector.

4 Discussion

Among 62 comparisons between Dick's K-X ray yield measurements and EGS4 calculations, $|C/M - 1|$ was within 0.15 for 41 cases. We suspect the largest source of the discrepancy between measurement and calculation is the error in EII cross section.

In the comparison of Dick's measurements and the EGS4 calculations, $C/M=0.79$ when electron energy=20 keV, target=Cu and $\theta = 120^\circ$. In the comparison of Acosta's measurement and EGS4 calculation, $C/M=0.83$. The close agreement of two C/M values suggests that both experiment values are consistent.

In the comparison of Acosta's measurement and EGS4 calculation, the high energy part of bremsstrahlung photon was underestimated. Similar underestimation of bremsstrahlung at high photon energy side was also seen in the com-

parison of photon spectra from a Sn target. We guess these underestimations can be corrected by using better bremsstrahlung photon generation cross sections.

5 Conclusion

Systematic comparison of measured and calculated K-X ray yield from various targets for electron beams of 0.01 to 3 MeV was performed without any normalization. General agreement between measurement and calculation show the validity of improved EGS4 code.

For Al, Ti, Cu and Ag samples, the dominant contribution of K-X ray is EII. For the Au sample, the dominant contribution of K-X ray is photoelectric effect of bremsstrahlung photon.

References

1. W.R. Nelson, H. Hirayama, D.W.O. Rogers: SLAC-265 (Stanford University, Stanford, 1985)
2. Y. Namito, H. Hirayama: Nucl. Instrum. and Meth. A **423**, 238 (1999)
3. Y. Namito, H. Hirayama: *LSCAT: Low-energy Photon-scattering Expansion for the EGS4 Code (Inclusion of Electron Impact Ionization)*, KEK Internal 2000-4 (2000)
4. ftp://ftp.kek.jp/kek/kek.egs4/kek.improve/kek.improve.*
5. C.M. Lederer V. S. Shirley, Eds.: *Table of Isotopes* 7th edn (Wiley-Interscience, New York, 1978)
6. W. Bambynek et al.: Rev. Mod. Phys. **44**, 716 (1972)
7. V.S. Shirley, Ed.: *Table of Isotopes* 8th edn. (Wiley-Interscience, New York, 1996)
8. W. Bambynek: post-deadline abstract published in the Proc. of the Conference on X-ray and inner-shell processes in atoms, molecules and solids, Leipzig, Aug 20-24 (1984)
9. Y. Namito, H. Hirayama: 'Improvement of the Cross-section and Branching-ratio Evaluation in EGS4 in the Energy Interval Which Has an Absorption-edge'. In: *8th EGS4 Users' Meeting in Japan, Japan, Aug. 1-3 1999* ed. by. H. Hirayama, Y. Namito and S. Ban, KEK Proc. **99-15**, (1999) pp.1-6
10. H. Hirayama, Y. Namito: *General Treatment of Photoelectric Related Phenomena for Compounds and Mixtures in EGS4*, KEK Internal 2000-3
11. L.M.N. Távora, E.J. Morton: Nucl. Instrum. and Meth. A **143**, 253 (1998)
12. J.M. Fernández-Varea, X. Lovet, E. Acosta, E. Benedito, F. Salvat: 'Simulation of X-ray Spectra Generated by Kilovolt Electron Bombardment'. These Proceedings p. 105
13. C.E. Dick, A.C. Lucas, J.M. Motz, R.C. Placious, J.H. Sparrow: J. Appl. Phys **44**, 815 (1973)
14. R. Placious, J. Appl. Phys. **38**, 2030 (1967)
15. E. Acosta, X. Llovet, E. Coleoni, J.A. Riveros, F. Salvat: J. Appl. Phys. **83**, 6038 (1998)
16. M.J. Berger, in: *Monte Carlo transport of Electron and Photons*, eds. T. M. Jenkins, W.R. Nelson and A. Rindi (Plenum, New York, 1988) pp.216, Figure 8.27b
17. M. Gryziński: Phys. Rev. **138**, A 305, A 322, A 336 (1965)
18. E. Casnati, A. Tartari, C. Baraldi: J. Phys. B **15**, 155 (1982)
19. E. Casnati, A. Tartari, C. Baraldi: J. Phys. B **16**, 505 (1983)

EGS4 Modelling of Coherent Scattering in the Biological Context

A. Taibi, A. Tartari, and M. Gambaccini

Dipartimento di Fisica, Università di Ferrara, via Paradiso 12, 44100 Ferrara, Italy

1 Introduction

Design of medical imaging systems based on the detection of small-angle x-ray scattering is a subject of renewed interest. The potential of coherent scatter-based techniques for tissue characterisation has been recently investigated both theoretically and experimentally by several authors [1–4]. Measured molecular form factor data are now available for some tissues and tissue-equivalent materials [5–8]. An adaptation of these data to the standard EGS4 code has been very recently performed as part of a Monte Carlo simulation study for mammographic applications [9]. The PEGS4NB mortran file, which is included in the LSCAT package [10] was modified in order to read new data (form factors and cross sections) that take into account the effects of molecular interference in coherent scattering. The interference effect in coherent scattering for seven materials of biological interest is now incorporated in the new version of LSCAT [11].

However, it is well known that the elemental composition of a body tissue is dependent upon the relative amounts of the various substances (water, lipid, minerals, etc.) which make up the tissue [12,13]. Woodard and White also report that for certain of these tissues, such as adipose tissue and mammary gland, the lipid content varies within a wide range, 61.4–87.3% and 5.6–56.2% by mass, respectively. Due to the natural variations in the composition of certain body tissues, measurements on unclassified excised samples are likely to exhibit an intensity scattering pattern which is significant only for that specific situation. This means that to thoroughly simulate real tissues the user needs to change the percentage constituents of the biological organs. To this aim a basis set of data for the simulation of body tissues was proposed by Tartari and co-workers [8]. They also showed that for water-like tissues (i.e. blood) the molecular form factor can be factorized as

$$F_{mol}^2(x) = F_{free}^2(x) \cdot [1 + H(x)] \quad (1)$$

where F_{free} is the form factor calculated by using the free-atom model, $x = \sin(\theta/2) \cdot E/hc$ is the momentum transfer, and $H(x)$ is the structure function which accounts for the interference effects. The structure function for liquid water at various temperatures was derived from x-ray diffraction data by Narten and Levy [14].

Soft tissue is mainly made up of fat and water whilst bone tissue can be considered as a mixture of osseous tissue (cortical and trabecular bone) and

soft tissue (red and yellow marrow). The dry bone has a mineral part, i.e. the hydroxyapatite (HA), and a ‘non-mineral’, i.e. the bone matrix (BM). Since both red and yellow marrow are mainly made up of fat and water, a set of four components, namely fat, water, bone matrix and hydroxyapatite, can represent a basis for the composition of the human tissues. Once the basis is defined one can simulate any tissue by linear combination.

The purpose of this work is to apply the above approach for generating molecular form factors and coherent cross sections within the PEGS4 data file in order to simulate body tissues as a mixture of basis components. The previous implementation [9] has been expanded by including the new set of data. The performance of the new EGS4 system has been tested with various configurations by changing both the tissue and its composition. Results for the intensity and angular distribution of scattered radiation from cylindrical absorbers will be presented and compared with known experimental data.

2 Simulation Model

The biological tissues were modelled by using the EGS4 code with the new version of LSCAT [11] to generate the pertinent PEGS4 data files. The molecular form factor data of the four substances used as basis to simulate human tissues were taken from [5] for fat, [15] for water, and [8] for BM and HA. The elemental composition of each basis component is reported in Tab. 1.

Table 1. Elemental composition by mass of the four basis materials

Substance	H	C	N	O	P	Ca	Density (g/cm ³)
Water	0.1119			0.8881			1.00
Fat	0.1190	0.7720		0.1090			0.9230
Bone Matrix	0.0344	0.7140	0.1827	0.0689			-
Hydroxyapatite	0.0020			0.4140	0.1850	0.3990	2.74

The measured molecular form factors were first interpolated and tabulated at the same momentum transfer values as the tables by Hubbell and Øverbø [16], i.e. the relativistic form factors used by the default version of the EGS4 code. The form factor values of the tissue to be simulated were calculated by using the formula:

$$F_{tissue}(x) = \sqrt{a_1 F_{fat}^2(x) + a_2 F_{water}^2(x) + a_3 F_{BM}^2(x) + a_4 F_{HA}^2(x)} \quad (2)$$

where a_i are the relative amounts of the basis components. The correspondent cross section values were calculated via numerical integration of the conventional

equation for the differential cross section:

$$\sigma_{coh} = \frac{r_e^2}{2} \int_0^\pi (1 + \cos^2\theta) F_{tissue}^2(x) 2\pi \sin\theta d\theta \quad (3)$$

To calculate the molecular form factors for water-like tissues the structure function tabulated in [14] was first interpolated in the same fashion as above. Then, the pertinent form factors of the ‘free’ molecule were calculated from the independent atomic scattering approximation:

$$\frac{F_{free}^2(x)}{W} = \sum_i \frac{w_i}{A_i} F^2(x, Z_i) \quad (4)$$

where w_i is the mass fraction of the element i , A_i is the atomic mass of the element i and W is the molecular weight. Finally, such form factors were multiplied by the structure function values according to (1). All these calculations were performed by making use of simple C programs specifically written.

In order to simulate a specific tissue the user has to calculate the elemental composition and density of the mixture by making use of Tab. 1. Once the PEGS4 input file is created the data file is generated by simply typing the pertinent form factor and cross section file names as required by the PEGS4NB program.

3 Results and Discussion

The first test that demonstrates the validity of this approach is a comparison between measured and calculated form factor data. In Fig. 1 the form factor of the adipose tissue measured by Peplow and Verghese [6] (*continuous curve*) is shown together with the form factor of the adipose tissue calculated as a mixture of 80% fat and 20% water (*dashed curve*). It is worth noting that three different sources of data were used in this example yet there is a very good agreement in the trend of the compared curves.

In Fig. 2 the form factor of blood (*continuous curve*) measured by Peplow and Verghese is compared to the form factor of blood calculated via (1) (*dashed curve*). The composition to calculate the free-atom form factor of blood was taken from [13]. The agreement is very good, thus showing that for water-like tissues molecular form factors can be easily extracted from known data.

3.1 Soft Tissue

It is well known that the relative proportion of adipose and fibroglandular tissue in the adult female breast varies between individuals and is age related. For this reason coherent scatter measurements of unclassified normal tissue samples cannot be used to simulate clinical examinations. A more useful approach would be a segmentation of breast tissue in fat and water components with variable

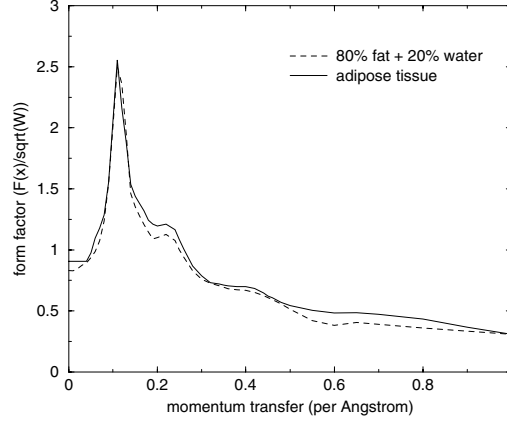


Fig. 1. Comparison of measured (*continuous curve*) and calculated (*dashed curve*) molecular form factor data for adipose tissue

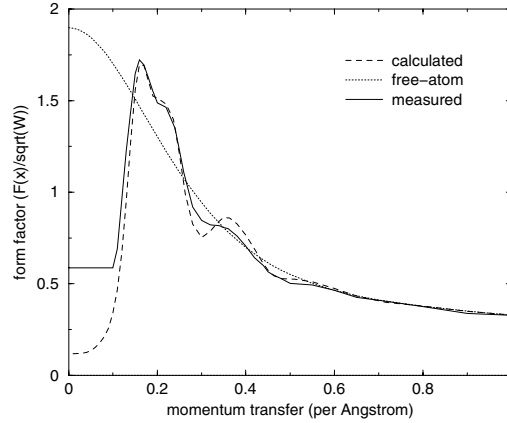


Fig. 2. Comparison of form factor data for blood tissue: Measured values (*continuous curve*), calculated values (*dashed curve*). The form factor of blood calculated in the free-atom approximation is also shown (*dotted curve*)

weight. Figure 3 shows in comparison the scatter profiles for a 20 keV monochromatic beam incident on a 5 cm-thick breast sample. The continuous curve is a simulation of an unclassified breast tissue by using the molecular form factor data of [6] whilst the other two curves represent a different mixture of fat and water calculated by using the molecular form factor data of the basis materials. The comparison reveals that the unclassified breast sample was made up of an amount of 40% fat and 60% water.

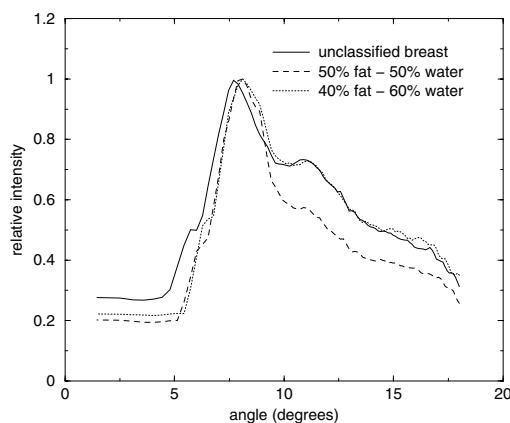


Fig. 3. Comparison of coherent scattered photons from a 5 cm-thick breast sample

3.2 Bone Tissue

Royle and Speller carried out a set of diffraction measurements in the diagnostic x-ray energy range by using human femoral head samples [17]. Their work aimed to obtain information on the relative quantities of bone and marrow tissue within trabecular bone. In fact, the bone-to-marrow ratio is a parameter to assess the osteoporotic state of the bone. The scattered intensity of a fresh femoral head was first simulated by using the proportions of osseous tissue and yellow marrow reported in [12,18] which refer to ‘healthy, adult humans’. The healthy bone was modelled as 15% water, 36% fat, 13% BM, and 36% HA and the simulation performed by using the experimental conditions described in [17]. Figure 4 shows that the experimental data are not in good agreement with the simulated data of healthy bone (*dotted curve*). The scatter profile exhibits two maxima due to the fat and hydroxyapatite content. A close agreement with the experimental data is obtained if the relative amount of marrow is increased for the femoral heads used in the experiment were osteoarthritic samples removed from elderly patients. The scatter profile of the osteoporotic bone (*continuous curve*) was modelled as 25% water, 55% fat, 5% BM, and 15% HA.

4 Conclusions

A basis set of molecular form factors have been implemented in the EGS4 code to enable the functionality for coherent x-ray scattering simulations in the field of diagnostic radiology. The segmentation of biological tissues in four components has been successfully tested and the scatter distributions compared with known experimental data. The results showed that in principle it is possible to simulate any experimental situation by simply changing the relative amount of the basis materials. As far as the investigation of coherent scatter-based techniques is concerned, it is believed that the described approach can represent a useful tool

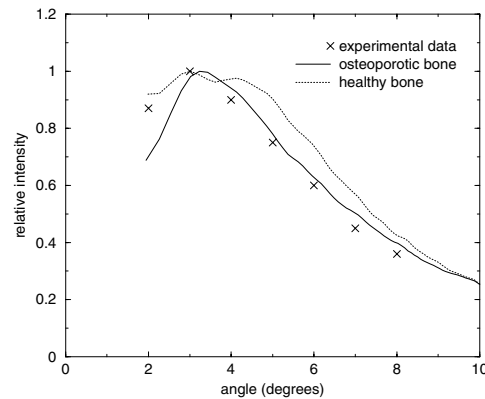


Fig. 4. Comparison of bone tissue simulations with experimental data

to model the widely varying composition of human tissues both in healthy and diseased persons.

References

1. R.J. Leclair, P.C. Johns: *Med. Phys.* **25**, 1008 (1998)
2. D.L. Batchelar, M.S. Westmore, H. Lai, I.A. Cunningham: *SPIE Proc.* **3336**, 707 (1998)
3. R.C. Barroso, R.T. Lopes, E.F.O. de Jesus, L.F. de Oliveira: 'Synchrotron Biomedical Applications using X-ray Diffraction Tomography'. In: *IEEE Nuclear Science Symposium Conference Record, Seattle, USA, 24-30 October 1999*
4. K. Kleuker, P. Suortti, W. Weyrich, P. Spanne: *Phys. Med. Biol.* **43**, 2911 (1998)
5. A. Tartari, E. Casnati, C. Bonifazzi, C. Baraldi: *Phys. Med. Biol.* **42**, 2551 (1997)
6. D.E. Peplow, K. Verghese: *Phys. Med. Biol.* **43**, 2431 (1998)
7. G. Kidane, R.D. Speller, G.J. Royle, A.M. Hanby: *Phys. Med. Biol.* **44**, 1791 (1999)
8. A. Tartari: *Rad. Phys. Chem.* **56**, 205 (1999)
9. A. Taibi, G.J. Royle, R.D. Speller: *IEEE Trans. Nucl. Science* **47**, (2000)
10. Y. Namito, S. Ban, H. Hirayama: *LSCAT: Low-energy Photon-Scattering Expansion for the EGS4 Code*, KEK Internal (1995)
11. Y. Namito, H. Hirayama: *LSCAT: Low-Energy Photon-Scattering Expansion for the EGS4 Code (Inclusion of Electron Impact Ionization)*, KEK Internal 2000-4, May (2000)
12. H.Q. Woodard, D.R. White: *Br. J. Radiol.* **59**, 1209 (1986)
13. F.A. Duck: *Physical Properties of Tissue: a Comprehensive Reference Book*, (Academic Press, London 1990)
14. A.H. Narten, H.A. Levy: *J. Chem. Phys.* **55**, 2263 (1971)
15. L.R.M. Morin: *J. Phys. Chem. Ref. Data* **11**, 1091 (1982)
16. J.H. Hubbell, I. Øverbø, *J. Phys. Chem. Ref. Data*, **8**, 69 (1979)
17. G.J. Royle, R.D. Speller: *Phys. Med. Biol.* **40**, 1487 (1995)
18. D.R. White, H.Q. Woodard, S.M. Hammond: *Br. J. Radiol.* **60**, 907 (1987)

Implementation of the Anomalous Dispersion of Rayleigh Scattered Photons in EGS4 Code

C. Baraldi, E. Casnati, G. Di Domenico, and A. Tartari

Università degli Studi di Ferrara, Dipartimento di Fisica, via Paradiso 12, I-44100 Ferrara, Italia

Abstract. Changes to the general purpose EGS4 code were performed in order to include anomalous dispersion effects in the simulation of elastic scattering from atomic bound electrons. Moreover, experimental checks with 59.54 keV photons incident on Hf and Pb targets, at 90° and 120° scattering angles, were carried out.

1 Introduction

The most rigorous procedure to evaluate the elastic collision cross section has its grounds in the QED approach with scattering matrix S restricted to the second perturbative order (SM) in the independent particle approximation as suggested by Kissel, Pratt and Roy [1]. This methodology was successfully applied in various experimental situations but its systematic use is impossible because the computing time grows prohibitively with the number and complexity of atomic orbitals. The Rayleigh scattering can be described also by one of the

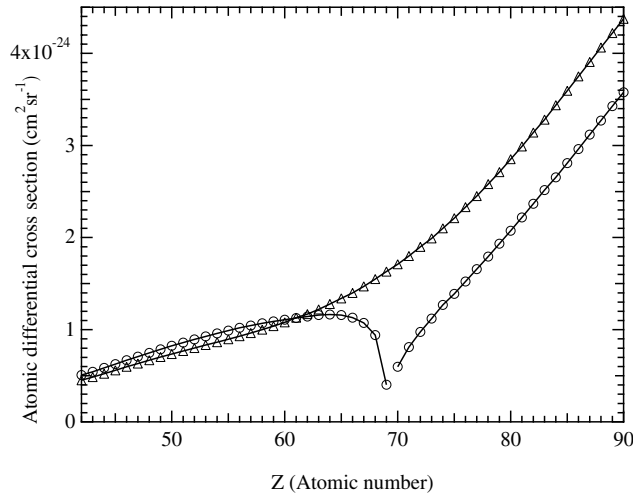


Fig. 1. Differential cross section of 90° elastically scattered 59.54 keV photons versus atomic number. Triangles: relativistic approximation of the atomic form factor; circles: relativistic approximation of the atomic factor corrected for anomalous dispersion

form factor theories. These procedures are simpler than the S matrix one, but their values are less rigorous and frequently show unacceptable deviations from experimental and SM values, e.g. when the incident photon energy is close to that of the target photoelectric threshold. To reduce such deviations Kronig [2] and Kramers [3] introduced the anomalous dispersion factor, independent from the scattering angle, that in combination with the form factor approximates better the experimental values of Rayleigh cross section. The elastic differential cross section of 59.54 keV photons scattered at 90° as given by the relativistic form factor approximation without and with anomalous dispersion correction suggested by Kissel and Bergstrom [4] are plotted in figure 1 as a function of the atomic number Z . The larger differences occur around 70 because here the binding energies of K electrons are very close to that of the incident photons. The difference is appreciable also for elements with atomic number greater than 70. In the general purpose EGS4 code [5] the elastic interactions of photons with bound electrons are described only by the relativistic form factor so that the addition of a correction for anomalous scattering should entail a real improvement. The present paper suggests a procedure to implement EGS4 code with the effects of anomalous dispersion and compares the simulations so obtained with experimental results at 59.54 keV energy.

2 Implementation of EGS4 Code

In using the independent electron atomic model with a central potential given by the charge distribution of nucleus and electrons, the atomic elastic scattering differential cross section of a photon of energy E at the scattering angle θ can be written as

$$\frac{d\sigma}{d\Omega} = \frac{r_o^2}{2} (1 + \cos^2\theta) F^2(E, \theta, Z) \quad (1)$$

where r_o is the classical electron radius and F the atomic scattering factor that is a function of incident photon energy, scattering angle and target atomic number. In the form factor theory F is approximated by a real function, said atomic form factor, function of a variable q which includes the photon energy and scattered angle dependence according to the definition

$$q = \frac{E \sin(\frac{\theta}{2})}{hc} \quad (2)$$

This property permits the shortening of computer time and makes $f(q, Z)$ tabulations easy. The atomic form factor can be evaluated by different wave functions. At present wide tabulations of values calculated by non relativistic wave function [6], the relativistic one [7] and relativistic with electron binding correction [8] are available. To improve the form factor results, two correction factors are applied to $f(q, Z)$. These f' and f'' anomalous dispersion factors are evaluated by the dispersion relations, which link the real and imaginary parts of the forward-scattering amplitudes, and the optical theorem, which relates the

imaginary part of the forward scattering amplitude to the photoabsorption cross section. Various tabulations of the anomalous scattering factors, differing mainly in the approximation used for the high-energy limit were worked out by many authors [4], [9–11]. The f' and f'' correction factors are assumed to be independent from the scattering angle and, therefore, the scattering factor becomes

$$F(q, E, Z) = f(q, Z) + f'(E, Z) + if''(E, Z) \quad (3)$$

In EGS4 transport code the relativistic values tabulated by Hubbell and Øverbø are used in PEGS4 program to evaluate the Rayleigh scattering cross section. To correct those values the anomalous dispersion factors tabulated by Kissel and Bergstrom were introduced in EGS4 pre-processor (PEGS4) and the new scattering factors calculated by equation (3) were used to tabulate the probability density function by which Rayleigh diffusion cross section was sampled on the angle.

3 Experimental Results

Accurate and precise measurements of the elastic differential cross section were obtained by the geometrical arrangement and experimental geometry described in detail elsewhere [12,13]; only the aspects useful to the understanding of the present results will be reminded. The experiment was carried out in specular geometry with source to target and target to detector distances practically equal one another and very large in respect of target thicknesses. Both source (18.5 GBq of ^{241}Am) and detector (HP-Ge 200 mm^2 in area and 10 mm in thickness) were provided with multivane collimators to limit the primary beam divergence and the detector acceptance angle. The scattering foil surface seen by the detector was well inside the irradiated one so that the areal emission was uniform for the detector. The advantage of this arrangement is a small angular dispersion. Measurements on pure target foils of Be, Al, V, Mo, Cd, Sn, Gd, Dy, Er, Yb, Hf, Ta, W, Pb at scattering angle of 60° , 90° and 120° were carried out with at least three independent observations for each element and angle. To check the reproducibility the measures were performed by alternating targets and angles. The thicknesses of most targets were of the order of at least three mean free paths to improve the signal to noise ratio [13]. Owing to the low angular dispersion both source to target and target to detector beams can be approximated by infinitely narrow beams the paths of which coincide with those of their central axes. Simulations with and without anomalous dispersion correction were carried out for Hf and Pb targets and 90° and 120° scattering angles. In all the simulations the LSCAT pack developed by Namito [14] was used. To compare EGS4 and experimental results, the areas of theoretical and experimental incoherent Compton distributions served for normalization. The incoherent experimental areas were compared also with those calculated by the model of Casnati et al. [15] to be sure of the absence of spurious signals. The corrections for the K-escape peak, and for the asymmetry of the instrumental peak were applied to the area evaluation of coherent signal. Moreover, the steps

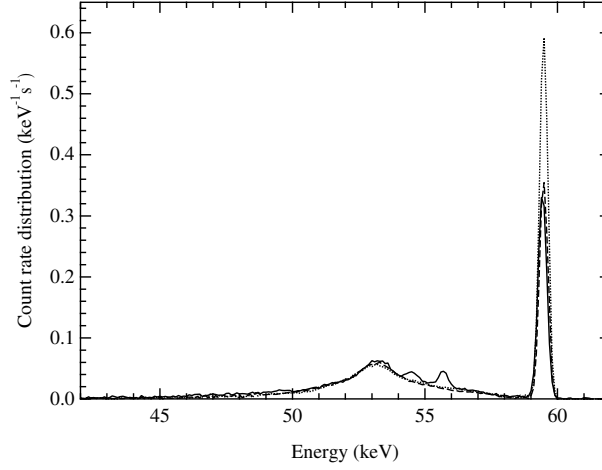


Fig. 2. Hf spectral distribution of 59.54 keV photons scattered at 90° . Continuous line: experimental data corrected; dotted line: EGS4 simulation without dispersion correction; dashed line: EGS4 simulation corrected for anomalous dispersion.

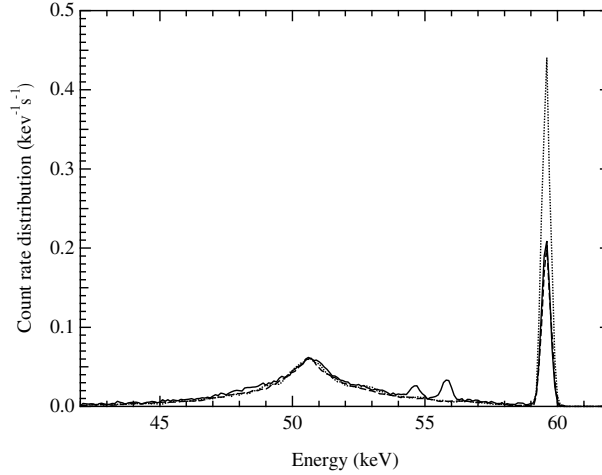


Fig. 3. Hf spectral distribution of 59.54 keV photons scattered at 120° . Continuous line: experimental data corrected; dotted line: EGS4 simulation without dispersion correction; dashed line: EGS4 simulation corrected for anomalous dispersion

of cumulative distribution function used by EGS4 code in Rayleigh simulation are too large with respect to the small angular dispersion of the experiment. As a consequence the Monte Carlo F^2 value resulted locally different from the Hubbell and Øverbø ones. Therefore, appropriate corrections were applied. The EGS4 normalized results and the experimental ones are shown in Figs. 2 and 3 for Hf target and 4 and 5 for Pb and their values are collected in Table 1. The

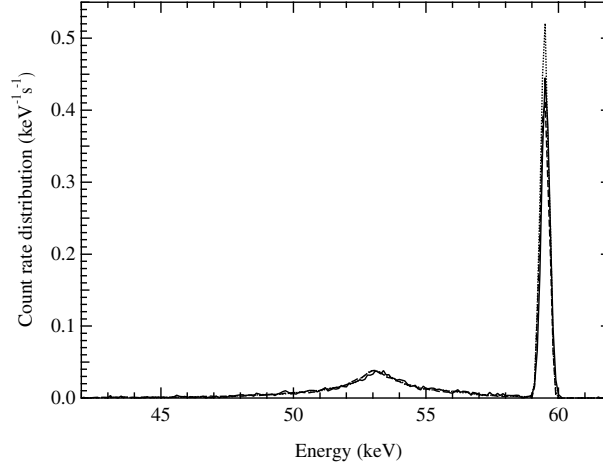


Fig. 4. Pb spectral distribution of 59.54 keV photons scattered at 90° . Continuous line: experimental data corrected; dotted line: EGS4 simulation without dispersion correction; dashed line: EGS4 simulation corrected for anomalous dispersion.

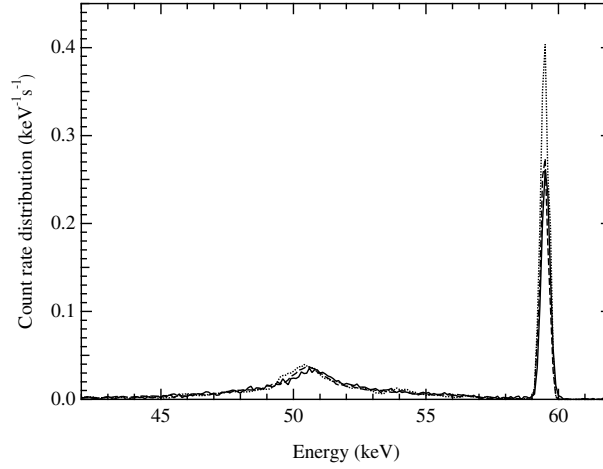


Fig. 5. Pb spectral distribution of 59.54 keV photons scattered at 120° . Continuous line: experimental data corrected; dotted line: EGS4 simulation without dispersion correction; dashed line: EGS4 simulation corrected for anomalous dispersion

improvement of the EGS4 performances with the introduction of the anomalous scattering implementation is evident. The differences between experimental and uncorrected EGS4 values are very large, up to 100%, whereas the implemented EGS4 values differ from the experimental ones by no more than 6%.

Table 1. Coherent experimental and theoretical areas. Z , atomic number; θ , scattering angle; Exp, experimental values, MC, EGS4 uncorrected values; MCI, EGS4 values corrected for the anomalous dispersion

Target Element	Z	θ	Exp	MC	MCI
Hf	72	90°	0.1396	0.2352	0.1426
Hf	72	120°	0.0854	0.1703	0.0803
Pb	82	90°	0.1784	0.2052	0.1721
Pb	82	120°	0.1068	0.1560	0.1056

4 Conclusion

The general purpose EGS4 code was implemented to transport photons of energy close to that of the K threshold of the medium they are crossing. Changes were introduced in PEGS4 program. The simulations worked out with and without implementation for 59.54 keV photons on Hf and Pb at 90° and 120° were compared with the corresponding experimental results and show evident improvements of the simulations performed by the implemented code.

References

1. L. Kissel, R.H. Pratt, S.C. Roy: Phys. Rev. A **22**, 1970 (1980)
2. R. Kronig: J. Opt. Soc. Am. **12**, 547 (1926)
3. H. Kramers: Atti Congr. Fis. Como **2**, 545, (1927)
4. L. Kissel, P.M. Bergstrom Jr.: <ftp://www-phys.llnl.gov/pub/rayleigh/SM>
5. W.R. Nelson, H. Hirayama, D.W.O. Rogers: *The EGS4 code system*, (SLAC-Report-265, Stanford University, Stanford, California, 1985)
6. J.H. Hubbell, W.J. Veigele, E.A. Briggs, R.T. Brown, D.T. Cromer, R.J. Hoverton: J. Phys. Chem. Ref. Data **4**, 471 (1975); **6**, 615 (E) (1977)
7. J.H. Hubbell, I. Øverbø: J. Phys. Chem. Ref. Data **8**, 69 (1979)
8. D. Schaupp, M. Schumacher, F. Smend, P. Rullhusen, J.H. Hubbell: J. Phys. Chem. Ref. Data **12**, 467 (1983)
9. D.T. Cromer, D.A. Liberman: J. Chem. Phys. **53**, 1891 (1970)
10. B.L. Henke, P. Lee, T.J. Tanaka, R.L. Shimabukuro, B.K. Fujikawa: At. Data Nucl. Data Tables **27**, 1 (1982)
11. C.T. Chantler: J. Phys. Chem. Ref. Data **24**, 71 (1995)
12. E. Casnati, C. Baraldi, A. Tartari: Phys. Rev. A **42**, 2627 (1990)
13. C. Baraldi, E. Casnati, A. Tartari, M. Andreis, B. Singh: Phys. Rev. A **54**, 4947 (1996)
14. Y. Namito, S. Ban, H. Hirayama: Nucl. Instrum. Methods Phys. Res. A **349**, 489 (1994)
15. E. Casnati, C. Baraldi, A. Tartari, B. Singh: Appl. Radiat. Isot. **44**, 1155 (1993)

Backscattering from Gold Irradiated with 15–40 keV Photons

N. Nariyama

Nuclear Technology Division, Ship Research Institute, Mitaka, Tokyo 181-0004, Japan

Abstract. To investigate the simulation of ionization process by synchrotron radiation, energy deposition by electrons reflected from gold irradiated with photons was calculated with a Monte Carlo transport code ITS and compared with measured backscattering factors for 10-40 keV monoenergetic photons from synchrotron radiation. The calculated factors almost agreed with the measured, while the agreement was not satisfactory at 15 and 40 keV. Without M- and N-shell electrons the degree of the agreement became worse. From calculated electron energy reflection and the spectra, the influence of the M- and N-shell electrons and Auger electrons was found to increase with approaching the absorption edges, especially L-shells more largely than K-shells.

1 Introduction

Using synchrotron radiation, biological researches [1] and medical treatments [2] have been conducted, which are mostly making use of the effect of secondary electrons from high-Z elements to DNA. For photon activation therapy (PAT), cell-seeking high-Z elements such as iodine are incorporated into DNA in the target cell [2–4]. When the cell is irradiated with monoenergetic photons above the K-absorption edge, Auger cascades induced give large biological damage to the critical site of the tumor. Thus photoelectrons and Auger electrons from high-Z elements play an important role in the applications. For the estimation of the effect, energy deposition becomes an important quantity. However, a nano-scale region has to be considered for the deposition and hence the measurements are extremely difficult: calculation becomes necessary. Auger cascade and the electron transport simulation have been made for Auger emitters krypton and iodine [5,6]. Nevertheless, the validity of the electron transport itself in the low energy and the small scale region composed of different materials has not been fully confirmed [7,8]. Moreover, just above the K- or L-absorption edge, large production of fluorescence photons and Auger electrons is originated in the complex shell structures of the high-Z elements. To what extent the ionization process is to be simulated for the energy deposition calculations is an important problem. In the general-purpose photon-electron transport codes such as EGS4 [9] and ITS [10], a condensed history technique using multiple scattering theory is employed for electron transport, in which individual collisions are not followed [11]. Moreover, transport of K- and L-shell electrons is considered but M- and N-shell photoelectrons and Auger electrons are often neglected or the accuracy of the production and transport has not been confirmed in detail [12].

In this study, to investigate the simulation of ionization process by synchrotron radiation and the electron transport, energy deposition by electrons reflected from gold irradiated with photons was calculated with a Monte Carlo transport code. The values are compared with measurements for 10-40 keV monoenergetic photons from synchrotron radiation, in which the influence of M- and N-shell and Auger electrons is discussed.

2 Calculation Method

For the calculations, a TIGERP program of the ITS Monte Carlo photon-electron transport code was used. The geometry used is one-dimensional slab, and in the photoelectric interaction, photoelectrons and Auger electrons from K-, L_1 -, L_2 -, L_3 -, average M- and N-shells are produced. The electron interaction includes bremsstrahlung production and electron impact ionization. In the electron transport, condensed-history technique is used [11,13]: electron trajectories are divided into path segments along which many interactions occur. To shorten the time consumed, angular deflection in the multiple scattering is sampled using Gaudsmitt-Saunderson theory [14]. Photon and electron transport was traced down to 1 keV.

For reflection energy, the backscattering factor was defined as the ratio of the energy deposition in a material with backing to that without backing. The energy deposition has been measured using thin $\text{Li}_2\text{B}_4\text{O}_7\text{:Cu}$ thermoluminescent dosimeters (TLDs) of 90- μm thickness on the 120- μm thick polyimide film [12] since the thinner detector exhibits stronger electron influence to the energy deposition. The TLD has been backed with a gold foil of 1- or 0.25- μm thickness and irradiated with 10-40 keV monoenergetic photons from synchrotron radiation. The experiment has been carried out at the Photon Factory in the High Energy Accelerator Research Organization (KEK). The K-edge energy of gold is 80.725 keV and the L_1 -, L_2 - and L_3 -edge energies are 14.35, 13.73 and 11.92 keV, respectively. The integral TL signal is proportional to the energy deposition in the 90- μm thick crystals in the corresponding energy region.

3 Results

Figure 1 shows the comparison between the experimental and calculated backscattering factors. The experimental values increase with energy and become larger for the 1- μm thickness than for 0.25- μm thickness. The ITS normal calculations showed that the values almost agreed with the measured but at 40 and 15 keV the agreement was not satisfactory. Without M- and N-shell electron transport, the calculated values decreased by about 20% even above the L-edge energies. No influence of Auger electrons was confirmed except for a 14% decrease of the factors observed at 15 keV.

The energy deposition in the 90- μm thick $\text{Li}_2\text{B}_4\text{O}_7\text{:Cu}$ TLDs directly given by the incident photons is obtained by multiplying the mass energy absorption coefficients of $\text{Li}_2\text{B}_4\text{O}_7\text{:Cu}$ [15] by the photon energy. Between 10 and 40 keV, the

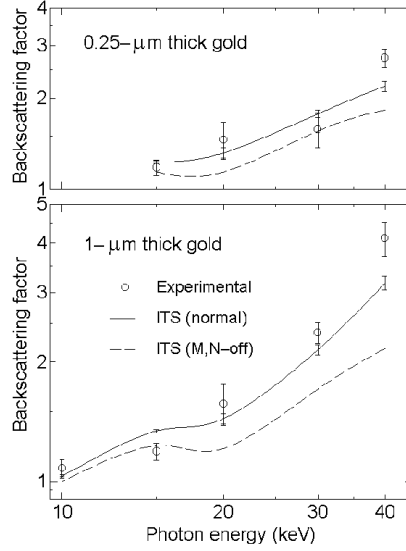


Fig. 1. Backscattering factor of 0.25- and 1- μm thick gold for 10–40 keV photons

deposition decreases with energy. On the other hand, electron energy reflection from gold becomes almost constant in the energy region [12]. As a result, with increasing energy the reflected electrons give rise to larger effect to the energy deposition, that is, the backscattering factor increases with energy as seen in Fig. 1.

More clearly to see the energy dependence of the influence of M- and N-shell and Auger electrons, respectively, ratios of the reflection electron energies to the incident photon energies were calculated with the TIGERP code below 200 keV. Calculations without M- and N-shell electrons and Auger electrons were also made. As shown in Fig. 2, the influence of M- and N-shell electrons increased markedly with approaching each absorption-edge energy. Auger electrons also give larger effect just above the L-edge energies than above the K-edge energy since the fluorescence yield is great near the K-absorption edge.

To see the electron spectra, calculations were made for 15–40 keV photons. The result is shown in Fig. 3. M-shell electron peak appears in each spectrum. For 15-keV photons, Auger electron peaks are observed clearly below 10 keV by comparison with the calculations without Auger electrons.

4 Discussion

In Fig. 1, worse agreement between the experiment and calculation was observed at 15 and 40 keV. For the 0.25- μm thick gold, the applicability of the multiple-scattering theory used has not been fully confirmed [7] because the thickness corresponds to only 7% of the 40 keV electron range in gold [16]. Even 1.0- μm

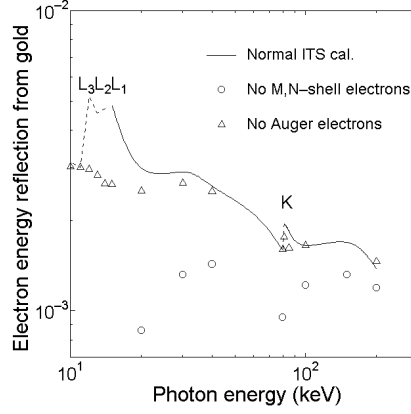


Fig. 2. Electron energy reflection from gold irradiated with photons

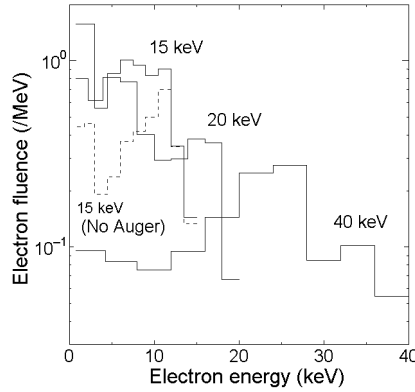


Fig. 3. Backscattered electron spectra from gold for 15-, 20- and 40-keV photons

thickness is still thin enough. The other possible reason is that the average binding energies are used for the M- and N-absorption edge in the code, and while the angular dependence of photoelectrons is considered [17], isotropic ejection is assumed for Auger electrons. Nevertheless, at 15 keV the experimental backscattering factor appears too small judging from the factor at 20 keV, which might be attributed to the electron attenuation in the air between gold and TLD and non-sensitive layer at the surface of the TLD that is believed to exist. Moreover, the discrepancy at 15 and 40 keV may be owing to the dependence of the TL efficiency on the electron energy because the electron spectra in the TLD with and without the backing differ from each other, while the efficiency does not change drastically between 15 and 40 keV [18].

In Fig. 2, even over the L-edge energies, the influence of M- and N-shell electrons to reflection energy was observed clearly. Moreover, Auger electrons

made the dose larger with approaching the edge energy. To clarify the reason, the physical data for gold related with photoelectric effect used in TIGERP need to be noted. The fraction of photoelectric interaction is 0.8 for K-shell, 0.15 for L-shells and 0.05 for M- and N-shells. The fluorescence yield is 0.96 for K-shell and 0.105, 0.357 and 0.327 for L₁-, L₂- and L₃-shell. For average M-shells, the small value of 0.029 is used. Here it should be noticed that since the average M-shell energy is 2.77 keV, the photoelectrons from M-shells have larger energy than from L-shells, and moreover the ratio of the two energies decreases with approaching the L-edge energies as shown in Fig. 3 from 0.69 at 40 keV to 0.05 at 15 keV. Furthermore, the fluorescence yield for M-shells is much smaller than those for L-shells. With regard to Auger electrons, the energies are also much greater than those of L-shell photoelectrons just above the edge: L₁MM Auger electrons have energy of 8.8 keV. As a result, the contribution of M-, N-shell and Auger electrons to the energy reflection increases largely just above the L-absorption edge.

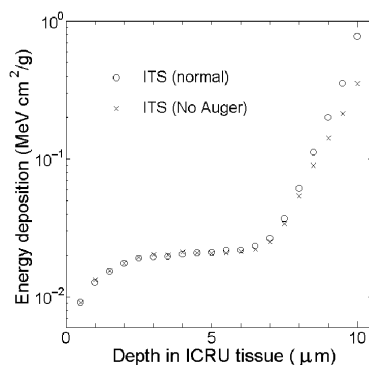


Fig. 4. Energy deposition distribution in ICRU tissue of 10- μ m thickness backed with gold for 15 keV photons

While the influence of Auger electrons is great for energy reflection just above the L-edge energies as shown in Fig. 1, the average energy is lower compared with that of M-shell electrons and the effect is restricted only to the interface. Figure 4 shows the energy deposition distribution in ICRU tissue of 10- μ m thickness backed with gold irradiated with 15-keV photons, which was calculated with TIGERP. It is shown that at about 2 μ m from gold the Auger electrons attenuate almost thoroughly.

5 Conclusions

The backscattering factors calculated with a Monte Carlo transport code ITS for Li₂B₄O₇:Cu TLDs backed with gold agreed with the measured except for 40 and

15 keV. The reason of the disagreement could be due to the experimental causes of the TL efficiency and non-sensitive layer at the surface of the TLD: for the confirmation, use of another thin dosimeter is effective. When the transport of M- and N-shell electron transport was neglected, the degree of agreement became worse. From the calculations of energy reflection and the spectra, the influence of M- and N-shell electrons and Auger electrons was found to increase just above L-absorption edges more greatly than above K-absorption edge. Judging from this consideration, it became clear that even above L-absorption energies, M, N-shell and Auger electrons have to be treated in detail depending on the photon energy.

References

1. K. Hieda, T. Ito: 'Radiobiological experiments in the x-ray region with synchrotron radiation'. In: *Handbook on synchrotron radiation*. (North-Holland, Amsterdam 1991) Vol. 4, ch. 13, pp. 431–465
2. B. Larsson, J. Stepanek: Nucl. Instrum. Meth. **A398**, 85 (1997)
3. R.G. Fairchild, V.P. Bond: Strahlentherapie **160**, 758 (1984)
4. B.H. Laster, W.C. Thomlinson, R.G. Fairchild: Radiat. Res. **133**, 219 (1993)
5. E. Pomplun, J. Booz, D.E. Charlton: Radiat. Res. **111**, 533 (1987)
6. E. Pomplun: Int. J. Radiat. Biol. **59**, 625 (1991)
7. N. Nariyama: KEK Proceedings **95-9**, 1 (1995)
8. C.T. Ballinger, J.A. Rathkopf, W.R. Martin: Nucl. Sci. Eng. **112**, 283 (1992)
9. W.R. Nelson, H. Hirayama, D.W.O. Rogers: SLAC-265 (1985)
10. Halbleib, J.A. R.P. Kensek, T.A. Mehlhorn, G.D. Valdez, S.M. Seltzer, M.J. Berger: SAND91-1634 (1992)
11. P. Andreo: Phys. Med. Biol. **36**, 861 (1991)
12. N. Nariyama, Y. Namito, S. Ban, H. Hirayama: Radiat. Prot. Dosim. **84**, 285 (1999)
13. M.J. Berger, R. Wang: 'Multiple-scattering angular deflections and energy-loss straggling'. In: *Monte Carlo transport of electrons and photons*. (Plenum Press, New York 1988) ch. 2, pp. 21–56
14. S. Gaudsmit, J.L. Saunderson: Phys. Rev. **57**, 24 (1949)
15. J.H. Hubbell: Int. J. Appl. Radiat. Isot. **33**, 1269 (1982)
16. International Commission on Radiation Units and Measurements, ICRU Report 37 (1984)
17. F. Sauter: Ann. Physik **11**, 454 (1931)
18. N. Nariyama, S. Tanaka, Y. Nakane, Y. Asano, H. Hirayama, S. Ban, Y. Namito: Radiat. Prot. Dosim. **74**, 155 (1997)

Monte Carlo Polarimetric Efficiency Simulations for a Single Monolithic CdTe Thick Matrix

R.M. Curado da Silva¹, M. Hage-Ali¹, E. Caroli², P. Siffert¹, and J.B. Stephen²

¹ Laboratoire PHASE, CNRS, Strasbourg, France

² Istituto TESRE/CNR, Bologna, Italy

Abstract. Polarimetric measurements for hard X- and soft gamma-rays are still quite unexplored in astrophysical source observations. In order to improve the study of these sources through Compton polarimetry, detectors should have a good polarimetric efficiency and also satisfy the demands of the typical exigent detection environments for this kind of missions. Herein we present a simple concept for such systems, since we propose the use of a single thick (~ 10 mm) monolithic matrix of CdTe of 32×32 pixels, with an active area of about 40 cm^2 . In order to predict the best configuration and dimension of detector pixels defined inside the CdTe monolithic piece, a Monte Carlo code based on GEANT4 library modules was developed. Efficiency and polarimetric modulation factor results as a function of energy and detector thickness, are presented and discussed. Q factor of the order of 0.3 has been found up to several hundreds of keV.

1 Introduction

Polarimetric measurements in the energy range of a few tens of keV up to several MeV is still a quite unexplored subject in several domains, mainly due to some complexity that such kinds of measurements need. In the past few years, there has been growing the interest over the domain of cosmological X- and gamma-ray radiation sources in the Universe. Light polarization studies of these emission sources, through Compton polarimetry, should give us a valuable information in order to discriminate between the different possible compact source models and obtain a unique insight into the composition and geometry of the source objects [1]. These objects can be such as Pulsars, Solar Flares, Active Galactic Nuclei, Galactic Black Holes or even unknown origin sources like those responsible for the production of Gamma-Ray Bursts.

These studies are generally carried out with satellite on board detection systems, where weight and simplicity are two key words. So far complex and expensive systems were originally proposed like the double layer configuration detectors. Generally these work under the principle of an event signal in a first detector layer in correlation with its escape Compton in a second detector layer. This second discrete layer detects the escaped Compton in order to accomplish the polarimetric measurement [2]. However several problems arise from such a system, which need delicate adjustment and more complex electronics, even if this set up presents some advantages in cosmic and medical field for precise angular determination, for example. Another kind of solution has been proposed

recently that consists of a thick CdTe discrete crystals matrix detector [3], but although this solution is not so exigent to implement on board flight modules, it's still quite complex and expensive.

Herein we present another concept for this kind of systems. The advantage arises from a relatively simple geometry to accomplish polarimetric observations, since instead of the double layer or a discrete detector matrix, we propose the use of a single thick (~ 10 mm) pixelated monolithic matrix of CdTe of 32×32 pixels, with an active area of about 40 cm^2 . It's simpler to manage than the former ones, less expensive and we have all the advantages offered by the CdTe semiconductor, namely its large cross section. This solution permits us to do polarimetry measurements as well as to have angular and energy resolution and eventually profit from the pixel effect [4] features.

2 Code Implementation: Polarimetry and Geometry

The Monte Carlo code based on GEANT4 library modules developed to simulate the detector behaviour has two main type files construction. First, the physical concepts associated to electromagnetic interactions and particularly the polarized Compton scattering. A second type, the beam, the detector and its read out geometry.

2.1 Polarimetry Physical Concepts and Modifications on GEANT4

The basic concept of the CdTe monolithic pixelated polarimeter functioning is the Compton scattering. Actually, in the considered energy range, this electromagnetic interaction is the one responsible for the non uniformity of the polarized beam photons distribution after the Compton scattering, furnishing us a method to obtain polarimetric data from the source beam and consequently from its source. The Klein-Nishina cross-section for linearly polarized photons gives us an azimuthal dependency for the scattered photons:

$$\frac{d\sigma}{d\Omega} = \frac{r_0^2}{2} \left(\frac{E'}{E} \right) \left[\frac{E'}{E} + \frac{E}{E'} - 2 \sin^2 \theta \cos^2 \varphi \right], \quad (1)$$

where r_0 is the classical electron radius, E and E' are respectively the energy of incoming and outgoing photon, θ the angle of the scattered photon and φ is the angle between the scattering plane (defined by incoming and outgoing photon directions) and incident polarization plane (defined by the polarization vector and the direction of the incoming photon). As can be seen from (1), fixing all other parameters the probability varies with the azimuthal angle φ . This feature makes the configuration of the proposed detector very suitable to polarimetric measurements since its planar configuration fits an essential condition for good polarimetric measurements. The maximum relative difference between the cross-section values for $\varphi = 0^\circ$ – when cross-section reaches a minimum – and $\varphi = 90^\circ$ – cross-section reaches a maximum – is obtained for an angle θ_M , dependent

of the incident photon energy. For soft gamma and hard X-rays θ_M is close to 90° . Due to its natural configuration the monolithic CdTe detector excludes the double event interactions for low values of θ – when polarimetric asymmetries are less evident – and collects preferentially double event interactions for angles closer to 90° .

The GEANT4 (version 4.1.1) code possesses an unfinished file for polarized scattering (G4PolarizedComptonScattering) that was here modified and a essential random number routine [5] was included in the code to generate the angle φ according to the distribution given by (1).

2.2 Beam and Detector Geometry

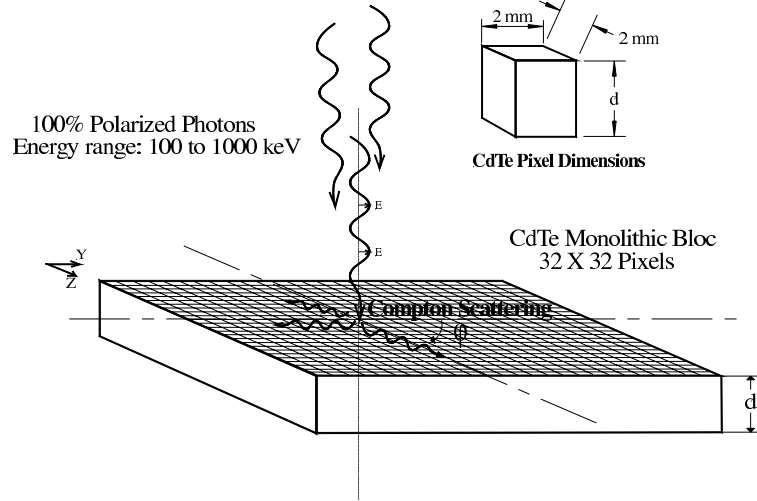


Fig. 1. Schematic representation of the monolithic CdTe detector and pixel dimensions (d is the detector thickness)

In order to predict the best configuration and dimension of the detector pixels defined inside the CdTe monolithic semiconductor detector an appropriate code was created. The simple geometric configuration of this detector (Fig. 1), a monolithic CdTe piece of 32×32 pixels (each $2 \times 2 \times d$ mm) defined by the x-axis direction electric field produced by the electrodes in contact with the bloc surface, was implemented using GEANT4 libraries facilities. Each pixel is then defined and labelled by an identification number (pixel ID) along the y- and z-axis parallel to the detector surface. Detector surface bloc irradiation is simulated by a 100% polarized beam orthogonal to y-z detection plane, covering uniformly a central pixel (y pixel ID 16 and z pixel ID 16). Then a read out geometry defined inside the detector is going to identify the pixels where double and other order events occur counting the number of these events for each pixel.

3 Results: Polarimetric Modulation Factor and Efficiency

In Fig. 2, two maps are presented showing double events distribution per pixel, corresponding to two different cases. In one case the map was produced by a 170 keV unpolarized beam, as described before, perpendicular to the detector plane, which covers uniformly a central pixel (16-16 pixel ID). As expected, the double events distribution is uniform in the y-z detector plane. In a second case a map corresponding to a 170 keV full polarized beam, for the same geometric conditions, is shown. We obtain an asymmetric double event distribution, as can be seen, more intense in Y direction and less significant in Z direction, the one of the electric vector. In order to evaluate the polarimetric performances of the

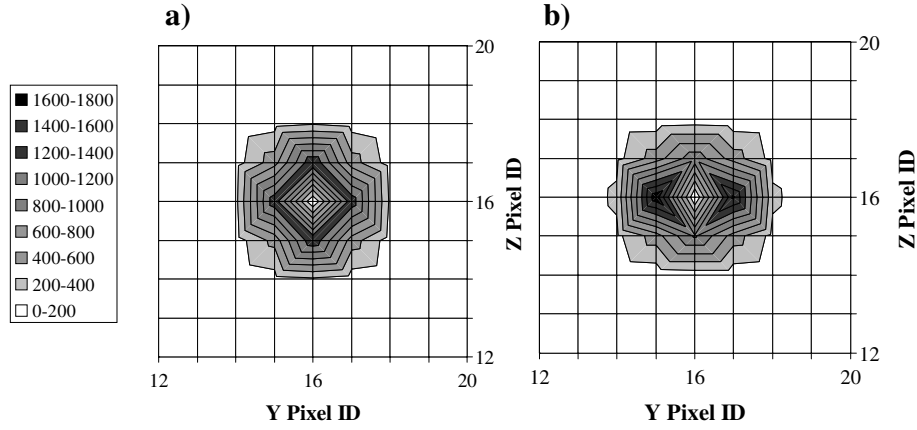


Fig. 2. Distribution map of double event interactions in y-z plane for: (a) unpolarized 170 keV photon beam. (b) 100% polarized 170 keV photon beam

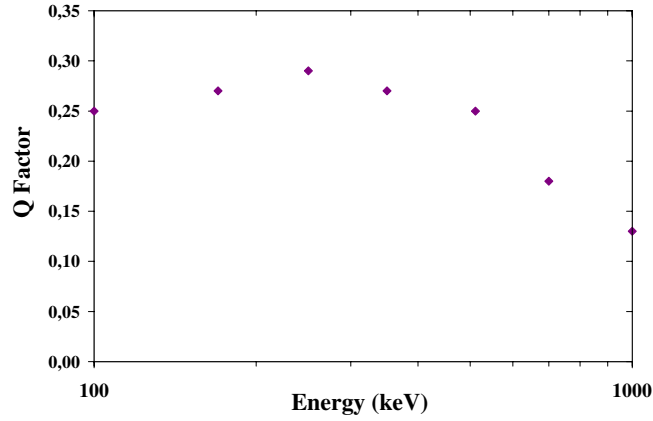
detector over the energy range of interest, results are presented in terms of the polarimetric modulation factor, Q . This is obtained by integrating the Compton polarimetric differential cross section formula over the solid angles defined by the physical geometry of the detection plane:

$$Q = \frac{N_y - N_z}{N_y + N_z}. \quad (2)$$

Here we obtain Q through the orthogonal directions y- and z-axis defined over the detector plane, to a 100% polarized beam which electric vector was in Z direction. N_y and N_z are the number of counts in each of the orthogonal directions. In Fig. 3 we present Q factor for beams of 100000 photons in the energy range from 100 keV to 1 MeV and for a 10 mm CdTe thickness. For lower energies polarimetric

Table 1. Efficiencies for the energy range between 100 keV and 1 MeV

Efficiencies (%)	100 keV	170 keV	250 keV	350 keV	511 keV	1 MeV
Double/Detected	2.0	12	21	25	27	23
Double/Total	2.0	11	15	14	11	6.8
Multiple/Detected	0.002	0.88	3.8	7.2	10	12
Multiple/Total	0.002	0.81	2.6	3.8	4.2	3.5
Detected photons	99	91	69	53	41	29


Fig. 3. Polarimetric modulation factor in the energy range from 100 keV to 1 MeV

modulation factor rises smoothly from 0.25 to about 0.3 between 200 and 300 keV, but for energies close 1 MeV it goes down to 0.15. This gives an indication of good polarimetric performances for this kind of simple system at least up to energies close to 1 MeV. Efficiencies for double events and other order events (multiple), referred to the number of detected and total number of sent photons, in this range are also showed in Tab. 1.

A study as been made concerning the thickness, d , of the semiconductor detector material. Tab. 2 shows obtained Q factor and double events efficiencies for lower CdTe thickness values at 170 keV. As can be seen, the Q factor becomes higher as we drop the detector thickness at the expense of double events efficiency. For $d < 8$ mm Q factor rises smoothly, for a large drop in double events efficiency, but 8 mm CdTe thickness presents also as a good alternative to 10 mm since Q factor is one tenth higher, although about one tenth lesser double events are detected. As in astrophysical polarimetric measurements the flux and beam duration may pose some limitations, 8 mm thickness presents a better solution for the study of long duration and greater flux polarized beams,

and 10 mm CdTe thickness as more appropriate to fainter polarized radiation beams, when efficiency becomes more important.

Table 2. Q factor and double events efficiency with CdTe thickness for 170 keV

<i>Thickness</i> (mm)	<i>Q factor</i>	<i>Double</i> events (%)
2	0.38	2.2
4	0.30	5.4
6	0.29	7.8
8	0.30	9.6
10	0.27	11

4 Conclusions

These results give us good perspectives for future polarimetric measurements through the use of a simple CdTe monolithic pixelated detection system. Not only the encouraging results presented in the range from 100 keV to almost 1 MeV but also the advantages arising from the simplicity and lower cost of this solution must be reminded to take part of a global analysis when choosing a polarimetric sensor to astrophysical applications. Finally these simulations have also the advantage of anticipating future experimental work and eventually complementing its developments.

Acknowledgements

This work was carried out in Laboratoire PHASE, CNRS, Strasbourg, France. One of the authors (R.M. Curado da Silva) was supported by the Fundação para a Ciência e Tecnologia through the research grant PRAXIS XXI/BD/16275/98.

References

1. F. Lei, A.J. Dean, G.L. Hills: Space Sci. Rev. **82**, 309 (1997)
2. R.A. Sareen, W. Urban, A.R. Barnett, B.J. Varley: Rev. Sci. Instrum. **66**, 3653 (1995)
3. E. Caroli, J.B. Stephen, W. Dusi, A.J. Bird, A.J. Dean, G. Bertuccio, M. Sampietro, W. Yu, C. Zhang, R.M. Curado da Silva, P. Siffert, V. Reglero: ‘The CIPHER Telescope for Hard X and Soft Gamma-Ray Polarimetry’. Accepted to be published on the Proceeding Series of American Institute of Physics
4. J.D. Eskin, H.H. Barrett, H.B. Barber: J. of Appl. Phys. **85**, 647 (1999)
5. G. Matt, M. Feroci, M. Rapisarda, E. Costa: Radiat. Phys. Chem. **48**, 403 (1996)

Simulations for X-Ray Synchrotron Beams Using the EGS4 Code System in Medical Applications

I. Orion¹, F.A. Dilmanian², Z. Zhong³, A.B. Rosenfeld⁴, A. Henn¹, I. Sagi¹,
and L. Peña²

¹ Weizmann Institute of Science, Rehovot 76100, Israel

² Medical Department, Brookhaven National Laboratory, Upton, NY 11973, USA

³ NSLS, Brookhaven National Laboratory, Upton, NY 11973, USA

⁴ University of Wollongong, PO Box 1144, Wollongong, New South Wales 2500,
Australia

Abstract. X-ray synchrotron beams are commonly used in biological and medical research. The availability of intense, polarized low-energy photons from the synchrotron beams provides a high dose transfer to biological materials. The EGS4 code system, which includes the photoelectron angular distribution, electron motion inside a magnetic field, and the LSCAT package, found to be the appropriate Monte Carlo code for synchrotron-produced x-ray simulations. The LSCAT package was developed in 1995 for the EGS4 code to contain the routines to simulate the linear polarization, the bound Compton, and the incoherent scattering functions. Three medical applications were demonstrated using the EGS4 Monte Carlo code as a proficient simulation code system for the synchrotron low-energy x-ray source.

1 Introduction

X-ray synchrotron beams are widely used in biological and medical researches. The availability of intense polarized low-energy photons produced from the synchrotron beams, offers a high dose transfer to biological objects. During the last decade, several experiments using synchrotron beams had demonstrated a possibility of designing a microbeam using a pinhole with a 30-mm width opening on a few mm length. This way of shaping of a beam is applicable only with a synchrotron beam due to its high intensity. A wiggler magnetic system including a proper filter provided the desired source energy distribution. The energy range for the microbeam study was set to be between 35- to 200-keV (60-keV mean), in order to enable the beam to penetrate through the skull and a few cm of tissue. The microbeam therapy method is based on the assumption that endothelial capillary cells in front of the beam die due to high dose exposure, while the surrounding cells survive and regenerate [1]. In a case of a tumor tissue, the cells will not perform an organized regeneration, and will leave the tissue to starve and to eventually die. A cell culture microbeam experiment was designed to investigate the validity of the microbeam therapy assumption. The change of the absorbed dose profile around a beam was tested for single cell dimensions (10–40 μm) along a 3 mm culture thickness using Monte Carlo simulations. Creating a confined absorbed dose range lead us to a 3-D reconstructed picture of

the damage to the cell culture caused by the radiation. A magnetic field of 6-T magnitude around the cell culture was considered necessary in order to provide the desired absorbed dose confinement along the sample depth.

RNA folding studies have a biological importance due to the diseases that can occur from the aberrant folding of the RNA caused by mutations. Changes in RNA conformation acted as regulatory switches in gene expression and development. X-ray synchrotron beam is used as a technique to resolve early steps in the ribozyme (a catalytic RNA molecule) folding pathway. The X-9A beam-line flux at NSLS (National Synchrotron Light Source) was in the order of 2×10^{11} photons $\text{s}^{-1}\text{mm}^{-2}$, which was sufficient to cleave 20% of the RNA molecules with duration of 10 ms exposure [2]. “Synchrotron x-ray footprinting” of nucleic acids and proteins, provided us with a unique tool of monitoring the formation of each tertiary contact during the RNA folding reaction

2 Method

The last developments of the EGS4 code system [3] for low energy scattering, and for polarization established the code system as one of the best tools for synchrotron based x-ray simulations. The modular structure of the low scattering photon transport routines, developed by the KEK EGS group [4], enabled us to prepare compound cross sections with form factors and scattering functions as H_2O , air, RNA (as a polymer of $\text{C}_5\text{O}_5\text{H}_7\text{-P}$), Lucite, and polypropylene.

The PRESTA (Parameter Reduced Electron-Step Transport Algorithm) [5], an essential procedure for electron transport, was included in every user code in this study due to high sensitivity of dose absorption to secondary electrons at the low energy photon transport. The photoelectron direction distribution was simulated due to the Sauter’s angular distribution equation for relativistic electrons [6].

The EMF_MAC.MOR macro was used in order to simulate the electromagnetic field in order to provide absorbed dose confinement in the cell culture application. This EMF_MAC.MOR macro was developed by Bielajew in order to simulate high-energy electron and photon beam dose deposition for radiotherapy [7].

3 Applications

3.1 X-ray Microbeam Radiotherapy

X-ray microbeam radiotherapy (MRT) is a therapy method based on inducing a high dose to an array of narrow regions inside a treated tissue. In the animal experiment stage, the MRT was tested for several brain tumor cases on rats. Other animal experiments were performed in order to ascertain normal brain tissue survival, and therefore the sparing of brain development disorders under the radiotherapy conditions. The MRT parameters such as microbeam array dimensions and spacing were investigated for peak-to-valley absorbed dose ratio

optimization [8]. The dose profile for a synchrotron - produced microbeam was simulated using the EGS4 code system including the low-energy code additions. The experimental results from a MOSFET monitoring micro-dosimeter at 1- μm resolution along 100- μm profile provided a verification for accuracy of the simulations as shown in Fig 1.

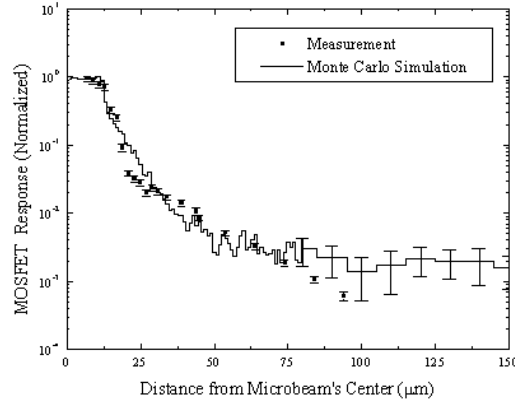


Fig. 1. A comparison of the MOSFET experimental results with the EGS4 simulation results along the microbeam profile up to 100 μm

3.2 Microbeam with Magnetic Confinement for Cell Culture Simulation

The radiation influence on cell damage and on cell survival is an important issue in therapy treatment studies. X-ray is one of the most common radiation sources to which humans are exposed, from medical treatments, from radiographic imaging, and from radiation working environments. We used the x-ray microbeam method in order to pinpoint the response of every individual cell inside a culture to a given radiation field. A low-energy x-ray source was chosen in order to apply appropriate LET (linear energy transfer) in a cell culture. The simulation included a 3-mm thickness cell culture placed in front of a low energy synchrotron x-ray microbeam (NSLS-beam-line X15). A narrow exposure profile along the whole object was essential in order to extract the cell death in slices along the sample depth.

In case of low energy x-rays, secondary photoelectrons can be emitted in an almost perpendicular direction due to the Sauter angular distribution. A 6-T magnetic field parallel to the x-ray beam direction was included to direct the energy deposition from electron transport along the original beam direction. A comparison of the beam profile with a 0.5-mm thickness central slice, with and without a magnetic field is shown in Fig. 2. It was essential to check the beam shape confinement along the cell culture depth when adding a magnetic field to

the simulation setup. The results of the simulation with the magnetic field are presented in Fig. 3, which provides an image of the microbeam profile along the sample depth.

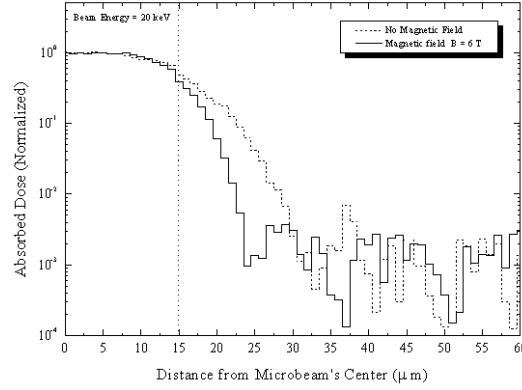


Fig. 2. The profile shape of central slice's absorbed dose for a 30 μm x-ray microbeam, with and without a magnetic field

3.3 Synchrotron x-ray RNA Footprinting

The need of a high LET radiation source with high intensity for x-ray RNA footprinting was recognized since 1993 [9]. The dose absorption in an RNA sample is highly depended on the source spectrum. The characteristics of x-ray generator were investigated in order to develop an available, and cheaper alternative source. The prepared RNA sample is a solution that was put into a polypropylene “Eppendorf” tube (0.5 ml) inside its conic shaped-end sealed by a 1 mm cover made of the same material. We compared the total absorbed dose, and the energy deposit spectra in an RNA sample from a synchrotron x-ray beam and from an x-ray generator source. The flux from the NSLS X9A beam-line was of the order of 2×10^{11} photons $\text{mm}^{-2}\text{s}^{-1}$, and the calculated flux of an x-ray generator with 50 kV, 250 mA was of the order of 2.5×10^8 photons $\text{mm}^{-2}\text{s}^{-1}$. The RNA sample inside the conic tube-end absorbed 72.7%, while the tube cover absorbed 24.2% of the beam energy, and the rest escaped or were absorbed by the tube's walls. The differences between the synchrotron beam and the generator source were as followed: spectral shape, polarization, rays divergence, and aperture dimensions.

Three x-ray tube source energies at 50 kV, from different target materials, were simulated in order to optimize the deposited energy on the RNA sample. The absorbed energy results versus the tube targets are summarized in Tab. 1.

Comparisons of the normalized source spectrum and deposited spectrum on the RNA sample are presented for the synchrotron beam and for x-ray tube with Mo target (Fig. 4).

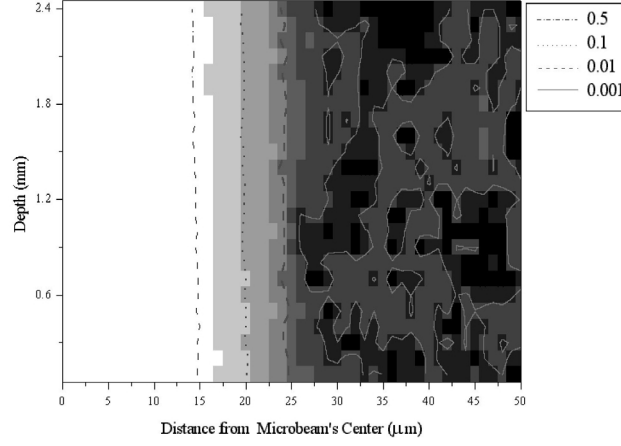


Fig. 3. Simulation results of 2-D image of the absorbed dose on 0.5 mm thickness cell culture slices that were exposed to a 30 μm microbeam (20 keV), with a longitudinal magnetic flux of 6 T

Table 1. The simulations results of x-ray tubes with three target materials: the deposited energy in the RNA sample region, in the sample cover, and the escaped energy to other regions. (The statistical error is of the order of 0.1%)

Target Material	Photon Energy (keV)	RNA (%)	Cover (%)	Escaped (%)
Cu	9.0	36.7	16.9	46.4
Mo	17.0	46.1	2.6	51.3
Ag	25.5	35.8	0.8	63.4

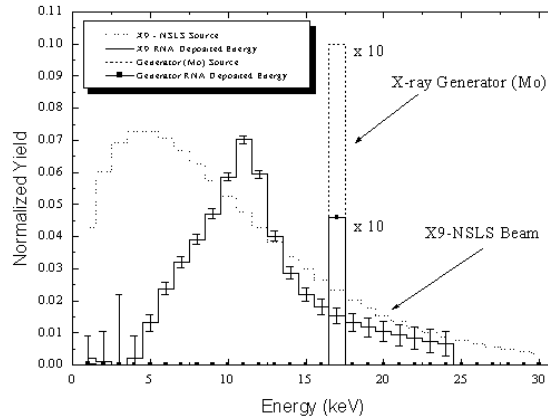


Fig. 4. Spectral distribution of the NSLS X9-A beam source (calculated using [10]), the x-ray tube source line, and the deposited energy on the RNA sample for each source

4 Conclusion

The MRT studies provided a highly spatial resolution measurement of dose distribution along a microbeam profile for 35-200 keV source energies. The comparison of the EGS4 simulation to such an experimental result enabled us to simulate and plan future experiments.

The simulation of cell culture 3-D image reconstruction was essential to set up an experiment that includes the needed electromagnet (6-T). The resolution (presented in Fig. 1), and the simulated results (presented in Fig. 2) indicate a possibility of measuring the profile change due to the magnetic field. Knowing the accurate shape of absorbed dose distribution close to the incident beam will provide a confident interpretation of the cell survival effected by well-defined radiation exposure.

The cover of the RNA sample was found to play an important rule in the energy deposition being in front of the source beam, and absorbing a significant fraction of the incident photon flux.

References

1. B. Sclavi, M. Sullivan, M.R. Chance, M. Brenowitz, S.A. Woodson: Science **279**, 1940 (1998)
2. K.J. Kim, B. Winer, J. Li, M. Armannini, N. Gillett, H.S. Phillips, N. Ferrara: Nature **362**, 841 (1993)
3. W.R. Nelson, H. Hirayama, D.W.O. Rogers: *The EGS4 Code System*, SLAC-Report-265, Dec. 1985
4. Y. Namito, S. Ban, H. Hirayama: Nucl. Instrum. Methods Phys. Res. A **332**, 277 (1993); Y. Namito, S. Ban, H. Hirayama: KEK National Laboratory for High Energy Physics KEK Internal 95-10, Japan; Y. Namito, S. Ban, H. Hirayama: Phys. Rev. A **51**, 3036 (1995)
5. A.F. Bielajew, D.W.O. Rogers: NRCC Internal Report No. PIRS-0042 (1986)
6. A.F. Bielajew, D.W.O. Rogers: *Photoelectron angular distribution in the EGS4 code system*, NRCC Internal Report No. PIRS-0058 (1986)
7. A.F. Bielajew: Med Phys, **20** 1171-9 (1993)
8. I. Orion et al.: 'Monte Carlo simulation of dose distributions from a synchrotron-produced microplanar beam array using the EGS4 code system', Phys in Med. and Bio. **45** (accepted)
9. A. Revzin (ed.): *Footprinting Techniques for Studying Nucleic Acid-Protein Complexes (A Volume of Separation, Detection, and Characterization of Biological Macromolecules)* (Academic Press, New York 1993)
10. <http://www-cxro.lbl.gov/optical.constants/bend2.html>

Applications of Monte Carlo Codes to a Study of Gamma-Ray Buildup Factors, Skyshine and Duct Streaming

H. Hirayama

KEK, High Energy Accelerator Research Organization, 1-1, Oho, Tsukuba, Ibaraki,
305-0801 Japan

1 Introduction

It has become possible to apply a Monte Carlo code to a specified shielding calculation, including deep-penetration problems, within a reasonable CPU time along with a recent drastic increase in computational power. It is, however, not reasonable to apply a Monte Carlo code to all shielding calculations at each step.

Many shielding calculations for gamma-rays have continued to rely on point-kernel methods incorporating buildup factor data. Line beam or conical beam response functions, which are calculated using a Monte Carlo code, for skyshine problems are useful to estimate the skyshine dose from various facilities. A simple calculation method for duct streaming was proposed using the parameters calculated by the Monte Carlo code.

It is therefore important to study, improve and produce basic parameters related to old, but still important, problems in the fields of radiation shielding using the Monte Carlo code. In this paper, these studies performed by several groups in Japan as applications of the Monte Carlo method are discussed.

2 Gamma-ray Buildup Factors

Gamma-ray buildup factors are key data of point-kernel methods which are widely using in gamma-ray shielding calculations. New gamma-ray buildup factor data were published as NUREG/CR-5740 [1] in 1991. These new data were prepared by Working Group ANS-6.4.3 (Chairperson: D. K. Trubey (ORNL)) as an international collaboration between US, Japan and India. The data, including this standard, were improved in energy range, number of materials, attenuation distance and secondary photons considered from the previous ones by Goldstein & Wilkins [2].

After publishing the NUREG-5740 data, systematic studies are continuing in Japan and France. It has become clear that parts of this new data must be re-evaluated to give more precise results for practical applications.

In Japan, the “Special Committee on the Shielding Safety Evaluation Methods and Related Data in Nuclear Facilities” was organized under the Atomic Society of Japan in 1995, and a re-evaluation of gamma-ray buildup factors was included as one of the jobs of this committee.

In this work, EGS4 [3] results with particle splitting [4] were used as reference data for results using the discrete ordinate method. It is not easy to apply the discrete ordinate method to a buildup factor calculation due to the drastic change of mfp after an interaction. An extremely fine space, angular and energy mesh, is required. The number of mesh size used, therefore, was verified by a comparison with the EGS4 results. Table 1 compares the buildup factors of lead for a 0.1MeV point isotropic source between the EGS4, ANS-6.4.3 data [1], the direct integration method code BERMUDA [5] and the angular eigenvalue method code AEM [6]. From this comparison, it is concluded that the mesh-size used in both BERMUDA and GEIET is sufficient for calculations including fluorescence photons. Clear differences exit between ANS-6.4.3 data.

Table 1. Gamma-Ray Exposure Buildup Factor of Lead for a Point Isotropic Source (0.1 MeV)

mfp	EGS4(PHOTX)			ANS-6.4.3	BERMUDA	AEM
1.0	2.17	±	0.003	2.04	2.14	2.16
2.0	3.53	±	0.005	3.39	3.45	3.51
3.0	5.57	±	0.010	5.60	5.47	5.55
4.0	8.99	±	0.020	9.59	8.84	8.94
5.0	14.8	±	0.023	17.0	14.7	14.8
6.0	25.0	±	0.036	30.6	24.7	25.0
7.0	43.2	±	0.067	54.9	43.2	43.1
8.0	75.9	±	0.11	94.7	75.4	75.7
10.0	243.	±	0.42	320.	248.	243.
15.0	5.12E+03 ^a	±	11.	5.80E+03	5.40E+03	5.14E+03
20.0	1.23E+03	±	300.	1.33E+05	1.33E+05	1.23E+05
25.0	3.17E+06	±	9.8E+3	3.34E+06	3.48E+06	3.19E+06
30.0	8.58E+07	±	3.0E+5	8.77E+07	9.48E+07	8.60E+07
35.0	2.38E+09	±	8.9E+6	2.36E+09	2.66E+09	2.37E+09
40.0	6.70E+10	±	2.7E+8	6.43E+10	7.51E+10	6.64E+10

^a Read as 5.12×10^3 .

Buildup factors for multilayer materials for various variations in the energy, attenuation depth and combinations of materials are desired for studying the empirical formula of multilayer gamma-ray buildup factors. EGS4 with particle splitting was applied to produce buildup factors for multilayer materials [7]. The double layer gamma-ray exposure buildup factors were calculated for combinations of water, iron and lead. As typical triple-layer shields, the calculations were

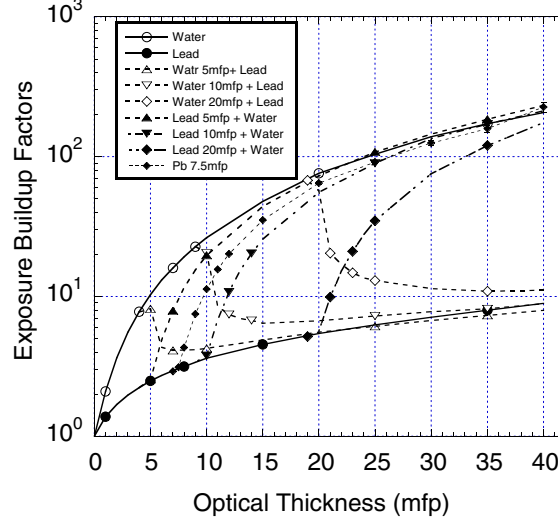


Fig. 1. Point isotropic buildup factor at 1MeV for single- double-layered shields of water and lead

performed for 4 different configurations of water, iron and lead. Figure 1 shows the point isotropic buildup factor at 1MeV for single- and double-layer shields of water and iron. Two different ways to express the multilayered buildup factors are proposed for continuing studies using these results by EGS4 [8,9].

3 Response Functions for Skyshine Calculations

The line beam response function (LBRF) is the skyshine dose, $R(E_0, \Phi, x)$, at a source-detector distance of x rising from a bare, collimated point source which emits one photon per unit time with energy E_0 to the direction Ω . The LBRFs are one of the key data for a line-beam method code for skyshine calculations, like the SKYSHINE code [10]. In the SKYSHINE code, the results by the COHORT Monte Carlo code [11] were used as the LBRFs. EGS4 [3] and MCNP [12] are used to study and improve the LBRFs for gamma-rays. Fig. 2 shows a comparison of the LBRFs obtained by EGS4, MCNP for 1MeV beam emitted at $\Phi=0, 0.1$ 2.5 and 5 degrees.

An approximate LBRF was obtained by fitting the following four-parameter empirical formula [13] to the LBRF values calculated with the EGS4 code:

$$R(x', E, \Phi)(\text{Gy/photon}) = \kappa E(\rho/\rho_0)^2 (x')^{b-dx'} \exp(a - cx'), \quad (1)$$

where, $x' = x\rho/\rho_0$, ρ_0 is the standard air density ($=0.001225\text{g cm}^{-3}$), ρ is the actual air density, E is the photon energy in MeV, and $\kappa = 1.308 \times 10^{-13}$. Values for parameters a, b, c and d , which depend on E and Φ , were obtained by fitting the above equation to values calculated with the EGS4 code.

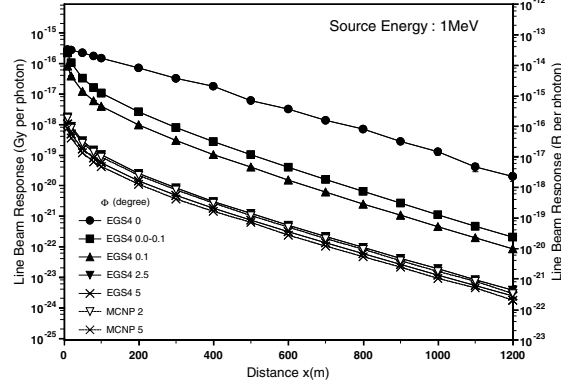


Fig. 2. Comparison of the LBRFs obtained by EGS4, MCNP for 1MeV beam emitted at $\Phi=0, 0.1, 2.5$ and 5 degrees

A similar technique was applied to SHINE-III, which is a simple code for a skyshine dose calculation up to 3 GeV neutrons by Tsukiyama et al. [14]. Skyshine conical beam response functions (CBRF) for high energy neutrons up to 3 GeV were obtained using NMTC-JAERI [15] and MCNP code [12]. Fig. 3 shows the calculated neutron dose distribution for an incident neutron energy of 3 GeV. This CBRF is fitted to a four parameters equation, which are same one used for the LBRFs. A simple code named SHINE-III using this equation with updated data has been developed. Equations (2) and (3) in Fig. 3 correspond to

$$D(r) = \frac{Q}{r} \exp \left[-\frac{r}{\lambda} \right], \quad (2)$$

$$D(r) = r^{b+dr} e^{a+cr}. \quad (3)$$

4 Duct Streaming Study

Miura et al. [16] presented a simple method to calculate radiation streaming through cylindrical ducts in a concrete shield. The method essentially involves summing the axial dose rate from the differential neutron and gamma components, which are functions of the energy and the angle of incident radiation, the duct diameter, the bend angle. etc. The axial dose rates are calculated by the MCNP code [12] for straight and bend ducts having diameters of 5, 10, 20, 30 and 40 cm. Radiation sources are plane mono-directional fission neutrons, intermediate neutrons, thermal neutrons and 1.25-MeV gamma rays. The incident angles are 0, 15, 30, 45 and 60 deg for straight ducts. For bent ducts, an isotropic plane source is placed inside the duct mouse to reduce the computation time. The bend angles are 30, 45, 60 and 90 deg. Figure 4 shows the dose rate distributions of neutrons in 90-deg bend ducts having diameter d .

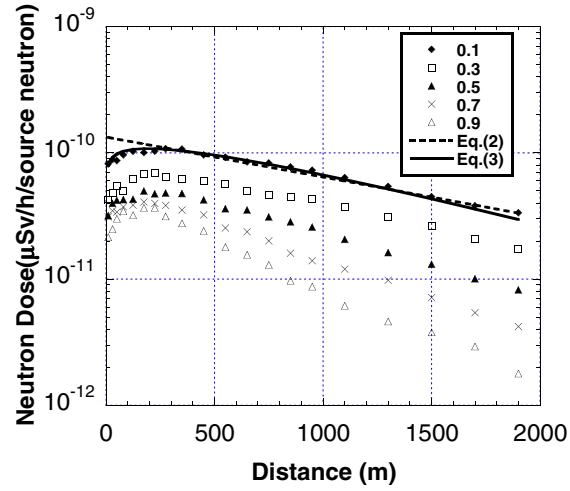


Fig. 3. Neutron dose distribution as a function of the distance from a 3-GeV neutron source in five angles (legend showing values of the emission angle, $\cos \theta$)

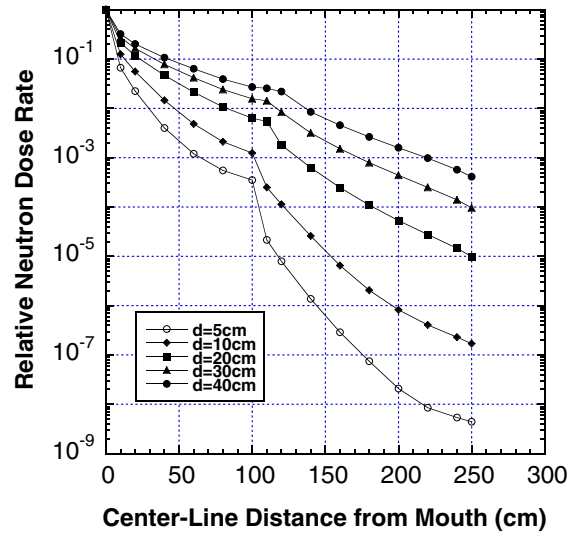


Fig. 4. Dose rate distribution of neutrons in 90-deg bend ducts having diameters of d

Nakano et al. [17] developed DUCT-III, which uses the albedo data for the streaming calculation. DUCT-III is a simple but useful streaming calculation method for high energy neutron facility. To provide the albedo data for high energy neutron streamings up to a few GeV, neutron scattering calculations were carried out for concrete and iron using NMTC/JAERI [15] and MCNP-4A

[12] with JENDL-3.2 [18]. The benchmark analyses of DUCT-III were carried out with neutron radiation streaming experiments at TIARA [19] and NIMROD [20].

References

1. D.K. Trubey: *New Gamma-Ray Buildup Factor Data for Point Kernel Calculations: ANS-6.4.3 Standard Reference Data*, NUREG/CR-5740 (1991)
2. H. Goldstein, J.E. Wilkins, NYO-3075, (1954)
3. W.R. Nelson, H. Hirayama, D.W.O. Rogers: *EGS4 Code System*, SLAC-265 (1985)
4. H. Hirayama: J. Nucl. Sci. Technol. **32**, 1201 (1995)
5. T. Suzuki, A. Hasegawa, S. Tanaka, H. Nakashima: *Development of BERMUDA: A Radiation Transport Code System, Part II. Gamma-Transport Code*, JAERI-M 93-143 (1993)
6. A. Shimizu: J. Nucl. Sci. Technol. **15**, 1201 (2000)
7. H. Hirayama, K. Shin: J. Nucl. Sci. Technol. **35**, 816 (1998)
8. K. Shin, H. Hirayama: J. Nucl. Sci. Technol. **35**, 865 (1998)
9. Y. Harima, Y. Sakamoto, N. Kurosawa, H. Hirayama: J. Nucl. Sci. Technol. Suppl. **1**, 488 (2000)
10. *SKYSHINE, Monte Carlo Integration of 6-MeV Gamma-Ray Transmission, Reflection, and Air Scattered Data to Compute Dose Rates*, CCC-298 (1977)
11. L. Soffer, L.C. Clemons Jr.: NASA-D-6170 (1975)
12. J.F. Briesmeister: LA-12625-M (1997)
13. N. Makoto, Y. Harima, H. Hirayama, Y. Sakamoto, K. Hayashi, Y. Hayashida, A. Ishikawa, O. Sato, R. Tayama: J. Nucl. Sci. Technol. Suppl. **1**, 616 (2000)
14. T. Tsukiyama, R. Tayama, H. Handa, K. Hayashi, K. Yamada, T. Abe, N. Kurosawa, N. Sasamoto, H. Nakashima, Y. Sakamoto: J. Nucl. Sci. Technol. Suppl. **1**, 640 (2000)
15. H. Yakada et al.: JAERI-Data/Code 98-005 (1998)
16. T. Miura, Y. Hirao, O. Sato, T. Ishida: J. Nucl. Sci. Technol. Suppl. **1**, 660 (2000)
17. H. Nakano et al.: 'Development of DUCT-III Code for Duct Streaming Calculation up to 3GeV', Presented at *Shielding Aspects of Accelerators, Targets and Irradiation Facilities (SATIF-5)*, Paris, France, July 17-21, 2000
18. T. Nakagawa et al.: J. Nucl. Sci. Technol. **32**, 1259 (1995)
19. Su. Tanaka et al.: to be submitted to Health Physics
20. G.R. Stevenson et al.: Health Physics **24**, 87 (1973)

Simulation of X-ray Spectra Generated by Kilovolt-Electron Bombardment

J.M. Fernández-Varea¹, X. Llovet², E. Acosta³, E. Benedito¹, and F. Salvat¹

¹ Facultat de Física (ECM), Universitat de Barcelona. Societat Catalana de Física (IEC). Diagonal 647, E-08028 Barcelona, Spain

² Serveis Científicotècnics, Universitat de Barcelona. Lluís Solé i Sabarís 1–3, E-08028 Barcelona, Spain

³ Facultad de Matemática, Astronomía y Física, Universidad Nacional de Córdoba. Medina Allende y Haya de la Torre, 5000 Córdoba, Argentina

Abstract. We describe an improved algorithm for calculating x-ray spectra emitted from targets bombarded with kilovolt electron beams. Electron tracks are generated by a modified version of PENELOPE in which radiative losses are obtained from tabulated partial-wave bremsstrahlung cross sections. Characteristic x-rays emitted after K-shell ionization by electron impact are simulated by using cross sections calculated from a model based on the plane-wave Born approximation. Simulation results are compared with available experimental data.

1 Introduction

The calculation of the continuous bremsstrahlung and characteristic x-ray spectra emitted from targets irradiated by low-energy (kilovolt) electrons is of interest in various fields, such as x-ray microanalysis, space physics and medical physics. Unfortunately, the description of both photon production channels is usually oversimplified or is not even considered in most general-purpose Monte Carlo simulation codes, since these processes occur with very small relative probability in comparison with that of elastic scattering or outer-shell ionization. For instance, in PENELOPE [1], the angular distribution of bremsstrahlung photons is described by means of a high-energy approximation which is not completely appropriate for kilovolt electron beams. In spite of this, PENELOPE gives a fairly realistic description of x-ray spectra generated in (mostly used) thick targets, because electron trajectories are rapidly randomized by elastic scattering and the angular distribution of emerging photons is practically insensitive to the intrinsic angular distribution. However, characteristic x-ray lines are not fully reproduced since PENELOPE only considers the generation of fluorescent radiation (characteristic x-rays and Auger electrons) after K-shell ionization by photon interaction, not by electron impact. Acosta et al. [2] included K-shell electron impact ionization by employing cross sections evaluated from the optical-data model proposed by Mayol and Salvat [3], and they also improved the angular distribution of bremsstrahlung photons at low energies by using an analytical distribution derived from the Kirkpatrick–Wiedmann–Statham formula [4]. In a similar way, other codes such as EGS4 have also been modified in order to improve the low-energy photon production [5–7].

In this work we further look into the algorithm proposed by Acosta et al. for the simulation of x-ray spectra from targets bombarded by kilovolt electrons. Radiative energy losses are simulated by interpolation from electron bremsstrahlung cross sections tabulated by Kissel et al. [8]. The new method splits radiative events into soft and hard contributions, and a suitable change of variables facilitates the random sampling of the energy of emitted photons in hard interactions. The complete procedure (generation of K-shell vacancies, energy and angular distributions of bremsstrahlung photons) is linked to a modified version of PENELOPE which uses partial-wave elastic cross sections [9]. Simulation results are compared with experimental data measured by our group and by other authors. Good agreement is generally found.

2 Updated Cross Sections

In this section we describe extensions of the original PENELOPE code, which are useful for the accurate simulation of x-ray spectra generated by keV electrons. The discussion is focused on the use of numerical differential cross sections (DCS) for elastic scattering and bremsstrahlung emission. For the sake of completeness, we will also consider inner-shell ionization by electron impact.

2.1 Elastic Scattering

The elastic scattering model adopted in PENELOPE yields accurate angular distributions under multiple scattering conditions, i.e. when at least about 20 interactions take place along an electron track. However, simulated distributions become less realistic for low-energy electron transport in high-atomic-number materials or cases of geometries where single or plural scattering prevails. To overcome this restriction, Benedito et al. [9] have recently developed an algorithm for the simulation of elastic scattering that uses numerical partial-wave cross sections. The method is based on a change of variables that absorbs most of the energy dependence of the DCSs. In other words, the scattering angle is replaced by a variable whose probability distribution function varies smoothly with the kinetic energy of the electron. This reduces the size of the required database and allows the use of simple, efficient sampling procedures. Moreover, the algorithm can be applied straightforwardly to mixed (class II) simulation. Results of simulated angular distributions of MeV electrons backscattered from aluminium and gold validated the correct coupling of this algorithm with the PENELOPE code system.

2.2 Bremsstrahlung Emission

For Monte Carlo simulation purposes, the DCS for bremsstrahlung emission is conveniently written as

$$\frac{d^2\sigma}{dW d\Omega} = \frac{d\sigma}{dW} \frac{1}{2\pi} p(\cos\theta) , \quad (1)$$

where W and θ are the energy and the polar angle, respectively, of the emitted photon; W is also the energy loss of the incident electron. The (normalized) angular distribution is given by $p(\cos \theta)$, and $d\sigma/dW$ gives the energy distribution in the bremsstrahlung process. Notice that, by starting from the double DCS instead of the triple DCS, changes of direction of the incident electron are disregarded; this is common practice in Monte Carlo simulation codes. Moreover, the factorization (1) neglects correlations between W and θ in a radiative event, but constitutes a practical approximation due to its simplicity.

In PENELOPE, the modified Bethe–Heitler DCS is used for $d\sigma/dW$ [10], and $p(\cos \theta)$ is taken from the classical dipole approximation [1]. This model is realistic enough in situations where elastic scattering effects can randomize the electron tracks to a large extent, or at high energies, where the bremsstrahlung photon distribution is strongly peaked in the forward direction.

At low energies, below a few hundred keV, Acosta et al. [2] modified PENELOPE in order to improve the angular distribution of emitted bremsstrahlung photons. They concluded that an analytical distribution derived from the Kirkpatrick–Wiedmann–Statham formula [4] predicts angular deflections in good agreement with the tabulation of Kissel et al. [8] (although it might not be very realistic below ~ 1 keV [11]). Due to its simplicity and accuracy, we will adopt this prescription for the sampling of the polar angle distribution.

The energy distribution $d\sigma/dW$ has a direct impact on simulated energy spectra. In this work, we resort to the partial-wave calculations of Pratt and co-workers [8,12]. These authors treated the electron-nucleus bremsstrahlung process as a single-electron transition in a relativistic self-consistent central field. Electron wave functions were expanded in partial-wave series and obtained by numerical solution of the radial Dirac equation. Kissel et al. carried out calculations for six elements with atomic numbers $Z = 2, 8, 13, 47, 79$ and 92 , electron energies $E = 1, 5, 10, 50, 100$ and 500 keV, and W/E values of $0, 0.4, 0.6, 0.8$ and 0.95 . From these calculations they prepared, by interpolation, a comprehensive tabulation of energy distributions $d\sigma_{\text{KQP}}/dW$ covering $2 \leq Z \leq 92$, $1 \text{ keV} \leq E \leq 500 \text{ keV}$ and $0 \leq W/E \leq 1$. In the kilovolt energy range, these theoretical cross sections are expected to be more reliable than the Bethe–Heitler DCS [13]. On the other hand, the electron-electron bremsstrahlung contribution can be safely disregarded [13].

Interpolation in the table of $d\sigma_{\text{KQP}}/dW$ values is facilitated by a change of variable $x = \ln(W/W_c)/\ln(E/W_c)$, where W_c is the selected cutoff energy for hard bremsstrahlung emission. The corresponding probability distribution function, $p(x) \propto Wp(W)$, varies smoothly with E , making linear interpolation accurate. Furthermore, the sampling method is readily adapted to perform mixed simulation.

2.3 Electron-impact Ionization of K Shells

Characteristic x-rays are emitted by relaxation of vacancies originated in atomic inner shells. In PENELOPE, only ionization of K shells is considered, either by photoelectric absorption or incoherent scattering of photons. However, in

applications involving keV electron beams, ionization by electron impact is the most important mechanism for inner-shell ionization. Here we will follow Acosta et al. [2] and evaluate K-shell ionization cross sections σ_{ion} from an optical-data model based on the plane-wave Born approximation, which incorporates relativistic and exchange effects and a simple Coulomb correction [3].

To simulate the generation of characteristic x-rays resulting from vacancies produced in a K shell, we proceed as follows [2]. For each free flight between consecutive interactions, the probability that an ionization has been produced in the considered shell is obtained from $p_{\text{ion}} = s \mathcal{N} \sigma_{\text{ion}}(E)$, where s is the length of the free flight and \mathcal{N} is the number of atoms per unit volume of the ionized element. We then sample a random value ξ uniformly in $(0, 1)$ and consider that the interaction is effective only if $\xi < p_{\text{ion}}$. When an ionization event occurs, its position is sampled uniformly along s . This procedure gives the correct average number of ionizations per unit path length since $p_{\text{ion}} \ll 1$.

3 Comparison with Experimental Data

As mentioned above, bremsstrahlung emission and inner-shell ionization by electron impact are processes that have small cross sections at the energies presently considered. The purely analogue simulation of x-ray spectra generated by these two processes is therefore very inefficient and time-consuming. In the simulations reported below, interaction forcing has been systematically employed to achieve higher efficiencies. In this variance-reduction technique, the cross sections associated with one or more interaction mechanisms are artificially increased, forcing them to occur with larger probabilities. Simulation results are kept unbiased by suitably modifying the “weight” assigned to each particle.

Figure 1 shows thick-target bremsstrahlung spectra produced by 70 keV electrons impinging at 45° on a 28.06-mg/cm²-thick slab of Pb. Emission angles of 45° and 90° with respect to the incident beam in transmission configuration are considered. Besides simulation results, experimental spectra measured by Ambrose et al. [14] are also displayed. Experimental data have been scaled to simulated data by fitting the area under each spectrum, excluding the region of characteristic x-rays (see [14]).

In Fig. 2 we show the x-ray spectrum produced by 20 keV electrons at normal incidence on a thick sample of Cu, as detected at 130° with respect to the direction of the incident beam. The simulated spectrum is in excellent agreement with experimental data measured by Acosta et al. [2].

Figure 3 displays K x-ray yields (Al K α and Si K α) as functions of the incident electron energy, produced by 5–30 keV electron beams impinging normally on 51 nm and 316 nm thick Al films deposited on Si, for an emission angle of 130° with respect to the direction of incidence. The Al and Si K x-ray intensities are normalized to the x-ray intensity yields from thick slabs of Al and Si, respectively. The agreement between simulated intensities and experimental data of Bastin and Heijligers [15] is very good.

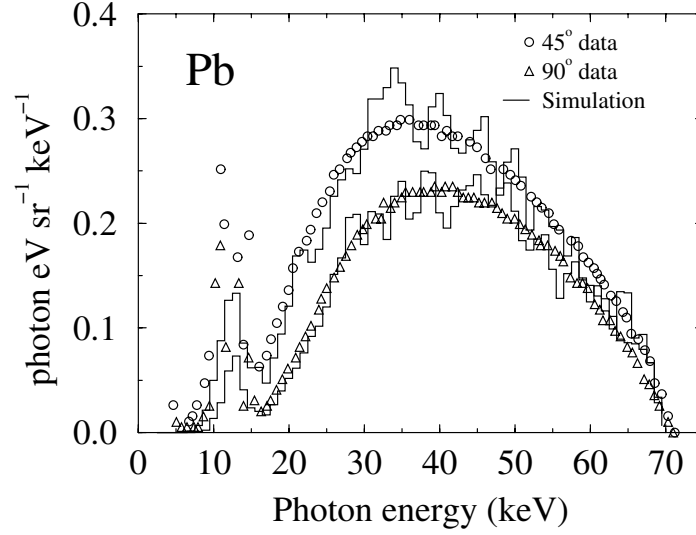


Fig. 1. Thick-target bremsstrahlung spectra (per incident electron) generated by 70 keV electrons impinging at 45° on a 28.06 mg/cm^2 -thick slab of Pb. The considered emission angles were 45° and 90° in transmission configuration. Symbols are experimental data of Ambrose et al. [14]. Histograms correspond to our simulation results

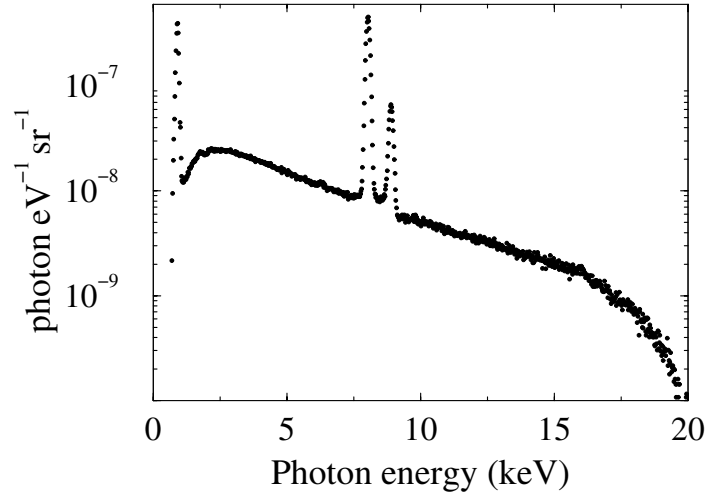


Fig. 2. Simulated (solid curve) and experimental (dots) x-ray spectrum (per incident electron) as a function of the radiated photon energy, generated by 20 keV electrons impinging normally on a thick slab of Cu; the detection angle was 130° . The experimental data are from [2]

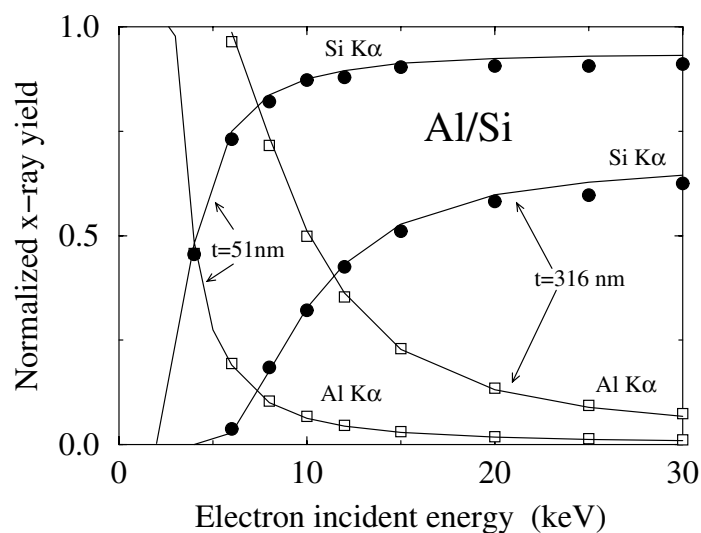


Fig. 3. Variation of the K x-ray intensity (Al K α and Si K α) with electron incident energy for Al films with thicknesses of 51 nm and 316 nm deposited on Si. Symbols represent experimental measurements of Bastin and Heijligers [15]. Continuous curves are our simulation results

References

1. J. Sempau, E. Acosta, J. Baró, J.M. Fernández-Varea, F. Salvat: Nucl. Instrum. Meth. B **132**, 377 (1997)
2. E. Acosta, X. Llovet, E. Coleoni, J.A. Riveros, F. Salvat: J. Appl. Phys. **83**, 6038 (1998)
3. R. Mayol, F. Salvat: J. Phys. B: At. Mol. Opt. Phys. **23**, 2117 (1990)
4. P.J. Statham: X-Ray Spectrom. **5**, 154 (1976)
5. Y. Namito, H. Hirayama, S. Ban: Radiat. Phys. Chem. **53**, 283 (1998)
6. L.M.N. Távora, E.J. Morton: Nucl. Instrum. Meth. B **143**, 253 (1998)
7. Y. Namito, H. Hirayama: Nucl. Instrum. Meth. A **423**, 238 (1999)
8. L. Kissel, C.A. Quarles, R.H. Pratt: At. Data Nucl. Data Tables **28**, 381 (1983)
9. E. Benedito, J.M. Fernández-Varea, F. Salvat: Nucl. Instrum. Meth. B (in press)
10. F. Salvat, J.M. Fernández-Varea: Nucl. Instrum. Meth. B **63**, 255 (1992)
11. N.S. Shin, Y.M. Koo, C.H. Chang, H. Padmore: J. Appl. Phys. **86**, 902 (1999)
12. R.H. Pratt, H.K. Tseng, C.M. Lee, L. Kissel, C. McCallum, M. Riley: At. Data Nucl. Data Tables **20**, 175 (1977)
13. S.M. Seltzer, M.J. Berger: Nucl. Instrum. Meth. B **12**, 95 (1985)
14. R. Ambrose, D.L. Kahler, H.E. Lehtinen, C.A. Quarles: Nucl. Instrum. Meth. B **56/57**, 327 (1991)
15. G.F. Bastin, H.J.M. Heijligers: X-Ray Spectrom. **19**, 212 (2000)

Particle Transport in Inhomogeneous Media

J. Tickner

CSIRO Minerals, PMB 5, Menai, NSW 2234, Australia

Abstract. A method is described for simulating particle transport in a medium which is homogeneous on a macroscopic scale but contains small regions having a different composition from the bulk medium. Modelling the regions explicitly becomes prohibitively expensive when their number density is large. Instead, a sampling scheme is developed which randomly positions regions in the path of the particle being tracked and then discards them once the particle moves on.

Two example applications of the method are described, namely modelling the transmission of beta-rays through pneumatically suspended finely ground coal and the gamma-ray energy deposition distribution in aerated water. In both cases, it is found that a detailed treatment of the inhomogeneous medium yields appreciably different results from assuming a uniform mean composition.

1 Introduction

Materials are commonly encountered in nuclear transport problems, which whilst homogeneous on a macroscopic scale, contain numerous regions of different composition and/or density. For example, many processes in the minerals industry use pneumatically conveyed powders, slurries or aerated liquids. For the purpose of simulating nuclear transport, it is commonly assumed that a uniform material of appropriate mean composition and bulk density can be substituted. The alternative approach of explicitly simulating all of the inhomogeneities is impractical for all but the simplest cases.

This paper describes an alternative method for simulating particle transport in a region which consists of a uniform background material containing a large number of randomly positioned spheres of a different material. The method has been implemented into a stand-alone EGS4 [1] code that allows the user to track particles through an arbitrary geometry.

2 Tracking Algorithm

Consider a region which is homogeneous apart from the inclusion of N spheres per unit volume of a different material, each having radius r . The cross-section for a particle (beta-ray, gamma-ray etc) entering a sphere, σ , is given simply by

$$\sigma = \pi r^2. \quad (1)$$

The probability, dp that a particle collides with a sphere after travelling a short distance dx is then

$$dp = N\sigma dx. \quad (2)$$

Consequently, the probability, $p(x)$, that a particle travels a distance x before colliding with a sphere is given by

$$p(x) = \frac{1}{\lambda} \exp\left(-\frac{x}{\lambda}\right) \quad (3)$$

where $\lambda = 1/N\sigma$ is the mean-free path (MFP) of particles in the inhomogeneous region for undergoing collisions with a sphere.

When a particle first enters the inhomogeneous region, the distance to the first collision with a sphere is sampled from equation 3. This is achieved conveniently by choosing the number of MFPs to the next collision to be

$$n_{\text{MFP}} = -\ln(\xi) \quad (4)$$

where ξ is a uniformly distributed random number on the interval $(0, 1]$. Every time the particle is transported a distance x , n_{MFP} is decreased by x/λ . If this results in n_{MFP} becoming negative, the particle is flagged as entering a sphere at the next step and the step length is adjusted to equal the remaining distance to the sphere.

The position on the sphere's surface where the particle enters must then be sampled. The position can be described in terms of a polar angle θ and an azimuthal angle ϕ . The polar angle varies from 0, corresponding to a glancing tangential collision, to $\pi/2$ for a head-on collision. The probability distribution for θ is given by

$$p(\theta) = 2 \cos \theta \sin \theta \quad (5)$$

Equation (5) can be sampled by setting

$$\cos \theta = \xi^{1/2} \quad (6)$$

where again ξ is a uniformly distributed random number in the interval $(0, 1]$.

The azimuthal angle ϕ is sampled uniformly in the interval 0 to 2π . Once θ and ϕ are known, the sphere can be positioned relative to the current position of the particle being tracked.

Normal tracking then resumes until the particle leaves the sphere. The distance to the next collision with a sphere is then re-sampled and the process repeated until the particle is terminated or leaves the inhomogeneous region.

Care has to be taken than any secondary particles produced by collisions inside the sphere are also correctly tracked. This is achieved by keeping information on the size and position of the current sphere separately for each particle on the tracking stack. It is also important not to discard a sphere immediately that a particle exits, as this removes the possibility of the particle scattering back in.

In practice, a sphere is not removed until the particle being tracked either enters a new sphere or escapes from the inhomogeneous region.

The method can be extended to track particles through a region where spheres of different sizes and/or compositions are present. If m types of sphere are present, with the i th type having radius r_i and number density N_i , then the MFP of the material is given by

$$\frac{1}{\lambda} = \sum_{i=1}^m \frac{1}{\lambda_i} \quad (7)$$

where $\lambda_i = 1/N_i\sigma_i$ and $\sigma_i = \pi r_i^2$. When a particle is flagged as entering a sphere, the type of sphere must be randomly sampled. The probability, p_i , of hitting a sphere of type i is

$$p_i = \frac{N_i\sigma_i}{\sum_{j=1}^m N_j\sigma_j} \quad (8)$$

Strictly, (3) for the distance between collisions is the distance between sphere centres. If the spheres occupy a large fraction of the total volume, then the distance between collision points measured from the spheres' surfaces will be smaller than predicted by (3). This can be accounted for by multiplying the attenuation length λ by a correction factor $1 - V$, where V is the fraction of the total volume occupied by the spheres and is given by $V = N \cdot 4/3\pi r^3$.

3 Application to Beta-ray Transmission

In the first example, the tracking algorithm is used to investigate the dependence on particle size of the transmission of beta-rays through a 50 cm thick slab of air (density 1.2 mgcm^{-3}) containing 0.8 mgcm^{-3} of pulverised coal. This configuration was chosen to approximately reproduce the conditions found in the fuel feed pipe of a coal fired burner [2].

The algorithm is implemented within the EGS4 framework including the PRESTA [3] electron tracking modification. Normally incident electrons are started on one face of the slab and the number of electrons exiting the opposite face is counted. Electrons are discarded inside the slab if their energy falls below 50 keV. The transmission of 300 keV and 600 keV electrons is measured as a function of particle size between 10 μm and 200 μm . These energies were chosen to illustrate the different effects of particle size on transmission when the transmission is either very small or close to unity. At 10 μm , the particle number density is approximately $1.1 \times 10^6 \text{ cm}^{-3}$.

Figures 1(a) and 1(b) plot the transmission as a function of particle size for the two energies. Also shown for the 600 keV case is the transmission for a homogeneous medium having the same average composition and bulk density as the air/coal mixture. For 300 keV electrons, the transmission through a uniform medium is zero.

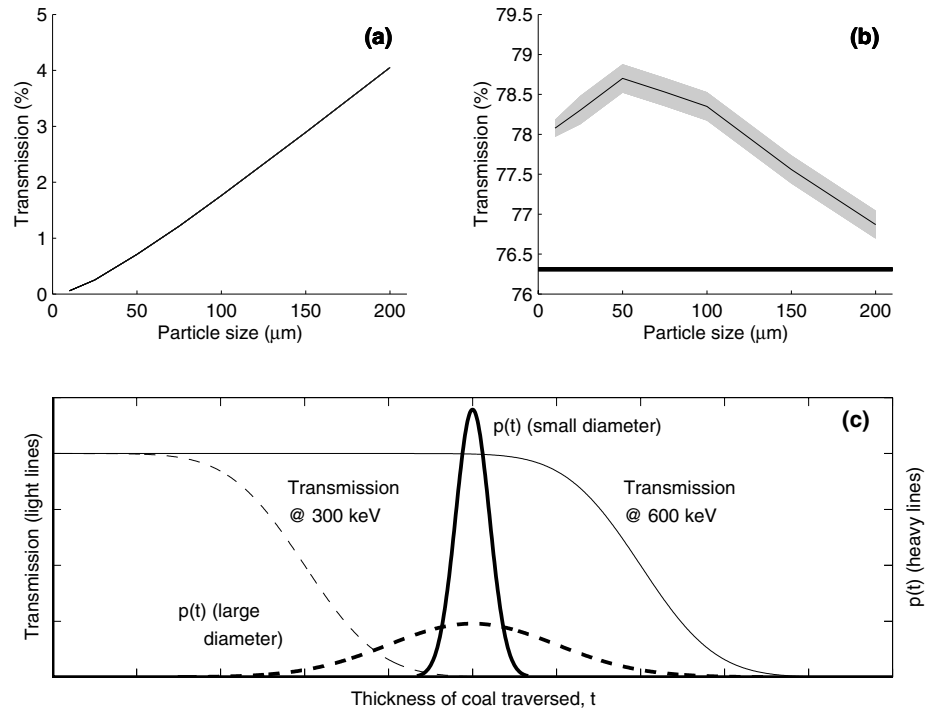


Fig. 1. (a) Transmission of 300 keV electrons through coal/air mixture as a function of coal particle size. The grey band denotes the 1σ statistical error. (b) As for (a) for 600 keV electrons. The horizontal line shows the transmission for a uniform material (c) The light lines sketch the transmission of 300 (*dashed*) and 600 keV (*solid*) electrons as a function of the total thickness of coal traversed whilst crossing the air/coal slab. The heavy lines show the probability, $p(t)$, of encountering a particular coal thickness t for smaller (*solid*) and larger (*dashed*) particle sizes

The behaviour of the transmission with respect to particle size can be understood qualitatively by referring to Fig. 1(c). The light solid and dashed lines sketch the probability of an electron being transmitted as a function of the total thickness of coal traversed for 600 and 300 keV electrons respectively. On purely statistical grounds, for a particular coal mass loading the probability of traversing either a very small or very large coal thickness increases as the coal particle size increases. This is because fewer coal particles are encountered on average and hence the *fluctuations* in the number of particles (and coal thickness) traversed increases. The heavy solid and dashed lines sketch the probability distributions for the amount of coal traversed for smaller and larger particle diameters.

In the 300 keV case, the transmission for small coal particles is low. As the particle size increases, an increasing fraction of electrons pass through significantly *less* coal than average and are transmitted. Consequently, the transmission increases with increasing particle size. The opposite happens in the 600 keV case.

Here, as the particle size increases, the reduced transmission of particles passing through *more* coal than average more than offsets the increased transmission due to electrons passing through less coal and so the transmission decreases.

Interestingly, the transmission through a uniform material is rather lower than that through the coal/air mixture. This is because energy loss and multiple scattering for a mixture are not equal to the sums of energy loss or scattering for the individual components [4].

4 Application to Gamma-ray Transmission

In the second example, the deposition of energy by gamma-rays is calculated as a function of depth in a semi-infinite volume of water containing 50% air by volume. For simplicity, the air is neglected and replaced by a vacuum. Normally incident 20 keV photons are started on the front face of the water volume and the energy deposited in 3 cm thick slabs is recorded. The slab thickness is chosen to be approximately 1 attenuation length for 20 keV photons. The energy deposition relative to the deposition recorded when the air/water mixture is replaced by a uniform material having one half the density of normal water is then calculated. The EGS4 code is used to perform the photon transport, together with the LSCAT [5] modification to improve the description of Compton scattering.

Figure 2 plots the relative energy deposition as a function of depth for air bubble sizes in the range 250 μm to 2000 μm .

As the air bubble size increases, the energy deposition at large depths increases. At the same time, the energy deposited close to the source decreases. When large bubbles are present in the water, the probability of a gamma-ray traversing substantially more air than average becomes significant. This tends to increase the number of gamma-rays that penetrate a long way into the water, which increases the energy deposition at large distances from the source. As the particle size decreases, the results of the detailed simulation approach those of where the material is taken to be homogeneous. This is to be expected as, at the level of detail simulated in EGS4, the gamma-ray transport properties of a mixture are equal to the sum of the properties of the individual mixture components.

5 Conclusions

An algorithm has been developed that allows the efficient simulation of particle transport in inhomogeneous materials, even when the number of inhomogeneities is very large (of order 10^6 cm^{-3} or higher). In the limit that all CPU time is consumed on boundary checks and that the mean distance between particle interactions is large compared to the distance between inhomogeneities, the CPU time required to track a particle should increase like $N^{1/3}$ where N is the number density of the inhomogeneities. In practice, the increase is found to be less severe than this. This compares with a theoretical $N^{4/3}$ dependence if all of the regions of different composition were simulated explicitly.

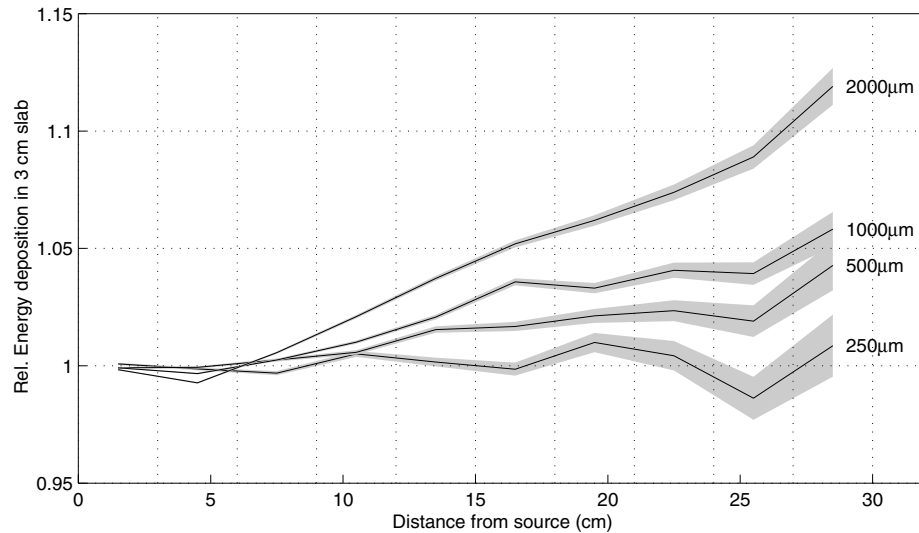


Fig. 2. Energy deposition in aerated water with 250, 500, 1000 and 2000 μm diameter bubbles relative to deposition in a homogeneous material having the same bulk density, plotted as a function of the distance from the source. The solid lines show the central values and the grey bars the 1σ statistical errors

The algorithm has been implemented into a stand-alone EGS4 code which allows the user to set up a problem with arbitrary geometry, source and tally descriptions using a graphical interface [6].

The application of the algorithm to an electron transmission and gamma-ray depth-dose calculation is demonstrated. In both cases, it is found that there is a substantial dependence on the size and number density of the inhomogeneous regions, even when the bulk density and composition of the material in which the particles are being tracked is kept constant. In particular, the standard practice of assuming a uniform mean composition and density is shown to yield inaccurate results.

References

1. W.R. Nelson, H. Hirayama, D.W.O. Rogers: SLAC-265
2. M.J. Millen et al: Flow Meas. and Instr.: **11** (in press) (2000)
3. A.F. Bielajew, D.W.O. Rogers: Nucl. Inst. Meth. **B18**, 165 (1987)
4. W.T. Scott: Rev. Mod. Phys. **25** 231 (1963)
5. Y. Namito, H. Hirayama, S. Ban: Rad. Phys. Chem. **53**, 283 (1998)
6. J.R. Tickner: *Poster presentation at MC2000 conference, 23-27 October, 2000 Lisbon*

Fast Simulation of X-ray Transition Radiation in the GEANT4 Toolkit

V.M. Grichine

CERN/IT, Geneva 23 CH-1211, Switzerland, on leave from P.N. Lebedev Physical Institute, Lenin Pr. 53, 117924 Moscow, Russia

Abstract. An implementation of fast simulation models provided by the GEANT4 package for the description of X-ray transition radiation (XTR) produced by a relativistic charged particle in a multi layered medium is discussed. The implementation allows us to calculate the number of XTR photons, their energy and angular spectra in a number of XTR radiators of practical interest. Ionisation produced by the relativistic particle and the XTR photons are also described in terms of fast parameterisation. Comparison of simulation with experimental data from gaseous detectors is presented.

1 Introduction

GEANT4 is an object-oriented toolkit for simulation in High Energy Physics (HEP), Astrophysics and medical imaging and therapy [1]. GEANT4 exploits advanced software engineering techniques and object-oriented technology to improve the validation of physics results for the simulation of relativistic particle transport through a complex geometry made of different materials and detectors. It is a completely new toolkit, engineered from the start with an object-oriented design. In several areas, though, it borrows physical models utilized in the GEANT3 simulation package [2]. GEANT4's design divides the responsibilities for different parts of the work into class categories. These include events, geometry, tracking, processes, user interfaces, visualization and so on [1].

X-ray transition radiation (XTR) is widely used in experimental high energy physics for particle identification, especially for identification of electrons in an environment of high hadron background [3]. XTR was not implemented in the GEANT3 package due to the following problems. XTR is a space distributed boundary process; XTR photon generation is distributed along the trajectory of the incident particle roughly within the limits of the XTR formation zone $\sim 10 - 100 \mu\text{m}$ around an interface. Moreover XTR is usually generated by a special radiator (stack of foils interspersed with gas gaps or foam); in this case the process of formation of the XTR photon is distributed over the whole radiator and is limited by the X-ray absorption path length. It is therefore difficult to describe XTR in terms of a point-like electro-magnetic process which was the standard approximation in GEANT3.

In this paper an implementation of XTR for the GEANT4 tracking package is discussed. The implementation is based on the fast simulation (parameterisation) approach developed in GEANT4 for the description of electro magnetic and hadronic shower development. Formulae describing different types of XTR

radiators written in physically clear form convenient for software implementation are presented. The results of simulation are compared with experimental data.

2 X-ray Transition Radiation from a Radiator

In practice XTR is generated by special radiators consisting of a stack of foils (plastics like polypropylene or mylar) with gas gaps or a foam. Suppose we have n foils with thickness t_1 interspersed by gas gaps with thickness t_2 . Both the foil and the gas gap thicknesses fluctuate according to the distribution $p(t_j)$, $j = 1, 2$. Then the mean number of XTR photons generated per unit energy ω and ξ , $d^2\bar{N}_{rad}/d\omega d\xi$, from the radiator is given by the following expression [4–9]:

$$\frac{d^2\bar{N}_{rad}}{d\omega d\xi} = \frac{\alpha}{\pi} \frac{\xi}{\omega} \left| \frac{1}{\gamma^{-2} + \eta^{(1)} + \xi} - \frac{1}{\gamma^{-2} + \eta^{(2)} + \xi} \right|^2 R, \quad (1)$$

where α is the fine structure constant, γ is the Lorentz factor of the particle, $\eta^{(j)} = (\omega_p^{(j)}/\omega)^2$, and $\omega_p^{(j)}$ is the plasma energy in the j -th medium ($j = 1, 2$), $\xi = 2(1 - \cos\theta) \sim \theta^2 \ll 1$, where the angle θ is counted from the particle direction, and R reflects the contribution of the radiator. In the most general form the factor R can be expressed as [9]:

$$R = \frac{1 - Q^n}{1 - Q} Re(F) + Re(G), \quad Q = Q_1 Q_2, \quad H = H_1 H_2, \quad (2)$$

$$F = \frac{(1 + Q_1)(1 + H) - 2H_1 - 2Q_1 H_2}{1 - H}, \quad G = \frac{2(1 - H_1)(Q_1 - H_1)H_2(Q^n - H^n)}{(1 - H)(Q - H)},$$

where the values Q_j and H_j , ($j = 1, 2$) are:

$$Q_j = \langle \exp[-\mu_j(\omega)t_j] \rangle, \quad H_j = \left\langle \exp \left[-\frac{\mu_j(\omega)t_j}{2} - i \frac{t_j}{Z_j} \right] \right\rangle. \quad (3)$$

In the latter expressions $\langle \dots \rangle$ means averaging over the distribution $p(t_j)$, $j = 1, 2$; μ_j is the linear absorption coefficient for XTR photons and Z_j is the formation zone of XTR in the j -th medium, respectively. In the energy range $\omega \geq 1$ keV, for plastics and gases the formation zone depends on the real part of the dielectric constant only:

$$Z_j = \frac{2c\hbar}{\omega} \frac{1}{\gamma^{-2} + \eta^{(j)} + \xi}, \quad \text{since } \mu_j Z_j \sim Im(\varepsilon_j) / |1 - Re(\varepsilon_j)| \ll 1. \quad (4)$$

Note that the factor F is responsible for the creation of XTR photons in each plate due to the interference between production at its surfaces, while the factor G describes creation of the XTR photon by interference of electro-magnetic waves generated from different plates. Both terms in (2) take into account absorption of the XTR photons in plastics and gas gaps of the radiator. The terms H_j are responsible for interference of the XTR photon yield from the radiator depending on the XTR photon energy and angle.

Since the t_j thicknesses are positive and Q_j , H_j have exponential form, it is convenient to represent the distribution $p(t_j)$ in the form of the Gamma distribution:

$$p(t_j) = \left(\frac{\nu_j}{\bar{t}_j}\right)^{\nu_j} \frac{\bar{t}_j^{\nu_j-1}}{\Gamma(\nu_j)} \exp\left[-\frac{\nu_j t_j}{\bar{t}_j}\right], \quad (5)$$

where Γ is the Euler gamma function, \bar{t}_j is the mean thickness of the j -th medium in the radiator and $\nu_j > 0$ is a parameter roughly describing the relative fluctuations of t_j . In fact, the relative fluctuation δ_j according to (5) is,

$$\delta_j = \frac{\sqrt{\langle(t_j - \bar{t}_j)^2\rangle}}{\bar{t}_j} = \frac{1}{\sqrt{\nu_j}}, \quad (j = 1, 2). \quad (6)$$

From the distribution (5) one can derive analytically the values Q_j and H_j :

$$Q_j = \left[1 + \frac{\mu_j(\omega)\bar{t}_j}{\nu_j}\right]^{-\nu_j}, \quad H_j = \left[1 + \frac{\mu_j(\omega)\bar{t}_j}{2\nu_j} + i\frac{\bar{t}_j}{Z_j\nu_j}\right]^{-\nu_j}. \quad (7)$$

The equations (7) allow us to calculate the factor R analytically and hence evaluate the density of XTR photons $d^2\tilde{N}_{rad}/d\omega d\xi$ according to expression (1) for any radiator tuning \bar{t}_j and ν_j . However in some practical cases it is possible to simplify expressions (7) and accelerate the calculation of R and $d^2\tilde{N}_{rad}/d\omega d\xi$. Let us consider some particular cases.

Suppose that $\nu_j = 1$, i.e., the gamma distribution reduces to the exponential one. We suppose that the following physical condition is satisfied:

$$Z_j \sim \bar{t}_j \ll \lambda_j = \mu_j^{-1}(\omega), \quad (8)$$

where λ_j is the mean path length of XTR photons in the j -th medium and we propose this be referred to as the foam approximation. Note that we can not neglect the small terms $\mu_j\bar{t}_j \ll 1$ in Q_j , i.e., neglect XTR photon absorption, since it results in numerical instability when F and G are calculated. If we replace the latter condition (8) by, $Z_j \ll \bar{t}_j$, i.e., $Z_j \ll \bar{t}_j \ll \lambda_j$, we can neglect the H_j values. In fact, $H_j \sim -iZ_j/\bar{t}_j \simeq 0$. Then the expression (2) for R is significantly simplified:

$$R = \frac{1 - Q^n}{1 - Q} (1 + Q_1), \quad Q_j = \frac{1}{1 + \mu_j(\omega)\bar{t}_j}. \quad (9)$$

This case corresponds to the fully irregular radiator, when R is independent of γ and ξ .

Let us consider now the case when plates with fixed thickness create a fully irregular stack, i.e., one can neglect interference between different plates:

$$\nu_1 \rightarrow \infty, \quad Z_1 \sim \bar{t}_1 \ll \lambda_1, \quad \text{and} \quad \nu_2 = 1, \quad Z_2 \ll \bar{t}_2 \ll \lambda_2. \quad (10)$$

Then the contribution of the radiator is described by:

$$R = \frac{1 - Q^n}{1 - Q} \left(1 + Q_1 - 2\sqrt{Q_1} \cos \frac{\bar{t}_1}{Z_1}\right) \quad (11)$$

$$\simeq n \left[(1 - \sqrt{Q_1})^2 + 4\sqrt{Q_1} \sin^2 \frac{\bar{t}_1}{2Z_1} \right] > 0, \quad (12)$$

where the right part is valid when the number of plates n is not very big, i.e., $n[\mu_1(\omega)\bar{t}_1 + \mu_2(\omega)\bar{t}_2] \ll 1$. Expression (12) describes the contribution from n different plates of fixed thickness without taking into account interference between them (irregular stack).

Finally we consider the case of the regular radiator, $\nu_j \rightarrow \infty$, $Z_j \sim \bar{t}_j \ll \lambda_j$. Then

$$Q_j = \exp[-\mu_j(\omega)\bar{t}_j], \quad H_j = \exp\left[-\frac{\mu_j(\omega)\bar{t}_j}{2} - i\frac{\bar{t}_j}{Z_j}\right] = \sqrt{Q_j} \exp\left[-i\frac{\bar{t}_j}{Z_j}\right]. \quad (13)$$

In this case it is convenient to represent the denominators of F and G by real numbers, since the denominators are small due to $Q \lesssim 1$. The corresponding formulae are considered in detail elsewhere [10].

3 Fast Simulation of X-ray Transition Radiation

XTR generation from radiators is described by a family of classes shown in Fig. 1. The class G4ForwardXrayTR is responsible for the description of XTR photon generation from one interface between two different materials.

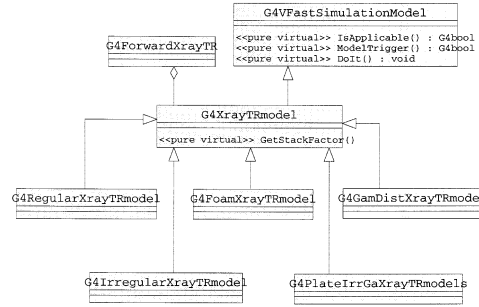


Fig. 1. A diagram for GEANT4 classes describing XTR generation from an XTR radiator. The base class G4XrayTRmodel inherits from G4ForwardXrayTR describing XTR formation from one interface and from G4FastSimulationModel which provides virtual function for fast simulation of XTR generation. Each particular XTR radiator model, like e.g., G4IrregularXrayTRmodel, implements pure the virtual function GetStackFactor calculating the factor R

Fig. 2 illustrates the working of the G4XrayTRmodel::DoIt function. The ionisation energy losses were simulated according to the Photo Absorption Ionisation (PAI) model described in detail elsewhere [11]. The PAI model is used also in the fast parameterisation mode.

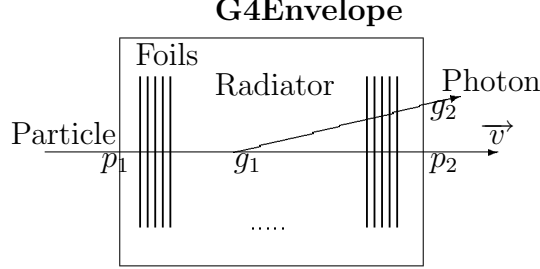


Fig. 2. A description of the G4XrayTRmodel::DoIt function. An incident charged particle with a Lorentz factor $\gamma \geq 500$ enters the logical volume G4Envelope at the point p_1 and exits at p_2 . It moves along the direction given by the unit vector \vec{v} . XTR photons are generated randomly along the particle trajectory inside G4Envelope with energies and polar angles relative to \vec{v} randomly selected from the corresponding tables of the integral and angular distributions. Each XTR photon is then moved to the border of G4Envelope. The sum of the XTR photon energies is subtracted from the kinetic energy of the incident particle

4 Comparison with Experimental Data

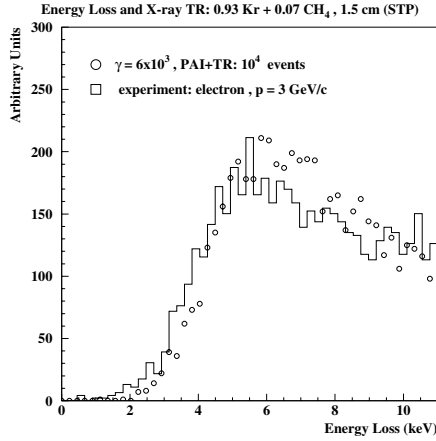


Fig. 3. The ionisation energy loss distribution produced by electrons with a momentum of 3 GeV/c in a gas mixture 93%Kr + 7%CH₄ with a thickness of 1.5 cm (STP). The histogram is experimental data [12], open circles are simulation according to the PAI model and the X-ray TR model

~ 0.5 allows us to get agreement between the experiment [13] and our simulation.

The implementation described above was compared with experimental data. We performed GEANT4 simulation of two experimental set-ups [12,13] where a clear energy calibration procedure was available.

Histograms in Fig. 3 and 4 are the experimental data and points are our simulations with the GEANT4 package. We used in both cases the irregular stack approximation since it provides a fast and numerically stable description of the XTR radiators and due to lack of data on the accuracy of positioning foils in the radiators. Note that direct application of (9) results in overestimation of the XTR yield for the case shown in Fig. 4.

Introduction of empirical factor

5 Conclusions

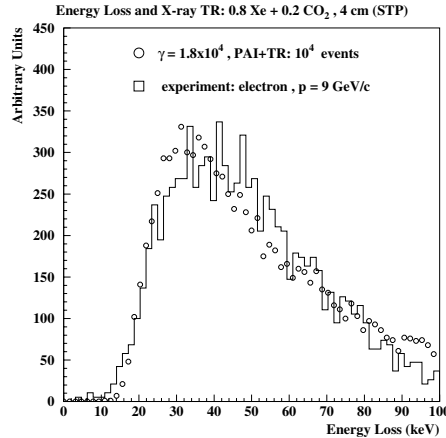


Fig. 4. The ionisation energy loss distribution produced by protons with a momentum of 9 GeV/c in a gas mixture $0.8\text{Xe} + 0.2\text{CO}_2$ with a thickness of 4 cm (STP). The histogram is the experimental data [13], open circles are simulation according to the PAI model and the X-ray TR model

the XTR photon yield as well as its energy and angular spectra.

The author is thankful to Drs. J. Allison, J. Apostolakis, D. Barberis, and B.M. Bolotovskii for useful discussions.

References

1. GEANT4 Collaboration: *GEANT4: An Object-Oriented Toolkit for Simulation in HEP*, CERN/LHCC 98-44,; see also the web site: <http://www.cern.ch/geant4>
2. *GEANT3, CERN Program Library Long Writeup*, W5013 (1993)
3. B. Dolgoshein: Nucl. Instr. and Meth. A **326**, 434 (1993)
4. B.M. Bolotovskiy: Lebedev Institute Proceedings, **140**, 95 (1982)
5. A.L. Avakian, G.M. Garibian, C. Yang: Nucl. Instr. and Meth., **129**, 303 (1975)
6. V.L. Ginzburg, V.N. Cytovitch: Soviet Physics (Uspekhi) **126**, 553 (1978)
7. G.M. Garibian, L.A. Gevorgian, C. Yang: Sov. Phys.- JETP **39**, 265 (1975)
8. G.M. Garibian, L.A. Gevorgian, C. Yang: Nucl. Instr. and Meth. **125**, 133 (1975)
9. G.M. Garibian, Yan Shi: *X-ray Transition Radiation* (Erevan 1983), in Russian
10. J. Apostolakis, S. Giani, M. Maire: to be published in Computer Physics Communications
11. J. Apostolakis, S. Giani, M. Maire: to be published in Nucl. Instr. and Meth. A
12. F. Harris, T. Katsura, S. Parker, V.Z. Peterson, R.W. Ellsworth, G.B. Yodh, W.W.M. Allison, C.B. Brooks, J.H. Cobb, J.H. Mulvey: Nucl. Instr. and Meth. **107**, 413 (1973)
13. M.L. Cherry, G. Hartmann, D. Muller, T.A. Prince: Phys. Rev. D **10**, 3594 (1974)

The fast simulation facility in the GEANT4 package was applied to the simulation of XTR generation in multi layered media. The implementation of the XTR generation in different types of radiators described above provides a satisfactory description of experimental data.

The object-oriented design of XTR models in GEANT4 allows a user to describe any specific radiator deriving a special class describing the radiator model. Only the virtual function, `GetStackFactor`, is required to be implemented for the description of the radiator contribution. Introducing empirical parameters and coefficients allows the user to tune

Optimization of a Tunable Quasi-Monochromatic X-ray Source for Cell Irradiations

W. Neubert¹, W. Enghardt¹, U. Lehnert¹, E. Müller¹, B. Naumann²,
A. Panteleeva¹, and J. Pawelke¹

¹ Forschungszentrum Rossendorf, 01314 Dresden, Germany

² TU Dresden, Institut für Kern- und Teilchenphysik, 01069 Dresden, Germany

Abstract. A setup for radiobiological studies using channeling radiation produced at a beamline of the superconducting electron accelerator ELBE has been optimized in order to reduce the bremsstrahlung and neutron background. The electron beam transport was designed using the code package PARMELA. The interaction of the electrons with the elements of the beam delivery and bremsstrahlung production has been calculated by means of GEANT. These results were used as input for EGS4 to calculate dose distributions in a biological specimen.

1 Introduction

A superconducting **E**lectron **L**inear accelerator of high **B**rilliance and low **E**mittance is under construction at the Forschungszentrum Rossendorf [1]. The electron beam with ps time structure, an energy up to 40 MeV and a maximum current of 1 mA is provided for various kinds of secondary radiation sources as free electron lasers in the infrared range and production targets for polarized bremsstrahlung, X-rays and neutrons. Quasi-monochromatic X-rays will be produced by electron channeling in crystals which will be applied to quantum energy dependent measurements of the relative biological effectiveness (RBE) for X-rays [2] within 10 keV and 50 keV.

Unlike synchrotron radiation facilities the biological samples are processed very close to the electron beamline at this novel compact X-ray source and, therefore, an efficient suppression of disturbing background radiation is required.

2 Electron Beam Transport

The beamline from the accelerator hall to the radiation physics cave, where the quasi-monochromatic X-rays will be generated (Fig. 1), was designed for a dispersion-free beam transport with minimal loss. It provides a versatile focusing at the channeling target and conserves the low transverse emittance of the electron beam.

For the beamline design first-order analytical calculations were verified with the PARMELA code [3]. The system delivers an electron beam with 3π mm mrad transverse emittance to the channeling target at focal spot diameters ranging from 4 mm to less than 1 mm. The interaction of the electron beam with the

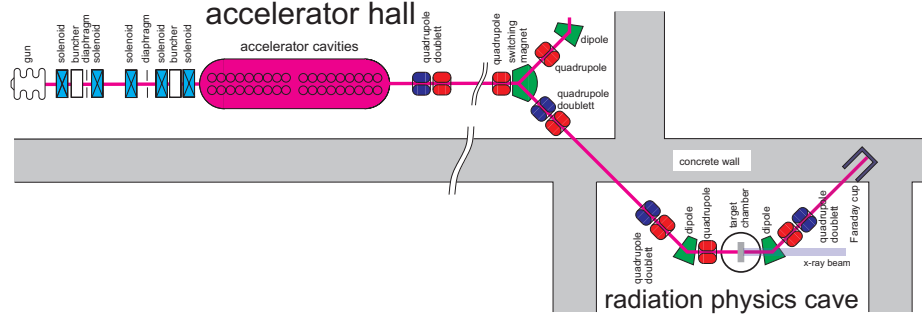


Fig. 1. The electron optical system of the ELBE accelerator and of the radiation physics cave, where quasi-monochromatic X-rays will be produced

X-ray production target increases the beam divergence and leads to collisions of electrons with the beamline elements downbeam the target. This causes a considerable bremsstrahlung background that may influence the radiobiological measurements, while the background contribution originating from the beam delivery to the target is negligible.

3 GEANT Simulation of the Radiation Physics Setup

The complete setup downbeam the target crystal as displayed in Fig. 2 has been taken into account in the GEANT [4] simulations. The background calculations have been started assuming a configuration with a distance of 123 cm between the crystal and the center of the bending magnet, which separates the electrons from the X-ray beam. The X-rays enter the cell irradiation chamber through a 100 μm beryllium window. They are filtered by a 70 μm Al absorber and hit the biological specimen as specified in sect. 5 at a distance of 1.5 m from the X-ray production target.

To evaluate the reliability of GEANT results, a similar experimental situation at the superconducting linear accelerator S-DALINAC of the Darmstadt University of Technology has been considered. There, channeling radiation was produced by bombarding a 42 μm diamond crystal with 9 MeV electrons [5]. GEANT calculations [6] reproduced the bremsstrahlung background measured in the energy region between 10 and 30 keV to an accuracy of 50 %. This encouraged us to perform simulations at the higher electron energy of 20 MeV which will be necessary to generate channeling radiation in the energy range from 10 to 30 keV. To obtain a channeling radiation intensity that is sufficiently high for biological applications (cell survival studies), a diamond crystal of 100 μm thickness has to be used.

In our calculations the electron beam was started at 1 cm in front of a carbon target that simulates the diamond crystal. The input parameters were taken from the beam transport calculations. Energy loss, multiple scattering, bremsstrahlung and pair production were considered in all construction materials.

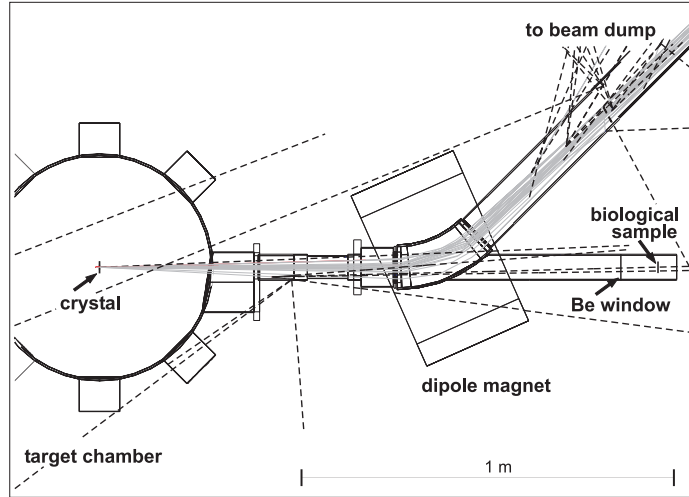


Fig. 2. The channeling radiation source with tracks of electrons (grey) and photons (dashed)

Multiple scattering in the target was found to be the dominating process which determines the beam divergence. Mainly electrons interacting in the entrance region of the bending magnet contribute to the bremsstrahlung background level. For the original setup this background contribution has been found to be about one order of magnitude larger than the bremsstrahlung from the target itself. A significant reduction was achieved by reducing the distance between the crystal and the magnet to $\simeq 80$ cm and by increasing the beam tube diameters from 40 to 63 mm and the magnet gap from 60 to 90 mm. This way, the bremsstrahlung

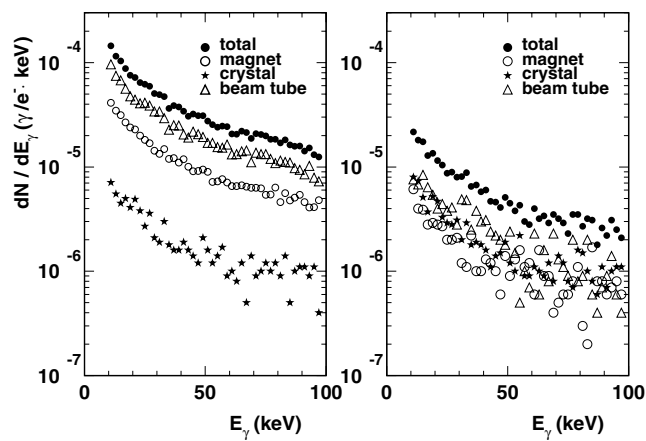


Fig. 3. Bremsstrahlung yields before (left) and after the setup optimization (right)

background could be reduced to the level of the target contribution (Fig. 3). The bremsstrahlung yields were extrapolated from the 10 keV lower tracking limit of GEANT to the 1 keV limit of EGS4 using the *Schiff* formula for thin radiators taken from [7,8]. This is justified since the *Schiff* formula reproduces the shape of the bremsstrahlung spectrum obtained with GEANT both for carbon and iron. The supplemented low energy part of the bremsstrahlung spectrum contributes 3–5 % to the background intensity.

4 Calculations of Channeling Radiation

Unlike bremsstrahlung, the channeling radiation cannot be treated by means of GEANT. It occurs if a charged particle is moving under a small angle along a closely packed atomic plane in a crystal structure. Perpendicular to these planes the electrons are trapped in a potential well and emit channeling radiation due to radiative transitions between different bound quantum states. The radiation spectrum was calculated using the dipole approximation [9] for 20 MeV electrons channeling along the (110) plane of a 100 μm thick diamond crystal. In Tab. 1 we compare the intensities of bremsstrahlung simulated by GEANT and of channeling radiation calculated according to [9].

Table 1. Comparison of channeling radiation (CR) and bremsstrahlung intensities for the optimized geometry at 20 MeV electron beam energy. The maximum energies of CR emitted in forward direction are 17.1 keV (2 \rightarrow 1 transition) and 29.9 keV (1 \rightarrow 0 transition)

Energy interval	Intensity of bremsstrahlung (at sample surface) (γ/e^-)	Intensity of CR (γ/e^-)
15.9 \pm 1.1 keV	$1.5 \cdot 10^{-5}$	$3.9 \cdot 10^{-4}$
28.0 \pm 2.0 keV	$8.38 \cdot 10^{-6}$	$6.4 \cdot 10^{-4}$
10keV–20MeV	$6.7 \cdot 10^{-4}$	

5 Dose Calculations Using EGS4

According to the energy dependent attenuation factors [10] the photon flux above 10 keV X-ray energy is attenuated only by a minor amount in the Be exit window of the beam tube while the bulk of low energy secondary electrons (≤ 100 keV) is absorbed there.

To calculate dose distributions in thin layers irradiated by a photon beam we used the capability of the EGS4 code [11]. The biological sample is assumed to consist of three layers: a monolayer of fibroblast cells (4 μm thick) placed on a 10 μm cellulose membrane and covered with a 8 mm thick medium layer [12]. We

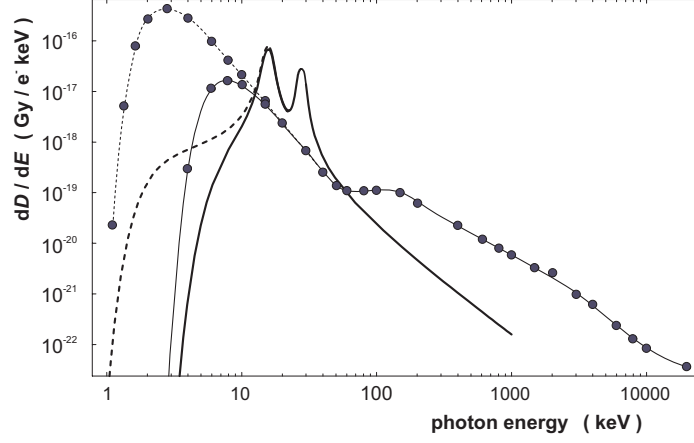


Fig. 4. Dose distributions obtained by EGS4 simulations for a $4 \mu\text{m}$ cell layer irradiated by bremsstrahlung (dots) and CR X-rays (thick line). The dotted and dashed lines are the corresponding calculations without the $70 \mu\text{m}$ Al absorber

Table 2. Expected doses in the biological sample

Photon energy	Dose in $10^{-16} \text{ Gy} / e^{-}$	
	with $100 \mu\text{m}$ Be window	with $70 \mu\text{m}$ Al absorber
1....10 keV background	13.00	0.70
10...100 keV background	1.04	0.86
≥ 100 keV background	0.29	0.29
17 keV CR line	3.23	2.82
29 keV CR line	1.53	1.49

studied both tracking and dose deposition in such thin layers. A lower thickness limit of $1 \mu\text{m}$ was found to be necessary to perform dose calculations within the photon energy region of 1.5-30 keV. The results of these dose calculations are summarized in Fig. 4 and Tab. 2. The dose provided by the discrete channeling lines exceeds the bremsstrahlung background by at least an order of magnitude. The introduction of a $70 \mu\text{m}$ Al absorber considerably reduces the low energy bremsstrahlung below 10 keV. However, the background dose is approximately the same as the channeling radiation dose.

The neutron dose produced by photons above the threshold of the (γ, n) reaction has been approximated using a method described in [13]. Based on the (γ, n) cross-sections of iron [14], a neutron energy distribution given in [15] and kerma factors for water [16] a neutron dose of $\simeq 10^{-19} \text{ Gy}/e^{-}$ is estimated which is negligible in comparison to the photon dose. We note that the neutron production is not reduced to the same extent as the bremsstrahlung level by

the improvement of the beam line. However, there is a need to confirm this estimation by forthcoming simulations with tools like FLUKA.

6 Conclusions

The application of Monte-Carlo simulation code packages is the only feasible way to estimate the real background level in case of a complex geometry and it allows, furthermore, sources of background radiation to be detected and the beam line geometry to be optimized. In a given energy interval, the intensity of the channeling radiation is expected to dominate over the bremsstrahlung background level. Still, the integral intensity of bremsstrahlung comes close to the intensity of channeling radiation which prevents energy selected cell irradiations. Therefore, a monochromatization of the photon beam becomes necessary whereas the dose deposition in the biological sample by the neutron background can be neglected. The design of an X-ray monochromator based on Bragg reflection at curved pyrolytic graphite crystals is in progress.

The EGS4 code makes it feasible to calculate dose distributions within the X-ray energy region from 1 to 30 keV in very thin samples like cell monolayers.

This work is supported by the Bundesministerium für Bildung, Wissenschaft Forschung und Technologie of Germany (06 DR 826).

References

1. W. Enghardt et al.: Acta Physica Polonica **30**, 1639 (1999)
2. D.T. Goodhead: 'Soft X-ray radiobiology and synchrotron radiation'. In: *Synchrotron Radiation in Biosciences*. ed. by B. Chance et al. (Clarendon Press/New York, Oxford University Press 1994)
3. L.M. Young, J.H. Billen: Los Alamos National Laboratory LA-UR-96-1835 (1996)
4. *GEANT: Detector Description and Simulation Tool*, CERN Program Library W 5013, March 1994
5. I. Reitz: *Untersuchung der Channelingstrahlung an Diamant am S-DALINAC bei einer Elektronenenergie von 9 und 10 MeV*. Diploma thesis, (TU Darmstadt 1999)
6. W. Neubert et al.: Report Jan. 1998 - June 1999, FZR-271, p. 25, Dresden (1999)
7. U. Kneissl: Atomkernenergie-Kerntechnik **42**, 151 (1983)
8. H.W. Koch, J.W. Motz: Rev. Mod. Phys. **31**, 920 (1959)
9. M. Kumakhov, R. Wedell: *Radiation of Relativistic Light Particles during Interaction with Single Crystals* (Akademie-Verlag, Berlin 1991)
10. <http://physics.nist.gov/PhysRefData/contents.html>
11. W.R. Nelson et al.: *The EGS4 code system*, SLAC-Report-265 (1985)
12. 'Tissue Substitutes in Radiation Dosimetry and Measurements'. In: ICRU Report **44**, (Bethesda, MD 1989)
13. B. Naumann et al.: *Entwicklung von Strahlfängern für maximale Elektronenenergie am Beschleuniger ELBE*, FZR-267, Dresden (1999)
14. S. Costa et al.: Nuovo Cimento B **51**, 199 (1967)
15. M. Barbier: *Induced Radioactivity* (North Holland Publ. Co, Amsterdam, 1969)
16. R.S. Caswell et al.: 'Tables of kerma factors'. In: *Monograph on basic physical data for neutron dosimetry*. ed. by J.J. Broerse (EUR 5629e, Euratom, Brussels, 1976)

Electron Photon Shower Simulation in TRIPOLI-4 Monte Carlo Code

Y. Peneliau

Commissariat à l'Énergie Atomique, CEA (France)

1 Introduction

TRIPOLI-4 [1] is a three dimensional polykinetic Monte Carlo code. It simulates the transport of neutral particles (neutrons, photons) at low energies (from 1.E-11 up to 150. MeV). It is parallelized and runs on either workstation networks or massively parallel machines.

The aim of the article is to present the electron photon shower implementation in the code.

Section 2 presents electron and positron physics and section 3 is dedicated to photon physics. In section 4, comparisons between MCNP4, PENELOPE and TRIPOLI-4 results in transmission particles currents through different layers, for different energy ranges are detailed.

2 Electron and Positron Physics

2.1 Differential Cross Sections (DCS) and Cross Sections (CS)

We use Riley cross sections [2] for energies from 1 keV to 256 keV and Mott cross section [3] to Rutherford cross section ratios [4] for energies from 256 keV to 1 GeV, in the multiple scattering formalism for elastic DCS. Inelastic DCS are Möller [5] cross section for electrons and Bhabha [6] cross section for positrons. Bremsstrahlung cross section is based on Berger and Seltzer recommendation of 1970 [7]. At the high frequency limit, Fano, Koch and Motz formula is used [8]. For positrons, electron bremsstrahlung DCS to which we apply theoretical positron cross section to electron cross section ratio is used [9]. Positron annihilation DCS is Heitler's one [10].

Electron or positron soft collisions and hard collisions are distinguished in TRIPOLI-4 simulation. The threshold between hard and soft collisions is determined by two energy cutoffs, one for inelastic scattering and one for radiative emission. CS are calculated either analytically for inelastic scattering or numerically for bremsstrahlung emission over a 1000 points energetic mesh. Inelastic and bremsstrahlung energy cutoffs are identical for electrons and positrons.

2.2 Multiple Scattering Formalism

Multiple scattering formalism is Goudsmit Saunderson formalism [11–13], based either on Mott to Rutherford cross sections ratios or on Riley cross sections.

The maximum amount of energy loss is 8.3 % of electron (or positron) energy. This determines the length of the step in the multiple scattering. When no hard collision occurs during a step, the deviation is applied randomly on the step. When a hard collision occurs, the deviation is applied in the middle of the step.

2.3 Collisional and Radiative Stopping Powers

Collisional stopping powers come from Berger and Seltzer theory [14]. Collisional continuous energy loss due to multiple scattering formalism is sampled from Landau distribution [15,16].

Radiative stopping power is numerically calculated from bremsstrahlung DCS. In the same time, the second moment of the energy loss is also calculated. Radiative continuous energy loss is sampled from a Gaussian distribution (this imposes that bremsstrahlung energy cutoff is low).

Continuous energy losses are applied at the end of each step in the multiple scattering formalism.

2.4 Hard Collision Simulation

For electrons and positrons hard inelastic collisions, normalized Möller cross section (for electrons) and Bhabha cross section (for positrons) are used to determine secondary electron energy. Angular deviation is calculated using the relativistic kinematic formulae.

For electrons and positrons hard bremsstrahlung emission, secondary photon energy is sampled from precalculated interpolated densities (one density per point in CS mesh). Angular deviation is sampled from Bielajew distribution [17].

Concerning positron annihilation, secondary photons energies are sampled from Heitler formula. Angular deviation is calculated using the relativistic kinematic formulae.

3 Photon Physics

3.1 Differential Cross Sections (DCS) and Cross Sections (CS)

Photons DCS and CS are read from ENDF format evaluation files, ENDF/B6 or JEF2. These files are tabulated in the energy range from 10 keV up to 100 MeV. That means that today TRIPOLI-4 can only perform calculations in this range. Data read from evaluation files are coherent form factors and coherent CS for coherent scattering (Riley scattering), incoherent scattering function and incoherent CS (Compton scattering), K, LI, LII, LIII shells and total photoelectric CS for photoelectric absorption, and pair effect CS for electron-positron pair emission. K, LI, LII and LIII shells photoelectric DCS come from Gavrila theory [18,19] and pair effect DCS comes from Bethe-Heitler formalism [20].

3.2 Coherent Scattering

Coherent DCS is defined with form factors, real and imaginary anomalous scattering factors depending on the recoil momentum of the atom.

Angular deviation is sampled from biased density $f(k, \mu) = \frac{1-\beta}{2^{1-\beta}} * (1-\mu)^\beta$ and photon simulation weight is modified by the ratio of natural density to biased density. β is chosen so that $f(E, \mu)$ is as close as possible to $\frac{d\sigma_{coh}(E, \mu)}{d\mu}$.

3.3 Incoherent Scattering

Incoherent DCS is defined with incoherent scattering function and Klein-Nishina cross section.

μ is sampled from Klein-Nishina formula, photon secondary energy is set to $k' = \frac{k}{1 + \frac{k}{E_0} * (1-\mu)}$ where E_0 is the electron at rest energy. Photon simulation weight is also modified in the same way as coherent scattering.

Secondary electron energy is set to $E = k - k' + E_0$ and secondary electron direction is calculated using the relativistic kinematic formulae.

3.4 Photoelectric Effect

K, LI, LII or LIII shell interaction is chosen according to the CS of each of the shells. Secondary electron energy is set to $E = k - E_{b(K, LI, LII, LIII)} + E_0$ where k is the photon energy, $E_{b(K, LI, LII, LIII)}$ is the corresponding shell binding energy and E_0 is the electron at rest energy. Secondary electron direction is sampled from K, LI, LII or LIII shell normalized DCS.

3.5 Pair Effect

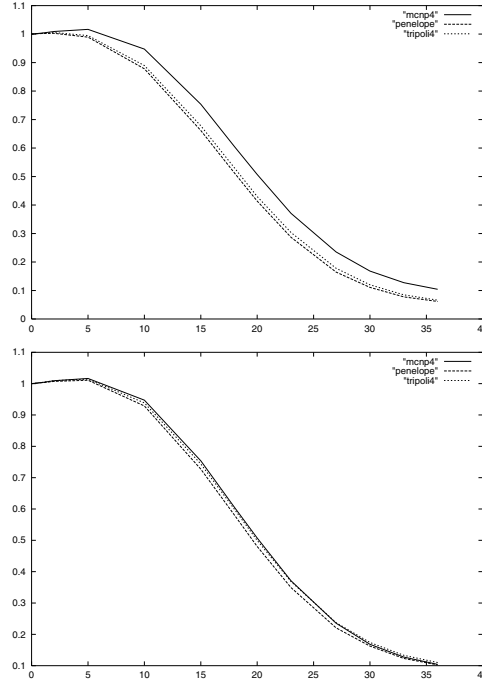
Secondary electron energy is sampled from normalized Heitler formula. Secondary positron energy is set to $E_+ = k - E_-$ where E_+ is the positron energy, E_- is the electron energy and k is the photon energy. Secondary electron and secondary positron directions are sampled from the Leading Order Approximate Distribution sampling method [21].

4 Transmission Experiments Comparisons between MCNP4, PENELOPE and TRIPOLI-4

The first experiment is a 100 MeV source electron transmission experiment through a pure iron layer. Particles are followed down to 10 MeV (kinetic energy for electrons, positrons and photons). Table 1 shows transmission rates calculated with MCNP4, PENELOPE and TRIPOLI-4 first for electrons and then for electrons and positrons. Figure 1 illustrates these results.

Table 1. 100 MeV electron transmission and electron/positron transmission rate through iron slab

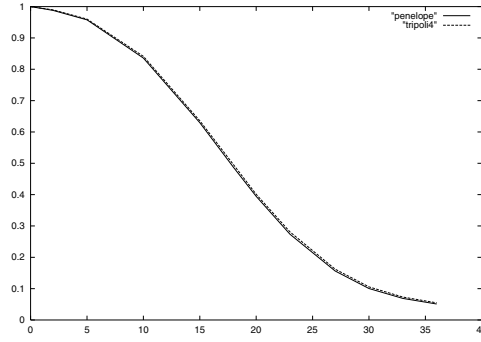
thickness (g/cm^2)	1.	5.	10.	15.	20.	27.	33.	36.
PENELOPE e^-	1.002+0 (0.02%)	9.893-1 (0.04%)	8.782-1 (0.16%)	6.616-1 (0.30%)	4.139-1 (0.51%)	1.645-1 (0.97%)	7.771-2 (1.41%)	6.167-2 (1.62%)
TRIPOLI-4 e^-	1.003+0 (0.01%)	9.948-1 (0.05%)	8.898-1 (0.08%)	6.783-1 (0.13%)	4.300-1 (0.20%)	1.779-1 (0.40%)	8.473-2 (0.67%)	6.613-2 (0.85%)
MCNP4 e^-/e^+	1.004+0 (0.03 %)	1.017+0 (0.08%)	9.473-1 (0.12%)	7.538-1 (0.17%)	5.075-1 (0.25%)	2.353-1 (0.44%)	1.275-1 (0.65%)	1.041-1 (0.73%)
PENELOPE e^-/e^+	1.003+0	1.011+0	9.288-1	7.273-1	4.803-1	2.206-1	1.230-1	1.026-1
TRIPOLI-4 e^-/e^+	1.004+0	1.014+0	9.386-1	7.437-1	4.999-1	2.373-1	1.330-1	1.100-1

**Fig. 1.** 100 MeV electron and electron/positron transmission rate through iron slab

The second experiment is a 100 MeV source positron transmission experiment through a pure iron layer. Particles are followed down to 10 MeV (kinetic energy for electrons, positrons and photons). MCNP4 does not calculate positrons sources. Table 2 and Fig. 2 illustrate these results.

Table 2. 100 MeV positron transmission rate through iron slab

thickness (g/cm^2)	1.	5.	10.	15.	20.	27.	33.	36.
PENELOPE e^+	9.941-1 (0.03%)	9.577-1 (0.09%)	8.357-1 (0.19%)	6.295-1 (0.32%)	3.947-1 (0.53%)	1.563-1 (0.96%)	6.890-2 (1.60%)	5.087-2 (1.83%)
TRIPOLI-4 e^+	9.948-1 (0.01%)	9.602-1 (0.04%)	8.413-1 (0.07%)	6.357-1 (0.11%)	4.010-1 (0.17%)	1.623-1 (0.33%)	7.310-2 (0.56%)	5.457-2 (0.60%)

**Fig. 2.** 100 MeV positron transmission rate through iron slab

The last experiment is a 10.2 MeV source electrons transmission experiment through a mixture (aluminium and lead) layer. Particles are followed down to 1 MeV (kinetic energy for electrons, positrons and photons). Table 3 and Fig. 3 illustrate these results.

Table 3. 10.2 MeV electron transmission rate through a mixture

thickness (g/cm^2)	0.1	0.25	0.5	1.	2.	3.	4.	5.
MCNP4 e^-/e^+	1.003+0 (0.01%)	1.002+0 (0.02%)	9.887-1 (0.03%)	9.045-1 (0.05%)	5.634-1 (0.13%)	2.312-1 (0.26%)	5.687-2 (0.58%)	1.075-2 (1.40%)
PENELOPE e^-	1.002+0 (0.02%)	1.001+0 (0.01%)	9.886-1 (0.05%)	9.026-1 (0.13%)	5.515-1 (0.38%)	2.163-1 (0.78%)	5.056-2 (1.84%)	9.174-3 (4.36%)
TRIPOLI-4 e^-	1.002+0 (0.01%)	1.001+0 (0.02%)	9.838-1 (0.03%)	8.9940-1 (0.06%)	5.463-1 (0.13%)	2.187-1 (0.28%)	5.416-2 (0.63%)	1.009-2 (1.69%)

5 Conclusion

TRIPOLI-4 now includes an electron/photon simulation package. It is based on Goudsmit-Saunderson multiple scattering formalism, hard and soft collisions treatment and distinguishes electron and positron physics.

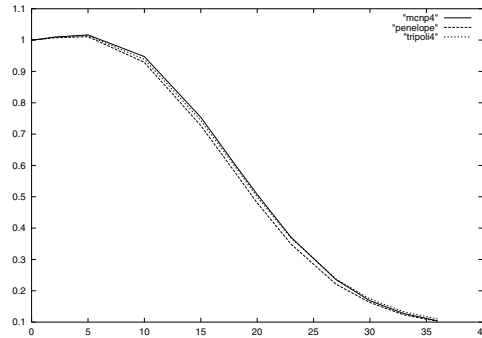


Fig. 3. 10.2 MeV electron transmission rate through a mixture

The first results, compared to other electron/photon simulation codes are very satisfying.

References

1. J.-P. Both, Y. Pénéliau: 'The Monte Carlo Code Tripoli-4 and its First Benchmark Interpretations'. In: *Physor 96 : International Conference on the Physics of Reactors, Mito, Ibaraki, Japan September 16-20, 1996*
2. M.E. Riley, C.J. MacCallum, F. Biggs: *Atom. Data and Nucl. Data Tables* **15**, 443 (1975)
3. N.F. Mott: *Proc. Roy. Soc. A* **124**, 425
4. N. Sherman: *Phys. Rev* **103**, 1601 (1956)
5. C. Möller: *Ann. Phys.* **14**, 531 (1932)
6. H.J. Bhabha: *Proc. Roy. Soc. A* **154**, 195 (1936)
7. M.J. Berger, S.M. Seltzer: *Phys. Rev.* **2(2)**, 621 (1970)
8. U.Fano, H.W. Koch, J.W. Motz: *Phys. Rev.* **112**, 1679 (1958)
9. L. Kim, R.H. Pratt, S.M. Seltzer, M.J. Berger: *Phys. Rev. A* **33**, 3002 (1986)
10. W. Heitler: *The Quantum Theory of Radiation* (Clarendon Press, Oxford 1954)
11. S. Goudsmit, J.L. Saunderson: *Phys. Rev.* **57**, 24 (1940)
12. S. Goudsmit, J.L. Saunderson : *Phys. Rev.* **58**, 36 (1940)
13. M.J. Berger: 'Monte Carlo Calculation of the Penetration and Diffusion of Fast Charged Particles'. In: *Methods in Computational Physics, vol. 1*, ed. by B. Adler, S. Fernbach and M. Rotenberg, (Academic Press, New York, 1963) pp. 135–215
14. S.M. Seltzer, M.J. Berger : *Nat. Aeron. and Space Adm. Rep. NASA-SP-3012* (1964)
15. L. Landau: *Journ. Phys.* **8**, 201 (1944)
16. W. Börsch-Supan: *Journ. of Res. of the Nat. Bureau of Stand. (B)* **65B(4)**, 245 (1961)
17. A.F. Bielajew: *Tech. Report PIRS-0203* (1989)
18. M. Gavril: *Phys. Rev.* **113**, 514 (1959)
19. M. Gavril: *Phys. Rev.* **124**, 1132 (1964)
20. H. Bethe, W. Heitler : *Proc. Roy. Soc. A* **146**, 83 (1934)
21. A.F. Bielajew: *Tech. Report PIRS-0287R1* (1994)

The EGSnrc System, a Status Report

I. Kawrakow and D.W.O. Rogers

Ionizing Radiation Standards, NRC, Ottawa, K1A 0R6, Canada

Abstract. EGSnrc [1] is a general-purpose package for the Monte Carlo simulation of coupled electron-photon transport that is based on the popular EGS4 system but incorporates a variety of improvements in the class II implementation of the condensed history technique and the modelling of the underlying physical processes. This paper gives a status report on the EGSnrc system and presents several examples demonstrating the importance of the improvements in the underlying cross sections undertaken recently.

1 Introduction

Code systems for the Monte Carlo (MC) simulation of coupled electron-photon transport, such as EGS4 [2], ITS [3] and MCNP [4] (the latter two being largely based on the ETRAN system [5] in their treatment of electromagnetic showers), have been extensively benchmarked and are known to reproduce experimental data well in a variety of situations. There are, however, situations where all these systems fail to produce reliable results. An excellent example of such a situation is the comparison between MC simulations and measurements of the response of a plane-parallel ionization chamber with a replaceable back wall as a function of the atomic number of the back wall, shown in Fig. 1. Experimental data are from [6], the front wall is aluminum and the curves are normalized to unity at aluminum ($Z = 13$). The two different EGSnrc simulations will be discussed later in the text. The up to 10% difference between measurements and EGS4/PRESTA and ITS simulations is rather striking and difficult to understand in view of differences between the underlying cross sections and in the implementation of the condensed history technique for electron transport (see *e.g.* the pioneering work by M. Berger who introduced the technique and coined the terminology [7]). Such large differences between measurements and calculations, together with the well known step-size dependence of simulation results and the failure of EGS4/PRESTA to converge to the correct answer for small step-sizes for certain type of situations [8], have prompted us to undertake a substantial rework of the EGS4 system. This paper gives a brief status report on the resulting MC package called EGSnrc.

2 EGSnrc

The work on the various changes of the EGS4 system that were implemented in EGSnrc can be grouped into two main phases:

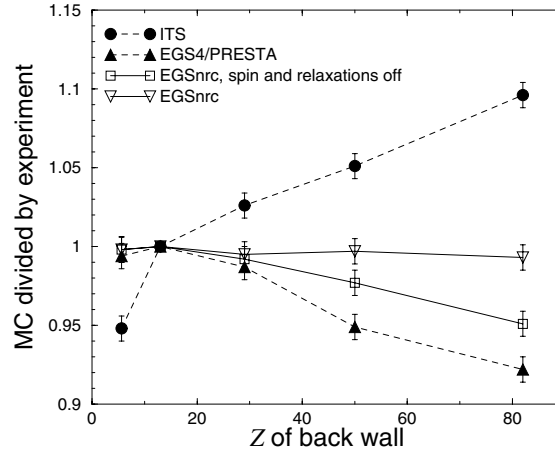


Fig. 1. MC simulations of a plane parallel chamber response in a broad parallel ^{60}Co beam as a function of the atomic number of the replaceable back wall. Results are divided by the experimental data of [6] (which has an uncertainty of 0.5%) and normalized to unity at $Z = 13$

1. Improved implementation of the condensed history (CH) technique
2. Improvements in the treatment of the various physical processes

Phase 1, which can be considered as completed, involved the following modifications

1. A new electron-step algorithm [9] with second order energy loss corrections as described in [10,11]
2. A new, any angle, any step, multiple elastic scattering theory based on the screened Rutherford cross section [12] with energy loss corrections discussed in [10,11]
3. Exact boundary crossing algorithm in single elastic scattering mode [10,11]
4. Correct implementation of the fictitious cross section method [10,11]
5. Exact evaluation of energy loss due to sub-threshold processes [10,11]

After completion of phase 1, EGSnrc was shown to produce step-size independent and artifact-free results at the 0.1% level when benchmarked against its own cross sections [10,13]. However, when applied to the plane-parallel chamber response situation described in the Introduction, phase 1 EGSnrc produced the curve labelled as “EGSnrc, spin and relaxations off” in Fig. 1. Although closer to the experiment than EGS4/PRESTA and ITS, there was still a significant difference between measurements and calculations for high atomic numbers (5% for lead). As artifacts due to the use of the CH technique can be excluded as a reason for the disagreement, the difference is clearly due to not sufficiently accurate cross sections which EGSnrc had inherited from the EGS4 system. The improvement of various cross section was undertaken in phase 2 which is still not completed. The current status can be summarized as follows:

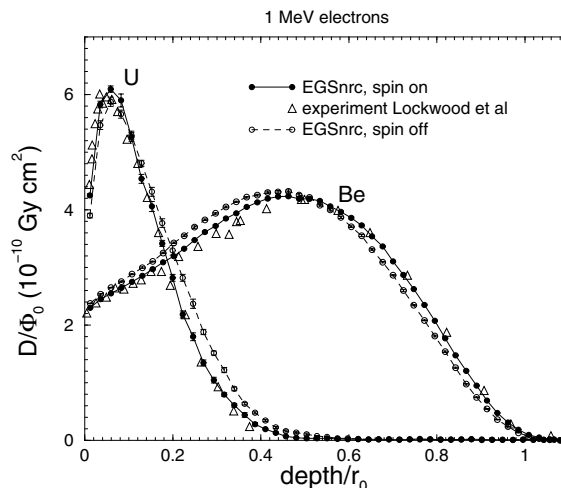


Fig. 2. Depth-dose curves for a broad parallel beam of 1 MeV electrons incident on a Beryllium or Uranium target as a function of depth expressed as a fraction of the CSDA range. The experimental data are from [22]

1. Electron elastic scattering is based on partial-wave analysis (PWA) cross section which take into account relativistic spin effects and are different for electrons and positrons. Sampling of multiple elastic scattering angles on the basis of the PWA cross sections requires one additional rejection loop in the sampling algorithm. For more details the reader is referred to [11]. To facilitate comparisons with EGS4 and in order to be able to study the effect of more accurate electron elastic scattering cross sections, the user is given the possibility to “turn off” spin effects.
2. In addition to the Bethe-Heitler cross sections for electron/positron bremsstrahlung used in EGS4, the possibility to use the NIST bremsstrahlung cross section data base [14,15], which is the basis for the radiative stopping powers recommended by the ICRU [16], has been implemented. In addition, sampling the angular distribution by the fixed angle approximation has been removed and is done either using equation 2BS from the article by Koch and Motz [17] (with a slight modification concerning the kinematics at low electron energies) or using the leading term of the distribution.
3. Binding effects and Doppler broadening in incoherent photon scattering are taken into account in the impulse approximation [18]. Shell-wise Compton profiles necessary for the sampling algorithm are approximated according to the formula suggested by the PENELOPE group [19]. The sampling algorithm makes use of the fictitious cross section method in order to avoid re-evaluation of total incoherent scattering cross sections. For more details see [11].
4. The sampling algorithm for photo-electric absorption has been modified (i) to explicitly sample the element in case of interactions with mixtures and (ii)

to explicitly sample the shell in the selected element absorbing the photon. In addition, the angular distribution of photo-electrons is modelled according to the Sauter distribution [20].

5. Atomic relaxations via the emission of characteristic X-rays, Auger and Coster-Kronig electrons are treated in a separate routine that can be called from any process generating inner shell vacancies (currently photo-electric absorption and incoherent scattering). Transition probabilities for the various de-excitation channels were taken from the Evaluated Atom Data Library (EADL) [21]. In order to keep the amount of data held in the memory at a reasonable level, transitions to and transitions from M and N shells are treated in an average way, see [11].

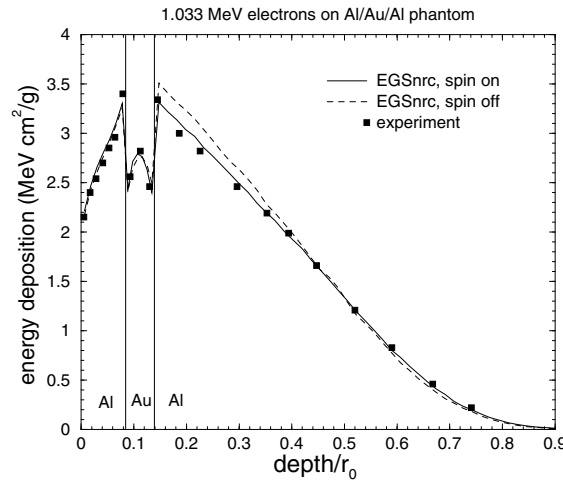


Fig. 3. Depth-dose curves for a broad parallel beam of 1 MeV electrons incident on an aluminum-gold-aluminum phantom as a function of depth expressed as a fraction of the CSDA range. The experimental data are from [22]

Simulation of the plane-parallel chamber situation described in the Introduction with EGSnrc in its current stage yields the curve labelled as “EGSnrc”. The agreement with the measurement is within 0.7% which is comparable with the stated experimental uncertainty of 0.5%. It is worth noticing that half of the simulated response increase for lead (compared to the simulation using EGS4 cross sections) was due to the inclusion of relativistic spin effects for electron elastic scattering, the other half resulted from the proper treatment of photo-electric absorption and the production of Auger electrons.

Improvements of the modelling of the underlying physical processes in the near future will concern

1. Better treatment of electron/positron inelastic scattering at low energies. In particular the creation of inner shell vacancies (electron impact ionization) will

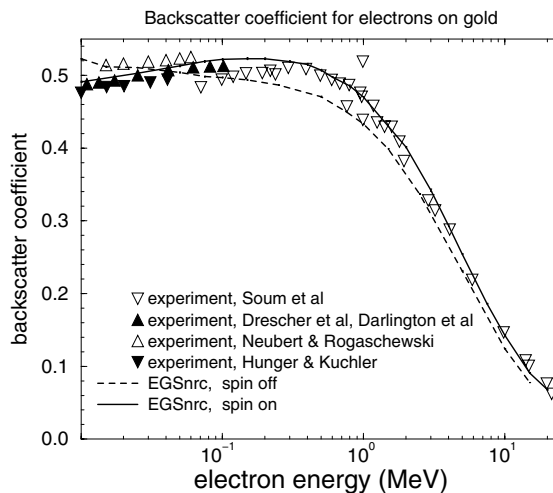


Fig. 4. Backscatter coefficients for electrons perpendicularly incident on a semi-infinite gold target

be taken into account

2. Implementation of energy loss straggling due to sub-threshold inelastic collisions. Although this could be considered to be part of the CH implementation, the precise shape of the straggling distribution depends on the small energy transfer inelastic cross section. Energy loss straggling can therefore be implemented only after completion of point 1.

3. Better modelling of coherent photon scattering.

Longer term goals could concern

1. Less important (at least from the point of view of the general user) cross section modifications such as differences between electron/positron bremsstrahlung cross sections, explicit treatment of triplet production, single and triple photon positron annihilation, etc.

2. Development of a general purpose geometry package for use with EGSnrc

3. Development of a general purpose source package

3 Examples

Perhaps the most important modification of cross sections in EGSnrc compared to EGS4 is the inclusion of spin effects for e^-/e^+ elastic scattering as it has an effect on the simulated results not only in the sub-MeV energy range. Figure 2 shows a comparison of calculated depth-dose curves in Beryllium and Uranium to measurements by Lockwood *et al* [22]. Both, the calculations and the measurements are absolute. The calculations with “spin on” are in much better agreement with the experiment. The effect of including spin is to make

the effective range of electrons longer for low- Z materials and shorter for high- Z materials. It is also present for the energy range relevant for radiation therapy. Fig. 3 shows comparisons of depth-dose curves in an aluminum-gold-aluminum phantom to experimental data from [22]. Again, the inclusion of spin effects leads to a much better agreement with the measurements. As a final example Fig. 4 presents a comparison between the calculated backscatter coefficients for electrons impinging on a semi-infinite gold target as a function of the incident electron energy and experimental data from various measurements.

References

1. EGSnrc main system, supporting documentation and user codes are available on-line at <http://www.irs.inms.nrc.ca/inms/irs/EGSnrc/EGSnrc.html>
2. W.R. Nelson, H. Hirayama, D.W.O. Rogers: Report SLAC-265, Stanford Linear Accelerator Center, Stanford, California, 1985
3. J.A. Halbleib, R.P. Kensek, T.A. Mehlhorn, G.D. Valdez, S.M. Seltzer, M.J. Berger: Sandia report SAND91-1634, 1992
4. J.F. Briesmeister (Editor): Los Alamos National Laboratory Report LA-12625-M (Los Alamos, NM), 1993
5. S.M. Seltzer: 'An overview of ETRAN Monte Carlo methods'. In: *Monte Carlo Transport of Electrons and Photons*, ed. by T.M. Jenkins, W.R. Nelson, A. Rindi, A.E. Nahum, D.W.O. Rogers, (Plenum Press, New York 1989) pp. 153–182
6. B. Nilsson, A. Montelius, P. Andreo, B. Sorcini. In *Dosimetry in Radiotherapy*, (IAEA, Vienna 1988) Vol 1, pp. 175 – 185
7. M. J. Berger: In B. Alder, S. Fernbach, M. Rotenberg, editors: *Methods in Comput. Phys.*, volume 1, pp. 135 – 215, (Academic, New York 1963)
8. D.W.O. Rogers: Med. Phys. **20**, 319 (1993)
9. I. Kawrakow, A.F. Bielajew: Nucl. Instr. Meth. B **142**, 253 (1998)
10. I. Kawrakow: Med. Phys. **27**, 485 (2000)
11. I. Kawrakow, D.W.O. Rogers: Technical Report PIRS-701, National Research Council of Canada, Ottawa, Canada (2000)
12. I. Kawrakow, A.F. Bielajew: Nucl. Instr. and Meth. **B134**, 325 (1998)
13. I. Kawrakow: Med. Phys. **27** 499 (2000)
14. S.M. Seltzer, M.J. Berger: Nucl. Inst. Meth. **B12**, 95 (1985)
15. S.M. Seltzer, M.J. Berger: Atomic Data and Nucl. Data Tables **35**, 345 (1986)
16. ICRU: ICRU Report 37, ICRU, Washington D.C., 1984
17. H.W. Koch, J.W. Motz: Rev. Mod. Phys. **31** 920 (1959)
18. R. Ribberfors: Phys. Rev. B **12**, 2067 (1975)
19. D. Brusa, G. Stutz, J.A. Riveros, J. M. Fernández-Varea, F. Salvat: Nucl. Instr. Meth. A **379**, 167 (1996)
20. F. Sauter: Ann. Physik **11** 454 (1931)
21. S.T. Perkins, D.E. Cullen, M.H. Chen, J.H. Hubbell, J.A. Rathkopf, J.H. Scofield: LLNL Report UCRL-50400, Volume 30, Livermore, Calif (1991)
22. G.J. Lockwood, L.E. Ruggles, G.H. Miller, J.A. Halbleib: Sandia Report SAND79-0414 (1980)

Status of MARS Electromagnetic Physics

O.E. Krivosheev and N.V. Mokhov

Fermilab, P.O. Box 500, Batavia, IL 60510, USA

Abstract. New modules for simulating electromagnetic showers at energies from 1 keV to a multi-TeV region have been developed and implemented into the MARS code. The entire shower and several “non-standard” processes essential at high energies are treated either exclusively or inclusively, according to the user’s choice. Results of calculations are in a good agreement with data.

1 Introduction

Developments in the MARS code [1] cover physics of hadron and lepton interactions from 100 TeV down to a fraction of an electron volt for neutrons and to about 100 keV for all other particles. Simulation of electromagnetic showers (EMS), although improved over the years, is still based – in the physics part – on the use of the AEGIS modules [2], which implies an inclusive approach and a simplified process description below a few MeV. This is quite acceptable for the majority of energy deposition and radiation applications, but in some cases a full analog simulation and a detailed physics description in the low energy domain are needed. New modules have recently been developed and implemented into MARS, as described in this paper. The main focus is given to electron and photon interactions in arbitrary composite solid, liquid and gaseous materials at low energies (1 keV to a few MeV). The high energy part is also completely re-built. A generic polarized photon transport algorithm is implemented. The entire shower, and such processes as emission of synchrotron photons, photohadron production, $\gamma Z \rightarrow \mu^+ \mu^-$ and $e^+ e^- \rightarrow \mu^+ \mu^-$, can be treated – in the spirit of the MARS framework – either exclusively or inclusively with corresponding statistical weights. The choice of method is left for the user to decide.

2 Photon Physics

Simulation of photon physics is based upon data from the EPDL library [3]. MARS stores the evaluated data, pre-compiled for fast interpolation for all 100 elements over a uniform, material- and element-independent, energy scale. The material is considered as an independent mixture of constituents. Total cross-sections and mean free paths are calculated, together with branching probabilities from these tables, as weighted sums over the elements in the mixture for four main processes: $e^+ e^-$ pair production, photoelectric effect, Compton scattering and coherent

scattering. Above 1 GeV, the photoelectric effect and coherent scattering cross-sections are assumed to be zero and high energy approximations are used for Compton scattering and e^+e^- pair production.

In the course of simulations – after sampling the process and the element – the particle phase coordinates are generated and stored on the stack for further processing. Compton scattering is simulated from the Klein-Nishina formula with the scattering function correction due to electron binding to the atom, essential at low energies $\omega \leq 1$ MeV. Coherent scattering is described in a form-factor approach, with data from EPDL. The scattering angle is sampled from the form-factor with the Rayleigh formula used to accept the sampled angle with a $\sim 2/3$ efficiency. The photoelectron energy is sampled using the subshell ionization probabilities and subshell energy levels, and the angle – from the Sauter distribution [4] for the K -shell, and from the Gavril distribution [5] for the L - and M -shells. The fluorescence probability is estimated from EPDL and the photon is sampled if its energy is above the transport threshold, otherwise it is deposited locally. Secondary energies in e^+e^- pair production are sampled in accordance with the Tsai approximation [6], with the Thomas-Fermi approximation for the elastic and inelastic screening functions for elements with $Z > 5$ and special screening functions for lighter elements. The pair angles are sampled as in [7].

3 Electron and Positron Physics

Total dE/dx_{tot} and restricted $dE/dx_{<}$ ionization stopping powers for electrons and positrons are calculated in accordance with ICRU-37 [8]. Ionization potentials and density corrections are included for all 100 elements. Special care is taken for gaseous mixtures. Due to the difference in the scattering laws – Möller for electrons and Bhabha for positrons – dE/dx is calculated separately for e^- and e^+ . The stopping power above the threshold ($dE/dx_{tot} - dE/dx_{<}$) is calculated in the assumption of scattering on free electrons and is expressed as an integral over the analytical Möller or Bhabha cross-sections from the threshold to the maximum energy transfer allowed.

The technique of [9] is employed for charged particle tracking without simulating the enormous number of low energy transfer collisions. For ionization collisions and bremsstrahlung, a threshold energy transfer Q_t is introduced. The processes with energy transfer $Q > Q_t$ – catastrophic events – are simulated individually. The collisions with $Q \leq Q_t$ are lumped together and treated in a continuous way. Two quantities are calculated at the initialization stage: $dE/dx_{<}$ and cross-sections above the threshold $\Sigma_{>}$ (to select a step length). A combination of $\Sigma_{>}$, $dE/dx_{<}$ and continuous slow down approximation (CSDA) allows one to sample the energy E at the end of the step from a relation

$$-\log \zeta = \int_E^{E_0} [\Sigma_{>}(E)/dE/dx_{<}(E)] dE, \quad (1)$$

where ζ is a uniform random number of $(0,1)$. A step size is sampled from the CSDA tables. After the step, the phase coordinates due to energy straggling and multiple scattering are sampled.

Multiple Coulomb scattering is simulated from a modified Molière theory. For the fast sampling, one uses a 2-D table for the inverse probability function to sample $\bar{\theta}^2(\zeta, B)$ directly. The straggling distribution function due to ionization collisions with $Q < Q_t$ is derived from the Vavilov distribution. The Rutherford part of the scattering cross-section is used, thus one deals with a generic probability distribution function applicable both for e^- and e^+ . Again, a 2-D table of the inverse probability function is pre-calculated and used in this sampling. The probability of a particular catastrophic event together with the element number are sampled the same way as for photons. The e^- and e^+ elastic scattering is described in a one-photon approximation using the Möller and Bhabha cross-sections. Sampling is quite similar, due to the common Rutherford parts. Energy transfer – and hence scattering angle – is sampled from the Rutherford part and then is rejected or accepted, in accordance with the rest of the cross-section.

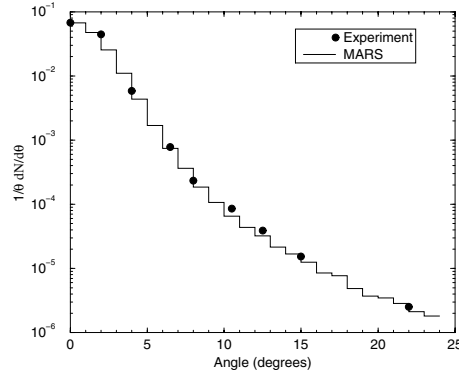


Fig. 1. 15.7 MeV e^- angular distribution after a 18.66 mg/cm² gold foil, data [11]

Bremsstrahlung data is taken from the tables [10] for differential cross-sections $\beta^2/Z^2 \cdot \omega d\sigma/d\omega$ for all 100 elements. The tables are for electrons with kinetic energies from 1 keV to 10 GeV. At $E > 10$ GeV, the Tsai analytical expression [6] is used for the differential cross-section with the same approximation for screening functions as used for e^+e^- pair production. The restricted bremsstrahlung stopping power and bremsstrahlung cross-section above the threshold are calculated using numerical integration over the tables [10]. Total and differential cross-sections for positron in-flight annihilation are taken from a one-photon exchange calculation [4]. Sampling is quite simple using a combination of the exact method and a von Neumann rejection. Figs. 1 and 2 show two examples of comparison of MARS calculations with the above algorithms and experimental data [11,12].

4 Muons, Photohadrons and Polarization

$e^+e^- \rightarrow \mu^+\mu^-$. A sampling algorithm for muon phase coordinates is based on a covariant method for a differential cross-section in a one-photon exchange approximation [4]

$$\frac{d\sigma}{ds} = \frac{4\pi e^4}{t(t-4m^2)} \frac{1}{t^2} \left\{ \frac{s^2 + u^2}{2} + (m^2 + \mu^2)(2t - m^2 - \mu^2) \right\}. \quad (2)$$

To enhance a muon pair production, MARS uses a forced e^+e^- to $\mu^+\mu^-$ conversion with a probability governed by the user.

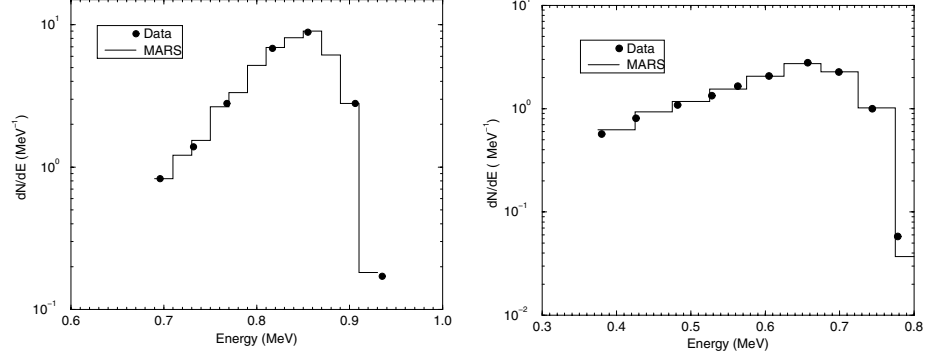


Fig. 2. 1 MeV e^- energy spectra after 0.36 (left) and 0.8 mm (right) Al foils, data [12]

$\gamma Z \rightarrow \mu^+ \mu^-$. An exact expression for $\frac{d\sigma}{d\varepsilon_\mu}$ is derived for nuclei using a dipole form-factor approximation. It is used for total cross-section numerical calculations and for a muon energy sampling via the von Neumann method. By default, this process is also forced with a production probability controlled by the user.

Photohadrons. Hadroproduction in photon-nucleus interactions is simulated as described in [1,13], with the analog or forced mode chosen by the user.

Low energy polarized photons. Generic polarized photon transport algorithms developed in [14] are implemented into MARS. A generic particle ID is introduced as a new MARS feature, which allows one to bind the Stokes param-

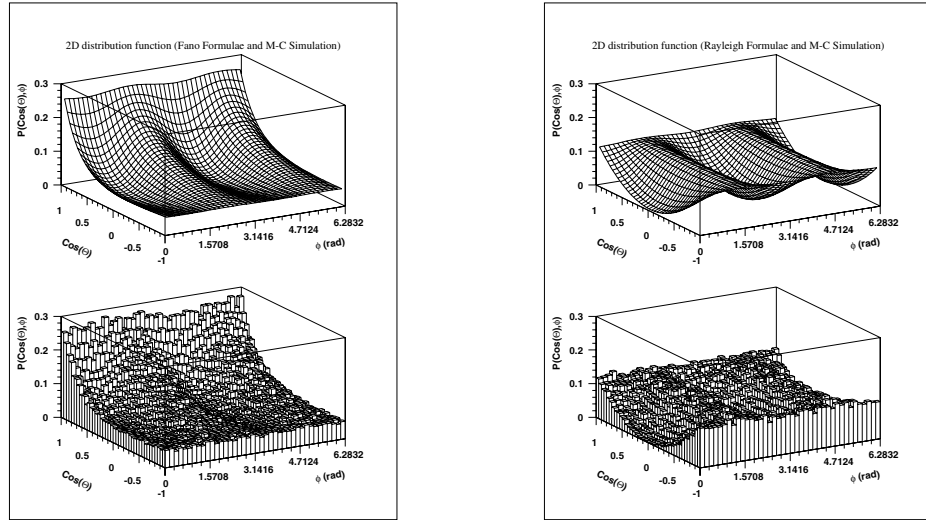


Fig. 3. 10 keV polarized photon angular distribution after Compton scattering, incoherent (left) and coherent (right)

ters and local coordinate axis to a low energy photon ID. Fig. 3 gives an example of polarized photon calculations.

5 EMS Vertex Biasing

The original MARS EMS module uses a leading particle biasing algorithm (LPBA) [2]. At each vertex, just one particle is picked up for further tracking, another particle is killed. With the probability E_{out}/E_{in} a secondary particle with energy E_{out} is selected and with the probability $1 - E_{out}/E_{in}$ it is rejected, and the other one is picked up. A statistical weight is adjusted correspondingly, $w_{out}=w_{in}E_{in}/E_{out}$, to fulfill energy conservation in the event. Such an approach obviously favors a more energetic particle which is appropriate for a deep penetration problem. This algorithm is also present in the new EMS module, as well as a fully analog simulation. Another inclusive algorithm is also introduced, with secondary particle rejection/selection with an equal probability. The choice of one of these three algorithms is controlled by the user.

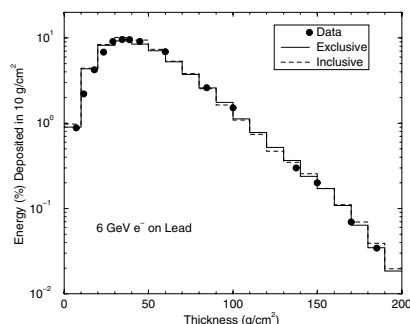


Fig. 4. 6 GeV e^- energy deposition in Pb, as calculated with MARS exclusive algorithm and LPBA *vs* data [15]

values of ϵ are 2190 and 6.3 in the original MARS LPBA with $E_{th}=100$ keV. In the new code with $E_{th}=1$ keV, t is noticeably longer, resulting in lower values of ϵ which are now 952 and 2.1 using the analog algorithm and 817 and 3.6 for LPBA. For averaged EMS characteristics, such as energy deposition, LPBA gives better efficiency at large distances compared to the analog algorithm.

6 Computing Issues

The new EMS modules are written in C, with proper interface to the Fortran parts of the code. An early decision was to embed all data necessary in the course of calculations via static arrays. Therefore there is no need for any additional data files and a file managing code. The price for that decision is the increase in the size of the code of about 20 Mb.

The analog algorithm, allowing one to calculate cascade-by-cascade fluctuations, consumes significant CPU-time per event – which grows linearly with the EMS energy. All three algorithms give similar results for inclusive type distributions, such as energy deposition as shown in Fig. 4 for a 6 GeV e^- on lead. However, computational efficiencies $\epsilon = (t\sigma^2)^{-1}$ are different, where t and σ are the CPU-time and RMS statistical error, both per event. In the above 6-GeV example, at two representative locations – the shower maximum and a maximum thickness of 200 g/cm² – the corresponding values

This work was supported by the U.S. Department of Energy. We thank A.A. Wehmann for useful comments.

References

1. N.V. Mokhov: 'The MARS Code System User's Guide', Fermilab-FN-628 (1995); O.E. Krivosheev, N.V. Mokhov: 'New MARS and its Applications', in: *Proc. of the Third Workshop on Simulating Accelerator Radiation Environments (SARE3)*, Tsukuba, Japan, May 7–9, 1997, KEK Proceedings 97-5, pp. 12–20 (1997), Fermilab-Conf-98/043 (1998); N.V. Mokhov, S.I. Striganov, A. Van Ginneken, S.G. Mashnik, A.J. Sierk, J. Ranft: in: *Proc. of the Fourth Workshop on Simulating Accelerator Radiation Environments (SARE-4)*, Knoxville, TN, September 14–16, 1998, pp. 87–99, Fermilab-Conf-98/379 (1998), nucl-th/9812038-v2-16-Dec-1998; N.V. Mokhov: in *Proc. of ICRS-9 International Conference on Radiation Shielding*, Tsukuba, Ibaraki, Japan, October 17–22, 1999, J. Nucl. Sci. Tech. **1**, pp. 167–171 (March 2000); Fermilab-Conf-00/066 (2000); <http://www-ap.fnal.gov/MARS/>
2. A. Van Ginneken: AEGIS – a Program to Calculate the Average Behavior of Electromagnetic Showers, Fermilab-FN-309 (1978)
3. D.E. Cullen et al.: *Tables of Graphs of Photon-interaction Cross-Section from 10 eV to 100 GeV Derived from the LLNL Evaluated Photon Data Library (EPDL)*, UCRL-50400, Vol. 6, Rev. 4, Oct. 31, LLNL (1989)
4. L.D. Landau, E.M. Lifshitz: *Theoretical Physics. Quantum Electrodynamics*, Vol. 4 (Moscow, Nauka 1984)
5. M. Gavrila: Phys. Rev. **124**, 578 (1961)
6. Y. Tsai: Rev. Mod. Phys. **46**, 815 (1974)
7. A. Borsellino: Nuovo Cimento **4**, 112 (1947)
8. ICRU Report 37: *Stopping Powers for Electrons and Positrons* (Bethesda) MD 20814 (1984)
9. A.M. Kolchuzhkin et al.: 'Monte Carlo Code for Simulation of Electron-Photon Showers and Pencil Beam Transport Studies', in: *Proc. of 8th Intl. Conf. on Radiation Shielding*, Arlington, TX, April 24–28, 1994 pp. 1346–1350
10. S.M. Seltser, M.J. Berger: Nucl. Instr. Methods **B12**, 95 (1985)
11. A.O. Hanson: Phys. Rev. **81**, 634 (1951)
12. H.D. Rester et al.: J. Appl. Phys. **41**, 714 (1971)
13. N.V. Mokhov, S.I. Striganov: in *Handbook of Accelerator Physics and Engineering*. Ed. by A.W. Chao, M. Tigner (World Scientific, Singapore 1999) pp. 234–240
14. A.M. Kolchuzhkin, O.E. Krivosheev: 'Monte Carlo Simulation of Polarized Photon Transport', in: *Proc. of ANS Radiation Protection and Shielding Topical Meeting*, Falmouth, MA, April 21–25, 1996, pp. 787–794
15. G. Bathow et al.: *Measurements of the Longitudinal and Lateral Development of Electromagnetic Cascades in Lead, Copper and Aluminum at 6 GeV*, DESY-69/39 (1969)

Status of PENELOPE

J. Sempau¹, J.M. Fernández-Varea², F. Salvat², E. Benedito², M. Dingfelder²,
H. Oulad ben Tahar², X. Llovet³, E. Acosta⁴, A. Sánchez-Reyes⁵, and
J. Asenjo⁵

¹ Institut de Tècniques Energètiques, Universitat Politècnica de Catalunya. Diagonal 647, E-08028 Barcelona, Spain

² Facultat de Física (ECM), Universitat de Barcelona. Societat Catalana de Física (IEC). Diagonal 647, E-08028 Barcelona, Spain

³ Serveis Cientifictècnics, Universitat de Barcelona. Lluís Solé i Sabarís 1–3, E-08028 Barcelona, Spain

⁴ Facultad de Matemática, Astronomía y Física, Universidad Nacional de Córdoba. Medina Allende y Haya de la Torre, 5000 Córdoba, Argentina

⁵ Hospital Clínic de Barcelona. Villarroel 170, E-08036 Barcelona, Spain

1 Introduction

PENELOPE (an acronym for PENetration and Energy LOSS of Positrons and Electrons) is a general-purpose Monte Carlo code system for the simulation of coupled electron-photon transport in complex material structures. Its most characteristic feature is the systematic use of mixed simulation (class II schemes in the terminology of Berger [1]) for electrons and positrons. This not only improves the accuracy of the simulation but also simplifies the structure and operation of the code. The reliability of the code has been tested by means of extensive comparisons with experimental data and with results from analog codes.

The core of the code system is a **FORTRAN** subroutine package that generates electron-photon showers in material systems consisting of a number of homogeneous regions of given composition (bodies). These subroutines are invoked from a main steering program, to be provided by the user, which controls the evolution of the tracks and keeps score of the relevant quantities. The code system also includes a subroutine package for simulation within quadric geometries (i.e. systems consisting of bodies limited by quadric surfaces) and a geometry viewer and debugger. The distribution package (**FORTRAN** source files, database and geometry viewer) is available from the NEA Data Bank¹. Recently, we have introduced various modifications, which improve the stability (thus allowing faster simulation) and the flexibility of the code.

¹ OECD Nuclear Energy Agency Data Bank. Le Seine Saint-Germain, 12 Boulevard des Iles, 92130 Issy-les-Moulineaux, France (e-mail: NEA@db.nea.fr; <http://www.nea.fr>)

2 Interaction Physics

To facilitate the formulation of the mixed simulation algorithm and to minimize the amount of numerical information needed for random sampling, the differential cross sections (DCS) of the various interaction mechanisms are approximated by analytical expressions derived from simple, but physically sound approximations. The accuracy of the simulation is ensured by fitting the DCS model parameters to reproduce the most accurate available values of relevant transport integrals.

2.1 Photon Interactions

Coherent (Rayleigh) scattering: The adopted DCSs are obtained from the Born approximation with the atomic form factor approximated by an analytical expression.

Incoherent (Compton) scattering: DCSs obtained from the relativistic impulse approximation [2], which accounts for electron binding effects and Doppler broadening. Contributions from different atomic electron shells are considered separately.

Photoelectric effect: Photoelectric cross sections are obtained by interpolation in a table that was generated by using the XCOM program of Berger and Hubbell [3]. The direction of the emitted photoelectron is sampled from Sauter's hydrogenic angular distribution [4].

Electron-positron pair production: The total cross sections are obtained by interpolation in a table generated with the XCOM program [3]. The kinetic energies and directions of the produced pair are sampled from a modified Bethe-Heitler DCS, which assumes an exponentially screened field and includes Coulomb and low-energy corrections. Although the total cross section accounts for pair and triplet production, all the events are simulated as if they were pairs.

2.2 Electron and Positron Interactions

Elastic scattering: Elastic collisions are simulated by means of the W2D model, which is a weighted admixture of screened Rutherford scattering and a fixed-angle process. The parameters of the model are determined so as to reproduce the values of the mean free path and the first and second transport mean free paths obtained from partial-wave calculations. The W2D model leads to multiple scattering angular distributions that agree closely with those that are obtained from the more accurate partial wave DCSs.

Inelastic collisions: The atomic DCSs are obtained from the Born approximation with a simple GOS model [5] in which the excitations of each electron shell are represented by a δ -oscillator with strength and resonance energies determined following the prescription of Sternheimer [6]. The model accounts for the density effect correction. The resulting stopping power agrees very closely with the tabulations of Berger and Seltzer [7].

Bremsstrahlung emission: Bremsstrahlung emission is described by using a modified Bethe-Heitler DCS that assumes exponential screening and includes Coulomb and low-energy corrections. The photon energy is sampled from the Bethe-Heitler energy-loss spectrum. The direction of the emitted photon is sampled from the dipole distribution in the rest frame of the projectile [8]. To improve the accuracy of the model, the DCS is renormalized so as to exactly reproduce Berger and Seltzer's radiative stopping powers for electrons.

Positron annihilation: Positrons annihilate in flight, or when they are brought to rest, with emission of two photons. The simulation is based on the Heitler DCS for annihilation with free electrons at rest.

2.3 Atomic Relaxation

PENELOPE simulates the emission of characteristic X-rays and Auger electrons that result from vacancies produced in a K-shell by photon interactions. Radiation resulting from the filling of vacancies in outer shells is not followed; in these cases, the excitation energy is taken out by the emitted Compton electron or photoelectron. This limits the validity of the simulation to photons with energies larger than the L-shell ionization energy of the heaviest element in the medium. The probability of inner-shell ionization by electron impact is very small; when it occurs, it is assumed that the excitation energy of the residual ion is locally deposited.

3 Simulation Algorithm

Photon simulation is performed by using the conventional detailed simulation scheme, i.e. all interactions in a photon history are sampled in chronological succession.

For the simulation of electrons/positrons, PENELOPE uses a mixed (class II) simulation scheme in which hard (catastrophic) events are simulated in a detailed way, whereas the effect of the soft interactions between each pair of hard events is described by means of simple approximations [9]. To separate soft and hard energy loss events, we introduce cutoff values W_{cc} and W_{cr} . Inelastic collisions with energy loss $W > W_{cc}$ and emission of bremsstrahlung photons with energy $W > W_{cr}$ are considered as hard interactions. For elastic scattering, instead of introducing the cutoff deflection μ_c ($\mu \equiv (1 - \cos \theta)/2$) directly, we define the mean free path between hard elastic events by

$$\lambda_{el}^{(h)}(E) = \max \left\{ \lambda_{el}(E), \min \left[C_1 \lambda_1(E), C_2 \frac{E}{S_{col}(E) + S_{rad}(E)} \right] \right\}, \quad (1)$$

where C_1 and C_2 are preselected small constants (less than ~ 0.05). The relation

$$\left[\lambda_{el}^{(h)} \right]^{-1} = \mathcal{N} \int_{\mu_c}^1 \frac{d\sigma_{el}}{d\mu} d\mu \quad (2)$$

determines μ_c as a function of energy. The average angular deflection $\langle\mu\rangle = (1 - \langle\cos\theta\rangle)/2$ and the average fractional energy loss $\Delta E/E$ in a path segment of length $\lambda_{\text{el}}^{(\text{h})}$ are then less than C_1 and C_2 , respectively.

Between a pair of consecutive hard interactions, an electron travels a certain path length t in which it may undergo multiple soft interactions, whose global effect is simulated by means of the random hinge method. In the first version of the code, the electron was moved a random distance $\tau = \xi t$ along the initial direction, then its energy and direction of motion were modified using simple multiple scattering theory and finally, the electron travelled the remaining step-length, $t - \tau$, in the final direction. Recently, we have introduced a slight modification of the algorithm to approximately account for energy variations along the step (which are caused only by soft interactions and, therefore, are small). Thus, the energy loss and angular deflection at the hinge are considered as separate processes and simulated in random order. In other words, the soft angular deflection is evaluated using the energy at either the beginning or the end of the step, with equal probabilities.

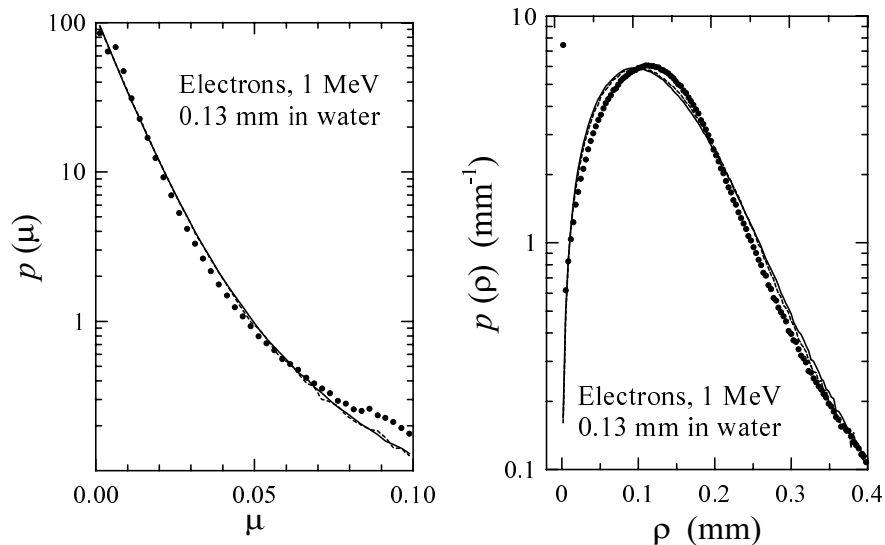


Fig. 1. Simulated angular distributions and lateral displacement distributions of 1 MeV electrons after traveling 0.13 mm in water. See the text for further details.

The main limitation of our mixed algorithm arises from the use of approximate energy loss and angular distributions in the description of soft events. These distributions have their first and second moments correct, but are otherwise arbitrary. This implies that we shall get reliable results only if each electron track involves (on average) a “statistically sufficient” number of soft events (hinges), say of the order of ten or larger, so that the details of the adopted distributions are washed out from the final distributions. We have modified the code to

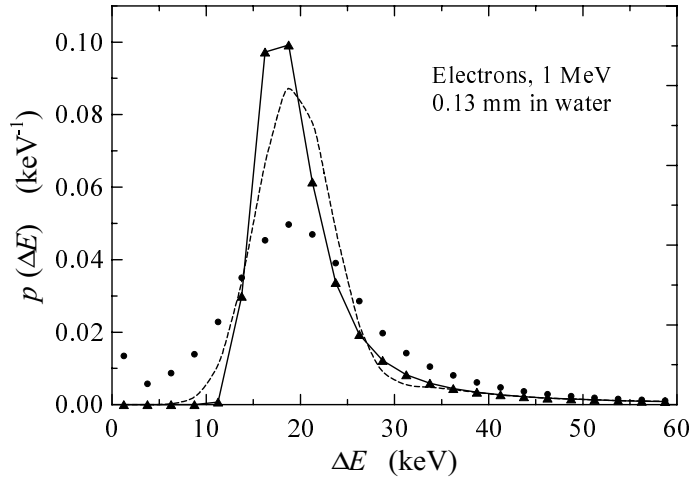


Fig. 2. Simulated energy-loss distributions of 1 MeV electrons after traveling 0.13 mm in water. Triangles have been joined with straight segments for visual aid. See the text for further details.

allow the user to set a maximum allowed step length, s_{\max} . When an electron intends to travel a length larger than s_{\max} without having a hard interaction, the step is truncated and no interaction occurs at the end point (for programming simplicity, PENELOPE simulates a δ -interaction, which does nothing). With the possibility of selecting s_{\max} , the user has direct control over the number of hinges per track and, therefore, on the accuracy of the simulation. Incidentally, limiting the step length is necessary to perform simulations of electron transport in external static electromagnetic fields [10]; with the current structure of the code, the coupling with an electromagnetic field is largely simplified.

Figures 1 and 2 display simulated angular, lateral and energy-loss distributions of 1 MeV electrons after travelling a path length of 0.13 mm in water (3% of the CSDA range). Continuous curves represent results of detailed (analog) simulations. The dots are distributions generated with $C_1 = 0.01$, $C_2 = 0.03$, $s_{\max} = \infty$ (i.e. step length control is switched off) and $W_{cc} = 10$ keV and $W_{cr} = 1$ keV. Dashed lines correspond to results with the same C_1 , C_2 , W_{cc} and W_{cr} and with s_{\max} equal to 1/10 of the total path length. In the latter case, step-length control is active and each electron undergoes, on average, 20 delta interactions. It is clear that, in the case of short path lengths, appropriate use of step-length control does improve the accuracy of the simulation. It should be noted that the considered case is fairly extreme (only ~ 2.4 hard interactions per electron history). In the case of longer path lengths, with multiple hard interactions (and hinges), the effect of s_{\max} on the simulation results is negligible. The user is cautioned against using values of s_{\max} that are too small, which may render the simulation unnecessarily slow.

Recent work of our group has been focused on the development of more elaborate interaction models for low-energy electrons and positrons. We have developed a new algorithm for the simulation of elastic scattering, using partial wave differential cross sections. Inelastic interactions are modelled by means of an optical-data model that combines calculated inner shell optical oscillator strengths with semiempirical models for valence shell excitations. The description of bremsstrahlung emission has been improved by the adoption of partial wave energy loss spectra [11] and angular distributions from Sommerfeld's theory. The resulting algorithm is currently being tested and will be made generally available in due course.

4 Acknowledgements

We would like to thank Prof. A.F. Bielajew for many enjoyable and helpful discussions and for useful suggestions which have lead, among other improvements, to the energy loss correction.

References

1. M.J. Berger: *Methods in Computational Physics*, vol. 1, ed. by B. Alder, S. Fernbach and M. Rotenberg (Academic Press, New York, 1963)
2. R. Ribberfors: Phys. Rev. A **27**, 3061 (1983)
3. M.J. Berger, J. H. Hubbell: National Bureau of Standards Report NBSIR 87-3797 (Washington, 1987)
4. F. Sauter: Ann. Phys. **11**, 454 (1931)
5. D. Liljequist: J. Phys. D: Appl. Phys. **11**, 839 (1978)
6. R.M. Sternheimer: Phys. Rev. **88**, 851 (1952)
7. M.J. Berger, S. M. Seltzer: National Bureau of Standards, Report NBSIR 82-2550 (Washington, 1982)
8. J. Sempau, E. Acosta, J. Baró, J.M. Fernández-Varea, F. Salvat: Nucl. Instrum. Meth. B **132**, 377 (1997)
9. J. Baró, J. Sempau, J.M. Fernández-Varea, F. Salvat: Nucl. Instrum. Meth. B **84**, 465 (1994)
10. A.F. Bielajew: In *Monte Carlo Transport of Electrons and Photons*, ed. by T.M. Jenkins, W.R. Nelson and A. Rindi (Plenum, New York 1988) p. 421
11. L. Kissel, C.A. Quarles, R.H. Pratt: At. Data Nucl. Data Tables **28**, 381 (1983)

Geant4 Electromagnetic Physics

S. Chauvie¹, V. Grichine², P. Gumplinger³, V. Ivanchenko⁴, R. Kokoulin⁵,
S. Magni⁶, M. Maire⁷, P. Nieminen⁸, M.G. Pia⁹, A. Rybin¹⁰, and L. Urban¹¹
(on behalf of the Geant4 Collaboration)

¹ Univ. of Torino and INFN Sezione di Torino, Italy

² LPI Moscow, Russia and CERN, Switzerland

³ TRIUMF, Canada

⁴ Budker Institute for Nuclear Physics, Russia

⁵ MePhi Moscow, Russia

⁶ INFN Sezione di Milano, Italy

⁷ LAPP, France

⁸ ESA/ESTEC, The Netherlands

⁹ INFN Sezione di Genova, Italy and CERN, Switzerland

¹⁰ IHEP Protvino, Russia

¹¹ KFKI Budapest, Hungary

Abstract. An overview of the main features of Geant4 electromagnetic physics is presented. The role played by advanced software engineering methodologies and of Object Oriented technology is illustrated. The main physics functionalities are described.

1 The Geant4 Object Oriented Simulation Toolkit

Geant4 [1] is a simulation toolkit designed for a variety of applications, including HEP, astrophysics and nuclear physics experiments, as well as medical physics and space science. GEANT4 provides functionalities for all the typical domains of simulation: geometry, tracking, detector response, run, event and track management, Particle Data Group compliant particle management, visualization and user interface, as well as a large variety of physics processes and models. It is also complemented by specific modules for space science applications.

Since the *R&D* phase of the Geant4 project, Software Engineering has played a fundamental role [1]. User Requirements were formally collected during the initial phase of the project, and were systematically reviewed and updated following the ESA PSS-05 framework [2] Standards. Object-Oriented methods (and the respective tools) have been employed for the analysis and design of the software, and to produce the corresponding deliverables. The spiral iterative approach for the development process demonstrated to be very effective also in the Production phase of the software product, allowing to apply successive refinements to the existing architecture, and experienced solutions to OOAD iterations. Software Processes have been monitored by following the ISO/IEC 15504 (SPICE) exemplar model [3], through regular assessments and improvements also from external professional companies.

By adopting OOP methodologies through the use of Software Engineering CASE tools and Quality Assurance techniques one guarantees that the code

quality will not degrade with time and a coherent development is also assured, where coupling will not increase with the complexity of the software.

Tools such as Insure++, CodeWizard, Purify and Logiscope have been used to assure and improve software quality and reliability. Scripts to automatically check the C++ coding guidelines recommended in the Project have been developed. Code inspections have been regularly held. Testing procedures are applied extensively, both at granular unit level and integration level, the latter being coordinated by a dedicated team through automated procedures based on the WWW.

The Geant4 source code is publicly distributed from the WWW [4], together with ample documentation.

2 General Features of Geant4 Physics

Object Oriented design provides the possibility to implement or modify any physics process in Geant4 without changing other parts of the software. This feature makes Geant4 open to the extension of its physics capabilities and to the implementation of alternative physics models. Via the use of virtual functions Geant4 provides transparent access to cross-sections (formulae, data sets, tables, etc.) and to models underlying the physics processes. For each process the generation of the final state is independent from the access and use of the cross sections. The transparency of physics implementation contributes to the validation of the experimental physics results.

By design Geant4 is independent from the units chosen by the user, so that one can use the most adequate units in different parts of the code.

In Geant4 there are no tracking cuts, but only production thresholds. Each physics process has its intrinsic limits to produce secondary particles, which can be tracked down to zero range; the cut associated to each particle represents only a recommended production threshold. In Geant4 the thresholds for producing secondaries are expressed in range, universal for all media. This range is converted in energy for each kind of particle and each material. The cuts in range allow one to say that the energy has been released at the correct space position, limiting the approximation within a given distance, while cuts in energy would imply accuracies of the energy depositions, which depend on the material.

Geant4 physics makes ample use of public evaluated databases, distributed by a variety of international sources; this feature also contributes to the reliability and the transparency of the physics implementation.

3 Overview of Geant4 Electromagnetic Processes

Geant4 Electromagnetic Physics manages electron processes, γ , X-ray and optical photon physics, muon processes and electromagnetic interactions of charged hadrons and ions. It exploits the features of transparency and extensibility provided by the Object Oriented technology. As shown in the top level class dia-

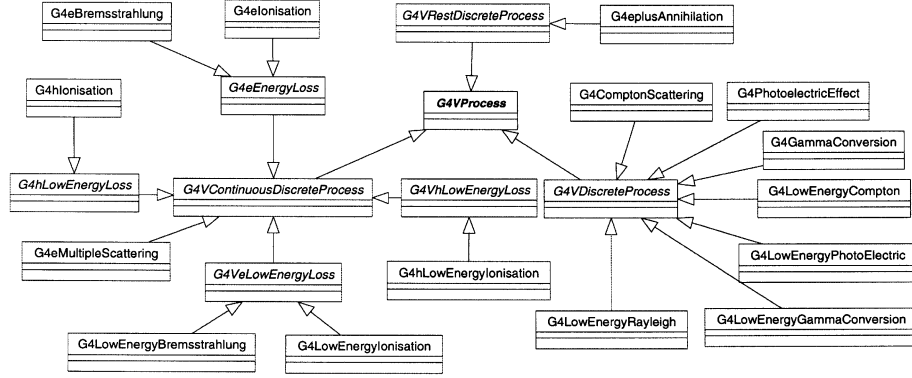


Fig. 1. Class diagram of electromagnetic processes

gram of Geant4 electromagnetic processes (Fig. 1), alternative models, obeying the same abstract interface, are often provided for the same physics interaction.

3.1 Standard Electromagnetic Processes

Geant4 *standard* electromagnetic physics provides a variety of implementations of electron, positron, photon and charged hadron interactions. Photon processes include Compton scattering, γ conversion and photoelectric effect. Electron/positron processes handle Bremsstrahlung, ionisation and δ ray production, positron annihilation and synchrotron radiation. The energy loss process manages the continuous energy loss of particles due to ionisation and Bremsstrahlung. An algorithm [5] is available to optimise the generation of δ rays only where they are needed, i.e. near the boundaries. The result can be a drastic improvement of the performance of the simulation, keeping the same quality of physics results as with the lowest cut. The ionisation and energy loss of hadrons can be simulated optionally with different models, including the PhotoAbsorption Interaction (PAI) one.

Geant4 multiple scattering [4] process can handle all the charged particles. It is based on a new model, which simulates the scattering of the particle after a step, computes the mean path length correction and the mean lateral displacement. Its performance is compared with experimental data in Fig. 2.

The ionisation, Bremsstrahlung, positron annihilation, energy loss and multiple scattering processes have been implemented both in the differential and in the so called 'integral' approach as well.

A shower profile resulting from Geant4 standard electromagnetic physics process is compared to and experimental data in Fig. 3.

3.2 Low Energy Extensions

A set of physics processes is implemented in Geant4 to extend the validity range of electromagnetic interactions down to lower energy than the standard Geant4

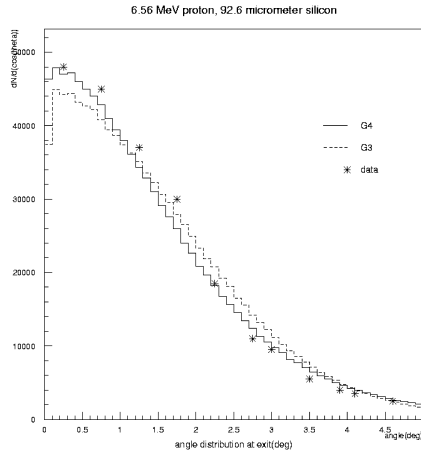


Fig. 2. Multiple scattering of 6.56 MeV protons on 92.6 μm Silicon: comparison of Geant4, Geant3 and experimental data from [19]

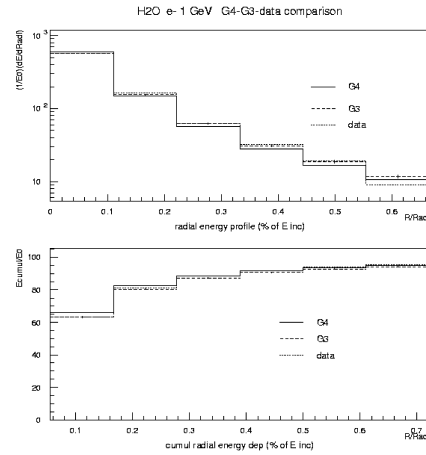


Fig. 3. Shower profile of 1 GeV electrons in water: Geant4, Geant3 and experimental data from [20]

electromagnetic processes. The currently available extensions cover processes for electrons, photons, positive and negative charged hadrons and positive ions; further extensions to cover positron and negative ion interactions are in progress.

Processes for Low Energy Photons and Electrons The current implementation of Geant4 Low Energy electron and photon processes [8] covers the energy range from 100 GeV down to 250 eV for elements with atomic number between 1 and 99. It includes photoelectric effect, Compton scattering, Rayleigh effect, Bremsstrahlung and ionization; for completeness, a photon conversion process has also been implemented based on the same data sources as the other Low Energy ones. In addition, fluorescence emission from excited atoms is also generated; the implementation of the Auger effect is in progress. The implementation is based on the exploitation of evaluated data libraries (EPDL97 [9], EEDL [10] and EADL [11]), that provide data for the determination of cross-sections and the sampling of the final state. A simulation based on Geant4 Low Energy processes for photons and electrons is compared with experimental data in Fig. 4, with evidence of shell effects.

Processes for Low Energy Hadrons and Ions A Low Energy process is available in Geant4 to handle the ionisation by hadrons and ions [12,13]. It adopts different models depending on the energy range and the particle charge. In the high energy ($E > 2 \text{ MeV}$) domain the Bethe-Bloch formula and in the low energy one ($E < 1 \text{ keV}$ for protons) the free electron gas model are applied respectively. In the intermediate energy range parameterized models based on experimental data from the Ziegler [14] and ICRU [15] reviews are implemented;

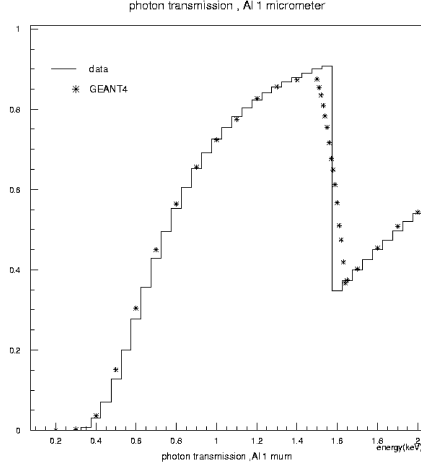


Fig. 4. Comparison of the Geant4 Low Energy photon simulation and experimental data, with relevance of shell effects: photon transmission in 1 μm Al; data from [21]

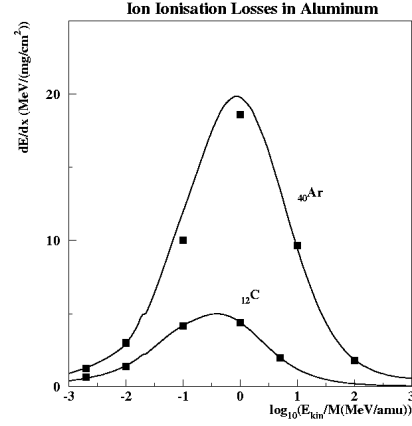


Fig. 5. Electronic stopping power of ions in Al; the accuracy of the data is approximately 5%; experimental data from [22]

corrections due to the molecular structure of materials [16] and to the effect of the nuclear stopping power [15] are taken into account. The Barkas effect is taken into account; a specialized quantum harmonic oscillator model [18] for negative charged hadrons, valid down to 50 keV, is available; this model is currently implemented for a set of materials only; extensions to other materials are in progress. Figure 5 shows a comparison with experimental data for ions.

3.3 Muon Processes

Muon processes available in Geant4 include Bremsstrahlung, ionisation and δ ray production, nuclear interaction and direct pair production. The Bremsstrahlung, ionisation and pair production processes give contributions to the total continuous energy loss.

The validity range of Geant4 muon processes, based on theoretical models, scales from 1 keV up to the 1000 PeV region, allowing the simulation of ultra-high energy and cosmic ray physics.

3.4 Physics Processes for Optical Photons

A photon is called optical when its wavelength is much greater than the typical atomic spacing, for instance when $\lambda \geq 10\text{nm}$ which corresponds to an energy $E \leq 100\text{eV}$. Production of an optical photon in a HEP detector is primarily due to Čerenkov effect and scintillation. In Geant4 optical photons are subject to in-flight absorption, Rayleigh scattering and medium boundary interactions.

3.5 Conclusions

An abundant set of physics processes is available in the Geant4 Toolkit for the simulation of electromagnetic interactions of electrons and positrons, photons, muons, charged hadrons and ions over an extended energy range. Many processes are available through alternative models. The Object Oriented technology plays a key role to achieve transparency of physics implementation and openness to extension to new physics processes and models. Geant4 electromagnetic physics is exercised in a variety of simulation domains; a selection of space and medical applications is presented elsewhere in these Proceedings [23] [24].

References

1. S. Giani et al.: *Geant4: an Object-Oriented toolkit for simulation in HEP*, CERN/LHCC/98-44 (1998)
2. ESA: *Guide to User Requirements Definition Phase*, ESA PSS-05 (1994)
3. *ISO/IEC DTR 15504 Software Process Assessment*, Project Editor: Terry Rout
4. The Geant4 Collaboration: <http://wwwinfo.cern.ch/asd/geant4/geant4.html>
5. J. Apostolakis et al.: CERN-OPEN-99-299 (1999)
6. S. Giani et al.: Phys. Lett. B **460**, 467 (1999)
7. J. Apostolakis et al.: *An implementation of ionisation energy losses in very thin absorbers for the Geant4 simulation package*, to be published in Nucl. Instr. Meth.
8. J. Apostolakis et al.: CERN-OPEN-99-034 and INFN/AE-99/18 (1999).
9. D. Cullen et al.: *EPDL97: the Evaluated Photon Data Library, 97 version*, UCRL-50400, Vol. 6, Rev. 5 (1997)
10. S.T. Perkins et al.: *Tables and Graphs of Electron-Interaction Cross Sections from 10 eV to 100 GeV Derived from the LLNL Evaluated Electron Data Library (EEDL)*, UCRL-50400 Vol. 31 (1997)
11. S.T. Perkins et al.: *Tables and Graphs of Atomic Subshell and Relaxation Data Derived from the LLNL Evaluated Atomic Data Library (EADL), Z=1-100*, UCRL-50400 Vol. 30 (1997)
12. S. Giani et al.: CERN-OPEN-99-121 and INFN/AE-99/20 (1999)
13. S. Giani et al.: CERN-OPEN-99-300 and INFN/AE-99/21 (1999)
14. H.H. Andersen, J.F. Ziegler: *The Stopping and Ranges of Ions in Matter* Vol.3, (Pergamon Press 1977)
15. ICRU (A. Allisy et al): ICRU Report 49 (1993)
16. J.F. Ziegler, J.M. Manoyan: Nucl. Instr. and Meth. B **35**, 215 (1988)
17. S. Chauvie et al.: INFN/AE preprint, in preparation
18. P. Sigmund: Nucl. Instr. Meth. B **85**, 541 (1994)
19. J. Vincour, P. Bem: Nucl. Instr. Meth. **148**, 399 (1978)
20. J.H. Crannel: Phys. Rev. **184**, 2 (1969)
21. R. Shimizu et al.: J. Phys. D **9**, 101 (1976)
22. H. Paul: <http://www.uni-linz.ac.at/fak/TNF/atomphys/STOPPING/welcome.htm>
23. E. Daly et al.: 'Space Applications of the Geant4 Simulation Toolkit'. These Proceedings p. 401
24. S. Chauvie et al.: 'Medical Applications of the Geant4 Simulation Toolkit'. These Proceedings p. 543

Electron–Photon Transport in FLUKA: Status

A. Fassò¹, A. Ferrari², and P.R. Sala²

¹ Stanford Linear Accelerator Center, USA

² CERN, Switzerland & Istituto Nazionale di Fisica Nucleare, Milano, Italy

1 Introduction

For historical reasons, FLUKA is best known for its hadron event generators: but the present version of the code can handle with similar or better accuracy also muons, low energy neutrons and electromagnetic effects. And, most important of all, it can simulate the transport of all these radiation components *and their reciprocal interactions* at the same time. This capability is especially important in accelerator shielding and in cosmic ray studies where the cross-talk at all energies between the different components is very complex and essential for an understanding of the radiation field.

At the MC93 Conference [1], we called into question a widespread opinion that electron-photon transport codes had already reached an unsurpassable degree of accuracy. To support our disagreement, we listed a number of weaknesses we found in the most popular codes, and we reported about our effort to overcome them in FLUKA.

About 8 years later, the situation is different. The challenge has been taken up. Several (although not all) of the issues we raised have now been addressed also in other programs, and new codes have appeared where new physical models have been implemented.

In this new emerging landscape, calculations made with different programs are often found now to be in similar (good) agreement with experimental data in most typical routine cases. However, we are convinced that FLUKA still offers a different approach which makes it an interesting alternative for a number of specialized problems.

Therefore, in the following the stress will be put more on the features which are not generally available elsewhere, than on the standard ones that FLUKA has in common with most other electron-photon Monte Carlo programs.

2 Energy Range

The energy range covered by FLUKA is probably unique: the program can transport photons and electrons over about 12 energy decades, between 1 PeV and 1 keV. Photonuclear reactions are implemented from threshold up to the maximum energy of the FLUKA hadron event generator (about 20 TeV).

A special care has been put in the description of both very high and very low energy effects (LPM effect, Ter-Mikaelyan effect, single scattering transport, photoelectron angular distribution, fluorescence).

3 Main Electromagnetic Physical Effects

A particular attention has been given to an accurate description of the most important electron and photon interactions, reproducing correlations as far as possible and avoiding unnecessary approximations.

3.1 Positrons

Electron and positron interactions are different [2], although the differences are often neglected. In FLUKA, these differences are taken into account both concerning stopping power and bremsstrahlung. The latter is not obtained by just rescaling the positron radiative power, but taking into account the actual spectral differences.

3.2 Bremsstrahlung

The bremsstrahlung differential cross-sections published by Seltzer and Berger [3] have been interpolated to a finer energy mesh and have been extended to 1000 TeV including the Landau-Pomeranchuk-Migdal suppression effect. A correction has been made to include the finite value at “tip” energy. The angular distribution of bremsstrahlung photons is sampled accurately, fully correlated with energy, and the Ter-Mikaelyan polarization effect in the soft part of the bremsstrahlung spectrum has also been implemented.

3.3 Other Effects

The treatment of pair production includes an accurate sampling from the energy and angular distribution of electrons and positrons. Common approximations used to sample electron energy at low photon energies have been avoided.

In the Compton effect, atomic bonds are accounted for using inelastic Hartree-Fock form factors.

The photoelectric effect is implemented with the actual relativistic photoelectron angular distribution according to Sauter [4], a detailed interaction on six K and L single sub-shells, emission of fluorescence photons and an approximate treatment of Auger electrons.

Photon polarization is taken into account for Compton, Rayleigh and Photoelectric effect.

4 Energy Loss Straggling

The Landau distribution, often used to describe ionisation fluctuations, is limited in several respects. Because the maximum energy of the δ rays is assumed to be infinite, it cannot be applied to long steps or to low velocities. On the other hand, since fluctuations connected with distant collisions are neglected, it cannot be applied for short steps either. More generally, the Landau distribution cannot be used if the code is required to produce explicitly δ rays above

any given energy threshold. In addition, the cross-section for close collisions is assumed to be the same for all particles. Some of these limitations can be avoided using instead the Vavilov distribution, but technical difficulties are met if the step length or the energy are not known in advance. The Vavilov distribution also lacks the contribution of distant collisions and does not account for electron-positron differences. In general, these difficulties are handled by means of empirical correction factors.

In FLUKA, on user’s request, an original treatment of ionisation fluctuations [5] can be applied for discrete losses below any predetermined δ ray production threshold. The new approach is based on very general statistical properties of the cumulants of a statistical distribution (in this case, the Poisson distribution convoluted with the differential cross-section for δ ray production). Since the necessary integrals can be calculated exactly and analytically *a priori*, the impact on CPU time is kept to a minimum.

In the present implementation, which includes “close” collisions and a two-oscillators model for “distant” collisions, the first 6 moments of the energy loss distribution are correctly reproduced.

This approach, as it is usual in FLUKA, is applied not only to electrons and positrons, but to all charged particles, taking into account the proper (spin-dependent) cross-section for δ ray production.

The scheme has proved so successful that it has been decided to extend it also to other Poisson-distributed effects, in particular multiple scattering (expressed as a function of projected angles in order to preserve additivity). A new scattering algorithm based on cumulants has already been thoroughly tested and will be available in the next version of FLUKA as a possible alternative to the present one, based on the Molière approach.

5 Variance Reduction

Several biasing options, which can be finely tuned as a function of energy, position, particle and material, allow the treatment of very deep photon and photon-neutron penetration problems and the simulation of rare events. Applications range from the simulation of very high energy showers to the calculation of very thick shielding with attenuation factors of the order of 10^{-10} , such as required by some high-intensity synchrotron radiation sources.

Most of the techniques available (importance biasing, weight windows) can be applied to electrons and photons as well as to all other particles, but one of them, leading particle biasing, is specifically designed to reduce the time spent in the simulation of electromagnetic showers. Experience has shown that this option, robust above all expectations, is indispensable for practically any high energy problem, and especially accelerator shielding. This option can be applied to selected physical effects (e.g. pair production only) and below a user-specified energy *on a region by region basis*.

Another biasing option, applicable also to hadrons but particularly useful with photons, is the reduction of the inelastic interaction length for hadronic interactions. Because photonuclear cross-sections are much smaller than those for

electromagnetic effects, calculations of photoneutron and photopion production or of photoactivation would be extremely inefficient if performed in analog mode. An artificial reduction of the photonuclear mean free path by a factor 0.01 to 0.05, compensated by a suitable adjustment of statistical weights, is commonly used in most electron accelerator shielding problems.

6 Transport

FLUKA includes an original transport strategy for charged particles, applied to both electrons/positrons and heavier particles. The general tracking system includes an optimized version of Combinatorial Geometry and a multiple scattering algorithm fully integrated with a special treatment of magnetic fields. During tracking, the minimum distance from any boundary (real or fictitious) is available at any time and is taken into account to establish the size of the next step. The approach of a charged particle to a boundary thus happens by progressively shortening the length of the steps.

6.1 Multiple Scattering

The multiple scattering algorithm of FLUKA [6] relies on an accurate calculation of the PLC (Path Length Correction). Sampling it from a distribution, rather than using an average value, gives a nearly complete independence of the results from step size. Correlations between path length corrections and lateral deflection are preserved, as well as those between lateral and longitudinal displacement and between the latter and scattering angle. The correct lateral displacement is ensured even near a boundary. The variation of the screening correction with energy is taken into account, and higher order corrections can be applied on user's request, such as spin-relativistic corrections (at the level of the first or second Born approximation) and the effect of the finite size of the nucleus.

Kawrakow and Bielajew [7] have criticized the FLUKA multiple scattering algorithm by alleging a pretended mathematical flaw. Actually the flaw was associated with some assumptions made by those authors while adjusting the original expression in order to compare it with other schemes. The derivation of the FLUKA model, which does not depend on such assumptions, is based on simple mathematics and can be easily checked.

The usefulness and the accuracy of the algorithm have been confirmed in practice by several years of experience and comparison with experimental data.

6.2 Single Scattering

Special tools take care of the actual crossing of a boundary, ensuring that the validity conditions of Molière theory are never violated and that no artifact is produced when the sampled step has to be cut due to boundary crossing.

One of such tools is a single scattering algorithm which can be activated on user's request. Originally intended mainly to improve the accuracy of tracking

at boundary crossing, it has been found extremely useful also to handle accurately very low energy electron problems, backscattering and transport in gases, especially in high-Z materials. The algorithm is based on the Rutherford formula with a screening factor in the form used by Molière (for consistency with the multiple scattering model used by FLUKA), integrated analytically without any approximation. Nuclear form factors and spin-relativistic corrections at the first or second Born approximation level are accounted for by a rejection technique.

The single scattering option can be used in a hybrid mode together with the condensed history scheme, by reverting to single scattering every time the validity conditions for Molière theory for the current step are not satisfied, or also alone. The latter choice, of course, is practicable only in very low-energy problems due to its large demand on CPU time.

As an example, we compare in Tab. 1 experimental values [8] of the backscattering coefficient for electrons of 9.3 and 102.2 keV, normally incident on a few materials, with the corresponding values calculated by FLUKA using the default multiple scattering algorithm and by a full single scattering calculation. It is worth noting that the two latter results coincide for gold at the lowest energy, because the validity conditions for applying Molière theory are never satisfied at low energies in high Z materials, and the code always automatically reverts to single scattering.

Table 1. Fraction of normally incident electrons backscattered out of a surface. All statistical errors are less than 1%

Energy (keV)	Material	Experimental (Drescher et al., 1970) [8]	FLUKA Single scattering	FLUKA Multiple scattering	CPU time ratio single/multiple
9.3	Be	0.050	0.044	0.040	2.73
	Cu	0.313	0.328	0.292	1.12
	Au	0.478	0.517		1.00
102.2	Be	0.035	0.036	0.031	5.48
	Cu	0.291	0.307	0.288	3.00
	Au	0.513	0.499	0.469	1.59

6.3 Variation of Energy Dependent Quantities over a Step

The cross-section for δ ray production at low energies is roughly inversely proportional to electron energy. Therefore, a fractional energy loss per step, typically of the order of 10–20%, would correspond to a similar variation in the cross-section.

The variations of the discrete event cross-sections and of the continuous energy loss in each transport step are taken into account *exactly* by a rejection technique based on the ratio between the cross-section value at the end of the step and its maximum value between the energies at either end of the step, independent of the fact that the cross-section be decreasing or increasing with energy.

7 Photonuclear Reactions

As already mentioned, in FLUKA there is a full exchange between the different radiation components. For instance, it is possible to simulate the electromagnetic showers generated by energetic knock-on electrons along a muon track, or by gammas from π^0 decay in hadronic cascades. A rather unique asset of FLUKA is its power to handle also exchanges in the opposite direction, i.e. from the electromagnetic to the hadronic compartment, at all energies below 20 TeV.

Photohadron production at high energy is described by the Vector Meson Dominance Model, fully coupled to the high and intermediate energy event generators of FLUKA. Giant Resonance and Quasideuteron interactions are also implemented. Photonuclear interactions include also virtual ones by high-energy charged hadrons and muons.

This capability has already originated a number of new applications in the field of shielding and radiation protection around electron accelerators. In this domain, the use of Monte Carlo programs has been traditionally limited mainly to dosimetry or to the separate study of the different components (bremsstrahlung, neutrons etc.), but most of the shielding and activation calculations were made by empirical or analytical techniques. It is now quite common to use FLUKA in the same way at electron and at proton accelerators, to calculate bulk shielding and to predict radionuclide production or radiation damage.

Applications have been found also in cosmic ray research, to calculate the residual activity produced by muons in rock and the production of muons by gamma rays from Gamma Ray Bursts.

8 Transport of Optical Photons

Recent improvements have been the generation and transport of Cherenkov light and the transport of light of a given wavelength in materials with user-defined optical properties. Unlike most existing programs specialized in this field, which can handle only simple geometrical arrangements for the transport of optical light, FLUKA can take full advantage of its powerful Combinatorial Geometry.

Part of this work was supported by the Department of Energy under contract DE-AC03-76SF00515.

References

1. P.A. Aarnio et al.: In *Proc. MC93 Int. Conf., Tallahassee 1993*. Ed. P. Dragovitsch, S.L. Linn and M. Burbank (World Scientific, Singapore 1994) p. 100
2. L. Kim et al.: *Phys. Rev. A* **33**, 3002 (1986)
3. S.M. Seltzer, M.J. Berger: *At. Data Nucl. Data Tab.* **35**, 345 (1986)
4. F. Sauter: *Ann. der Phys.* **9**, 217 (1931); **9**, 454 (1931)
5. A. Fassò, A. Ferrari, J. Ranft, P.R. Sala: *Proc. SARE3 Workshop*, Ed. H. Hirayama, KEK Proceedings 97-5 (1997)
6. A. Ferrari et al.: *Nucl. Instr. Meth. in Phys. Res. B* **71**, 412 (1992)
7. I. Kawrakow, A.F. Bielajew: *Nucl. Instr. Meth. B* **142**, 253 (1998)
8. H. Drescher et al.: *Z. Angew. Phys.* **29**, 331 (1970)

Random, Quasirandom and Hybrid Methods for Transport Problems

J. Spanier

Claremont Research Institute of Applied Mathematical Sciences, 925 North
Dartmouth Avenue, Claremont Graduate University, Claremont, CA 91711, USA

Abstract. Quasi-Monte Carlo methods may be regarded as fully deterministic substitutes for Monte Carlo methods. Their potential superiority to conventional (pseudorandom) Monte Carlo methods relies on the use of decision-making numbers that are more regularly distributed than pseudorandom ones. Understanding these newer methods requires replacement of the probability model that represents conventional Monte Carlo by an asymptotic frequency model that is totally devoid of probabilistic structure. Hybrid sequences are decision-making sequences designed to achieve convergence superior to that available using either pseudorandom or quasirandom methods. The elements of the theory needed will be outlined here.

1 Introduction

In the past thirty years or so there has been a surge in the number of publications (see, e.g., [1–4]) that recommend the use of quasirandom sequences (i.e., sequences more regular than pseudorandom ones) in place of pseudorandom sequences for difficult problems requiring lengthy Monte Carlo simulations. These *quasi-Monte Carlo methods*, as they are sometimes called, have become the methods of choice recently for many problems involving financial modeling [5–8], radiosity and global illumination problems [9–12], and other applications. Quasirandom methods promise improved convergence *rates* when compared with pseudorandom methods and have performed even better, in many applications, than can easily be explained by existing theory. Consequently, a sizeable research effort is presently devoted to obtaining a deeper understanding of these methods.

A hybrid sequence is one that combines pseudorandom and quasirandom components for the purpose of improving on both. Most of the literature dealing with methods that use either quasirandom or hybrid sequences, however, studies their use in estimating high dimensional integrals, rather than in solving integral, or integro-differential equations such as those describing particle transport. In this paper we will emphasize the latter, describing what we have learned about the application of quasi-Monte Carlo methods to particle transport problems.

2 Conventional (Pseudorandom) Monte Carlo

Conventional Monte Carlo methods have been successfully applied to the estimation of finite-dimensional integrals:

$$I \equiv \int_{I^s} f(x) dx \quad (1)$$

where $f(x)$ is known (i.e., is evaluable) and I^s is the unit hypercube in s dimensions, as well as to infinite-dimensional (random walk problems), both discrete and continuous:

1. Discrete case: estimate

$$\langle \mathbf{g}, \mathbf{x} \rangle \quad (2)$$

where

$$\mathbf{x} = \mathbf{H}\mathbf{x} + \mathbf{a}. \quad (3)$$

and \mathbf{g} , \mathbf{a} and \mathbf{H} are known. Here \mathbf{g} , \mathbf{a} and \mathbf{x} are s -dimensional vectors and \mathbf{H} is an $s \times s$ matrix of transition probabilities.

2. Continuous case: estimate

$$\int_{\Gamma} g(x) \Psi(x) dx \quad (4)$$

where $\Psi(x)$ satisfies

$$\Psi(x) = \int_{\Gamma} K(x, y) \Psi(y) dy + S(x) \quad (5)$$

and g , S , and K are known and Γ is a physical phase space. For all of these problems, a probability model is used to demonstrate that convergence is $O(N^{-1/2})$ when pseudorandom numbers are used to generate the “random” samples.

3 Quasi-Monte Carlo Methods

For finite-dimensional integrals, quasi-Monte Carlo methods replace *probability* with *asymptotic frequency*:

$$\lim_{N \rightarrow \infty} \frac{1}{N} \sum_{i=1}^N f(x_i) = \int_{I^s} f(x) dx \quad (6)$$

for a reasonable class of f (and (6) can be used to define x_1, x_2, \dots *uniformly distributed* in I^s).

For integral equations, the appropriate condition is

$$\lim_{N \rightarrow \infty} \frac{1}{N} \sum_{i=1}^N \xi(\omega_i) = \int_{\Omega} \xi d\mu \quad (7)$$

and ξ (which is an estimator of the functional $\int_{\Gamma} g(x)\Psi(x)dx$ of the solution $\Psi(x)$ of the integral equation) must satisfy mild smoothness restrictions (and (7) then defines the μ -uniformity of $\omega_1, \omega_2, \dots, \omega_N$ in Ω). The idea of μ -uniformity was introduced by Chelson [13] who showed that replacing pseudorandom sequences by uniformly distributed sequences produces μ -uniformity in Ω . Chelson's construction, modified slightly in [14], is simply to sample one dimensional conditional probability density functions derived from the source and kernel of the transport equation by using low discrepancy sequences, rather than pseudorandom ones. However, the correlation that is characteristic of low discrepancy sequences means that care must be exercised in the sampling details to ensure that the random walks simulated are, indeed, independent realizations of the physical system modelled.

The heart of the theory justifying quasi-Monte Carlo methods can be exhibited very easily using one dimensional integration to illustrate the ideas involved. For a given sequence $Q = \{x_1, x_2, \dots\} \subset [0, 1]$, first define a *counting function*

$$A([0, t]; N, Q) = \text{number of } x_i, 1 \leq i \leq N, \text{ with } x_i \in [0, t] \quad (8)$$

and then define the $*$ -discrepancy of Q to be

$$D_N^*(Q) = \sup |L_N([0, t])| \quad (9)$$

where

$$L_N([0, t]) = \frac{A([0, t]; N, Q)}{N} - t. \quad (10)$$

Thus, $D_N^*(Q)$ provides a quantitative measure of the nonuniformity of the sequence Q .

Theorem 1. Let $Q = \{x_1, x_2, \dots\} \subset [0, 1]$ & let f be a function of bounded variation on $[0, 1]$. Then

$$\begin{aligned} |\delta_N(f)| &= \left| \frac{1}{N} \sum_{i=1}^N f(x_i) - \int_0^1 f(t)dt \right| \\ &\leq D_N^*(Q)V(f) \end{aligned} \quad (11)$$

where $D_N^*(Q) = *$ -discrepancy of Q , $V(f) = \text{total variation of } f$.

Proof. (sketched assuming f is continuous):

$$\begin{aligned} \delta_N(f) &= \frac{1}{N} \sum_{i=1}^N f(x_i) - \int_0^1 f(t)dt \\ &= \int_0^1 f(t)d\left(\frac{A([0, t]; N, Q)}{N} - t\right) \\ &= \int_0^1 f(t)dL_N([0, t]) \\ &= L_N([0, t])f(t)|_0^1 - \int_0^1 L_N([0, t])df(t). \end{aligned}$$

Thus,

$$\begin{aligned} |\delta_N(f)| &= \left| \int_0^1 L_N([0, t)) df(t) \right| \\ &\leq D_N^*(Q) \int_0^1 |df(t)| \\ &= D_N^*(Q) V(f). \end{aligned} \quad (12)$$

When extended to finite dimensional integrals, this result is known as the *Koksma-Hlawka inequality* [3]. A similar result is also valid in the random walk case. That is,

$$|\delta_N(\xi)| \leq \hat{C} D_N^* \quad (13)$$

where $\delta_N(\xi) \equiv \frac{1}{N} \sum_{i=1}^N \xi(\omega_i) - \int_{\Omega} \xi d\mu$. For random walk applications, this generalization of the Koksma-Hlawka inequality was also established in Chelson's thesis [13].

The constant \hat{C} in (13) measures the variation of ξ ; reductions in \hat{C} can be accomplished by importance sampling and similar conventional variance reduction mechanisms, as described in [4,13,15]. But improvements in the *rate* of convergence as $N \rightarrow \infty$ can be obtained only as a result of the factor D_N^* . The key question then becomes: How rapidly can D_N^* converge to 0?

The answer is widely believed to be $D_N^* = O[(\log N)^s/N]$, s = "effective" dimension of the problem (though slightly more rapid convergence cannot yet be ruled out theoretically). Integral equations are really infinite-dimensional problems in the sense that normally, no *a priori* upper bound exists for the number of steps in a random walk. However, one might use the product of the average number of steps and $\dim(\Gamma)$ as an effective dimension.

Sequences in s dimensions whose discrepancies are $O[(\log N)^s/N]$ are called *low discrepancy sequences* and are the ones typically used in quasi-Monte Carlo implementations. A very general family of extremely low discrepancy sequences are the (t, s) -sequences [3,17,18] and are in wide use for quasi-Monte Carlo implementations.

4 Examples

A low discrepancy infinite sequence in $[0, 1)$ is the *Van der Corput sequence*, which is defined by

$$\phi_2(n) = \sum_{j=0}^N a_j(n) 2^{-j-1} \quad (14)$$

where

$$n = \sum_{j=0}^N a_j(n) 2^j. \quad (15)$$

Then we find that $\phi_2(1) = 1/2$, $\phi_2(2) = 1/4$, $\phi_2(3) = 3/4$, $\phi_2(4) = 1/8$, $\phi_2(5) = 5/8$, ... and the numbers $\{\phi_2(n)\}_{n=1}^{\infty}$ are much more uniformly distributed in the unit interval than pseudorandom numbers are.

In similar fashion, one can define the *radical inverse function* for any number base b by

$$\phi_b(n) = \sum_{j=0}^N a_j(n) b^{-j-1}; \quad (16)$$

it enjoys properties very similar to the $b = 2$ case when b is a prime larger than 2.

The *Halton sequence* is an infinite, s -dimensional, low discrepancy sequence defined by $\{\phi_{b_1}(n), \phi_{b_2}(n), \dots, \phi_{b_s}(n)\}$, where b_1, b_2, \dots, b_s are relatively prime in pairs (for example, the first s primes). It is useful for generating very uniform s -dimensional vectors, as when random walks in an s -dimensional phase space are required.

For more about important low discrepancy sequences the reader is referred to [3].

5 Summary: Pseudorandom vs. Quasirandom Methods

For fixed s (here s should be thought of as the actual dimension of a multidimensional integral or as the effective dimension of a discrete or continuous random walk problem), quasi-Monte Carlo methods will be superior to pseudorandom methods as $N \rightarrow \infty$ because of the inequality (13) and because $[(\log N)^s/N]$ becomes much smaller than $N^{-1/2}$ in this limit. However, for *practical* values of N and moderate values of s , such a comparison may well favor the pseudorandom convergence rate. In fact when s is only 3, N must be larger than 10^7 for quasirandom sampling to have a chance of improving upon pseudorandom sampling. There is also some evidence to support the fact that N must be exponential in s before the advantages of quasi-Monte Carlo methods over conventional Monte Carlo using pseudorandom sequences can be realized [18]. Model problem analyses reported in various publications support these findings.

Another possible drawback to using quasirandom methods is the lack of an effective and low cost error analysis when it is used. The use of sample standard deviation or variance in conventional Monte Carlo applications as a measure of uncertainty in the answer is simple and inexpensive. By contrast, the terms entering the right hand side of (13) are both difficult and expensive to estimate sharply. Quite recently, Halton has advocated analyzing low discrepancy sequences as though they were independent and identically distributed uniform sequences [19] but this device entails generating low discrepancy sequences in dimensions much higher than actually needed for the simulation itself, and there are disadvantages to doing so. When we discuss hybrid sequences below we will mention a similar error analysis suggested by Okten [20].

6 Hybrid Sequences

Hybrid sequences are meant to combine the best features of both pseudorandom (convergence rate is independent of dimension) and quasirandom (asymptotic rate of convergence is greater than $N^{-1/2}$). Ideas for generating hybrid sequences seem to rely either on randomly scrambling the elements of a low discrepancy sequence or restricting the use of the low discrepancy component to a lower dimensional portion of the problem and filling out the remaining dimensions with pseudorandom sequence elements. Thus, Spanier [21] introduces both a “scrambled” and a “mixed” sequence based on these ideas, Owen [22] describes a method for scrambling (t, m, s) –nets and (t, s) –sequences, Faure [23] describes a method for scrambling the Halton sequence to achieve lowered discrepancy, Wang and Hickernell [24] randomize Halton sequences, and Moskowitz [25], Coulibaly and Lecot [26], and Morokoff and Caflisch [18] present various methods for renumbering the low discrepancy components. Okten [27,28] has introduced a generalization of Spanier’s mixed sequence and Moskowitz’s renumbering method and also indicated how error estimation may be performed when using such sequences. Because of its generality, we will describe Okten’s ideas briefly here.

In [2], Okten provides the following

Definition 1. Let $\pi = \{i_1, \dots, i_d\}$ ($i_1 < \dots < i_d$) be a subset of the index set $\{1, \dots, s\}$. For a given d –dimensional sequence $\{q_n\}_{n=1}^\infty$, a $\text{mixed}_\pi(s, d)$ sequence is an s –dimensional sequence $\{m_n\}_{n=1}^\infty$ ($s \geq d$) such that $m_n^{i_k} = q_n^k$, $k = 1, \dots, d$ and all other components of m_n (i.e., m_n^i for $i \in \{1, \dots, s\} - \pi$) come from independent realizations of a random variable uniformly distributed on $[0, 1]^{s-d}$.

This definition is useful inasmuch as it specializes to a number of interesting sequences introduced by other authors earlier. For example, Spanier’s mixed sequence corresponds to the choices $\pi = \{1, \dots, d\}$ with $s = \infty$; i.e., it is a $\text{mixed}_\pi(\infty, d)$ sequence that can be used for either high dimensional integration or random walk problems. Also, the continuation method introduced in [25] amounts to using a $\text{mixed}_\pi(s, d)$ sequence with $\pi = \{s - d + 1, s - d + 2, \dots, s\}$. Furthermore, the Spanier mixed sequence clearly degenerates to an ordinary pseudorandom sequence when $d = 0$ and π is empty, while if $\pi = \{1, \dots, d\}$ and $s = d$, the resulting $\text{mixed}_\pi(d, d)$ sequence is clearly completely deterministic, with no random components at all.

Okten [3] also introduces a family of hybrid sequences obtained by randomly sampling from a universe consisting of low discrepancy sequences of the appropriate dimension for the problem. This idea permits the use of conventional statistical analyses to be performed on the resulting estimates and therefore helps to overcome one of the major drawbacks of using low discrepancy sequences: the unavailability of an effective and convenient error analysis.

Hybrid sequences are designed to produce good results for general problems with dimensions s that are too large for pure low discrepancy sequences to be

effective. Such sequences should, therefore, be effective for s -dimensional integration of arbitrary functions or for arbitrary random walks problems of high effective dimension. But one should not overlook the possibility that for *certain* integrands or random walk problems, special features of that problem might suggest the use of special sequences designed to take advantage of additional information about the problem. For example, if the s -dimensional integrand is, in fact, independent of several of the s variables, the properties of the hybrid sequence with respect to these variables becomes irrelevant. More generally, if an s -dimensional integrand exhibits diminished dependence on some subset of the variables, it makes sense to design a hybrid sequence that takes advantage of that information. Similar special considerations would apply in the case of certain random walk problems

Based on this sort of reasoning, quite recently some authors have focused attention on restricting the class of integrands treated by each method in an attempt to explain why some sequences perform surprisingly well for certain problems. Interest in taking this point of view might have been picqued by provocative results reported when purely quasirandom sequences were used to estimate some very high dimensional integrals arising in financial applications [30,5]. This has led to a rash of publications in which the sensitivity of an integrand function with respect to its independent variables and/or parameters is studied ([32–37]).

7 Summary and Conclusions

1. Quasi-Monte Carlo and hybrid methods can be very effective for random walk problems.
2. Substantial savings over pseudorandom Monte Carlo are possible (even when Neumann series converges slowly).
3. Matrix transport problems provide very useful models for studying convergence and are much easier to analyze than continuous transport problems.

Continuing research is needed to understand more completely when each method might prove of most value.

References

1. S.K. Zaremba: ‘The Mathematical Basis of Monte Carlo and Quasi-Monte Carlo Methods’, SIAM Rev. **10** (1968)
2. S. Haber: ‘The Numerical Evaluation of Multiple Integrals’, SIAM Rev. **12** (1970)
3. H. Niederreiter: ‘Random Number Generation and Quasi-Monte Carlo Methods’, SIAM (1992)
4. J. Spanier, E.H. Maize: ‘Quasi-Random Methods for Estimating Integrals Using Relatively Small Samples’, SIAM Rev. **36** (1994)
5. P. Boyle: Options: ‘A Monte Carlo Approach’, J. Fin. Econ. **4** (1997)
6. W.J. Morokoff, R.E. Caflisch: ‘Quasi-Monte Carlo Simulation of Random Walks in Finance’. In: *Monte Carlo and Quasi-Monte Carlo Methods 1996*, Lecture Notes in Statistics 127 ed. by H. Niederreiter, P. Hellekalek, G. Larcher, P. Zinterhof (Springer-Verlag, New York 1998)

7. C. Joy, P. Boyle, K.S. Tan: 'Quasi-Monte Carlo Methods in Numerical Finance. Management Science' **42** (1996)
8. S. Tezuka: 'Financial Applications of Monte Carlo and Quasi-Monte Carlo Methods'. In: *Random and Quasirandom Point Sets*, Lecture Notes in Statistics 138 ed. by P. Hellekalek, G. Larcher (Springer-Verlag, New York 1998)
9. M. Cohen, J. Wallace: *Radiosity and Realistic Image Synthesis* (Academic Press Professional, Cambridge, 1993)
10. A. Keller: 'A Quasi-Monte Carlo Algorithm for the Global Illumination Problem in the Radiosity Setting'. In: *Monte Carlo and Quasi-Monte Carlo Methods in Scientific Computing*, Lecture Notes in Statistics 106 ed. by H. Niederreiter, P.J. Shiue (Springer-Verlag, New York 1995)
11. A. Keller: 'The Quasi-Random Walk'. In: *Monte Carlo and Quasi-Monte Carlo Methods 1996*, Lecture Notes in Statistics 127 ed. by H. Niederreiter, P. Hellekalek, G. Larcher, P. Zinterhof (Springer-Verlag, New York 1998)
12. E. Lafortune: *Mathematical Models and Monte Carlo Algorithms for Physically Based Rendering*. Ph. D. dissertation (Katholieke Universiteit Leuven, Belgium 1996)
13. P. Chelson: *Quasi-Random Techniques for Monte Carlo Methods*. Ph. D. dissertation (The Claremont Graduate School, Claremont 1976)
14. J. Spanier, L. Li: 'Quasi-Monte Carlo Methods for Integral Equations'. In: *Monte Carlo and Quasi-Monte Carlo Methods 1996*, Lecture Notes in Statistics 127 ed. by H. Niederreiter, P. Hellekalek, G. Larcher, P. Zinterhof (Springer-Verlag, New York 1998)
15. E.H. Maize: *Contributions to the Theory of Error Reduction in Quasi-Monte Carlo Methods*. Ph. D. dissertation (The Claremont Graduate School, Claremont 1981)
16. H. Niederreiter, C. Xing: 'The Algebraic-Geometry Approach to Low-Discrepancy Sequences'. In: *Monte Carlo and Quasi-Monte Carlo Methods 1996*, Lecture Notes in Statistics 127 ed. by H. Niederreiter, P. Hellekalek, G. Larcher, P. Zinterhof (Springer-Verlag, New York 1998)
17. H. Niederreiter: 'Construction of (t, m, s) -Nets'. In: *Monte Carlo and Quasi-Monte Carlo Methods, 1998* ed. by H. Niederreiter, J. Spanier (Springer-Verlag, New York 2000)
18. W.J. Morokoff, R.E. Caflisch: 'A Quasi-Monte Carlo Approach to Particle Simulation of the Heat Equation'. SIAM J. Num. Anal. **30** (1993)
19. J. Halton: *Independence of Quasi-Random Sequences and Sets*. Working Paper CB#3175 University of North Carolina, Chapel Hill (1998)
20. G. Okten: 'Error Estimation for Quasi-Monte Carlo Methods'. In: *Monte Carlo and Quasi-Monte Carlo Methods 1996*, Lecture Notes in Statistics 127 ed. by H. Niederreiter, P. Hellekalek, G. Larcher, P. Zinterhof (Springer-Verlag, New York 1998)
21. J. Spanier: 'Quasi-Monte Carlo Methods for Particle Transport Problems'. In: *Monte Carlo and Quasi-Monte Carlo Methods in Scientific Computing*, Lecture Notes in Statistics 106 ed. by H. Niederreiter, P.J. Shiue (Springer-Verlag, New York 1995)
22. A. Owen: 'Randomly Permuted (t, m, s) -Nets and (t, s) -Sequences'. In: *Monte Carlo and Quasi-Monte Carlo Methods in Scientific Computing*, Lecture Notes in Statistics 106 ed. by H. Niederreiter, P.J. Shiue (Springer-Verlag, New York 1995)
23. H. Faure: 'Good Permutations for Extreme Discrepancy'. J. Number Theory **42** (1992)
24. J. Wang, F.J. Hickernell: 'Randomized Halton Sequences'. Math. Comp. Modelling (to appear)

25. B. Moskowitz: 'Quasirandom Diffusion Monte Carlo'. In: *Monte Carlo and Quasi-Monte Carlo Methods in Scientific Computing*, Lecture Notes in Statistics 106 ed. by H. Niederreiter, P.J. Shiue (Springer-Verlag, New York 1995)
26. I. Coulibaly, C. Lecot: 'Monte Carlo and Quasi-Monte Carlo Algorithms for a Linear Integro-Differential Equation', In: *Monte Carlo and Quasi-Monte Carlo Methods 1996*, Lecture Notes in Statistics 127 ed. by H. Niederreiter, P. Hellekalek, G. Larcher, P. Zinterhof (Springer-Verlag, New York 1998)
27. G. Okten: *High Dimensional Integration: A Construction of Mixed Sequences Using Sensitivity of the Integrand*. Technical Report, (Ball State University, Muncie IN 1999)
28. G. Okten: 'Applications of a Hybrid Monte Carlo Sequence to Option Pricing'. In: *Monte Carlo and Quasi-Monte Carlo Methods, 1998* ed. by H. Niederreiter, J. Spanier (Springer-Verlag, New York 2000)
29. G. Okten: *Random Sampling from Low Discrepancy Sequences: Applications to option Pricing*. Technical Report, (Ball State University, Muncie IN 1999)
30. S.H. Paskov: 'New Methodologies for Valuing Derivatives, in *Mathematics of Derivative Securities*, ed. by S. Pliska, M. Dempster (Isaac Newton Institute, Cambridge University Press, Cambridge, UK, 1997)
31. S.H. Paskov, J.F. Traub: 'Faster Valuation of Financial Derivatives'. *The Journal of Portfolio Management* **22** (1995)
32. R.I. Cukier, H.B. Levine, K.E. Shuler: 'Nonlinear Sensitivity Analysis of Multiparameter Model Systems'. *J. Comput. Phys* **26** (1978)
33. I.M. Sobol': 'Sensitivity Estimates for Nonlinear Mathematical Models'. *MMCE* **1** (1993)
34. A. Owen: 'Orthogonal Arrays for Computer Experiments, Integration and Visualization'. *Statistica Sinica* **2** (1992)
35. I. Radovic, I.M. Sobol', R.F. Tichy: 'Quasi-Monte Carlo Methods for Numerical Integration: Comparison of Different Low Discrepancy Sequences'. *Monte Carlo Methods and Applications* **2** (1996)
36. I.H. Sloan, H. Wozniakowski: 'When Are Quasi-Monte Carlo Algorithms Efficient for High Dimensional Integrals?'. *J. Complexity* **1** (1998)
37. H. Wozniakowski: 'Efficiency of Quasi-Monte Carlo Algorithms for High Dimensional Integrals'. In: *Monte Carlo and Quasi-Monte Carlo Methods, 1998* ed. by H. Niederreiter, J. Spanier (Springer-Verlag, New York 2000)

On the Use of Antithetic Variates

M.S. Milgram

Consulting Physicist, Box 1484, Deep River, Ont. Canada, K0J 1P0, e-mail:
gmtrcs@magma.ca; temporary address(Jan-June 2001: Mechanical Engineering
Faculty, Technion, Haifa, Israel)

Abstract. The use of antithetic variates as a variance reduction method is investigated by numerical experimentation. It is found that if *variance reduction* is not carefully defined, it can go undetected. With this caveat in mind, it is shown that antithetic variates can reduce variance up to a point. The phenomenon of *spontaneous correlation* is identified as the cause of failure. The surprising result that it can pay to use non-scoring histories is demonstrated. A total energy deposition problem is studied.

1 Introduction

The use of antithetic samples variates [1,2] in a Monte Carlo implementation of particle transport problems is appealing yet challenging. The simplicity of the method suggests that it could be a powerful tool for variance reduction, but few successful applications have been reported. The basic idea is to obtain two anti-correlated estimates of the mean $\mu = \frac{1}{2}(\mu_2 + \mu_1)$ noting that the estimate of variance is reduced by a covariance term.

Using a random sample, an estimator μ for the quantity of interest $\langle g \rangle = \int_0^1 g(x)p(x)dx$ is conventionally obtained. Introduce σ^2 , the variance of $g(x)$,

$$\sigma^2 \equiv \int_0^1 \{g(x) - \langle g \rangle\}^2 p(x)dx = \int_0^1 g(x)^2 p(x)dx - \langle g \rangle^2 \equiv \langle g^2 \rangle - \langle g \rangle^2. \quad (1)$$

An estimator of σ^2 , the *sample variance* can be obtained by evaluating

$$s^2 \equiv \left(\frac{1}{N-1} \right) \sum_{i=1}^N (t_i - \mu)^2 = \left(\frac{1}{N-1} \right) \left(\sum_{i=1}^N t_i^2 - \frac{1}{N} \left(\sum_{i=1}^N t_i \right)^2 \right), \quad (2)$$

with $t_i = g(R_i)$, and s_μ^2 , the *variance of the mean*

$$s_\mu^2 = s^2/N. \quad (3)$$

If μ were to be calculated many (say L) times, the estimates μ_i would collectively form a distribution about the mean of the means $\bar{\mu}$, s_μ^2 being an estimator of the variance $\text{var}(\bar{\mu})$ of this second distribution. Recognize that the equality in (3) is derived, assuming that the samples t_i , are independent measurements, but if any subsets are correlated, substitute the general rule

$$s_\mu^2 = \frac{1}{N} \left[s^2 + 2 \sum_{p < q} \text{covar}(t_p, t_q) \right]. \quad (4)$$

Since this is rarely done, if correlation exists, s_μ^2 as computed by (3), will be a poor measure of $\text{var}(\mu)$. As well, a distinction must be made between reduction of a sampling variance e.g. (3) and reduction of true variance ((1)), without which, it is possible, with antithetic variates, to observe false, or paradoxical instances of variance reduction. Three possibilities are [3]:

- reduction of both σ^2 and s_μ^2 (case A), the goal;
- reduction of σ^2 but not s_μ^2 (case B);
- reduction of s_μ^2 but not σ^2 (case C).

2 Antithetic Variates

The choice of antithetic transformations is very large [4]. The simplest considers another estimator μ_2 , an antithetic pair for μ_1 , defined by

$$\mu_2 = (1/N) \sum_{i=1}^N g(1 - R_i). \quad (5)$$

The corresponding set of sample variables $R_i \Leftrightarrow 1 - R_i$ are antithetic (*mirror*) variates, and it is known [1] that choosing a corresponding transformation can reduce σ^2 , accompanied by a reduction in $\text{var}(\mu)$, if $g(x)$ is such that $g(R_i)$ is small when $g(1-R_i)$ is large or the reverse. In this case, the elements of μ_1 and μ_2 will be anti-correlated, and, calculated properly, the reduction in σ^2 will be detected by a reduction in s_μ^2 (case A). Calculated improperly, it is possible to reduce σ^2 and $\text{var}(\mu)$ but not s_μ^2 , (case B).

This use of antithetic variates demands batch sampling. It has been proven [5,6] that “single batch” grouping minimizes the estimator of the “*variance of the variance*”, apparently contradicting (4); the resolution lies in the fact that the cited proofs are only valid for independent, unbiased samples.

3 Two Integration Examples

Trials of the antithetic method on multi-dimensional integrals are of interest. First, consider the function

$$\begin{aligned} g(x) &= 1 & 0 \leq x \leq 1/2 \\ &= 0 & \text{otherwise} \end{aligned} \quad (6)$$

and draw random variables R_i N times. Antithetically, use mirror variates, scoring either individually or in paired batches (Tab. 1).

Scored individually, mirror variates eventually converge to the limiting (large N) results in line one. In pairs, the use of mirror variates gives a zero variance solution. With reference to Section 1, the antithetic transform has reduced σ^2 , as well as s_μ^2 but only if the samples are grouped in pairs - case A. Tallied

Table 1. Evaluation of $\langle g \rangle$ with the integrand of (6), using single batch random samples, compared with antithetic mirror variates, in single and paired batches

	mean μ		s^2		$s/\sqrt{N}=s_\mu$	
Random (large N)	$\rightarrow 1/2$		$\rightarrow 1/4 \text{ ((3))}$		$\rightarrow 0$	
	random samples	mirror samples	random samples	mirror samples	random samples	mirror samples
N=2	0.500	0.500	0.500	0.500	0.500	0.500
N=3	0.667	0.667	0.333	0.333	0.333	0.333
N=4	0.500	0.500	0.333	0.333	0.289	0.289
...						
N=21	0.476	0.524	0.262	0.262	0.112	0.112
N=28	0.464	0.500	0.258	0.259	0.096	0.096
mirror antithetic (batches of 2)						
all N/2	0.500		0		0	

individually, case B arises. Notice that no-scores ($x > 1/2$) represent beneficial non-contributions to the tally, demonstrating (in a transport analog) that it can pay to track histories into regions of sample hyper-space where they do not score!

Second, I evaluate the volume V_n of a unit sphere in “n” dimensions by scoring if a vector $\mathbf{R}_i = (R_{i,1}, \dots, R_{i,n})$ chosen at random satisfies $\mathbf{R}^2 \leq 1$. Antithetic, multi-dimensional mirror variates are not well-defined, so try the vectors

$$\begin{aligned} \hat{R}_{i,k} &= 1 - R_{i,k} && \text{if } i = 2, 4, \dots, N \\ &= R_{i,k} && \text{otherwise.} \end{aligned} \quad (7)$$

From these two sets, estimates v_n and \hat{v}_n of the known result V_n were obtained, and estimates of the corresponding errors ε_μ and $\hat{\varepsilon}_\mu$ were conventionally calculated, terminating at a value of N where estimates of these parameters reached 0.01. Estimates of the real error $\varepsilon_n = 1 - v_n/V_n$, $\hat{\varepsilon}_n = 1 - \hat{v}_n/V_n$ and the variances $s_{v_n}^2$ and $s_{\hat{v}_n}^2$ were simultaneously calculated repeating $L=5000$ times, each with a different pseudo-random sequence, to measure the variance of the parent distribution, which should equal 0.01, if the estimators $s_{v_n}^2$ and $s_{\hat{v}_n}^2$ were accurately obtained using (3). Additionally, the number of samples N, adopted at the termination of each calculation was collected and the mean (\bar{N}) and variance $s_{\bar{N}}^2$ was calculated. The mean error $\bar{\varepsilon}$, as well as $\text{var}(\bar{\varepsilon}_n)$ for each of the three methods was obtained from the 5,000 entry distributions. The results, summarized in Tab. 2, demonstrate that:

1. Sampling with single batch antithetic variates does not improve the efficiency of the calculation *vis-a-vis* using independent samples. The subtle advantage appears in the estimate of $s_{\bar{N}}^2$ and $\text{var}(\bar{\varepsilon}_n)$, the former estimate being consistently less for the antithetic cases; as well, $\sqrt{\text{var}(\bar{\varepsilon}_n)}$ is always less than its expected value of 0.01, indicating that the use of single batch antithetic variates has made the calculation more reliable, but has not improved its

efficiency, and the estimates of accuracy are not very accurate. In contrast, for $K=2$, (̈) the efficiency of the calculation as measured by \tilde{N} has been improved for some values of “n”, and the estimator $\tilde{s}_{\tilde{N}}$ is not greater than that for the case of independent variates. For this case, $\sqrt{\text{var}(\tilde{\varepsilon}_n)}$ equals .01 as expected, verifying the accuracy of (3).

2. Although there is a small (10-20%) reduction between the case of independent and antithetic variates ($K=1$), an advantage is obtained by trading increased reliability (lower values of $\text{var}(\tilde{\varepsilon}_n)$) for efficiency with $K=2$.
3. All estimates of $\tilde{\varepsilon}_n$ are small, indicating that the use of (anti-)correlated sampling has not affected the means.

Table 2. Number of samples required to obtain $\tilde{\varepsilon}_\mu=.01$ in a Monte Carlo evaluation of V_n and the observed distribution of error

Dimensions	Method	\tilde{N}	$s_{\tilde{N}}$	$\tilde{\varepsilon}_n$	$\sqrt{\text{var}(\tilde{\varepsilon}_n)}$
n=2	independent variates	2,737	145	$-.7 \times 10^{-3}$	0.01
	(mirror) variates $K=1$	2,740	129	$-6. \times 10^{-3}$	0.0087
	(mirror) variates $K=2$	1,987	58	$-6. \times 10^{-3}$	0.01
n=3	independent variates	9,122	190	$-.17 \times 10^{-3}$	0.01
	(mirror) variates $K=1$	9,122	110	$-.1 \times 10^{-3}$	0.0058
	(mirror) variates $K=2$	3,033	174	$-.31 \times 10^{-3}$	0.01
n=4	independent variates	22,500	323	$-.14 \times 10^{-3}$.0099
	(mirror) variates $K=1$	22,500	245	$-.15 \times 10^{-3}$.0075
	(mirror) variates $K=2$	22,500	328	$-.33 \times 10^{-3}$.01
n=5	independent variates	50,900	600	$-.66 \times 10^{-4}$.0098
	(mirror) variates $K=1$	50,900	542	$-.43 \times 10^{-4}$.0089
	(mirror) variates $K=2$	40,940	620	$-.53 \times 10^{-4}$.01
n=6	independent variates	114,100	1210	$-.13 \times 10^{-4}$.0097
	(mirror) variates $K=1$	114,100	1180	$-.21 \times 10^{-4}$.0095
	(mirror) variates $K=2$	104,500	1293	$-.14 \times 10^{-4}$.0098

Finally, a well-known [7] result has been reproduced: the method of antithetic variates fails as “n” increases. Consider Tab. 3, listing both V_n and V_n/V_T , the probability that a sample point selected by \mathbf{R}_i or $\hat{\mathbf{R}}_i$ will fall in the interior of V_n , V_T being the hyper-cube volume enclosing the unit hyper-sphere. Calculate the joint probabilities that successive samples will either (i) both fall inside V_n , (ii) both fall outside, or (iii) one will fall inside, the other outside.

Table 3 gives such probabilities, showing that antithetic sampling has its greatest advantage for $n=3$ and 4, but that the advantage decreases as “n” increases, because of the tendency of the independently and antithetically selected samples to “spontaneously correlate” to similar limits, demonstrating that independently selected variates can naturally mimic anti-correlation.

Table 3. Showing the probability that successive samples will be correlated in pairs, for both independent and antithetic sampling, for the problem of finding V_n

n	V_n	V_n/V_T		both inside	one inside, one outside	both outside
2	π	0.78	independent	0.617	0.337	0.046
			antithetic	0.571	0.429	0.
3	$4\pi/3$	0.52	independent	0.274	0.499	0.227
			antithetic	0.047	0.935	0.
4	$\pi^2/2$	0.31	independent	0.095	0.427	0.478
			antithetic	0.	0.616	0.384
5	$8\pi^2/15$	0.16	independent	0.027	0.274	0.698
			antithetic	0.	0.328	0.671
6	$\pi^3/6$	0.08	independent	.006	0.148	.845
			antithetic	0.	0.161	.838

4 An Example from Electron Transport

The problem is to determine the energy deposition of a 1 MeV photon beam impinging on a 25 cm H_2O slab, 100 cm in extent, using a modified version of EGS4 [8]. It was found that the first-drawn pseudo-random number, $R_{i,1}$, governs the parent particle displacement: if $R_{i,1} < 0.17$, the particle will (likely) traverse the medium without interacting. How can this be used to reduce variance? Since $R_{i,1}$ governs total energy deposition, use the antithetic transform [1]

$$g_a(x) \equiv \alpha g(\alpha x) + (1 - \alpha)g(\alpha + (1 - \alpha)x) \quad 0 \leq \alpha \leq 1 \quad (8)$$

setting $\alpha=0.17$, noting that each of the $g(x)$ on the RHS represents the contribution of a (biased) individual history to the tally. Denote these by ${}^\alpha R_{i,1}$, and recall that the antithetic history (${}^\alpha R_{i,1} < 0.17$) is unlikely to score, meeting the antithetic criterion by correlating high- with “no”-scoring tallies.

The results are presented in Tab. 4, where the number of histories tracked was noted, and the problem was terminated when the estimated fractional error, ε_Ω , in the total energy deposition Ω was less than 0.01. The first case is the usual solution with independently chosen random numbers. 950 repetitions were performed and \bar{N} , the average number of histories required to meet the accuracy criterion was computed (except for case 2), along with the variance $s_{\bar{N}}^2$.

Assuming that the correct answer is known, I also calculated the mean, $\bar{\varepsilon}_\Omega$, and the observed variance of the mean $\text{var}(\bar{\varepsilon}_\Omega)$. Independently, the mean of the estimates of variance, $\bar{s}_{\varepsilon_\Omega}^2$, used to truncate each of the 950 calculations was established. If the estimate of sample variance is correct, this quantity should approximate $\text{var}(\bar{\varepsilon}_\Omega)$.

Table 4. Number of histories, and variances in the total energy deposition problem

case	α	first random number	\bar{N}	$s_{\bar{N}}$	$\bar{\varepsilon}_\Omega$	$\sqrt{\text{var}(\bar{\varepsilon}_\Omega)}$	$\bar{s}_{\varepsilon_\Omega}$
1		independent	3830	117	-0.0005	0.01	0.01
2	0.17	${}^\alpha R_{i,1}$ (K=1)	4000	0	-0.0005	0.008	0.018
3		${}^\alpha R_{i,1}$ (K=2)	2960	166	-0.0002	0.01	0.01

From Tab. 4, the most important test comes from a comparison of cases 1 and 3, where it can be seen that the use of antithetic variates along with batch sampling in pairs, increases the efficiency of the calculation by $1-2960/3830=23\%$. In fact, the observed improvement was about 50% as measured by CPU time, since half of the histories in the antithetic case did not score, simplifying the tracking effort. However, the observed variance s_N^2 was increased for case 3 relative to case 1, since fewer histories were tracked.

Also, a comparison of columns 7 and 8 of the table for case 2 shows that the estimate of error obtained from s_μ^2 is more than twice that observed, demonstrating that the use of antithetic variates improves reliability, which is not reflected in the estimates of s_μ^2 , in the absence of batch sampling.

5 Summary

It is shown that antithetic variates are a promising technique to consider in those problems in which last event estimators are sought that can be classified on the basis of sharply delineated scoring regions in sample space. However, the beneficial effects are sometimes not detected, unless the sample variance is calculated appropriately. Batch sampling is a simple way to do this is, choosing batch sizes consistent with the antithetic scheme. A few simple problems were studied, and, the efficiency of an energy deposition problem was doubled. In no case did the failure of an antithetic variance reduction method result in an incorrect estimate of the corresponding mean, in agreement with expectations [7].

6 Acknowledgment

This paper summarizes work funded by Lawrence Livermore National Laboratory under contract W-7405-ENG-48.

References

1. L. Carter, E.D. Cashwell: *Particle Transport Simulation with the Monte Carlo Method*, (ERDA Critical Review Serites, TID-26607, 1977)
2. J.M. Hammersley, K.W. Morton: Proc. Camb. Phil. Soc. **52**, 449 (1956)
3. M. Milgram: Annals of Nuclear Energy **28**, 297 (2001)
4. J.H. Halton: Nucl. Sci. Eng. **98**, 299 (1998)
5. A. Dubi: Nucl. Sci. Eng. **72**, 108 (1979)
6. I. Lux: Nucl. Sci. Eng. **92**, 607 (1979)
7. J.M. Hammersley, D.C. Handscomb: *Monte Carlo Methods*, (Methuen 1967)
8. W.R. Nelson, H. Hirayama, D.W.O. Rogers: *The EGS4 Code System*, SLAC-265 (1985)

Adjoint Monte Carlo Simulation of Fixed-Energy Secondary Radiation

N.M. Borisov¹ and M.P. Panin²

¹ Institut de Protection et de Sûreté Nucléaire, rue Auguste Lemaire, BP 6,
Fontenay-aux-Roses, F92265 France

² Moscow Engineering Physics Institute, 31, Kashirskoe Shosse, Moscow, 115314
Russia

Abstract. Fixed energy secondary generation for adjoint Monte Carlo methods constitutes certain difficulties because of zero probability of reaching fixed value from continuous distribution. This paper proposes a possible approach to adjoint Monte Carlo simulation with fixed energy secondary radiation which does not contain any simplifying restriction. This approach uses the introduced before generalized particle concept developed for description of mixed-type radiation transport and allows adjoint Monte Carlo simulation of such processes. It treats particle type as additional discrete coordinate and always considers only one particle even for the interactions with many particles outgoing from the collision. The adjoint fixed energy secondary radiation simulation is performed as local energy estimator through the intermediate state with fixed energy. The proposed algorithm is tested on the example of coupled gamma/electron/positron transport with generation of annihilation radiation. Forward and adjoint simulation according to generalized particle concept show statistically similar results.

1 General Approach to Adjoint Fixed Energy State Generation

Monte Carlo simulation technique for adjoint transport equation reached a considerable number of sophistication. Yet there is still a problem of fixed energy secondary radiation (annihilation photons, characteristic X-rays, Auger electrons etc.), mentioned in [1]. These difficulties are caused by zero probability of reaching fixed value from continuous distribution. The paper [2] proposed only a restricted method for these problems. Here is presented the possible approach to the problem without any restrictions.

In [3] we developed a generalized particle concept, which can be an universal approach to Monte Carlo simulation of mixed type particle radiation transport. According to generalized particle concept the particle type is associated to discrete phase coordinate $1 \leq \zeta \leq N$, where N is number of particle types taken to account. The differential linear cross section of particle reproduction, which has the meaning of expected number of particles with coordinates E, Ω, ζ outgoing from the unit path length near the phase point $\mathbf{r}, E, \Omega, \zeta$ is equal to

$$\Sigma_s(E', \Omega', \zeta' \rightarrow E, \Omega, \zeta | \mathbf{r}) = \sum_{\mu=1}^{\infty} \mu \Sigma_{\mu\zeta}(\mathbf{r}, E', \zeta') f_{\zeta}(E, \Omega), \quad (1)$$

where $\Sigma_{\mu\zeta}$ is section of process with μ outgoing particles of type ζ and $f_\zeta(E, \boldsymbol{\Omega})$ is energy-angular pdf of ζ -particle emerging from the collision.

With this reproduction section one can write down both forward and adjoint integral transport equations for both forward incoming ψ and outgoing χ , adjoint incoming χ^+ and outgoing ψ^+ collision densities:

$$\begin{cases} \psi(\mathbf{r}, E, \boldsymbol{\Omega}, \zeta) = \int T(\mathbf{r}' \rightarrow \mathbf{r} | E, \boldsymbol{\Omega}, \zeta) \chi(\mathbf{r}', E, \boldsymbol{\Omega}, \zeta) d\mathbf{r}' \\ \chi(\mathbf{r}, E, \boldsymbol{\Omega}, \zeta) = \sum_{\zeta'=1}^N \iint C(E', \boldsymbol{\Omega}', \zeta' \rightarrow E, \boldsymbol{\Omega}, \zeta | \mathbf{r}) \psi(\mathbf{r}, E', \boldsymbol{\Omega}', \zeta') dE' d\boldsymbol{\Omega}' + \\ \quad + S(\mathbf{r}, E, \boldsymbol{\Omega}, \zeta), \end{cases} \quad (2)$$

$$\begin{cases} \chi^+(\mathbf{r}, E, \boldsymbol{\Omega}, \zeta) = \int T(\mathbf{r}' \rightarrow \mathbf{r} | E, \boldsymbol{\Omega}, \zeta) \psi^+(\mathbf{r}', E, \boldsymbol{\Omega}, \zeta) d\mathbf{r}' \\ \psi^+(\mathbf{r}, E, \boldsymbol{\Omega}, \zeta) = \sum_{\zeta'=1}^N \iint C^+(E', \boldsymbol{\Omega}', \zeta' \rightarrow E, \boldsymbol{\Omega}, \zeta | \mathbf{r}) \chi^+(\mathbf{r}, E', \boldsymbol{\Omega}', \zeta') dE' d\boldsymbol{\Omega}' + \\ \quad + D(\mathbf{r}, E, -\boldsymbol{\Omega}, \zeta). \end{cases} \quad (3)$$

Here S is source density, D is detector response from unit path length, T is conventional transport kernel, which is happily self-adjoint, and

$$C(E', \boldsymbol{\Omega}', \zeta' \rightarrow E, \boldsymbol{\Omega}, \zeta | \mathbf{r}) = \frac{\Sigma_s(E', \boldsymbol{\Omega}', \zeta' \rightarrow E, \boldsymbol{\Omega}, \zeta | \mathbf{r})}{\Sigma_t(\mathbf{r}, E', \zeta')}, \quad (4)$$

$$C^+(E', \boldsymbol{\Omega}', \zeta' \rightarrow E, \boldsymbol{\Omega}, \zeta | \mathbf{r}) = \frac{\Sigma_s(E, -\boldsymbol{\Omega}, \zeta \rightarrow E', -\boldsymbol{\Omega}', \zeta' | \mathbf{r})}{\Sigma_t(\mathbf{r}, E', \zeta')}, \quad (5)$$

are forward and adjoint collision kernels respectively.

The concept assumes simulation of only one outgoing particle even for collisions with many outgoing particles (the effect produced by other particles is taken into account by statistical weight correction). It makes forward simulation algorithms free of remembering the intermediate states and allows to perform adjoint Monte Carlo calculations of coupled particle transport (for more details, see [3]).

The generation of secondary fixed energy radiation can be described by introduction of “singular” member to generalized particle cross section. This part has Dirac $\delta(\dots)$ function in energy:

$$\Sigma_{\text{sing}}(E', \boldsymbol{\Omega}', \zeta' \rightarrow E, \boldsymbol{\Omega}, \zeta | \mathbf{r}) = \mu \Sigma_X(\mathbf{r}, E', \zeta') \delta(E - E_X) f(\boldsymbol{\Omega}' \rightarrow \boldsymbol{\Omega}) \delta_{\zeta X}, \quad (6)$$

where Σ_X – cross section of generation process, μ – number of particles of type X with fixed energy E_X emerging from a collision. Because of this singularity, the integrals of “regular-singular” and “regular-regular” transition kernels do not have equal dimension:

$$P_{\text{reg} \rightarrow \text{sing}}^+(\mathbf{r}') = \Sigma_{\text{reg}}(E_X, X \rightarrow E', \zeta' | \mathbf{r}') / \Sigma_t(\mathbf{r}', E', \zeta'), \quad (7)$$

$$P_{\text{reg} \rightarrow \text{reg}}^+(\mathbf{r}') = \sum_{\zeta=1}^{\infty} \int \Sigma_{\text{reg}}(E, \zeta \rightarrow E', \zeta' | \mathbf{r}') dE / \Sigma_t(\mathbf{r}', E', \zeta'). \quad (8)$$

Fortunately, the subsequent “singular-regular” transition is described by the kernel, which integral through all the outgoing coordinates is

$$P_{\text{sing} \rightarrow \text{reg}}^+(\mathbf{r}) = \mu \int \Sigma_X(\mathbf{r}, E, \zeta) dE / \Sigma_t(\mathbf{r}, E_X, X). \quad (9)$$

The product of $P_{\text{reg} \rightarrow \text{sing}}^+ \times P_{\text{sing} \rightarrow \text{reg}}^+$ has unitary dimension and may be compared with $P_{\text{reg} \rightarrow \text{reg}}^+$.

Now we can formulate an approach to simulation of adjoint fixed energy radiation for adjoint particle, entering a collision in “regular” state $\mathbf{r}', E', \boldsymbol{\Omega}', \zeta'$.

Step 1. With the probability $P_{\text{reg} \rightarrow \text{sing}}^+ P_{\text{sing} \rightarrow \text{reg}}^+ / (P_{\text{reg} \rightarrow \text{sing}}^+ P_{\text{sing} \rightarrow \text{reg}}^+ + P_{\text{reg} \rightarrow \text{reg}}^+)$ play transition to the singular state, set $E = E_X$, $\zeta = X$ and choose $\boldsymbol{\Omega}_X$ from the proper distribution. With the probability $P_{\text{reg} \rightarrow \text{reg}}^+ / (P_{\text{reg} \rightarrow \text{sing}}^+ P_{\text{sing} \rightarrow \text{reg}}^+ + P_{\text{reg} \rightarrow \text{reg}}^+)$ play the transition to the regular state $\mathbf{r}', E, \boldsymbol{\Omega}, \zeta$ according to the regular part of adjoint collision kernel. Finally multiply the statistical weight of the particle by a factor of $P_{\text{reg} \rightarrow \text{sing}}^+ P_{\text{sing} \rightarrow \text{reg}}^+ + P_{\text{reg} \rightarrow \text{reg}}^+$.

Step 2. Simulate the transport kernel T to move the particle from the point \mathbf{r}' to the point \mathbf{r} .

Step 3. If on the step 1 the regular channel was chosen, just return to step 1 again. Otherwise simulate the transition to regular state from proportionally to function $C_{\text{sing} \rightarrow \text{reg}}^+(\mathbf{r})$ and multiply the statistical weight of the particle by a factor of $P_{\text{sing} \rightarrow \text{reg}}^+(\mathbf{r}) / P_{\text{sing} \rightarrow \text{reg}}^+(\mathbf{r}')$. Then return to step 2.

The presence of fixed energy state in transport model adds the extra part with delta function to detector function: $S(\mathbf{r}, E, \boldsymbol{\Omega}, \zeta) \delta(E - E_X) \delta_{\zeta X}$, and we must begin some adjoint random walk stories from this state directly.

2 Example of Adjoint Fixed Energy State Generation

We tested the model on coupled transport of gamma rays ($\zeta = \gamma$), secondary electrons ($\zeta = e$) and positrons ($\zeta = e^+$). For gamma rays we simulated photoelectric absorption, Compton scattering and pair production. Transport of charged particles was calculated in continuous-slowing-down approximation (CSDA). The fixed energy state was considered to occur in positron annihilation. Positrons, in their own turn, can be produced during pair generation, which differential section was considered the following:

$$\begin{aligned} \Sigma_{\varkappa}(E', \boldsymbol{\Omega}', \gamma \rightarrow E, \boldsymbol{\Omega}, \zeta | \mathbf{r}) &= \Sigma_{\varkappa}(\mathbf{r}, E') \left((1 - P_{\gamma}(E', E_t^{e^+})) \times \right. \\ &\times f_{\varkappa}(E' \rightarrow E) \frac{1 - b^2}{4\pi(1 - b\boldsymbol{\Omega}\boldsymbol{\Omega}')^2} (\delta_{\zeta e} + \delta_{\zeta e^+}) + 2P_{\gamma}(E', E_t^{e^+}) \delta(E - \varepsilon) \frac{1}{4\pi} \delta_{\zeta \gamma} \Big). \end{aligned} \quad (10)$$

Here $\Sigma_{\mathcal{K}}$ is total pair production linear section, $f_{\mathcal{K}}(E' \rightarrow E)$ is normalized pdf for electron or positron energy, described in [4], $b = v/c$ is electron or positron velocity in speed of light units and ε is electron rest mass energy. The second element of the sum describes annihilation of positron *in situ* (energy of this positron is lower than termination threshold $E_t^{e^+}$, and

$$P_{\gamma}(E', E_t^{e^+}) = \int_0^{E_t^{e^+}} f_{\mathcal{K}}(E) dE \quad (11)$$

is the probability of immediate annihilation.

The collision kernel for positron annihilation can be written as follows:

$$C_{\text{an}} \left(\frac{E_t^{e^+}}{1-\eta} < E' \leq E_t^{e^+}, \boldsymbol{\Omega}', e^+ \rightarrow E, \boldsymbol{\Omega}, \zeta \right) = \frac{2}{4\pi} \delta_{\zeta\gamma}, \quad (12)$$

where η is the energy loss fraction in CSDA, H is Heavyside function. With introduced in [3] concept of CSDA “total interaction section” $\Sigma_t(\mathbf{r}, E, \zeta = e, e^+) = \beta(\mathbf{r}, E, \zeta = e, e^+)/(\eta E)$ (β is stopping power) the annihilation differential cross section can be defined as:

$$\Sigma_{\text{an}}(\dots) = C_{\text{an}}(\dots) \frac{\beta(\mathbf{r}, E, \zeta = e, e^+)}{\eta E}. \quad (13)$$

Forward photon, electron and positron interaction channels for this model are shown in the left column of Fig. 2. Briefly, “KN” denotes Compton effect, “ph” – photoelectric absorption, “ \mathcal{K} ” – pair production, and “an” – annihilation.

The transposition of differential cross section arguments and substitution of incoming state total cross section with outgoing state total cross section gives us adjoint collision kernels. Adjoint photons have regular $C_{\text{KN}}^+(\gamma \rightarrow \gamma)$ and singular $C_{\text{KN}}^+(\gamma \rightarrow \gamma)\delta(E-\varepsilon)$ “transposed Compton scattering” as “interaction channels”. Adjoint annihilation photons can produce adjoint positrons

$$C_{\text{an } e^+}^+(\varepsilon, \boldsymbol{\Omega}', \gamma \rightarrow E, \boldsymbol{\Omega}, \zeta | \mathbf{r}) = \frac{\beta(\mathbf{r}, E')}{\eta E' \Sigma_t(\mathbf{r}, \varepsilon)} 2H(E - E_t^{e^+}) H\left(\frac{E_t^{e^+}}{1-\eta} - E\right) \frac{1}{4\pi} \delta_{\zeta e^+} \quad (14)$$

or directly adjoint photons:

$$C_{\text{an } \gamma}^+(\varepsilon, \boldsymbol{\Omega}', \gamma \rightarrow E, \boldsymbol{\Omega}, \zeta | \mathbf{r}) = 2P_{\gamma}(E, E_t^{e^+}) \Sigma_{\mathcal{K}}(\mathbf{r}, E) \frac{1}{4\pi} \delta_{\zeta\gamma}. \quad (15)$$

For adjoint electrons there are possible regular “transposed Compton effect” $C_{\text{KN}}^+(e \rightarrow \gamma)$, singular “transposed Compton effect” $C_{\text{KN}}^+(e \rightarrow \gamma)\delta(E-\varepsilon)$, regular “transposed photoelectric effect” $C_{\text{ph}}^+(\dots)$, singular “transposed photoelectric effect” (when incoming adjoint electron energy $(1-\eta)\varepsilon < E' \leq \varepsilon$): $C_{\text{ph}}^+(\dots) \times \delta(E-\varepsilon)$, transposed pair generation process

$$C_{\mathcal{K}}^+(E', \boldsymbol{\Omega}', e \rightarrow E, \boldsymbol{\Omega}, \zeta | \mathbf{r}) = \frac{\Sigma_{\mathcal{K}}(E, \boldsymbol{\Omega}, \zeta \rightarrow E', \boldsymbol{\Omega}', e | \mathbf{r}) \delta_{\zeta\gamma} \eta E'}{\beta(\mathbf{r}, E')}, \quad (16)$$

and gaining energy in the process, transposed to continuous slowing down model C_{CSDA}^+ . Two last processes are regular and also possible for adjoint positrons. A brief diagram of adjoint particle “interaction channels” is given in the right column of Fig. 1.

Compton scattering, photoelectric absorption and continuous-slowing-down transport model for charged particles (both mathematical formulae and forward and adjoint simulation algorithms) were described previously [3].

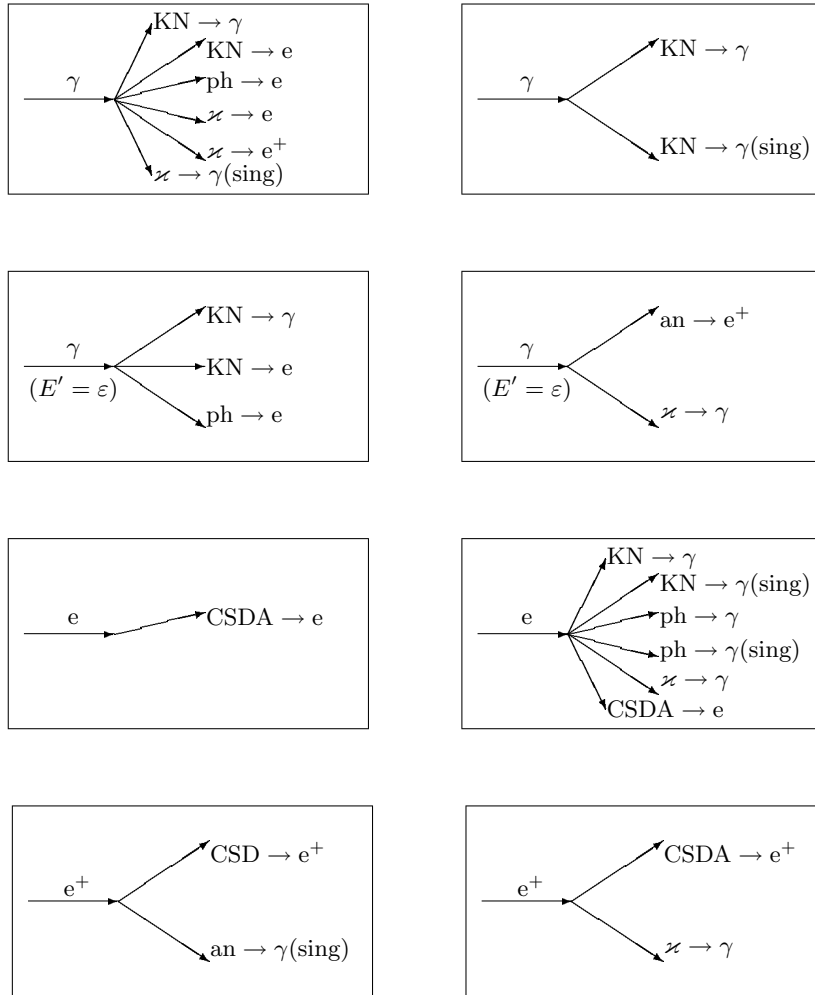


Fig. 1. Possible “scattering channels” for forward (left column) and adjoint (right column) particles

To verify adjoint simulation algorithm for fixed energy states, we compared the results of forward and adjoint Monte Carlo calculations of absorbed energy in thin (0.01 mean free path) water slab from the photon 9 MeV point source located at the boundary of the slab. Absorbed energy from annihilation radiation and particles generated by it is shown in Tab. 1. The relative error indicates one standard deviation, so forward and adjoint results are statistically similar. The relative FOM indicates the ratio of adjoint FOM to forward. In thin sub-slabs (ten times thinner than whole slab), relative efficiency of adjoint method is higher because of detector localization.

Table 1. Absorbed energy in slab, MeV per source photon

Particle and energy	Forward method	Adjoint method	Relative FOM
γ , $E = 0.511$ MeV	$4.26 \cdot 10^{-5} \pm 1.0\%$	$4.28 \cdot 10^{-5} \pm 2\%$	0.6
γ , $E < 0.511$ MeV	$4.72 \cdot 10^{-6} \pm 3\%$	$4.74 \cdot 10^{-6} \pm 3\%$	1.0
e , $E < 0.511$ MeV	$5.21 \cdot 10^{-5} \pm 3\%$	$4.94 \cdot 10^{-5} \pm 2\%$	2.8

References

1. M. Kalos: Nucl. Sci. and Eng. **33**, 284 (1968)
2. J.A. Halblieb: Nucl. Sci. and Eng. **50**, 162 (1982)
3. N.M. Borisov, M.P. Panin: Monte Carlo Meth. and Applic. **4**, 341 (1998)
4. P.V.C. Hough: Physical Review **73**, 266 (1948)

Symmetry-Based Variance Reduction Applied to ^{60}Co Teletherapy Unit Monte Carlo Simulations

D. Sheikh-Bagheri

MDS Nordion, 447 March Rd., Kanata, Ontario, Canada

Abstract. A new variance reduction technique (VRT) is implemented in the BEAM code [1] to specifically improve the efficiency of calculating penumbral distributions of in-air fluence profiles calculated for isotopic sources. The simulations focus on ^{60}Co teletherapy units. The VRT includes splitting of photons exiting the source capsule of a ^{60}Co teletherapy source according to a splitting recipe and distributing the split photons randomly on the periphery of a circle, preserving the direction cosine along the beam axis, in addition to the energy of the photon. It is shown that the use of the VRT developed in this work can lead to a 6-9 fold improvement in the efficiency of the penumbral photon fluence of a ^{60}Co beam compared to that calculated using the standard optimized BEAM code [1] (*i.e.*, one with the proper selection of electron transport parameters).

1 Introduction

^{60}Co teletherapy has been in use for the past 50 years to treat over 25 million patients. Recently the BEAM code [1] was used to model a typical ^{60}Co therapy source [2] with excellent results in predicting depth-dose behaviour and output factors. Similar simulations are very CPU intensive and could benefit from improvements in calculation efficient. This work aims at introducing a variance reduction technique (VRT) into the BEAM code for the simulation of isotopic sources such as ^{60}Co .

The efficiency (ϵ) of a Monte Carlo calculation, with respect to a specific endpoint, can be defined as [3–6]:

$$\epsilon = \frac{1}{T \cdot \sigma^2} \quad (1)$$

where, T is the total CPU time for the run and σ^2 is the variance of the endpoint of interest. In practice one uses s , an estimator for σ , in (1). When variance reduction techniques are employed, the computing time, T , for a given number of histories may increase. However, the goal is to make the product $T\sigma^2$ (Ts^2) decrease, by reducing variance to a greater extent.

2 Methods

The number of splits is determined for each photon individually based partially on the likelihood of a photon contributing to the penumbral fluence (see Fig. 1).

The recipe used here is a combination of a linear function which increases (up to a user-specified radius) with the radial distance from the axis of symmetry of the beam and then falls off according to a Gaussian afterwards (see (2)). The recipe uses 4 user-specified parameters which allow problem-specific optimization. The basic idea is to have more photons generated which aim at the edges of the collimating system, compared to the number of photons emitted towards inside or outside the field, as shown in Fig. 3.

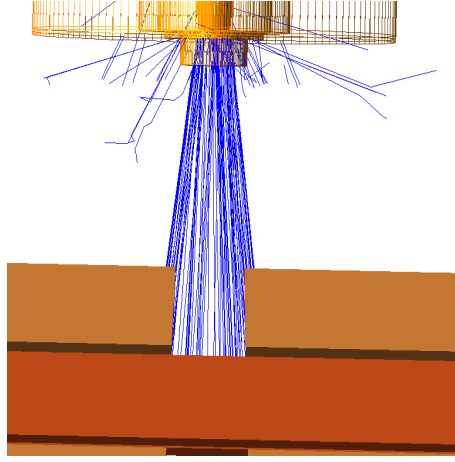


Fig. 1. The basic idea behind this splitting routine is to make use of the cylindrical symmetry of a ^{60}Co beam exiting the source capsule. The beam is no longer cylindrically symmetric after passing through the (non-cylindrically symmetric) collimators

Photon splitting is performed, according to the function $f(R_p)$, as the photon is being transported out of the exit window of the radioactive source, which has its axis of symmetry aligned with the beam axis. The splitting function $f(R_p)$ is defined by:

$$f(R_p) = \begin{cases} N_{\max} \left(\frac{R_p}{R_f} \right) + N_{\min} & \text{if, } R_p \leq R_f \\ N_{\max} \exp(-\ln(2) \frac{(R_p - R_f)^2}{R_w}) + N_{\min} & \text{if, } R_p > R_f, \end{cases} \quad (2)$$

where, R_f is a parameter representing the field radius, N_{\max} and N_{\min} are the maximum and the minimum splitting numbers allowed, R_w , the FWHM of the Gaussian, is a parameter which specifies how fast the splitting should fall off as a function of R_p , and R_p is the distance from the central axis projected to the scoring plane and is defined as:

$$R_p = \left[\left(x + \frac{u}{w} (SSD - Z_{\text{split}}) \right)^2 + \left(y + \frac{v}{w} (SSD - Z_{\text{split}}) \right)^2 \right]^{1/2}, \quad (3)$$

where, u, v , and w are the direction cosines; x and y the co-ordinates of the photon at the splitting plane which itself is specified by Z_{split} , and SSD is the

distance from the bottom of source to the scoring plane. Then $f(R_p)$ copies of the photon exiting the source's bottom exit plane are generated and each sampled randomly on a circle, while maintaining the same w direction cosine (along the symmetry axis of the beam). To keep the game fair and preserve the physics, the split particles are assigned reduced weights equal to the reciprocal of the splitting number. Any electron or positron set in motion (inside the photon collimators) by the split photons, is then subject to a roulette game to minimize the time needed to track electrons inside the high-density collimating system. Any bremsstrahlung or annihilation photon generated by the electrons or positrons surviving the roulette game, is split isotropically. If such a photon is not split, it will have an importance weight assigned to it which can be substantially larger than the rest of the photons (which were split). It has been shown that when such a photon reaches the scoring region it will adversely affect the efficiency of the quantities of interest [7].

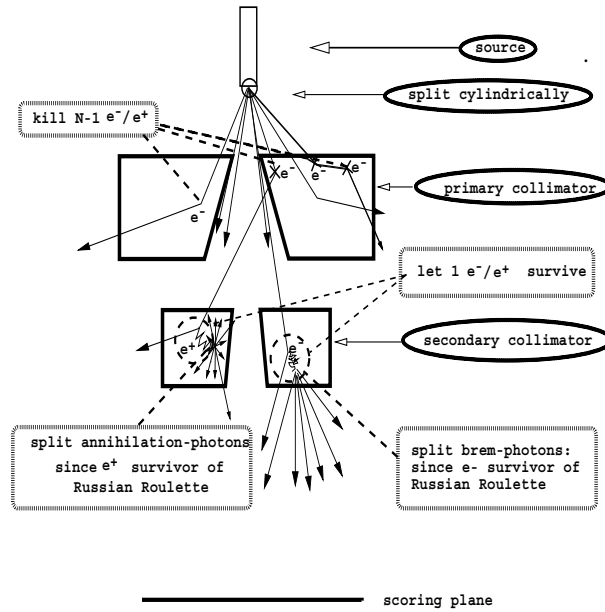


Fig. 2. Schematic showing the splitting of first-generation photons according to (2), the Russian Roulette of secondary electrons, and the splitting of second generation bremsstrahlung, and annihilation photons which is necessary for the success of a photon splitting routine (performed together with Russian Roulette of secondary electrons) as discussed in [7]. The X's denote electrons which have not survived Russian Roulette and therefore have been terminated

The end point used in the assessment of the efficiency using the VRTs developed in this work is the statistical uncertainty of the calculated fluence in the penumbral region of the in-air photon fluence profile at 90 cm from the source.

The calculation of the in-air penumbral width and its associated uncertainty for each source-collimator configuration consists of statistically analyzing 20 photon beam profiles from 20 complete yet independent MC simulations of the teletherapy machine. The independence of these sub-simulations is assured since each one uses a different random number (RN) sequence of the Marsaglia-Zaman [8] RN generator.

The fluence profiles are histogrammed by properly accounting for the weight of all the events in that bin. This means the content of a bin is the sum of the weights of all the entries in that bin. The uncertainty in each bin is equal to the square root of the sum of the squares of the weights in that bin. This is based on Poisson statistics and the assumption that the entries are uncorrelated. All the histograms contain 100 equal-width bins, to provide good resolution. The overall variance assigned to the end-point is estimated as the sum of the variances (square of the uncertainties) of all bins. This ensures a more proper estimate for the variance when the corresponding distribution of the end-point is not flat.

Having estimated the variance of the end-point of interest in a proper fashion, (1) is used to calculate the efficiency.

3 Results

Figure 3 shows the variation of the improvement in efficiency as the various parameters in the splitting recipe are varied. Figure 3a shows an improvement in efficiency of about a factor of 8-9 over the standard BEAM code, for as long as R_f does not substantially exceed the actual field dimensions. Figure 3b shows overall improvements in efficiency of factors between about 10 and 5, when R_w is increased from 1 to 20 cm. Panels c and d in Fig. 3 show the variation of efficiency when N_{\max} is varied from 10 to 200, when N_{\min} is selected as 3 or 10, respectively. The efficiency, generally speaking, increases as N_{\max} is increased, but eventually reaches a plateau.

Results show that the VRT proposed in this work can lead to improvements in efficiency of photon fluence outside the penumbral region of factors up to 20. Typically the improvement in efficiency of fluence in a narrow band inside the field is not more than a factor of 8. The latter is only achievable with a smaller choice of N_{\min} like 3, when $N_{\min} = 10$ is chosen the efficiency of fluence in a band inside the field is not more than a factor of 5.

Figure 4a shows a fluence profile simulation with the standard BEAM code and Fig. 4b shows one using the VRT proposed in this work. Both simulations took about 2400 s CPU time.

4 Summary and Conclusions

The use of the VRTs developed in this work can lead to a 6-9 fold improvement in the efficiency of calculating the penumbral width of the photon fluence profile of a ^{60}Co beam compared to that calculated using the standard optimized BEAM code [1] (*i.e.*, one with a proper selection of electron transport parameters).

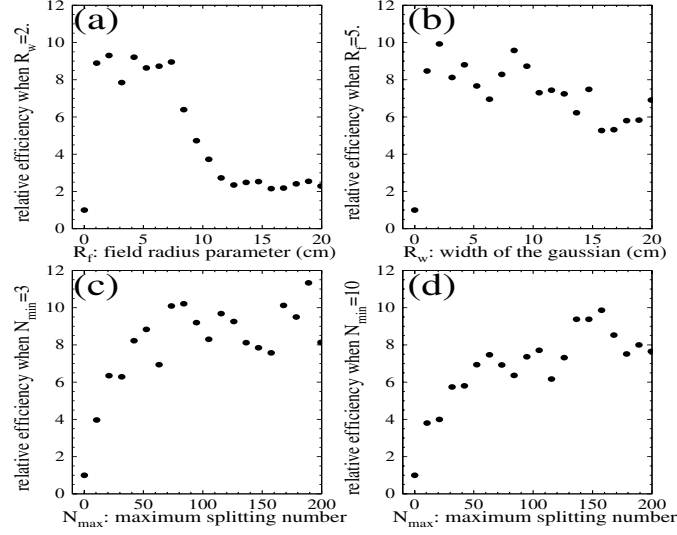


Fig. 3. Optimization of some of the parameters used in (2). The panels show the achievable relative gain in the efficiency of calculating the fluence in the penumbral region using the VRTs proposed in this work, normalized to a calculation performed with the standard BEAM code [1] (see also Fig. 4). When not explicitly specified, the following (or a subset thereof) were used as defaults: $N_{\max} = 180$, $N_{\min} = 10$, $R_f = 5$ cm, and $R_w = 8$ cm (both specified at 100 cm). The field is collimated to a 10×10 cm² field at 100 cm in all the simulations. In all four panels the filled circle corresponding to an abscissa of 0, represents the standard BEAM code

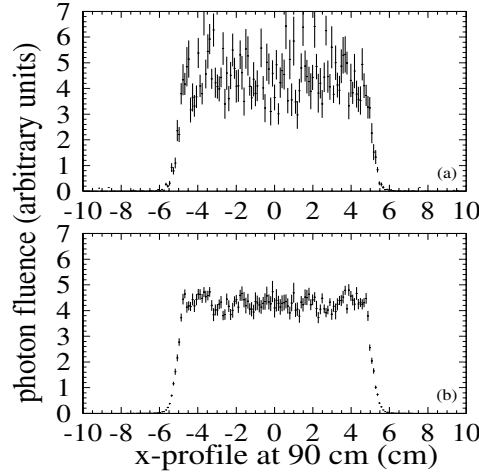


Fig. 4. Photon fluence profiles at 90 cm from the source calculated using equal amount of CPU time. (a) using the standard BEAM code [1], and (b) using the VRT proposed in this work with maximum splitting number of 180, minimum splitting number of 10, 4 cm width for the Gaussian and 5 cm radius assumed for the field. Both simulations took approximately 2400 seconds on a single 500 MHz machine

Splitting second-generation photons together with a proper selection of splitting parameters will ensure uniformity of weights in the photon population and leads to improved efficiency. The design of the splitting routine is such that it leads to an improved efficiency in the case of both on-axis and off-axis fields. One should be aware that VRTs, in general, do not improve the efficiency of all physical quantities in the problem at hand, but only that of a subset.

References

1. D.W.O. Rogers, B.A. Faddegon, G.X. Ding, C.-M. Ma, J.Wei, T.R. Mackie: Med. Phys. **22**, 503 (1995)
2. G.M. Mora, A. Maio, D.W.O. Rogers: Med. Phys. **26**, 2494 (1999)
3. E.J. McGrath, D.C. Irving: *Techniques for Efficient Monte Carlo Simulation*, Vols. I, II, and III. Report ORNL-RSIC-38, Radiation Shielding Information Center, Oak Ridge National Laboratory, Oak Ridge, Tennessee, 1975
4. M.H. Kalos, P.A. Whitlock: *Monte Carlo methods*. Wiley, New York, 1986
5. D.W. Rogers, A.F. Bielajew: 'Monte Carlo techniques of electron and photon transport for radiation dosimetry'. In: *The Dosimetry of Ionizing Radiation*, Vol. III, ed. by K. R. Kase, B. E. Bjarngard, and F. H. Attix (Academic Press, 1990) pp. 427 - 539
6. I. Lux, L. Koblinger: *Monte Carlo particle transport methods: neutron and photon calculations* (CRC Press, New York, 1991)
7. D. Sheikh-Bagheri: *Monte Carlo Study of Photon Beams from Medical Linear Accelerators: Optimization, Benchmark and Spectra*. PhD Thesis (Carleton University, Ottawa, Canada 1998)
8. G. Marsaglia, A. Zaman: Annals of Applied Probability **1**, 462 (1991)

Importance Biasing Quality Criterion Based on Contribution Response Theory

N.M. Borisov¹ and M.P. Panin²

¹ Institut de Protection et de Sûreté Nucléaire, rue Auguste Lemaire, BP 6, Fontenay-aux-Roses, F92265 France

² Moscow Engineering Physics Institute, 31, Kashirskoe Shosse, Moscow, 115314 Russia

Abstract. The report proposes a visual criterion of importance biasing both of forward and adjoint simulation. The similarity of contribution Monte Carlo and importance biasing random collision event distribution is proved. The conservation of total number of random trajectory crossings of surfaces, which separate the source and the detector is proposed as importance biasing quality criterion. The use of this criterion is demonstrated on the example of forward vs. adjoint importance biasing in gamma ray deep penetration problem. The larger amount of published data on forward field characteristics than on adjoint leads to the more accurate approximation of adjoint importance function in comparison to forward, for it adjoint importance simulation is more effective than forward. The proposed criterion indicates it visually, showing the most uniform distribution of random trajectory crossing events for the most effective importance biasing parameters and pointing to the direction of tuning importance biasing parameters.

1 Relations between Contribution Monte Carlo Simulation and Importance Biasing

Importance biasing is a commonly used approach for variance reduction in Monte Carlo calculation. Unfortunately, one can not define the importance function exactly, and that is why there is a risk of wrong estimation of importance function with crucial decrease of calculation efficiency. This paper proposes a visual criterion of importance biasing both of forward and adjoint simulation.

To formulate it, recollect that the importance of forward collisions is adjoint flux-like function, and adjoint collision importance function has the dimension of forward flux [1]. Importance biasing includes implicitly the bilinear combination of forward and adjoint field characteristics. In transport theory there is certain concept of a contribution – a fictitious particle, whose flux is the product of forward and adjoint fluxes [2,3]. The kinetic equation for contribution flux has the following form:

$$\begin{aligned} & \boldsymbol{\Omega} \nabla \Phi(\mathbf{r}, E, \boldsymbol{\Omega}) + \varphi(\mathbf{r}, E, \boldsymbol{\Omega}) \iint \Sigma_s(E, \boldsymbol{\Omega} \rightarrow E', \boldsymbol{\Omega}' | \mathbf{r}) \varphi^+(\mathbf{r}, E', \boldsymbol{\Omega}') dE' d\boldsymbol{\Omega}' = \\ & = \varphi^+(\mathbf{r}, E, \boldsymbol{\Omega}) \iint \Sigma_s(E', \boldsymbol{\Omega}' \rightarrow E, \boldsymbol{\Omega} | \mathbf{r}) \varphi(\mathbf{r}, E', \boldsymbol{\Omega}') dE' d\boldsymbol{\Omega}' + \\ & + \hat{S}(\mathbf{r}, E, \boldsymbol{\Omega}) - \hat{D}(\mathbf{r}, E, \boldsymbol{\Omega}), \end{aligned} \tag{1}$$

where $\Phi = \varphi\varphi^+$, $\hat{S} = \varphi^+S$, $\hat{D} = \varphi D$, and

$$\Theta(E', \boldsymbol{\Omega}' \rightarrow E, \boldsymbol{\Omega}|\mathbf{r}) = \Sigma_s(E', \boldsymbol{\Omega}' \rightarrow E, \boldsymbol{\Omega}|\mathbf{r}) \frac{\varphi^+(\mathbf{r}, E, \boldsymbol{\Omega})}{\varphi^+(\mathbf{r}, E', \boldsymbol{\Omega}')} \quad (2)$$

are contribution flux, source and disappearance densities and differential cross section respectively, while S and D are source density and detector response from unit path length respectively.

Let us determine the relations between importance biasing and contribution simulation both in forward and adjoint case. First we introduce contribution scattering cross section Θ_s as integral from Θ over all the outgoing coordinates, absorption cross section $\Theta_a = D/\varphi^+$ and total cross section $\Theta_t = \Theta_s + \Theta_a$. Then the (1) can be rewritten as:

$$\begin{aligned} \boldsymbol{\Omega} \nabla \Phi(\mathbf{r}, E, \boldsymbol{\Omega}) + \Theta_t(\mathbf{r}, E, \boldsymbol{\Omega}) \Phi(\mathbf{r}, E, \boldsymbol{\Omega}) = \\ = \iint \Theta(E', \boldsymbol{\Omega}' \rightarrow E, \boldsymbol{\Omega}|\mathbf{r}) \Phi(\mathbf{r}, E', \boldsymbol{\Omega}') dE' d\boldsymbol{\Omega}' + \hat{S}(\mathbf{r}, E, \boldsymbol{\Omega}). \end{aligned} \quad (3)$$

This equation can be called “forward contribution transport equation” for all the functions in it are biased proportionally forward importance functions, i. e. adjoint functions:.

To derive the integral equation, convenient for Monte Carlo, we can substitute the flux-like function Φ with incoming $\Psi = \Theta_t \Phi$ and outgoing X contribution collision densities, like in [4,5]. Finally, the integral equation is:

$$\begin{cases} \Psi(\mathbf{r}, E, \boldsymbol{\Omega}) = \int T_c(\mathbf{r}' \rightarrow \mathbf{r}|E, \boldsymbol{\Omega}) X(\mathbf{r}', E, \boldsymbol{\Omega}) d\mathbf{r}' \\ X(\mathbf{r}, E, \boldsymbol{\Omega}) = \iint C_c(E', \boldsymbol{\Omega}' \rightarrow E, \boldsymbol{\Omega}|\mathbf{r}) \Psi(\mathbf{r}, E', \boldsymbol{\Omega}') dE' d\boldsymbol{\Omega}' + \hat{S}(\mathbf{r}, E, \boldsymbol{\Omega}), \end{cases} \quad (4)$$

where

$$T_c(\mathbf{r}' \rightarrow \mathbf{r}|E, \boldsymbol{\Omega}) = \frac{\Theta_t(\mathbf{r}, E, \boldsymbol{\Omega}) \exp(-\tau_c(\mathbf{r}' \rightarrow \mathbf{r}|E, \boldsymbol{\Omega})) \delta\left(\boldsymbol{\Omega} - \frac{\mathbf{r} - \mathbf{r}'}{|\mathbf{r} - \mathbf{r}'|}\right)}{|\mathbf{r} - \mathbf{r}'|^2} - \quad (5)$$

forward contribution transport kernel,

$$\tau_c(\mathbf{r}' \rightarrow \mathbf{r}|E, \boldsymbol{\Omega}) = \int_0^{|\mathbf{r} - \mathbf{r}'|} \Theta_t\left(\mathbf{r}' + \frac{\mathbf{r} - \mathbf{r}'}{|\mathbf{r} - \mathbf{r}'|} R, E, \boldsymbol{\Omega}\right) dR, \quad (6)$$

$$C_c(E', \boldsymbol{\Omega}' \rightarrow E, \boldsymbol{\Omega}|\mathbf{r}) = \frac{\Theta(E', \boldsymbol{\Omega}' \rightarrow E, \boldsymbol{\Omega}|\mathbf{r})}{\Theta_t(\mathbf{r}, E', \boldsymbol{\Omega}')} - \quad (7)$$

forward contribution collision kernel.

Now introduce adjoint contribution scattering cross section, biased proportionally the ratio of forward fluxes (i.e. adjoint importance functions) with the transposition of cross section arguments:

$$\Theta^+(E', \boldsymbol{\Omega}' \rightarrow E, \boldsymbol{\Omega}|\mathbf{r}) = \Sigma_s(E, -\boldsymbol{\Omega} \rightarrow E', -\boldsymbol{\Omega}'|\mathbf{r}) \frac{\varphi(\mathbf{r}, E, -\boldsymbol{\Omega})}{\varphi(\mathbf{r}, E', -\boldsymbol{\Omega}')}, \quad (8)$$

as well as adjoint absorption and total cross sections respectively:

$$\Theta_a^+(\mathbf{r}, E, \boldsymbol{\Omega}) = \frac{S(\mathbf{r}, E, -\boldsymbol{\Omega})}{\varphi(\mathbf{r}, E, -\boldsymbol{\Omega})}, \quad \Theta_t^+ = \Theta_s^+ + \Theta_a^+. \quad (9)$$

The integro-differential adjoint contribution transport equation can be derived from (1):

$$\begin{aligned} & -\boldsymbol{\Omega} \nabla \Phi(\mathbf{r}, E, -\boldsymbol{\Omega}) + \Theta_t^+(\mathbf{r}, E, -\boldsymbol{\Omega}) \Phi(\mathbf{r}, E, \boldsymbol{\Omega}) = \\ & = \iint \Theta^+(E', -\boldsymbol{\Omega}' \rightarrow E, -\boldsymbol{\Omega} | \mathbf{r}) \Phi(\mathbf{r}, E', \boldsymbol{\Omega}') dE' d\boldsymbol{\Omega}' + \hat{D}(\mathbf{r}, E, \boldsymbol{\Omega}). \end{aligned} \quad (10)$$

The integral adjoint contribution equation for incoming and outgoing collision densities, $X^+(\mathbf{r}, E, \boldsymbol{\Omega}) = \Theta_t^+(\mathbf{r}, E, \boldsymbol{\Omega}) \Phi(\mathbf{r}, E, -\boldsymbol{\Omega})$ and Ψ^+ respectively is the following:

$$\begin{cases} X^+(\mathbf{r}, E, \boldsymbol{\Omega}) = \int T_c^+(\mathbf{r}' \rightarrow \mathbf{r} | E, \boldsymbol{\Omega}) \Psi^+(\mathbf{r}', E, \boldsymbol{\Omega}) d\mathbf{r}' \\ \Psi^+(\mathbf{r}, E, \boldsymbol{\Omega}) = \iint C_c^+(E', \boldsymbol{\Omega}' \rightarrow E, \boldsymbol{\Omega} | \mathbf{r}) X^+(\mathbf{r}, E', \boldsymbol{\Omega}') dE' d\boldsymbol{\Omega}' + \hat{D}(\mathbf{r}, E, -\boldsymbol{\Omega}) \end{cases} \quad (11)$$

Here

$$T_c^+(\mathbf{r}' \rightarrow \mathbf{r} | E, \boldsymbol{\Omega}) = \frac{\Theta_t^+(\mathbf{r}, E, \boldsymbol{\Omega}) \exp(-\tau_c^+(\mathbf{r}' \rightarrow \mathbf{r} | E, \boldsymbol{\Omega})) \delta\left(\boldsymbol{\Omega} - \frac{\mathbf{r} - \mathbf{r}'}{|\mathbf{r} - \mathbf{r}'|}\right)}{|\mathbf{r} - \mathbf{r}'|^2} - \quad (12)$$

adjoint contribution transport kernel,

$$\tau_c^+(\mathbf{r}' \rightarrow \mathbf{r} | E, \boldsymbol{\Omega}) = \int_0^{|\mathbf{r} - \mathbf{r}'|} \Theta_t^+\left(\mathbf{r}' + \frac{\mathbf{r} - \mathbf{r}'}{|\mathbf{r} - \mathbf{r}'|} R, E, \boldsymbol{\Omega}\right) dR, \quad (13)$$

$$C_c^+(E', \boldsymbol{\Omega}' \rightarrow E, \boldsymbol{\Omega} | \mathbf{r}) = \frac{\Theta^+(E', \boldsymbol{\Omega}' \rightarrow E, \boldsymbol{\Omega} | \mathbf{r})}{\Theta_t^+(\mathbf{r}, E', \boldsymbol{\Omega}')} - \quad (14)$$

adjoint contribution collision kernel.

During forward contribution transport simulation random trajectories emerge in the source, reach the detector without absorption and terminate in the detector. During adjoint contribution simulation random trajectories start from the detector and terminate in the source. Contribution collision densities have the meaning of contribution to the functional of interest from all the forward (or adjoint respectively) trajectories with the collision in unit phase volume around the certain point, and absolute value of scalar contribution current $|J| = \Phi \cdot |\mathbf{n}, \boldsymbol{\Omega}|$ through the certain surface where \mathbf{n} is normal vector, has the meaning of contribution to the functional from all the trajectories crossing the unit area of this surface in certain direction. with certain energy.

Despite the found in [3] principal difference between importance biasing and contribution Monte Carlo method there is a close genetic relation between each other. One can see that defined in [1] forward and adjoint, respectively, importance biased initial probability densities f_0 and f_0^+ , collision kernels \tilde{C} and \tilde{C}^+ , as well as absorption probability densities f_a and f_a^+ are similar to analogous contribution functions. To prove it, consider:

$$\Theta_t = \Sigma_t \frac{\psi^*}{\chi^*}, \quad f_0 = \frac{\hat{S}}{F}, \quad f_a = \frac{D}{\Theta_t \chi^*} \equiv \frac{D}{\Sigma_t \psi^*}, \quad (15)$$

$$C_c(E', \boldsymbol{\Omega}' \rightarrow E, \boldsymbol{\Omega} | \mathbf{r}) = C(E', \boldsymbol{\Omega}' \rightarrow E, \boldsymbol{\Omega} | \mathbf{r}) \frac{\chi^*(\mathbf{r}, E, \boldsymbol{\Omega})}{\psi^*(\mathbf{r}, E', \boldsymbol{\Omega}')} \equiv \tilde{C}, \quad (16)$$

$$\Theta_t^+ = \Sigma_t \frac{(\chi^+)^*}{(\psi^+)^*}, \quad f_0^+(\mathbf{r}, E, \boldsymbol{\Omega}) = \frac{\hat{D}(\mathbf{r}, E, -\boldsymbol{\Omega})}{F}, \quad (17)$$

$$f_a^+(\mathbf{r}, E, \boldsymbol{\Omega}) = \frac{S(\mathbf{r}, E, -\boldsymbol{\Omega})}{\Theta_t^+(\mathbf{r}, E, \boldsymbol{\Omega})(\psi^+)^*(\mathbf{r}, E, \boldsymbol{\Omega})} \equiv \frac{S(\mathbf{r}, E, -\boldsymbol{\Omega})}{\Sigma_t(\mathbf{r}, E)(\chi^+)^*(\mathbf{r}, E, \boldsymbol{\Omega})}, \quad (18)$$

$$C_c^+(E', \boldsymbol{\Omega}' \rightarrow E, \boldsymbol{\Omega} | \mathbf{r}) = C^+(E', \boldsymbol{\Omega}' \rightarrow E, \boldsymbol{\Omega} | \mathbf{r}) \frac{(\psi^+)^*(\mathbf{r}, E, \boldsymbol{\Omega})}{(\chi^+)^*(\mathbf{r}, E', \boldsymbol{\Omega}')} \equiv \tilde{C}^+, \quad (19)$$

where ψ^* and χ^* are forward incoming and outgoing collision importance, while $(\chi^+)^*$ and $(\psi^+)^*$ are adjoint incoming and outgoing collision importance, and F is the functional of interest (as defined in [1]).

As to contribution T_c and importance biased \tilde{T} transport kernels, one can mention:

$$T_c(\mathbf{r}' \rightarrow \mathbf{r} | E, \boldsymbol{\Omega}) = \tilde{T}(\mathbf{r}' \rightarrow \mathbf{r} | E, \boldsymbol{\Omega}) \frac{\chi^*(\mathbf{r}', E, \boldsymbol{\Omega})}{\chi^*(\mathbf{r}, E, \boldsymbol{\Omega})} \times \quad (20)$$

$$\times \exp \left(\int_0^{|\mathbf{r}-\mathbf{r}'|} \Sigma_t(\mathbf{r}' + R\boldsymbol{\Omega}, E) \left(1 - \frac{\psi^*(\mathbf{r}' + R\boldsymbol{\Omega}, E, \boldsymbol{\Omega})}{\chi^*(\mathbf{r}' + R\boldsymbol{\Omega}, E, \boldsymbol{\Omega})} \right) dR \right). \quad (21)$$

Taking into account the following relation between outgoing and incoming collision importance functions:

$$-\boldsymbol{\Omega} \nabla \chi^*(\mathbf{r}, E, \boldsymbol{\Omega}) + \Sigma_t(\mathbf{r}, E) \chi^*(\mathbf{r}, E, \boldsymbol{\Omega}) = \Sigma_t(\mathbf{r}, E) \psi^*(\mathbf{r}, E, \boldsymbol{\Omega}), \quad (22)$$

and substituting the variables in the previous integral, it is possible to see that $T_c \equiv \tilde{T}$. In the same manner one can also obtain, that $T_c^+ \equiv \tilde{T}^+$.

Thus, we see that ideal importance biasing produces the same phase states as ideal contribution simulation both for forward and adjoint cases. It allows the use of contribution response theory conclusions for evaluation of real importance biasing “quality”. Contribution response theory is known to contain the theorem of total contribution current J conservation through all the surfaces separating the source and the detector. With this conservation, we should organize importance biasing to keep invariant total number of events, when random trajectory crosses these surfaces.

2 Example of Importance Biasing Criterion Application

We demonstrated the use of importance biasing quality criterion on gamma ray deep penetration problem, described in [1]. We considered a gamma-emitting source in the infinite atmosphere, which size is negligible in comparison with the distance to the detector. In such simple geometry the buildup factor concept can be used for importance function estimation. We calculated air absorbed dose in point of detection as the functional of interest. For transport calculation Compton scattering and photoelectric absorption were taken into account.

We compared the efficiency of forward and adjoint importance simulation for this problem. The importance of forward collisions is related to adjoint flux, of adjoint collisions – to forward flux. The larger amount of published data on forward functions rather than adjoint makes the estimation of adjoint importance function more accurate and adjoint importance simulation – more effective. It was demonstrated both by the comparison of FOM and the proposed contribution quality criterion.

The Tab. 1 shows data on dose buildup factor with the standard deviation σ of point isotropic monoenergetic (0.5 MeV) source and detector at the distance of 10 mean free path for different lower thresholds of weight window W .

Table 1. Comparison of dose buildup factor for different importance biasing parameters

Method	W	B_d	$\sigma, \%$	Relative FOM
Forward	10^{-5}	54	6	0.37
— —	10^{-3}	55	5	1.0
— —	10^{-2}	66	12	0.34
Adjoint	10^{-6}	63	5	5.8
— —	10^{-3}	61	8	2.3
Data of [6]	—	60.6	—	

The Fig. 1 shows the distribution of random trajectory crossing events with the planes perpendicular to the axis “source-detector” for forward and adjoint importance biasing. For forward simulation the distance x is counted from the source, for adjoint $(\tau - x)$ – from the detector. The phase state distribution indicates that in our scheme weight window is an essential tuner of importance biasing, which is able to affect crucially the distribution of phase states. Taken by itself, variance reduction methods are powerful but “blind” tools, and their optimization is not trivial. Our quality criterion allows to visualize the similarity of real and ideal variance reduction parameters. The best results were achieved where the crossing distribution is maximally uniform and reaches the plateau after several mean free paths from the source (in adjoint case – from the detector).

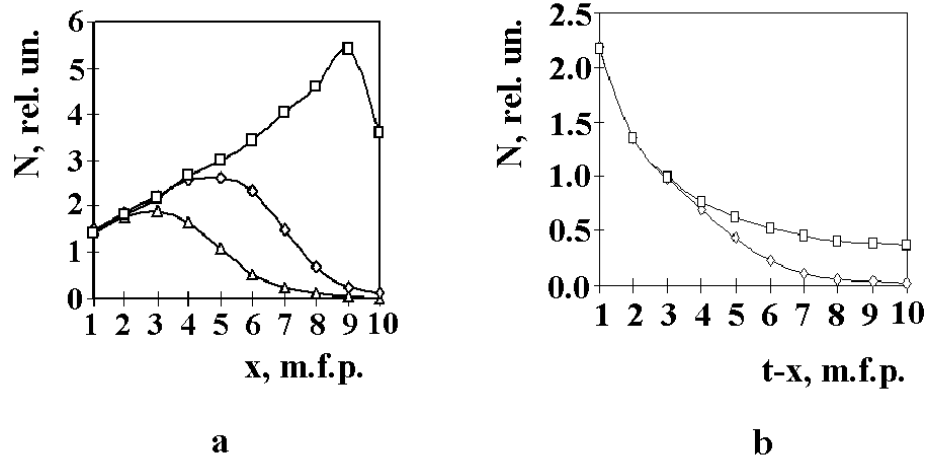


Fig. 1. Distribution of crossing events for forward (a): $\square - W = 10^{-5}$, $\diamond - W = 10^{-3}$, $\triangle - W = 10^{-2}$ and adjoint (b): $\square - W = 10^{-6}$, $\diamond - W = 10^{-3}$ importance biasing

References

1. N.M. Borisov, M.P. Panin: Monte Carlo Meth. and Applic. **3**, 241 (1997)
2. M.L. Williams: Nucl. Sci. and Eng. **108**, 355 (1991)
3. C.H. Aboughantous: Nucl. Sci. and Eng. **118**, 160 (1994)
4. D.C. Irving: Nucl. Eng. and Design **15**, 273 (1971)
5. N.M. Borisov, M.P. Panin: Monte Carlo Meth. and Applic. **4**, 341 (1998)
6. A.B. Chilton, C.M. Eisenhauer, G.L. Simmons: Nucl. Sci. and Eng. **73**, 97 (1980)

Calculations of Electron Deep Penetration Using the Method of Trajectory Rotation

V. Moskvina¹, L. Papiež¹, T. Tabata², and I.J. Das³

¹ Department of Radiation Oncology, Indiana University, Indianapolis, USA

² IDEA, Osaka, Japan

³ University of Pennsylvania, Philadelphia, USA

Abstract. The method of trajectory rotation (Lazurik and Moskvina, Nucl. Instr. and Meth. **B134**, 1998, p. 1-12) has been modified for calculations of deep penetration of electron beams through thick targets. The new algorithm obtained is presented together with its efficiency evaluated for calculations of the average energy of electrons transmitted through thick targets. The appearance of artifacts in calculations of the above problem by conventional binary-encounter Monte Carlo techniques is discussed.

1 Introduction

For semi-empirical modeling of electron depth-dose curves, the knowledge on the average energies of transmitted electrons and transmission coefficients for different target materials is essential [1]. The same knowledge is also important in the measurement and use of electron beams. However, poor statistics in conventional Monte Carlo calculations for deep penetration of electron beams produce unsatisfactory results. For example, the general purpose Monte Carlo codes using the binary-encounter technique yield average energies of transmitted electrons with strange behavior or artifacts in deep regions of a target (see Fig. 1).

To decrease such effects one may combine the use of symmetry in uniform media and information contained in trajectories to improve the efficiency of evaluation by Monte Carlo codes. One specific technique of this type is the Method of Trajectory Rotation (MTR). The MTR uses induced correlations between contribution of a given trajectory of a particle at various depths in a target [2]. We have tried to modify the MTR to calculations of deep penetration of electron beams in thick targets. The present paper describes the algorithm of the modified MTR and results on its efficiency for calculations of the average energy of transmitted electrons as a function of the depth in thick targets. The reasons for the appearance of artifacts in calculations of electron deep penetration by conventional Monte Carlo methods is discussed.

2 Modified Method of Trajectory Rotation

The MTR relies on rotational and translational symmetry of a uniform medium. A set of trajectories is created by rotation of the part of the trajectory around the direction of electron movement at some arbitrary point of the track. We

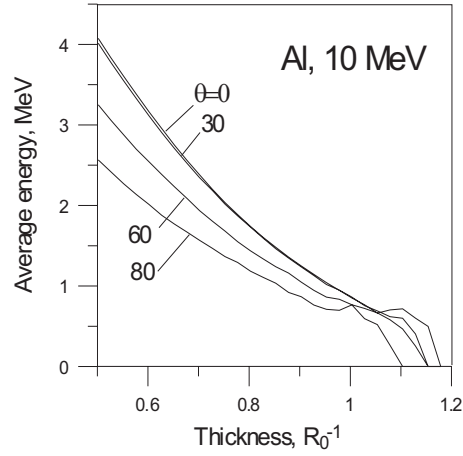


Fig. 1. Strange behaviour of average energy of electrons as a function of target thickness at deep penetration

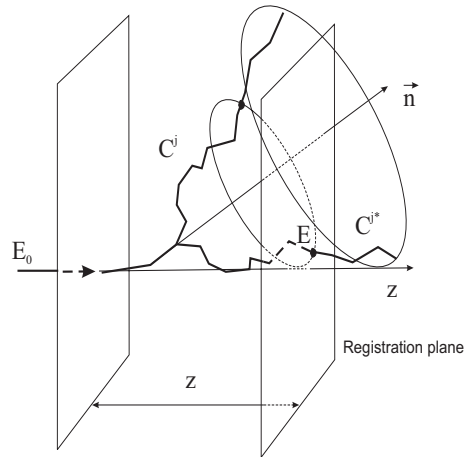


Fig. 2. Method of trajectory rotation

used this set of trajectories to evaluate the weight of the contribution by a given trajectory to average energy E_{av} at depth z (we set axis z to be normal to a target). The algorithm of the MTR works as follows.

1. An electron trajectory C^j is simulated in an infinite medium from initial energy E_0 to the cut-off energy E_c and stored in memory as a set of (x_i, y_i, z_i, E_i) , where i is the index of the trajectory steps.
2. The trajectory C^j is placed in a set of thick targets D (see Fig. 2).
3. The point of the trajectory where the electron has a given energy E_r is a rotation point. The direction of the electron motion at this point is considered

as a rotation axis. Note that any value can be taken for E_r except E_0 and E_c . We have chosen $E_r = 0.9E_0$ based on the discussion presented in [2].

4. The part of the trajectory C^j , where electron has the energy $E < E_r$ is selected. A set of trajectories is created by rotating this part of the base trajectory around the rotation axis.

5. The deeper region of the target is considered. If the indicator of rotation (see below) $\zeta^j(E, z)$ for a given depth z and energy E on the trajectory equals 1, then go to 4'; if $\zeta^j(E, z)$ equals 0 it is necessary to consider another z and E .

6. A weight factor of the trajectory C^j in scoring the spectrum of electrons transmitted through the target of thickness z is calculated (see [2]) as

$$W_S^j(E; z) = \frac{1}{2\pi} \left(\frac{d\varphi}{dE} \right)_E \zeta^j(E, z) \sum_{m=1}^2 |\gamma^m| \xi^{j,m}(E) \quad (1)$$

where

$$\left(\frac{d\varphi}{dE} \right)_E = \left(\frac{d\varphi}{dz} \right) \frac{|\gamma^m|}{\left(\frac{dE}{dl} \right)_E} \quad (2)$$

and ϕ is the rotation angle, γ^m is the directional cosine relative to z-axis (normally directed to a target), $(dE/dl)_E$ is a linear stopping power of electron with an energy E .

$(d\varphi/dz)$ is given in an analytical form as

$$\left(\frac{d\varphi}{dz} \right) = \frac{1}{\sqrt{(R_E^2 - (\mathbf{R}_E, \mathbf{n}_\varphi)^2)(1 - \gamma_r)^2 - (z - (z_r + \gamma_r(\mathbf{R}_E, \mathbf{n}_\varphi)))^2}}, \quad (3)$$

where z_r is the z -coordinate of the rotation point (i.e. the trajectory point with the energy E_r); \mathbf{R}_E is the radius-vector from the rotation point to the point of a trajectory where an electron has energy E ; \mathbf{n}_φ is the rotational axis defined by the direction $\boldsymbol{\Omega}_r = (\alpha_r, \beta_r, \gamma_r)$ of electron motion in the rotation point; $(\mathbf{R}_E, \mathbf{n}_\varphi)$ is the dot product of \mathbf{R}_E and \mathbf{n}_φ .

The binary indicator of rotation $\zeta^j(E, z)$ determines the intersection of a given trajectory created by rotation of the basic trajectory with a set of trajectories that produce contributions to a spectrum of transmitted electrons. $\xi^{j,m}(E)$ is the binary region indicator which determines boundary conditions for a given trajectory created by rotation.

The indicator of rotation $\zeta^j(E)$ can be written as

$$\zeta^j(E, z) = \begin{cases} 1, & \text{if } ((R_E^2 - (\mathbf{R}_E, \mathbf{n}_\varphi)^2)(1 - \gamma_r)^2 - (z - (z_r + \gamma_r(\mathbf{R}_E, \mathbf{n}_\varphi)))^2) \geq 0 \\ 0, & \text{in other case} \end{cases} \quad (4)$$

7. The average energy E_{av} of transmitted electrons is calculated as the average of the transmitted electron spectrum:

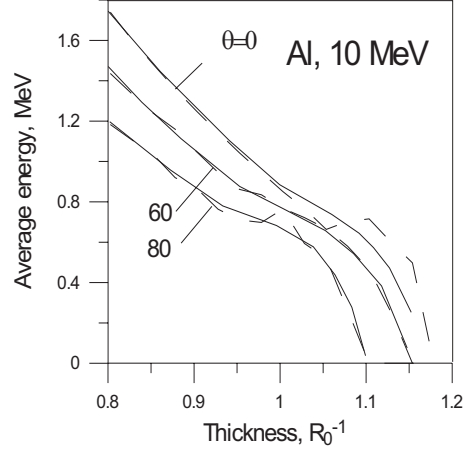


Fig. 3. Average energy of electrons transmitted through thick targets vs. thickness of the target. Solid lines, MTR; dashed lines, conventional Monte Carlo technique

$$E_{av} = \frac{1}{N} \int_0^{E_0} E \sum_{j=1}^N W_S^j(E; z) dE \quad (5)$$

MTR has been tested in calculations of electron range straggling distribution and spectrum near the target surface (see [2]).

3 Results of Calculations

The algorithm described above was implemented in a FORTRAN subroutine and integrated with PENELOPE code [3], and the efficiency of the usage of the MTR was evaluated.

A set of calculations of average energy for thick targets shows the high efficiency of the MTR in providing data for deep penetration of electrons. The amount of primary MTR trajectories that are needed to reach the same statistics as conventional Monte Carlo method can be reduced by a factor of 50 for depths of the order of one CSDA (continuous slowing down approximation) range R_0 of electrons. The use of the MTR increases the time for one trajectory processing by about a factor of 2; thus the efficiency of the MRT is about a factor of 25 in comparison to the conventional Monte Carlo technique.

The reason for such an efficiency increase is that when using the MRT, we create an additional set of trajectories that may also reaches deeper regions in a target. The artificiality of these trajectories is weighted by the weight factor given by (1).

We compared data on average energy E_{av} of electrons penetrating thick targets calculated by the use of PENELOPE in conventional binary Monte Carlo

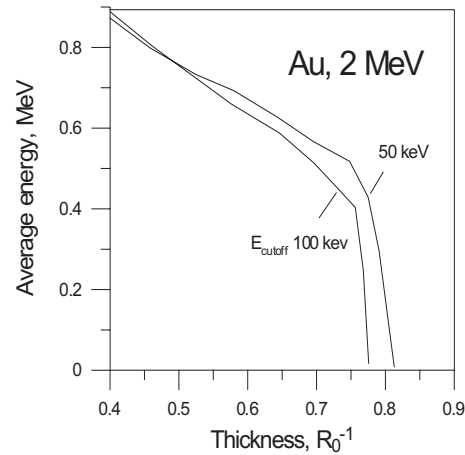


Fig. 4. Average energy of electrons transmitted through thick targets vs. thickness of the target calculated with 100 keV and 50 keV cutoff energies

mode with the data provided by the MTR technique. Figure 3 shows how much the statistical uncertainty of the results can be reduced by the MTR technique (solid lines). The data given by the dashed line are the results of conventional calculations that has been presented in [1]. The number of primary electrons has been 100,000 in the calculation by the conventional Monte Carlo method, while it has been 5,000 with the application of the MTR.

The behaviour of the curve describing the dependence of E_{av} on target thickness at deep penetration is determined by the range struggling of electrons. The slope of this curve becomes steeper at a large thickness, but this is an artifact associated with the energy cutoff used as a set-up parameter of the Monte Carlo simulation. The cut-off energy of 100 keV was used in the present calculations. The decrease of the cut-off value from 100 keV to 50 keV leads to a slight shift of the position of the change of the slope (see Fig. 4). Ideally the dependence of average energy on target thickness should be studied with a cut-off energy comparable to the energy of electron thermalisation in solids. The use of a low cut-off energy increases the computation time, so that the application of the MTR would also be effective in reducing the artifact of the type described above as well as the artifact due to statistical fluctuations.

References

1. T. Tabata, V. Moskvina: 'Transmission Coefficients and Residual Energies of Electrons: PENELOPE Results and Empirical Formulas', *Third International Workshop on Electron and Photon Transport Theory Applied to Radiation Dose Calculation*, Indianapolis, Indiana, August 8–12, (1999)
2. V. Lazurik, V. Moskvina: Nucl. Instr. and Meth. **B 134**, 1 (1998)

3. F. Salvat, J.M. Fernández-Varea, J. Baró, and J. Sempau: *PENELOPE, an algorithm and computer code for Monte Carlo simulation of electron-photon showers*. Informes Tecnicos CIEMAT n. 799, CIEMAT, Madrid, June, (1996)

The Impact of Monte Carlo Dose Calculations on Intensity-Modulated Radiation Therapy

J.V. Siebers, P.J. Keall, and R. Mohan

Medical College of Virginia, Virginia Commonwealth University, USA

Abstract. The effect of dose calculation accuracy for IMRT was studied by comparing different dose calculation algorithms. A head and neck IMRT plan was optimized using a superposition dose calculation algorithm. Dose was re-computed for the optimized plan using both Monte Carlo and pencil beam dose calculation algorithms to generate patient and phantom dose distributions. Tumor control probabilities (*TCP*) and normal tissue complication probabilities (*NTCP*) were computed to estimate the plan outcome. For the treatment plan studied, Monte Carlo best reproduces phantom dose measurements, the *TCP* was slightly lower than the superposition and pencil beam results, and the *NTCP* values differed little.

1 Introduction

The ultimate success of intensity modulated radiation therapy (IMRT) may rest in the accuracy of dose calculation. While Monte Carlo dose calculation algorithms are recognized as the most accurate way of computing patient dose [1], they are currently considered too time consuming to be used for iterative IMRT dose calculations. Monte Carlo, however, may be the only method that can accurately account for the leakage radiation (transmission plus scatter) from the multi-leaf collimator (MLC) which contributes substantially to the total dose at low intensity levels.

Most implementations of IMRT use fast pencil beam or superposition dose calculation algorithms to optimize the beam intensities. Differences between pencil beam computations and measurements are well documented for static field treatments, and differences with respect to superposition calculations have recently been studied [2]. Similar differences may exist for IMRT treatments. In addition to the dose calculation error, evidence exists that use of an inaccurate dose calculation in the IMRT optimization process results in the IMRT plan converging to a plan that differs from that which would be developed using the most accurate dose calculation algorithm [3]. This so-called convergence error obscures the optimal solution. An obvious method to correct this situation is to use more accurate dose calculation methods for dose computation during the optimization process, such as Monte Carlo.

The aim of the current work was to compare dose distributions for an IMRT plan computed with the pencil beam, a superposition/convolution (SC), and a Monte Carlo algorithms so as to ascertain the dose error introduced by using inaccurate dose computation algorithms.

2 Method

An IMRT treatment plan for a head and neck cancer patient was optimized using our in-house IMRT program [4]. The IMRT case study was performed for a 61 year old male with a stage T2N2bM0 squamous cell carcinoma of the right palate. The intent was to deliver 68 Gy in 30 fractions to the gross tumor volume (GTV), with the left parotid, cord, and larynx specified as critical structures. Although dose was scored for the right parotid, it was not restricted. A dose-volume based objective function was minimized. The superposition/convolution dose calculation algorithm used during the iterative optimization process was the collapsed cone convolution (CCC) from Pinnacle¹. The optimized plan was recalculated using both Monte Carlo and a pencil beam algorithm to evaluate the effect of the dose calculation algorithm on the optimized dose distribution. The Monte Carlo code used was MCV, an EGS4 [5] based Monte Carlo system that uses the EGS user codes BEAM [6] and DOSXYZ [7], which we have directly coupled to the Pinnacle treatment planning system. Photon transport through the dynamically moving multi-leaf collimator (MLC) was incorporated into the Monte Carlo algorithm by reducing photon weights by the probability of transmission through the MLC [8]. For each beam, the Monte Carlo statistical uncertainty was 2% (1σ) at the depth of maximum dose. The pencil beam is that developed by Mohan [9], which we have modified to integrate into the Pinnacle treatment planning system. All of the dose calculation algorithms predict the dose per monitor unit in the patient, thus, absolute dose values are compared.

The treatment plans were analyzed both by visual examination of isodose distributions and the dose volume histograms, and by calculating tumor control probability (*TCP*) and normal tissue complication probability (*NTCP*). The *TCP* was calculated using

$$TCP = 0.5^{exp\left[\frac{2\gamma_{50}}{\ln 2}\left(1 - \frac{EUD}{D_{50}}\right)\right]} \quad (1)$$

with a γ_{50} value (the percent increase in *TCP* per percent increase in dose at *TCP* = 50%) of 3.0 [10]. The equivalent uniform dose (*EUD*) was calculated from

$$EUD = 2 \cdot \frac{\ln \left[\frac{1}{V} \sum_i v_i SF_2^{\frac{D_i}{2}} \right]}{\ln SF_2} \quad (2)$$

V is the volume composed of elements v_i , and SF_2 , the surviving fraction of cells after irradiation of 2 Gy, was set to 0.5. Equation (1) can be derived from Niemierko [11].

The *NTCP* was calculated using the Lyman model [12]. The volume dependence parameter, slope of the complication probability vs. dose parameter and the dose to the whole organ which would lead to a complication probability of 50% values were tabulated in Burman et al. [13], based on data taken from Emami et al. [14].

¹ ADAC Laboratories, Milpitas, CA USA

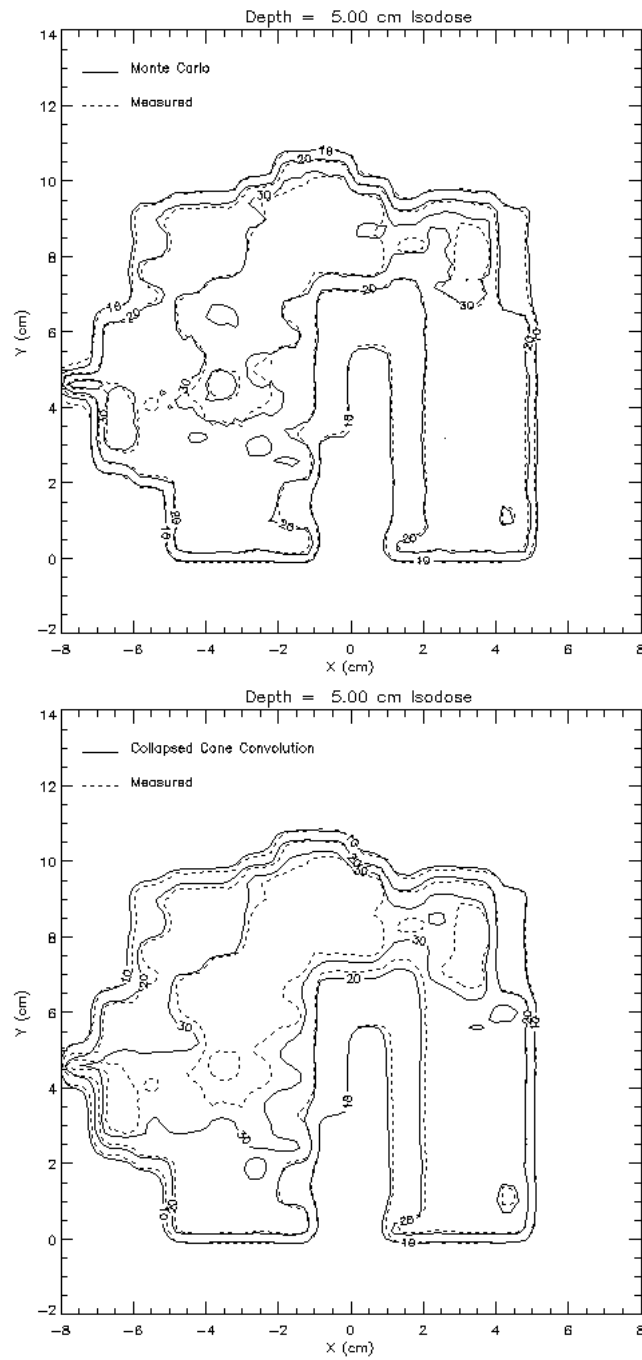


Fig. 1. Isodose comparisons with measurement (film) at 5 cm depth in a water phantom. (a) (top) Monte Carlo, (b) (bottom) Superposition/Convolution

To compare computed dose distributions with measurements, the patient was replaced with a flat water phantom and the dose calculations were repeated. Dose measurements were made at 5 cm depth using film. Film optical density results were converted to dose using calibration films exposed and developed in the same session as the field measurement films.

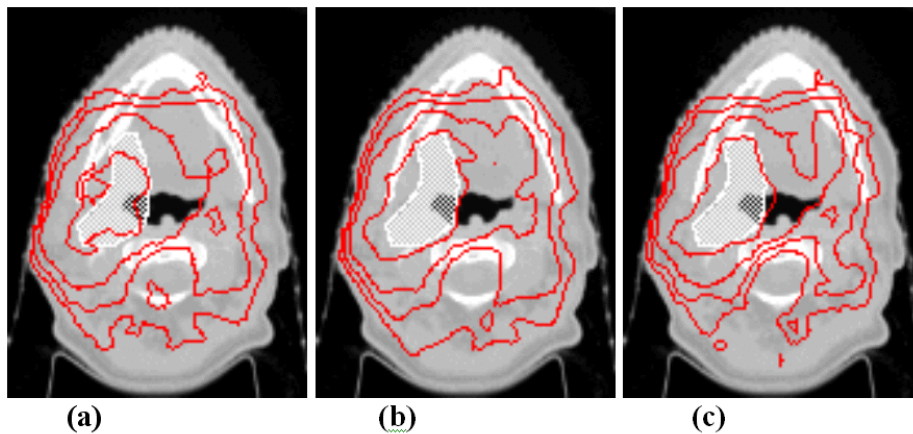


Fig. 2. Isodose plans calculated using (a) Monte Carlo, (b) Superposition and (c) Pencil Beam. The shaded area is the GTV. The isodose levels are 40, 50, 60 and 70 Gy

3 Results

Figure 1 compares the measured isodose distributions with those computed using Monte Carlo and SC algorithms for one of the patient's IMRT beams incident upon a flat water phantom. The pencil-beam results (not shown) are nearly identical to the SC results in the homogeneous phantom. While both algorithms predict the general shapes of the isodose distributions, the Monte Carlo better reproduces the fine-structure of the isodose profiles.

Figure 2 compares isodose distributions on one slice of the treatment plan for all beams computed using the three dose algorithms. Predicted target (shaded on figure) coverage by the dose algorithm varies substantially. Dose-volume histograms (DVHs) for the target, cord and left parotid are shown in Fig. 3. Within the target all three calculation algorithms yield DVHs that agree to within 2%. However, due to the lack of accounting for lateral scatter, the pencil beam algorithm significantly underpredicts the dose to the left parotid and spinal cord.

Table 1 summarizes the *TCP* and *NTCP* values computed for the patient plan. The *TCP* calculations yield a maximum difference of 4% in *TCP* prediction by the three algorithms, and a maximum difference of 3% for *NTCP*.

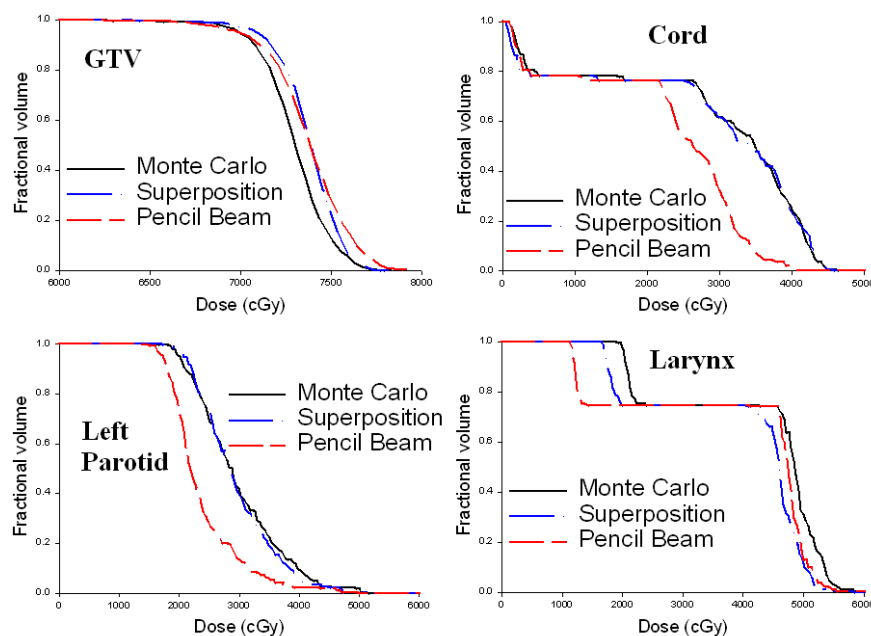


Fig. 3. Dose Volume Histogram comparison for the GTV, cord, left parotid and larynx

Table 1. *TCP* and *NTCP* values for an IMRT plan as calculated by Monte Carlo, superposition and pencil beam dose calculation algorithms

Tissue Type	Dose Calculation Algorithm		
	Monte Carlo	Superposition	Pencil Beam
<i>TCP</i> of GTV	86%	90%	89%
<i>NTCP</i> Cord	1%	1%	0%
<i>NTCP</i> Right Parotid	92%	95%	95%
<i>NTCP</i> Left Parotid	2%	3%	0%
<i>NTCP</i> Larynx	4%	3%	3%

4 Conclusions

Monte Carlo IMRT dose calculations reproduce film dosimetry measurement results more accurately than the superposition and pencil beam calculations.

For the head and neck cancer treatment plan evaluated, the three dose calculation algorithms predicted different patient outcomes (*TCP* and *NTCP*). It is anticipated that when the different algorithms are used for the dose calculation during optimization process, different intensity patterns (and different dose distributions) will result.

5 Acknowledgements

This work is supported by the grants CA74043 and CA74158 from the National Cancer Institute.

References

1. R. Mohan: 'Why Monte Carlo?', presented at the XII International Conference on the Use of Computers in Radiotherapy, Salt Lake City, Utah (1997)
2. P.J. Keall, J.V. Siebers, R. Mohan: 'The impact of Monte Carlo dose calculations on treatment outcomes', presented at the XIII International Conference on the Use of Computers in Radiation Therapy, Heidelberg, Germany (2000)
3. R. Jeraj, P.J. Keall: 'Errors in inverse treatment planning based on inaccurate dose calculation', presented at the XIII International Conference on the Use of Computers in Radiation Therapy, Heidelberg, Germany (2000)
4. Q. Wu, R. Mohan: *Med. Phys.* **27**, 701 (2000)
5. W.R. Nelson, H. Hirayama, D.W.O. Rogers: *The EGS4 Code System*, Report No. SLAC-265, Stanford Linear Accelerator Center (1985)
6. D.W.O. Rogers, B.A. Faddegon, G.X. Ding, C.M. Ma, J. We, T.R. Mackie: *Med. Phys.* **22**, 503 (1995)
7. C.-M. Ma, P. Reckwerdt, M. Holmes, D.W.O. Rogers, B. Geiser, B. Walters: *DOSXYZ users manual*, Report No. PIRS-0509b, National Research Council of Canada (1995)
8. J.V. Siebers, P.J. Keall, M. Arnfield, J.O. Kim, R. Mohan: 'Dynamic-MLC modeling for Monte Carlo dose calculations', presented at the XIII International Conference on the Use of Computers in Radiation Therapy, Heidelberg, Germany (2000)
9. R. Mohan, C.S. Chui: *Medical Physics* **14**, 70 (1987)
10. J.E. Munzenrider, A.P. Brown, J.C.H. Chu, L.R. Coia, K.P. Doppke, B. Emami, G.J. Kutcher, R. Mohan, J.A. Purdy, B. Shank, J.R. Simpson, L.J. Solin, M.M. Urie: *Int J. of Radiation Oncology, Biology and Physics* **21**, 147 (1991)
11. A. Niemierko: 'Treatment Evaluation'. In *Teletherapy: Present and Future*, ed. by T.R. Mackie and J.R. Palta (Madison, WI: Advanced Medical Publishing 1996)
12. J.T. Lyman: *Radiation Research* **104**, S13 (1985)
13. C. Burman, G.J. Kutcher, B. Emami, M. Goitein: *Int J. of Radiation Oncology, Biology and Physics* **21** 123 (1991)
14. B. Emami, J. Lyman, A. Brown, L. Coia, M. Goitein, J.E. Munzenrider, B. Shank, L.J. Solin, M. Wesson: *Int. J. of Radiation Oncology, Biology and Physics* **21**, 109 (1991)

PC-Based Process Distribution to Solve Iterative Monte Carlo Simulations in Physical Dosimetry

A. Leal^{1,3}, F. Sánchez-Doblado^{1,2}, M. Perucha¹, M. Rincón¹, R. Arrans², C. Bernal³, and E. Carrasco¹

¹ Dpto. Fisiología y Física Médica. Fac. Medicina. Univ. Sevilla, Spain

² Serv. Oncología Radioterápica. H.U.V.M. Sevilla, Spain

³ C.I.C.A. Sevilla, Spain

Abstract. A distribution model to simulate physical dosimetry measurements with Monte Carlo (MC) techniques has been developed. This approach is indicated to solve the simulations where there are continuous changes of measurement conditions (and hence of the input parameters) such as a TPR curve or the estimation of the resolution limit of an optical densitometer in the case of small field profiles. As a comparison, a high resolution scan for narrow beams with no iterative process is presented.

The model has been installed on a network PCs without any resident software. The only requirement for these PCs has been a small and temporal Linux partition in the hard disks and to be connecting by the net with our server PC.

1 Introduction

Some Monte Carlo (MC) simulations are tedious due to the need of a continuous change of the input parameters. While for a Percentage Depth Dose (PDD) curve the dose deposition along the central axis can be obtained with a single simulation [1], this is not the case in those curves where the Source to Surface Distance (SSD) is not constant, such as the Tissue Phantom Ratio (TPR). The process distribution could be then especially indicated for these cases. To share the work out, our approach uses a set of PCs connected to the network without the need of any software installation in the *clients*.

This work presents the resolution of two specific physical situations: the measurement of TPR curve above mentioned and the simulation of an optical densitometer for either very small fields or step gradient dose regions. Films are considered to be one of the dosimeters with highest spatial resolution. However, this detector has to be evaluated by means of a reader which has some intrinsic limitations. The restriction values provided by the manufacturer are not reliable, due to the complex geometrical relationship between the light emitter and the reader. We have prepared a tool which simulates an optical densitometer by an iterative process consisting of a moving voxel array. The physical resolution is obtained by varying the voxel size until a match with the empirical result is achieved. Therefore, the corresponding voxel size can be considered as the actual resolution limit on the detector. In this sense, we have developed the software to distribute the different process involved in this physical situation. This approach is entirely dissimilar to the one customarily used to obtain a profile with MC

in which, a fixed voxel array is considered. For comparison, both situations are presented.

2 Materials and Methods

The code used for the simulation has been *EGS4* [2,3], integrated in the *OMEGA-BEAM* package [4,5]. This code has the possibility of distributing the processes through a queue manager (*NQS*) [6,7]. This option would require the installation of the code in all the machines. With our method, however, no resident software is necessary. The Operating System and simulation code, as well as the data files and distribution scripts, are exported by the network from another PC, acting as a server. The server machine is a Pentium III, 500 MHz and 256 Mbytes RAM with an Ultra Wide hard disk SCSI of 9 Gb connected to the network via 3 Com Fast Ethernet XL 10/100 Mbytes card. Only a small *LINUX* partition (300 Mbytes hard disk) is necessary in each PC client in order to make a temporal file while the simulation is carried on. A floppy disk with a minor kernel was designed in order to boot the client PCs from the server connected to the net. No boot sector of the local disks was therefore needed. Making the remote boot of the system in the client nodes is based on two reasons: The high number of machines and the fact that they do not have to be exclusively dedicated for MC calculations. This way, administration from the server is easier. With the collaboration of the Engineering School of the University of Seville, a prototype was mounted with 36 client PCs connected with our server. These PCs are Pentium II with 64 Mbytes RAM of memory. The area of the server disk, which contains the simulation code, is exported by *NFS* (Network File System). Each machine participates only with its processor and physical memory. The orders are executed by means of the *rsh* (remote shell) command on each client. When the simulation finishes, nothing is left in the client hard disks.

The beam distribution was made by means of a task manager written with the *awk* tool within a *Bourne-shell script*. The initial parameters are modified as the processes are distributed among the PC nodes according to a defined sequence. The script “reads” the input parameters through a friendly graphical interface designed with *tcl/tk*.

2.1 TPR Curve Simulation

For simulating TPR curves (see Fig. 1), the distribution of the processes was made writing a *script* of *shell*, which modifies the input file parameters (the SSD and detector depth) to send a different task to each machine connected to network. As the processes are ending, the cumulative dose in the voxel corresponding to the isocentre is stored in the server for every simulated situation and performed by each CPU. Consequently, the TPR function can be obtained straight forward.

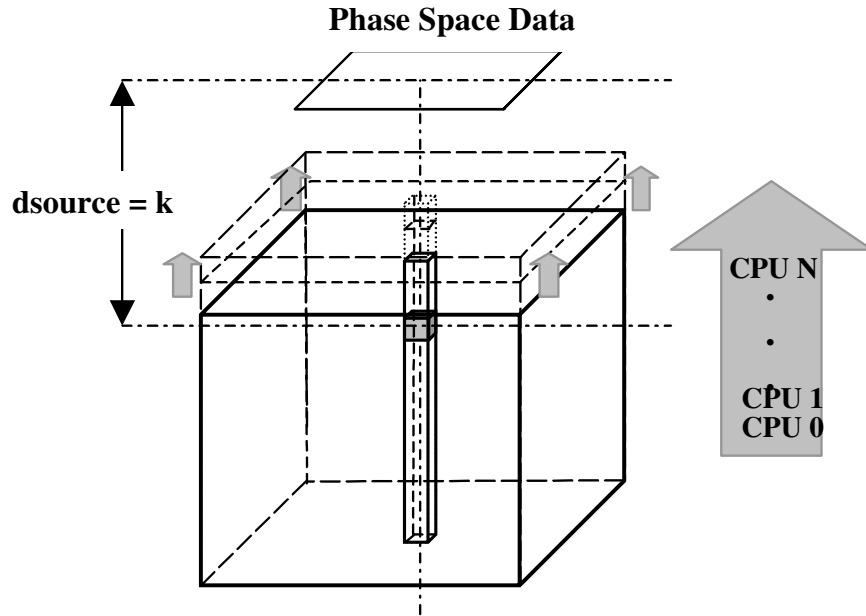


Fig. 1. Each PC simulates the phantom in a different position along the beam axis. The distance from the Phase Space Data (PSD) to the isocentre remains constant. The voxel where the dose is delivered remains always at the same position (isocentre) but at a different depth

2.2 Profile Curve Simulation

To obtain an accurate profile of a small field or the exact shape of the penumbra, a detector with a good resolution is necessary. To reproduce this physical situation, phantoms with very small voxels can be simulated with MC. This implies more histories to maintain the statistical uncertainty with an associated increasing of CPU task. Reasonable times can be achieved by distributing the total number of particles between the available machines. The chosen special resolution was 1 mm while the total number of particles was 2×10^8 .

2.3 Optical Densitometer Simulation

To obtain this high resolution, film dosimetry is commonly used, even though MC calculation (taken as a reference) may differ, in some special case where a high definition is required (see Fig. 2). This is due to the fact that the resolution of the optical densitometer is larger than that of the film. To assess the precision limits, scans with different reader sizes have been simulated by varying the voxel dimensions until a match with the empirical results is achieved. The simulation is designed so that the movement of detector is taken into account.

A task manager program was developed which modifies the input parameters for the simulation assigning different voxel position to each PC (see Fig. 3). To optimise the calculation time, the number of voxels considered along the profile is taken as a function of the scanning length and the resolution chosen. To simulate the continuous scan, intermediate positions have to be considered.

The number of processes depends on the accuracy required, the number of points of the profile curve and the number of available machines. In our case, two arrays with 9 voxels (having 0.36 cm and 0.50 cm, respectively) were chosen with a number of steps of 4 for a field size of 3 mm in diameter. The number of CPU assigned to each step was 9, as a result of the total number of machines (36) divided by the number of steps (4).

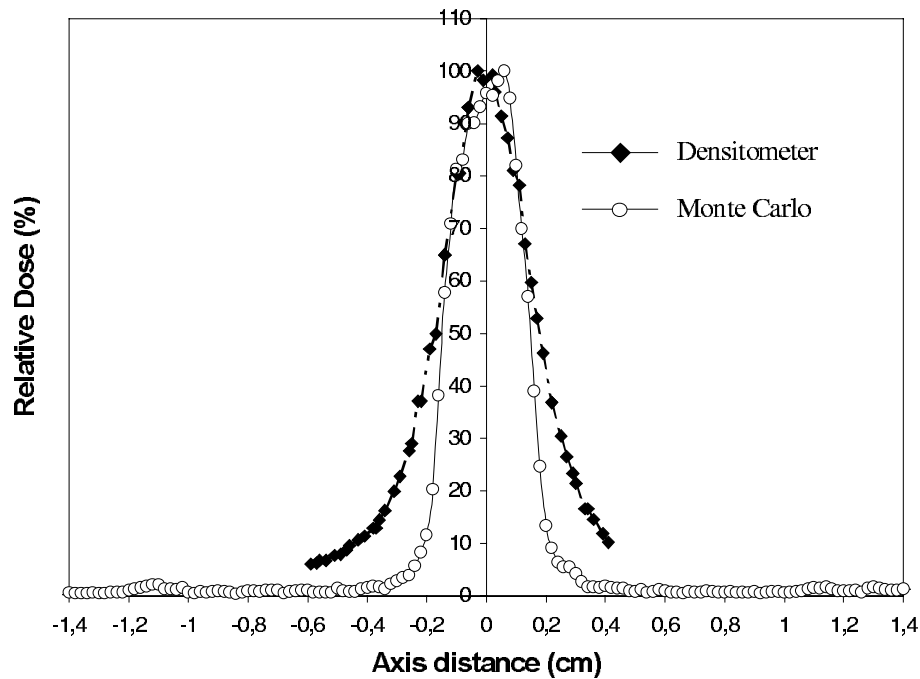


Fig. 2. Comparison between profiles of a 3 mm in diameter field size obtained with a conventional film densitometer and with MC using a voxel width of 0.2 mm

3 Results

CPU times obtained for the calculation of TPR and the simulation of an optical densitometer, as well as profile curves are shown in Tab. 1. The considered CPU time corresponds to the processor that took the longest from the 36 PCs available. Notice the relationship between CPU time, number of machines and histories.

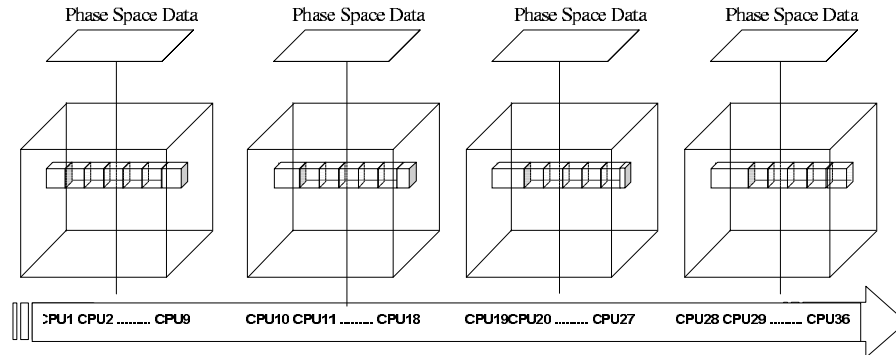


Fig. 3. Every group of PCs simulates the phantom with the array of voxels in a different position along the profile until one voxel size is reached. Each PC in the group simulates (1/Number of PC) of the total histories for that position

Table 1. CPU time spent to simulate a) TPR curve, b) fix high resolution profile and c) profiles with an optical densitometer

Curve	Voxel size	Histories	CPU time
a) TPR	0.20 cm <i>z-voxel</i>	1×10^8 / CPU	41 min. 22 s
b) Profile	0.10 cm <i>x-voxel</i>	2.0×10^8 / 36CPU	6 min. 22 s
c) Profile	0.36 cm <i>x-voxel</i>	3.6×10^7 / 6CPU	8 min. 58 s
c) Profile	0.50 cm <i>x-voxel</i>	3.6×10^7 / 6CPU	8 min. 05 s

z-voxel: boundary voxel in the beam axis; *x-voxel*: boundary voxel in the profile direction

4 Conclusions

A distribution model for the simulation of dosimetric curves has been developed. This approach is especially useful when dealing with processes in which the physical situation varies and therefore, they can be emulated by a series of simulations with different input data. The model has been implemented for two clinical cases: TPR curves and a optical densitometer simulation.

Furthermore, this model has been performed by using a set of PCs connected to the network, with no need of software installation. This prototype is affordable, allowing the PC clients their normal use, when the simulation code is not running.

References

1. C-M. Ma, E. Mok, A. Kapur, T. Pawlicki, D. Findley, S. Brain, K. Forster, A.L. Boyer: Med. Phys. **26**, 10 (1999)
2. A.F. Bielajew: *How to manage the EGS4 system* (National Research Council of Canada report PIRS-0391, Ottawa 1993)
3. A.F. Bielajew: *Running EGS4 on different architectures* (National Research Council of Canada report PIRS-0392, Ottawa 1993)
4. C-M. Ma, S.B. Jiang: Phys. Med. Biol. **44** (1988)
5. D.W.O. Rogers, B.A. Faddegon, G.X. Ding, C-M. Ma, J. We: Med. Phys. **22**, 5 (1995)
6. D.W.O. Rogers, C-M. Ma, B. Walters, G.X. Ding, D. Sheikh-Bagheri, G. Zhang: *BEAM Users Manual* (NRCC report PIRS-0509B(revC), Ottawa 1998)
7. C-M. Ma, P. Reckwerdt, M. Holmes, D.W.O. Rogers, B. Geiser, B. Walters: *DOSXYZ Users Manual* (NRCC report PIRS-0509B(revC), Ottawa 1998)

Inverse Treatment Planning for Radiation Therapy Based on Fast Monte Carlo Dose Calculation

M. Fippel¹, M. Alber¹, M. Birkner¹, W. Laub¹, F. Nüsslin¹, and I. Kawrakow²

¹ Radiologische Universitätsklinik Tübingen, Germany

² Institute for National Measurement Standards Ottawa, Canada

Abstract. An inverse treatment planning system based on fast Monte Carlo (MC) dose calculation is presented. It allows optimisation of intensity modulated dose distributions in 15 to 60 minutes on present day personal computers. If a multi-processor machine is available, parallel simulation of particle histories is also possible, leading to further calculation time reductions. The optimisation process is divided into two stages. The first stage results in fluence profiles based on pencil beam (PB) dose calculation. The second stage starts with MC verification and post-optimisation of the PB dose and fluence distributions.

Because of the potential to accurately model beam modifiers, MC based inverse planning systems are able to optimise compensator thicknesses and leaf trajectories instead of intensity profiles only. The corresponding techniques, whose implementation is the subject for future work, are also presented here.

1 Introduction

Inverse or optimised treatment planning becomes more and more important especially for intensity modulated radiation therapy (IMRT). Iterative optimisation algorithms provide primary fluence profiles based on given treatment objectives (motivated by physical [1] and/or biological assumptions [2]) and dose calculation methods. Monte Carlo (MC) dose calculation [3] will be the preference in future because of the potential to accurately model treatment machines as well as photon and electron transport in heterogeneous human tissue [4–6]. Computation time will be irrelevant in future because of the rapidly increasing CPU speed and the development of optimised MC codes designed for the material and energy range of radiation therapy, e.g. the X-ray Voxel Monte Carlo [7–9] (XVMC) algorithm. XVMC is coded in C++ and allows parallel computation of particle histories on multiple processor units. Special combinations of variance reduction techniques like photon splitting, electron history repetition and Russian Roulette allow the calculation of dose distributions within minutes or seconds for photon respectively electron beams.

For the present investigation the XVMC code has been integrated into “Hyperion” [10], an IMRT planning system based on constrained biological optimisation and a gradient method to calculate the primary fluence updates. The treatment planning starts with the definition of critical organ structures and corresponding maximum damages measured by an effective dose. The implemented

optimisation algorithm tries to maximise the dose (or damage) in the tumor volume by retaining the organ constraints, which can be changed by the user during the planning process.

2 Monte Carlo Optimisation Procedure

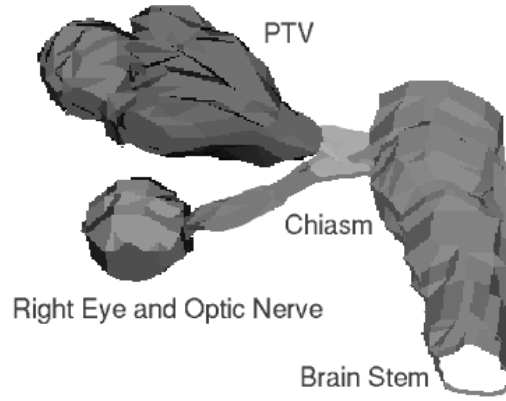


Fig. 1. Beam's eye view of one of the four 6 MV photon beams to irradiate a optical nerve carcinoma. PTV means planning target volume and denotes the tumor region

The first IMRT optimisation stage employs a finite size pencil beam (PB) algorithm for calculating the dose distribution and the objective function derivatives with respect to the primary fluence elements. The second stage starts with MC verification ($D_{MC}^0(\mathbf{r})$) of the PB dose distribution ($D_{PB}(\mathbf{r})$). Differences between $D_{MC}^0(\mathbf{r})$ and $D_{PB}(\mathbf{r})$ are subject to further optimisation, but this time employing XVMC for dose calculation. To obtain the fluence updates for the next iteration step we have to know the dose contribution $T(i, \mathbf{r})$ of each beam element i . In principle, it is possible to compute these values also by Monte Carlo. However, the function $T(i, \mathbf{r})$ is frequently used and the storage and calculation time requirements are huge. Therefore, to differentiate the objective function we still use $T_{PB}(i, \mathbf{r})$ of the PB algorithm. The convergence of this approach is still unproven, but it could be shown that there are problem dependent (heterogeneity of the treatment volume, beam parameters, objective function) convergence conditions [6].

During each iteration step the fluence updates are transformed into corresponding initial particles with positive or negative statistical weights. Positive weight particles increase and negative weight particles decrease the dose along their trajectory. This procedure corrects the dose distribution $D_{MC}^k(\mathbf{r})$ of the previous step k due to the fluence of the present step. Additionally, the statistical fluctuations are smaller for the new distribution $D_{MC}^{k+1}(\mathbf{r})$. The optimisation ends if the objective function changes are smaller than a user provided value.

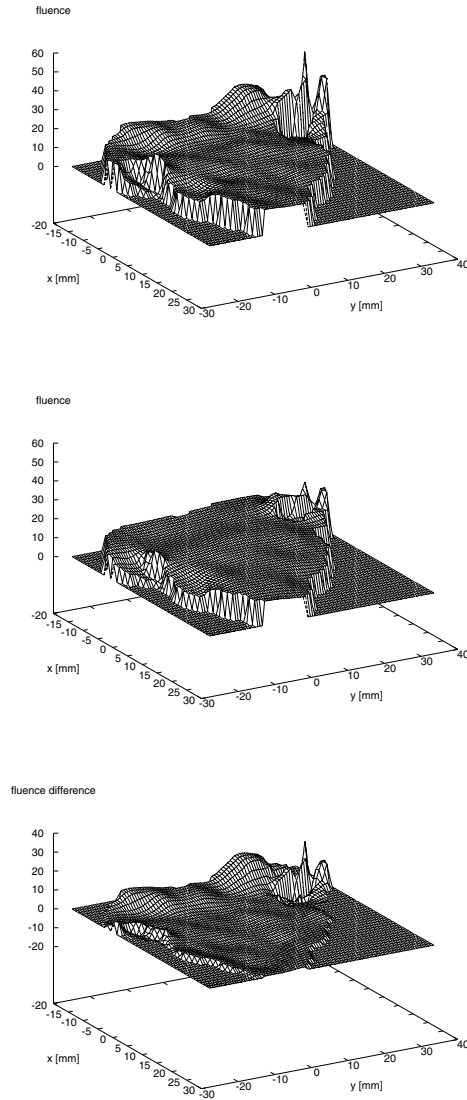


Fig. 2. The intensity profile of the beam from Fig. 1 after PB and MC optimisation (upper plot), PB optimisation only (central plot) and the difference between both distributions (lower plot)

As an example we simulated the treatment of a carcinoma near the right eye and optical nerve. In this region we find large density variations (soft tissue, bone, air). Therefore, the quality of dose calculation will have significant influence on

the resulting intensity profiles. For the treatment of this patient four beams of 6 MV photon energy have been arranged with different directions. Figure 1 shows one beam’s eye view of the tumor (PTV = planning target volume) and the critical structures. In Fig. 2 the fluence profiles of this beam after optimisation with Monte Carlo (upper plot) and pencil beam dose calculation (central plot) are represented. The lower plot shows the fluence difference between the MC and PB profiles which are in the order of 50% especially in the third quadrant. There, the MC algorithm has to compensate for lateral electron scatter by increasing the primary photon fluence. A pencil beam algorithm, however, is not able to model electron transport correctly. Therefore, the corresponding profile is too flat.

3 Beam Modifiers

Beam modifiers like multi-leaf collimators (MLC) or compensators can be integrated directly into the optimisation procedure and to the MC simulation by retaining the fluence update approach. In the following we will explain the corresponding techniques, which will be implemented into “Hyperion”.

3.1 Compensators

Intensity modulated beams can be generated by inserting a compensator into the beam line. Generally, a compensator is a block of lead with varying thickness d leading to variable attenuation and photon fluence. Usually, the result of “conventional” IMRT planning systems are fluence profiles. After finishing the iteration procedure, these profiles are converted into compensator shapes. However, the compensator produces additional photon scatter and electron contamination, which should be taken into account by the optimisation process. Only Monte Carlo algorithms are able to model compensators correctly. Therefore, MC based IMRT planning systems should optimise compensator shape and thickness rather than fluence profiles.

Assume that after the iteration k the compensator thickness at a definite location is $d^k(x, y)$ (x and y denote the coordinates within the compensator system). After the next iteration ($k + 1$) the compensator thickness changes to $d^{k+1}(x, y)$, which can be larger, smaller, or equal to $d^k(x, y)$. A photon hitting the compensator may be absorbed by the compensator material or it survives with or without scattering. This depends on the sampled free photon path length. Furthermore, Compton, pair and photo electrons (positrons) and additional bremsstrahlung photons can be produced. To calculate the dose update for iteration $k + 1$, we perform the following steps repeatedly, if $d^k(x, y)$ and $d^{k+1}(x, y)$ differ for the given beam element:

- Take an initial photon from the fluence distribution above the compensator.
- For $d^k(x, y)$ and $d^{k+1}(x, y)$ sample the particle states behind the compensator using identical random numbers.

- If the states are identical, do nothing.
- If the states are different, simulate the first photon history (k) in the patient volume using a negative weight and the second photon history ($k + 1$) using a positive weight.
- The corresponding history simulation is unnecessary, if one of the photons is absorbed by the compensator completely, i.e. also the secondary particles of this history are absorbed.
- Take the next photon from the fluence distribution above the compensator, etc.

Secondary electrons produced within the compensator can be rejected if their energy is too small to reach the patient surface (range rejection). On the other hand, electrons arising from the compensator's bottom side must be simulated because of their additional patient dose contribution (electron contamination).

3.2 Dynamic Multi Leaf Collimators

An alternative method to deliver intensity modulated beam profiles in radiation therapy is the use of dynamic multi-leaf collimators (DMLC). The Monte Carlo implementation of DMLCs is comparable to the compensator case. If the positions are given by a set of time dependent functions $x_l(t)$ (l denotes the leaf number and x stands for all geometrical parameters necessary to model the leaf position), continuous leaf motion can be simulated by choosing the time t randomly from a uniform distribution. Therefore, the IMRT planning system should be able to find the optimum by iterating a sequence of leaf trajectories $x_l^k(t)$ similar to the sequence of compensator thicknesses $d^k(x, y)$ (see Sec. 3.1).

4 Conclusion

The new system allows MC optimisation of IMRT dose distributions in 15 to 60 minutes on present day personal computers. If a multi-processor machine is available, the calculation time can be reduced further. Therefore, it is a practical tool improving the treatment of cancer. Especially for the modelling of beam modifiers (compensators, MLC) and in regions with large density variations (lung, head and neck) the benefit of MC algorithms compared to conventional dose determination is indispensable.

References

1. A. Brahme, J. E. Roos, I. Lax: Phys. Med. Biol. **27**, 1221 (1982)
2. M. Alber, F. Nüsslin: Phys. Med. Biol. **44**, 479 (1999)
3. W. R. Nelson, H. Hirayama, D. W. O. Rogers: *The EGS4 code system*, SLAC Report **265** (1985)
4. R. Jeraj, P. Keall: Phys. Med. Biol. **44**, 1885 (1999)
5. L. Bogner, J. Scherer, M. Herbst: Physica Medica **15**, 111 (1999)

6. W. Laub, M. Alber, M. Birkner, F. Nüsslin: Phys. Med. Biol. **45**, 1741 (2000)
7. I. Kawrakow, M. Fippel, K. Friedrich: Med. Phys. **23**, 445 (1996)
8. M. Fippel: Med. Phys. **26**, 1466 (1999)
9. I. Kawrakow, M. Fippel: Phys. Med. Biol. **45**, 2163 (2000)
10. M. Alber, M. Birkner, W. Laub, F. Nüsslin: 'Hyperion: An integrated IMRT planning tool'. In Proc.: *13th International Conference on the Use of Computers in Radiation Therapy, Heidelberg, Germany, May 23-26, 2000* ed. by W. Schlegel and T. Bortfeld (Springer-Verlag Berlin Heidelberg New York) pp. 46-48

Macro Monte Carlo: Clinical Implementation in a Distributed Computing Environment

H. Neuenschwander¹, W. Volken², D. Frei², C. Cris², E. Born², and R. Mini²

¹ Radio-Oncology Dept., Lindenhof Hospital, Bremgartenstr. 117, CH-3001 Bern, Switzerland,

² Div. of Medical Radiation Physics, Clinic for Radio-Oncology, Inselspital, CH-3010 Bern, Switzerland

1 Introduction

The Monte Carlo (MC) method is the most accurate method for the calculation of dose distributions in radiotherapy treatment planning (RTP) for high energy electron beams, if the source of electrons and the patient geometry can be accurately modeled and a sufficiently large number of electron histories are simulated. Due to the long calculation times, MC methods have long been considered as impractical for clinical use. Two main advances have improved the situation and made clinical MC RTP feasible: The development of highly specialized radiotherapy MC systems, and the ever-falling price/performance ratio of computer hardware. Moreover, MC dose calculation codes can easily be parallelized, which allows their implementation as distributed computing systems in networked departments. This paper describes the implementation and clinical validation of the Macro Monte Carlo (MMC) method, a fast method for clinical electron beam treatment planning.

2 Methods

A Monte Carlo (MC) dose calculation system for radiotherapy treatment planning purposes consists of two essential parts: A beam model describing the particles emerging from a medical accelerator treatment head and an algorithm for the transport of these particles through a patient geometry. The MMC code system consists of the scaled multiple source beam model (SMSM) and the Macro Monte Carlo (MMC) dose calculation engine.

2.1 Beam Model

MC codes can only predict clinical dose distributions accurately if the initial phase space of particles (electrons and photons) emerging from a medical linear accelerator is known in detail. For electron beams, there are approaches to determine this phase space directly from measurements [1] or from Monte Carlo simulations of the linear accelerator treatment head [2].

For the clinical implementation of MMC, a hybrid beam model was developed. For a certain type of linear accelerator (eg. Varian high-energy Clinac)

detailed simulations of particle transport through the treatment head are performed using the BEAM code system. As the number of particles required for an accurate patient dose calculation is of the order of 10^7 , the resulting raw phase space files for all combinations of accelerators, energies and electron applicators encountered in a typical clinic would be unfeasibly large. Therefore, the BEAMDP utility [3] is applied to the raw phase space data to extract the parameters of several predefined particle sources. The final result of the BEAM simulation is a ‘reference set’ of multiple source models of all energy/electron applicator combinations of a certain accelerator type. As an example, the MSM of a Varian high energy Clinac consists of 6 sources: A point source for direct electrons, a planar ‘square ring’ source for electrons scattering at the X-ray jaws, 3 planar ‘square ring’ sources for electrons scattering at the applicator scrapers, and a point source for contaminating photons. Actual clinical beams of accelerators of the same type as the reference machine are obtained by scaling the reference MSM to the clinical beam based on a small set of measurements (SMSM [4]). Individual metallic inserts to shape the electron beam are taken into account by partly blocking the phase space and adding an additional, scatter kernel based line source to the MSM.

2.2 Transport Model

The MMC method [5,6] has been developed to increase the speed of traditional MC methods to make MC feasible for electron beam RTP. MMC is an example of a Local-To-Global (LTG) transport scheme [7,8], which consists of two steps: In the first step, conventional MC simulations (single scatter or condensed history) of electron transport are performed in a well defined ‘local’ geometry. The result of these ‘local’ calculations is a library of probability distribution functions (PDF) of particles emerging from the ‘local’ geometry. These PDFs are calculated only once for a variety of relevant materials and energies and represent the combined effect of many individual collisions of the electron. The second step in LTG MC consists of an absorber-specific ‘global’ MC calculation. Electrons are transported in ‘macroscopic’ steps through the absorber, with the particle parameters after each step sampled from the PDFs generated in the ‘local’ calculations. For the ‘local’ calculations MMC uses the EGS4 code system [9] to transport electrons through spherical or ellipsoidal volume elements. The ‘global’ calculation is performed on a 3D rectangular grid based on computer-tomographic patient data. The adaptive step-size algorithm used in MMC allows to take large, efficient steps through homogeneous parts of the patient and to reduce step sizes to maintain the accuracy of the transport near significant material boundaries. The concept of MMC is illustrated in Fig. 1 for a spherical ‘local’ geometry element (‘kugel’). Although not shown in Fig. 1, the MMC algorithm takes into account the production and transport of secondary electrons and bremsstrahlung photons and the transport of contaminating photons contained in the electron beam of a medical linear accelerator.

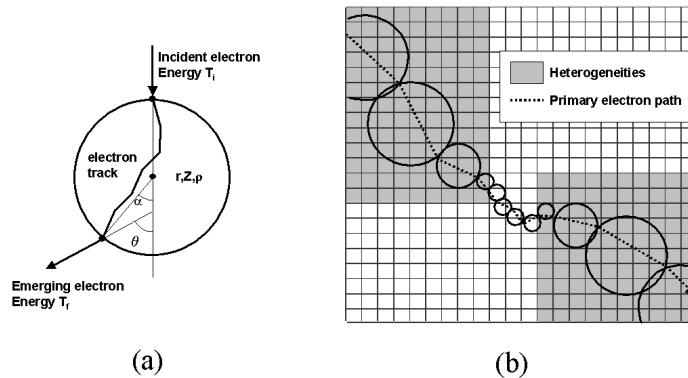


Fig. 1. Illustration of the MMC concept. (a) Local calculation (b) Global calculation

2.3 Implementation

Besides being available as a stand-alone application, the MMC code system has been implemented as a dose calculation server in a commercial treatment planning system. In clinical MMC treatment planning, the user has the choice of an ‘accurate’ and a ‘fast’ dose calculation mode by specifying the target accuracy and the resolution of the requested results. The ‘fast mode’ is especially useful in the initial beam setup and optimizing stage of treatment planning, because it allows the user to get a good overview of the resulting dose distribution in a matter of seconds. The high speed in the MMC ‘fast mode’ is obtained by reducing the number of histories at the expense of an increased statistical uncertainty. This flexibility is an exclusive feature of MC codes.

It has been shown previously that the MMC code can be easily parallelized and implemented on parallel hardware [10] with a speedup depending on the number of processing nodes. In the present work, a parallel version of the MMC code system has been developed and implemented in a distributed computing environment using the PVM (parallel virtual machine) software package [11]. This parallel version is based on a master/slave model. The PVM master processor receives the patient data from the dose planning front-end and distributes it to the slaves over the network using the PVM communication facilities. All slaves then start independent MMC dose calculations and regularly report their calculation status back to the master. An essential feature in the design of the MMC/PVM implementation is the fact, that an automatic dynamic load balancing on the different processing nodes is guaranteed.

3 Results

3.1 Clinical Validation

During the validation process, the MMC system was tested in various experimental set-ups, similar to the work of the NCI (National Cancer Institute) collabo-

rative working group on electron beam RTP [12]. The experimental conditions were aimed at reproducing realistic clinical situations. Therefore absorbers of different complexity, from homogeneous water to highly heterogeneous situations, were designed. The beam energies chosen for the tests span the range of energies encountered in clinical routine. Corresponding MMC and pencil beam dose calculations were performed and the resulting dose distributions were compared with the measured data. Whenever necessary, EGS4 calculations were also performed and the results were used as benchmarks for MMC dose distributions. As an example, Fig. 2 shows profiles measured and calculated at various depths in a water phantom with an irregular surface ('nose phantom', cf. [12]). Discrepancies near the edges of the field are mainly due to uncertainties in the experimental setup. The validation process has shown that in terms of accuracy MMC performs better than conventional pencil beam algorithms. Results of MMC calculations with the SMSM beam description are in good agreement with measurements, both for homogeneous and heterogeneous phantom setups.

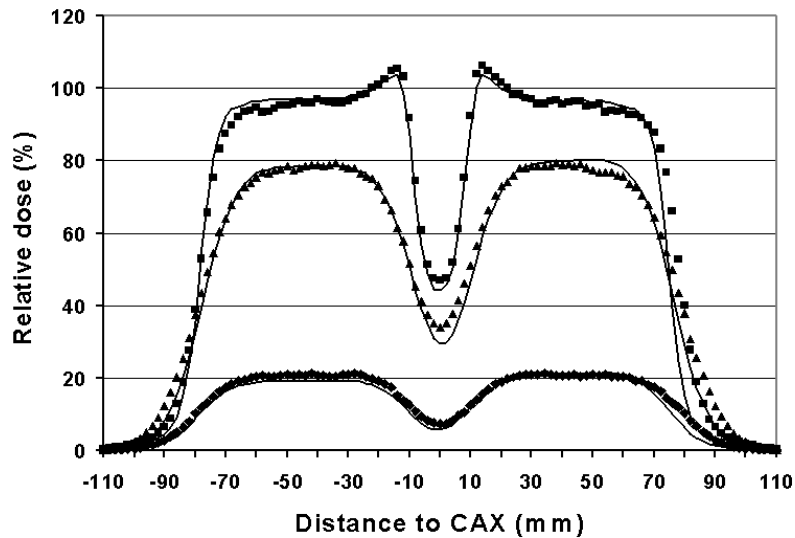


Fig. 2. Experimental validation of the MMC code system. 9 MeV, 15 cm x 15 cm electron beam on a 'nose phantom'. Statistical uncertainty of MMC results 1.5%. Measurements (*lines*) vs. MMC calculation (*symbols*). Profiles at depths of 1.7 cm (*squares*), 3.2 cm (*triangles*) and 4.2 cm (*diamonds*)

3.2 Speed

To obtain results with a statistical uncertainty of about 1.5% standard deviation for typical clinical situations, it is necessary to simulate 10^6 - 10^7 electron histories.

On an Intel Pentium III Xeon Processor (500 MHz), an MMC simulation in homogeneous water runs at a rate of 12'000 10 MeV electron histories/sec. MMC volume calculation times are therefore of the order of 1-20 minutes per beam in the 'accurate mode' and as low as a few seconds in the 'fast mode'.

For the present study, up to 11 workstations in a typical networked radio-oncology department have been linked together in a 'star-topology' on one network segment as a virtual parallel computer. The results of a timing study with up to 8 equally powerful PCs (Pentium III, 350 MHz, 100 Mbit/s network interface) are summarized in Tab. 1 and Fig. 3. The maximum speedup that can be obtained mainly depends on the communication overhead in the chosen topology of processing nodes. Because of this overhead, the optimal number of nodes for a simulation with 10^6 histories is already reached at 6 nodes, whereas for the calculation of 10^7 histories the speedup is almost linear up to 8 nodes. Network traffic can be optimized with processing nodes running on separate segments of the network. Moreover, in future 1'000 Mbit/s networks network traffic time will be reduced accordingly, making distributed computing efficient also for simulations of a small number of histories.

Table 1. Network traffic time and total simulation time for distributed MMC simulations of 10 MeV electrons on N processing nodes. CT-Grid 256 x 256 x 30, dose grid 128 x 128 x 30

<i>N</i>	<i>Network</i> (<i>sec</i>)	<i>10⁶histories</i>		<i>10⁷histories</i>	
		<i>Total</i> (<i>sec</i>)	<i>Network</i> (%)	<i>Total</i> (<i>sec</i>)	<i>Network</i> (%)
1	0.0	130.4	0.0	1304	0.0
2	6.3	71.3	8.9	656	1.0
4	10.0	43.0	23.4	340	3.0
6	14.4	36.4	39.5	234	6.1
8	22.0	38.5	57.1	187	11.8

4 Conclusions

The MMC code system is a fast MC calculation system for electron beam RTP. For clinical purposes, MMC calculation times are feasible and the accuracy of MMC results sufficient. In terms of accuracy, speed and flexibility, the MMC system is superior to traditional pencil beam algorithms. The inherent parallel character of the MC method allows an easy implementation of the MMC code system in a distributed computing environment. By linking them together as a virtual parallel machine, idle computing resources in a radio-oncology department can thus be put to good use.

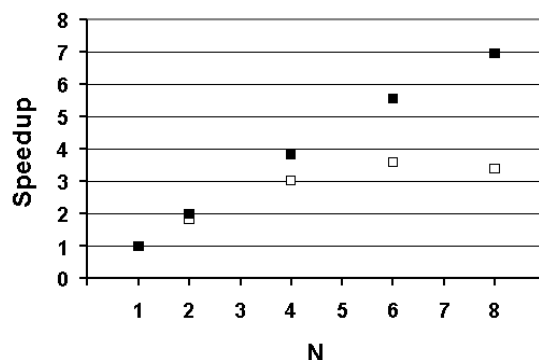


Fig. 3. Speedup of a distributed MMC simulation as a function of the number N of processing nodes. 10^7 histories (*full squares*) and 10^6 histories (*empty squares*)

5 Acknowledgements

Part of this work has been financially supported by the Swiss KTI (projects 3023.1 (EUREKA 1326), 3680.1 (EUREKA 1734)) and Varian Oncology Systems.

References

1. J.J. Janssen, E.W. Korevaar, L.J. van Battum, P.R.M. Storchi, H. Huizenga: Proc. XIIth ICCR (Salt Lake City, USA), p. 195 (1997)
2. D.W.O. Rogers, B.A. Faddegon, G.X. Ding, C.M. Ma, J. Wie, T.R. Mackie: Med. Phys. **22**, 503 (1995)
3. C.M. Ma, D.W.O. Rogers: NRCC Report PIRS-0509(D)rev, 1996
4. C. Cris, E. Born, D. Frei, R. Mini, H. Neuenschwander, W. Volken: *Proc. XIIIth ICCR (Heidelberg, Germany)*, p. 411, 2000
5. H. Neuenschwander, E.J. Born: Phys. Med. Biol. **37**, 107 (1992)
6. H. Neuenschwander, T.R. Mackie, P.J. Reckwerdt: Phys. Med. Biol. **40**, 543 (1995)
7. M.M. Svatos, C.T. Ballinger, H. Neuenschwander, T.R. Mackie, W.P. Chandler, C.L. Hartmann Siantar, J.A. Rathkopf, P.J. Reckwerdt: *Proc. ANS Topical Meeting 'Int. Conf. on Mathematics and Computations, Reactor Physics and Environmental Analyses' (Portland, Oregon)*, Vol. 2, pp. 866–75 (1995)
8. H. Neuenschwander: Rad. Phys. Chem. **53**, 346 (1998)
9. W.R. Nelson, H. Hirayama, D.W.O. Rogers: Stanford Linear Accelerator Center Report **265** (1985)
10. H. Neuenschwander, W. Volken, C. Cris, R. Mini, P. Schwab: *Proc. XIIth ICCR (Salt Lake City, USA)*, p. 23 (1997)
11. G.A. Geist, A. Beguelin, J. Dongarra, W. Jiang, R. Manchek, V. Sunderam: *PVM: Parallel Virtual Machine, A User's Guide and Tutorial for Networked Parallel Computing* (The MIT Press, 1994)
12. A.S. Shiu, S. Tung, K.R. Hogstrom, J.W. Wong, R.L. Gerber, W.B. Harms, J.A. Purdy, R.K. Ten Haken, D.L. McShan, B.A. Fraass: Med. Phys. **19**, 623 (1992)

VMC⁺⁺, Electron and Photon Monte Carlo Calculations Optimized for Radiation Treatment Planning

I. Kawrakow

Ionizing Radiation Standards, NRC, Ottawa, Canada

Abstract. VMC⁺⁺ is a package for the class II condensed history Monte Carlo simulation of coupled electron-photon transport optimized for three dimensional dose calculations used in the treatment planning of cancer patients irradiated with photons and/or electrons (RTP). VMC⁺⁺ is partially based on ideas developed for the VMC and xVMC algorithms but incorporates a variety of improvements in the modelling of the underlying physical processes and simulation geometry. This paper describes a new variance reduction technique, called STOPS, and discusses the use of quasi-random number sequences.

1 Introduction

The large amount of CPU time required by general purpose Monte Carlo (MC) codes such as EGS4 [1], ITS [2], MCNP [3] or PENELOPE [4], has prevented so far their use for routine dose distribution calculations for the radiation treatment planning (RTP) process of cancer patients. To facilitate the application of MC techniques for routine clinical calculations, several MC algorithms specialized for use in the external beam RTP energy/material regime (100 keV – 50 MeV, low atomic numbers) have been developed in recent years, *e.g.* MMC [5,6], VMC and xVMC [7–10], SMC [11], PEREGRINE [12], and more recently MCDOSE [13] and DPM [14].

VMC⁺⁺ [15] is a package for the class II condensed history¹ (CH) MC simulation of coupled electron-photon transport optimized for three dimensional dose calculations for external beam RTP. It is partially based on ideas and algorithms developed for VMC/xVMC but incorporates a variety of improvements in the modelling of the underlying physical processes and the CH implementation. VMC⁺⁺ is implemented in C++ using object-oriented design. In particular, all interactions relevant for the MC simulation of coupled electron/photon transport are represented by separate interaction objects. This approach makes the implementation of enhancements/modifications in the modelling of the underlying physical processes very easy. In addition, the interaction of the simulation package with the objects responsible for geometry, external source and scoring is realized via specific methods of abstract classes. In this way the flexibility of the code is greatly improved.

¹ See the pioneering article by M. Berger, [16], who introduced the condensed history technique and coined the terminology.

A detailed description of the VMC⁺⁺ physics will be given elsewhere. This paper introduces a new variance reduction technique, called STOPS, and discusses the use of quasi-random number sequences.

2 STOPS

If one uses a small-angle approximation to describe multiple elastic scattering (MS) and ignores differences in the discrete interaction cross sections per unit energy loss between different materials, one can transform an electron track simulated in a homogeneous medium into an electron track in an arbitrary heterogeneous geometry. This fact has prompted the re-use of electron histories generated in a homogeneous water phantom in the VMC and xVMC algorithms. This technique is also employed in SMC and MCDOSE, these two algorithms using EGS4/PRESTA to generate the homogeneous particle tracks. A typical gain in efficiency due to re-using particle tracks is about a factor of 2.

The use of the small-angle approximation for RTP type simulations can be justified *e.g.* by the success of EGS4/PRESTA, which employs the small-angle approximation theory of Molière [17] for MS. Ignoring the material variation of the discrete interaction cross section per unit energy loss causes a systematic error in the simulation. It can be shown that this error is small (less than 1%) in the RTP energy/material regime [18]. It is worth noticing that DPM, where a similar set of approximations is used and therefore re-using at least portions of particle histories would be possible, does not employ this technique thus giving up a factor of ~ 2 gain in efficiency.

VMC⁺⁺ uses Simultaneous Transport Of Particle Sets (STOPS), a newly developed variance reduction technique. The motivation for the implementation of STOPS was the desire to extend the applicability of VMC⁺⁺ to arbitrary materials and energies without giving up the efficiency gain due to re-using electron tracks. The idea behind STOPS is as follows:

Several particles that have the same energy but not position, direction, or statistical weight, form a “particle set”. A single particle is a special case of a particle set that has just one particle in it. In VMC⁺⁺ both, electrons and photons, are transported using particle sets (PS). The main gain in efficiency results from the electron transport and therefore the focus will be given to the details of transporting electron sets. If one uses a CSDA model for sub-threshold energy loss processes, the transport equation can be formulated in terms of energy instead of path-length, relating the latter to the former using the restricted stopping power $L(E)$,

$$s = \int_E^{E_0} \frac{dE'}{L(E')} \quad (1)$$

Distances between discrete interactions are then expressed as energy loss and sampled using total discrete interaction cross sections per unit energy loss,

$\Sigma_E(E)$,

$$\Sigma_E(E) = \frac{\Sigma(E)}{L(E)} , \quad (2)$$

where $\Sigma(E)$ is the usual macroscopic cross section (number of interactions per unit length). Unlike Σ , which may exhibit a sharp maximum if the δ -particle production threshold energy is sufficiently low, Σ_E is a fairly flat function of energy [18]. This fact allows the use of the fictitious cross section method (sometimes also referred to as Woodcock scheme) for sampling distances between discrete interactions without loss of efficiency [18]. In addition, differences between cross sections in different materials become very small. One can therefore use the global maximum (the maximum Σ_E for all energies below the maximum energy of the external source and all materials involved in the geometry under consideration) for the fictitious cross section method. By doing so, the geometry becomes homogeneous in terms of number of interactions (fictitious or real) per unit energy loss. Thus all particles in the set will have the same energy when reaching the interaction site. If the energy loss between discrete interactions is too large for the accuracy of the CH algorithm, one divides this energy loss into shorter steps of a user-specified, maximum acceptable energy loss per step. In this way all particles in the set have the same energy at any stage of the simulation until a discrete interaction occurs. This permits various material independent quantities needed for the simulation, such as interpolation indexes, azimuthal scattering angles, distances to discrete interactions, etc., to be calculated or sampled just once for the entire set. For instance, to sample the azimuthal scattering angles for 1 million electrons slowing down in 20 CH steps, one needs of the order of 10 seconds on a present day computer. By transporting 20 electrons simultaneously, this time is reduced to 0.5 seconds. Given the fact that the CPU time for simulating the transport of 1 million electrons (50000 sets with 20 electrons per set) using VMC⁺⁺ is of the order of 30 seconds, it becomes clear that the saving in CPU time due to the STOPS technique can be substantial. Material dependent quantities, such as MS angles and stopping powers, are calculated or sampled separately for each particle in the set, depending on the stopping and scattering properties of the media being traversed. Furthermore, when a discrete interaction site is reached, the type of interaction is also sampled separately for each particle in the set using the interaction probabilities for the current energy and material. If one uses the same random number for all electrons in the set, the probability that all particles in the set undergo the same type of interaction (fictitious *vs* Møller/Bhabha *vs* bremsstrahlung *vs* in-flight annihilation, if a positron set) is very high, in particular if the transport takes place in a geometry containing only human tissue materials where the material variation of Σ_E is very weak. If it nevertheless happens that different interactions are selected for the different particles in the set, or the interaction selected is material dependent (bremsstrahlung), the set is split into separate sets and each new set transported individually. In this way the approximations associated with re-using histories are eliminated and the transport algorithm becomes applicable to arbitrary materials and energies.

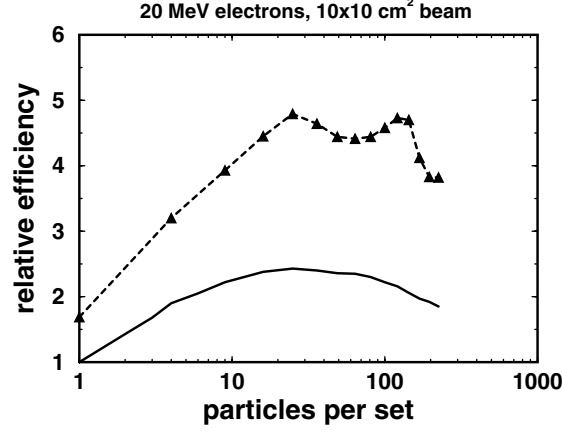


Fig. 1. The relative efficiency of VMC⁺⁺ simulations as a function of the number of particles per set using pseudo-random (solid line) and quasi-random (dotted line) sequences

The effect of the use of the STOPS technique is illustrated in Fig. 1. This figure shows the relative efficiency of VMC⁺⁺ calculations of the dose distribution deposited by a 20 MeV 10x10 cm² electron beam in a phantom made of 4 randomly distributed materials (lung, carbon, water, aluminum) and 5 mm voxels as a function of the number of electrons per set. The solid line is the result of simulations using a pseudo-random sequence, the dotted line represents simulations using a quasi-random sequence (see next section). For the purposes of this figure, the efficiency ε is defined as

$$\varepsilon = \frac{1}{\langle \Delta D^2 \rangle T}, \quad \langle \Delta D^2 \rangle = \frac{1}{N_{50}} \sum_{D > D_{50}} \left(\frac{\Delta D_i}{D_i} \right)^2 \quad (3)$$

where T is the CPU time of the simulation, D_i and ΔD_i the dose in the i 'th voxel and its statistical uncertainty, and where the summation runs over all voxels with a dose larger than 50% of the maximum dose. The statistical uncertainties were determined using a “history-by-history” scoring according to an idea by F. Salvat as described in [19]. For the sake of the statistical analysis, a statistically independent “history” is a PS and all its descendent sets, should the set be broken due to material dependent interactions. We can see from Fig. 1 that initially the efficiency increases, reaching a maximum at about 20–30 particles per set (PPS), and then declines for larger numbers of PPS. The initial rise is due to the CPU time saved via the STOPS technique. When the number of PPS becomes sufficiently high, the probability that two electrons are transported on trajectories very close to each other using the same random number sequence becomes significant. In this case no new information is gained but the time for transporting the particles still spent and therefore the decline in efficiency.

Ultimately, if the entire simulation is realized via a single PS, the statistical uncertainty will become infinite and the efficiency will drop to zero.

3 Quasi-Random Sequences

The use of quasi-random sequences for RTP class MC simulations of photon beams was discussed already in [10]. For VMC⁺⁺ the use of quasi-random sequences was extended to electron beams and to the transport of electrons set in motion by photons (in external photon beams or bremsstrahlung photons). For this purpose a 500-dimensional Sobol's random number generator was implemented (see *e.g.* [20] and references therein for a discussion of quasi-random sequences). In addition, in order to maximize the gain in efficiency due to the quasi-random sequence, sampling techniques using a single random number were developed for Møller/Bhabha scattering, bremsstrahlung, and MS. The additional gain of efficiency for external photon beams, compared to the efficiency gain reported in [10], due to this extension is relatively modest ($\sim 10\%$), but it is significant for electron beams, as can be seen from Fig. 1. The reason for the increase in efficiency is two-fold: (i) reduced variance per particle (ii) "maximum avoidance" of initial electron positions and directions when using a quasi-random number sequence to sample particles from the external source. This "maximum avoidance" has the effect that the onset of the decline of the efficiency for large numbers of PPS, discussed in the previous section, occurs later, permitting a stronger gain from the STOPS technique. The combined gain in efficiency from the use of a Sobol's sequence and the STOPS technique for external electron beams is of the order of a factor of 4.5 – 5.

4 Discussion

After a profiling study of the DPM code, the authors of [14] concluded that their algorithm "exhibits close to the maximum achievable efficiency for CH CSDA MC codes". This conclusion was based on the observation that DPM spends 41% (for 1 mm voxels) of the CPU time for voxel-to-voxel boundary crossing and energy loss deposition, two unavoidable tasks. Given the factor of 4.5 – 5 increase in efficiency due to the two techniques presented here, which are not used in DPM, this conclusion appears questionable.

The CPU time T for a RTP type MC simulation using algorithms that do not truncate steps at boundaries (*e.g.* VMC/xVMC, DPM or VMC⁺⁺), is

$$T = N \left(T_0 + \frac{\alpha}{\Delta x} \right) . \quad (4)$$

Here, N is the number of particle histories and T_0 the average time per history needed for the simulation of geometry independent quantities. T_0 depends on the number of CH steps taken (via the need to sample a MS angle for each step) and the selected particle production cut-off energies, which determine the number of discrete interactions. The time $\alpha/\Delta x$ represents the CPU time spent for

voxel-to-voxel boundary crossing and energy loss deposition. It is proportional to the number of voxel boundaries crossed by the particle track and therefore proportional to the inverse of the voxel resolution Δx . The speed of a MC simulation has reached the theoretical maximum when $T_0 \ll \alpha/\Delta x$, *i.e.* the entire time is spent for geometry checks and scoring. One can therefore conclude that DPM operates at 41% of the maximum possible speed for 1 mm voxels. This is not to be confused with the efficiency, which also depends on the number of histories N to achieve a certain statistical uncertainty.

If using the STOPS technique with n PPS, (4) becomes

$$T = \frac{N}{n} \left(T_0 + n \frac{\alpha}{\Delta x} \right) = N \left(\frac{T_0}{n} + \frac{\alpha}{\Delta x} \right). \quad (5)$$

If the number of PPS is sufficiently high, T_0/n becomes negligible compared to $\alpha/\Delta x$ and the simulation speed approaches the theoretical limit. Figure 2 shows the relative CPU time of VMC⁺⁺ simulations as a function of $1/\Delta x$ for two different numbers of PPS. This figure confirms the linear dependence with $1/\Delta x$ and the parallel shift of the CPU time curve due to the STOPS technique. A linear fit to the two curves reveals that, for 1 mm voxels, VMC⁺⁺ spends about 35% for geometry checks and scoring with a single PPS, but already 94% when using the STOPS technique! Thus VMC⁺⁺ operates at 94% of the theoretical speed limit for a resolution of 1 mm. The slight difference between VMC⁺⁺ simulations with a single PPS and DPM is most likely due to various approximations used in the DPM method, such as the approximated treatment of the bremsstrahlung process, the neglect of the energy variation of total discrete interaction cross sections, the approximate treatment of the pair production process, or the use of fixed multiple scattering steps. Assuming that geometry checks and scoring are done with comparable efficiency in VMC⁺⁺ and DPM, VMC⁺⁺ is about $94\%/41\% \approx 2.3$ times faster than DPM for 1 mm voxels². If one uses a voxel size of 2.5 mm, which is perhaps more realistic for present day clinical dose calculations, the speed advantage of VMC⁺⁺ compared to DPM becomes $\sim 3.2 - 3.5$. Keeping in mind that the goal of a MC simulation for RTP is to calculate a dose distribution to a prescribed statistical uncertainty, and not to simulate a given number of histories, and taking into account the factor of ~ 2 increase in efficiency due to the use of a quasi-random sequence, one can conclude that VMC⁺⁺ is $\sim 6.4 - 7$ times more efficient than DPM for realistic clinical dose calculations.

An important point for clinical use of MC techniques is accuracy. Larsen has shown that any CH MC algorithm will converge to the correct answer, provided that the multiple scattering of electrons is faithfully simulated [22]. VMC⁺⁺ uses a multiple scattering theory [23], which is exact and applicable for

² A similar estimate results from the DPM timing reported in [14]. Using the EGS4 benchmark list [21], and assuming that the 400 MHz HP PA8500 CPU used to obtain the timing results for DPM is $400/175 \approx 2.3$ times faster than the 175 MHz HP PA7200 CPU, available in the benchmark list, one arrives at a speed factor of 2.5 for VMC⁺⁺ compared to DPM.

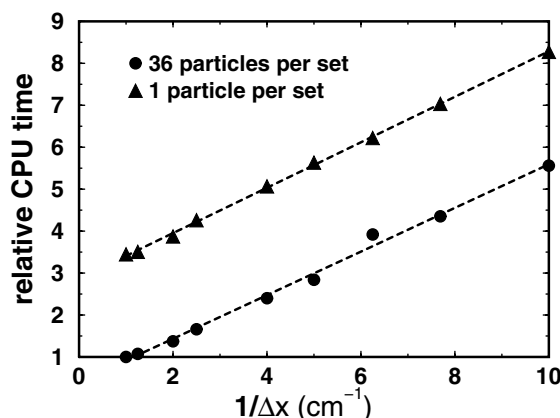


Fig. 2. The relative CPU time of VMC⁺⁺ simulations as a function of the inverse of the voxel resolution Δx for two different numbers of particles per set

arbitrary step-sizes, and will therefore always deliver the desired accuracy using the appropriate CH step-length. It was demonstrated in [15] that VMC⁺⁺ indeed agrees on a sub-percent level with EGSnrc simulations, being at the same time more than 50 times faster than EGS4/PRESTA. The accuracy benchmarks used, proposed by D. Rogers and R. Mohan [24], which involve situations with a strong charged particle disequilibrium (narrow beams, sharp inhomogeneities), were specifically designed to represent a severe test on the accuracy of MC codes specialized for use in RTP. As a conclusion it is worth pointing out that, due to the use of the STOPS technique, CPU time variation with step-length is much weaker for VMC⁺⁺ than it is for algorithms such as DPM. For instance, an increase of T_0 by a factor of two will result in a $\sim 6\%$ increase in CPU time for a VMC⁺⁺ simulation in 1 mm voxels using 36 PPS, but cause a 60% increase in CPU time for a VMC⁺⁺ simulation with a single PPS or a DPM simulation!

References

1. W.R. Nelson, H. Hirayama, D. W. O. Rogers: *The EGS4 Code System*, Report SLAC-265, Stanford Linear Accelerator Center, Stanford, California (1985)
2. J.A. Halbleib et al: *ITS Version 3.0: The Integrated TIGER Series of Coupled Electron/Photon Monte Carlo Transport Codes*, Sandia Report SAND91-1634 (1992)
3. J.F. Briesmeister (Editor): *MCNP – A general Monte Carlo N-particle transport code*, LANL Report LA-12625-M (Los Alamos, NM) (1993)
4. F. Salvat et al: *PENELOPE, an algorithm and computer code for Monte Carlo simulation of electron-photon showers*, University of Barcelona preprint (1996)
5. H. Neuenschwander, E.J. Born: *Phys. Med. Biol.* **37**, 107 (1992)
6. H. Neuenschwander et al.: *Phys. Med. Biol.* **40**, 543 (1995)
7. I. Kawrakow, M. Fippel, K. Friedrich: *Med. Phys.* **23**, 445 (1996)

8. I. Kawrakow: Med. Phys. **24**, 505 (1997)
9. M. Fippel: Med. Phys. **26**, 1466 (1999)
10. I. Kawrakow, M. Fippel: Phys. Med. Biol. **45**, 2163 (2000)
11. P.J. Keall, P.W. Hoban: Med. Phys. **23**, 2023 (1996)
12. C.L. Hartmann-Siantar et al: 'LLNL's PEREGRINE project'. In *Proceedings of the XII-th Conference on the Use of Computers in Radiotherapy, May 27-30, 1997* (Medical Physics Publishing, Madison, Wisconsin 1997), pp. 19–22
13. C.-M. Ma, J.S. Li, T. Pawlicki, S. B. Jiang, J. Deng: 'MCDOSE - A Monte Carlo dose calculation tool for radiation therapy treatment planning'. In *The Use of Computers in Radiotherapy, XIIIth Int'l Conf., Heidelberg* ed. by W. Schlegel and T. Bortfeld, (Springer-Verlag, Heidelberg 2000) pp. 123 – 125
14. J. Sempau, S.J. Wilderman, A. F. Bielajew: Phys. Med. Biol. **45**, 2263 (2000)
15. I. Kawrakow, M. Fippel: 'VMC++, a fast MC algorithm for radiation treatment planning'. In *The Use of Computers in Radiotherapy, XIIIth Int'l Conf., Heidelberg* ed. by W. Schlegel and T. Bortfeld (Springer-Verlag, Heidelberg 2000) pp. 126 – 128
16. M.J. Berger: 'Monte Carlo Calculation of the penetration and diffusion of fast charged particles'. In *Methods in Comput. Phys.* ed. by B. Alder, S. Fernbach, and M. Rotenberg, Vol. 1, (Academic, New York 1963) pp. 135 – 215
17. G.Z. Molière: Z. Naturforsch **3a**, 78 (1948)
18. I. Kawrakow: Med. Phys. **27**, 485 (2000)
19. J. Sempau, A.F. Bielajew: Phys. Med. Biol. **45**, 131 (2000)
20. W.H. Press et al: Numerical Recipes in Fortran, 2nd Ed, (Cambridge University Press, New York 1992)
21. A.F. Bielajew, D.W.O. Rogers: Medical Physics, **19**, 303 (1992)
22. E.W. Larsen: Ann. Nucl. Energy **19**, 701 (1992)
23. I. Kawrakow, A. F. Bielajew: Nucl. Instr. and Meth. B **134**, 325 (1998)
24. D.W.O. Rogers, R. Mohan: 'Questions for comparison of clinical Monte Carlo codes'. In *The Use of Computers in Radiotherapy, XIIIth Int'l Conf., Heidelberg* ed. by W. Schlegel and T. Bortfeld, (Springer-Verlag, Heidelberg 2000) pp. 120 – 122

The Track Structure of Photons, Electrons and α -Particles from the Point of View of the Formation of Ionization Clusters

B. Grosswendt

Physikalisch-Technische Bundesanstalt, Bundesallee 100, D-38116 Braunschweig, Germany

1 Introduction

It is commonly accepted that the spatial distribution of ionization events or of energy depositions caused by ionizing radiation in sub-cellular structures is decisive for the initiation of radio-biological effects. In this sense, radiation damage to cellular DNA is assumed to be initiated by the direct ionization of the DNA and subsequent reactions with reactive species produced by ionization of neighbouring molecules. As was shown, for instance, in [1], the yields of clusters of multiple ionizations produced by ionizing radiation of different quality within sites, 2–3 nm in size, correlate well with observed yields of double strand breaks. By the analysis of ionization clusters, it was concluded that two ionizations are required for the induction of one double strand break of DNA. Similarly, by modelling of the DNA damage induced by Auger electrons of incorporated ^{125}I , it was found out [2] that two ionizations are necessary to induce one single strand break and four ionizations to induce one double strand break.

The importance of ionization yields to explain radiation damage is also suggested by the dependence of bio-effect cross sections on the mean free path length with respect to primary ionization produced by different radiation qualities in some types of mammalian cells [3]. In this context, one should have in mind that even the concept of restricted LET [4–6], which is experimentally identified to determine the yield factor α of various cellular radiation effects, is based on the fact that for sites of nanometre dimensions the restricted LET, L_{100} , is directly proportional to the linear primary ionization density [6].

Despite the importance of ionization yields in sub-cellular structures, a few nm in size, with respect to radiation damage, our present knowledge is almost exclusively based on Monte Carlo simulations using cross section sets for water vapour or liquid water [7–11]. Measurements would be desirable but are missing because the direct measurement of ionizations in cells or even in nanometric volumes of liquid water are not yet possible.

The most feasible way, at present, to overcome this problem and to put finally our knowledge of ionization yields in nanometric volumes on an experimental basis is the use of highly sophisticated counters filled with gases at low operating pressure to simulate a spherical target volume a few nm in diameter at a density of 1.0 g/cm^3 . Based on such instruments, ionization yields in sub-cellular structures could be simulated if (i) the interaction mechanisms of ionizing radiation

in the counter gas are similar to those in cell material or, at least, in liquid water, (ii) the interaction cross sections and the number or kind of the most important energy loss channels are almost independent of gas density, and (iii) the particle tracks are not noticeably disturbed by any component of the measuring device. The first of these three requirements is the most critical one since it is hardly conceivable that gaseous systems well suited to proportional counter experiments show the same mechanisms of radiation interaction as sub-cellular material which, in addition, are also not really known. In this respect, one should have in mind that even the radiation interaction in water vapour is quite different from that in liquid water as discussed extensively in [7,11,12,14]. If, however, the reliable interaction mechanisms of ionizing radiations are satisfactorily known in an appropriate gas, its use for the above purpose would be reasonable since the measurements could be traced to primary interaction processes by combined Monte Carlo simulations. After this traceability has been established, the measurements can be compared and analysed with the corresponding data for liquid water or sub-cellular structures if available.

Because of this fact, the track structure formation of photons, electrons and α -particles in water and propane-based tissue-equivalent gas (composition by volume: 55% C_3H_8 , 39.6% CO_2 , 5.4% N_2) was studied by Monte Carlo simulation with special emphasis on the formation of ionization clusters. After a short summary of the most important physical aspects of ionization cluster formation, new results are presented and discussed from the point of view of radiation biology, radiation protection and radiation therapy.

2 General Aspects of Ionization Cluster Formation

Let $P(T, \nu)$ be the probability that exactly the number ν of ionizations is produced in a piece of matter of specified size and shape, by charged particles at initial energy T . The mean number of ionizations produced within the target volume is then given by the first moment $M_1(T)$ of the distribution $P(T, \nu)$ according to (1) and is called mean cluster size in the following.

$$M_1(T) = \sum_{\nu=0}^{\infty} \nu P(T, \nu) \quad (1)$$

This moment $M_1(T)$ is one of the most important quantities to describe ionization clusters and depends strongly on the size and material properties of the target volume, and, in addition, on the kind of ionizing radiation. Here, the ionization cross sections of the primary radiation and of all types of potential secondary particles are of particular importance.

If we assume (i) that T_1 is the mean particle energy after penetrating through the piece of matter and (ii) that, in the case of a very small target volume, the greater part of the energy loss $\Delta T = T - T_1$ is not absorbed, $M_1(T)$ depends almost exclusively on the ratio of the target size along the primary particle's track and its mean free path length $\lambda_{\text{ion}}(T)$ with respect to primary ionization, which is proportional to the reciprocal ionization cross section.

To give an impression of such data for different kinds of ionizing particles, Fig. 1 shows the mean free path length $(\lambda\rho)_{\text{ion}}$ with respect to ionization of electrons, α -particles and photons in liquid water or propane-based tissue-equivalent gas at density ρ as a function of energy T . Here, the energy of the α -particles is expressed by the energy T of electrons at the same velocity: $T = (m_{\text{el}}/m_{\alpha})T_{\alpha} \approx T_{\alpha}/7345$, where m_{el} and m_{α} represent the particle masses. The values of $(\lambda\rho)_{\text{ion}}$ for electrons were determined on the basis of [15] in the case of the tissue-equivalent gas and on the basis of [16] for liquid water; the data for α -particles were determined in the same way as described in [17] using the parameters for protons of [18] with regard to the constituents of the tissue-equivalent gas and the parameters of [19] in liquid water, after scaling by Z^2 and applying a correction factor with respect to the atomic number Z [20]. The mean free path lengths of photons were calculated on the basis of the mass attenuation coefficients with respect to the photoelectric effect and to Compton scattering taken from [21] for $T \geq 1$ keV and on those from [22] at lower energies.

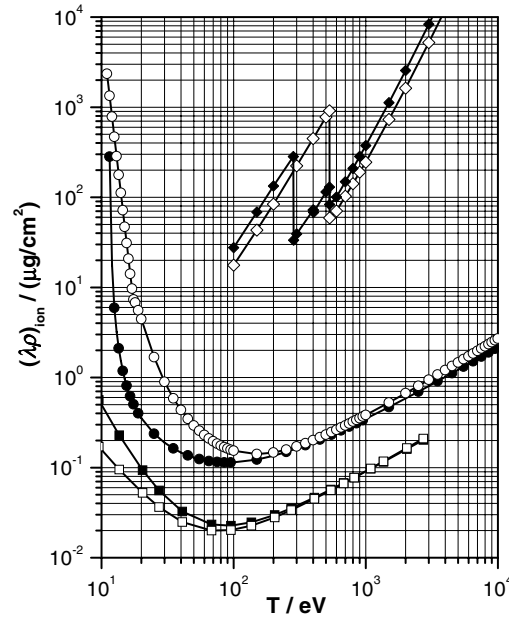


Fig. 1. Mean free path length $(\lambda\rho)_{\text{ion}}$ with respect to ionization in water (*open symbols*) or in propane-based tissue-equivalent gas (*solid symbols*), as a function of particle energy T : (*circles*) electrons, (*diamonds*) photons and (*squares*) α -particles plotted at the energy of electrons at same velocity

If we compare the mean free path lengths of photons with those of electrons, a completely different behaviour of both particle types in matter becomes obvious. The path lengths of photons are much longer than those of electrons, at least,

down to 100 eV, which means that photon tracks can be clearly interpreted as a collection of single electron tracks. As far as the behaviour of electrons in the two different media is concerned, it can be emphasized that the electron path lengths in water are very similar to those in the tissue-equivalent gas at energies greater than about 200 eV but clearly longer at smaller energies. In addition, the data for electrons at around 100 eV are comparable with those of α -particles at higher energies thus demonstrating the strong ionization capability of low-energy electrons.

In larger target volumes where the mean particle energy T_1 after penetration is comparable with the initial energy T but the energy loss ΔT is totally absorbed, $M_1(T)$ is related to the differential value $\omega(T)$ of the mean energy required to produce an ion pair formed [23] in the following way:

$$M_1(T) = \int_{T_1}^T \frac{dE}{\omega(E)} \quad (2)$$

Here, $\omega(T)$ is defined as the quotient dT/dN , where dT is the mean energy lost by a charged particle of energy dT in traversing an absorber of thickness dx , and dN is the mean number of ion pairs produced if dT is completely dissipated in the material.

In the special case that the initial particle energy T is completely absorbed in the target volume which, at the same time, means that T_1 is smaller than the lowest ionization threshold energy, the moment $M_1(T)$ is equal to the mean number $N(T)$ of ion pairs formed which is conventionally expressed by $N(T) = T/W(T)$, where $W(T)$ represents the so-called W-value [23].

3 Monte Carlo Simulation of Ionization Clusters

As stated in the introduction, the measurement of ionization clusters in nanometric volumes is, at present, one of the most important needs in the field of radiation metrology. But, because of the fact that such measurements are exclusively performed in gaseous systems, it is necessary to estimate the difference between cluster distributions produced by ionizing radiation in gases and those produced in liquid water. For this purpose, the formation of ionization clusters caused by electrons or α -particles was simulated in two different nanometric targets comparable with those actually used in experiments [24,25], but consisting on the one hand of liquid water and on the other hand of propane-based tissue-equivalent gas.

In order to simulate the irradiation geometry described in [24] for 5.4 MeV α -particles, the distribution of ionization clusters was calculated in spherical target volumes of a homogeneous medium consisting of tissue-equivalent gas or liquid water, at different distances to the particle beam. To study the cluster formation by primary electrons, one of the experimental devices described in [25] was simulated. For this purpose, the distribution of ionization clusters was calculated for cylindrical target volumes surrounded by a vacuum and penetrated by a primary

electron beam perpendicularly to its main axis. In order to study the formation of ionization clusters by photons, the photon attenuation in and the penetration through a half-infinitely extended water phantom was simulated to calculate the spectral distribution of electron fluence as a function of phantom depth. These spectral distributions were used afterwards for cluster size analysis.

3.1 Simulation of the Cluster Formation by α -Particles

To calculate the ionization yield distribution caused by α -particles at energies of a few MeV during their penetration through material layers of small mass per area, it was assumed that (i) the energy loss due to impact ionization or excitation along short track segments does not appreciably change the initial particle energy, (ii) the influence of elastic scattering on the particle's energy and flight direction can be neglected in the case of short track segments, and (iii) the primary particle energy is high enough to allow charge changing processes also to be neglected. The first of these assumptions is justified if the energy loss during the penetration of a material layer is only of the order of a few percent. The validity of the second assumption is obvious from the detour factor of α -particles, which is equal to 0.9931 in liquid water and 0.9952 in propane-based tissue-equivalent gas at 5 MeV [26] thus demonstrating that the particles' projected ranges are almost equal to their travelling lengths within the limits of the continuous-slowing-down approximation. The validity of the third assumption becomes obvious if one considers the influence of charge changing processes of protons on their W-value at higher energies [27].

In view of these facts, the structure of α -particle track segments at an energy of a few MeV is almost exclusively based on their ionization cross section, on the spectral and angular distribution of secondary electrons produced by impact ionization, and on the properties of secondary electron degradation. The main steps for simulating their track segments in matter are, therefore, (i) the determination of the distance to the subsequent point of ionization interaction, (ii) the determination of the energy and direction of the secondary electron set in motion, and (iii) the simulation of electron transport.

In consequence of this simulation strategy, the ionization pattern of an α -particle track can be subdivided into two contributions where the first one represents the ionization pattern directly produced by the α -particles and the second one that produced during the degradation of secondary electrons if their initial energies are greater than the lowest ionization threshold energy of the stopping material.

As described in Sect. 2, the distance between two subsequent ionization events within the track segment of an α -particle at energy T was calculated on the basis of cross sections for protons [17–19] at the same velocity, after scaling with the square of the atomic number Z . To simulate the secondary electron distribution after impact ionization, the single-differential ionization cross section with respect to the secondary-electron energy of the Hansen-Kocbach-Stolterfoht model (HKS) was applied, which is published in [20] for specified subshells κ of binding energy B_κ and electron occupation number N_κ . For the present purpose,

the values of B_κ and N_κ were taken from [28]. The advantage of using the semi-empirical HKS model is that it has no adjustable parameters and gives not only the single-differential but also the double-differential cross section with respect to the energy and the emission angle of the secondaries.

After the determination of the secondary electron energy, the polar angle θ of the electron's flight direction relative to that of the α -particle was sampled, using the double-differential cross section of the HKS model at specified electron energy as the probability density. Before that, the double-differential cross section was normalized to its integral over $\cos(\theta)$ within the limits $-1 \leq \cos(\theta) \leq 1$. The azimuthal angle of the electron direction was assumed to be uniformly distributed between 0 and 2π . These data were used later as input parameters to the Monte Carlo model for electrons.

3.2 Simulation of the Cluster Formation by Electrons

To investigate the cluster distributions produced by primary electrons or photons and to study the contribution of secondary electrons to the cluster distributions of α -particles, the Monte Carlo model for electrons must be able to follow electron histories down to the ionization threshold energy of 11.08 eV in the case of propane-based tissue-equivalent gas and of 10.79 eV in the case of liquid water, taking into account elastic electron scattering, impact ionization and the reliable excitation processes influencing electron degradation. At each interaction point, the electron flight direction after interaction in the case of elastic scattering and, in addition, the energy loss of the primary electron in the case of inelastic scattering have to be calculated, possibly supplemented by the energies and flight directions of secondary particles directly liberated by the scattering process.

In view of these facts, the main steps for simulating electron histories are (i) the determination of the distance to the subsequent point of interaction, (ii) the determination of the type of interaction the electron suffers at this point, and (iii) the sampling of the energy loss and the new flight direction caused by the selected interaction process, possibly supplemented by the energies and flight directions of secondary particles if liberated at all. For a detailed description of procedures useful for purposes of low-energy electron transport simulations see, for instance, [29–31].

To simulate the electron transport in the tissue-equivalent gas mixture, the same sets of cross sections were used as those described in [15] for nitrogen, carbon dioxide and propane. In the case of liquid water, the ionization cross section was taken from [16], the cross sections for discrete electronic excitations were taken from [32], and those for vibrational excitation from [11]. Elastic scattering was treated in a similar way as described in [29] at energies greater than 200 eV, but according to [33] at lower energies.

3.3 Simulation of the Cluster Formation by Photons

The photon transport was simulated in the energy range between 10 keV and 10 MeV from one interaction point to the other according to [34], taking into

account: (i) the photoelectric effect, (ii) Rayleigh scattering including electron binding, (iii) Compton scattering again with electron binding, and (iv) electron-positron pair creation followed by the annihilation of positrons. The distance between two succeeding interaction points and the probabilities of the four photon interaction processes were calculated using the total mass attenuation coefficients and interaction cross sections of [35], assuming that the independent atom model is valid for water.

The photon direction after Rayleigh scattering was simulated from the differential Thomson cross section, multiplied by the square of the atomic form factor to include electron binding. The energy and direction of the photons after Compton scattering were sampled from the Klein-Nishina differential cross section for inelastic scattering of unpolarized photons by free electrons, multiplied by the incoherent scattering function to include electron binding.

Electron-positron pair creation followed by positron annihilation were simulated in the conventional way, assuming that each positron is annihilated directly at its point of creation by isotropic emission of two 511 keV photons of opposite directions. Both photons are treated afterwards like the primaries.

The creation of fluorescence radiation and of bremsstrahlung quanta were not taken into account. The details of photon sampling including the formation of Auger electrons are described in detail in [34].

4 The Cluster Formation by α -Particles, Electrons or Photons: a Comparison

In order to give an impression of the results for α -particles, Fig. 2a shows the probability $P(T, \nu)$ that in liquid water a particle at energy $T_\alpha = 5.4$ MeV produces exactly ν ionizations in a spherical target with a diameter D of mass per area $0.2 \mu\text{g}/\text{cm}^2$ if the midpoint of the sphere is localized at distances d to the particle beam between zero and $1.4 \mu\text{g}/\text{cm}^2$. Two different shapes of the probability as a function of the number of ionizations can be clearly recognized: a first one which shows a maximum at around 2.5 ionizations and represents the cluster distribution if the target sphere is directly penetrated by the α -particle beam, and a second one which is valid at distances d greater than or equal to the sphere radius. This second shape shows high probabilities at $\nu = 0$ and strongly decreasing values with increasing cluster size representing cluster distributions which are exclusively caused by secondary electrons. An interesting aspect of the latter type of probability curves is the fact that their slope is almost independent of distance d , on a logarithmic scale. Similar results for protons are discussed in detail in [10].

For a comparison of cluster distributions produced in liquid water or in propane-based tissue-equivalent gas at the same irradiation geometry, Fig. 2b shows the first moment M_1 of the probability $P(T, \nu)$ of cluster size ν in spherical targets with diameters D of mass per area between 0.2 and $0.8 \mu\text{g}/\text{cm}^2$ (corresponding to 2 – 8 nm in a material of density $1.0 \text{ g}/\text{cm}^3$) as a function of distance d . At a first glance, it can be stated that the mean cluster size M_1 in

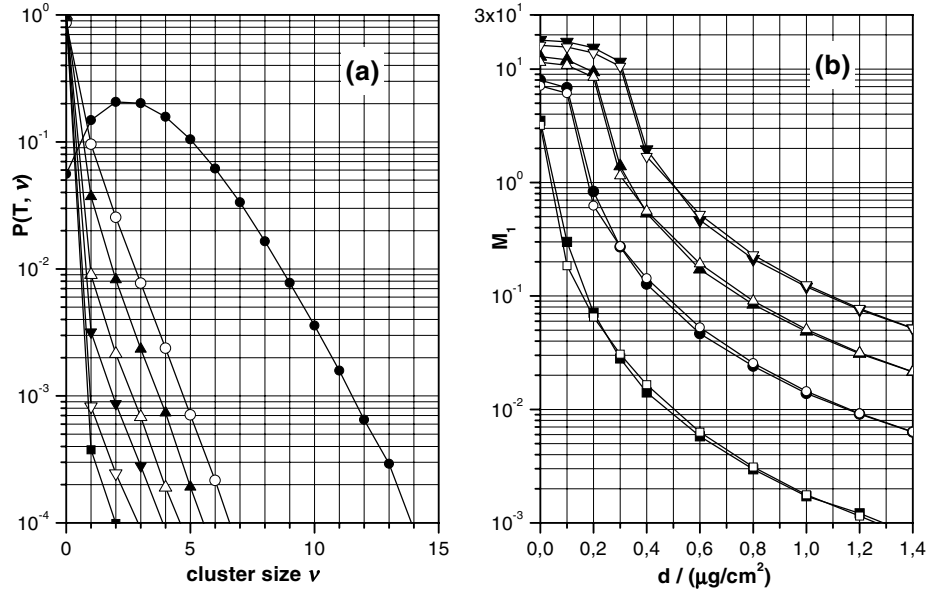


Fig. 2. Formation of ionization clusters by 5.4 MeV α -particles in spherical targets of diameter D centred at a distance d to the particle beam: (a) probability $P(T, \nu)$ that exactly ν ionizations are produced in a sphere of liquid water ($0.2 \mu\text{g}/\text{cm}^2$ in diameter), with distance d as a parameter: $d = 0 \mu\text{g}/\text{cm}^2$ (\bullet), $0.1 \mu\text{g}/\text{cm}^2$ (\circ), $0.2 \mu\text{g}/\text{cm}^2$ (\blacktriangle), $0.4 \mu\text{g}/\text{cm}^2$ (\triangle), $0.6 \mu\text{g}/\text{cm}^2$ (\blacktriangledown), $1.0 \mu\text{g}/\text{cm}^2$ (\triangledown), and $1.4 \mu\text{g}/\text{cm}^2$ (\blacksquare); (b) first moment M_1 of the cluster distribution as a function of distance d in liquid water (open symbols) or in propane-based tissue-equivalent gas (solid symbols), with the sphere diameter D as a parameter: $D = 0.8 \mu\text{g}/\text{cm}^2$ (down triangles), $0.6 \mu\text{g}/\text{cm}^2$ (up triangles), $0.4 \mu\text{g}/\text{cm}^2$ (circles), and $0.2 \mu\text{g}/\text{cm}^2$ (squares)

the tissue-equivalent gas is very similar to that in liquid water proving that, at least, mean cluster sizes measured in spherical targets of small mass per area in the tissue-equivalent gas mixture can be reasonably used to estimate cluster sizes produced by 5.4 MeV α -particles in nanometric spheres of liquid water.

To discuss the formation of ionization clusters by electrons, Fig. 3a presents the probability $P(T, \nu)$ that in liquid water an electron at energy T produces exactly ν ionizations in a cylindrical target, $0.2 \mu\text{g}/\text{cm}^2$ in diameter and $0.2 \mu\text{g}/\text{cm}^2$ in height, if the cylinder is penetrated perpendicularly to its main axis, on a radius at half of the normal height. As expected, the probability as a function of cluster size shows a maximum in the case of lower energies, but a strong decrease with increasing number of ionizations at higher energies.

For the analysis of the influence of the target material on the formation of ionization clusters, Fig. 3b shows the first moments M_1 of the probability $P(T, \nu)$ of cluster size ν and of the conditional probability of cluster size $\nu \geq 1$ in the cylinder target as a function of electron energy T in both media, again at the same irradiation geometry. At first glance, it is obvious that both types

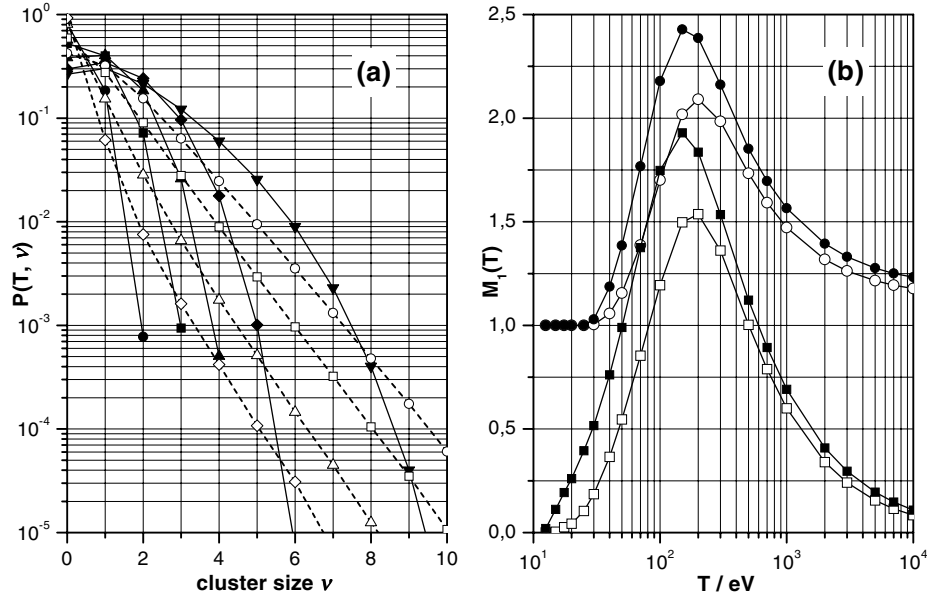


Fig. 3. Formation of ionizations clusters by electrons at energy T in a cylindrical target, $0.2 \mu\text{g}/\text{cm}^2$ in diameter and height: **(a)** probability $P(T, \nu)$ that exactly ν ionizations are produced in liquid water, with the energy T as a parameter: $T = 30 \text{ eV}$ (\bullet), 50 eV (\blacksquare), 70 eV (\blacktriangle), 100 eV (\blacklozenge), 200 eV (\blacktriangledown), 500 eV (\circ), 1 keV (\square), 3 keV (\triangle), and 10 keV (\diamond); **(b)** first moments M_1 of the probability distribution $P(T, \nu)$ (squares) or of the conditional probability distribution for $\nu \geq 1$ (circles) as a function of electron energy T , in liquid water (open symbols) or propane-based tissue-equivalent gas (solid symbols)

of moments in the tissue-equivalent gas mixture are greater than those in liquid water due to the smaller mean free path length concerning ionization in the case of the gas mixture (see Fig. 1). The maximum values of the moments which are localized at an energy of about 150 eV in the case of the gas mixture are shifted to about 200 eV in water. Nevertheless, it can be stated that in both target systems the energy dependence of the moments is quite similar.

As already mentioned, the formation of ionization clusters by photons was studied in two steps. In a first step, the spectral electron fluence produced by photon interaction in liquid water was calculated as a function of depth and, in a second step, these electrons were treated like primary electrons. To give an overview of the electron energy distribution at different depths of liquid water, Fig. 4a shows the normalized spectral electron fluence $(d\Phi/dT)_d/\Phi_d$ produced at depth d by mono-energetic primary photons of 100 keV , where Φ_d is the integral of $(d\Phi/dT)_d$ over T up to the primary photon energy. The increasing fraction of low energy electrons with increasing depth is obvious. The shape of the electron distribution at lower energies, however, is almost independent of depth. Since the greater part of ionizations is produced by the electrons at lower energies, the

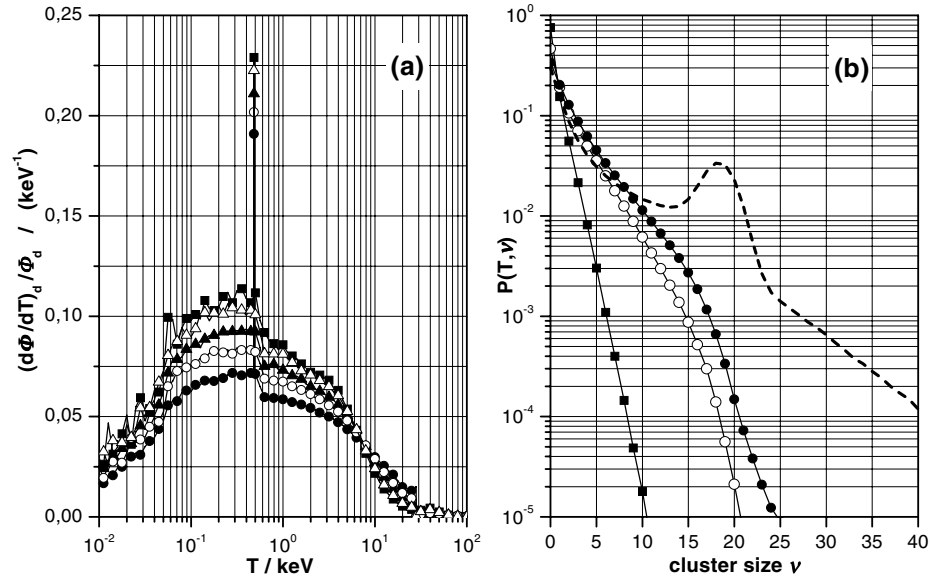


Fig. 4. Formation of ionization clusters by mono-energetic photons in liquid water: (a) normalized spectral electron fluence $(d\Phi/dT)_d / \Phi_d$ produced by 100 keV photons at depth d : $d = 1$ cm (\bullet), 5 cm (\circ), 10 cm (\blacktriangle), 20 cm (\triangle), and 30 cm (\blacksquare); (b) probability $P(T, \nu)$ that exactly ν ionizations are produced in cylindrical targets, $0.2 \mu\text{g}/\text{cm}^2$ in height and $0.2 \mu\text{g}/\text{cm}^2$ in diameter (\blacksquare), $1.0 \mu\text{g}/\text{cm}^2$ in diameter (\circ) or $2.0 \mu\text{g}/\text{cm}^2$ in diameter (\bullet), or in a cylinder, $2.0 \mu\text{g}/\text{cm}^2$ in diameter and $10.0 \mu\text{g}/\text{cm}^2$ in height (*broken curve*)

probability $P(T, \nu)$ of cluster formation in nanometric target volumes does not strongly depend on the depth in water.

To give an impression of the cluster distribution caused by photons in nanometric targets, Fig. 4b shows the probability $P(T, \nu)$ as a function of ν produced by 100 keV photons at a depth of 5 cm in cylindrical volumes, $0.2 \mu\text{g}/\text{cm}^2$ or $1.0 \mu\text{g}/\text{cm}^2$ in diameter and $0.2 \mu\text{g}/\text{cm}^2$ in height, and, in addition, also for volumes, $2.0 \mu\text{g}/\text{cm}^2$ in diameter and $0.2 \mu\text{g}/\text{cm}^2$ or $10.0 \mu\text{g}/\text{cm}^2$ in height. As is obvious from the figure, the cluster distributions produced in the cylinders, $0.2 \mu\text{g}/\text{cm}^2$ in height, show a very pronounced decrease with increasing cluster size ν whereas that in the cylinder, $2.0 \mu\text{g}/\text{cm}^2$ in diameter and $10.0 \mu\text{g}/\text{cm}^2$ in height, extends to much higher values of the cluster size and shows a second maximum. The reason of this behaviour is the fact that a remarkable fraction of the electrons set in motion by photon interaction has an energy smaller than 500 eV and a range of mass per area less than $2.0 \mu\text{g}/\text{cm}^2$. These electrons are completely stopped within the cylinder, $2.0 \mu\text{g}/\text{cm}^2$ in diameter and $10.0 \mu\text{g}/\text{cm}^2$ in height, but not in the smaller ones. In consequence, the larger cylinder can be interpreted as a macroscopic target for these electrons, with a most probable cluster size of about 18. This value agrees very well with the mean number

$N = T/W(T)$ of ion pairs formed in liquid water, due to a W-value of 25.5 eV at an electron energy T of 500 eV. In the smaller target volumes, the W-value or its differential value $\omega(T)$ cannot not be applied since the greater part of secondary electrons produced during electron degradation is not completely absorbed within the targets.

5 Consequences for Radiation Protection and Radiation Therapy from the Point of View of Radiation Biology

As mentioned in the introduction, the yields of clusters of multiple ionization in sites, 2–3 nm in size, correlate well with observed yields of double strand breaks of DNA. If one now has in mind that the mean cluster size produced by ionizing radiation in nanometric volumes is governed to the greater part by the mean free path length $(\lambda\varrho)_{\text{ion}}$ with respect to ionization of a particle at energy T (see Sect. 2), it can be expected that the yields of clusters with size $\nu \geq 2$ as a function of $(\lambda\varrho)_{\text{ion}}$ are independent of the kind of ionizing particle.

To check this assumption, the cumulative distribution function $F_2(T) = \sum P(T, \nu)$ for $\nu \geq 2$ was calculated and plotted as a function of path length. Figure 5a shows (i) the results for 5.4 MeV α -particles in the case of a target sphere, $0.2 \mu\text{g}/\text{cm}^2$ in diameter, at zero distance to the particle beam, (ii) those for primary electrons in the energy range between 20 eV and 100 keV in a cylinder, $0.2 \mu\text{g}/\text{cm}^2$ in diameter and height, and (iii), in the same target volume, those for secondary electrons produced by 100 keV photons at a depth of 5 cm in water. For the latter purpose, the mean free path length of the spectral distribution of secondary electrons was defined as the reciprocal ionization cross section of mono-energetic electrons averaged over the electron energy distribution, using the energy dependence of $(\lambda\varrho)_{\text{ion}}$ for electrons as presented in Fig. 1.

In the case of electrons, the distribution function $F_2(T)$ versus $(\lambda\varrho)_{\text{ion}}$ looks like an arrow showing its top at $F_2 = 0.44$ and $(\lambda\varrho)_{\text{ion}} = 0.141 \mu\text{g}/\text{cm}^2$ where the latter value corresponds to an electron energy of 150 eV. The right hand side of the arrow represents the probability of multiple ionization as a function of path length at energies between 150 eV and 100 keV, whereas the left hand side represents $F_2(T)$ at lower energies. Because of this fact, a specified value of $F_2(T)$ cannot be related unambiguously to the mean free path length $(\lambda\varrho)_{\text{ion}}$. If we now look at the values of F_2 for electrons produced by the photons or for 5.4 MeV α -particles, it becomes obvious that the photon value fits well to the high-energy electron branch, and the α -particle value at $(\lambda\varrho)_{\text{ion}} = 0.0708 \mu\text{g}/\text{cm}^2$ to the extrapolation of the high-energy branch of the electrons, thus confirming the dependence of $F_2(T)$ as a function of $(\lambda\varrho)_{\text{ion}}$ if the low-energy branch with regard to electrons is not taken into account.

$$\sigma_B(\lambda)/(10^{-8} \text{ cm}^2) = 3 \left[1 - \exp \left(- \frac{0.36 \mu\text{g}/\text{cm}^2}{(\lambda\varrho)_{\text{ion}}} \right) \right]^2 \quad (3)$$

In order to apply the probability of multiple ionization to radiation biology, $F_2(T)$ was scaled at an electron energy of 200 eV to the bio-effect cross section σ_B

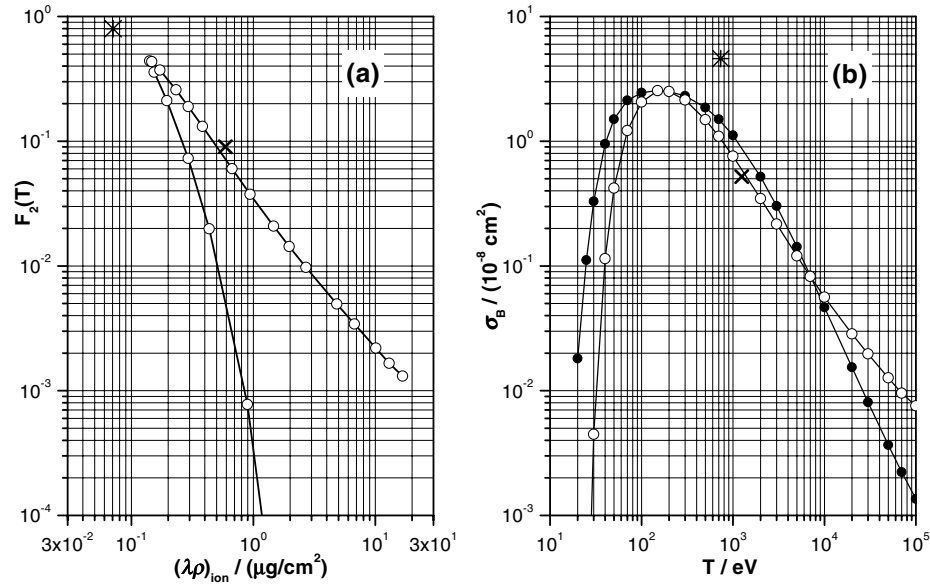


Fig. 5. Probability of multiple ionization and its relation to the bio-effect cross section of [3] for different radiation qualities. **(a)** cumulative distribution function F_2 as a function of the mean free path length $(\lambda\rho)_{\text{ion}}$ of ionizing particles in liquid water: (o) electrons in a cylinder, $0.2 \mu\text{g}/\text{cm}^2$ in diameter and height, (x) secondary electrons produced by 100 keV photons at a depth of 5 cm in water in the same cylindrical target, and (*) 5.4 MeV α -particles in a sphere, $0.2 \mu\text{g}/\text{cm}^2$ in diameter, at zero distance to the particle beam. **(b)** bio-effect cross section in various types of mammalian cells as a function of particle energy T : cross section σ_B (•) according to (3) using the energy dependence of $(\lambda\rho)_{\text{ion}}$ presented in Fig. 1, cumulative distribution function $F_2(T)$ scaled at an electron energy of 200 eV to σ_B for electrons (o), for 5.4 MeV α -particles plotted at the energy of electrons with the same velocity (*), and for secondary electrons of 100 keV photons plotted at the mean value of the secondary electron energy with respect to $F_2(T)$ of primary electrons (x)

given by (3) for electrons and X-rays and extensively discussed in [3]. Figure 5b shows the scaled values of $F_2(T)$ in comparison with the results of (3) as a function of energy T . At first glance, it can be seen that the energy dependence of the bio-effect cross section and of that of the scaled distribution function for the primary electrons are quite similar. In addition, it can be stated that the scaled F_2 -value of the secondary electrons produced by 100 keV photons fits very well to the electron data, whereas the corresponding data of 5.4 MeV α -particles is much greater than that of electrons at the same velocity. The latter fact can be understood if one has in mind that $(\lambda\rho)_{\text{ion}}$ of the α -particles is much smaller than that of the electrons and, therefore, leads to higher values of the bio-effect cross section according to (3). Nevertheless, the scaled value of F_2 for 5.4 MeV α -particles, which is equal to $4.59 \times 10^{-8} \text{ cm}^2$, is much smaller

than the bio-effect cross section of $46.5 \times 10^{-8} \text{ cm}^2$ to be expected for heavy charged particles of $(\lambda\varrho)_{\text{ion}} = 0.0708 \mu\text{g}/\text{cm}^2$ according to [3]. The reason for this discrepancy is the fact that the range of α -particles at 5.4 MeV is much greater than the diameter of a chromatin fibre of about $4 \mu\text{g}/\text{cm}^2$ (30 nm at a mean density of $1.35 \text{ g}/\text{cm}^3$ [36]). Hence, for the α -particles, the chromatin fibre represents a very complex and heterogeneous target of high multiplicity with respect to DNA damage. In contrast, the 95% ionization range of electrons at an energy of 150 eV is about $0.5 \mu\text{g}/\text{cm}^2$ and, therefore, markedly smaller than the diameter of a chromatin fibre. In consequence, the target multiplicity for the electrons is strongly reduced despite the fact that, in liquid water, 150 eV electrons have the shortest mean free path length $(\lambda\varrho)_{\text{ion}}(T)$ as compared with electrons at other energies and, consequently, the highest value of the distribution function $F_2(T)$ or of the bio-effect cross section σ_B when considering electrons or X-rays according to (3).

Because of these facts, the measurement of the distribution of ionization clusters produced by ionizing particles in multiple targets consisting of several volumes, a few nm in size, could be used in the field of radiation protection to define measuring quantities which directly take into account radiation quality and are strongly related to radiation biophysics. As was shown in Sect. 4, such measurements could even be performed with gas-filled counters, due to the similarity of the cluster size distributions produced in nanometric targets of liquid water with those produced in targets of propane-based tissue-equivalent gas. Similar measurements would also be useful in the field of radiation therapy, for instance, to optimize the treatment of individual tumors with respect to radiation quality or to estimate the dependence of cell killing as a function of depth in the human body.

References

1. D.J. Brenner, J.F. Ward: *Int. J. Radiat. Biol.* **61**, 737 (1992)
2. H. Nikjoo, R.F. Martin, D.E. Charlton, M. Terrissol, S. Kandaiya, P. Lobachevsky: *Acta Oncol.* **35**, 849 (1996)
3. J.A. Simmons, D.E. Watt: *Radiation Protection Dosimetry: A Radical Reappraisal*, 1st edn. (Medical Physics Publishing, Madison, WI, USA 1999)
4. R. Blohm, D. Harder: *Radiat. Prot. Dosim.* **13**, 377 (1985)
5. D. Harder, R. Blohm, M. Kessler: *Radiat. Prot. Dosim.* **23**, 79 (1988)
6. E.R. Bartels, D. Harder: *Radiat. Prot. Dosim.* **31**, 211 (1990)
7. H.G. Paretzke, J.E. Turner, R.N. Hamm, R.H. Ritchie, H.A. Wright: *Radiat. Res.* **127**, 121 (1991)
8. V. Michalik: *Phys. Med. Biol.* **36**, 1001 (1991)
9. A.V. Lappa, E.A. Bigildeev, D.S. Burmistrov, O.N. Vasilyev: *Radiat. Environ. Biophys.* **32**, 1 (1993)
10. W.E. Wilson, H.G. Paretzke: *Radiat. Prot. Dosim.* **52**, 249 (1994)
11. E.A. Bigildeev, V. Michalik: *Radiat. Phys. Chem.* **47**, 197 (1996)
12. R.N. Hamm, J.E. Turner, H.A. Wright, R.H. Ritchie: *Radiat. Res.* **97**, 16 (1984)
13. H.G. Paretzke, D.T. Goodhead, I.G. Kaplan, M. Terrissol: 'Track Structure Quantities'. In: *Atomic and Molecular Data for Radiotherapy and Radiation Research*. IAEA-TECDOC-799 (IAEA, Vienna, Austria 1995) pp. 633–721

14. S.M. Pimblott, J.A. LaVerne, A. Mozumder: J. Phys. Chem. **100**, 8595 (1996)
15. B. Grosswendt, W.Y. Baek: 'Basic Physical Data in Organic Gases'. In: *Radiation Quality Assessment Based on Physical Radiation Interaction at Nanometer Level*. Report 161 ed. by P. Colautti (INFN-Laboratori Nazionali di Legnaro, Padova, Italy 2000) pp. 5–26
16. M. Dingfelder, D. Hantke, M. Inokuti, H.G. Paretzke: Radiat. Phys. Chem. **53**, 1 (1998)
17. B. Grosswendt, W.Y. Baek, A. Alkaa, A. Breskin, P. Colautti, R. Chechik, V. Conte, L. De Nardo, P. Ségur, S. Shchemelinin, G. Tornielli, J.Y. Tamboul, I.C. McDougall, D.E. Watt, S. Pszona, J. Kula, S. Marjanska: 'Ionisation-pattern Investigation in Nanometric Gas Volumes'. In: *Radiation Quality Assessment Based on Physical Radiation Interaction at Nanometer Level*. Report 161 ed. by P. Colautti (INFN-Laboratori Nazionali di Legnaro, Padova, Italy 2000) pp. 61–70
18. M.E. Rudd, Y.-K. Kim, D.H. Madison, J.W. Gallagher: Rev. Mod. Phys. **57**, 965 (1985)
19. M. Dingfelder, M. Inokuti, H.G. Paretzke: Radiat. Phys. Chem. **59**, 255 (2000)
20. ICRU: *Secondary Electron Spectra from Charged Particle Interactions*, Report 55 (ICRU, Bethesda, MD, USA 1996)
21. M.J. Berger, J.H. Hubbell: *XCOM: Photon Cross Sections on a Personal Computer*, Report NBSIR 87-3597 (National Bureau of Standards, Gaithersburg, MD, USA 1987)
22. Wm.J. Veigele: Atomic Data Tables **5**, 51 (1973)
23. ICRU: *Average Energy Required to Produce an Ion Pair*, Report 31 (ICRU, Washington, DC, USA 1979)
24. A. Alkaa, A. Breskin, P. Colautti, R. Chechik, V. Conte, L. De Nardo, P. Ségur, S. Shchemelinin, G. Tornielli: 'Detectors for Track-nanodosimetry'. In: *Radiation Quality Assessment Based on Physical Radiation Interaction at Nanometer Level*. Report 161 ed. by P. Colautti (INFN-Laboratori Nazionali di Legnaro, Padova, Italy 2000) pp. 27–40
25. J.Y. Tamboul, I.C. McDougall, D.E. Watt, S. Pszona, J. Kula, S. Marjanska: 'Nanometric Gas Counters'. In: *Radiation Quality Assessment Based on Physical Radiation Interaction at Nanometer Level*. Report 161 ed. by P. Colautti (INFN-Laboratori Nazionali di Legnaro, Padova, Italy 2000) pp. 41–60
26. ICRU: *Stopping Powers and Ranges for Protons and Alpha Particles*, Report 49 (ICRU, Bethesda, MD, USA 1993)
27. W.Y. Baek, B. Grosswendt: Radiat. Prot. Dosim. **52**, 97 (1994)
28. W. Hwang, Y.-K. Kim, M.E. Rudd: J. Chem. Phys. **104**, 2956 (1996)
29. B. Grosswendt, E. Waibel: Nucl. Instrum. and Meth. **155**, 145 (1978)
30. H.G. Paretzke: 'Radiation Track Structure Theory'. In: *Kinetics of Nonhomogeneous Processes*. ed. by G.R. Freeman (Wiley-Interscience Publication, John Wiley & Sons, New York, Chichester, Brisbane, Toronto, Singapore 1987) pp. 89–170
31. B. Grosswendt: 'Low-energy Electron Transport Using the Monte Carlo Method'. In: *Use of MCNP in Radiation Protection and Dosimetry, Training Course at Bologna, Italy, May 13–16, 1996*, ed. by G. Gualdrini, L. Casalini (ENEA, Bologna 1998) pp. 201–229
32. G.J. Kutcher, A.E.S. Green: Radiat. Res. **67**, 408 (1976)
33. D.J. Brenner, M. Zaider, Phys. Med. Biol. **29**, 443 (1983)
34. B. Grosswendt: Radiat. Environ. Biophys. **38**, 147 (1999)
35. J.H. Hubbell: Radiat. Res. **70**, 58 (1977)
36. W. Friedland, P. Jacob, H.G. Paretzke, T. Stork: Radiat. Res. **150**, 170 (1998)

Track Structure in Molecular Radiation Biology

H. Nikjoo¹, S. Uehara², I.K. Khvostunov³, and F.A. Cucinotta⁴

¹ MRC Radiation and Genome Stability Unit, Harwell, OX11 0RD, UK

² School of Health Sciences, Kyushu University, Fukuoka, Japan

³ Medical Radiological Research Centre, Obninsk, Russia

⁴ NASA Johnson Space Center, Houston Texas 77058, USA

1 Introduction

The initial physical structure of charged particle tracks plays an important role in understanding the basic mechanism of radiation action on biological material. To date, there are a number of Monte Carlo electron and ion track structure codes which have been developed independently to investigate the microscopic features of ionising radiation, the ensuing chemical pathways and the molecular nature of the damage in biomolecular targets. The paper reviews the essential input data for simulation of ionising particles and recent advances including development of new cross sections for energetic electrons and ions in water and extension of track-segment simulation to lower energies below Bragg-peak. The paper presents two examples of application of track structure in biophysical studies of ionising radiation.

2 Data Base for Electron Cross Sections in Water

2.1 Ionization

The experimental ionization cross sections are shown in Fig. 1a) for water in the energy range 10 eV to 10 keV. Experimental ionization cross sections included in the analysis were those given in absolute scale by Hayashi [1], Djuric *et al.* [2], Olivero *et al.* [3], Bolorizadeh and Rudd [4], and Schutten *et al.* [5]. Although there exists close agreement between some of the measurements of ionization cross sections over part of the energy spectrum, there is considerable variation in the range 50 eV to 1 keV. The experimental data shown in Fig. 1 were least square fitted (shown by a solid line), using the function

$$\sigma_{\text{exp}} = f + at^d e^{-(bt+ct^2)} \quad (1)$$

and

$$t = \frac{\ln T}{15} \quad (2)$$

where σ is in 10^{-16} cm^2 and T , the particle kinetic energy, is in eV. The fitting parameters are shown in Tab. 1. The single differential cross sections for ejection of an electron generated by the collision of the primary electron with water can

be described by various theoretical treatments. These include Born and Bethe [6], Jain and Khare [7], Gryzinski [8], Kim and Rudd [9], Vriens [10], Dingfelder [11]. Figure 1b) shows the calculated total ionization cross sections in the range 10 eV to 10 keV primary electron energy. The dipole oscillator strength for water vapour given by Berkowitz [12], and the partial photoelectric cross section given by Uehara and Nikjoo [13], used in the evaluations of equations given by Born-Bethe and Jain-Khare. The fitted experimental data (solid line) (obtained in Fig. 1a) and data of the code *KURBUC* [14] are shown for comparison. A summary of cross sections used by various codes can be found in Nikjoo *et al.* [15].

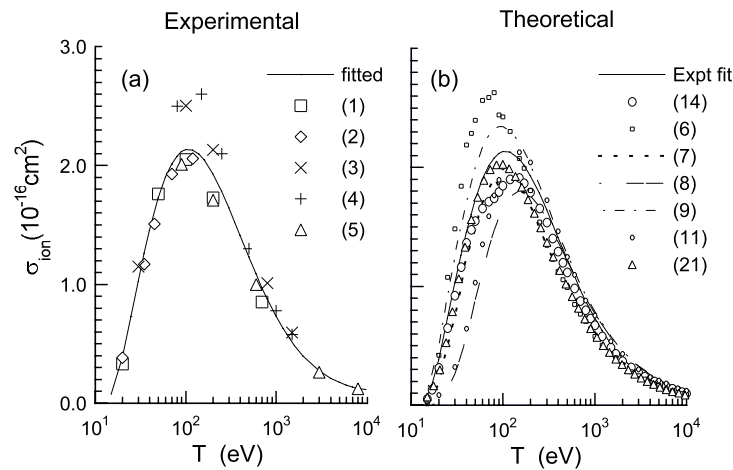


Fig. 1. Experimental and calculated ionization cross sections as a function of electron energy. The solid line is the least square fit to all experimental data shown in the figure

2.2 Excitation

There are very few experimental excitation cross sections reported in the literature and these are fragmentary. We use the compiled data by Paretzke [16], Olivero *et al.* [3] and Zaider *et al.* [17] which encompass almost all major excitation modes. These authors used a combination of model functions and the equation of Green and Stolarski [18] to obtain the fitting parameters for the individual excitation states. A summary of analytical functions for excitation cross section used is given Uehara *et al.* [19]. Total excitation cross section was obtained by summing up all the individual cross sections. Figure 2a) shows the total excitation cross section for electrons in the range of 10 eV to 10 keV. The differences observed arise from the differences in the theoretical treatment and the experimental data used. For the purposes of comparison, the excitation cross sections for liquid water as used in the codes OREC [20] and CPAT [21] and

calculated in a recent calculations by Dingfelder *et al.* [11] is also included. The total excitation cross section used in *KURBUC* was obtained by summing all the 10 mode of excited states using the empirical formula of Berger and Wang [22]. These data were then fitted by a function in the form

$$\sigma_{excit} = a + bx + cx^2 + dx^f e^{-gx} \quad (3)$$

where $x=\log(t)$. The fitting parameters are given in the Tab. 1.

Table 1.

Cross-section	Ionization	Excitation	Elastic	Elastic
Function	σ_t^{exp}	σ_{excit}	σ_{ela}	σ_{ela}
			(10eV<T<120eV)	(120eV<T<10keV)
a	2.07201	0.01608355	-667.2442	27.45452
b	0.271302	2.875443	949.465	-9.232332
c	0.119638	11.5376	-507.5807	1.056612
d	1.46521	-0.4113672	131.2099	-0.04093413
f	0.074664	0.1302236	-16.58025	—
g	—	—	0.8234437	—

2.3 Elastic Scattering

In a similar manner as adopted in Fig. 1a), a least square fitted cross section for elastic scattering, including both experimental and theoretical data, was compared with calculations by Moliere's formula which is adopted in the codes *KURBUC*. Experimental elastic scattering cross sections included in the analysis were those of Shyn and Cho [23], Katase *et al.* [24], Hayashi [1], Nishimura [25] and Danjo and Nishimura [26]. Theoretical cross sections used in the analysis were obtained by a linear combination of composite atoms, i.e. $2\sigma_H + \sigma_O$. Using these six sets of data, a fitted cross section (in units of 10^{-16} cm^2) was obtained by a polynomial function of the form

$$\sigma_{ela} = \sum a_i (\ln T)^{i-1} \quad (4)$$

where a_i are the parameters a to g listed in Tab. 1 and $i=1, \dots, 6$. The parameters of the fitting function are presented in Tab. 1. The experimental, theoretical and the fitted excitation cross sections are shown in Fig. 2. Solid lines represent the least squares fit to all experimental data.

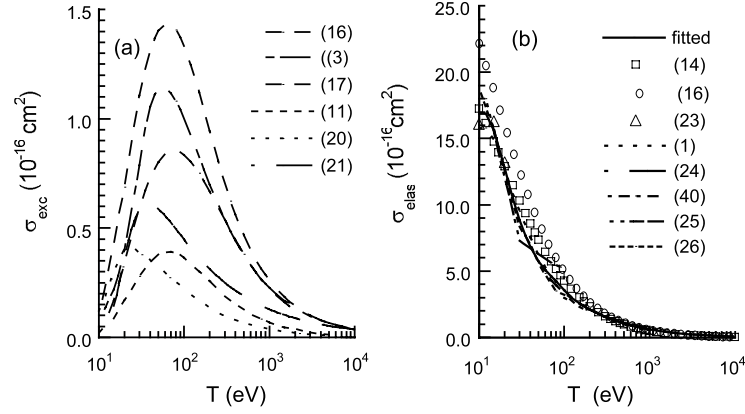


Fig. 2. Excitation and Elastic scattering cross sections as a function of energy

3 Track Structure of Low Energy Protons

As charged particles pass through matter they lose energy primarily through collisions with bound electrons. For fast protons, the majority of energy is transferred in ionising collisions, resulting in energetic free electrons and the potential energy of residual ions. A summary of these interactions are presented in Tab. 2.

Table 2.

Interactions	Proton	Neutral Hydrogen
Elastic scattering	$p + H_2O \rightarrow p' + H_2O$	$H + H_2O \rightarrow H' + H_2O$
Target Ionization	$p + H_2O \rightarrow p' + H_2O^+ + e$	$H + H_2O \rightarrow H' + H_2O^+ + e$
Target Excitation	$p + H_2O \rightarrow p' + H_2O^*$	$H + H_2O \rightarrow H' + H_2O^*$
Electron Capture	$p + H_2O \rightarrow H' + H_2O^+$	—
Electron loss	—	$H + H_2O \rightarrow p' + e + H_2O$

Total ionisation cross sections for proton and neutral hydrogen impact were obtained from experimental data for water vapour [27]. As fast protons slow-down, interactions involving electron capture and loss by the moving protons become an increasingly important component of the energy loss process. For incident protons with speeds comparable to or lower than the orbital speeds of the bound electrons in the target, the capture of electrons from the target is a significant mechanism for ionisation of the target but does not produce secondary electrons. After the charge transfer process the neutral hydrogen atom becomes either stripped or ionises a water molecule. In the first case, a proton and an excited water molecule remain, an electron is ejected in forward direction with

nearly the same velocity as the proton. In the latter case, the neutral hydrogen, an ionised water molecule and an ejected electron with a similar distribution of electron energy and ejection angle as for protons result. The electron capture and loss cross sections were obtained using previously published models fitted experimental data [28].

There are no experiments on excitation cross sections for proton and neutral hydrogen impact for water vapour. We adopted the semi-empirical model developed by Miller and Green [29], which is based on the electron impact excitation. Generally, high-energy protons proceed along a straight-line trajectory. However, the effects of elastic nuclear collisions will also become more prominent in the low energy region. Elastic collisions that transfer little or no energy but might have a notable effect on the spatial character of the track structure at very low energies. Elastic scattering cross sections were evaluated using the classical-mechanics trajectory calculations assuming Coulomb potentials with screening functions.

Analytical calculations of nuclear and electronic stopping cross sections were performed using the cross sections and mean energy loss per collision data. Figure 3 shows the calculated stopping cross sections of water vapour in comparison with the published data [30,31]. A more comprehensive derivation of all cross sections can be found in Uehara *et al.* 2000 [32].

4 Model Applications

4.1 Response of a TEPC Counter

High energy protons and heavy ions have distinct advantage for use in radiotherapy and radiobiological experiments. On the other hand, the solar energetic particles such as protons and galactic cosmic radiation (GCR) which contain heavy nuclei are the main source of risk to astronauts in long term flights. Use of heavy charged particles for therapy is advantageous over the conventional methods because of long range, high-LET, high dose-depth distribution and increase in density of energy deposition with increasing penetration giving high values of RBE at the end of the particle track. For practical situations, in therapy or in risk estimation from exposure to ionising radiation, one needs to measure the absorbed dose. TEPC is a device which can be used for this purpose.

Tissue Equivalent Proportional Counter (TEPC) is the principle instrument for measuring the distribution of energy deposited in a specific volume. The instrument is commonly designed as a spherical or a cylindrical volume with varying sensitive volume. The principle feature of the instrument is based on the similarity between the energy loss in the solid wall and the gas cavity as these are made of equivalent density material. Figure 4 shows the distribution of mean events size and the lineal energy as a function of impact parameter b normalised by the radius of the sensitive volume. The parameter b (the eccentricity) is the distance from the centre of the cavity to the chord of the ion cutting the sphere and R_{sv} is the radius of the counter. Distribution of Mean event size

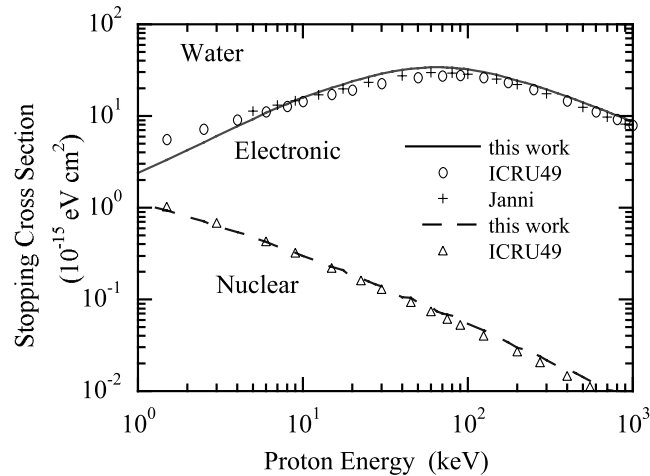


Fig. 3. Electronic and nuclear stopping cross sections for water as a function of proton energy

were simulated for 1 MeV protons generated by the code PITS [33] through a wall-less counter 0.01 μm diameter. The walled counter calculations were made in a TEPC 1 μm diameter. The data shows the edge effect of the wall of the counter. The small peak shown indicates the small contribution of the secondary electrons generated in the wall of the counter to the detector response.

4.2 Data Base for Energy Deposition in Molecular Targets

Relevant biological effects of radiation are mostly due to damage to individual cells. Assuming DNA is the target for ionising radiation, then understanding of the mechanism of radiation damage requires a knowledge of the spatial distribution of energy deposition by the track at sub-cellular structures such as DNA and chromatin. Therefore these distributions must be considered if we are seeking either practical quantities for comparison of radiation of different quality in radiation protection or therapy, or if we are seeking fundamental understanding of the mechanism of radiation action. We have compiled an extensive data-base of energy deposition at DNA and higher order molecular structures by electrons, protons, alpha-particles and selected heavy ions. These studies have been used in variety of ways to seek quantities of energy deposition that correlate with observed biological effectiveness of radiations of different qualities [34–36]. Alternatively, these studies provide a detailed analysis in which the energy is deposited inside a target. These energy distributions along with the distribution of reaction site by reactive radical species with DNA have provided a means of obtaining patterns of the initial DNA damage by ionising radiations [37,38]. Figure 5 shows comparison of distribution of absolute frequency of energy depositions in a cylindrical volume of dimensions similar to DNA and a chromatin.

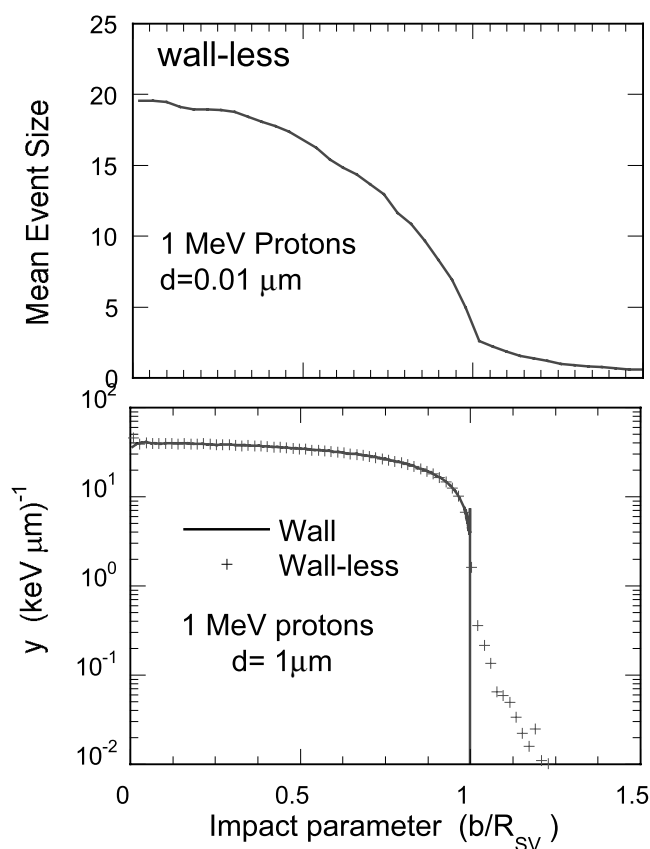


Fig. 4. Energy deposition in simulated wall and wall-less proportional for site diameters $0.01 \mu\text{m}$ and $1 \mu\text{m}$ counters

Such calculations are very cpu time consuming which makes them practically prohibitive in many situations. Recently Cucinotta *et al.* [39] developed a deterministic approach to obtain these distributions which are needed especially for energetic heavy ions in space radiation risk determination. Table 3 shows a summary of data for frequency-averaged specific energy and dose-averaged frequency for selected energies of electrons, protons, alpha-particles and heavy ions.

5 Conclusions

The Monte Carlo track structure method provides a powerful tool to obtain information on the basic mechanisms of radiation action in mammalian cells where experimental methods at sub-cellular levels lack the required resolutions. It has provided insight into the patterns of initial DNA damage by ionising radiations of different qualities which can be served as a guide in the design and

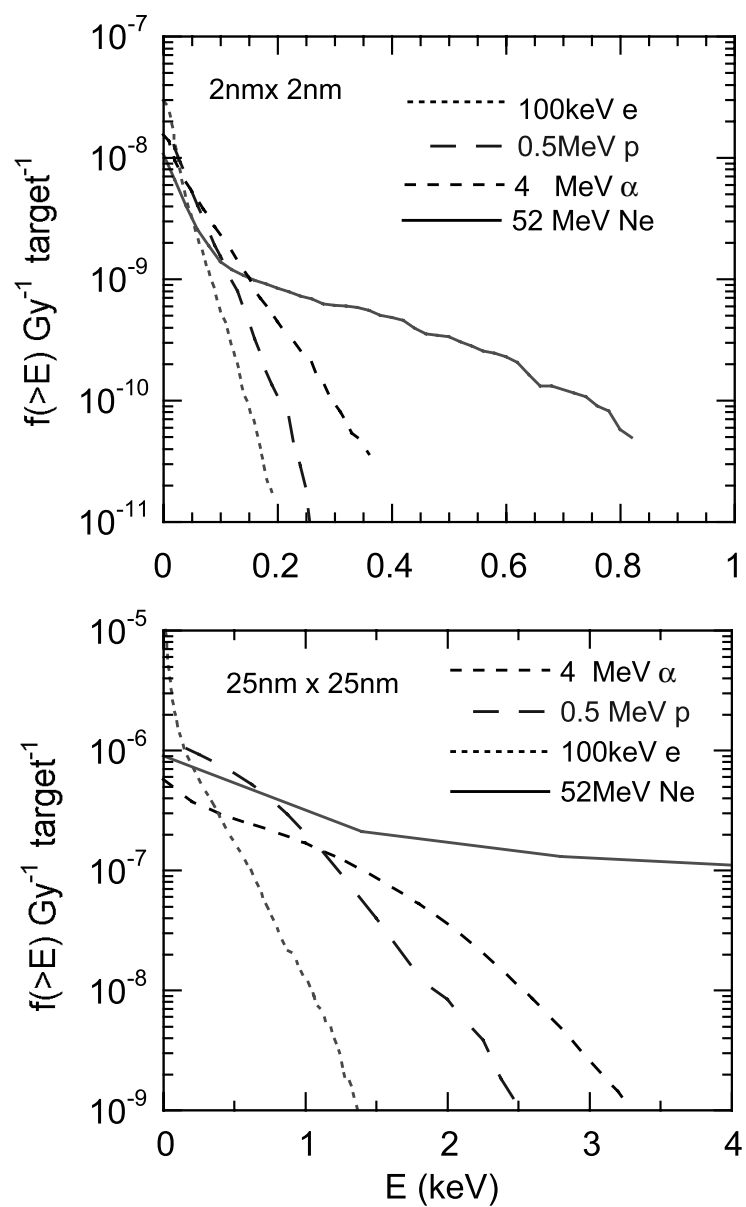


Fig. 5. Frequency distribution of energy deposition in target corresponding in size to a volume of DNA and a segment of chromatin in water irradiated with 1 Gy of a given radiation

development of experiments such as those in the investigation of the nature of molecular damage in the cell and in the measurement of dose and the spectra of radiations of different qualities.

Table 3. \bar{Z}_D data taken from reference [39]

Particle	LET (KeV/ μ m)	Energy (MeV/u)	\bar{Z}_F (kGy)	\bar{Z}_D (kGy)
Electron	—	0.001	830	1500
Electron	—	0.100	630	1310
Proton	8.8	4	650	1300
Proton	16.0	2	710	1390
Proton	25.8	1	750	1580
^4He	32.2	5	720	1480
^4He	40.3	4	780	1550
^4He	61.4	2	930	1800
^4He	103.0	1	1090	2260

6 Acknowledgements

The authors wish to thank Alex Wingent and Anne Johnson for help with preparation of the manuscript. This work was partially supported by the European Community programme FIGHT-CT-1999-00005.

References

1. M. Hayashi: IAEA-TECDOC-506, 194-200 (1989)
2. N. Lj Djuric, I.M. Cadez, M.V. Kurepa: Int. J. Mass Spectrum Ion Proc. **83**, R7 (1988)
3. J.J. Olivero, R.W. Stagat, A.E.S. Green: J. Geophys. Res. **77**, 4797 (1972)
4. M.A. Bolorizadeh, M.E. Rudd: Phys. Rev. A **33**, 882 (1986)
5. J. Schutten, F.J. de Heer, H.R. Moustafa, A.J.H. Boerboom, J. Kistemaker: J. Chem. Phys. **44**, 3924 (1966)
6. M. Inokuti: Rev. Mod. Phys. **43**, 297 (1971)
7. D.K. Jain, S.P. Khare: J. Phys. **B9**, 1429 (1976)
8. M. Gryzinski: Phys. Rev. **138**, A336 (1965)
9. Y.K. Kim, M.E. Rudd: Phys. Rev. **A50**, 3954 (1994)
10. L. Vriens: Proc. Phys. Soc. **89**, 13 (1966)
11. M. Dingfelder, D. Hantke, M. Inokuti, H.G. Paretzke: Radiat. Phys. Chem. **53**, 1 (1998)
12. J. Berkowitz: *Photoabsorption, photoionisation and photoelectron spectroscopy* (Academic Press, New York, 1979)
13. S. Uehara, H. Nikjoo: Radiat. Environ. Biophys. **35**, 153 (1996)
14. S. Uehara, H. Nikjoo, D.T. Goodhead: Phys. Med. Biol. **38**, 1841 (1993)
15. H. Nikjoo, S. Uehara, W.E. Wilson, M. Hoshi, D.T. Goodhead: Int.J.Radiat.Biol. **73**, 355 (1998)

16. H.G. Paretzke: 'Radiation track structure theory'. In *Kinetics of Nonhomogeneous Processes*. ed. by G.R. Freeman (John Wiley and Sons, New York 1987) pp. 89–170
17. M. Zaider, D.J. Brenner, W.E. Wilson: *Radiat. Res.* **95**, 231 (1983)
18. A.E.S. Green, R.S. Stolarski: *J. Atm Terr. Phys.* **34**, 1703 (1972)
19. S. Uehara, H. Nikjoo, D.T. Goodhead: *Radiat. Res.* **152**, 202 (1999)
20. R. N. Hamm, J.E. Turner, R.H. Ritchie, H.A. Wright: *Radiat. Res.* **104**, S20 (1985)
21. M. Terrissol: *Int. J. Radiat. Biol.* **66**, 447 (1994)
22. M. Berger, R. Wang: 'Multiple scattering angular deflections and energy-loss straggling'. In *Monte Carlo transport of Electrons and Photons*. ed. by T.M. Jenkins, W.R. Nelson and A. Rindi (Plenum Press, New York 1988) pp. 21–56
23. T.W. Shyn, S.Y. Cho: *Phys. Rev. A* **36**, 5138 (1987)
24. A. Katase, K. Ishibashi, Y. Matsumoto, T. Sakae, S. Maezono, E. Murakami, K. Watanabe, H. Maki: *J. Phys. B* **19**, 2715 (1986)
25. H. Nishimura: 'Elastic scattering cross-sections of H₂O by low energy electrons'. In *Electronic and Atomic Collisions, Proc. XIth Int. Conf.* ed. by N. Oda and K. Takayanagi (North-Holland, Amsterdam 1979) p. 314
26. A. Danjo, H. Nishimura: *J. Phys. Soc. Jpn.* **54**, 1224 (1985)
27. M.E. Rudd, T.V. Goffe, R.D. DuBois, L.H. Toburen: *Phys. Rev. A* **31**, 492 (1985)
28. L.H. Toburen, M.Y. Nakai, R.A. Langley, *Phys. Rev.* **171**, 114 (1968)
29. J.H. Miller, A.E.S. Green: *Radiat. Res.* **54**, 343 (1973)
30. ICRU Report 49, International Commission of Radiation Units and Measurements, Bethesda, MD (1993)
31. J.F. Janni: *At. Data Nucl. Data Tables* **27**, 147 (1982)
32. S. Uehara, L.H. Toburen, W.E. Wilson, D.T. Goodhead, H. Nikjoo: *Radiat. Phys Chem.* **59**, 1 (2000)
33. W.E. Wilson, H. Nikjoo: *Radiat. Environ. Biophys.* **38**, 97 (1999)
34. D.E. Charlton, D.T. Goodhead, W.E. Wilson, H.G. Paretzke: *Radiat. Prot. Dosim.* **13**, 123 (1985)
35. H. Nikjoo, D.T. Goodhead, D.E. Charlton, H.G. Paretzke: *Phys. Med. Biol.* **34**, 691 (1989)
36. H. Nikjoo, D.T. Goodhead, D.E. Charlton, H.G. Paretzke: *Int. J. Radiat. Biol.* **60**, 739 (1991)
37. H. Nikjoo, P. O'Neill, D.T. Goodhead, M. Terrissol: *Int. J. Radiat. Biol.* **71**, 467 (1997)
38. H. Nikjoo, P. O'Neill, M. Terrissol, D.T. Goodhead, *Radiat. Environ. Biophys.* **38**, 31 (1999)
39. F.A. Cucinotta, H. Nikjoo, D.T. Goodhead: *Radiat. Res.* **153**, 459 (2000)
40. *Elastic-electron-scattering cross section database*. NIST standard reference database no. 64. (US Dept. of Commerce, Gaithersburg 1996)

Analogue Monte Carlo to Model Radiation-Induced DNA Damage

M. Terrissol and J. M. Vrigneaud

CPAT Université Paul Sabatier, 118, Route de Narbonne, F-31062 Toulouse, cedex 4, France

1 Introduction

Radiation induced DNA damage is dependent on the inchoative distributions of direct ionisations and excitations, and of the indirect action of all species and radicals created or set in motion at early times within a few angstroms distance. These distributions are used to initiate the physico-chemical, chemical and biological stages, with reactions, attacks, repair, non-repair, . . . So, a simple target model like a small piece of DNA cannot be considered as an homogeneous medium but as a composite one with

- i) DNA structure with nucleotides, bases, sugar and phosphate,
- ii) hydration shell tightly bound, and
- iii) surrounding bulk water where active species and radicals are created.

2 Mean Free Paths and Target Dimensions

With impinging electrons, the great majority of secondary ones are created with energies much lower than 1 keV. If one irradiates DNA with X-rays, in addition to the photoelectron, a low energy Auger electron spectrum is set in motion: from a few eV to about 2 keV for the KXX phosphorus case. The ranges of secondary or Auger electrons and fluorescence X-rays are of order of magnitude of these fundamental biological targets. Moreover, their mean free paths are sometimes lower than the distances between two neighbouring molecules of water or two neighbouring atoms of a nucleotide. If we take the case of one 500 eV electron slowing down in liquid water, its mean free path is about 10 angstroms and then about 30 percent of sampled exponential paths will be smaller than interatomic distances, leading for instance to have several events on the same atom!

3 DNA Damage

The action of radiation on DNA can be quantified by scoring of single strand break (SSB) and double ones (DSB) more or less complex. Guided by literature [1], we used the following:

- Ionisations in sugar phosphate group: creation of a SSB

- Bases ionisations : transfer on Guanine
- Other inelastic event on bases: base damage
- Hydration shell ionisations :
 - linked to bases, go to bases (G)
 - linked to sugar phosphate: 60% give one SSB and 40% go to bulk
- Events in bulk water :
 - creation of species e-aq, OH., H., H₃O+, H₂O₂, ...
 - diffusions and reactions up to 10⁻⁶ second, attack on DNA gives a SSB
- 2 SSB within 10 basepairs give one DSB.

So to model the action of radiation at the chromatin fibre and DNA levels we have to describe the complete transport of low energy -say 0...2 keV- electrons and photons, and to model the ensuing chemistry up to 10⁻⁶ second. To build an analogue Monte Carlo transport we need total and differential cross sections of all possible events and they are not yet known! Only now becomes available, say down to tens of eV, liquid water total and differential cross sections. The hydration shell structure being quasi crystalline, one can use some existing data on ice [2]. Some rare data exist for nucleotides [3], but since many experiments have shown the similarity of comportment with water, that missing cross sections can be replaced by those of liquid water. When we do not know the total interaction cross section for a biological molecule, we use the fact that macroscopic mean free paths are quite identical with those of liquid water [4] to recalculate for each atom of that molecule a cross section weighted by its Van der Waals radius. So, if $\sigma_W(E)$ is the interaction cross section of a liquid water molecule for an electron of energy E, A_W and A_M the molecular weight of the water and the concerned molecule M, R_i the Van der Waals radius of atom i of that molecule M, then the cross section $\sigma_{M_i}(E)$ of that atom is evaluated by:

$$\sigma_{M_i}(E) = \frac{A_M R_i \sigma_W(E)}{A_W \sum R_i} \quad (1)$$

where the summation runs over all atoms of the molecule M. For this atom if individual and/or differential cross sections are not known, those of liquid water [5] are taken.

4 Transport in Heterogeneous Medium

To sample the path lengths in the composite medium (see Fig. 1), we first determine each distance to a boundary between two media. S_j is the partial distance travelled in the j^{th} medium and S the total distance travelled. In the case of a homogeneous medium composed of n_j targets of type j per unit volume, σ_{τ_j} being their total cross section, then we used a macroscopic cross section Σ_j , defined as:

$$\Sigma_j = n_j \sigma_{\tau_j} \quad (2)$$

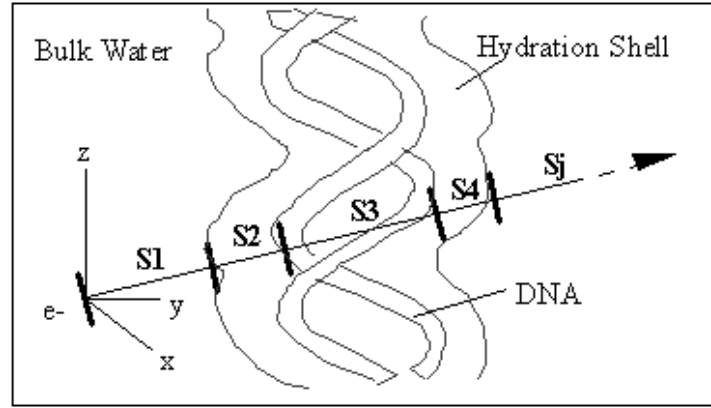


Fig. 1. Modelling of the electron transport through the DNA helix

For a heterogeneous medium, we considered an arbitrary volume around the path containing n_j atoms or molecules with total cross section σ_{k_j} then

$$\Sigma_j = \sum_{k=1}^{n_j} \sigma_{k_j} \quad (3)$$

If ξ is a uniform random number between 0 and 1, then the m^{th} medium was determined such as:

$$\sum_{j=1}^{m-1} (\Sigma_j S_j) \leq -\log \xi < \sum_{j=1}^m (\Sigma_j S_j) \quad (4)$$

it gives the path

$$S = \sum_{j=1}^{m-1} S_j - \frac{\sum_{j=1}^{m-1} \Sigma_j S_j + \log \xi}{\Sigma_m} \quad (5)$$

with $\sum S_j = 0$ for $j = 1$, and the electron interacts with the closest atom or molecule of its new sampled position.

The DNA helix plus its hydration shell is considered as a set of n_j independent targets with cross section σ_{T_j} , the sampled path S is the path from the origin to the first target with distance d_j between this target and the direction of travel such that:

$$d_j^2 \leq \frac{\sigma_{T_j}}{\pi} \quad (6)$$

and the interaction is modelled with this atom or molecule.

The method is efficient when the number of targets (atoms or molecules) is rather low, about say 200. So to model the transport in the chromatin (Fig. 2), we developed a three-steps sampling, based on the same scheme :

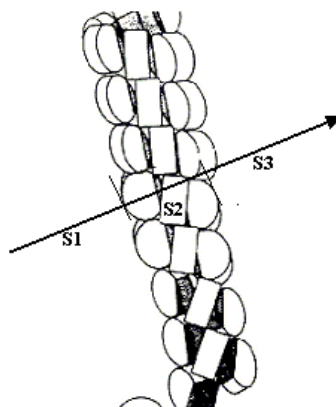


Fig. 2. Selection of a nucleosome

1. for all nucleosomes of the considered fibre, we calculated their macroscopic cross-sections, and applying the same method to their barycentre, one nucleosome is selected among about 50,
2. for each nucleotide of the selected nucleosome (about 300 elements of Adenine, Guanine, Cytosine and Thymine per nucleosome) macroscopic cross-sections are calculated and a nucleotide is sampled. If the sampled path falls inside the histone's region (S3 on Fig. 3), the region is considered as passive bulk water with histone density: energy absorption but no effect and no chemistry. Regarding the possible overlap of nucleotides, 6 nucleotides around the selected one and their attached waters are taken into account and then,
3. all their atoms or molecules are considered (about 220 targets for 7 nucleotides) to find the interaction target. Then the type of interaction is sampled according to the total cross-sections, energy loss and deviations according to differential ones and eventual damages scored.

All events in the bulk water create species and radicals: e^-_{aq} , OH^\cdot , H^\cdot , H_3O^+ , H_2O_2 , \dots . Their behaviour is simulated with a Smoluchowski diffusion controlled scheme. All OH radical reactions with nucleotides give a SSB.

This method can be used to sample down to tens of eV and has been successfully used to model damage induced by ultra soft X-rays [6], or Auger emitters incorporated to the DNA molecule. But the limits of validity are reached, and at this level, interactions could not be longer considered binary and now we will need to incorporate quantum dynamics and/or quantum chemistry modelling. All other details to build targets, simulate the transport or modelling the chemistry can be found in [7].

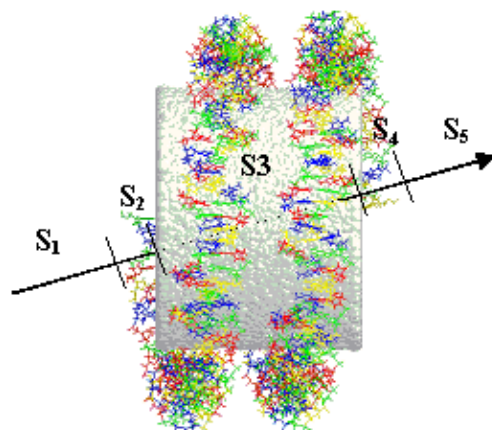


Fig. 3. Selection of nucleotides

5 Acknowledgment

This work was supported by the European Community under contract 'Biophysical Models for the Induction of Cancer by Radiation'.

References

1. C. Von Sonntag: *The chemical basis of Radiation Biology* (Taylor and Francis, London 1987)
2. M. Michaud, L. Sanche: Phys. Rev. A **36**, 4672 (1987)
3. D. Inagaki et al.: J. Chem. Phys. **61**, 4246 (1974)
4. A. La Verne, S. Pimblott: Rad. Res. **141**, 208 (1995)
5. M. Dingfelder et al.: Radiat. Phys. Chem. **70**, 53? (1998)
6. M. Terrissol, J.M. Vrigneaud: 'Modelling Ultrasoft X-rays Effects on DNA'. These proceedings p. 279
7. J.M. Vrigneaud: *Modele Biophysique pour L'Evaluation des Dommages Radio-Induits dans la Fibre Chromosomique*. PhD Thesis (University Paul Sabatier, Toulouse, France, July 2000)

Basic Data for Track Structure Simulations: Electron Interaction Cross-Sections in Liquid Water

M. Dingfelder^{1,2} and W. Friedland¹

¹ GSF–National Research Center for Health and Environment, Institute of Radiation Protection, Ingolstädter Landstraße 1, D–85764 Neuherberg, Germany

² Universitat de Barcelona, Facultat de Física, Departament d'Estructura i Constituents de la Matèria, Diagonal, 647, E–08028 Barcelona, Spain

Abstract. A model for the dielectric response function of liquid water is presented. Interaction cross sections are deduced within the framework of a Born approximation and compared with water vapour calculations. The liquid water cross sections are implemented in the biophysical simulation code PARTRAC. Electron tracks are simulated for different starting energies. Track-lengths are calculated, as well as radial energy depositions for the vapour and the liquid phase.

1 Introduction

Monte Carlo track structure simulation uses the classical trajectory picture and follows the incident particle, as well as all produced secondary particles, from starting (MeV) or ejection energies down to total stopping (a few eV), by processing elastic and inelastic scattering events. This kind of simulation requires reliable cross sections for interaction of radiation with atoms and molecules of the material under study. In the biological cell of soft tissue, water is the dominant component and is largely in the liquid state. Electron cross sections are of special interest because electrons are generated as secondary particles by all kinds of primary radiation.

In the past most of the older simulation codes use water in the vapour phase as a transport medium because there is a good experimental data base for water vapour, while there is only scarce experimental information on liquid water. Most of the existing simulation codes used the concept of the inverse mean free path (IMFP). Theoretically, within the framework of standard perturbation theory, these cross sections are based on the dielectric response of the material under consideration. Indeed, this method allows us to account for the liquid phase of water and to include pertinent information on the different phases of water.

In this paper a short summary on the deviation of the interaction cross sections of electrons in liquid water is presented, followed by a description of some modules of the simulation program PARTRAC. Finally, some applications are given to show how information from the simulation can be used.

2 Interaction Cross Sections

Interaction cross sections are calculated within the framework of the Born approximation in the non relativistic case and within the framework of the Bethe approximation in the relativistic case. Both approximations are first-order perturbation theories and are valid for incident electron energies T much larger than the binding energies E_j of the atoms or molecules under consideration, $T \gg E_j$. For low incident electron energies, corrections have to be introduced which account for higher order effects. Furthermore, in the case of electron impact, the indistinguishability of the incoming and target electron has to be considered.

In the Born- or Bethe approximation, cross sections depend on the energy loss function $\eta_2(E, K)$. Here E is the energy transfer and $\hbar K$ the momentum transfer. The energy loss function is related to the dielectric response function: $\eta_2(E, K) = \text{Im}(-1/\varepsilon(E, K))$. Therefore, we model the dielectric response function and fit it to available experimental information.

2.1 Dielectric Response Function

As described in a previous work [1], the imaginary part of the dielectric response function $\varepsilon_2(E, 0)$ is modelled in the optical limit ($K = 0$) by representing each excitation level by a derivative Drude function and each ionization shell by a Drude function truncated and smeared out at the ionization threshold. Different parameters are the excitation and ionization energies E_j , widths γ_j and heights (oscillator strengths) f_j , and in the case of ionization there is additionally the width of the smear out Δ_j . The real part of the dielectric response function $\varepsilon_1(E, 0)$ is then calculated using the Kramers-Kronig relations, which can be done analytically in this case. The momentum dependence is added in the sense of an impulse approximation. A detailed description can be found in [1].

2.2 Liquid Water

Our model for liquid water considers five excitation levels (two electronic excitations \tilde{A}_1B^1 and \tilde{B}_1A^1 , two Rydberg series states, Ryd A+B and Ryd C+D, and diffuse bands; no collective excitation is considered) and five ionization shells called $1b_1$, $3a_1$, $1b_2$, $2a_1$ and the K-shell.

ε_2 was fitted to the optical reflectance data obtained by Heller and co-workers about 25 years ago [2], which is (to the present) the only available experimental information on the dielectric response of liquid water. The dielectric response function as well as the energy loss function fulfills all important sum rules, the mean excitation value yields $I = 81.6$ eV, which is close to the recent experimental value, 79.75 ± 0.5 eV [3].

The parameters used for the different excitation levels of liquid water are given in Tab. 1 of [1], those for the ionization shells are displayed in Tab. 1. This table should substitute Tab. 2 of [1]. Please note, that the f_j values differ from those given in Tab. 2 of [1] by a factor of $1/(2\Delta_j)$, which arises from

the now correct normalization of the $d\Omega$ integration (see Eq. (15) of [1]), and an additional factor of around 1.035, which arises from a numerical inaccuracy in the integration routines used before. The dimension of f_j , energy^{-1} , is now correct, in order to cancel the dimension of energy coming from the $d\Omega$ integration.

Table 1. Parameters used for the ionization shells of the dielectric response function in liquid water

j	shells	E_j^{ion} (eV)	E_j (eV)	γ_j (eV)	Δ_j (eV)	f_j (eV) $^{-1}$	% sum rule
1	1b ₁	10.79	11.95	12.50	1.16	0.1516	22.50
2	3a ₁	13.39	14.70	16.10	1.31	0.1222	20.62
3	1b ₂	16.05	16.60	19.40	0.55	0.2253	16.11
4	2a ₁	32.30	33.30	95.00	1.00	0.0826	12.08
5	K-shell	539.00	540.00	220.00	1.00	0.1608	17.87

This dielectric response function was also used to calculate inelastic interaction cross sections for energetic protons in liquid water [4].

Very recently a new measurement using inelastic x-ray scattering has become available [5]. Hayashi et al. measured the energy loss function of liquid water in an energy range from 0 to approximately 100 eV at very low momentum transfer (approximately zero). This new measurement looks promising to improve our cross sections, but we possibly have to refine our parameters and perhaps our models. The same group also recently published measurements of the Bethe surface of liquid water [6], i. e., the energy loss function at momentum transfers (much) larger than zero. In general, a theoretical Bethe surface calculated with our model [7], showed no alarming discrepancy to the newly available data.

2.3 Mean Free Path

As already stated, interaction cross sections for the different ionization shells and excitation levels are calculated within the framework of the Born-approximation. Electron exchange effects are considered and relativistic energies treated in the Bethe approach. At low incident energies (below 500 eV) empirical correction factors are added which account for the invalidity of perturbation theory at these low energies and which are obtained from water vapour data. Elastic scattering cross sections are calculated using semi-empirical models and are corrected for properties of the liquid phase. Total cross sections are used to determine the distance to the next collision and to determine the type of interaction (excitation level or ionization shell or elastic scattering), while energy differential cross sections are used to determine the energy transfer in the case of inelastic events. The angular distributions of the secondary electron emission spectra are calculated using semi-empirical models based on experimental data of the vapour phase.

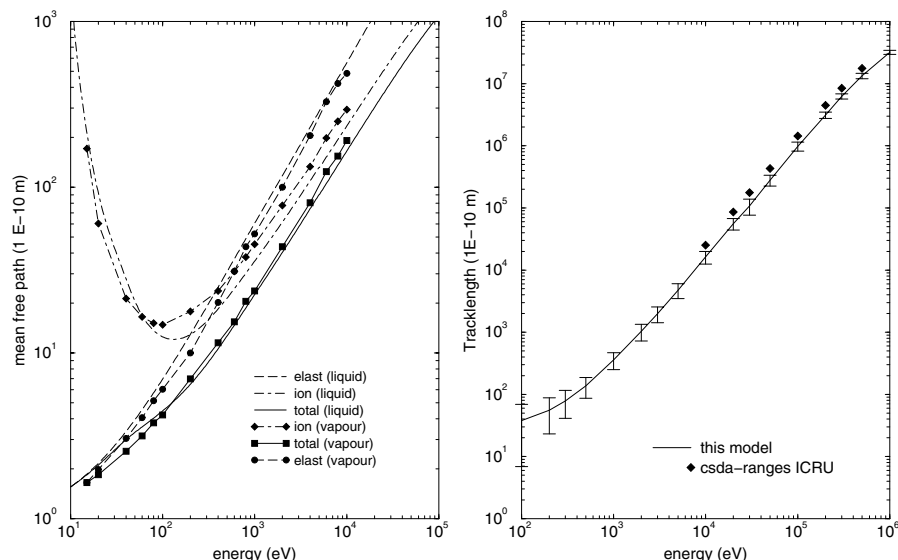


Fig. 1. Left panel: Mean free path of water vapour and liquid water. Right panel: Track length (primary particle) of simulated tracks using this mean free path

The mean free paths for liquid water are shown in Fig. 1, left panel, (total, ionization and elastic), as well as for water vapour, taken from [8]. The ionization as well as the total mean free path of liquid water is smaller than that of water vapour. This leads to a larger G-value in liquid water, i. e., to more ionizations in liquid water for the same incident electron energies. The calculated G-values (number of ionizations per 100 eV) for a 10 keV electron are 3.92 for liquid water and 3.29 for water vapour.

3 Simulation Program: PARTRAC

The biophysical radiation track structure simulation code PARTRAC is used to simulate radiation transport and radiation action of photons, electrons and protons in biologically relevant structures from a molecular level (DNA) up to higher order structures (chromosome domains) [9]. This is done in three major steps: the interaction part simulates the initial track structure from radiation fields, the geometrical part superimposes the track structures upon the DNA target model, and the effect part analyzes the effect on the biochemical structure.

The particle transport module uses Monte Carlo techniques to follow the complete history of the primary and all created secondary electrons by simulating inelastic (ionizations, excitations) and elastic collisions step by step down to total stopping of the particle. This is done in specified scoring regions of homogeneous target materials under consideration (energy range of liquid water: 10 MeV – 10 eV; water vapour: 100 keV – 10 eV). All important quantities of

(all) interactions are reported such as type and coordinates of the interaction, the deposited energy, secondary electron starting energy and direction. This information can be further used by other modules of PARTRAC such as the geometrical structure part or by special applications. A more detailed description of PARTRAC can be found in [9] and literature quoted therein.

4 Applications

In this work we focus on simple applications to check our model and to show how spatial information can be used. Spatial information on energy deposition is the main input for determining radiation damage in biological systems. Therefore, we first simulate the total track length of electrons in liquid water, i.e., the distance the primary electron travels until it has lost all its kinetic energy. All particles start at the origin with a fixed starting energy in a random direction, the region of interest is a sphere with a sufficiently large radius. The results are shown in Fig. 1, right panel. The error bars refer to a standard deviation of 1σ (simulation of 10000 histories for each energy). The simulated track lengths are, as expected, somewhat smaller than the calculated ranges using the continuous slowing down approximation (csda) (diamonds) [10]. This approximation uses a fixed mean energy loss per unit length and is based on the mean excitation value $I = 75.0$ eV in the case of liquid water.

As a second application we simulate the deposited energy per track and per length (μm) as a function of the radial distance r from the origin, i. e., the source of electrons. Here, all energy deposited from the primary as well as from all secondary electrons is considered. The results are shown in Fig. 2 for 10 keV electrons (again 10000 histories) starting again at the origin in a random direction

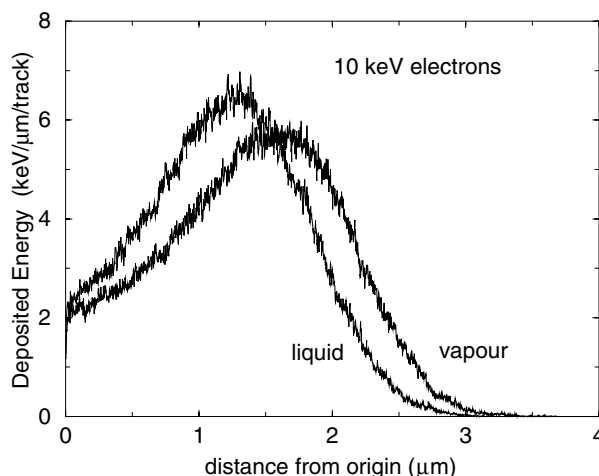


Fig. 2. Deposited energy per track and per μm versus radial distance from the origin for 10 keV electrons

and traveling in water vapour and liquid water. We see that energy is deposited at smaller distances in liquid water, and there is a slightly larger deposition of energy at shorter distances than in the vapour phase. The mean free path in liquid water is somewhat smaller than in the vapour phase, as seen in Fig. 1. Therefore, the distance between two interactions is on average smaller. Furthermore, the G-value (the mean number of ionizations per 100 eV) is larger in the liquid phase, which leads to more ionizations. Even if the ionisation thresholds, or the deposited energy per interaction, are somewhat smaller in the liquid phase than in the vapour phase, there is a larger energy deposition for radial distances below the maximum in liquid water. These differences in radial distributions can be very important in simulations of biologically relevant structures.

5 Acknowledgments

MD thanks the European Community for the Marie-Curie Fellowship “Low Energy Electrons in Microdosimetry and Health” under Contract No. FIGD-CT-1999-50002. This work was partly supported by the European Community under Contract No. FI4P-CT95-0011 “Biophysical Models for the Induction of Cancer by Radiation” and Contract No. FIGH-CT-1999-00005 “Low-dose risk models”.

References

1. M. Dingfelder, D. Hantke, M. Inokuti, H.G. Paretzke: *Radiat. Phys. Chem.* **53**, 1 (1998)
2. J.M. Heller, R.N. Hamm Jr., R.D. Birkhoff, L.R. Painter: *J. Chem. Phys.* **60**, 3483 (1974)
3. H. Bichsel, T. Hiraoka: *Nucl. Instr. Meth.* **B 66**, 345 (1992)
4. M. Dingfelder, M. Inokuti, H.G. Paretzke: *Radiat. Phys. Chem.* **59**, 255 (2000)
5. H. Hayashi, N. Watanabe, Y. Udagawa, C.-C. Kao: *Proc. Natl. Acad. Sci.* **97**, 6264 (2000)
6. N. Watanabe, H. Hayashi, Y. Udagawa: *Bull. Chem. Soc. Jpn.* **70**, 719 (1997)
7. M. Dingfelder, M. Inokuti: *Radiat. Environ. Biophys.* **38**, 93 (1999)
8. H.G. Paretzke: ‘Radiation Track Structure Theory’. In: *Kinetics of Nonhomogeneous Processes*. ed. by G.R. Freeman (John Wiley & Sons, New York 1987) pp. 89–170
9. W. Friedland, P. Jacob, H. G. Paretzke, M. Merzagora, A. Ottolenghi: *Radiat. Environ. Biophys.* **38**, 39 (1999)
10. International Commission on Radiation Units and Measurements: *Stopping Powers for Electrons and Positrons* (ICRU, Bethesda 1984)

Inelastic Cross-Sections for Use in Monte Carlo Track Structure Codes

D. Emfietzoglou

Dept. of Medical Physics, University of Ioannina Medical School, 451 10 Ioannina,
Greece

1 Introduction

The difficulty to solve with the needed accuracy (for finite inhomogeneous media) the Boltzmann transport equation together with advances in computer power have motivated the widespread application of Monte-Carlo (MC) codes for the (stochastic) simulation of particle tracks. To develop such codes it is vital that the physics of the penetration and diffusion of charged particles in matter, in terms, for example, of straggling distributions and interaction cross sections, is adequately known and amenable to a computationally convenient description.

The following classification is pertinent in terms of the physics incorporated in an MC code for the stochastic simulation of charged particle tracks. Macroscopic codes make use of the so called “condensed-history” (CH) technique, where a sufficiently large number of collisions (practically at least 20) along each track are grouped together and their effect is treated by an appropriate multiple-scattering-theory (MST). Therefore, the term macroscopic denotes, in essence, that each track is simulated as a collection of path segments (steps) sufficiently long compared to the mean free path of the charged particles to justify the applicability of the adopted MST. Two different schemes utilizing the CH technique are in use. The continuous-slowing-down (CSD) scheme is the simplest and least demanding in computer power. Each elastic collision is explicitly modeled while in between such events the energy loss from inelastic collisions is estimated from stopping power theory. A serious deficiency of this scheme is the complete neglect of energy straggling. The next level of sophistication is the so called condensed random walk scheme. In accordance with Berger’s original terminology [1] we may distinguish within this scheme between class I and class II algorithms. In class I codes (e.g. MCNP) both the energy loss and the angular deflection of the particles after traversing a preselected step are sampled from appropriate MSTs. Although class I codes fully account for straggling, and thus are considered to be more advanced than the CSD schemes, their main drawback is the limitations posed by the adoption of the appropriate step size. For example, close to interfaces (between media of different composition) the step size may have to be considerably reduced so the assumptions inherent in the MSTs may be questioned. Additionally, the application of MSTs systematically errors as far as the lateral displacement of particles after each step is concerned. To better deal with boundary effects, class II codes (e.g. EGS) introduce a cut off value where only collisions associated with energy loss and angular deflection below

the cut off are grouped together, while the occasional production of fast secondaries is treated individually on the basis of single scattering cross sections. Therefore, class II codes are more suitable for transport near interfaces than class I codes and also more accurate in terms of spatial distribution. The main shortcoming associated with class II codes is the fact that, although straggling in hard events is accounted naturally, soft events have either to be treated on the basis of an appropriate CSD scheme or employ restricted straggling distributions which are known only roughly [2]. Obviously, to best deal with interfaces the cut off will ultimately have to be eliminated. Then, class II codes reduce to the microscopic regime and an event-by-event simulation (denoted as class III hereafter) is obtained. To account for all collisions individually, the development of single scattering cross sections is mandatory. Obviously, the computer time required increases dramatically, rendering this scheme practical only for low and intermediate energy particles (i.e. electrons in the eV–keV region). Apparently, in class III codes, straggling is included naturally at all levels. The main difficulty is constructing reliable elastic and inelastic cross sections for the entire range of impact velocity and energy loss. In fact, this is where the differences between existing class III codes essentially lie [3].

2 Model Inelastic Cross-Sections

The inelastic cross sections used in class II codes are based on the binary approximation, that is, either the target electrons are treated as being free and at rest or the influence of the electronic configuration of the target on the collision dynamics is treated only roughly (e.g. by subjecting the target electron to a velocity distribution). Thus, optically allowed transitions are not properly accounted for. This is not problematic as long as the cut off value is kept sufficiently higher than the electronic binding energies. For the transport of low and medium energy electrons (10–10,000 eV) which is the main subject of class III codes (or when in class II codes the cut-off is sufficiently decreased), the binary approximation alone is entirely inadequate, since the details of the electronic structure of the target become critical. Thus, collision parameters specific to the target need to be established.

The statistical nature of the MC technique restricts rather severely the complexity of the formulae adopted. Thus, all inelastic cross sections employed in class III codes work under the theoretical framework of the (1st) Born approximation, i.e., the interaction potential is treated at the level of first order perturbation. This, formally restricts its range of validity to impact velocities much higher than the orbital velocities of the target electrons. Although the precise way the first order cross sections deviate from the true cross sections is only poorly understood, it is generally assumed that the Born approximation is sufficient for electron impact above a few tens of eV (e.g. 50–100 eV), that is, sufficiently above the binding energies of the outer shells. Below this energy range corrections usually apply. In addition, exchange corrections need to be introduced into the Born cross sections for electron impact ionization.

The main result of the Born approximation is that the inelastic cross section is factorized and essentially becomes a study of the energy structure of the target. In accordance with the nomenclature mostly used in atomic and molecular physics it is reduced to the study of the generalized-oscillator-strength (GOS), or, in an alternative formulation more appropriate for condensed targets, to the energy-loss-function (ELF); the latter being the imaginary part of the inverse dielectric response function. Both the GOS and ELF are directly related to the form-factor of the inelastic collision process and may heuristically be interpreted as the conditional probability that the target makes a transition to a particular excited state (discrete or continuum) upon receiving a particular energy (E) and momentum transfer (q). Hence, a three dimensional representation of the GOS or ELF (the so called Bethe surface) completely describes the inelastic process within the range of validity of the Born approximation [4]. For example, integration over the q variable yields the energy loss differential cross section, while a full integration over the E - q plane yields the (inverse) mean free path for inelastic collisions. Other important quantities, such as the collision stopping-power and the energy loss straggling parameter may be obtained from the first and second moment, of the energy loss differential cross section, respectively.

A formal complete mapping of the Bethe surface requires that the wavefunctions and eigenvalues (of both the ground and excited states) of the system to be known. Hence, an analytic representation of the Bethe surface is only possible for the hydrogen atom and the free electron gas. Even then, the formal solutions appear too involved for MC transport problems. First-principle numerical calculations are a truly demanding task for all but the hydrogen like systems, due to the correlation energy correction which especially affects the excited states. Moreover, in contrast to dilute systems where accurate numerical solutions of the atomic or molecular Hamiltonian may be obtained from standard Hartree-Fock techniques and variational or many-body perturbation corrections, the relevant task for condensed targets appears to be formidable, especially if one is reminded of the statistical nature of the MC transport. Thus, semi-theoretical cross sections where full advantage of experimental data is taken seems mandatory.

In constructing the ELF of a condensed target, it is convenient to divide the electronic subsystem into tightly bound (innershell or core) electrons and weakly bound (outershell or valence) electrons. The former are associated with relatively large binding energies and therefore they are practically unaffected by the remaining electronic subsystem. Hence, a suitable binary approximation (i.e. a semiclassical scheme) is well suited for innershell impact ionizations [5]. For weakly bound electrons, a further distinction must be made between conduction or nearly free electrons and electrons in non-conduction bands. In general, nearly free electrons are associated with collective excitations of the plasmon type. The ELF may be obtained in this case from Lindhard's expression (or Mermin's modification) for the free electron gas [6] or simplifications of it [7]. For valence electrons, though, associated with interband (instead of intraband) transitions, the assumption of a nearly free like behavior may be problematic. Hence, for a wide range of nonorganic (semiconductors and insulators) and organic materials

and water, a physically motivated scheme for modeling the ELF of weakly bound electrons must be devised [8].

In contrast to gas targets where well tested data are usually available, scattering experiments in solid targets are scarce and restricted to a limited range of impact energies and momentum transfer [9]. Hence, advantage is taken of the numerous optical measurements on the basis of which the optical limit ($q=0$) of ELF (denoted hereafter as OELF) may be obtained [10]. Despite the fact that the OELF denotes well the spectrum of the most probable collisions (i.e. the soft collisions involving small momentum transfer), an accurate description of particle transport in terms of distance to the next inelastic interaction and energy loss therein necessitates that the effect of finite momentum transfer collisions is also taken into account. In other words, a dispersion relation for extending the OELF into the E - q space is essential. To avoid inconsistencies, the extension algorithm, though approximate, needs to be guided by sound physical arguments. For example, it is known that for optically allowed transitions, the ELF is a slowly varying function of q for small values of q (reaching the OELF at $q=0$), while it diminishes quickly at $Q=E$ and is practically vanished for Q larger than E (with Q the recoil energy of a free electron). On the other hand, for optically forbidden transitions, the ELF sharply peaks at $Q=E$ with the width of the peak related to binding which, in effect, smears out the δ -function (free electron limit) to the E - Q space.

3 Results

In order to model the Bethe surface of liquid water, and thus establish differential and total inelastic cross sections, the electronic subsystem of liquid water was divided into eight weakly bound (non-conducting) electrons and two core electrons (in the oxygen K shell). The latter were assumed to be unperturbed from the remaining electronic subsystem and thus treated by a binary formula including exchange corrections [11]. The dielectric approach was used for the interband transitions associated with the former. In that respect, experimental data on the optical properties (reflectance) of liquid water were used [12]. The experimentally obtained OELF was analytically represented by a sum of Drude type functions, where the oscillator strengths, transition energies, and damping constants were considered as fitting parameters. In particular, a sum of derivative Drude functions which are more sharply peaked were used for discrete excitations [13]. The Drude expansion representation of the dielectric function is in close agreement with that in [14]. However, the methodology followed in [14], where a step function along with a Gaussian smearing was employed for avoiding the unrealistic extension of the Drude ionization functions below the ionization threshold, is computationally demanding and thus not very suitable for MC simulation. Therefore, a simple smoothing procedure with a cut off was used in the present work. Figure 1 shows the real and imaginary part of the optical dielectric response function (ODRF) of liquid water along with the OELF as obtained after the fitting procedure. The extension algorithm applied to the OELF for

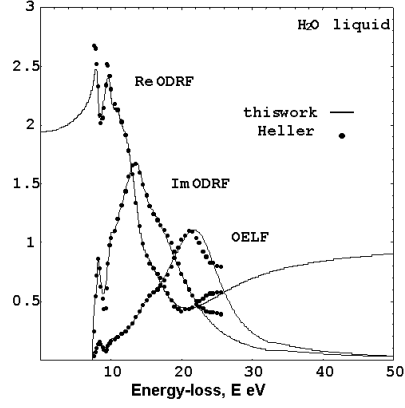


Fig. 1. Dielectric response and energy loss function of the optical limit for liquid water obtained by present model and the data of [12]

constructing the full ELF is based on an exponentially decreasing damping relationship for the GOS of discrete transitions which has been found empirically [14], while the GOS for the continuum was subsequently obtained from the Bethe sum rule. In addition, the full Drude functions were appropriately modified to allow a free electron like dispersion for ionizations [15]. The resulting Bethe surface is thus properly forced to reduce to the Bethe ridge at large values of E and q , while the discrete excitations are damped but not dispersed. In Figs. 2 and 3 the differential and total inverse mean free path for inelastic collisions, respectively, are shown and compared with the results of [13]. In the present study low energy and exchange

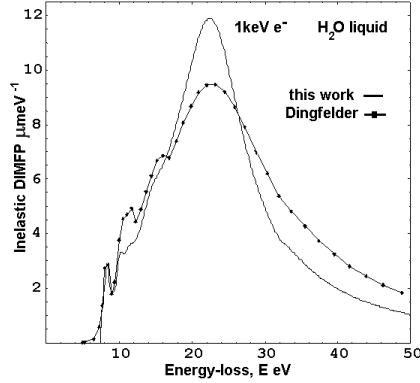


Fig. 2. Differential inverse mean free path (DIMFP) for inelastic collisions for 1 keV electron impact in liquid water obtained by the present work and the calculations of [14]

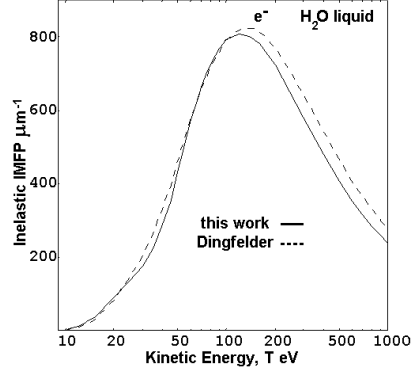


Fig. 3. Inverse mean free path (IMFP) for inelastic collisions for electron impact in liquid water obtained by the present model and the calculations of [14]

4 Conclusion

A model based on the dielectric formalism for calculating inelastic cross sections for liquid water has been established. The Bethe surface is constructed by

first fitting optical data by a sum of Drude type functions where discrete and continuum excitations are explicitly separated. Extension to the E - q space is accomplished by a simple algorithm with a dispersion relationship for ionizations leading to the Bethe ridge and an empirical damping function for (discrete) excitations. The results of the model compare well with that of [13]. The present model, though primarily suited for event-by-event simulations, may also contribute to condensed-history mixed algorithms (i.e. class II codes) by allowing a reliable evaluation of energy straggling parameters for soft collisions. This is important because the use of the binary approximation alone in class II codes imposes the adoption of high cut off values which, in turn, result in increased straggling of soft events (below the chosen cut off). Equally important, the allowance of reliably increasing the cut off will significantly decrease the simulation time.

References

1. M.J. Berger: 'Monte Carlo Calculation of the Penetration and Diffusion of Fast Charged Particles'. In: *Methods in Computational Physics Vol. 1* ed. by B. Adler, S. Ferubach, M. Rotenberg (Academic, New York 1963) pp. 135–215
2. P. Andreo: *Phys. Med. Biol.* **36**, 861 (1991)
3. S. Uehara, H. Nikjoo, D.T. Goodhead: *Rad. Res.* **152**, 202 (1999)
4. M. Inokuti: *Rev. Mod. Phys.* **43**, 297 (1971)
5. L. Vriens: *Phys. Rev.* **141**, 141 (1966)
6. D.J. Planes, R. Garcia-Molina, I. Abril, N.R. Arista: *J. Electron Spectrosc. Relat. Phenom.* **82**, 23 (1996)
7. J.M. Fernandez-Varea, R. Mayol, F. Salvat, D. Liljequist: *J. Phys.: Condens. Matter* **4**, 2879 (1992)
8. J.M. Fernandez-Varea, R. Mayol, D. Liljequist, F. Salvat: *J. Phys.: Condens. Matter* **5**, 3593 (1993)
9. W.E. Wilson, H. Nikjoo: *Radiat. Environ. Biophys.* **38**, 97 (1999)
10. E.D. Palik: *Handbooks of Optical Constants I and II* (Academic, New York, 1985 and 1991)
11. D. Emfietzoglou, G. Papamichael, M. Moscovitch: *J. Phys. D: Appl. Phys.* **33**, 932 (2000)
12. J.M. Heller, R.N. Hamm, R.D. Birkhoff, L.R. Painter: *J. Chem. Phys.* **60**, 3483 (1974)
13. R.H. Ritchie, R.N. Hamm, J.E. Turner, H.A. Wright: 'The Interaction of Swift Electrons with Liquid Water'. In: *6th Symposium on Microdosimetry at Brussels, Belgium, 1978* ed. By J. Booz, H.G. Ebert (Harwood Academic, Luxemburg 1978) pp. 345–354
14. M. Dingfelder, D. Hantke, M. Inokuti, H. Paretzke: *Radiat. Phys. Chem.* **53**, 1 (1998)
15. A.E.S. Green, S.K. Dutta: *J. Geophys. Res.* **72**, 3933 (1967)
16. R.N. Hamm, H.A. Wright, R.H. Ritchie, J.E. Turner, T.P. Turner: 'Monte Carlo Calculation of Transport of Electrons Through Liquid Water'. In: *5th Symposium on Microdosimetry at Verbania, Pallanza, 1975* ed. By J. Booz, H.G. Ebert, B.G.R. Smith (EUR-5452, 1975) pp. 1037–1050

Modelling Ultrasoft X-ray Effects on DNA

M. Terrissol and J.M. Vrigneaud

CPAT Université Paul Sabatier, 118, Route de Narbonne, F-31062 Toulouse, cedex 4, France

1 Introduction

Between 100 eV and 3 keV, X-rays interact in biological media almost exclusively by photoelectric effect, producing low-energy electrons (photoelectron and Auger electrons), depositing their energy in volumes comparable with DNA dimensions. These electrons are emitted in abundance as secondary particles in all low linear energy transfer (LET) radiations and are supposed to play an important role in the clustering of damages. It has been shown both from experiments [1] and theoretical calculations [2] that these low-energy, track end electrons contribute significantly to critical biological damage. However, recent cell studies with the use of synchrotron-produced ultrasoft X-rays contradict these conclusions with no significant differences in survival results between 273, 860 eV ultrasoft X-rays and 250 kVp X-rays [3]. In this energy range, photon cross-sections present singularities due to ionisation thresholds of Carbon (C), Nitrogen (N), Oxygen (O) and Phosphorus (P) atoms. Enhancement of damage has already been observed from X-rays experiments above the Carbon K (~ 290 eV) [4] and the Phosphorus K (~ 2130 eV) [5] thresholds. Monte Carlo track structure calculations were used to study the influence of all DNA atoms ionisation thresholds on strand breakage. The code cpa100 was used to follow the histories of photons and electrons ejected through a hydrated DNA model and the ensuing chemistry was taking into account up to 1 nanosecond. Induced single and double strand breaks were analysed as a function of energy and compared with studies highlighting the effect of track structure on DNA damage [6,7].

2 Modelling Photon Irradiation

To model the biological target we used an atomistic linear B-DNA model, built from the molecular simulation software MSI. The first hydration shell, namely 20 water molecules per nucleotide, was added using available crystallographic coordinates (~ 8 water molecules per nucleotide) and completed in MSI. The hydration shell was divided into two layers to model quasi-direct effect between the most bounded water molecules and the biomolecule. The linear hydrated DNA was centred in a block of 200 angstroms long, filled with bulk water Fig. 1. Photons were uniformly emitted from a face and all photoelectric interactions scored. The photoelectrons were ejected according to the Fisher differential cross-section [8] and its azimuthal angle was assumed to be isotropic. After

photoelectric effect, the residual atom is left in an ionised state with a vacancy in its inner shells, usually in the K shell. This vacancy is filled afterwards by electrons from higher shells accompanied by the emission of fluorescence X-rays or Auger electrons. In the present study, which deals with low-energy photons in low-Z materials, radiative transitions have been neglected. We used binding energies and non radiative transitions probabilities of Perkins [9] to take into account the ejection of the emitted Auger electron if the initial vacancy took place on K-shell of C, N or O atoms. For P atoms, cascade of transitions were calculated from a Monte Carlo reorganization code and resulting electrons were used as input each time an interaction occurred on these atoms. When the initial vacancy was on the K (2130 eV), L1 (187 eV) and L2 (139 eV) P shells we had respectively about 3, 2 and 1 emitted electrons. The angular distribution of all ejected Auger electrons was assumed to be isotropic.

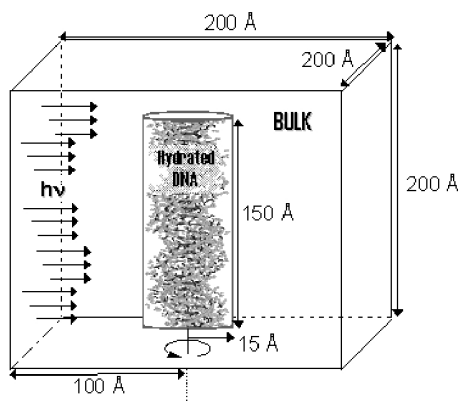


Fig. 1. Scheme illustrating the geometry of irradiation used in the calculation

Fig. 2 shows photon cross-sections per nucleotide between 100 and 3000 eV. In this energy range, variations are due to K ionisation thresholds of C, N, O and P atoms and to L-shells of P atoms. About the relative importance of each cross-section, two main areas can be distinguished as a function of energy. Towards 450–500 eV, we expect more photoionisations on DNA since cross-sections of C and N atoms are the most important. On the contrary, cross-section of O is greater almost elsewhere. This means that photoionisations are likely to occur mainly in the bulk water that surrounds DNA. That's actually what we find when we plot the spatial distribution of photoelectric effects in the block (not shown). Even above the K-ionisation threshold of P (2130 eV), there are still many interactions in the environment and DNA is poorly photo ionised.

3 Calculation of DNA Damage

The next step is to follow in an analogue Monte Carlo simulation [10] the histories of all primary and secondary electrons created in the cube until they come to rest. The main feature concern the electronic path sampling that takes into account the atomic nature of the target. During the subsequent stages (up to 10^{-9} s.), water species created along the track are allowed to react and diffuse according to the diffusion-controlled scheme of Smoluchowsky. To model DNA attacks, each DNA constituent (sugar-phosphate, base, water molecules of the hydration shell) may react with these chemical species to lead to indirect damages

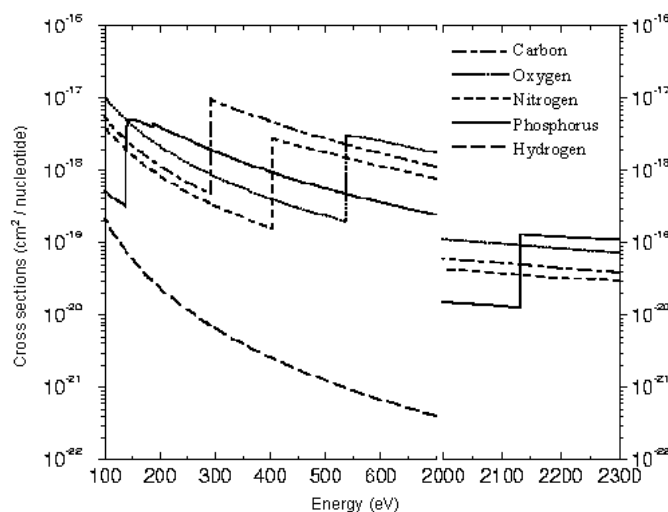


Fig. 2. Photon cross-sections (cm^2 per nucleotide). Mean elemental composition of our dry DNA segment : Carbon 10, Oxygen 6, Nitrogen 4, Phosphorus 1, Hydrogen 11

The hypothesis used in the modelling of DNA damage are the following : we assumed that one ionisation on a sugar-phosphate or on a water molecule attached to the sugar-phosphate moiety led to a direct single strand break (SSBd). Any radicals which interacted in the same way with sugar-phosphate or water molecules linked to the sugar-phosphate backbone produced an indirect single strand break (SSBi). Two SSB on opposite strands with a distance of no more than 10 base pairs were scored as one double strand break (DSB). We also present results with a classification scheme which separate breaks arising solely from direct effect (SSBd, DSBd), solely from indirect effect (SSBi, DSBi) or from any combination of these two (SSBm, DSBm). Over the full-length DNA segment, only one class of damage amongst these six was assigned for one photon absorbed in the block. The following discussion focuses specially on DSB whose repair is presumed to play an important role with respects to cell lethality.

4 Results and Discussion

Statistics were done for 200 000 absorbed photons in the block. In Fig. 3 we present contribution of induced DSB on the hydration shell (HYD) and on dry DNA (DNA). Regarding the influence of ionisation thresholds on the yield of damage, the knowledge of the number and energy of emitted electrons and the spatial distribution of interactions are very important. We found that electrons ejected above a threshold become more and more efficient to induce DSB as the photoelectron energy increases. Furthermore, electrons whose energies are in the range 400-500 eV are particularly effective since they produce the most dense interactions in water all along their quite large track. To fine-tune these preliminary observations, we divide the curves as a function of energy :

- Between 125 and 520 eV, the yield of damage increases rapidly with the number of DSB 8 times greater at 520 eV than at 125 eV. In the first part (125 - 280 eV), around the L-ionisation thresholds of P (139 and 187 eV), calculations have shown that electrons produced in bulk water around DNA are mainly responsible for this enhancement. The reason is that cross-section of O is still important and so the contribution to damage of electrons released from P is quite small. On the contrary, electrons ejected in situ on DNA just after the K-ionisation thresholds of C and N can explain the increase between 280 and 520 eV. As one goes further away above the thresholds, photoelectrons become more and more efficient to produce DSB, especially those ejected from C atoms, which are in higher proportions in DNA (~ 10 per nucleotide). At 520 eV, results show that ~ 40 % of all DSB are due to electrons emitted from C or N and 50 % of all SSB are direct.
- At 550 eV, beyond the K-ionisation threshold of O, there is a sudden yield decrease because all the interactions are uniformly distributed in the environment. A photoelectric effect on O atoms gives 2 electrons : one ~ 520 eV Auger electron and one photoelectron with a too weak energy to reach DNA.
- From 550 eV to 1 keV, the increasing DSB yield is due to the increasing photoelectron energy from several eV to 400-500 eV between 550 eV and 1 keV. Beyond 1 keV, tracks of photoelectrons created in bulk water become more and more sparse and particles rapidly escape from the block after a few interactions. Consequently the yield of DSB is expected to decrease progressively down to the value obtained at 550 eV where only the Auger electron has sufficient energy to induce DNA damage.
- Influence of the K-ionisation threshold of P atoms is very small, with little enhancement due to the 4 electrons (1 photoelectron and an average of 3 Auger electrons) ejected from P atoms above 2130 eV. Even here, most DSB are due to electrons emitted from O atoms especially located in bulk water.

Table 1 presents data for the relative yields of strand breakage according to their source (Tab. 1). For all energies, the predominant damage is an indirect SSB alone : the yield ranges from 45% at 520 eV when electrons are ejected from DNA to 57% at 250 eV when interactions occurred mainly in bulk water. This is quite in good agreement with the well-known value of $2/3$ indirect damages

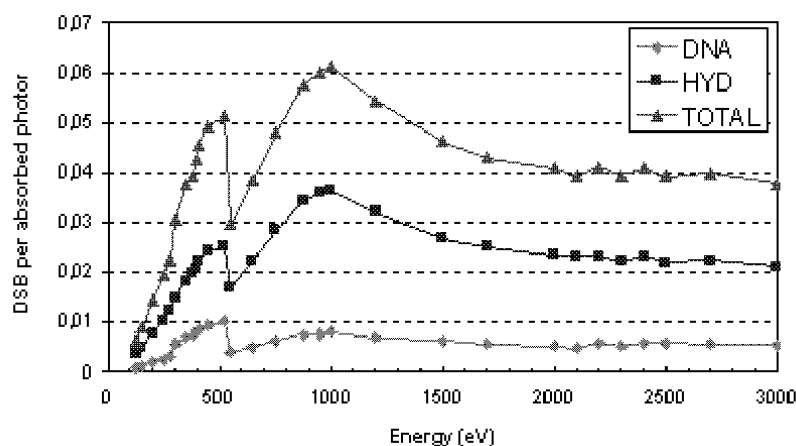


Fig. 3. Yield of DSB obtained at 10^{-9} second per absorbed photons in the cube

for low-LET radiations. Furthermore, ultrasoft X-rays are supposed to produce more complex damage than high-energy photons leading to more SSBm, DSBm and to a decrease in the yield of SSB relative to that of DSB. Table 4 shows that the complexity of clustered damage seems to be greater for the 520 eV radiation (see SSB/DSB) since low-energy electrons are ejected in abundance directly from DNA. Comparisons can be made with experiments on plasmids, keeping in mind that no calibration was included in the calculation as well as no scavengers.

Table 1. Relative yields of breaks according to the source (direct, indirect or mixed)

Energy ^a	SSBd ^b	SSBi ^b	SSBm ^b	DSBd ^b	DSBi ^b	DSBm ^b	SSB/DSB ^c
250	20.0	57.2	6.2	4.3	5.6	6.7	6.2
520	19.8	44.8	8.6	8.1	7.5	11.2	3.8
1000	15.3	52.7	8.1	5.0	9.6	9.3	4.3
1500	17.4	53.8	8.0	4.7	8.0	8.1	5.0
2200	18.6	52.7	7.5	5.0	7.7	8.5	4.8

^a Energy in eV.

^b in percent.

^cFor all energies, ratios are calculated for the same absorbed dose in the block.

Experimentally, enhancement ratios of 1.2 and 1.17 around the carbon K [11] and phosphorus K [5] ionisation thresholds have been reported and we found 1.6 and 1.08 respectively. Gould and al. [3] found no differences on survival results of cells between 273 eV and 860 eV. Our model predicts that the most strik-

ing feature is the biological importance of energies just below the K-ionisation threshold of oxygen. Recent studies [6,7] tried to link the yield of OH radicals created in aqueous solutions to the ionisation density of the track, which is strongly dependent on photon energy. They showed that the number of OH radicals escaping intratrack recombination events is minimum around 1-2 keV, indicating that ionisation density is the most important at these energies. It is interesting to note that we found a maximum of DSB around 1 keV (Fig. 3) corresponding to dense tracks of electrons emitted from bulk water.

Taking into account ionisation thresholds of each DNA atoms, this model seems to be a powerful tool to investigate low-energy photon induced DNA damage. Sophistications (such as inclusion of scavengers or DNA concentration) for direct comparison with experiments are currently processed.

5 Acknowledgment

This work was supported by the European Community under contract 'Biophysical Models for the Induction of Cancer by Radiation'.

References

1. H. Nikjoo, D. T. Goodhead: *Phys. Med. Biol.* **36**, 229 (1991)
2. S.W. Botchway, D.L. Stevens et al.: *Rad. Res.* **148**, 317 (1997)
3. M.N. Gould et al.: In *Proceedings of the eleventh international congress of radiation research, Dublin, Ireland, 1999* Vol. 2, pp. 157-159
4. M.A. Hervé du Penhoat et al.: *Rad. Res.* **151**, 649(1999)
5. K. Hieda et al.: *Int. J. Radiat. Biol.* **70**, 437 (1996)
6. J. Fulford et al.: *J. Phys. Chem. A* **103**, 11345 (1999)
7. S.M. Pimblott In: *Proceedings of the eleventh international congress of radiation research, Dublin, Ireland, 1999*, Vol. 2, pp. 122-125
8. F. Fisher: *Ann. Phys.* **8**, 821 (1931)
9. S.T. Perkins: *Tables and graphs of atomic sub shell and relaxation data derived from the LLNL evaluated atomic data library (EADL), Z=1,100*, UCRL-50400, Vol. 30, (1991)
10. M. Terrissol, J.M. Vrigneaud: 'Analogue Monte Carlo to Model Radiation Induced DNA Damage', These proceedings p. 261
11. B. Fayard et al.: *J. Chem. Phys.* **96**, 147 (1999)

Radiobiological Modeling in Voxel Constructs

R.D. Stewart and R.J. Traub

Radiation and Health Technology, Pacific Northwest National Laboratory, Richland, WA, 99352, USA

Abstract. Although great strides have been made towards integrating the anatomical characteristics of specific patients into Monte Carlo dosimetry calculations, efforts to further improve the effectiveness of radiation treatments for cancer are ultimately limited by our ability to predict, for specific patients, the cell-killing effects of temporally and spatially complex irradiation schemes. To better integrate patient- and tumor-specific data into the treatment planning process and provide the research community with the enabling technologies needed to exploit the full potential of radiation therapy, the Pacific Northwest National Laboratory (PNNL) is developing new software to estimate tumor control probabilities (TCPs) using three-dimensional tissue constructs. To illustrate the potential impact on treatment planning of more detailed tumor response modeling, we present the results of several studies characterizing the effects on the TCP of modulating the temporal and spatial distribution of radiation delivered to an idealized tumor with heterogeneous biophysical properties.

1 Introduction

To exploit the full potential of radiation therapy, treatment designs must consider the so-called four R's [1]: repair effects, cell-cycle redistribution (or resensitization) effects, reoxygenation effects, and repopulation effects. As illustrated in Fig. 1, as the time between radiation “pulses” increases, repair and repopulation effects tend to **decrease** cell killing, whereas reoxygenation and cell-cycle redistribution effects tend to **increase** cell killing. The effort to design more effective radiation treatments must ultimately consider the interplay between all four of these effects. However, treatment outcome is determined by the compounded

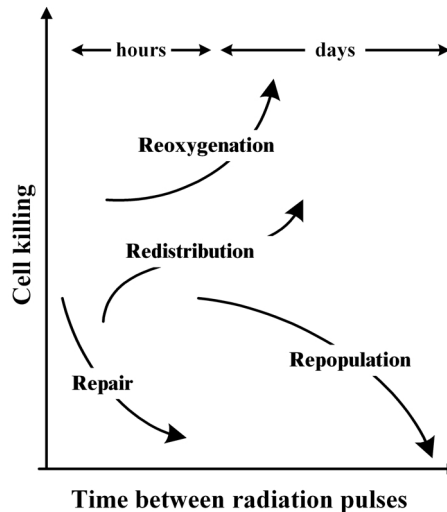


Fig. 1. An idealized schematic illustrating trends in cell killing associated with repair effects, cell-cycle redistribution effects, reoxygenation effects, and repopulation effects. The relative importance of the four effects are not drawn to scale

cell-killing effects of individual dose fractions, and any temporal or spatial change in the way that a dose fraction is delivered that enhances tumor-cell killing should also increase the cell-killing effects of the entire treatment. In the typical 30 to 60 minute timeframe needed to deliver a dose fraction, damage repair effects will be far more important than reoxygenation, redistribution, and repopulation effects.

Dose fractions are usually delivered using collimators with multiple beam or leaf configurations to shape the radiation field to the contours of the tumor and minimize the dose to surrounding normal tissues. Because irradiator systems cannot be moved instantaneously from one beam or leaf configuration to another, tumor cells experience small pulses of radiation separated by time intervals that range from a few seconds up to a few minutes. Also, cells in different regions of a tumor experience slightly different sequences of radiation pulses because of attenuation and scattering of the radiation beam. Cells are exquisitely sensitive to the size and timing of the radiation pulses they experience, and more realistic, three-dimensional tumor models are needed to better predict the outcome of intensity-modulated radiation therapy (IMRT) treatment designs. To improve tumor response modeling, the Pacific Northwest National Laboratory (PNNL) is developing new software to calculate tumor control probabilities (TCPs) using three-dimensional tissue constructs and an exact description of the series of radiation pulses experienced by tumor cells during the course of a radiation treatment. To illustrate the potential impact on treatment planning of more detailed tumor response modeling, we present the results of several studies characterizing the effects on the TCP of modulating the temporal and spatial distribution of radiation delivered to an idealized tumor with heterogeneous biophysical properties.

2 Methodology

PNNL has developed a computer application called VOXEL, which is based on the Kinetic Biological Effects Modeling (KBEM) software library (<http://www.pnl.gov/berc/>), to perform TCP calculations using the Lethal and Potentially Lethal (LPL) radiobiological model [2] and tabulated dose distributions. In the LPL model, a system of coupled, non-linear ordinary differential equations are used to model DNA damage repair and misrepair processes. The LPL model explicitly accounts for dose and dose-rate effects. Moreover, the widely used linear-quadratic (LQ) formalism [3] is a special case of the more general LPL model [2]. Briefly, the methodology used to compute tumor control probabilities is as follows.

2.1 Dosimetry

The MCNP Monte Carlo code [4] was used to compute absorbed dose distributions for a cylindrical tissue construct irradiated by broad parallel 1 MeV photon beams from eight different directions as illustrated in Fig. 2. Given the

tabulated dose distribution for the eight beam directions (labeled A through H in Fig. 2), the time required to re-orient the accelerator system (e.g., from configuration A to B), and the time of day when delivery of the dose fraction is initiated, the VOXEL application constructs an absorbed dose rate function, $\dot{D}(t)$ to describe the sequence of radiation pulses experienced by cells in each voxel. The total treatment dose, D , is the integral of $\dot{D}(t)$ over all time. The relative intensity of the radiation beams and the beam sequence (e.g., Beam A followed by Beam B followed by Beam C and so on) are user-configurable at runtime. MCNP-calculated dose distributions are re-normalized so that the total treatment dose delivered to a target voxel located near the center of the tissue construct equals a prescribed value, as recommended by the International Commission on Radiation Units and Measurements [6].

2.2 Tumor Control Probability

To estimate the fraction of the initial number of cells that survive in each tissue region, the LPL model is solved by numerical integration, and the probability of tumor control is calculated using the Poisson TCP model [7], i.e.,

$$\text{TCP} = \exp \left\{ - \sum_{i=1}^Q N_i S_i(D) \right\} \quad (1)$$

Here, Q is the number of voxels, N_i is the initial (pre-treatment) number of tumor cells in the i th voxel, and $S_i(D)$ is the fraction of the initial number of tumor cells in the i th voxel that survive a treatment, as calculated by solving the LPL model with a specific dose rate function $\dot{D}(t)$.

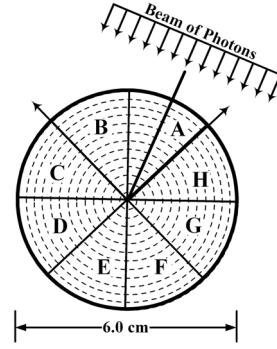


Fig. 2. MCNP geometry and 1 MeV photon beam configurations used for absorbed dose distribution calculations. The tissue construct, a right circular cylinder 6 cm high with a diameter of 6 cm, is composed of soft tissue at a density of 1.04 g cm^{-3} [5]. For dose tallying purposes, the construct is sub-divided into 2,328 annular voxels as illustrated

3 Results

Figure 3 (inset) shows the fraction of irradiated tumor cells that are expected to survive a single dose of low Linear Energy Transfer (LET) radiation delivered at 10 Gy min^{-1} . The cell survival estimates predicted by the LQ model ($\alpha=0.22 \text{ Gy}^{-1}$ and $\beta=6.47 \times 10^{-2} \text{ Gy}^{-2}$) are within 1 to 5% of the values predicted by the LPL model using three different *biologically plausible* parameter sets: $\eta_{PL} = 2.98 \text{ Gy}^{-1} \text{ cell}^{-1}$; $\eta_L = 0.154 \text{ Gy}^{-1} \text{ cell}^{-1}$; (a) $\varepsilon_{PL} = 1.39 \text{ h}^{-1}$, $\varepsilon_{2PL} = 3.15 \times 10^{-2} \text{ h}^{-1}$; (b) $\varepsilon_{PL} = 0.693 \text{ h}^{-1}$, $\varepsilon_{2PL} = 1.57 \times 10^{-2} \text{ h}^{-1}$; (c) $\varepsilon_{PL} = 0.346 \text{ h}^{-1}$, $\varepsilon_{2PL} = 7.81 \times 10^{-2} \text{ h}^{-1}$. That is, the LQ model and the LPL model yield the same

“intrinsic radiosensitivity”, Although the models predict the same level of cell survival for a single, acute dose of radiation, the TCP calculations shown in Fig. 3 clearly demonstrate that cells with the same apparent intrinsic radiosensitivity but slightly different damage repair characteristics (i.e., the ε_{PL} and ε_{2PL} parameters) respond very differently to the same multi-fraction radiation treatment; the difference is due to damage repair effects. These data highlight the need for detailed modeling of the interplay between damage repair processes and the complex sequence of radiation pulses experienced by cells during the course of a radiation treatment.

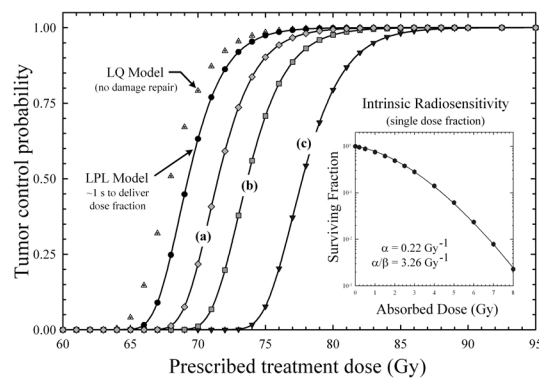


Fig. 3. Effects on TCP of intrinsic cell radiosensitivity. LQ model parameters are for colon adenocarcinoma cells [11]. TCP calculations are for a uniformly irradiated tumor (30 dose fractions, 1 dose fraction per day) composed of a homogeneous population of 6.9×10^{10} cells. The dose fraction delivery time is 21 minute (8 pulses separated by a 3 minute time interval). LPL model parameters are listed in the main text. Inset figure: (●) LQ model; solid lines LPL model

For a cylindrical tumor with homogeneous radiosensitivity parameters irradiated by a broad parallel beam of photons, beam sequence most likely has little effect on treatment outcome [8]. However because of microenvironmental factors (e.g., presence or absence of nutrients or oxygen), genome instability [9], and cell signaling phenomena [10], cells in different regions of a tumor most likely have very different biophysical (dose-response) characteristics. For a tumor composed of a non-uniform spatial distribution of radioresistant and radiosensitive cells (Fig. 4), the results shown in Fig. 5 suggest that the sequence of beams used

to deliver a dose fraction affects treatment outcome. Moreover, these results suggest that less uniform dose distributions can sometimes produce better treatment outcomes than more uniform dose distributions.

4 Conclusions

Results for an idealized tumor with asymmetrical biophysical properties suggest that biological optimization of the way dose fractions are delivered (beam sequence and intensities) could improve some radiation treatments by factors on the order of 5 to 20% (iso-effect dose). The dose distribution that best maximizes the TCP may or may not be a uniform dose distribution. However, when information about the three-dimensional properties of a tumor is not available, the

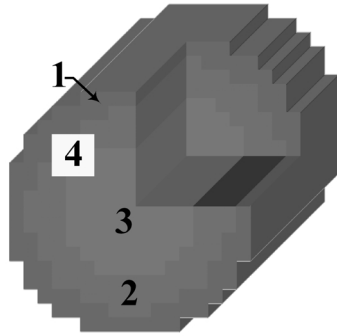


Fig. 4. Cylindrical tumor model with heterogeneous biophysical properties. Tumor parameters are: (1) 10^8 cells cm^{-3} and LPL parameter set (c); (2) 5×10^8 cells cm^{-3} and LPL parameter set (c); (3) 10^8 cells cm^{-3} and LPL parameter set (b); (4) 10^{10} cells cm^{-3} and LPL parameter set (a). For visualization purposes, the cylindrical tumor is sub-divided into 3,133 rectangular voxels and shown with a section cutout. Tissue region 4 is a particularly radioresistant portion of the tumor

recommended strategy is to deliver a uniform dose of radiation to the planning target volume [6] **as rapidly as possible**. The compounded effects of delivering the individual dose fractions in a few minutes instead of an hour could improve the effectiveness of some treatments by factors on the order of 1 to 5% [8]. To fully exploit all four R effects (Fig. 1), will, no doubt, require a three-dimensional tumor model that accounts for dynamic changes in the tumor-cell population during the course of the entire treatment. However, static tumor models that capture some of the essential three-dimensional properties of the tumor (e.g., the initial location of hypoxic or rapidly proliferating cells) may prove useful for treatment optimization. With continuing improvements in computer technology and non-invasive imaging techniques, full (all four R) biological optimization of radiation treatments for cancer seems an ambitious but not unreachable goal for the coming decade [12]. Three-dimensional tumor modeling using software such as our VOXEL application will be needed to unlock the full potential of radiation therapy.

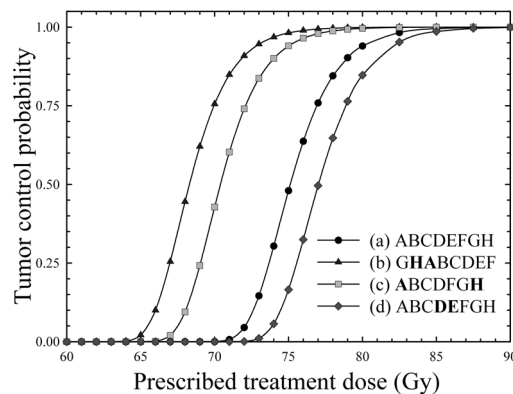


Fig. 5. Effects on the TCP of modulating the beam sequence and beam intensities (30 dose fractions, 1 dose fraction per day, dose fraction delivery time of 28 minutes). (a) uniform beam weights; (b), (c) beams A and H 10 times stronger than the other beams; (d) beams D and E 10 times stronger than the other beams. Curve (b) and (c) are different because of beam sequence effects

References

1. *Moss' Radiation Oncology. Rationale, Technique, Results, 7th edition.* ed. by J.D. Cox (Mosby - Year Book, Inc. St. Louis, MO 1994)
2. S.B. Curtis: Radiat. Res. **106**, 252 (1986)
3. D.J. Brenner, L.R. Hlatky, P.J. Hahnfeldt, Y. Huang, R.K. Sachs: Radiat. Res. **150**, 83 (1998)
4. J.F. Briesmeister, Ed.: *MCNP - A General Monte Carlo N-Particle Transport Code*, Los Alamos National Laboratory Report, LA-12625-M (March, 1997)
5. M. Cristy, K.F. Eckerman: *Specific Absorbed Fractions of Energy at Various Ages from Internal Photon Sources. I. Methods*, ORNL/TM-8381/V1, Table A-1. Oak Ridge National Laboratory, Oak Ridge, TN 37831 (1987)
6. ICRU: *Prescribing, Recording, and Reporting Photon Beam Therapy*, Report 50. International Commission on Radiation Units and Measurements. Bethesda, Maryland (1993)
7. S. Webb, A.E. Nahum: Phys. Med. Biol. **38**, 653 (1993)
8. R.D. Stewart, R.J. Traub, 'Temporal optimization of radiotherapy treatment fractions', in *Proceedings of the ANS, Radiation Protection for our National Priorities, Medicine, the Environment, and the Legacy, Spokane, Washington, September 17-21, 2000*. In press
9. K.R. Loeb, L.A. Loeb: Carcinogenesis **21**, 379 (2000)
10. M.H. Barcellos-Hoff: Radiat. Res. **150**(5 Suppl), S109 (1998)
11. P.J. Deschavanne, B. Fertil, N. Chavaudra, E.P. Malaise: Radiat. Res. **122**, 29 (1990)
12. C.C. Ling, J. Humm, S. Larson, H. Amols, Z. Fuks, S. Leibel, J.A. Koutcher: Int. J. Radiat. Oncol. Biol. Phys. **47**, 551 (2000)

Monte Carlo Techniques for Primary Standards of Ionizing Radiation and for Dosimetry Protocols

D.W.O. Rogers

Ionizing Radiation Standards, Institute for National Measurement Standards,
National Research Council of Canada, Ottawa K1A 0R6, Canada

Abstract. This is a brief, highly biased, review of how Monte Carlo techniques of electron and photon transport have been applied to radiation dosimetry. The major emphasis is on radiotherapy dosimetry protocols and primary standards for air kerma.

1 Introduction to Radiation Dosimetry

In radiotherapy treatments for cancer patients it is critical to have an accurate measure of the dose delivered to the patient since survival rates peak within a narrow range of dose. To establish this dose accurately consists of 3 linked steps. The first step is the establishment of primary standards of air kerma or absorbed dose to water. The second step is the use of dosimetry protocols based on ion chambers calibrated using these primary standards to establish the dose under reference conditions in a clinical therapy beam. The final step is to establish the dose distribution in individual patients specified by CT data.

Monte Carlo (MC) simulation of electron-photon transport has long played a role in all three components in this chain and its role is increasing substantially as processor speed and algorithm accuracy are improving. The focus of this paper is the first two steps while the third step is being dealt with extensively elsewhere at this meeting.

Monte Carlo has played an important role in radiation dosimetry for many years because of the importance of stopping-power ratios (sprs). These play a central role in Spencer-Attix cavity theory [1] which is used to relate the dose in a medium to the dose in a small cavity in that medium (eg an ion chamber).

Although sprs were originally calculated using complex analytic techniques to approximate electron fluence spectra, an early application of Monte Carlo techniques in radiation dosimetry was to calculate these spectra for use in calculating sprs. These spectra vary significantly with depth and beam quality, especially for electron radiotherapy beams. This meant that extensive calculations were needed. In the last few years there have been significant advances in how these calculations are done. Much of this paper will be a description of these advances and of some calculations of how the presence of a real ion chamber affects the situation.

Spencer-Attix cavity theory is also used to establish primary standards for air kerma. There have been some controversial MC contributions regarding the correction factors in this equation and these are discussed.

2 Role of Monte Carlo in Clinical Dosimetry Protocols

2.1 Stopping-power Ratios (sprs)

The major protocols for radiotherapy reference dosimetry need sprs [1–4]. The early sprs for electron beams were calculated by Berger and Seltzer using the NIST Monte Carlo code ETRAN [1,5]. Nahum [6] made a significant step forward by including track-ends in sprs and in using Monte Carlo calculations for photon beams. The extensive Monte Carlo calculations of Andreo and Brahme [7] for photon beams are used in the IAEA and other protocols [3].

The calculation of sprs in photon beams has not changed substantially since the 70s except for a study by Malamut et al who used EGS4 [8] to study the effect of accounting for electron-positron differences [9]. Although positron stopping powers differ from electron stopping powers by up to 10%, but typically by 2%, they showed there is no effect on the MC calculated sprs at the 0.1% level.

One of the major restrictions of the sprs for electron beams was that they were for mono-energetic incident beams. The protocols used the sprs as a function of depth for the incident monoenergetic electron beam which matched the R_{50} value of the clinical beam (R_{50} is the depth at which the dose falls to 50% of its maximum and incidentally, the association between R_{50} and E_o was also based on Monte Carlo calculations, eg, [10]). This approach was found to be inadequate once a flexible code for simulating radiotherapy accelerators was developed.

BEAM Code for Simulating Radiotherapy Sources

The EGS4 user-codes, BEAM, for simulating radiotherapy sources, and DOSXYZ, for calculating dose in a CT phantom, were developed at NRC [11–13] in collaboration with Rock Mackie's group in Wisconsin. The BEAM system makes it possible to model realistic electron and photon radiotherapy beams using powerful graphical user interfaces for input [14] and the Linux/X compatible version 4 of EGS_Windows allows full 3-D display of the EGS simulation [15]. BEAM builds the accelerator models from individual component modules. It is widely used and has been cited about 100 times. An extensive review of BEAM and earlier work has been published by Ma and Jiang [16].

Returning to the issue of stopping-power ratios, Ding et al used the BEAM code and found that using realistic incident electron beams instead of monoenergetic beams caused the sprs at dose maximum to change by up to 1.8% [17]. In a related study, they showed that R_{50} did not accurately reflect the mean energy of the electrons incident on a water phantom although it was reasonably well correlated to the mean energy of the direct electrons in the beam [19]. David Burns made the valuable observation that moving the reference depth for electron beam dosimetry from the depth of dose maximum to $d_{ref} = 0.6 R_{50} - 0.1$ cm

and also using R_{50} directly as the beam quality specifier, caused both problems to be overcome: the sprs at d_{ref} are all given very accurately by a simple analytic expression (instead of tables of sprs vs depth) and one doesn't need to worry about E_o [19]. Figure 1 shows this remarkable relationship. This approach has been adopted by both of the new dosimetry protocols [4,20].

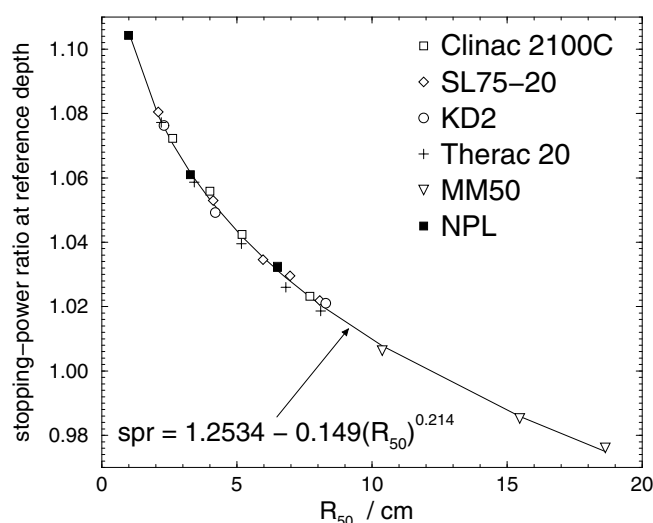


Fig. 1. Burns et al [19] found that at $d_{ref} = 0.6 R_{50} - 0.1\text{cm}$ the Spencer-Attix water to air sprs for realistic electron beams are uniquely specified by R_{50} . The calculated sprs are from Ding et al [17] who used the BEAM code

2.2 Other Detector Correction Factors

Stopping-power ratios vary by up to 5% (11%) in photon (electron) beams of different qualities and are the most critical dosimetry factors calculated with Monte Carlo techniques. However there are many other, usually smaller effects, which have been calculated this way. Ma and Nahum have used the EGS4 code and correlated sampling techniques to calculate the effects of a 1 mm aluminium electrode in an ion chamber instead of an electrode made out of the wall material (usually graphite or plastic) [21]. This calculation is very difficult because the effect is typically less than 1%. The 0.8% effect in a ^{60}Co beam was totally ignored in the TG-21 protocol of the AAPM [2], however for photon beams it nearly cancelled out because it affected the chamber response more or less equally in-air and in-phantom. The major effect on dosimetry protocols is in electron beams where the electrodes have least effect! The AAPM's TG-51 fully incorporates these MC calculated results [4].

Ma et al have used correlated sampling techniques to study the effects of the walls of glass vials used for Fricke dosimetry to prevent chemical effects [22].

Their calculations showed that 1 mm walls could have up to a 2% effect in photon beams. This was verified experimentally in the same work and caused significant changes in the primary standards and Fricke calibration services at major standards laboratories since these corrections were ignored previously.

When using ion chambers, one must account for the fact that the chamber walls are not a single material and often differ from the phantom material. Many experiments had demonstrated that the response of plane-parallel chambers in ^{60}Co beams did not agree with the standard theory. Detailed Monte Carlo calculations of the response of these ion chambers showed that for the NACP and Capintec PS-033, the thin insulating layers behind the air cavity (0.2 mm of polystyrene and 1 mm of C-552 air equivalent plastic respectively) were causing -2% and $+4\%$ changes in the chamber response and this explained the previously unexplained experimental results [23]. Similar calculations [24] are the basis of the so-called k_{ecal} factors used in the AAPM's TG-51 protocol [4].

3 Role of Monte Carlo in Primary Standards of Air Kerma

3.1 K_{wall} and K_{an} Correction Factors

Primary standards for air kerma in ^{60}Co beams are based on graphite walled ion chambers. There are two controversial aspects of these standards, namely the correction for attenuation and scatter in the wall of the chamber, K_{wall} , and the correction which accounts for the radiation being from a point source rather than a parallel beam, K_{an} . Most standards labs determine K_{wall} by measuring ion chamber response as a function of wall thickness and linearly extrapolating the response to zero wall thickness. In contrast, MC simulations predict K_{wall} is up to 1% different from the extrapolated value. At the same time, MC correctly predicts the variation in response with wall thickness to about 0.1% [25,26]. The resolution of this discrepancy is that the extrapolation to zero wall thickness is non-linear [27]. Labs determine the K_{an} correction using two different techniques and the two approaches disagree by up to 0.8% [28]. Early in the 90's, EGS4/PRESTA MC calculations using correlation techniques demonstrated a preference for Bielajew's theory in two cases, but were limited by the 200 days of CPU time required for the calculations [29]. A recent set of calculations was done with the EGSnrc code [30,31] and using a brute force method in which ion chamber response in a parallel or point source beam was calculated directly. The K_{an} values calculated for 19 cases with a precision of 0.01% to 0.04% confirmed that the factors used by several major standards labs are inappropriate [26] and required corrections of up to 0.9%. As shown in Fig. 2, if the MC values of K_{wall} and K_{an} are both applied instead of the values currently used by the primary standards labs, the implication is an increase in the world's primary standards of air kerma by an average of 0.8% [26].

There has been considerable resistance to making these changes because very tight agreement in the "as reported" results has been taken as evidence that the

old techniques work. However, as Fig. 2 shows, with the exception of 2 or 3 labs, the variation of the “revised” results is equally good, despite the 0.8% shift. My own lab is one of the outliers, but as discussed below, this may not continue.

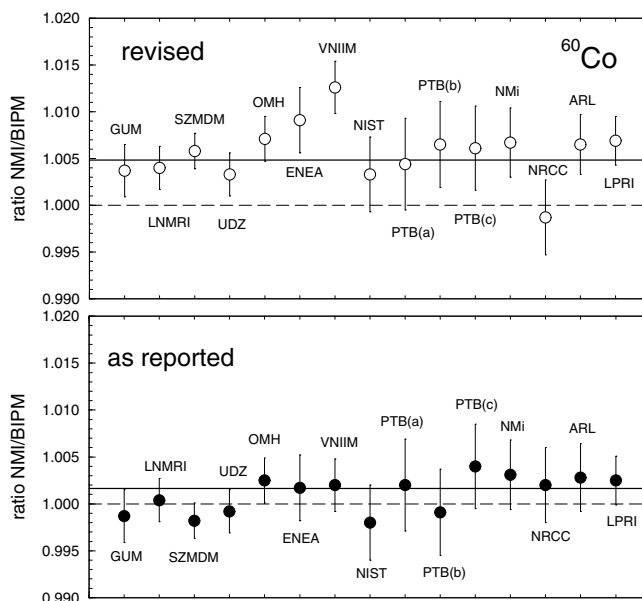


Fig. 2. The “as reported” ratios of air-kerma rates measured by various national lab’s vs that measured by the BIPM and the “revised” results after applying both the K_{wall} and K_{an} corrections as obtained from Monte Carlo calculations. Note that there is a change in the BIPM baseline of about 0.4%. From [26]

3.2 Verification of Spencer-Attix Cavity Theory

In a “Fano” ion chamber in which the gas is made of the same material as the wall and the density effect for the wall material is used to model the gas, the response of the ion chamber is known and one can use this to test a Monte Carlo code’s ability to calculate this response. In this way, Kawrakow has demonstrated that the EGSnrc code is capable of calculating ion chamber response with an accuracy of 0.1% relative to its own cross sections [31].

Given this unprecedented accuracy, one can ask questions about the accuracy of Spencer-Attix (S-A) cavity theory. Borg et al [32] have taken a simple approach and asked the question, “If S-A cavity theory is applied with a standard calculation of sprs and other factors, do we predict the correct air kerma given the measured or calculated dose to the gas in the ion chamber?”. For ^{60}Co beams, all primary standards of air kerma assume the answer is yes. But Ma and Nahum have shown, using MC calculations, that at 300 keV (the mean energy

of an ^{192}Ir source) 3% of the ion chamber response comes from photon interactions in the cavity, thereby invalidating an assumption of S-A cavity theory. This theory also assumes that the cavity does not change the particle fluence and this assumption may break down, as may the standard method for calculating photon beam sprs as photon energy is reduced. Borg et al calculated the dose to the gas in an ion chamber using EGSnrc and calculated the factors needed for standard S-A cavity theory. They calculated K_{SA} , the correction needed to standard S-A cavity theory to get the correct air kerma, by comparing the cavity theory estimate of the air kerma to the air kerma determined from the known fluence of photons [32]. Figure 3 presents their calculated Spencer-Attix correction factors, in this case when using the NRC primary standard cavity chamber (the “3C”). The factor is not unity, even at ^{60}Co energies. If a more appropriate value of Δ is used to calculate the spr, K_{SA} is within 0.05% of unity at ^{60}Co and 0.15% at ^{192}Ir energies. These calculations demonstrate that Spencer-Attix cavity theory is more accurate than one might expect, at least for graphite-walled ion chambers. These results do not generalise to other wall materials.

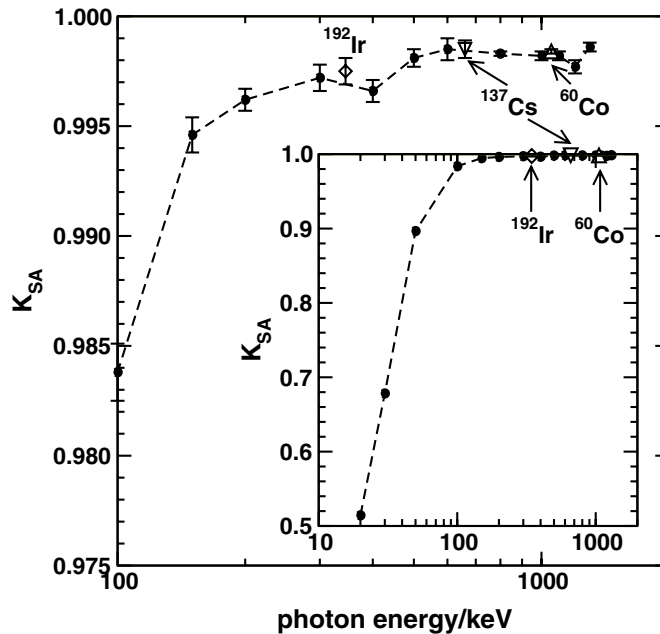


Fig. 3. Values of K_{SA} , for the NRC 3C cylindrical ion chamber, if made entirely of graphite, as a function of energy for monoenergetic photon beams and for 3 spectra. Sprs were calculated with $\Delta = 10$ keV. Statistical uncertainties are 1 standard deviation. The inset shows the agreement for the interval from 20 to 1300 keV. From [32]

3.3 Composite Wall Corrections for the NRC Chamber

The standard S-A cavity theory applied above is for an ion chamber made of one material (graphite). However, all chambers require insulators and the NRC 3C chamber has a polystyrene insulator in its base. Careful but difficult measurements had indicated that its effect was negligible [33]. In the process of Borg et al's study they calculated that the polystyrene insulator produced an 0.4% decrease in the ion chamber response. They showed that this agreed with a very simple analytic calculation of the correction and this implies that the Canadian primary standard for air kerma will have to be increased by 0.4% to account for this effect. Note that this brings the NRC result in the upper part of Fig. 2 into much better agreement with the other standards, except for the BIPM standard.

4 Summary

MC techniques have become an essential element of radiation dosimetry standards and protocols for clinical dosimetry. I have discussed a biased selection of applications but there are many others. While a great deal has already been done, with the advent of the much improved accuracy of the EGSnrc code, there are many projects which can and should be undertaken to improve the accuracy of previous calculations. Furthermore, with the increasing computing power available in most labs, the ability to do meaningful ion chamber simulations in-phantom will lead to further improvements in radiation dosimetry.

References

1. ICRU: *Radiation Dosimetry: Electron beams with energies between 1 and 50 MeV*, ICRU Report 35, (ICRU, Washington D.C. 1984)
2. AAPM TG-21: *Med. Phys.* **10**, 741 (1983)
3. IAEA: *Absorbed Dose Determination in Photon and Electron Beams; An International Code of Practice, Technical Report Series-277*, (IAEA, Vienna 1987)
4. P.R. Almond et al.: *Med. Phys.* **26**, 1847 (1999)
5. M.J. Berger, S.M. Seltzer, S.R. Domen, P.J. Lamperti: *Stopping-power ratios for electron dosimetry with ionization chambers, in Biomedical Dosimetry*, (IAEA, Vienna 1975), pp 589 – 609
6. A.E. Nahum: *Phys. Med. Biol.* **23**, 24 (1978)
7. P. Andreo, A. Brahme: *Phys. Med. Biol.* **31**, 839 (1986)
8. W.R. Nelson, H. Hirayama, D. W. O. Rogers: *The EGS4 Code System*. Report SLAC-265, Stanford Linear Accelerator Center, Stanford, California (1985)
9. C. Malamut, D.W.O. Rogers, A.F. Bielajew: *Med. Phys.* **18**, 1222 (1991)
10. D.W.O. Rogers, A.F. Bielajew: *Med. Phys.* **13**, 687 (1986)
11. D.W.O. Rogers, B.A. Faddegon, G.X. Ding, C.M. Ma, J. Wei, T. R. Mackie: *Med. Phys.* **22**, 503 (1995)
12. D.W.O. Rogers, C.M. Ma, G.X. Ding, B. Walters, D. Sheikh-Bagheri, G.G. Zhang: *BEAM98 Users Manual*, NRC Report PIRS 509(a)revC (1998)
13. C.M. Ma, D.W.O. Rogers, B. Walters: *DOSXYZ99 Users Manual*, NRC Report PIRS 509b(revD) (1999)

14. J.A. Treurniet, D.W.O. Rogers: *BEAM, DOSXYZ and BEAMDP GUI User's Manual*, NRC Report PIRS 0623(rev A) (1999)
15. J.A. Treurniet, D.W.O. Rogers: *EGS-Windows4.0 User's Manual*, NRC Report PIRS-0669, 1999
16. C.-M. Ma, S. B. Jiang: Phys. Med. Biol. **44**, R157 (2000)
17. G.X. Ding, D.W.O. Rogers, T.R. Mackie: Med. Phys. **22**, 489 (1995)
18. G.X. Ding, D.W.O. Rogers, T.R. Mackie: Med. Phys. **23**, 361 (1996)
19. D.T. Burns, G.X. Ding, D.W.O. Rogers: Med. Phys. **23**, 383 (1996)
20. P. Andreo et al: *Absorbed Dose Determination in External Beam Radiotherapy based on Absorbed-Dose-to-Water Standards: An International Code of Practice for Dosimetry*, draft V.7. (IAEA, Vienna 2000)
21. C.M. Ma, A.E. Nahum: Phys. Med. Biol. **38**, 267 (1993)
22. C.M. Ma, D.W.O. Rogers, K.R. Shortt, C.K. Ross, A.E. Nahum, A.F. Bielajew: Med. Phys. **20**, 283 (1993)
23. D.W.O. Rogers: Med. Phys. **19**, 889 (1992)
24. D.W.O. Rogers: Med. Phys. **25**, 310 (1998)
25. D.W.O. Rogers, A.F. Bielajew: Phys. Med. Biol. **35**, 1065 (1990)
26. D.W.O. Rogers, J. Treurniet: *Monte Carlo calculated wall and axial non-uniformity corrections for primary standards of air kerma*. NRC Report PIRS-663, NRC, Ottawa (1999)
27. A.F. Bielajew: Med. Phys. **17**, 583 (1990)
28. A. F. Bielajew: Phys. Med. Biol. **35**, 517 (1990)
29. A.F. Bielajew, D.W.O. Rogers: Phys. Med. Biol. **37**, 1283 (1992)
30. I. Kawrakow: Med. Phys. **27**, 485 (2000)
31. I. Kawrakow: Med. Phys. **27**, 499 (2000)
32. J. Borg, I. Kawrakow, D.W.O. Rogers, J.P. Seuntjens: Med. Phys. **27**, Aug, 2000
33. K.R. Shortt, C.K. Ross: *The Canadian ^{60}Co Exposure Standard*, National Research Council of Canada Report PIRS-0052 (1986)

Many of the above NRC papers are at <http://www.irs.inms.nrc.ca/inms/irs/irs.html>

Absorbed Dose Conversion Factors for Megavoltage Photon Beams

R. Nutbrown, S. Duane, D. Shipley, and R. Thomas

National Physical Laboratory, UK

1 Introduction

For high-energy photon radiation the IPEM recommends its 1990 Code of Practice [1], in which radiotherapy dosimetry is traceable to the UK standard of absorbed dose to water. This standard consists of a graphite calorimeter used to calibrate reference standard ionisation chambers in terms of dose to graphite, and a method [2] to convert this calibration to one in terms of absorbed dose to water. The aim of the present work [3] is to re-evaluate these conversion factors. We compare results previously obtained using cavity ionisation theory and the photon fluence scaling theorem (PFST), for lightly filtered X-ray beams generated by the NPL linac, to recent measurements and EGS4 Monte-Carlo simulations in both lightly and heavily filtered X-ray beams.

2 General Overview of the Method of Dose Ratios

The absorbed dose calibration factor, N_m , converts the electric charge Q_m from ionisation in the chamber cavity, to the absorbed dose D_m at the position of the chamber in the undisturbed medium, m:

$$N_m = D_m / Q_m \quad (1)$$

Under the assumptions of the photon fluence scaling theorem, when all dimensions are scaled in the inverse ratio of the electron densities, the ratio of calibration factors in water (w) to graphite (c) is given by:

$$\frac{N_w}{N_c} = \frac{Q_c}{Q_w} \cdot \frac{f_c^2}{f_w^2} \cdot \frac{\int_0^{E_0} dE \cdot w[E] \cdot (\mu_{en}[E] / \rho)_w \cdot \beta_w[E]}{\int_0^{E_0} dE \cdot w[E] \cdot (\mu_{en}[E] / \rho)_c \cdot \beta_c[E]} \quad (2)$$

Where E is the energy of the photon fluence with maximum energy E_0 , f is the source-chamber distance, μ_{en}/ρ is the mass-energy absorption coefficient of the medium, β is the ratio of absorbed dose to collision kerma at a point and w is a weighting factor common to both numerator and denominator.

Equation (3) is obtained using the relation between photon fluence and absorbed dose from the more general form:

$$\frac{N_w}{N_c} = \frac{D_w}{D_c} \cdot \frac{Q_c}{Q_w} \quad (3)$$

In the present work, Monte-Carlo simulation was also used to estimate the absorbed doses D_w , D_c .

3 Overview of Methods A and B

Ionisation measurements were made in graphite and in water under two sets of conditions. In method (A) both the chamber-source distance and the chamber depth in phantom were scaled by the inverse electron density of the media, while in method (B) the chamber-source distance was kept fixed, and only the depth was scaled. The effective position of the source was determined from the inverse square law, after correcting for scatter and air-attenuation.

The ratio of absorbed doses at the chamber position was obtained using (A) the PFST and (B) Monte-Carlo simulation. The required conversion factor is the product of this dose ratio with the ratio of measured ionisations, and the results of the two methods were compared. The second method avoids the need to estimate various corrections to the PFST, but places more reliance on Monte-Carlo calculations.

3.1 Virtual Source Correction

It has been assumed that as the primary component of the photon fluence obeys the inverse square law the chamber response to this fluence would vary similarly. Chamber response measurements made at depth in a water phantom at varying source to chamber distances were corrected to give the chamber response to the primary contribution. The EGS4 usercode DOSRZPAR (see section 4.2) was used to calculate the ratio of primary to total dose which was used to correct measurements of total collected charge to give the chamber response to the primary component. The calculations determined dose rather than charge ratios and so it was necessary to assume that chamber response (charge/dose) is the same for primary and scattered radiation. After correcting also for air attenuation the chamber response in water to the primary fluence should obey the inverse square law. Any deviation from this was assumed to be due to a displacement of the virtual source of X-radiation from the centre of the target.

3.2 Air Attenuation Correction

As measurements were made at different target-chamber distances it is necessary to apply a correction for the differing amount of attenuation of the intervening air. Narrow beam attenuation coefficients for air were applied to the binned photon energy fluence at the scoring plane to give the fluence at the front face of the phantom. The effective value of the attenuation of the air between the scoring plane and phantom is given by the ratio of the photon energy fluences at the front face and at the scoring plane integrated over all energies. The air attenuation correction is determined by taking the ratio of this value for the water and graphite setups.

3.3 Correction for Pair Production

The PFST assumes that photons interact only by Compton scattering whose cross-section is proportional to the electron density of the medium. This ensures

that the primary and the proportion of scattered to primary photon fluence at corresponding scaled depths in the two media is the same. In contrast bremsstrahlung and pair production do not obey the PFST as their differential effect in two phantoms scaled by electron density does not cancel.

The correction to account for the different proportion of the primary photon fluence scattered out of the beam due to pair production in the two phantoms can be determined by considering the narrow-beam attenuation of the photons that includes attenuation due to pair production. Firstly the correction for narrow beam attenuation of the beam in air was applied to the binned photon energy fluence from the scoring plane to the front face of the corresponding phantom. For each set-up the correction for narrow beam attenuation of the beam from the front face of the phantom to the point of measurement in the medium was applied to this corrected photon energy fluence. The effective attenuation factor of the medium that includes attenuation due to pair production is given by the integrated ratio of the photon energy fluence at the depth in the medium to the front face of the phantom. The pair production correction can then be determined by taking the ratio of the attenuation factors in water and graphite.

3.4 Correction for Bremsstrahlung and Annihilation Radiation

The intensity and spectrum of radiation due to bremsstrahlung and annihilation will differ in the two media. Positrons produced from pair production events give rise to annihilation photons which can add to the scattered radiation reaching the point of measurement. Compton scattered electrons may subsequently create bremsstrahlung radiation that will also add to the scattered radiation reaching the point of measurement.

DOSRZPAR can score the dose due to Compton and Rayleigh scattered photons separately to that due to bremsstrahlung and annihilation photons. Estimated values of the average energy of the primary and scattered components of the fluence were used to give an estimate of the average mass-energy absorption coefficients and the correction for the centre of electron production for the two components. Values for the ratio of the scatter factors in water and graphite at a point in the undisturbed medium could then be determined for the situation when bremsstrahlung and annihilation radiation was included in the total dose and when it was excluded. The maximum correction was of the order +0.05% with uncertainties of the same order of magnitude and so it was decided not to apply any correction to account for bremsstrahlung and annihilation.

3.5 Ratio of Mass-Energy Absorption Coefficients

Values of the photon mass-energy absorption coefficients for water and graphite at the point of measurement in the respective phantoms were determined by taking a weighted average over the photon energy fluence at the measurement depth. Values were interpolated from the tabulated data of Hubbell [4].

3.6 Correction for Centre of Electron Production

In a slab of material with a broad parallel beam of high-energy photons (free of electron contamination) perpendicularly incident on it, at depths greater than the maximum electron range, transient charged particle equilibrium exists. Kase [5] defines a mean distance \bar{x} that the secondary electrons carry kinetic energy “downstream” before depositing it as absorbed dose. The value of \bar{x} is given by the horizontal separation of the curves for absorbed dose and collision kerma anywhere past the build-up.

The correction for centre of electron production was determined by interpolating values of \bar{x} obtained from Attix [6] and taking a weighted average over the photon energy fluence at depth in the water and graphite phantoms.

4 EGS4 Monte Carlo Simulations

The Monte-Carlo calculations described here were carried out using the EGS4 code system [7] with the PRESTA [8] electron transport algorithm. Appropriate values for the electron transport cut-offs were chosen for the NPLLINAC and DOSRZPAR calculations and the PEGS4 datasets. The IAPRIM and EPSTFL options were used with density effect corrections obtained using EPSTAR. Where possible correlated sampling techniques were employed in the calculations of absorbed dose in the graphite and water phantoms by using the same phase space data generated in the linac simulation.

4.1 Simulations of the NPL LINAC

A detailed model of the NPL linac (the EGS4 usercode NPLLINAC) was used to generate phase space data representing the X-ray beam as it emerges from the collimator, filter and transmission monitor. These data were validated by comparing simulated central axis depth dose curves and beam quality parameters with measured data. In the model the electrons incident on the X-ray target were taken to form a pencil beam, with no attempt to include the angular distribution produced by the focussing magnets. Particular care has been taken to minimise the effects of this incorrect angular dependence in all the simulations which used these phase space data.

NPLLINAC stores the full phase space information of each particle striking a predefined scoring plane that is perpendicular to the beam axis. The code has been validated extensively by comparing TPR values for calculated spectra with measured values. Depth dose curves for measured and calculated spectra have also been compared and good agreement has been found. In all cases, the phase space spectra was binned into 200 energy bins.

4.2 Simulations of the Measurement Set-up

Simulations of the measurement set-up were carried out using the usercode DOSRZPAR which has been well tested and validated against the established code

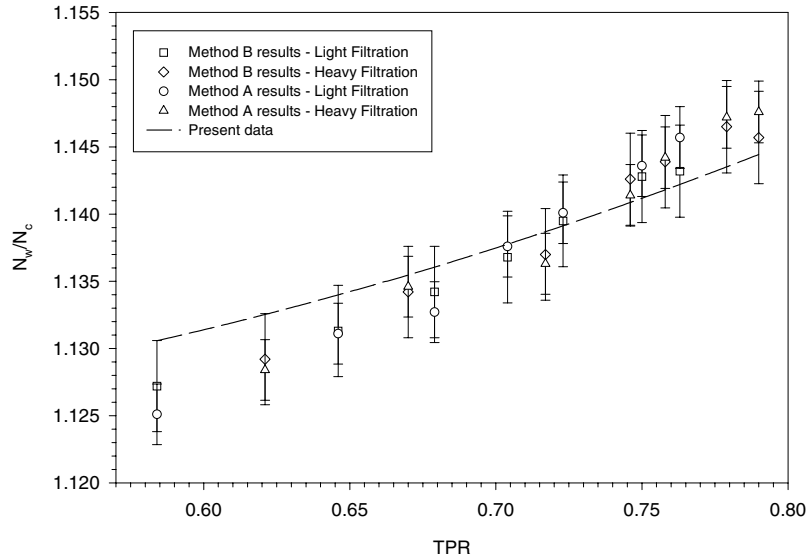


Fig. 1. Plot of N_w/N_c versus TPR ([2,3]) with uncertainties shown at 1σ level

DOSRZ. DOSRZPAR calculates the dose to the internal regions of a cylindrical-slab geometry and so it was necessary to approximate the measurement set-up by using a cylindrical water or graphite phantom with a radius chosen to give the same area as the front face of the respective phantom. The phase space spectra were used with DOSRZPAR to calculate the total and primary dose to the scoring region at the points of measurement in the respective phantoms. The scoring region was approximated by a cylinder of length 1 cm, and radius 0.5 cm for target-chamber distances of 125 cm or less and radius 1 cm for greater target-chamber distances. In the case of the water phantom, the Perspex walls were replaced by water.

5 Results

The total uncertainty in the determination of N_w/N_c at the 1σ level was calculated to be 0.32% using method A and 0.37% using method B. The non-random uncertainty in the ratios of mass-energy absorption coefficients is present in each total uncertainty for methods A and B and should be ignored when comparing results from these two methods. Also, all random uncertainties can be reduced by a factor of \sqrt{N} , where N is the number of estimates made.

The values of N_w/N_c determined using methods A and B agree to within 1σ uncertainty where the uncertainties on method A results are 0.20% and the uncertainties on method B results are 0.30%. Non-random uncertainties common to both methods have not been included in each total uncertainty and all random

uncertainties are reduced by a factor of \sqrt{N} . The best fit to both sets of results agrees with values determined in previous work to within 2σ uncertainty, the greatest discrepancy being found at the lowest and highest energies.

One of the main aims of this work was to test the interpolation and extrapolation of results obtained for light filtration to give values for heavy filtration. It can be seen from Fig. 1 that, for this work, no noticeable difference was observed between results for light and heavy filtration measurements. It can therefore be concluded that interpolation and extrapolation was adequate.

The values of N_w/N_c determined in this work agree to within 1σ uncertainty to values in present use at the NPL. The uncertainty quoted on the values in present use is $\pm 0.5\%$. It is worth noting that much of the work used to determine the values of N_w/N_c in both cases makes use of the PFST and so non-random uncertainties common to both results should not strictly be included when comparing values. The greatest discrepancy between the two sets of results is observed to be at the extremes of the energy range with the largest difference (0.4%) at 4 MV with light filtration. Further work is required to determine the value of N_w/N_c for a ^{60}Co beam. New facilities are soon to be commissioned at the NPL that will allow measurements in ^{60}Co to be made at a greater range of distances. However, extrapolation of the data given in Fig. 1 of N_w/N_c versus TPR gave values for ^{60}Co which are in good agreement (within 0.3%) to the average value obtained by the Australian Radiation Laboratory [9] using the PFST.

References

1. S.C. Lillicrap, B. Owen, J.R. Williams, P.C. Williams: Phys. Med. Biol. **35**, 1355 (1990)
2. J.E. Burns, J.W.G. Dale: NPL Report RSA(EXT) 7, National Physical Laboratory, Teddington, UK (1990)
3. R.F. Nutbrown, S. Duane, D.R. Shipley, R.A.S. Thomas: NPL Report CIRM 37, National Physical Laboratory, Teddington, UK (2000)
4. J.H. Hubbell, Int. J. Appl. Radiat. Isot. **33**, 1269 (1982)
5. K.R. Kase, B.E. Bjärngard, F.H. Attix: *The Dosimetry of Ionizing Radiation Metrology* (Academic Press, London 1985)
6. F.H. Attix: Health Physics **36**, 347 (1979)
7. W.R. Nelson, H. Hirayama, D.W.O. Rogers: Report SLAC-265, Stanford Linear Accelerator Center, Stanford, CA (1985)
8. A.F. Bielajew, D.W.O. Rogers: Nucl. Instr. and Meth. **B18**, 165 (1987)
9. R.B. Huntley, J.F. Boas: Report ARL/TR126, Australian Radiation Laboratory, Victoria (1998)

Is the Spencer–Attix Cavity Equation Applicable for Solid-State Detectors Irradiated in Megavoltage Electron Beams?

P.N. Mobit^{1,2} and G.A. Sandison^{1,2}

¹ Department of Medical Physics, Tom Baker Cancer Centre, 1331-29 Street NW, Calgary, Alberta, T2N 4N2, Canada.

² Departments of Oncology, Physics and Astronomy, University of Calgary 1331-29 Street NW, Calgary, Alberta, T2N 4N2, Canada

Abstract. The applicability of the Spencer–Attix cavity equation in determining absorbed doses in water using solid state detectors irradiated by megavoltage electron beams have been examined. The calculations were performed using the EGSnrc Monte Carlo code. This work is an extension of a recently published article examining the perturbation of dose by solid state detectors in megavoltage electron beams. The use of the Spencer–Attix cavity equation is based on the assumption that the charge particle fluence in the uniform medium and in the detector material are the same. Previous Monte Carlo simulation of the perturbation correction for common TLD materials in electron beams show that for solid state detectors having a density of at least double that of water, there is a significant difference at all depths between the energy spectra present in the water phantom and that in the solid state cavity. This means the assumption that the detector does not perturb the charged particle fluence is not valid. As the cavity size is increased, the difference between the energy spectra in the solid cavity and medium increases as expected. At depths beyond d_{max} not only is there a significant difference between energy spectra but there is also a significant difference in the number of low energy electrons which can not travel across the solid cavity (i.e. stopper electrons whose residual range is less than the cavity thickness). The number of these low energy electrons that are not able to cross the solid state cavity increases with depth. They also increase with the dimension of the cavity in the beam direction. These differences in the energy spectra and increasing percentage of the total dose in the cavity due to these stopper electrons means that the shape of the depth dose curve measured by a solid detector depends on its effective thickness and may differ from that measured with detectors of different effective thickness. The results show that for a 1 mm thick LiF solid cavity, the stopper to crosser ratio at a depth of 1 cm for a 5 MeV incident electron beam is about 0.2 but this ratio increases to 0.3 and 0.5 at a depth of 1.4 cm and 1.9 cm, respectively. For a 2.64 mm thick water cavity, the stopper to crosser ratio at a depth of 1 cm is 0.25 and this value rises to 0.38 and 0.95 at depths of 1.4 and 1.9 cm, respectively. The results show that even for a 1 mm thick LiF-cavity the response of the detectors is dominated by stoppers for depths equal or greater than R_{50} .

1 Introduction

The main assumption in the use of the Spencer–Attix cavity equation [1] for the determination of absorbed dose in electron beams is that the cavity does not

perturb the electron spectrum from that experienced in the uniform medium at the same point. Mobit et al. [1] have shown that for incident electron beams, the electron spectra in the medium and in a solid detector material are significantly different when the density of the detector is at least double that of the medium. So for these solid state detectors, the assumption that the cavity does not perturb the electron spectrum is not valid. An assumption made in the derivation of the Bragg-Gray cavity equation is that the cavity is infinitely small so that the dose deposited in the detector is primarily by electrons whose range is much greater than the thickness of the cavity i.e. the dose is deposited by crossers. The Spencer-Attix cavity equation represented a major improvement of the Bragg-Gray cavity equation by allowing for a finite size cavity. The dose due to stoppers was incorporated into the Spencer-Attix equation by the track end terms [3]. If the cavity is large compared to the range of the electrons incident on it, then the response of the detector may be dominated by these electrons (stoppers) which are not energetic enough to travel across the cavity. The ratio of the number of stoppers to the number of crossers is therefore very important in the measurement of relative and absolute absorbed doses in charged particle beams because the variation of the stopper to crosser ratio might not be uniform through out the entire range of the incident charged particles. The purpose of this work is to evaluate the stopper to crosser ratio in a 5 MeV electron beam incident upon a water phantom. We have also studied how the size of a solid cavity affects the stopper to crosser ratio and the influence of the cavity size on the depth dose curve.

2 Monte Carlo Simulations

The EGSnrc Monte Carlo System [4,5] was used for all simulations reported in this work. The EGSnrc user codes DOSRZnrc and FLURZnrc were used in the calculation of absorbed doses and the electron fluence respectively. Both codes incorporate the much improved electron PRESTA-II algorithm. The fractional energy loss per electron step (ESTEPE) was set to 0.25 and ECUT and PCUT were 0.521 MeV and 0.010 MeV respectively. The field size of the incident electron beam had a radius of 5 cm at the phantom surface. The calculations were performed on two Pentium III, 500MHz Personal Computers loaded with 320Mb of RAM.

3 Results and Discussions

3.1 Depth Dose Curve

Figure 1 shows the depth dose curve for 5 MeV monoenergetic electron beams calculated with DOSRZnrc with different scoring slab thickness in a water phantom. The scoring radius was 1.805 mm which is equivalent to the surface area of a typical 3.2 mm \times 3.2 mm TLD chip. The slab thickness were set to 1 mm and 2.64 mm. The thickness of 2.64 mm slab was chosen to simulate a 1 mm thick

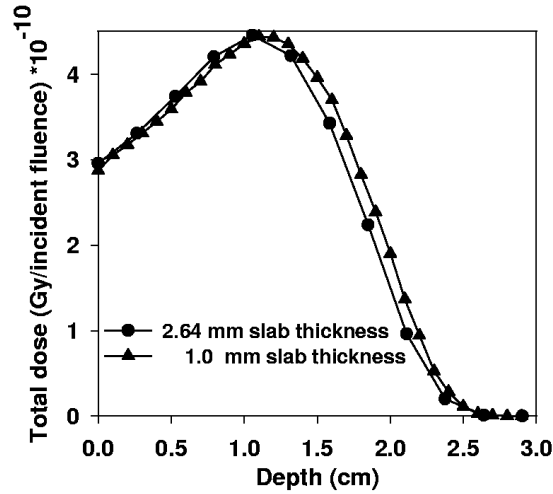


Fig. 1. Absolute depth dose curve for a 5 MeV electron beam in water scored in different thicknesses of water

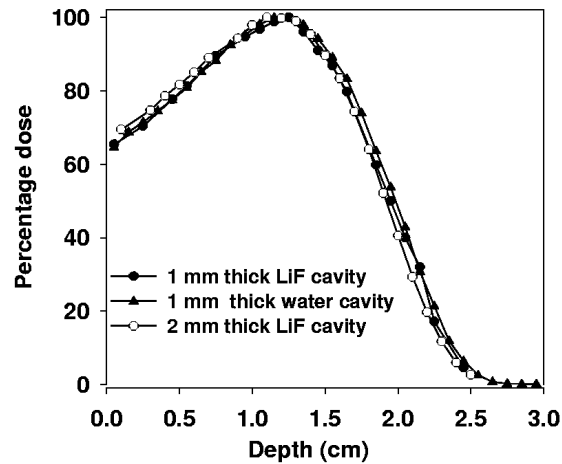


Fig. 2. Percentage depth dose curve for a 5 MeV electron beam in water scored in different thicknesses of LiF-TLD

LiF-TLD rod. Since LiF-TLD has a density of 2.64g/cm^3 , this means that a 1 mm thick LiF-TLD is approximately equivalent to 2.64 mm of water. The results shown in Fig. 1 indicate very clearly that even in a uniform water phantom with no region of inhomogeneity the depth dose curves are different for different scoring slab thicknesses. Also noticeable is the more rapid build up of dose for depths less than d_{max} , the shift in the d_{max} towards the surface and the reduced apparent electron range for the 2.64 mm slab compared to the 1 mm slab thickness. Figure 2 shows the depth dose curve obtained by scoring the dose in

a 1 mm and 2 mm LiF-TLD disc at various depths in a 5 MeV electron beam. The radius used for calculation was also set to 1.805 mm. The data presented in Fig. 2 is equivalent to performing depth dose measurements with LiF-TLDs. We see that there is a difference in the percentage depth dose curve for all depths. R_{50} determined by the 2 mm thick LiF-TLD is 1 mm less than that determined for 1 mm water cavity. In addition to the volume averaging effect of a dosimeter which will result in differences in the percentage depth dose data, the number of low energy electrons (stopper) also has a significant influence on measurement of the depth dose curve as demonstrated in section 3.2

3.2 Stopper to Crossers Ratio as a Function of Depth

To investigate how the stopper to crosser ratio varies with depth, simulations were performed using the FLURZnrc user code for a 5 MeV monoenergetic electron beam incident on a water phantom. The stopper to crosser ratio was examined at 4 different depths (0.9-1.0 cm, 1.2-1.3cm, 1.4-1.5 cm and 1.9-2.0 cm). The electron energy spectrum at these depths is shown in Fig. 3 and the stopper to crosser ratio at each depth is shown in Fig. 4. For a small cavity size (lineal density less than 0.01 g/cm^2) there is essentially no difference between the stopper to crosser ratio at all depths. However for a 1 mm thick water-equivalent cavity the stopper to crosser ratio at a depth of 1 cm for a 5 MeV incident electron beam is about 0.2, i.e. approximately 20% of the dose deposited in the cavity is deposited by stoppers. For this size detector, the stopper to crosser ratio increases to 0.3 and 0.5 at a depth of 1.4 cm and 1.9 cm, respectively, indicating that up to 50 percent of the dose is due to stoppers in a 5 MeV incident electron beam at depths less than R_{50} . In the case of a 1 mm LiF-TLD cavity (which is equivalent to a 2.64 mm thick water cavity) the stopper to crosser ratio at a depth of 1 cm is 0.25 and this value rises to 0.38 and 0.95 at depths of 1.4 and 1.9 cm, respectively. The results indicate that a 1 mm thick LiF-TLD cannot be considered as a Bragg-Gray cavity at depths greater than or equal to R_{50} for a 5 MeV incident electron beam. The Spencer-Attix cavity theory does take into account the dose contributed by stoppers and hence should be able to predict the dose to medium accurately even for depths greater than R_{50} . However due to perturbation by the cavity, the energy distribution of the electrons in the medium and in a solid cavity are significantly different [2], and the Spencer-Attix cavity equation is not able to predict the dose to the medium from the dose deposited in the LiF-TLD. The only way to determine the dose accurately is to use the Spencer-Attix cavity equation and the actual electron fluence in the medium and in the detector material as performed by Mobit et al. [2]. A thick solid state cavity therefore represents a situation in which there is a breakdown of the Spencer-Attix cavity equation and therefore dose measurements by such solid state detectors in charged particle beams is unreliable. The results also indicate that a gas ionization chamber may be the only dosimeter that can be used to measure dose accurately at all depths in charged particle beams since the stopper to crosser ratio remains low e.g. less than 1% for electron beams at all depths. Although the results presented here are for a low energy electron beam,

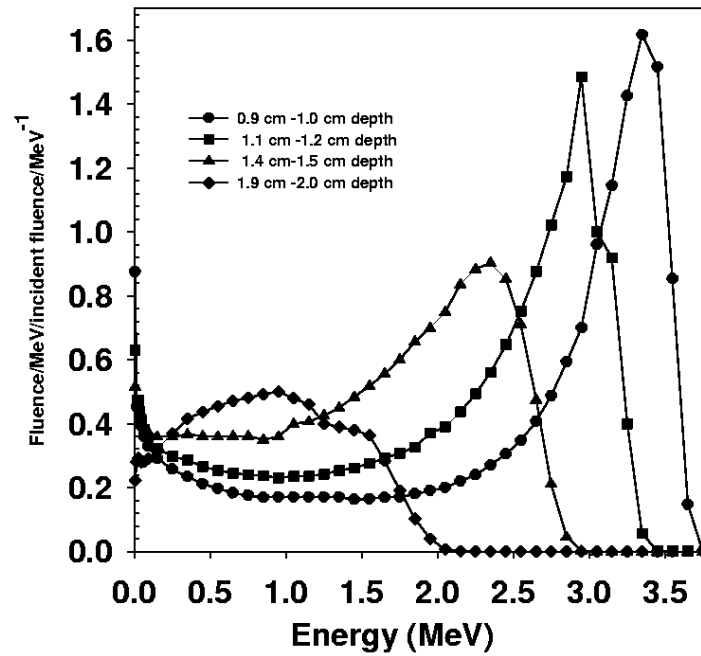


Fig. 3. Electron spectra at various depths in water for a 5 MeV incident electron beam

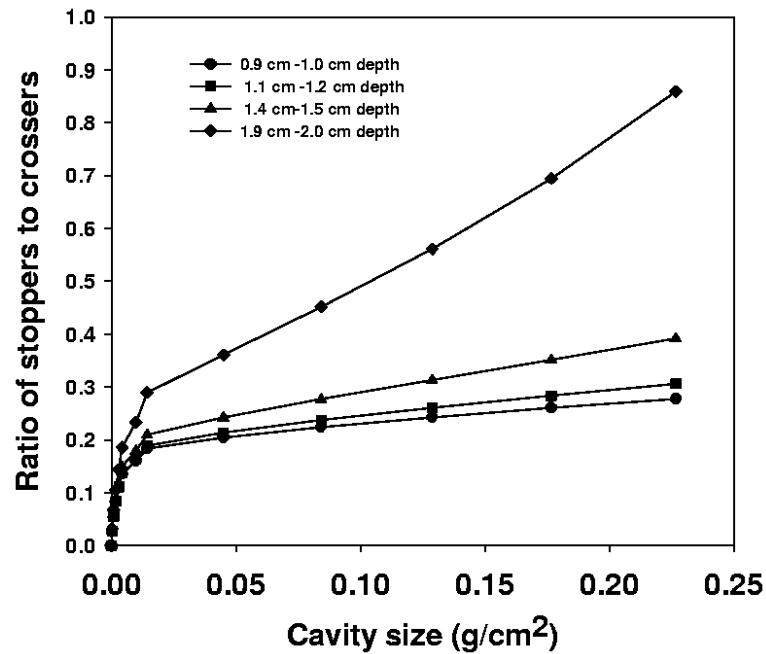


Fig. 4. Stopper to crosser ratio at various depths in water for a 5 MeV electron beam

proton beams and heavier charged particle beams will be even more sensitive to this breakdown of the Spencer–Attix cavity equation in application to dose measurement, especially in the Bragg peak region.

4 Conclusions

- The stopper to crosser ratio increases with depth because of the increased energy spread of electrons with depth.
- At depths greater than d_{\max} , the dose deposited in the cavity by stoppers can be a significant proportion of the total dose deposited in the cavity.
- Even for a water cavity irradiated in a water phantom, different dose averaging volumes lead to differences in the depth dose data obtained. This indicates that for a solid state detector, the cavity should be made as thin as possible to reduce the cavity-size dependent effects of the detector that may lead to inaccurate determination of dose or such quantities as R_{50} .
- The results also indicate that a gas ionization chamber may be the only dosimeter that can be used to measure dose accurately at all depths in an electron beam since the stopper to crosser ratio remains less than 1% at all depths.
- The breakdown of the Spencer–Attix equation is a major concern for dose measurements in all types of charged particle beams when thick solid state detectors are used.

References

1. L.V. Spencer, F.H. Attix: *Rad. Res.* **3**, 239 (1955)
2. P.N. Mobit, S.A. Sandison, A.E. Nahum: *Phys. Med. Biol.* **45** (2000)
3. A. E. Nahum: *Phys. Med. Biol.* **41**, 1531 (1996)
4. I. Kawrakow: *Med. Phys.* **27**, 485 (2000)
5. I. Kawrakow: *Med. Phys.* **27** 499 (2000)

Monte Carlo Simulation of Electron Beams for Radiotherapy – EGS4, MCNP4b and GEANT3 Intercomparison

A. Trindade¹, P. Rodrigues¹, C. Alves², A. Chaves², M.C. Lopes², C. Oliveira³,
and L. Peralta¹

¹ LIP, Laboratório de Instrumentação e Física Experimental de Partículas, Av. Elias Garcia, 14-1, 1000-149 Lisboa, Portugal

² CROC, Centro Regional de Oncologia de Coimbra do IPOFG, Av. Bissaya Barreto, 3000-075 Coimbra, Portugal

³ ITN, Instituto Tecnológico e Nuclear, Estrada Nacional 10, 2685-953 Sacavém, Portugal

Abstract. In medical radiation physics, an increasing number of Monte Carlo codes are being used, which requires intercomparison between them to evaluate the accuracy of the simulated results against benchmark experiments. The Monte Carlo code EGS4, commonly used to simulate electron beams from medical linear accelerators, was compared with GEANT3 and MCNP4b. Intercomparison of electron energy spectra, angular and spatial distribution were carried out for the Siemens KD2 linear accelerator, at beam energies of 10 and 15 MeV for a field size of 10×10 cm². Indirect validation was performed against electron depth doses curves and beam profiles measured in a MP3-PTW water phantom using a Markus planar chamber. Monte Carlo isodose lines were reconstructed and compared to those from commercial treatment planning systems (TPS's) and with experimental data.

1 Introduction

Monte Carlo (MC) simulation is regarded as a precise technique for radiotherapy and radiation dosimetry. In this field, Monte Carlo codes can be used to characterize electron or photon beams produced by clinical linear accelerators. While photon beams are used to deep-seated radiation therapy, electron beams are used for superficial pathologies due to their dose deposition characteristics.

EGS [1] is the most used MC code for electron beam simulation, and the results it provides are well established against experimental data. MCNP4b [2], due to the enhanced electron physics, is also currently used for electron beam simulation. In the present work, EGS4 has been compared with MCNP4b and GEANT3 [3]. This code, although used for hadron-therapy, has been less benchmarked for conventional radiotherapy. It was found that electron transport simulations are sensible to fine details of accelerator geometry and to different electron transport algorithms [4]. This motivates the intercomparison between different codes. For this purpose, two different intercomparison stages have been considered. First stage comprehended spatial and angular distribution simulations for electrons and contaminant photons along the accelerator head. In the second

stage, indirect validation of these results have been performed against experimental central axis depth dose curves and profiles measured in water. However, the information provided by the simulation of the central depth dose curves is not sufficient to fully characterize the spatial radiation distribution produced by the beam. In clinical practice, calculation of radiation dose distributions is performed by treatment planning systems (TPS's) through the display of isodose lines, so a two dimensional method of representation was required for more accurate results. Reconstructed isodose lines from the simulation results of EGS4, MCNC4b and GEANT3 have been compared with commercially available TPS's, and experimental results.

2 Materials and Methods

A Siemens KD2 in electron mode with a square applicator of $10 \times 10 \text{ cm}^2$ for 10 and 15 MeV nominal energies was simulated. Detail technical construction data was kindly provided by Siemens AG Medical Engineering. During preliminary simulations, energy tuning was performed for the incident electron beam. Identical values were then use in all MC codes and electron sources were assumed to be point-like and monoenergetic. Along the beam line, phase space distributions were obtained at pre-determined planes, stored into data *Ntuples* and intercompared using PAW software package [5]. Energy values for photons and electrons cut-offs were the same for all codes, respectively 10 and 700 keV (total energy) in the accelerator head, and 10 keV and 521 keV in the water phantom.

The experimental data, depth doses and profiles, were obtained in a MP3-PTW water phantom using a Markus planar chamber.

2.1 GEANT3 Code

Originally designed for detector simulation in High Energy Physics, GEANT3 features cross-sections for physical processes spanning a wide energy range. In simulations, user selection of tracking parameters were used. Maximum fractional energy loss due to continuous processes in an electron step, DEEMAX, was chosen to be a material-dependent parameter. After preliminary runs DEEMAX was set to 0.3% – 0.5% (high-Z materials) and 1% (low-Z materials). Built-in variance reduction techniques, such as electron range rejection, were switched off for this set of results. By default, GEANT3 simulates hadron-photon-lepton coupled transport. In order to decrease total CPU time only relevant electromagnetic process to low energy photon-electron simulation were included: photoelectric effect, Compton scattering, pair production, positron annihilation and bremsstrahlung photon production. Energy loss straggling for charged particles was accounted by explicit generation of δ -rays. Below the threshold for charged secondaries particle production, continuous energy fluctuations were sampled from a restricted Landau distribution. In GEANT3 an interactive graphics interface, capable of displaying 3D geometrical setup (see Fig. 1) and particle transport on real-time is also available.

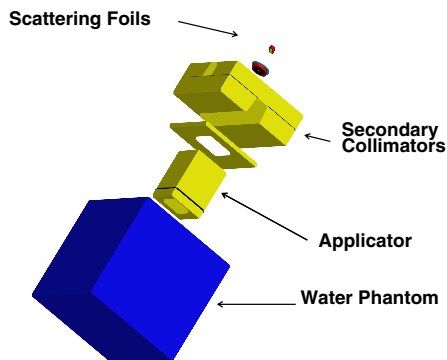


Fig. 1. Siemens KD2 displayed in GEANT 3.21

2.2 EGS4 User Code

The accelerator head was modeled with an EGS4 User Code, using a general purpose geometry package previously developed [6]. This User Code contains also several auxiliary subroutines used for I/O operations, histogram booking and scoring.

The PRESTA electron transport algorithm was switched off. Maximum fractional energy loss due to continuous processes, ESTEPE, was set to 0.5% in the accelerator and 1% in the water phantom. Since EGS4 does not account for continuous energy loss straggling, lower thresholds were used for secondary particle production (AE and AP). This option is required to account for the correct energy distribution on the final electron beam. Thresholds values were set to 521 keV (total energy) for electrons (AE) and 10 keV for photons (AP). For dose calculations, in the water phantom, AE was set to 512 keV [7].

2.3 MCNP4b Code

Concerning this work the enhanced electron physics, to the level of ITS-3, is the most important aspect of the MCNP4b. It takes into account collision energy loss straggling (Landau), angular distributions with partial sub-step to boundary, forward scattering and energy indexing. The tabular region is increased in resolution and an analytic asymptotic form of treatment is used for large energy losses. Material and energy dependent cut-offs are applied to obtain the correct mean energy loss; the Gaussian width is empirically corrected following Seltzer [8]. To obtain the dose values that allowed to draw the isodose curves the water phantom was divided into small cells using the lattice capacities of MCNP. Due to the very small dimensions of the scoring cells, particularly along the beam axis, special attention has been put on the number of the electron sub-steps. For this purpose, ESTEP parameter was set at 15 and 25 for electron source energy of 10 MeV and 15 MeV, respectively.

3 Results and Discussion

3.1 Accelerator Simulation

Phase space distributions were obtained at the end of scattering foils, secondary collimator and electron applicator. Intercomparison has focused electron and photon energy spectra and polar angular distributions. Plots were normalized to total number of simulated events. Overall agreement is good at the different planes. Electron energy and polar angular distribution at the phantom surface are present in Fig. 2.

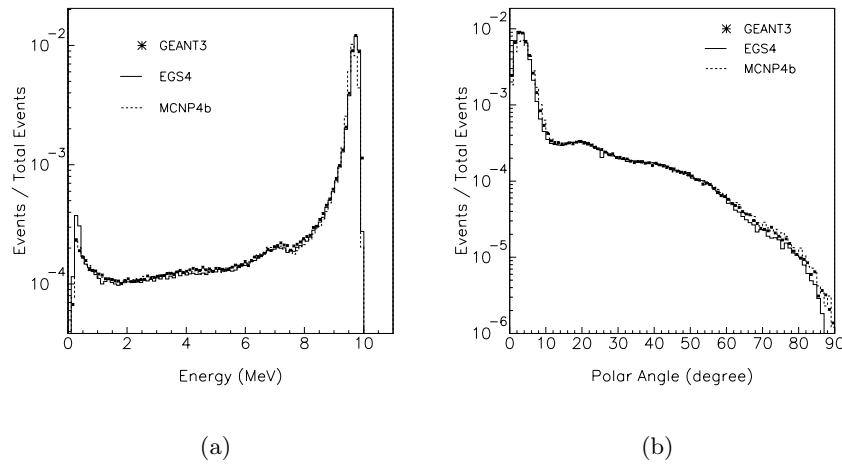


Fig. 2. (a) Electron energy spectra and (b) polar angular distribution at phantom surface, for a 10×10 cm² square field at 10 MeV nominal energy

3.2 Phantom Simulation

Although the agreement between EGS4, MCNP4b and GEANT3 was achieved in a great extent along the beam line, final validation was performed in water. Central axis depth doses and profiles at several depths have been simulated and compared with experimental data. Scoring volumes were chosen with dimensions similar to the Markus planar chamber. In Fig. 3, 10 and 15 MeV depth dose curves are shown. Each curve was normalized at maximum dose on the central axis. Agreement in depth dose curves achieved by EGS4 and GEANT3, for the two energies, were at the 1% level. It was found that MCNP4b slightly underestimates dose deposition at larger depths, demonstrating an adjustment to experimental points identical to the one obtained by Jeraj *et al* [9]. For isodose reconstruction, dose values were scored on a 3D cross-plane grid, filled with voxels. Using a linear interpolation algorithm available in PAW, points with equal dose were joined. The curves were normalized to 100% at depth of maximum dose on the central axis. Monte Carlo isodose lines were then compared with experimental data. From Fig. 4(a), EGS4 and GEANT3 were found to be in close agreement with each other and the experimental points. Disagreement for

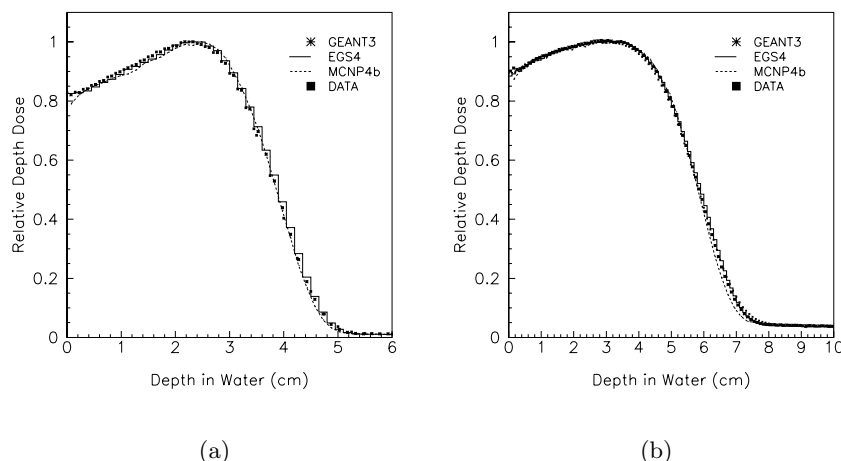


Fig. 3. Comparison between experimental and simulated central axis depth doses for 10 MeV (a) and 15 MeV (b) nominal energy

MCNP4b at the 10% isodose line is related with differences shown in the simulated central axis depth dose curve. For all MC codes lateral adjustment is less than 1 mm, denoting a good agreement with experimental beam profiles and a clearly definition of the field edges.

Data for 10 and 15 MeV isodose lines were calculated with two current commercial TPS, PLATO (version 2.2.15 from Nucletron) and TMS (version 5.0A from HELAX). These lines were then reconstructed with PAW's linear interpolation algorithm. Isodose curves from PLATO and TMS were compared with GEANT3. The good agreement at the central axis seen in Fig. 4(b), indicates that electron depth dose curves are usually very well calculated by TPS's. However, a quite different behavior is demonstrated at the field edges, namely concerning one of the systems and mainly for the lower level isodose curves (below 50%). Indeed, for the PLATO system, the process of commissioning and validation includes, after the input of the basic data (depth dose curves and output factors for each field size), the adjustment of the initial angular spread parameter. This parameter has been adjusted for each energy, in order that the best fit corresponds to the higher level isodose curves - calculated isodose widths at the maximum dose depth, should coincide as much as possible with the experimental and simulated ones (arrows) downgrading the adjustment for lower isodose lines.

4 Conclusions

From the comparison with the Monte Carlo code EGS4, it was found that GEANT3 is a reliable system with excellent capabilities for clinical electron beam simulations. Unclear differences in depth dose curves calculated with MCNP4b affect the adjustment of lower isodose lines. However, comparisons along the accelerator head at different levels reveals a good agreement with GEANT3 and EGS4. This kind of study is very important for the therapeutic

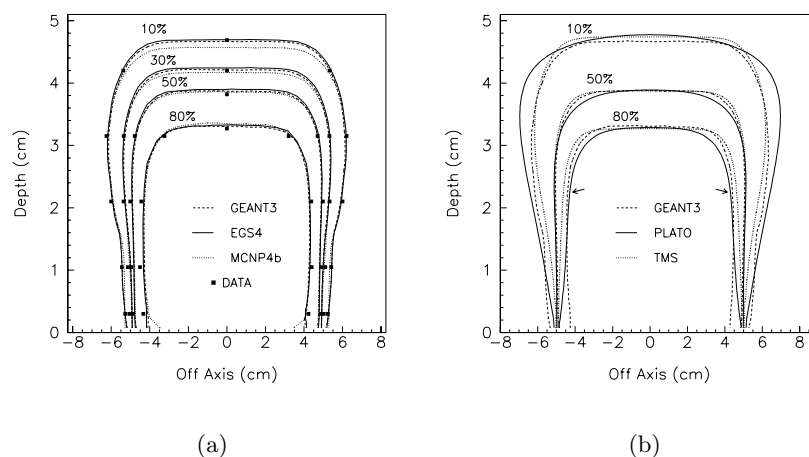


Fig. 4. (a) 10 MeV Monte Carlo reconstructed isodose curves compared with experimental data. (b) Isodose curves from PLATO and TMS compared with GEANT3

tic use of electron beams. Indeed, quite frequently in clinical practice, several electron fields are used together covering extended regions of the patient skin (for instance along a scar). For decision on field separation, a good dosimetric description at the beam edges and shallow depths is crucial in order to determine the homogeneous dose distribution. The isodose configuration calculated in superficial depths by treatment planning systems, would predict an erroneous overdosage for two adjacent beams at the skin level. On the other hand, both experimental and MC results show an isodose configuration at the beam edges enabling the adjacency of two fields without overdosage in depth.

References

1. W.R. Nelson, H. Hirayama, D.W.O. Rogers: *The EGS4 Code System* Report SLAC-265, Stanford Linear Accelerator Center (1985)
2. J.F. Briesmeister: *MCNP-general Monte Carlo N-particle transport code-version 4B* Report LA-12625, Los Alamos National Laboratory (1997)
3. S. Giani, S. Ravndal, M. Maire: *GEANT: Detector Description and Simulation Tool*, CERN Program Library, Long Writeup W5013 (1994)
4. C.M. Ma, S.B. Jiang: *Phys. Med. Biol.* **44**, R157 (1999)
5. R. Brun, O. Couet, N.L. Cremel, C. Vandomi, P. Zarini: *PAW – Physics Analysis Workstation*, CERN Program Library, Long Writeup Q121 (2000)
6. M. Fragoso, A. Chaves, M.C. Lopes, C. Oliveira, L. Peralta, J. Seco: ‘MC simulation of a linear accelerator treatment head – EGS4 and MCNP-4B intercomparison’. In: *8th Int. Conf. on Calorimetry in High Energy Physics 1999*, ed. G. Barreira (World Scientific, Singapore 2000) pp 697–702
7. D.W.O. Rogers: *Nucl. Instrum. Methods Res. B* **227**, 535 (1984)
8. S.M. Seltzer: ‘An overview of ETRAN Monte Carlo methods’. In *Monte Carlo Transport of Electrons and Photons*, ed. by T.M. Jenkins (Plenum Press, New York 1988)
9. R. Jeraj, P. Keall, P.M. Ostwald: *Phys. Med. Biol.* **44**, 705 (1999)

Evaluation of a 50-MV Photon Therapy Beam from a Racetrack Microtron Using MCNP4B Monte Carlo Code

I. Gudowska¹, B. Sorcini^{1,2}, and R. Svensson¹

¹ Dept. of Medical Radiation Physics, Karolinska Institutet and University of Stockholm, PO Box 260, S-171 76 Stockholm, Sweden

² Huddinge University Hospital, Dept. of Medical Physics, Dosimetry Division, RT, Stockholm Söder Hospital, S-118 83 Stockholm, Sweden

Abstract. High energy photon therapy beam from the 50 MV racetrack microtron has been evaluated using the Monte Carlo code MCNP4B. The spatial and energy distribution of photons, radial and depth dose distributions in the phantom are calculated for the stationary and scanned photon beams from different targets. The calculated dose distributions are compared to the experimental data using a silicon diode detector. Measured and calculated depth-dose distributions are in fairly good agreement, within 2–3% for the positions in the range 2–30 cm in the phantom, whereas the larger discrepancies up to 10% are observed in the dose build-up region. For the stationary beams the differences in the calculated and measured radial dose distributions are about 2–10%.

1 Introduction

Monte Carlo (MC) simulation of therapy beams provides an useful information about the phase-space description (PSD) for the treatment machine and allows to accurately predict the radiation dose distribution delivered to a patient. A detailed spatial and energy distribution of the photon beam can be calculated for the complex therapy head configurations of a modern medical accelerator that uses advanced field shaping techniques with multileaf collimators and electromagnetic scanned beams. This information is of particular importance both for accurate treatment planning as well as for intensity and energy modulation of narrow elementary beams operating in the scanned mode.

The Monte Carlo N-Particle code MCNP [1], with both versions MCNP4A and -4B, became a widely used Monte Carlo code in medical applications, specially for modeling the photon and electron beams from medical accelerators in a range of accelerating potentials from 4 to 25 MV [2–8]. The bremsstrahlung production from a target and photon depth dose distributions calculated by MCNP have been verified by a number of the experimental data [2,3,5–7,10,11] showing a good agreement, within the 0.5–3% (1σ), in all parts of the depth dose curves for the low energy photon beams of 4–6 MV. However, for photon beams of higher energy like 25 MV the larger discrepancies, up to 10%, between measurement and calculation are observed in the dose build-up region [7].

Also the comparison between MCNP4B and the MC code EGS4 [12] is satisfactory [6,9] when used to generate the PSD of the photon beam. In the work by Siebers et al [6] the bremsstrahlung productions for 6 and 18 MV beams are about 10 and 5% respectively less using MCNP4B than EGS4 code, but consistent with the differences in the bremsstrahlung cross section data used by these codes. For 3 and 6 MV beams the dose profiles agree within 1-2% statistical uncertainty beyond the build-up region. Some larger discrepancies up to 7% are observed in the build-up region, mainly due to different electron transport algorithms used by EGS4 and MCNP4B codes.

There is a lack of validation of the MCNP code regarding high energy photons around 50 MeV and its application for the therapy beams operating in the scanning mode. In this work the MCNP4B code was used to evaluate photon beam from the 50 MV racetrack microtron (MM50) at Karolinska Hospital, Stockholm. Calculated dose distributions have been compared to experiments using a silicon diode detector.

2 Materials and Method

Treatment Unit The 50 MV racetrack microtron (MM50) provides electron and photon beams with maximum energies in the range 2 - 52 MeV. The accelerator is equipped with an electron and photon beam scanning system instead of conventional flattening filters [13]. Narrow elementary electron and photon beams are scanned in different scanning patterns to generate homogeneous or intensity modulated fields. Three different composite targets for bremsstrahlung production are used: two almost fully absorbing targets of 9 mm beryllium + 6 mm tungsten (9Be6W) and of 5.5 mm tungsten + 6.5 mm copper (5.5W6.5Cu) respectively, and a thin beryllium transmission target of 3 mm Be. All of them were used in the present studies to calculate the bremsstrahlung production for stationary and scanned electron beams of the nominal energy 50 MeV. In the scanned mode the photon radiation fields of 10 x 10 and 30 x 30 cm² at 1 m SSD (source-to surface-distance) were generated by the elementary beams scanned in two different scanning patterns. The first pattern consisted of two concentric circles of the radius of 5 and 14.5 cm at 1 m SSD containing 6 and 115 elementary beams for the inner and outer scanning circles, respectively. The second one of 64 elementary beams formed one circular pattern of 14.5 cm radius at 1m SSD.

Calculation Method The electron - photon mode of MCNP4B with a detailed physics treatment was used to calculate the bremsstrahlung production in the target and the photon transport through the treatment head and the water phantom. The physics of electron and photon transport used in MCNP code is described elsewhere [1,11,14].

The electron source has been defined in the input file by a source-definition (SDEF command) assuming the specific source distributions for stationary and scanned beams. For the MM50 accelerator the emittance of the source electron pencil beam has certain radial spread both in the x- and y- directions. It was

assumed that the source electron beams formed a nearly circular spots on the target surface of about 1.5 and 2 mm diameter for stationary and scanned beams respectively. For the simulation of the stationary beam impinging almost perpendicularly to the target an angular spread of the incident electrons on the target surface was also taken into account. In this case the stationary electron beam had a Gaussian distribution of the poloidal angle in the range 0° – 0.4° around the central axis [15]. For electron beams scanned around the central axis the incident angles on the target matched the radius of the circular patterns at 1m SSD. The beam direction and the distributions of the elementary electron beams in every scanning circle were specified in the SDEF command.

Photon transport was simulated through the detailed geometry corresponding to the technical drawings of the treatment head and subsequently through the phantom modeled by a $30 \times 40 \times 40$ cm³ box. The settings of the multi-leaf collimators and irradiated volume corresponded to the used radiation fields 10×10 or 30×30 cm² at the phantom surface at 1m SSD.

Bremsstrahlung production was improved by increasing the sampling of electron interactions in the target. Therefore, the target was divided into several layers to break the electron path into many small steps and to ensure detailed multiple scattering. The 9Be6W target was divided into two Be layers of 4 and 5 mm thickness and six 1 mm thick W layers. The 5.5W6.5Cu target was divided into 1 and 1.5 mm thick layers whereas a very thin 3 mm Be target was modeled by three 1 mm thick layers. The step parameters [1] for Be, Cu and W in the material input data were taken equal to 25, 12 and 12, respectively. The electron and photon cut-off energies in the gantry cells were 0.75 and 0.5 MeV respectively. For the calculations in the phantom the cut-off energies were 0.01 and 0.05 MeV for photons and electrons respectively. Using a 50 MeV electron beam only 5.5W6.5Cu target fully absorbs electrons. For other targets, 3Be and 9Be6W, the remaining transmitted electrons have to be removed by the purging magnet [15]. In this work the removal of transmitted electrons was simulated by an energy cut-off of 50 MeV for all electrons transmitted through the target and transported to the 0.5 cm thick cell of He gas placed in the position 1 cm below the target. All secondary electrons produced in the gantry and He gas beyond this thin cell were further transported to the phantom.

For the stationary beams the MC calculations were performed in a one-step process i.e. the bremsstrahlung production in the target and electron-photon transport through the treatment head and the phantom were performed in a one run. In order to optimise the calculation time for the scanned beam the simulations were divided into two steps. In the first one, the bremsstrahlung production in the target and photon beam transport through the treatment head were simulated and resulting particles, primary photons and secondary photons and electrons, were stored in the surface source located at the position behind the treatment head. This surface source containing the information about energy, location, direction and particle type crossing the surface were used in the second calculation step for the particle transport through the air between the gantry window and the phantom, and subsequently through the phantom.

The calculations were performed on a 500 MHz Intel Celeron (Mendocino) processor using a PC - Linux-RedHat 6.2 operating system.

3 Measurements

The photon radial and depth-dose distributions of the 50 MV beam have been measured in a water phantom using p-type Scanditronix silicon diode detector [16]. Its sensitive volume is about $0.2\text{--}0.3\text{ mm}^3$. The water phantom was a PMMA tank $60\times60\times50\text{ cm}^3$ (RFA 300, Scanditronix) with a resolution of 0.1 mm in the position and 0.1% in the relative response. Depth dose measurements were made at depth increments of 2 mm in the build-up region and with 5 mm at the descending part of dose distribution. The accuracy of the silicon diode detector was verified prior to the measurements by a small cylindrical ionization chamber (RK-Scanditronix) at 1 m SSD and a field size of $10\times10\text{ cm}^2$. The agreement between these two detectors was found to be better than 0.5% at all depths.

4 Results and Discussion

The spatial distributions of the photon fluence and energy fluence differential in energy were calculated for the stationary and scanned beams.

Figure 1 shows the calculated photon fluence and energy fluence differential in energy normalised per source electron for the stationary 50 MV photon beam from the 3 mm Be target. The calculation was performed for a small cylindrical voxel of 0.25 cm^3 at 1m SSD on the central axis. The statistical uncertainties in this case are less than 1.5% (1σ) for all energy bins using the calculations with 6×10^8 starting electrons. Figure 2 shows the calculated and measured radial dose profiles normalised to the integral and projected at 1m SSD for 50 MV beam and 3Be target. A full width at half maximum (FWHM) of 34 mm from experiments and 30 mm from MC calculations is evaluated for this very narrow photon beam. The differences between calculated and measured radial dose profiles are up to 10% depending on the radial bin size and are much higher than the statistical uncertainties of the MC calculations and the experimental uncertainties, both less than 0.5%. Probably these discrepancies could be diminish if the radial bin size used in the calculations are decreased and the geometrical properties of the source electron beam are better modeled. A flat energy dependence of the energy fluence for 3Be target shows that this very narrow forward bremsstrahlung beam has unique therapeutical properties.

The calculated and measured radial dose profiles for 9Be6W target and 50 MV stationary beam are shown on Fig. 3. The discrepancies up to 10% between the calculation and the measurement are observed mainly for the radii in the range 0–4 cm from the central axis. Also the MC results underestimate the radial dose in this region, similar to the work by S  therberg et al [17] where the 50 MV photon beam from the racetrack microtron was evaluated by the ITS3.0 MC code. The calculated radial dose profile for the 5.5W6.5Cu target, also shown on Fig. 3, is very similar to the profile for 9Be6W. The calculated

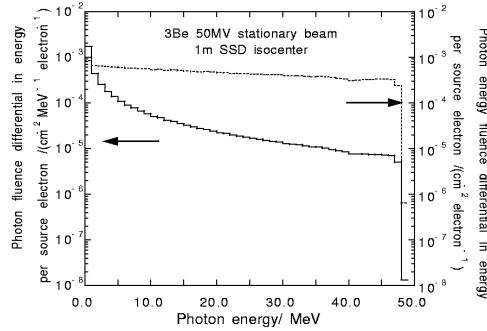


Fig. 1. Calculated photon and energy fluence differential in energy for 50 MV stationary photon beam from 3Be target. 1m SSD at the isocentre.

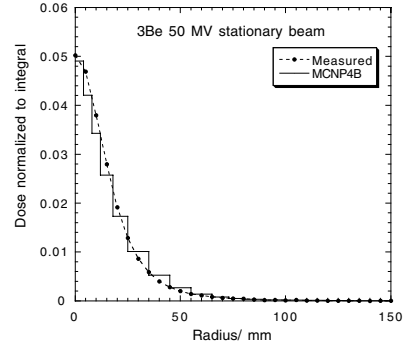


Fig. 2. Calculated and measured radial dose profiles normalised to the integral for 50 MV photon beam from 3Be target

and measured FWHM for 9Be6W target are 70 and 73 mm respectively. The statistical uncertainties of the calculated dose are less than 2% (1σ) for the voxels on the central axis and about 0.5% (1σ) for the positions larger than 0.5 cm from the central axis using the calculations with 1.8×10^6 starting electrons. Error bars on the all experimental curves are within the size of the symbols.

Figure 4 shows the calculated and measured depth dose profiles normalised to the integral for 50 MV photon beam from the 9Be6W target, radiation field $10 \times 10 \text{ cm}^2$ and a scan pattern of the radius 14.5 cm at 1m SSD. The statistical uncertainties of the calculated dose for the depth bins in the build-up region are 2–7% (1σ) and less than 2% (1σ) at the descending part of depth dose

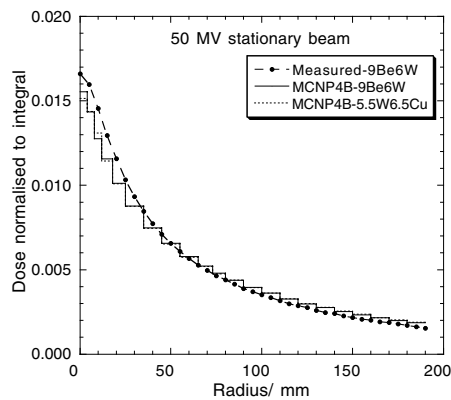


Fig. 3. Calculated and measured radial dose profiles normalised to the integral for 50 MV photon beams from 9Be6W and 5.5W6.5Cu targets.

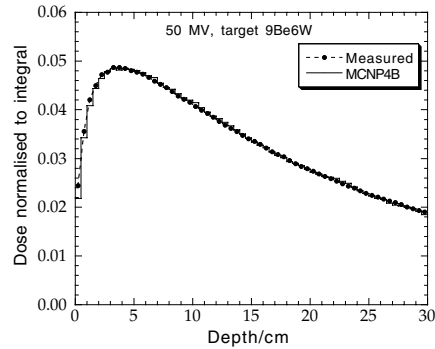


Fig. 4. Calculated and measured depth dose profiles normalised to the integral for 50 MV scanned photon beam from 9Be6W target and scan pattern of the radius 14.5 cm at 1 SSD. Radiation field $10 \times 10 \text{ cm}^2$

distribution for the calculations with 1.9×10^6 photons stored in the surface source. Measured and calculated depth-dose distributions in the water phantom are in good agreement, within about 2–3% for the positions in the range 2–30 cm, whereas larger discrepancies up to 10% are observed in the build-up region close to the phantom surface (0–2 cm). The beam contamination by the secondary electrons arising from the primary and multileaf collimators, and the large dose gradient in the build-up region have a significant influence on the accuracy of both calculation and measurement for the small depth intervals. The similar discrepancies in the build-up region have been observed for the 25 MV photon beam by Chetty et al [7]. The comparison between the calculated and measured dose profiles for the 5.5W6.5Cu target, a composite scan pattern of the radii 5 and 14.5 cm performed for the radiation fields 10×10 and 30×30 cm² showed the same agreement as discussed for the results shown on Fig. 4.

MCNP4B code can fairly good predict dose distribution in the patient for high energy photon beam of 50 MV operating in the scanned and stationary modes. However, a clinical application requires the dose determination with a statistical error less than 0.5%, that implies the use of very fast processors or parallel processing to get a reasonable running time using the MCNP4B code.

5 Acknowledgments

The project was partly supported by the Swedish Radiation Protection Institute, SSI P 949.96.

References

1. J. Briesmeister: *MCNPTM - A general Monte Carlo N-Particle Transport Code Version 4B*, LA-12625-M, Los Alamos National Laboratory (1997)
2. J.J. DeMarco, T.D. Solberg, J.B. Smathers: *Med. Phys.* **25**, 1 (1998)
3. T.D. Solberg, J.J. DeMarco et al.: *Radioth. Oncol.* **49**, 73 (1998)
4. A.E. Schach von Wittenau, L.J. Cox et al.: *Med. Phys.* **26**, 1196 (1999)
5. R.D. Lewis, S.J.S. Ryde et al.: *Phys. Med. Biol.* **44**, 1219 (1999)
6. J.V. Siebers, P.J. Keall et al.: *Phys. Med. Biol.* **44**, 3009 (1999)
7. I. Chetty, J.J. DeMarco, T.D. Solberg: *Med. Phys.* **27**, 166 (2000)
8. J.V. Siebers, P.J. Keall et al.: *Phys. Med. Biol.* **45**, 983 (2000)
9. P.A. Love, D.G. Lewis et al.: *Phys. Med. Biol.* **43**, 1351 (1998)
10. J.J. DeMarco, T.D. Solberg et al.: *Med. Phys.* **22**, 11 (1995)
11. D.P. Gierga, K.J. Adams: *Electron/Photon verification calculations using MCNP4B*, LA-13440, Los Alamos National Laboratory (1999)
12. W.R. Nelson, H. Hirayama, D.W.O. Rogers: *The EGS4 Code System*, Report SLAC-265, Stanford, CA: Stanford Linear Accelerator Center (1985)
13. A. Brahme, T. Kraepelien, H. Svensson: *Acta Radiol. Oncol.* **19**, 305 (1980)
14. H. G. Hughes: *Treating electron transport in MCNPTM*, <http://www-xdiv.lanl.gov/XCI/PROJECTS/MCNP>
15. R. Svensson, A. Brahme: *Phys. Med. Biol.*, **41**, 1353 (1996)
16. G. Rikner: *Acta Radiol. Oncol.* **24**, 65 (1985)
17. A. S  therberg, P. Andreo, M. Karlsson: *Med. Phys.* **23**, 495 (1996)

Energy Spectra and Dose Distributions of a Medical Linear Electron Accelerator Simulated with BEAM/EGS4 and MCNP

D. Albers, F. Cremers, I. Eggers, M. Todorovic, and R. Schmidt

Dept. of Radiotherapy and Radiooncology / Clinic of Radiology, University Hospital
Eppendorf, Martinistr. 52, 20246 Hamburg, Germany

1 Introduction

The energy distribution of photons from a medical linear electron accelerator is an important characteristic of a radiotherapy photon beam. The knowledge of clinical beams is essential for dosimetry, treatment planning, and design of an accelerator. We are especially interested in the response of various dosimetry devices towards radiation. Knowledge of the energy spectrum is important since the response of these devices is generally energy dependent, thus varies with depth in the irradiated material.

Generally the photon energy spectrum is unknown, and the therapeutic beam is only characterized by the maximal energy in MeV or by a quality index Q . A direct measurement of the spectrum is difficult because of the high photon fluence and energy. We have simulated the photon beam of a 6 MV clinical accelerator (Siemens MDX2) using two different Monte Carlo codes: the EGS4 Monte Carlo code BEAM and MCNPX. Moreover we indirectly derived the energy spectrum from transmission measurements.

2 Materials and Methods

2.1 Monte Carlo Simulation

BEAM BEAM is an EGS4-based code for modelling beams in a component-by-component way and predicting beam characteristics from clinical accelerators [1]. The generic accelerator consists of a number of predefined components that enable simulation of most linear accelerators. Materials and dimensions have to be defined in associated files. The components were applied to model the target, primary collimator, flattening filter, chamber, mirror and jaws. The vendor specific data were obtained from R. Siochi [2]. A $10 \times 10 \text{ cm}^2$ beam was modelled in a distance of 100 cm from the target. Initially 10^9 electrons with an energy of 5.58 MeV impinged on the target. No variance reduction techniques were used.

The output of the code produces phase space information for histories crossing a plane (here 100 cm from focus). The phase space file contains all necessary information of each particle, i. e. charge, energy, position in terms of x-, y-, and z-coordinates, impulse (direction), and z-position of the last interaction.

Irradiating a water phantom the depth dose curve is dependent on the energy distribution of the irradiating photons. As a test for the reliability of the simulation the phase space data was taken as an input for a simulation of a depth dose curve in water. This was carried out with the EGS4 code DOSXYZ and will be compared to measured data.

In addition the photon spectrum was simulated for a $3 \times 3 \text{ cm}^2$ beam in a distance of 184.5 cm from the focus in order to compare the result to a spectrum derived from transmission data measured under these conditions (see below).

MCNPX MCNPX is based on MCNP, that has originally been developed in Los Alamos to simulate neutron transport [3]. The geometry in MCNP is set up by surfaces and cells that have to be specified by cell and surface cards. These cards are command or data lines limited to 80 columns. Surfaces are defined by supplying coefficients to the analytic surface equations. Cells are determined by the surrounding surfaces. The user can instruct MCNP to make various tallies related to particle current, particle flux, and energy deposition. In contrast to BEAM a phase space file that can be used as input for further simulations is not produced.

The head of the accelerator was modelled, and as above a $10 \times 10 \text{ cm}^2$ beam in a distance of 100 cm from the focus was simulated. Therefore 10^6 electrons with an energy of 5.58 MeV were used as an initial input. “Photon splitting” was used as a technique for variance reduction.

2.2 Experiment

Photon energy spectra can also be determined by measuring the photon transmission through polymethyl methacrylate (PMMA). The transmission $T(x)$ is the ratio of measured transmission dose $D(x)$ through a material of thickness x and the dose $D(0)$ without absorbing material in the beamline:

$$T(x) = \frac{D(x)}{D(0)} \quad (1)$$

$D(x)$ and $D(0)$ are measured with an ionization chamber carrying a build-up cap.

The spectral photon fluence Φ_E is derived from the transmission $T(x)$ by inverse Laplace transformation L^{-1} :

$$\Phi_E = -\frac{D(0)}{E \left(\frac{\mu_{en}}{\rho} \right)_m} L^{-1} \{T(x)\} \frac{d\mu_E}{dE} \quad (2)$$

$\left(\frac{\mu_{en}}{\rho} \right)_m$ is the mass energy-absorption coefficient of the build-up cap and μ_E the attenuation coefficient of PMMA.

Applying the 4 parameter model from Archer et. al. [4] the transmission can be written as:

$$T(x) = \left(\frac{ab}{(x+a)(x+b)} \right)^c e^{-\mu_E^0 x} \quad (3)$$

with the parameters a , b , c , and the attenuation coefficient μ_E^0 for the maximal photon energy. The transmission $T(x)$ was measured using a 3×3 cm beam in 184.5 cm distance from the focus.

3 Results

The energy spectra simulated with BEAM/EGS4 and MCNPX show a good agreement (Fig. 1). The maximal energy of the photons is limited by the acceleration voltage to 5.58 MeV. The average photon energy amounts to an evidently lower energy of 1.55 MeV.

The experimentally derived photon energy spectrum depends on 4 parameters only. That means that the spectrum cannot take on any shape but is somehow predetermined by the maximal energy of the photons, the attenuation

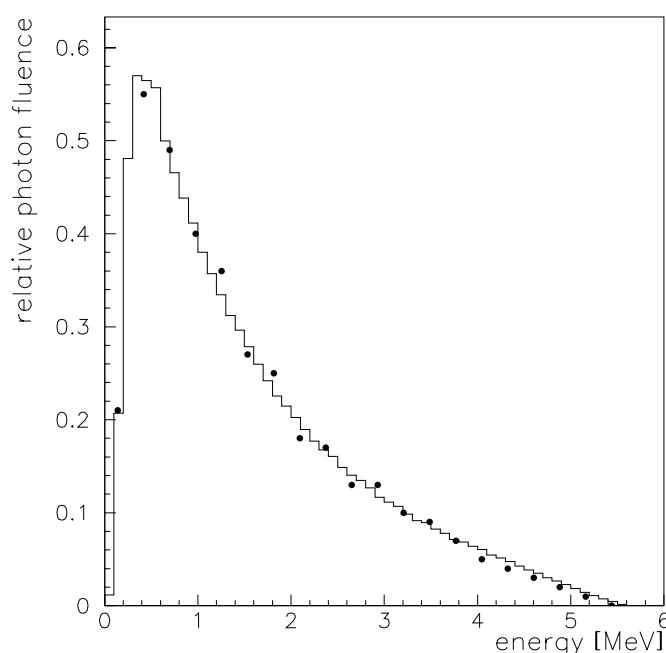


Fig. 1. Simulated photon spectrum of a clinical linear electron accelerator (Siemens MDX2) with an acceleration voltage of 5.58 MV (nominal 6 MV). The bar chart shows the spectrum simulated with BEAM/EGS4, the marker indicate the spectrum simulated with MCNPX

coefficient of lucite, and the absorption coefficient of the build-up cap. Nevertheless, Fig. 2 shows that the experimentally derived spectrum agrees quite well with the simulated spectrum.

As the measured spectrum depends sensitively on the maximal energy of the photons, it was important to use the exact acceleration voltage of 5.58 MeV for the calculation instead of the nominal voltage of 6 MeV.

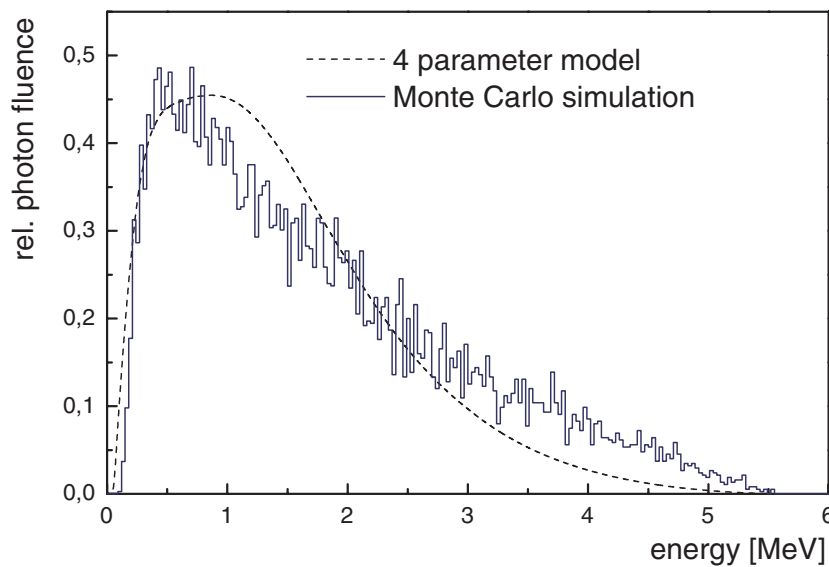


Fig. 2. Comparison of simulated and experimentally derived photon energy spectrum of a clinical linear electron accelerator (Siemens MDX2) with an acceleration voltage of 5.58 MV (nominal 6 MV). The simulation was carried out with BEAM/EGS4 and for the experiment the 4 parameter model from Archer et al. was applied

The energy dose deposited in various depth of a water phantom is very dependent on the energy distribution of the radiation. A test of the quality of the determined photon energy spectra can be achieved by investigating the attenuation of the radiation. Figure 3 compares the simulated depth dose curve in a water phantom to a measured depth dose curve. The shapes of the curves agree well and confirm the simulated photon energy spectrum. As the Bragg-Gray condition is not fulfilled near the surface the dose could only be simulated in that region.

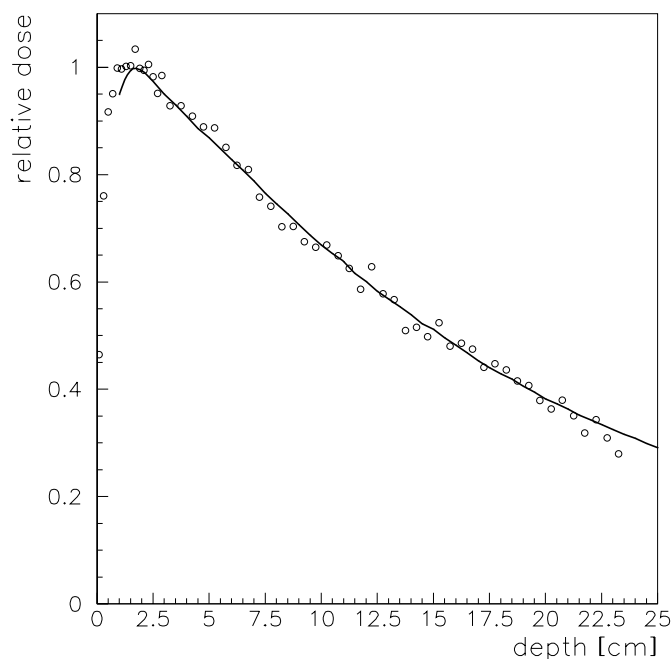


Fig. 3. Comparison of simulated (marker) and measured (line) depth dose curve. The phase space data of the simulated therapeutic beam was taken as an input for the simulation of the depth dose curve with the EGS4 code DOSXYZ

References

1. D.W.O. Rogers, B.A. Faddegon, G.X. Ding, C.-M. Ma, J. We: *Med. Phys.* **22**, 5 (1995)
2. R.A.C. Siochi: 'Requirements for Manufacturer Supplied Data for Monte Carlo Simulation: A BEAM Perspective'. In: *Proc. of the 15th Int. Conf. on the Appl. of Accelerators in Research and Industry* ed. by J.L. Duggan and I.L. Morgan (The American Institute of Physics 1999) pp. 1060–1065
3. J.F. Briesmeister, Ed.: *MCNP - A General Monte Carlo N-Particle Transport Code, Version 4B*, (<http://www-rsicc.ornl.gov/rsic.html>), LA-12625-M (1997)
4. B.R. Archer: *Med. Phys.* **9**, (1982)

Monte Carlo Simulation of an Arc Therapy Treatment by Means of a PC Distribution Model

A. Leal^{1,3}, F. Sánchez-Doblado¹, M. Perucha¹, M. Rincón¹, R. Arráns², C. Bernal³, and E. Carrasco¹

¹ U. Sevilla. Fac. Medicina. Dpto. Fisiología y Física Médica, Spain

² H.U.V.M. Serv. Oncología Radioterápica. Sevilla, Spain

³ C.I.C.A. Sevilla, Spain

Abstract. It would be always desirable to have an independent assessment of a planning system. Monte Carlo (MC) offers an accurate way of checking dose distribution in non homogeneous volumes. Nevertheless, its main drawback is the long processing times needed.

A distribution model to simulate arc-therapy treatments with Monte Carlo techniques has been developed. This model divides the individual tasks with a physical sense. In this way, not only the CPU time is substantially reduced but a detailed analysis can be achieved. A distribution program modifies the input parameters in the code to send a different task to each processor. This model has been installed on a PC network without any resident software. This model works independently of the operating system pre-installed. The PC acting as a server exports the required operating system (Linux), the MC code and the input data, as well as it stores all the results.

Some very complex radiosurgery treatments simulated using this model leads a CPU time about one hour.

1 Introduction

Monte Carlo (MC) calculation is one of the most precise ways of calculating the dose delivered on a heterogeneous medium [1]. Nevertheless, the main drawback of this technique is the long CPU time needed [2]. Although several reduction variance techniques have decreased considerably processing times MC calculation is hard to be used yet as an alternative verification tool not [3]. A possible solution to overcome this problem could be to share the task out between a set of processors. This approach is valid as the histories are independent for every particle.

Distributed simulation on a single multiprocessor machine has been successfully achieved [3], but this expensive computers are not affordable by every hospital. The fast growth of PC speed, the accessibility of LINUX, and the network hardware available at the moment, suggest a new cheap and efficient solution.

One typical case which could be faced with this approach is the radiosurgical treatments by means of an arc therapy strategy.

A PC network based process distribution model with this MC technique has been developed. This model divides the different tasks with a physical sense. In this way, not only a CPU time saving is obtained but a detailed analysis of the individual beam contribution can be achieved.

2 Material and Method

For the simulation, the *EGS4* code [5,6] was used operating under UNIX and implemented in the *OMEGA-BEAM* package, developed by D. Rogers and collaborators at the NRCC (National Research Council Canada).

With the *BEAM* code [7,8], a phase space file can be obtained with the position, angle of incidence and energy data of every particle. Three phase space files were calculated, considering the linac head plus a 7 mm, 20 mm and a 15 mm additional collimators especially designed for radiosurgery. These phase spaces were obtained right at the end of the collimator, and were used as input data to simulate the beam impinging on the patient. The patient geometry was build by a file created from the CT slices of the area to be treated.

The clinical case simulated is a radiosurgery treatment performed in our hospital. A total number of 72 images were chosen, having each a resolution of 512×512 pixels. *DOSXYZ* software [9] calculates the dose in cubic elements or voxels. For this reason, a program was developed which converts the CT data into a file readable by *DOSXYZ*. In this MC geometry, four media (bone, tissue, lung and air) and 4096 density levels could be differentiated. This file is distributed in $72 \times 256 \times 256$ voxels which represents a resolution of $1.34 \times 1.34 \times 2$ mm³.

The simulation approach consisted of 48 beams forming 8 arcs around 2 different isocenters. The Monitor Units (MU) used were weighted for each arc according to a total of 8×10^7 histories simulated.

The current treatment strategy determines the starting and final angle of the accelerator gantry, as well as the angle of the treatment couch for each arc. The dose per arc is adjusted by selecting the corresponding number of MUs. These parameters were translated and substituted by those required by the MC code to simulate all the treatment. A rotation axis algorithm relates the reference system in the bunker with the one used by the code. Furthermore, the number of histories used to simulate each arc is proportional to the number of MUs per arc.

As MC simulation considers particle histories independently, the whole task could be divided into processes with small number of histories. In our case, 48 processes needed to be simulated consecutively, as the angles of both gantry and treatment couch change with every beam the simulation consists of.

For this reason, the smallest process sent to each CPU unit was every single beam constituting the whole treatment (see Fig. 1). The distribution of the beams and arcs was made by writing a "*script*" or "*shell*" (available in graphics interface) which modifies the initial parameters of the input file as it shares the task out between each machine connected to the network.

In collaboration with the Engineering School of the University of Seville, a model prototype was installed on a local network of 36 PCs. These PCs had the minimum necessary requirements for our simulations (Pentium II processors with 64 Mbytes of memory). No software was necessary to be installed. The only requirement was a small Linux partition (300 Mbytes of hard disk) on each PC. The operating system and the simulation code, as well as the data file and

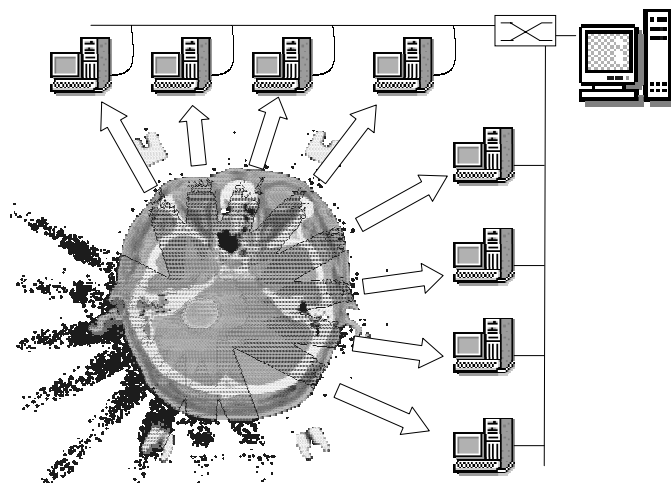


Fig. 1. Each beam is simulated in a different PC. The results are download to the server when the processes finishes

distribution programs, where all exported by network from another PC outside the local network, acting as a server (a Pentium III, 500 MHz and 256 Mbytes RAM with an Ultra Wide hard disk SCSI of 9 Gb connected to the network via a *3 Com* Fast Ethernet XL 10/100 Mbytes card). The starting of each PC clients was achieved by means of a floppy disk with a minor kernel. Therefore, no boot sector of the local disks is needed. The system kernel was the 2.2.10, which included the NFS (Network File System) as part of its nucleus. Furthermore, the remote boot of the system in the client nodes lies on two reasons: The high number of client machines and the fact that they do not need to be exclusively dedicated for MC calculations. Each machine contributes to the simulation with its processor and physical memory. No information remains in the hard disks when the simulation finishes. The machines were then switched off and rebooted under Windows98.

To minimise the CPU time, different locations of the files required by the code simulation were studied. These files were placed either in the PC local disks executing the code, or in the server disk for remote access. CPU time using different configurations in the NFS block size was also studied. Furthermore, temporary memory consumption per partition was also analysed for an intelligent simulation distribution according to the available resources.

3 Results

Concerning locations of input files, the best option was the unique installation of the code in the server machine, as the CPU time saved is cancelled by downloading time.

Regarding the NFS block size, there was a maximum difference of 9 minutes in the real time obtained by using a block size of 8 Kbytes instead of blocks of 1 Kbyte.

The memory requirements conducts to a single beam as the minimum partition sent to each machine simultaneously. The very complex (seventy-two 256×256 CT slices, 8 arcs, 2 isocenters, 4096 density levels) radiosurgery treatment simulated leads to a total real time of 1 hour and 23 minutes and a CPU time of 1 hour and 7 minutes.

4 Conclusions

A model for a distribution of processes applied to MC simulation of radiosurgery treatments has been developed. This model allocates the work in a way with which a double aim is covered: a significant reduction in CPU time and the resolution of a difficult problem by its division in simpler tasks keeping their physical sense. Moreover, a flexible and immediate installation of the code through the network is achieved and hence, the PC clients can be operated when not in their normal use. Therefore, an intensive utilization of the available resources could make MC simulation affordable to every institution with no additional cost. This accessibility and efficiency lead to a substantial reduction in the processing time, presenting MC simulation as a powerful treatment verification tool.

References

1. C-M. Ma, S.B. Jiang: Phys. Med. Biol. **44** (1988)
2. C-M. Ma, E. Mok, A. Kapur, T. Pawlicki, D. Findley, S. Brain, K. Forster, A.L. Boyer: Med. Phys. **26**, 10 (1999)
3. A.F. Bielajew, D.W.O. Rogers : Nucl. Instrum. Methods B **18** (1987)
4. C-M. Ma : Parallel Computing. **20** (1994)
5. A.F. Bielajew: *How to manage the EGS4 system* (National Research Council of Canada report PIRS-0391, Ottawa 1993)
6. A.F. Bielajew: *Running EGS4 on different architectures* (National Research Council of Canada report PIRS-0392, Ottawa 1993)
7. D.W.O. Rogers, B.A. Faddegon, G.X. Ding, C-M. Ma, J. We: Med. Phys. **22**, 5 (1995)
8. C-M. Ma, P. Reckwerdt, M. Holmes, D.W.O. Rogers, B. Geiser, B. Walters: *BEAM Users Manual* (NRCC report PIRS-0509B(revC), Ottawa 1998)
9. C-M. Ma, P. Reckwerdt, M. Holmes, D.W.O. Rogers, B. Geiser, B. Walters: *DOSXYZ Users Manual* (NRCC report PIRS-0509B(revC), Ottawa 1998)

Analysis of the Influence of the Radial Displacement of the Source in the Simulation of Ge-Detector Calibration Using MCNP Code

J. Ródenas¹, A. Martinavarro¹, and V. Rius²

¹ Departamento de Ingeniería Nuclear, Universidad Politécnica de Valencia

² Iberdrola, Central Nuclear de Cofrentes, Valencia (Spain)

1 Introduction

Dose reduction programs in Nuclear Power Plants include a measurement campaign to determine activities and doses in several areas of the plant. A gamma spectrometry device is used for direct on-site measurements during that campaign. The equipment includes a heavily shielded HP Germanium detector.

One of the most important purposes of the measurement campaign is to estimate the average level of radioactive contamination on specific plant component surfaces such as the inner side of the pipes in the Recirculation System or the Reactor Water Cleanup System of a BWR.

The detector calibration is not easy because the measurements have to be performed in difficult-to-access plant locations with high dose rates. The experimental duplication of the source is complicated and expensive, so it is more convenient to apply a numerical solution for the detector efficiency calibration. MCNP [1] code based on the Monte Carlo method is used to simulate the detection process and to obtain spectrum peaks [2,3].

The computational calibration procedure was validated experimentally using gamma sources in the laboratory. Measurements were compared with the results of the simulation [4].

In order to evaluate the contribution to detector efficiency from sources placed away from the detector axis, an analysis of the radial displacement was performed moving the source on a perpendicular to the detector axis. The results of this analysis allow us to determine the minimum length of the pipe considered, since the contribution of further sources can be neglected [5].

Measurements and simulation results match well while the detector and source are aligned. However, as the source is moved away from the detector axis some discrepancies appear. They are probably due to the geometric model used, so it should be carefully reviewed.

In order to optimise the MC simulation, the parameters involved in the geometry are estimated. Thus, those that better reproduce the actual situation during measurements are determined. Different hypotheses are considered and results are compared with laboratory measurements to find out the lowest discrepancies.

2 Analysis of the Solid Angle Model

In order to improve variance reduction and hence reduce the number of photons to be started, obtaining good results with lower computing time, an anisotropy is introduced in the source model. Photons are emitted within a cone which has its vertex placed on the source and its base on the detector front side. Results must be later corrected for the bias introduced. That is, multiplying by the ratio of solid angles. Being θ the cone opening angle, the bias can be calculated as:

$$B = \frac{\int_0^\theta 2\pi \sin(\theta') d\theta'}{4\pi} = \frac{1 - \cos(\theta)}{2}. \quad (1)$$

In Fig. 1, a sketch showing the angles when the source is placed out of the detector axis, can be seen. From the diagram in Fig. 1,

$$\varphi_1 = \psi_2 - \psi_1, \quad \varphi_2 = \psi_3 - \psi_2, \quad (2)$$

and,

$$\tan(\psi_1) = \frac{b-r}{d}, \quad \tan(\psi_2) = \frac{b}{d}, \quad \tan(\psi_3) = \frac{b+r}{d}. \quad (3)$$

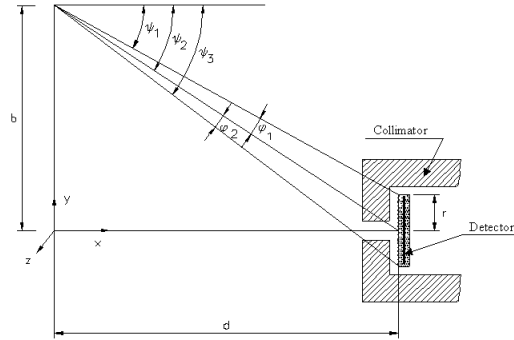


Fig. 1. Angular diagram

If $b = 0$ (no displacement) $\varphi_1 = \varphi_2 = \theta$, but if $b \neq 0$ then an asymmetry appears since $\varphi_1 \neq \varphi_2$. That asymmetry will be greater when b increases. As $\varphi_1 > \varphi_2$, it will be usually taken $\theta = \varphi_1$ in order to be sure that the photon beam covers the maximum area on the detector front side.

In the first set of simulations, $\cos(\theta)$ is maintained constant for every radial displacement. The value used is the corresponding to the no-displacement position. Results

obtained with MCNP for different radial displacements are listed in Tab. 1, where I is the intrinsic efficiency and A is the absolute efficiency obtained multiplying I by the bias B . Absolute and experimental efficiencies are normalised dividing by the value corresponding to the position without any displacement. The ratio between calculated and experimental normalised values is also listed in the table. There is a good agreement between calculated and experimental values for $b \leq 10$ cm, even for $b = 12$ cm the deviation is lower than 7%.

In a second approach, $\cos(\theta)$ was calculated for each displacement and another set of simulations was run. Results are listed in Tab. 2. Comparing last columns in Tabs. 1 and 2, it can be said that although a variable cosine is a better approximation to reality, results does not differ very much, so using a

Table 1. Results for the constant solid angle model

b	I	B	A	Norm.	Exp.	Norm.	Ratio
0	6.525E-03	1.806E-05	1.178E-07	1	1.110E+05	1	1
2	5.839E-03	1.806E-05	1.054E-07	0.894	9.845E+04	0.886	1.008
4	4.766E-03	1.806E-05	8.602E-08	0.730	8.131E+04	0.732	0.996
6	3.693E-03	1.806E-05	6.659E-08	0.565	6.230E+04	0.561	1.006
8	2.643E-03	1.806E-05	4.760E-08	0.403	4.535E+04	0.408	0.988
10	1.679E-03	1.806E-05	3.019E-08	0.256	2.920E+04	0.263	0.973
12	8.890E-04	1.806E-05	1.595E-08	0.135	1.611E+04	0.145	0.932

constant $\cos(\theta)$ provides a simple and good simulation. Intrinsic efficiency, I , calculated by MCNP is higher for the variable angle than for the constant cosine as the geometry is more efficient since the angle coupled to the detector front side is smaller. However, a smaller angle produces a lower bias, so the absolute efficiency, A , is very similar in both simulation models.

Table 2. Results for the variable solid angle model

b	I	B	A	Norm.	Exp.	Norm.	Ratio
0	6.525E-03	1.806E-05	1.178E-07	1	1.110E+05	1	1
2	5.841E-03	1.805E-05	1.054E-07	0.895	9.845E+04	0.886	1.009
4	4.771E-03	1.804E-05	8.611E-08	0.730	8.131E+04	0.732	0.997
6	3.693E-03	1.803E-05	6.659E-08	0.565	6.230E+04	0.561	1.006
8	2.641E-03	1.801E-05	4.756E-08	0.403	4.535E+04	0.408	0.987
10	1.697E-03	1.798E-05	3.051E-08	0.258	2.920E+04	0.263	0.984
12	8.930E-04	1.794E-05	1.602E-08	0.135	1.611E+04	0.145	0.936

3 Detector Surface Covered by Photon Beam

Intrinsic efficiency may decrease due to various phenomena. When the radial displacement increases, less photons reach the detector as they pass through a thicker shielding. On the other hand, the plane containing the detector front side is not perpendicular to the cone axis and consequently the intersection between detector front side and photon beam is not a circle but an ellipse. That may be important, since some part of the detector may not receive photons. Therefore, a study of this intersection has been carried out. Let us consider mathematics of the involved surfaces.

Taking origin in the point source and the x-axis as the line that joins the source with the detector front side centre, the equation of the conic surface

generated around the x-axis with the vertex on the origin can be written as:

$$x \tan(\theta) = \sqrt{y^2 + z^2} . \quad (4)$$

After that, a reference axis rotation is done to match the cone and detector axis. The spin equations of angle ψ_2 are (see Fig. 1):

$$\begin{aligned} x &= x' \cos(\psi_2) - y' \sin(\psi_2) , \\ y &= x' \sin(\psi_2) + y' \cos(\psi_2) , \\ z &= z' . \end{aligned} \quad (5)$$

So the equation of the conic surface surrounding the photon beam is:

$$(x' \cos(\psi_2) - y' \sin(\psi_2)) \tan(\theta) = \sqrt{z'^2 + (x' \sin(\psi_2) + y' \cos(\psi_2))^2} . \quad (6)$$

And the detector external surface (front side) equation is the plane:

$$x' = d . \quad (7)$$

Substituting (7) in (6) one can find the equation of a line representing the intersection of the photon beam with the detector front side,

$$(d \cos(\psi_2) - y' \sin(\psi_2)) \tan(\theta) = \sqrt{z'^2 + (d \sin(\psi_2) + y' \cos(\psi_2))^2} . \quad (8)$$

Equation (8) can be transformed to match the general equation for an ellipse:

$$\frac{(z' - z_0)^2}{\alpha^2} + \frac{(y' - y_0)^2}{\beta^2} = 1 , \quad (9)$$

where (y_0, z_0) are the ellipse centre coordinates, and α, β the major and minor axis length. Those parameters can be found in terms of d, b and r . With no radial displacement, $b = 0$, the intersection is a circumference, as $y_0 = z_0 = 0$ and $\alpha = \beta = 2r_0$, the circumference diameter.

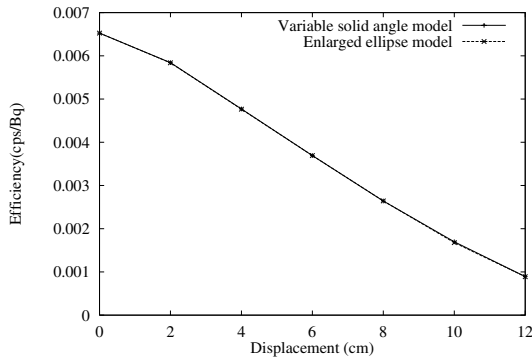
Once b and d are set, only the value of r can be varied, that is, the diameter ($2r$) of a circle placed on the detector front plane. For each r value, α and β can be calculated and it can also be determined whether the photon beam fully covers the detector or not.

Taking $r = r_0$ the major axis is always greater than $2r_0$, but the minor axis is lower, so the photon beam does not cover the whole detector front side. In order to achieve this, the minor axis α has to be greater or equal than $2r_0$. If that happens for the maximum radial displacement simulated, the detector will be covered for lower displacements. However, the solution would depend on the maximum displacement value. To obtain a better solution the r value that makes the ellipse as small as possible covering the whole detector front side has to be estimated for each radial displacement.

With this model, efficiency is calculated once more using MCNP. Results are listed in Tab. 3 as well as experimental efficiencies and the ratio MCNP/Experimental for normalised values. Now this ratio is always greater than 1, increasing as b does. That is, MCNP estimation for this model overvalues experimental measurements. This is due to the fact that the bias introduced is higher when displacement increases, since $\cos(\theta)$ decreases.

Table 3. Results for the enlarged ellipse model

b	I	B	A	Norm.	Exp.	Norm.	Ratio
0	6.525E-03	1.806E-05	1.178E-07	1	1.110E+05	1	1
2	5.839E-03	1.819E-05	1.062E-07	0.901	9.845E+04	0.886	1.016
4	4.766E-03	1.875E-05	8.936E-08	0.758	8.131E+04	0.732	1.035
6	3.693E-03	1.929E-05	7.126E-08	0.604	6.230E+04	0.561	1.077
8	2.643E-03	2.013E-05	5.321E-08	0.451	4.535E+04	0.408	1.105
10	1.679E-03	2.315E-05	3.887E-08	0.329	2.920E+04	0.263	1.253
12	8.890E-04	2.808E-05	2.496E-08	0.211	1.611E+04	0.145	1.459

**Fig. 2.** Intrinsic efficiency comparison

Discrepancies can be explained comparing results from the last two models. Results in Tab. 3 were obtained using an enlarged ellipse, estimated for each displacement. No attention to intersection shape is paid in the variable solid angle model, whose results were listed in Tab. 2. It can be seen from Fig. 2 that intrinsic efficiencies are very similar in both models.

However, absolute efficiencies show discrepancies increasing

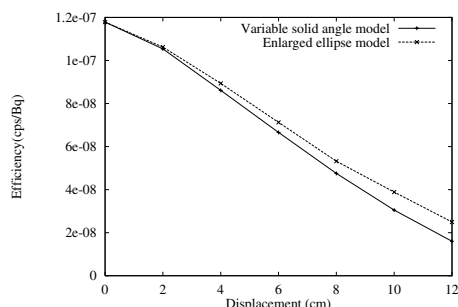
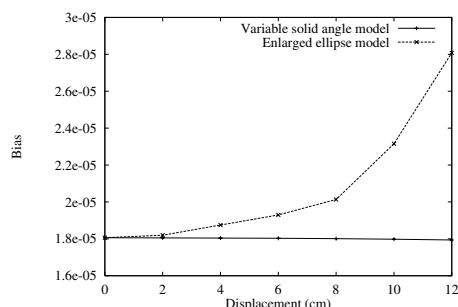
with the radial displacement as we can see in Fig. 3. As it is clearly shown in Fig. 4 discrepancies are due to the strong bias introduced in the enlarged ellipse model. This model simulates larger solid angle to avoid that some part of the detector surface does not receive photons, hence, more photons are started at the source, but these extra photons are mostly useless as they are attenuated by the collimator or do not reach the detector surfaces at the major axis zone.

Consequently, in the enlarged ellipse model the intrinsic efficiency scarcely changes while the bias introduced is higher and modifies the absolute efficiency out of experimental values. Therefore results definitely show that the hypothesis involved in the enlarged ellipse model and the model itself are not good.

4 Conclusions

MCNP code, based on the Monte Carlo method, was used to analyse the source radial displacement influence on the Ge-detector calibration.

Two models considering the cone with a vertex in the point source and its base on the detector were compared. A variable cone model is more realistic, but

**Fig. 3.** Absolute efficiency comparison**Fig. 4.** Bias comparison

results differ scarcely from those obtained with a constant cone model, which is a simpler model.

On the one hand, it is considered that some part of the detector front side will not receive photons as the intersection of the photon beam with the detector surface is not a circumference but an ellipse. A convenient model is developed in order to get an ellipse covering the whole detector surface.

Calculated efficiencies with this model do not differ from the previous ones, but the bias introduced is high and increasing with the displacement so that absolute efficiencies show hard discrepancies with experimental measurements and previous values. Therefore, the model is not good.

The main conclusion of this analysis developed is that the simpler model is better than the more realistic one, at least for the considered cases.

References

1. J. F. Briesmeister (Editor): *MCNP - A General Monte Carlo N-Particle Transport Code, Version 4B*, LA-12625-M, Los Alamos National Laboratory, Los Alamos, New Mexico (1997)
2. J. Ródenas, V. Rius: 'Application of Monte Carlo method to the simulation of Ge-detector calibration', TOPSAFE'98, Valencia, 15-17 April 1998
3. J. Ródenas, 'Simulation of Ge-Detector Calibration Using MCNP Code', Monte Carlo Methods and Models Applications in *Energy and Technology, Workshop held at Forschungszentrum, Karlsruhe (Germany), May 12-14, 1998*
4. J. Ródenas, A. Martinavarro, V. Rius: 'Validation of the MCNP code for the simulation of Ge-detector calibration', Accepted for publication in Nucl. Instr. and Meth. (Section A)
5. J. Ródenas: *Calibración de un equipo de espectrometría gamma, mediante el método de Monte Carlo, para su uso en el programa de reducción de dosis (ALARA) de la Central Nuclear de Cofrentes*, DIN-CNC 4663-97-003, Informe Final (Departamento de Ingeniería Química y Nuclear, Universidad Politécnica de Valencia 1997)

Monte Carlo Simulations of Photon Field Characteristics for In Situ Gamma Spectrometry Applications

J. Klusoň

Czech Technical University, Fac. of Nucl. Sci. & Phys. Eng., Břehová 7, Prague 1, 11519, Czech Republic

1 Introduction

In-situ gamma spectrometry makes it possible to determine concentrations of the natural as well as man made radionuclides in the environment and represents the significant method for the radiation monitoring (e.g. operational and accidental monitoring of the nuclear facilities vicinity, spent fuel storage, uranium industry and waste depositories, radioactive contamination measurements, environmental studies, geological prospection and mapping, etc.) [1]. Two arrangements are usually used: 1) the ground measurements (typically in the reference height 1 meter above ground) or 2) airborne measurements (enable fast and effective monitoring/scanning of large areas).

To interpret the full information inherent in the spectrometry data it is necessary to know the used detection system response function (response matrix) for the real photon field (i.e. for the photons energy-angular distribution) in the point of measurement. In the most common case of environmental measurements the photon field (terrestrial component) originate from radionuclides in the soil saturated surface layer and depend on many parameters (height above ground, soil composition, density and humidity, radionuclides depth distributions, character of terrain, vegetation cover, etc.). The semi-infinite size of such source is usually considered.

Two Monte Carlo codes were designed (on base of earlier works [2,3]) for this purposes. The first one enable to calculate the photon field energy-angular distributions for user definable source configurations and second one calculation of detectors responses in such photon fields.

2 Simulation of the Photon Fields

The Monte Carlo photon transport simulation code for calculation of the photon field energy- angular distributions originated from the specified source configurations was written. The code was designed namely for simulation of fields in given heights above the semi-infinite soil surface layer with given radionuclides and their depth distributions in this layer (typical source configuration for in-situ measurements). The model is based on the Mayneord's reciprocal theorem [4] and takes into account all photon interactions in the soil and air (including skyshine).

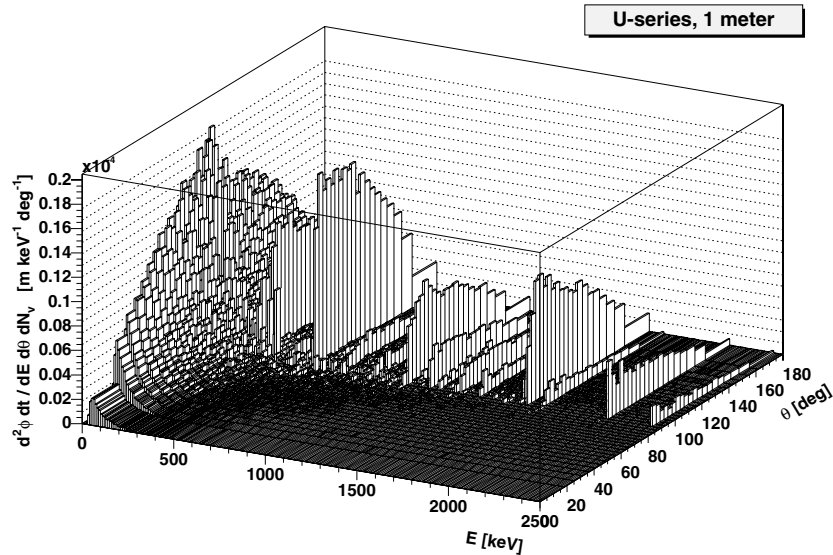


Fig. 1. Calculated photon flux density energy-angular distribution in reference height 1 meter for the U-series radionuclides (in equilibrium) homogeneously dispersed in the saturated soil surface layer, normalised to activity concentration 1 Bq m^{-3}

Photon cross sections from the [6,7] are used. Any radionuclide source and its distribution in depth can be described through the input data. Resulting photon field in any required height above ground is described by the energy-angular distribution matrix (with optional number and widths energy and angular intervals, standard setting is 256 equidistant energy and 40 no equidistant angular intervals) normalised to the unit specific or superficial activity concentration. Examples of results, calculated for the natural radionuclides of the U-series (reference height 1 meter – for ground measurements) and for ^{137}Cs contaminant with exponential depth distribution (altitude 100 meters – for airborne monitoring) are in Figs. 1 and 2.

3 Calculation of the Detection Systems Responses

The Monte Carlo electron-photon transport simulation is effective tool also for the modelling of the detection systems response functions (response matrices). The corresponding code for cylindrical and block scintillation detectors was designed and written. The code enables to use the calculated matrices, describing the photon field energy-angular distribution (see previous paragraph) as input data. The typical arrangements of the source (photon field) and detector (point source, parallel beam, isotropic or 2π -isotropic field) are also available. The all interactions of the primary photons and secondary electrons are taken into account. The photon cross sections from the [6,7] and electron energy loss, range

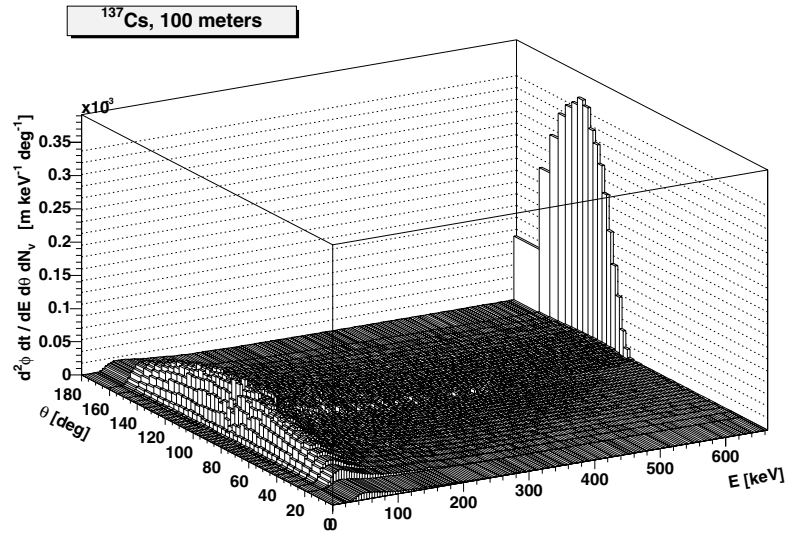


Fig. 2. Calculated photon flux density energy-angular distribution in altitude 100 meters for the radionuclide ^{137}Cs with exponential depth distribution (relaxation length 3 cm) in the soil surface layer, normalised to effective superficial activity 1 Bq m^{-2}

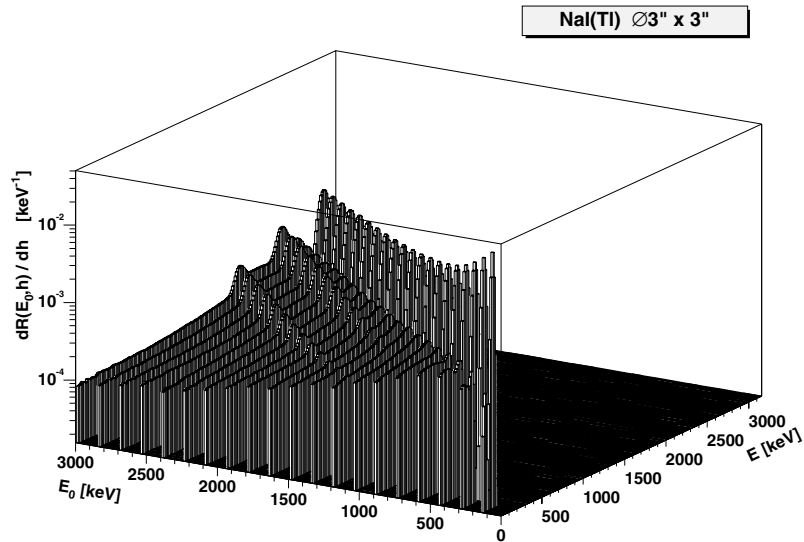


Fig. 3. Calculated response matrix for NaI(Tl) $\phi 3'' \times 3''$ bare detector, broad parallel beam perpendicular to the detector endface and energy interval up to 3 MeV (only each 10-th row drawn)

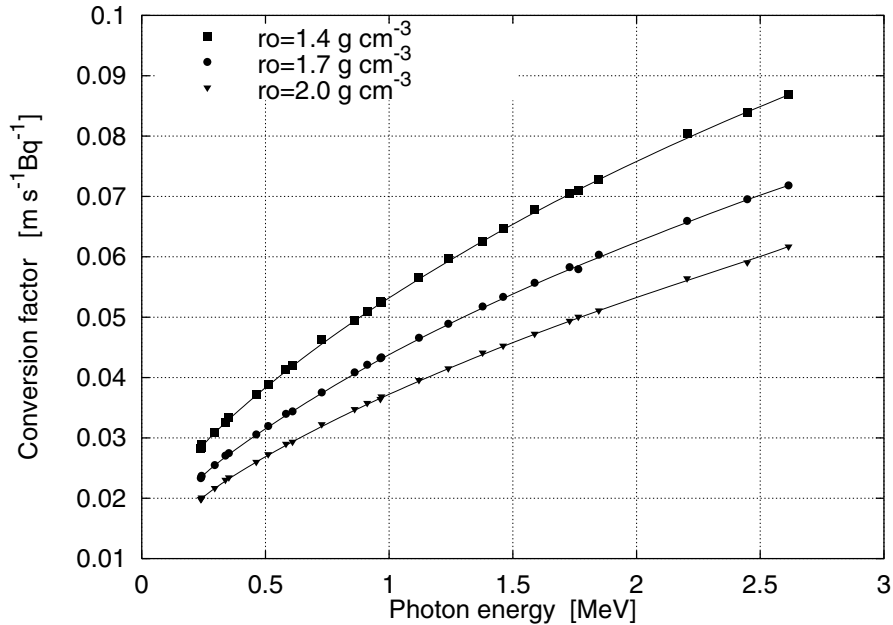


Fig. 4. Calculated conversion factors for the most significant energy lines of natural radionuclides (homogeneously dispersed in the soil surface layer), for reference height 1 meter and for soil densities 1.4, 1.7 and 2.0 gcm⁻³

and bremsstrahlung yield data from [8] are used. The output of the program is calculated spectrum of energy deposited in the detector active volume. Convoluting the deposition spectrum with detector resolution function, we can obtain the modelled detector response for given energy line (or photon field). Making such calculations for the set of energies covering the required energy interval, we can construct the response matrix for this interval. Matrices for several sizes (shapes) of the NaI(Tl) and BGO detectors were calculated and applied for the in-situ spectrometry data deconvolution and analysis. Example of the calculated response matrix for the NaI(Tl) $\phi 3'' \times 3''$ bare detector is in the Fig. 3. The model responses and response matrix for the ENMOS airborne scintillation spectrometer ($4'' \times 4'' \times 16''$ NaI(Tl) detector, Picodas Group Inc., Canada) and environmental monitoring applications were also calculated.

4 Conversion Factors for the Ground Measurements

The semiconductor spectrometers are often used for in-situ activity concentrations ground-level measurements. Semiconductor detector provides high resolution (comparing with scintillation one) that enables to distinguish and identify all radionuclides. To preserve the high resolution, the extremely large response

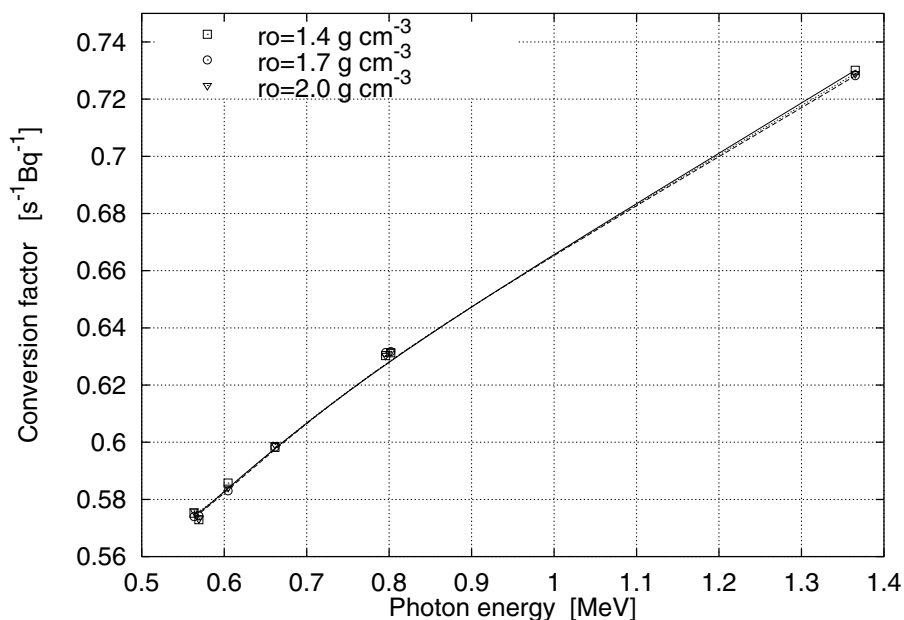


Fig. 5. Calculated conversion factors for the energy lines of ^{134}Cs and ^{137}Cs radionuclides dispersed exponentially in the soil surface layer (with relaxation length 3 cm) for reference height 1 meter and for soil densities 1.4, 1.7 and 2.0 g cm^{-3}

matrix should be necessary and deconvolution technique (mentioned above) is not applicable for this reason. The experimental calibration of the energy and directional dependence of detection efficiency and conversion factors (describing relation between individual radionuclides concentrations and corresponding peaks areas in the standard experimental arrangement) are usually used for the semiconductor spectrometers. The database of these conversion factors was prepared using Monte Carlo code discussed in the paragraph 2. Example of the calculated conversion factors for the natural radionuclides is in the Fig. 4. The same calculations were done for some expected man made contaminants. Example of results for the energy lines of the ^{134}Cs and ^{137}Cs with exponential depth distribution in the soil surface layer (relaxation length 3 cm) shows Fig. 5. The conversion factors for the continuous set of sublayers of the soil surface layer and most significant expected contaminants were also calculated. Conversion factors for the user definable radionuclides depth distribution models can be derived from this data to improve the experimental spectrometry data processing and interpretation.

5 Conclusion

The effective methods for in-situ gamma spectrometry data processing and interpretation were developed on the base of electron-photon transport Monte Carlo simulation techniques. Discussed codes were successfully used also for the additional studies of data processing methods dependence on the variation of used model parameters (representing factors, which are not known a priori or are known with some uncertainties in real conditions). Influence of the soil composition, density and humidity, airborne spectrometer sensitivity and spatial resolution as function of altitude, vegetation cover density, etc. were studied and some corrections proposed.

References

1. *Gamma-Ray Spectrometry in the Environment*, ICRU Report 53 (1994)
2. J. Klusoň: Progress in Nuclear Energy, **24**, 377 (1990)
3. T. Čechák, J. Klusoň, A. Malušek: *Spectra Processing in Airborne Gamma-Ray Spectrometry Using the ENMOS Detection System*, Report of contract No. 402994, CTU Prague, FJFI KDAIZ (1994)
4. G.J. Hine, G.J. Brownell: *Radiation Dosimetry* (Academic Press Inc. Publishers, New York 1956)
5. J. Klusoň, T. Čechák: 'Some Improvements of In-situ Gamma Spectrometry Data Processing'. In: *Proceedings of the 21st Radiation Hygiene Days, Jasná pod Chopkom, Slovakia, 23–27 November, 1998*, ed. by H. Cabaneková, M. Ďurčík, D. Nikodemová (Graft3, Bratislava 1998) pp. 183-186
6. E. Storm, H. Israel: *Photon Cross Sections from 0.001 to 100 MeV for elements 1 through 100* (Los Alamos Scientific Laboratory, New Mexico 1967)
7. M.J. Berger, J.H. Hubbell: *XCOM V 1.2 – Photon Cross Sections on a Personal Computer* (CRR-NBS, MD 20899, 1987)
8. L. Pages et al.: Atomic Data **4**, 1 (1972)

Visual Monte Carlo and Its Application to Internal and External Dosimetry

J.G. Hunt¹, F.C. da Silva¹, D. de Souza-Santos¹, I. Malatova², S. Foltanova², B.M. Dantas¹, A. Azeredo¹, and M. Isakson³

¹ Instituto de Radioproteção e Dosimetria, Rio de Janeiro, Brazil.

² National Radiation Protection Institute, Prague, Czech Republic.

³ Göteborg University, Sweden.

1 Introduction

The program Visual Monte Carlo (VMC), combined with voxel phantoms, and its application to three areas of radiation protection: calibration of *in vivo* measurement systems, dose calculations due to external sources of radiation, and the calculation of Specific Effective Energies is described in this paper. The simulation of photon transport through a voxel phantom requires a Monte Carlo program adapted to voxel geometries. VMC is written in Visual Basic[®], a Microsoft Windows based program, which is easy to use and has an extensive graphic output. The voxel phantoms used were developed by the National Radiological Protection Board (NRPB) and by Yale university.

The use of a voxel phantom and MCNP for the estimation of the activity of an internally deposited radionuclide was demonstrated by Mallett [1]. Voxel phantoms have been used to estimate counting efficiencies for whole-body ¹³⁷Cs body burdens [2–4]. Voxel phantoms have also been used to calculate external doses and Specific Effective Energies [5,6]. In this paper, the results of the application of VMC are shown for 5 cases of ²⁴¹Am bone surface contamination, one natural uranium, one ²⁴¹Am lung contamination and one ¹³⁷Cs whole body contamination. The three applications were benchmarked against similar physical systems. The measurements for VMC benchmarking were made at the Radiation Protection Institute (NRPI) and at the Instituto de Radioproteção e Dosimetria. The results of the benchmarking show that VMC and voxel phantoms can provide adequate photon transport results.

2 Materials and Methods

2.1 The Monte Carlo Program

The Monte Carlo technique is used to simulate a tissue contamination (or an external source of radiation), to transport the photons through the tissues and, where necessary, to simulate the detection of the radiation. The graphic output of VMC was extensively used for debugging. The program XGEN 3.0 [7] was used to obtain the mass absorption coefficients based on the tissue compositions given in the ICRU report number 44 [8]. A curve was then adjusted for each tissue,

for example, bone marrow. The total, photoelectric and Compton cross sections ($\sigma_{\text{photo, Compton or total}}$) in relation to the photon energy (ϵ) are determined by the following equation:

$$\sigma_{\text{photo, Compton or total}} = \exp(a_0 + a_1 \cdot \epsilon + a_2 \cdot \epsilon^2) \quad (1)$$

3 The Voxel Phantoms

For the simulation of *in vivo* measurement systems, a voxel phantom with a format of 871 “slices” each of 277×148 picture elements was used. The voxel phantom, called NORMAN, is derived from a whole body Magnetic Resonance Image (MRI) scan with contiguous slices [9]. The scanning data were kindly supplied by the Non-Ionising Radiation Department of NRPB. The size of each voxel is 2.08 mm x 2.08 mm x 2.02 mm. The voxel phantom was scaled so that the height (1.76 m) and the mass (73 kg) conforms to the values for reference man stated in ICRP 66 [10]. The version of NORMAN supplied by NRPB for this work is divided into the following tissue types: adipose tissue, hard bone, bone marrow and lungs. The other tissues and muscles are grouped together. For the calculation of dose received from external sources and for the calculation of SEE's, the Yale voxel phantom [11] with a format of 493 “slices” each of 87×147 picture elements was used. The size of each voxel is 3.6 mm x 3.6 mm x 3.6 mm. The Yale voxel phantom contains 36 tissue types.

4 Real Internal Contamination Cases Used for the Benchmarking

The real internal contamination cases used were: (a) Subject with internal contamination of ^{241}Am . A 62 year old male was internally contaminated probably during work with open ^{241}Am oxide for Am Be source production between 1969 and 1973 (b) Subject with internal contamination of ^{137}Cs . A 42 year old, 1.62 m high male was internally contaminated with ^{137}Cs during the radiological accident in Goiânia, 1987.

4.1 Phantoms Used for the Benchmarking

The phantoms used for *in vivo* benchmarking were the NRPI skull phantom [12], the Bfs skull phantom, the BPAM - 001 skull phantom [13], the UCin skull phantom, the LLNL lung phantom [14] and the UCin knee phantom. For external dose calculations, a male, RANDO Dosimetric whole body anthropomorphic [14] phantom was irradiated with a ^{137}Cs source of known activity placed one meter from the front centre of the phantom. 23 cylindrical, glass encapsulated LiF TLDs were placed in the phantom.

5 Results

5.1 Results for *in vivo* Calibration Benchmarking

- Measurement of an individual internally contaminated with ^{241}Am . A whole body cortical bone surface contamination with ^{241}Am measured with a low energy germanium (LEGe) detector (model GL2020R) was simulated. The mathematical detector was first “calibrated” through a simulation of a point ^{241}Am source of 18 kBq located at 5.5 cm from the Ge crystal, on the detector centerline. A whole body cortical bone surface contamination was simulated, and the calculated activity was 4.6 ± 0.3 kBq of ^{241}Am deposited on the external and internal bone surfaces. The activities reported by five laboratories were in the range of 2.3 to 5.5 kBq of ^{241}Am . Figure (1) is an example of the screen image produced by VMC.



Fig. 1. Simulated ^{241}Am contamination of the bone surface being counted with a Germanium detector. The circles are photon interactions in the LEGe detector

- Measurement of an individual internally contaminated with ^{137}Cs . A whole body contamination with ^{137}Cs was simulated, using the $8'' \times 4''$ NaI(Tl) detector. Due to the high activity present, the detector was placed 1.84 m above the patient. An activity of 5.8×10^6 Bq was estimated using a physical phantom. A run of VMC for the same geometry gave a calculated activity of 6.9×10^6 Bq, which is 19% higher than the previously evaluated activity.
- Measurement of head and knee phantoms contaminated with ^{241}Am . VMC was used to calculate the ^{241}Am activities of the Bfs, USTUR, NRPI and UCin head phantoms, using the same detector and measurement geometry as before. The UCin knee phantom was counted with a Ge detector at the IRD. The results of the ^{241}Am activity calculations were all between +40% and -33% of the expected values.
- Measurement of the lung phantom contaminated with U_{nat} and ^{241}Am . VMC was used to calculate the U_{nat} and ^{241}Am activities of the lung of the LLNL torso phantom. The results of the calculations were an overestimation of 46% in the case of U_{nat} , and an underestimation of 9% in the case of the ^{241}Am activity.

6 Results for Specific Effective Energy Benchmarking

VMC was modified to enable the calculation of (SEEs). Figure (2) shows the graphics output of the program, in this case calculating the dose to the lung due to ^{60}Co in the liver.

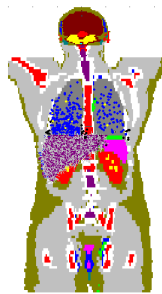


Fig. 2. Coronal view of a SEE calculation: liver (source) to lung (target), ^{60}Co . The circles are photon interactions in the lung

SEE's are quantities defined in the computation of equivalent dose rate in a target organ of the human body. The International Commission on Radiological Protection (ICRP), in its publication 30 [15], tabulates values of SEE's. Table 1 shows calculated SEEs obtained for an adult male. The table contains a comparison of the results with the SEEs cited in the ICRP 30.

Table 1. SEE's calculated using VMC and as given in the ICRP 30

Radionuclide	Source to Target	VMC SEEs	ICRP 30 SEEs
		$(\text{MeV} \cdot \text{g}^{-1} \cdot \text{Trans}^{-1})$ $\times 10^{-7}$	$(\text{MeV} \cdot \text{g}^{-1} \cdot \text{Trans}^{-1})$ $\times 10^{-7}$
^{235}U	Lung to Marrow	4.6	9.3
^{57}Co	Lung to Gonads	0.25	0.41
^{60}Co	Liver to Gonads	0.044	0.042
^{60}Co	Liver to Lung	240	200
^{60}Co	Liver to Marrow	72	81
^{99}Mo	Kidney to liver	39	20

VMC can simulate the photon emission of a radioactive nucleus such as ^{192}Ir , which has a complicated decay scheme, so avoiding the transport errors produced by averaging the photon energy. The results (for mono-energetic photons) show that the differences between the voxel SEEs and the ICRP 30 SEEs are less than a factor of 2.5.

7 Results for External Dose Calculation Benchmarking

VMC has been developed to calculate external doses due to environmental, occupational or accidental exposures. The program calculates tissue and effective dose. The geometries accepted are cloud immersion, ground contamination, X-ray irradiation, point source irradiation or others.

For the benchmarking, cylindrical LiF TLDs were placed at 23 points inside the RANDO phantom which was then irradiated with a point ^{137}Cs source of activity 6.6×10^{10} Bq placed at one meter from the front center of the phantom. The geometry used is shown in Fig. 3.

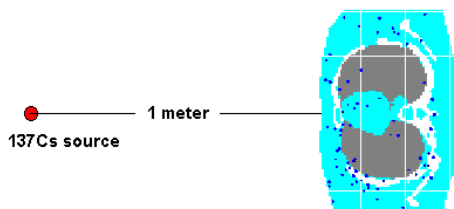


Fig. 3. A transverse view of the Yale phantom showing the ^{137}Cs source and phantom geometry. The circles represent photon interaction points in the phantom

At each point, the value F_i ($i = 1$ to 23) which is the Monte Carlo calculated absorbed dose divided by the TLD measured absorbed dose was calculated. The average of the F_i was 1.01. The standard deviation of the F_i was 0.29.

8 Future Work

The usefulness of VMC can only be shown through the continued benchmarking of the program. The first author is therefore interested in receiving *in vivo* data with reference to the counting of individuals with known body burdens, or data of irradiation with a source of known activity of anthropomorphic phantoms containing TLDs so that the benchmarking can continue. It is planned to apply the VMC code to the calibration of *in situ* gamma spectrometry geometries and to the calibration of systems for *in vivo* measurements of stable lead in bone using X-ray fluorescence. A BOMAB [14] geometry has been “voxelised” and will be used for planning and building BOMAB phantoms. More complicated detector geometries have been simulated, such as the case of the two plastic scintillator detectors with light pipes, as shown in Fig. 4. This geometry will be used to simulate the measurement of ^{40}K in phantoms and in people.

9 Discussion and Conclusions

The results of *in vivo* calibrations and external dose and SEE calculations using voxel phantoms and VMC indicate that diverse photon transport calculations may be made using this system. Hopefully, in the future, mathematical phantoms will complement the use of physical phantoms in the routine calibration of *in vivo* measurement systems.

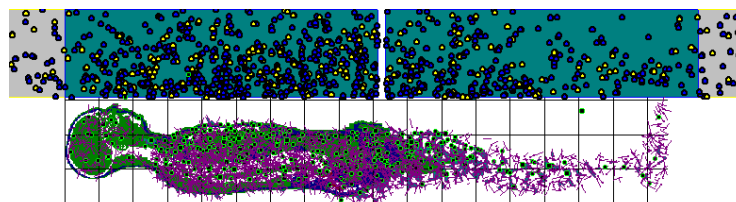


Fig. 4. Coronal slice of NORMAN with two plastic scintillator detectors, radionuclide ^{40}K distributed in the whole body. The circles represent photon interactions in the detector

References

1. M.W. Mallett, D.P. Hickman, D.A. Knuchen: *Health Phys.* **68**, 773 (1995)
2. I. Ishikawa, M. Uchiyama: *Radiat. Prot. Dosim.* **69**, 199 (1997)
3. I. Ishikawa, M. Uchiyama: *Radiat. Prot. Dosim.* **71**, 195 (1997)
4. J.G. Hunt, L. Bertelli, B.M. Dantas: *Radiat. Prot. Dosim.* **76**, 179 (1998)
5. M. Zankl, G. Drexler, N. Petroussi-Heins: *The calculation of dose from external photon exposures using reference Human Phantoms and Monte Carlo methods*. GSF report 8/97, Munich (1997)
6. N. Petroussi-Heins, M. Zankl, and K. Henrichs: *Tomographic Anthropomorphic Models. Part I: Specific Absorbed Fractions of energy for a baby and a child from internal photon sources*. GSF report 7/97, Munich (1997)
7. J.A. Halbleib, R.P. Kensek, T.A. Mehlhorn, S.M. Valdez, *ITS version 3.0: The integrated TIGER series of coupled electron/photon Monte Carlo transport codes*. Sandia National Laboratories SAND91 - 1634, Albuquerque (1992)
8. International Commission on Radiation Units and Measurements: *Tissue substitutes in Radiation Dosimetry and Measurements*; ICRU Publication 44 (Pergamon Press, Oxford 1989)
9. P.J. Dimbylow: 'The development of realistic voxel phantoms for electromagnetic field dosimetry'. In: *Voxel Phantom Development, proceedings of an international workshop, National Radiological Protection Board, Chilton, 1-7* (1996)
10. International Commission on Radiological Protection: *Human Respiratory Tract Model for Radiation Protection*. ICRP Publication 66, Ann. ICRP 24 (1 - 3) (1994)
11. I.G. Zubal, C.R. Harrell, E.O. Smith, Z. Rattner: *Med. Phys.* **21**, 299 (1994)
12. I. Malátová, S. Foltánová: 'A case of internal contamination with ^{241}Am - different methods for whole body content assessment'. In: *Radioaktivität in Mensch und Umwelt. 30. Jahrestagung der FS und OVS, Lindau, 28 Sept. - 2 Oct. 1998*, Vol. 1, pp.40-45 (1998)
13. G. S. Roessler, B. Magura: *Health Phys.* **49** (1985)
14. International Commission on Radiation Units and Measurements: *Phantoms and Computational Models in Therapy, Diagnosis and Protection*; ICRU Publication 48 (Pergamon Press, Oxford 1992)
15. International Commission on Radiological Protection: *Limits for Intakes of Radionuclides by Workers*. ICRP Publication 30, Part 1. Annals of the ICRP, Vol. 2, No. 3. (Pergamon Press, Oxford 1979)

Monte Carlo Simulation of Mammography X-ray Units: a Comparison Between Different Electron Extensions of the EGS4 Code System

M. Marziani¹, M. Gambaccini¹, L.M.N. Távora², and A. Taibi¹

¹ Dipartimento di Fisica, Università di Ferrara and INFN, 44100 Ferrara, Italy

² Inst. Centre, Departamento de Física, U. Coimbra, 3004-516 Coimbra, Portugal

1 Introduction

The knowledge of diagnostic X-ray spectra is a parameter of primary importance for optimising radiologic examinations and for the evaluation of organ doses. The last decade of improvements in the diagnostic X-ray unit technology has brought an array of several anode and filter material combinations for X-ray tubes, notably in mammography. The direct measurement of X-ray spectra generated from such tubes is rarely practical, especially in a hospital or any other clinical environment. Moreover, the recorded pulse spectra have to be corrected for efficiency, resolution and energy dependence of the detector. Even resorting to tabulated spectra from published catalogues [1–3] could be impractical since for the most part the desired combination of target and exit window materials, anode angle, added filtration and peak-kilovoltage can't be easily found in such databases. Moreover, published tabulations are often based on semi-empirical models or fitting procedures which rarely try to mimic the underlying physics.

The advantages of a direct Monte Carlo simulation of spectra from diagnostic X-ray tubes consist principally in a more realistic simulated production process than semi-empirical models and in a greater flexibility as far as the variability of input parameters is concerned. Changes in any of the input values can be easily implemented in the code, thus allowing an easy way of testing various anode, filter material and target angle combinations.

This paper is focused on the Monte Carlo simulation of X-ray tubes used in mammography. The simulation work is based on enhanced versions of the EGS4 code system [4], that incorporate different improvements to deal with the ionisation of the K-shell by electron impact, namely those proposed by Namito and Hirayama (EII model) [5] and the generalised oscillator strength (GOS) model [6,7] with an improved scheme for the angular distribution of bremsstrahlung radiation. These recent enhancements should further improve the usefulness of a direct Monte Carlo simulation of X-ray tubes, inasmuch as they reproduce the electron–electron interaction more closely. In order to assess the importance of such extensions, we used the above codes to build realistic simulations of a General Electric GS 512–4 mammography tube. This choice is due to the fact that the tube is a part of the General Electric 600T mammography unit, in widespread use all over the world.

2 Methods

2.1 Monte Carlo Simulations

The EGS4 code system [4] was used to simulate the response of the General Electric tube at typical diagnostic kilovoltage settings (26–30 kVp). Since the tube is powered by a high-frequency generator which approximately mimics a constant potential generator, then a fixed energy (e.g. 30 keV for a setting of 30 kVp) can be assumed in the simulation for the beam of incident electrons. Thus the high-frequency tube-voltage ripple (less than 2% at 30 kVp) was not taken into account in this work. The molybdenum anode target, the beryllium exit window and molybdenum added filtration were modelled accurately according to the manufacturers' specifications [8]. The tube geometry is given in Fig. 1 where parts are not drawn to scale. The three boxes represent right circular cylinders. The electron beam is perpendicular to the anode target cylindrical surface and the output photon spectrum was scored at the exit surface of the Mo added filter. The symmetry axis of both the Be window and the Mo filter was chosen as the z axis of the geometry, directed downwards. Energy, x – y coordinates and w direction cosines of the output photons were scored with associated statistical weights. The focal spot size of the tube was ignored, i.e. incident electrons were assumed to form a pencil beam. Reflected electrons from the anode were simply discarded, thus disregarding the production of off-focus radiation.

2.2 Electron Impact Ionisation (EII) Model

A modification [5,9] to the default EGS4 code was used in order to include K-shell electron impact ionisation, i.e. the transport of fluorescent photons emitted after the scattering of an incident electron with an inner K-shell electron. Material data were prepared with the latest implementation of PEGS4 developed at KEK [10], including flags for generating K X-ray energy related data and Rayleigh scattering cross-sections. Suitable PEGS4 input data files were prepared for each of the six values for the IMPACT flag corresponding to different EII cross-section models [9]. The option for normalizing bremsstrahlung cross sections to ICRU Report 37 radiative stopping powers was also activated.

The electron transport algorithm PRESTA [11] was used. Energy cut-offs were set to 10 keV for electrons and 1 keV for photons. Improved bremsstrahlung angular sampling based on the 2BS formula [12] was included. A bremsstrahlung splitting variance reduction technique was applied with splitting factors as high as 200. X-ray fluorescence photon transport was obviously taken into account. To simulate the Mo anode the MARYMAC Mortran package [13] for generalised cylinder geometry was employed. A variance reduction splitting technique for EII photons was applied, with a splitting factor of 100. The code (briefly called EGS4+EII system) was compiled on a Pentium-II PC with a 400 MHz clock using the Lahey Fortran 90 compiler. Run times were in the order of 18 s per 10^5 incident electrons.

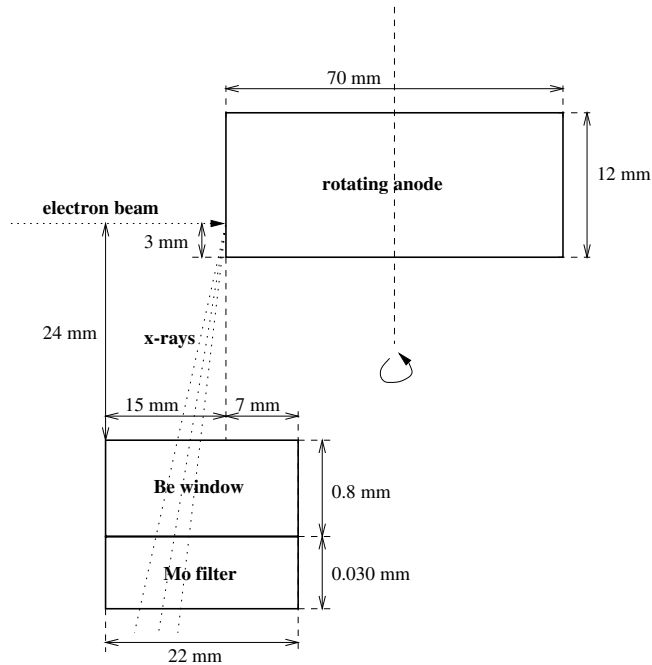


Fig. 1. Schematic representation of the tube geometry. The electron beam hits the target material at an angle of 90° and the emitted X-rays are scored at the exit of the added molybdenum filter

2.3 Generalised Oscillator Strength (GOS) Model

The differential cross section for inelastic collisions of non-relativistic electrons with atoms may be treated (within the Born approximation) in terms of a function called the *generalised oscillator strength* (GOS) [14], which describes the inelastic properties of the target atom. Although total inelastic cross sections and stopping powers could be accurately estimated with the GOS model, the same did not apply to partial ionisation cross sections, especially near shell thresholds. That motivated the development of an improved version of the GOS model [6] especially suited for events involving the ionisation of the K-shell by electron impact. This model has been implemented in the EGS4 code system. The code (briefly called EGS4/GOS system) can be used to predict photon spectra produced in X-ray tubes operating at diagnostic energies [15] and different sets of data for the electron impact ionisation of the K-shell can now be used [7].

Simulation runs were set to use the GOS cross sections and in this case the bremsstrahlung splitting based on the 2BN formula was used [6]. Energy cut-offs were set to 9 keV for electrons and 1 keV for photons. The code was compiled on a PC as above, with run times in the order of 50 s per 10^5 incident electrons.

3 Results

Output energy spectra from the above simulations were studied as a function of the tube kilovoltage in the range 25–40 kVp. Here, results for a typical diagnostic setting of 30 kVp are only presented. Planar fluence and angular distribution of photons at Mo filter exit were evaluated. The angular distribution of exit photons exhibited the expected peak at about 22° [16].

Results were compared with tabulated data from the IPEM database [3]. While being the most recent catalogue of diagnostic X-ray spectra, it only allows effective target angles in the range 9° – 23° for molybdenum anodes. Reference spectra presented in older databases [1,2] had a fixed 17° target angle and a fixed 1.0 mm thickness for the Be window. The simulated GS 512–4 tube, however, has a 0.8 mm Be window and a 0° effective angle [16]. In order to assess how results of the simulations are affected by the chosen model for the EII cross section, the K_α to bremsstrahlung continuum ratio was evaluated for every calculated spectrum. Values were averaged among several runs of the codes with different random number starting seeds. In Tab. 1 values of this ratio are presented as a function of the simulation model and compared with those of IPEM reference spectra for various target angles.

Table 1. Values of the K_α to bremsstrahlung ratio as a function of either the simulation model or the reference spectrum at 30 kVp

Monte Carlo code name	EII cross-section model	K_α /bremsstrahlung
EGS4+EII	Casnati	12
EGS4+EII	Kolbenstvedt (revised)	14
EGS4+EII	Kolbenstvedt	19
EGS4+EII	Jakoby	12
EGS4+EII	Gryzinski	6.6
EGS4+EII	Gryzinski (relativistic)	6.8
EGS4/GOS	GOS	10
EGS4 (default)		3.5
Reference spectrum	Target angle	K_α /bremsstrahlung
IPEM	9°	9.2
IPEM	17°	9.0
IPEM	23°	9.0

A 9° target angle IPEM spectrum at 30 kVp is compared in Fig. 2 with output spectra from the codes EGS4+EII, EGS4/GOS and the default EGS4 (no EII included). The EGS4+EII spectrum was employing the Casnati’s cross-section model. Simulated spectra were calculated with 10^7 incident electrons and normalized to the total photon count of the IPEM spectrum. Both EGS4+EII and

EGS4/GOS results exhibit a good overall agreement with the IPEM reference spectrum, with a slight overestimate for both K-peaks. In contrast, the default EGS4 heavily underestimates the K characteristic contributions.

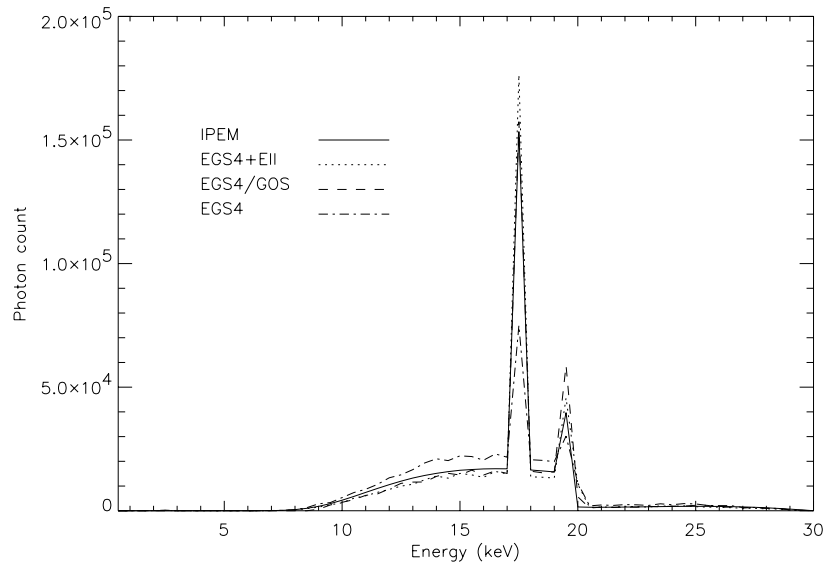


Fig. 2. Photon spectra obtained with the X-ray tube operated at 30 kVp. The simulated EGS4+EII spectrum using Casnati's model (*dotted line*), the EGS4/GOS spectrum (*dashed line*) and the default EGS4 output (*dotted-dashed line*) are compared with a 9° IPEM spectrum (*solid line*)

The above photon spectra were further converted to kerma-in-air spectra using the photon-to-kerma conversion factors included in [3]. Tube output, mean photon energy and HVL of the filtered spectra were computed for an attenuation due to 75 cm of air and are presented in Tab. 2.

4 Conclusion

The results presented exhibited an overall good agreement between simulated and reference data. The accuracy of simulated results has been shown to heavily depend on the model used to deal with the ionisation of the K-shell. Both EGS4+EII and EGS4/GOS codes seem promising in this respect. The latter is able to reproduce the K_{α} to bremsstrahlung ratio within about 10%, while the former approximates better the K_{β} to bremsstrahlung ratio. Furthermore, the apparent discrepancies between the results presented and reference data might be ascribed to the lack of both a 0° effective angle reference spectrum and of the modelling of electrons reflected from the anode.

Table 2. Tube output, mean photon energy and HVL values of both simulated and reference spectra at 30 kVp, 75 cm air

Code name or reference	Tube output ($\mu\text{Gy/mAs}$)	\bar{E} (keV)	HVL (mm Al)
IPEM (9°)	114.1	17.0	0.33
EGS4+EII (Casnati)	110.5	17.1	0.36
EGS4/GOS	109.5	17.2	0.36
EGS4 (default)	118.8	16.7	0.30

References

1. T.R. Fewell, R. Shuping: *Handbook of mammographic X-ray spectra* (FDA, Rockville 1978)
2. R. Birch, M. Marshall, G.M. Ardran: *Catalogue of Spectral Data For Diagnostic X-rays* (The Hospital Physicist's Association, London 1979)
3. K. Cranley, B.J. Gilmore, G.W.A. Fogarty, L. Desponds: *Catalogue of Diagnostic X-ray Spectra and Other Data* (The Institute of Physics and Engineering in Medicine, York 1997)
4. W.R. Nelson, H. Hirayama, D.W.O. Rogers: SLAC-265, Stanford University, Stanford (1985)
5. Y. Namito, H. Hirayama: Nucl. Instrum. and Methods A **423**, 238 (1999)
6. L.M.N. Távora, E.J. Morton: Nucl. Instrum. and Methods B **143**, 253 (1998)
7. L.M.N. Távora, E.J. Morton, F.P. Santos, T.H.V.T. Dias: 'Simulation of X-ray tubes for imaging applications'. In *1999 IEEE Nuclear Science Symposium Conference Record, Seattle, USA, 24–30 October, 1999*
8. General Electric document GS 512–4 DTP C00G61M.03 (1988)
9. Y. Namito, H. Hirayama: *LSCAT: Low-Energy Photon-Scattering Expansion for the EGS4 Code (Inclusion of Electron Impact Ionization)*, KEK Internal 2000-4, KEK, Japan (2000)
10. H. Hirayama, Y. Namito, S. Ban: *Implementation of a General treatment of Photoelectric-Related Phenomena for Compounds or Mixtures in EGS4*, KEK Internal 2000-3, KEK, Japan (2000)
11. A.F. Bielajew, D.W.O. Rogers: Nucl. Instrum. and Methods B **18**, 165 (1987)
12. A.F. Bielajew, R. Mohan, C.S. Chui: *Improved bremsstrahlung photon angular sampling in the EGS4 code system*, National Research Council of Canada Report PIRS-0203 (1989)
13. M. Udale-Smith: *Code developed at the Cookridge Hospital, Leeds, UK* (1988); EGS4 contributors area: <ftp://www.irs.inms.nrc.ca/pub/inms/egs4/contributors/>
14. M. Inokuti: Rev. Mod. Phys. **43**, 297 (1971)
15. L.M.N. Távora, E.J. Morton and W.B. Gilboy: 'Enhancing the ratio of fluorescence to bremsstrahlung radiation in X-ray tube spectra'. Accepted for publication in Appl. Rad. and Isotopes
16. G.T. Barnes: 'Tube Potential, Focal Spot, Radiation Output and HVL Measurements on Screen–Film Mammography Units', In: *Screen Film Mammography – Imaging Considerations and Medical Physics Responsibilities*, ed. by G.T. Barnes and G.D. Frey (Medical Physics Publishing, Madison, Wisconsin 1991) pp. 67–113

The Use of MCNP in Flash Radiographic Applications at AWE

S. Quillin, I. Crotch, S. McAlpin, and J. O'Malley

AWE Aldermaston, Berkshire, UK

1 Introduction

AWE performs experiments to investigate the hydrodynamic behavior of explosive metal systems in order to underwrite the UK nuclear deterrent. The experiments involve the manufacture of a device to mock up some aspect of the weapon. Inert simulant materials replace fissile weapon components. The device is then detonated under remote control within specially designed explosive containment buildings called firing chambers. During the experiment a very brief, intense, collimated flash of high energy x-rays are used to take a snapshot of the implosion (see Fig. 1). From the resulting image measurements of the dynamic configuration and density distribution of the components in the device are inferred. These are then used to compare with calculations of the hydrodynamic operation of the weapon and understand how the device would perform under various conditions. This type of experiment is known as a core punch experiment.

The core punch experiment poses several unique challenges to radiography. The object under investigation is extremely opaque to x-rays. It is both dense and of high atomic number and therefore is equivalent to many tens of cm of lead in terms of transmission to 3-5MeV photons. The object density distribution is also rapidly moving (\sim several kms^{-1}) and therefore a 50ns flash of x-rays is typically used. Finally, the experiment is an explosive experiment, therefore the x-ray source, detectors and facilities must be protected against explosive blast and fragmentation attack.

The Monte Carlo n-particle transport code (MCNP) [1] has been used for the approximately five years at AWE to aid in the design and analysis of core punch experiments. This paper gives a brief review of current areas of research in which the code is being employed. The areas are loosely grouped under the topics of x-ray source and source shielding design, signal to noise calculations and detector response investigations.

2 X-ray Source and Source Shielding Design

In addition to the intensity of the x-ray source, three characteristics of the source are important in the design and analysis of core punch experiments. The first is the spatial intensity distribution of the x-ray source. The second is the spectral distribution of x-rays from the target and the third is the degree to which any radiation away from the collimated primary beam is shielded. Figure 2 shows

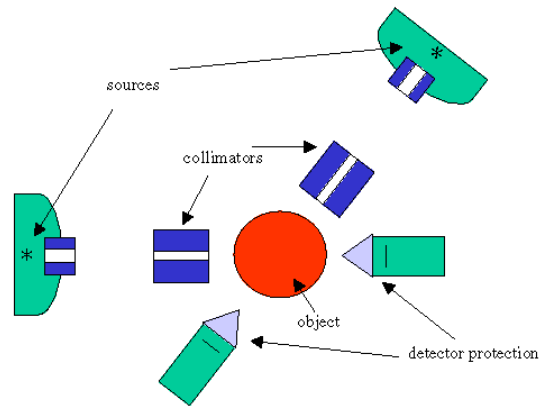


Fig. 1. Plan schematic of core punch flash radiographic experiment

a cross section through the conversion target of a typical flash x-ray machine used at AWE. These typically use a paraxial diode on a single pulse forming line though a variety of machine types operate at AWE.

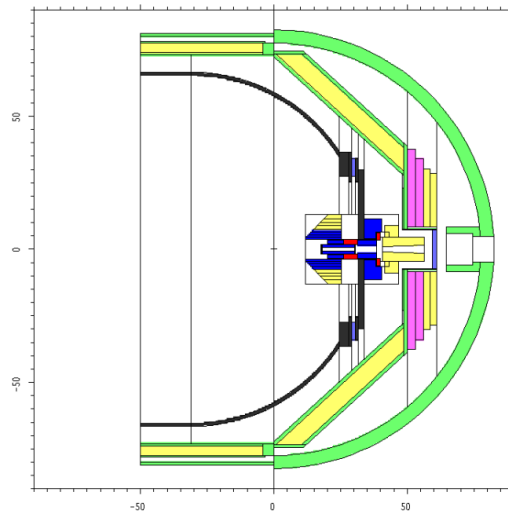


Fig. 2. MCNP flash x-ray machine shielding geometry showing complex shielding

Two types of MCNP calculation are performed. In order to establish the spectral distribution of the primary beam simple geometries are modelled in coupled electron/photon mode in which a narrow beam of electrons are normally

incident on a conversion target (typically tantalum) of the correct thickness for the machine in question, including electron beam stopping material. The photon flux then tallied as a function of energy using surface tallies and next event estimators (f2 and f5).

Investigations have been performed to investigate the effect of non-normally incident electrons on the target and non-mono-energetic electron beams. The degree of electron angular spread at the target can be inferred from experimental measurements of the machine intensity with respect to angle from the main beam. The electron energy spread can be inferred from voltage measurements at the machine anode/cathode arrangement. These effects can also therefore be modelled to give the deviation of the spectrum from pure Bremsstrahlung and include effects of target absorption.

The design of high intensity flash x-ray sources used at AWE results in an impedance mismatch between the conversion diode and the transmission line. This means that from an initial 100kA of beam current only 30kA reaches the load and is converted. The remaining 70kA will in general spray into the forward part of the machine where it will be converted and generate an undesirable secondary “glow” of photons of various energies. MCNP is being used in conjunction with e-beam transport codes to investigate this effect and enhance the design of pulsed power machines and source shielding. Figure 3 shows results from a coupled electron/photon calculation in which a fan of electrons is sprayed out in a disk from the central beam. Photo-weighted flux (see section 4) is tallied as a function of angle around the outside of the machine and compared with dose measurements on the front of the machine. It can be seen whilst there is some qualitative agreement between the code and experiment, the precise details of this sprayed electron current are still unknown.

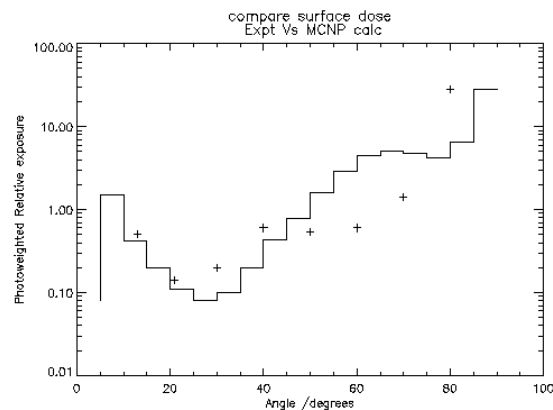


Fig. 3. MCNP photoweighted flux vs measured dose for a flash x-ray machine (using 70% sprayed electrons into vacuum dustbin)

3 Signal to Noise Calculations

One of the major applications of MCNP at AWE is in the investigation of background dose distributions on core punch images. Figure 1 shows a schematic of a core punch experimental configuration. One can see various explosive protection systems, collimators etc. Photons will interact with collimators, explosive containment systems and the object itself and be scattered, but may still interact with the detector to produce a background on the image which is not correlated to the signal. It is this background which will be referred to as scatter or noise in this paper. Random noise, though an issue for core punch radiography, is not discussed. Scatter arises from multiple sources in the experiment. The systematic uncertainty in this background is one of the major sources of uncertainties in density measurement from core punch images. In order to be able to make density measurements in the object to the percent level it is necessary to either reduce current core punch background levels or characterize them on dynamic experiments to a few percent. This is extremely challenging.

A second major uncertainty in deriving density from core punch images is related to uncertainties due to the three-dimensionality of the implosion. Increasing the number of simultaneous images of the implosion would reduce this uncertainty, however it is then important to assess how multiple beams may increase scatter backgrounds and how this scatter may be either reduced and/or quantified. Work is therefore underway to assess the characterization of scatter in multiple axis core punch radiography.

The scatter research programme at AWE comprises of three main experimental and calculational programmes. These are described below.

3.1 Small Angle Compton Scattering Investigations

Experiments have been carried out at the Microtron facility at LANL. The microtron is an x-ray source capable of delivering large dose rates $\sim 1000\text{R/min}$ at 1m at variable peak Bremsstrahlung energies of 6MeV, 10MeV, 15MeV and 20MeV. The source size is small, equivalent to a uniformly filled disc of 0.6mm diameter. The small angle Compton scatter investigations were designed to investigate to what degree single scatter events from photon interactions with detector protection materials could be modelled using MCNP.

The experimental arrangement is shown in schematic in Figure 4. The method used was to take attenuation images of a simple circular tungsten alloy step wedge at a low magnification ~ 1.3 . A large scattering mass was also imaged. By variation of the distance between the scattering mass and the detector and the area of collimated beam the ratio of small angle, Compton scattered radiation from the scattering mass to the signal transmitted through the scattering mass and step wedge can be varied. Scatter to signal levels from $\sim 1\%$ to 100% have been obtained. Calculational comparisons were then made with MCNP simulations of the experiment. In particular the degree to which relative step heights in the image were predicted in high and low scatter situations was investigated.

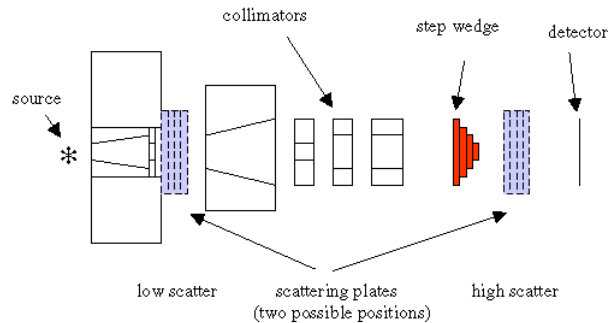


Fig. 4. Experimental geometry for low angle Compton scattering investigations

Experiments were performed in four different scatter geometries varying from low to high scatter at four different peak Bremsstrahlung energies, 6 MeV, 10 MeV, 15 MeV and 20 MeV. Images have been recorded on two types of phosphor storage screen (Fuji BAS IIIs and AC3 plates) and also on direct record x-ray film with varying thicknesses of metal intensifying screens either side of the detector.

MCNP calculations consisted of a photo-weighting calculation for the detector used, a calculation to obtain the spectral source distribution (using the known target configuration for the microtron) and numerous calculations of photo-weighted flux at the detector position (see section 4).

The effects of electron transport and coherent scattering modelling was investigated by comparison with MCNP calculation with these aspects of physics turned on and off. Surface flux tallies were also compared with next event estimators. Figures 5 and 6 show comparison between measured distributions and those calculated using MCNP 4B. It can be seen that the agreement is reasonable good <5%. Several issues were noted in the comparison.

1) The modelling of coherent scattering is important to match the scatter distribution at the edge of the collimated beam.

2) Electron transport in the flux calculations had <1% effect on the agreement with experiment at the expense of significant calculation time.

3) The understanding of detector response is a key issue in accurately modelling these backgrounds, in particular the energy response of different detectors. This will be discussed further in section 3.

4) Surface tallies and detectors show a ~1% disagreement in well converged problems with full electron transport and coherent scatter modelled. This is still under investigation and has been reproduced in simpler geometries.

5) Photoneutron production in the Microtron conversion target above 6 MeV limits high energy experimental agreements with MCNP 4B which did not model such production in the form used. This capability would be useful for core punch radiography applications of the code.

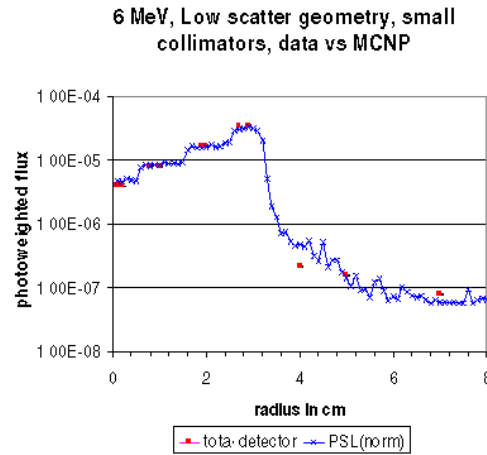


Fig. 5. 6 MeV, Low scatter geometry experiment vs MCNP (stars = experiment, square = MCNP ring detectors)

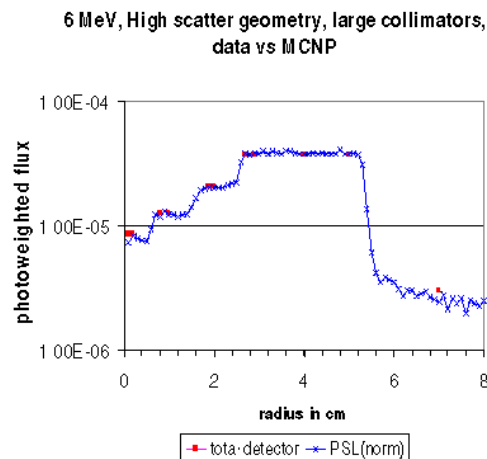


Fig. 6. 6 MeV, High scatter geometry experiment vs MCNP (stars = experiment, square = MCNP ring detectors)

3.2 Large Angle Compton Scattering Investigations

In order to understand twin or multiple axis radiography, experiments have been carried out to investigate how well the scatter from a simple spherical steel ball vs angle from the incident beam could be modelled using MCNP 4B. These experiments were also performed in collaboration with LANL at the microtron facility. Figure 7 shows the geometry. Measurements were made at five different scattering angles from 60 to 130 degrees from the forward beam direction. Fuji Bas IIIS phosphor storage screens were used behind a 13cm thick focussed collimator. A lead castle was built around the detector and boron carbide loaded

wax blocks also used in the higher energy measurements to reduce photo-neutron backgrounds in the detector. Measurements were made at two peak Bremsstrahlung energies, 6MeV and 15MeV.

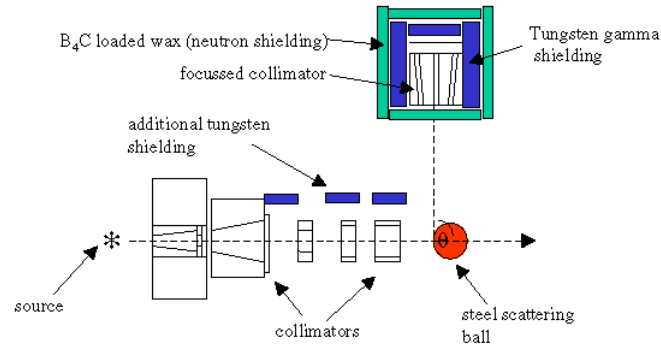


Fig. 7. Experimental geometry for high angle Compton scattering investigations

MCNP calculations consisted of a photo-weighting calculation for the detector used, a calculation to obtain the spectral source distribution (the beam was hardened by 1.25cm of tungsten alloy) and a simple calculation of photoweighted flux from the ball vs angle using ring detectors.

Figure 8 shows a comparison of photoweighted flux vs angle for 6MeV and 15MeV peak energy Bremsstrahlung beams respectively. Reasonable qualitative agreement was obtained in the relative scattered dose intensity vs angle. The agreement is sensitive to the detailed modelling of the detector in the photo-weighting calculation and also to the density and material of the scattering sphere. The boron carbide loaded wax blocks are vital in removal of photo-neutron backgrounds for the 15MeV measurements.

3.3 Integrated Core Punch Scatter Experiments

In addition to the modelling of simple experimental configurations discussed above, which attempt to investigate how well the code can model scatter backgrounds in core punch experiments, integrated experiments are being performed to obtain a gross estimate of scatter levels in multi-axis core punch experiments. MCNP is being used to attempt to model these integrated experiments and calculationally extrapolate to geometries not amenable to experimental measurement. A 10MeV linear accelerator (LINAC) with $\sim 100\text{R}$ per minute dose rate from a $\sim 2\text{mm}$ uniformly filled spot size was used at AWE. Figure 9 shows the experimental arrangement. Collimators and detectors for up to five x-ray beams were arranged within a 6 foot tall, 6 foot diameter 5cm thick steel cylinder which modelled a possible explosive containment system for a core punch

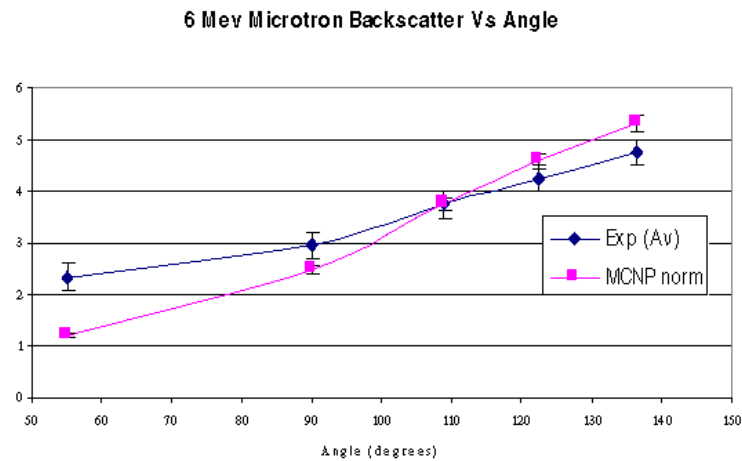


Fig. 8. Experiment vs MCNP, photoweighted flux vs angle for the backscatter experiments

experiment. A simple tungsten object was used which was elongated along the axis of the primary beam to mock up the transmission properties of a core punch experiment.

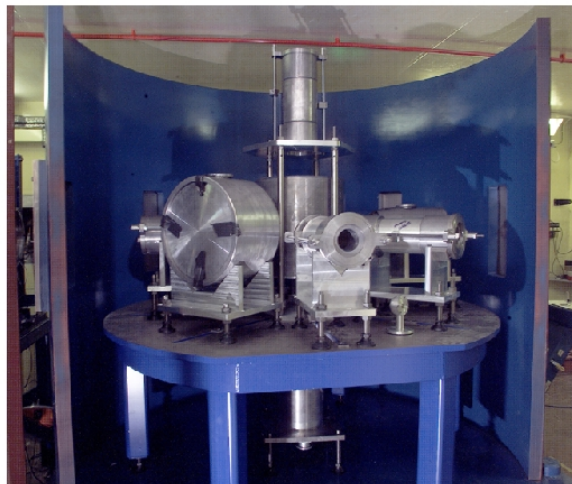


Fig. 9. Photograph of integrated multi-axis scattering experiments

The LINAC was used to provide radiation along one axis of the experiment and (film) detectors were placed within all the off-axis protection systems to measure the contribution that the main beam makes to scatter background on

off-axis views. This was done for a simple twin axis geometry and components added until five axis were used.

The facility space currently renders the positioning of the mock up in all the necessary orientations to enable five different beams to be employed impractical. Therefore MCNP is being used to match experiments with a single source and one to five axis of components before being used to model multiple beams along all axis.

The geometry for this experiment was extremely complex and the requirement to model scattered photons from multiple components presented significant variance reduction problems. Figure 10 shows the MCNP geometry which includes all the main core punch components. Photons only were run in the flux calculation and single point detectors were placed in all film positions to estimate direct and collided flux. A DXTRAN sphere and forced collisions were used to attract particles to the object and then scatter them within components of relevance. Figure 11 shows the agreement between MCNP and experiment for one to five axes of core punch components using a single source. The agreement was deemed sufficient to enable the programme to proceed to use MCNP to investigate multiple beams.

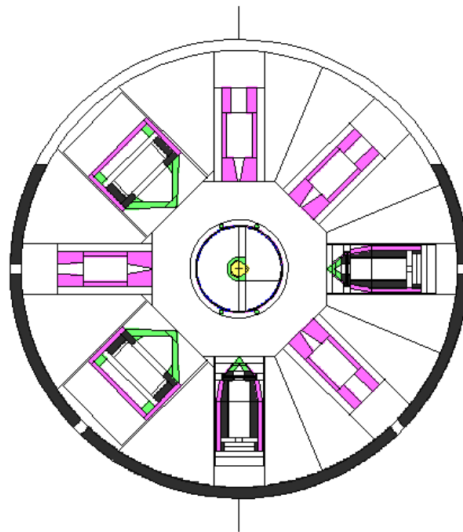


Fig. 10. Plan MCNP geometry of multi-axis scattering experiments showing complex geometry of collimators and detectors

4 Detector Modelling

Three main x-ray imaging detector types are currently being employed at AWE to record the images in flash radiographic experiments. These are x-ray recording film, phosphor storage screens and opto-electronic gamma camera systems. All

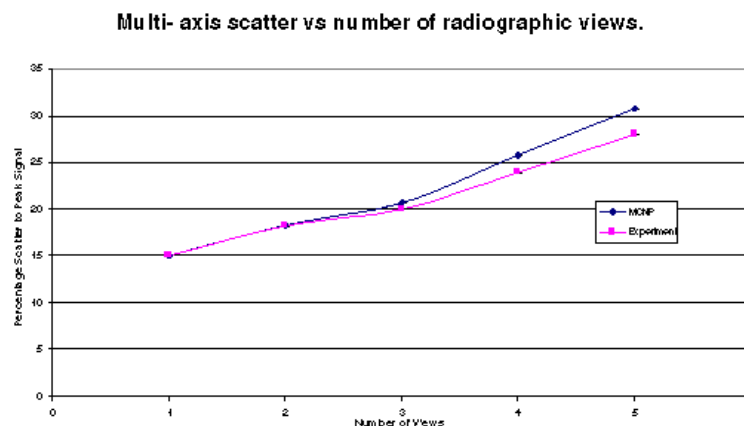


Fig. 11. Experiment vs calculation in multi-axis scatter experiments showing scattered photoweighted flux vs number of radiographic views

detectors have some common issues which can be investigated using MCNP. This is done in conjunction with a variety of alternative techniques to look at detector specific issues, for example effects due to film densitometry or optical wavelength light spread within scintillators used with gamma cameras. The main areas of detector response being investigated using MCNP is spectral response of the detectors and blur effects. These are described below.

4.1 Energy Deposition Calculations (The Photoweighting Function)

Sections 2 and 3 above highlight the importance of an understanding of the relative amount of energy different photons deposit within a particular detector system. In order to reduce calculation times for MCNP modelling of complex core punch geometries it is usual for a calculation to be run in which photon flux only is tallied at the detector position. An energy dependent function is then used to modify the tally to account for the dose absorbed by the detector. This flux modifier is known as a photoweighting function. It is generated by running a calculation for a specific type of detector in which all the details of the detector are explicitly modelled, including, for example any small air gaps which may exist between films and metal intensifying screens, substrates on films etc. A series of monoenergetic photon sources are run normal to the detector and the energy per source particle, within the active region of the detector, that each of these source photons deposits is tallied. The results are then normalised to cobalt 60 energies (AWE measures all doses relative to a cobalt 60 standard source). The flux from a core punch MCNP simulation is then multiplied by photon energy and the photoweighting function to tally cobalt equivalent dose absorbed within the detector without recourse to explicit detector modelling in full electron/photon mode for every calculation. Figure 12 gives an example of a photoweighting function calculated for Fuji BAS IIs phosphors with 0.254mm

thick tantalum metal intensifying screens. This function was calculated for use with the large angle scattering experiments described in section 3.2. Two curves are shown with different phosphor densities. The correct density for the IIIs phosphor is believed to be 3.9g/cc.

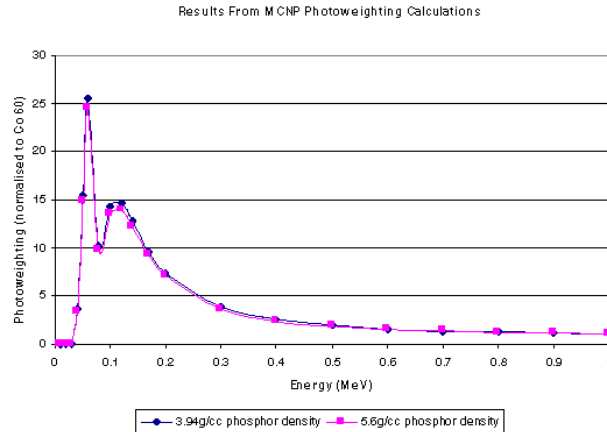


Fig. 12. “Photoweighting” function for Fuji BAS IIIs image phosphors for two different densities of phosphor component

The use of photon heating tallies and energy deposition tallies (f6 and *f8) have been investigated in MCNP 4B for the construction of photoweighting functions. It has been shown that f6 tallies give inappropriate results for thin systems but may be used in thick detectors.

4.2 Point Spread Function Calculations

The resolution of a core punch radiographic experiment depends critically upon the source intensity distribution, the experimental geometry and also the resolving characteristics of the detector. For x-ray recording films the resolving power of the detector is dominated by considerations of the range of secondary electron populations generated within the detector from absorbed x-ray distributions. MCNP is being used to calculate this energy spread for various detector types in order to optimise core punch experimental geometries and also to enhance analysis of core punch images.

A narrow beam of photons is modelled normally incident upon an explicitly modelled detector and collisions forced in the detector cells along the beam. Energy deposition in the active parts of the detector is then tallied. This effectively gives the point response of the system or point spread function for the detector due to x-ray electron interactions. Figure 13 shows a typical result for a 1cm thick slab of CsI. The results from these calculations in scintillators are used in optical Monte Carlo techniques in order to investigate further spatial blurring due to light spread within the scintillator.

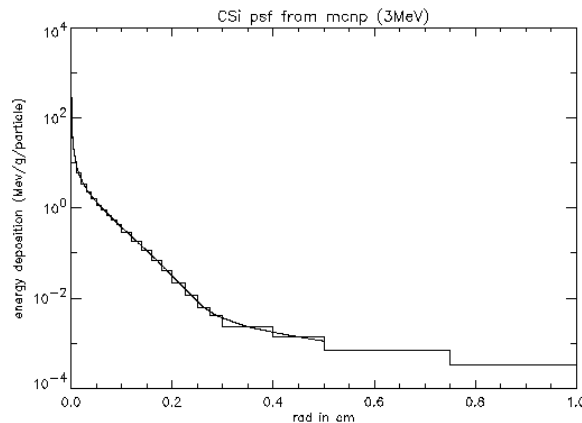


Fig. 13. Point spread function for 3MeV photons in 1cm thick CsI scintillator using *f8 tallies

5 Summary and Conclusions

MCNP is a useful tool in the development and characterization of flash radiographic experiments at AWE. MCNP areas of research at AWE encompass many areas common to the fields of medical physics and oncology. These areas include high energy (several MeV) source shielding, scatter background reduction and detector modelling. Many areas of experimental comparison with MCNP have been described. With care agreement between calculation and experiment $<5\%$ can be obtained. The details of detector response are a critical area of work for these detailed comparisons and it is important that balances between the use of the MCNP code and alternative calculational techniques and experiments be maintained.

Whilst this paper has dealt with the use of version 4B of the MCNP code MCNP 4C is now being employed at AWE in the areas described. In particular, detailed comparison between the results of MCNP 4B and MCNP 4C in photoweighting calculations is being carried out in light of electron physics enhancements in MCNP 4C.

6 Acknowledgements

The authors would like to acknowledge the work of Todd Kauppila and Karl Mueller at LANL and Dr Andrew Gregory at AWE in the fields of scatter background characterization and detector research. Many thanks also to T F Pang for his assistance in the production of this paper.

References

1. J.F. Briesmeister (ed.): *MCNPTM – A General Monte Carlo N-Particle Transport Code – Version 4B*, LA-12625-M (Los Alamos National Laboratory 1997)

Comparison of Monte Carlo Simulation and Measurement of Electron Reflection from Solids

V. Starý

Dept of Materials Engn., Faculty of Mech. Engn., CTU, Karlovo nám. 13, 121 35
Prague, CR

Abstract. Using our Monte-Carlo (MC) code, we simulated the energy-angular distribution of electrons elastically reflected from Au at relatively low electron energy 0.2 – 5.0 keV. The MC data were compared with experimental values measured at energy 0.4 – 2.0 keV and 0.1 – 1.5 keV, respectively, and in the emission angle range 15 – 70°. Taking into account only simple elastic and inelastic scattering, some discrepancies appeared. The positions of the peaks in the angular distributions agreed well, while the MC values at a maximum of 60° peak, were rather different. To explain the difference, we first considered the possibility that energy is lost during “elastic” collision, i.e., by excitation of continuum (X-ray) radiation, and then the possibility of surface plasmon generation. The inclusion of these processes in our MC code improves the agreement somewhat.

1 Introduction

A MonteCarlo simulation (MC) of electron transport in solids can give us reasonable results [1] in electron microscopy, spectroscopy and microanalysis, where knowledge of certain quantities is very often needed for proper analytical measurement. The reliability of physical models incorporated in MonteCarlo code is usually checked by comparing with experimental results. In our MC code the single scattering model is employed, where each scattering event is simulated individually. Elastic or inelastic collisions are usually considered as the basic interactions of electrons with atoms. The interaction efficiencies are defined by differential cross-sections (DCS).

For elastic scattering the DCSs are calculated using quantum physics methods (e.g., [2]). In recent years, several calculated tables of differential cross-sections (DCS) and total cross-sections have been published; cross-sections can also be calculated by suitable programs (e.g., [3]).

In single scattering calculations, we need to know the inelastic cross section, which is double differentiated over the scattering angle and the energy loss. The dependence of inelastic DCS on angle depends on the nature of the inelastic scattering. The integration of an inelastic DCS over the scattering angle should enable us to describe the inelastic scattering by energy loss distribution $d\sigma_{in}(W)/dW$, where W is energy loss. This integration is not simple and should be done sequentially for various interactions. Fortunately, in [4] simple hyperbolic dependence was suggested, which can approximate the real dependence of $d\sigma_{in}(W)/dW$ for all inelastic losses simultaneously. Supposing no energy exchange between two electrons, a simple dependence like W^{-2} is suitable. In this

model, due to the divergence of function W^{-2} when W tends to zero, minimal energy loss W_{min} must be defined. This parameter is connected with the inelastic mean free path λ_{in} by the relation [4]

$$\lambda_{in} = \frac{W_m}{S_B}, \quad (1)$$

where S_B is the Bethe stopping power and W_m is the mean energy loss,

$$W_m = \int_{W_{min}}^E W f(W) dW \simeq W_{min} \ln \left(\frac{E}{W_{min}} \right); \quad (2)$$

$f(W)$ is the normalized distribution function (in our case a hyperbole of the second order) and E is electron energy.

In our recent work [5], we systematically changed the value of W_{min} in our MC code, and we obtained the dependencies of the coefficient of elastic electron reflection R_e on primary electron energy E_o for several elements (C, Al, Ni, Cu, Ag and Au). The optimal values of W_{min} and λ_{in} were found by comparing the MC data with experimental data from [6], which were taken for an acceptance angle between 6 and 52°; the optimal values of λ_{in} agreed well with the theoretical values in [7]. Because the classical formula for S_B diverges when the electron energy tends to zero, we used an empirical correction of ionisation potential according to [8]. The shape and the absolute values of calculated and measured dependencies of R_e were nearly identical for light elements, while for Ag and mainly for Au, the decrease of MC calculated $R_e(E)$ was faster than for the measured curves.

Finally, we studied the energy-angular distribution of elastically reflected electrons to a fixed, relatively narrow acceptance angle; it is given by the coefficient of elastic reflection $R_e(E, \theta)$, where θ is the emission electron angle [9]. We followed the position, width and height of the peaks of $R_e(E, \theta)$ and of the theoretical elastic DCS calculated using PWADIR code [3]. λ_{in} was defined for electron reflection as above, i.e., taking into account only elastic collisions without energy loss and bulk inelastic collisions. We found that there is reasonable agreement in the positions of the peaks (the maximum difference between DCS, MC results and measurement [10] is about 5°). The position of the peaks in [11] differs slightly. The peaks in the MC simulation were wider than the experimental peaks. The ratio of maximum intensity of low angle ($\sim 15^\circ$) and high angle ($\sim 60^\circ$) peaks of the measured and MC calculated values of R_e differed slightly from the experimental data of [10] and [11].

The purpose of this work was to add to the physical model of electron backscattering some possible further process(es), which might improve the agreement of the Monte Carlo calculated and experimentally measured energy-angular distribution of elastically reflected electrons $R_e(E, \theta)$.

2 New Processes Incorporated into the Model

The real process of electron transport through matter is more complicated than the simple model shown above. At least the process of surface plasmon generation and also the generation of continuum radiation should proceed.

To explain some XPS and EELS results, in [12] the model of the next type of inelastic scattering was developed and added to MC calculations, where the electrons crossing the surface lose energy by excitation of surface plasmons. The number of surface plasmons excited during transfer through the surface is given by the Poisson distribution. Here, the probability $p(N)$ of exciting N surface plasmons is

$$p(N) = \frac{P_s^N}{N!} \exp(-P_s); \quad (3)$$

P_s is the mean energy loss (the surface excitation parameter in [12]) given as

$$P_s = K \frac{\pi}{\sqrt{2E}} \frac{1}{\cos \theta}. \quad (4)$$

Because P_s is different for various elements, K should depend only on the type of atoms, i.e., on the atomic number Z . Thus, we can simply calculate the number of excited plasmons and using the magnitude of surface plasmon loss we can also calculate the energy loss of the emitted electron using a standard MC algorithm

$$R = \frac{\sum_0^N p(N)}{\sum_0^\infty p(N)}, \quad (5)$$

where R is a random number ($R \in (0, 1)$). Because $p(N)$ is normalized, the denominator is equal to unity.

The process of generating continuum radiation, i.e., energy loss on “elastic” collision, is given by the change of electron direction connected with some additional acceleration. The differential cross-section of photon production with frequency ω (i.e., electron energy loss $W = \hbar\omega$), with the change of electron direction by angle ϑ is given as [13]

$$\frac{d\sigma}{d\omega d\Omega} = \frac{8}{3\pi} Z^2 \alpha c^2 \left(\frac{e^2}{mc^2} \right)^2 \frac{1}{\omega} \frac{v'}{v} \frac{1}{(\mathbf{v} - \mathbf{v}')^2} \quad (6)$$

where $d\Omega$ is the solid angle, \mathbf{v} and \mathbf{v}' are the velocities of the electron before and after collision, ϑ is the angle between them, and the other symbols are the usual atomic constants. The angle ϑ is standardly calculated during MC calculations; it defines the term $\mathbf{v} - \mathbf{v}'$ and also $d\Omega$. To calculate the probability of any energy loss, we must integrate (6) over the photon energies. Fortunately, even though the DCS diverge, the equation (6) can be integrated analytically. Finally, again using the MC algorithm, now for continuous probability $p(\omega)$, the real energy loss at given electron energy and direction change can be calculated. Because the formula diverges when ω tends to zero, the integrals in the MC algorithm

are limited to some very low value ω_{min} determined by the maximum number accepted by the programming language (PASCAL).

3 Conditions of MC Calculation

For elastic scattering, we used the tables of DCS calculated by the PWADIR program [3], using the muffin-tin potential for atoms in solids with relativistic partial wave analysis. The cut-off limit for electron energy was 0.1 keV. We simulated the process till the number of electrons elastically reflected to the detector in a defined position reached 2000 (i.e., the number of trajectories was usually 10^6). Electrons with only elastic collisions were followed. The surface plasmon loss was supposed to be 2.5 eV [12]. The MC data were compared with two sets of experiments [10,11]. In the calculations, we copied the measurement conditions of [10], especially the solid angle of the detector.

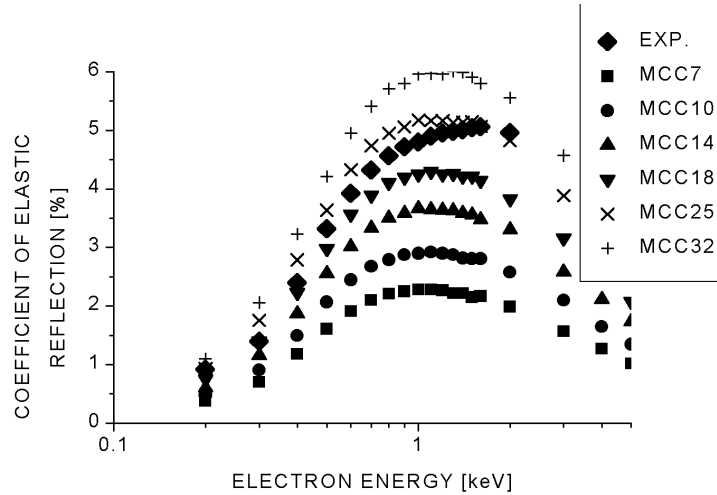


Fig. 1. Comparison of energy dependence of R_e for various W_{min} ; model EC

Firstly, using a free parameter of energy loss distribution (e.g., minimal energy loss W_{min}), λ_{in} was defined for electron reflection taking sequentially into account either only elastic scattering without energy losses (EC), or only bulk energy losses at elastic collisions (EL), or only surface energy losses (SL), or all the mentioned physical processes (AL). The calculations were performed for several defined values of W_{min} (see Fig. 1); the numerical integrals of single curves were again compared with experimental data in [6]. Secondly, we compared the position, width and height of the peaks of $R_e(E, \theta)$ of experimental data and this MC data, calculated with the values of λ_{in} that gave the best agreement for single models.

4 Results and Discussion

We obtained the optimum values of W_{min} and using (1) also the values of the inelastic mean free path λ_{in} for single models defined above (EC, EL, SL, and AL). The optimal values of W_{min} were 18, 32, 25, and 40 eV for single models, respectively. The results are shown in Figs. 1,2 and Tab. 1.

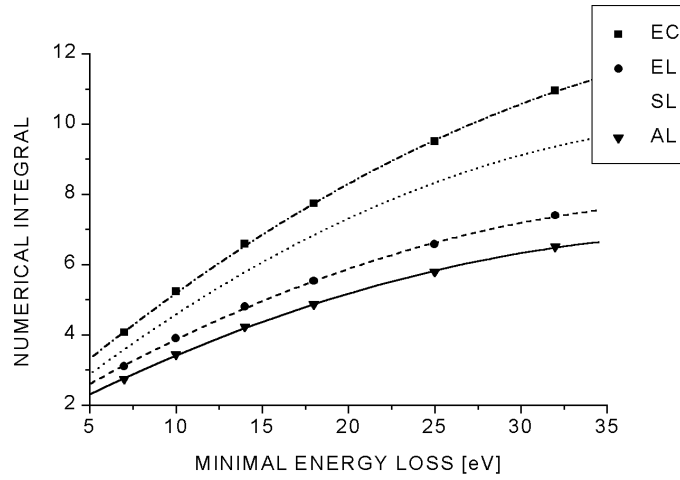


Fig. 2. The dependence of numerical integral of $R_e(E)$ on W_{min} for various models

Table 1. The values of inelastic mean free path λ_{in} for Au, calculated using a comparison of MC data and experimental data

INTER-ACTION	Elastic collisions without energy losses (EC)	Losses due to excitation of radiation (EL)	Losses due to surface plasmon generation (SL)	Losses due to both processes (AL)	Theoretical calculations from optical data [7]
ENERGY [keV]					
0.2	0.64	0.92	0.79	1.07	0.51
0.3	0.76	1.11	0.93	1.28	0.60
0.4	0.86	1.27	1.07	1.48	0.71
0.6	1.05	1.57	1.31	1.83	0.91
0.8	1.22	1.84	1.53	2.16	1.11
1.0	1.38	2.09	1.74	2.46	1.29
1.5	1.71	2.63	2.17	3.12	1.74
2.0	2.11	3.25	2.68	3.86	2.16

Next, we compared the angular distributions (to the fixed solid angle) of elastically reflected electrons for Au. The example is shown in Fig. 3.

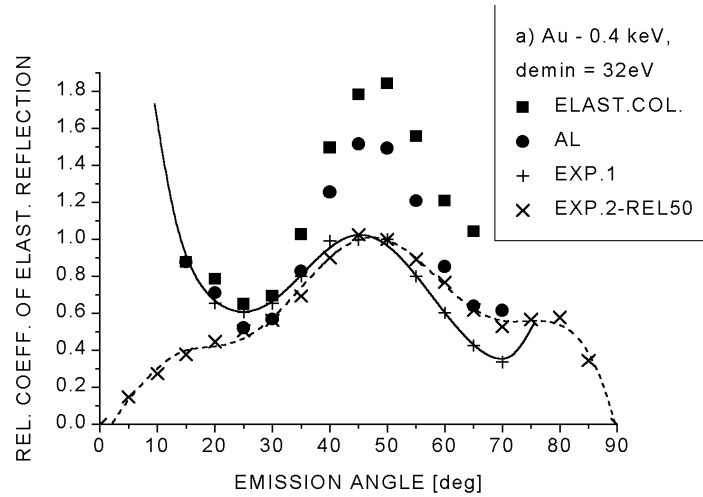


Fig. 3. The measured and MC values with ElasticCollision and AL models at energy 0.4 keV. EXP.1 are the data from [10] and EXP.2 from [11]

Taking into account not only elastic and simple inelastic collisions but also the energy losses in “elastic” collisions and energy losses in surface transfer, with the aid of these rarely used models of physical interaction of electrons in matter we achieved more reasonable agreement between the calculated and measured R_e values for Au. Although the calculated values when there is a high angle peak remain slightly higher than the measured ones, mainly for energies under 1 keV, correction of the MC code by including these models decreased the difference, in comparison with the difference in the case when no corrections were made. The best agreement appears using the AL model, i.e., including all sources of energy losses. We also found that the shape of $R_e(E, \theta)$ changes very slowly with change of W_{min} in the model.

We suppose the main reason for these relatively low discrepancies lies in the use of a very simple model of inelastic losses. The advantage of this model seems to lie in the existence of two free parameters – the minimum energy loss and the shape of the functional dependence of $d\sigma_{in}(W)/dW$. The simple model also strongly decreases the time of calculation. The disadvantage is in the fact that the process of inelastic scattering is rather oversimplified. Both the model supposition of the zero probability of inelastic collision with loss lower than W_{min} and application of the Bethe stopping power (even though with correction) are far from the exact physical solution and thus should not work properly at the very low energies of primary electrons. Because the loss function of inelastic collisions in Au is relatively complicated [12], at least the starting

part of energy loss distribution $d\sigma_{in}(W)/dW$ should be different from simple hyperbolic dependence.

Because of the reasonable agreement in the positions of the peaks (the maximum difference between DCS, MC results and measurement [10] is about 5°), it seems that the model of elastic collisions used in our MC code agrees well with physical reality, even though the position of the peaks in [11] differs slightly. It is known that the position of the reflection peaks is given by the nodes of DCS (e.g., [10]) and at this point the agreement between experiment and MC simulation is good. On the other hand, the size and width of $R_e(E, \theta)$ is affected very strongly by these values of elastic DCS. This should account for some discrepancies, because, firstly, we exceeded the recommended low limit of the PWADIR program, which was about 1 keV, and secondly, the best model would be defined preferably by comparison with experimental data. In our opinion, the slight shift and mainly the increased width can be caused by some uncertainties of the elastic scattering model.

We tried to achieve the best agreement between calculated and experimental values of the coefficient of elastic reflection $R_e(E, \theta)$. A problem can appear in the selection of suitable experimental results. Usually, several sources produce the more or less different measured data. In this case the data taken in a relatively large range of parameters should be better than data obtained at the very specific definition of experimental parameters (e.g., the values of intensities measured for an exactly defined value of the emission angle and in a relatively narrow solid angle). In our recent comparison with data measured using a retarding field analyser [9], where electrons were detected with a rather large solid angle and the dependencies $R_e(E)$ were followed, the absolute calculated and experimental values of R_e in the wide energy range were in very good agreement (see Fig. 1).

Also, the limited ranges of experimental data in [10,11], and only relative measurement of R_e complicate the sufficient accuracy of comparison. In our case, due to the limited measured angular range the first peak at $\sim 15^\circ$ and the third peak at $\sim 80^\circ$ appeared only partially; and, due to the theoretical DCS, we suppose the first peak really exists around of 15° .

It seems that the next free parameter of energy loss distribution (the degree of hyperbole) should be better specified and/or physical processes not included till now in the model should be utilized in the MC code. Nevertheless, in our opinion, the next study should better define the low energy losses and should check the more pronounced models of differential cross-section in elastic scattering.

5 Conclusions

We have developed a versatile Monte-Carlo code, which can be used for simulating interesting quantities in electron beam interaction with solids. In this work, we have tried to improve the agreement between MC calculated and experimental values of the coefficient of elastic reflection by incorporating some other physical processes (i.e., by exciting surface plasmons and energy losses in nominally “elastic” collisions), into our general code. The decrease of R_e values

due to these processes substantially improved the agreement, so we can at least partially explain the difference between experimental and MC results in a simple simulation with and without taking these processes into account. The better agreement between the MC calculated and experimental values of R_e took place at energy > 1 keV.

6 Acknowledgments

For kindly making the PWADIR program available I should like to thank Dr. F. Salvat. For analytical integration, I thank to Dr. J. Stará. For helpful discussions, Prof. R. Hrach and for English review Mr Robin Healey are gratefully acknowledged. The work was supported by GA-CR grant No. 106/97/S008 and Ministry of Education, Youth and Sport project No. 210000021.

References

1. R. Shimizu, Z.-J.: Rep. Prog. Phys. **55**, 487 (1992)
2. A. Jablonski: Phys. Rev. B **13**, 7546 (1991)
3. F. Salvat, R. Mayol: Comp. Phys. Comm. **74**, 358 (1993)
4. D. Liljequist: J. Phys. D: Appl. Phys. **11**, 839 (1978)
5. V. Starý, Brit: J. Phys D: Appl. Phys. **32**, 1811 (1999)
6. R. Schmid, H.K. Gaukler, H. Seiler: Scan. Electr. Micr. (1983), Vol. II, p. 501
7. S. Tanuma, C.J. Powell, D.R. Penn: Surf. Interf. Anal. **17**, 911 (1991)
8. D.C. Joy, S. Luo: Scanning **11**, 176 (1989)
9. V. Starý, J. Zemek: *Proc. of EMAG'99, Sheffield, August 1999*, p. 231
10. A. Jablonski, J. Zemek: Surf. Sci. **347**, 207 (1996)
11. I.M. Bronstejn, V.P. Pronin: Fizika Tverdovo Tela **17**, 2086 (1975)
12. C.M. Kwei et al.: J. Phys. D: Appl. Phys. **30**, 13 (1997) Y.F. Chen, Y.T. Chen: Phys. Rev. B **53**, 4980 (1996)
13. L.D. Landau, E.M. Lifschic: *Quantum Mechanics* (Pergamon Press, Oxford 1974), p. 337

Low-Energy Electron Response of CsI(Tl) and BGO

A. Martínez-Dávalos and J.M. López-Robles

Instituto de Física, UNAM, A.P. 20-364, 01000 D.F., México

Abstract. A Compton coincidence experiment has been implemented to measure the electron response of CsI(Tl) and BGO in the energy range 1–1000 keV. The experimental results were compared with calculations made with a Monte Carlo simulation of the system. Good agreement between the experimental and simulation results has been found.

1 Introduction

During the last decade there has been an increasing interest in the use of large scintillator arrays for charged particle detection and identification. A common problem encountered in these detectors is the non-linear response of their light output, which means that a large fraction of the beam time has to be dedicated to the calibration of each crystal in the detector array.

For this reason, a number of theoretical models describing the luminescent response of scintillators have been proposed (see [1] and references therein), but they are normally too complex to be used in routine calibration procedures, and have not proved to accurately and unambiguously describe the data over a wide range of incident charges and energies. Moreover, we have found [2] that even recently proposed analytical models fail to reproduce experimental data of ion-induced luminescence at energies near the Bragg peak.

Since the detection mechanism for both, charged and uncharged ionising radiation, relies ultimately in the process of energy deposition by low to intermediate energy electrons, it is important to understand the fundamental processes involved. In fact many of the problems of the existing models arise from the complicated nature of electron production cross sections and the simplifications used for low energy electron scattering and backscattering. However, although there has been a long standing interest in studying the electron response of scintillators [3] and the associated problems of the experimental techniques to measure these quantities, there is still a general lack of published data for the scintillator materials most commonly used nowadays.

The aims of this work have been to measure the light-output response of CsI(Tl) and BGO for low-energy electrons, and to develop accurate Monte Carlo simulations of the experimental setup to compare with our data.

2 Materials and Methods

2.1 The Experiment

The light yield non-linearity was measured by means of a Compton coincidence experiment. This technique is used to measure the nearly mono-energetic scintillator electron response by recording events only when energetic electrons are produced by gamma rays that are Compton scattered through a specific angle [3,5]. It also provides the ability to accurately determine the light yield non-proportionality of scintillation materials as a function of electron energy while minimizing the potential complicating effects of surface interactions and escape. Figure 1 shows a schematic diagram of the experimental setup; the scintillator to be studied (detector 1) is exposed to a collimated beam of mono-energetic gamma rays of known energy $h\nu$. The signals from this detector are recorded only when they are in coincidence with detector 2, which is placed at an angle θ with respect to the original incident axis.

In our experiment the energy range of interest was covered using three different γ -ray sources; ^{133}Ba was useful from 4 to 14 keV, ^{137}Cs from 30 to 342 keV and ^{60}Co from 374 to 958 keV. The scintillator crystals used were a 2.5×2.5 cm BGO cylinder and a $1 \times 1 \times 1$ cm Cs(Tl) cube. Both scintillators were coupled to Hamamatsu photomultipliers, and were used as primary and secondary detectors (see Fig. 1) in turns.

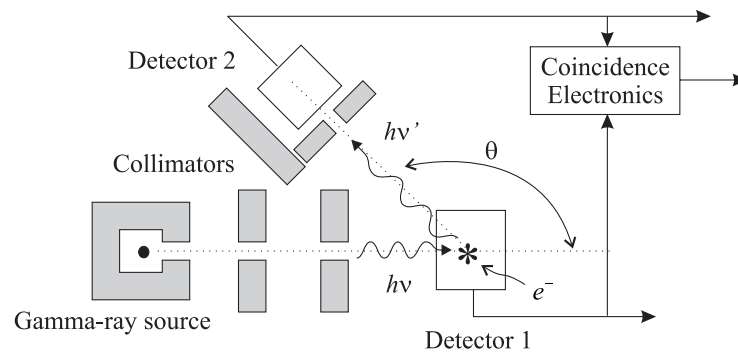


Fig. 1. Schematic diagram of the setup of the Compton coincidence experiment

2.2 Monte Carlo Simulation

We are currently using the Monte Carlo subroutine package PENELOPE [6,7] to develop our simulations. This code performs Monte Carlo radiation transport of coupled electron-photon showers in arbitrary materials, in the energy range from 1 keV to 1 GeV. It includes a geometry module that allows the programmer to describe complicated structures using simple quadratic surfaces. The structure

of the main program only provides control of the evolution of photon-electron showers, and scores the relevant physical quantities, such as particle energy, position and direction, deposited energy, kind of event (Compton, photoelectric, etc.).

The Monte Carlo code was used to optimise the geometry of the experimental setup and to calculate the light-output response of each scintillator in terms of the energy deposition process. It was validated using both published data [4] and our own experimental results. As an example, Fig. 2a shows a comparison of a measured (symbols) and calculated (line) energy spectrum of 662 keV γ -rays (^{137}Cs) obtained with a 1×1 inch cylindrical BGO crystal coupled to an R1668 Hamamatsu photomultiplier. The Monte Carlo data was convolved with an appropriate Gaussian function to reproduce the energy resolution of the detector. Figure 2b shows the coincidence spectrum for the same detector using a secondary detector placed at $\theta = 20^\circ$. It can be observed that there is very good agreement between the calculated and the measured data.

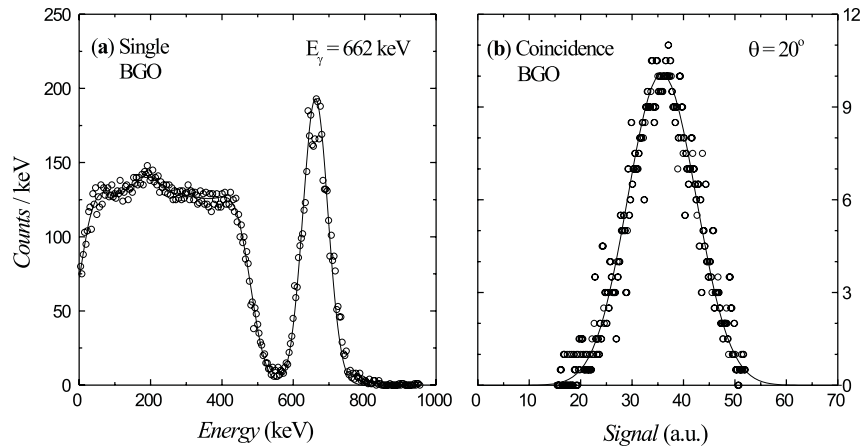


Fig. 2. Measured and calculated energy spectra of 662 keV γ -rays on BGO. (a) Single events in the primary detector. (b) Coincidence spectrum

3 Results and Analysis

Scintillation pulses from the primary scintillator were included in the analysis only if the coincidence signal had previously opened the ADC gate. This produced a coincidence spectrum similar to the one showed in Fig. 2b for each angle θ , which in turn corresponded to a fixed energy of the Compton electron E_c for a given radioactive source. The resulting experimental coincidence pulse-height

spectra were fitted with a Gaussian function using Chi-square minimization to obtain the centroids, which represent the mean light-output at energy E_c . The light-output response vs. E_c data for relatively high energies (above 500 keV) were fitted using a linear function, and the fitted straight line was used to normalize all the data.

Figures 3a–b show the result of this analysis when Cs(Tl) and BGO were used as the primary detectors, respectively. The energy axis is plotted in a log scale in order to show more clearly the effect of the non-linearities in the low-energy end of the scale. The error bars of the relative light-output correspond to $\pm 1\sigma$ deviation obtained from the Gaussian fits, and the error bars in energy were determined by the angular aperture of the collimators. It can be observed that the maximum of the non-linearity of response occurs between 10 and 20 keV in both cases.

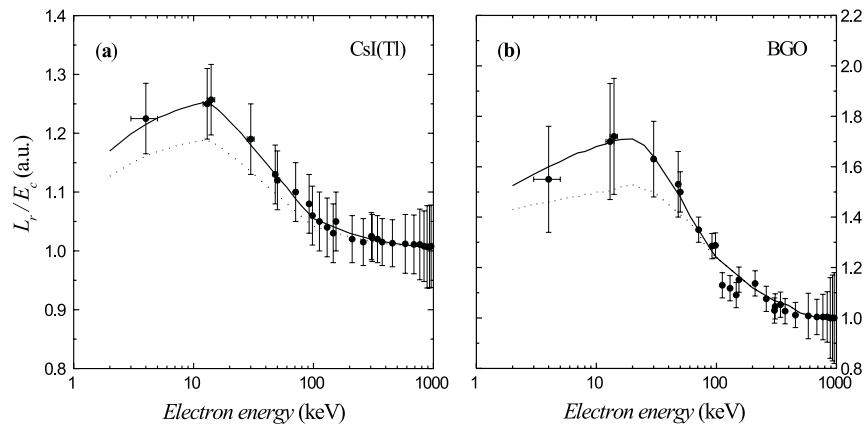


Fig. 3. Normalised light-output per unit electron energy as a function of the energy of the Compton electron. **(a)** CsI(Tl). **(b)** BGO

The lines in the same figures correspond to the results of the Monte Carlo simulation using either the default values (dotted lines) for the energy and oscillator strength of plasmon excitations, or adjusted values (continuous lines) that produced a better fit. These data were calculated using smaller energy steps, specially at energies under 100 keV, in order to obtain slightly smoother curves in the energy region where the non-linearities are bigger. Again, the results were normalised using the high-energy data as a reference, and are given in arbitrary units. It can be observed that the adjusted values reproduce very well the response function over the whole energy range.

4 Conclusions

We have measured the scintillation response of CsI(Tl) and BGO in the energy range 1–1000 keV using the Compton coincidence technique. The experimental results show a non-linear behaviour in both scintillators extending downwards from approximately 500 keV, with the maximum of the non-linearity occurring between 10 and 20 keV. A Monte Carlo simulation was developed in order to test the performance and the geometrical characteristics of the experimental setup, and to calculate the electron response function. The Monte Carlo code was validated using both published data, and our own experimental results. It was found that excellent agreement between the experimental and the calculated response functions could be obtained if suitable energy and oscillator strength of plasmon excitations for each scintillator were introduced into the calculations.

Acknowledgments

Partial support from grants DGAPA IN101599 and CONACYT 34526-E is gratefully acknowledged.

References

1. K. Michaelian, A. Menchaca-Rocha: *Phys. Rev. B* **49**, 15550 (1994)
2. A. Martínez-Dávalos, E. Belmont-Moreno, K. Michaelian, A. Menchaca-Rocha: *J. Lumin.* **72**, 769 (1997)
3. F.T. Porter, M.S. Freedman, F. Wagner, I.S. Sherman: *Nucl. Instr. and Meth.* **39**, 35 (1966)
4. J.D. Valentine, B.D. Rooney: *Nucl. Instr. and Meth. A* **353**, 37 (1994)
5. B.D. Rooney, J.D. Valentine: *IEEE Trans. Nucl. Sci.* **43**, 1271 (1996)
6. J. Baró, J. Sempau, J.M. Fernández-Varea, F. Salvat: *Nucl. Instr. and Meth. B* **100**, 31 (1995)
7. J. Sempau, E. Acosta, J. Baró, J.M. Fernández-Varea, F. Salvat: *Nucl. Instr. and Meth. B* **132**, 377 (1997)

Monte Carlo Estimate to Improve Photon Energy Spectrum Reconstruction

S. Sawchuk

University of Calgary and Tom Baker Cancer Centre, Medical Physics Department,
1331 29 St. NW, Calgary, Canada

1 Introduction

Improvements to planning radiation treatment for cancer patients and quality control of medical linear accelerators (linacs) can be achieved with the explicit knowledge of the photon energy spectrum. Monte Carlo (MC) simulations of linac treatment heads and experimental attenuation analysis are among the most popular ways of obtaining these spectra. Attenuation methods which combine measurements under narrow beam geometry and the associated calculation techniques to reconstruct the spectrum from the acquired data are very practical in a clinical setting and they can also serve to validate MC simulations. A novel reconstruction method [1] which has been modified [2] utilizes a Simpson's rule (SR) to approximate and discretize (1)

$$T = \int_{E_0}^{E_{\max}} \exp[-\mu(E)x]F(E)dE \quad (1)$$

where the variables are defined in the abstract. However, this approximation may not be accurate enough for low transmission with a fixed, but acceptable resolution of the energy spectrum. Retaining the accuracy is crucial for an accurate reconstruction. For this reason a straightforward MC estimate to the integral in (1) is used which can increase the accuracy by increasing N, the sampling size. Energy binning must be introduced in the real situation of solving for the unknown spectrum and this results in a slight loss of the accuracy gained in the straightforward (non-binning) MC. Techniques such as non-uniform energy binning and importance sampling have been tested on realistic cases where the solution is known. These techniques have been applied to a real case of an unknown spectrum and the results are compared to that of using SR.

2 Method

2.1 Reconstruction

Equation (1) is discretized in terms of E and x. The discretized equation can be written in matrix form $T_i = A_{ij}F_j$ and the unknown spectrum vector F is obtained by finding the inverse of the attenuation matrix A which is based on the exponential attenuation factor and the coefficients of the SR approximation,

i.e., $F = A^{-1}T$. The inversion process exploits the spectral vectorial algebra of matrix A and the unknown vector components of F can be obtained. The modified reconstruction process follows from (1), using the following:

$$T = \int_{E_0}^{E_{\max}} \exp[-\mu(E)x] G(E) \left[\frac{F(E)}{G(E)} \right] dE \quad (2)$$

$$T_i = \sum_{j=1}^n A'_{i,j} B_j \quad (3)$$

where the new matrix $A'_{i,j}$ now includes the factor $G(E)$ as well and the vector B has unknown components representing $F(E)/G(E)$. This mathematical trick utilizes $G(E)$ which changes nothing in the theory, but alters much in the Eigen-system of the matrix A' such that the inversion process is less subject to ill-conditioning. Simpson's rule is applied and after the inversion the vector of components $F(E)/G(E)$ are obtained. Then a simple multiplication of $G(E)$ captures the unknown energy spectrum vector $F(E)$.

2.2 Accurate Transmission

The reconstruction process deals with the inversion of the quasi-ill-conditioned matrix A . Increasing the number of components in the spectrum vector (increased resolution) would lead to further ill-conditioning. The SR approximation for low transmission values may not be sufficient to reconstruct the spectrum accurately especially in the tail section. Since we are bound to a fixed resolution, MC is used as an alternative because the resolution of the spectrum need not be increased to increase the accuracy. Instead, the number of random samples needs to be increased only since the error is $O(\frac{1}{\sqrt{N}})$. Thus, the most efficient MC scheme should be used to estimate the integral in (1). However, since our final goal is to obtain the unknown spectrum vector $F(E)$ which we treat as a vector of unknown constants, we must use energy binning. Energy binning results in a decrease in accuracy compared to non-binning MC. However, the most efficient sampling scheme for non-binning MC yields the most accurate scheme for MC with energy binning.

2.3 Analytic Transmission

A known flexible function was used to simulate a realistic 4 MV spectrum defined by (4) and (5).

$$F(E) = F_{\text{norm}} \exp[-p(E - E_0)] \sin\left[\pi \frac{E - E_0}{E_{\max} - E_0}\right] \quad (4)$$

$$F_{\text{norm}} = \frac{1}{\int_{E_0}^{E_{\max}} F(E) dE} \quad (5)$$

The parameter p may be varied to reposition the height and placement of the mode of the spectrum. In this case the attenuation coefficient is also analytic and is a linearly decreasing function of energy, viz, $\mu = 4 - E$. Replacing $F(E)$ and $\mu(E)$ in (1) yields the analytic expression:

$$T(x) = F_{\text{norm}} \exp[-\{4 - E_0\}x] (E_{\text{max}} - E_0) \frac{\pi[1 + \exp[-(p - x)(E_{\text{max}} - E_0)]]}{\pi^2 + (p - x)^2 (E_{\text{max}} - E_0)^2} \quad (6)$$

2.4 Importance Sampling

Various importance sampling methods have been used to solve the analytic case putting the function in (4) into (1). Use of non-uniform energy binning requires an intimate knowledge of the integrand or specifically the spectrum. Again, in a real situation the spectrum is unknown. Thus a technique such as importance sampling is used instead where only an approximate knowledge of the spectral shape is an aid, but not a necessity. These techniques were first applied to the non-binning MC to assess the improvement in accuracy. Then energy binning MC was used. The two most successful schemes were sampling from the following distributions:

Rectangular Distribution The rectangular distribution uses the following probability density function (pdf), cumulative distribution function (cdf), and the resulting sampling using the uniformly distributed random number $R \in (0, 1)$

$$pdf_R = \frac{1}{E_{\text{max}} - E_0} \quad (7)$$

$$cdf_R = \frac{E - E_0}{E_{\text{max}} - E_0} \quad (8)$$

$$E = E_0 - R(E_{\text{max}} - E_0) \quad (9)$$

Exponential Distribution The exponential distribution uses the following pdf, cdf and sampling:

$$pdf_{\text{exp}} = \frac{p \exp[-p\{E - E_0\}]}{1 - \exp[-p(E_{\text{max}} - E_0)]} \quad (10)$$

$$cdf_{\text{exp}} = \frac{1 - \exp[-p(E - E_0)]}{1 - \exp[-p(E_{\text{max}} - E_0)]} \quad (11)$$

$$E = E_0 - \frac{1}{p} \ln[1 - R(1 - \exp[-p(E_{\text{max}} - E_0)])] \quad (12)$$

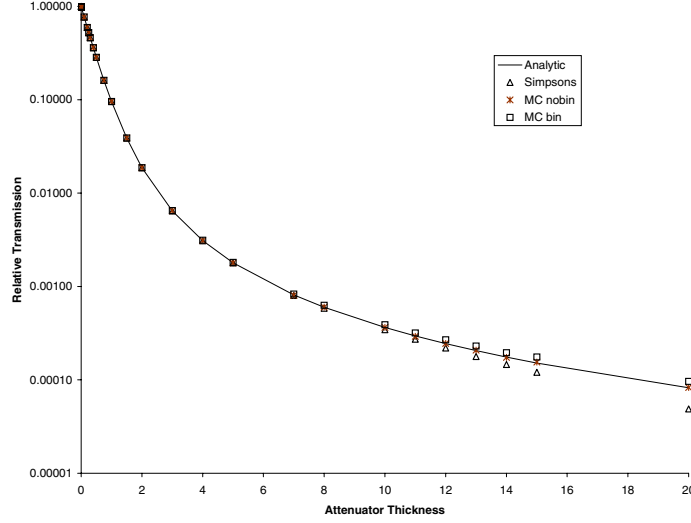


Fig. 1. Comparison of analytic semi-log transmission (Analytic) to SR (Simpsons) and to MC calculations using an exponential importance sampling distribution for the case of energy binning (MC-bin) and not binning (MC-nobin). Note $p=1$

Analysis of Analytic Case Figure 1 indicates that results agree well except for low transmission where the non energy binning MC (straightforward) is the most accurate, and the binning MC is not as accurate but better than using SR.

This is the case for both sampling methods used. The loss of accuracy when energy binning is introduced is similar for both the rectangular and exponential MC. Figure 3 shows the actual percentage differences of the transmission values for each calculation type compared with the analytic transmission. Again, the non energy binning MC is the most accurate for low transmission followed by the energy binning MC and then SR technique.

3 Real Measurement and Results

Narrow beam transmission measurements were performed using an ionization chamber with water as the attenuator in front of a 6 MV beam. The resulting smoothed transmission vector was used for the reconstruction using SR, rectangular MC sampling, and the exponential MC sampling. The MC estimates of the integral in (2) are given by:

$$T(x) = \frac{1}{N} \sum_{i=1}^N G(E) \frac{\exp[-\mu_{\text{water}}(E)x]}{\text{pdf}_R} B \quad (13)$$

$$T(x) = \frac{1}{N} \sum_{i=1}^N G(E) \frac{\exp[-\mu_{\text{water}}(E)x]}{\text{pdf}_{\text{exp}}} B \quad (14)$$

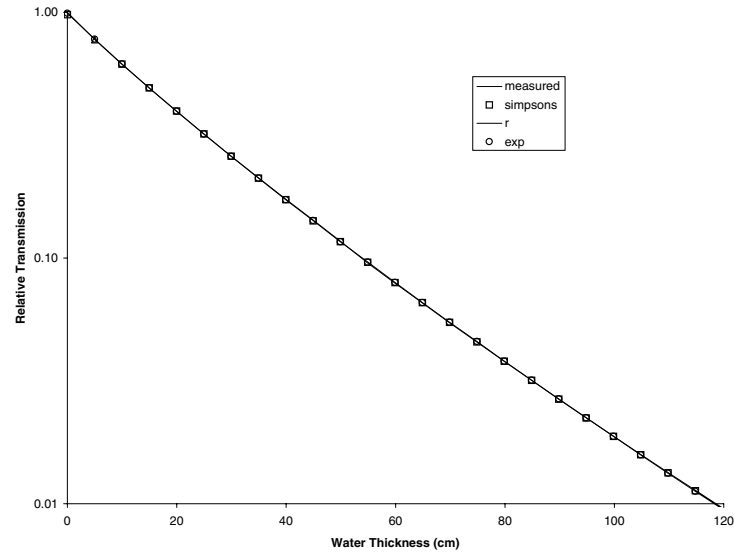


Fig. 2. Comparison of measured semi-log transmission (measured) to calculated transmission using SR (Simpsons), MC using rectangular sampling (r) and MC using exponential importance sampling (exp)

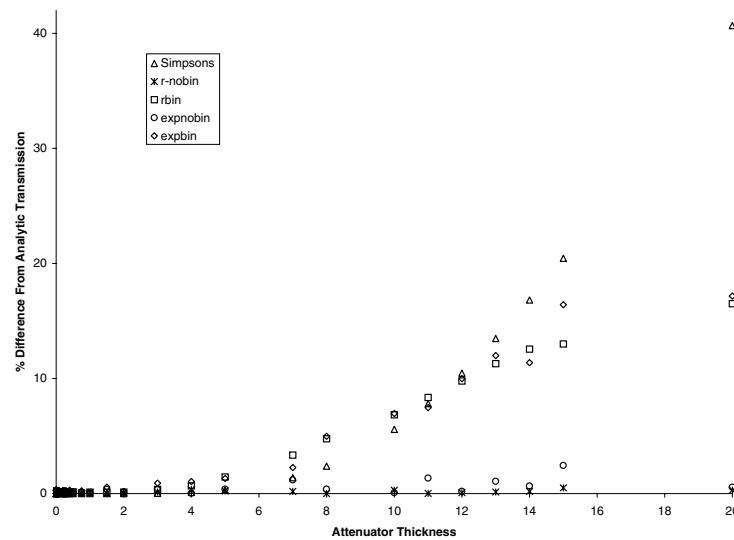


Fig. 3. Comparison of percentage differences of SR (Simpsons), and MC sampling from a rectangular distribution with energy binning (r-bin), without energy binning (r-nobin) and MC sampling from an exponential importance sampling with binning (expbin) and without (expnobin). Note $p=1$

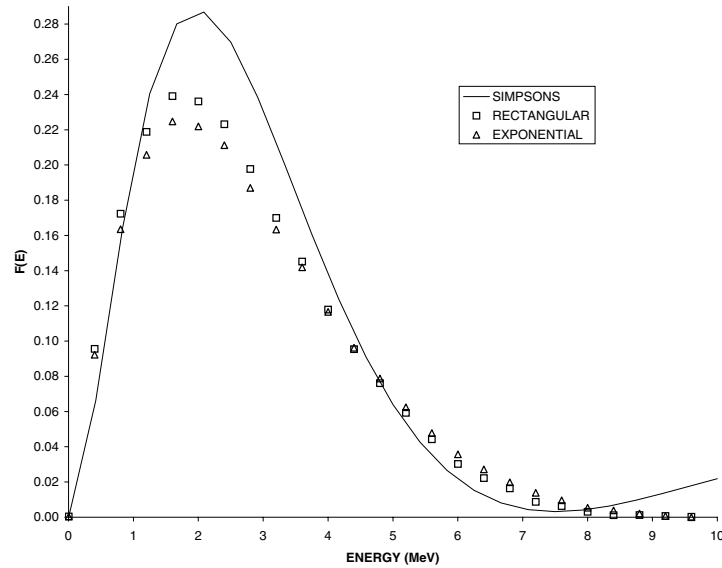


Fig. 4. Comparison of reconstructed photon energy spectra using SR (Simpsons), MC calculation using rectangular sampling (RECTANGULAR) and MC using exponential importance sampling (EXPONENTIAL)

where $G(E)=E$ and after the inversion $B=F/G$ is obtained. Note that the E is the mid-binned value of energy. Figure 2 shows that after obtaining the unknown spectrum the calculated transmission values agree very well. However, even the slightest differences especially at low transmission are related to marked differences in the reconstructed spectrum (see Fig. 4). The two MC calculation estimates agree reasonably well but are quite different from the SR approximation.

References

1. Catala, P. Francois, J. Bonnet, Ch. Scourarnec: Med. Phys. **22**, 3 (1995)
2. S. Sawchuk: *Improved Precision To Photon Energy Spectrum Reconstruction Algorithm*, Med. Phys. Aug. 1998 WIP-T43

Monte Carlo Simulations on Rough and Porous Alumina

L. Sorbier¹, E. Rosenberg¹, and C. Merlet²

¹ Institut Français du Pétrole, 1 et 4 Avenue de Bois Préau 92852 Rueil Malmaison Cedex, France

² ISTEEM, CNRS, Université de Montpellier II, Sciences et Techniques du Languedoc, Place E. Bataillon 34095 Montpellier Cedex 5, France

1 Introduction

Heterogeneous catalysts are of primary importance for many industrial processes. Catalysts are frequently obtained by including small amounts of active species on a porous carrier having a very high specific surface. For design and optimization purposes, electron probe micro analysis (EPMA) is routinely used in our laboratory. With EPMA, the sample is irradiated by a monoenergetic keV electron beam. X-ray Bremsstrahlung and characteristic photons are then selected by either an energy dispersive spectrometer (EDS) or a wavelength dispersive spectrometer (WDS). The characteristic line intensity (of relaxation of inner-shell ionisation photons) of the unknown sample is measured as well as the intensity of this same line emerging from a standard of a well known composition. Correction procedures are applied to achieve a quantification of the elements. Yet when traditional EPMA correction procedures are processed for our porous alumina samples, unrealistically low total composition are observed. The alumina porous samples (porosity $\approx 68\%$, specific surface $\approx 250\text{ m}^2/\text{g}$, pore size $\approx 10\text{ nm}$) emit about 10% less photons on Al K_α line than a massive sample of same composition.

Monte Carlo simulations [1] have shown that for a nanometric pore size, the porosity of the sample is not directly responsible for the observed signal loss. Some authors have suggested charge trapping effects [2] as a possible explanation since the porous samples are also insulating. Simulation work including charges trapping [3] has been adapted to our material but the simulated intensities do not agree with experimental data. The aim of this work is to study the influence of the roughness of samples and energy loss at interfaces through surface plasmon excitation on emerging X-ray signal.

2 Numerical Methods

A program using the PENELOPE [4] package has been written to simulate photon emission from rough and porous samples. The characteristic X-ray photons emission is simulated with the optical data model cross section proposed by R. Mayol et al. [5].

2.1 The PENELOPE Package

The PENELOPE version used in this work uses elastic cross section from partial wave analysis [6] and a generalized oscillator strength model for inelastic collision. For Bremsstrahlung, the photon energy is sampled from a Bethe-Heitler cross section modified by an empirical correction at low energy. The direction of emission is sampled from the Kirkpatrick-Wiedmann-Statham distribution [7]. Although PENELOPE uses a mixed algorithm to simulate electron transport, the algorithm has been forced to work with fully detailed elastic interaction. Full detailed interactions are requested to describe accurately interface crossing which should play an important role for rough and porous samples.

2.2 Forcing Photon Emission

Since Bremsstrahlung and characteristic photon emission probabilities are very low, interaction forcing is applied. Photon emission probability is increased by a factor F and the photon and all its secondary particles (if any) are affected the weight $W = 1/F$. X-ray line emission probability is multiplied by a constant factor F whereas Bremsstrahlung production mean free path is forced to a fixed value λ_f far smaller than the physical one λ_0 , giving a factor F equal to λ_0/λ_f . In the same manner, because of the very small solid angle of EDS and WDS spectrometers, and the dependence of X-ray intensities on emerging angle, the photon emission is partially forced in the solid angle $\Delta\Omega$ at the take-off angle of the experimental detector. Only a fraction $(1 - \alpha)$ of photons is forced in this direction, the fraction α being used to allow secondary processes in the depth of the sample. The weight of the photon is corrected, i.e. multiplied by $W_{\Delta\Omega}(\theta)$ if emitted in $\Delta\Omega$ and else by $W_{(4\pi-\Delta\Omega)}(\theta)$. The weights are calculated to preserve probability of emission.

$$\begin{aligned} W_{\Delta\Omega} &= \frac{\Delta\Omega}{(1 - \alpha)} Q_p(\theta) , \\ W_{(4\pi-\Delta\Omega)} &= \frac{4\pi - \Delta\Omega}{\alpha} Q_p(\theta) . \end{aligned} \quad (1)$$

where $Q_p(\theta)$ is the probability to emit a photon in the direction having an angle θ with the direction of primary electron. This probability depends only on θ since we assume spherically symmetric diffusion centers. Then the main steps of the algorithm are:

- Choose emission in $\Delta\Omega$ with probability $(1 - \alpha)$ or emission in $(4\pi - \Delta\Omega)$ with probability α .
- Sample isotropically the direction of emission within the chosen angle.
- Compute angle θ between initial direction of primary electron and sampled direction. If (u_p, v_p, w_p) are direction cosines of the electron and (u_s, v_s, w_s) the direction cosines of the sampled direction, we have $\cos(\theta) = u_p u_s + v_p v_s + w_p w_s$.
- Correct the weight of the photon.

2.3 Handling the Geometry

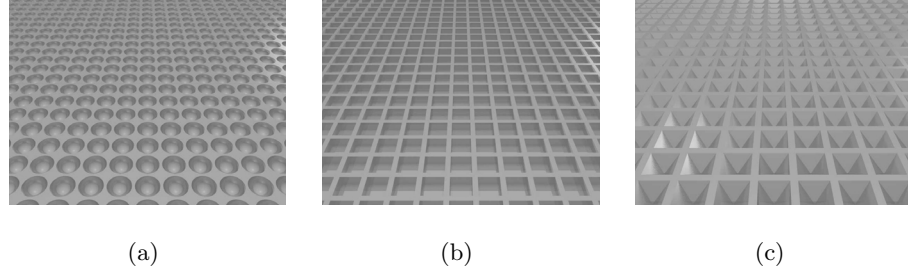


Fig. 1. Different models of rough samples: (a) cubic lattice of cubic voids, (b) cubic lattice of spherical voids, (c) cubic lattice of pyramidal voids

The geometry of the sample (rough surface, porous sample) is described by the porosity models developed for a previous work [1] based on cubic body centered lattice of voids of very simple shapes (spheres, cubes and pyramids). These models have been adapted to generate easily a rough surface as shown in Fig. 1. For the following simulations, the size of voids (sphere radius, cube side, pyramid side) is calculated to obtain a 30% porosity. Specific energy loss at interfaces is taken into account by assuming that a mean energy loss ΔE occurs for each interface crossing. This mean energy loss ΔE can be related with the probability P_s to excite a surface plasmon and the energy of the surface plasmon E_s as defined by Egerton [8] ($\Delta E = P_s \times E_s$). Typical values for alumina are $P_s \approx 0.066$ and $E_s \approx 13$ eV which lead to an expected value of $\Delta E \approx 0.9$ eV.

3 Simulation Results

Table 1. Simulation parameters

α	$\Delta\Omega$	Take-Off Angle	Number of Trajectory	Electron Beam Energy	Sample Composition	Simulated X-ray Line
0.1	10^{-3} sr.	40°	10^6	20 keV	Al_2O_3	$Al K_\alpha$

All results presented here have been obtained for a defocused beam of $100\ \mu\text{m}$ diameter impinging normally on the sample. The other parameters are specified in Tab. 1. The error bars (often smaller than the symbols) represent the 3σ confidence level.

3.1 Influence of Roughness

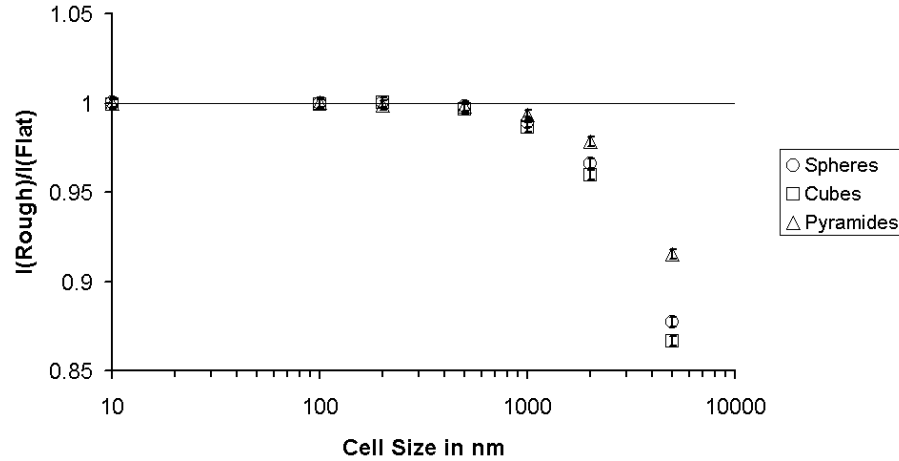


Fig. 2. Effect of roughness, cell size dependence

Simulated X-ray intensities emerging from a rough and a flat sample are compared in Fig. 2 by forming the ratio I_{Sample}/I_{Flat} . This figure shows that the signal loss and the influence of the exact geometry of the roughness become significant when the roughness size reaches the micrometer scale. Atomic Force Microscope measurements have shown that the maximum height difference in surface topography of the alumina sample is about 140 nm, thus not large enough to imply a signal loss.

The Peak-to-Background ratio correction procedure [9] has been proposed to correct the effect of roughness. It uses the ratio between the intensity of a characteristic line with the background at the same energy. The Fig. 3 shows that the Peak-to-Background method applied on simulated data provides a good correction for sample roughness effects up to the micron scale. Experimental Peak-to-Background ratio is however lower for porous alumina than for a massive alumina. This confirms that sample roughness cannot explain our experimental results.

3.2 Influence of Energy Loss at Interfaces

Here, the porous samples are compared with full massive sample. The ratio between the simulated intensities emerging from a full massive sample and a porous sample is plotted in Fig. 4. As expected, the signal loss is increasing with increasing the mean energy loss at interface crossing. The results can be approximated with great accuracy by a linear fit. Discrepancies between the different models, only visible for high $\overline{\Delta E}$, are directly correlated with the number of crossed interfaces (334 ± 1 for spheres 390 ± 1 for cubes and 413 ± 1 for pyramides,

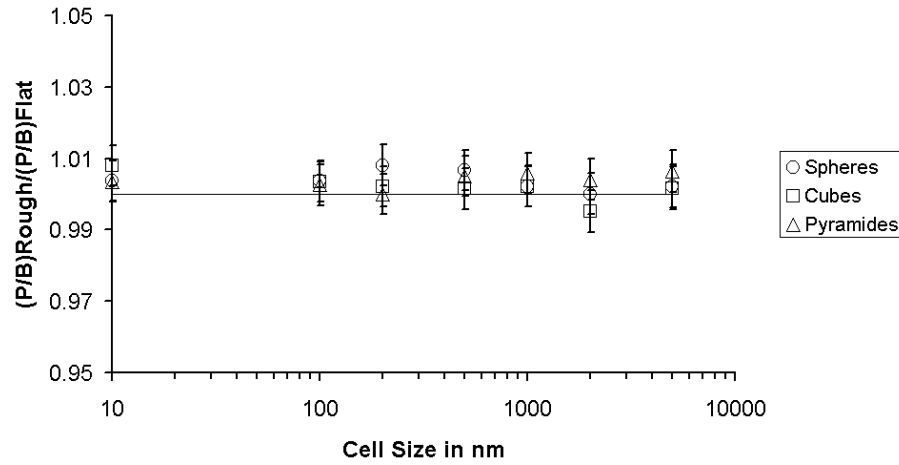


Fig. 3. Cell size dependence of Peak-to-Background ratio

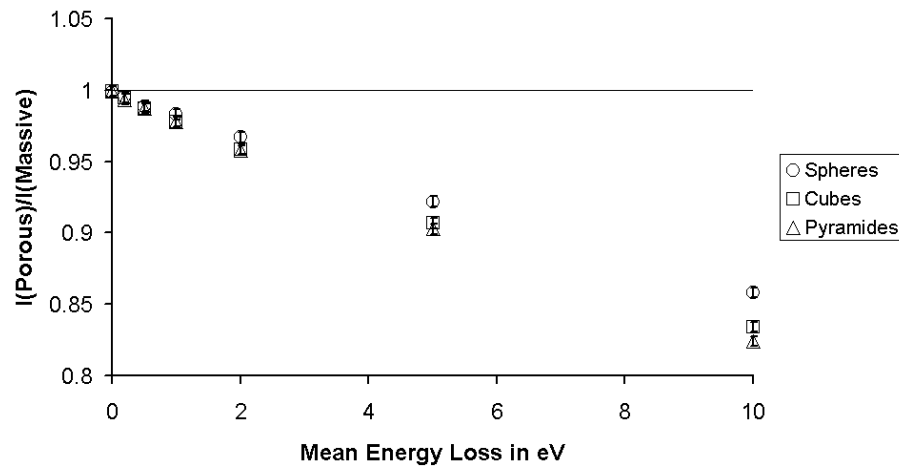


Fig. 4. Mean energy loss dependence for 10 nm cell size

at $\overline{\Delta E} = 10 \text{ eV}$ and 30% porosity). A simulation obtained for a porosity closer to the alumina sample (70% porosity, only possible for the cubic void model) show for $\overline{\Delta E} = 1 \text{ eV}$ a signal loss equal to $7.5\% \pm 0.3\%$. For a calculated mean energy loss at interfaces of 1 eV, these simulations show that the influence of surface plasmon is not negligible for 30% porosity alumina and sensitive for 70% porosity, more representative of experimental samples.

4 Conclusion

Simulations of electron trajectories in rough alumina show that Al K $_{\alpha}$ signal loss at 20 keV is not expected for roughness less than 1 μm and that, even in this case, a Peak-to-Background method would successfully correct it. Simulation on porous alumina show that specific electron energy loss at interfaces by surface plasmon excitation may generate a significant signal loss on Al K $_{\alpha}$ line. The order of magnitude of the signal loss is important and justify further investigations on surface plasmons for quantification purposes of nanoporous alumina in EPMA.

5 Acknowledgements

The authors would like to thank F. Salvat and X. Llovet for fruitful discussions.

References

1. L. Sorbier, E. Rosenberg, C. Merlet, X. Llovet: *Mikrochimica Acta* **132**, 189 (2000)
2. J. Cazaux: *X-ray Spectrometry* **25**, 265 (1996)
3. O. Jbara, B. Portron, D. Mouze, J. Cazaux: *X-ray Spectrometry* **26**, 291 (1997)
4. J. Baró, J. Sempau, J.M. Fernández-Varea, F. Salvat: *Nuclear Instruments and Methods B* **100**, 31 (1995)
5. R. Mayol, F. Salvat: *Journal of Physics B* **23**, 2117 (1990)
6. E. Benedito, J.M. Fernández-Varea, F. Salvat: *Radiation Physics Group Internal Report No. UBRGP-1998-02* (1999)
7. E. Acosta, X. Llovet, E. Coleoni, J.A. Riveros, F. Salvat: *Journal of Applied Physics* **83**, 6038 (1998)
8. R.F. Egerton: *Electron Energy Loss Spectroscopy in the Electron Microscope* (Plenum Press, New York 1986)
9. S.A. Abo-Namous: 'On the Peak-to-Background ratio in microprobe analysis of porous materials'. In: *Microbeam Analysis*. ed. by P. E. Russel (San Francisco Press, San Francisco 1989) pp. 239–241
10. R.E. Lakis, C.E. Lyman, J.I. Goldstein: 'Electron probe microanalysis of porous materials'. In: *50th Annual Meeting of the Electron Microscopy Society of America, 1992*. ed. by G. W. Bailey, J. Bentley, J. A. Small (San Francisco Press, San Francisco 1992) pp. 1660–1661
11. V.V. Tretyakov, S.G. Romanov, A.V. Fokin, V.I. Alperovich: *Mikrochimica Acta [Suppl.]* **15**, 211 (1998)

Simulation of the Response Function of an Amorphous Silicon Flat-Panel Array

F. Cremers, C. Kausch, D. Albers, M. Todorovic, and R. Schmidt

Dept. of Radiotherapy and Radiooncology / Clinic of Radiology, University Hospital
Eppendorf, Martinistr. 52, 20246 Hamburg, Germany

1 Introduction

Electronic portal imaging devices (EPIDs) in radiotherapy are mainly used to verify patients' alignment. It is necessary to ensure that a high dose is delivered to the tumor while the healthy tissue is spared. Most of these EPIDs consist of a metal plate/phosphor screen combination which transforms some of the MeV x-rays into optical light. In a fluoroscopic system the generated optical photons are reflected by a mirror and read out with a CCD-camera.

Portal images have a very poor image quality. There are several reasons: The contrast of images between bone and tissue is very low in the MeV-range. Since only a small fraction of x-rays interacts with the metal plate/phosphor screen and interacting x-rays deposit differing amounts of energy portal images are very noisy. In addition, in a fluoroscopic device many optical photons created in the phosphor are lost due to the optical chain. To improve image quality one came up with different imaging devices. Devices with improved image quality are flat-panel imagers since the phosphor is bonded directly to a flat-panel light sensor consisting of photodiodes. Image quality of these devices were studied by different groups (see [1,2]).

In addition to verifying field shape and position, another very interesting application is to use these devices for patient dose verification. 3-D compensation devices used in conformal radiotherapy will make it necessary to verify dose to ensure that the compensators are mounted correctly. EPIDs offer digital images ready for dose evaluation. Images produced by electronic portal imaging devices cannot be converted directly to portal dose images (PDI) since these devices are energy dependent. To do dosimetry the knowledge of the energy dependency of the EPID is of special interest. Adopting a two step Monte Carlo simulation which was previously used to determine the detective quantum efficiency (*DQE*) of different metal plate/phosphor screen combinations [3] the energy dependency of a flat-panel imager based on amorphous silicon will be determined.

2 Materials and Methods

2.1 The Amorphous Silicon Flat-Panel Array (ADAS)

The amorphous Si-detector, which will be modeled is a prototype manufactured by Wellhöfer Dosimetrie, Schwarzenbruck, Germany. ADAS is the short form of

Acquiring Device of Amorphous Silicon and will be used throughout this paper. The device is 8 mm thick and consists of 134 mg/cm² Gd₂O₂S (Kodak Lanex fast back), an amorphous silicon flat-panel light sensor, both embedded in polyethylene (3 mm on top and 4 mm at the bottom) and associated readout electronics. The phosphor screen is made of small phosphor grains mixed with a polymer and pressed. The flat-panel light sensor consists of 128×128 elements with a pixel pitch of 0.75 mm and hence forming a sensitive field of 9.6 cm². Impinging high-energy x-rays produce electrons in the polyethylene and the phosphor layer which will be partially converted into optical photons in the phosphor. The optical photons will be read out by photodiodes.

2.2 The Simulation of the ADAS

EGS4 Monte Carlo Calculation The interaction of x-rays in the MeV energy range with the polyethylene plate/phosphor screen was simulated using the electron gamma shower code (EGS4) [4]. The simulations presented here have been performed with the DOSXYZ code for calculating dose distributions in a rectilinear voxel phantom. It is part of the OMEGA-BEAM system of codes developed at the National Research Council Canada NRCC. This user code includes the parameter reduced step transport algorithm (PRESTA). The geometry is a rectilinear volume consisting of voxels of variable dimensions. A rectangular parallel beam (1×1 mm²) is incident at the center of the x-y surface. The minimum total energy of photons and electrons which are transported were set to PCUT= 10 keV (photons) and ECUT= 521 keV (electrons). With the Monte Carlo code the history of each individual MeV x-ray was tracked and the energy which was deposited in the phosphor by electrons and positrons was calculated and summed.

Optical Transport The energy which was deposited in the phosphor was partially converted into optical light. Since EGS4 can only calculate the transport of particles down to 1 keV the optical transport in the phosphor is modeled by a self-written code based on an algorithm by Radcliffe et al. [5]. Values considering absorption length, scattering length and reflection were adopted from this work. The conversion efficiency of the deposited energy into optical photons is 0.16 and the average energy of optical photons amounts to 2.2 eV [6]. The optical photons are scattered at the boundaries between the plastic binder and the phosphor grains. At the front surface they are scattered back into the phosphor or exit the phosphor hence contributing to the signal. Optical photons hitting the metal plate are either absorbed or backscattered into the phosphor. In addition optical photons can be reabsorbed. A detailed description of the code can be found in [3].

The phosphor was subdivided into layers with a thickness of 100 μm. In the center of each layer 300000 optical photons were generated (Fig. 1). Taking the above described scattering and absorption events into account number and position of the optical photons exiting the front surface of the phosphor are calculated. The collection of the optical photons dependent on the position results

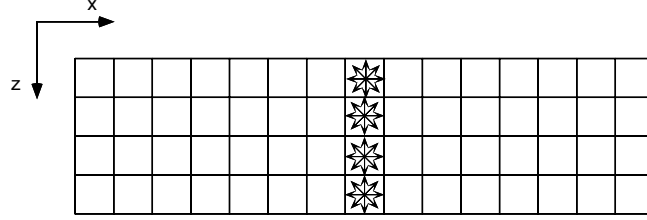


Fig. 1. For the simulation of the optical transport the phosphor screen is subdivided into layers 0.1 mm thick. In the middle of each layer 300000 optical photons are generated and then transported. Collecting the optical photons exiting the front layer leads to a line spread function of each layer

in a line spread function $LSF_z(x)$ of each phosphor layer z . x is the x-coordinate of the exit point of an optical photon at the front surface of the phosphor.

The convolution of the optical line spread function $LSF_z(x)$ with the energy deposition $E_i(x, z)$ in the phosphor calculated in step 1 yields the optical distribution function $g_i(x)$ of each deposited x-ray photon i :

$$g_i(x) = \sum_z LSF_z(x) * E_i(x, z) = \sum_{x'z} LSF_z(x - x') \cdot E_i(x', z). \quad (1)$$

The optical quanta exiting the voxels are gathered according to the pixel size of the detector. To determine the response function for each energy all photons escaping from the phosphor were integrated over all pixels.

3 Results

3.1 The Energy Deposition in the Phosphor

The deposition of energy in the phosphor is dependent on the energy of the impinging photons and on the depth in the phosphor (Fig. 2).

At high energies ($E > 4$ MeV) the energy deposition is increasing with depth along the central axis. Between $E = 4$ MeV and $E = 1$ MeV the deposition first ascends and then descends again. At low energies ($E < 1$ MeV) the deposition decreases. This is due to the small range of electron in the polyethylene (PE) and the phosphor. At $E = 1$ MeV the range of electrons in PE is 4.4 mm, so that a depth dose maximum is reached in the beginning of the phosphor and falls then with increasing depth. Since the energy dependence varies with depth the optical transport must be considered. In addition the fraction of optical photons escaping the phosphor is strongly dependent on the starting position of the photons in the screen. Considering a phosphor layer of 1 mm thickness 70 % of the optical photons starting in the bottom layer escape the phosphor while only 4.5 % of the optical photons starting in the top can escape the phosphor [3].

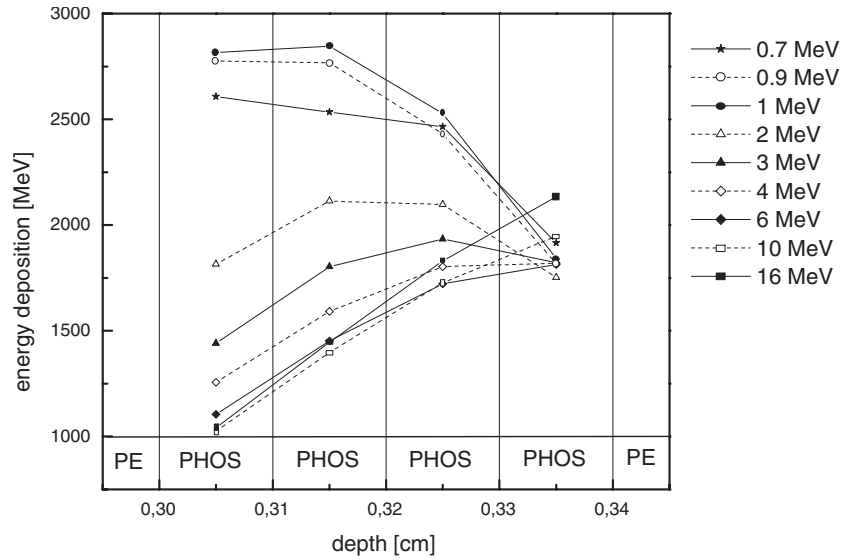


Fig. 2. Energy deposition in the voxels around the central beam depending on the phosphor layer. PHOS denotes the $\text{Gd}_2\text{O}_2\text{S}$ -layer, PE is the surrounding polyethylene. To distinguish between different energies the deposition values for each energy are connected by straight lines. At high energies ($E > 2$ MeV) the energy deposition is increasing with depth, at low energies ($E < 2$ MeV) the deposition is decreasing with depth

3.2 The Response Function

The response of the ADAS-detector is depicted in Fig. 3. The number of optical photons escaping the phosphor versus the energy of incident x-ray photons is plotted. At low energies the number of escaping photons per incoming high energy x-ray photon is relatively high, which is due to the high photon cross section in this energy range. Going to higher energies the response of the detector decreases. The small increase between 0.7 MeV and 2 MeV is probably due to Compton scattering. At high energies the response increases slightly again which is caused by pair production events.

4 Forthcoming Work

Using a deconvolution method the response of the amorphous silicon array is supposed to be determined experimentally from transmission data.

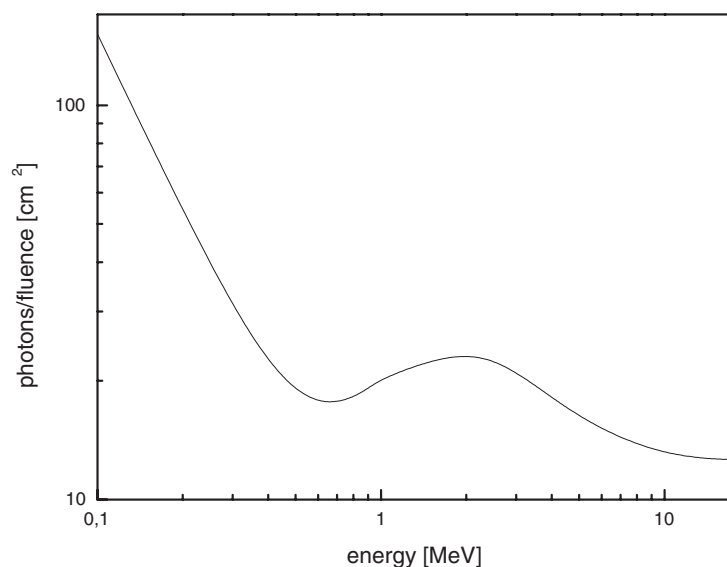


Fig. 3. The response of the ADAS-detector depending on the energy

References

1. P. Munro, D.C. Bouius: Med. Phys. **25**, 689 (1998)
2. F. Cremers, C. Kausch, D. Albers, T. Frenzel, and R. Schmidt: Accepted by Med. Phys. (2000)
3. C. Kausch, B. Schreiber, F. Kreuder, R. Schmidt, O. Dössel: Med. Phys. **26**, 10 (1999)
4. W.R. Nelson, H. Hirayama, D.W.O. Rogers: SLAC-Report 265, Stanford University (1985)
5. T. Radcliffe, G. Barnea, B. Wowk, R. Rajapakshe, S. Shalev: Med. Phys. **20**, 4 (1993)
6. J.P. Bissonnette, I.A. Cunningham, D.A. Jaffray, A. Fenster, P. Munro: Med. Phys. **24**, 815 (1997)

Space Applications of the Geant4 Simulation Toolkit

E. Daly¹, H. Evans¹, F. Lei², F. Longo³, S. Magni⁴, R. Nartallo¹,
P. Nieminen¹, M.G. Pia⁵, and P.R. Truscott²

¹ ESA/ESTEC, The Netherlands

² DERA, The United Kingdom

³ University and INFN Ferrara, Italy

⁴ INFN Milan, Italy

⁵ INFN Genova, Italy, and CERN, Switzerland

Abstract. The space radiation environment is highly variable and dynamic. With the increasing number and complexity of space missions, the detailed analysis of the effects of that environment often requires the use of advanced Monte Carlo radiation transport tools. In this presentation, various space-oriented developments and applications based on the Geant4 particle transport toolkit are described.

1 Introduction

There are various undesirable effects the space radiation environment can induce in spacecraft and their instrumentation. These include total dose effects and single event effects phenomena in electronic components, material degradation, and biological effects in astronauts. On the other hand, for a variety of scientific missions the radiation “background” in sensitive detectors, in addition to the actual signal to be measured, is an important factor to be. With the increasing number of complex space missions and their instrumentation, the detailed and accurate analysis of the space radiation effects increasingly requires the use of Monte Carlo radiation transport tools.

Geant4 [1] is a new-generation, Object-Oriented particle transport toolkit that allows full and fast 3D simulation in a user-defined geometry. Due to its versatility, the toolkit has found use in various diverse fields, including high-energy physics, medical and biological applications [2], and nuclear physics. The wide selection of physics processes and the modular, Object-Oriented implementation of Geant4 also make it an ideal platform for space applications, including cosmic ray and astrophysics.

In this presentation, we summarize a number of space applications and developments utilizing Geant4. A number of future activities are also presented.

2 Simulation of Radiation Effects on X-ray Telescopes

It has been found that protons of energies in the range of hundreds of keV to a few MeV can scatter at low angles through the mirror shells of space-based X-ray

astronomy missions. These protons, because of their low energy can produce a high non-ionising dose in unshielded CCDs and are therefore a potential threat. This is the most likely cause of the degradation in the charge transfer efficiency reported to have occurred in the CCDs of the ACIS instrument on NASA's Chandra X-ray observatory [3].

An extensive analysis of this process both on Chandra and on ESA's XMM-Newton observatory was carried out utilising Geant4 [4]. The mirror systems of both spacecraft were modelled in 3D, with some supporting analysis of the scattering off the mirror surface performed in 2D. The Geant4 model of XMM mirrors, consisting of more than 1000 individual elements, is shown in Fig. 1. From the right, this shows three baffles, the set of nested mirror shells and the reflection gratings. It was not necessary to model the spacecraft telescope tube that closes the optical axis between the gratings and the detectors 7 m away. The source of the incident protons was placed just outside the telescope baffle structure, covering it in its entirety. The energy range of incident protons simulated was from 100 keV to 1.5 MeV. Protons reaching the focal plane at the other end of the telescope, where the two separate XMM detectors EPIC and RGS reside, were registered.

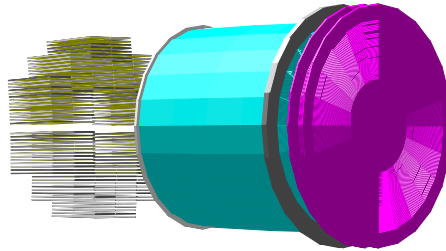


Fig. 1. XMM geometric model used in Geant4 simulations

Based on this analysis, it was concluded that as long as protective measures (i.e. detector shield closure) are adopted to protect the XMM EPIC instrument during passages through the Earth's radiation belts, no damage is expected to occur to its CCDs. The CCDs on the RGS instruments, for which no protective measures can be taken, are on the other hand not expected to be significantly affected by radiation damage. The analysis has shown, however, that low-energy protons both in the radiation belts and in the interplanetary medium need to be taken into account in the design and simulations of future in-orbit X-ray observatories.

3 Simulations of Gamma Ray Space Missions

The gamma ray missions GLAST [5] and AGILE [6] are sensitive in analogous energy bands, between 30 MeV and around 100 GeV. The main physics process

involved is gamma conversion. These instruments are essentially made of certain converter material and a number of tracking detectors, in particular, in these two missions, consisting of similar Si detectors. In this energy range it is essential to establish the contribution from the cosmic ray flux and that from the 'real' astronomical gamma ray fluxes, which are several orders of magnitude lower than the former one.

Several attempts are being performed to evaluate this background, with the current activity concentrating on building small prototypes of the two instruments in Geant4 (see Fig. 2), using both the Low-Energy extension of Geant4 [7] and the General Source Particle Module developed by ESA [8] (see below). The usefulness of Geant4 for AGILE detector is motivated also by the presence on board of AGILE of an X-ray instrument, sensitive in a totally different energy band between 10 and 40 keV, where the Low-Energy extension could be particularly interesting.

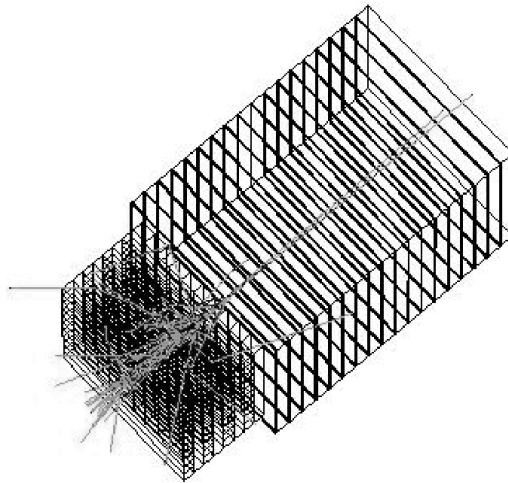


Fig. 2. Geant4 model of the basic tracker and calorimeter structures of GLAST mission

4 Mineralogical X-ray Surveys of Asteroids and Moons

Most solid bodies in the solar system do not contain a substantial atmosphere. Thus they are effectively exposed to the ambient space radiation environment. This consists to a large degree of electromagnetic radiation (particularly X-rays and UV) from the Sun, but also include charged solar particles, Jovian electrons and cosmic rays originating from outside the Solar System. These radiations interact with the surface materials of the target body, the reflection and emission spectra being characteristic of the composition of the surface.

By observing the Sun at soft X-ray wavelengths (~ 0.1 -10 keV) and simultaneously the X-ray spectra from the illuminated body it is possible to determine the surface geology of the body. There is currently activity in the ESA Space Science Department to develop a standard X-ray survey instrument for mapping this way most of the bodies of the Solar System that retain no atmosphere on future ESA Solar System missions. Such hardware needs to be combined with a solid predictive capability for the expected emission spectra from the various target bodies.

Geant4 low-energy electromagnetic physics extensions down to 250 eV allow for such a capability. Example simulations for a representative composition of basalt [9] have been performed for a range of solar conditions. The results of this analysis for a major X-ray flare spectrum are shown in Fig. 3. Although the input data of the spectrum is limited above 1 keV, it can be seen that the major K-shell emissions are clearly visible in the simulation. Further Geant4 simulation work with other spectra and charged particles is foreseen in the near future.

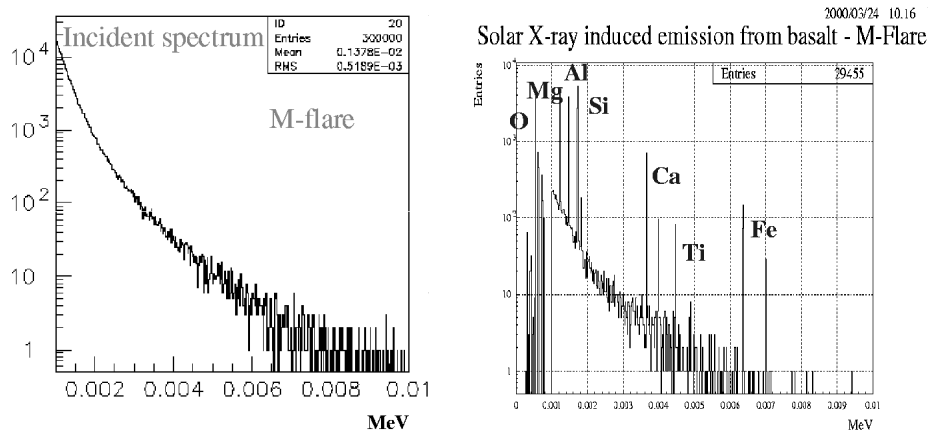


Fig. 3. Left: modelled major solar flare X-ray spectrum. Right: simulated response from a representative composition of basalt

5 Space-Specific Modules in Geant4

As a member of the world-wide Geant4 Collaboration, ESA has sponsored [8] the development of a number of space-specific software modules in Geant4, tailored to the demands of the European space radiation community. The main features of these modules are briefly summarized below.

5.1 Low-Energy Electromagnetic Processes Extension

The low-energy cutoff of electromagnetic physics in the earlier Geant3 code was 10 keV, and many other electron-photon transport codes have their cutoff at 1

keV. In Geant4 this lower limit has been extended to allow the physical processes of electrons and photons to be modelled as low as 250 eV. This feature enables studies of the characteristic X-ray line emissions down to Carbon, and has been applied e.g. in the simulation work for geological surveys of asteroids and moons (see above). Wide use in medical, biological and fundamental physics applications have also been found, and low-energy extensions with protons, ions and antiprotons have also been completed [2,7,10].

5.2 Sector Shielding Analysis Tool (SSAT)

This tool performs a ray-tracing analysis of a user-defined geometrical configuration to yield the distribution of shielding material and thickness as viewed from a given point within the configuration. The fictitious *geantino* particle is used for the purpose. This approach is highly useful for calculating the absorbed radiation dose and for finding optimal shielding geometries.

5.3 Front-End for CAD Software

This module uses the STEP AP-203 protocol to provide an interface to standard computer-aided design tools which facilitates the transfer of instrument engineering designs to Geant4 simulations and vice versa. In addition to geometrical data, materials information may also be included.

5.4 General Source Particle Module (GSPM)

This module allows the user to apply various simulation scenarios assuming unidirectional or omnidirectional incidence of particles with a defined energy spectrum instead of a monoenergetic source. This gives a more realistic analysis of the effects of the radiation environment encountered in many space applications.

5.5 Radioactive Decay Module (RDM)

Traditionally, Monte Carlo transport codes only consider the prompt component of an atomic or nuclear reaction. This module introduces a delayed component, which can be a significant contributor to undesirable instrument background radiation experienced in certain types of mission (e.g. gamma ray observatories, such as ESA's INTEGRAL), particularly during and after passage through the radiation belts. The decay branching ratios are based on data from the Evaluated Nuclear Structure Data File (ENSDF). Decays can be performed over multiple nuclide generations. The RDM includes biasing techniques to increase the sampling of events within the user-chosen observations times. Furthermore, other variance reduction techniques such as splitting are included to increase the sampling of the nuclear decay scheme.

6 Discussion and Future Developments

Geant4 has proven to be a powerful tool for modelling the interactions between spacecraft and their radiation environments. A number of future developments utilizing Geant4 capabilities are currently planned. An activity will be started at ESA later this year to implement further space-specific software modules in Geant4, with the emphasis on electronic components and circuits. In 2001, a project will be started to transfer the old Geant 3.21 simulation models of the ESA Standard Radiation Environment Monitor (SREM) [11] to Geant4. A Phase-A study on the ESA Charged Particle Telescope (CPT) has also addressed simulation requirements, and concluded that Geant4 is the preferred tool for design and optimisation of this instrument when eventually constructed.

Recently, a program has been initiated to ultimately enable the simulation of the interactions of radiation with biological systems at the cellular and DNA level [12]. This project, coordinated by ESA and INFN, will in its first phase concentrate on a rigorous collection of user requirements, and has generated wide interest in the European space, medical, and biological communities. Geant4 has been chosen as a platform for this work. The current Geant4-DNA Collaboration consists of some 25 experts in astrophysics, nuclear physics, microbiology, genetics and Object-Oriented software design, and is an excellent example of a multidisciplinary approach to a demanding software development project.

References

1. <http://wwwinfo.cern.ch/asd/geant4/geant4.html>
2. S. Chauvie et al.: 'Medical Applications of the Geant4 Simulation Toolkit'. These Proceedings p. 543
3. <http://www1.msfc.nasa.gov/NEWSROOM/news/status/chandrastatus/chandrasatus49.html>
4. R. Nartallo et al.: *Modelling the Interaction of the Radiation Environment with the XMM-Newton and Chandra X-Ray Telescopes and its Effects on the On-board CCD Detectors*, in the Space Radiation Environment Workshop and Workshop on Radiation Monitoring for the International Space Station, Farnborough, U.K., November 1–25, 1999
5. <http://glast.gsfc.nasa.gov>, <http://glast.stanford.edu>
6. <http://www.ifctr.mi.cnr.it/> Agile
7. M.G. Pia et al.: 'Geant4 Electromagnetic Physics'. These Proceedings 153
8. http://www.space.dera.gov.uk/space.env/geant_mn.html/
9. P.R. Truscott et al.: *Basalt X-Ray Fluorescence Study*, Technical Note to ESA, DERA/CIS/CIS2/7/36/4/1/3 (1999)
10. <http://www.ge.infn.it/geant4/lowE/>
11. <http://pc1582.psi.ch:80/SREM/>
12. <http://www.ge.infn.it/geant4/dna/>

Introduction of the Muonic and Cerenkov Effects in the EGS4 Code

E. Duverger¹, A. Mishev², R.I. Gschwind¹, L. Makovicka¹, and J. Stamenov²

¹ RMC LMIT Université de Franche Comté, BP 427, F-25211 Montbéliard cedex, France

² INRNE, Bulgarian Academy of Sciences, 72, Tsarigrad.chausse, 1784 Sofia, Bulgaria

1 Introduction

Some studies have been made in order to study the cosmic rays solar component variations. It's a method particularly interesting to obtain information about the solar activity. Actually, we search more precisely to measure the flux of the secondary muons created by cosmic rays during their interactions in the atmosphere. In this aim, a muonic Cerenkov Telescope developed by the INRNE (Institute for Nuclear Research and for Nuclear Energy) and the SWU "Neofit Rilsky"- Blagoevgrad Bulgaria is used [1]. The Experimental measures are made with a coincidence geometry. However, the electronic noise is very important. That 's why, in this work, an absolute calibration and a signal modelling is realised to diminish the discrepancies of the results. In a first part, we redefine rapidly the Cerenkov effect and the model introduced inside the EGS4 Monte Carlo Code in order to simulate it. This approach permits the development of new technics for the registration of cosmic rays based on Cerenkov light in the atmosphere and the estimation of atmospheric transparency. In a second part we describe the telescope used and the comparison between the experimental and theoretical results obtained.

1.1 The Cerenkov Effect

The cosmic rays is an isotropic flux of particles with high and very high energy (nearly 90% are protons) [2]. The fluctuation in the muonic component are strongly interesting because it's correlated with the flux variation of the solar contribution. During the interactions between the atmosphere and the cosmic rays flourish the secondary particles (the muonic component, the electromagnetic, the hadronic cascade and the Cerenkov light) [3]. When a particle crosses in a medium in which its speed is more important that the relative speed of light, a photon is emitted with an angular distribution limited by the maximum angular value given by (1).

$$\theta_{\max} = \arccos\left(\frac{1}{n}\right) \quad (1)$$

where n is the optical index in function of the wavelength. The number of photons emitted in function of the mean path is given by the relation (2) where α is a fine structure constant.

$$\frac{dN}{dx} = 2\pi\alpha \int_{\beta n > 1} \left(1 - \frac{1}{\beta^2 n^2(\lambda)}\right) \frac{d\lambda}{\lambda^2} \quad (2)$$

For the optical spectrum, n is a constant and we can rewrite the formula (2) in the form (3).

$$\frac{dN}{dx} = 2\pi\alpha \sin^2 \theta \left[\frac{1}{\lambda_1^2} - \frac{1}{\lambda_2^2} \right] \quad (3)$$

Finally by integration of (3), between 350 and 500 nm in the optical spectrum, we obtain the relation defined by (4) which gives the number of photons by centimeter.

$$N_{\text{tcher}} = 390 \sin^2 \theta \quad (4)$$

1.2 Modifications Introduced in EGS4

In most of the Monte Carlo code as CORSIKA, the simulation of the cosmic ray transport is only for one medium and more precisely for the atmosphere [4]. What's more the simulation is incomplete because often the Cerenkov effect isn't introduced for the fixed geometry. It exists a possibility to introduce the Cerenkov effect in the EGS4 Monte Carlo Code and to take advantages of the simulation of the electromagnetic cascade in different media and different geometries [5]. In the EGS4 code, inside a subroutine named AUSGAB, we have added a program in an additional subroutine for the production of Cerenkov photons. When a charged particle enter in a medium and its velocity exceeds the local speed of light in the medium, some photons are created according to the equation determined by (3).

We check, if the region presents some interests. If the particle is charged we determine the Lorentz Factor γ (5).

$$\gamma = \frac{1}{\sqrt{1 - \frac{1}{n^2}}} \quad (5)$$

$$\gamma \leq \frac{E}{m_e c^2} \quad (6)$$

If we verify (6) with E the total energy of the charged particle, we call our subroutine of production of Cerenkov photons. In the subroutine the energy

losses of photon produced is not taken in counts because it's negligible compared to the losses by ionisation of the charged particles [6]. The total number of photons creates is given by the product of the distance travelled by the charged particle in the medium by the result given in (2). In this simple model the simulation of the diffusion angle is not taken in counts because we want recorded all the photons generated in the water Cerenkov detector in total reflection configuration. Before any modification of the model, we have searched to validate our assumption. The medium chosen has been the water because the simulation of the atmosphere and the comparison with CORSIKA taken a more great CPU time. So, the comparison have been made with the muonic telescope built at the Blagoevgrad University.

2 The Cerenkov Telescope

The telescope is based on 18 water tanks mounted in 2 slabs of 3 by 3 cells (Fig. 2). Each tank have the same shape and geometry (49 cm x 49 cm x 12.5 cm). The water level is of 10 cm. Every detector is connected with a photomultiplier FEU-110 and FEU-139. The distance between the two planes is optimised in order to measure the muonic component in different direction. The telescope is isolated by two plates of lead [1]. One is at the bottom of the structure, the second between the two planes defines by the 9 cells. The energy loss of the muons between the first and the second slab are below 1 GeV, so the energy threshold is equal at this value.

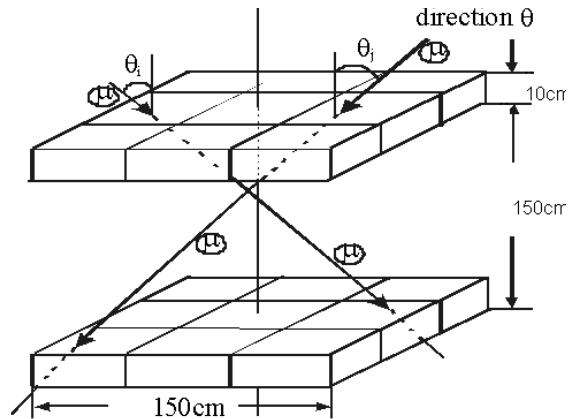


Fig. 1. Scheme of the Cerenkov Telescope

When a muon pass toward a tank, some Cerenkov photons are created recorded by the photomultiplier (PM). By integration of the muonic component, we have determined the intensity I recorded by the telescope (10^{-2} s^{-1}

$\text{cm}^{-2} \text{ster}^{-1}$). The mean number N of events for two tanks separated by a distance of 150 cm is 130 photons by minute. At any time, the tension for the PM (FEU-110 and FEU-139) is put between 1700-2000 V and the threshold tension at 25 mV. The detection window is regulated at 60 ns.

2.1 Experimental Studies

The experimental studies was realised using a tank and a gamma source Co^{60} . The gamma photons penetrating in the detector creates Compton electrons giving Cerenkov photons. For the calibration of the telescope and experimental verification of the model, we needed different quantities of photons produced in the tank. We have chosen to make the measures for three depths of water in function of the threshold tension. Each experience was made during 15 minutes for each point in the Fig. 2.

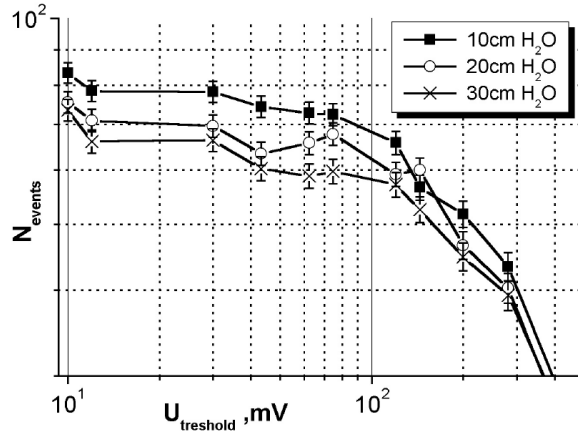


Fig. 2. Experimental number of Cerenkov photon in function of the threshold energy

All the curves have the same behaviour. One can see three parts. At the beginning of each curve the electronic noise is particularly high. At the middle, we find a plateau. Near its end, the tension at the output is proportional with the number of photons recorded by the photomultiplier. So, when we use the photomultiplier in spectrometric mode the response is linear. The third part of the curve is necessary to obtain the end of the plateau. If we make the assumption that each curve are the sum of two function describe by the relation (7).

$$Y(x) = a + bx^c \quad (7)$$

A simple fit permits to determine with a great precision the spectrometric point. With these different experimental data, we have determined three points

in function of the count speed and the threshold energy of the photomultiplier. These results have been compared to the theoretical results obtained with the EGS4 code for the same water depth (Fig. 3).

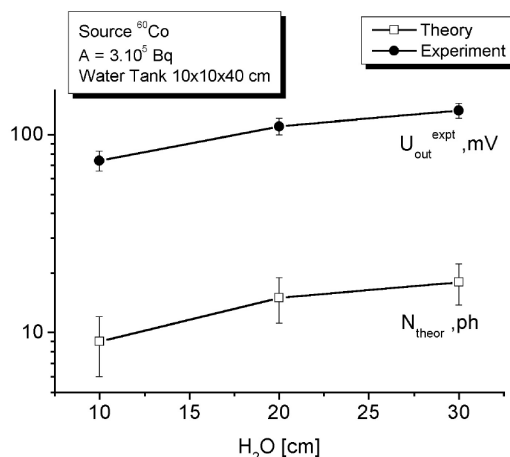


Fig. 3. Comparison between experimental and theoretical results

2.2 Additional Studies

One more possible verification of the model is the comparison with another code written for the simulation of the Cerenkov effect. We have introduced a simple model of the atmosphere in the EGS4 code. The atmosphere is divided in 21 layers with a thickness of 5 km [7,8]. The variation of the refractive index is taken into account [9]. It is important for the lateral distribution of the particle in function of the Cerenkov light. This simple model permits also to track the secondary particles. The angle of the Cerenkov photons emission is also simulated. The comparison with CORSIKA code is realized for a large energetic range until 1000 GeV. We take into account only the total number of the Cerenkov photons at the sea observation level. The results are shown in Fig. 4.

We have a great correspondence between the source of the different results. So replacing in EGS4 the electron rest mass with a muon rest mass and using our model authorize the simulation of the response of the telescope.

3 Conclusion

It exists a concordance between the model and the experimental results for the water detector. We can notice that the ratio between the Cerenkov determined for a water depth of 10 cm and 20 cm in theory (simulated in EGS4) is twice and

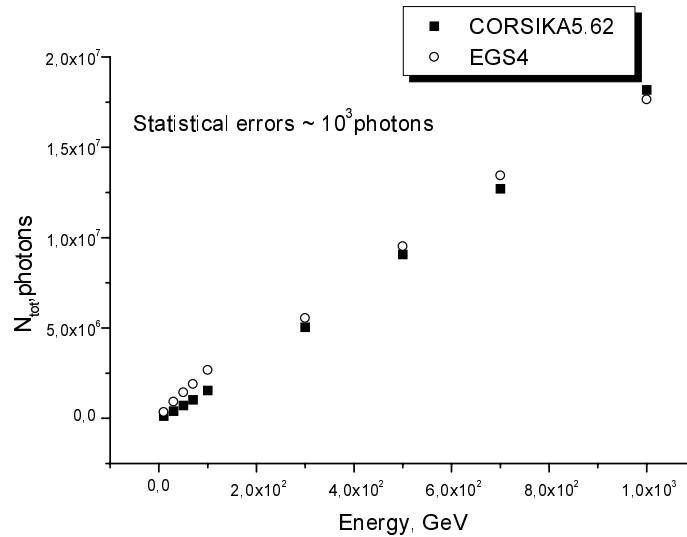


Fig. 4. Comparison between EGS4 and CORSIKA codes

in the case of the experience it is 1.75. The discrepancies in the results is due to the fact that for the experimental curve, it's particularly difficult to determine the spectrometric point and the efficiency of registration of the photons in the tank. This study shows however that the theoretical model is correct and that we can begin to make the simulation of the atmosphere.

References

1. I. Angelov, I. Kalapov, E. Malamova, J. Stamenov: 'Muon Cerenkov Telescope'. In: *National Conference of Electronics at Sozopol, Bulgaria, September 18–September 21, 1999*, to be published
2. M.S. Longuyr: *High Energy Astrophysics*, 1st edn. (Cambridge University Press, London 1981)
3. I.M. Frank: *Vavilov Cerenkov Radiation. Theoretical aspects*, 1st edn. (Nauka, Moscow 1988)
4. D. Heck, J. Knapp, J.N. Capdevielle, G. Schatz, T. Thouw: *Corsika a Monte Carlo Code To Simulate Extensive Air Showers*. Report-FZKA 6019, Forschungszentrum Karlsruhe, Karlsruhe (1998)
5. W. Nelson, H. Hirayama, D.W.O. Rogers: *The EGS4 Code System*. SLAC-Report-265, Stanford University, California (1985)
6. D. Blanc: *Les Rayonnements Ionisants*, 2nd edn. (Masson, Paris 1990)
7. G. Brasseur: *Physic and Chemistry of the Earth Atmosphere*, 1st edn. Masson Press, Paris 1982)
8. *Manual Of The ICAO Standard Atmosphere*, 3rd edn. (ICAO Press 1993)
9. E.J. McCarthy: *Optics of the Atmosphere. Scattering By Molecules And Particles*, 2nd edn. (John Willy and Sons Press, New York 1977)

Spectrum Shape Analysis Applied to Radioactive Waste Gamma-Ray Spectroscopy

B. Perot¹, J.-L. Artaud¹, B. Chabalier¹, J. Misraki², and P. Chany³

¹ CEA/DESD/SCCD/LECD, 13108 ST Paul lez durance Cedex, France

² GIE CODEM, Château de Paniscoule, 30200 Bagnols-sur-Cèze Cedex, France

³ COGEMA, Marcoule/PRG, BP 170, 30200 Bagnols-sur-Cèze Cedex, France

Abstract. Gamma ray spectroscopy of radioactive waste drums is often difficult at low energy (less than 200 keV) because of high photon attenuation in the matrix. This paper deals with the assay of 225 liters packages (about 60 US gallons) filled with radioactive salts mixed with bitumen.

The presence of high-Z elements, such as barium ($Z=56$) or uranium ($Z=92$), has a great impact on the low energy photon attenuation. As these elements appear in various quantities in the waste, the attenuation corrections required for activities calculations is quite delicate.

We propose to take this effect into account through the analysis of the spectrum shape. The low energy continuum due to scattered photons (partly in the matrix and partly in the germanium detector), is indeed very related to the heavy elements content, whereas this is not the case of the 661.7 keV peak of ^{137}mBa (^{137}Cs radioactive daughter), main gamma emitter in this waste.

1 Introduction

The CEA (French Atomic Energy Commission) has developed a combined passive and active non destructive assay system for 225 litres bitumized waste drums produced at the nuclear fuel reprocessing plant of Marcoule (France) [1] including a gamma-ray spectroscopy device.

This work deals with the precision improvement of activity determination in the case of low energy gamma rays. As a matter of fact, photon attenuation corrections accuracy is lowered by the presence of heavy elements, such as uranium or barium, which appear in various quantities in the matrix composition (up to a few percent). For a given activity in the drum and a given matrix density, a small variation in the amount of these components implies a significant change of the photon attenuation below 200 keV.

We present here a numerical feasibility study for a correction method based on the analysis of the gamma spectrum shape, performed with the transport code MCNP (Monte Carlo N-Particle) Version 4B [2]. We first describe shortly the numerical model, and then present parametrical calculations related to several heavy material contents.

2 Numerical Model

In order to accelerate the statistical convergence (calculation time reduction) and to simplify the spectrum shape analysis (discrimination of the photons scattered in the matrix or in the germanium detector), we separate the calculation in two stages : the first one consists in evaluating the photon flux at the measurement distance with the “Flux at a point detector tally (F5)” of MCNP; the second one consists in simulating the high purity germanium detector (planar design: diameter 25 mm, thickness 13 mm) spectrum with the “Energy distribution of pulses created in a detector tally (F8)”.

For the spectrum shape calculations, we describe a single-energy photon source of 661.7 keV which is the dominant gamma-ray in these waste drums, uniformly sampled in the bitumized matrix (density of 1.3). Then, we carry out a set of parametrical simulations with different barium and uranium contents, covering the expected range.

We also perform photon attenuation calculations with the same matrix compositions, using a multi-energy source (discrete values between 60 keV and 1 MeV), also uniformly distributed in the matrix.

3 Heavy Elements Effect on Photon Attenuation

We present on Fig. 1 the relative effect of barium and uranium on the flux at the detector position. The different curves are normalised to the one corresponding to the matrix without heavy materials. We use the notations $M(\text{Ba})_{\text{max}}$ and $M(\text{U})_{\text{max}}$ for the maximum masses of barium and uranium.

One can observe a great influence of barium and uranium below 200 keV. The flux attenuation is the highest at 60 keV, reaching a factor of 4 with the maximum amount of these elements. On the other hand, it is less than 10 percent above 400 keV, and negligible at 1 MeV.

The discontinuities observed in the curves corresponding to a matrix with uranium are due to the absorption-edge discontinuities of the photon mass attenuation coefficients, see Fig. 2.

At each energy, the ratio between the fluxes calculated with an without heavy elements (see Fig. 1) can directly be used to correct the photon efficiency corresponding to a matrix without barium or uranium.

We aim to find a way to determine which correction factor has to be used, for any given waste package, through the analysis of the gamma spectrum shape (see following sections).

4 Spectrum Shape Analysis

We have examined different ways to take into account the changes in the low energy photon attenuation due to heavy materials, and we notably studied a low energy photon transmission method. Unfortunately, it was unpractical to bring it into operation because of the rather high density of the matrix (about 1.3),

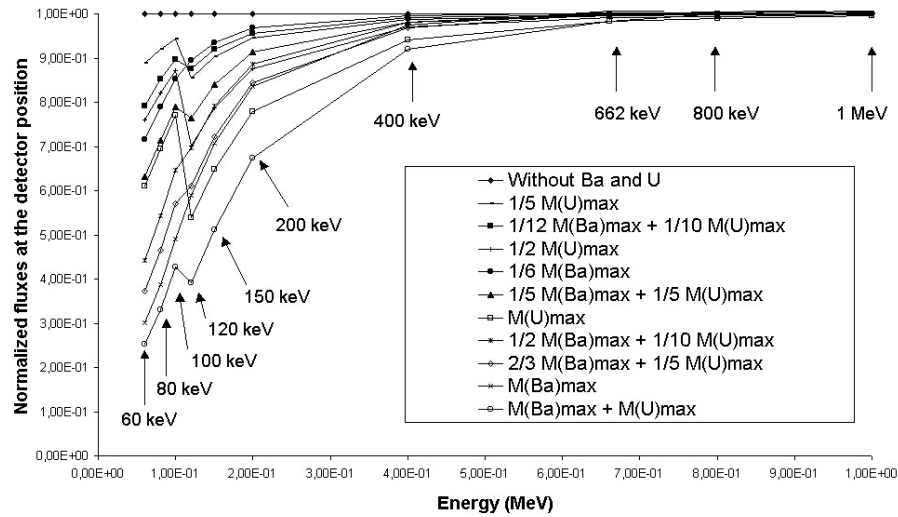


Fig. 1. Normalised photon fluxes emergency from waste drum at the detector location as a function of energy and heavy materials content

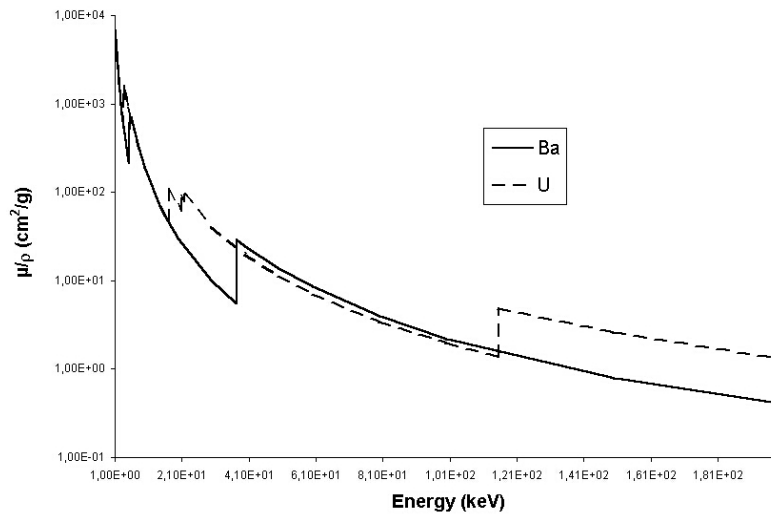


Fig. 2. Energy dependence of barium and uranium photon mass attenuation coefficients [3]

which would have required a very high activity transmission source. We could have possibly used a tangential measurement, but this would have led to a poor precision, because many drums have not a perfect cylindrical shape.

We finally decided to study a new method based on the analysis of the gamma spectrum shape. In our case, this shape is primarily due to direct and scattered

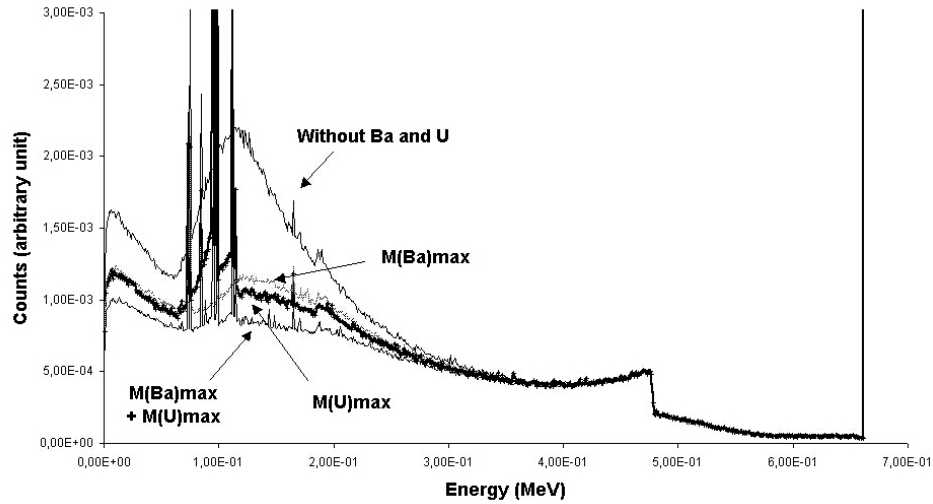


Fig. 3. Spectrum shape as a function of barium and uranium contents

photons of the main gamma ray emitted in the drum, which energy is 661.7 keV. On the one hand, as shown in the former section, the unscattered 661.7 keV peak is almost insensitive to the presence of high-Z constituents. On the other hand, the low energy continuum due to scattered photons is severely attenuated by the absorption in these elements, see Fig. 3.

Our goal is to find out a spectrum shape indicator and a correlation with the photon efficiency correction factor described in section 3. One can see on Fig. 3 that a simple indicator could be the ratio between the surfaces of a low energy region of interest (ROI) and the 661.7 keV peak.

In fact, we have to select different ROIs according to the energy of the efficiency correction factor, because of the absorption-edge discontinuities (see Figs. 1 and 2).

More precisely, a ROI must not cover a discontinuity and furthermore, as far as the correlation with the correction factors is concerned, the spectrum shape indicator is only relevant in the same energy area. For instance, any ROI chosen between the K-edges of barium (37.4 keV) and uranium (115.6 keV) will be convenient for the determination of the correction factors belonging to this energy area (see Fig. 2).

However, the choice of the ROI is not only based on the absorption edges because we also must avoid low energy perturbing peaks, such as fluorescence X-rays (collimator or shielding lead, uranium of the matrix...). In our case, for the former energy region, we have selected a ROI located at about 80 keV with a width of a few keV.

5 Photon Attenuation Corrections

In our application, the determination of ^{241}Am activity is one of the main objectives of the gamma-ray spectroscopy device. For this purpose, we use the 59.5 keV gamma-ray emitted by this radioisotope.

Figure 4 presents the correlation between the photon attenuation correction factor at 60 keV and the spectrum shape indicator based on the 80 keV ROI (see section 4) for a wide range of barium and uranium masses in the matrix.

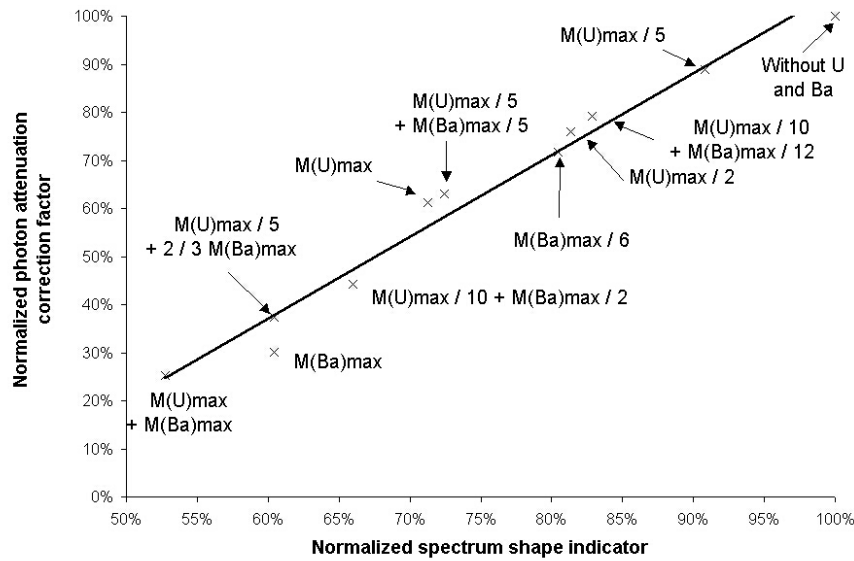


Fig. 4. Relationship between the photon attenuation correction factor and the spectrum shape indicator

This linear correlation can be used to correct the low energy photon efficiency, for any waste drum with any unknown barium or uranium contents. One must merely evaluate the shape indicator value on then gamma spectrum and deduce the correction factor with the help of the correlation.

6 Conclusion

We have performed a numerical feasibility study of a gamma-ray spectrum shape analysis method intended to improve the accuracy of activity determination in the case of low energy gamma emitter in radioactive bitumized waste drums.

The results prove that it is possible to use the spectrum shape in order to take into account the presence of high-Z elements such as barium or uranium in the waste matrix. Actually, these elements have a strong effect on low energy

photon attenuation, and the variability of their quantity involves an important incertitude on the activity calculation.

The proposed method uses the difference of sensibility observed in the gamma spectrum between low and high energy regions, as a function of barium and uranium contents. It could lead to a substantial improvement of the activity precision, with the great advantage that the needed information can be found directly in the spectrum and requires no additional assay.

An experimental validation of this numerical feasibility study will soon be possible thanks to the assay of real bituminized waste drums on a gamma spectroscopy prototype currently under construction [1].

We must also investigate the different parameters that could disturb the method, such as a potential matrix or activity heterogeneity, the presence of other high-Z elements, the modification of the theoretical spectrum shape due to electronics set-up or to photons scattered in the experimental environment.

References

1. B. Chabaliér, J.L. Artaud, B. Perot, C. Passard, J. Romeyer Dherbey, A.C. Raoux, J. Misraki, P. Chany, S. Dogny: ‘Developpement of the “Measurement and Sorting” Device for Bituminized Waste Drums at COGEMA Marcoule’. In *Safewaste 2000, 2th International Conference at Montpellier, France, 2-4 October 2000*
2. J.F. Briesmeister, Editor: *MCNP, A General Monte Carlo N-Particle Transport Code, Version 4B*. Manual LA-12625-M (1997)
3. M.J. Berger, J.H. Hubbell : *Data Library PHOTX, Version 2.0. 24 Feb 1988. Cross Sections for Interactions of Photons with Atoms*, Photon and Charged Particle Data Center, National Bureau of Standards, Gaithersburg, MD 20899

Assessment of a Compton Suppression Spectrometer for the Measurement of Medium- and High-Level Radioactive Waste Packages

J.-L. Artaud¹, B. Perot¹, B. Chabalier¹, and H. Toubon²

¹ CEA/DESD/SCCD/LECD, 13108 ST Paul lez durance Cedex, France

² COGEMA, 78182 ST Quentin en yvelines Cedex, France

1 Introduction

A study has been carried out by the CEA (French atomic energy commission) in Cadarache to estimate the potential gain brought by a Compton Suppression Spectrometer (CSS) for the measurement of medium and high level radioactive waste packages.

Many articles have already been published in the field of environmental and low level waste CSS applications [1]. The originality of the current study lies in the application of that concept to industrial devices devoted to medium and high level waste measurement.

2 Principle of a Compton Suppression Spectrometer

The gamma-ray spectroscopy is often complicated by a continuum that raises significantly the limits of detection and makes it difficult to detect the peaks of low intensity.

This continuum stems partly from Compton scattering of higher energy gamma rays in the crystal of the detector. During that process a photon hits an electron, and yields a fraction of its energy in the crystal before escaping [2]. This partial depositing of energy is materialised by a pulse that is not representative of the incident photon and so impossible to use. The reproduction of this phenomenon for a lot of incident photons and for various deposits of energy fuels the continuum detrimental to the measurement.

The principle of a Compton Suppression Spectrometer (CSS) consists of detecting the photons escaping from the germanium crystal after scattering in order to eliminate the corresponding pulses. The detection is performed by a scintillator (usually NaI or BGO) surrounding the germanium. An electronic device, devoted to the detection of the coincidence of events occurring in the two detectors (germanium and scintillator), sends a signal to the ADC in order to reject the “Compton” pulse.

Finally, we get a “cleaned” spectrum, where the continuum level is reduced and the peak/Compton ratio is increased.

The reduction of the continuum level is quantified by the suppression factor (SF) which is the ratio of the spectrum with and without CSS.

3 Limitations

A Compton edge corresponds to photons backscattered in the germanium: they leave the crystal by the entrance window towards the source and cannot be detected by the scintillator. For that reason, a swell appears on the “CSS spectrum” at every Compton edge.

In the case of a waste drum, the continuum stems partly from the scattering in the detector and partly from interactions produced outside the detector, particularly in the matrix. Depending on the ratio of the two contributions, the efficiency of the CSS can be very low.

4 Optimisation of the System

By the mean of the relation (see Fig. 1) linking the energy yield to the angle of scattering [2] where m_0c^2 is the rest-mass energy of the electron (0.511 MeV), it is possible to calculate the scattering angle θ corresponding to a given incident energy.

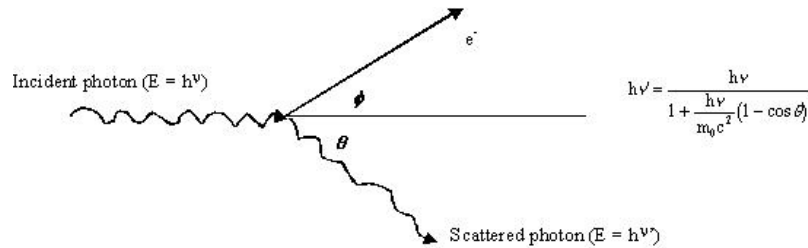


Fig. 1.

Hence, it is possible to compute the minimum and maximum scattering angles for the energy of the considered incident photons, in order to define the low and high threshold of the device, as for a pass band filter. After that, it is easy to define the shape and the dimensions of the scintillator allowing to stop the corresponding scattered photons.

5 Simulation Tool

In our laboratory, we frequently use MCNP (version 4B [3]), in order to design and evaluate the performances of gamma spectroscopy [4] or imaging [5] devices. This Monte-Carlo code, describes particularly the interactions of photons with matter from the geometrical and physical description of the studied device, allowing to design and simulate, for instance, a complete gamma spectroscopy

measurement device, from the source (waste drum) to the final spectrum. The methodology has been described in [4] and [5].

However, with this code we cannot simulate a CSS in a standard way. We have customised it by adding a subroutine capable of detecting the events produced by the same photon in the germanium and in the scintillator of the CSS. The software, playing then the part of “veto” instead of the electronic device in a real application, rejects those events.

6 First Possible Application

The first possible application is the gamma spectroscopy device of the “ACC”. A new facility devoted to the compaction of hulls and endpieces at the nuclear fuel reprocessing plant of COGEMA la Hague, which has been studied by our laboratory [4].

The measurement system, located at about 5 meters from the drum, is made up of five identical detection sets, each aiming at a fifth of the drum height. Each set is made up of a planar high purity germanium detector (area 500 mm², 13mm depth) located behind a collimator adapting the flux of photons to the performances of the electronic system components.

The drum is an inox cylinder (diameter 40 cm, height 120 cm) which can contain from 5 to 7 disks of compacted hulls and endpieces and various technological waste. The mean activity is equal to 15 TBq for the two main radionuclides : ⁶⁰Co and ¹³⁷Cs.

The continuum stemming mainly from ⁶⁰Co and ¹³⁷Cs, is located at energies less than 1117 keV (Compton edge of the 1332 keV ray of ⁶⁰Co). The gamma rays we aim to measure in the continuum zone of the spectrum are located between 427 keV (¹²⁵Sb) and 834 keV (¹⁵⁴Mn). Hence, the CSS must be optimised for that stretch of energy.

The contribution to the continuum stemming from Compton scattering in the matrix, the drum wall and the collimator for which the CSS is inoperative, is quite important. Therefore, that application is then a quite difficult case.

6.1 CSS Optimisation

The incident photons stem from ¹³⁷Cs (661.6 keV) and from ⁶⁰Co (1173 and 1332 keV). For those rays, the angles of scattering are included between 33.3 and 100.3 degrees.

The Fig. 2 shows how the dimensions of a ring of BGO have been calculated from the most penalising possible interaction points. However, these calculations consider only a single interaction in the crystal. In fact a photon can undergo several successive scattering and leave the crystal in an unpredicted direction. If there is not scintillator in this direction, then the escaping photon is not detected.

The exponential photon attenuation law of Beer-Lambert [2] allows us to compute the thickness needed to absorb the scattered photons we want to intercept and, to optimise the dimensions of the BGO.

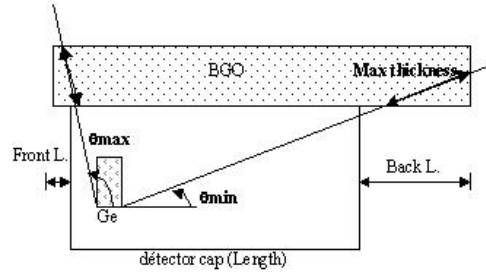


Fig. 2. Scintillator length calculation

6.2 Result

The Fig. 3 shows the spectra with and without CSS.

The suppression factor is included between 2 and 4 between 550 and 850 keV. The poor result between 400 and 500 keV is due to the Compton edge of the 661.5 keV ray of ^{137}Cs at 477 keV.

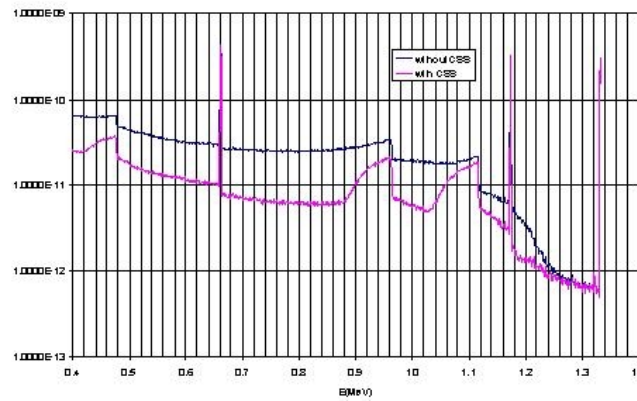


Fig. 3. Spectrum with and without CSS

At the first sight, the gain brought can seem quite weak. However, we recall that the scattered photons coming from the drum is important, and this reduces strongly the benefit of the CSS.

7 Second Possible Application

The second possible application concerns the “AD2” facility of COGEMA la Hague that deals with technological waste coming from the UP2 and UP3 re-processing plants. The problem is very different from the first application. Here,

the potential measurement difficulties are located at low energies, particularly : ^{241}Am at 59.5 keV and ^{239}Pu at 129.3 keV.

The package is a steel cylinder drum (120 l, about 76 cm of height and 46 cm of diameter). The matrix, (density of 0.19), is composed of polyvinyl chloride (PVC). An activity of 80 MBq of ^{60}Co and of 6.6 MBq of ^{137}Cs is representative of a real drum characterised in the facility.

For this evaluation the geometry has been simplified. The distance between the wall of the drum and the detector has been set to 1.5 meter, in the way to measure the entire drum with only one detector, whereas there is three detectors close to the drum in the real device.

7.1 CSS Optimisation

The angles of scattering are very small, because in the aimed range of energies, the incident photons yield very little energy (from 50 to 200 keV). In this case, They are slightly deflected and escape mainly toward the back of the detector.

We have assessed a compact geometry, with an enveloping back part of the BGO, which dimensions have been optimised according to the methodology described previously.

7.2 Result

The Fig. 4 shows the spectra with and without CSS.

The suppression factor is equal to 8 at 59.5 keV and about equal to 2.5 at 129 keV. Logically, the gain brought for that application more favourable than the first one, is quite interesting.

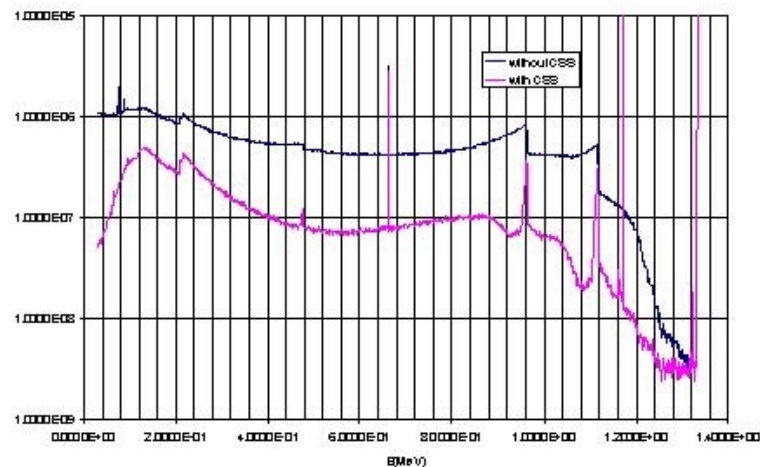


Fig. 4. Spectrum with and without CSS

8 Conclusion

After a remainder of the principle and the main limits of a Compton suppression spectrometer, we have showed how to optimise and assess the performances of a CSS, depending on a specific problem, by mean of numerical simulations.

This methodology has been applied to two examples of industrial measurement devices, which are very different in terms of geometry, packages and measurement objectives. For each of them, we have designed an optimised device.

The numerical results show a significant improvement in the two cases allowing either to lower the limits of detection, or to reduce the time of measurement while maintaining the same limits of detection.

If these CSS were to be brought into operation, the protection of the scintillator would be very effective to avoid accidental coincidences due to direct irradiation of the BGO crystal which result in the suppression of “good” pulses and therefore loss of counts in the full energy peaks. In our simulations this has been taken into account.

Even with a good protection, the BGO crystal is irradiated by the direct flux. And because its detection efficiency is very high, the count rate must be kept low enough to avoid accidental coincidences. In our simulations this is obtained by the mean of a collimator which limits the flux.

For application to medium and high level waste measurement, these two recommendations are of the highest importance.

References

1. J. Konin, P. Goudsmit, E. Lingemang, G.F. Knoll: *Radiation detection and measurement*, Second edition
2. G.F. Knoll: Nucl. Instr. Meth. **109** (1973)
3. Los Alamos National Laboratory, “MCNP4B : Monte-Carlo N-Particle Transport Code System”
4. J.-L. Artaud: *Atelier de compactage des coques et embouts, Dimensionnement du poste de mesures par spectrométrie gamma, avec le détecteur EGP 500-13 TR Evaluation des limites de détection*, NT SCCD/LECD 98-12
5. J.-L. Artaud: *Définition du poste d'imagerie gamma active du système de tri UP1*, NT SCCD/LECD 98-16

The Degradation of the Energy of Primary Photons Described through the Entropy

A.D. Oliveira¹ and J.J. Pedroso de Lima²

¹ Instituto Tecnológico e Nuclear, DPRSN - E.N 10 - Apartado 21, 2686-953
Sacavém, Portugal

² Instituto Biomédico de Investigação da Luz e Imagem, Az. de S.ta Comba, Celas,
3000 Coimbra, Portugal

Abstract. The photons of a radiation beam incident on a material suffer energy degradation as a consequence of multiple collisions between photons and matter. The aim of this work is to apply the concept of entropy of a probability distribution to quantify the degradation of energy. The probability distribution of energy deposited in the medium is obtained by a home made Monte Carlo code.

1 Introduction

Apart from the classical quantities of radiation dosimetry, i.e., energy imparted and absorbed dose, and considering the physical, chemical or biological effects of the ionising radiation, other physical concepts better correlated to the track structure of any radiation quality in matter are necessary [1].

For an alternative description of the radiation scattering we presented the concept of entropy to describe the diversity of energy in a given energy spectrum, as a result of the interaction of the radiation with matter.

The entropy is an old concept with recent applications like the entropy of a probability distribution [2]. We use the entropy to measure the disorder of the spectra of energy deposited in matter, which is related with the quality of the deposited energy. With this new method we describe the degradation of the energy of the primary photons as a function of the depth in water.

2 Methods

We considered water as scatter medium and a beam of monoenergetic photons with perpendicular incidence in a half-extended geometry. The energy of the primary photons was 10–150 keV. We chose this range because the quality factor is higher than 1 for energies below 300 keV [3].

We need to consider only three interactions. For the photoelectric effect we considered the deposition of energy in the interaction point. In the Compton scattering we used the Klein-Nishina cross-section modified by the incoherent scattering function. In the coherent scattering we used the Thomson cross-section modified by the atomic form factor. Grosswendt [4] describes the approaches used in this range of energy in full detail. The code was implemented following Chan and Doi [5].

For a monoenergetic beam with energy E , before interaction in the medium the probability of a photon with energy E is one and the entropy is zero. We divided the water in plane-parallel layers of 1 cm and for each one we obtained a sample of the distribution of the energy deposited. We applied the concept of entropy to this energy distribution which is obtained by Monte Carlo simulation. For the layer m , with $m = 0, 1, 2, \dots$, we define the entropy as $S_m = -\sum p(E_i) \ln p(E_i)$, where the summation is for $i = 1, \dots, N_m$ and where N_m is the number of different values of the energy in the spectrum (we used steps of 1 keV) and $p(E_i)$ is the probability of finding a photon with energy E_i .

3 Results

Bryan [6] concluded that after several collisions, energy and direction of the photons have small correlation with the primary photons. The deposited energy reaches an equilibrium distribution from a given depth. Our results do not fit to this concept. In the range of energy used the Compton shift is the main mechanism in the degradation of the energy of the primary photons. The coherent scatter does not contribute to the deposition of energy, however it is important in relation to the space distribution of the radiation. The spectrum of energy deposited varies with the depth as a function of the material and of the primary energy.

Using the Monte Carlo code we obtained spectra of energy deposited in layers of 1 cm. For each spectrum we calculated the entropy accordingly the previous section.

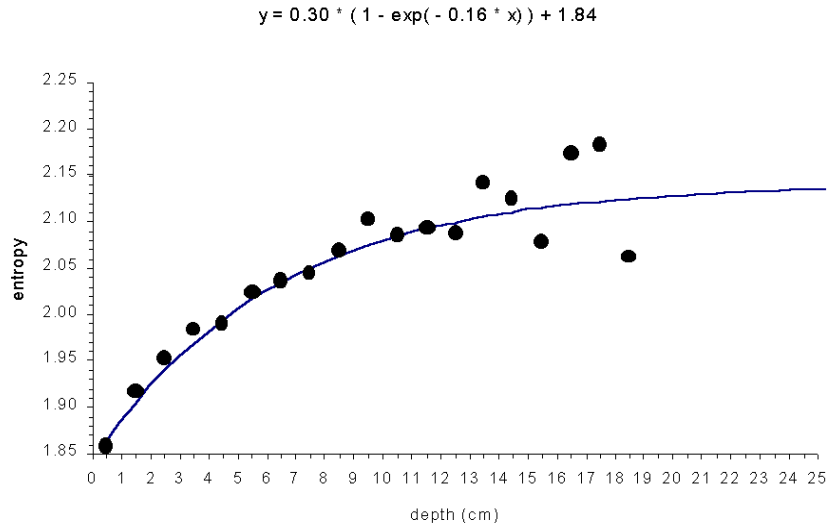


Fig. 1. Entropy for the degradation of primary photons with 30 keV as a function of depth. Results obtained approximately with 90000 photons

In the next figure we present the entropy for primary photons with 30 keV.

This result confirm the Bryan analysis [6]. The entropy tends for a constant value. Fitting the data we obtained a equilibrium value of 2.14.

In the next figure we present the same result for primary photons with 100 keV.

In this figure we see that increasing the number of photons simulated we obtained a convergence in the curve of the entropy. The function to fit the data in Fig. 1 no longer can be used. This result is in disagreement with Bryan [6] and with the result for 30 keV. We made simulations for another values of the primary energy and the results obtained are presented in the next figure.

This figure we presented is our main result, however, followed we presented the concept of accumulated entropy that allows a better discussion of the results and comparison with the quality factor.

The accumulated entropy is not a summation of values. We defined layers of 1 cm previously, for sampling the spectrum of energy. In the accumulated entropy the sampling layer is going increasing progressively with increments of 1 cm. When we included in the sampling all of the deposition points, we obtain the global entropy of the energy deposited.

Next, we define relative entropy:

$$\text{Relative entropy} = \text{layer entropy} / \text{accumulated entropy}$$

In the next figure we presented the relative entropy for the data of Fig. 4.

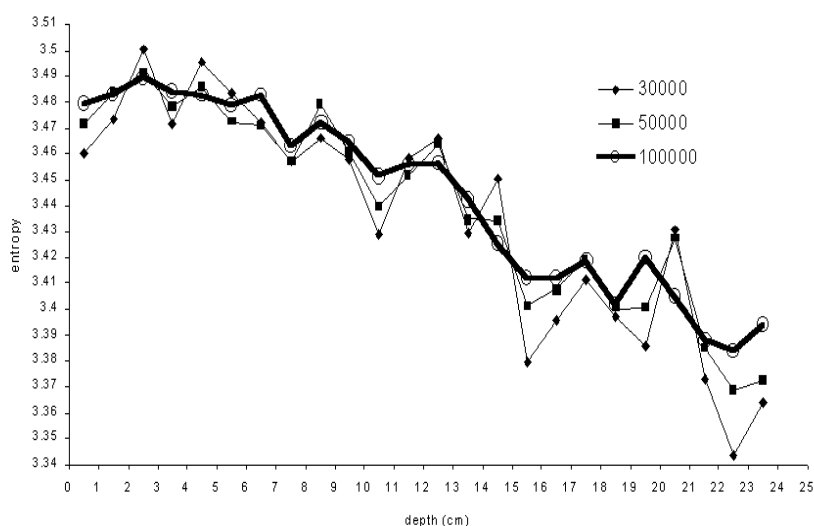


Fig. 2. Entropy for primary photons with energy 100 keV. Results obtained with 30000, 50000 and 100000 photons

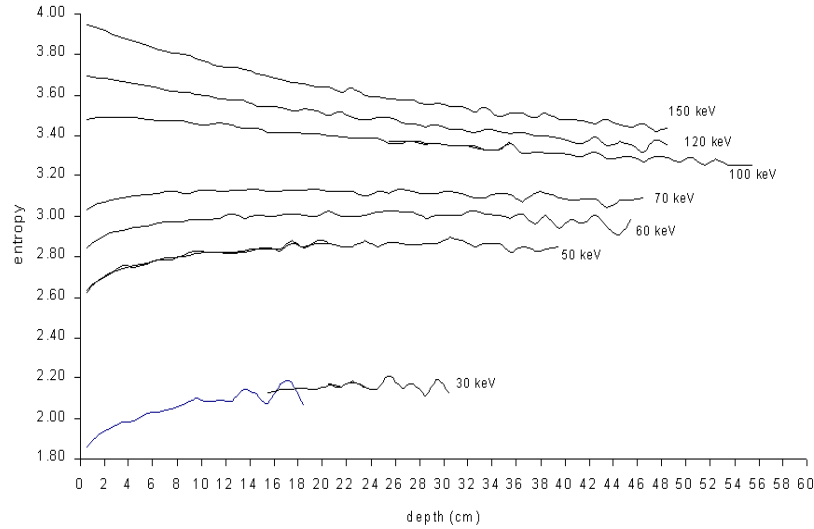


Fig. 3. Entropy in water as a function of the depth with the energy as parameter

4 Discussion

We observed in Fig. 4 three types of different behaviour:

- For values of primary energy below 50 keV the relative entropy is always higher than one.
- Between 50 keV and 120 keV is higher or lower than 1, depending on the depth considered.
- Above 120 keV the relative entropy is always lower than one.

We concluded that the values of energy (50 keV and 120 keV) are the limits of three zones of different behaviour of the entropy. As we can associate the entropy to the quality of the energy then those limits also defines three zones of the quality of the energy deposited in matter.

The traditional concept used in radiation protection is the quality factor. Drexler et al [3] calculated the effective quality factor for the ambient dose equivalent. We can also define three zones for the quality factor:

- The quality factor increases from 1 to a maximum at 50 keV.
- Between 50 keV and 300 keV decreases to the unit.
- For values above 300 keV maintains the unitary value.

The quality factor is calculated from the secondary electrons whose initial energy is determined by the same spectra of energy that we calculated the entropy.

We concluded that both approaches, the entropy and the quality factor, they present similar behaviours as a function of the primary energy. However we will

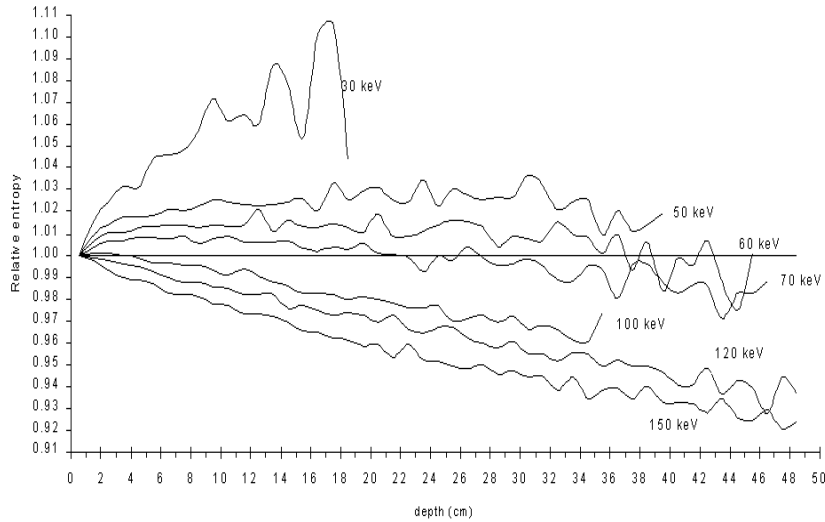


Fig. 4. Relative entropy for primary energies in the range 30-150 keV

still discuss the difference among the values of energy: 120 keV for the entropy and 300 keV for the quality factor.

For each value of the energy of the secondary electrons it corresponds a value of LET . Several proposals exist for the function $Q(LET)$. Drexler et al [3] discusses the influence of $Q(LET)$ in the effective quality factor, \bar{Q} . Depending on the specific choice of the function $Q(LET)$, the value of 300 keV referred above varies between 100 keV and 500 keV. Then, we concluded that both approaches, the entropy and the effective quality factor, are in agreement. The entropy, as it does not include any consideration on the secondary electrons, provides a much simpler approach to the quality of the energy deposited in matter.

5 Conclusion

The concept of entropy of a probability distribution applied to the distribution of energy deposited in matter by the radiation allows a quantitative analysis of the degradation of the energy of the primary photons. Unexpectedly, for the highest energies in the range studied, the entropy decreases when the depth increases. Both, the quality factor and the entropy present three zones of behaviour defined by the energy of the primary photons. These values of energy present a good agreement. Both approaches are based in the same spectra of energy. However the entropy is a much simpler approach than the effective quality factor.

This new application of the entropy allows new insights of the radiation physics. The results we obtained allow further research, for example they suggest that the distribution of the energy deposited by the photons can have an importance up to now unsuspected in the value of the quality factor.

References

1. B. Grosswendt: Radiat. Prot. Dosim. **52**, 237 (1994)
2. J.P. Peixoto, F.C. Rodrigues: *Sistemas. Entropia e Coesão*, (Discordia Editores, Lisboa 1991)
3. G. Drexler, R. Veit, M. Zankl: Radiat. Prot. Dosim. **32**, 83 (1990)
4. B. Grosswendt: Radiat. Environ. Biophys. **38**, 147 (1999)
5. H.-P. Chan, K. Doi: 'Monte Carlo Simulation in Diagnostic Radiology'. In: *Monte Carlo Simulation in the Radiological Sciences*, ed. by R.L. Morin (CRC Press, Florida 1988)
6. F. A. Bryan: 'Differential Energy Spectra'. In: *Engineering Compendium on Radiation Shielding*, ed. by R. G. Jaeger et al (Springer-Verlag, Heidelberg 1968)

Monte Carlo Simulation of the Conversion Electron Scattering in Targets for the Synthesis of Superheavy Elements

A. Špalek and O. Dragoun

Nuclear Physics Institute, Acad. Sci. Czech Rep., CZ 25068 Řež near Prague, Czech Republic

Abstract. The Monte Carlo simulation of conversion electron scattering in the targets, used in the experiments with superheavy elements synthesis, is presented. The calculations were performed for electron energies of 10, 100 keV and lead targets of 200, 600 and 2000 nm thicknesses. The results indicate the feasibility of internal conversion electron spectroscopy as a significant tool for the studies of superheavy nuclei.

1 Introduction

One of the important nuclear physics tasks is the investigation of the structure of heavy nuclei with atomic numbers $Z > 100$ and especially the search for the “island of stable nuclei” with Z from 114 to 126 [1]. Some of the nuclei with $Z > 100$ were already synthesized in the reactions of a heavy ion beam with the target of heavy nuclei; e.g. Reiter et al [2] investigated the $Z=102$ isotope ^{254}No produced in the reaction $^{208}\text{Pb}(^{48}\text{Ca}, 2n)^{254}\text{No}$. The superheavy nucleus is synthesized in an excited state from which it goes to the ground state through the sequence of depopulating electromagnetic transitions. Important part of these transitions corresponds to the rotational band. In the heavy even–even nuclei, the rotational transitions usually have energies in the range from tens to hundreds of keV ($2^+ \rightarrow 0^+ \sim 40$ keV, $4^+ \rightarrow 2^+ \sim 100$ keV, $6^+ \rightarrow 4^+ \sim 150$ keV, $8^+ \rightarrow 6^+ \sim 200$ keV etc.).

In the region of $Z > 100$, a large part of the transitions proceed via emission of the internal conversion electrons that prevail the photon emission (corresponding internal conversion coefficients are of the order of $10^1 - 10^2$ [3]). Until now, the rotational transitions in very heavy nuclei were observed only with the γ -ray detectors [2]. By means of multidetector γ -ray spectrometer, the authors identified the ground-state band of the even-even nucleus up to spin 20. This means relatively low sensitivity, mainly for the lowest rotational transitions with an extremely low probability of corresponding γ -ray emission. In such situation, the spectroscopy of internal conversion electrons would be worthwhile. The conversion electrons are emitted from the superheavy atom produced in the volume of the irradiated target. For planning the conversion electron spectra measurements it is necessary to take into account the electron scattering within the target material. With this aim, we performed the Monte Carlo calculations of electron scattering for the conditions typical in the experiments with superheavy elements.

2 Calculations and Results

In Monte Carlo calculations, the individual elastic and inelastic electron collisions were simulated in the way described in our previous works on electron scattering within the radioactive sources [4,5]. The distribution of electron losses W in the inelastic collisions was sampled according to the differential inelastic cross section (or differential inverse mean free path DIMFP for the inelastic collisions). This quantity is usually available only for energy losses up to ~ 100 eV; its shape for higher energy losses was extrapolated using $1/W^2$ dependence. The condition to obtain realistic results is

$$W_{av} = S\lambda_{inel}, \quad (1)$$

where W_{av} , S and λ_{inel} are the mean energy loss in an inelastic collision, the stopping power and the inelastic mean free path, respectively. This condition can be satisfied by a proper choice of the point, where $1/W^2$ function is joined to the DIMFP function relevant to the given scattering material. In this paper, we considered the case of a lead target used in the recent experiments [6,1]. Since the DIMFP function for lead is not available we used an approximate Lorentz-like shape with the maximum at 25 eV. The $1/W^2$ function was joined to the Lorentz one at 33 eV.

We simulated the electron scattering in lead targets of three different thicknesses, i.e. 200 and 600 nm (227 and 680 $\mu\text{g}/\text{cm}^2$) as typical examples used in the experiments [6,1] and 2000 nm (2.3 mg/cm^2) for the case of rather thick target. The initial electron energies were chosen to be 10 and 100 keV as typical values of the kinetic energy of conversion electrons that could be emitted with relatively high intensity during deexciting nuclear transitions in the superheavy nuclei. For calculations the computer codes developed in our laboratory were employed. In each case $10^7 - 10^8$ electron trajectories were simulated.

At first, the isotropic initial angular distribution of emitted electrons was assumed apart from a possible angular dependence of the electron emission for nuclei produced in the reaction. Also the homogeneous distribution of electron sources in the target volume was used corresponding to prompt electron emission from the created superheavy atoms. In further simulations, we took into account also the angular anisotropy of the conversion electrons emitted from the nuclei oriented after creation in the nuclear reaction. The angular distribution was described according to the relation [7]

$$W(\theta) = 1 + A_2 B_2 P_2(\cos \theta), \quad (2)$$

where A_2 and B_2 are γ -ray angular distribution coefficients and particle parameters [8], respectively. The $P_2(\cos \theta)$ is the Legendre polynomial. For a typical situation of the K or L conversion electrons emitted at the nuclear transition from 8^+ to 6^+ state, the value of $A_2 B_2 = 0.6$.

The examples of simulated spectra are displayed in Figs. 1 – 4. The energy distribution of the electrons emitted from the target has a smooth shape with monotonous fall towards the low energies. The distributions corresponding to different conditions have very similar form. Particularly, the considered anisotropy

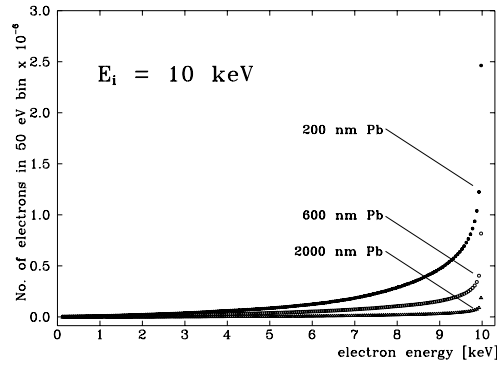


Fig. 1. The Monte Carlo calculated distribution of electrons emitted from the 200, 600, and 2000 nm thick lead targets into the forward half of the full solid angle. The electron sources are uniformly distributed in the target volumes and the initial energy of electrons is 10 keV. The initial angular distribution of the electrons is isotropic. The data presented are scaled to the 10^8 initially emitted electrons. The same scaling is used in all figures

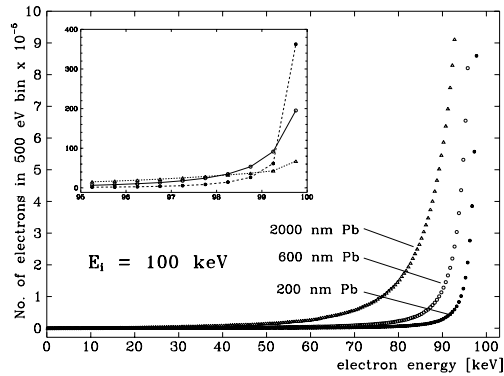


Fig. 2. The MC calculated energy distribution of electrons from the 200, 600, and 2000 nm thick lead targets. The initial electron energy is 100 keV. All other conditions are the same as in Fig. 1. In the insert, the energy interval 95–100 keV is depicted in more detail. (The lines connecting the points are only to guide the eye)

of initial angular distribution gave only small difference from the results corresponding to the isotropic angular distribution. The mean energy loss of emitted electrons is about 1–2 keV depending on the initial emission energy and the target thickness. The ratio (with respect to the total number of electrons originated in the target volume) of electrons emitted from the target into the forward half of the full solid angle decreases with the target thickness. These ratios are summarized in Tab. 1.

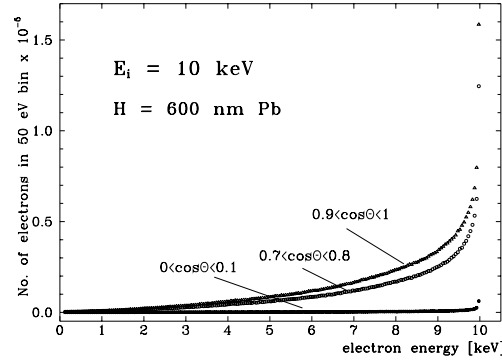


Fig. 3. The MC simulated energy distribution of electrons emitted from the 600 nm thick lead target into three different angular intervals. Θ is the angle of electron emission with respect to the target surface normal

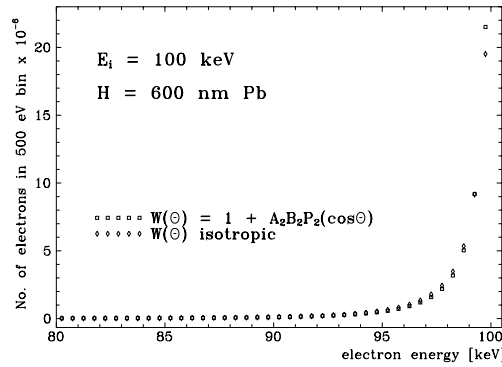


Fig. 4. The energy distribution of electrons emitted from the 600 nm thick lead target into the forward half of the full solid angle. The initial electron energy is 100 keV. The diamonds correspond to the isotropic initial angular distribution of electrons, the squares correspond to the anisotropic angular distribution following the above formula. The coefficient $A_2 B_2$ is equal to 0.6 (see text)

Due to the symmetry the same values correspond to the backward half of the full solid angle behind the target. Some electrons are emitted from the target with zero energy loss and their fraction, in the case of 200 nm lead target, varies from 2.7 to 14 % of the total number of emitted electrons for 10 and 100 keV initial energies, respectively (the corresponding values are 0.9 and 4.9 % for the 600 nm lead target). The intensity of emitted electrons is almost linearly dependent on the cosine of the angle of electron emission with respect to the target surface normal (this holds for the sum of the electrons over all energies as well as for the zero-loss electrons).

Table 1. Fraction (in %) of electrons emitted into the forward hemisphere

Initial electron energy (keV)	Target thickness (nm)		
	200	600	2000
10	21.7	13.2	4
100	50	50	49.6

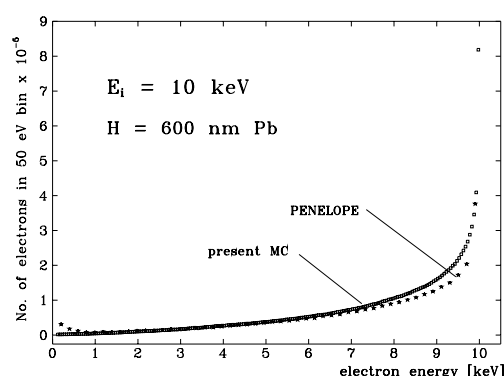


Fig. 5. The energy distribution of electrons emitted from the 600 nm thick lead target into the half of the full solid angle. The initial electron energy is 10 keV. The squares correspond to the MC simulation approach described in this paper. The asterisks were obtained from calculations using the PENELOPE [9]. The deviations in the low-energy region (<1 keV) could correspond to the secondary electrons considered in the PENELOPE program

We performed also similar calculations with the PENELOPE algorithm devised by J. Baró et al. [9]. As seen in Fig. 5 for the case of 10 keV energy and the 600 nm thick lead target, the PENELOPE energy distribution is similar to that simulated by the above described approach of our laboratory. Some deviation could be caused by different treatment of inelastic collisions in the lead target.

To express the effect of electron scattering on the spectra analyzed in a future experiment, we convoluted the Gaussian spectrometer response function with the $\text{FWHM} = 0.5$ and 2 keV with the MC calculated distribution corresponding to the 10 keV electron energy and 600 nm thick lead target, see Fig. 6. It is seen that in the case of realistic instrumental resolution the electron scattering in the target causes increase of the spectral line width but it does not hinder the observation of internal conversion line. Moreover, with increasing electron energy and for thinner targets the effect of electron energy losses and scattering will be smaller. In addition, the superheavy atoms move after the recoil in nuclear reaction and therefore some conversion electrons can be emitted in the sites closer to the target surface or even outside of the target.

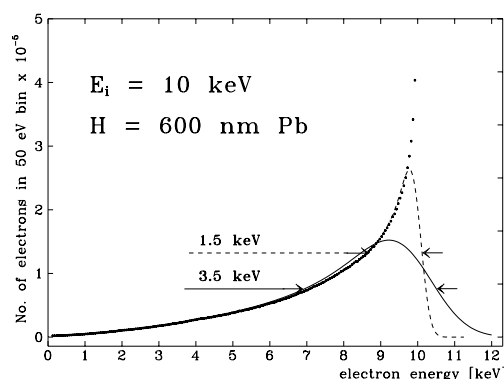


Fig. 6. Energy spectrum of electrons with initial energy of 10 keV emitted from the 600 nm thick lead target (see Fig. 1). The dashed and full lines correspond to the convolution of the given energy distribution with a Gaussian spectrometer response function of 0.5 and 2 keV FWHM, respectively

3 Conclusion

We have demonstrated the feasibility of internal conversion spectra measurement in the experiments with superheavy elements synthesis, supposing the use of an electron spectrometer with the energy resolution of about 1 keV and sufficient transmission.

4 Acknowledgments

The authors are grateful to Dr. F. Salvat for delivering of the program PENELOPE and valuable help with its use. Supported by the Grant Agency of the Czech Republic under contact 202/00/1625.

References

1. V. Ninov et al.: Phys. Rev. Lett. **83**, 1104 (1999)
2. P. Reiter et al.: Phys. Rev. Lett. **82**, 509 (1999); P. Reiter et al.: Phys. Rev. Lett. **84**, 3542 (2000)
3. O. Dragoun, M. Ryšavý, A. Špalek: J. Phys. G., submitted
4. S. Müller et al.: Z. Naturforsch. **a49**, 874 (1994)
5. O. Dragoun et al.: J. Phys. G **25**, 1839 (1999)
6. M. Leino et al.: GSI Scientific Report 1998, p.12
7. J.O. Newton et al.: Nucl. Phys. A **95**, 357 (1967)
8. R.S. Hager, E.S. Seltzer: Nucl. Data A **4**, 317 (1968)
9. J. Baró, J. Sempau, J.M. Fernández-Varea, F. Salvat: Nucl. Instr. Meth. B **100**, 31 (1995)

Monte Carlo Simulations on a 9-node PC Cluster

J. Gouriou

BNM-LNHB, CEA/Saclay, F-91191 Gif-Sur-Yvette Cedex, France

Abstract. Monte Carlo simulation methods are frequently used in the fields of medical physics, dosimetry and metrology of ionising radiation. Nevertheless, the main drawback of this technique is to be computationally slow, because the statistical uncertainty of the result improves only as the square root of the computational time. We present a method, which allows to reduce by a factor 10 to 20 the used effective running time. In practice, the aim was to reduce the calculation time in the LNHB metrological applications from several weeks to a few days. This approach includes the use of a PC-cluster, under Linux operating system and PVM parallel library (version 3.4). The Monte Carlo codes EGS4, MCNP and PENELOPE have been implemented on this platform and for the two last ones adapted for running under the PVM environment. The maximum observed speedup is ranging from a factor 13 to 18 according to the codes and the problems to be simulated.

1 Introduction

Monte Carlo simulation methods are frequently used in the fields of medical physics, dosimetry and metrology of ionising radiation. Nevertheless, the main drawback of this technique is to be computationally slow, because the statistical uncertainty of the result improves only as the square root of the computational time. To reduce the effective running time two approaches were studied, i.e. the use of powerful workstations (Dec-Alpha XP 1000) and a cluster of standard PCs. The choice of the best solution was determined by the performance/cost ratios calculated using the EGS4 user program XYZDOS [1]. In practice, due to budget considerations, the choice had to be made between a set of three DEC-Alpha work stations and a cluster of 16 P II 400 MHz processors. The cluster option was found to be the most powerful solution with a factor 1.8 better than the workstation option. Moreover, this option allowed to upgrade the cluster without modifying the implemented softwares and codes.

2 Material and Method

The cluster, see Fig. 1, is made up of 9 distinct nodes, i.e. 8 of them are workers and the last one is the master node that manages the local network and the interface between the cluster and the external network. Each worker node includes two P II 400 MHz processors with 256 MB SDRAM memory (one P II 400 MHz with 128 MB SDRAM for the master node). The local network uses a

classic 100 MHz Fast-Ethernet structure. The Linux operating system and the Fortran compiler are respectively a Debian version 2.1 and a g77 version 0.5.24. The MPI [2] and PVM [3] communication softwares were also implemented.



Fig. 1. LNHB cluster [Left: master node; Right: worker nodes]

Few works have been made in the field of parallel computing with public radiation transport Monte Carlo codes. To our knowledge, MCNP4 is the only code to have a PVM version [4,5]. For this work, the version 4b of MCNP was used [6]. In the case of EGS4 [7], the only bibliographic reference to a parallel version on a massive transputer dealt with the program Dosimeter [8]. Unfortunately, this approach is not directly usable in the case of the PVM environment.

Consequently, for the Dosimeter program (EGS4 code with PRESTA I [9]) and Pendoses program (PENELOPE code [10]) we developed appropriate algorithms to run under PVM (version 3.4). The selected algorithm architecture includes a master program and several worker sub-programs. The first one launches the workers, one per available processor without any other running task if it is possible, sends them essential parameters and receives from them the calculated results. Each task runs asynchronously, i.e. when a sub-program finishes a task, a new task is given to him. This means that the architecture does not keep the workers waiting while other workers complete their tasks.

The parallel simulation requires the use of a particular sampling technique of random numbers, which prevents from taking twice the same random number for the same action. The method used was to choose for the initial random number of history number n , the initial random number of history $n-1$ after two more successive samplings (random number stride of 2).

3 Results and Discussion

Test problems, representing a wide range in geometry and complexity, were chosen for this study (one specific problem for each code, i.e. calculation of dosimetric perturbation correction factor for a graphite calorimeter for Dosimeter, fluence calculation for internal dosimetry (MIRD phantom [11]) for MCNP and

fluence calculation in a NaI detector for Pendoses). Execution times were calculated on the master node with a statistical uncertainty (1σ) less than 2 %. They included the CPU time wasted during communications. These times were made long enough to eliminate any effect of initialisation time (approximately 2 hours).

Table 1. Execution times observed on the LNHB cluster. The times reported are elapsed execution time in seconds (not total CPU time). The numbers of simulated histories for Dosimeter, MCNP-4b and Pendoses are respectively 640 000, 39 000 000 and 580 000.

Number of Processes	Program used		
	Dosimeter	MCNP-4b	Pendoses
Linear (1)	4385	7083	7169
1	4450	7040	5602
2	2224	3870	2820
4	1181	1872	1398
6	768	1267	976
8	611	973	778
12	412	693	499
16	328	552	403

The running times spent in linear mode and in parallel mode with 1, 2, 4, 6, 8, 10, 12, 14 and 16 processes, and best optimization level on the compiler, were measured and summarized as raw data in Tab. 1 and as normalized data in Figs. 2 and 3. The linear process was done on the master node with the standard code under Linux environment. For MCNP-4b, the PRDMP default card parameters were used, i.e. 10 synchronized task rendezvous during execution. For Pendoses and Dosimeter, each worker sub-program sent results after 10 000 histories.

The maximum observed linear/parallel computing time ratios (R), represented in Fig. 2, were respectively 18 for Pendoses and 13 for the two other programs. The theoretical limit approach led to the assumption of a linear increase of the performance in function of the number of worker processes. The curves showed that above 8 processes the performances started to decrease. The fact that in a worker node the SDRAM memory was shared in between two separate processors could partly explain this.

For one process in parallel mode with Pendoses, the ratio (R) was found equal to 1.3. This effect was also observed with Dosimeter for a simplified model problem. Moreover, the ratio of running time ratios (R) between Pendoses and the two other codes (Dosimeter and MCNP) remained relatively constant for all

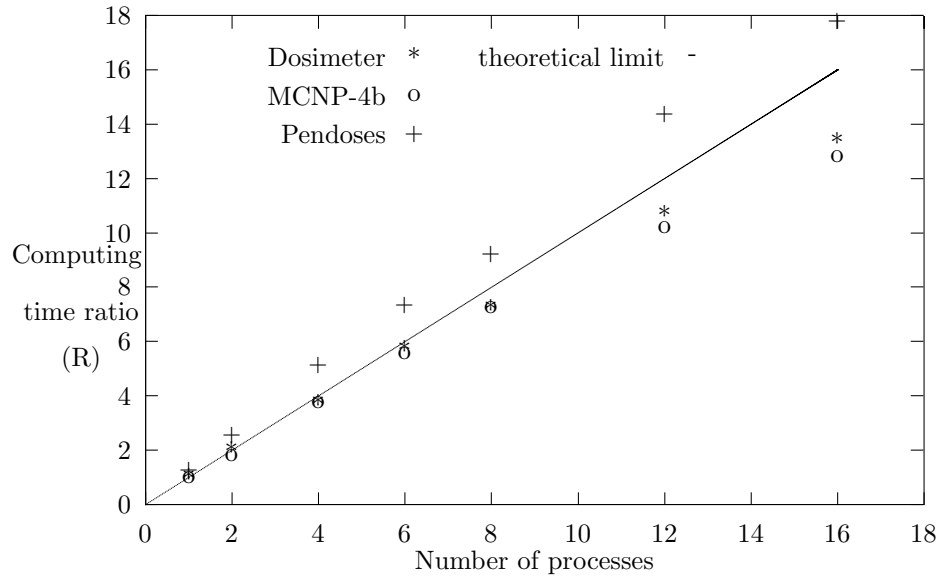


Fig. 2. Time ratios (R) observed on the LNHB Cluster. The running times were normalized to the execution time for a linear process for the same number of histories

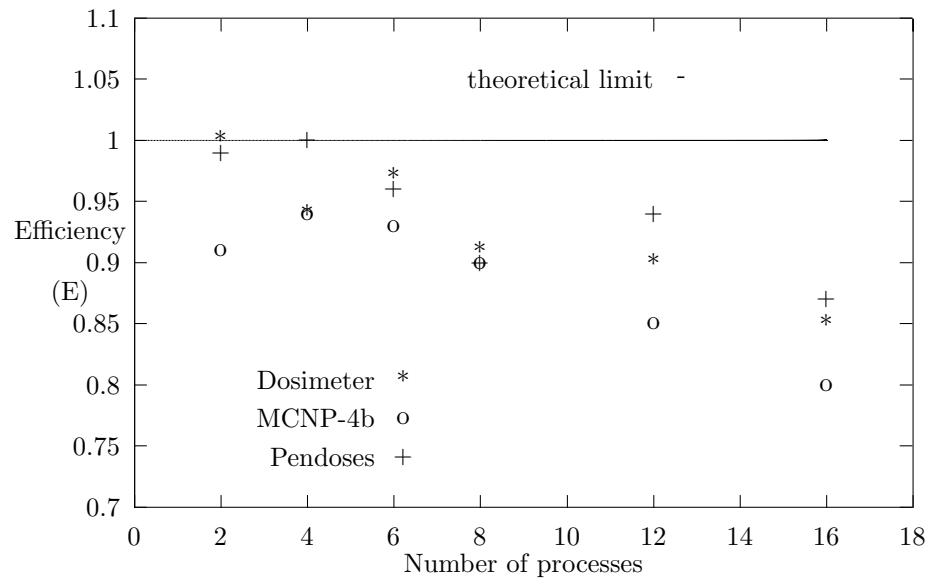


Fig. 3. Efficiencies (E) observed on the LNHB Cluster. The running times were normalized to the product of the execution time for one single parallel process by the number of active processors

process numbers. Thus in some particular conditions using a simpler structure and the PVM library, the new modified program could be faster than the classic one.

The influence of process communications on the performance degradation was observed. The efficiency (E), defined here as the ratio of computing times in parallel mode for several processes and for one single parallel process, divided by the number of active processors, was found, see Fig. 3, better than 0.90 up to 8 distinct processes and minimum for 16 processes. Unlike Fig. 2 for Pen-doses, all values were significantly below the theoretical limit, set equal to one. Moreover, there was also no much difference between the Dosimeter and Pen-doses performances. MCNP was slower because it required several synchronized communications. In fact for this code, different tasks ran on the master node, with only one single processor, and the other processes waited for them to be finished.

Generally speaking, for any code used for a quite short run, the ratio (R) decreases with increasing complexity of the problem to be simulated, for instance the geometry or the number of parameters to be extracted.

MCNP gives the same results for the two different modes (linear and parallel). Only the parallel versions of EGS4 and PENELOPE had to be validated. To take into account all the parameters, especially for the random sampling technique, the parallel calculated values were compared with the linear ones as an example of long term calculation.

With this aim in view, the value of the perturbation correction factor due to the vacuum gaps, existing in the LNHB graphite calorimeter, was calculated for different high-energy photon beams with the program Dosimeter. The parallel values were in good agreement with the linear ones, the largest discrepancy being about 0.16 % with a statistical uncertainty (1σ) of 0.13 % for each calculated factor.

In conclusion, it was possible to make several run tasks with a parallel version of different standard Monte Carlo codes. The observed ratios (R) for a 2 hours linear execution time, ranging from a factor 13 to 18, correspond to the expected values. A more important number of histories allows to increase the value of these ratios (R). Considering our limited experience, it seems that, for parallel versions of EGS4 and PENELOPE, the ratio (R) could reach a value equal to the number of processors, i.e. when the communications between programs are minimal.

References

1. S. Walker, A.F. Bielajew et al.: *Med. Phys.* **19**, 303 (1992)
2. M. Snir, S. Otto et al.: *MPI: The complete reference* (Massachusetts Institute of Technology Press 1996)
3. A. Geist, A. Beguelin et al.: *PVM: Parallel virtual machine -A users' guide and tutorial for networked parallel computing* (Massachusetts Institute of Technology Press 1994)
4. G.W. McKinney: Report LA-UR 93-1338 (1993)
5. G.W. McKinney: Report LA-UR 94-2523 (1994)

6. J.F. Briesmeister: Report LA-M 12626 (1997)
7. W.R. Nelson, H. Hirayama et al.: Report SLAC-265 (1985)
8. C.M. Ma: *Monte Carlo simulation of dosimeter response using transputers*. Thesis (London University, London 1991)
9. A.F. Bielajew and D.W.O. Rogers: Nucl. Instr. and Meth. **B18**, 165 (1987)
10. J. Sempau: *Development and applications of a computer code for Monte Carlo simulation of electron-photon showers*. Thesis (Barcelona University, Barcelona 1995)
11. W.S. Snyder, M.R. Ford et al.: *Estimates of specific absorbed fractions for photon sources uniformly distributed in various organs of a heterogeneous phantom*, MIRD pamphlet no. 5 revised (The Society of Nuclear Medicine 1978)

Application of Numerical Phantoms and MCNP Calculation for In Vivo Calibration

D. Franck, N.M. Borisov, and L. Laval

Institut de Protection et de Sûreté Nucléaire, rue Auguste Lemaire, BP 6,
Fontenay-aux-Roses, F92265 France

Abstract. The paper reports on development of numeric phantoms for Monte Carlo calculations for in vivo measurements of radionuclides deposited in tissues. The individual properties of each person require rather precise geometric representations. It is particularly important for low energy gamma ray emitting sources as thorium, uranium, plutonium and other actinides. The new utility which allows automatic creation of MCNP initial file from individual scanning information, was developed. It includes segmentation of voxel matrix, obtained with computer tomography, for distinguishing tissues by level of brightness, association colors with certain tissues, source and detector specification and, finally, voxel coupling to reduce the consumed memory and increase speed of calculations.

Although great efforts have been made to improve the physical phantoms used to calibrate in vivo measurement systems, these phantoms represent a single average counting geometry and usually contain a uniform distribution of the radionuclide over the tissue substitute. As a matter of fact, significant corrections must be made to phantom-based calibration factors in order to obtain absolute calibration efficiencies applicable to a given individual. The importance of these corrections is particularly crucial by considering in vivo measurements of low energy photon emitting radionuclides deposited in the lung such as actinides. Thus, it is desirable to develop a method for calibrating in vivo measurement systems that is more sensitive to these types of variability.

The crucial point is to use individual scanning data for creating a person-specified numeric phantom which will be both adequately representing the body structure and allowing three-dimensional transport calculations. Such calculations in real geometry without any restrictions can be done practically only with Monte Carlo method which is rather time-consuming. Previous works [1,2] have demonstrated the possibility of such a calibration using the Monte Carlo technique (MCNP code). Unfortunately, they use rough resolution images for numeric phantoms due to memory capacity and calculation speed restrictions.

Our research program extended such investigations to the reconstruction of numeric adequate anthropomorphic phantoms with the highest possible resolution based on personal physiological data. For automatization of preparation process for initial MCNP file we developed a special utility named *Anthropo* based on PV-Wave[®] visual data analysis developer's system. It can be run both on Intel[®] and DEC Alpha[®] platforms under MS Windows[®] and UNIX systems respectively. The visual representation of input and output data of *Anthropo* is

shown on Fig. 1. Input data describes the three-dimensional voxel matrix, different slides of this matrix are presented in the left part of the figure. Different colors represent different levels of brightness of the image. On the right side of the figure there is shown Sabrina[®] visualization of MCNP geometry, restored by our utility after segmentation and MCNP file creation. Different colors represent different materials associated with geometrical zones. Also our utility specify the source and the detector for MCNP calculations.

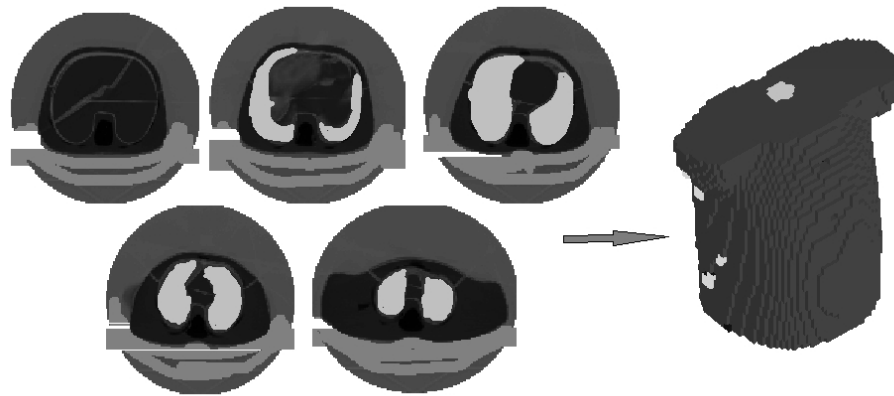


Fig. 1. Input and output data for *Anthro* utility

Before segmentation it is possible to decrease the resolution of the image and to cut margins of each slide which can contain several artifacts. The segmentation itself does distinguish tissue from tissue by brightness level for given level boundaries, improve the homogeneity of segmented image with erosion and dilatation procedures and, finally, associate colors with tissues. The segmentation window is shown on Fig. 2. The upper left window represents slices of the original CT image, the lower left window — of the segmented image with several large areas with uniform color. The histogram at upper right corner shows the brightness profile of current slide, clearly showing peaks corresponding to bones, lungs, soft tissues and external air.

From this point it is possible to specify sources: on the user's choice either point source, specifying the contamination points by mouse-clicking and visualizing in the window shown at the lower part of Fig. 3, or source distributed through the tissue. The user can choose either a certain nuclide from the menu shown in upper figure, or compose the custom set of energies and quantum release factors as it is shown in the upper part Fig. 3. The total activity and time of measurement can be also specified from the proper window.

Then the user can specify the proper detector (we involved three types of germanium detectors and one type of silicon detector). After choosing the detector can be placed to proper position and oriented properly (see Fig. 4).

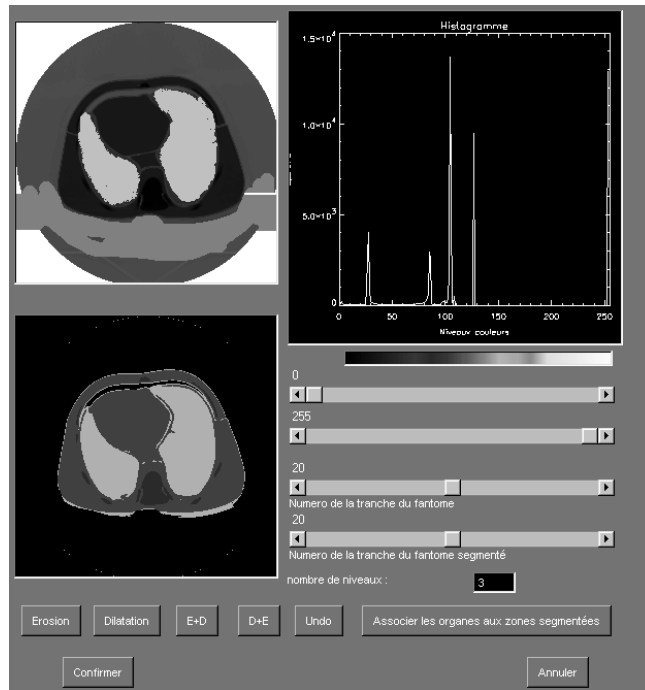


Fig. 2. Segmentation window

Finally, the data can be written as initial MCNP file to calculate pulse-height-spectrum in the detector. To take advantage of high-resolution images we developed the procedure of coupling the neighboring voxels with the same density and material to unitary MCNP cells. For internal MCNP reason the primitive solids constructing the cells must not be scooped and that means that only rectangular boxes can be used as three-dimensional coupled cells. Also we provided the procedure of one-dimensional coupling in which only neighbors along one axis can be coupled. The difference between coupled and non-coupled cell representation of MCNP file is shown on Fig. 5 . Different colors represent different cells.

The advantage of voxel coupling procedure is shown in Tab. 1, where the comparison of cell numbers both for rough ($32 \times 32 \times 17$ voxels) and realistically high ($128 \times 128 \times 40$ voxels) resolution phantoms is done. The number of cells for high resolution without voxel coupling exceeds the maximal possible number for MCNP, so any calculations are absolutely impossible. Also the table contains the data on required computation time for one random story produced by lung ^{241}Am source located in lungs for DEC Alpha[®] professional workstation (frequency 1 GHz, memory 512 Mb) and (in parentheses) Intel Pentium[®] III PC (frequency 400 MHz, memory 64 Mb). Voxel coupling allows decreasing of memory capacity and calculation time by an order. This advantage is more essential

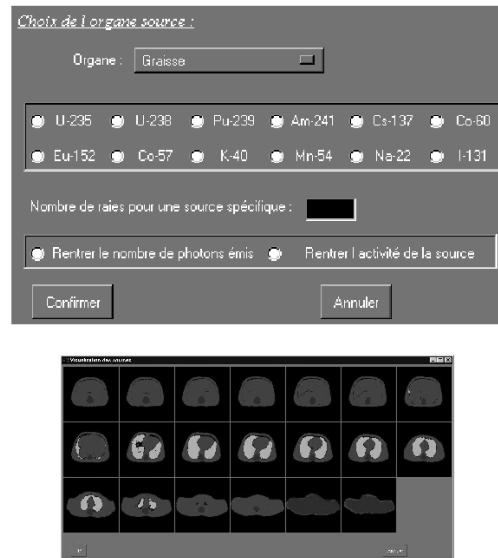


Fig. 3. Source specification windows

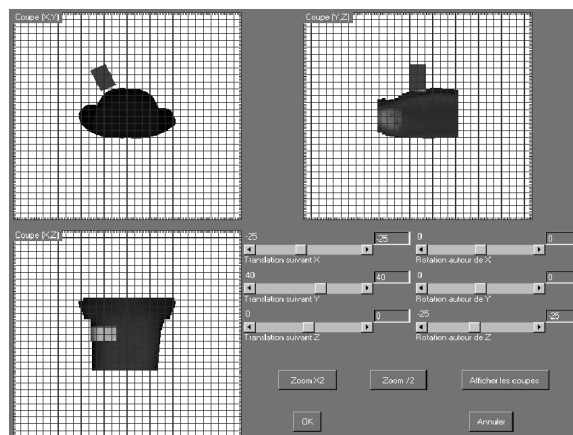


Fig. 4. Detector placement window

for distributed source calculation, when the computation time for high-resolution phantom and even coupled voxel cells takes a day or more.

The comparison of calculated spectrum with experimentally measured for uniform lung contamination of ^{241}Am is shown in Fig. 6. Experimental data

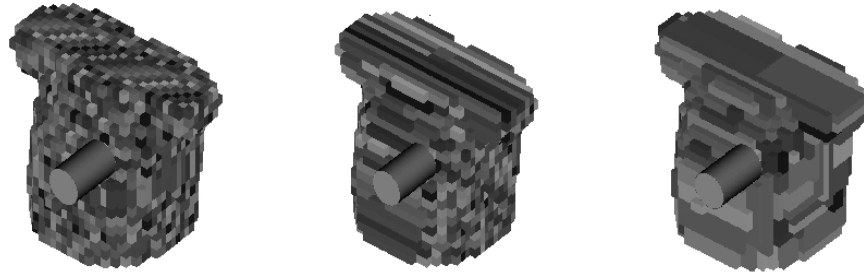


Fig. 5. Voxel coupling. From left to right: no coupling, one-dimensional coupling, three-dimensional coupling

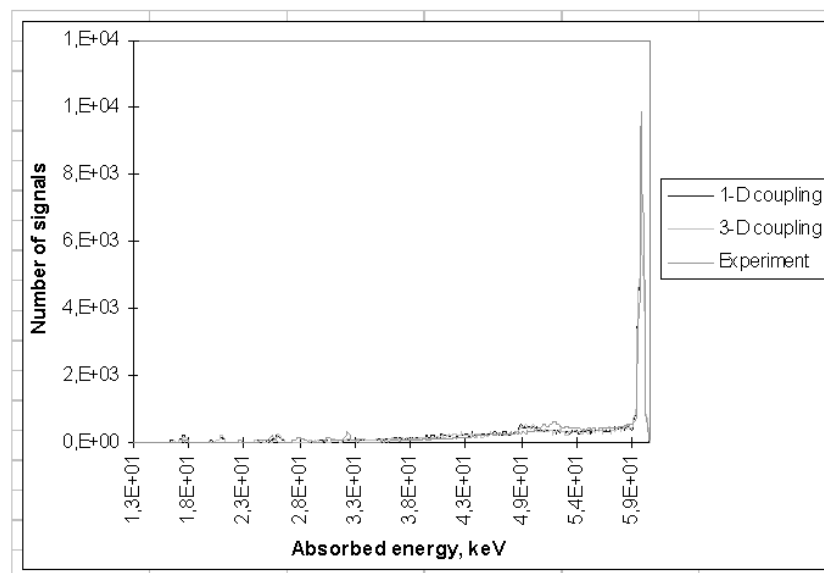


Fig. 6. Comparison of experimental and MCNP pulse-height-spectrum

(medium darkness line) show the good consistence with simulation (bright and dark lines) both in full absorption peak of the most powerful ^{241}Am line and in Compton scattering area.

Other point of current development of the utility is to involve MRI images for numeric phantom reconstruction because such images do not require radiation exposure and are more precise, but less convenient for distinguishing organs and tissues by colors. Now some real measurements for comparison with MRI-based numerical phantom data are planning.

Table 1. Number of cells/Computation time for one random story with ^{241}Am lung source, 10^{-6} min

	No coupling	1-D coupling	3-D coupling
Rough resolution	6468/157.0(484.9)	1466/36.1(111.5)	448/14.6(45.1)
High resolution	—	11389/281.7(886.9)	4437/106.7(329.6)

References

1. M.W. Mallet et al.: Health Physics, **68**, 773 (1995)
2. D. Franck et al.: Radioprotection (accepted for publication)

Use of Monte Carlo Method in Support of Medical Applications of Radiation

N. Cerullo¹, G. Curzio², G. Daquino³, and A. Mariani²

¹ DITEC, University of Genova, Via All'Opera Pia 15/A, I-16145 Genova, Italy

² DIMNP, University of Pisa, Via Diotisalvi 2, I-56100 Pisa, Italy

³ LNGS, National Institute for Nuclear Physics, S.S. 17/bis km 18.910 I-67010 Assergi (AQ), Italy

Abstract. The first application concerned the simulation of a PET Tomograph performing a fine analysis of the photon spurious events, namely scattering and multiple coincidences, in order to obtain correction factors to apply to image reconstruction [1,2].

Following the PET experiences we have applied this computing tool to BNCT in evaluating the tumour and healthy tissue dose ratio after the neutron irradiation. This procedure allowed to create an original TPS, to be used in BNCT [3–5]. Furthermore, other work was done on the Monte Carlo evaluation of the detection efficiency of a particular superheated drop neutron detector [6].

1 Introduction

Calculation based on Monte Carlo method may often be the only means to explore phenomena requiring coupling of multiple physical events. This is the case of simulation of physical situations that we can find in the medical activities, particularly the diagnostic systems. We can add the statement that often Monte Carlo simulation can give information that cannot be reached in the experimental way. This is the case of PET (Positron Emission Tomography) and of BNCT (Boron Neutron Capture Therapy). In the former case the simulation allows to check and to perform the correction algorithms. Besides, in the latter case, we can reach higher precision in evaluating the tumour and tissue dose distribution. Some years ago, our research group, previously involved in use of MC in the field of the nuclear power plants evaluation, design and shielding decided to apply the acquired experience to the simulation of the radiation behaviour in support to some Medical Applications.

The MCNP is the more experienced Monte Carlo code in the research community (since by 1940) and is being continuously updated.

2 PET Simulation

Positron Emission Tomography (PET) is a quantitative and not invasive diagnostic method for the study of the biochemistry and of the metabolism: it furnishes an assessment of the concentration of a particular radioisotope, previously inserted in an organ. This process is based on the measurement of the

emitted radiation from several angles. The study of the relationships between the imaging properties of a positron tomograph and the set up variables is difficult.

The availability of the modern Monte Carlo codes, like MCNP, has induced our group to use the great possibilities of this program for the PET simulation. To this purpose new original options have been created.

The work performed at Pisa University, in collaboration with IFC-CNR of Pisa, has allowed to show the possibility to simulate, through adequate codes [1], the PET processing, following all the steps. In fact the MCNP-4A code is able to simulate the physics of the problem; therefore we can reconstruct the image utilising its outputs, in the same way followed by the real tomograph software. In addition we can also operate a filter action, because it is possible to establish the noise due to scattering, multiple coincidences, detectors efficiency and so on. This particularity will allow in the future to have diagnostic systems more and more efficient. The work on the PET simulation consists principally on three steps:

1. *The simulation of the photons emission through the MCNP-4A code through the addition in the code of an original subroutine(POSITRON);*
2. *The simulation of the PET acquisition through particular programs, ad hoc originated (DEIMOS);*
3. *Data analysis and image reconstruction.*

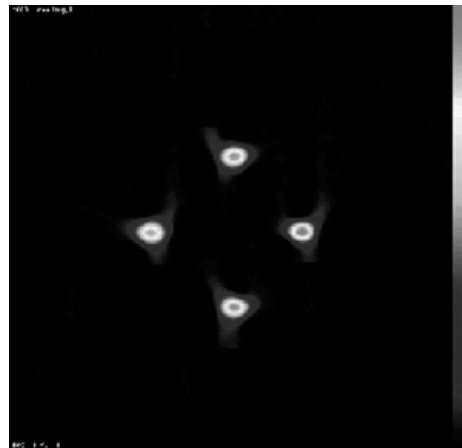


Fig. 1. Image reconstruction of the four spherical sources

To test the system operations, different simulations have been performed, and an image reconstruction using the tomograph software have been done. In Fig. 1 also the image reconstruction of the simulation of four spherical sources, obtained through the software of the ECAT III tomograph, is represented as well.

3 BNCT Treatment Planning System (TPS)

Immediately after the discovery of neutrons by Chadwick in 1932, Locher proposed the general concept of NCT and, subsequently, Sweet proposed BNCT application to treat intracranial tumours. Despite significant difficulties encountered in early US trials, NCT has continued to be of expanding interest worldwide, especially because of the encouraging results obtained by researchers in Japan.

In NCT, a neutron capture agent (^{10}B in current practice) is inserted into the malignant tissue after the administration of a suitable boronated drug. When the boron reaches the max concentration value in the tumour tissue, the treatment volume is exposed to a field of epithermal neutrons, produced by small nuclear reactors or by suitable accelerator facilities. The neutrons interact with the ^{10}B nucleus that has a very high thermal cross section and which, should be present only in the tumour zone. This nuclear reaction emits an α particle and a ^7Li recoil nucleus, both particles characterised by a high LET. In this way a high selective tumour cell killing, saving the surrounding healthy tissue, is obtained.

A lot of effort has been devoted in order to be able to predict the doses associated to a patient treatment through suitable Treatment Planning Systems (TPS). A flow sheet of TPS is represented in Fig. 2.

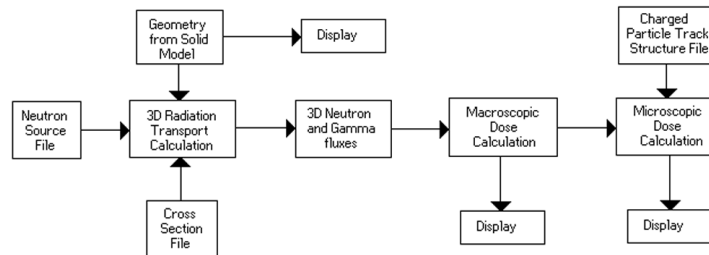


Fig. 2. Flow diagram showing BNCT neutron transport and dosimetric analysis

The TPSs are normally focused on the macrodosimetric analysis of the dose distribution in the human head, following an uniform boron distribution description. Nevertheless, an accurate microdosimetric analysis is very important because, for certain types of nuclear reactions, as the boron one, the dose distribution is dramatically dependent upon the exact positioning of the boron nucleus in the cell.

The core of a TPS is the module for the calculation of the solution of the 3D Boltzmann transport equation for neutrons, given certain descriptive information as input. Among these descriptive informations, it is important to point out:

1. *the geometric model of the irradiation volume;*
2. *a mathematical description of the treatment beam, namely intensity and spectral shape;*

3. *a complete set of coupled neutron and photon interaction cross section data for all significant elements in the irradiation volume.*

As regards the calculation methods used to evaluate the particle transport into the matter, the Monte Carlo method, which is based on the *simulation* of the particle history during its path in the matter, has been largely used. This technique can provide very detailed spatial dose distributions and dose-volume histogram information as well as other types of integral data of interest.

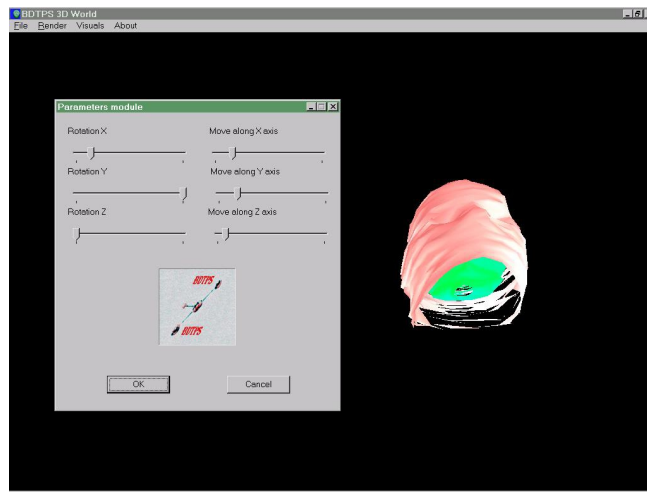


Fig. 3. Dialog Box related to the parameters change and the patient head in BDTPS

Our research group has involved a lot of effort trying to develop a new TPS, which must be able to consider the **real** macroscopic boron distribution, that should be obtained through PET or MRI analysis of the patient head. This TPS was called CARONTE in its first version.

More recently, CARONTE has been upgraded on the basis of the past experience in the same field [3–5] and in the PET analysis, by Monte Carlo technique (MCNP code). In this way **BDTPS** (**Boron Distribution Treatment Planning System**) [7] has been implemented.

4 MC Guided Experimental Tests

Confidence in MC calculations may ask support from comparison with experimental data when they can be obtained in the same assembly studied by MC code. Several problems of this type were faced in supporting our BNCT activities. Two kinds of detection methods were developed and used: the first one employs superheated drop detectors (SDD) for patient neutron dosimetry and spectral characterization of neutron fluxes and the second uses classical sandwich activation detectors for the thermal and epithermal flux measurement. In

each case the response of the detection system to the neutron flux as a function of the beam characteristics (energy and angular distribution) was evaluated on the basis of MC calculation and verified with standardized neutron sources and beams.

SDD (or bubble detectors) employ a wide variety of halocarbon droplets and emulsifier gel combinations, all sharing the same fundamental properties. The metastable droplets vaporize in bubbles when they are nucleated by the energy deposition from charged particles generated by neutron interactions. Bubbles can be recorded by counting the acoustic pulses arising from the explosive boiling as well as optically or through volume variation of the emulsion. Dichlorofluoromethane (R-12) is sensitive to slow neutrons through the $^{35}\text{Cl}(n,p)^{35}\text{S}$ reaction and to fast neutrons through recoils from scattering reactions. Several experimental determinations of the detector sensitivity at neutron energies up to 20 MeV and Monte Carlo calculations by MCNP code, in the energy range where no reference sources are available (epithermal energies), showed that a proper choice of the working temperature makes the response of the detector suitable for personal dose measurements [6]. Neutron patient dosimetry was performed at the Brookhaven BNCT facility by SDD's on a phantom out of the irradiation field. Comparison of the obtained value with MC calculation is in progress.

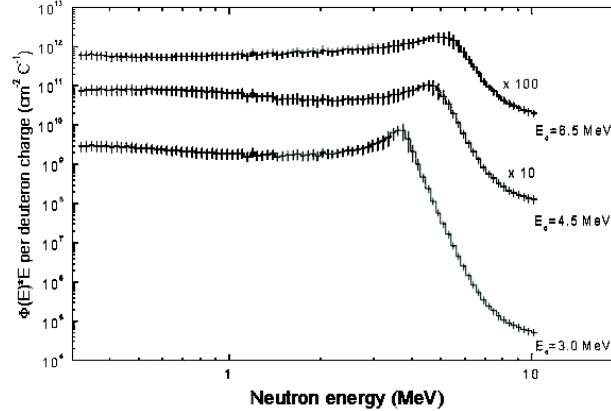


Fig. 4. Energy spectrum obtained by SSD for BNCT accelerator based source at LNL

The SDD may be used also for fast neutron spectrometry. In this case the superheated liquid in the SDD's doesn't contain chlorine. The energy threshold of sensibility depends on the working temperature and liquid characteristics (boiling and critical temperature). Therefore, varying these parameters, it is possible to choose appropriate energy thresholds. The neutron energy spectra may be obtained through unfolding codes. Fig. 4 shows the energy spectrum we obtained [8] at the experimental structure of the accelerator based neutron

source for the BNCT of skin melanoma installed at the Van de Graaf accelerator of the Laboratori Nazionali di Legnaro (Italy).

Standard activation detectors may be efficiently used for thermal and epithermal flux measurements. In case of neutron sources for BNCT of deep tumor treatment, the shape of the epithermal spectrum plays an important role in treatment planning and it would be important to confirm the outputs of MC calculations. A classic method [9] with a particularly selective sensitivity to neutron energy employs sandwiches of foils of resonance detectors (In, Au, W, etc.). The method was successfully tested in a laboratory irradiation rig with two moderated 200 mCi AmBe neutron sources. Measured and calculated fluxes give values within the experimental statistical uncertainties.

All the exposed methods will be used in the next months at the BNCT experimental source we have designed, that is being assembled at the TAPIRO research reactor of ENEA Casaccia (Rome).

References

1. N. Cerullo, M. Bogliardi, R. Guzzardi, P. Riscossa: 'Petsi, a package based on Monte Carlo Techniques to simulate the Positron Emission Tomography'. In: *Advanced Monte Carlo Computer Programs for Radiation Transport, Nuclear Energy Agency, OECD-NEA Saclay (France) 27-29 April 1993* pp. 341-345
2. A. Mariani, N. Cerullo, G. Curzio, R. Guzzardi, R. Plenteda: 'Positron Emission Tomography Simulation Using MCNP-4a Code'. In: *European Radiation Research '98 - Capri (Italy) 3-7 October 1998*
3. N. Cerullo, G. Daquino: 'Use of Monte Carlo code in neutrons behaviour simulation in BNCT (Boron Neutron Capture Therapy)'. In: *Technologies for the New Century, ANS, Nashville (TN), 19-23 April 1998* pp. II-236-243
4. N. Cerullo, G. Daquino: 'Tumour and Healthy Tissues Dose Calculation Using Monte Carlo Code and PET Information on Boron Distribution in Tissues'. In: *Boron Neutron Capture Therapy, Oncological, Radiobiological, Chemical and Radiation Physics Aspects in the BNCT Technique. Present and Future in Italy, G. Tornielli ed., INFN Acts, Padova (Italy), February 24-25, 1998* pp. 55-62
5. N. Cerullo, G. Daquino: 'CARONTE. A Treatment Planning System Based on Real Macroscopic Boron Distribution and MCNP-4A Code: Results and Discussion'. In: *Frontiers in Neutron Capture Therapy - "Eight International Symposium on Neutron Capture Therapy", La Jolla (CA), Plenum Press, New York, September 13-18 1999* to be published
6. G.F. Gualdrini, F. d'Errico, P. Noccioni: *Radiation Protection Dosimetry* **65**, 397 (1996)
7. N. Cerullo, G. Daquino, J. Esposito: 'The Real ^{10}B Macro-Distribution in Treatment Planning System'. In: *Proceeding of Ninth International Symposium on Neutron Capture Therapy for Cancer, Osaka (Japan), October 2-6 2000* to be presented
8. S. Agosteo, G. Curzio, F. d'Errico, R. Tinti: 'Characterization of an accelerator based neutron source for BNCT versus beam energy'. In: *Int. Workshop on Neutron Field Spectrometry in Science, Technology and Radiation Protection, Pisa (Italy) 4-8 June 2000* to be published
9. K.H. Beckurst, K. Wirtz: *Neutron Physics* (Springer Verlag, New York 1964)

Intra-Operative Radiation Therapy Optimization Using the Monte Carlo Method

M. Rosetti¹, M. Benassi², V. Bruzzaniti³, A. Bufacchi², and M. D'Andrea²

¹ ENEA, Via Don Fiammelli 2, 40129 Bologna, Italy

² Istituto Regina Elena, Via Delle Messi D' Oro 156, 00158 Rome, Italy

³ ENEA, Via Anguillarese 301, 00060 S. Maria di Galeria (Rome), Italy

1 Introduction

Intra-Operative Radiation Therapy (IORT) [1] is an innovative cancer treatment technique which consists in delivering during a surgical operation a radiation dose on the order of 10–20 Gy to a tumor bed or to a tumor residual after the resection. In this way it is possible to destroy the residual malignant cells. IORT is generally performed by means of electron beams produced by linear accelerators (linacs) in the range 3–12 MeV.

As in the case with any kind of radiotherapy it is important that the dose delivered to the target volume be well-known and as uniform as possible. To achieve this aim it is essential to optimize both the treatment head design and the Treatment Planning System (TPS). The treatment head is the assembly which follows the exit window of the accelerator tube whereas the TPS is the software system which allows to calculate the dose distribution inside the patient. The present paper describes the work done on the subject using the Monte Carlo code system OMEGA-BEAM; the study has been performed in the framework of ENEA's IORT project funded by MURST, the Italian Ministry of University and of Scientific and Technological Research.

The problem addressed with reference to the treatment head optimization has been the choice of the proper design of the head of a new 12 MeV linear accelerator in order to have the required dose uniformity on the target volume while keeping the dose rate sufficiently high and the photon production and the beam impact with the head walls within acceptable limits. The second part of the optimization work, concerning the TPS, is based on the rationale that the TPSs generally used in radiotherapy use semi-empirical algorithms whose accuracy can be inadequate particularly when irregular surfaces and/or inhomogeneities, such as air cavities or bone, are present. The Monte Carlo method, on the contrary, is capable of accurately calculating the dose distribution under almost all circumstances. Furthermore it offers the advantage of allowing to start the simulation of the radiation transport in the patient from the beam data obtained with the transport through the specific treatment head used. Therefore the Monte Carlo simulations, which at present are not yet widely used for routine treatment planning due to the required computing time, can be employed as a benchmark and as an optimization tool for conventional TPSs.

2 Materials and Methods

2.1 The Linear Accelerators and the Treatment Heads

The present work refers to two linacs which are produced by Hitesys S.p.A., Aprilia, Italy. The first one, IORT Novac7, accelerates electrons up to 9 MeV nominal energy, whereas the second one, IORT-ENEA, is in a developmental stage and will accelerate electrons up to 12 MeV.

The treatment heads of both accelerators have cylindrical symmetry. The beam is collimated to the target volume by applicators which in Novac7 have internal diameters up to 10 cm, lengths up to 87 cm and Perspex walls 0.5 cm thick. The applicator set includes both unbeveled and beveled ends, with 15°, 30° and 45° bevel angles, to treat sloping surfaces.

2.2 The OMEGA-BEAM Monte Carlo System

The OMEGA-BEAM software, which is based on the EGS4 Monte Carlo system [2], has two main components, BEAM and DOSXYZ. BEAM [3] simulates the electron-photon transport through the linac treatment head; this is modeled by means of a series of individual component modules (CM), each of which occupies a slab at right angles to the beam axis. BEAM is able to produce a phase-space output file of the beam (i.e. the position, energy, direction, charge and history tag for each particle) at the back plane of any CM. The phase-space file can either be re-used by BEAM itself to simulate the radiation transport through a downstream head part or used as an input to DOSXYZ, i.e. the phantom dose computation code. DOSXYZ simulates the electron-photon transport in a Cartesian volume and scores the dose in the specified voxels. To each voxel the material and density data obtained with Computed Tomography (CT) scans can be assigned.

2.3 The Modeling and the Monte Carlo Simulation

The IORT treatment head has been divided in 5 sections modeled by means of the FLATFILT CM. As in every CM the scoring plane is perpendicular to the head axis whereas the beveled applicators require a scoring plane oblique to this axis, it has been necessary to modify FLATFILT. A scoring plane with variable obliquity angle has been introduced into the HOWFAR geometry routine of FLATFILT and it has been allowed for the calculation of the distance of the transported particle from the current position to this plane along the motion direction. When a step has to be taken, this distance is compared to USTEP, the requested step length, and to the particle distance from the next region along the motion direction; if it results to be the smallest of the three the particle is transported to the oblique plane, its parameters are scored and its transport terminated. An axis rotation is performed before scoring the particle parameters in order to set the Z axis, i.e. the dose reference axis, perpendicular to the exit surface of the beveled applicator. This is necessary for the subsequent

simulation with DOSXYZ as the information which is clinically relevant is the dose calculated with reference to an axis perpendicular to the phantom surface. As HOWFAR is called only when USTEP is larger than DNEAR, the lower bound of the particle distance from the nearest region boundary, the calculation of DNEAR has been modified to take into account the oblique plane as well.

Furthermore, as electron impacts damage the head walls, a counter has been introduced in the HOWFAR routine of FLATFILT to calculate the amount of these impacts with the narrowest head part.

The electron source has been specified with the energy spectrum, radial distribution and divergence obtained by means of beam dynamics simulations.

The cutoff energy for electron transport, ECUT, has been set at 0.700 MeV corresponding to 0.189 MeV kinetic energy, whereas that for photon transport, PCUT, has been set at 0.010 MeV. PRESTA (Parameter Reduced Electron Step Transport Algorithm) has been used in all the calculations.

The statistical uncertainty of the simulations has been kept better than 1 %.

3 Results

3.1 Treatment Head Optimization

The improvement of the dose uniformity for the head of the new 12 MeV linac has been obtained increasing the thickness of the titanium exit window and the Perspex applicator length; the former modification has the side effect of increasing the bremsstrahlung production and the beam impact with the head walls and both of them of diminishing the dose rate. The uniformity index (u.i.) has been calculated according to the following expression:

$$u.i. = 100 \cdot \frac{D_{\max} - D_{\min}}{D_{\max} + D_{\min}} \% \quad (1)$$

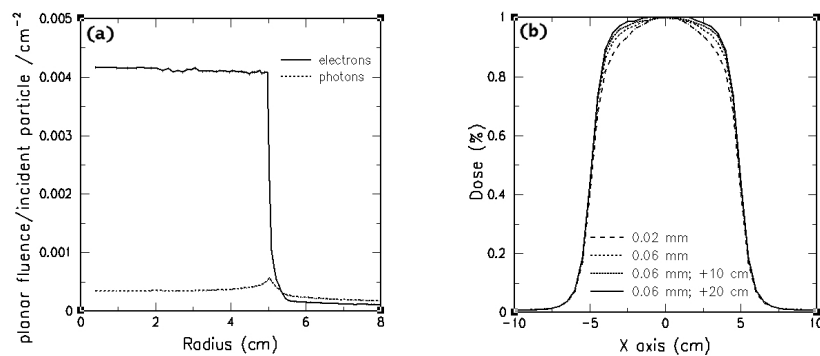
where D_{\max} and D_{\min} are respectively the maximum and the minimum value of the dose inside a circle whose diameter is 80 % of the field width. The uniformity has been determined in correspondence of the depth of the dose maximum. The aim of the optimization work has been to obtain an uniformity index lower than 5 %. Another constraint came from the fact the applicator length increase could not exceed 20 cm, due to the necessity of limiting the overall dimensions of the linac, which has to be housed in standard operating rooms.

The starting configuration had a 0.02 mm thick titanium window and a 87 cm long applicator. The applicator radius was of 5 cm. The calculations have involved the simulation of the radiation transport through various treatment head configurations with the BEAM code and subsequently in a water phantom with the DOSXYZ code. The dose rate has been evaluated considering the maximum of the dose per primary electron (e_p^-) whereas the photon production has been evaluated as the percentage of the maximum photon dose with respect to the maximum total dose. The percentage of electron impacts per primary electron with the head walls in correspondence of the narrowest head part of 0.65 cm

Table 1. Results of the simulations for the optimization of a 12 MeV linac head. In the linac operating conditions $1 \cdot 10^{-12} \text{ Gy/e}_p^-$ corresponds to 8.1 Gy/min

Window thickness (mm)	Additional appl. length (cm)	Uniformity index (%)	Dose rate (Gy/e_p^-)	Photon product. (%)	Wall impacts (%)
0.02	0.0	9.08	$2.40 \cdot 10^{-12}$	0.06	0.49
0.04	0.0	7.90	$2.18 \cdot 10^{-12}$	0.07	0.69
0.04	5.0	7.14	$2.02 \cdot 10^{-12}$	0.07	0.69
0.04	10.0	6.36	$1.86 \cdot 10^{-12}$	0.07	0.69
0.04	15.0	5.65	$1.72 \cdot 10^{-12}$	0.08	0.69
0.04	20.0	5.49	$1.61 \cdot 10^{-12}$	0.08	0.69
0.06	0.0	6.71	$1.95 \cdot 10^{-12}$	0.07	0.92
0.06	5.0	5.67	$1.80 \cdot 10^{-12}$	0.08	0.92
0.06	10.0	5.36	$1.68 \cdot 10^{-12}$	0.08	0.92
0.06	15.0	5.07	$1.56 \cdot 10^{-12}$	0.09	0.92
0.06	20.0	4.64	$1.44 \cdot 10^{-12}$	0.09	0.92
0.08	0.0	5.78	$1.76 \cdot 10^{-12}$	0.08	1.17
0.08	5.0	5.56	$1.64 \cdot 10^{-12}$	0.08	1.17
0.08	10.0	4.90	$1.52 \cdot 10^{-12}$	0.09	1.17
0.08	15.0	4.79	$1.40 \cdot 10^{-12}$	0.09	1.17
0.08	20.0	4.32	$1.30 \cdot 10^{-12}$	0.10	1.17

radius has been evaluated as well. The results, reported in Tab. 1, allow to conclude that the best compromise is given by a window thickness of 0.06 mm and an additional applicator length of 20 cm. In fact this configuration allow to have an uniformity index lower than 5 %, fewer impacts with the walls than in the case of the other possible choices, a dose rate sufficiently high and an acceptable photon production. Figure 1 reports some examples of the simulations.

**Fig. 1.** (a) Fluence vs. radius for the optimized head at the exit of the 5 cm radius applicator. (b) Dose profiles perpendicular to the beam axis in a water phantom at the depth of the dose maximum, for different window thicknesses and additional applicator lengths

3.2 Treatment Planning System Optimization

The treatment planning systems for IORT are still in a developmental stage. At Istituto Regina Elena hospital, Rome, an IORT TPS is being developed according to the Hogstrom algorithm [4]. The comparison between the depth dose distributions in a water phantom calculated with this algorithm and with the Monte Carlo method shows a good agreement. However the comparison of the dose profiles perpendicular to the beam axis shows a significant difference (see Fig. 2). This reveals the necessity of improving the dose computation algorithm. The related work is in progress.

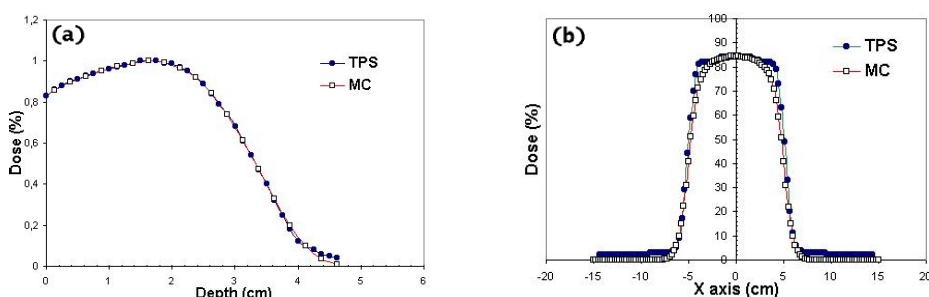


Fig. 2. 9 MeV dose calculations in a water phantom with both TPS and Monte Carlo. (a) Percentage depth dose distribution. (b) Dose profile at 2.6 cm depth

To test thoroughly the modifications of the algorithm, Monte Carlo simulations have been performed in the most challenging irradiation conditions for these algorithms, i.e. those with beveled applicators and with the presence of inhomogeneities such as bone and lung. Some results for a 9 MeV beam are re-

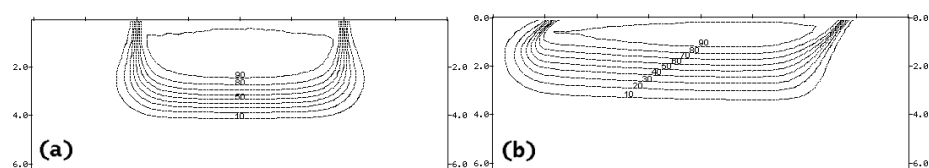


Fig. 3. Isodose curves. (a) With unbeveled applicator. (b) With 45° beveled applicator

ported in Figs. 3 and 4. To the same purpose isodose curves have been calculated in anthropomorphic phantoms obtained from CT scans of patients. An example referring to a beveled applicator is given in Fig. 5.

4 Conclusions

The treatment head of a new 12 MeV linac for IORT has been optimized by means of Monte Carlo simulations. To perform the same optimization without

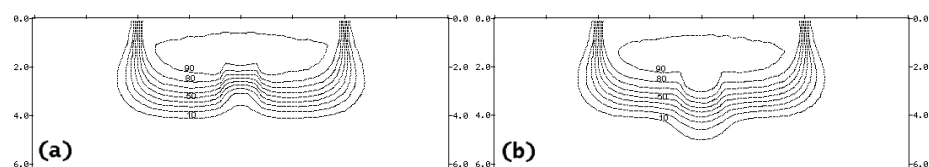


Fig. 4. Isodose curves with the presence of an inhomogeneity consisting in a cube of 1.75 cm side placed at 1.5 cm depth. (a) Bone inhomogeneity. (b) Lung inhomogeneity

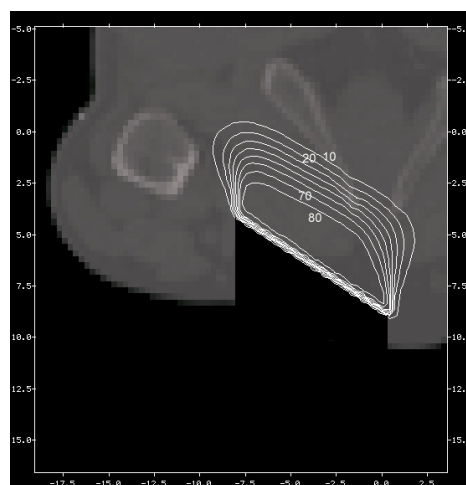


Fig. 5. Isodose curves in an CT phantom, representing an abdomen, irradiated by a 12 MeV beam by means of the optimized treatment head. A 30° beveled applicator has been considered. The surgical opening is shown

Monte Carlo would have required to fabricate various modifications of the apparatus and to perform laborious measurements. Furthermore the Monte Carlo simulations have revealed the necessity of improving the IORT dose computation algorithm; simulations in the most challenging irradiation conditions have been performed to provide benchmarks for the algorithm improvement work. The OMEGA-BEAM code system has proved to be an excellent tool for the described optimization work.

References

1. J.M. Vaeth (Ed.): *Intraoperative Radiation Therapy in the Treatment of Cancer* (Karger, Basel 1997)
2. W.R. Nelson, H. Hirayama, D.W. Rogers: *The EGS4 Code System*, Stanford Linear Accelerator Center Report SLAC-265, Stanford, CA (1985)
3. D.W. Rogers, B.A. Faddegon, G.X. Ding, C.M. Ma, J. We, T.R. Mackie: *Med. Phys.* **22**, 503 (1995)
4. K.R. Hogstrom, M.D. Mills, P.R. Almond: *Phys. Med. Biol.* **26**, 445 (1981)

Coupling Photon Monte Carlo Simulation and CAD Software. Application to X-ray Nondestructive Evaluation

J. Tabary and A. Glière

LETI - CEA Technologies Avancées, F-38054 Grenoble, France

Abstract. A Monte Carlo radiation transport simulation program, EGS Nova, and a Computer Aided Design software, BRL-CAD, have been coupled within the framework of Sindbad, a Nondestructive Evaluation (NDE) simulation system. In its current status, the program is very valuable in a NDE laboratory context, as it helps simulate the images due to the uncollided and scattered photon fluxes in a single NDE software environment, without having to switch to a Monte Carlo code parameters set. Numerical validations show a good agreement with EGS4 computed and published data. As the program's major drawback is the execution time, computational efficiency improvements are foreseen.

1 Introduction

A wide range of applications of numerical simulation have been pointed out in the field of X-ray Nondestructive Evaluation (NDE). These applications are as diverse as assistance to X-ray hardware designers, help in validation of inspection procedures, defect detectability assessment, operators education and training, etc. Designers of digital processing techniques, such as tomography, tomosynthesis and automated defect detection can also take advantage of realistic simulated images.

The necessity to have fast and practical software tools at disposal lead, during the last decade, to the development of solutions based on Computer Aided Design (CAD) model of the examined part and Graphical User Interface (GUI). In a first stage, analytical models using ray tracing techniques were developed in order to address the straightforward problem of the uncollided flux (i.e. the flux of photons which have not been subjected to any interaction inside the examined part) computation [1–4].

However, a X-ray radiographic image is generated by both uncollided photons and photons scattered inside the examined part. The latter phenomena is a major source of unwanted noise which accounts, in usual NDE conditions, from a few percent to more than half the overall measured intensity. Quantitative evaluation of the scattered flux is therefore of primary interest, for instance to correctly evaluate flaw detectability. In order to address this problem, several approaches have been proposed, ranging from rough approximations, such as build up factors to sophisticated numerical procedures solving integral transport equations [5]. Solutions based on the Monte Carlo method have also been implemented [6,7] but the lack of flexibility in the description of the examined

part and experimental setup and the relatively long execution time have, to date, prevented a widespread use.

As desktop computers power increases continually and variance reduction techniques can drastically improve calculation efficiency, we decided to couple, within a NDE simulation system called Sindbad, a Monte Carlo radiation transport simulation code with a CAD and ray tracing package. This provides the simulation of photon scattering inside the examined part with the established accuracy of the Monte Carlo method and the mechanical parts design flexibility of CAD solid modelers.

This paper first presents an overview of the models used by the NDE simulation software in order to compute the radiographic image due to the uncollided flux. It focuses in a second part on the use of the CAD model of the examined part and a Monte Carlo simulation to compute the image due to the scattered flux. A validation of the model is then established by comparison with published data. At last, an example of application is presented.

2 Presentation of the Pre-existing NDE Analytical Simulation Package

The physics of the radiographic inspection process can be divided into three separate parts, namely the photon beam generation in the X-ray source, the beam interaction with the examined part, and the imaging process (detection of the remaining photon flux and transformation into a measured signal). They have been addressed as follows in the Sindbad NDE simulation package.

The X-ray tube model semi-empirically simulates the physical phenomena involved in bremsstrahlung and characteristic photons production. It takes into account the anode angle and composition and the inherent and additional filtration. It can be used in the range 30–450 kV. Experiments, previously performed in CEA-LETI experimental facility, show an agreement usually better than 20% between calculated and measured doses.

The uncollided flux analytical simulation relies on the computation of the attenuation of the incident flux, binned in narrow energy channels, by the examined part. This is performed by tracing rays from the source point to every pixel of the detector through the part CAD model, built with BRL-CAD [8], a Constructive Solid Geometry based CAD and ray tracing package, and by calculating the energy dependent attenuation due to the crossed materials. The attenuation coefficients are those described in Storm–Israël data tables [9]. Cross sections for compounds or mixed materials are obtained by linear combination of elemental data.

Detectors are modeled in two successive steps. The first one, common to all types of detectors, computes the energy deposition in the sensing part of the detector, using the energy absorption attenuation coefficients. The second stage, specific to each type of detector, simulates the successive physical phenomena involved in the energy to signal transformation. For instance, in the case of a scintillating screen viewed by a CCD camera, it accounts for energy to light

photons transformation, light photon absorption in the screen and optical coupling system, and photon to electron conversion in the CCD device. Noise and blurring, defined by the system Modulation Transfer Function, can be added on the final image.

User's interaction with non computing intensive modules is performed by the means of a Motif based GUI.

3 Monte Carlo Radiation Transport in CAD Models

Sindbad has recently been improved by the development of a module dedicated to the Monte Carlo simulation of the radiation scattered in the examined part. In order to facilitate the software use in our laboratory context and to limit the development task, it has been decided to keep using the CAD model of the examined part, as well as the usual NDE parameters set and thus, to couple, within our NDE simulation system, a Monte Carlo radiation transport simulation code, with the BRL-CAD CAD and ray tracing package. Because of its availability in the C programming language and the established reliability of the models used in EGS4 [10], EGS Nova [11], a functionally equivalent adaptation of the default EGS4 code, has been chosen as a basis for our application. The CAD coupled software major features are as follows:

- The incident photon energy is sampled from a cumulated distribution function obtained from modeled or measured X-ray tube spectra as well as from radioisotope source data. A cone beam point source or an evenly distributed circular focal spot can be taken into account to determine the photon initial position and direction.
- Once the incident photon parameters are defined, the particles interaction and particles stack are managed by the EGS Nova shower simulation.
- The medium cross section data are generated beforehand by PEGS4, the EGS4 preprocessor.
- The examined part geometry interrogation function, whose goal is to compute the distance from the current particle position to the next boundary that will be crossed and the next region index, uses the ray tracing functions provided by BRL-CAD. Several CAD formats are accepted.
- As in EGS Nova, user has easy access to the physical models switches and cutoffs. However, the electron energy cutoff is defaulted to a high value in order to limit unnecessary computation.
- In the scoring function, every photon that reaches the front side of the detection system deposits, in a single detector pixel, an amount of energy related to the pre-calculated energy dependent detection efficiency of the detector material. History flags are used in order to distinguish between uncollided photons, once scattered photons and several times scattered photons.

The pre-existing simulation software and its GUI manage the remaining tasks, namely the X-ray source modeling, the overall parameterization of the

radiography setup and the detection system modeling. The knowledge of the analytically computed uncollided flux and the Monte Carlo computed uncollided to scattered ratio can be used to eventually scale the scattered flux image to the actual experimental conditions.

4 Implementation Validation and Application Example

A first validation study has been performed on steel slabs of various thickness. The front side of the slab is placed one meter away from a ^{60}Co gamma rays source. The detection system is directly placed on the plate back side. The comparison with results obtained in the same modeling conditions using the EGS4 code shows a very close agreement (the difference is less than one percent). The computation time ratio, approximately longer by a factor of 1.5 in this slab geometry case, would probably improve for more complex part geometries.

In the same configuration, the comparison between analytical and Monte Carlo computations of the uncollided flux exhibits a slight difference, which remains in the few percent range. This discrepancy is probably caused by differences between the Storm–Israël and PEGS4 cross sections databases, respectively used by the analytical and Monte Carlo simulations.

A second validation set uses a study by Inanc [12] in which comparisons between a deterministic scattering computation code and MCNP [13] are carried out. The radiography setup is formed by flat aluminum plates irradiated by a 140 kV X-ray tube, placed one meter away. The plate thickness is varied between 1 and 5 cm. The detection system, assumed perfect, is placed on the plate back side. Normalized uncollided and scattered photon fluxes are plotted with respect to plate thickness in Fig. 1.

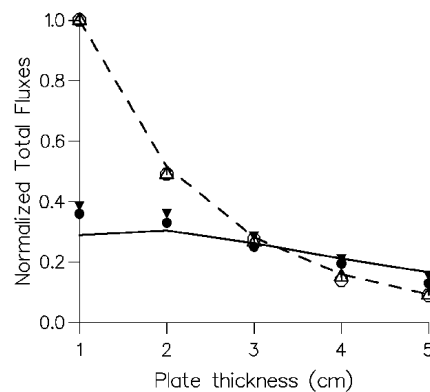


Fig. 1. Comparison with published data. Normalized uncollided (empty triangle: deterministic code, empty circle: MCNP, dashed line: present results) and scattered (solid triangle: deterministic code, solid circle: MCNP, solid line: present results) flux magnitude versus plate thickness

The agreement between uncollided flux computations by the three codes is very good. However, our CAD coupled implementation underestimates the scattered flux for thin plates. The discrepancy, which remains acceptable for our applications, is probably caused by a combination of differences in X-ray tube spectra, which are not exactly similar, and differences in the materials cross sections and models used by EGS Nova and MCNP.

A realistic geometry example has been simulated in order to demonstrate the capabilities of the CAD coupled code. The test sample is a small mechanical part made of aluminum (cf. Fig. 2 left) placed 70 cm away from a 110 kV X-ray tube. The electron cutoff energy is set in order to discard any electron transport inside the sample. 2.10^9 photons histories were computed (at a 16,000 histories/s rate on a SUN Ultra workstation). Computed radiographs (top views) relative to the uncollided and scattered photon fluxes are presented in Fig. 2. In agreement with experimental data, the computed amount of scattered radiation represents a small percentage of the uncollided flux.

5 Conclusion

A Monte Carlo radiation transport simulation program, EGS Nova, and a CAD software, BRL-CAD, have been coupled within the framework of Sindbad, a NDE simulation system. A first level set of validation has been performed. In its current status, the program is very valuable in a NDE laboratory context, as it helps compute the magnitude and spatial distribution of the scattered flux in a NDE software environment, without having to switch to a Monte Carlo code parameters set.

The major drawback is the execution time, usually more than one hour on a SUN UltraSparc workstation, which remains at present too long for everyday production use. The foreseen computational efficiency improvements are as follows. Firstly, as scattering contributes only to the low frequency details of the radiographic image, the pixel size used for the Monte Carlo computation will be increased. An interpolation will then be performed on the low resolution Monte

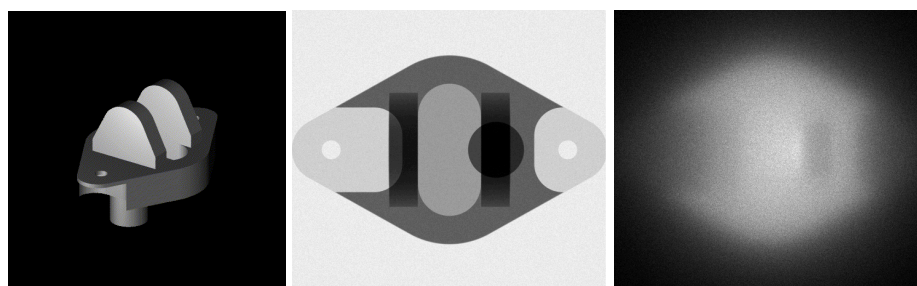


Fig. 2. Application example. Test part geometry (left), simulated uncollided flux image (center) and scattered flux image (right)

Carlo computed scattered flux image before addition to the high resolution analytically computed uncollided flux image. Secondly, we will take advantage of the computation of the uncollided flux with an analytical method to force interaction of all photons within the examined part and thus reduce variance. These improvements will be carried out in a near future.

References

1. F. Inanc, J.N. Gray: 'A CAD interfaced simulation tool for X-ray NDE studies'. In *Rev. Prog. Quant. Nondestructive Evaluation*, Vol. 9A (Plenum Press, New York 1990)
2. C. Bellon, G.R. Tillack, C. Nockemann, L. Stenzel: 'Computer simulation of X-ray NDE process coupled with CAD interface', In *Rev. Prog. Quant. Nondestructive Evaluation*, Vol. 16A (Plenum Press, New York 1996)
3. P. Duvauchelle, N. Freud, V. Kaftandjian, G. Peix, D. Babot, 'Development of a simulation tool for X-ray imaging techniques', In: *Workshop on the application of X-ray tomography in materials science, Villeurbanne, Oct. 28-29, 1999*, ed. by J. Baruchel et al. (Hermes, Paris 2000)
4. A. Glière: 'Sindbad. From CAD model to synthetic radiographs', In *Rev. Prog. Quant. Nondestructive Evaluation*, Vol. 17A (Plenum Press, New York 1998) pp. 387-394
5. F. Inanc, J.N. Gray: *Applied Radiation and Isotopes* **48**, 1299 (1997)
6. Z.W. Bell: *Rev. Prog. Quant. Nondestructive Evaluation* Vol. 10A (Plenum Press, New York 1991)
7. C.J. Leliveld, J.G. Mass, V.R. Bom, C.W.E. Van Eijk: *IEEE Trans. Nucl. Sci.* **41**, 1 (1994)
8. P.C. Dykstra, M.J. Muus: 'The BRL-CAD Package: An overview', In: *USENIX, Proceedings of the Fourth Computer Graphics Workshop* (1987)
9. E. Storm and H.I. Israël: *Nuclear Data Tables A* **7**, 565 (1969)
10. W.R. Nelson, H. Hirayama, D.W.O. Rogers: *The EGS4 code system*, SLAC Report 265 (1985)
11. J.C. Satterthwaite: <http://www.nemc.org/nova>
12. F. Inanc: *Journal of Nondestructive Evaluation* **18**, 2 (1999)
13. J.F. Briesmeister, Editor: *MCNP – A General Monte Carlo N-Particle Transport Code*, Los Alamos National Laboratory report LA-13709-M (2000)

Dose Rate Calculations from Radioactive Vascular Stents: DPK Versus Exact MC Approach

S. Gorodkov¹, A. Möslang², and P. Vladimirov¹

¹ RRC “Kurchatov Institute”, Kurchatov sq. 1, 123182 Moscow, Russia

² Forschungszentrum Karlsruhe, Postfach 3460, D-76021 Karlsruhe, Germany

Abstract. Vascular stents activated with radioactive isotopes are planned to be used in clinical practice to prevent restenosis in human coronary arteries after balloon angioplasty. Medical stents are cylindrical meshes and their complex geometry is usually treated for energy dose calculation with approximate dose point kernel (DPK) approach. The important point missed in the DPK approach is the absence of the stent material and, hence, the absence of energy absorption inside the stent. We have performed a comparison between DPK and exact Monte Carlo calculations for some simplified stent models. It appears that DPK approximation significantly overestimates pike dose values especially for the case of γ -emitting sources. We suggest DPK kernel normalization, which minimizes the difference at relatively far distances, while significant discrepancies near the stent surface still remain.

1 Introduction

Narrowing or blockage of coronary arteries caused by build-up of fat (cholesterol) within the artery wall, called atherosclerosis, will result in restricted blood flow that could lead to serious consequences for human arteries. A common way to overcome this disease without surgical operation is a PTCA¹, which uses balloon dilatation catheters to open and treat blocked coronary arteries. Very often PTCA treatments are followed by the implantation of metallic mesh tubes (stents) to maintain the arteries open.

Despite the well-elaborated implantation technique in-stent restenosis, that is significant reduction of artery cross section, still occurs within a few months after PTCA treatment at unacceptably high rate. It was demonstrated that in-stent restenosis is mainly caused by fast smooth muscle cell multiplication and migration. Then it was suggested to activate the stent surface with radioactive isotopes and reduce cell multiplication under impact of ionizing radiation. First trials were performed with stents activated by ^{32}P β -emitting isotope.

Ongoing clinical trials are clearly showing that ^{32}P activated stents can suppress nearly completely in-stent restenosis. However, researches met with a new problem: a severe restenosis at the stent edges, so called “candy wrapper” effect. The “candy wrapper” effect is assumed to be related with the insufficient impact

¹ PTCA: “Percutaneous”—through the skin; “Transluminal”—within the artery; “Coronary”—the artery supplying the heart; “Angioplasty”—remodeling the artery

of low dose radiation in these areas. In particular, it was supposed that using gamma radiation source would shift these low dose regions outside the part of an artery being disturbed during stent implantation.

The application of radioactive stents in stimulated considerably the interest for the calculation of the absorbed energy (dose) distribution in tissue and γ -emitting isotopes and for different stent designs.

Commercial medical stents have a form of metal mesh cylinder and their geometry is usually too complex to be satisfactory taken into account by direct Monte Carlo (MC) simulation. One way to overcome this complexity is to calculate dose distribution from a point source of radiation, a dose point kernel (DPK), and then obtain the dose distribution around the stent model by numerical integration over its shape. It should be emphasized that in the frame of this approach, the stent phantom is supposed to be made of infinitely thin wires. This approach provides fast calculation of the dose distribution around complex geometry stent and is widely used in practice [1,2].

This work describes the differences between DPK approximation and exact MC calculations using some simplified stent models activated with β - and γ -emitting isotopes.

2 Calculation Method

DPK approach implicitly involves the following approximations:

- The source shape is changed by shrinking finite size stent wires into infinitely thin lines;
- The absence of the stent material and, in particular, the absence of energy absorption inside a stent;
- The absence of perturbation of radiation field emitted by one part of a stent induced by the presence of the other stent parts.

It should be noted that in this work we have studied the consequences of the first two approximations on the calculated dose distribution.

One of the questions arising on application of DPK approximation for a stent phantom is one concerning the placement of the line source. For DPK simulation we placed the source, having the form of infinitely thin rings, at the same position (0.015 cm from the stent axis) as the activated phantom stent outer surface. This is a common practice to report DPK calculation results in terms of the distance from the stent surface and with this choice we followed this practice. The choice can significantly affect the results for DPK to MC dose ratio.

To clarify the differences between DPK and MC methods we have performed 2D MC calculations using infinite straight wires embedded into homogeneous tissue with circular and rectangular cross sections of equal area as well as line source (representing DPK approach).

Besides 2D model calculations we have performed 3D MC dose distribution calculations for a more advanced stent model. Our stent phantom consists of a set of twelve rings with equal gaps in between. Each ring is formed by two

coaxial cylinders and two planes perpendicular to cylinder axis OZ. The ring cross section has the same area as in the case of infinite circular and rectangular wires. The stent phantom was embedded in homogeneous tissue. Surface area of rings amounts to 15% of the outer cylinder surface and stent thickness is equal to 0.1 mm. Both values correspond to those used in practice.

Being relatively easy to implement in computer simulation, the model allows the calculation of a set of maximums in the dose distribution near the stent surface as well as the study of the long range behavior at the stent ends [3].

For 3D simulation of the DPK approach we have substituted the stent material with tissue and changed the source geometry by shrinking the finite cross section stent rings to infinitely thin wires. So there was no need to really perform DPK calculations with the advantage that using the same approach allows a direct comparison between DPK-like and MC methods.

All calculations were performed using a combination of MC packages MCU [4], which was initially developed for nuclear reactor neutron transport calculation, and EGS4 [5]. The coupled electron-photon transport was calculated using EGS4, while source simulation and description of the problem geometry as well as energy deposition scoring were performed by MCU.

3 Results and Discussion

The analytical calculation of the dose distribution from a point source of radiation is rather difficult due to complexity of electron and gamma interaction with matter, while using EGS4 code it is relatively easy to obtain “high-quality” DPKs in tissue. For illustration we have calculated DPK for ^{32}P β -source (average energy released per one decay ~ 0.7 MeV) and for ^{103}Pd γ -source (average released energy ~ 16 keV) (see Fig. 1).

Figure 1 demonstrates a pronounced difference between β - and γ -sources. The energy deposited by beta source absorbed inside a sphere with a radius of

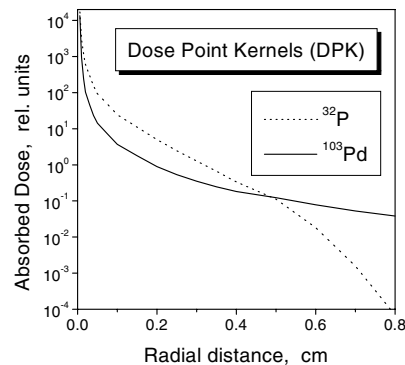


Fig. 1. ^{32}P (dotted line) and ^{103}Pd (solid line) dose point kernels, normalized to the same total energy released

about 0.8 cm. The radius depends on the average energy of beta electrons. In contrast the gamma source energy is distributed over larger distances, but is less homogeneously deposited in the vicinity of the source. Hence, gamma sources can be used to extend the volume affected by radioactive stent and therefore have the potential to decrease the “candy wrapper” effect, while increasing pike doses near the stent surface. Presently it is not clear how the shape of the dose rate distribution influences the healing of PTCA treated vessels. The accurate study of dose distributions and ways of their optimization for particular stent design is necessary before new radioactive sources will be used in clinical practice.

To elucidate the differences between DPK and MC methods, we started with simple 2D calculations for infinitely straight steel wires of different cross section form embedded into homogeneous tissue. The cross section of the wire is either rectangular (0.005x0.01923 cm) or circular of the same area. Also we calculated dose distribution for the infinitely thin wire source (line source) representing DPK approach.

These calculations revealed that DPK approximation predicts dose distribution significantly different from that calculated with MC method. The DPK to MC results ratio tends to become rapidly a constant value with increasing distance from the wire axis. For all cases considered this value is greater than unity. The data on the amount of the energy absorbed inside the stent material represented in Tab. 1 provide us with a clue to understand the behavior.

Table 1. Percent of energy absorbed in the stent volume for all type of stent models for typical β (^{32}P) and γ (^{103}Pd) sources

Source of Radiation	Absorbed Energy, %			
	Circular Wire	Rect. Wire	DPK	Stent Phantom
^{32}P	7.2	8.6	2.8	7.9
^{103}Pd	34.8	36.1	1.7	38.5

It is remarkable that in-stent absorbed energy very slightly depends on the form of the wire cross section. The percent of the energy absorbed inside metal wires is not negligible, especially for the case of low-energy ^{103}Pd source. Based on these findings we suggest to decrease the activity of the DPK source, so that the energies absorbed outside the stent will be the same in both cases of DPK and wire sources. In the case of the circular wire these scaling factors are 0.94 for ^{32}P and 0.65 for ^{103}Pd sources.

Figure 2 shows that the suggested scaling improves the DPK results in most parts of the volume. The remaining difference near the stent surface, which can not be removed by scaling of the source activity, is attributed to the change of the source form and the presence of the stent material inherent for DPK approach.

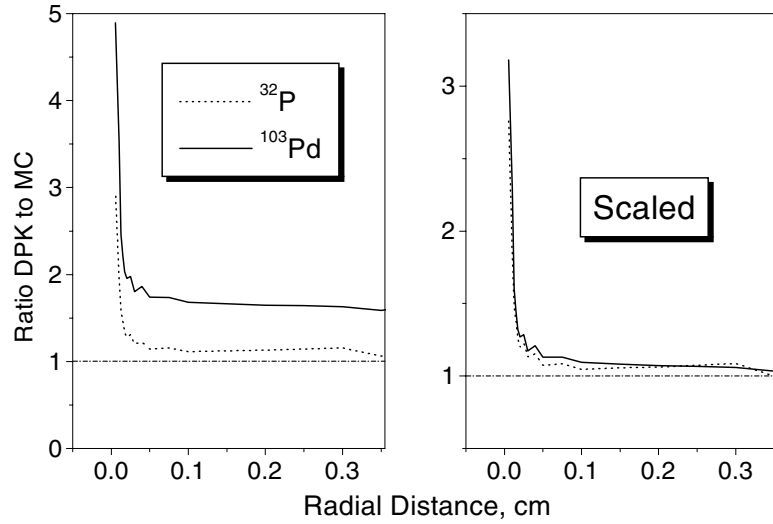


Fig. 2. Ratio of DPK to MC results for an infinite straight wire both as calculated (a) and scaled to the same energy absorbed outside the stent volume (b) (infinite cylinder of 0.055 cm radius)

Using these results we can conclude that at least for gamma emitters the DPK approach is of little use for the calculation of the near surface pike dose.

For an improvement of the DPK results by appropriate scaling, we can suggest the following approach for the dose calculation. At the first stage one can calculate the DPK for the radioactive source of interest using MC electron-photon transport code (e.g. EGS4). Then the correction factor for the in-stent absorption should be determined by MC calculation for infinite straight circular wire of given cross section. After this DPK approach is applied to the elaborated stent model, the resulting dose distribution should be multiplied by the obtained factor. This approach was realized in our calculations for 3D stent phantom (see Fig. 3). Before the scaling procedure maximum DPK to MC ratio were 2.4 for ^{103}Pd source and 1.6 for ^{32}P . The influence of the geometry and of the radiation field interference from different part of stents on the energy absorbed inside the stent material is demonstrated by comparison of circular wire and stent phantom results represented in Tab. 1.

4 Conclusions

In this paper we have investigated errors induced by DPK approximation for dose calculation using simplified stent models. It appears that the DPK method provides better approximation to dose distribution for the case of ^{32}P β -emitting source, where less than 10% of deposited energy are absorbed inside the stent material. On the other hand, DPK essentially overestimates dose values for ^{103}Pd soft γ -emitting source where about 40% of the released energy is absorbed inside

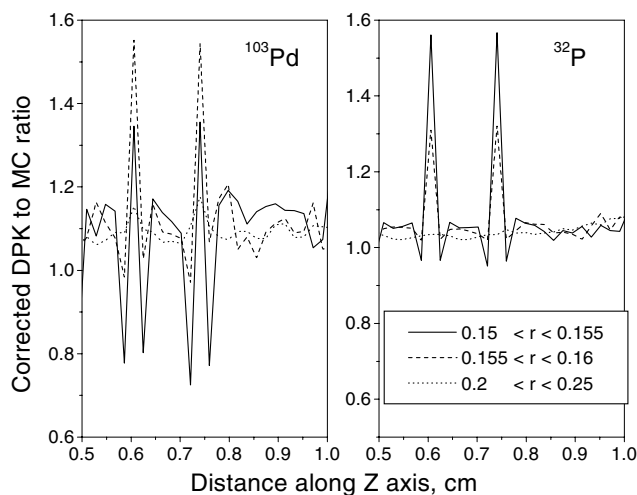


Fig. 3. Scaled ratio of DPK to MC dose results for 3D stent model for ^{103}Pd (a) and ^{32}P (b), with infinitely thin sources placed at the same distance from axis as the outer stent phantom surface

the stent. It was shown that the suggested scaling of the source activity taking into account the absorption inside the stent material is able to keep the DPK dose overestimation for wires within few percent in comparison with exact MC calculation. Even being properly normalized, DPK approximation significantly distorts pike doses near the stent surface, which definitely lower the usefulness of this approach. In the case of the stent phantom significant discrepancies still remain even after the suggested scaling. Full-scale MC calculations, though costly, may be the only help in this case.

References

1. C. Janicki, D.M. Duggan, C.W. Coffey: *Med. Phys.* **24**, 437 (1997)
2. W.V. Prestwich, T.J. Kennet, F.W. Kus: *Med. Phys.* **22**, 313 (1995)
3. A. Frey, S. Gorodkov, A. Möslang, A. Przykutta, P. Vladimirov: 'Development of ^{103}Pd X-Ray emitting stents', *Atherosclerosis 2000 – Disease patterns and Frontiers in Medical and Invasive Therapy*, March 31–April 1, 2000, Freiburg, Germany
4. E.A. Gomin, L.V. Maiorov: 'The MCU–RFFI Monte Carlo Code for Reactor Design Applications,' *Int. Conf. on Mathematics and Computation, Reactor Physics, and Environmental Analyses at Portland, Oregon, USA, April 30–May 4, 1995* (American Nuclear Society) vol. 2, p. 1136
5. W.R. Nelson, H. Hirayama, A.F. Bielajev: *The EGS4 Code System*, Stanford Linear Accelerator Center Report SLAC-265 (Stanford Calif) 1985

Dosimetric Study of a Low-Dose-Rate Brachytherapy Source

M. Rodríguez-Villafuerte¹, S. Arzamendi¹, and R. Díaz-Perches²

¹ Instituto de Física, UNAM, A.P. 20-364, 01000 D.F., México

² Hospital General de México, SSA, Dr. Balmis 148, México D. F., México

1 Introduction

Carcinoma of the cervix is the most common malignancy – in terms of both incidence and mortality – in Mexican women. Low dose rate (LDR) intracavitary brachytherapy is normally prescribed for the treatment of this disease to the vast majority of patients attending public hospitals in our country. However, most treatment planning systems being used in these hospitals still rely on Sievert integral dose calculations. Moreover, experimental verification of dose distributions are hardly ever done. In this work we present a dosimetric characterisation of the Amersham CDCS-J ^{137}Cs source, an LDR brachytherapy source commonly used in Mexican hospitals. To this end a Monte Carlo simulation was developed, that includes a realistic description of the internal structure of the source embedded in a scattering medium. The Monte Carlo results were compared to experimental measurements of dose distributions. A lucite phantom with the same geometric characteristics as the one used in the simulation was built. Dose measurements were performed using thermoluminescent dosimeters together with commercial RadioChromic dye film. A comparison between our Monte Carlo simulation, the experimental data, and results reported in the literature is presented.

2 Materials and Methods

2.1 Monte Carlo Simulation

The Electron Gamma Shower code [1] was used to calculate the dose in water per unit air-kerma strength around an Amersham CDCS-J ^{137}Cs source (see Fig. 1). In this source the ^{137}Cs is uniformly distributed in 9 Pyrex spheres which are surrounded by a cylindrical stainless steel shield. A 0.1 cm diameter hole drilled through the lower part of the shield is present in the real source, but this structure was not included in the simulation.

For the dose in water calculations the source was assumed to be placed in the centre of a cylindrical water phantom of 30 cm diameter and 30 cm height, with its long axis parallel to the axis of the cylinder. Photoelectric absorption, Rayleigh and Compton scattering were taken into account. Photons and electrons were followed through the different structures of the geometry until they were absorbed, escaped the boundary of the system or reached the specific cut-off energy (10 keV for photons and 50 keV for electrons). The dose (defined as the

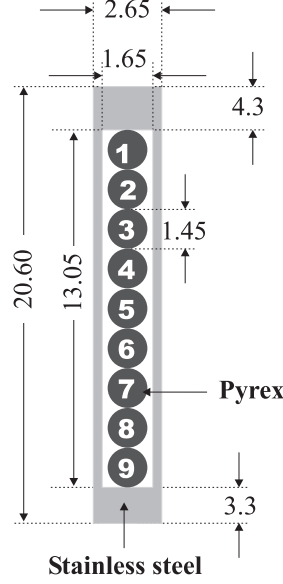


Fig. 1. Geometry of the Amersham CDCS-J ^{137}Cs source (units in mm)

energy deposited by the secondary electrons per unit mass of water) was recorded in 0.1 cm steps both in the radial and axial directions.

The air-kerma strength, S_k , of the source [2] was calculated by recording the energy fluence spectrum reaching a 100 cm air-filled sphere. The dose rate in water per unit air-kerma strength (in $\text{cGy h}^{-1} \text{U}^{-1}$) was obtained in the following manner [3]:

$$\frac{\dot{D}}{S_k} = \frac{D(y, z)/N_D}{1.602 \times 10^{-10} \sum_{E_{\min}}^{E_{\max}} (\varphi(E_i)/N_s) E_i (\mu_{en}/\rho)_{E_i} r^2} \quad (1)$$

where $D(y, z)$ is the dose in water (in Gy) and N_D is the total number of photon histories for dose in water calculations. 1.602×10^{-10} is a conversion factor from MeV g^{-1} into Gy, $\varphi(E_i)$ is the photon fluence (in cm^{-2}) at energy E_i (in MeV) and N_s is the number of photons for air-kerma strength calculations. μ_{en}/ρ are the mass-energy absorption coefficients of air (in $\text{cm}^2 \text{g}^{-1}$) at energy E_i , and $r = 100$ cm is the sphere radius at which S_k was evaluated.

2.2 Dose Distributions Measurements

Spatial dose distributions were measured using TLD-100¹ thermoluminescent (TL) dosimeters and RadioChromic MD-55-2 dye film². Slabs of lucite of 29 cm

¹ Harshaw/Bicron Solon technologies Inc., 6801 Cochran Road, Solon OH 44139

² International Specialty Products, 1361 Alps Road, Wayne, NJ 07470

diameter of different thicknesses were stacked one on top of the other to assemble a 30 cm height cylindrical phantom. Five thin slabs, with a 0.3 cm diameter hole located in their centre to accommodate the source, were placed in the middle of the phantom. A series of cavities were made in all the slabs at 2, 3, 4, 5, 7, 9, and 11 cm in order to place the TL dosimeters, two at the same radial distance. The RF was used to measure dose distributions at radial distances smaller than 2 cm, while the TL dosimeters were used for radial distances beyond this value.

The calibration of the TL dosimeters and the RadioChromic film was performed using ^{60}Co γ -rays. In both cases, a special structure of lucite was used to guarantee charge particle equilibrium. The TLDs were calibrated in the 0.1 to 12 Gy dose interval, while the GafChromic film was calibrated between 5 and 50 Gy.

The comparison between MC and experimental results required the use of a scaling factor (SF) to take into account the differences in attenuation properties between plastic (used in the experiment) and water (used in the MC) [4]. Our experimental data required $SF = 1.0867$ to scale the distances in plastic to those in water.

3 Results and Discussion

The Monte Carlo calculations for dose rate in water per unit air-kerma strength were performed using 8×10^7 histories. The calculated errors in the dose rate in water per unit air-kerma strength for transversal distances greater than 0.25 cm were 2.9% on the average (range: 0.6% to 14.8%). The comparison between our data and reported values of dose rate in water per unit air-kerma strength [5] shows good agreement. Differences of 1.0% were found on the average (range: -3.5 to 4.3%).

The comparison between the MC simulation and the experimental measurements with both types of dosimeters are shown in Fig. 2. The uncertainties of the measurements with TLD-100 are of the order of the symbol size. It can be observed from the graphs that there is an excellent agreement between the MC results and the experimental measurements. The differences found between both sets of data are on the average 1.0% (range: -0.2 to 12%). However, the agreement between the MC and the RadioChromic film results is not as good as the one achieved with the TL dosimeters. Our protocol developed to measure absolute doses with RF produced relatively good results only when the dose received by the RF was greater than 7 Gy.

4 Conclusions

In this work we have presented a Monte Carlo simulation of the Amersham CDCS-J ^{137}Cs source which considers its geometric structure in detail. The MC predictions of the dose rate in water per unit air-kerma strength are in excellent agreement with Williamson's reported values for the same source [5]. The MC results were validated with experimental measurements of the dose rate in

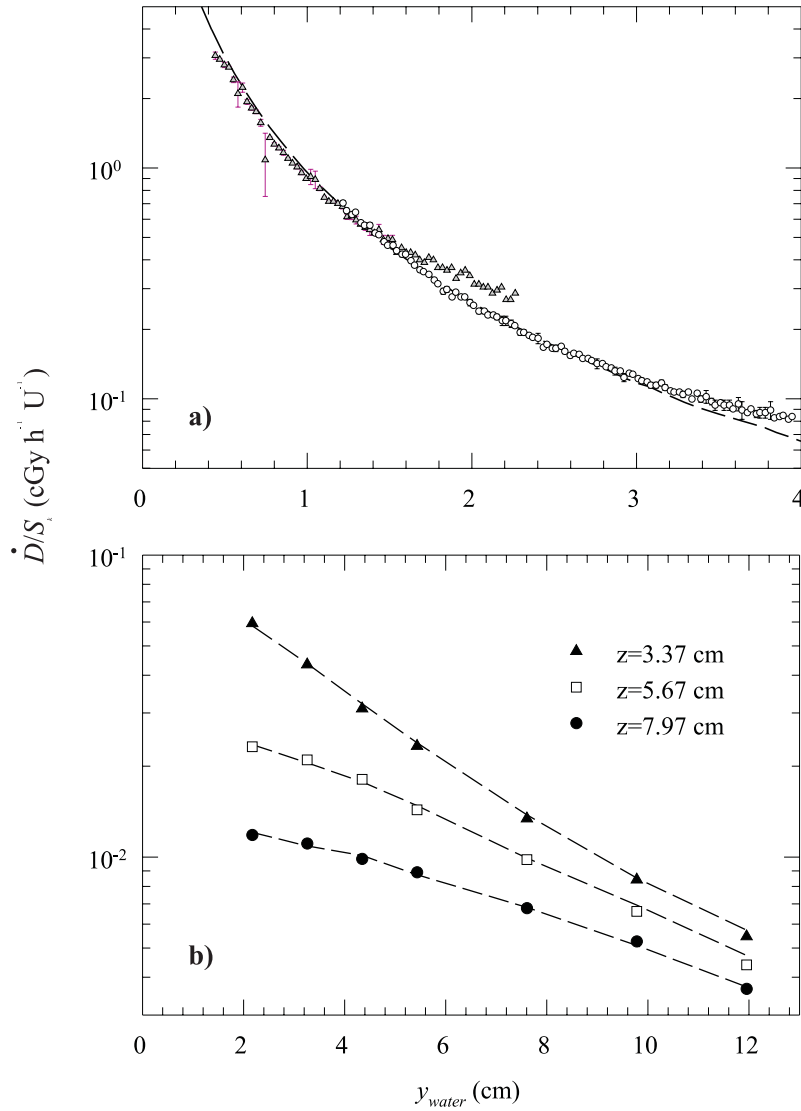


Fig. 2. MC results (dashed lines) and experimental measurements (symbols) of the dose rate in water per unit air-kerma strength ($\text{cGy h}^{-1} \text{U}^{-1}$) for different z -distances along the longitudinal axis of the source. (a) RadioChromic film, (b) TLD-100

water per unit air-kerma strength using TLD-100 dosimeters for transversal distances greater than 2 cm. Given the excellent agreement between the experiment and the MC predictions, it is worth noting the high capability of the protocols developed in our laboratory to measure absolute dose with extreme precision. Additionally, RadioChromic film was used to measure dose rate in water per unit

air-kerma strength for transversal distances smaller than 2 cm and the results were also compared with the MC. In this case, the agreements was good for dose measurements in the 7 to 50 Gy dose interval. Further experimental work is still under way to measure lower doses with higher precision than the one achieved in this work.

5 Acknowledgements

This work was partially funded by DGAPA-UNAM IN101399 and CONACYT 32226-E. The technical support of R. Ramírez in the construction of the phantom and of J. Montoya in the experimental measurements is greatly acknowledged.

References

1. W. R. Nelson, D. W. O. Rogers, H. Hirayama: *The EGS4 Code System*, Stanford Linear Accelerator Center Report SLAC-265 (1985)
2. R. Nath., L. Anderson et al.: Med. Phys. **22**, 209 (1995)
3. J. Borg, D.W.O. Rogers: Med. Phys. **26**, 2441 (1999)
4. R.J. Schulz, P.R. Almond, J.R. Cunningham et al.: Med. Phys. **10**, 741 (1983)
5. J.F. Williamson: Int. J. Radiat. Oncol. Biol. Phys. **41**, 959 (1998)

Electron Transport Simulation in the Range 1 keV–4 MeV for the Purpose of High-Resolution Dosimetric Application

V. Cobut¹, L. Cirioni², and J.P. Patau²

¹ Laboratoire Pharmacophores Rédox, Phytochimie et Radiobiologie, Université de Cergy-Pontoise, 5 Mail Gay-Lussac, Neuville/Oise, 95031 Cergy-Pontoise, France

² Faculté de Pharmacie, Université Paul Sabatier, 35 chemin des Maraîchers, 31062 Toulouse Cedex 4, France

Electron and photon transport problems are rarely absent-minded in radiation protection or dosimetry. Knowing how beam characteristics evolve in irradiated structures, and which physical or chemical effects may happen in them is of major interest.

Experimental spectrometry and dosimetry can offer some reliable answers. However, they are not easy to implement in some specific situations. Furthermore, information on dose distributions cannot always be obtained with the desirable geometrical resolution.

In order to circumvent these difficulties and deficiencies, Monte Carlo simulations provide convenient alternatives since they allow to reproduce the stochastic feature of primary and secondary particles interactions in the irradiated media. In the case of electrons, several computer codes are based on sampling of energy straggling and multiple scattering distributions, while for photons, individual interaction simulation is practised. These codes (ETRAN, EGS, MNCP, PENELOPE, etc.) can calculate energy deposition distributions. Founded on general theories, they are performed to solve a wide range of dosimetric problems, but they fail in specific situations where the physico-chemical composition of the matter is of importance on the electron interactions. Their accuracy may depend on certain restricting conditions. In particular, these methods are revealed unsuitable as far as we are concerned with electron transport in very thin slabs or in high atomic number materials. Even in infinite media, problems arise if we need a high-resolution spatial description of the energy losses. Such a problem is encountered in the evaluation of high gradient distributions of dose deposited in matter by beta sources, or in the response simulation of a detector composed of very thin sensitive slabs.

A way to get rid of these disadvantages consist in simulating every successive individual interactions suffered by electrons and photons along their path. We applied this principle to simulate the response of a detector placed in the field of beta-gamma sources, which maximum energy does not exceed 4 MeV. A part of this work is presented here, which concerns Monte Carlo simulation of electron transport in materials encountered in experimental dosimetric devices. Electrons were followed down to a cutoff energy of 1 keV.

In the framework of the simulation model developed, an electron history consists in a succession of free linear flies interrupted by elastic or inelastic interactions. The energy dependent interaction mean free path is deduced from the total interaction cross section, which itself depends on total individual cross sections for all kinds of interactions.

Then, differential cross sections enable to determine, after Monte Carlo-type stochastic sampling, the state of the particle system following the interaction. Each of the random variables (deflection angle, energy loss, etc.), necessary in course of the simulation, is sampled from its specific law of probability derived from the corresponding cross section. A brief summary of the data and interaction cross sections used are given below.

1 Inelastic Cross Sections

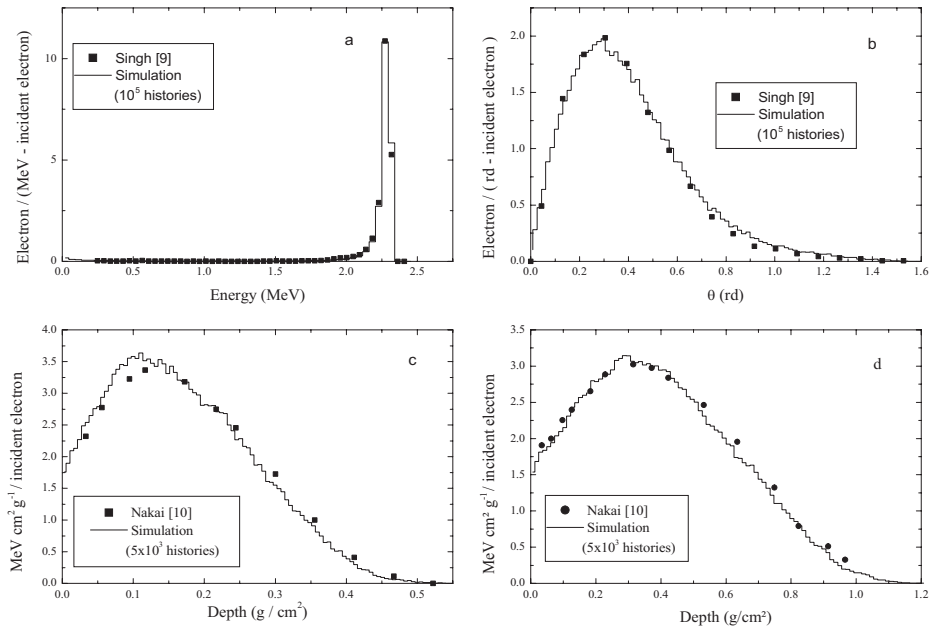
Since we are concerned with electrons of energy greater than 1 keV, angular deflections during an inelastic event can be neglected. As Bichsel [1] did for silicon, but with other means, we calculated, for any element of interest, the cumulative energy loss function $Q(W,E)$, where W is the energy lost in an inelastic collision by an incident electron of energy E . This function depends on inelastic differential cross sections (IDCS). These IDCS were computed according to the theoretical model of Martinez et al. [2]. This one is attractive since it is build up to describe energy losses in insulators, as well as in metals, where collective excitations (plasmons) occur.

2 Elastic Cross Sections

We used gas phase total elastic cross sections compiled in Cullen's database [3]. On the other hand, gas phase differential elastic cross sections (DECS) were taken from a program edited by Berger [4]. These cross sections can be tabulated for electrons of energies between 1 keV and 1024 keV for scattering targets of atomic number from 1 to 100. They have been calculated using Riley's computer code [5], which numerically solves the Dirac equation including screened Coulomb potentials. Above 1024 keV we used Mott's DECS [6] according to the "Berger factorization" [7], where the ratio of Mott to Rutherford cross sections includes a Rutherford cross section form with the screening factor adopted by Chibani [8].

Cross sections have been computed and validated for several materials encountered in experimental dosimetric devices. With this aim, we developed a code simulating the transport of monoenergetic electron beams impinging on slabs of different thicknesses and compositions. As an example, Figures (a) and (b) present simulation results for 2.43-MeV electrons slowing down in a 0.113 g/cm² thick silicon slab. On Figure (a) appears the energy spectrum of transmitted electrons (irrespective of the observation angle), while Figure (b) presents the angular spectrum of all transmitted electrons (irrespective of their energy).

Excellent agreement with experimental data [9] is observed. As other example, Figures (c and d) show depth energy deposition in semi-infinite aluminum targets for incident electrons of 1 and 2 MeV respectively. Comparison with experimental data ([10]) shows again an excellent agreement.



References

1. H. Bichsel: Nucl. Instr. and Meth. **B52**, 136 (1990)
2. J.D. Martinez, R. Mayol, F. Salvat: J. Appl. Phys. **67**, 2955 (1990)
3. D.E. Cullen, Program Epicshow, Version 96-1, Lawrence Livermore National Lab
4. M.J. Berger, S.M. Seltzer, R. Wang, A. Schechter: *Elastic Scattering of Electrons and Positrons by Atoms: Database ELAST*, NISTIR 5188 (1993)
5. M.E. Riley, C.J. MacCallum, F. Biggs: Atomic Data and Nuclear Data Tables **15**, 443 (1975)
6. N.F. Mott: Proc. R. Soc. **A 124**, 475 (1929)
7. M.J. Berger, in: Methods in computational Physics, Vol. 1 (Academic Press, New York, 1963) p. 135
8. O. Chibani, J.P. Patau: Nucl. Instr. and Meth. **B94**, 1 (1994)
9. J.J. Singh: *Transmission of 2.43 MeV Electrons Through Thick Silicon Targets*, NASA Technical Note D-5075 (1969)
10. Y. Nakai: Jpn. J. Appl. Phys. **2**, 743 (1963)

Shield Optimization for X-rays Using the Monte Carlo Method Combined with Analytical Calculation

Zhang Dian-hui, Huang Liu-xing, and Niu Sheng-li

Northwest Institute of Nuclear Technology, P.O. Box 69, Section No.15, 710024,
Xi'an, China

Abstract. Shielding for X-ray multi-layer single/composite material has been studied. The transmitted energy fluence and the corresponding total ionizing dose (TID) in Silicon were computed using a Monte-Carlo code (MCNP 4B) and an analytical model applying the “modified beam attenuation law”. With optimum shielding solution, the total shield weight to achieve a given TID or the TID for a given total shield weight can be greatly reduced.

1 Introduction

Shielding has long been used to alleviate radiation damage effects. In most cases, additional shielding (AS) is needed for electronic systems that must work in high-fluence-level, high penetrating radiation (e.g., high energy X-rays) environment even if radiation hardened (RH) parts are used. The brute force solution of adding shielding (AS) to crucial components (package level) or the composite electronic boxes is frequently the lowest cost solution.

The AS solution is contradictory to the requirement to build system weighing possibly less, especially for space vehicle system. Usually very little weight of shielding material is permitted in order to get lower weight and also get as more payload weight as possible. So a compromise will be needed and shield optimization play an important role in system hardening design. Shield optimization is based on the accurate calculation of the radiation transport. Monte Carlo method can give accurate results especially in dealing with radiation transport in complex structure, but is relatively not much effective when the consuming time to run M-C code is considered. Other method such as narrow-beam calculations used in photon transport can provide satisfactory estimate in many simple cases. So some compromise is also needed in calculation method.

For X-radiation, effectively shielding for soft X-rays (10^0 keV) is inherently provided by the spacecraft/vehicle shell itself (inherent shielding, IS). The AS will be directed against the X-rays with higher energy (10^1 – 10^2 keV) in a given spectrum. In practical designing, the shield usually must be chosen from a list of limited number proposed materials in order to meet other physical and chemical property requirements. So a tradeoff study is often desirable to determine the optimum combination of intrinsic hardness and special X-ray shielding to realize greater weight savings.

In this paper, the transport process of X-rays in an additional shield with single/composite materials has been studied with Monte-Carlo method and analytical model. The most important factor concerned is the expected TID from the emerging energy X fluence. X rays of blackbody radiator with single/composite temperature were considered.

2 Physical Model

For a composite-blackbody radiator, the normalized energy fluence spectrum can be written as

$$F_E(E)dE = \sum_i \alpha_i \frac{15u_i^3}{\pi^4(e^{u_i} - 1)} du_i \quad (1)$$

The associated differential energy distribution (X-rays/unit energy) is

$$F_n(E)dE = \sum_i \alpha_i \frac{15}{\pi^4 kT} \frac{u_i^2}{(e^{u_i} - 1)} du_i \quad (2)$$

where E is photon energy, $E = h\nu$, $u_i = h\nu/kT_i$, and α_i is the energy percent for temperature T_i .

To estimate the dose at a specified depth in a material due to a source with a known energy spectrum, the methodology of “broad beam attenuation law” or “narrow beam attenuation law” can be used [1], noted as analytical model in the following.

To compare the results with that of Monte-Carlo method, the Monte-Carlo calculation is done with MCNP(4B) using a multi-layer slab geometry as shown in Fig. 1. The source defined as mono-directional inward-directed at the front surface.

For X-rays with intensity $I_0(E)$ transporting through n layer materials, the emerging fluence spectrum $I(E)$ can be calculated using analytical model as

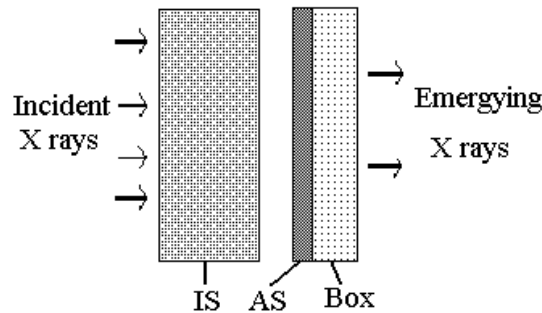


Fig. 1. Geometry for X rays shielding

following,

$$I(E) = I_0(E) \exp\left[-\sum_{i=1}^n t_i \sigma_i(E)\right] \quad (3)$$

where E_{\min} and E_{\max} are the spectral photon energy limits, t_i (in g/m²) is the thickness of the i th layer t , and σ_i the mass attenuation i th layer shielding material.

Taken σ_i as the “energy absorption coefficient” or “total attenuation coefficient” [2], (3) is corresponding to the “broad beam attenuation law” (BBA) or “narrow beam attenuation law” (NBA). In our calculation the “total absorption coefficient” was also used for comparison, we called equation (3) as “modified beam attenuation law” (MBA) in this case.

3 Dose Calculation

TID (Si) due to the emerging X-rays can be calculated as follows:

$$R = \int_{E_{\min}}^{E_{\max}} \sigma_{\text{aSi}}(E) I(E) dE \quad (4)$$

where σ_{aSi} is the total absorption cross section (cm²/g) of Silicon [2], E_{\max} and E_{\min} are taken 0.1 keV and 500 keV in our calculation. In our calculation, the TID only include the dose due to the emerging photons, dose from the electrons were omitted because the low penetrating (100–101 keV) secondary electrons will be absorbed by the devices package so contribute not too much to the TID in the sensitive region.

In our analytical model, $I(E)$ was obtained using (3). The emerging fluence spectrum for Monte-Carlo method (noted as FMC(E)) was recorded using MCNP tally *F1:P n. It's noted that there is no obvious difference in FMC(E) data between a point source and a uniformly distributed surface source in our multi-layer slab geometry.

For transmission simulating with MCNP, source photon number distribution (in unit energy) was calculation with (2) and was normalized to one photon. Due to the lower energy cutoff in MCNP (default 1 keV for photon), the average source energy EAV sampled by MCNP is larger than that calculated with (2), especially for blackbody spectrum of lower temperature. Using EAV from (2) and FMC(E), the dose for MCNP results can be written as

$$R = \frac{I_0(E)}{E_{\text{AV}}} \int_{E_{\min}}^{E_{\max}} \sigma_{\text{aSi}}(E) F_{\text{MC}}(E) dE \quad (5)$$

To compare the results of MCNP and analytical model, for a various combination of blackbody source and shield the expected emerging energy X fluence and the corresponding dose (Si) have been calculated. Some dose results are given in Tab. 1. For $kT=12\text{keV}$, Fig. 2 shows the emerging fluence of one source photon

Table 1. Dose after shield for a blackbody source with fluence $1\text{Cal}/\text{cm}^2$

Shield Configuration (thickness in cm)	kT(keV)	Dose 10^5 rad(Si)		
		MCNP	Narrow beam*	MBA
0	9		49.85(49.371)	
	12		24.07(24.39)	
	15		13.56(13.936)	
Al(0.1)	9	3.249	3.081	3.077
	12	2.349	2.256	2.254
	15	1.714	1.661	1.659
Al(0.15)	9	2.349	2.274	2.270
	12	1.798	1.761	1.758
	15	1.362	1.343	1.342
Al(0.30)	9	1.240	1.269	1.265
	12	1.065	1.098	1.095
	15	0.869	0.900	0.898
Ta(0.00125)	9	3.139	2.961	2.6371
	12	2.245	2.090	1.901
	15	1.648	1.520	1.400
Ta(0.0025)	9	1.367	1.276	1.154
	12	1.158	1.070	0.984
	15	0.9401	0.864	0.801
Ta(0.005)	9	0.3596	0.317	0.2846
	12	0.5731	0.5395	0.4919
	15	0.5176	0.4841	0.440
Ta(0.00125) +Ni(0.01) +Al(0.254)	9	0.4397	0.4782	0.4451
	12	0.4605	0.4956	0.4665
	15	0.4270	0.4573	0.4327
Ta(0.0025) +Ni(0.01) +Al(0.254)	9	0.3365	0.3685	0.3403
	12	0.3631	0.4007	0.3727
	15	0.3530	0.3815	0.3550
Ta(0.005) +Ni(0.01) +Al(0.254)	9	0.2133	0.2374	0.2160
	12	0.2532	0.2801	0.2539
	15	0.2546	0.2809	0.2523
*data in bracket are from [3]				

calculated with MCNP and analytical model (using “narrow beam attenuation law”(NBA) and MBA).

Our conclusion is that analytical method such as “narrow beam attenuation”(NBA) can provide a reasonable estimate for X-rays (1keV–200keV) transportation through an appropriate shield thickness. In our analytical model, using NBA law or MBA law results no much difference for low Z material Al shield up to 0.3 cm, but an about 10% difference may be resulted for high Z material Ta.

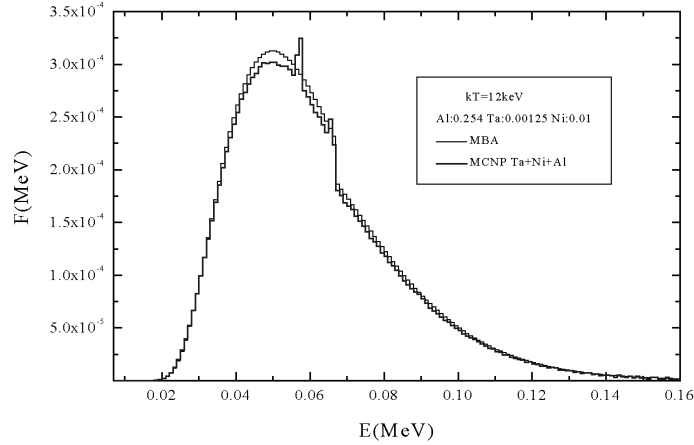


Fig. 2. Emerging fluence of one source photon

It also can be seen from Tab. 1 and Fig. 2 that the results using analytical model (MBA law) agreed surprisingly well with that using MCNP code for composite shield with low and high Z material. MBA law was also applied in the following analysis.

4 Shield Optimization

Based on the conclusion that analytical model can give a satisfactory estimate for the fluence and dose in our multi-layer slab geometry, we applied the MBA law as a tool to fast predicate the optimum shield configuration for a specified X-rays source. A list of AS material t was also specified. The optimum shield configuration will be checked by MCNP calculation.

Considering the (Ta, Ni, Al) composite shield configuration in Tab. 1, the 0.254 cm Al was regarded as a structure shell, the combination of Ta and Ni was regarded AS. First, we use MCNP to study the influence of the material sequence in the shield. Fig. 3 shows the results for two configuration of the same shield material.

Dose due to the emerging fluence is 4.605×10^4 rad(Si) cal/cm² for Ta+Ni+Al and 5.407×10^4 rad(Si) cal/cm² for Al+Ta+Ni, the difference comes from the secondary photons at K absorption edge of the shield material which can be seen clearly in the figure. For Ta+Ni+Al shield configuration, the secondary photons at K absorption edge of Ni and Ta can be absorbed by Al, so the dose is reduced obviously.

Now, we try to replace the Ta with other material in the Ta+Ni+Al shield configuration. For $kT = 12$ keV, fluence=1 cal/cm² and a 0.01 cm Ta + 0.01 Ni + 0.254 cm Al shield, the emerging dose will be 1.389×10^4 rad(Si) and 1.371×10^4 rad(Si) by MCNP and MBA. Using MBA analytical model, a fast predicated

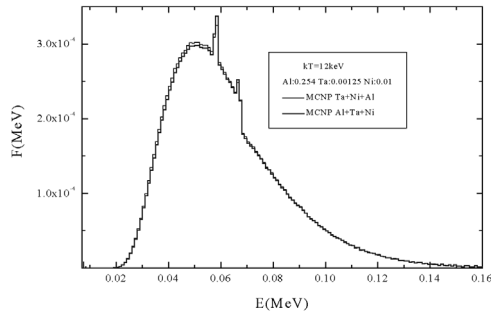


Fig. 3. Emerging fluence for same shield materials of different sequence

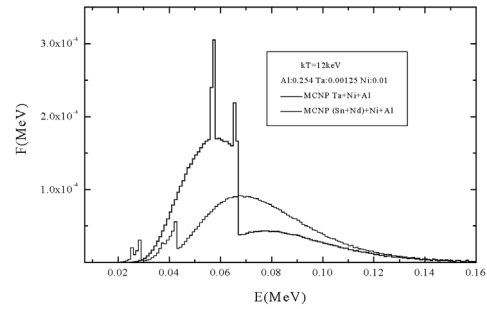


Fig. 4. Emerging fluence for optimum shield

optimum shield will be 61%Sn+39%Nd with the same mass thickness of 0.01cm Ta ($0.1668\text{g}/\text{cm}^2$), the corresponding dose is $8.594 \times 10^3 \text{ rad}(\text{Si})$. For the same shield configuration, MCNP predicated dose is $8.925 \times 10^3 \text{ rad}(\text{Si})$, reduced approximately 35% as compared to the Ta+Ni+AL shield. The emerging fluence was shown in Fig. 4.

5 Summary

For a variety of blackbody sources, X-rays transport in a shield of single/composite materials has been studied with Monte-Carlo method and analytical model, the expected emerging energy fluence and the corresponding dose in Silicon were calculated. Based on the modified beam attenuation law, an analytical model and code was developed to fast predicate the fluence and dose of X-rays after a shield of simple material composition, and to provide a fast estimate for optimum shield configuration. It can be concluded that using analytical model base on the “narrow beam attenuation law” or the “modified beam attenuation law” can provide a satisfactory estimate for the emerging X-ray fluence and dose after a shield of simple configuration. It is appropriate to use the analytical method to fast construct an optimum shield configuration.

It should be noted that the contribution to dose from the emerging secondary electron is omitted and the dose enhancement effects that may occur in devices with high Z package is not considered. So the optimum shield configuration may be not optimum in real cases.

References

1. J.C. Garth, J.R. Turinetti: IEEE Trans. Nucl. Sci. **44**, 2058 (1997)
2. E. Storm, H.I. Israel: *Photon Cross Section from 0.001 to 100 MeV for elements 1 through 100*, LA-3753, 1967
3. N.J. Rudie: *Principles and techniques of radiation hardening*, 3rd ed, Vol.3 (Western Periodical Company, California 1986)

MCNP Analytical Models of a Calibration Head Phantom for Bone-Seeker Nuclides In Vivo Measurements

G. Gualdrini¹, P. Ferrari², P. Battisti¹, P. De Felice³, and L. Pierotti⁴

¹ ENEA-IRP v. Dei Colli 16 I-40136 Bologna Italy

² Department of Physics University of Bologna Viale C. Berti Pichat 6/2 I-40127 Bologna Italy

³ ENEA - INMRI v. Anguillarese, 301, I-00060 S. M. Galeria-Roma Italy

⁴ Health Physics Service, Az. Osp. S.Orsola, v. Massarenti 35 I-40138 Bologna Italy

1 Introduction

Dosimetric studies related to internal contamination from actinides, characterised by a gamma or X-ray emission, can be done using Whole Body Counters (WBC), equipped with Germanium detectors. Their calibration requires suitable plastic phantoms, activated with a known quantity of the investigated radionuclide, to reproduce the contamination of the individual, or of the particular target organ. In order to detect low energy photon emitters, some long-lived daughter nuclei, characterised by higher energy emission, are usually selected as markers. In the case of Plutonium the internationally accepted practice is to employ ^{241}Am (nearly 60 keV gamma emission) taken as a marker of actinide previous contamination [1]. These actinides deposit, during their long retention period (over 20 years), in the skeleton and in the liver. Taking into account that the low energy of the emitted photons makes the measurement strongly sensitive to the thickness of the soft tissue surrounding the bones (and therefore very much subject-dependent), it is advised to perform the measurement on the head, to minimise the individual variation of the soft tissue thickness. The measured head activity can be thereafter extrapolated to the whole skeleton. The previous considerations justify the importance of developing a suitable head calibration phantom to be activated with known activity radioactive sources in order to well approximate the assumed homogeneous contamination encountered in the real practice. The main difficulty is represented by the complexity of the radioactive source itself which is the skull of the plastic phantom. Since many years Monte Carlo techniques have been used to simulate internal dosimetry measurements with satisfactory results [2–4]. This paper describes the method followed to work out this problem relying on the capabilities of the Monte Carlo code MCNP [5]. The code was employed both to determine the best distribution a set of 24 point sources, to simulate a homogeneous activity in the plastic phantom, and to calculate a correction coefficient to be associated to the calibration factor. It should be mentioned that some of the results of this paper have already been presented in a previous work [6], although in non-Monte Carlo forum. Particular

emphasis was devoted here to the numerical analyses concerning the modelling of progressively more complex skull phantoms.

2 Materials and Methods

2.1 The *AldersonTM* Angiographic Phantom

At the moment a standard head calibration phantom for actinides has not been defined at the international level. Our aim was therefore to adopt a reasonably suitable head commercial phantom (an *AldersonTM* plastic head phantom, usually adopted for angiography studies (Fig. 1)) and adapt it to our problem. Its characteristics are the following:

- *AldersonTM* cortical bone [$\rho = 1.88(g/cm^3)$; $\mu(60keV) = 0.587 (cm^{-1})$]
- *AldersonTM* trabecular bone [$\rho = 1.17(g/cm^3)$; $\mu(60keV) = 0.274 (cm^{-1})$]
- *AldersonTM* soft tissue [$\rho = 1.09(g/cm^3)$; $\mu(60keV) = 0.223 (cm^{-1})$]

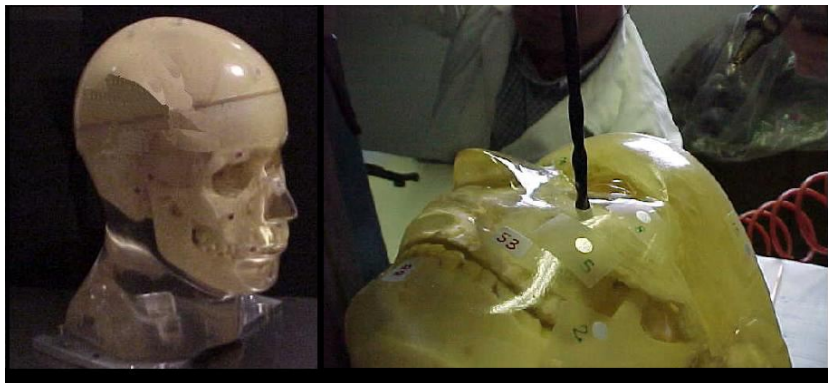


Fig. 1. (left to right) The commercial *AldersonTM* angiographic phantom and the drilling operation

2.2 ^{241}Am Calibrated Sources

In order to best approximate a uniform contamination condition of the head bone, a set of 24 nearly point calibrated ^{241}Am sources were developed at the ENEA-National Metrology Institute of Ionising Radiations (ENEA-INMRI). The sample was characterised by a mean activity value of 122.9 Bq with a percentage standard deviation of 2.9%. The adopted solution of very thin disk sources allowed minimising the source volume at the same time reducing the self absorption. The head phantom was mounted on a spherical co-ordinates rotating base that was positioned onto the working plane of a precision milling machine by which a number of 24 cylindrical holes were made on the head phantom (Fig. 1).

3 MCNP Analytical Models

The problem of producing a reliable and rigorous mathematical model of the employed experimental phantom played a crucial role in the context of the work. The skull within the head is a very heterogeneous structure and the relatively weak energy of the source photons (nearly 60 keV) can be significantly sensitive to the geometric model. This consideration implied the need of a realistic model of the skull to be developed according to the MCNP formalism. The study was performed in three steps relying on three different analytical models of the head: ADAM, SAM and CAM. This allowed analysing the level of accuracy introduced by the adoption of models characterised by a different degree of complexity.

3.1 The MIRD-5 Model: ADAM

The ADAM model is based on the mathematical equations [8] originally written to describe the standard man organs at the Oak Ridge National Laboratory (ORNL) since the end of the 60s. The head, that was modelled for MCNP (Fig. 2), is constituted by the union of two half-ellipsoids to describe the top of the skull and an elliptical cylindrical segment to describe the facial skeleton. The MCNP model is made of 10 cells (five describing the bone volumes) and 24 surfaces (12 for the bones).

3.2 The Simplified Analytical Model: SAM

The Simplified Analytical Model, SAM (Fig. 2), is a mathematical model developed on the basis of direct measurements made on plastic skull phantoms similar to the *AldersonTM* one. A 14 pieces decomposable skull developed for didactic purposes helped in these evaluations. The 14 pieces were weighted using high precision instrumentation and the corresponding volumes calculated assuming a constant average density of the bone (a mixture of trabecular and cortical bone). SAM is made of 43 cells (15 of bone) and 88 surfaces (74 for the bones).

3.3 The Complex Analytical Model: CAM

Using a Computed Tomography (GE Hi Speed Adv RP) a number of 248, 1 mm thick, axial slices of the *AldersonTM* phantom were obtained. Only a subset of them were used for the production of the 3-dimensional MCNP model of the skull. An example of a CT slice together with its MCNP representation is shown (Fig. 3). The final geometry is made of 54 layers, 277 MCNP cells and 1929 surfaces (Fig. 2). The capability of the MCNP code to evaluate spatial cell volumes in a satisfactory way was employed (as for SAM) to determine the ^{241}Am sources positions, imposing that each of the 24 sources should be placed in the centroid of 24 equal volume sub-regions to obtain a nearly homogeneous distribution of the radioactivity.

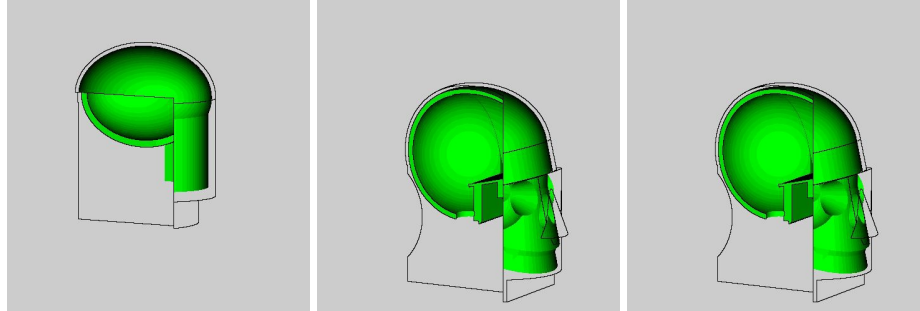


Fig. 2. (left to right) SABRINA [7] cut of ADAM, SAM and CAM MCNP models

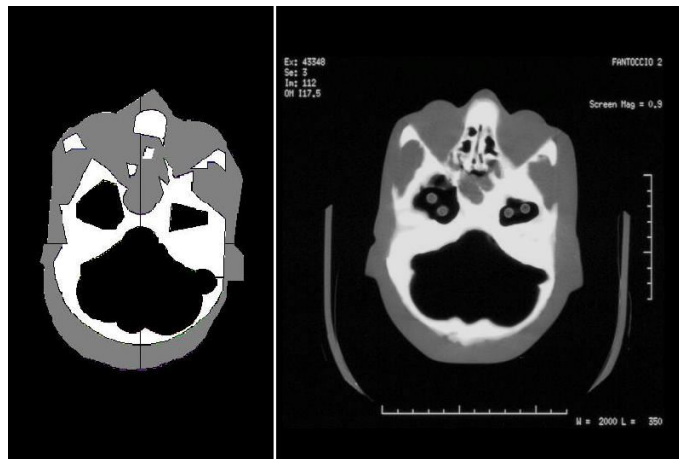


Fig. 3. An axial skull CT scan (right) with its MCNP model (left)

3.4 MCNP LGe Detector Measurement Simulations

The experimental procedure used in the routine assessment of internal contamination of actinides is based on the use of two *CanberraTM* LGe GL3825S (76 mm diameter, 25 mm thickness, 38 cm^2 detection window surface) that can be placed symmetrically at a fixed distance from the head surface (1 cm on average). Three measurement conditions were simulated for each model using MCNP, to cover a significant number of routine situations (Fig. 4) : Frontal Bone; Temporal Bone; Upper Parietal Bone

An homogeneous nuclide distribution throughout the skull was simulated with MCNP. The employed estimator was a pulse-height tally (F8 in the MCNP syntax) within the sensitive volume of the Germanium detector. An energy segmentation of the response was adopted to obtain the full absorption energy peak

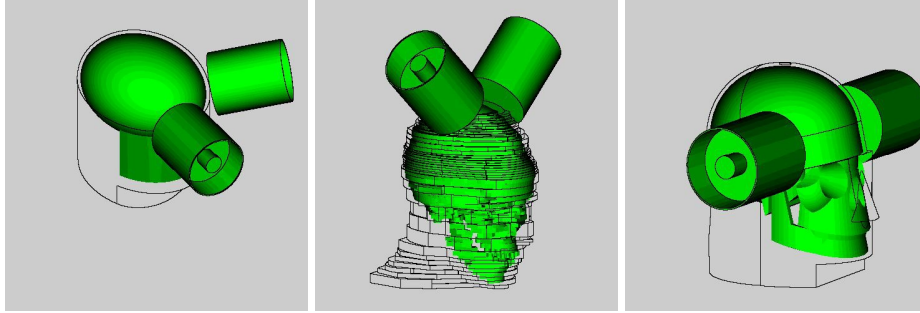


Fig. 4. (left to right) Some MCNP measurement simulations for ADAM, SAM and CAM

counts per Bq. The efficiencies obtained in this way for the three MCNP models are reported in Tab. 1.

Table 1. Uniform Distributed Source - Efficiencies Comparison at 1 cm from the head surface (Cps/Bq)

<i>Detector Position</i>	<i>MIRD model</i>	<i>SAM</i>	<i>CAM</i>
Upper parietal	$6.14 * 10^{-3} (0.1\%)$	$5.43 * 10^{-3} (0.1\%)$	$6.70 * 10^{-3} (0.2\%)$
Temporal	$6.03 * 10^{-3} (0.1\%)$	$5.70 * 10^{-3} (0.1\%)$	$7.25 * 10^{-3} (0.2\%)$
Frontal	$6.57 * 10^{-3} (0.1\%)$	$6.32 * 10^{-3} (0.1\%)$	$6.60 * 10^{-3} (0.2\%)$

It can be in general noted a spread in the results due to the arbitrary assumptions made for ADAM and SAM models. This spread is mainly due to the different bone spatial distributions, significantly influencing the detector efficiency depending on each selected measurement position. On the other hand the discrepancy, bounded within about 20%, can be considered rather limited, taking into account the strong diversity of the developed models. CAM, being based on tomographic analyses of the plastic phantom, was taken as the reference head model in the present work.

4 Optimising the Experimental Phantom Design Using MCNP

As already mentioned the positions of the 24 point sources were selected on the basis of the MCNP evaluation of 24 equal-volumetric zones in which centroids each source was placed. To reproduce the volume ratios as obtained through the MCNP calculations, that reasonably confirmed the Reference man parameters

[10], eight sources were placed in the facial skull whilst the other sixteen were distributed in the rest of the skull bones according to the respective volumes. It has to be pointed out that the adopted heterogeneous source distribution strongly influences the system counting efficiency. As a matter of fact the closer to the head surface the detector is placed, the higher is the heterogeneity effect on the measurement. The Monte Carlo modelling allowed not only simulating the various possible measurement configurations, but also calculating a correction coefficient to be applied to the calibration factor. This allows taking into account the heterogeneous source distribution (calibration condition) as compared with the real in vivo homogeneous distribution of the contaminant. The following computational steps were followed:

- A uniform ^{241}Am distribution was modelled within the CAM phantom bone
- A suitable 24 ^{241}Am point source distribution was selected on the basis of the MCNP volume calculations.
- The positioning of the detectors on the head was studied, relying of an accurate fluence mapping (within the detector Region Of Interest, ROI) through an azimuthal-polar grid representing a large number of potential measurement positions. This mapping was obtained for the two source configurations (homogeneous and 24 points).

Relying on the data obtained, the ratios between homogeneous and 24 point source fluences within the detector ROI were plotted for different head-detector distances (Fig. 5); that allowed analysing the degree of heterogeneity due to the non homogeneous source distribution. Some conclusions can be drawn:

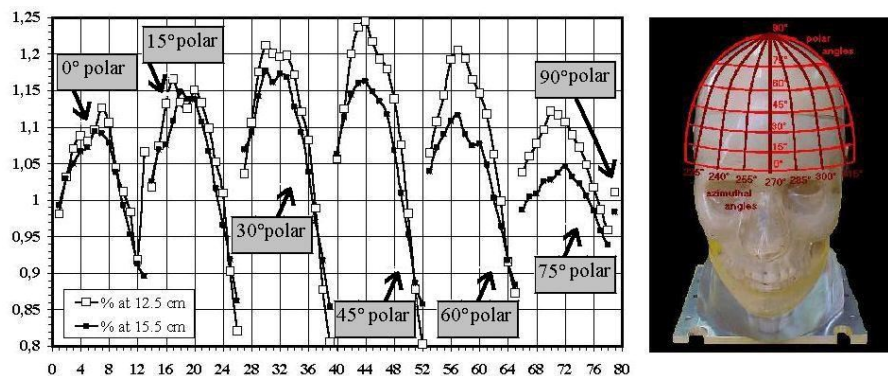


Fig. 5. Head Top mapping scheme of Photon Fluences: the left plot supplies the ratios between Homogeneous and Heterogeneous Source Distribution Photon Fluences. The six curves correspond to the six polar angles (bottom to top). Each of the six curves is described by 13 azimuthal detection points from 180 to 360 degrees. The detection positions are located within a grid on the head top (right) centered on the centre of gravity of the top of the skull. The results are presented for two different distances from the centre of gravity of the top of the skull and the detector (12.5 and 15.5 cm)

- The agreement between the two models (fully homogeneous and 24 sources heterogeneous) is bounded within maximum $\pm 20\%$
- The agreement is improved at higher distances from the skull surface.

5 Calibration Measurements and Monte Carlo Simulations

An accurate calibration campaign was carried out on the developed plastic phantom at the ENEA - Institute for Radiation Protection Casaccia (Rome) Research Centre. The detector position had to satisfy two main requirements: the need to reduce the photon fluence variations due to the heterogeneous source distribution, and to assure a minimum detectable activity (MDA) [10] of about 3–4 Bq in the skull in 20–30 minutes measurement times. The obtained results in terms of counting efficiency (Tab. 2), show a progressively better agreement between the Monte Carlo results and the WBC measurements as a function of the increasing distance of the detector from the phantom external surface, reaching a nearly perfect agreement at 15–20 cm. At this kind of distances the efficiency factors observed are on the other hand too low to guarantee the desired MDA values in reasonable counting times. These considerations implied the adoption of an operative procedure allowing to maximise the counting efficiency in the measurement. The adopted procedure can be summarised as follows:

- Measurement of the efficiency factor $\epsilon_{\text{calib}/15}$ at 15 cm from the head surface (calibration distance) to limit as much as possible the local effects on the photon fluence due to the 24 heterogeneous sources.
- Monte Carlo calculation of the efficiency correction factors due to the change in distance (CFd) and to the non homogeneous distribution of the calibration sources (CFh). CFd is the ratio of the MCNP efficiencies at calibration and at in vivo measurement distance, assuming the real-homogeneous source distribution. CFh is the ratio of the MCNP efficiencies at calibration distance, between the real-homogeneous and calibration-heterogeneous source distributions.

Table 2. Full Energy Peak Efficiencies at various Head Surface-Detector Distances: MCNP and Experimental values

Detector to Head distance cm	MCNP Hom /Exp Data	MCNP Hom Source 10^{-3} Cps/Bq	MCNP 24 Point /Exp Data	MCNP 24 point-source 10^{-3} Cps/Bq	MCNP Hom /MCNP 24 Point	Experimental WBC efficiency: 10^{-3} Cps/Bq
-1	0.77	6.70 (0.2%)	0.86	7.54 (0.2%)	0.89	8.70 (1.0%)
-10	0.85	2.10 (0.5%)	0.89	2.21 (0.4%)	0.96	2.48 (1.0%)
-15	0.99	1.37 (0.6%)	1.00	1.40 (0.6%)	0.99	1.41 (1.0%)
-20	1.00	0.95 (0.5%)	1.02	0.97 (0.5%)	0.98	0.95 (1.0%)

- Determination of the values of the in vivo efficiency for the assumed in vivo homogeneous distribution and detection distance of 1 cm from the head surface according to: $\epsilon_{\text{in vivo}/1} = \epsilon_{\text{calib}/15} * CFd * CFh$
- In vivo measurements at 1 cm distance from the subject head.

6 Conclusions

The adopted procedure, based on the use of known activity point sources, can be considered a valuable alternative to the employment of skull phantoms painted with a thin coat of radioactive paint, for which it is difficult to guarantee an homogeneous distribution on the head surface and to quantify suitable correction factors. The employed methodology, relying on a rigorous Monte Carlo simulation, allowed determining the approximation level introduced and evaluating a corresponding correction factor. The comparison with the measurements demonstrated the reliability of the approach, that can therefore be standardised in the calibration procedures. A further implementation could consist in the development of a multi-purpose phantom for a large variety of osteotropic nuclides to be placed in the same plastic matrix: this could enhance the flexibility of the phantom to become a new calibration standard in this field of applications.

References

1. R. Toohey: Health Phys. **60**, 7 (1991)
2. G.H. Kramer, L.C. Burns, S. Yiu: Rad. Prot. Dosim. **74**, 173 (1997)
3. N. Petoussi-Henss, M. Zankl: Rad. Prot. Dosim. **79**, 415 (1998)
4. J.Hunt, B.M. Dantas, E.Lucena: Rad. Prot. Dosim. **79**, 425 (1998)
5. J.F. Briesmeister [editor]: *MCNP – A general Monte Carlo N-Particle Transport Code Version 4B*, LA-12625 Los Alamos National Laboratory (1997)
6. G. Gualdrini, P. Battisti, R. Biagini, P. De Felice, A. Fazio, P. Ferrari: Appl. Rad. Isot. **53** 387 (2000)
7. K. Van Riper: *Sabrina User's Guide* (White Rock Science, 1997)
8. W.S. Snyder et al.: *Estimates of specific absorbed fractions for photon sources uniformly distributed in various organs of a heterogeneous phantom*. Health Physic Division, Oak Ridge Nat. Lab., Tennessee 37830 (1978)
9. AA.VV.: *Report of the task group on Reference Man*, ICRP Publication 23 (Pergamon Press, 1974)
10. L.A. Currie: Analytical Chemistry **40** (1998)

Monte Carlo Studies of the Portuguese Gamma Irradiation Facility. The Irradiator Geometry and Its Influence on Process Parameters

C. Oliveira, L. Ferreira and J. Salgado

Instituto Tecnológico e Nuclear, Est. Nacional 10, 2686-953 Sacavém, Portugal

Abstract. The paper describes a Monte Carlo study of dose distributions, minimum dose and uniformity ratio for the Portuguese Gamma Irradiation Facility. These process parameters are calculated using the MCNP code for several irradiator geometries. The comparison of the simulated results with the experimental results carried out using Amber Perspex dosimeters in a routine process of the gamma facility for a given material composition and density reveals good agreement. The results already obtained allow to conclude that the dose uniformity is not very sensitive to the irradiator geometry for density value $\rho = 0.1$ and for a dynamic process.

1 Introduction

Considering that there are more than 200 Gamma Irradiator Facilities in the world and the relatively short half-life of Co sources, substitution of these sources is a relevant issue.

Gamma irradiation facilities have been studied previously using mathematical methods such as the point kernel approach [4] and the Monte Carlo approach. The most used Monte Carlo codes are the EGS4 [2–4], the ITS [5,6] and the MCNP [7,8].

This work reports a Monte Carlo application for the Portuguese Gamma Irradiation Facility (UTR). The MCNP [9] code has been used for this study. A specific code C, whose input is the output of MCNP code, gives, for several irradiator configurations, the process parameters: average dose, minimum and maximum dose and dose uniformity. The experimental results have been obtained using Amber Perspex dosimeters in a routine process of the UTR.

This study can be an important tool in order to optimize replacement the old sources by new ones according to some pre-defined statements.

2 Materials and Methods

The UTR has already been described elsewhere [10]. The product to be irradiated is placed in vertical carriers suspended from a monorail conveyor. Each carrier can be loaded with 4 product boxes. There are 2 rows of carriers in each side of the source plaque and 7 irradiation positions (i.e. 7 carriers) in each row. Each

carrier has four levels. To ensure the two-sided irradiation of the boxes the carrier is reversed by 180° at the end of the second row on one side of the source rack. One complete irradiation run consists of two cycles. After the completion of the first cycle the two product boxes on the first and second levels are transferred to the third and fourth levels and irradiated in the second cycle.

The source rack has an area of $0.9 \times 0.9 \text{ m}^2$, and contains 30 stainless steel tubes. In the current geometry the irradiator contains 156 ^{60}Co sources, doubly encapsulated in welded stainless steel so that two tubes in the middle of the rack contain 8 sources each, while 7 tubes to the left and right of the middle ones contain 10 sources each [11]. In this configuration there are 7 empty stainless steel tubes in the left and 7 empty stainless steel tubes in the right of the source rack (see Fig. 1a)).

For this study two boxes ($40 \times 40 \times 40 \text{ cm}^3$) filled with paper were used. Each of them was conceptually divided in 64 small cubic volumes ($10 \times 10 \times 10 \text{ cm}^3$). Sixty-four Amber-Perspex dosimeters were put in the positions corresponding to the centre of each of these volumes. The boxes were placed in the carrier and a complete irradiation was run.

MCNP4B2 was used for simulation. The motivations for using this code are: (a) it is a very well benchmarked code; (b) it allows the use of some variance-reducing techniques; (c) it has ten statistical checks to test the validity of results; (d) the repeated structure feature of the code is appropriate to design the Gamma Irradiation Facility and to obtain results corresponding to the routine (dynamic) process. In fact, the 28 carriers having each 4 levels which correspond to 4 boxes, are identical and were appropriately designed using the *universe* and *fill* capacities of the MCNP code and also the *like... but* (with a translation) card. The same method has been adopted for designing the sources that can have equal or different intensities between them. The way to ask the results benefits also of the repeated structure capacities.

In order to compare the experimental results with the simulated results, the MCNP code calculates the average photon flux into each cubic volume ($10 \times 10 \times 10 \text{ cm}^3$) and it directly converts the flux estimates to absorbed dose rates in the paper by using the flux multiplier card *FM*. The correction factor (ratio between the mass energy-absorption coefficient of the water and the paper) was applied in order to convert these values in absorbed dose in water. The platform used for the code was an Alpha Personal Workstation running Digital Unix with 64 Mbytes RAM and a 433 MHz CPU. The physical parameters selected in MCNP were the same that was described elsewhere [8].

3 Results and Discussion

As it has been previously mentioned, for each of the two boxes pertaining to level 1 and 3, and to level 2 and 4, the MCNP code calculates the dose in each 64 small volumes, for each of the 28 positions in each level (56 positions for the two levels). A specific C code sums the dose values of each volume for the 56 positions, in a similar way that occurs in the real process.

Besides the current irradiator geometry used to validate the followed methodology (*a*), three other configurations have been studied: (*b*) a mixture of the current 156 sources with 140 new ones (whose activity correspond to the initial activity of the current sources) filling all empty positions; (*c*) 296 new sources; (*d*) 196 new sources positioned in the middle of the source rack. These configurations are drawn in Fig. 1.

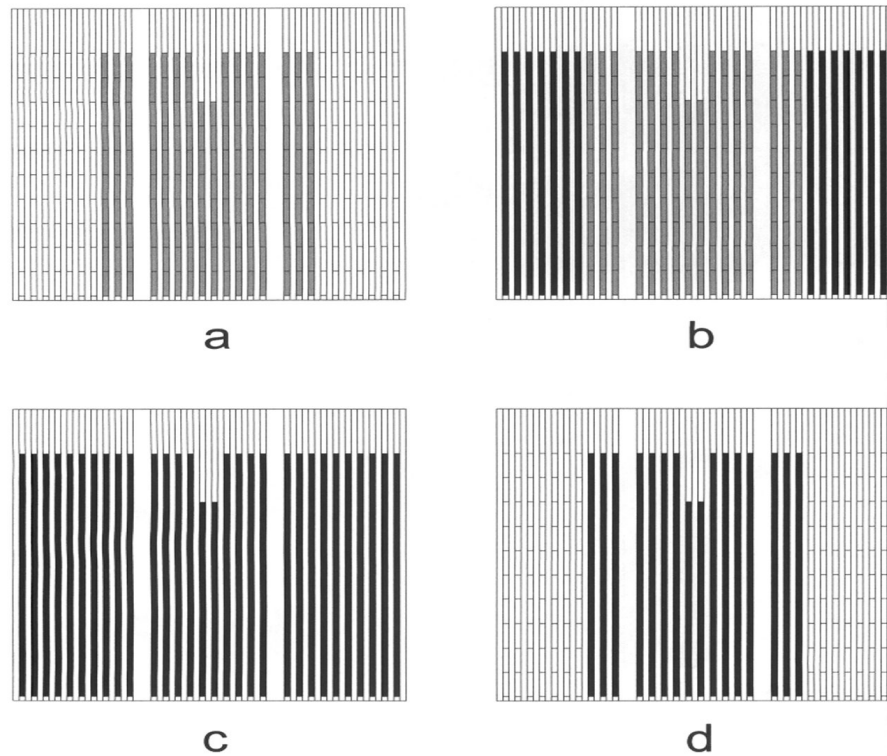


Fig. 1. The four studied irradiator configurations. *a*) Current configuration; *b*) mixture of lower (grey) and higher (black) activity sources; *c*) 296 new sources; *d*) 196 new sources

For the current geometry, the experimental results - absorbed dose (after the second cycle) are shown together with the simulation results in Fig. 2. The experimental data are systematically about 2% higher than the simulated values for both product boxes. Taking into account the uncertainty in the source activity, and in the experimental and simulated errors, there is a good agreement between simulated and experimental results.

The results, average dose rate, minimum and maximum dose rate and dose uniformity, for the current configuration and for the other configurations, are

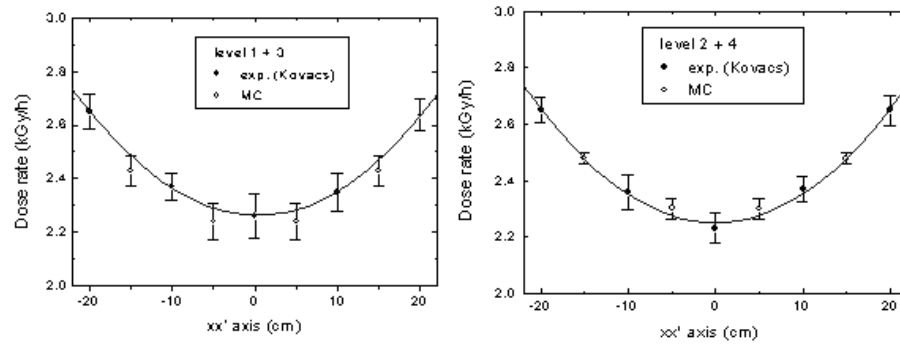


Fig. 2. Experimental and simulated results for the current geometry for a material density of $\rho = 0.1$

shown in Tab. 1. The material density is 0.1 and the activity is reported to October 1999.

Table 1. Activity, average dose rate (\dot{D}), minimum dose rate (\dot{D}_{\min}), maximum dose rate (\dot{D}_{\max}), and dose uniformity (U) for the current geometry (case *a*) and for three studied cases.

Configuration	Activity (Bq)	\dot{D} (kGy/h)		\dot{D}_{\min} (kGy/h)		\dot{D}_{\max} (kGy/h)		U	
		Level 1-3	Level 2-4	Level 1-3	Level 2-4	Level 1-3	Level 2-4	Level 1-3	Level 2-4
Case <i>a</i>) $\rho = 0.1$	2.71E15	0.610	0.622	0.576	0.592	0.654	0.662	1.14	1.12
$\rho = 0.2$		0.557	0.569	0.522	0.536	0.609	0.620	1.17	1.16
Case <i>b</i>)	1.42E16	3.080	3.150	2.969	3.044	3.309	3.374	1.11	1.11
Case <i>c</i>)	2.43E16	5.280	5.390	5.090	5.210	5.690	5.790	1.12	1.11
Case <i>d</i>)	1.61E16	3.58	3.65	3.40	3.48	3.48	3.91	1.13	1.12

The data show that the dose uniformity is independent of the irradiator configuration.

The average, maximum and minimum doses are proportional to the source activity. Simulated and experimental data previously obtained by Kovács [11] have also been compared in Fig. 3. In this case the density was $\rho = 0.2$.

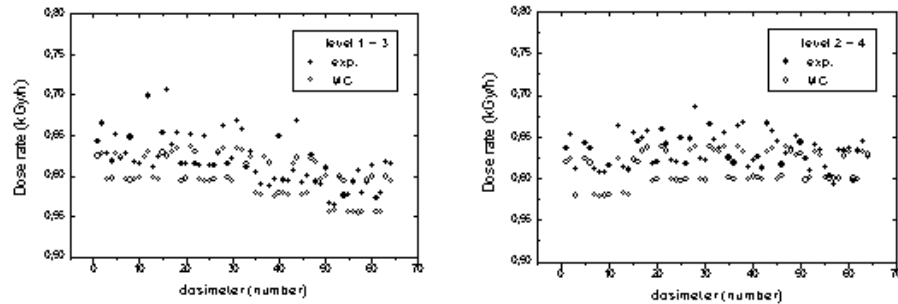


Fig. 3. Experimental (from reference [11]) and simulated data for a material density of 0.2

The xx' axis is perpendicular to the source rack plan and its center is located in the center of the box. The bars in the experimental values represent the dispersion of the values on the plan perpendicular to the xx' axis. It measures the dispersion along the yy' and zz' axis. From the data it is evident that the variation of the absorbed dose inside the box with the distance to the source is dominant relatively to others variations. The simulated values fit well the experimental ones.

Reporting to the Tab. 1 it can be observed a light decrease on the absorbed dose for $\rho = 0.2$ as compared to the dose corresponding to $\rho = 0.1$. This effect is due to the increase of the absorption of gamma radiation in material as it has already been mentioned previously [12]. On the other hand the dose uniformity worsens with the density.

4 Conclusions

The results obtained allow concluding that the dose uniformity and the dose normalised by source activity are not sensitive to the irradiator geometry. On the contrary they are sensitive to the density. The final option for a given irradiator geometry which is supposed to irradiate material with a given density should be made taking into account, besides the process parameters already mentioned, economical aspects.

Another aspect is the importance that non-routine irradiations could assume for some facilities. Generally these are static irradiations. For them, the effects on dose uniformity depend on the irradiator configuration. Note that this aspect has not discussed in this work.

5 Acknowledgements

The authors wish to thank Eng. Pedro Gomes for his contribution in the writing of C code for this work.

References

1. G. Pina-Villalpando, D.P. Sloan: Radiat. Phys. Chem. **52**, 563 (1998)
2. W.R. Nelson, D.W.O. Rogers: 'Structure and operation of the EGS4 code system'. In *Jenkins, T.M., Nelson, W.R. and Rindi, A. eds. Monte Carlo transport of electrons and photons*, 287-305 (1988)
3. R. McIntyre, C.J. Huntzinger, W.R. Nelson: Radiat. Phys. Chem. **35**, 762 (1990)
4. G.R. Raisali, M. Sohrabpour: Radiat. Phys. Chem. **42**, 799 (1993)
5. J. Halbleib: 'Structure and operation of the ITS code system'. In *Jenkins, T.M., Nelson, W.R. and Rindi, A., eds. Monte Carlo transport of electrons and photons* (Plenum Press, New York 1988) pp. 249-262
6. D.E. Weiss, W.C. Johnson, R.P. Kensek: Radiat. Phys. Chem. **50**, 475 (1993)
7. M.C. Saylor, T.M. Jordan: Radiat. Phys. Chem. **52**, 563 (1998)
8. C. Oliveira, J. Salgado, M.L. Botelho, L.M. Ferreira: 'Monte Carlo application for irradiation process planning at the Portuguese Gamma Irradiation Facility'. Radiat. Phys. Chem. in press (1999)
9. J.F. Briesmeister (ed.): *MCNP - A General Monte Carlo N-Particle Transport Code*, LA 12625-M, Version 4B (1997)
10. C.M. Mendes, J.C. Almeida, M.L. Botelho, M.C. Cavaco, E. Almeida-Vara, M.E. Andrade: Radiat. Phys. Chem. **35**, 576 (1990)
11. A.V. Kovács: *Initial commissioning of the UTR Gamma-Pi ^{60}Co irradiation facility*. Final Report. Internal Publication of ITN, Portugal (1988)
12. C. Oliveira, J. Salgado: 'Isodose distributions and dose uniformity in Portuguese Gamma Irradiation Facility calculated using the MCNP code'. Presented at 8th *International Symposium on Radiation Physics*, ISRP-8, Prague, Czech Republic, June 2000

Multiple Scattering in GEANT4. A Comparison with Molière Theory and L3 Detector Data

P. Arce¹, M. Maire², L. Urbán³, and M. Wadhwa⁴

¹ Instituto de Física de Cantabria, Av. los Castros s/n, E-39005 Santander, Spain

² LAPP, BP 110, F-74941 Annecy-le-vieux Cedex, France

³ KFKI Research Institute for Particle and Nuclear Physics, H-1525 Budapest,
P.O.Box 49, Hungary

⁴ University of Basel, Klingelbergstraße 82, CH-4056 Basel, Switzerland

Abstract. We have compared a new model used in GEANT4 for multiple scattering and the model based in the Molière theory used in GEANT3 with the data collected in the L3 detector for the case of muons of momentum around 45 GeV. We have found some disagreement in the case of GEANT3 but a good matching to the data in the case of GEANT4.

1 Multiple Scattering in GEANT4

GEANT4 [1] uses a new multiple scattering model instead of the Molière formalism ([2]) used in GEANT3 and other software.

This model simulates the scattering of the particle after a given step, calculating first the transformation ‘true’ path length, ‘t’ (total length travelled by the particle), and the ‘geometrical’ path length, ‘z’ (straight distance between the starting and end point of the step) with the equation

$$z = \lambda * (1. - \exp(-t/\lambda)) \quad (1)$$

where λ is the transport mean free path. This formula is an exact result for the mean values of ‘z’, if the differential cross section has an axial symmetry and the energy loss can be neglected. This formula and some other expressions for the first moments of the spatial distribution after a given ‘true’ path length ‘t’ have been calculated by Goudsmit and Saunderson [3] and Lewis [4].

The mean value of $\cos(\theta) - \theta$ is the scattering angle after a true step length ‘t’ – is

$$\langle \cos(\theta) \rangle = \exp(-t/\lambda) \quad (2)$$

As described by Liljequist [5], the mean properties of the multiple scattering process are mainly determined by the transport mean free path (also called first transport mean free path in the literature), which is a function of the energy in a given material. Some of the mean properties – the mean lateral displacement and the second moment of $\cos(\theta)$ – depend on the second transport mean free path, too.

The transport mean free path values have been calculated by Liljequist et al. [6] for electrons and positrons in the kinetic energy range 0.1 keV–20 MeV in 15 materials. The multiple scattering model uses these values with an appropriate interpolation or extrapolation in the atomic number Z and in the velocity of the particle β , when necessary. In the case of heavy charged particles (μ , π , proton, etc.) the mean transport free path is calculated from the $e^+ / e^- \lambda$ values with a ‘scaling’.

The quantity $\cos(\theta)$ is sampled in the model according to a function $f(\cos(\theta))$. The function has been chosen in such a way that it reproduces the results of the direct simulation of the particle transport and (2) is satisfied. The functional form of this model function is

$$f(x) = p \frac{(a+1)^2(a-1)^2}{2a} \frac{1}{(a-x)^3} + (1-p) \frac{1}{2} \quad (3)$$

where $x = \cos(\theta)$, $0 \leq p \leq 1$ and $a > 1$. The model parameters p and a depend on the path length ‘ t ’, the energy of the particle and the material. They should satisfy the constraint

$$\frac{p}{a} = \exp\left(-\frac{t}{\lambda}\right) \quad (4)$$

which follows from (2).

After calculating the scattering angle, the model computes the mean lateral displacement, using a more complicated formula [7], but using as only ‘random’ quantity the same scattering angle θ .

It is worth to note that in this multiple scattering model there is no step limitation originated from the multiple scattering process. Another important feature of this model is that the total ‘true’ path length of the particle does not depend the length of the steps. Most of the algorithms used in simulations do not have these properties.

A first comparison of this model with L3 data was presented at [8]. A discrepancy of the order of 20% was discovered then and it was found to be due to a missing nuclear size effect correction, increasing with the energy of the particle. The formulae to include this effect have been taken from [5]. This implementation is a semiempirical one, leaving free one parameter. To adjust this parameter, the data from [9] have been used, where the deviation of pions, kaons and protons from 50 to 200 GeV traversing thin layers of lead, tin and copper has been studied. The average value obtained for the parameter is

$$\log(\text{nucl.size.effect.param}) = -2.79 \pm 0.69$$

We present here the new results obtained with this improved model of multiple scattering.

2 Method

To check the results of this new model against data, we have chosen a sample of muons of momentum around 45 GeV collected in the L3 detector during the

years 1994 and 1995. A selection procedure is done to identify the muons coming from the process $e^+e^- \rightarrow Z/\gamma \rightarrow \mu^+\mu^-$. With this selection a purity bigger than 99.5% is reached with an efficiency of 15.3%. Fig. 1 shows the distribution of the generated momentum for the Monte Carlo (MC) $e^+e^- \rightarrow Z/\gamma \rightarrow \mu^+\mu^-$ sample after selection.

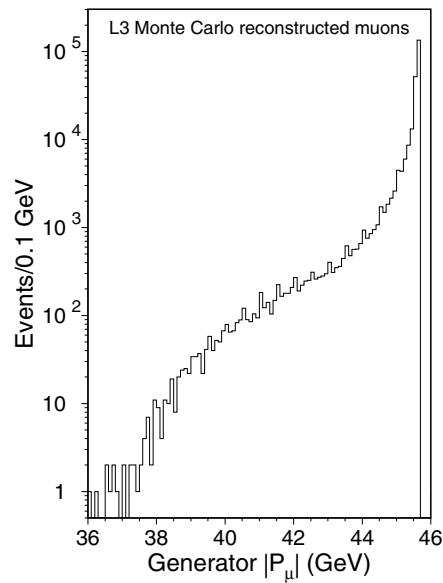


Fig. 1. Distribution of generated muon momentum for the selected muons of the MC $e^+e^- \rightarrow Z/\gamma \rightarrow \mu^+\mu^-$

From its creation at the L3 interaction vertex until they hit the first muon chamber, these muons travel 213 cm. The main materials found include 24 cm of BGO, 25 cm of iron, 28 cm of brass and 28 cm of uranium. Of course, all this numbers have to be divided by $\cos\theta$, being θ the angle between the muon and the beam direction (the Z direction). All the subdetectors (including the muon chambers) are immersed in an homogeneous solenoidal field of 0.5 Tesla. A detailed description of the L3 detector can be found in [10,11].

We have only studied the deviation of the muons in the R- ϕ plane, as the Z measurements in L3 do not give enough precision to study the deviation in the RZ plane.

There are several contributions to the end point deviations of muons (the distance between the real point of the muon track in the inner muon chamber

and the point at the same radius that it would reach if it would have followed an straight line trajectory):

- First, the ones we are interested in, the **deviation from multiple scattering and from energy conservation when emitting a secondary particle**. We cannot split in the data these two contributions and therefore we will treat them together as the ‘deviation from matter interaction’. We will mention here that the deviation due to secondary particles production is only of the order of 10–20% of the one due to multiple scattering and it is almost fully due to the production of delta rays, while the contributions from bremsstrahlung, pair production and nuclear interaction is less than 1% of the total.

The other contributions to the deviation of muons in L3, that we should subtract, are:

- **The magnetic field.** This is the biggest contribution of all, because the 0.5 Tesla solenoidal field deviates 45 GeV muons around 12.5 mm from

the vertex to the inner muon chamber. To subtract it, we have simulated a sample of single muons of different momentum and theta and used the method described below.

- **Errors in the vertex position, the ϕ angle at vertex and the position of the point at the inner muon chamber.** The first one is around 200 μm , the second one around 10^{-4} radians (what means around 200 μm at 2.1 meters) and the third one is less than 100 μm . All three are therefore negligible compared to the expected 6–7 mm deviation from matter interaction. We have not subtracted them in our distributions, but we have included them in the GEANT3 and GEANT4 simulations.

2.1 Subtracting the Deviation from Magnetic Field

The deviation due to the magnetic field is different for different momenta of the muons and it also depends on the area of the detector traversed by the muon. As the L3 magnetic field is solenoidal, we have assumed axial symmetry around Z . To get the dependences on momentum and Z of the point in the inner muon chamber, we have run the full GEANT3.15 L3 simulation for muons of momentum of different momentum and initial θ , switching off the deviation from matter interaction. We have not changed the energy lost by secondary particles production, as this would affect the deviation caused by the magnetic field. As the reconstruction process consumes too much time for L3, we have opted to include in this simulated sample the effects needed to reproduce the data sample of reconstructed muons. To do this, we have first reweighted the distributions of the variables on which the deviation depends more, namely the generator momentum and the radius of the point of intersection of the muon with the inner muon chamber, to make them equal to those of the reconstructed sample. We have then smeared with the data resolution the distributions of inverse muon momentum and also the distributions of θ and ϕ and distance of closest approach to vertex.

The momentum dependence of the deviation caused by the magnetic field can be approximated by a circle with a curvature radius proportional to $1/P_\mu$. For Z the dependence is more difficult to parametrize. To do it, we have split the sample in twenty equally spaced bins of Z . For each bin independently we have extrapolated all the muons along a trajectory with a curvature radius $F \times 1/P_\mu$, and we have got the value of the factor F that makes the distribution of the distance of the trajectories to the real point in the inner muon chamber be centered at zero (as it should be because all the other contributions to this deviation are centered at zero). The adjusting of these factors serves also to account for the deviation from an exact $1/P_\mu$ dependence due to the energy lost by the muon on its way through the L3 detector and for the dependence of the magnetic field with the radius.

3 Comparison of GEANT3.15 with Data

After subtracting the deviation due to the magnetic field with the method described in the previous section, we compare in Fig. 2(a) the distribution of end point deviation for MC reconstructed muons for positive and negative muons. We see that both distributions are centered at zero and have very similar width, what gives us confidence on the method used for subtracting the magnetic field deviation.

In Fig. 2(b,c) the same distributions are shown for 1994 and 1995 reconstructed data. In this case, they are also very similar for positive and negative muons, but they are not centered at zero. This is due to the misalignment of the muon chambers with respect to their nominal positions. After correcting this effect octant by octant the distributions appear centered at zero.

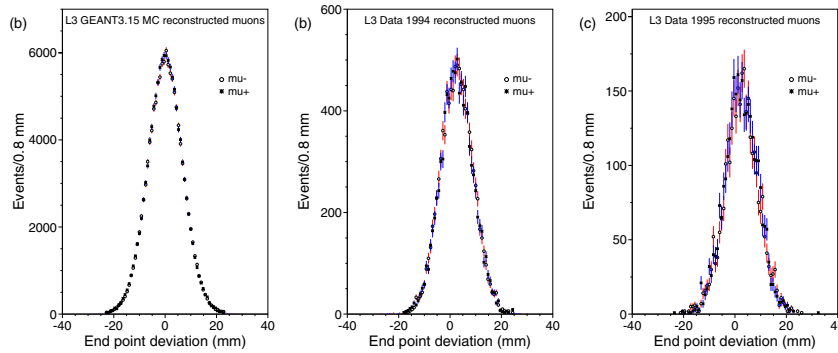


Fig. 2. End point deviation of positive and negative reconstructed muons after subtracting the magnetic field deviation. (a) GEANT3 MC. (b) Data 1994. (c) Data 1995

Merging the positive and negative muons distributions, the widths of the distributions of the deviation of a muon while traversing the L3 detector, once the magnetic field contribution is subtracted, for the MC GEANT3, the data 1994 and the data 1995, are:

GEANT3.15: 6.871 ± 0.011 mm

Data 1994: 6.066 ± 0.032 mm

Data 1995: 6.120 ± 0.061 mm

3.1 Systematics for the GEANT3.15 - Data Comparison

We have studied every possible source of systematic error we could think it may affect the previous results, and we have given a conservative estimation of their magnitude.

Contamination from other Channels: It is negligible thanks to the stringent selection cuts used.

Wrong Simulation of the Detector: After ten years of running a precision experiment like L3, we have the assurance that a 1% systematic error is quite conservative.

Misalignment of the Muon Chambers: The correction done for the misalignment could induce a systematic error if the misalignment changes with time. We have split the yearly samples in three periods and we have corrected the 1994 with the 1995 misalignments and vice versa. This way we can estimate a systematic error of ± 0.013 mm.

Subtracting the Deviation from Magnetic Field: After this subtraction the width of the deviation is changed of the order of 0.1 mm, therefore the change cannot be very different in MC and data. We will take as systematic error the difference between the variation in MC and in data, that is ± 0.017 mm.

Radius of Muon Chamber Point: The dependence of the end point deviation is very big with this variable, what made us reweight the MC distribution to match that of data (although differences were small). Even so, we account for a systematic error as the variation in deviation due to an error in this variable of ± 10 mm, what means ± 0.049 mm.

Initial Muon Momentum: The momentum dependence of the deviation is also quite big, but again the distributions of data and MC are similar. There could be two main sources of error related to the momentum: a different initial momentum for data and MC and a different loss of momentum for data and MC.

The distribution of initial momentum cannot be obtained for data, but we are confident that the MC program used in L3 (KoralZ) reproduces it quite well. In any case, we have studied the dependence of the deviation with the initial momentum. Assuming conservatively a discrepancy of the MC and data initial momentum of 0.5 GeV we can then quote an error of ± 0.059 mm.

Energy Lost by the Muon: We have made a similar study of the dependence of the deviation with the total energy lost by the muon before reaching the first muon chamber. A discrepancy as big as 1 GeV in this variable (the mean energy deposited is 2.5 GeV) means an error of ± 0.036 mm.

Resolutions Applied to Simulated Muons: We have changed the inverse momentum resolution of the simulated muons used to subtract the magnetic field by $\pm 33\%$ and the θ and ϕ resolutions by $\pm 20\%$. This way we can estimate a systematic error of ± 0.006 mm.

Small Changes in the Method: We have also made small changes in the method used to subtract the magnetic field contribution. The systematic error obtained from these changes is ± 0.002 mm.

Selection: Finally, we have changed the cuts used in the reconstructed sample and at the same time in the simulated sample. We get a combined systematic error for the cuts ± 0.074 mm.

Adding all the above mentioned errors, we can quote a
total systematic error: ± 0.134 mm

4 GEANT4 Simulation of L3

We have simulated the full geometry of the L3 detector with the help of an enhanced version of the package g3tog4, part of the GEANT4 software [1]. We have used GEANT4.0.1 with the correction to account for the nuclear size effect in the multiple scattering described in the first section (later released in GEANT4.1.0).

To make possible a comparison with the L3 reconstructed data, we have applied to the simulated muons the same cuts, reweighting and smearing we applied to the GEANT3 simulated sample when subtracting the magnetic field.

For comparing to data, a final correction is needed. We have realized that the width of the end point deviation for GEANT3 simulated muons is slightly different from that of the GEANT3 reconstructed muons, the ratio being $102.20 \pm 0.64\%$. We have tracked this problem to the Gaussian smearing we have used for the simulated sample, specially for the momentum variable. After this correction, the width of the GEANT4 deviation is

GEANT4.1.0: 6.233 ± 0.046 mm

4.1 Systematics of the GEANT4 Simulation

We have analysed with care the simulation for a few muons with GEANT3 and GEANT4 and checked that they traverse the same detector parts at the same points. We have also simulated 25 cm blocks of the main materials in L3, namely uranium, iron, lead and BGO, and checked that the average difference in the deviation of GEANT4 and GEANT3 is about the same than the observed difference in the simulation of L3.

Most of the systematics that affect the GEANT3 simulation will probably also affect the GEANT4 simulation. Applying the same relative error of the GEANT3 simulation to the GEANT4 one, we quote a systematic error of ± 0.121 mm.

Another source of error is the correction factor 102.20 % applied to the GEANT4 data to account for the difference between the simulated (reweighted and smeared) sample and the reconstructed one. We will conservatively quote an error of 2.20 % as possible systematic error, this means ± 0.137 mm.

The last relevant systematic error is related to the correction applied to the GEANT4 code to account for the screening of the nucleus to the multiple scattering. Including the error in the nuclear size correction parameter as described in the first section, we obtain a systematic error of ± 0.112 mm.

Adding all this errors, we can quote for the GEANT4 simulation a

Total systematic error: ± 0.214 mm

5 Conclusions

We have studied the model used in GEANT4 for the multiple scattering of charged particles and compared it with the GEANT3 model and with a sample of 45 GeV muons collected in the L3 detector during the years 1994 and 1995.

The widths of the end point deviation distributions in the first muon chamber are:

$$\text{Data: } 6.078 \pm 0.028 \text{ mm}$$

$$\text{GEANT3.15: } 6.871 \pm 0.011 \pm 0.134 \text{ mm}$$

$$\text{GEANT4.1.0: } 6.233 \pm 0.046 \pm 0.214 \text{ mm}$$

where the first errors are statistical and the second is systematic. This deviations can be seen in Fig. 3.

We conclude that Molière theory implemented in GEANT3.15 shows some difference with the L3 data while the new model of multiple scattering of GEANT 4.1.0 shows a good agreement.

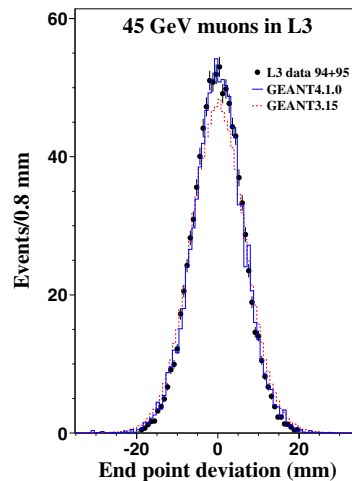


Fig. 3. Comparison of end point deviation for L3 data 1994+1995 reconstructed muons, L3 MC GEANT3.15 reconstructed muons and GEANT4.1.0 simulated and corrected muons

References

1. <http://wwwinfo.cern.ch/asd/geant4/geant4.html>
2. G.Z. Molière: Z. Naturforsch. **3a**, 78 (1948)
3. S. Goudsmit, J. L. Saunderson: Phys. Rev. **57**, 24 (1940)
4. H. W. Lewis: Phys. Rev. **78**, 256 (1950)
5. D. Liljequist: J. Appl. Phys. **68**, 3061 (1990)
6. D. Liljequist, M. Ismail: J. Appl. Phys. **62**, 342 (1987)
7. J.M. Fernandez-Varea et al.: Nucl. Instr. Meth. B **73**, 447 (1993)
8. <http://www.estec.esa.nl/CONFANNOUN/99c09/index.html>
9. G. Shen et al.: Phys. Rev. D **20**, 1584 (1979)
10. L3 Collaboration, B. Adeva et al.: Nucl. Instr. Meth. A **289**, 35 (1990)
11. L3 Collaboration, O. Adriani et al.: Phys. Rep. **236**, 1 (1993)

On the Use of CAD Geometry for Monte Carlo Particle Transport ^{*}

H. Tsige-Tamirat

Forschungszentrum Karlsruhe, Institut für Reaktorsicherheit, P.O. Box 3640,
76021 Karlsruhe, Germany

Abstract. This paper deals with the conversion of geometric data generated by Computer Aided Design (CAD) systems into a representation appropriate for Monte Carlo (MC) Particle Transport codes.

1 Introduction

Currently, geometry models for MC codes are mostly provided manually by collecting coordinates and vectors from engineering drawings. This process is time consuming and error prone. A better solution would be to use geometric data from CAD systems to directly generate a geometry representation appropriate for MC particle transport. This requires, however, the following steps: (i) access to the data of a CAD system, and (ii) conversion of the CAD geometry into a representation appropriate for MC codes. While the first step is merely technical, the second step seems to be a basic problem which has been a major obstacle in the past for the development of a CAD interface for MC codes. In this paper, we primarily deal with this problem for solids given by boundary representation as used in most commercial CAD systems.

2 Preliminary

2.1 Basic Topological Notions

In what follows we introduce some elementary topological notions which we use later [1]. Let F be a subset of topological space X . F is said to be closed if its complement is open. We denote the interior, closure, and boundary of F by $\text{int}F$, $\text{cl}F$, and $\partial F = \text{cl}F \setminus \text{int}F$, respectively.

A set F is regular closed if $F = \text{cl}(\text{int}F)$ and regular open if $F = \text{int}(\text{cl}F)$. A subset F of a topological space X is said to be dense in X if $\text{cl}F = X$ and F is said to be nowhere dense if $X \setminus \text{cl}F$ is dense. A collection of open sets $\mathcal{B} = \{B_\alpha\}$ is a base for a topology on X if (i) $X = \cup B_\alpha$, and if p is a point in X such that $p \in B_\alpha \cap B_\beta$, then there exists $B_\gamma \in \mathcal{B}$ containing p and which itself is contained in $B_\alpha \cap B_\beta$. A collection of open sets \mathcal{O} is a subbase for a topology

^{*} This work has been performed in the framework of the nuclear fusion programme of Forschungszentrum Karlsruhe and is supported by the European Union within the European Fusion Technology Programme.

\mathcal{J} on X iff the collection of finite intersection of elements \mathcal{O} is a base for \mathcal{J} . A collection of closed sets \mathcal{C} is a base for closed sets if every closed set in X is an intersection of members of \mathcal{C} , i.e., when \mathcal{C} is a base and whenever F is a closed set and $x \in X \setminus F$, there is a member of \mathcal{C} that contains F but not x .

Let X be a topological space with topology \mathcal{J} . If Y is a subset of X , the collection $\mathcal{J}_Y = \{Y \cap U \mid U \in \mathcal{J}\}$ is a topology on Y , called the subspace topology. Equipped with this topology, Y is said to be a subspace of X . If \mathcal{B} is a base for topology of X , then the collection $\mathcal{B}_Y = \{B \cap Y \mid B \in \mathcal{B}\}$ is a base for the subspace topology on Y . A collection of sets \mathcal{A} is said to be a cover of a topological space X if X is contained in the union of elements of \mathcal{A} . A subcover is a subset which covers X . A topological space is compact if every open cover of it has a finite subcover.

Let $\{X_\alpha\}$ be family of topological spaces. A topology \mathcal{J} on a set Y is said to be final with respect to the function $f_\alpha : X_\alpha \rightarrow Y$ iff for any topological space Z and a function $g : Y \rightarrow Z$ is continuous iff $g f_\alpha : X_\alpha \rightarrow Z$ is continuous. Given a set X , a family $\{X_\alpha\}$ of topological spaces, and a family of injective maps $f_\alpha : X \rightarrow X_\alpha$ for each X_α . Then a topology \mathcal{J} on X is initial with respect to the family $\{f_\alpha\}$ iff there exists a topological space Y and a map $g : Y \rightarrow X_\mathcal{J}$ is continuous iff $g f_\alpha : Y \rightarrow Z$ is continuous. A decomposition X/\mathcal{D} of a topological space X is a disjoint family \mathcal{D} of X whose union is X . The quotient map of X onto the decomposition X/\mathcal{D} is a continuous surjection $pr : X \rightarrow X/\mathcal{D}$. The quotient topology on X/\mathcal{D} is the final topology with respect to pr . The Tychonoff topology on the product $X = \prod_{\alpha \in A} X_\alpha$ is the initial topology with respect to the projections $\pi_\alpha : X \rightarrow X_\alpha$. If each X_α is compact, then by the Tychonoff theorem [1] the product is compact.

A sequence X_0, X_1, \dots of subsets of a topological space X is a filtration of X if the sequence is ordered by inclusion, i.e., $X_0 \subset X_1 \subset \dots$, and the sets X_i form a cover of X . A filter \mathcal{F} in a set X is a family of non-empty subsets of X such that (i) $A, B \in \mathcal{F} \Rightarrow A \cap B \in \mathcal{F}$, and (ii) $A \in \mathcal{F}, B \in X, A \subset B \Rightarrow B \in \mathcal{F}$. A filter \mathcal{F} is a prime filter if the union of two sets belongs to \mathcal{F} , then one of them belongs to \mathcal{F} . A filter is a ultrafilter iff it is not properly contained in no other filter in X .

2.2 Basic Semi-Algebraic Geometry

Let \mathbb{R}^n denotes the affine n -space. A subset S of \mathbb{R}^n is said to be semi-algebraic if it can be represented by a Boolean combination of polynomials equations and inequalities as follows; $S = \cup_i^s \cap_j^{r_i} \{x \in \mathbb{R}^n \mid P_{i,j} *_{i,j} 0\}$, where $P_{i,j} \in \mathbb{R}[X_1, \dots, X_n]$ and $*_{i,j} \in \{<, =, >\}$, for $i = 1, \dots, s$ and $j = 1, \dots, r_i$. Semi-algebraic subsets of \mathbb{R}^n form the smallest family of subsets that contain all sets of the form $\{x \in \mathbb{R}^n \mid P(x) \geq 0\}$ and are closed with respect to set-theoretic operation of finite union, intersection, and complement.

The following properties of semi-algebraic sets will be needed later. Let S be a semi-algebraic subset of \mathbb{R}^n . A point $x \in S$ is said to be a regular point if there exists a neighborhood U of x which is homeomorphic to a manifold of

some-dimension ¹. Points which fail to be regular in a given dimension are called singular. Every non-empty semi-algebraic set contains at least one regular point. The set of regular points of a semi-algebraic set lies dense.

We perform two topological constructions on the same space and gain thereby equivalent families of bases and filters which we shall use later. Let $\mathcal{P} = P_1, \dots, P_s \subset \mathbb{R}[X]$ be a finite set of irreducible monic polynomials used for the representation of some semi-algebraic set S . Denote by $U_i(P_i) = \{x = x_{reg} \in S \mid P_i(x) \geq 0\}$ and by $U_i^c(P_i) = \{x = x_{reg} \in S \mid P_i(x) < 0\}$. Let $V_i = cl(int(U_i))$ or $V_i = cl(int(U_i^c))$ be in the strong topology. Let \mathcal{V} be a family of non-empty sets of V_i .

The family \mathcal{V} covers the set $X \subset \mathbb{R}^n$ containing regular points and as such a subbase for a unique topology on X . Therefore, any finite intersection of elements of \mathcal{V} is a base for this topology. Let $\mathcal{P}(\mathcal{V})$ be the power set generated by elements of \mathcal{V} . Let \mathcal{F} be a filter in $\mathcal{P}(\mathcal{V})$ in the specialization ordering. Let $\mathcal{F} \rightarrow \mathcal{F}_u$ be the quotient map which sends each filter \mathcal{F} in $\mathcal{P}(\mathcal{V})$ onto its maximal element \mathcal{F}_u , i. e., its ultrafilter, which is an identity surjection on \mathcal{F}_u . The composite map of the injection of filters into the power set containing it and the surjection onto maximal elements is again an identity map. Clearly, final and initial topologies with respect to the identity map coincide with the strong topology. By abuse of notation, we call the covering of X by filters in $\mathcal{P}(\mathcal{V})$ a pre-decomposition of X and covering of X by disjoint elements or equivalently by ultrafilters in $\mathcal{P}(\mathcal{V})$ a decomposition X/\mathcal{D} of X . Then X/\mathcal{D} can be seen as natural semi-algebraic cell decomposition of X where by a cell is meant a compact subset of regular points.

We introduce now the Tychonoff topology on the set of regular points X of \mathbb{R}^n covered by the family \mathcal{V} . Let $f_{V_i}(x)$ be a characteristic map from X to the discrete space $\{0, 1\}$ such that $f_{V_i}(x) = 0$ if $V_i(x) \geq 0$, and $f_{V_i}(x) = 1$ if $V_i(x) < 0$ for all $V_i \in \mathcal{V}$. Let $f_{\mathcal{V}}(x) = (f_{V_1}(x), \dots, f_{V_n}(x))$ be the map from X to the product space $\prod_i^n \{0, 1\}$. If we require that the composite of the projection $\pi_{f_{V_i}}$ of $f_{\mathcal{V}}$ and $f_{\mathcal{V}}$ itself to coincide with f_{V_i} , i. e., $f_{V_i} = \pi_{f_{V_i}} \circ f$ for $i = 1, \dots, n$, then the final topology with respect to $f_{\mathcal{V}}$ and with respect to f_{V_i} coincide. It is exactly the Tychonoff topology with subbases $f_{V_i}^{-1} = V_i$ for $V_i \in \mathcal{V}$. It can be easily shown using complementary elements from the family \mathcal{V} and DeMorgan's law that X is compact. The set of regular points X equipped with the Tychonoff topology becomes a compact totally disconnected space. Obviously, the Tychonoff topology on the set of regular points X has the same subbase as the quotient topology on the decomposition X/\mathcal{D} . Therefore, both topologies and consequently bases and filters coincide.

3 Geometry Representation

3.1 Geometry for MC Particle Transport

It is clear from the definition of semi-algebraic sets that primitive solids and algebraic half-spaces, and any Boolean combination of them are semi-algebraic.

¹ The dimension of non-empty semi-algebraic set is defined to be the maximal dimension of its regular points.

In most MC particle transport codes, the three-dimensional problem space is subdivided using Boolean combinations of primitive solids and algebraic half-spaces into connected disjoint regions of constant ray attenuation coefficient so that the line integral for a particle path is transformed into summation over regions.

Formally, the representation needed at the algorithmic level amounts to be a semi-algebraic cell decomposition. To show this, let the set $X \subset \mathbb{R}^n$ be the problem space. Let X/\mathcal{D} be a semi-algebraic cell decomposition of X as described above. The particle tracking problem, which is a combination of ray classification and point location problem, can be stated as following; Let r be a ray segment starting at $r_0 \in D_0 \in X/\mathcal{D}$ and ending at $r_q \in D_q \in X/\mathcal{D}$. The first problem is then to find all cells $\{D_i, \dots, D_n\} \in \mathcal{D}$ which contain r . The second problem is: given a cell $D_i \in \mathcal{D}$ and a query point $r_q = r - r_0 \in X$, decide whether $r_q \in D_i$. The solutions yield then the set of cells traversed by a ray and the position of a particle among with the cell containing it.

3.2 Boundary Representation of a Solid

A manifold solid is a regular closed subset of Euclidean 3-space with a compact orientable boundary. Most CAD systems represent the shape of such a solid by a collection of its boundary elements among with their topological connectivity and orientation. In practice, the Boundary representation (B-rep) of a solid consists of two parts, a topological description of the connectivity and orientation of the collection of boundary elements consisting of vertices, edges, and faces and a geometric description of the affine supports of these elements [2]. Faces are assumed to be either disjoint or intersect transversally.

The affine supports are mostly smooth surfaces given by irreducible monic polynomials among with normal vectors pointing to the interior of the solid. The B-rep of a solid is thus essentially the union of algebraic sets bounding the solid. Clearly, this representation is semi-algebraic, and is unique up to the reordering of the elements of the collection.

4 Conversion between Representation Schemes

The aim is to solve the following problem: Given a solid by its boundary representation, find a semi-algebraic description for each cell defining its interior and exterior. The first step in solving the problem is to find a set of polynomials sufficient for semi-algebraic description of the cells defining the solid. Next to that, we regard limit points in a semi-algebraic decomposed space. Using filters convergent to given limit points we are then able to write semi-algebraic descriptions of cells in the solid and its exterior.

4.1 Definability

In general, the polynomials supporting the boundary of a solid in its boundary representation are not sufficient for its semi-algebraic description. The topolog-

ical formulation of the problem leads to the concept of definability. Recall that if a family of sets \mathcal{B} is a base for a topology on a set X , then the elements of \mathcal{B} define open sets and points of X completely.

Let S be a solid given by a boundary representation. Note that S is a regular closed set with a compact boundary. Let $\mathcal{P} = \{P_1, \dots, P_s\} \subset \mathbb{R}[X]$ be a finite set of polynomials supporting the boundary of the solid and whenever they intersect on the boundary let it be transversally. Let \mathcal{V} be the family defined as above and let X/\mathcal{D} be the decomposition of the space containing regular points. We regard the solid S as a subspace of X/\mathcal{D} with the Tychonoff topology generated by the family \mathcal{V} . The boundary ∂S of the solid is a closed nowhere dense subset of S , for $\partial S = cl(S) \setminus int(S)$ and $int(S)$ is dense open. As S is closed subspace of X , its intersection with the Tychonoff subbase \mathcal{V} , that is, $\mathcal{C} = \{S \cap V_i | V_i \in \mathcal{V}\}$, is a subbase for closed sets in S . Hence a closed subbase for the boundary sets ∂S . With this in mind, we reformulate our problem as follows. Given a closed subbase \mathcal{C} for a topology on ∂S , under what circumstance is there exists a closed base \mathcal{C} for a the topology on ∂S ? If this topology exists, it will clearly be unique. By definition of a closed base; a family \mathcal{C} is a closed base for the closed sets in ∂S iff every closed set in ∂S is an intersection of elements of \mathcal{C} . An equivalent way to say the above is, if G is a closed semi-algebraic subset of ∂S and x is a point $\partial S \setminus G$, then there exists a semi-algebraic set G' containing x such that $G \cap G' = \emptyset$. A subset ∂S_j of a boundary ∂S then is said to be definable if it can be represented as a semi-algebraic set by the available elements of \mathcal{V} as $\partial S_j = \cap_i^n \{(S \cap V_i) | V_i \in \mathcal{V}\}$. The whole boundary is definable if every subset is definable.

If a given family \mathcal{V} is sufficient for a representation of the boundary then it is also sufficient for a representation of the interior of the solid it bounds by the duality between open and closed bases. A defining family \mathcal{V} is usually called a separating family. If the family \mathcal{V} is not separating, it can be enlarged to be so. There is a separation theorem [3] which says that every family \mathcal{V} can be augmented into a separating family. Note that the polynomials occurring in the definition of a solid are usually linear half-spaces, quadric surfaces, etc. which are irreducible monic polynomials. In this case, a separating family can be generated by adding partial derivatives and resultants to the available set. Applied to our problem, this gives us a constructive method to achieve a sufficient set of polynomials for the semi-algebraic description of cells involved in the representation of a solid.

4.2 Constructing Cell Representation

The availability of a sufficient set of polynomials implies the existence of a subbase \mathcal{V} for a topology on S . Any finite intersection of elements of \mathcal{V} is a base for Tychonoff topology on S . Since S is compact and Hausdorff, we have also filters \mathcal{F} converging to distinct limit points. The boundary of a solid is just the set of its limit points in the strong topology. Since the Tychonoff topology on S coincides with the strong topology, points in the boundary can be regarded as limit

points for filters in the Tychonoff topology. The construction of a semi-algebraic representation for cells in S is based on the following topological construction.

Let X be the set containing regular points generated by the family \mathcal{V} and let $x_\mu \in X$ be a collection of limit points in X . Let the family \mathcal{B} be an open base for the strong topology on X . Let \mathcal{F} be a family of filters in the Tychonoff topology converging to the limit points $x_\mu \in X$. A filter F is said to be convergent to a point $x_\mu \in B_i$ if $F \supset B_i(x_\mu)$. If a limit point x_μ is contained in some $\{B_i, \dots, B_n\} \subset \mathcal{B}$, then let all filters converging to x_μ contain $\{B_i, \dots, B_n\} \subset \mathcal{B}$. Now let \mathcal{C} be a family containing the collection of $\{B_i, \dots, B_n\} \subset \mathcal{B}$ which contain limit points and themselves are contained in filters. As it can be easily checked the family \mathcal{C} defines a topology on X .

Recall that S is a subspace of X and the subspace topology on S is the Tychonoff topology. Therefore, our problem amounts to a computing of an appropriate set of filters converging to boundary points of S . A plane filtration by the family \mathcal{V} results in the decomposition of S by ultrafilters. The union of the ultrafilters convergent to points in ∂S is a semi-algebraic representation for the interior points of the solid and by DeMorgan's law the intersection of the unions of the complementary ultrafilters is a semi-algebraic representation for the exterior points of the solid. There exists, however, an optimal pre-decomposition using distinguished limit points which we are not able to give account of due to space limitation.

5 Summary and Outlook

To use geometric data generated by CAD systems in MC Particle Transport codes, one has to convert the CAD geometry into a representation appropriate for MC particle transport. It has been shown in this paper that the conversion problem, in principle, can be solved using standard methods from semi-algebraic geometry. In a next phase, we will be dealing with the implementation of a conversion algorithm and a CAD data access interface.

References

1. J.R. Munkers: *Topology a First Course* (Prentice-Hall, Inc. 1975)
2. C.M. Hoffmann: *Geometric and Solid Modeling* (Morgan Kaufmann 1989)
3. J. Bochnak et al.: *Real Algebraic Geometry* (Springer Verlag 1998)

Analysis of the Simulation of Ge-Detector Calibration for Environmental Radioactive Samples in a Marinelli Beaker Source Using the Monte Carlo Method

J. Ródenas¹, J. Ortiz², L. Ballesteros², and V. Serradell²

¹ Departamento de Ingeniería Nuclear

² Laboratorio de Radiactividad Ambiental, Universidad Politécnica de Valencia, Apartado 22012 E-46071 Valencia, Spain

1 Introduction

Gamma spectrometry devices are one of the most powerful instruments used in laboratories for radioactive measurements. The equipment usually includes a HP Germanium semiconductor detector.

Different recipients can be used to contain environmental samples whose radioactivity is to be determined in laboratory. The Marinelli beaker is one of the most frequently used recipients, so it has been chosen for this analysis. The volume of the Marinelli beaker can vary in a wide range from 0.5 to 4 litres. And the detector should be calibrated in efficiency for each geometry, that is, for each different volume.

The calibration of radioactivity measurement devices implies the use of certified radioactive sources. The optimal geometry election for a particular analysis is frequently not a simple problem, which needs to be carefully analysed. Therefore, the simulation of the calibration procedure with a validated computer program becomes an important auxiliary tool for a laboratory of environmental radioactivity. In the paper, a computational method for the detector calibration is proposed in order to optimise calibration procedures for different geometries and reduce the amount of radioactive wastes.

A potentially useful tool is Monte Carlo modelling. The Monte Carlo method is applied to the detector calibration by means of MCNP 4B code [1]. MCNP (Monte Carlo N-Particles Transport Code) is an advanced Monte Carlo simulation program, which contains all the necessary cross section data for neutron, photon and electron transport calculations. The 4B version is suitable for modelling the detector response, since it contains a tally (F8), which is specific for detector pulse height determination. Thus, the detection process is simulated with MCNP 4B to obtain spectrum peaks for each modelled geometry [2]. The procedure was validated for point source geometry [3].

In the paper, different models have been developed considering some features of the attenuating geometry. An ideal bare Marinelli model has been compared with the actual plastic model. Concerning the detector, a bare detector model has been improved including an Aluminium absorber layer and a dead layer of

inactive Germanium. Calculation results of the Monte Carlo simulation have been compared with experimental measurements carried out in laboratory for various radionuclides from a calibration gamma cocktail solution with energies ranging in a wide interval.

2 Marinelli Model

An homogeneous source containing 1 litre volume solution with the shape of a Marinelli beaker has been considered for the simulation. A model for an homogeneous water matrix source with two energy peaks 0.364 MeV from I-131 and 0.667 MeV from Cs-137 has been developed in the first approach. A bare model was designed with no material around the solution, so the calculated efficiency was overestimated since the shielding provided by the plastic was neglected. In this model, three different volumes were considered starting from a rough model (1.6 l) and adjusting the geometric model until reaching a more exact shape and volume (1.001 l).

The efficiency calculated by MCNP increased slightly when volume decreased. Anyway, the variation was minimal – some thousandths – for both nuclides considered as it can be seen in Tab. 1.

Table 1. Calculated efficiency for different volumes

Volume	I-131	Cs-137
(litres)	Efficiency (cps/Bq)	
1.68	0.023	
1.117	0.025	0.015
1.001	0.028	0.017

In the second approach the material – polypropylene – forming the beaker was considered. As expected, efficiencies obtained with this model were lower than for the bare model, but not too much. In Tab. 2 results for I-131 and Cs-137 are listed and compared.

Furthermore, MCNP was also run for various radionuclides from a calibration gamma cocktail solution with energies varying from 59 up to 1836 keV. The ratio between MCNP results from the plastic model and the bare model remains between 0.96 and 0.99.

3 Detector Model

A GEM Series HP Ge (High Purity Germanium) coaxial detector system has been used for measurements. For all runs presented so far the detector model

Table 2. Comparison of efficiencies for bare and plastic beaker models

Isotope	Energy (Mev)	Efficiency		Ratio EC/ES
		plastic EC	bare ES	
Cs-137	0.66167	1.6576E-02	1.6985E-02	0.97592
I-131	0.364	2.7282E-02	2.7672E-02	0.98591

was the simplest possible. Just a cylinder made up of Germanium, that is, a bare detector model where no absorber nor dead layers have been considered. The Marinelli beaker source sits right on the top of the detector. No directional bias is necessary because this is a relatively high efficiency geometry.

When results from MCNP were compared with experimental measurements, significant discrepancies were found. The ratio for calculated to laboratory efficiencies was about 1.6 for Cs-137 and I-131.

For all of the nuclides contained in the gamma cocktail solution used for calibration, results from MCNP were also compared with laboratory measurements. The ratio stays around 1.6 for central energies (300-700 keV), but harder discrepancies are found for lower and higher energies, with ratios up to 1.96 for Co-57 (122 keV) and 1.97 for Y-88 (1836 keV). Even for the lowest energies, i. e., peaks from Am-241 (59.5 keV) and Cd-109 (88 keV) the ratio shoot up to 9.6 and 3.1 respectively.

Such a strong discrepancy can be attributed without doubt to the bare detector model used. When some absorber layer is included around the detector, efficiencies decrease quickly. For instance, when a layer of Al 1.27 mm thick is considered in calculations, the efficiency for Am-241 passes from 5.975 E-02 to 5.3872E-02. Increasing the Aluminium thickness up to 2.87 mm the efficiency goes down to 3.5 E-02. This attenuation effect is more apparent for lower energies.

Another important characteristic to be considered in detector model is a dead layer in germanium, that is, a layer of inactive germanium, which is not useful for detection, but attenuates photons.

Data provided by the manufacturer read 1.27 mm for aluminium absorber layer and 0.7 mm for inactive germanium. Including these data in our detector model, the efficiency calculated by MCNP for Am-241 is equal to 1.745 E-02 giving a ratio MCNP/Experimental equal to 2.6 that is still high. We found in literature [4,5] that such a disagreement is usually found between experimental and simulated efficiency values when manufacturer data are used. That is due to the existence of a transition zone between the inactive layer and active Ge in the crystal. Photons absorbed in the transition zone will not contribute to the full energy peak count rate, and thus, concerning detector efficiency, transition zone behaves as a inactive layer [4].

In order to determine the thickness of the transition layer, we increased the inactive Ge layer thickness, comparing the estimated efficiency with laboratory measurements. We tried different dead layer thickness for the simulation of Am-241 peak. We chose this nuclide since it has the lowest energy in the gamma cocktail used and the attenuation is more important for lower energies. But other peak energy could have been selected for the adjustment.

A good agreement between experimental and simulated efficiency values was found for an inactive Ge layer thickness of 1.35 mm instead of the value of 0.7 mm given by the manufacturer. Obviously, the absorbing layer (1.27 mm Aluminium) has been also included in our new detector model.

Using this model, efficiency for all nuclides contained in the calibration gamma cocktail solution is recalculated using MCNP. Results are listed in Tab. 3, where it can be seen the good agreement, also showed in the Fig. 1 where the efficiency is plotted in terms of energy for both MCNP and experimental values. A bar diagram showing the ratio MCNP/Exp is presented in Fig. 2 where it can be seen that the ratio remains between 1 and 1.5 for all nuclides analysed.

Table 3. Comparison of calculated and experimental efficiencies

Isotope	Energy (Mev)	Calculated EC	Experimental EX	Ratio EC/EX
Am-241	0.05954	6.951E-03	6.683E-03	1.040
Cd-109	0.08803	2.371E-02	2.057E-02	1.152
Co-57	0.1221	3.159E-02	2.794E-02	1.131
Ce-139	0.1659	3.293E-02	2.875E-02	1.145
Hg-203	0.2792	2.500E-02	2.096E-02	1.193
Sn-113	0.3917	1.890E-02	1.580E-02	1.196
Sr-85	0.514	1.550E-02	1.249E-02	1.242
Cs-137	0.66166	1.264E-02	1.024E-02	1.235
Y-88	0.898	1.031E-02	7.617E-03	1.354
Co-60	1.17324	8.662E-03	6.077E-03	1.425
Co-60	1.3325	7.946E-03	5.513E-03	1.441
Y-88	1.836	6.393E-03	4.225E-03	1.513

4 Conclusions

MCNP code based on the Monte Carlo method is a powerful tool to simulate a Ge-detector calibration. It permits to establish a useful and simple computa-

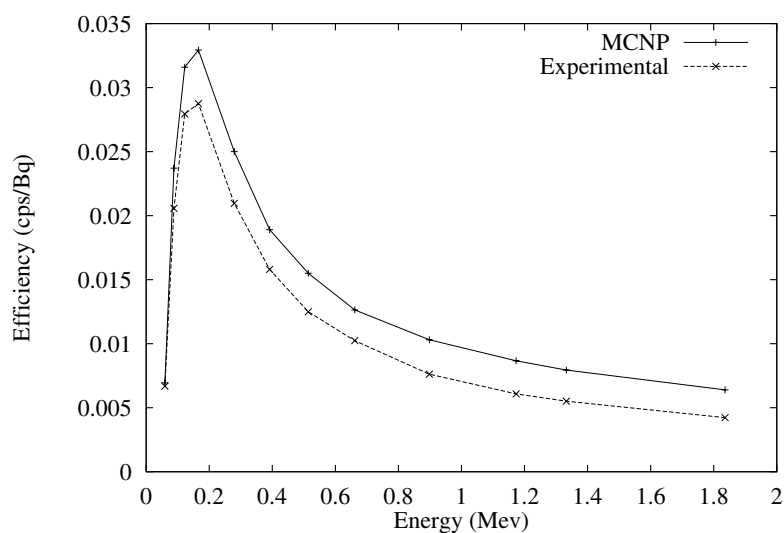


Fig. 1. Comparison of calculated and experimental efficiencies

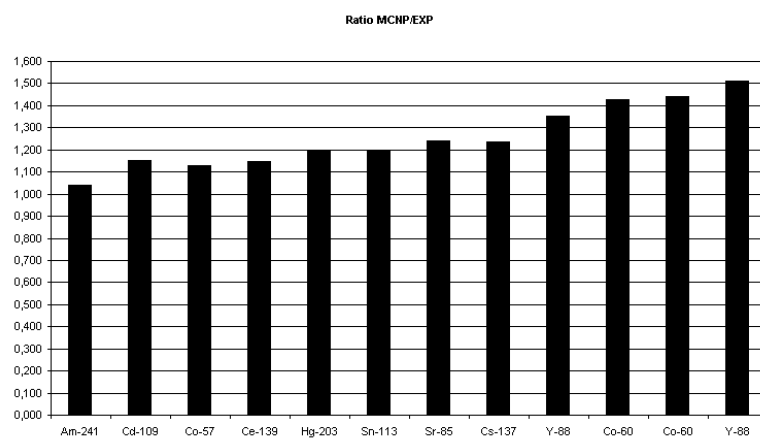


Fig. 2. MCNP to experimental efficiency ratio

tional tool to assess with reasonable accuracy the detector efficiency for environmental radioactive sample measurements, avoiding some cumbersome experimental calibration as well as decreasing the generation of radioactive wastes.

Validation was carried out comparing results from MC simulation with laboratory measurements. A calibration gamma cocktail solution was used for the comparison.

The detector model is a very important feature in the simulation. An extra inactive germanium layer has to be included in the model in order to achieve a good agreement between simulation and measurements.

On the other hand, the Marinelli beaker model can be simplified since the accuracy in the solution volume as well as the photon attenuation produced by the beaker material have a lower influence on calculated efficiency values.

The calibration simulation might be still improved using a better model, which include all detector features that could modify the process of charge collection.

References

1. J.F. Briesmeister (Editor): *MCNP – A General Monte Carlo N-Particle Transport Code, Version 4B*, LA-12625-M, Los Alamos National Laboratory, Los Alamos, New Mexico (1997)
2. J. Ródenas, V. Rius: ‘Application of Monte Carlo method to the simulation of Ge-detector calibration’. In *TOPSAFE’98, Valencia, 15–17 April 1998*
3. J. Ródenas, A. Martinavarro, V. Rius: ‘Validation of the MCNP code for the simulation of Ge-detector calibration’. Nuclear Instruments & Methods in Physics Research (Section A), (In print), Accepted for publication on December 21, 1999 REG. No.: KNO-99-619 (R1) NIMA 40372
4. A. Clouvas, S. Xanthos, M. Antonopoulos-Domis, J. Silva: Health Physics **74**, 216 (1998)
5. F. Sánchez, E. Navarro, A. Moreno, C. Roldán: Nucl. Instr. Meth. B **61**, 535 (1991)

Simulation of a ^{32}P Sourcewire and a $^{90}\text{Sr}/^{90}\text{Y}$ Sourcetrain Using MCNP4b and EGS4

M. Todorovic, F. Cremers, D. Albers, and R. Schmidt

Dept. of Radiotherapy and Radiooncology / Clinic of Radiology, University Hospital Eppendorf, Martinistr. 52, 20246 Hamburg, Germany

1 Introduction

The two simulated sources, the ^{32}P sourcewire and the $^{90}\text{Sr}/^{90}\text{Y}$ sourcetrain, are parts of catheter-based systems developed for vascular brachytherapy. Percutaneous transluminal coronary angioplasty (PTCA) is a widely accepted therapy for symptomatic coronary disease, but within the first 6 months often restenosis occur. The intracoronary brachytherapy is a new method to help avoiding restenosis [1].

For dosimetry and treatment planning, the knowledge of the source is essential. Therefore we simulated the depth dose curve and the change of the energy-spectra in dependence on the depth in polymethyl methacrylate (PMMA). To compare the results, we used two codes: the MCNP4b [2,3] code and BEAM/EGS4 [4].

2 Materials and Methods

2.1 The ^{32}P Sourcewire

The simulated source is ^{32}P , hermetically sealed in a flexible Nitinol wire. ^{32}P is a pure β^- emitter with a half-life of 14.1 days. The maximal energy is 1.71 MeV and the average energy is 0.695 MeV. The active length is 27 mm and the source diameter is 0.46 mm. Modeled with MCNP4b and BEAM, the source was simulated in PMMA. The theoretical beta-particle energy spectrum for ^{32}P used as input for the simulation was taken from Cross et al. [5]. For MCNP4b, a surface Tally (Tally 2) was used to simulate the energy spectrum in different depths. The PMMA phantom and the tally surfaces had cylindrical geometry. For the EGS4 simulation, BEAM was used. Instead of building an accelerator, we formed a uniform isotropically radiating internal source (source type 3) with a sidetube around it.

2.2 The $^{90}\text{Sr}/^{90}\text{Y}$ Sourcetrain

The simulated $^{90}\text{Sr}/^{90}\text{Y}$ sourcetrain consists of 12 seeds. Each seed has a length of 25 mm, an outer diameter of 0.64 mm, and an inside diameter of 0.56 mm. Inside are the radioactive isotopes ^{90}Sr and ^{90}Y . Both isotopes are pure β^-

emitters. The combined beta-particle energy spectrum used as input for the simulation was also taken from Cross et al. [5]. The maximum energy is 2.273 MeV and the average energy is 0.934 MeV. The half-lives are 28.1 years (^{90}Sr) and 64.2 hours (^{90}Y). Like the ^{32}P source, the source train was simulated using MCNP4b with the surface Tally 2. The change of the energy spectrum in different depths of PMMA and the depth dose were simulated.

3 Results

3.1 The ^{32}P Source

The energy spectrum was simulated in different distances from the source, using MCNP4b and BEAM/EGS4. Only electrons were counted. Fig. 1 shows the results for BEAM/EGS4 and MCNP4b in 2 mm PMMA. They both match very well. With increasing depth the energy spectra become softer. Due to the fact that the electrons interacted with the PMMA and lost some of their energy, the low energy bins of the spectrum became more populated. The maximum energy is 1.375 MeV and the average energy is 0.4 MeV (MCNP4b)/ 0.425 MeV (BEAM).

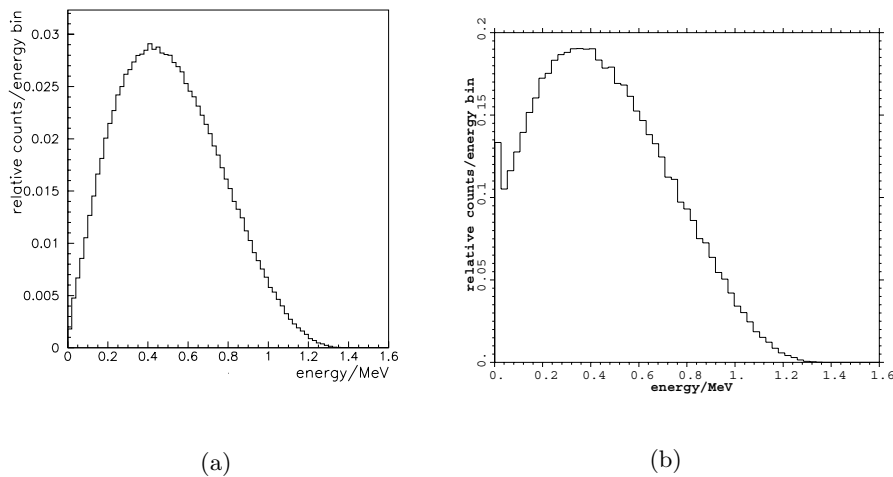


Fig. 1. Energy spectrum of the ^{32}P source simulated with (a) BEAM and (b) MCNP4b in 2 cm PMMA

MCNP4b was used to simulate the energy spectra in different depths of the PMMA phantom. The results are shown in Fig. 2. As expected, with increasing depth in the phantom the energy spectrum is shifted towards lower energies. The maximum energy decreases from 1.45 MeV (for 1 mm PMMA) to 1.20 MeV

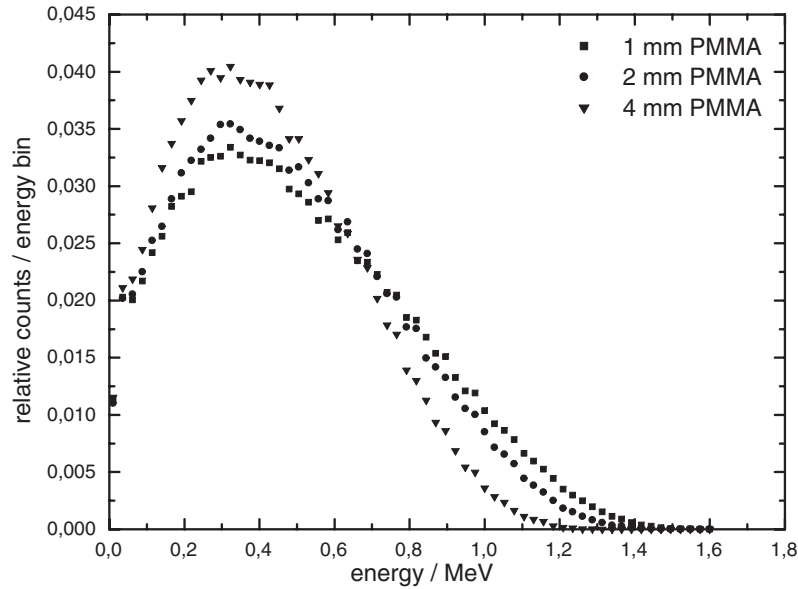


Fig. 2. Energy spectrum of the ^{32}P source simulated in dependence on the depth in PMMA simulated with MCNP4b

(4 mm PMMA). The average energy stays nearly the same for all 3 different depths. It extends from 0.4 MeV for a depth of 1 mm to 0.3 MeV for 4 mm PMMA. This is a result of the fact, that the high energetic electrons were slowed down, while the electrons with the low energy were completely stopped. In this way, the amount of low energetic electrons stays nearly the same and the average energy will decrease only slightly.

3.2 The $^{90}\text{Sr}/^{90}\text{Y}$ Sourcetrain

For the $^{90}\text{Sr}/^{90}\text{Y}$ sourcetrain, the change of the energy spectrum with increasing depths in the PMMA phantom was simulated using MCNP4b. The results are shown in Fig. 3. As expected, the simulations show the same effect. With increasing depth, the energy spectrum also shifted towards lower energies. In 1 mm PMMA, the maximum energy is 1.95 MeV, in 4 mm it is 1.38 MeV. On the other hand, the change in the average energy is quiet small. It changes from 0.48 MeV (for 1 mm) to 0.38 MeV (in 4 mm PMMA). The difference in the maximum energy is about 0.57 MeV, while the change in the average energy is 0.1 MeV.

3.3 The Depth Dose Curves

For both types of sources, the depth dose curves in PMMA were simulated using MCNP4b. Figure 4 shows the results for this simulations. Both depth dose

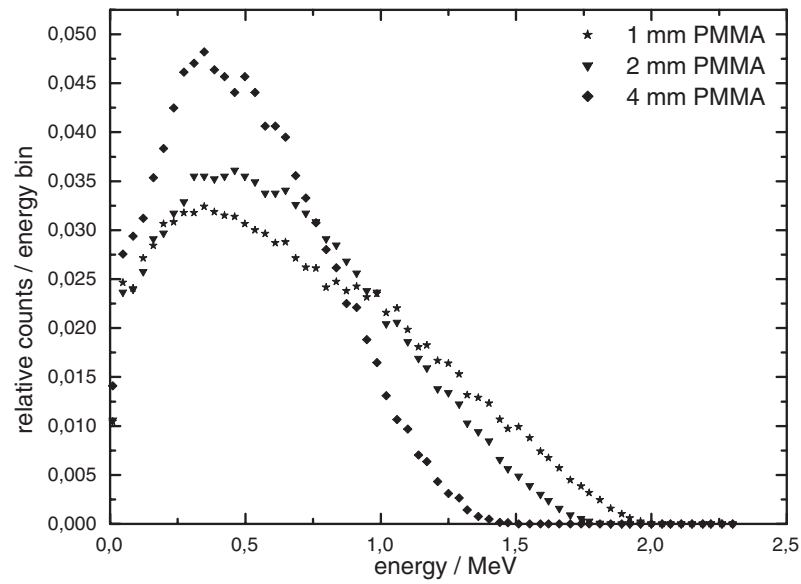


Fig. 3. Energy spectrum of the $^{90}\text{Sr}/^{90}\text{Y}$ source in dependence on the depth in PMMA simulated with MCNP4b

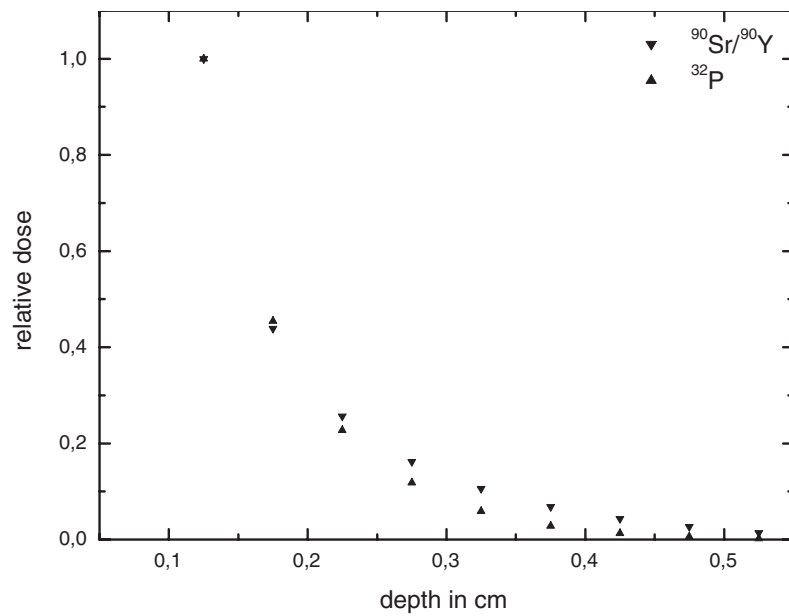


Fig. 4. Comparison of the $^{90}\text{Sr}/^{90}\text{Y}$ source train and ^{32}P source wire depth dose curves in PMMA

curves show the same trend. With increasing depth in the PMMA phantom the dose decreases rapidly. At a distance of 0.175 cm the dose dropped down to approximately 40% of the dose value at 0.125 cm (norm. point). At 0.475 cm, the dose for the $^{90}\text{Sr}/^{90}\text{Y}$ sourcechain is 0.027 % , for the ^{32}P sourcewire the dose is 0.005 % of the dose at 0.125 cm. As expected, the simulated depth dose curve for ^{32}P reveals lower dose values as the $^{90}\text{Sr}/^{90}\text{Y}$ sourcechain for the same depth. The maximum depth in PMMA for the ^{32}P source is 0.525 cm, for the $^{90}\text{Sr}/^{90}\text{Y}$ sourcechain it is approximately 0.575 cm.

References

1. R. Waksman: *Vascular Brachytherapy Second Edition* (Futura Publishing Company, New York 1999)
2. J.F. Briesmeister: *MCNP-A General Monte Carlo N-Particle Transport Code*, RS-ICC, Oak Ridge (1997)
3. R.H. Olsher, D.T. Seagraves: *Practical MCNP for the Health Physicist, Rad Engineer, & Medical Physicist*, National Laboratory, Los Alamos
4. D.W.O. Rogers, B.A. Faddegon, G.X. Ding, C.-M. Ma, J. We: *Med. Phys.* **22**, 5 (1995)
5. W.G. Cross, H. Ing, N. Freedman: *Phys. Med. Biol.* **28**, 1251 (1983)

Monte Carlo Simulations for the Estimation of Dose Rates During Handling of Spent Fuel at the Portuguese Research Reactor

A. Kling^{1,2}, J.G. Marques^{1,2}, and A.J.G. Ramalho¹

¹ Instituto Tecnológico e Nuclear, Estrada Nacional n°10, P-2686-953 Sacavém, Portugal

² Centro de Física Nuclear da Universidade de Lisboa, Av. Prof. Gama Pinto 2, P-1649-003 Lisboa, Portugal

Abstract. During the shipment of spent fuel of the Portuguese Research Reactor (RPI) the fuel assemblies had to be transferred from the reactor pool to a transport cask located outside the reactor building. The expected dose rates for the staff performing the transfer of the fuel had to be estimated in advance in order to determine the optimum conditions to minimize their radiation exposure. The MCNP4B code was used to determine the γ -exposure during loading of the fuel into the transport cask under various conditions. The calculations were compared with the actual dose rates measured during the transfer process.

1 Introduction

During the shipment of spent fuel of RPI the fuel assemblies had to be transferred from the reactor pool to a transport cask. As the handling of the fuel cask inside the containment building was not possible, mainly due to the low capacity of the reactor crane and the characteristics of the floor at the service entrance which had been planned for a load of less than 7 t/m², the loading of the transport cask had to be done outside the building where a loading station was erected. The transport cask used has a diameter of 1.6 m and is able to store up to 40 fuel assemblies. It was provided with two major accessories: a small transfer cask capable of handling a single MTR assembly and a loading skirt adaptable to the top of the cask. The skirt was used to create a water basin where the assemblies could be manipulated. Its bottom part was covered with an 8 cm thick lead shield as biological protection. A sketch of the set-up is shown in Fig. 1.

The radiation exposure of the staff, especially during the loading into the transport cask, had to be estimated in advance in order to optimize the handling procedure. Since this was the first time that spent fuel was shipped from the RPI no previous data on the dose rates occurring during handling and the optimum procedure for the handling of the fuel were available on site. The main exposure was expected to occur during the transfer of the fuel assemblies from the transfer cask into the transport cask. At this stage the shielding is provided only by the water-filled skirt and the biological shield. In contrast, the loading of the fuel assemblies into the transfer cask was regarded as unproblematic since this procedure was performed in the reactor pool which provided sufficient shielding

due to a thick water layer and the concrete lining. The use of the Monte Carlo method was expected to yield a good estimate of the gamma dose rates to be expected for various possible situations during the handling procedures at the transport cask.

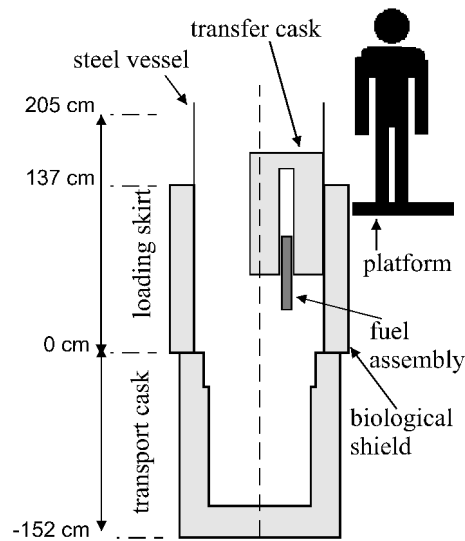


Fig. 1. Sketch of the setup used for the loading of the spent fuel into the transport cask

2 Calculations

To determine the relevant sources of γ -radiation calculations of the radioactive inventory of the fuel assemblies (the spent fuel itself and the structure material aluminum) were performed using the program PHDOSE [1]. Although the inventory of fission products consists of many isotopes [2] it was found that due to a long decay time of the fuel assemblies in the reactor pool only ^{137}Cs played a role in terms of radiation exposure [3]. The second isotope that had to be considered was ^{60}Co originating from the neutron activation of approximately 100 ppm Co in the aluminum structural material. On the other hand, β -emitters like ^{90}Sr had not to be taken into account. The activities to be handled ranged from 0.01 to 0.28 Ci for ^{60}Co and from 9.4 to 90 Ci for ^{137}Cs for different fuel assemblies.

The MTR fuel assemblies were modeled by rectangular homogeneous blocks (dimensions $8.1\text{ cm} \times 7.6\text{ cm} \times 60\text{ cm}$) since the production of neutrons was neglected. The assumed composition was 42.6 at.% Al, 1.7 at.% U (representing

the structural material and fuel), 37.1 at.% H and 18.6 at.% O (representing the water between the fuel elements). The source of gamma radiation was assumed to be uniformly distributed in the volume of the fuel assembly along an active length of 45 cm.

The dimensions and material compositions of transfer cask, transport cask, loading skirt and biological shield were supplied the company carrying through the transport (Transnucleaire). The structure of these devices was slightly simplified by omitting details corresponding to piping, transport hooks etc. in order to save computing time. In the resting position the fuel assembly is located only 18 cm from the wall of the loading skirt after release from the transfer cask.

The main interest laid in the determination of the gamma dose rates to be expected for an operator standing on the platform as close as possible to the fuel assembly position and its variation along the length of the body. Calculations were performed for different situations which could arise during the transfer of the fuel from the transfer cask into the loading skirt:

1. The fuel assembly resting unshielded at the bottom of the loading skirt. This condition was encountered during the identification of the fuel assembly during the actual loading procedure.
2. The fuel assembly unshielded at the top of the loading skirt with the top end corresponding to the surface of the water filling of the loading skirt. This situation served as a worst case estimate.
3. The fuel assembly sticking out 15 cm from the bottom of the transfer cask. The position of the transfer cask with respect to the top of the biological shield was varied between 0 cm and -30 cm (i.e., 30 cm below the top end of the biological shield). These cases were investigated in order to determine a position of the transfer cask at which the dose rate does not exceed significantly that encountered in the first case.

The calculations were performed using the MCNP4B [4] code. For each case two calculations (one assuming a ^{60}Co source, one assuming a ^{137}Cs source in the fuel assembly) were performed using 10^7 photon histories. The photon fluxes computed at different height positions were distributed into energy bins corresponding to the intervals for the flux-to-equivalent dose conversion factors recommended by ICRP [5]. Using these factors the expected gamma dose rates for a fuel assembly containing 0.2 Ci ^{60}Co and 90 Ci ^{137}Cs were computed.

Fig. 2 depicts the results for the situations 1 and 2. The computations show that the dose rates for the situation 1 are in a safe range for performing operations on the working platform. The sharp increase in the dose rate at a height of 140 cm coincides with the top end of the biological shield. The maximum dose rate is expected to occur below the knees of the operator and it is strongly reduced in the region of the gonads. On the other hand situation 2 leads to intolerable gamma dose rates and has to be strictly avoided.

The dependence of the dose rates on the position of the transfer cask as described in case 3 is shown in Fig. 3 for five different distances. The results indicate that the dose rate is significantly decreasing the deeper the transfer

cask dives into the loading skirt. If the bottom of the transfer cask is located 30 cm below the top end of the biological shield the order of magnitude of the computed radiation doses corresponds to those for case 1 enabling a safe handling of the fuel.

3 Comparison with Measurements Performed During Loading of the Spent Fuel

During the actual loading procedure of the spent fuel the gamma dose rates were determined at three well-defined positions at the loading skirt for 13 different fuel assemblies. The fuel assembly rested during the measurement at the bottom of the loading skirt corresponding to situation 1. The observed dose rates are plotted in Fig. 4 against the ^{137}Cs activity of the fuel elements determined with PHDOSE. The straight line shows the dose rate dependence derived from the Monte Carlo calculation using MCNP4B. The computed dose rates for the fuel assemblies with the highest activities agree well with the measurements indicating that the maximum dose rates were correctly estimated.

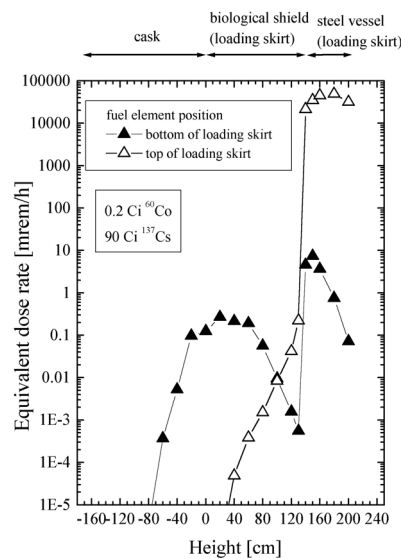


Fig. 2. Equivalent dose rate for a fuel assembly containing 90 Ci ^{137}Cs and 0.2 Ci ^{60}Co resting at the bottom or top of the loading skirt.

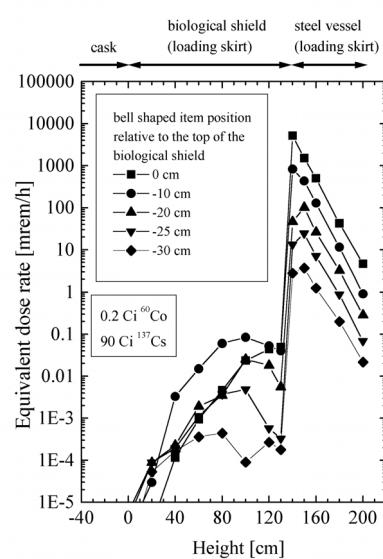


Fig. 3. Equivalent dose rates for a fuel assembly containing 90 Ci ^{137}Cs and 0.2 Ci ^{60}Co sticking out 15 cm from the bottom of the transfer cask for different positions with respect to the biological shield

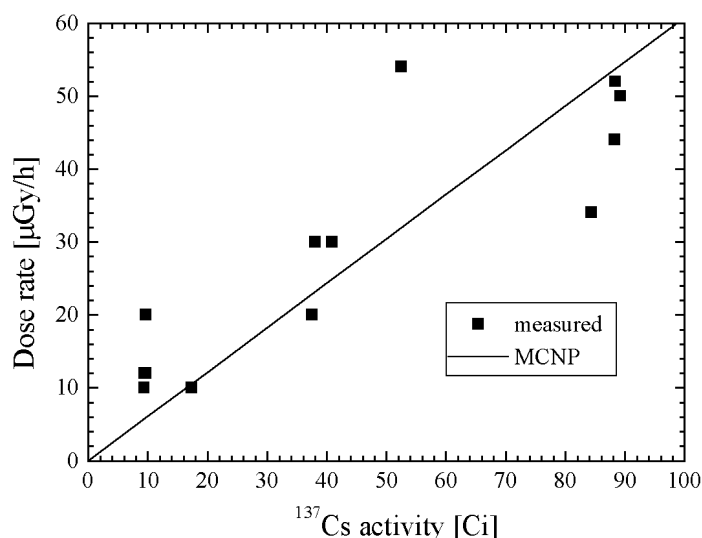


Fig. 4. Comparison of the measured gamma dose rate in dependence of the ^{137}Cs activity for 13 different fuel assemblies during the loading process with the results obtained by MCNP4B. The position of the measurement corresponds to the height of the working platform

4 Conclusions

Monte Carlo simulations using the MCNP4B code were successfully employed to estimate the gamma dose rates occurring during the handling of spent fuel for shipment. It demonstrated the feasibility of the Monte Carlo method to model the dose rates to be expected during procedures that have not been performed before and help to plan the tasks so that they can be carried out in a safe way with respect to radiation protection.

References

1. R.B. Pond, J.E. Matos: *Photon Dose Rates from Spent Fuel Assemblies with Relation to Self-Protection*, ANL/RERTR/TM-25 (Argonne National Laboratory, Argonne 1996)
2. S. Glasstone, A. Sesonske: *Nuclear Reactor Engineering*, 4th edn. (Chapman and Hall, New York 1994)
3. A.J.G. Ramalho, J.G. Marques, F.M. Cardeira: 'Return of Spent Fuel from the Portuguese Research Reactor'. In: *Proc. 4th Int. Meeting on Research Reactor Fuel Management, Colmar, France, March 19-21, 2000* (European Nuclear Society, Bern 2000) pp. 75-79
4. J.F. Briesmeister (ed.): *MCNPTM - A General Monte Carlo N-Particle Transport Code - Version 4B*, LA-12625-M (Los Alamos National Laboratory, Los Alamos 1997)

5. ICRP Committee 3 Task Group, P. Grande, M.C. O'Riordan (chairmen): *Data for Protection Against Ionizing Radiation from External Sources: Supplement to ICRP Publication 15*, ICRP-21, International Commission on Radiological Protection (Pergamon Press, Oxford 1972)

Photoelectron Collection Efficiency in Rare Gases: A Monte Carlo Study

P.J.B.M. Rachinhas¹, J.A.M. Lopes^{1,2}, T.H.V.T. Dias¹, F.P. Santos¹,
C.A.N. Conde¹, and A.D. Stauffer³

¹ Departamento de Física, Universidade de Coimbra, Coimbra 3004-516, Portugal

² Instituto Superior de Engenharia de Coimbra, Ap. 4065, Coimbra 3030, Portugal

³ Physics and Astronomy Department, York University, Toronto, Canada M3J 1P3

Abstract. A detailed Monte Carlo simulation is used to investigate the effective collection efficiency of photocathodes in xenon, neon, and mixtures of xenon with neon, in order to obtain a better understanding of the physics involved in the emission of electrons by photoelectric effect from photocathodes in gaseous media in the presence of an applied electric field. The case of the 7.2 eV photon-induced electron emission from a CsI photocathode is analyzed, and results are presented for applied reduced electric fields E/N in the range 0.1 to 40 Td. The calculations take into account the variation of the electron energy along the free paths and the anisotropy of the scattering. The contribution of the cathode electron-image potential to the total potential is assessed.

1 Introduction

The gas proportional scintillation counter (GPSC) is a noble gas detector used to detect x-rays in the 0.25 to 60 keV range, which has demonstrated superior performance in applications for which large detection area and room temperature operation are required [1,2]. The energy resolution of the GPSC can be better than standard proportional counters by a factor of ~ 2 .

To detect the ultraviolet (UV) scintillation photons from the noble gas, in particular from xenon, a quartz-window photomultiplier tube (PMT) is currently required, and this has limited the use of the GPSC for more general applications. Quartz-window PMTs are bulky, expensive, fragile, and sensitive to gain fluctuations, and lack the uniformity of spatial response for large-area detectors. Moreover, if the GPSC is operated at xenon pressures above several atmospheres, the quartz windows must be thick, and UV scintillation losses become significant.

Many authors have recently investigated the use of integrated UV sensors as an alternative to the standard PMT [3]. In particular, in references [4–6], a CsI photocathode is used in direct contact with a pure xenon atmosphere.

In recent years interesting work has been developed, which assesses the collection efficiency of photoelectrons in gaseous media [7,8]. For the case of He- and Ar-based mixtures a significant backscattering effect has been reported in [7,8], the magnitude of which depends on the rare gas component.

In the present work we use Monte Carlo simulation to investigate the effective collection efficiency of CsI photocathodes in xenon, neon and in xenon-neon mixtures. The goal of this study is a better understanding of the physics involved

in the collection of electrons emitted from photocathodes by the photoelectric effect, by investigating the collection efficiency in rare gas media at varying applied electric fields.

2 Monte Carlo Method

The purpose of this work is to calculate which fraction of the photoelectrons emitted from a CsI photocathode into a rare gas atmosphere is transmitted, and which fraction is backscattered, in the presence of an applied electric field E , when compared with the case of photoelectrons injected into vacuum.

The results are presented for atmospheric pressure (760 Torr) and for reduced electric fields E/N in the range 0.1 to 40 Td, where E is field strength and N is the number density.¹ This E/N limit guarantees that ionization by electron impact is low.

The results apply to the emission of photoelectrons induced by the absorption of 7.2 eV photons (173 nm) in CsI. This energy value corresponds to the peak of the xenon scintillation spectra at atmospheric pressure.

Single photoelectrons are released at the photocathode surface with energy ε_0 , which is sampled from a distribution whose mean value and FWHM (0.4 and 0.5 eV, respectively) are based on the results in [9,10] for 7.2 eV photons and a 11 nm thick reflective CsI photocathode. The emission angle θ_0 is chosen randomly from a uniform angular distribution in $[0, \pi/2]$, where $\theta = 0$ is the forward direction perpendicular to the photocathode surface.

If the contribution of the cathode electron-image potential is taken into account within a classical frame [11,12], the potential energy $U(x)$ of an electron at a distance x from the photocathode surface is given by

$$U(x) = -Ex - B/x + 2(BE)^{1/2} \quad (1)$$

where $B = ke/4$ with $k = 1/(4\pi\epsilon_0)$, where ϵ_0 is the permittivity of the vacuum, and e is the elementary electron charge. This function exhibits a maximum $U = 0$ at $x = \hat{a} = (B/E)^{1/2}$ and diverges to $-\infty$ at $x = 0$. Since $U(x)$ must approach the finite constant value $U_a = -0.1$ eV inside the photocathode (U_a is the electron affinity for CsI [13]) we truncate $U(x)$ near the surface at x_0 where $U(x_0) = U_a$, and adopt $U(x \leq x_0) = U_a$ ("truncated barrier model" [12]). If T is the electron kinetic energy, the total electron energy ε between successive collisions is given by

$$\varepsilon = U + T = U(x) + T_x(x) + T_{yz} , \quad (2)$$

or, making $\varepsilon_x = U(x) + T_x(x)$,

$$\varepsilon = \varepsilon_x + T_{yz} . \quad (3)$$

¹ 1 Td = 10^{-17} Vcm²; $E/N = 3.034 E/p$ (Vcm⁻¹Torr⁻¹) at 293 K.

All photoelectrons emitted into vacuum with $\varepsilon_{x0} < 0$, i.e., with $T_{x0} < |U_a|$, cannot overcome the potential barrier, and the electron will inevitably be recaptured by the photocathode in its single trajectory. This way, the photoelectrons emitted in vacuum with an angle $\theta_0 > \theta_{0m}$,

$$\begin{aligned}\theta_{0m} &= \arccos(|U_a|/T_0)^{1/2} \\ &= \arccos(|U_a|/(\varepsilon_0 + |U_a|))^{1/2},\end{aligned}\quad (4)$$

are reabsorbed, and all those within the cone $\theta_0 < \theta_{0m}$ are transmitted.

In the case where the photoelectrons are injected into the gas, the simulation follows the histories of the individual electrons along the various paths determined by the multiple elastic and inelastic collisions with the gas atoms. The condition $\varepsilon_x < 0$ at some position $x < \hat{a}$ behind, or $x > \hat{a}$ beyond the potential-barrier maximum is not sufficient now to decide the destiny of the electron as final recapture or transmission, respectively. In fact for $\varepsilon > 0$ the energy ε_x may become positive after an electron collision with a gas atom (see (3)), and the barrier may still be crossed in either direction. Therefore, in the gas, an electron is counted as backscattered either when it reaches $\varepsilon < 0$ at a position $x < \hat{a}$, or when it hits the photocathode surface ($x = 0$), whatever occurs first, and it is counted as transmitted when it reaches $\varepsilon < 0$ at a position $x > \hat{a}$.

In order to assess the effect that the image-charge attraction may have on the results, calculations were also made neglecting the image-charge potential. In this case, all the electrons emitted with $\theta_0 > \theta_{0m}$ are counted as recaptured, and those emitted in the cone $\theta_0 < \theta_{0m}$ are followed in the gas. These are recaptured when they hit the surface ($x = 0$), and are transmitted when they reach $\varepsilon < 0$ at a position $x > 0$.

To follow the electron histories, the null collision technique is used to determine the time of flight of the electrons between successive collisions [14,15]. The equations of motion of the electrons are integrated in six-dimensional phase space by the fast “leap-frog” numerical method [16]. The electron scattering cross sections in xenon and neon used in this work have been described in earlier publications [17–19].

3 Results and Discussion

The results of the Monte Carlo simulations for the ratios f_{Xe} and f_{Ne} between the average number of transmitted electrons in the xenon or neon gas, respectively, and in vacuum are shown in Fig. 1, as a function of the reduced electric field E/N . The dashed and the full curves represent the results obtained when the contribution of the image-charge attraction to the potential is included or is neglected, respectively.

All f results have been averaged over a sample of $\sim 10^5$ photoelectrons, corresponding to an uncertainty lower than $\sim 2\%$.

We observe that the values for the collection efficiency in xenon, f_{Xe} , are always lower than 30%, showing that backscattering effects are very important in

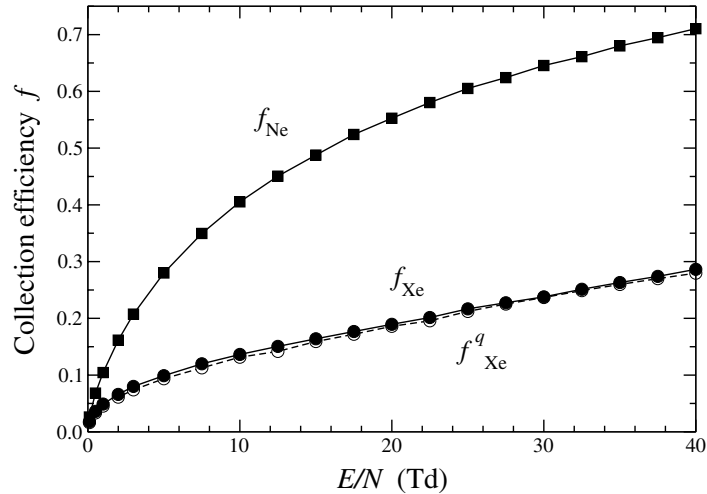


Fig. 1. Monte Carlo results for the ratio f_{Xe} and f_{Ne} between the average number of photoelectrons emitted from CsI that are transmitted in xenon or neon, respectively, and in vacuum, as a function of the density-reduced applied electric field E/N in the range 0.1 to 40 Td. The results refer to the electron emission from CsI induced by 7.2 eV photons. The dashed curve, f_{Xe}^q , includes the contribution of the electron-image attraction

the range of E/N investigated. This is because electrons are scattered mostly in elastic collisions for this range, where direction can change but energy loss is very small, so that during a large number of collisions recapture stays energetically possible and the backscattering chances stay high. However, the collection effect of the applied electric field is evident in Fig. 1, where for the xenon and the neon curves the backscattering is progressively reduced for increasing E/N . In addition, the frequency of excitation collisions gradually increases with E/N , and the larger energy losses involved efficiently reduce the chance of backscattering.

For neon, the collection efficiency is always higher than in xenon. For the lower E/N , where elastic collisions are predominant, f_{Ne} is lower than f_{Xe} because energy losses in elastic collisions are higher in neon, since neon is a lighter gas. As we move to higher E/N , inelastic scattering becomes the main loss channel, and a higher transmission efficiency in neon is observed because electrons reach excitation threshold more rapidly in neon. This is related to the higher energy gains between successive collisions, since in neon the total collision frequency is lower and electron paths are longer.

To our knowledge, the only published work that deals with photoelectron emission from a photocathode into xenon or into neon is [20], for 760 Torr and in the limited range $E/N \leq 4$ Td. Although the situation examined in [20] – the 337 nm photon-induced emission from a Mg cathode – is somewhat different from ours, we observe that a picture similar to our results emerges from their experimental data.

A comparison between the curves for xenon in Fig. 1, where f_{Xe}^q and f_{Xe} include or exclude the contribution of the cathode image-charge potential, shows that f_{Xe}^q is systematically lower than f_{Xe} , but indicates that the effect on the results for the present 7.2 eV photon-induced emission from the CsI photocathode, although increasing as we approach the lower E/N values, is in general small. As illustrated in Fig. 2 for xenon, this behaviour can be related to the increase in the ratios λ^q/\hat{a} , as we move to higher E/N , where λ^q is the calculated mean length of the first free path of the photoelectrons injected in the gas. Note that the region where the image-charge attractive field predominates over the applied collecting electric field is given by the magnitude of the parameter \hat{a} .

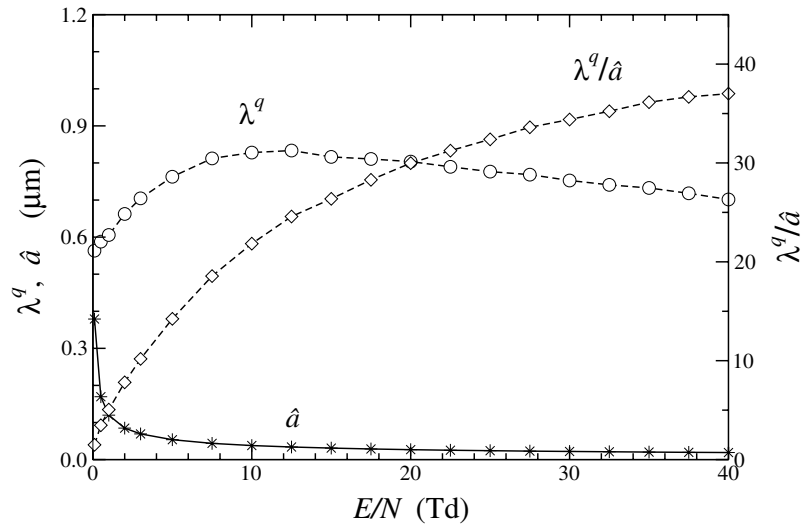


Fig. 2. The Monte Carlo mean length λ^q of the first free-path of the photoelectrons injected in Xe when the cathode image-charge attraction is included, the distance \hat{a} from the photocathode surface where the potential energy barrier is maximum, and the ratio λ^q/\hat{a} , as a function of the applied reduced electric field E/N in the range 0.1 to 40 Td ($p=760$ Torr, $T=293$ K)

For neon, the distinction between f and f^q will be lower than for xenon, since the collision frequency is higher and the free paths and ratios λ^q/\hat{a} are therefore higher than in xenon.

In Fig. 3, the collection efficiencies calculated for mixtures of xenon with neon, $f_{\text{Xe-Ne}}$, are shown as a function of mixture composition, for the reduced electric fields $E/N = 1, 10, 20$, and 40 Td. For each applied field, the results increase gradually from f_{Xe} to f_{Ne} , the values in the pure gases, showing that the transmission can be significantly improved by the addition of a small percentage of neon to xenon, especially for the higher E/N values.

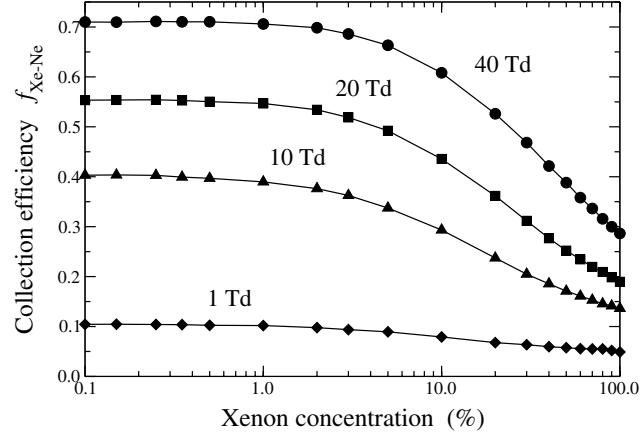


Fig. 3. Monte Carlo results for the ratio $f_{\text{Xe-Ne}}$ between the average number of photoelectrons emitted from CsI that are transmitted in xenon-neon gas mixtures and in vacuum, as a function of xenon concentration for the applied reduced electric fields $E/N = 1, 10, 20$ and 40 Td

Although in GPSC applications the energy resolution of a xenon counter will in general deteriorate with the addition of neon (because xenon is the scintillating gas), some beneficial compromise may be found between the lower scintillation yield and the improved photoelectron collection efficiency when an integrated CsI photocathode is used as the photosensor. This may be particularly relevant for the detection of x rays with energies below 2-3 keV, where the addition of neon also improves the collection of the primary electron cloud near the detector entrance window [19,21].

4 Conclusions

In this work, the Monte Carlo simulation method is used to examine the photoelectron collection efficiency and backscattering in pure xenon, pure neon and xenon-neon mixtures. The results apply to the case where photoelectron emission is induced by the absorption of 7.2 eV photons in an 11 nm reflective CsI-photocathode. The ratio f between the number of transmitted photoelectrons in the gas media and in vacuum is calculated, and results are presented at 760 Torr for applied reduced electric fields E/N in the range 0.1 to 40 Td.

The behavior of the results indicates that in this range the influence of the CsI-photocathode image-charge attractive field is small. This is correlated with the increasing λ^q/\hat{a} ratios as E/N is increased, where λ^q is the first free-path of the photoelectrons in the gas and \hat{a} is the distance from the photocathode surface for which the potential energy barrier is maximum, a measure of the effective reach of the image-charge attraction.

The calculations show that the photoelectron collection efficiencies in the E/N range studied are always lower than 30% for xenon, while in neon they are

much higher, reaching 70% at 40 Td. The results for xenon-neon mixtures show that the addition of a small amount of neon to xenon can improve significantly the photoelectron transmission for the higher E/N applied electric fields. At present work is in preparation to investigate the backscattering effects in argon and noble gas mixtures involving argon.

5 Acknowledgments

This work was carried out at Grupo de Instrumentação Atômica e Nuclear, Centro de Instrumentação (UO-217/94), Departamento de Física, Universidade de Coimbra, and received support from Fundação para a Ciência e Tecnologia (FCT) Lisboa, through Project CERN/P/FIS/15193/1999.

References

1. A. Peacock, R.D. Andresen, E.A. Leimman, G. Manzo, B.G. Taylor: Nucl. Instrum. Meth. **169**, 613 (1980)
2. A. Smith, M. Bavdaz: Rev. Sci. Instrum. **63**, 689 (1992)
3. A. Breskin: Nucl. Instrum. Meth. A **371**, 116 (1996)
4. J.F.C.A. Veloso, J.A.M. Lopes, J.M.F. dos Santos, C.A.N. Conde: IEEE Trans. Nucl. Sci. **43**, 1232 (1996)
5. J.A.M. Lopes, J.M.F. dos Santos, C.A.N. Conde, R.E. Morgado: IEEE Trans. Nucl. Sci. **44**, 517 (1997)
6. J.A.M. Lopes, J.M.F. dos Santos, C.A.N. Conde, R.E. Morgado: Nucl. Instr. Meth. A **426**, 469 (1999)
7. A. Breskin, A. Buzulutskov, R. Chechik, D. Vartsky, G. Malamud, P. Miné: Nucl. Instrum. Meth. A **344**, 537 (1994)
8. A. Di Mauro, E. Nappi, F. Posa, A. Breskin, A. Buzulutskov, R. Chechik, S.F. Biagi, G. Paic, F. Piuz: Nucl. Instrum. Meth. A **371**, 137 (1996)
9. A. Akkerman, T. Boutboul, A. Breskin, R. Chechik, A. Gibrekhterman: J. Appl. Phys. **76**, 4656 (1994)
10. T.H. Di Stefano, W.E. Spicer: Phys. Rev. B **7**, 1554 (1973)
11. P.J. Kuntz, W.F. Schmidt: J. Chem. Phys. **76**, 1136 (1982)
12. P.J. Jennings, R.O. Jones: Advances in Physics **37**, 341 (1988)
13. R.T. Poole, J.G. Jenkin, J. Liesegang, R.C.G. Leckey: Phys. Rev. B **11**, 5179 (1975)
14. S.L. Lin, J.N. Bardsley: Computer Phys. Communications **15**, 161 (1978)
15. M.J. Brennan: IEEE Trans. Plasma Sci. **19**, 256 (1991)
16. D. Potter: *Computational Physics* (Wiley, New York 1973)
17. P.J.B.M. Rachinhas, P.C.P. Simões, J.A.M. Lopes, T.H.V.T. Dias, R.E. Morgado, J.M.F. dos Santos, A.D. Stauffer, C.A.N. Conde: Nucl. Instrum. Meth. A **441**, 468 (2000)
18. T.H.V.T. Dias, F.P. Santos, P.J.B.M. Rachinhas, F.I.G.M. Borges, J.M.F. dos Santos, C.A.N. Conde, A.D. Stauffer: J. Appl. Phys. **85**, 6303 (1999)
19. F.P. Santos, T.H.V.T. Dias, P.J.B.M. Rachinhas, C.A.N. Conde, A.D. Stauffer: to be submitted to J. Appl. Phys.
20. E.M. Gushchin, A.N. Lebedev, S.V. Somov, V.P. Protasov, M.K. Timofeev, G.I. Tipografshchik: Instr. Exp. Tech. **36**, 754 (1993)

21. H. Inoue, K. Koyama, M. Matsuoka, T. Ohashi, Y. Tanaka, H. Tsunemi: Nucl. Instrum. and Meth. **157**, 295 (1978)

Medical Applications of the Geant4 Toolkit

S. Agostinelli¹, S. Chauvie^{2,5}, F. Foppiano¹, S. Garelli¹, F. Marchetto²,
M.G. Pia⁴, P. Nieminen³, V. Rolando², and A. Solano²

¹ Istituto Nazionale per la Ricerca sul Cancro, Italy

² Univ. of Torino and INFN Sezione di Torino, Italy

³ ESA/ESTEC, The Netherlands

⁴ INFN Sezione di Genova, Italy and CERN, Switzerland

⁵ IRCC Institute for Cancer Research and Treatment, Italy

Abstract. A powerful and suitable tool for attacking the problem of the production and transport of different beams in biological matter is offered by the Geant4 Simulation Toolkit. Various activities in progress in the domain of medical applications are presented: studies on calibration of brachytherapeutic sources and termoluminescent dosimeters, studies of a complete 3-D inline dosimeter, development of general tools for CT interface for treatment planning, studies involving neutron transport, etc. A novel approach, based on the Geant4 Toolkit, for the study of radiation damage at the cellular and DNA level, is also presented.

1 The Geant4 Object Oriented Simulation Toolkit

Geant4 [1] is a general purpose code providing a complete set of tools for the simulation of particle passage in matter. It provides tools for Tracking, Geometry, Detector Response, Run, Event and Track management, Visualisation and User Interface. A variety of physical processes describes interactions of hadrons, leptons and bosons in a large energy range. In particular, the new low energy extensions of electromagnetic interactions [2] are relevant in the domain of medical simulations. A fundamental requirement for physics validation of the Geant4 simulation results is to make transparent how the software produces the results. This is one of the major requirements and achievements of Geant4 and it is exploited through advanced Software Engineering and Object Oriented Technology. The OO technology allows fast and easy implementation of new features without modifying the preexistent code. Geant4 is supported for both UNIX and Windows platforms. The source code of Geant4 is freely available [1] and distributed by the Geant4 Collaboration. A User Support service is also available. The Geant4 software has been developed by a world-wide collaboration of over 100 scientists from Europe, Canada, Russia, Japan and USA.

2 Geant4 Features Relevant for Medical Applications

The capabilities of the Geant4 toolkit include a very powerful kernel, transparency and evidence of physics model and several auxiliary capabilities. The latter include the ability to visualise the detector, particle trajectories and hits, and the creation of a persistent geometry and persistent events.

The kernel of Geant4 handles the management of Run, Event and Track to perform the act of simulation. Geant4 Run encapsulates the possibility to create different geometry configurations and/or several beam types within a single computer job. Geant4 does not apply tracking cuts but only secondary production cuts, so that the validity range of physical models can be fully exploited and all particles are tracked down to 0 range. Cuts can be given in energy or in range so that the accuracy of spatial energy deposition becomes independent of the material. The Geant4 framework allows Fast Monte Carlo simulation that co-works with the full event simulation, for example, by plugging-in a user's parameterisation. This can be interesting, for example, to simulate treatment planning: full simulation will be in charge of inhomogeneous parts while fast simulation will be applied to homogeneous media. In this way it is easy to describe local energy deposition in small volumes with high density differences.

The role of geometry in Geant4 consists of providing tools to describe the complete environment. This can result in interesting medical applications in which beam sources and the patient can be described in the same frame. Geant4 handles the equation of motion solver in an electromagnetic field. An object geometry can be described in several different ways: via the geometrical definition of solid with Constructive Solid Geometry module, describing a solid as an intersection of surfaces with Boundary REPresented Solid (BREPS), or using geometry definition from commercial tools such as CAD via an ISO STEP compliant solid modeller. Geant4 itself treats the response of the object hit by the beam, including readout and digitisation. Geometry can be modified run-time, for example by a particle interaction with a volume of the geometry itself. This can be useful, for example, in the simulation of cell survival after irradiation, in which cells which have been hit, can send biochemical signals to neighbouring cells and modify their structure.

Geant4 Electromagnetic Physics manages electrons, positrons, γ -rays, X-rays, optical photons and muon interactions, as well as hadrons and ions interactions. A complete set of electromagnetic processes has been created and specialised processes extend the treatment of photons and electrons down to 250 eV [2] as well as for hadrons and ions. Hadronic processes are implemented for all hadrons in a variety of models over a wide energy range. For the neutron transport all data bases available are used. These features are relevant for particle cancer treatments such as Boron Neutron Capture Therapy or Hadrontherapy, in which a high definition description of the patient is needed.

The visualisation and GUI design is based on an object oriented abstract interface that makes Geant4 independent from any particular graphics system. At the same time, this interface allows multiple implementation of drivers for graphical libraries; the implemented visualisation drivers support the use of X11, PostScript, OpenGL, OpenInventor, RayTracer, DAWN and VRML. A friendly user interface offers batch or command line approaches and also fully graphical user interface such as OPACS, Momo, GPE and VRML. Due to the versatility of Object Oriented Technology it is possible to add modules for interfacing Geant4 with different tools or graphical systems in an easy and powerful way. The ability

to store relevant data in a persistent object storage has been developed in Geant4 for event data, hits and geometry description.

3 Brachytherapy Applications

The role of Monte Carlo simulation in Brachytherapy is mainly to obtain complex physical parameters not directly available by experimental measurements, used in treatment planning. The task described here [3] is to simulate a commercial ^{192}Ir source in order to:

- verify the anisotropy function,
- verify the dose distribution in a tissue equivalent phantom,
- compare the simulated air kerma strength with the measured value.

As a first test of Geant4 capabilities for Brachytherapy, the attenuation coefficient μ/ρ in different materials of interest has been simulated. Because of the energy and the accuracy required, the new features contained in Low-Energy Electromagnetic processes have been used. The tests involved one million photons of various energies passing through a thin layer of material and detected by a long-distance sensitive detector. Each test took approximately 2 minutes on a Windows Intel PC running at 300 MHz. Simulation results for water versus literature experimental values available at NIST [4] are shown in Fig. 1. Geant4 simulation is able to simulate with great accuracy (error less than 1%) the attenuation for photons.

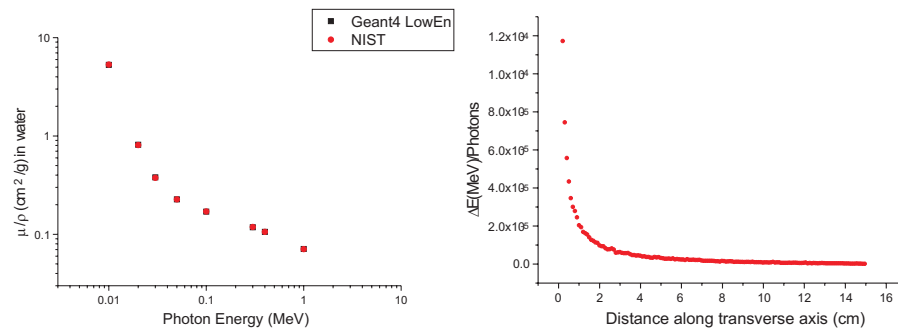


Fig. 1. Left: μ/ρ simulation results, with GEANT4 versus NIST tabulated values
Right: Simulation results for ΔE as a function of axial distance

The Geant4 simulated energy absorption in 20 cm water phantom (Fig. 1) of 10 millions of photons of energy equal to ^{192}Ir mean energy was also simulated.

The picture shown in Fig. 2 describe the anisotropy function obtained at 6 cm distance from axis by re-sampling in polar coordinates the available data with nearest neighbour interpolation.

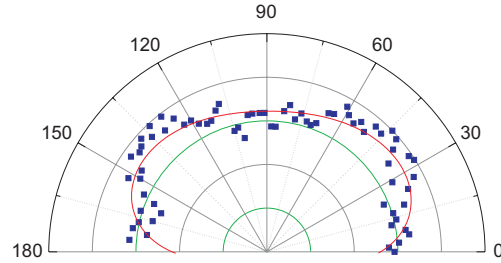


Fig. 2. Simulated anisotropy function at 6 cm axial distance

4 Dosimeter Studies

Thanks to its physics performance and easy geometry management, Geant4 is suitable for electron and photon beam studies. At INFN Torino, within the TERA project, a simulation of a pixel ionization chamber to measure the relative dose with therapeutical photon beam is under development. The photon energy beam follows a typical bremsstrahlung spectrum extended through 6 MeV. A comparison between experimental data and simulation is shown in Fig. 3, where the deposited energy in function of depth in water is shown. The agreement is fairly good; further attempts to shape the beam transverse profile are under way. The CPU time measured on a 500 MHz PC Linux platform is about 5 msec/photon.

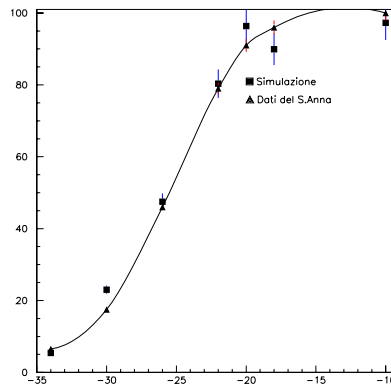


Fig. 3. Comparison between experimental data (triangle) and simulation (squared line)

Studies have already been undertaken for proton beams; Bragg peak reconstructed from experimental data taken at PSI compared with simulation 4 show a good agreement [5].

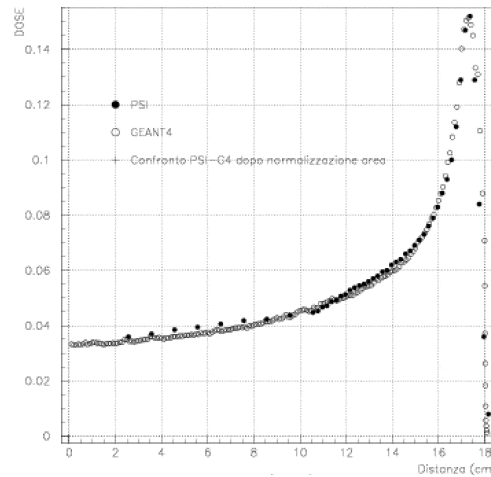


Fig. 4. Simulated versus experimental energy deposition in function of the depth in water

Characterisation of Thermoluminescent Detectors used in in-vivo dose estimation in radiological examination is also in progress in collaboration with Institute for Cancer Research and Treatment.

5 CT Image Interface

To simulate a full radiotreatment planning it is necessary to have the complete geometrical description of the patient; this is done through a CT scan image. An activity is in process to interface Geant4 with DICOM CT scan images format in order to perform direct simulation in an ad hoc described tissue, with the definition of organ at risk and target tumour volume.

6 Particle Interaction with DNA

Estimating cancer risk for human exposures to space radiation is a challenge which involves a wide range of knowledge in physics, chemistry, biology and medicine. Traditionally, the biological effects of radiation are analysed in top-bottom order, i.e. evaluation of the absorbed macroscopic radiation dose at a given location in the biological tissue is translated to the degree of danger it presents, and dose limits are consequently set that are considered to be acceptable. A novel approach that proceeds in a reverse order, from bottom to top, by analysing the nano-scale effects of energetic particles at the cellular and DNA molecule level, has been started [6]. In the framework of this project nanodosimetric studies are in progress, involving the application of Low Energy electromagnetic processes. In Fig. 5 we can see an α particle of 5.3 MeV from

an ordinary Po^{210} source producing δ electrons traversing a cylindrical volume inside a modelled cell nucleus. The particle is followed in steps of 1 nanometer in water and with δ emission. A definition of tissue and cell within the framework of Geant4 using the Object Oriented approach, as well as a detailed modelling of the DNA double helix, are in progress.

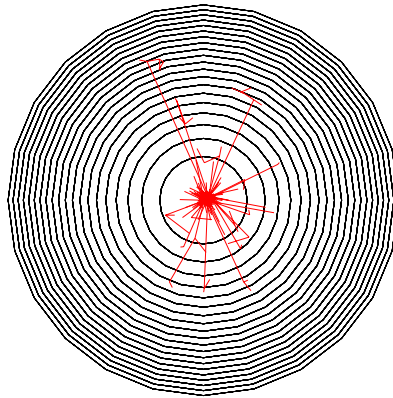


Fig. 5. 5.3 MeV alpha particle in cylindrical volume inside cell nucleus. The inner cylinder has radius 50 nm

The DNA-Geant4 project is sponsored by the European Space Agency (ESA) and National Institute of Nuclear Physics (INFN) and is pursued by a multi-disciplinary European Collaboration of biologists, physicians, physicists, space scientists and software engineers.

References

1. The Geant4 Collaboration: <http://wwwinfo.cern.ch/asd/geant4/geant4.html>
2. M.G. Pia et al.: 'Geant4 electromagnetic physics'. These Proceedings p. 153
3. F. Foppiano, S. Garelli, P. Moresco, G. Paoli, S. Agostinelli: 'The application of GEANT4 simulation code to the verification of a brachytherapy calibration procedure'. In *Proceedings of the XIII International Conference on the Use of Computers in Radiation Therapy, Heidelberg, Germany 22-26 May 2000*
4. National Institute of Standards and Technology: <http://physics.nist.gov>
5. R. Gotta: *Monte Carlo Simulation with Geant4 of a 3D dosimeter for therapeutical proton beams*. Thesis. (University of Torino 1999)
6. The Geant4-DNA Collaboration: <http://www.ge.infn.it/geant4/dna/index.html>

Effect of Voxel Size on Monte Carlo Dose Calculations for Radiotherapy Treatment Planning

G. Mora¹, T. Pawlicki², A. Maio¹, and C.-M. Ma²

¹ CFNUL, Lisbon University, Portugal

² Stanford Medical Center, Stanford University, USA

1 Introduction

The ability of CT (Computer Tomography) to measure the distribution of absorption coefficient in the patient body opens up the possibility of improving the accuracy of the dose calculation. On the other hand, the implementation of the Monte Carlo (MC) techniques in the treatment planning system is becoming a practical possibility [1]. The actual trends of the radiotherapy society are to combine the benefits of CT and MC dose calculations to design higher accuracy radiotherapy treatments.

The 3-D information of the anatomical structures given by the CT image data is used as input to MC dose calculations for radiotherapy treatment planning. The material and density information of the patient simulation geometry is derived from the patient CT data. An ideal conversion scheme would be using the same voxel size as that of the CT data (about 1 mm resolution) in order to eliminate the effect of CT data resizing. Because the CPU time required to perform dose calculations in a patient phantom with the same statistical uncertainty increases rapidly with decreasing voxel size and because of the computer memory size, it is more practical to use large dose calculation voxels (2–10 mm depending on the treatment site). However, resizing the CT voxels will change the material and density distribution in the converted patient simulation geometry and therefore affect the dose distributions. In this work we have investigated the voxel size effect on the dose distributions calculated by Monte Carlo for clinical photon and electron beams from Varian Clinac 2100C and 2300C/D linear accelerators.

2 Materials and Methods

2.1 Conversion of CT Data

In order to investigate the voxel size effect described above, patient simulation phantoms of different voxel sizes (2–10 mm), were built from the same patient CT data using the same CT number to material and density conversion algorithm. CTCREATE [2] was used to convert the patient's CT data to the desired dimensions, material types, and mass densities. Table 1 gives the CT number

range and density range for the three materials used in the conversion procedure. The use of these materials as tissues substitutes is consistent with the recommendations in an ICRU report [3]. The density for a given voxel was assigned by linear interpolation of a mass density versus CT number curve.

The resizing process groups a given number of original CT image pixels into one converted simulation phantom voxel. A resulting voxel has a new CT number which is equal to the average of the individual original pixels CT numbers. Hence, some variations of the material types of the resulting converted simulation phantoms relative to the original CT material types must be considered. These variations obviously are expected more pronounced at the interfaces of two or three different materials. In Figs. 1 and 2, we show the same slices ($Z = -74$) of the simulation phantoms built from the head patient CT data using 2, and 5 mm voxel sizes in the conversion procedure.

Table 1. Density range for the three materials used to build the Monte Carlo simulation phantoms

Material	Air	Tissue	Bone
CT number range	0-100	100-1125	1125-3500
Density range	0.001-0.1	0.1-1.125	1.125-2.65

2.2 Dose Calculations

Monte Carlo dose calculations were performed in the CT based simulation phantoms described above using the EGS4/MCDOSE code [4]. Both the phase space particles obtained from a previous BEAM [5] simulations of *4 and 6 MeV photon beams* [6,7] and the source models [8,9] of *6, 12 and 20 MeV electron beams* were used as input of MCDOSE phantom calculations. In both cases, the particles were transported from the source plane to the anterior-posterior part of the phantom. MCDOSE produced a data file that contained the dose values and the associated statistical uncertainties in the individual voxels. The dose distributions were analyzed and plotted using a STATDOSE [10] code.

3 Results

By comparison of Figs. 1 and 2, we clearly see a change in the material and density distribution of the converted patient simulation geometry as a result of resizing the voxel size (*V.S.*) from 2 to 5 mm. Bone/muscle/air and muscle/bone interfaces are replaced by homogeneous regions with a density higher than muscle and lower than bone. This change is more pronounced in the previous part of the phantom which include the nasal cavities.

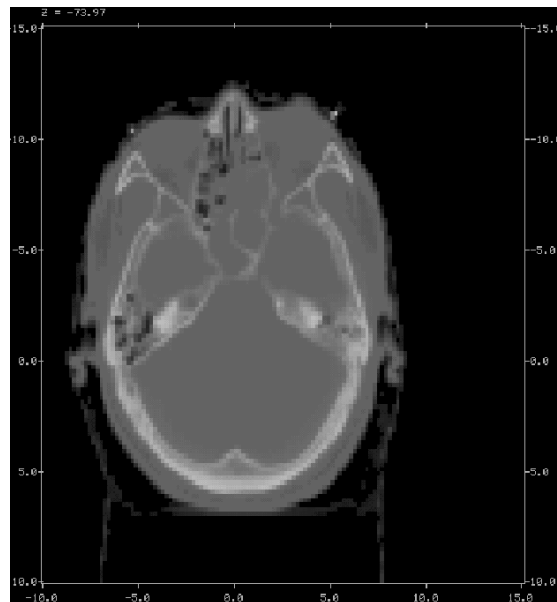


Fig. 1. CT based phantom simulation geometry of 2 mm Voxel Size

The above described phantom variations affect dose distributions. This effect is clearly observed in Figs. 3 and 4, which compare the dose profiles calculated in the simulation phantoms of different voxel sizes (2-10 mm) for a $6 \times 6 \text{ cm}^2$ field size of 6 and 20 MeV electron beams from Varian Clinac linear accelerators. The both figures show the X dose profiles plotted in the same slice of the phantom ($Z = -74 \text{ cm}$) and at the same depth ($Y = -9.5 \text{ cm}$).

In Fig. 3, we present the dose profiles calculated for 6 MeV electron beam and we can see a dramatic variation on the shape of the dose profile with voxel size. Although this effect is most significant in the central-axis region (*c.a.r.*), it is observed along all field size. It is very difficult to predict exactly quantitative differences between the dose values of the dose curves calculated with different geometry resolution phantoms because the obvious dependence on the interpolation one used to join the points. However, the change of resolution from 2mm to 4mm *V.S.* geometry would change the dose values by about 13 % in the *c.a.r.* (1.5 cm) and about 4% in the off-axis region (*o.a.r.*). Increasing the *V.S.* to 5 mm, the differences on the *c.a. r.* dose values would reach 25% and 20% on the *o.a.r.* dose values. The extremely effect of *V.S.* on dose distribution is observed in Fig. 3 by the comparison of 2 mm and 10 mm *V.S.* curves. The *c.a.r.* dose values would change by about 30% while the *o.a.r.* values by about 15%.

Fig. 4 shows also the X profiles calculated in different *V.S.* geometry phantoms, but in this case for 20 MeV electron beam. As in the previous case, the change on the profile shape with *V.S.* is also noted. But in this case it occurs only in the *c.a.r.* (about 1.5 cm), and the differences on the dose values are less

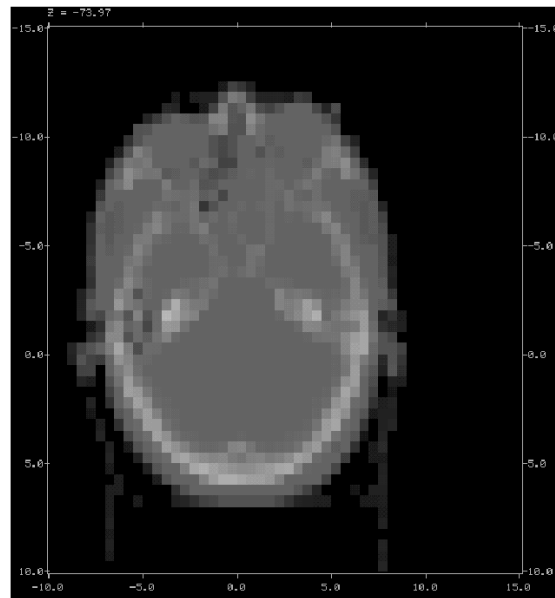


Fig. 2. CT based phantom simulation geometry of 5 mm Voxel Size

pronounced than in the 6 MeV case. Increasing *V.S.* from 2 to 4 mm, would vary the c.a.r. dose values about 15%, and there are no significant variations between 4, 5, and 6 mm *V.S.* curves.

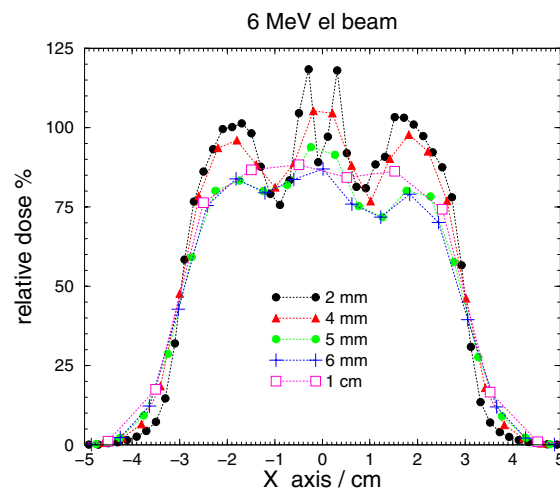


Fig. 3. Comparison of X dose profiles calculated in the CT based simulation phantoms of different voxel sizes

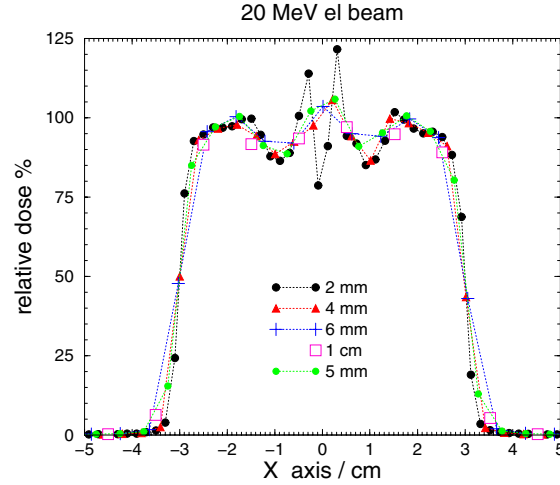


Fig. 4. Comparison of X dose profiles calculated in the CT based simulation phantoms of different voxel sizes

Table 2. Simulation results versus *VoxelSize*

Voxel Size cm	Number of histories	Dose at D_{\max} (Gy)	1σ uncert	D_{\max} cm	CPU time ratio
0.2	15×10^6	1.12E-10	0.96	-8.91	1
0.4	15×10^6	1.06E-10	0.75	-8.31	1.14
0.5	15×10^6	1.02E-10	0.62	-8.19	1.18
0.6	15×10^6	1.02E-10	0.52	-8.52	1.21
1	15×10^6	0.97E-10	0.43	-8.15	1.27

In Tab. 2 is observed that the value of dose at D_{\max} changes about 15% from 2 to 10 mm *V.S.* while the position of D_{\max} varies from 8.91 to 8.15 cm. At the same time, the simulation in the phantom of 2 mm voxels required 1.27 more CPU time than the simulation in the 10 mm voxels. However, the relative uncertainty in the dose value at D_{\max} decreases by about 50%.

4 Conclusions

- Significant voxel size effect is observed on the dose distributions calculated in the nasal cavity region for both cases, 6–20 MeV electron beams and 4 and 15 MeV photon beams.

- The difference in the isodose values is more than 25% between a phantom of 2 mm voxels and a phantom of 10 mm voxels.
- The effect decreases with beam energy

Our results suggest that 3 mm or smaller voxels should be used for the head and 5 mm or smaller voxels should be used for the body for accurate Monte Carlo dose calculations.

References

1. C.-M. Ma, E. Mok, A. Kapur, T. Pawlicki, D. Findley, S. Brain, K. Forster, A.L. Boyer: 'Clinical Implementation of a Monte Carlo treatment planning system', Med. Phys. (1999)
2. C.-M. Ma, P.J. Reckwerdt, M. Holmes, D. W. O. Rogers, and B. Geiser: 'DOSXYZ Users Manual', National Research Council of Canada Report: PIRS-509B, 1995
3. ICRU: *Tissue Substitutes in Radiation Dosimetry and Measurements*, ICRU Report 44, ICRU, Washington D.C. (1989)
4. C.-M. Ma, T. Pawlicki, M.C. Lee, S.B. Jiang, J.S. Li, J. Deng, E. Mok, B. Yi, G. Luxton, A.L. Boyer: Phys. Med. Biol. **45**, 2293 (2000)
5. D.W.O. Rogers: 'BEAM: A Monte Carlo code to simulate radiotherapy treatment units', Med. Phys. (1995)
6. A. Kapur: *Monte Carlo dose calculations for clinical electrons and intensity modulated photons in radiotherapy*. PhD Thesis. (Stanford University 1999)
7. G. Mora, T. Pawlicki, A. Kapur, A. Maio, C.-M. Ma: 'Monte Carlo Simulation of 4 MeV photon beam from Varian Clinac 2100C medical accelerator'. In *Proceedings of the World Congress on Medical Physics and Biomedical Engineering*, Chicago (2000)
8. C.-M. Ma, B.A. Faddegon, D.W.O. Rogers, T. R. Mackie: Med. Phys. **24**, 401 (1997)
9. S.B. Jiang, A. Kapur, C.M. Ma: Med. Phys. **27**, 180 (2000)
10. H.C.E. McGowan, B.A. Faddegon, C.-M. Ma: *STATDOSE for 3D Dose Distributions*, National Research Council of Canada Report: PIRS-509F (1995)

Monte Carlo Physical Dosimetry for Small Photon Beams

M. Perucha¹, F. Sánchez-Doblado^{1,2}, M. Rincón¹, A. Leal¹, L. Núñez³,
R. Arráns², E. Carrasco¹, J.A. Sánchez-Calzado², and L. Errazquin²

¹ Universidad de Sevilla. Facultad de Medicina. Dpto. Fisiología Médica y Biofísica.
Avda. Sánchez Pizjuán, 4. E41009. Sevilla. Spain

² Hospital Universitario Virgen Macarena. Servicio de Oncología Radioterápica.
Avda. Dr. Fedriani, 3. E41071. Sevilla. Spain

³ Clínica Puerta de Hierro. Servicio de Radiofísica. C/ Martín de Porres, 4. E28035.
Madrid. Spain

Abstract. Small field dosimetry is complicated due to the lack of electronic equilibrium and to the high steep dose gradients. This work compares PDD curves, profiles and output factors measured with conventional detectors (film, diode, TLD and ionisation chamber) and calculated with Monte Carlo. The 6 MV nominal energy from a Philips SL-18 linac has been simulated by using the OMEGA code. MC calculation reveals itself as a convenient method to validate OF and profiles in special conditions, such as small fields.

1 Introduction

Radiosurgery [1] is a radiotherapy technique in which the target volume has usually a reduced size. This implies the use of very small beams with the associated dosimetrical inconveniences, among them the absence of lateral electronic equilibrium and the sharp profiles which make the penumbra difficult to be quantified accurately. Usual detectors [2,3] have not an active volume small enough to measure the beam with precision. Furthermore, some of them exhibit the additional drawback of the energy dependence. The Monte Carlo (MC) approach may solve these problems, as the dose delivery for every particle can be studied in a volume size according to the field dimension.

2 Material and Method

The code OMEGA (based on EGS4) was used to simulate the particle transport. Basically, it consists of two parts: BEAM [4] and DOSXYZ [5]. The former simulates the linac head, while the second allows the dose calculation in either a phantom or a patient. The hardware used was an Octane Silicon Graphics with two R10000 processors and 384 Mbytes RAM. The beam simulated was a 6 MV from a Philips SL-18. The secondary collimator is fixed to a 10×10 cm² field size. Additional radiosurgery collimators of 2, 7, 9, 11, 15, 20 and 35 millimetres of diameter (30.4 cm far from the isocenter) were attached to the linac head. Several detectors (TLD [6], film, semiconductor [7] and ionisation chamber) were

used. Due to the versatility of the BEAM [8] module FLATFIL, it has been used to simulate the target, the flattening filter and additional collimators. CONS3R was used for the primary collimator as well as the specific modules CHAMBER, MIRROR and JAWS. The $10 \times 10 \text{ cm}^2$ phase space is first obtained and used as a source to calculate the corresponding ones for each additional collimator. A water phantom has been emulated to obtain PDD curves ($2 \times 2 \times 4 \text{ mm}^3$ voxel size), profiles (different voxel dimensions depending on the field size; in particular, a resolution of $0.2 \times 0.2 \times 2 \text{ mm}^3$ was used for the smallest collimator) and output factors ($1.5 \times 1.5 \times 4 \text{ mm}^3$).

3 Results

Monte Carlo calculated PDD curves are compared with those measured with diode and ionisation chamber. The agreement is good for every collimator (Fig. 1) except for the smallest one, where the RK ionisation chamber measurement deviates significantly (Fig. 2)

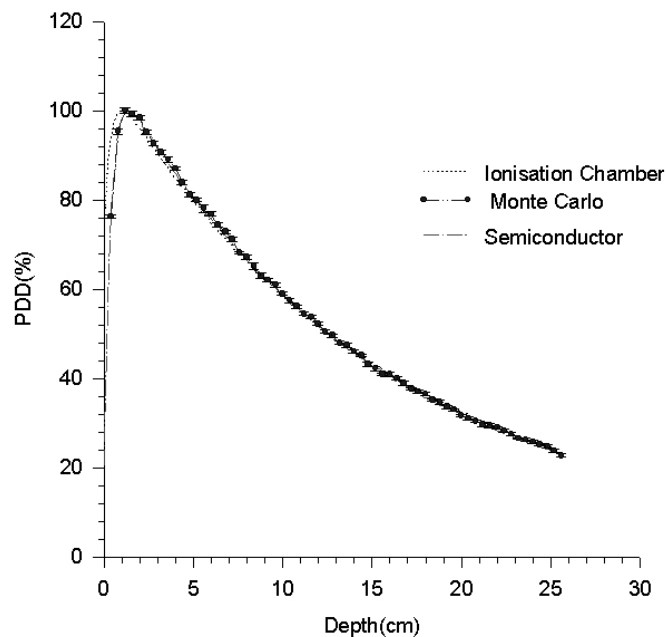


Fig. 1. PDD curve for the collimator with diameter of 7 mm (10.1 mm at the isocenter)

Profiles (OAR) measured with film, TLD, diodes and ionisation chamber were also compared with the MC simulation (Fig. 3). As the field size becomes smaller, the detector measurements are further from the calculations, except the film.

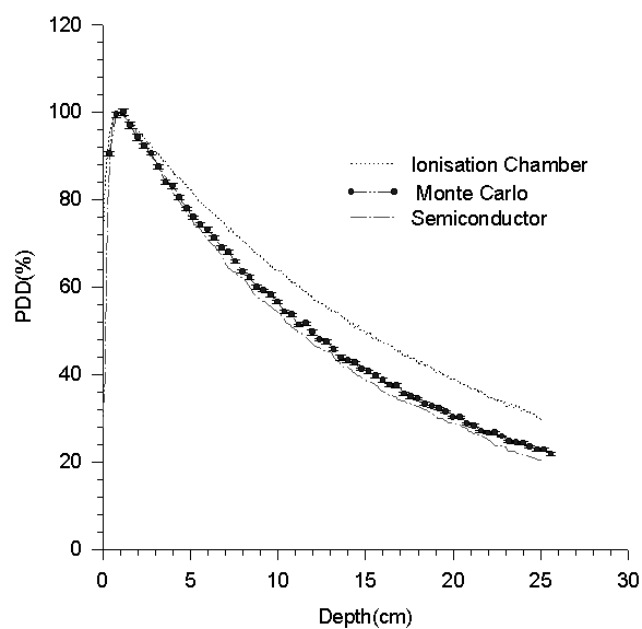


Fig. 2. PDD curve for the collimator with diameter of 2 mm (2.9 mm at the isocenter)

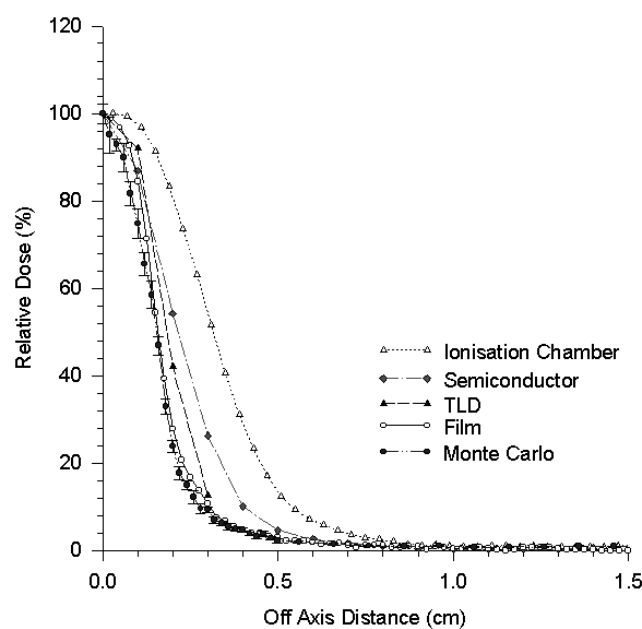


Fig. 3. OAR for the collimator with diameter of 2 mm (2.9 mm at the isocenter)

Regarding the OF, the most representative differences are again for the smallest one (Fig. 4).

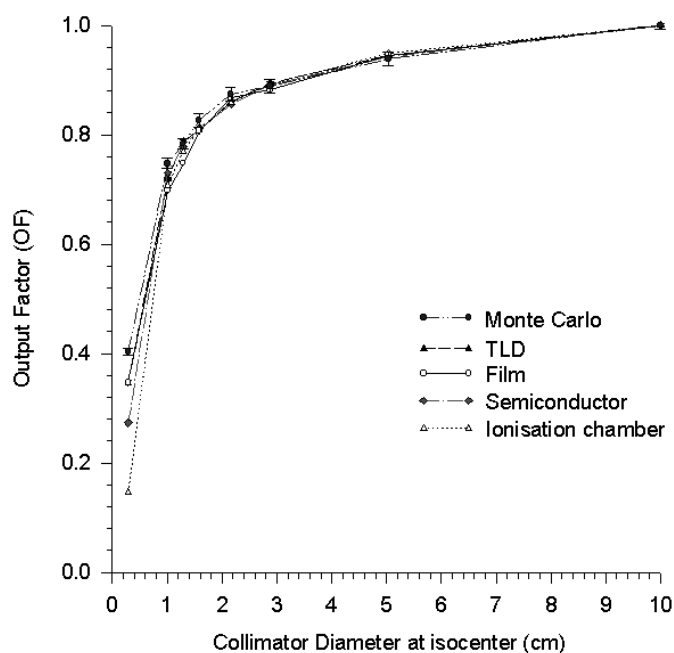


Fig. 4. Outputs Factors for all collimators

4 Conclusions

Both ionisation chamber and diode reproduce the PDD curves calculated with MC in the whole field size range, with the exception of the 2 mm diameter collimator, in which the former deviates significantly. OF measurement for the smallest field size is critical. The active volume for the conventional detectors used is too big and hence their response has a non correct value. The accurate reproduction of the penumbra region of a profile can be achieved with the help of MC as far as the voxel size, statistics and cut-off energies have appropriate values.

References

1. Med. Dosim. **23**, 3 (1998)
2. L. Núñez, F. Sánchez-Doblado, J.L. Muniz, M.C. Ispizua, J.C. Medrano, M.I. Gallardo, A. Delgado: Radiat. Protect. Dosim. **85**, 405 (1999)

3. L. Núñez, F. Sánchez-Doblado: *Small field dosimetry in Radiosurgery* (Dynarad, Seville 1999)
4. C-M. Ma, P. Reckwerdt, M. Holmes, D.W.O. Rogers, B. Geiser, B. Walters: *BEAM Users Manual* NRCC report PIRS-0509B(revC), (Ottawa 1998)
5. C-M. Ma, P. Reckwerdt, M. Holmes, D.W.O. Rogers, B. Geiser, B. Walters: *DOSXYZ Users Manual* NRCC report PIRS-0509B(revC), (Ottawa 1998)
6. J.L. Muniz, A. Delgado, J.M. Gómez Ros, A. Brosed: *Phys. Med. Biol.* **40**, 253 (1995)
7. G. Rikner: Silicon Diodes as detectors in relative Dosimetry of Photon, Electron and Proton Radiation Field. MA Thesis, Uppsala University, Uppsala (1983)
8. M. Perucha, F. Sánchez-Doblado, A. Leal, M. Rincón, L. Núñez, J. Roselló, R. Arráns, E. Carrasco, L. Errazquin, J.A. Sánchez-Calzado: *Physica Medica*. XV **3**, 188 (1999)

Monte Carlo Dose Distributions for Radiosurgery

M. Perucha¹, F. Sánchez-Doblado^{1,2}, A. Leal¹, M. Rincón¹, L. Núñez³,
R. Arráns², E. Carrasco¹, B. Sánchez-Nieto⁴, J.A. Sánchez-Calzado², and
L. Errazquin²

¹ Universidad de Sevilla. Facultad de Medicina. Dpto. Fisiología Médica y Biofísica.
Avda. Sánchez Pizjuán, 4. E41009. Sevilla. Spain

² Hospital Universitario Virgen Macarena. Servicio de Oncología Radioterápica.
Avda. Dr. Fedriani, 3. E41071. Sevilla. Spain

³ Clínica Puerta de Hierro. Servicio de Radiofísica. C/ Martín de Porres, 4. E28035.
Madrid. Spain

⁴ Joint department of physics. Royal Marsden NHS Trust and the Institute of Cancer
Research. Dows Road. Sutton, Surrey SM2 5PT, UK

Abstract. The precision of Radiosurgery Treatment planning systems is limited by the approximations of their algorithms and by their dosimetrical input data. This fact is especially important in small fields. However, the Monte Carlo methods is an accurate alternative as it considers every aspect of particle transport. In this work an acoustic neurinoma is studied by comparing the dose distribution of both a planning system and Monte Carlo. Relative shifts have been measured and furthermore, Dose-Volume Histograms have been calculated for target and adjacent organs at risk.

1 Introduction

The main objective of radiosurgery [1] is the delivery of a high and precise dose on the target volume, while keeping the morbidity of adjacent organs at risk as low as possible. Treatment Planning Systems (TPS) use approximate algorithms based on experimental data, which are some times measured with detectors with limited resolution for small fields [2]. The Monte Carlo (MC) method [3,4] allows an accurate calculation of the dose by considering all the electron and photon interactions. In this work, a clinical case has been studied and its results from a conventional TPS compared with a MC simulation.

2 Material and Method

A Philips SL18 linac with 6 MV nominal energy was simulated [5]. The secondary collimator is set to 10x10 cm² at the isocenter and the additional collimators used had 7, 15 and 20 mm. The particle transport was simulated by the OMEGA code which basically consists of the BEAM [5,6] and the DOSXYZ [8] codes. The former simulates the accelerator head geometry while the second determines the dose distribution in a patient. The hardware used was a Octane Silicon Graphics work station with two R10000 processors and 384 Mbytes RAM. A program

was developed to calculate Dose Volume Histograms (DVH) which outlines the contour of Regions of Interest (ROIs) and integrates the dose delivered in each voxel. The CT patient information is converted into MC geometry, which requires four media (air, lung, tissue and bone) and physical densities instead of Hounsfield numbers. It is also necessary to translate from the linac reference system to MC coordinates. A case of acoustic neurinoma has been studied. The planning strategy consisted of two isocenters with 6 and 2 arcs, respectively. The comparison between the planning system and MC followed three different methods. First, from a qualitative point of view, by calculating isodose lines in axial, sagittal and coronal planes (Fig. 1).

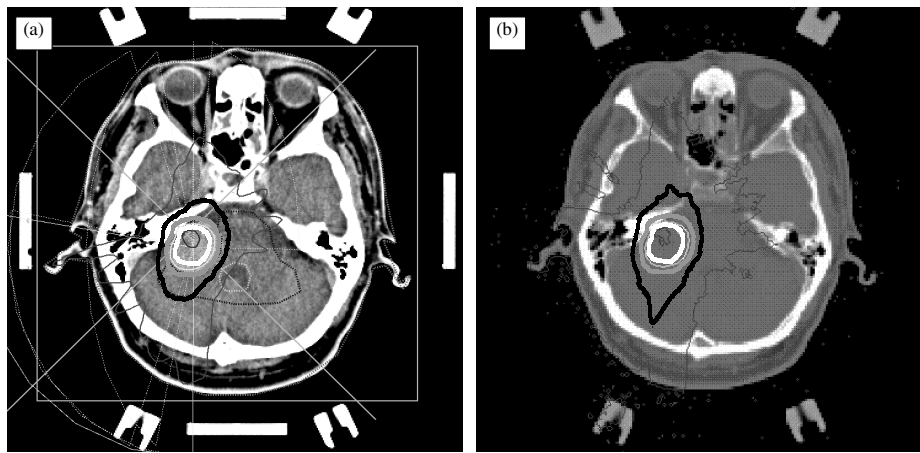


Fig. 1. Identical plans in the acoustic neurinoma treatment using (a) the conventional planning system and (b) Monte Carlo method. The 85% (*white*), 50% (*grey*) and 20% (*black*) isodose lines in axial plane have been highlighted

Second, by quantifying the deviations along X and Y directions of some given isodoses. Finally, to estimate the dose distribution in certain ROIs, a program which calculated DVH has been developed. It allows a more objective comparison between planning system and MC by evaluating the overall dose delivered to both target and critical organs.

3 Results

For the case being studied, the deviation between the 50% and 85% isodose lines is negligible. However, there are significant discrepancies with the 20% isodose lines (on the axial and sagittal plane 8 mm far from the isocenter). Figure 2 shows the comparison for the DVHs obtained with a conventional planning system and MC, for the target volume and an organ at risk.

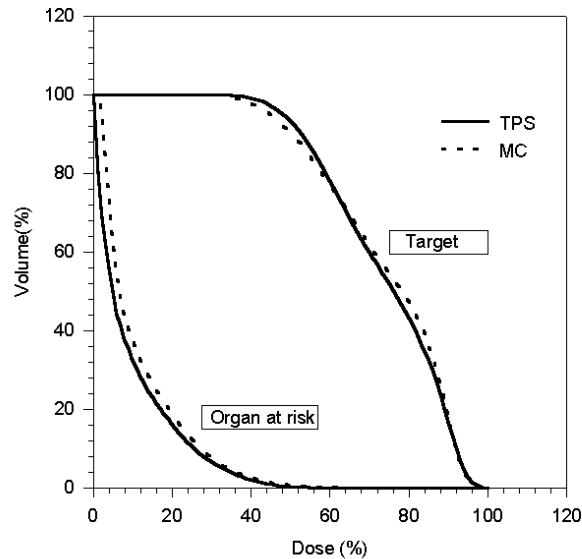


Fig. 2. Dose Volume Histograms for target and organ at risk from conventional treatment planning system (*straight line*) and Monte Carlo method (*dotted line*)

Comparison between conventional planning system and Monte Carlo method for Tumour Control Probability (TCP) and Normal Tissue Complication Probability (NTCP) [9,10] shows no differences.

4 Conclusions

Results show significant differences in certain isodose lines. Nevertheless, in the case presented, these discrepancies are not relevant from the radiobiological point of view. This reinforces the importance of a more accurate calculation in some critical situations in radiosurgery. The possibility to evaluate DVHs with MC makes feasible a radiobiological comparison between conventional planning systems and Monte Carlo calculations.

References

1. Med. Dosim. **23**, 3 (1998)
2. L. Núñez, F. Sánchez-Doblado: *Small field dosimetry in Radiosurgery* (Dynarad, Seville 1999)
3. F. Sánchez-Doblado, M. Perucha, L. Núñez, A. Leal, M. Rincón, R. Arráns, E. Carrasco, J. Roselló, L. Errazquin, J.A. Sánchez-Calzado: *Physica Medica*. XV **3**, 188 (1999)
4. C-M. Ma, E. Mok, A. Kapur, T. Pawlicki, D. Findley, S. Brain, K. Forster, AL. Boyer: *Med. Phys.* **26**, 2133 (1999)

5. M. Perucha, F. Sánchez-Doblado, A. Leal, M. Rincón, L. Núñez, J. Roselló, R. Arráns, E. Carrasco, L. Errazquin, J.A. Sánchez-Calzado: *Physica Medica*. XV **3**, 188 (1999)
6. C-M. Ma, P. Reckwerdt, M. Holmes, D.W.O. Rogers, B. Geiser, B. Walters: *BEAM Users Manual* NRCC report PIRS-0509B(revC), (Ottawa 1998)
7. D.W.O. Rogers, B.A. Faddegon, G.X. Ding, C-M. Ma, J. We: *Med. Phys.* **22**, 503 (1995)
8. C-M. Ma, P. Reckwerdt, M. Holmes, D.W.O. Rogers, B. Geiser, B. Walters: *DOSXYZ Users Manual* NRCC report PIRS-0509B(revC), (Ottawa 1998)
9. B. Sánchez-Nieto, A. E. Nahum: *Rad. Oncol.* **48**(S1), 152 (1998)
10. B. Sánchez Nieto, A.E. Nahum: *International Journal of Radiation Oncology Biology and Physics*, **44**, 369 (1999)

Monte Carlo Conformal Treatment Planning as an Independent Assessment

M. Rincón¹, F. Sánchez-Doblado^{1,2}, A. Leal¹, M. Perucha¹, R. Arráns²,
J.C. Medrano³, E. Carrasco¹, J.A. Sánchez-Calzado², and L. Errazquin²

¹ Universidad de Sevilla. Facultad de Medicina. Dpto. Fisiología Médica y Biofísica.
Avda. Sánchez Pizjuán, 4. E41009. Sevilla. Spain

² Hospital Universitario Virgen Macarena. Servicio de Oncología Radioterápica.
Avda. Dr. Fedriani, 3. E41071. Sevilla. Spain

³ Clínica Puerta de Hierro. Servicio de Radiofísica. C/ Martín de Porres, 4. E28035.
Madrid. Spain

Abstract. The wide range of possibilities available in Radiotherapy with conformal fields cannot be covered experimentally. For this reason, dosimetrical and planning procedures are based on approximate algorithms or systematic measurements. Dose distribution calculations based on Monte Carlo (MC) simulations can be used to check results. In this work, two examples of conformal field treatments are shown: A prostate carcinoma and an ocular lymphoma. The dose distributions obtained with a conventional Planning System and with MC have been compared. Some significant differences have been found.

1 Introduction

Whenever it is necessary to conform the field shape [1] in a radiotherapy treatment, conventional planning systems may lay to some uncertainties. This is so, because their algorithms [2] employ regular fields as input data. For this reason, it may be useful to have an alternative tool, such as the Monte Carlo (MC) method, for independent assessment. As representative cases, an ocular lymphoma [3] and a prostate carcinoma [4–6] treated with electron [7] and photon beams [8] respectively, are presented.

2 Material and Method

In this work, the Monte Carlo [9–11] techniques have been utilized by using the program BEAM [12,13] (to simulate every component of the linac head) and DOSXYZ [14] (to calculate the dose distribution in the patient). Both software packages are based in the EGS4 [15,16] code, running under UNIX operating system and developed by the OMEGA project (Ottawa Madison Electron Gamma Algorithm).

The conformation of the electron beam [17] for the ocular lymphoma starts with a lengthener directly attached to the electron applicator, to fit the anatomical contour. At the end of the lengthener (radius = 2.4 cm), a PMMA plate (radius = 2 cm) energy degrader and a lead circular shielding (radius = 0.6 cm)

to prevent any damage to either the cornea or the eye lens were located. A ring shaped small field was then obtained (Fig. 1)

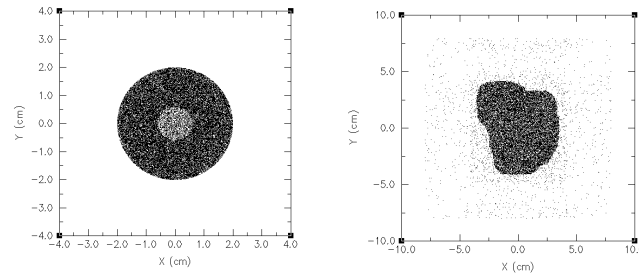


Fig. 1. X-Y scatter plot of particles from conformal electron and photon beam

In the case of the photon beam (prostate carcinoma), blocks have been used to conform the field. All the needed elements to carry out the beam shaping [18] have been simulated. Analogously, Philips SL18 linac head was simulated for photon beam geometry and Siemens Mevatron 74 linac head for electron beam. The nominal energy used was 6 MV and 6 MeV, respectively.

BEAM has a series of modules for this purpose. For the electron beam configuration, the FLATFILT module was used for the electron vacuum window, the secondary scattering foils, the applicator and the flattening filter. The CONS3R module was employed for the primary scattering foils and the primary collimator. The ionisation chamber and secondary collimator were simulated with the CHAMBER and JAWS modules, respectively. Additional elements were built with the FLATFILT module. For the photon beam geometry, the FLATFILT module was used for target and flattening filter, CONS3R for the primary collimator, CHAMBER for the ionisation chamber, MIRROR for the mirror, SLABS for the aluminium slab underneath the ionisation chamber and the mylar slab under the secondary collimator and JAWS for the collimator. Blocks, simulated with the BLOCK module, were the most difficult element to construct, due to their geometry. This module needs the coordinates of each point of the block geometry with respect to a coordinate system, having its origin at the centre of the block. A digitiser-based method has been developed for the block contour acquisition. These blocks stand on a PMMA plate provided with a 2D fixation hole array. This complex element was also simulated with the BLOCK module.

The BEAM code has implemented some variance reduction techniques [19] like Bremsstrahlung photon splitting. This technique offers the possibility to improve the statistics of bremsstrahlung photons resulting from electron interactions by producing NBRSP photons (instead of one) in every bremsstrahlung event. This parameter was set to 25. To reduce the CPU time following all of the electrons created by the split photons, a Russian roulette technique was used. The electron path length was calculated with the PRESTA [20] algorithm.

A Fortran 77 program was developed to convert the patient CT information to a MC geometry. This takes into account three main requisites: the voxel boundary co-ordinates, the index assigned to each medium (medium 1 = AIR, medium 2 = LUNG, medium 3 = TISSUE and medium 4 = BONE) and the density of the medium in each voxel (4096 levels). To correlate the Hounsfield number with the corresponding medium and density, several experiments were carried out. In the case of the prostate carcinoma, the CT studies have been performed with a radio-opaque substance filling the bladder and adjacent anatomical structures. This adds an extra problem, as this is not the treatment situation. Therefore, a program has been developed which converts the Hounsfield number of the voxels with contrast to tissue-like numbers. Thirty-one 340×340 CT slices 0.5 cm apart were taken in the case of the ocular lymphoma. This implies a voxel size of $0.12 \times 0.12 \times 0.5 \text{ cm}^3$. Analogously, for the prostate treatment, thirty 256×256 CT slices 1 cm apart, lead to a voxel size of $0.23 \times 0.23 \times 1 \text{ cm}^3$. This voxel size influences the cut-off energy value. For electrons, 700 keV (electron rest mass plus its kinetic energy) was chosen, while 10 keV was selected for photons. The coordinates of the isocenter in the MC geometry and in the planning system are related by an equation obtained by linking several reference marks in the CT study.

The patient dose distribution was obtained by two means: Full Monte Carlo (FMC) calculation, using DOSXYZ package, and two conventional planning systems (PLATO and FOCUS).

The hardware used in the MC calculation was a Octane Silicon Graphics workstation with two R10000 processors and 384 Mbytes RAM memory. The CPU time required for the calculation of the dose distribution was approximately three hours for the ocular lymphoma. The prostate treatment was calculated with a cluster of four 500 MHz Pentium III having each 256 Mbytes RAM memory. A process distribution model [21] has been developed to share the calculation tasks out between these machines. The CPU time required in this case was half an hour.

3 Results

The comparison between both dose distributions obtained with these two methods (FMC and PLATO treatment planning), in the case of the conjunctival lymphoma, shows significant discrepancies when comparing isodose lines. This is due to the implementation of the modifiers (applicator lengthener, PMMA plate energy degrader and lead shielding). For example, as you can see in Fig. 2, at a distance of 1.5 cm from the isocentre, differences up to 1.7 cm can be found in the penetration of the 75% isodose lines in the malar bone.

Furthermore, the 90% isodose line does not appear in the MC calculation, however, in the calculation made with PLATO, it goes as far as 0.8 cm into the orbital bone. The influence of the lead shielding is clearly shown in the CT slice corresponding to the isocenter when using MC. Nevertheless, this effect does not appear in the conventional planning system calculation (Fig. 3)

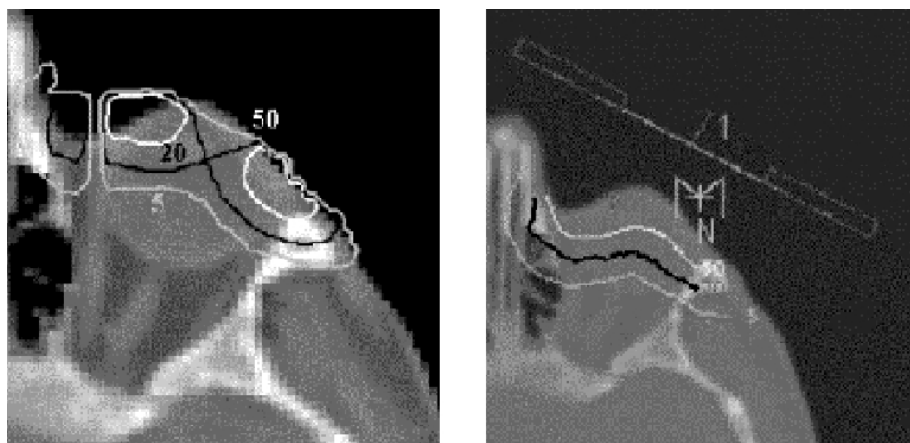


Fig. 2. Identical plans in the ocular lymphoma treatment using the conventional planning system PLATO (right) and Monte Carlo method (left). The 90% (grey), 75% (white) and 20% (black) isodose lines in the axial slice at 1.5 cm above the isocenter are observed. Note the absence of the 90% isodose line with the MC calculation

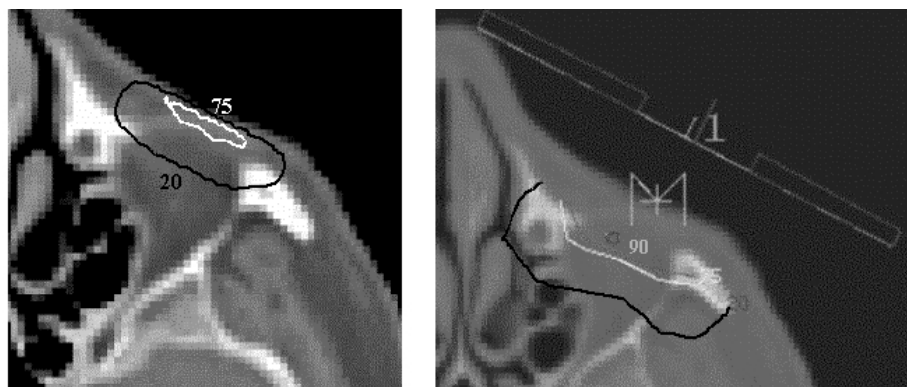


Fig. 3. Identical plans in the ocular lymphoma treatment using the conventional planning system PLATO (right) and Monte Carlo method (left). The 50% (white), 20% (black) and 5% (grey) isodose lines in the axial slice where the isocenter is placed are shown. The most importance fact is the penetration of the 50% isodose line inside the eyeball with PLATO calculation. This therefore suggests that the circular lead shield does not conveniently protect the cornea from a possible radiation harm

In the prostate treatment the most relevant fact, as shown in Fig. 4, is an overdose (about 50%) in the femoral head when comparing MC with a conventional (FOCUS) treatment planning system.



Fig. 4. Identical plans in the prostate cancer using FOCUS treatment planning system (up) and the Full Monte Carlo system (down). The 85% (yellow), 50% (green) and 5% (pink) isodose lines are shown in the axial slice where the isocentre is placed. Note the 50% isodose line with the Monte Carlo simulation over the femoral head

4 Conclusions

These results show that in treatments where conformal beams (photon or electron) are needed, the traditional planning methods can have some limitations and Monte Carlo simulation is a very useful tool to know the dose deposition accurately and to verify the results.

References

1. J. Hubert, D. Rossi, V. Beckendorf: Prog-Urol. **9**, 3 (1999)
2. H.E. Johns, J. R. Cunningham: *The physics of radiology*, 4th edn. (Thomas, Springfield 1983)
3. P.G. Isaacson, J. Spencer: Histopathology **11** (1987)
4. E.J. Small: Curr-Opin-Oncol. **11**, 3 (1999)
5. J.P. Gerard, C. Xie, C. Carrie, P. Romestaing, P. Pommier, F. Mornex, S. Clippe, I. Sentenac, C. Ginestec: Aust-N-Z-J-Surg. **69**, 10 (1999)
6. J.L. Bedford, V.S. Khoo, S. Webb, D.P. Dearnaley: Int. J. Radiat. Oncol. Biol. Phys. **46**, 1 (2000)
7. F.M. Khan, K.P. Doppke, K.R. Hogstrom: Med. Phys. **18**, 1 (1991)
8. J. Deng, S.B. Jiang, A. Kapur, J. Li, T. Pawlicki, C-M. Ma: Phys. Med. Biol. **45** (2000)
9. A.F. Bielajew: *Electron Monte Carlo simulation*, (National Research Council of Canada, Ottawa 1993)
10. C-M. Ma, S.B. Jiang: Phys: Med. Biol. **44** (1999)
11. C-M. Ma, E. Mok, A. Kapur, T. Pawlicki, D. Findley, S. Brain, K. Forster, A.L. Boyer: Med. Phys. **26**, 10 (1999)
12. C-M. Ma, P. Reckwerdt, M. Holmes, D.W.O. Rogers, B. Geiser, B. Walters: *BEAM Users Manual*, (National Research Council of Canada, Ottawa 1988)
13. D.W.O. Rogers, B.A. Faddegon, G.X. Ding, C-M. Ma, J. We: Med. Phys. **22**, 5 (1995)
14. C-M. Ma, P. Reckwerdt, M. Holmes, D.W.O. Rogers, B. Geiser, B. Walters: *DOSXYZ Users Manual*, (National Research Council of Canada, Ottawa 1988)
15. A.F. Bielajew: *How to manage the EGS4 system*, (National Research Council of Canada, Ottawa 1993)
16. A.F. Bielajew: *Running EGS4 on different architectures*, (National Research Council of Canada, Ottawa 1993)
17. R. Arráns, S. Alonso, F. Sánchez-Doblado, J.A. Sánchez-Calzado, A. Leal, M. Perucha: Radiother. Oncol. **49** (1999)
18. E. M. Soffen, G. E. Hanks, M. A. Hunt, B. E. Epstein: Int. J. Radiat. Oncol. Biol. Phys. **24**, 3 (1992)
19. A.F. Bielajew and D.W.O. Rogers: *Variance-reduction techniques in Monte Carlo Transport of Electrons and Photons*, (Plenum Press, New York 1988)
20. A.F. Bielajew, D.W.O. Rogers: Nucl. Inst. Meth. B **18** (1987)
21. A. Leal, F. Sánchez-Doblado, M. Rincón, M. Perucha, I. Camacho, M. Sierra, R. Arráns, E. Carrasco, J.A. Sánchez-Calzado, L. Errazquin: Physica Medica. **XV**, 3 (1999)

Modelling of Multiple Scattering Distributions by Mixture Models

R. Frühwirth and M. Regler

Institute of High Energy Physics of the Austrian Academy of Sciences, Nikolsdorfer Gasse 18, A-1050 Wien, Austria

Abstract. We present a new mixture model for the precise modelling of multiple scattering in thin to medium layers. The model is a mixture of a Gaussian core and single-scattering tails. Its parameters are estimated by minimizing the Kullback-Leibler divergence from the true density. We present the results and derive a simple parametrisation for computing the mixture for scatterers of different thickness and material.

1 Introduction

It is well known that the multiple scattering (MS) distribution of heavy particles (muons, pions, protons) has long tails that are normally neglected, both in simulation and in track reconstruction. For instance, the popular formula of Highland [1] and the improved formula of Lynch and Dahl [2] give the width of the Gaussian core, but no information on the tails. In a recent report [3] a mixture model of MS has been presented that models both the core and the tails by Gaussians. This model has been developed mainly for advanced track reconstruction methods [4]. In thin layers it is possible to obtain a considerably better approximation by using a mixture model with a Gaussian core and non-Gaussian tails, the tails of the MS distribution being mainly due to single scattering events with large deflection angles. The approximation of the MS tails by the single scattering tails is therefore natural as long as the probability of two or more large single scatters is small. We will show that this approximation is excellent in thin layers. In addition, simulation from the single scattering density is very fast, making the new model eminently suitable for simulation purposes.

2 The Mixture Model

The probability density function of the projected MS angle x is approximated by a mixture of the following form:

$$f(x) = (1 - \varepsilon) \cdot \varphi(x; 0, \sigma^2) + \varepsilon \cdot g(x; a, b) \quad (1)$$

where $\varphi(x; 0, \sigma^2)$ is the Gaussian density with mean 0 and variance σ^2 , and $g(x; a, b)$ is the density of the projected single scattering angle [3]:

$$g(x) = \frac{a^2}{\pi} \left[\frac{\sqrt{b^2 - x^2}}{(b^2 + a^2)(x^2 + a^2)} + \frac{\arccos(\sqrt{x^2 + a^2}/\sqrt{b^2 + a^2})}{(x^2 + a^2)^{3/2}} \right] \quad (2)$$

a and b being the minimum and the maximum scattering angle, respectively [5].

3 Estimation of Mixture Parameters

The mixture model (1) has four free parameters $(a, b, \varepsilon, \sigma^2)$. If the estimation is carried out in standard measure one of the parameters can immediately be eliminated. Using the fact that the total variance is equal to 1, the core variance σ^2 can be expressed in terms of a , b , and ε :

$$\sigma^2 = \frac{1 - \varepsilon a^2 [\ln(b/a) - 0.5]}{1 - \varepsilon} \quad (3)$$

The parameter b can be fixed *a priori* by using the observation that up to large N the effective range of the MS distribution in standard measure is proportional to $1/\sqrt{N}$, where N is the number of scatters. A simple and precise parametrisation of b in standard measure is given by [3]

$$b = \frac{\varrho}{\sqrt{N(\ln \varrho - 0.5)}}, \quad \text{with} \quad \varrho = \frac{b}{a} \approx \frac{41000}{Z^{2/3}} \quad (4)$$

We have estimated the remaining two free mixture parameters a and ε by three different methods:

1. Maximum-likelihood estimation
2. Minimize the Kullback-Leibler (KL) divergence

$$D(f||h) = \int f(x) \ln(f(x)/h(x)) dx$$

3. Minimize the χ^2 -distance

$$D_{\chi^2}(f, h) = \int [f(x) - h(x)]^2 / h(x) dx$$

Here f denotes the mixture density (1), and h denotes the true MS density as obtained in [3]. The maximum-likelihood estimate has been found by means of the EM algorithm; numerical minimization of $D(f||h)$ and $D_{\chi^2}(f, h)$ has been carried out via the Newton-Raphson algorithm. A detailed description can be found in [3].

The quality of the approximation can be assessed by various distance measures, for instance the L_1 -distance, the L_2 -distance, $D(f||h)$, and $D_{\chi^2}(f, h)$. It turns out that in all cases methods 2 and 3 give virtually the same result, whereas method 1 is significantly worse. In order to ensure compatibility with the results in [3] the final estimate is the one from method 2.

Figure 1 shows the KL divergence between the approximating mixture (1) and the true density (open triangles), for (a) carbon, (b) silicon, and (c) iron. For comparison the figure also shows the KL divergence of a purely Gaussian mixture as obtained in [3] (open circles). The new mixture model (1) is superior up to $N \approx 1.25 \cdot 10^5$ in carbon, $N \approx 4.3 \cdot 10^4$ in silicon, and $N \approx 1.9 \cdot 10^4$ in iron. In terms of the radiation length X_0 this corresponds to about 14.4% in carbon, 7.3% in silicon, and 4.4% in iron, or approximately $0.6X_0/Z^{0.8}$. For thicker layers, the purely Gaussian mixture is to be preferred.

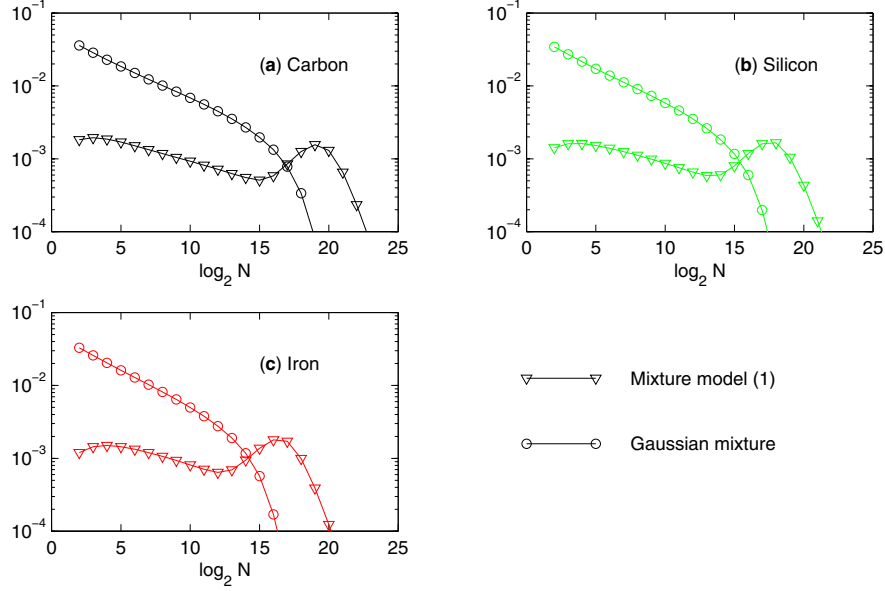


Fig. 1. KL divergence between approximating mixture and true density, for (a) carbon, (b) silicon, and (c) iron. The open triangles correspond to the new model presented here, the open circles correspond to the purely Gaussian mixture of [3]

4 Results of the Approximation

Figure 2 shows the parameters of the approximating mixture with the smallest KL divergence from the true distribution, for carbon, silicon and iron. Although the picture is similar for the three materials, a slight dependence of the core variance σ^2 and of the tail parameter a on Z is obvious.

A material-independent representation in the required range can be achieved if the core variance σ^2 and the tail parameter a are considered as functions of $Z^{0.1} \log_2 N$. A simple parametrisation of σ^2 and a in terms of $Z^{0.1} \log_2 N$ can be obtained by fitting polynomials of order 2 and 4, respectively. The coefficients of the polynomials can be found in Tab. 1. The fitted curves are also shown in Fig. 2(a,b). The tail weight can be computed from σ^2 and a :

$$\varepsilon = \frac{1 - \sigma^2}{a^2 [\ln(b/a) - 0.5] - \sigma^2} \quad (5)$$

The corresponding curves are shown in Fig. 2(c). They exhibit an excellent agreement with the estimated mixture parameters.

If the parametrisation is to be of practical use, the average number N of scattering processes has to be related to the material and to the thickness of the scatterer. Assume that d is the thickness of the scatterer and X_0 is its radiation

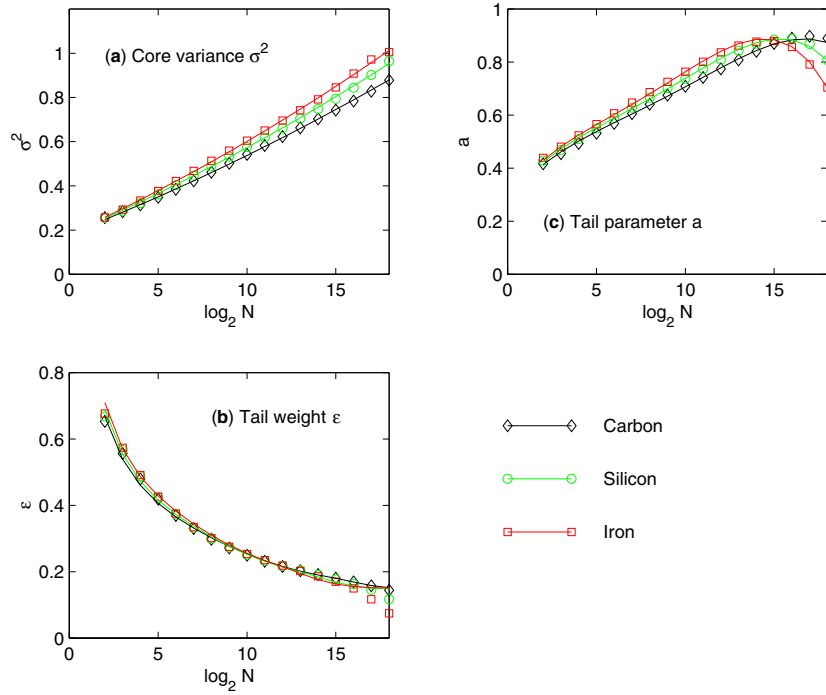


Fig. 2. Parameters of the approximating mixture for carbon (diamonds), silicon (circles), and iron (squares): (a) core variance σ^2 , (b) tail parameter a , (c) tail weight ϵ . The fitted polynomials (solid lines) are superimposed on the estimated mixture parameters

length, where d and X_0 are both given in g/cm^2 . Let $d' = d/X_0$. Then

$$N(d) = \frac{d N_0}{X_0} = d' N_0 \approx \frac{d' \cdot 1.587\text{E}7 \cdot Z^{1/3}}{\beta^2 (Z + 1) \ln(287 Z^{-1/2})} \approx \frac{d \cdot 2.215\text{E}4 \cdot Z^{4/3}}{\beta^2 A} \quad (6)$$

where N_0 is the average number of scattering processes per radiation length, A is the atomic mass number of the material and $\beta = v/c$ is related to the velocity of the scattered particle [3].

We recall that the approximating mixtures have been obtained in standard measure. The mixture distribution has therefore to be scaled with the total

Table 1. Coefficients of the polynomial parametrisation in terms of $Z^{0.1} \log_2 N$

Parameter	c_0	c_1	c_2	c_3	c_4
σ^2	1.827E-1	2.636E-2	2.778E-4		
a	2.822E-1	6.812E-2	-6.511E-3	4.428E-4	-1.060E-5

standard deviation $\sigma_T(d)$ of the MS distribution [6]:

$$\sigma_T(d) = \frac{0.015}{\beta p} \sqrt{\frac{d}{X_0}} \quad (7)$$

where p is the momentum of the scattered particle in GeV/ c .

Finally, Fig. 3 illustrates the excellent quality of the mixture model by plotting the mixture densities (solid lines) and the true densities (dashed lines) for a few values of the scatterer thickness d , in standard measure. All plots are for silicon. The average number of scattering processes is 2^4 , 2^7 , 2^{10} , and 2^{13} , respectively.

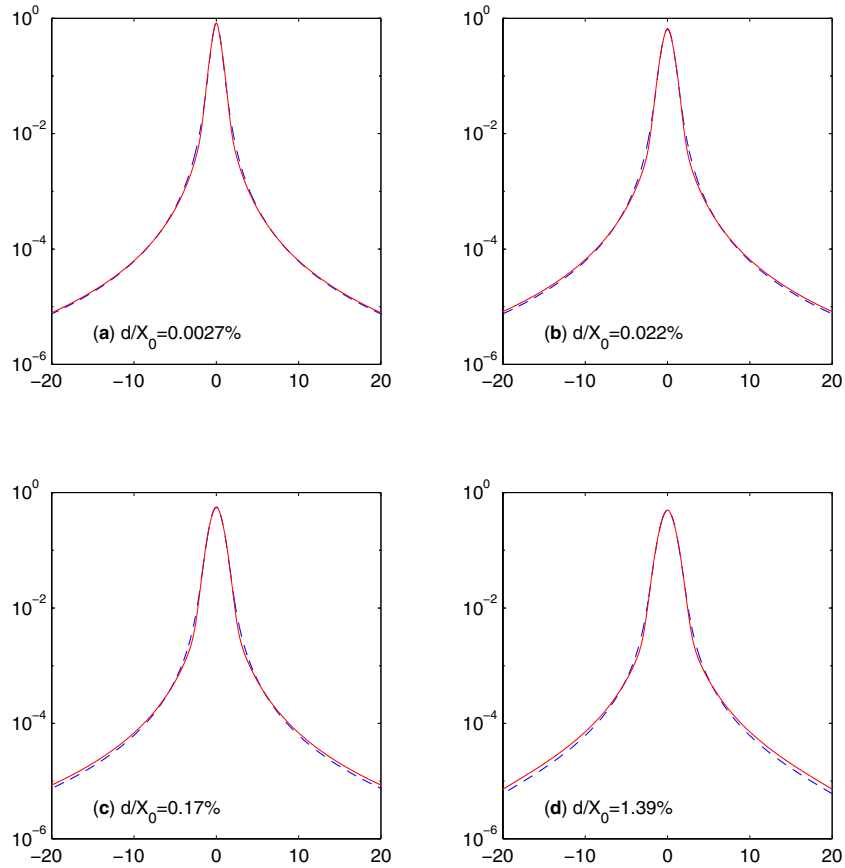


Fig. 3. Mixture densities (solid lines) and true densities (dashed lines) in standard measure, for a few values of the scatterer thickness d . The material is silicon

5 Simulation from the Mixture Model

Up to now multiple scattering in a projection has been considered. In practice one usually has to generate two scattering angles x and y in two orthogonal projections. The two scattering angles are uncorrelated but not independent, except in the Gaussian limit. In order to get the correct dependency structure one has to go back to the scattering angle θ in space. Although the distribution of $\theta = (x^2 + y^2)^{1/2}$ is not uniquely determined by the marginal densities of x and y , there is a very plausible mixture model of the distribution of θ which yields the marginal mixture densities of the desired form (1):

$$f(\theta, \varphi) = \frac{1}{2\pi} \left[(1 - \varepsilon) \cdot \frac{\theta \exp(-\theta^2/2\sigma^2)}{\sigma^2} + \varepsilon \cdot \frac{2a^2\theta}{(\theta^2 + a^2)^2} \cdot I_{[0,b]}(\theta) \right] \quad (8)$$

where the second component is the density of the single scattering angle in space [3]. It is not difficult to see that the marginal distributions of $x = \theta \cos \varphi$ and $y = \theta \sin \varphi$ have exactly the required form (1). Drawing a random number from the distribution with density (8) can be accomplished in the following way:

$$\theta = \begin{cases} \sigma \sqrt{-2 \ln u} & \text{if } v > \varepsilon \\ ab \sqrt{\frac{1-u}{u b^2 + a^2}} & \text{if } v < \varepsilon \end{cases} \quad (9)$$

where u and v are independent and uniformly distributed in $[0,1]$.

We now can summarize the generation of a pair (x,y) of multiple scattering angles in two orthogonal projections:

1. From the thickness d of the scatterer compute N , using (6)
2. Compute b , using (4)
3. Evaluate the polynomials in $Z^{0.1} \log_2 N$ for σ^2 and a , using Tab. 1
4. Compute ε from σ^2 , a and b , using (5)
5. Draw θ from (8), using (9)
6. Draw φ from a uniform distribution in $[0, 2\pi]$
7. Compute $x = \theta \cos \varphi$, $y = \theta \sin \varphi$
8. Multiply x and y by the total standard deviation $\sigma_T(d)$, using (7)

References

1. V. Highland: Nucl. Instr. and Meth. **129**, 497 (1975)
2. G. Lynch, O. Dahl: Nucl. Instr. and Meth. B **58**, 6 (1991)
3. R. Frühwirth, M. Regler: Nucl. Instr. and Meth. A (in press)
4. R. Frühwirth: Comp. Phys. Comm. **100**, 1 (1997)
5. J.D. Jackson: *Classical electrodynamics* (John Wiley & Sons, New York 1999)
6. R. Frühwirth, M. Regler *et al.*: *Data Analysis Techniques for High-Energy Physics* (Cambridge University Press, Cambridge 2000)

Radiative Transport in Multiple Scattering Media

E.J.N. Pereira¹, J.M.G. Martinho², and M.N. Berberan-Santos²

¹ Dep. de Física, Universidade do Minho, Portugal

² Centro de Química Física Molecular, IST, Portugal

Abstract. A general purpose stochastic theory for the propagation of radiation of arbitrary polarization in a medium where it can suffer reabsorption as well as multiple light scattering events is briefly presented. The Monte Carlo computation of the numerical coefficients is outlined and relative merits are discussed.

1 Introduction

Radiative transfer of energy in optically dense random media is relevant in areas as diverse as stellar atmospheres [1], plasmas and atomic vapors luminescence [2,3], terrestrial atmospheric and ocean optics [4], molecular luminescence [5], and energy (heat) transfer in the infrared [6]. Radiative transfer comprises both radiation trapping (or reabsorption) of resonance energy and photon migration by repetitive light scattering events. Both phenomena occur in photoexcited biological tissues and in strongly scattering lasing media.

This contribution presents a proposal of computation of the dynamics of radiation transport of trapped resonance radiation with simultaneous multiple scattering of both trapped and nontrapped radiation. It generalizes a previous developed stochastic description of time-dependent photon migration developed by the authors and includes a Monte-Carlo computation proposal of the parameters using Stokes polarization parameters and Mueller calculus.

The stochastic theory for arbitrary polarized radiation propagation in a medium with simultaneous reabsorption and light scattering is briefly presented in the following section with particular emphasis on the Stokes parameters description of the radiation field. The theory for multiple light scattering is given essentially as a product of standard Mueller matrices for single light scattering. In real cases, these matrices can be difficult to estimate but the general theory remains unchanged. Finally, a Monte Carlo simulation procedure is proposed to compute the numerical coefficients of the theory by recording the Stokes vector for a mimic of individual classical photon trajectories inside a given sample cell. The merits of the proposal are discussed in the end.

2 Stochastic Formulation

In the case of the *classical trapping problem*, it is possible to ignore photon propagation times and nonlinear effects [2]. In this case, it can be shown that

the spatial and temporal dependencies of the dynamics of the photon migration can be factored into a product of \mathbf{f}_n^Ω and $g_n(t)$ where the first factor accounts for the spatial details of the photon migration [7]. The remaining factor $g_n(t) = \Gamma \frac{(\Gamma t)^{n-1}}{(n-1)!} e^{-\Gamma t}$ gives the probability density for radiation emission from each one of the n^{th} generation of excited species [5] and it is shown in Fig. 1 as function of generation number. Γ is the emission rate constant. Each generation of excited species is created by the reabsorption of the radiation emitted by species belonging to the previous generation: second generation molecules result from the reabsorption of radiation emitted by first generation species, third generation species are created by trapping of the emission of second generation, etc. The separation of the spatial details from the temporal evolution of the radiation emitted by each generation ensemble represents a considerable economy in computation time. It also allows to account for the complex influence of radiation trapping and multiple light scattering in the spatial factor f_n^Ω alone.

The proposal uses Stokes polarization parameters and Mueller calculus [8] to give a stochastic theory for radiation propagation of arbitrary polarization state under the simultaneous influence of multiple reabsorption and light scattering events. The Stokes polarization parameters for the emitted radiation in a given solid angle Ω from the experimental sample is formulated as [9]:

$$\mathbf{S}(\nu, t) = \sum_{n=1}^{+\infty} \mathbf{f}_n^\Omega g_n(t) \quad (1)$$

The sum automatically incorporates the contribution of all the generations of excited species at a given time t and detection solid angle. The \mathbf{f}_n^Ω have the same dimensions as the standard column array of Stokes polarization parameters and take into account the spatial details of photon migration under the simultaneous influence of multiple trapping. These factors are defined as [9]:

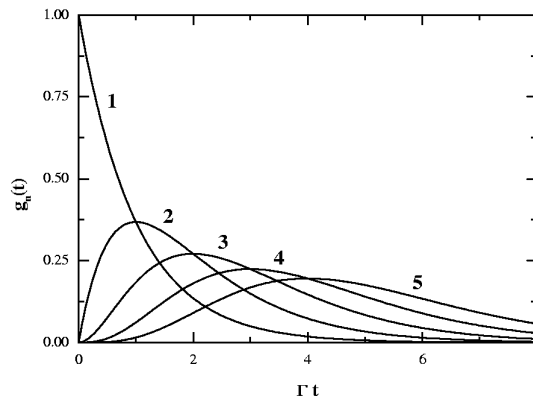


Fig. 1. Probability density for the time distribution of the emission from the n^{th} generation of excited species

$$\begin{aligned}
\mathbf{f}_n^\Omega(\nu) = & \int_\Omega \int_V \left\{ \int_0^\infty \cdots \int_0^\infty \int_0^\infty \int_V \cdots \int_V \int_V \mathbf{f}_{bn}(\hat{\mathbf{k}}_{n-1}, \nu_{n-1}; \hat{\mathbf{k}}_b, \nu) \right. \\
& \Phi_0 \mathbf{f}_{n-1}(\hat{\mathbf{k}}_{n-2}, \nu_{n-2}; \hat{\mathbf{k}}_{n-1}, \nu_{n-1}) \\
& \Phi_0 \mathbf{f}_{n-2}(\hat{\mathbf{k}}_{n-3}, \nu_{n-3}; \hat{\mathbf{k}}_{n-2}, \nu_{n-2}) \cdots \Phi_0 \mathbf{f}_2(\hat{\mathbf{k}}_1, \nu_1; \hat{\mathbf{k}}_2, \nu_2) \\
& \left. \Phi_0 \mathbf{f}_1(\hat{\mathbf{k}}_p, \nu_p; \hat{\mathbf{k}}_1, \nu_1) d\mathbf{r}_{n-1} \cdots d\mathbf{r}_2 d\mathbf{r}_1 d\nu_{n-1} \cdots d\nu_2 d\nu_1 \right\} d\mathbf{r}_n d\mathbf{r}_b
\end{aligned} \tag{2}$$

where the generic terms $\mathbf{f}_n(\hat{\mathbf{k}}_{n-1}, \nu_{n-1}; \hat{\mathbf{k}}_n, \nu_n)$ are the excitation transition probabilities between emission and reabsorption coordinates. These transition probabilities are defined as functions of the propagation directions $\hat{\mathbf{k}}_n$ and optical frequencies ν_n . The photon migration is described as a stochastic process in physical space and frequency space coordinates – each photon in the overall sequence is characterized by coordinates \mathbf{r}_n and ν_n where the n stands for the number of previous absorptions in the media. $\hat{\mathbf{k}}_b$ represents the direction of the radiation escaping from the experimental volume at a given boundary coordinate \mathbf{r}_b and arbitrary frequency ν . The last two integrals in the previous equation take into account the details of the radiation that is emitted into the solid angle for detection, summed up over the entire volume of the experimental sample. In the case of a media in which there is only trapping of the emitted radiation, the \mathbf{f}_n factors are given by:

$$\begin{aligned}
\mathbf{f}_n(\hat{\mathbf{k}}_{n-1}, \nu_{n-1}; \hat{\mathbf{k}}_n, \nu_n) = \\
= \frac{\Phi(\nu_n|\nu_{n-1}) \mathbf{M}_e(\hat{\mathbf{k}}_{n-1}; \hat{\mathbf{k}}_n)}{4\pi |\mathbf{r}_{n+1} - \mathbf{r}_n|^2} k(\nu_n) e^{-k(\nu_n) |\mathbf{r}_{n+1} - \mathbf{r}_n|}
\end{aligned} \tag{3}$$

where $\Phi(\nu_n|\nu_{n-1})$ is the conditional emission spectra (emission probability at frequency ν_n given that the frequency of the radiation absorbed to create the emitting species was ν_{n-1}) and $\mathbf{M}_e(\hat{\mathbf{k}}_{n-1}; \hat{\mathbf{k}}_n)$ is the Mueller matrix for the process of absorption followed by reemission (gives the Stokes parameters after emission as function of the corresponding Stokes parameters of the absorbed radiation for the particular directions $\hat{\mathbf{k}}_{n-1}$ and $\hat{\mathbf{k}}_n$). The exponential term in the previous equation accounts for the Beer-Lambert attenuation of radiation between emission and reabsorption with an absorption coefficient $k(\nu_n)$.

In the case of allowing for light scattering between the emission and reabsorption coordinates, the previous equation should be modified to [9]:

$$\begin{aligned}
& \mathbf{f}_{S,n}(\widehat{\mathbf{k}}_{n-1}, \nu_{n-1}; \widehat{\mathbf{k}}_n, \nu_n) = \\
& = \frac{\Phi(\nu_n | \nu_{n-1}) \mathbf{M}_e(\widehat{\mathbf{k}}_{n-1}; \widehat{\mathbf{k}}_n)}{4\pi |\mathbf{r}_{n+1} - \mathbf{r}_n|^2} k(\nu_n) e^{-(k(\nu_n) + \beta) |\mathbf{r}_{n+1} - \mathbf{r}_n|} + \\
& \sum_{m=1}^{\infty} \left\{ \underbrace{\int_V \dots \int_V}_{m \times} \frac{\mathbf{M}_S(\widehat{\mathbf{k}}'_m; \widehat{\mathbf{k}}_{n+1})}{4\pi |\mathbf{r}_{n+1} - \mathbf{r}'_m|^2} k(\nu_n) e^{-(k(\nu_n) + \beta) |\mathbf{r}_{n+1} - \mathbf{r}'_m|} \times \right. \\
& \quad \left\{ \prod_{k=m}^2 \frac{\mathbf{M}_S(\widehat{\mathbf{k}}'_{k-1}; \widehat{\mathbf{k}}'_k)}{4\pi |\mathbf{r}'_k - \mathbf{r}'_{k-1}|^2} \beta e^{-(k(\nu_n) + \beta) |\mathbf{r}'_k - \mathbf{r}'_{k-1}|} \right\} \\
& \quad \left. \frac{\Phi(\nu_n | \nu_{n-1}) \mathbf{M}_e(\widehat{\mathbf{k}}_{n-1}; \widehat{\mathbf{k}}'_1)}{4\pi |\mathbf{r}'_1 - \mathbf{r}_n|^2} \beta e^{-(k(\nu_n) + \beta) |\mathbf{r}'_1 - \mathbf{r}_n|} \underbrace{dV \dots dV}_{m \times} \right\} \quad (4)
\end{aligned}$$

β is now the attenuation coefficient due to light scattering alone and the first term of the right hand side has the same meaning as (3). The remaining terms account for the influence of a variable m number of light scattering events between absorption and reabsorption coordinates. Primed and k indexed quantities are associated with light scattering events and unprimed and n indexed quantities quantify the emitted/reabsorbed radiation propagation direction and frequencies. Equation (4) assumes isotropic medium (non changing Stokes polarization parameters apart from the obvious intensity attenuation as a result of radiation propagation in the medium) and frequency coherent light scattering events.

The corresponding terms for the first generation of excited molecules is slightly modified from the previous two equations by right multiplying by the Stokes polarization vector for the external exciting radiation [9]. The previous equations allow a stochastic formulation of the propagation of radiation of arbitrary polarization in media with concurrent trapping and light scattering. For any particular medium, it is necessary to characterize the angular distributions of both the reemission and the light scattering processes using standard Mueller matrices. In this respect, the theory is particularly suited for the difficult case of multiple scattering or turbid media because it is formulated from the Mueller matrix for the single scattering case. This matrix can be always estimated with a sufficient degree of accuracy either from theoretical data (in the most simple cases) or from experimental measurements (made in single scattering conditions). For instance, for the well known case of Rayleigh scattering, standard Mueller calculus procedures [8,10] allow the definition of the single scattering angular phase function as [9] :

$$g_s(\widehat{\mathbf{k}}', \widehat{\mathbf{k}}) = \frac{3}{4} \left[(1 + \cos^2 \theta) - \sin^2 \theta \left(\cos(2\varphi) \frac{S'_1}{S'_0} + \sin(2\varphi) \frac{S'_2}{S'_0} \right) \right] \quad (5)$$

for an arbitrary polarization radiation initially propagating in the z axis direction with Stokes parameters $\mathbf{S}'(S'_0, S'_1, S'_2, S'_3)$. θ and φ are the standard spherical angles and primed quantities now stand for quantities before interaction, primed after. Fig. 2 shows this function for the two special cases of scattering of linear x -polarized $\mathbf{S}'(1, 1, 0, 0)$ and unpolarized $\mathbf{S}'(1, 0, 0, 0)$ radiation. For the case of reabsorption followed by reemission, two realistic angular phase functions include isotropic emission $g_e(\hat{\mathbf{k}}', \hat{\mathbf{k}}) = 1$ and dipolar like absorption/reemission in a media with frozen rotation $g_e(\hat{\mathbf{k}}', \hat{\mathbf{k}}) = \frac{3}{5} [2 - \sin^2 \theta \cos^2 \varphi]$.

3 Monte Carlo Simulation Procedure

It is proposed to compute the numerical coefficients of the Stokes column array in (1) by a Monte Carlo simulation procedure that mimics the photons classical trajectories inside a realistic sample cell. This was previously tested for the particular case of radiation trapping alone without the possibility of light scattering [11].

The Monte Carlo simulation should consider each individual event at a time and compute photon propagation directions after either reemission or light scattering from the corresponding angular phase functions $g(\hat{\mathbf{k}}', \hat{\mathbf{k}})$. In either case, $g(\hat{\mathbf{k}}', \hat{\mathbf{k}})/4\pi$ is the probability density for photons redirection from $\hat{\mathbf{k}}'$ to $\hat{\mathbf{k}}$. After the random generation of the $\hat{\mathbf{k}}$ direction, the Stokes parameters of the radiation should be computed from the corresponding Mueller matrices and Stokes parameters before interaction defined in the direction $\hat{\mathbf{k}}'$. For each generation n , it is further necessary to compute each photon trajectory contribution for the

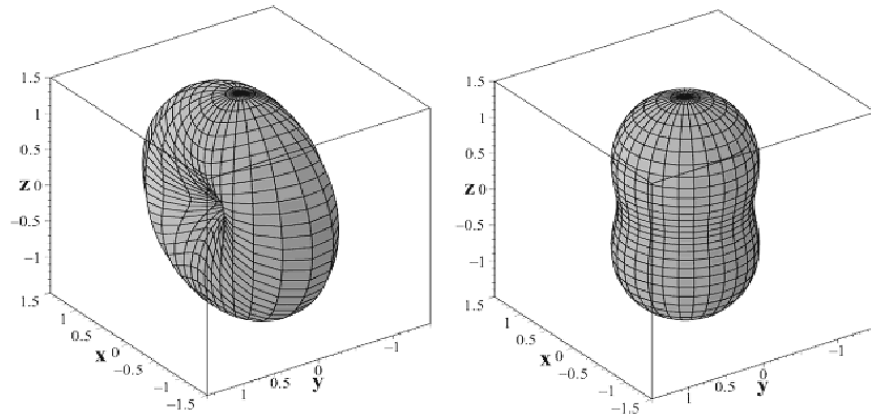


Fig. 2. Angular phase function for Rayleigh scattering of radiation initially propagating along z direction: linear x -polarized (left) or nonpolarized (right)

detected radiation macroscopic Stokes vector in the chosen laboratory reference frame according to (1). The column array thus obtained will contain not only the intensity decay but also the polarization decay and this will allow (assumed linear regime) the theoretical prediction of the time-resolved and steady-state intensity and polarization spectra.

The formulation differs from previous treatments of multiple light scattering because no use is made of the radiative transfer equation or its diffusion approximation in random media. The innovative aspects of the proposed work include: (i) the description of the time-resolved intensity of radiation for simultaneous trapping and light scattering in optically dense media, (ii) the inclusion of multiple scattering, (iii) consideration of the joint influence of trapping and scattering on the polarization, (iv) a Monte-Carlo general purpose algorithm valuable in practical applications. This last aspect is particularly important since most of the work done in the radiation trapping literature is focused on ideal 1D geometries with the same qualitative behavior of the real geometries but with important quantitative differences. The Monte-Carlo procedure is the same for any geometry, however complex, and for any single scattering angular phase function (including the ill behaved but important case of strongly forward scattering in biological tissues and atmospheric turbid media).

References

1. D. Mihalas: *Stellar Atmospheres*, 2nd edn. (W.H. Freeman, San Francisco 1978)
2. A.F. Molisch, B.P. Oehry: *Radiation Trapping in Atomic Vapours* (Oxford University Press, Oxford 1998)
3. J.M. Proud, L.H. Luessen, editors: *Radiative Processes in Discharge Plasmas*, NATO ASI Series, Series B Physics (Plenum Press, New York 1986)
4. G.E. Thomas, K. Stamnes: *Radiative Transfer in the Atmosphere and Ocean* (Cambridge University Press, Cambridge 1999)
5. M.N. Berberan-Santos, E.J.N. Pereira, J.M.G. Martinho: 'Dynamics of Radiative Transport'. In: *Resonance Energy Transfer*, ed. by D.L. Andrews, A.A. Demidov (John Wiley & Sons, Chichester 1999) pp. 108–149
6. M.F. Modest: *Radiative Heat Transfer* (McGraw-Hill, New York 1993)
7. M.N. Berberan-Santos, E.J.N. Pereira, J.M.G. Martinho: *J. Chem. Phys.* **103**, 3022 (1995)
8. E. Collett: *Polarized Light, Fundamentals and Applications* (Marcel Dekker, New York 1993)
9. E.J.N. Pereira, M.N. Berberan-Santos, J.M.G. Martinho: submitted for publication
10. W.A. Shurcliff: *Polarized Light, Production and Use* (Harvard University Press, Cambridge Mass. 1962)
11. E.J.N. Pereira, M.N. Berberan-Santos, J.M.G. Martinho: *J. Chem. Phys.* **104**, 8950 (1996); E.J.N. Pereira, M.N. Berberan-Santos, A. Fedorov, M. Vincent, J. Gallay, J.M.G. Martinho: *J. Chem. Phys.* **110**, 1600 (1999)

Markov Chain Monte Carlo Methods in Radiotherapy Treatment Planning

R.P. Hugtenburg

U. Hospital Trust, Birmingham, B15 2TH, United Kingdom

1 Introduction

In radiotherapy, it is recommended that a dosimetric precision of 3%(s.d.) and 3 mm is necessary to achieve local tumour control. Standardised measurements and theoretical extrapolation must be used in combination for the highest dosimetric precision. The Markov chain method can be used to incorporate measured data in Monte Carlo based radiotherapy treatment planning (RTP). This paper shows that convergence to the measured data, within the target precision, is achievable. Relative output factors for blocked fields and oblique beams are shown to compare well with independent measurements according to the same criterion.

Markov chain convergence can be used to include measured data in Monte Carlo based radiotherapy treatment planning (RTP) [1–3]. Conventional RTP uses dose related measurements, performed under standardised conditions, as a first approximation to the dose in the patient. Conventional planning algorithms are based on simplistic representations of the radiation transport and their formulae can be inverted relatively easily. This process of inversion enables the measured data to form the bounding conditions for the distribution of dose in the more complex circumstance of the patient treatment.

Monte Carlo offers a considerable improvement in the quality of the radiation transport and is favoured as a next step in the process of improvement of RTP. However, inverse solutions of Monte Carlo based radiation transport problems are difficult given the dimensionality of the problem and resolutions required. Workers have tended towards highly detailed simulations of the therapeutic linear accelerator to achieve consistency with measured data. Some input parameters, such as the electron potential of the accelerator, are not known, *a priori*, to adequate precision and inevitably a degree of iteration is required. The CPU time required to simulate a therapeutic linear accelerator in sufficient detail to perform MC RTP is currently months [4]. The storage requirements for the phase-space data generated is Gigabytes. This paper proposes that a less detailed simulation of the accelerator hardware and smaller phase-space files will be adequate for RTP if measured data is incorporated into the calculation.

2 The Markov Chain Monte Carlo Method

Markov chain Monte Carlo is a method for mixing prior and posterior information in the Bayesian sense [5]. In the case of RTP, one has *a priori* information

about the linear accelerator hardware (or other radiation source) and *a posteriori* information from sets of standardised measurements that are performed on the source. Particles are sampled from a prior domain and expectations of the dose or similar quantities are formed with large numbers of particle histories. The quality of each new expectation compared to the measured data is considered for each sample and the contribution may be accepted or rejected. The sequence of acceptable contributions forms a Markov chain which can be shown to converge to the measured distribution in a finite number of steps. Source particles, deemed to belong to the measured distribution, can be simulated anew or correlated within a model that describes the patient treatment.

Hastings [6] shows that a Markov chain that transits from state X to state Y according to the probability,

$$\alpha(X, Y) = \min \left\{ 1, \frac{\pi(Y) q(Y, X)}{\pi(X) q(X, Y)} \right\}, \quad (1)$$

where $\pi(X)$ is the probability of state X in the distribution π and $q(X, Y)$ is the probability of the transition from X to Y , converges in the limit to the distribution π . In particular, $\int \pi d\mathcal{R}^d = 1$ where \mathcal{R}^d represents the, potentially d -variate, domain. When computing (1) for each iteration, it is possible to take advantage of massive cancellation of the nominator and denominator generating relative probabilities of single events close to unity.

Tierney [7] demonstrates two special classes of Markov chain. An independence sampler is where $q(X, Y) = q(Y)$. This chain has predictable convergence properties because if $q(Y) > 0$ for all \mathcal{R}^d then all of π will eventually be sampled. A simple and useful form of the, so called, random walk sampler chooses a transition such that $q(X, Y) = q(Y - X)$. The transition is independent of the location of the states so this chain also has good visitation properties. The Monte Carlo method used for the radiation transport problem is an example of a random walk chain where the n th expectation, $E_n = Y$, is determined from a running average, $\sum_i^n \varepsilon_i / i$, where ε_i is the distribution of energy absorbed during the i th history.

A transition probability based on the variance, σ^2 , has been used here. σ^2 decreases at a rate $1/n$ sharing this and other similarities with fast simulated annealing [8]. The following, much simplified, expression for the transition probability, proves to be very powerful random walk sampler such as described above.

$$\begin{aligned} \alpha(E_n) &= 1, \text{ if } \frac{\Delta^2}{\sigma^2} < 1 \text{ or } n = 1, \\ &= 0, \text{ otherwise,} \\ \text{where, } \Delta^2 &= (E_n/n - \pi)^2, \\ \text{and, } \sigma^2 &= \frac{n-1}{n^2} ((E^2)_n/n - (E_n)^2/n^2). \end{aligned} \quad (2)$$

If π is multivariate it is usual to multiply the probabilities as if independent. This independence is assured as E tend towards π . In the above formulation the exponential function has been dropped, the nominator and denominator are

formed into separate sums which help to exclude effects due to high variance when the algorithm is starting. It is usual to have a burn-in period where the earliest samples are ignored for the same reason.

Independent sampling of either Y or $Y - X$ has a draw-back if π cannot be sampled directly and is computed as a function of samples from a further distribution, ψ . This is the case with the radiation transport problem where π is a function of the phase space distribution of the incident radiation. If $\psi(Y)$ is sampled independently of $\psi(X)$ then the distribution that π returns is biased in ψ . Random walk sampling on ψ reduces biasing as the step size decreases but suffers from poor guarantees of convergence if ψ is multimodal. Increasing the number of draws/histories per sample has also proved to reduce bias [9]. As an independent sampler of ψ , this method has preferable convergence guarantees but is inefficient if ψ is highly peaked. Repetitious sampling and the random walk sampler are closely related and may be used in combination to ensure high acceptance rates and good coverage of the domain.

3 Implementation

A phase space file of 10^5 incident particles has been generated from a detailed Monte Carlo model of the accelerator beam shaping and collimating hardware. This data has been generated for the 6 MeV electron modality of a Varian 2100C linear accelerator with a $10 \times 10 \text{ cm}^2$ applicator.

This phase space file gives inadequate information about the spatial distribution of dose for conventional Monte Carlo. Resampling the same data set will tend to create spikes at the entry points of the particle set and these will be visible in off-axis profiles and isodose distributions. To ensure a more even and extensive coverage of the phase space domain, the particles have been perturbed in energy, angle and position of incidence by a Gaussian function. The spread (FWHM) is approximately 10% of the domain, the standard deviations are given in Tab. 3.

Table 1. Standard deviation of Gaussian modifications to incident energy, ε , trajectory, θ and ϕ , and position x and y of particles extracted from the phase space file

Parameter	std. dev.
Energy ε	$\varepsilon/20$
Trajectory ϕ	$\pi/20$
θ	$\pi/10$
Position x, y	1 cm

Inevitably, smoothing causes a reduction in resolution, in particular, in the quality of the beam penumbra (see Fig. 1b). However, if a Markov chain is used to force the calculation to adhere to the measured profile enabling then the resolution dictated by the measurements can be maintained.

The measurement data consists of a percentage depth dose (PDD) and off-axis ratios (OAR) at several depths (0.5 cm, 1.0 cm and 2.0 cm) with the phantom surface at 100 cm from the source. This is a typical set of measurements used for the commissioning of an electron energy and applicator cone combination. The data has been extended to a 3D array according to the formula $\pi(x, y, z) = \text{PDD}(z) \cdot \text{OAR}(x) \cdot \text{OAR}(y)$, with 2 mm graduations in the x and y directions and 1 mm graduations in the z direction.

Samples, ψ_n , are taken from the phase space distribution and radiation transport through a regular water phantom to compute E_n is performed using EGS4 [10] implemented on a Sparc Ultra II. Each new set of expectations, E_n , in this case dose, determined from the transport, are compared to π and a contribution accepted if the conditions in (3) are met.

The sampled particle is transported multiple times. The number of histories is increased in proportion to the iteration number (by 1 every 10000 iterations). The Gaussian modification to the spatial origin of the particle occurs within the iterative loop but energy and angle of incidence are sampled only once per iteration.

Concurrent computation of various related quantities has been performed. Relative output measures for an obliquely incident beam and for a $2 \times 2 \text{ cm}^2$ field have been computed. Markov chain Monte Carlo has been used in this manner to compute a radiotherapy treatment plan for a patient [2]. Oblique beams have been used to previously demonstrate the predictive capability of the algorithm beyond normal commissioned data [3]. A typical role for a Monte Carlo based electron planning is to predict output factors [11]. In full detail, this calculation should involve the effect of the cut-out. Here, the cut-out is treated as a perfect shield by ignoring those particles emanating outside the fields definition. Transport of particles in the cut-out is feasible but time consuming.

4 Results and Discussion

8×10^5 iterations were performed in 8 batches with approximately 3.2×10^8 particles transported. The first batch is regarded as a burn-in and does not contribute to the calculation of the dose array. The overall rejection rate is 91%. This high rejection rate is partly due to the poor statistical quality of the phase space file. 10^5 particles will lead to statistical uncertainty in a $2 \times 2 \text{ mm}^2$ isodose profile of at best 15% (s.d.). To compensate, a relatively broad Gaussian is required and, consequently, many of the phase space samples produce dose distributions that diverge from π .

A further source of inefficiency is the updating of the 62500 element array of the dose scored at each iteration. The array must be added to the total dose and zeroed at every iteration. An alternative, amongst several optimisation options here, would be to store the energy deposition events in a stack.

Figure 1 demonstrates the quality of the Markov chain MC convergence to the measured distributions. The percentage depth dose is well matched to the measured data and is considerably better than the conventional computation

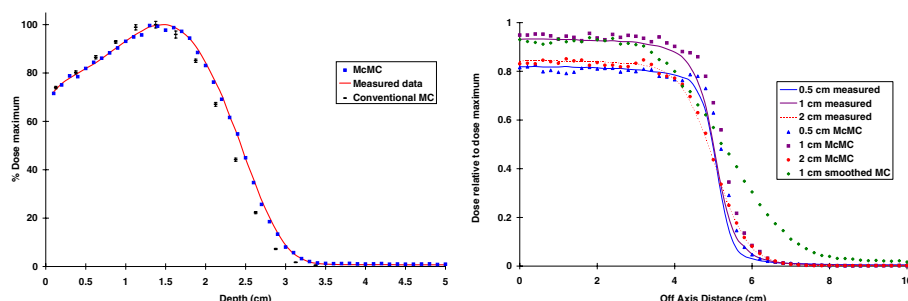


Fig. 1. Percentage dose versus depth and off-axis ratios determined by the Markov chain MC method compared to conventional Monte Carlo and measurement

using a full phase space file. The off-axis ratios show the systematic noise has not been removed completely but that, in comparison, smoothing without Markov chain sampling leads to a greatly broadened penumbra.

Plots of the convergence of the concurrently computed relative outputs at dose maximum with batch number for a 45° oblique beam and a $2 \times 2 \text{ cm}^2$ applicator demonstrate the effect of bias in ψ (Fig. 2). The determination of the relative output of the oblique beam gives a dose maximum at 7 mm of 101% in accord with previous work [3]. The computation of the relative output of the blocked field converges to 65%. This is lower than an experimental measurement (75.5%) but higher than the conventional MC calculation (51.6%).

It is important to batch and examine such extrapolated quantities for signs of convergence and plots as a function of batch number are very useful. This examination underlines the importance of testing the algorithm in a predictive capacity beyond what would normally comprise a commissioned data set.

While we have used a reduced length phase space file in this study, an alternative solution to the storage of large phase-space files is to process the data into

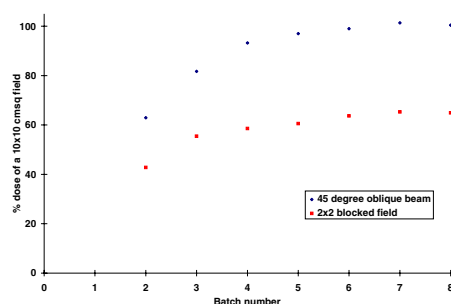


Fig. 2. Convergence of relative output factors biased by the Markov chain sampling of ϕ . Factors for a 45° oblique beam and a $2 \times 2 \text{ cm}^2$ applicator cut-out are determined at peak relative to dose maximum of a $10 \times 10 \text{ cm}^2$ field

a beam model [12]. This procedure yields a compact representation of the linear accelerator. However, many components may be required to maintain the precise correlation of the particle origin with trajectory and energy. Alternatively, a broad featured beam model would benefit from the use of a Markov chain.

One criticism of the technique might be the following. While Monte Carlo has the potential to improve upon experimental measurement, this technique compromises the accuracy of Monte Carlo to the level of experimental error. In answer, Markov chain Monte Carlo provides the formalism for incorporating knowledge of experimental uncertainty as a prior.

5 Conclusion and Acknowledgements

To achieve a dosimetric precision of the order of 3%(s.d.) and 3 mm, RTP must incorporate standardised measurements and high quality predictive calculations in combination. A method is proposed that enables smaller phase space data sets to be honed to measured data and corrected for statistical and parametric errors. The method incorporates the precision of Monte Carlo calculations with the assurance of a clinical data set.

This work demonstrates that a relatively small phase-space file contains enough information, regarding the correlation between the energy, trajectory and spatial origin of particles, to perform Monte Carlo based RTP. A Markov chain formalism enables information provided from measured beam data to be used in an Monte Carlo calculation to accurately predict dose within the patient.

Dr Frank Verhaegen is especially thanked for supplying the phase space data and measurements.

References

1. R.P. Hugtenburg. *Computational methods in radiation oncology*. PhD thesis, Department of Physics and Astronomy, University of Canterbury, Jul 1998.
2. R.P. Hugtenburg: Radiotherapy and Oncology, **51** (1999)
3. R.P. Hugtenburg, N. Thorp: Journal of Computer Simulation and Modelling in Medicine **1**, (2000)
4. C.-M. Ma, S.B. Jiang: Phys. Med. Biol., **44**, R157 (1999)
5. J. Besag, P. Green, D. Higdon, K. Mengersen: Statistical Science, **10**, 3 (1995)
6. W.K. Hastings: Biometrika, **57**, 97 (1970)
7. L. Tierney: Annals of Statistics, **22**, 1701 (1994)
8. H. Szu, R. Hartley: Phys. Lett. A, **122**, 157 (1987)
9. R.P. Hugtenburg, S. Duane, A.R. de Sautoy: 'Energy resolution of in-phantom dose and charge measurement techniques used in the reconstruction of electron spectra'. Technical report, National Physical Laboratory, 2000
10. W.R. Nelson, H. Hirayama, D.W.O. Rogers: *The EGS4 code system, rep. SLAC-265*. Stanford Linear Accelerator Center, California, 1985
11. A. Kapur, C.-M. Ma, E.C. Mok, D.O. Findley, A.L. Boyer: Phys. Med. Biol., **43**, 3479 (1998)
12. C.M. Ma, B.A. Faddegon, D.W.O. Rogers, T.R. Mackie: Med. Phys., **24**, 401 (1997)

Research Themes of Broad Transport Applicability

J. Spanier

Claremont Research Institute of Applied Mathematical Sciences, 925 North
Dartmouth Avenue, Claremont Graduate University, Claremont, CA 91711, USA

Abstract. This paper describes two current examples of research being undertaken at the Claremont Research Institute of Applied Mathematical Sciences. The first concerns the development of geometrically convergent Monte Carlo algorithms to estimate global solutions of transport problems. The second initiative is aimed at the solution of certain inverse problems arising in biomedical applications. Only the main ideas for both techniques are sketched here; algorithmic details and numerical examples are presented elsewhere.

1 Introduction

The Claremont Research Institute of Applied Mathematical Sciences (CRIAMS) at Claremont Graduate University is a small institute where research aimed at the development of new methods for solving practical problems is performed. Currently, emphasis is on Monte Carlo methods for transport problems; two recent and ongoing examples of such work are described in this article.

The first is an ambitious program, performed in collaboration with researchers at Los Alamos National Laboratory since 1996, with the goal of constructing adaptive, geometrically convergent algorithms for estimating global solutions of transport problems. Two distinctly different methods – correlated sampling and importance sampling – form the basis for these algorithms. Both algorithms use information generated from a block of particle histories in the k th stage to improve the sampling strategy in the $(k + 1)$ st stage. The methods have been tested extensively on a series of model transport problems of ever increasing difficulty; the most recent of these computations is presented here.

The second effort has been performed in collaboration with scientists at the Beckman Laser Institute and Medical Clinic of the University of California at Irvine since 1997. Motivated by a desire to solve a class of inverse problems arising in the field of biomedical optics, use is made of a technique based on perturbation Monte Carlo methods to produce a sensitivity analysis that can be performed outside the main Monte Carlo generation code. The resulting optimization routine characterizes the optical properties of heterogeneous tissue that best match data measured in the clinic.

2 Geometric Convergence for Global Transport Solutions

The main idea underlying our methods is easy to describe. Each random walk generated in a typical Monte Carlo simulation adds information to the total

available for analyzing results. How can this information be used to improve the estimates steadily? That is, how can the incremental information be used to achieve systematic variance reduction? Since atypical individual random walks could well add to the variance, our strategy has been to process random walks in blocks, or stages, each consisting of many histories, and to revise the sampling method only at the end of each stage. The goal then becomes to achieve

$$E_k < \lambda E_{k-1} < \lambda^k E_0, \quad 0 < \lambda < 1 \quad (1)$$

$k = \text{stage number}$

where E_k = error after the k th stage. Equation (1) is normally taken as the definition of *geometric convergence*. Of course, when pseudorandom numbers are used to generate the random walks, strict error reduction in stages can only be assured with probability 1, and this will be our objective here. An early mention of sequentially improved Monte Carlo methods (for solving matrix equations) is in [1]; see also [2].

We are interested in studying both discrete and continuous transport problems. The discrete problems serve as models for examining multigroup transport equations and the matrix formulation of such problems promotes an easier understanding of some of the key questions, such as the dependence on rate of convergence of the Neumann series for the solution. On the other hand, our principal objective – and the one that has occupied the bulk of our attention to date – has been the solution of continuous transport problems expressed as integral equations. Both kinds of problems can be expressed using a convenient operator formulation.

2.1 Operator-Theoretic Formulation

We consider the abstract transport equation

$$\phi = \mathcal{K}\phi + \sigma \quad (2)$$

in which σ represents a source term and \mathcal{K} is either a matrix or an integral operator. The solution ϕ is most commonly interpreted as a (discrete or continuous) collision density, so that σ describes the density of initial collisions and \mathcal{K} incorporates information that describes the probability of transfer from a given state in phase space to the next one. Then the iterative, or multistage procedure that we have in mind can be written quite generally as

$$\phi = \mathcal{K}^{(k)}\phi + \sigma^{(k)} \quad \sigma^{(0)} = \sigma, \quad \mathcal{K}^{(0)} = \mathcal{K}. \quad (3)$$

Thus, using (3) we reserve the right to modify both the source term and the operator kernel term after each stage of our adaptive algorithm, but our first stage only makes use of the source and kernel of the original transport equation.

The global solution of (2) is obtained by expanding each approximate solution $\hat{\phi}$ as a finite linear combination of appropriately chosen basis functions

$$\hat{\phi} = \sum_{i=1}^M a_i B_i \approx \phi = \sum_{i=1}^{\infty} a_i B_i \quad (4)$$

and determining the coefficients a_1, \dots, a_M by adaptive Monte Carlo methods. In the most general case, there will be six independent variables (representing position, direction and energy for a steady-state transport problem) and the number of coefficients needed might increase rapidly depending upon the accuracy required for the approximation (4). Accordingly, a premium is placed on selecting basis functions that represent the solution economically.

In the context of (3), the correlated sampling algorithm may be characterized by writing

$$\sigma^{(k+1)} = \sigma^{(k)} + \mathcal{K}\hat{y}^{(k)} - \hat{y}^{(k)}, \quad \sigma^{(0)} = \sigma, \quad (5)$$

where $\hat{y}^{(k)}$ is an approximate solution to (3). Then as $\sigma^{(k)} \rightarrow 0$, $\hat{y}^{(k)} \rightarrow 0$ and $x^{(k)} = \hat{y}^{(k)} + \hat{y}^{(k-1)} + \dots + \hat{y}^{(0)} \rightarrow \phi$

and convergence should be geometric with sufficient care. Thus, we subtract an approximate solution from both sides of the transport equation and solve for the difference between the approximate and exact solutions in each stage. The geometric convergence of an algorithm based on this idea was established rigorously in [3]. For details about the implementation of the sequential correlated sampling (SCS) algorithm that produces geometric convergence, the interested reader should consult [4,5]. Here we content ourselves with a summary of the advantages and disadvantages of using SCS to solve either discrete or continuous transport problems based on our experience to date.

We notice that (5) indicates that only the analog kernel \mathcal{K} is needed to implement SCS. This makes sampling the transition probabilities easiest, and is a distinct advantage. However, the reduced source, $\sigma^{(k)}$, is nonvanishing everywhere, it is small and it is of mixed sign, normally. Most of the cost of using SCS stems from the complexity of dealing with this reduced source. As well, one might anticipate that transport problems not well suited to analog treatment (e.g., shielding, or streaming types of problems) will not fare well under SCS. This will reveal itself in the need to generate very large numbers of random walks in each stage of the computation in order to reduce the error with probability one.

Partly because of these potential problems with SCS, we have developed entirely independent algorithms based on an adaptive modification of importance sampling rather than correlated sampling. In this case, use is made of an approximate importance function (as obtained from approximate solutions of an appropriate adjoint transport equation) to modify both the source and kernel of the original transport equation at each adaptive stage. In other words, (3) is used in its full generality for adaptive importance sampling (AIS) and now both $\sigma^{(k)}$ and $\mathcal{K}^{(k)}$ will change with k . Provided that an improving approximation to the exact importance function can be assured, convergence will also be geometric for this method. Proof of this fact can be found in [5], and details about implementing AIS may be found in [5,6]. In these references and in [7] one can also find descriptions of how use is made of importance sampling theory, based on the duality between the original transport equation and one adjoint to it, to modify both the source and kernel in each adaptive stage.

As for the benefits and disadvantages of AIS, the most serious objection to its use arises because sampling the non-analog, importance-modified kernel can be very costly. On the plus side, however, use of an importance function in the sampling usually results in the need for fewer random walks in each adaptive block of histories than is the case for SCS. Also, convergence rates obtained from a fixed number of histories in each stage tend to be more favorable for especially difficult (i.e., slowly convergent) problems when AIS is used than when SCS is used. Overall, however, each of the two methods is very problem-dependent and one cannot state categorically that it is always better to use one algorithm or the other. It is an interesting and challenging question to determine *a priori* criteria for deciding which method will be superior for any given transport problem.

2.2 Summary & Conclusions

1. Geometric convergence has been established, both theoretically and numerically, using both correlated and importance sampling “learning” algorithms.

2. Use of transport constraints (e.g., finding angular flux in terms of angular moments of scalar flux) greatly reduces effort, increases accuracy in many problems. Use of one method or the other then amounts to a choice between larger numbers of expansion coefficients and greater sampling complexity.

3. Use of variance reduction methods can lower computational costs per adaptive stage.

Some outstanding research questions remain:

- A. How can one effectively combine the use of both global and local basis functions?

- B. How can one best capture the behavior near singularities?

- C. What sort of error analysis is possible and useful in conjunction with these new methods?

Ongoing research at CRIAMS is addressing these issues.

3 Monte Carlo for Inverse Problem Solutions

The second area of intensive study concerns the application of perturbation Monte Carlo methods to perform sensitivity analysis on various complex systems. The general goal is to analyze the impact on overall system performance of small changes in subsystem components. The technique has been applied successfully to the solution of certain inverse problems in biomedical optics, in collaboration with scientists at the Beckman Laser Institute and Medical Clinic of the University of California at Irvine. More specifically, we have developed an algorithm whose purpose is to estimate the heterogeneous tissue optical properties (i.e., absorption and scattering characteristics) that best match clinical measurements. The technique is useful in support of laser probes as diagnostic tools for the early detection of cancer and other tissue anomalies.

3.1 Problem Description

An assumption is made that ultrasound and/or MRI imaging can be used to describe the size and shape of a tumor or suspicious mass beneath the surface of the tissue. A continuous, pulsed or intensity-modulated laser light source is launched into the tissue from above and measurements are made of the amount of light reflected or transmitted at various locations at the surface of the skin. Previously performed measurements made on unaffected tissue of the same patient are used as baseline measures of healthy tissue optical properties. Small differences in the optical response of healthy and suspicious tissues are associated with cell transformations (dysplasia) that might indicate malignancy. The challenge is to provide computational support for use of laser instruments that are exquisitely sensitive to such subtle cell transformations so that very early diagnosis and intervention can be accomplished noninvasively.

3.2 Correlated Sampling Monte Carlo

The method developed at CRIAMS to solve this problem uses correlated sampling techniques to extract information about the differential effects caused by varying optical properties in the tissue. The novelty of our approach is that a single Monte Carlo simulation plus a small amount of additional computation can be used to solve an *inverse* problem: given a tumor of known size and shape but unknown optical properties, determine its optical properties from knowledge of the reflected or transmitted laser radiation.

The correlated sampling method invoked can be traced to [9–13] and may be described in our setting as follows:

1. generate N photon histories from the laser source using the background (normal tissue) optical properties μ_a, μ_s, g (these are, respectively, the absorption coefficient, scattering coefficient and average cosine of the scattering angle);
2. estimate the reflectivity $R(t; \alpha)$ or transmissivity $T(t; \alpha)$, $t = \text{time}$, $\alpha = \text{parameter (or vector of parameters) representing absorption coefficient, } \hat{\mu}_a, \text{ and/or scattering coefficient, } \hat{\mu}_s, \text{ and/or anisotropy factor, } \hat{g} \text{ in the tumor}$;
3. perform a sensitivity analysis by reweighting the photon histories according to assumed tumor optical properties;
4. use the sensitivity results to solve the inverse problem, matching the tumor optical properties by a least squares fit to the measured data.

The key is to track a pair of tallying random variables $\xi, \hat{\xi}$:

$\xi = \text{reflectivity or transmissivity in the unperturbed problem,}$

$\hat{\xi} = \text{reflectivity or transmissivity with a perturbing region (tumor) present.}$

Then one will have

$$\int \hat{\xi} d\mu = \int \xi d\hat{\mu} \quad (6)$$

if

$$\hat{\xi} = \xi \frac{d\hat{\mu}}{d\mu}. \quad (7)$$

Defining $\hat{\xi}$ in this way serves to correlate estimates of $\int \xi d\mu, \int \hat{\xi} d\mu$. In (6), the left hand side is the expected photon reflectivity averaged over the background optics; the right hand side is the expected photon reflectivity averaged over the assumed two region optics. Here,

$$\begin{aligned}\mu &= \text{measure induced by healthy tissue optics} \\ &\quad \text{everywhere} \\ \hat{\mu} &= \text{measure induced by combined healthy tissue} \\ &\quad \text{and assumed tumor optics.}\end{aligned}$$

A single set of random walks is thus used to represent the solution of **two** (or more) problems: one, with no perturbation, another with the perturbation of known size and shape but unknown optical properties.

Specifically, if the simple estimator

$$\xi = (\mu_s/\mu_t)^k \quad (8)$$

is computed for each particle reaching a detector after k collisions, then $\hat{\xi}$ becomes

$$\hat{\xi} = (\mu_s/\mu_t)^k (w)^{j_1} \left(\frac{\hat{\mu}_t}{\mu_t}\right)^{j_2} \exp(-(\hat{\mu}_t - \mu_t)S) \quad (9)$$

if the photon reaches a detector after making k collisions, j_1 of which occur in the perturbed region, and after leaving portions of j_2 tracks in the perturbed region of total length $S = \sum_{l=1}^{j_2} s_l$, where $w = \frac{\hat{\mu}_s/\hat{\mu}_t}{\mu_s/\mu_t}$.

Using similar derivations, one can estimate rates of change of output quantities with respect to changes in input. That is, one can estimate the derivatives $\frac{\partial^k R(t;\alpha)}{\partial \alpha_1^{k_1} \dots \partial \alpha_m^{k_m}}$ or $\frac{\partial^k T(t;\alpha)}{\partial \alpha_1^{k_1} \dots \partial \alpha_m^{k_m}}$. This information can be used to determine optical properties in the perturbed region that best match clinical measurements of reflectivity.

Results we have obtained using this method suggest that perturbation Monte Carlo methods, coupled with low cost sensitivity analysis, are much faster and much more accurate than could be obtained using independent Monte Carlo simulations.

3.3 Summary & Conclusions

1. Perturbation Monte Carlo can be effective in providing sensitivity analysis based on a single, large simulation + slight additional post-processing computation.
2. Monte Carlo estimation of derivatives enables the effective solution of inverse problems.
3. Introduction of weight control, improved estimators, adaptive strategies will enhance the algorithm's performance.

4. Similar methods have great potential in other areas requiring inverse problem solutions (e.g., inverse radiation therapy planning, oil well logging).

Two key research questions can be mentioned in connection with this method:

A. Establish the theoretical and practical limits of this perturbation-based approach.

B. Verify the accuracy of confidence region predictions based on the optimization algorithm.

Work continues at CRIAMS aimed at polishing these useful techniques.

References

1. J. Halton: Proc. Comb. Phil. Soc. **58** (1962)
2. J. Halton: J. Sci. Comp. **9** (1994)
3. R. Kong, J. Spanier: 'Error Analysis of Sequential Monte Carlo Methods for Transport Problems.' In: *Monte Carlo and Quasi-Monte Carlo Methods, 1998* ed. by H. Niederreiter, J. Spanier (Springer-Verlag, New York 2000)
4. R. Kong, J. Spanier: 'Sequential Correlated Sampling Methods for Some Transport Problems.' In: *Monte Carlo and Quasi-Monte Carlo Methods, 1998* ed. by H. Niederreiter, J. Spanier (Springer-Verlag, New York 2000)
5. R. Kong: Transport Problems and Monte Carlo Methods. Ph. D. dissertation (Claremont Graduate University, Claremont 1999)
6. Y. Lai, J. Spanier: 'Adaptive Importance Sampling Algorithms for Particle Transport Problems.' In: *Monte Carlo and Quasi-Monte Carlo Methods, 1998* ed. by H. Niederreiter, J. Spanier (Springer-Verlag, New York 2000)
7. J. Spanier: 'Geometrically Convergent Learning Algorithms for Global Solutions of Transport Problems.' In: *Monte Carlo and Quasi-Monte Carlo Methods, 1998* ed. by H. Niederreiter, J. Spanier (Springer-Verlag, New York 2000)
8. J.F. Briesmeister (ed.): *MCNP - A General Monte Carlo N-Particle Transport Code, Version 4A*, Los Alamos National Laboratory Report LA-12212 (1993)
9. J. Spanier, E.M. Gelbard: *Monte Carlo Principles and Neutron Transport Problems* (Addison-Wesley 1969)
10. H. Rief: Ann. Nucl. Energy, **11** (1984)
11. H. Rief, E.M. Gelbard, R.W. Schaefer, K.S. Smith: Nucl. Sci. Eng. **92** (1986)
12. H. Rief: Adv. Nucl. Sci. and Techn. **23** (1996)
13. I. Lux, L. Koblinger: *Monte Carlo Transport Methods: Neutron and Photon Calculations*. (CRC Press Inc. USA 1991)

Response Decomposition with Monte Carlo Correlated Coupling

T. Ueki¹, J.E. Hoogenboom², and J.L. Kloosterman²

¹ Somewhere on the Earth (virtual address; taroueki85@hotmail.com)

² Delft University of Technology, Interfaculty Reactor Institute, Mekelweg 15, 2629 JB Delft, The Netherlands

1 Introduction

Particle histories that contribute to a detector response are categorized according to whether they are fully confined inside a source-detector enclosure or cross and recross the same enclosure. The contribution from the confined histories is expressed using a forward problem with the external boundary condition on the source-detector enclosure. The contribution from the crossing and recrossing histories is expressed as the surface integral at the same enclosure of the product of the directional cosine and the fluxes in the forgoing forward problem and the adjoint problem for the whole spatial domain. The former contribution can be calculated by a standard forward Monte Carlo. The latter contribution can be calculated by correlated coupling of forward and adjoint histories independently of the former contribution. We briefly describe the computational method and discuss its application to perturbation analysis for localized material changes.

2 Theory

Let V stand for the entire spatial domain of a physical source-detector problem and V_{sd} the spatial subdomain that contains both the source and detector. The spatial subdomain outside V_{sd} , $V \setminus V_{sd}$, is assumed to occupy non-zero volume. The forward transport equation for V_{sd} is

$$\underline{\Omega} \cdot \underline{\nabla} \psi_{sd}(\underline{r}, \underline{\Omega}, E) + \sigma_t(\underline{r}, E) \psi_{sd}(\underline{r}, \underline{\Omega}, E) = \int_0^{E_0} \int_{4\pi} \sigma_s(\underline{r}, \underline{\Omega}' \rightarrow \underline{\Omega}, E' \rightarrow E) \psi_{sd}(\underline{r}, \underline{\Omega}', E') d\Omega' dE' + S(\underline{r}, \underline{\Omega}, E), \quad \underline{r} \in V_{sd}, \quad (1)$$

$$\psi_{sd}(\underline{r}, \underline{\Omega}, E) = 0 \quad \text{for } \underline{r} \in \partial V_{sd} \text{ and } \underline{\Omega} \cdot \underline{n} < 0, \quad (2)$$

and the adjoint transport equation for V is

$$-\underline{\Omega} \cdot \underline{\nabla} \psi_i^*(\underline{r}, \underline{\Omega}, E) + \sigma_{i,t}(\underline{r}, E) \psi_i^*(\underline{r}, \underline{\Omega}, E) = \int_0^{E_0} \int_{4\pi} \sigma_{i,s}(\underline{r}, \underline{\Omega} \rightarrow \underline{\Omega}', E \rightarrow E') \psi_i^*(\underline{r}, \underline{\Omega}', E') d\Omega' dE' + D(\underline{r}, \underline{\Omega}, E), \quad \underline{r} \in V, \quad (3)$$

$$\psi_i^*(\underline{r}, \underline{\Omega}, E) = 0 \quad \text{for } \underline{r} \in \partial V \text{ and } \underline{\Omega} \cdot \underline{n} > 0, \quad (4)$$

$$\sigma_{i,t}(\underline{r}, E) = \begin{cases} \sigma_t(\underline{r}, E) & \text{for } \underline{r} \in V_{sd} \\ \sigma_{i,t}(\underline{r}, E) & \text{for } \underline{r} \in V \setminus V_{sd} \end{cases}, \quad (5)$$

$$\sigma_{i,s}(\underline{r}, \underline{\Omega} \rightarrow \underline{\Omega}', E \rightarrow E') = \begin{cases} \sigma_s(\underline{r}, \underline{\Omega} \rightarrow \underline{\Omega}', E \rightarrow E') & \text{for } \underline{r} \in V_{sd} \\ \sigma_{i,s}(\underline{r}, \underline{\Omega} \rightarrow \underline{\Omega}', E \rightarrow E') & \text{for } \underline{r} \in V \setminus V_{sd} \end{cases}, \quad (6)$$

where S is a source distribution, D a detector response function, $S = D = 0$ in $V \setminus V_{sd}$, and the expressions in (5) and (6) are intended to imply that $V \setminus V_{sd}$ is occupied by material i and the material inside V_{sd} remains unperturbed. The detector response R_i due to material i in $V \setminus V_{sd}$ is expressed as

$$\begin{aligned} R_i &= \int_{V_{sd}} \int_{4\pi} \int_0^{E_0} S \psi_i^* dE d\Omega dV \\ &= \int_{V_{sd}} \int_{4\pi} \int_0^{E_0} D \psi_{sd} dE d\Omega dV + \int_{\partial V_{sd}} \int_{\underline{n} \cdot \underline{\Omega} > 0} \int_0^{E_0} \underline{n} \cdot \underline{\Omega} \psi_{sd} \psi_i^* dE d\Omega dA, \end{aligned} \quad (7)$$

where dV corresponds to volume elements and dA to surface elements. The physics implied in (7) is discussed in section V in [1] based on duality and Green's functions.

As in [2,3] and references therein, coupling calculations based on surface integral have been employing an enclosure separating source and detector regions. In the expression after the second equality in (7), the first term is the contribution from histories confined inside V_{sd} and is calculated by a standard forward Monte Carlo, and the second term is the contribution from histories crossing and recrossing ∂V_{sd} and is calculated by Monte Carlo correlated coupling independently of the first term. Here, correlated coupling is a recently developed calculational tool where forward and adjoint histories are initiated in exactly opposite directions at the enclosure with no tally discretization [2,4,5]. We rewrite the second term after the second equality in (7) as

$$\int_{\partial V_{sd}} \int_{\underline{n} \cdot \underline{\Omega} > 0} \int_0^{E_0} \frac{\pi A(\partial V_{sd})}{f(E)} \psi_{sd} \psi_i^* \frac{\underline{n} \cdot \underline{\Omega} f(E)}{\pi A(\partial V_{sd})} dE d\Omega dA \quad (8)$$

where $A(\partial V_{sd})$ is the area of ∂V_{sd} and $f(E)$ is an arbitrary positive function that satisfies $\int_0^{E_0} f(E) dE = 1$. Since

$$\int_{\partial V_{sd}} \int_{\underline{n} \cdot \underline{\Omega} > 0} \int_0^{E_0} \frac{\underline{n} \cdot \underline{\Omega} f(E)}{\pi A(\partial V_{sd})} dE d\Omega dA = 1, \quad (9)$$

$\underline{n} \cdot \underline{\Omega} f(E) / [\pi A(\partial V_{sd})]$ can be interpreted as the probability density function for selecting an initial energy variable from $(0, E_0)$, initial position variables from ∂V_{sd} and initial direction variables from the unit hemisphere centered at the origin. Upon selecting $E = E_I$, $\underline{r} = \underline{r}_I$ and $\underline{\Omega} = \underline{\Omega}_I$, one can simulate the problem formally adjoint to (1)-(2) to estimate $\psi_{sd}(\underline{r}_I, \underline{\Omega}_I, E_I)$ and the problem formally

adjoint to (3)-(6) to estimate $\psi_i^*(\underline{r}_I, \underline{\Omega}_I, E_I)$. The product of the scores from the two simulations becomes a coupled score with the initial variable dependent multiplier $\pi A(\partial V_{sd})/f(E_I)$. Since the two simulations can be performed independently of each other after fixing the initial variables E_I , \underline{r}_I and $\underline{\Omega}_I$, conditional independence [6] guarantees that the conditional expectation of the coupled score is

$$\frac{\pi A(\partial V_{sd})}{f(E_I)} \psi_{sd}(\underline{r}_I, \underline{\Omega}_I, E_I) \psi_i^*(\underline{r}_I, \underline{\Omega}_I, E_I).$$

The theory of conditional expectation [7] ensures the unbiasedness of the coupled score.

Table 1. Calculation of R_1 in (7) with $i = 1$ [first group isotropic particle source; response is normalized per particle born at source; $D = 1$ inside detector and 0 otherwise; $\sigma_{t,1} = \sigma_{1,t,1} = 0.333333$, $\sigma_{s,1 \rightarrow 1} = \sigma_{1,s,1 \rightarrow 1} = 0.294$ $\sigma_{s,1 \rightarrow 2} = \sigma_{1,s,1 \rightarrow 2} = 0.0326666$, $\sigma_{s,1 \rightarrow 3} = \sigma_{1,s,1 \rightarrow 3} = 0.0$, $\sigma_{t,2} = \sigma_{1,t,2} = 0.5$, $\sigma_{s,2 \rightarrow 1} = \sigma_{1,s,2 \rightarrow 1} = 0.0$, $\sigma_{s,2 \rightarrow 2} = \sigma_{1,s,2 \rightarrow 2} = 0.441$, $\sigma_{s,2 \rightarrow 3} = \sigma_{1,s,2 \rightarrow 3} = 0.049$, $\sigma_{t,3} = \sigma_{1,t,3} = 0.666666$, $\sigma_{s,3 \rightarrow 1} = \sigma_{1,s,3 \rightarrow 1} = 0.0$, $\sigma_{s,3 \rightarrow 2} = \sigma_{1,s,3 \rightarrow 2} = 0.0$, $\sigma_{s,3 \rightarrow 3} = \sigma_{1,s,3 \rightarrow 3} = 0.653333$ (all in cm^{-1}); source and detector are sphere with 1.5 cm radius and separated by 20 cm; spatial domain is cylinder with 45 cm radius and 90 cm length and its axis coincides with the line connecting the centers of the source and detector; the distance to the nearer top or bottom cylinder surface is the same for both the source and detector; source-detector enclosure is sphere with 18 cm radius and its center coincides with the middle point between the centers of the source and detector]

standard forward for whole spatial domain , cpu time = 1265 min. [calculation of the expression after the first equality in (7)]		
1st 7.552×10^{-5} (0.0072 ^a)	2nd 6.381×10^{-5} (0.0075 ^a)	3rd 3.589×10^{-4} (0.0029 ^a)
response decomposition [the expression after the second equality in (7)]		
standard forward for confined component, cpu time = 541 min. (calculation of the first term)		
1st 7.022×10^{-5} (0.0056 ^a)	2nd 5.803×10^{-5} (0.0059 ^a)	3rd 2.719×10^{-4} (0.0026 ^a)
correlated coupling ^b for crossing and recrossing component, cpu time = 634 min. (calculation of the second term)		
1st 5.509×10^{-6} (0.0399 ^a)	2nd 5.595×10^{-6} (0.0361 ^a)	3rd 8.740×10^{-5} (0.0089 ^a)
total, cpu time = 1175 min. (sum of the first and second terms)		
1st 7.573×10^{-5} (0.0060 ^a)	2nd 6.362×10^{-5} (0.0062 ^a)	3rd 3.593×10^{-4} (0.0029 ^a)

a) fractional standard deviation

b) 4 adjoint and 40 forward histories per initial variable

Numerical results for a three energy group problem are shown in Tab. 1. It is observed that the calculation by the decomposition performs correctly. In the actual correlated coupling calculation for the second term in the expression after the second equality in (7), the adjoint simulation for $\psi_{sd}(\underline{r}_I, \underline{\Omega}_I, E_I)$ precedes the

forward simulation for $\psi_i^*(\underline{r}_I, \underline{\Omega}_I, E_I)$. If the preceding simulation yields a zero score, the succeeding simulation is skipped, the coupled score becomes zero and the next initial variables are selected. Both the simulations consist of a batch of histories because batch-average product processing generally raises the efficiency in correlated coupling [4,5].

3 Perturbation Analysis

The significance of response decomposition can be found in a new possibility of perturbation analysis [8]. The key idea is to initiate forward and adjoint histories in exactly opposite directions at the boundary between perturbed and unperturbed materials. The histories that have influence on the variation of a detector response can exclusively be simulated.

When material in $V \setminus V_{sd}$ is changed from material k to material j , the response variation, $R_j - R_k$, is expressed by (7) as

$$R_j - R_k = \int_{\partial V_{sd}} \int_{\underline{n} \cdot \underline{\Omega} > 0} \int_0^{E_0} \underline{n} \cdot \underline{\Omega} \psi_{sd}(\psi_j^* - \psi_k^*) dE d\Omega dA. \quad (10)$$

Note that the first term after the second equality in (7) is invariant with respect to perturbations in $V \setminus V_{sd}$. We rewrite the right hand side of (10) as

$$\int_{\partial V_{sd}} \int_{\underline{n} \cdot \underline{\Omega} > 0} \int_0^{E_0} \frac{\pi A(\partial V_{sd})}{f(E)} \psi_{sd}(\psi_j^* - \psi_k^*) \frac{\underline{n} \cdot \underline{\Omega} f(E)}{\pi A(\partial V_{sd})} dE d\Omega dA. \quad (11)$$

This can be calculated by the methodologies in correlated coupling for reflection control [4,5]. In (11), $\underline{n} \cdot \underline{\Omega} f(E) / [\pi A(\partial V_{sd})]$ is again interpreted as the probability density function for selecting the initial variables $E = E_I$, $\underline{r} = \underline{r}_I$ and $\underline{\Omega} = \underline{\Omega}_I$. One can then simulate the problem formally adjoint to (1)-(2) to estimate $\psi_{sd}(\underline{r}_I, \underline{\Omega}_I, E_I)$ and the two problems formally adjoint to (3)-(6) with $i = j$ and $i = k$ to estimate $\psi_j^*(\underline{r}_I, \underline{\Omega}_I, E_I)$ and $\psi_k^*(\underline{r}_I, \underline{\Omega}_I, E_I)$. The product of the score for $\psi_{sd}(\underline{r}_I, \underline{\Omega}_I, E_I)$ and the score difference for $\psi_{sd}(\underline{r}_I, \underline{\Omega}_I, E_I)$ and $\psi_k^*(\underline{r}_I, \underline{\Omega}_I, E_I)$ becomes a coupled score with the initial variable dependent tally multiplier $\pi A(\partial V_{sd}) / f(E_I)$. The three simulations are independently performed after fixing the initial variable E_I , \underline{r}_I and $\underline{\Omega}_I$.

Numerical results are shown in Tab. 2. The perturbed region therein corresponds to the inside of the cube containing material 2 or 3, which is located at the midway between the source and detector. The surface of the cube corresponds to $\partial V_{sd} \setminus \partial V$. It is observed that response variation is correctly evaluated by correlated coupling. As in the previous section, the adjoint simulation for $\psi_{sd}(\underline{r}_I, \underline{\Omega}_I, E_I)$ precedes the forward simulations for $\psi_i^*(\underline{r}_I, \underline{\Omega}_I, E_I)$ ($i = j, k$). When the adjoint simulation yields a zero score, the forward simulations are skipped, the coupled score is zero and the next initial variables are selected. These procedures are the same as the corresponding ones in the previous section. Only when the adjoint simulation yields a non zero score, the two forward simulations are performed.

Table 2. Response variation ($R_2 - R_3$), caused by the perturbation from material 3 to material 2 inside a cube between a source and detector (first group isotropic particle source; response is normalized per particle born at source; $D = 1$ inside detector and 0 otherwise; material 1 in Tab. 1 occupies the outside of the cube; $\sigma_{2,t,1} = 0.333333$, $\sigma_{2,s,1 \rightarrow 1} = 0.27$, $\sigma_{2,s,1 \rightarrow 2} = 0.03$, $\sigma_{2,s,1 \rightarrow 3} = 0.0$, $\sigma_{2,t,2} = 0.5$, $\sigma_{2,s,2 \rightarrow 1} = 0.0$, $\sigma_{2,s,2 \rightarrow 2} = 0.405$, $\sigma_{2,s,2 \rightarrow 3} = 0.045$, $\sigma_{2,t,3} = 0.666666$, $\sigma_{2,s,3 \rightarrow 1} = 0.0$, $\sigma_{2,s,3 \rightarrow 2} = 0.0$, $\sigma_{2,s,3 \rightarrow 3} = 0.6$, $\sigma_{3,t,1} = 0.333333$, $\sigma_{3,s,1 \rightarrow 1} = 0.255$, $\sigma_{3,s,1 \rightarrow 2} = 0.028333$, $\sigma_{3,s,1 \rightarrow 3} = 0.0$, $\sigma_{3,t,2} = 0.5$, $\sigma_{3,s,2 \rightarrow 1} = 0.0$, $\sigma_{3,s,2 \rightarrow 2} = 0.3825$, $\sigma_{3,s,2 \rightarrow 3} = 0.0425$, $\sigma_{3,t,3} = 0.666666$, $\sigma_{3,s,3 \rightarrow 1} = 0.0$, $\sigma_{3,s,3 \rightarrow 2} = 0.0$, $\sigma_{3,s,3 \rightarrow 3} = 0.566666$ (all in cm^{-1}), non-listed group transfer cross sections are zero; the whole spatial domain is a cylinder with the radius of 45 cm and the length of 90 cm; the source and detector are sphere with 1.5 cm radius, and their centers lie on the cylinder axis and are separated by 16 cm; the midpoint of these centers is located at that of the cylinder axis; the center of cube 1 coincides to the midpoint; the side of cube 1 is 6 cm in length; two faces of cube 1 are vertical to the cylinder axis.)

	difference of two independent forward calculations	correlated coupling
first group	7.28×10^{-6} (0.103)*	5.90×10^{-6} (0.110)*
second group	8.77×10^{-6} (0.071)*	8.19×10^{-6} (0.060)*
third group	5.16×10^{-5} (0.022)*	5.03×10^{-5} (0.016)*
cpu time (min.)**	10366***	3870****

* fractional standard deviation

** measured by Digital AlphaStation 600 5

*** $2 \times 100,000,000$ histories

**** 20,000,000 initial variable selections based on (11);

4 adjoint and 2×40 forward histories per initial variable

4 Summary and Discussion

We have decomposed a detector response according to whether particle histories cross and recross a source-detector enclosure or not. The decomposition was applied to calculate the variation of a detector response due to material perturbations in a region isolated from both the source and detector. The characteristic of the perturbation analysis is to initiate forward and adjoint histories in exactly opposite directions at the internal boundary between perturbed and unperturbed materials. The methodologies in correlated coupling [4,5] play a crucial role.

A particle history in Monte Carlo perturbation analysis is divided into three parts; the path from the birth to the first entrance into a perturbed region, the path toward a detector after the last exit from the perturbed region, and the path in between. A method of separately constructing these three parts may be sought with appropriate coupling techniques. The work described in this paper

is an attempt aiming to concentrate the computational effort on the path in between.

References

1. R. Sánchez: Transport Theory and Statistical Physics **27**, 445 (1998)
2. S.N. Cramer: Nucl. Sci. Eng. **124**, 398 (1996)
3. I.V. Serov et al.: Nucl. Sci. Eng. **133**, 55 (1999)
4. T. Ueki et al.: ‘Analysis of Correlated Coupling of Monte Carlo Forward and Adjoint Histories’, Nucl. Sci. Eng., accepted.
5. T. Ueki, J.E. Hoogenboom: ‘Particle Reflection in Correlated Coupling of Monte Carlo Forward and Adjoint Histories’. In CD Proceedings: *PHYSOR 2000, ANS International Topical Meeting on Advances in Reactor Physics and Mathematics and Computation into the Next Millennium, Pittsburgh, Pennsylvania U.S.A., May 7-11, 2000* (American Nuclear Society, Inc., La Grange Park, Illinois)
6. M. Løve: *Probability Theory II*, 4th Edition (Springer-Verlag, New York U.S.A. 1978)
7. P. Billingsley: *Probability and Measure*, Third Edition (John Wiley & Sons, New York U.S.A. 1995)
8. T. Ueki, J.E. Hoogenboom: ‘Exact Monte Carlo Perturbation Analysis By Forward-Adjoint Coupling in Radiation Transport Calculations’, J. Comput. Phys., submitted

The Geometrical Sensitivity Option in MCBEND

T. Shuttleworth

The ANSWERS Software Service, AEA Technology plc, Winfrith Technology Centre,
Dorchester, Dorset DT2 8ZE, United Kingdom

1 Introduction: the Differential Sensitivity Algorithm in Monte Carlo

A scored result, R , in a Monte Carlo calculation may be represented in the form:

$$R = Q \prod_i P_i \quad (1)$$

Where P_i are the probabilities associated with a each event, i , in the random walk of a particle and Q is a scaling constant. If the result is sensitive to some parameter, s , then:

$$\frac{dR}{ds} = Q \sum_j \left(\frac{dP_j}{ds} \prod_{i \neq j} P_i \right) = Q \prod_i P_i \left(\sum_i \frac{1}{P_i} \frac{dP_i}{ds} \right) = R \sum_i \frac{1}{P_i} \frac{dP_i}{ds} \quad (2)$$

The summation of the terms $(1/P \cdot dP/ds)$ is effectively a weight factor that is accumulated during the calculation. It is applied to the scored result to give its differential with respect to parameter s .

In the Monte Carlo code MCBEND [1], geometry models use the differences and intersections of simple solid bodies to define volumes of space occupied by a uniform material. The geometrical sensitivity option allows the perturbation 'ds' to represent a differential displacement of a body along one of its local co-ordinate axes or a change to one of its dimensions - e.g. the radius of a cylinder.

The differential sensitivity method has advantages over making finite perturbations and observing the changes in results. If the overhead for evaluating sensitivity terms is less than a factor two then it is more efficient than executing two calculations. If small, finite changes are made to the model then the precise difference in the results will be masked by the Monte Carlo statistical noise. If larger changes are made they may be physically unrealistic.

2 The Probability of Reaching a Boundary without a Collision

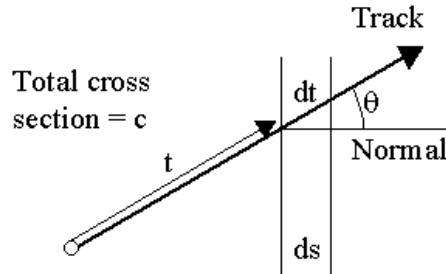
From any arbitrary point on a particle track approaching a boundary, the probability of reaching that boundary without a collision is simply:

$P = e^{-ct}$ t = the geometrical distance to the boundary
 c = the total cross section of the material before the boundary

$$\frac{dP}{dt} = -ce^{-ct} \quad \text{and} \quad \frac{1}{P} \frac{dP}{dt} = -c \quad (3)$$

The term may be related to a geometrical displacement of a parameter, s , as follows:

$$\frac{1}{P} \frac{dP}{ds} = \frac{1}{P} \frac{dP}{dt} \frac{dt}{ds} = -c \frac{dt}{ds} \quad (4)$$



The differential dt/ds is purely geometrical. The example in the sketch illustrates a case where the specified geometrical perturbation is the displacement of a plane surface along its normal. The term dt/ds is then the secant of the angle (Θ) at which the particle track crosses the surface. For first order sensitivities, the same result applies to curved surfaces – e.g. the crossing of a cylindrical boundary with ds representing a change in its radius.

The crossing of a perturbed boundary is a well defined event in the history of a particle; the above term may be evaluated and accumulated in a sensitivity weight register with little additional effort.

3 The Probability of Colliding before Reaching a Perturbed Boundary

From any arbitrary point on a particle track approaching a boundary, the probability of colliding before reaching that boundary is given by:

$$P = e^{-ct} \quad \frac{dP}{dt} = -ce^{-ct} \quad \text{and} \quad \frac{1}{P} \frac{dP}{dt} = \frac{ce^{-ct}}{1 - e^{-ct}} = \frac{c}{e^{+ct} - 1} \quad (5)$$

However, it is not appropriate to apply this weight term to every collision event. Pre-boundary collisions could occur several mean-free-paths before a boundary and it would be illogical to weight them for a perturbation that has not been reached or even approached.

The sensitivity term for the crossing of a perturbed boundary (equation 4) is negative for a displacement along the particle track: fewer particles reach the boundary as a result of the displacement. The number of pre-boundary collisions increases (equation 5) but the increase should be confined to collisions within the differential limit of the boundary. In a practical Monte Carlo calculation the probability of such events is vanishingly small.

One solution attempted during development of the sensitivity algorithm was to confine the application of sensitivity weights to collisions that occurred *close* to a boundary: say within 0.1mfp. This leads to the following weight term to apply to collisions that occurred within Δt of a boundary:

$$\frac{1}{P} \frac{dP}{dt} = \frac{c}{e^{+c\Delta t} - 1} \approx 9.5 \text{ for } c\Delta t = 0.1 \quad (6)$$

Thus we would be applying a relatively high weight to a relatively small number of events.

This solution met with limited success: if the chosen interval was reduced then the approximation became more valid but the statistical noise on the sensitivity results increased; if the interval was increased then the statistics improved but the approximation became greater. The method was found to be entirely inadequate for second order sensitivity calculations.

A practical solution was found by re-examining the basic form of the sensitivity calculations (equation 2). Consider a less formal representation involving only three probabilities:

$$\begin{aligned} R &= QP_1P_2P_3 \\ \frac{dR}{ds} &= QP_1P_2P_3 \left(\frac{1}{P_1} \frac{dP_1}{ds} + \frac{1}{P_2} \frac{dP_2}{ds} + \frac{1}{P_3} \frac{dP_3}{ds} \right) \end{aligned} \quad (7)$$

Suppose one of the probabilities is extremely small (e.g. $P_2 = \varepsilon$) but its differential is not. The equation reduces to:

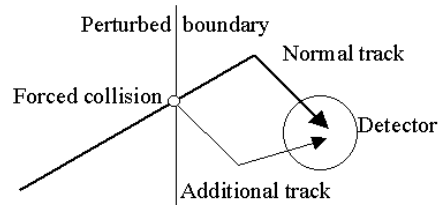
$$\begin{aligned} \frac{dR}{ds} &= Q \left(P_2P_3 \frac{dP_1}{ds} + P_1P_3 \frac{dP_2}{ds} + P_1P_2 \frac{dP_3}{ds} \right) \\ &= Q \left(\varepsilon P_3 \frac{dP_1}{ds} + P_1P_3 \frac{dP_2}{ds} + P_1\varepsilon \frac{dP_3}{ds} \right) \\ &= QP_1P_3 \frac{dP_2}{ds} \text{ as } \varepsilon \rightarrow 0 \end{aligned} \quad (8)$$

A collision within the differential limit of the perturbed boundary is such an event. Its probability and differential are:

$$P = 1 - e^{-c\delta t} \quad (\rightarrow c\delta t = \varepsilon); \quad \frac{dP}{dt} = ce^{-c\delta t} \quad (\rightarrow c) \quad (9)$$

Such an event may be forced to happen in a Monte Carlo calculation when a particle track crosses a perturbed boundary. The progeny of the collision are assigned an extremely low weight so that the contribution they make to any detectors which they enter is negligible. The chosen weight is arbitrary - say 10^{-6} - and may be equated to ε in the above analysis.

$$\begin{aligned} R &= QP_1\varepsilon P_3 &&= \text{negligible} \\ \frac{dR}{ds} &= QP_1\varepsilon P_3 \left(\frac{\varepsilon}{\varepsilon} \right) &&= \text{finite} \end{aligned} \quad (10)$$



By this method, we have represented a very rare event and given it a very large sensitivity weight. However, we have made the event frequent (by forcing it) so the statistical noise does not become unacceptable. An example of such an event is sketched on the right.

There is clearly a computational overhead here: additional tracks from the forced collisions must be traced. The severity depends on how late in the particle history the perturbed boundary is crossed; if it is near the detector then the extra tracks are relatively short. In MCBEND, provision is made for restricting the frequency of forced collisions with a compensating weight enhancement for those that do occur.

4 Post-boundary Even

The above analysis has been confined to events in the material preceding a perturbed boundary. Contributions to the sensitivity weight are also generated by the fact that the path length of the particle in the material beyond the boundary is reduced when the boundary is displaced along the track. If c' is the total cross section of the material beyond a boundary then the sensitivity weight for a particle track that crosses it is increased by $c' dt/ds$. A forced collision must be generated immediately after the boundary with a sensitivity weight $(-c'/\varepsilon) dt/ds$. Quite correctly, these terms cancel those of the pre-boundary events when the material on either side of the boundary is the same.

5 Types of Perturbation

The simplest form of perturbation is one in which a single surface is moved. Applications include the following examples.

Assessing the sensitivity of reactor pressure vessel damage to its inner radius. A large pressure vessel may change its radius significantly due to thermal expansion. There may be some uncertainty over the difference between the design radius and the 'as-built' dimension.

The biological dose beyond a shield wall will depend upon its thickness. During a cycle of design calculations, the outer boundary of the shield may be declared as a perturbed boundary to provide an estimate of the gradient of the dose vs thickness curve. This can reduce the number of survey calculations required and allow rapid convergence on the thickness required to attain a given dose level.

A more complex application is one in which a component of the geometrical model may be displaced - particularly if it contains a source.

In a well logging calculation the source and detector are contained within a tool that is lowered down a bore hole. The measurements obtained will be sensitive to the position of the tool relative to the bore hole centre. The geometrical sensitivity option allows this to be quantified.

In this mode, the source point and the particle tracks undergo the same differential displacement as the tool. Boundary crossings within the tool and at its surface are not deemed to be perturbed relative to the track. Differential sensitivity terms are derived when the displaced track crosses the fixed surfaces of the bore hole and its environment.

6 Second Order Sensitivities

In many applications, the variation of the result with a geometrical change is non-linear; usually it is the sum of a series of exponentials. The curvature of the variation may be assessed by evaluating the second differential terms. A simple approach here is to take the mean gradient of the first order sensitivities between two points and use it as an estimate of the second order differential.

Alternatively, the method of evaluating the first order sensitivities may be extended to second order. The following terms can be derived for the probability of a particle reaching a perturbed boundary.

$$\frac{d^2 P}{ds^2} = \frac{d^2 P}{dt^2} \left(\frac{dt}{ds} \right)^2 + \frac{dP}{dt} \frac{d^2 t}{ds^2} \rightarrow \frac{1}{P} \frac{d^2 P}{ds^2} = c^2 \left(\frac{dt}{ds} \right)^2 - c \frac{d^2 t}{ds^2} \quad (11)$$

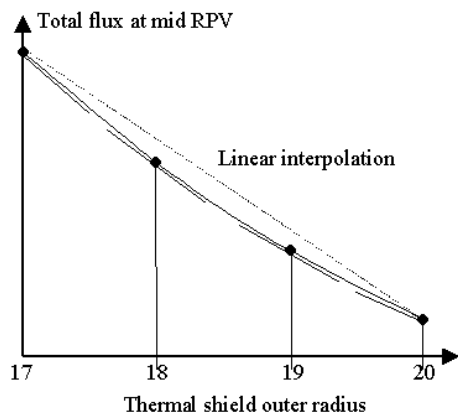
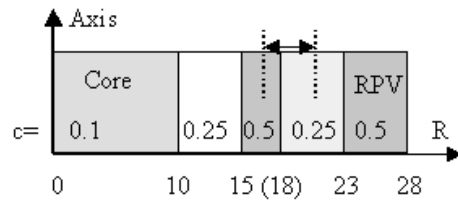
Terms such as the above are generated when the second differential of the result, R , is taken with respect to a geometrical parameter s . For plane surfaces, the geometrical term $d^2 t/ds^2$ is zero; for curved surfaces it is dependent on the shape of the surface and its curvature.

Detailed analysis of the provision to be made for forced boundary collisions shows that *two* collisions must be forced to obtain the second order sensitivity contributions. A number of combinations are required for distributing these two collisions about a perturbed boundary.

The complexity of this process, and the extra computing effort required to track the plethora of extra particles associated with second order sensitivities renders the method unattractive compared with the relative simplicity of the first order evaluation. A prototype implementation has been attempted in MCBEND with limited success. The statistical uncertainties on the second order sensitivities were very poor compared with those obtained for first order.

7 Example Application

The following example illustrates the type of calculation that may be executed. The materials are formed from a fictitious nuclide that has the property of scattering isotropically with the loss of half the incident energy. The calculation records the fluxes in groups representing 0 - 4 scattering events together with a response function that is the sum over all groups.



The geometry is a cylindrical system representing a notional reactor system.

The outer radius of the thermal shield (nominally 18.0 units) is defined as a perturbed boundary. Calculations were executed for specific variations: 17.0, 18.0, 19.0, 20.0.

The sketch right plots the results of calculations with explicit variations of the thermal shield radius. Superimposed are the gradients at each point provided by the geometrical sensitivity results. Had the variations been confined to the two end points ($R=17$ and $R=20$) then, in the absence of geometrical sensitivity results, a linear interpolation would not give correct intermediate values. The gradients at these points could be used to provide a reasonable estimate of the variation between them rather than requiring three or four executions.

In this example, inclusion of a geometrical sensitivity estimation extended the execution time by about 25%. The uncertainty on the scored values of dR/ds was of the order 4%.

8 Summary

The method of estimating differential sensitivities in Monte Carlo calculations has been extended to perturbations of the geometry model. The problem of representing differential changes in collision rates near perturbed boundaries has been resolved by forcing extra collisions at these boundaries. The extension to second order has been outlined. Some potential applications of the technique have been listed. An example application illustrates its usefulness.

References

1. N.R. Smith et al.: 'The Current Status and Future Plans for the Monte Carlo Codes MONK and MCBEND', These Proceedings p. 637

An Alternative Monte Carlo Method for the k -Eigenfunction?

T.E. Booth

Los Alamos National Laboratory, Los Alamos NM 87545 USA

Abstract. Major Monte Carlo codes such as MCNP [1] typically use variations on the power iteration [1,2] method to obtain the fundamental mode k -eigenvalue and eigenfunction. This paper describes an alternative to the power iteration method. The new method builds the eigenfunction, one source particle at a time, by starting each new source particle at a location chosen so that the source density tends to better approximate the fundamental eigenfunction. That is, the method adds new source points to regions where the empirical source density appears too low to satisfy the eigenfunction equation.

1 Introduction

The eigenfunction problem seeks to obtain a source density $\Psi(P)$ that satisfies the equation:

$$A\Psi(P) = k\Psi(P) \quad (1)$$

where A is the operator that transports neutrons from the current fission source site to the next fission source site. Suppose that $S(P)$ is the best current guess for $\Psi(P)$. Let $I(P) = AS(P)$ be called the “image” of $S(P)$. Define

$$k_e = \frac{\int AS(P) dP}{\int S(P) dP} = \frac{\text{total number of image points}}{\text{total number of source points}} \quad (2)$$

If $S(P) = \Psi(P)$, then the number of image points will be exactly $k_e = k$ times the number of source points in any region of the problem. Otherwise, some regions of the problem will have an excess of image points and some regions of the problem will have an excess of source points. The new method finds the region with the largest excess of image points and adds a new source particle to this region. The new source particle is then transported to produce an updated image. This process then repeats with both the source points and image points accumulating.

As a simple illustration, consider a discrete two-state transport problem. Suppose that S_1 and S_2 particles have been sourced into states 1 and 2 resulting in I_1 and I_2 image particles in states 1 and 2. Now suppose

$$\frac{I_i}{S_i} > \frac{I_1 + I_2}{S_1 + S_2} > \frac{I_j}{S_j} \quad (3)$$

The ratio I_i/S_i is too large and the method tries to reduce this ratio by adding another particle to state i , thereby increasing S_i . The new particle is then transported to produce new image particles and the process is repeated.

2 Procedure for a Slab Problem

The n^{th} source particle's position is determined by dividing the entire problem into two intervals. One then computes k_1 and k_2 corresponding to the lower and upper intervals. One then adds the n^{th} source particle to the half-space with the largest k . This half-space is further divided into two quarter-spaces and the quarter-space with the largest k gets n^{th} source particle. This dividing process continues until the interval selected only contains one image particle. The n^{th} source particle is then placed coincident with the image particle. The n^{th} source particle is then transported and the set of image particles is updated with any resulting fission particles. The entire process is now repeated for the $n + 1^{st}$ source particle.

3 Results

A slab problem with thickness $T = 20\lambda$, isotropic scattering, $\nu = 2$ neutrons per fission, absorption probability $p_a = 1/3$, scattering probability $p_s = 1/3$, and fission probability $p_f = 1/3$ is considered herein.

For reference, an independent solution was obtained for reference using the fission matrix method. That is, the interval $0 \leq x \leq T$ was divided into 2000 intervals. For each interval, i , a Monte Carlo run of one million particles (started uniformly in interval i) estimated the number of fission particles, $F(j, i)$ produced in interval j per source particle in interval i . The matrix eigenfunction equation

$$FS = kS \quad (4)$$

was then solved deterministically. Note that the ratio of the two largest eigenvalues is .9774.

Figure 1 shows a comparison of 100 independent calculations with the power iteration method versus 100 independent calculations with the new method. Both methods used 100,000 particles for each calculation. Both particles started with the initial source point near the left edge at $x = .2$. The power iteration method ran for 1000 iterations with 100 particles per iteration. The 1000 iterations included the first 200 iterations that were not tallied followed by 800 tallied iterations. Note from Fig. 1 that the error bars for the two methods are very similar. The power iteration method took 60 seconds and the new method took 287 seconds.

Figure 2 shows a comparison of 20 independent calculations with the power iteration method versus 20 independent calculations with the new method. Both methods used one million particles for each calculation. Both particles started with the initial source point near the left edge at $x = .2$. The power iteration method ran for 1000 iterations with 1000 particles per iteration. The 1000 iterations included the first 200 iterations that were not tallied followed by 800 tallied iterations. Note from Fig. 2 that the error bars for the two methods are very similar. The power iteration method took 103 seconds and the new method took 754 seconds.

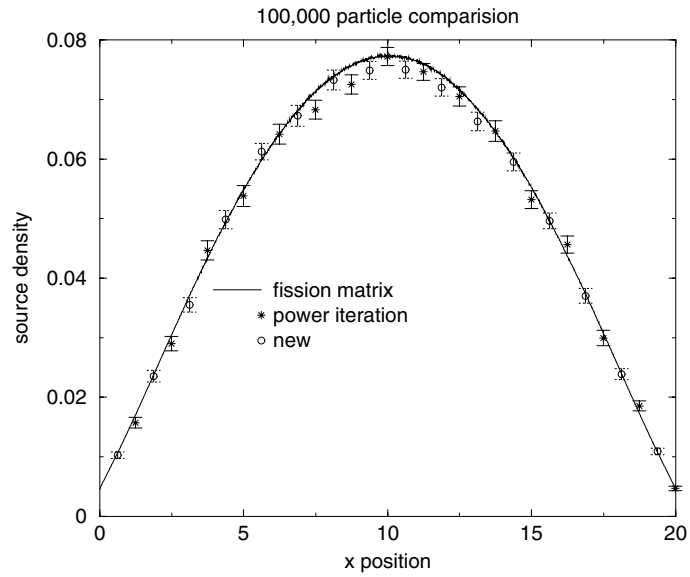


Fig. 1. Comparison of Alternative Method versus Power Iteration Method for One Hundred Thousand Particles

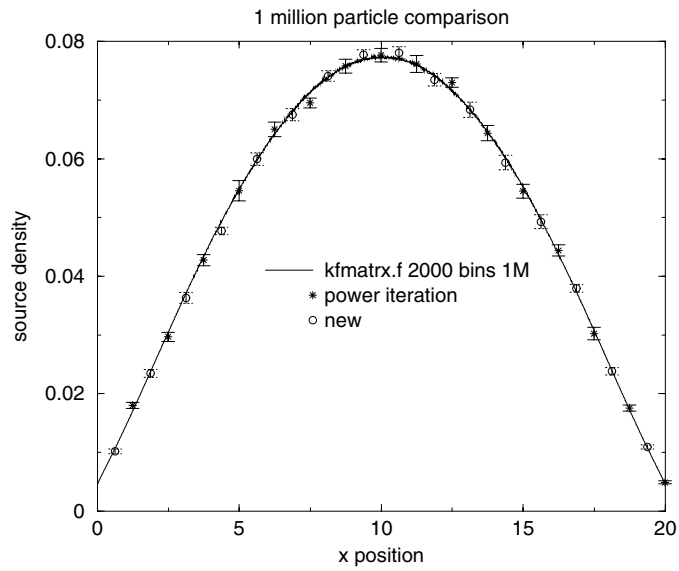


Fig. 2. Comparison of Alternative Method versus Power Iteration Method for One Million Particles

4 Summary

For the same number of particles, the quality of the eigenfunction generated by the new method seems roughly comparable to the quality of the eigenfunction generated by the author's best choice of the power iteration parameters. (It should be noted that the author has little experience with the optimal choice for these parameters. Ideally these comparisons should be done by an expert in the power iteration method.) However, the new method requires substantially more computer time per particle because a lot more effort is expended deciding where to place the source particles.

Despite that fact that the new method appears to be computationally less efficient than the power iteration method for simple problems, there are three reasons that the method is worth considering. First, it is useful to have two different methods to check against each other. Second, perhaps the new method might be improved by some simple modifications. Third, one advantage of the new method is that there are no parameters for the user to pick.

References

1. J. Briesmeister, editor: *MCNP – A General Monte Carlo N-Particle Transport Code Version 4A*, Los Alamos National Laboratory manual LA-12625-M, (November 1993)
2. G. Bell, S. Glasstone: *Nuclear Reactor Theory*, Van Nostrand Reinhold Company, Copyright 1970 by Litton Educational Publishing (see sec 4.4d)

Continuous Energy Adjoint Monte Carlo for Coupled Neutron–Photon Transport

J.E. Hoogenboom

Delft University of Technology, Interfaculty Reactor Institute, Mekelweg 15, 2629 JB Delft, The Netherlands

Abstract. Although the theory for adjoint Monte Carlo calculations with continuous energy treatment for neutrons as well as for photons is known, coupled neutron-photon transport problems present fundamental difficulties because of the discrete energies of the photons produced by neutron reactions. This problem was solved by forcing the energy of the adjoint photon to the required discrete value by an adjoint Compton scattering reaction or an adjoint pair production reaction. A mathematical derivation shows the exact procedures to follow for the generation of an adjoint neutron and its statistical weight. A numerical example demonstrates that correct detector responses are obtained compared to a standard forward Monte Carlo calculation.

1 Introduction

Adjoint Monte Carlo methods are useful in situations with a small detector (either geometrically or with regard to the energy sensitivity range), for which a regular forward Monte Carlo calculation may break down as only few particles will actually hit the detector. In an adjoint Monte Carlo calculation the hypothetical particle that obeys the adjoint transport equation starts at the detector, will gain energy in collisions and contributes to the result when it crosses the original source region. Therefore, a small detector volume is no problem at all.

Adjoint Monte Carlo is generally provided in general purpose Monte Carlo codes like MCNP, but only in multigroup approximation. To retain the full advantages of a Monte Carlo simulation a continuous energy mode for adjoint Monte Carlo calculations is necessary. For neutron transport the theory was developed many years ago [1,2]. For photon transport the theory was developed only recently [3]. Instrumental for the Monte Carlo solution of the adjoint transport equation is the concept of so-called adjoint cross sections [2]. Using this concept the Monte Carlo simulation of the adjoint transport equation can be made very similar to that of regular neutron or photon history simulation. In coupled neutron-photon problems the discrete nature of the photons generated by neutron capture or neutron inelastic scattering processes prohibits a direct simulation of the adjoint equations. For the generation of an adjoint neutron from an adjoint photon interaction, the adjoint photon should have exactly the discrete energy with which a photon is produced in the real physical process.

The paper concentrates on the simulation of the source term in the adjoint neutron transport equation, i.e. the generation of adjoint neutrons from adjoint photon processes. Because of the artificial nature of adjoint particles the correct

procedure of generating adjoint photons must be derived by an extensive mathematical derivation. This is followed by a Monte Carlo interpretation in terms of probability density functions to be sampled and factors defining the statistical weight of an adjoint particle.

2 Theory of Coupled Neutron–Photon Adjoint Monte Carlo

To simplify the formulas we will deal only with the energy dependence of the coupled neutron-photon transport, as energy is the most important variable for continuous energy adjoint Monte Carlo. However, the theory can be derived for the case with space and direction dependence included. We start with the coupled neutron-photon transport equations for the neutron and photon emission densities χ_n and χ_γ , respectively. With only energy dependence these quantities are equal to the respective collision densities.

$$\chi_n(E) = S_n(E) + \int K_n(E' \rightarrow E) \chi_n(E') dE' , \quad (1)$$

$$\chi_\gamma(E) = S_\gamma(E) + \int K_\gamma(E' \rightarrow E) \chi_\gamma(E') dE' , \quad (2)$$

with the source function of photons determined by the neutron emission density

$$S_\gamma(E) = \int G_{n\gamma}(E' \rightarrow E) \chi_n(E') dE' . \quad (3)$$

The detector response to be calculated is given by

$$R = \int \eta_\chi(E) \chi_\gamma(E) dE . \quad (4)$$

with η_χ the detector response function with respect to the photon emission density χ_γ . These equations can be solved by the Monte Carlo method in a standard way. The detector response can be estimated for instance with a collision estimator. The kernel $G_{n\gamma}$ represents the process of discrete photon generation from neutron reactions and can be written as

$$G_{n\gamma}(E' \rightarrow E) = \sum_l \frac{\Sigma_{n\gamma}^l(E')}{\Sigma_{tn}(E')} \delta(E - E_\gamma^l) , \quad (5)$$

with E_γ^l the discrete photon energy produced at neutron process l , which can be neutron capture and discrete level inelastic collision.

The equations adjoint to (1) and (2) involve the adjoint functions $\chi_n^+(E)$ and $\chi_\gamma^+(E)$ and the kernels K with their arguments interchanged. However, for a proper Monte Carlo sampling of the adjoint equations, it is useful (especially

for the space-dependent case) to consider the quantity $\xi^+(E) = \Sigma_t(E)\chi^+(E)$, leading to the following adjoint equations

$$\xi_\gamma^+(E) = \Sigma_t(E)\eta_\chi(E) + \int L_\gamma^+(E' \rightarrow E)\xi_\gamma^+(E')dE' , \quad (6)$$

$$\xi_n^+(E) = S_n^+(E) + \int L_n^+(E' \rightarrow E)\xi_n^+(E')dE' , \quad (7)$$

with the kernels L defined by

$$L^+(E' \rightarrow E) = \frac{\Sigma_t(E)}{\Sigma_t(E')}K(E \rightarrow E') , \quad (8)$$

both for adjoint photons and neutrons, and the source of adjoint neutrons S_n^+ given by

$$\begin{aligned} S_n^+(E) &= \int \frac{\Sigma_{tn}(E)}{\Sigma_{t\gamma}(E')}G_{n\gamma}(E \rightarrow E')\xi_\gamma^+(E')dE' \\ &= \sum_l \int \frac{\Sigma_{n\gamma}^l(E)}{\Sigma_{t\gamma}(E')}\delta(E' - E_\gamma^l)\xi_\gamma^+(E')dE' = \sum_l \frac{\Sigma_{n\gamma}^l(E)}{\Sigma_{t\gamma}(E_\gamma^l)}\xi_\gamma^+(E_\gamma^l) . \end{aligned} \quad (9)$$

Now we can proof that the detector response R is also equal to

$$R = \int \frac{S_n(E)}{\Sigma_{tn}(E)}\xi_n^+(E)dE . \quad (10)$$

In Monte Carlo terms this means that we have to solve the adjoint equations (6) and (7) and use a collision estimator with $\frac{S_n(E)}{\Sigma_{tn}(E)}$ as the scoring function.

The main problem is that for sampling the source of adjoint neutrons S_n^+ we need a sample of the adjoint function ξ_γ^+ at the discrete energy E_γ^l , which will not be obtained in a continuous energy Monte Carlo calculation in a natural way. To overcome this problem, we have to sample (6) with a next-event estimator to force the outcoming energy of the adjoint photon collision to be E_γ^l . However, the photon collision kernel $K_\gamma(E' \rightarrow E)$ also contains a delta function because of the pair production process resulting in a discrete energy $E_C=0.511$ MeV. So we can split that kernel in a Compton part and a pair production part as follows

$$K_\gamma(E' \rightarrow E) = \frac{\Sigma_C(E' \rightarrow E) + 2\Sigma_{pp}(E')\delta(E - E_C)}{\Sigma_{t\gamma}(E')} , \quad (11)$$

with the two photons from annihilation taking together by doubling the statistical weight. This is also allowed in a direction dependent case, provided that no angular correlation between photons needs to be investigated.

The delta function in (11) also introduces a problem in sampling the adjoint photon transport equation, which problem can be solved using a next-event estimator to get an adjoint photon at energy E_C , after which an adjoint pair production reaction can take place [3]. To obtain an expression for $\xi_\gamma^+(E_\gamma^l)$ we

use (11) and (8) and substitute the result in (6) setting $E = E_{\gamma l}$. Then we have for the source term of adjoint neutrons from (9)

$$S_n^+(E) = \sum_l \frac{\Sigma_{n\gamma}^l(E)}{\Sigma_{t\gamma}(E_{\gamma}^l)} \left[\eta_{\Phi}(E_{\gamma}^l) + \int \frac{\Sigma_C(E_{\gamma}^l \rightarrow E')}{\Sigma_{t\gamma}(E')} \xi_{\gamma}^+(E') dE' \right. \\ \left. + 2 \frac{\Sigma_{pp}(E_{\gamma}^l)}{\Sigma_{t\gamma}(E_C)} \eta_{\Phi}(E_C) + 2 \frac{\Sigma_{pp}(E_{\gamma}^l)}{\Sigma_{t\gamma}(E_C)} \int \frac{\Sigma_C(E_C \rightarrow E')}{\Sigma_{t\gamma}(E')} \xi_{\gamma}^+(E') dE' \right], \quad (12)$$

with η_{Φ} the detector response function for the photon flux Φ , i.e. $\eta_{\Phi} = \eta_{\chi}/\Sigma_{t\gamma}$.

Now the coupled neutron-photon adjoint problem has four statistically independent source terms. Two in the adjoint photon equation (6) in which application of (11) leads to an additional source term $2\Sigma_{pp}(E)/\Sigma_{t\gamma}(E_C)\eta_{\Phi}(E_C)$ [3]. Moreover, the source of adjoint neutrons (12) contains two independent source terms S_{n1}^+ containing $\eta_{\Phi}(E_{\gamma}^l)$ and S_{n2}^+ containing $\eta_{\Phi}(E_C)$, respectively. These source terms are sampled as follows. Rewrite

$$S_{n1}^+(E) = \sum_l \frac{\Sigma_{n\gamma}^l(E)}{\Sigma_{t\gamma}(E_{\gamma}^l)} \eta_{\Phi}(E_{\gamma}^l) = \sum_l \frac{\Sigma_{n\gamma l}^+}{\Sigma_{n\gamma}^+} \frac{\Sigma_{n\gamma}^l(E)}{\Sigma_{n\gamma l}^+} \frac{\Sigma_{n\gamma}^+}{\Sigma_{t\gamma}(E_{\gamma}^l)} \eta_{\Phi}(E_{\gamma}^l). \quad (13)$$

The discrete photon energy E_{γ}^l is selected from the probability density function (pdf) $p_l = \Sigma_{n\gamma l}^+/\Sigma_{n\gamma}^+$ with the adjoint photon production cross section defined by

$$\Sigma_{n\gamma l}^+ = \int \Sigma_{n\gamma l}^+(E) dE, \quad (14)$$

and $\Sigma_{n\gamma}^+ = \sum_l \Sigma_{n\gamma l}^+$. Next the energy of the adjoint photon is sampled from the pdf $p_l(E) = \Sigma_{n\gamma}^l(E)/\Sigma_{n\gamma}^+$ and the remaining term $\eta_{\Phi}(E_{\gamma}^l)\Sigma_{n\gamma}^+/\Sigma_{t\gamma}(E_{\gamma}^l)$ is taken into account as a starting weight of the particle. The second source term S_{n2}^+ is rewritten in the same way and l and E sampled as for S_{n1}^+ . Here the weight factor becomes $2 \frac{\Sigma_{n\gamma}^+}{\Sigma_{t\gamma}(E_{\gamma}^l)} \frac{\Sigma_{pp}(E_{\gamma}^l)}{\Sigma_{t\gamma}(E_C)} \eta_{\Phi}(E_C)$. Of course, these source terms are only non-zero if the sensitive energy range of the detector determined by $\eta_{\Phi}(E)$ encompasses one or more of the discrete photon energies E_{γ}^l and the energy E_C , respectively. Finally, sampling the terms of (12) containing ξ_{γ}^+ is analogous to sampling S_{n1}^+ and S_{n2}^+ . Given a sample of $\xi_{\gamma}^+(E')$ we select l from the discrete pdf p_l and the energy from $p_l(E)$. Now the weight factor to be applied is $\frac{\Sigma_{n\gamma}^+}{\Sigma_{t\gamma}(E_{\gamma}^l)}$ $\frac{\Sigma_C(E_{\gamma}^l \rightarrow E')}{\Sigma_{t\gamma}(E')}$ and $2 \frac{\Sigma_{n\gamma}^+}{\Sigma_{t\gamma}(E_{\gamma}^l)} \frac{\Sigma_{pp}(E_{\gamma}^l)}{\Sigma_{t\gamma}(E_C)} \frac{\Sigma_C(E_C \rightarrow E')}{\Sigma_{t\gamma}(E')}$, respectively.

3 Numerical Example

To demonstrate the correctness of the scheme developed we studied an artificial coupled neutron-photon problem with sufficiently realistic energy dependence of cross sections, that allowed an analytic calculation of the adjoint cross sections.

The neutron transport includes a $1/v$ capture cross section, generating photons of 1.0 MeV. There is elastic scattering with a constant cross section and two discrete levels of inelastic scattering with different threshold energies, delivering photons with 1.5 and 2.0 MeV, respectively. The neutron source has a flat distribution between 4 and 5 MeV. The neutron transport was cut off at 0.1 MeV for simplicity. The photon transport features the photo-electric effect with a E^{-3} energy dependence, Compton scattering with differential cross section according to the Klein-Nishina formula and pair production above 1.022 MeV with a logarithmic energy dependence. The detector registers the photon flux for a variable energy range. This means that $\eta_{\phi} = 1$ for the considered energy range.

A code was written to simulate the coupled adjoint photon-neutron transport process as outlined above. For a comparison of the results the forward Monte Carlo simulation was also programmed in a separate code.

Table 3 shows the results for various photon energy ranges of interest. In the forward calculation 10^4 neutron histories were followed. The adjoint calculation has to be repeated for every energy range. For all non-zero source terms in the coupled equations 10^5 particles were started.

Table 1. Comparison of detector response for various energy ranges from a forward Monte Carlo calculation and the newly developed adjoint Monte Carlo calculation

Energy range (MeV)	Forward continuous energy		Adjoint continuous energy	
	ϕ	σ (%)	ϕ	σ (%)
0.1-0.2	0.00782	1.3	0.00726	7.0
0.2-0.510	0.787	0.5	0.741	2.5
0.510-0.512	0.863	1.6	0.852	0.4
0.512-0.999	3.183	0.7	3.163	3.0
0.999-1.001	6.104	0.2	6.145	4.0
1.001-1.499	1.901	1.8	1.882	0.4
1.499-1.501	6.770	0.7	6.754	0.4
1.501-1.999	0.263	1.8	0.264	1.1
1.999-2.000	1.813	1.9	1.827	0.3

The table shows an excellent agreement between the forward and the adjoint results which validates the continuous energy adjoint Monte Carlo technique for coupled neutron-photon transport. To demonstrate the power of the adjoint Monte Carlo method we also calculated with the continuous energy adjoint Monte Carlo program the results of a point energy photon flux spectrum which is shown in Fig. 1. The group fluxes from Tab. 1 are also included after division by the energy group width. The figure shows the detailed energy dependence of the photon spectrum, especially below 1 MeV, which can not be obtained from the group flux results in Tab. 1. The discrete photon lines are indicated schematically. Note the discontinuity of the smooth parts of the photon spectrum near the discrete energy lines.

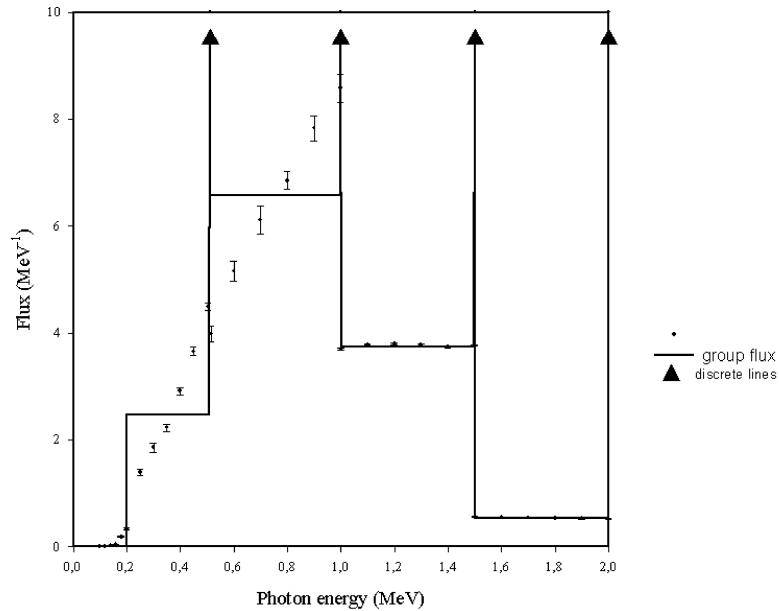


Fig. 1. Point energy photon flux as a function of energy

4 Conclusion

From the theory developed in this paper and the demonstration for a numerical case, we can conclude that coupled neutron-photon transport problems can be solved by continuous energy adjoint Monte Carlo techniques. Adjoint Monte Carlo is the more efficient if more detailed (energy) resolution is needed in the quantity to be calculated.

References

1. B. Eriksson et al.: Nucl. Sci. Eng. **37**, 410 (1969)
2. J.E. Hoogenboom: Nucl. Sci. Eng. **79**, 357 (1981)
3. J.E. Hoogenboom: 'Adjoint Monte Carlo Photon Transport in Continuous Energy Mode with Discrete Photons from Annihilation'. In: *Proceedings PHYSOR 2000 conference on CD-Rom, Pittsburgh, USA, 7-12 May 2000*, (American Nuclear Society 2000)

Application of A³MCNPTM to Radiation Shielding Problems

A. Haghighat¹ and J.C. Wagner²

¹ The Pennsylvania State University, Mechanical and Nuclear Engineering, 137
Reber Building, University Park, PA 16802

² Oak Ridge National Laboratory, P.O. Box 2008, Oak Ridge, TN 37831-6370

Abstract. This paper briefly discusses the theory of the A³MCNPTM code and its application to three real-world shielding/fixed-source problems; including PWR cavity dosimetry, DPA estimation at a BWR core-shroud weld, and dose estimation at the surface of a storage cask. These problems all address major concerns of nuclear utilities and are very important for the continued safe and economical operation of nuclear power plants. The paper demonstrates that A³MCNPTM, with its automated variance reduction capability, is able to solve these problems in a relatively short time with modest computational resources, while significantly reducing the engineer's time and effort for performing these calculations.

1 Introduction

The Monte Carlo (MC) method is considered to be one of the most accurate techniques for simulation of radiation transport. The major drawback associated with using the MC method for simulation of real-world problems is its exorbitant computational expense. To overcome this shortcoming, numerous variance reduction (VR) techniques have been devised and implemented in production codes such as MCNPTM [1]. Effective use of VR techniques for large/complex problems, however, is not straightforward and can be very time consuming. To surmount this difficulty, we have developed a new automatic VR methodology, CADIS (Consistent Adjoint Driven Importance Sampling) [2,3], that formulates both source and transport biasing in a consistent manner based on importance sampling. The space- and energy-dependent source and transport biasing parameters are generated by deterministic transport calculations and used with the weight window technique. The CADIS methodology, along with capabilities for automatic mesh generation and input preparation for a deterministic transport code, has been implemented into the MCNPTM code. This new version of MCNPTM is referred to as A³MCNPTM (Automated Adjoint Accelerated MCNP) [3].

In this paper, we briefly discuss the performance of A³MCNPTM for three major problems of interest to the nuclear industry; including PWR cavity dosimetry [4], DPA estimation at a BWR core-shroud weld [5], and gamma dose estimation over a storage cask.

2 Description of A³MCNPTM

A³MCNPTM (Automated Adjoint Accelerated MCNP) automatically generates a deterministic “importance” function that is used within the CADIS (Consistent Adjoint Driven Importance Sampling) methodology. CADIS performs source and transport biasing using a space-energy dependent weight-window technique. It determines the biased source and weight-window lower bounds via a deterministic adjoint function. Below, we summarize functions performed by A³MCNPTM

1. Generation of a mesh distribution for the deterministic S_N calculation.
2. Preparation of input file for the TORT S_N code [6].
3. Determination of material compositions and preparation of the necessary input files for the GIP code [6] for generation of multi-group mixture cross-sections.
4. Reads the adjoint “importance” function and prepares a biased source as

$$\hat{q}(P) = \frac{\Psi^\dagger(P)q(P)}{\int_P \Psi^\dagger(P)q(P)dP} \quad (1)$$

and the corresponding formulation for particle statistical weight as

$$W(P) = \frac{\int_P \Psi^\dagger(P)q(P)dP}{\Psi^\dagger(P)} = \frac{R}{\Psi^\dagger(P)} \quad (2)$$

where, R is the response, P refers to the independent variables, e.g., space (r), energy (E), and direction (Ω), and Ψ^\dagger , q , and \hat{q} are the importance function, “unbiased” source, and “biased” source, respectively.

5. Superimposes the deterministic S_N spatial-mesh distribution and energy-group structure onto the MC model in a “transparent” manner.
6. Calculates space- and energy-dependent weight-window lower bounds (W_l) for the “transparent” space-energy mesh according to

$$W_l(r, E) = \frac{W}{(\frac{C_u+1}{2})} = \frac{R}{\phi^\dagger(r, E)} \frac{1}{(\frac{C_u+1}{2})} \quad (3)$$

where ϕ^\dagger is the scalar adjoint function and $C_u = \frac{W_u}{W_l}$ is the ratio of upper and lower weight window values.

7. Updates the particle weight, as each particle is transported through the “transparent” mesh using the following formulation:

$$W(r, E) = W(r', E') \frac{\phi^\dagger(r', E')}{\phi^\dagger(r, E)}. \quad (4)$$

3 Performance of A³MCNPTM

In this section, the performance of A³MCNPTM for three different problems that are important for nuclear safety and operation is discussed.

3.1 Cavity Dosimetry for a PWR

Problem Description - The embrittlement of a reactor pressure vessel (RPV) is primarily due to the bombardment of high-energy neutrons and cannot be directly determined from measured quantities. Cavity dosimetry calculations attempt to estimate high-energy reaction rates in a small volume outside of the RPV at a distance of ~ 350 cm from the core centerline. These reaction rates are used to validate methods/models that are subsequently used to estimate RPV neutron fluence. The problem is illustrated in Fig. 1, which shows one octant of the Three Mile Island Unit 1 (TMI-1) reactor.

Performance - Without the use of VR techniques, one could allow MCNPTM to run this problem continuously for weeks and still not obtain statistically significant/reliable results [3]. Before the CADIS methodology and the A³MCNPTM code were developed, this problem was manually optimized with existing VR methods [2]; including, source biasing, weight windows, exponential transformation, and energy cutoff. This manual optimization required a great deal of time and effort to develop, but proved to be very successful in terms of both computational performance and calculational reliability (i.e., enabled problem objectives to be accomplished with available computational resources). Upon completion and implementation of the automated VR methodology, the problem was used to evaluate the efficiency of the automated VR approach. Application of the CADIS methodology increased the calculational efficiency by a factor of more than 4 with respect to our best manually optimized model and by a factor of $\sim 50,000$ with respect to the analog case. Furthermore, the automatic VR approach required very little user time, effort, or experience.

We have performed [2] a number of studies to evaluate the relationship between the accuracy of the adjoint function and its effectiveness for VR of the MC calculation. The effectiveness of the adjoint function for VR was found to be rather insensitive to the accuracy of the adjoint function, and in some cases, due

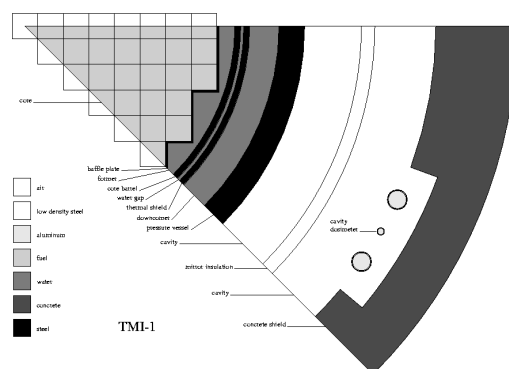


Fig. 1. One octant of TMI-1

to the reduction in data volume and CPU time required for the S_N calculation, less detailed adjoint functions actually yielded greater effectiveness.

3.2 Estimation of DPA at a BWR Core Shroud Weld

Problem Description - The core shroud is an ~ 5 cm thick stainless steel annulus located between the core and the pressure vessel of a BWR reactor. Figure 2 depicts the axial locations of the core-shroud welds (H1 to H8) relative to the reactor core and other structural components. We have developed a model of size $300 \times 300 \times 381$ cm³ and estimated the DPA at a small segment ($2 \times 2 \times 2$ cm³) of the H4 weld, which is located ~ 63.5 cm above the core mid-plane.

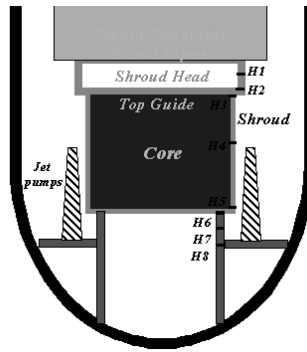


Fig. 2. Schematic of a BWR core shroud and its welds

Performance - We examined the performance of A^3MCNP^{TM} for different mesh distributions (uniform and variable) that are used for the deterministic S_N calculation. Here, for brevity, we present only three cases with uniform meshes of 86,400, 10,800, and 300. Figure 3 shows a sample mesh distribution for each case. The xy mesh intervals for cases 1 to 3 are 5, 10, and 60 cm, and z -mesh intervals are 15.875, 31.75, and 31.75 cm, respectively. As expected, due to the coarse meshing, large ($>$ several orders of magnitude) differences are observed in the calculated adjoint function distributions for the different cases.

The estimated FOM of the unbiased case after 2000 CPU-min with a relative error of 14.97% is only 0.022, while cases 1 to 3 show significantly higher FOMs, which are larger by factors of 4123, 2945, and 131, respectively. As expected, case 1, with the finest TORT mesh distribution, achieves the best FOM, but requires the longest CPU time among the three cases. For example, to achieve a 1σ statistical uncertainty of 1.0%, case 1 requires a total CPU of 534.9 min, from which 424.6 min is consumed by TORT. Our estimated total CPU times, for 1.0% uncertainty, for the unbiased case and cases 2 and 3 are 448,201, 223.5, and 3462.7 min, respectively. This means that case 2 yields the largest CPU speedup of 2005, and even case 3 with its very inaccurate “importance” function yields a speedup of 129.

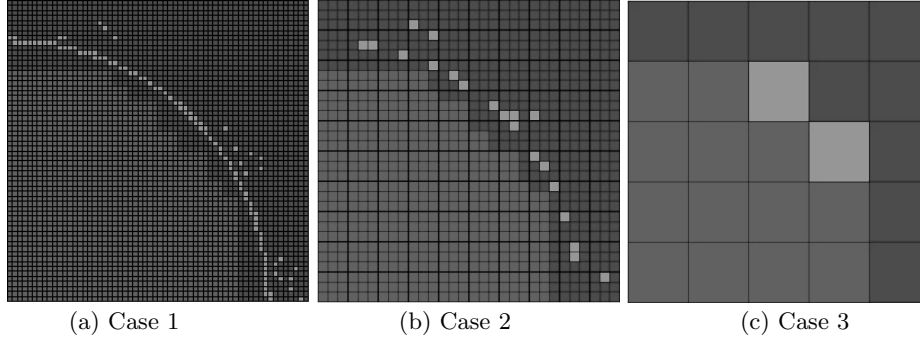


Fig. 3. Mesh distributions from A³MCNPTM for the TORT adjoint calculations

3.3 Storage Cask

Problem Description - To expand storage capacity and prevent premature plant shutdown, utilities are storing their Spent Nuclear Fuel (SNF) on-site in dry casks. Multidimensional MC codes such as MCNPTM are used for this application. Because of the large size of the physical model (~ 3.3 m diameter and ~ 6 m height) and the need for detailed information with high precision, VR methods are necessary. Here, we consider a concrete cask of size $178.3 \times 178.3 \times 838.2$ cm³, and evaluate the gamma dose on the outer surface, as a whole and over axial segments. Figure 4a shows an axial cross section of the MCNPTM model [7] (developed by Holtec Int.), which represents one quarter of a 24-assembly PWR storage cask, used for this study.

Performance - For the unbiased case, a 1σ uncertainty of 0.0376 and FOM of 0.12 are achieved after 6000 CPU-min. For the A³MCNPTM run, after 180 min, we achieve a 1σ uncertainty of 0.0047 with a FOM of 254. This means that to evaluate the dose over the surface, as a whole, A³MCNPTM performs ~ 2117 times faster than the unbiased MCNPTM. For this, besides the CPU for MC simulation, we have used ~ 20 CPU-min for determination of the 3-D “importance” function distribution using the TORT code. We have also examined the performance of A³MCNPTM for evaluation of dose along axial segments. Figure 4b shows the ratio of FOMs (A³MCNPTM to unbiased MCNPTM) and the FOM of the unbiased MCNPTM as a function of axial position. As expected, the performance of A³MCNPTM improves significantly as one moves away from the fuel assembly mid-plane; this is specially evident at the regions above and below the fuel assemblies, i.e., < 116.55 cm and > 482.3 cm.

4 Conclusions

This paper briefly described the A³MCNPTM code and its automated VR, based on the CADIS methodology. We examined the performance of A³MCNPTM

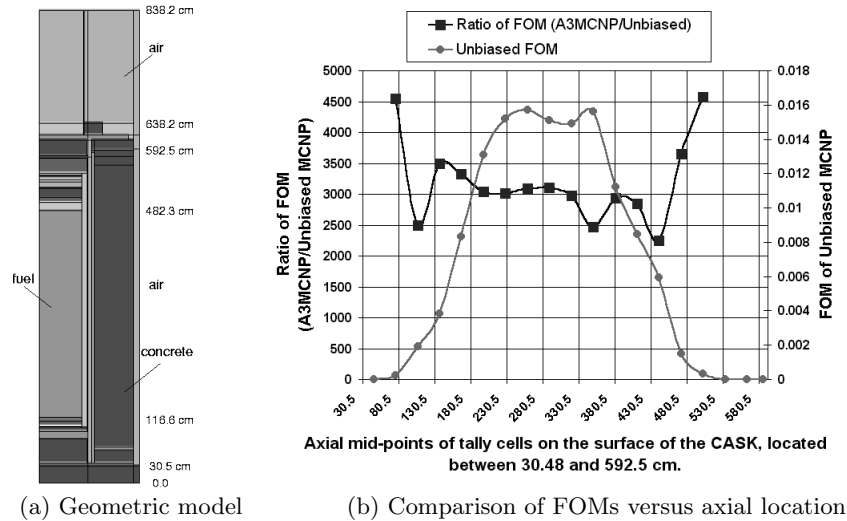


Fig. 4. Storage cask geometry and FOM comparison

for several real-world problems and demonstrated significant improvements in computational efficiency. Perhaps more important than its ability to increase the calculational efficiency, is the fact that A^3MCNP^{TM} does so in a way that requires very little time or experience on the part of the user.

References

1. J.F. Briesmeister, Editor: *MCNPTM - A General Monte Carlo N-Particle Transport Code, Version 4C*, LA-13709-M, Los Alamos National Laboratory (April 2000)
2. J.C. Wagner: *Acceleration of Monte Carlo Shielding Calculations with an Automated Variance Reduction Technique and Parallel Processing*. Ph.D. Thesis (The Pennsylvania State University, Nuclear Engineering Dept. 1997)
3. J.C. Wagner, A. Haghighat: Nucl. Sci. Eng. **128**, 186 (1998)
4. J.C. Wagner, A. Haghighat: 'Acceleration of Monte Carlo Reactor Cavity Dosimetry Calculations with the Discrete Ordinates Adjoint Function'. In *Reactor Dosimetry*, Prague, Czech Republic, 2-6 Sept. 1996, (World Scientific, 1998) pp. 754-761
5. A. Haghighat, H. Hiruta, B. Petrovic: 'Performance of A^3MCNP^{TM} for Calculation of 3-D Neutron Flux Distribution in a BWR Core Shroud'. In *Reactor Dosimetry*, ASTM STP 1398, John G. Williams, David W. Vehar, Frank H. Ruddy and David M. Gilliam, Eds., American Society for Testing and Materials, West Conshohocken, PA, 2000
6. *DOORS3.2 - One, Two- and Three-Dimensional Discrete Ordinates Neutron/Photon Transport Code System*, available as CCC-650 from the Radiation Safety Information Computational Center, Oak Ridge, TN (1998)
7. E. L. Redmond II, S. Antone, Holtec International: Personal Communication

Status of JAERI's Monte Carlo Code MVP for Neutron and Photon Transport Problems

T. Mori, K. Okumura, and Y. Nagaya

Japan Atomic Energy Research Institute, Tokai-mura, Ibaraki-ken, 319-1195, Japan

Abstract. The special features of MVP are (1) vectorization and parallelization, (2) multiple lattice capability and statistical geometry model, (3) probability table method for unresolved resonance, (4) calculation at arbitrary temperatures, (5) depletion calculation, (6) perturbation calculation for eigenvalue (k_{eff}) problem, and so on.

1 Introduction

A general-purpose continuous-energy Monte Carlo code MVP for neutron and photon transport calculations, together with its multi-group version GMVP, has been developed since late 80s at Japan Atomic Energy Research Institute (JAERI). These two codes were designed for vector supercomputers at the first stage, and then parallel processing capability was added for several computers including UNIX work station clusters. The first version of the code was released for domestic use in 1994, with cross section libraries based on JENDL, ENDF/B, etc. After that, functions have been extended for geometry description capability, depletion calculations, realistic calculations of power reactor at arbitrary temperatures, perturbation calculation for eigenvalue problems, and so on. Most of functions for production use are implemented in the code. The MVP code is widely used in Japan, especially in the field of reactor physics analyses. This paper describes the current capability and special features of MVP. Some applications of those special features are also presented.

2 Special Features and Main Capability

2.1 Calculation Algorithm Suitable for Vector Supercomputers

MVP is fully vectorized by the stack-driven zone-selection method [1,2]. In this method, the random walk process is divided into 7 basic tasks; source particle generation, free flight analysis, next zone search, lattice treatment, reflection treatment, neutron collision and photon collision analyses. Each task has its own stack for queuing up particles. The simulation proceeds by selecting a task, processing the task and dispersing processed particles to other stacks. The order of processing tasks depends on the numbers of queued particles in the stacks. Two tasks of the free flight and next zone search are carried out for particles on one geometric zone at a time (zone-selection), while the other tasks are performed for all particles in the stacks.

A speedup, more than 10 times, has been achieved on vector supercomputers for wide applications compared with conventional codes like MCNP [3].

2.2 Geometry Description

MVP adopts the Combinatorial Geometry with multiple square and hexagonal lattice capability to describe easily pin-by-pin models of power reactors. Vacuum, perfect or white reflection and periodic boundary conditions are available.

Recently, a new method based on the statistical geometry model [4] was developed to treat a great number of randomly distributed spherical fuels (coated fuel particles, CFPs) in high-temperature gas-cooled reactors. In this model, location of a spherical fuel is sampled probabilistically along a neutron flight path as shown in Fig. 1.

As the probability distribution for sampling (NND), MVP can use not only an accurate NND calculated with the Monte Carlo hard sphere packing simulation code MCRDF [4] but also the theoretical NND based on the assumption of statistical uniformity [4]:

$$\frac{d}{dr}(\text{NND}(r)) = \frac{3}{2} \frac{f_p}{1 - f_p} \exp\left(-\frac{3}{2} \frac{f_p}{1 - f_p} r\right), \quad (1)$$

where f_p and r are the packing fraction and the distance from the reference position in unit of a spherical fuel diameter, respectively. By using this model, the heterogeneity effect of spherical fuels can be taken into account without any loss of the advantage of the continuous energy method.

2.3 Physics Model, Cross Sections and Calculation at Arbitrary Temperature

All neutron reactions given in evaluated nuclear data files in the ENDF-6 format are explicitly taken into account. Resolved resonance and smooth cross sections are represented pointwisely, while unresolved resonances are described by the cross section probability table method. By using these cross sections, MVP gives an accurate solution for fast reactors which require an accurate treatment of unresolved resonances of U-238. In the thermal energy region, neutron scattering is treated based on the free gas, the inelastic scattering ($S(\alpha, \beta)$) models, and so on. The physics model of photon reactions is similar to that in MCNP4A including Bremsstrahlung photons.

MVP can generate cross section data at an arbitrary temperature from its master cross section library [6]. The master library is produced by the LICEM system [6] and includes temperature-dependent data such as the cross section probability tables and thermal scattering data at several different temperatures. By applying an interpolation to these temperature-dependent values and making Doppler broadening for pointwise cross sections, MVP obtains those at a specified temperature.

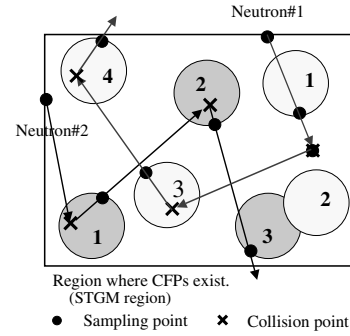


Fig. 1. Arrangement of CFPs in the statistical geometry model

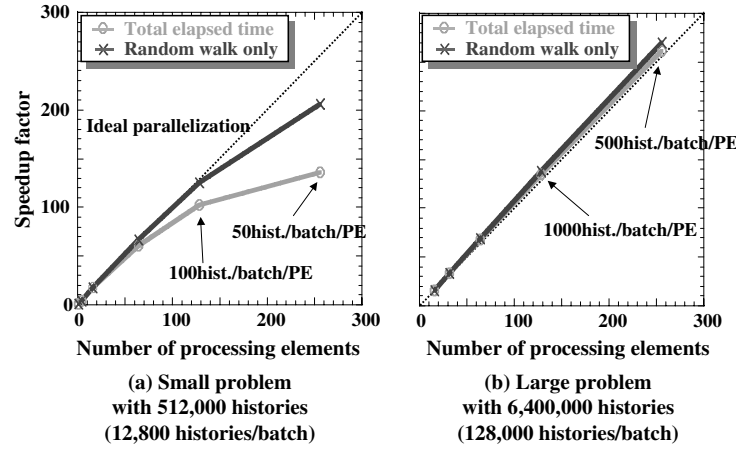


Fig. 2. Speedup factors for the FBR assembly by parallel processing on Intel-Paragon

2.4 Tallies, Estimators and Variance Reduction Techniques

MVP evaluates fluxes, reaction rates, multi-group effective macroscopic/microscopic cross sections and their variances by the track length, collision, surface and point estimators. The eigenvalue (k_{eff}) is calculated by two methods: the multiplication of source neutrons and the neutron balance. The estimates by both methods are obtained by three different estimators (track length, collision and analog), and the final result is evaluated from all estimates on the basis of the method of maximum likelihood. MVP can estimate a real variance of the result taking account of correlation between successive generations [5].

We can obtain results with less statistical errors with MVP owing to its high computation speed by the vectorization and/or parallelization. In addition, MVP includes reliable and widely used variance reduction techniques such as splitting/Russian roulette kill based on cell importance or weight window.

2.5 Parallel Processing Capability

Parallel processing of MVP has been made since early stage of the development work. Recently, the code was parallelized by using MPI for a massively parallel distributed-memory computer Intel-Paragon [6]. The parallelization efficiency was evaluated by analyzing an infinite lattice of FBR fuel assembly with 256 processor elements (PEs) at maximum. We compared two cases, small and large problems. Speed-up factors are depicted in Fig. 2. It can be seen that the parallelization efficiency is quite high and almost an ideal one even with 256 PEs for the large problem although it decreases to about 50% with 256 PEs for the small problem. With 512 PEs, a whole core calculation of a commercial type PWR with 13 million histories can be carried out within about 1 hour.

2.6 Continuous Energy Monte Carlo Burn-up Calculation Code MVP-BURN

In order to apply MVP to various burn-up calculation problems, the MVP-BURN code [7] has been developed by implementing an auxiliary modular code BURN which carries out depletion calculations based on Bateman's method. MVP-BURN has lots of useful functions such as cooling-calculation, branch-off calculation, use of the predictor-corrector method, and so on. The reliability of the code was confirmed by wide benchmark calculations and PIE analyses [7].

2.7 Perturbation Calculation for Eigenvalue Problem

Perturbation effects in eigenvalue (k_{eff}) problems can be evaluated by the correlated and 2nd order differential operator sampling methods with MVP [8]. The effect on k_{eff} due to fission-source change is well evaluated by our method, as shown below.

3 Application of MVP Special Functions

3.1 Analysis of Heterogeneity Effect of Coated Fuel Particles in High Temperature Engineering Test Reactor HTTR

In order to evaluate the heterogeneity effect of CFPs in the fuel compacts, fuel rod cells of HTTR of JAERI [9] were analyzed with and without the statistical geometry model (STGM). The calculation model is an infinite hexagonal cell consisting of a fuel compact, a graphite sleeve of fuel rod, helium coolant and graphite moderator. The JENDL-3.2 cross section library was used in the analysis. The total number of neutron histories for each calculation was about 1,000,000. The results are shown in Tab. 1, which are summarized as follows.

- The heterogeneity effects evaluated with the NND by the MCRDF code and the theoretical one show good agreement with each other, though the latter NND is quite different from the former at a small distance in case of low packing fraction [4].
- The heterogeneity effect strongly depends on fuel rod pitch and U-235 enrichment. This fact means that whole core calculations are necessary to evaluate accurately the heterogeneity effect in such a complicated core as HTTR.

3.2 Analysis of OECD/NEA/NSC Benchmark on MOX BWR

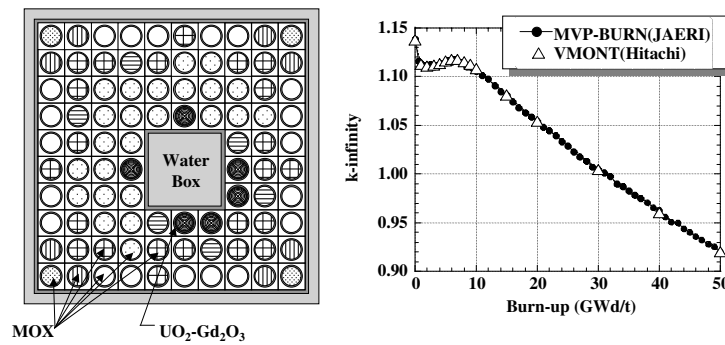
The result of MVP-BURN for OECD/NEA/NSC MOX BWR benchmark problem [10] is shown in Fig. 3. In this figure, the MVP result is compared with that of the VMONT multigroup Monte Carlo burn-up code [11]. The both results show fairly good agreement.

Table 1. Heterogeneity effect of coated fuel particles in HTTR fuel rod cell^a

Fuel rod pitch	U-235 enrichment	k-infinity (heterogeneity effect(% $\Delta k/k'$))		
		Smeared density in fuel compact	STGM with NND by MCRDF	STGM with theoretical NND
5.16cm ^b	3w/o	1.21928 \pm 0.043%	1.25142 \pm 0.045% (2.106 \pm 0.050)	1.25318 \pm 0.045% (2.219 \pm 0.050)
	10w/o	1.36986 \pm 0.042%	1.40173 \pm 0.043% (1.660 \pm 0.043)	1.40181 \pm 0.042% (1.664 \pm 0.043)
6.27cm ^c	3w/o	1.37032 \pm 0.035%	1.39238 \pm 0.041% (1.156 \pm 0.039)	1.39293 \pm 0.035% (1.185 \pm 0.036)

^a Fuel compact: outer diameter=2.6cm, inner diameter=1.0cm, packing fraction=30%.

^b Nominal fuel rod pitch. ^c Fuel rod pitch averaged over fuel assembly.

**Fig. 3.** Calculation geometry and results for the MOX BWR benchmark

3.3 Evaluation of Perturbation Effect on k_{eff}

The perturbation effect on a thermal system was investigated by analyzing an infinite cylindrical core containing a uranyl nitrate solution fuel of the STACY facility [12]. The calculation model is an infinite cylinder with a radius of 22 cm and 1 cm thick water reflector. A perturbation was introduced by decreasing the density of the reflector region by 10%. The results of MVP perturbation calculations are shown in Tab. 2. This table also includes the result of a MCNP4B perturbation calculation and that by two independent MVP calculations. The MVP results with the fission source change effect are in good agreement with that evaluated from two independent calculations, though their statistical uncertainties are slightly large. On the other hand, the large discrepancies are observed for the results obtained without the fission source change effect, including the MCNP4B result.

Table 2. Change in the effective multiplication factor for the simplified STACY model

Method		Δk	1σ
2 MVP Runs		-1.690E-3	0.145E-3
MCNP4B		-3.642E-3	0.042E-3
MVP Correlated Sampling	Without perturbation effect due to fission-source change	-3.658E-3	0.025E-3
(Without any approximation)	With perturbation effect due to fission-source change	-1.537E-3	0.229E-3
MVP 2nd-Order Differential Operator	Without perturbation effect due to fission-source change	-3.655E-3	0.028E-3
Sampling	With perturbation effect due to fission-source change	-1.607E-3	0.261E-3

4 Summary

This paper describes main capability and special features of JAERI's Monte Carlo code MVP, together with some examples of its applications. Now, the study is concentrated on perturbation and high energy particle transport.

References

1. M. Nakagawa, T. Mori, M. Sasaki: Nucl. Sci. Eng. **107**, 58 (1991)
2. T. Mori, M. Nakagawa, M. Sasaki: J. Nucl. Sci. Technol. **29**, 235 (1992)
3. J.F. Briesmeister (ed.): *MCNPTM - A General Monte Carlo N-Particle Transport Code - Version 4B*, LA-12625-M (Los Alamos National Laboratory, Los Alamos 1997)
4. I. Murata, T. Mori, M. Nakagawa: Nucl. Sci. Eng. **123**, 96 (1996)
5. T. Ueki, T. Mori, M. Nakagawa: Nucl. Sci. Eng. **125**, 1 (1997)
6. Mori T., et al.: *Proc. Int. Conf. Math. and Compu., Madrid*, p. 987 (1999)
7. K. Okumura, et al.: J. Nucl. Sci. Technol. **37**, 128 (2000)
8. Y. Nagaya, T. Mori: *Proc. PHYSOR 2000, Pittsburgh, May 7-12, 2000* (2000)
9. K. Yamashita, et al.: Nucl. Sci. Eng. **122**, 212 (1996)
10. OECD/NEA: *Physics of Plutonium Recycling*, to be published in OECD DOC
11. H. Maruyama, et al.: Nucl. Technol. **118**, 3 (1997)
12. Y. Miyoshi, et al.: Nucl. Technol. **118**, 69 (1996)

Current Status of the Oak Ridge Monte Carlo Codes: MORSE/SAS4 and KENO

M.B. Emmett and D.F. Hollenbach

Oak Ridge National Laboratory, MS-6370, Oak Ridge, TN 37831-6370, USA

Abstract. Over the years, the Oak Ridge National Laboratory staff have developed a number of Monte Carlo codes. KENO V.a and KENO-VI are criticality safety codes that can be run stand-alone or by using the criticality safety analysis sequences CSAS and CSAS6. MORSE is a shielding analysis code that can be run stand-alone or through use of the shielding analysis sequences SAS3 and SAS4. All of these codes are part of the SCALE code system, which is widely distributed and used all over the world. As with any major computer code system, changes and improvements are inevitable. These changes occur for multiple reasons, including release of new compilers, faster and improved computers, and changing customer requirements. This paper provides a current overview of these Monte Carlo codes and a look at possible future enhancements.

1 Monte Carlo Criticality Safety Codes

The first part of this presentation covers the criticality safety codes and code sequences that are available in the SCALE [1] code system.

1.1 KENO V.a

KENO V.a is a multigroup Monte Carlo criticality program used to calculate the k-effective of a three-dimensional (3-D) system. KENO V.a's geometry input allows the use of nonconcentric cuboidal, cylindrical, and spherical shapes and has "array-of-arrays" and "holes" capabilities. The array-of-arrays option allows construction of arrays from other arrays. The hole option allows placing a unit or an array at any desired location within a geometry region. This option is quite useful for describing shipping casks and reflectors that have gaps. KENO V.a also has the capability of supergrouping energy-dependent information such as cross sections. Supergrouping is a process that allows a problem to run with only part of the data in core, rather than the entire energy range.

1.2 KENO-VI

KENO-VI contains all the features of KENO V.a plus a more flexible geometry package. The KENO-VI geometry package is capable of modeling any volume that can be constructed using quadratic equations. Other geometry features such as intersections, body rotations, hexagonal arrays, and array boundaries make the code more flexible. The ability to intersect volumes makes it possible to model such things as pipe intersections exactly, which were previously impossible with KENO V.a.

1.3 The CSAS Sequences

CSAS was developed to provide automated, problem-dependent cross-section processing followed by calculation of the neutron multiplication factor for the system being modeled. CSAS executes BONAMI, NITAWL-II, and KENO V.a. Control sequences ending in “X” also execute XSDRNPM to provide a cell-weighted mixture cross section; CSASI and CSASIX use ICE to provide a Monte Carlo formatted mixed cross-section library. CSAS6 is a version of CSAS written explicitly for KENO-VI.

1.4 The KENO3D Visualization Tool

A recent addition to the KENO code systems is KENO3D [2]. KENO3D is a state-of-the-art visualization tool for KENO geometry models that allows the user to interactively display a 3-D geometry model. The KENO V.a version is currently available to the public; the KENO-VI version should be available sometime during the fall of FY 2000. A paper on KENO3D is being presented at this conference.

2 Monte Carlo Shielding Codes

This section will present the Monte Carlo shielding codes that are modules in the SCALE code system.

2.1 MORSE

The Multigroup Oak Ridge Stochastic Experiment code, MORSE [3], is a 3-D multipurpose neutron and gamma-ray transport code that has been in use for nearly 30 years and has undergone several evolutions during that time. Oak Ridge National Laboratory (ORNL) has two versions that are distributed by the Radiation Safety Information Computational Center (RSICC): MORSE-CGA and MORSE-SGC. MORSE-SGC is part of the SCALE [1] computer code system, both as a stand-alone program and as part of two of the shielding analysis sequences, SAS3 and SAS4.

Both SGC and CGA use the Multiple Array System (MARS) geometry package. The primary difference in the two versions is the cross-section structure. MORSE-SGC has a supergrouping capability that allows a problem to run with only part of the cross-section groups in core rather than the entire energy range. Because of the amount of memory available in today’s computers, this feature is not nearly as important now as it was when the code was originally developed. The other major difference in the two versions is that SGC has built-in routines for the source selection and estimation routines, whereas the user can supply his or her own routines and override the provided versions in CGA.

2.2 SAS4

SAS4 was developed to solve spent fuel shipping cask problems and, as a result, has an automated geometry-modeling procedure. When the SAS4 shielding analysis sequence was being developed, one of the objectives was to automate the selection of biasing parameters for MORSE and the preparation of cross-section data. As a result of this, SAS4 runs cross-section resonance-processing modules BONAMI and NITAWL and an adjoint case using the one-dimensional code XSDRNPM prior to executing the MORSE module. The adjoint XSDRNPM results are used to generate biasing parameters for MORSE.

Another feature of SAS4 is that the PICTURE program, which generates 2-D color plots, or printer plots can be run from within SAS4. A number of changes were required for MORSE-SGC to implement a new SAS4 option for surface detectors and subdetectors. Prior to these changes, SAS4 restricted the number of surface detectors to four preset locations for all of the geometry options. This update allows the use `r` to specify up to 36 surface detectors when using the MARS geometry option rather than the simplified geometry input options; furthermore, each surface can be subdivided into spatial and azimuthal segments. This option is only available when running SAS4; i.e., it is not an option when running MORSE-SGC stand-alone.

2.3 SAS3

The SAS3 shielding analysis sequence runs the cross-section modules and MORSE. At present, there is no automated selection of biasing parameters. SAS3 can, however, solve many problems that the specialized SAS4 can not handle. Examples of such problems are streaming through ventilation ducts and cask penetrations and applications to more generalized shielding problems. Currently, SAS3 or MORSE-SGC can treat any of these applications. However, the user must generate and input very detailed biasing parameters.

3 Graphical User Interfaces

One current project under development is a SCALE shielding analysis graphical user interface (GUI) for Windows 95/98/NT/2000. This GUI, known as ESPN for Easy Shielding Processor iNput, will provide an easy-to-use system to assist the occasional and inexperienced SCALE users in the setup and execution of SAS4/MORSE. The material information cross-section portion is nearly identical to that in CSPAN (Criticality Safety Input Processor for Analysis), the GUI for the CSAS criticality sequence that is already complete. CSPAN and ESPN are specifically designed for SCALE 4.4 or 4.4a on a WINDOWS PC. For ESPN, the primary development effort will be in the geometry input specifications. A preliminary version of ESPN, without the geometry input, is being tested at ORNL. CSPAN is being distributed with the SCALE 4.4a package. Both the initial release and future updates to ESPN and CSPAN can be found on the SCALE Download page (<http://www.cped.ornl.gov/scale/download.html>).

4 SCALE 5 Development

Work currently in progress on the SCALE code system includes the development of SCALE 5. Although version 4.4a, the current release of SCALE, is FORTRAN-90 compatible, it requires using several of the extensions to the language. The FORTRAN routines for version 5 will be pure FORTRAN-90 and, as such, will not require use of extensions. SCALE 5 will, however, still have some library routines written in the C language. Several new features are being added to the Monte Carlo codes.

4.1 New Features of the Criticality Safety Codes

Recent development for the SCALE 5 version of the KENO control sequences includes a new pointwise discrete-ordinates neutron-transport code called CENTRM (Continuous ENergy TRansport Model) [4] which is based on the 1-D discrete ordinates code XSDRNPM. One of the features of CENTRM is the ability to explicitly model flux distributions radially across a pin, an option that allows the user to model fuels and dissolvers in solutions containing fissile materials (e.g., a fuel pellet). CENTRM uses a 1-D point flux distribution to collapse the point cross sections read from a CENTRM point cross-section file. This method produces more accurate group cross sections. Enhancements, expected to be ready this fall, include the extension of the pointwise solution into the thermal energy range. A complete ENDF/B-V CENTRM library is available for use with ENDF/B-V group cross-section libraries. Presently, an ENDF/B-VI CENTRM library is available, but it contains no thermal data. An ENDF/B-VI multi-group cross-section libr SCALE 5 criticality control sequences will also include NITAWL-III, which contains a more sophisticated method for the resonance parameter processing. NITAWL-III is the latest variation of the modules that have served as the primary resonance self-shielding module in SCALE. The primary functional difference between NITAWL-III and its predecessor, NITAWL-II, is the capability of using multipole parameters for the resolved resonance in addition to the Briet-Wigner parameters. The multipole parameter method can be used to generate cross-section values that are equivalent to the widely used Reich-Moore data.

KENO-VI for SCALE 5 has recently been updated to include the capability to calculate volumes. SCALE 5 will have the ability to explicitly enter multiple unit cells. Currently, only one unit cell is allowed; all other material is treated as infinite homogeneous media. Dancoff factors can be incorporated in the non-unit cell materials (thus treating them as part of a unit cell) by adding them in the MORE DATA section of the problem. The ability to have multiple unit cells will allow search cases to properly modify the cross sections of any material in a unit cell during a pitch search.

4.2 Future Directions for the Monte Carlo Codes

Because unbiased Monte Carlo methods are not practical for real reactor and away-from-reactor applications which are typically large and geometrically com-

plex and which also involve significant attenuation, the development of a 3-D Monte Carlo shielding analysis sequence with automatic variance reduction is highly desirable. As indicated above, the SAS4 sequence uses the 1-D code XSDRNPM to produce biasing parameters for MORSE; however, for general-purpose 3-D shielding calculations, use of 3-D adjoint functions is necessary. For this reason, ORNL expects to develop a code sequence that uses the SN adjoint output from the 3-D discrete ordinates transport code TORT [5] to produce variance reduction parameters for use in MORSE. Development of this capability will require significant changes to MORSE and to the shielding sequence in which it is implemented. This sequence may be an update to the SAS3 sequence discussed above or it may be an additional shielding sequence. Sources of funding are being investigated; several proposals are in process. Additional biasing options for SAS3 and SAS4 are also possible, and future development projects are under consideration.

Development of additional features for the criticality safety codes will continue. In FY 2001, work is scheduled to begin on a continuous energy version of KENO V.a. As stated above, KENO3D development for KENO-VI is another ongoing project.

5 Summary

All of the codes discussed here run on multiple computer platforms, including DEC-Alpha, IBM RISC 6000 series, Sun and HP workstations, and on personal computers. Codes in the SCALE system are under configuration control and have been validated and verified. A set of shielding benchmarks has been documented in [6], and a set of criticality safety benchmarks has been documented in [7]. Both sets are available on the SCALE website (<http://www.cped.ornl.gov/scale>). A set of neutronic benchmarks for mixed oxide fuel has been calculated using the SCALE/CENTRM sequence and is documented in [8].

References

1. *SCALE: A Modular Code System for Performing Standardized Computer Analyses for Licensing Evaluation*, NUREG/CR-0200, Rev. 5 (ORNL/NUREG/CSD-2/R5), Vols. I, II, and III, March 1997. Available from Radiation Safety Information Computational Center at Oak Ridge National Laboratory as CCC-545
2. J.E. Horwedel, S.M. Bowman: *KENO3D, A Visualization Tool for KENO V.a and KENO-VI Geometry Models*, NUREG/CR-6662 (ORNL/TM-1999/284), U.S. Nuclear Regulatory Commission, Oak Ridge National Laboratory, 2000
3. M.B. Emmett: *MORSE-CGA: A Monte Carlo Radiation Transport Code with Array Geometry Capability*, ORNL-6174, Martin Marietta Energy Systems, Inc., Oak Ridge National Laboratory (April 1985)
4. M. Williams, M. Asgari: Nucl. Sci. Eng. **121**, 173 (1995)
5. W.A. Rhoades, D.B. Simpson: *The TORT Three-Dimensional Discrete Ordinates Neutron/Photon Transport Code (TORT Version 3)*, ORNL/TM-13221, Lockheed Martin Energy Research, Inc. (October 1997)

6. B.L. Broadhead, M.B. Emmett, J.S. Tang: *Guide to Verification and Validation of the SCALE-4 Radiation Shielding Software*, NUREG/CR-6484 (ORNL/TM-13277), U.S. Nuclear Regulatory Commission, Oak Ridge National Laboratory (December 1996)
7. M.B. Emmett, W. C. Jordan: *Guide to Verification and Validation of the SCALE-4 Criticality Safety Software*, NUREG/CR-6483 (ORNL/TM-12834), U.S. Nuclear Regulatory Commission, Oak Ridge National Laboratory (December 1996)
8. D. F. Hollenbach, P.B. Fox: *Neutronics Benchmarks of Mixed Oxide Fuels Using the SCALE/CENTRM Sequence*, ORNL/TM-1999/299, Lockheed Martin Energy Research Corp., Oak Ridge National Laboratory (February 2000)

The Current Status and Future Plans for the Monte Carlo Codes MONK and MCBEND

N. Smith¹, T. Shuttleworth¹, M. Grimstone¹, L. Hutton¹, M. Armishaw¹,
A. Bird¹, N. France¹, and S. Connolly²

¹ The ANSWERS Software Service, AEA Technology plc, Winfrith Technology Centre, Dorchester, Dorset DT2 8ZE, United Kingdom

² BNFL

Abstract. MONK and MCBEND are software tools used for criticality/reactor physics and shielding/dosimetry/general radiation transport applications respectively. The codes are developed by a collaboration comprising AEA Technology and BNFL, and AEA Technology's ANSWERS Software Service supplies them to customers throughout the world on a commercial basis. In keeping with this commercial nature it is vital that the codes' development programmes evolve to meet the diverse expectations of the current and potential customer base. This involves striving to maintain an acceptable balance in the development of the various components that comprise a modern software package. This paper summarises the current status of MONK and MCBEND by indicating how the task of trying to achieve this difficult balance has been addressed in the recent past and is being addressed for the future.

1 The Challenge of Commercial Software Development

MONK and MCBEND are commercial software products, a unique attribute in a market place where large-scale government support and free access is the norm. Why is this so and how can the codes survive? The reason why is easy to address. For some time, the civil nuclear industry in the traditional UK home of the codes has operated in an entirely commercial manner. Development of software is no exception. Hence for the ANSWERS codes to remain in existence they had to become commercial codes. As to how the codes have survived and indeed grown in this environment for more than a decade is perhaps less obvious.

Planning the development of MONK and MCBEND involves maintaining a difficult balancing act between many different aspects of a commercial service. We are required to:

- Develop methods to provide solutions to emerging customer problems;
- Enhance the product image to facilitate use for existing customers and attract new customers;
- Produce nuclear data libraries to meet local needs and specific requirements;
- Provide supporting productivity tools taking advantage of the capabilities of modern computing facilities;
- Enhance documentation and validation (and the means of accessing both);
- - Commit to the provision of a wide range of support services to maximise customer productivity (e.g. help-desk, consultancy, training).

For each of the above items, the individual ANSWERS customers may have widely varying requirements and priorities. The development of the ANSWERS products therefore seeks to achieve a balance, to try and meet as many of the customers' expectations as possible, within the constraints of available resources. Whether this balance is achieved or not is ultimately up to the individual customers to decide. This paper sets out our recent efforts and future plans aimed at ensuring their continued custom.

2 Background

MONK is primarily used for the solution of nuclear criticality safety and reactor physics problems. Major features such as hyper-fine energy nuclear data libraries, continuous energy collision modelling, superhistory powering and hole geometry modelling provide real application benefits to code users in terms of increased accuracy, efficiency, confidence and flexibility. MCBEND is a general-purpose radiation transport package that can calculate neutron, gamma-ray and electron transport in sub-critical systems; coupling of the different radiation types is also possible and powerful variance reduction techniques allow for wide ranging code application. With an extensive track record of use in support of nuclear operations across the whole fuel cycle, both codes provide sophisticated modelling capabilities in easy-to-use packages. Both codes are developed within a partnership between AEA Technology and BNFL.

3 Status of MONK and MCBEND

The production of MONK8 and the recent versions of MCBEND have brought into general use a number of facilities to extend the accuracy and efficiency of reactor physics, criticality and shielding analyses.

3.1 Geometry

MONK and MCBEND share a common geometry modelling package comprising two major components:

- A geometry body-based system built around hierarchically structured collections of bodies of general orientation. The collections of bodies can have simple relationships (e.g. nested or arrays) or complete freedom of overlap. Particle tracking is performed using conventional ray tracing techniques.
- A system of 'hole' geometry options that provides detailed structure and repeating configurations within the body-based system. The particle tracking in this option is performed using Woodcock tracking, which allows for a considerable increase in modelling capability and efficiency.

In combination, these options provide almost unlimited modelling capability, yet retain the simplicity of concept of the originators. Major extensions to both options have taken place in the recent past to meet emerging customer needs.

3.2 Nuclear Data

The recent past has also seen a major development of the nuclear data options available with MONK and MCBEND, particularly for neutron applications. Traditional use of UK nuclear data library-based compilations has declined in preference for more modern evaluations such as JEF2.2 [1]. In addition, other options have been provided to meet the broader international usage of the codes. A summary of the neutron options available is as follows:

- UK nuclear data library-based hyperfine energy group library (8,220 groups) using a continuous energy/angle slowing down treatment;
- JEF2.2-based hyperfine energy group library (13,193 groups) using a continuous energy/angle slowing down treatment;
- This has been followed by ENDF/B-VI-based and JENDL3-based libraries with the same characteristics as the JEF2.2-based library;
- UK-based and JEF2.2-based WIMS multigroup libraries (69 or 172 groups).

3.3 MCBEND Acceleration

For many years, MCBEND has contained an integral adjoint multigroup diffusion capability that can be used to calculate importances on an orthogonal mesh overlaying the problem space. These are used to control particle splitting/Russian roulette and weighted source sampling. In many diverse applications, this method has proved very effective in accelerating radiation transport calculations. However, there are cases, principally those dominated by voids and ducts, in which the limitations of a deterministic approach leads to inefficiencies in the Monte Carlo calculation. Alternative ways of generating importances have therefore been developed based on Monte Carlo methods [2]:

- Importance values can theoretically be estimated by sprinkling the entire problem with test sources and tracking them, with scoring samples contributing to the adjoint estimate at their birth site. Although impractical for large cases, a refinement of this technique has been implemented in MCBEND and has been assigned the name ‘recursive’.
- The adjoint flux in a given space/energy cell may be interpreted as the expected score produced by introducing a particle into that cell. An estimator based on this definition can be used during a forward calculation to score the adjoint. The results may be combined with an initial guess of the importance function to improve the efficiency of the calculation.

3.4 Major New Development

Point Energy Adjoint. An alternative approach to some problems is to perform a Monte Carlo calculation in adjoint mode. For example, detector reaction rates can be calculated by integrating the product of the adjoint function and the source function. To-date, the adjoint capability in MCBEND has been solely

a multigroup one. However, MCBEND has now been extended to provide the option of performing adjoint calculations using point energy data [2].

Reactor Burnup. The MONK code now includes a microscopic burn-up capability which enables the code to treat whole core burn-up in small reactors. In a reactor core the material compositions change continuously with time during burnup. Monte Carlo calculations are used to calculate the flux at a given time point and this flux is used to determine the reaction rates of the materials in the problem. These reaction rates are then used to calculate the new material compositions by solving the depletion equations.

Sensitivity Options. The ability to calculate the sensitivity of scored fluxes and responses to changes in cross-sections has long been a feature of MCBEND. It has been used to good effect for application uncertainty analysis and to guide data improvement studies. Three recent developments have extended the range of sensitivity calculations:

- The original first order MCBEND sensitivity approximation has been extended to cover second order terms.
- A sensitivity option has been added to MONK to enable the sensitivity of k-effective to changes in cross-sections to be determined.
- A geometry sensitivity option is available in MCBEND to calculate the flux and response sensitivity to source and model geometry changes [3].

3.5 Ease of Use

To enable our customers to make best use of the power available from the combination of Monte Carlo techniques and high performance computers, new options have been developed to aid input specification and output analysis:

- Input data parameters are available to facilitate the setting up of calculations. The use of algebraic expressions as input data is possible. Automatic calculation sequences can be specified;
- MONK and MCBEND share a common nuclide and materials database, so that standard mixtures can be easily specified. This database can be augmented by user additions and provides a link between the various nuclear data libraries used with the codes;
- Output from MONK and MCBEND can be requested in standard and customisable formats, to provide direct links with other software packages such as spreadsheets.

3.6 Productivity Tools

A range of supporting productivity tools [4] continue to be developed for use with MONK and MCBEND as follows:

- VISAGE provides detailed interactive viewing of 2D slices of a geometry model, using the tracking routines of MONK/MCBEND;

- VISTA-RAY provides detailed interactive viewing of 3D images of a geometry model, again using MONK/MCBEND tracking;
- VISTA-WIRE gives rapid interactive viewing of a wire-frame representation of a model;
- VISTA-MOVIE can be used to show animated sequences of 3D model images;
- VISTA-GRAPH enables interactive presentation of calculated results;
- VISTA-TRACK displays Monte Carlo particle trajectories;
- LAUNCHPAD is an easy to use interface for preparing calculations.

3.7 Code Structure and Infrastructure

In addition to development of the codes, data libraries and supporting tools, several changes to the code structure and infrastructure have been made:

- The codes are assembled from a collection of independent functional and service modules, for optimum developer convenience; - For the FORTRAN code components, extensive use is made of FORTRAN90 constructs, to provide significant structural simplifications;
- Embedded commentary and PDL (Programme Definition Language) is used to 'self document' the source code;
- Validation programmes continue on various fronts. The MONK programme now makes substantial use of ICSBEP [5] data;
- Commercial packages are used to prepare the software to ease customer installation;
- A modern commercial package is being used to service and monitor help-desk enquiries, to help provide the level of support expected in a commercial environment. Dedicated staff deal with enquiries from customers, with working hours scheduled to match the international nature of the business;
- The internet is being used not only to promote products but also, in a protected area, to provide an on-line information resource for customers;
- A range of computer platforms continue to be supported, the most popular being Sun/Solaris and PC/Windows;
- In addition to hardcopy, all user documentation is now provided as Adobe AcrobatTM PDFs.

4 On-Going and Future Plans

The previous section indicated the breadth of activity undertaken in the recent past for MONK and MCBEND in order to try and provide the essential balance required for successful commercial software development. However, development of both MONK and MCBEND is a continuing process and a summary of current major developments is given below.

Automatic Importance Mesh Generation. The in-built importance value generation option of MCBEND has proved very successful over the last decade or more but the requirement still exists for the code user to select the orthogonal

mesh that overlays the problem geometry. For some systems, this is not a difficult requirement but for others some automatic assistance would be of value. The latest MCBEND acceleration development is seeking to provide this assistance.

Unified Source Capability. A replacement unified source specification capability is being developed for MONK and MCBEND aimed at rationalising the existing options and providing more widely applicable implementations of variance reduction options such as source weighting. Additional user convenient features such as source contribution analysis will also be provided.

The BINGO Project. The module DICE is the collision processing engine within MONK and MCBEND; DICE assesses the outcome of particle interactions with nuclides. DICE is one of the longest-standing modules of MONK and MCBEND and despite its excellent service over many years, has been a candidate for replacement for some time. A new nuclear data library and collision processing package (BINGO) is therefore being developed for MONK and MCBEND aimed at making even better use of the available ENDF-6 format data (as used in JEFF, ENDF/B-VI and JENDL3). BINGO will exploit improvements in hardware, software and programming languages and incorporate new/extended physics modelling. In addition, the following technical developments will be implemented: fine-point cross-sections with interpolation; better unresolved resonance representations; delayed neutron treatment; enhanced thermal scattering; improved temperature capability; coupled and fully integrated $n/\gamma/e^\pm$ physics.

5 Conclusion

This paper has reviewed the current status of the uniquely commercial Monte Carlo codes MONK and MCBEND. Recent developments have been highlighted and on-going programmes outlined, all aimed firmly at meeting the diverse current and future needs of our customers. By focussing on issues as identified by our customers around the world and developing the products accordingly, we continue to strive to maintain the codes' leading edge position and develop the staff required to achieve this.

References

1. J.L. Rowlands (Editor): *The JEF2.2 Nuclear Data Library*, JEF Report No. 17
2. E. Shuttleworth, M.J. Grimstone, S.J. Chucas: 'Application of Acceleration Techniques in MCBEND'. In *Proceedings of ICRS'9, Tsukuba (October 1999)*
3. E. Shuttleworth: 'The Geometrical Sensitivity Option in MCBEND'. These Proceedings p. 603
4. M.J. Armishaw, A. Bird, H. Crofts and N. Smith: 'The Role of Graphical Supporting Tools for Monte Carlo Analysis'. These Proceedings p. 827
5. *International Handbook of Evaluated Criticality Safety Benchmark Experiments*, NEA/NSC/DOC(95)03

MCNP Capabilities at the Dawn of the 21st Century: Neutron–Gamma Applications

E.C. Selcow, G.W. McKinney, T.E. Booth, J.F. Briesmeister, L.J. Cox, R.A. Forster, J.S. Hendricks, R.D. Mosteller, R.E. Prael, A. Sood, S.W. White

Los Alamos National Laboratory, Diagnostic Applications Group, X-5, P.O. Box 1663, MS F663, Los Alamos, NM 87545, USA

Abstract. The Los Alamos National Laboratory Monte Carlo N-Particle radiation transport code, MCNP, has become an international standard for a wide spectrum of neutron-gamma radiation transport applications. These include nuclear criticality safety, radiation shielding, nuclear safeguards, nuclear oil-well logging, fission and fusion reactor design, accelerator target design, detector design and analysis, health physics, medical radiation therapy and imaging, radiography, decontamination and decommissioning, and waste storage and disposal. The latest version of the code, MCNP4C [1], was released to the Radiation Safety Information Computational Center (RSICC) in February 2000. This paper describes the new features and capabilities of the code, and discusses the specific applicability to neutron-gamma problems. We will also discuss some of the future directions for MCNP code development.

1 Introduction

MCNPTM is a general purpose, three-dimensional, time-dependent, continuous-energy Monte Carlo fully-coupled N-Particle transport code. Neutrons are modeled from 0–20 MeV, and photons and electrons are modeled from 1 keV to 100 GeV. The high fidelity simulation capability that MCNP provides is widely used as a standard for predicting the interaction of radiation with matter in complex systems. This simulation tool, used for design, experimentation, and safety assessments, often eliminates the need for expensive hardware manufacturing and testing.

The overall development philosophy revolves around the edicts of quality, value, and features. MCNP4C contains ten new features [2,3] since version 4B, including macrobodies, unresolved resonances, superimposed weight windows, perturbation enhancements, electron physics enhancements, delayed neutrons, ENDF/B-VI upgrade, alpha eigenvalue, parallelization advances, and PC enhancements. The portability of the code is demonstrated by the support of nine computer platforms, including SGI IRIX, Sun Solaris, DEC Ultrix, HP HPUX, IBM AIX, Cray Unicos, Linux, and Windows 9x/NT. These new features and capabilities are summarized in the next section, followed by the highlights of a recent MCNP timing study and a description of some of the new developments for future versions of the code. Finally, several neutron-gamma applications of MCNP are presented.

2 New Capabilities in MCNP4C

2.1 Macrobodies

Macrobodies are a geometry feature for MCNP, which bears similarity to the combinatorial geometry modeling used in MORSE [4], KENO [5], and the Integrated Tiger Series (ITS) [6] codes. These new geometries supplement MCNP's fully three-dimensional surface-sense geometry that is capable of modeling any space bounded by first and second degree surfaces (conic sections) and fourth degree elliptical tori. The usage of macrobodies can significantly reduce the amount of input required to describe some geometric configurations.

2.2 Unresolved Resonances

MCNP4C has added unresolved resonance range probability tables [7]. The statistical nature of this treatment may impact the calculation of criticality eigenvalues, especially in cases where neutron resonance self-shielding is important. In particular, it can make significant differences in the calculation of the criticality eigenvalue for plutonium critical assemblies with intermediate spectra, and substantial increases in reactivity for systems with a large amount of U [2,3,8] and intermediate spectra.

2.3 Superimposed Weight Windows

A major improvement in variance reduction has been implemented with the superimposed mesh weight window generator [8,9]. The geometry specification for importance functions can now be specified with an importance mesh superimposed on the regular geometry. This superimposed mesh can be in either rectangular or cylindrical geometry and eliminates the need to define finely detailed subdivided geometries in order to specify smoothly changing importances. In addition, the weight window generator can determine the optimum importance function for the superimposed mesh.

2.4 Perturbation Enhancements

The perturbation capability used in MCNP4B has been upgraded to enable perturbations of cross-section dependent tallies [10]. This significantly facilitates the calculation of perturbations to reaction rate tallies that depend on cross sections, as well as perturbations to k_{eff} values.

2.5 Electron Physics Enhancements

The electron physics enhancements include upgrading the radiative stopping powers to the Seltzer model found in the ITS 3.0 code, adding a new electron library, EL3, and the ITS 3.0 density correction and bremsstrahlung production models. In addition, the sampling of photons produced from a bremsstrahlung

event has been improved with enhanced variance reduction. Lastly, the fluorescence and k x-ray relaxation models in MCNP have been made more consistent with each other.

2.6 Delayed Neutrons

MCNP4C has added a time-dependent delayed neutron treatment [11]. This has improved the accuracy of criticality calculations using either fixed sources or k_{eff} (kcode) calculations. The default for eigenvalue calculations is a natural sampling of both prompt and delayed neutrons. A delayed neutron biasing scheme was added due to the low probability of delayed neutron occurrence.

2.7 ENDF/B-VI Upgrade

The nuclear data cross sections for MCNP4C have been improved with the addition of new ENDF/B data library sampling schemes. This has enabled utilization of the forthcoming ENDF/B-VI revision 5 data. These new angular sampling distributions have been added to the MCNP ACE format and represent differential angular cross section information in finer detail than with the existing thirty-two equi-probable bin distribution. In addition, neutrons and photons are now handled consistently within the energy-sampling portion of the ENDF laws 4, 44, and 61, which use emission-energy tables.

2.8 Alpha Eigenvalue

MCNP4C now includes an alpha eigenvalue search in addition to the criticality eigenvalue search [12]. This time dependent eigenvalue search is characterized by $e^{\alpha t}$, where the neutron population evolves with time from an initial state. This can be used to describe a subcritical, critical, or supercritical system. This feature allows positive and negative eigenvalue searches, as well as a fixed positive or negative alpha value to be used in a k_{eff} calculation.

2.9 Parallelization Advances

MCNP4C has further enhanced the capability to compute on multiple processors. The ability to perform high fidelity simulations on massively parallel machines will enable users to enhance their predictive capability of radiation transport problems in times approaching real time. The current version of the code supports distributed-memory multiprocessing (DMMP), shared-memory multiprocessing (SMMP), and the combined modes. DMMP is currently supported only through PVM [13], but future versions will also support MPI [14].

2.10 PC Enhancements

The operation of MCNP4C on personal computers now uses the Compaq Visual Fortran 90 compiler [15] or the Lahey Fortran 95 compiler [16]. The X-windows graphics option is available with either compiler. In addition, the QuickWin graphics option is available with the Compaq Visual Fortran compiler and the Winteracter graphics option is available with the Lahey Fortran compiler.

3 Results of Recent Timing Study

A timing study has recently been performed for MCNP4C [17] in which thirteen computer platforms were tested with MCNP4C using sequential processing. The results show that the fastest machine is the Compaq Alpha XP1000, with the 800 MHz PC showing comparable performance. The fastest machine in the last timing study for version 4B [18] was the DEC Alphastation 500, a predecessor to the XP1000. The timing performance between these two machines for MCNP4C is within a factor of two. In the last timing study, which was performed in 1997, the tested PC was approximately a factor of four slower than the DEC Alphastation 500. The recent study also highlighted that the MCNP timing comparisons are test problem dependent. Overall, the timing study illustrated the fact that the developments in personal computers have made them an attractive option for the international MCNP user community.

4 Future Directions

The next version of MCNP will contain several new and enhanced features, including additional macrobodies, charged particle transport [19], further upgrades to the parallel processing capabilities, and an interactive plotter [20] which significantly enhances the flexibility of geometry plotting with point-and-click features. The additions to the parallelization features include the implementation of DMMP with MPI and SMMP with OpenMP [21]. The MCNP Software Quality Assurance (SQA) [22] practices, configuration management, regression testing, and bug tracking are also being upgraded. Further MCNP modernization includes converting the code from Fortran 77 to Fortran 90.

5 Neutron-Gamma Applications

There exists a wealth of applications for neutron and photon transport with MCNP. This section presents examples of four selected applications.

5.1 Radiography

MCNP has been used to design and test a number of concepts for neutron radiography. Radiography can be used for the interrogation of materials to detect

specific elements or combinations of materials. The specific applications include inspection of packages or luggage for explosives, detecting landmines in battle fields, and detecting impurities in the environment. A concept was developed at Brookhaven National Laboratory (BNL) for thermal neutron imaging [23] that can be used to detect explosives in packages. Neutron radiography has also been considered for the detection of low concentrations of halogens and heavy metals in plastics. The specific interest was to produce low-impurity plastics and minimize the economic and environmental burden for disposal.

There are several improvements for MCNP4C that favorably impact the modeling and execution of these problems. These include macrobodies to simplify the input, parallelism to speed-up the time to produce results, and the superimposed mesh weight window generator to increase tally convergence.

5.2 Medical Applications

MCNP has been used for a variety of medical applications, including therapy, imaging, and the measurement of body composition. Monte Carlo analysis has been used to design collimator/filter systems for Boron Neutron Capture Therapy (BNCT) facilities, shielding systems for health physics concerns in therapy and imaging systems, and dosimetry predictions. Specific anatomical structures of different organs can be well represented and the shielding/detector systems can be efficiently modeled.

There have been two different clinical trials for BNCT, one at BNL and the other at the Massachusetts Institute of Technology (MIT), both using reactors for the neutron source to treat brain cancer. MIT has also treated skin cancer. There are, however, alternate sources of neutrons, such as that from accelerator systems. One concept for this utilizes an array of pulsed neutron generators to irradiate a tumor [24]. Figure 1 shows an MCNP cross sectional view of an array of twelve pulsed neutron generators irradiating a brain tumor in the center. The 14 MeV neutrons are slowed down to epithermal energies with the use of a collimator/filter system, shown as concentric rings surrounding the tumor in Fig. 1.

Monte Carlo analysis can also be used in three-dimensional treatment planning. The advantages of Monte Carlo include the ability to model small anatomical heterogeneities that are often obscured in conventional treatment planning techniques. The principal criticism of using Monte Carlo for this purpose is the significant amounts of computer time required to track the large number of particle histories needed for a converged answer. The advances in multiprocessing in MCNP4C together with the development of faster microprocessor chips help to counter this criticism and make Monte Carlo a viable tool for three-dimensional treatment planning.

MCNP has also been used to simulate the images from Single Photon Emission Computed Tomography (SPECT). The specific interest is to determine scatter and attenuation correction factors with MCNP that are important for the clinical application of SPECT and Positron Emission Tomography (PET) imag-

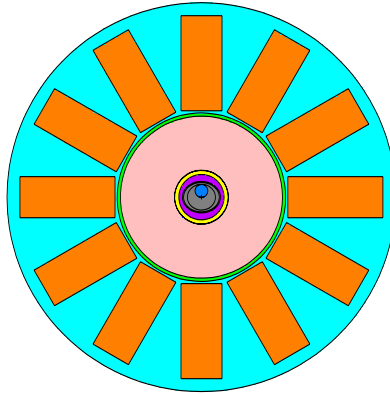


Fig. 1. Concept for BNCT using Pulsed Neutron Generators as the Neutron Source

ing. Detailed anthropomorphic models of the body have been constructed with MCNP for this purpose.

Another medical application of MCNP was the design of a facility for body composition at St. Luke's Roosevelt hospital in New York [25]. This is a concept for in-vivo neutron activation that has been clinically implemented at St. Luke's to determine the amount of nitrogen and carbon in the human body. This is used as an important signature to monitor the advancement of several diseases such as AIDS and cancer.

Several advances in MCNP4C improve these medical applications, including macrobodies, parallelism, and the improved nuclear physics with the ENDF data upgrades.

5.3 Criticality experiments

MCNP has been used to design and benchmark nuclear criticality experiments. The benchmarked quantities include criticality, spectra, flux and power profiles, differential worths, and temperature coefficients. Figure 2 is a MCNP cross sectional view of a critical experiment that was performed at Sandia National Laboratories to test the neutronics of a nineteen element particle bed reactor concept [26].

The use of MCNP4C features, such as macrobodies, alpha eigenvalue search, perturbation improvements, unresolved resonances, delayed neutrons, improved ENDF data and parallelism, will benefit these calculations.

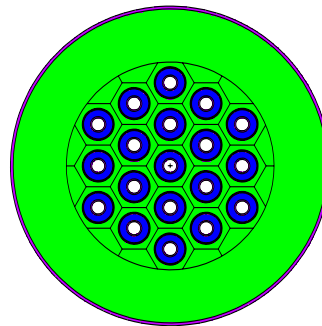


Fig. 2. Cross Sectional view of Nineteen Element Critical Experiment of Particle Bed Reactor Concept

5.4 Aerospace Applications

There have been several concepts for space nuclear thermal propulsion. One example is a program from the early 1990's for a particle bed nuclear propulsion concept. Figure 3 is a MCNP elevation view of a particle bed reactor rocket concept designed to fly to Mars [27]. The MCNP4C improvements listed above for critical experiments will also benefit this application, in addition to the utilization of the mesh-based weight window generator to expedite the dose and component heating computations.

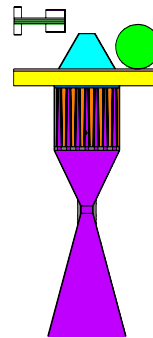


Fig. 3. Elevation view of a Rocket Ship Powered by a Particle Bed Reactor

6 Summary

MCNP continues to provide an invaluable modeling and simulations tool for a wide spectrum of radiation transport applications. The code development efforts focus on enhancing the physics features as well as upgrading the code to take advantage of the evolving capabilities in computer technologies. This will further enable users throughout the 21st century to simulate more complex problems, with improved fidelity, and in significantly faster time periods. These code development efforts are conducted in an environment that revolves around quality.

References

1. J.F. Briesmeister, Editor: *MCNPTM – A General Monte Carlo N-Particle Transport Code, Version 4C*, Los Alamos National Laboratory Report LA-13709-M (April 2000)
2. G.W. McKinney et al.: ‘MCNP Applications for the 21st century’. In *Proceedings of the SNA 2000 Conference*, (Tokyo, Japan), LA-UR-00-4098 (September 2000)
3. J.S. Hendricks: ‘Advances in MCNP4C’. In *Proceedings of the Conference on Radiation Protection for our National Priorities*, (Spokane, Washington), LA-UR-00-2643 (September 2000)
4. M.B. Emmett: *The MORSE Monte Carlo Radiation Transport Code System*, ORNL-4972 (February 1975); ORNL-4972/R1 (February 1983); ORNL-4972/R2 (July 1984)
5. L.M. Petrie et al.: *KENO V.a: An Improved Monte Carlo Criticality Program with Supergrouping*, NUREG/CR-0200 (ORNL/NUREG/CSD-2/R6) (March 2000)
6. J.A. Halbleib et al.: *ITS Version 3.0: The Integrated TIGER Series of Coupled Electron/Photon Monte Carlo Transport Codes*, Sandia National Laboratories Report SAND91-1634 (March 1992)
7. L.L. Carter et al.: *New Probability Table Treatment in MCNP for Unresolved Resonances*, 1998 Radiation Protection and Shielding Division Topical Conference on Technologies for the New Century, Sheraton Music City, Nashville, TN, vol. II, p. 341 (April 1998)

8. L. Liu, et al.: Nuclear Science and Engineering **125**, 188 (1997)
9. C. N. Culbertson: et al.: *Assessment of MCNP4C Weight Windows*, Los Alamos National Laboratory Report, LA-13668 (December 1999)
10. J.S. Hendricks et al.: 'MCNP Perturbation Capability for Monte Carlo Criticality Calculations'. In *Proceedings of the Sixth International Conference on Nuclear Criticality Safety, September 20-24, 1999, Palais des Congres, Versailles, France, Volume 1, pg 269-277 (1999)*
11. C.J. Werner: 'Delayed Neutron Model in MCNP', submitted to Progress in Nuclear Energy (Special Issue on Delayed Neutron Research) (2000)
12. D. Brockway et al.: 'Monte Carlo Eigenvalue Calculation', Lecture Notes in Physics, *Monte Carlo Methods and Applications in Neutronics, Photonics, and Statistical Physics*, Proceedings, Cadarache Castle, France, 1985 (Springer-Verlag, Berlin 1985)
13. A. Geist. et al.: *PVM 3 User's Guide and Reference Manual*, ORNL/TM-12187 (1993)
14. <http://www-unix.mcs.anl.gov/mpi>
15. <http://www5.compaq.com/fortran>
16. <http://www.lahey.com>
17. E.C. Selcow et al.: 'Quadrennial MCNP Timing Study'. In *Proceedings of the Conference on Radiation Protection for our National Priorities*, (Spokane, Washington), LA-UR-00-3103 (September 2000)
18. H.E. McLaughlin et al.: Nucl Sci. Eng. **129**, 311 (1998)
19. H.G. Hughes et al.: 'Recent Developments in MCNPX', *Proceedings of the Second International Topical Meeting On Nuclear Applications of Accelerator Technology, 281, Gatlinburg, TN, (September 1998)*
20. J.S. Hendricks: 'Point-and-Click Plotting with MCNP', in *Proceedings of the Conference on Radiation Protection for our National Priorities*, (Spokane, Washington), LA-UR-00-2642 (September 2000)
21. <http://www.openmp.org>
22. H.M. Abhold et al.: *MCNP Software Quality Assurance Plan*, LA-13138 (April 1996)
23. P.E. Vanier et al.: 'A Thermal Neutron Source Imager Using Coded Apertures', *Proceedings of the 36th Annual Meeting of the Institute of Nuclear Materials Management, Palm Desert, CA, 24*, Journal of Nuclear Materials Management, pp.842-847, (1995)
24. E.C. Selcow et al.: *Medical Physics Program Development*, Laboratory Directed Research and Development, Annual Report, Brookhaven National Laboratory (December 1997)
25. E.C. Selcow et al.: *Final Report on Monte Carlo Simulation Work to Provide Design Guidance for the St. Luke's PGNA Facility*, Advanced Energy Systems, Inc. Medford, NY, (October 1999)
26. E.C. Selcow et al.: 'MCNP Benchmark Analyses of Critical Experiments for the Space Nuclear Thermal Propulsion Program'. In *Proceedings of the 10th Symposium on Space Nuclear Power Systems, Albuquerque, NM, (January 1993)*
27. E.C. Selcow et al.: *Component Shielding Requirements for Mars Mission*, The Case for Mars IV Conference, Boulder, CO, (June 1990)

TRIPOLI-3: A Neutron/Photon Monte Carlo Transport Code

J.C. Nimal, T. Vergnaud

Commissariat à l'Energie Atomique, Service d'Etudes de Reacteurs et de
Mathematiques Appliquees, DRN/DMT/SERMA/LEPP, 91191 Gif sur Yvette cedex,
France

1 Introduction

The present version of TRIPOLI-3 [1–3] solves the transport equation for coupled neutron and gamma ray problems in three dimensional geometries by using the Monte Carlo method. This code is devoted both to shielding and criticality problems. The most important feature for particle transport equation solving is the fine treatment of the physical phenomena and sophisticated biasing technics useful for deep penetrations. The code is used either for shielding design studies or for reference and benchmark to validate cross sections. Neutronic studies are essentially cell or small core calculations and criticality problems. TRIPOLI-3 has been used as reference method, for example, for resonance self shielding qualification.

Let respectively T and C be the transport and the collision kernel of the Boltzmann equation and Φ and S the angular and energetic distributions of flux and sources respectively:

$$T^{-1} \Phi = \Omega \text{grad} \Phi(\mathbf{r}, E, \Omega) + \Sigma_T(\mathbf{r}, E) \Phi(\mathbf{r}, E, \Omega) \quad (1)$$

$$C \Phi = \int_0^\infty dE' \int \int_{4\pi} d\Omega' \Phi(\mathbf{r}, E', \Omega') C(E', \Omega' \rightarrow E, \Omega)$$

TRIPOLI-3 can solve :

- problems with external sources, stationary or time dependent, for neutrons and gamma rays :

$$\frac{1}{v} \frac{d\Phi}{dt} + T^{-1} \Phi = C\Phi + S \quad (2)$$

- criticality problems with calculations of the multiplication factor and neutron distribution according to the fundamental mode :

$$T^{-1} \Phi = C\Phi + \frac{P\Phi}{K_{\text{eff}}} \quad \text{where } P \text{ is the neutron production by fission operator.}$$

- subcritical problems with both multiplication by fissions and external sources ($K_{\text{eff}} < 1$):

$$T^{-1} \Phi = C\Phi + P\Phi + S$$

2 Geometry Description

The geometry is a gathering of any volumes limited by first and second degree surfaces. Then very general configurations can be represented. Geometries can be repetitive by rotation, symmetry and translation. Leakage or albedo conditions can be given on the outer boundaries.

3 Neutron Nuclear Data

Neutron cross sections come from ENDF/B/6. Two libraries are available respectively with 315 or 3209 energy groups, between 20 MeV and 1.E-05 eV. The multigroup representation is completed with the probability tables [4].

The probability table method allows to treat with an excellent accuracy the resonance of the cross sections. With a fine multigroup structure, we can treat almost exactly core neutronic problems without hypothesis of the selfshielding.

The cross section representation using the probability table method was proposed independently by NICOLAEV (1970) and LEVITT (1972). The principles of this method were developed some years ago by P. RIBON at Saclay [5].

The probability method uses a multigroup structure. But contrary to the classical method the probability table method assumes several values of the cross section in one group associated with their probabilities of appearance.

Thus, for each interaction X , for each energy group g , there are N cross section values $\sigma_{X,g,i}$ with N occurrence probabilities $p_{X,g,i}$. The suffix i takes the values from 1 to N . The $2N$ values $\sigma_{X,g,i}$ and $p_{X,g,i}$ are determined by solving the following system :

$$\sum_{i=1}^N p_{X,g,i} \times \sigma_{X,g,i}^m = \int_{E_g}^{E_g-1} \sigma^m(E) dE \quad m \in \{-N+1, -N+2, \dots, N-1, N\}$$

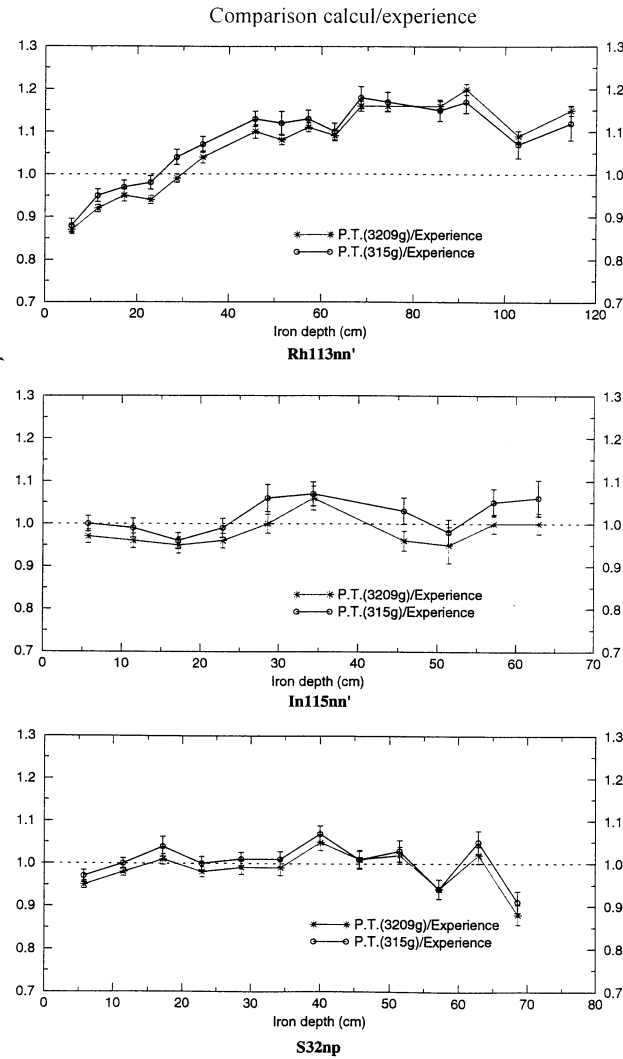
In this relation, m takes the values from $-N+1$ to N . E_g and E_g-1 are the energy boundaries of the group g .

Comparisons with punctual representation of the cross sections have been made successfully. The used reference code was TRIPOLI 4. The cases we have treated contained U^{238} , U^{235} , Pu^{239} and Pu^{240} . Uranium oxide pins, surrounded by water, were used for this comparison. The reaction rates, such as fission and capture, were compared energy group by energy group.

Neutron energy and direction are studied in a continuous way and scattering laws on each nuclide are differentiated. For neutron, TRIPOLI-3 treats continuous and discrete level inelastic scattering, (n,2n), (n,3n), elastic scattering, capture and fission. For thermal range, there are 70 thermal groups below 5eV. Direction and energy are sampled using the $S(\alpha, \beta)$ functions deduced from the frequency spectrum or using the free gas model for structural materials.

The following example (see figure) is relative to a benchmark interpretation. It is the matter of the iron benchmark ASPIS made at Winfrith. A one meter

thick iron block is put behind a fission converter plate. Then, the source has a pure fission spectrum and a well known spatial distribution. The figure represents comparisons between TRIPOLI3 calculations and experiments made with activation detectors such as Rh103(n,n'), In115(n,n') and S32(n,p). Two libraries issued from ENDF/B6 are used, the first one is described with 315 energy groups and probability tables, the second one with 3209 groups with probability tables too.



4 Photon Data

Photon cross sections come from JEF2 evaluation. The representation has 220 energy groups between 15 MeV and 1 keV. Like neutron energy, the photon

energy is followed continuously and the interactions taken into account are : coherent and incoherent scattering, photoelectric and pair effects. The photon direction is sampled using 64 equal probability intervals.

5 Biasing Technic Principles

Deep penetration studies need biasing technics to reduce the variance on the results with consuming a reasonable computer time. In TRIPOLI-3 a continuous importance function $I(\mathbf{r}, E, \boldsymbol{\Omega})$ is assigned to each point of the phase space . In other words, a particle weight $W(\mathbf{r}, E, \boldsymbol{\Omega})$ is assigned after each event undergone by the particle. This weight is the inverse of the importance.

For each zone Z_J , this weight is factorized as a product of a function $\pi_1(\mathbf{r})$ by two functions $\pi_2(\Omega)$ and $\pi_3(E)$. The relation (3) shows the expression of the assigned weight $\pi(P)$:

$$\pi(P) = \pi_1(\mathbf{r})^{\chi(E)} \times \pi_2(\boldsymbol{\Omega}) \times \pi_3(E) \quad P = (\mathbf{r}, \boldsymbol{\Omega}, E) \quad \mathbf{r} \in Z_j \quad (3)$$

P symbolizes the general phase point. We recall that the assigned weight is the inverse of the well known importance function $I(P)$. The principle of TRIPOLI 3 biasing is to make a change of the solution Φ (unknown function) by means of the relation (4) :

$$\Phi^+ = \frac{\Phi(P)}{\pi(P)} = I(P) \Phi(P) \quad (4)$$

Φ^+ is the flux of biased particles, i.e., for particles weighted by $\pi(P)$. π decreases like the unknown solution Φ , since the importance I increases asymptotically like the inverse of the flux from the source to the detector. Thus, the non analog flux Φ^+ is almost constant between the source and the tally: the biased particles undergone a very small attenuation.

Φ is solution of the integro-differential transport equation (5) :

$$\begin{aligned} & \boldsymbol{\Omega} \text{grad} \Phi(\mathbf{r}, E, \boldsymbol{\Omega}) + \Sigma_T(\mathbf{r}, E) \Phi(\mathbf{r}, E, \boldsymbol{\Omega}) \\ &= \int_0^\infty dE' \int \int_{4\pi} d\boldsymbol{\Omega}' \Phi^+(\mathbf{r}, E', \boldsymbol{\Omega}') \times C(E', \boldsymbol{\Omega}' \rightarrow E, \boldsymbol{\Omega}) + S(\mathbf{r}, E, \boldsymbol{\Omega}) \end{aligned} \quad (5)$$

If we put the expression (4) of Φ in the last equation (5), we obtain the equation (6) :

$$\begin{aligned} & \boldsymbol{\Omega} \text{grad} \Phi^+(\mathbf{r}, E, \boldsymbol{\Omega}) + \Sigma_T^+(\mathbf{r}, E) \Phi^+(\mathbf{r}, E, \boldsymbol{\Omega}) \\ &= \int_0^\infty dE' \int \int_{4\pi} d\boldsymbol{\Omega}' \Phi(\mathbf{r}, E', \boldsymbol{\Omega}') \times C^+(E', \boldsymbol{\Omega}' \rightarrow E, \boldsymbol{\Omega}) + S^+(\mathbf{r}, E, \boldsymbol{\Omega}) \end{aligned} \quad (6)$$

This equation (6) will be solve using Monte Carlo. It is important to notice that Φ^+ has no attenuation between the source and the tally; therefore the Monte Carlo game will be very efficient. It can be noted that (5) and (6) have

the same form. Φ satisfies the transport equation with natural nuclear constants. Φ^+ satisfies a transport equation with biased cross sections. This last equation is solved using a non analog game, still called biased game. In the biased equation (6) Σ_T^+ , C^+ and S^+ are respectively defined by the relations (7), (8) and (9) :

$$\Sigma_T^+ = \Sigma_T - K \Omega \Omega_0 \quad (7)$$

$$K = \frac{|\mathbf{grad}\pi_1(\mathbf{r})|}{\pi_1(\mathbf{r})} \quad (7\text{bis})$$

$$\Omega_0 = -\frac{\mathbf{grad}\pi_1(\mathbf{r})}{|\mathbf{grad}\pi_1(\mathbf{r})|} \quad (7\text{ter})$$

$$C^+(\mathbf{E}' \rightarrow \mathbf{E} \setminus \mathbf{r}) = C(\mathbf{E}' \rightarrow \mathbf{E} \setminus \mathbf{r}) \times \frac{\pi_2(\Omega') \pi_3(E')}{\pi_2(\Omega) \pi_3(E)} \quad (8)$$

$$S^+ = \frac{S(P)}{\pi(P)} = S(P) \times I(P) \quad (9)$$

The non analog simulation is carried out such as the particle weight remains in accordance with the assigned weight $\pi(P)$. The particle track is sampled with an adapted exponential transform. The local parameter of this exponential transform is K, defined by (7bis), which allows to define the biased cross section Σ_T^+ (7). The vector Ω_0 is the local direction of interest. This vector shows the shortest way, in optical term, to reach the tally leaving the location \mathbf{r} .

We can prove that the best choice for the function $\pi_2(\Omega)$ is given by the relation (12) :

$$\pi_2(\Omega) = \frac{\Sigma_T^+(\mathbf{r}, \mathbf{E})}{\Sigma_T(\mathbf{r}, \mathbf{E})} \quad (12)$$

This choice assumes that the weight at each collision is independent of the direction of the incoming particle.

In TRIPOLI 3, the weight variation versus energy is initialized by the user, locally proportional to $\frac{1}{E^\alpha}$. During the simulation, this function $\pi_3(E)$ is adjusted by TRIPOLI itself, to provide that the particle population size is almost constant during the slowing down in energy.

Concerning the collision biasing parameters after collision (energy and direction), they are sampled according to the biased collision kernel C^+ . An iterative rejection technique is used to sample the direction and energy after collision versus the parameters before collision. This collision biasing is only useful if the parameter K is close to Σ_T . In this case, Σ_T^+ can be very small and the biased track length can be very long near the direction of interest. In other case, if Σ_T^+ is not too small, no collision biasing is needed. It is necessary to notice that this collision biasing is time consuming. In TRIPOLI 3, the number of iterations used in the rejection technique is associated to the presence of negative resonances.

The most important problem is to define the importance function. There are two ways to define the importance function in TRIPOLI 3. The first one is the old way which consists to define analytically the shape of the equiweight surfaces in each set of volumes. The second one is completely automatic and is used now almost exclusively. In this second way, TRIPOLI-3 carries out a three dimensional discretization in meshes. A removal cross section data base is proposed and adjustable to provide the users with the K values. The INIPOND module calculates the importance at each node by determining the shortest optical way to reach the tally. This importance distribution is close to the solution of the adjoint problem.

This automatic importance determination is easier to implement and very useful.

6 Check Up and Vizualisation

TRIPOLI-3 allows to test the geometry input data : vizualisation of sections according to any plane, dimension of all volumes found along straight lines, recovered volumes or hole in geometrical definition. The code permits to help the user by plotting the equiweight surfaces. TRIPOLI-3 vizualises also the collisions undergone by a particle sample with a color which depends on the particle energy.

Post treatment routines are available and make easier the user task :

- several calculations can be run on different workstations , then be managed to obtain a better statistical accuracy ; it is a kind of “parallelism” ;
- result values can be printed directly on geometrical sections.

7 Availability

The version TRIPOLI-3.5 is unrestricted and will be available at the end of this year; the package is still prepared by the NEA Data Bank. Two languages will be possible: English and French.

8 Acknowledgment

The authors thank J. Bord and A. Tsilanizara for the help during typing.

References

1. L. Bourdet, S. Katz, J.C. Nimal, T. Vergnaud: *Programme de Monte Carlo a 3 dimensions polycinetique TRIPOLI* ICRS 4 (Paris 9-12 Octobre 1972), in French
2. J.C. Nimal et al.: *TRIPOLI 1 Energy dependent Three Dimensional Monte Carlo Program* ORNL -tr-4085 Translated by Dr Ernest G. Silver for RSIC ORNL Tennessee USA , June 1976
3. J.C. Nimal, T. Vergnaud: Prog. in Nucl. Energy **24**, 195 (1990)
4. S.H. Zheng, T. Vergnaud, J.C. Nimal: Nucl. Sci. and Eng. **128**, 321 (1998)
5. P. Ribon, J.M. Maillard: *les tables de probabilite, application au traitement des sections efficaces pour la neutronique*, Note CEA N2485 (1986)

Modern Nuclear Data for Monte Carlo Codes

R.C. Little, S.C. Frankle, M.C. White, R.E. MacFarlane, Ch.J. Werner, and J.M. Campbell

Los Alamos National Laboratory, Los Alamos NM 87545, USA

1 Introduction

Much emphasis has been placed on the fact that the explosion in computer power has enabled Monte Carlo transport simulations to be performed that were previously impractical. Much less attention has been given to the idea that simply being able to calculate hundreds of millions, or even billions of particle histories may not ensure an accurate solution if the simulation is limited by nuclear data approximations inherent in the Monte Carlo code.

The purpose of this paper is to describe several such nuclear data approximations that have recently been eliminated (or mitigated) from the MCNP family of codes [1,2] and associated nuclear data libraries. Specific examples described are probability tables in the neutron unresolved resonance region, delayed neutrons from fission, secondary charged particles from neutron collisions, photonuclear physics, table-based charged-particle transport, and improvements in secondary scattering representations. We will also describe remaining nuclear data approximations in MCNP and the prospects for addressing them.

2 Unresolved Resonance Probability Tables

The neutron unresolved resonance range is that energy region between low neutron energies, where cross sections are derived from explicit resonance parameters, and high neutron energies, where cross sections are relatively smooth and are obtained from slowly-varying tabulations. It is an energy region where experimentalists have difficulty resolving individual resonances. Therefore, nuclear data evaluations in ENDF format [3] often provide statistical information in this energy range, including average level spacings and average neutron, radiative, fission, and competitive widths. As examples, the unresolved resonance range in ENDF/B-VI extends from 2.65 to 100 keV for ^{184}W , from 2.25 to 25 keV for ^{235}U , and from 10 to 149 keV for ^{238}U .

Versions of MCNP up through and including 4B did not take full advantage of the unresolved resonance data provided by evaluators. Instead, smoothly-varying average cross sections were used in the unresolved range. As a result, any neutron self-shielding effects in this energy range were unaccounted for. Better utilizations of unresolved data have been known and demonstrated for some time [4,5], and in MCNP Version 4C the probability table treatment was incorporated [6].

In this model, a processing code (NJOY [7]) is used to generate ladders of resonances that obey the chi-square distributions for widths and Wigner distribution for spacing. Cross sections are sampled from the ladders at randomly selected energies and accumulated into probability tables until reasonable statistics are obtained. MCNP then samples the cross sections from these probability tables when a neutron is in the unresolved region. A data library for MCNP including probability tables for 27 isotopes has been generated and distributed [8].

Calculations for a variety of uranium and plutonium criticality benchmarks have been performed with and without the probability-table treatment [9]. Small but significant reactivity changes are seen for plutonium and ^{233}U systems with intermediate spectra. More importantly, substantial reactivity increases can be obtained for systems with large amounts of ^{238}U and intermediate spectra when the probability-table method is used.

3 Delayed Neutrons from Fission

A small but important fraction of the neutrons emitted in fission events are delayed neutrons, emitted as a result of fission-product decay at times much later than prompt fission neutrons. MCNP users have always been able to specify whether or not to include delayed fission neutrons by using either total nubar (prompt plus delayed) or prompt nubar only. However, in versions of MCNP up through and including 4B, all fission neutrons (whether prompt or delayed) were produced instantaneously and with an energy sampled from the spectra specified for prompt fission neutrons.

For many applications this is adequate. However, it is another example of a data approximation that is unnecessary. Therefore, Version 4C of MCNP allows delayed fission neutrons to be sampled (either analog or biased) from time and energy spectra as specified in nuclear data evaluations. There are two impacts. One is that the delayed neutron spectra are softer than the prompt spectra. The second is that experiments measuring neutron decay after a pulsed source can now be modeled with MCNP because the delay in neutron emission following fission is properly accounted for. A library based on ENDF/B-VI including detailed delayed fission neutron data for 20 isotopes has been prepared and is part of the MCNP 4C data distribution package.

Reference 10 describes the impact of sampling delayed neutron energy spectra on reactivity calculations. As expected, most of the reactivity impacts are very small, although changes of 0.1-0.2% in k_{eff} were observed. Overall, using the delayed neutron spectra produced small positive reactivity changes for most fast and intermediate HEU systems and small negative changes for some systems in which a significant fraction of the fissions occurs in ^{238}U .

4 Neutron-Induced Charged Particles

All versions to date of MCNP assume that charged particles produced by neutron collisions are deposited locally. This assumption has been eliminated, however, in the MCNPX code. In MCNPX, neutron induced charged particles (isotopes of hydrogen and helium) are sampled and banked for subsequent transport at the option of the user.

This capability was enabled by utilization of changes in the ENDF6 format that allowed evaluators to fully specify charged-particle reaction products. In particular, Chadwick and Young at Los Alamos have produced over 40 neutron evaluations to 150 MeV in ENDF6 format [11]. In these evaluations, they include production cross sections and energy-angle correlated spectra for secondary light particles. The format of MCNP neutron data was modified to include secondary charged-particle data, and NJOY was updated to process evaluated data into this new format. Implementation in MCNPX is described in [12]. A library based upon Los Alamos evaluations including neutron-induced charged particle data for 41 isotopes has been prepared and is part of the MCNPX 2.1.5 distribution.

One additional aspect warrants mention. Whereas previous MCNP neutron transport had assumed that the energies of all secondary charged particles would be deposited locally, users of MCNPX are now given flexibility to decide whether to transport some or all of the light charged particles. This required expansion of the MCNP heating (energy deposition) values to include not only the total, but also the partial contributions due to each secondary charged particle. In MCNPX if a particular charged particle is being transported, its contribution to the heating is subtracted from the total. After production, of course, the energy of the charged particle itself may be deposited elsewhere in the geometry as a result of transport.

5 Photonuclear Physics

MCNP through Version 4C and MCNPX through Version 2.1.5 account for only photoatomic processes; photonuclear physics is completely ignored. This limitation will be removed in MCNP 4D and MCNPX 2.2.

Substantial work to produce complete nuclear data evaluations for incident photons, including multiplicities and spectra of secondary particles, has enabled this work. A library based upon Los Alamos evaluations for 12 isotopes has been processed with NJOY and will be distributed with the code versions mentioned in the last paragraph. The Los Alamos evaluations are part of an international collaboration organized by the IAEA [13].

The photonuclear physics implementation is complete and consistent with existing photoatomic physics and other code features. Secondary neutrons and photons may be created in MCNP from a photonuclear collision; in addition, light charged particles may be created in MCNPX. The implementation includes the ability to bias photonuclear events. Complete documentation, including validation examples, is available in [14].

6 Charged-Particle Tables

Until recently, the only possibility in MCNP for charged-particle transport (other than for electrons) was by using the multigroup Boltzmann-Fokker-Planck option. MCNPX also has featured continuous-energy light charged-particle transport by use of various physics models, primarily intranuclear cascade for energies below 150 MeV.

Recently, complete nuclear data evaluations have been prepared for incident protons and a table-based continuous-energy transport capability has been included in MCNPX 2.2. Evaluations have been completed for 42 isotopes [11], processed by NJOY, and a library for MCNPX based on these data will be distributed with Version 2.2.

The implementation of table-based proton transport in MCNPX relies on the data tables to describe nuclear reactions and large-angle scattering. Non-table-based continuous slowing down and multiple scattering models are used for small-angle scattering. The implementation is described more fully in [15]. Results of benchmark calculations using table-based proton transport in MCNPX have been reported in [16,17]. The capability will be generalized in the future to include table-based transport for additional light charged particles.

7 Secondary Scattering Distributions

Angular distributions of secondary particles have traditionally been represented in the MCNP family of codes by using 32 equally-probable cosine bins. This representation has the advantages of being compact and very easy to sample. Stimulated initially by the highly forward-peaked nature of proton scattering distributions, a new, more rigorous angular distribution representation has been implemented in MCNP 4C and in MCNPX 2.1.5.

The new representation features a tabulation of the probability density function (pdf) as a function of the cosine of the scattering angle. Interpolation of the pdf between cosines may be either histogram or linear-linear. The new tabulated angular distribution allows more accurate representations of original evaluated distributions in both high-probability and low-probability regimes. NJOY now processes angular distribution data for certain reactions for all incident particles into the new representation.

ENDF6 format also has featured various formalisms to describe correlated secondary energy-angle spectra. The MCNP family of codes samples from many such representations. In connection with the discussion in the previous paragraphs, we have recently added a correlated representation that presents data as tabulated angular distributions that are a function of tabulated energy distributions. This capability exists in MCNP 4C and in MCNPX 2.1.5. Libraries described in Sections 4-6 all include the new secondary scattering representations described here.

8 Remaining Approximations

Many challenges remain in terms of eliminating nuclear data approximations in the MCNP family of codes. Among those that might be addressed in the relatively near future are:

- The number of fission neutrons is always sampled as one of the nearest integers to $\nu(E)$
- Neutron F6 heating (energy deposition) tallies are the same whether or not secondary photons are transported
- There is no consideration of delayed photon production from fission

Other approximations that are much more challenging include:

- The type of reaction responsible for the creation of various secondary particles at a single nuclear collision is not correlated
- Each secondary particle from a collision is sampled independently
- The treatment of temperature effects is limited in its range of validity

Of course, no matter how many approximations are removed, it must be remembered that the ultimate accuracy of a Monte Carlo simulation can never be better than that of the fundamental evaluated data upon which it is based.

9 Summary

In summary, several physics improvements have been made recently to the MCNP family of codes by eliminating or mitigating previous nuclear-data assumptions. These physics improvements complement other capability improvements resulting from the explosion in computing power. Together, they enlarge the suite of applications that can be performed with Monte Carlo and allow improved fidelity and accuracy of all simulations.

References

1. J.F. Briesmeister, Editor: *MCNP - A General Monte Carlo N-Particle Transport Code, Version 4B*. Los Alamos National Laboratory report LA-12625-M, Version 4B (March 1997)
2. H.G. Hughes, K.J. Adams, M.B. Chadwick, J.C. Comly, L.J. Cox, H.W. Egdorf, S.C. Frankle, J.S. Hendricks, R.C. Little, R.E. MacFarlane, S.G. Mashnik, R.E. Prael, A.J. Sierk, L.S. Waters, M.C. White, P.G. Young, F.X. Gallmeier, E.C. Snow: 'MCNPX for Neutron-Proton Transport'. In: *Mathematics and Computations, Reactor Physics and Environmental Analysis in Nuclear Applications*, September 27-30, 1999, Madrid, Spain, ed. by J.M. Aragonés, C. Ahnert, and O. Cabellos (Senda Editorial, Spain, 1999), pp. 939-948
3. V. McLane, C.L. Dunford, P.F. Rose, Editors: *ENDF-102 Data Formats and Procedures for the Evaluated Nuclear Data File ENDF-6*. Brookhaven National Laboratory report BNL-NCS-44945, Revised (November 1995)

4. J.M. Otter, R.C. Lewis, L.B. Levitt: *UBR, A Code to Calculate Unresolved Resonance Cross Section Probability Tables*. Atomics International report AI-AEC-13024 (July 1972)
5. R.N. Blomquist, R.M. Lell, E.M. Gelbard: 'VIM - A Continuous Energy Monte Carlo Code at ANL'. In: *Proceedings of a Seminar-Workshop, A Review of the Theory and Application of Monte Carlo Methods*, April 21-23, 1980, Oak Ridge, Tennessee, Oak Ridge National Laboratory report ORNL/RSIC-44
6. L.L. Carter, R.C. Little, J.S. Hendricks, R.E. MacFarlane: 'New Probability Table Treatment in MCNP for Unresolved Resonances'. In: *Proceedings of the 1998 ANS Radiation Protection and Shielding Division Topical Conference*, April 19-23, 1998, Nashville, Tennessee, pp. II-341 - II-347
7. R.E. MacFarlane, D.W. Muir: *The NJOY Nuclear Data Processing System, Version 91*. Los Alamos National Laboratory report LA-12740-M (1994)
8. R.C. Little, R.E. MacFarlane: *ENDF/B-VI Neutron Library for MCNP with Probability Tables*. Los Alamos National Laboratory report LA-UR-98-5718 (December 1998)
9. R.D. Mosteller, R.C. Little: 'Impact of MCNP Unresolved Resonance Probability-Table Treatment on Uranium and Plutonium Benchmarks'. In: *Sixth International Conference on Nuclear Criticality Safety*, September 20-24, 1999, Versailles, France, pp. 522-531
10. R.D. Mosteller and C.J. Werner: *Trans. Am. Nucl. Soc.* **82**, 235 (2000)
11. M.B. Chadwick, P.G. Young, S. Chiba, S.C. Frankle, G.M. Hale, H.G. Hughes, A.J. Koning, R.C. Little, R.E. MacFarlane, R.E. Prael, L.S. Waters: *Nucl. Sci. Eng.* **131**, 293 (1999)
12. R.C. Little, S.C. Frankle, H.G. Hughes, R.E. Prael: 'Utilization of New 150-MeV Neutron and Proton Evaluations in MCNP'. In: *Proceedings of the International Conference on Nuclear Data for Science and Technology*, May 19-24, 1997, Trieste, Italy, ed. by G. Reffo, A. Ventura, and C. Grande (1997) pp. 1446-1448
13. P. Oblozinsky, M.B. Chadwick, A.I. Blokhin, T. Fukahori, Y.O. Lee, M.N. Martins, V.V. Varlamov, B. Yu, Y. Han, S.F. Mughabghab, J. Zhang: *Handbook on Photonuclear Data for Applications: Cross Sections and Spectra*. International Atomic Energy Agency TEC-DOC In Press (To be published in 2000; see <http://iaeaand.iaea.org/photonuclear> for draft)
14. M.C. White: *Development and Implementation of Photonuclear Cross-Section Data for Mutually Coupled Neutron-Photon Transport Calculations in the Monte Carlo N-Particle (MCNP) Radiation Transport Code*. Los Alamos National Laboratory report LA-13744-T (July 2000)
15. R.C. Little, M.B. Chadwick, S.C. Frankle, H.G. Hughes, R.E. MacFarlane, R.E. Prael, M.C. White, P.G. Young: '150 MeV Nuclear Data: Evaluations and Utilization in MCNPX'. In: *Proceedings of the Fourth Workshop on Simulating Accelerator Radiation Environments (SARE4)*, September 14-16, 1998, Knoxville, Tennessee, ed. by T.A. Gabriel pp. 163-170
16. M.B. Chadwick, H.G. Hughes, R.C. Little, E.J. Pitcher, P.G. Young: *Nuclear Data for Accelerator-Driven Systems*. Los Alamos National Laboratory report LA-UR-00-30 (2000) to be published in *Progress in Nuclear Energy*
17. H.G. Hughes, M.B. Chadwick, H.W. Egendorf, R.C. Little, R.E. MacFarlane, S.G. Mashnik, E.J. Pitcher, R.E. Prael, A.J. Sierk, L.S. Waters, M.C. White, P.G. Young, F.X. Gallmeier, E.C. Snow, R.K. Corzine: 'Status of the MCNPX Transport Code'. These Proceedings p. 961

The MCNP Code in Planning and Interpretation of Thermal Neutron Pulsed Experiments

J. Dąbrowska, K. Drozdowicz, and U. Woźnicka

The Henryk Niewodniczański Institute of Nuclear Physics ul. Radzikowskiego 152,
PL-31-342 Kraków, Poland

Abstract. A possibility to use the MCNP code to support planning and interpretation of the neutron pulsed experiments is discussed. Example of the simulated experiments for polyethylene are shown and compared to the real experimental results. A usefulness of the MCNP code for consideration of the time-dependent thermal neutron fields is stated. There are indicated some properties of the code and cross-section libraries which create problems or make impossible its using for many hydrogenous materials when the thermal neutron transport has to be considered with a high accuracy.

Samples in pulsed neutron experiments can be irradiated by a short burst of fast neutrons. After a time, long enough to slow down the neutrons, the exponentially decaying in time of the thermal neutron flux $\phi(t)$ is observed. The decay constant λ of its fundamental mode is equal [1] to

$$\lambda = \langle v\Sigma_a \rangle + D_0 B^2 - C B^4 + F B^6 - O(B^8), \quad (1)$$

where

$\langle v\Sigma_a \rangle$ – the thermal neutron absorption rate,

D_0 – the diffusion constant,

C – the diffusion cooling coefficient,

F – a correction to the diffusion cooling coefficient,

B^2 – the geometric buckling, a function of a size and a shape of the sample.

The above dependence gives a base of the so-called buckling experiment which is a classic method for the determination of the thermal neutron diffusion parameters of various media: the macroscopic absorption cross-section, the diffusion constant and the diffusion cooling coefficient. The first two parameters define properties of an infinite medium; the third one describes the behaviour of neutrons in a bounded (finite) medium. The experiment is performed using a pulsed neutron source (e.g. a pulsed neutron generator) and consists of a measurement of the time decay constant of thermal neutrons in a series of volumes of the investigated material.

The method has been well elaborated for many years but difficulties still arise, e.g. when samples are small (Corngold's limit and the extrapolation length), when material is heterogeneous in a sense of the density and/or a presence of

absorbing centers. Another problem appears when the buckling experiment is planned for bulk materials. The bulk density can change with the volume of the sample and it is almost impossible to keep the same density for all samples in one series.

A method proposed by Czubek [2] to make the buckling experiment independent of the density fluctuations has been tested by a fully simulated Monte Carlo experiment. The MCNP code [3] has been used. Three series of the buckling experiment for polyethylene $(\text{CH}_2)_n$ spherical samples of three different densities ($\varrho_0=0.95 \text{ g cm}^{-3}$, $\varrho_1=0.85 \text{ g cm}^{-3}$, $\varrho_2=0.57 \text{ g cm}^{-3}$) were carried out. The radii of the samples covered the range $0.04\text{--}3.0 \text{ cm}^{-2}$ of the buckling. Considering the neutron source, the test was made using 14 MeV, 1 keV, and Maxwellian-distributed thermal neutrons. No influence of the pulsed source type on the resulting decay constant was observed. Therefore, the Maxwellian source at the room temperature was applied, which assures the shortest time of the Monte Carlo runs.

The thermal neutron source was isotropic and the neutrons were uniformly generated inside the sample within a $100 \mu\text{s}$ time interval with a constant probability, which corresponds to a square $100 \mu\text{s}$ in width neutron burst in a real experiment. After the neutron burst, the neutron flux in the sample was scored in 900 time channels, 1 or $2 \mu\text{s}$ in width. The time-decay constant λ was determined using the procedure [4] like in a real pulsed experiment. The number of histories in the MCNP runs was chosen for each sample to assure the final standard deviation $\sigma(\lambda)$ not worse than 0.5% of λ . Cross-section tables were taken from the rmccs and tmccs libraries. Three series of the decay constants $\lambda(B^2)$ corresponding to the three different polyethylene densities were obtained. For each density the thermal diffusion parameters were evaluated. The results are collected in Tab. 1.

Table 1. The thermal neutron diffusion parameters obtained from the MCNP simulations for polyethylene

Density (g cm^{-3})	$\langle v\Sigma_a \rangle$ (s^{-1})	D_0 ($\text{cm}^2 \text{s}^{-1}$)	C ($\text{cm}^4 \text{s}^{-1}$)	F ($\text{cm}^6 \text{s}^{-1}$)
0.95	6068 ± 28	27069 ± 109	1897 ± 111	136 ± 27
0.85	5435 ± 14	30256 ± 61	2674 ± 68	242 ± 19
0.57	3684 ± 17	44699 ± 102	7923 ± 153	1145 ± 56

The density-removed parameters:

$$\langle v \Sigma_a^M \rangle = \frac{\langle v \Sigma_a \rangle}{\varrho}, \quad D_0^M = \varrho D_0, \quad C^M = \varrho^3 C, \quad F^M = \varrho^5 F, \quad (2)$$

were the final result of the simulated buckling experiment [5] (Tab. 2).

Table 2. The thermal neutron diffusion density-removed parameters for polyethylene from the MCNP simulations

Density (g cm ⁻³)	$\langle v \Sigma_a^M \rangle$ (cm ³ g ⁻¹ s ⁻¹)	D_0^M (cm ⁻¹ g s ⁻¹)	C^M (cm ⁻⁵ g ³ s ⁻¹)	F^M (cm ⁻⁹ g ⁵ s ⁻¹)
0.95 and 0.85	6390	25721	1636	106
	± 13	± 41	± 35	± 7

The density-removed diffusion parameters give a possibility to calculate the λ value for the polyethylene sample of any bulk density in a limited range of the fluctuations [5]. Such Monte Carlo simulations are a valuable tool to pre-define experimental conditions of a real experiment. A new buckling experiment for polyethylene cubes was planned in our Laboratory and the results from the above simulations were used to evaluate the λ value before performing the experiment. The λ values (Tab. 3) for two polyethylene cubes of the density $\varrho=0.946$ g cm⁻³ and sides $a=5.94$ cm and 8.90 cm were calculated using (1), (2) and the data from Tab. 2. The needed geometric buckling is defined for the cube by

$$B^2 = 3 \left(\frac{\pi}{a + 2d} \right)^2, \quad (3)$$

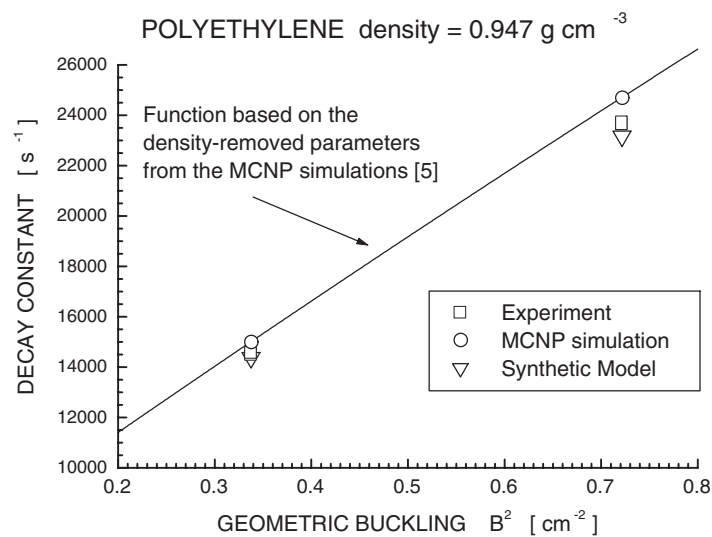
where d is the extrapolation length (dependent on the diffusion constant of a material).

The real experiment was carried out on the experimental set-up at the 14 MeV pulsed neutron generator in the Institute of Nuclear Physics in Kraków. The experimental λ values (Tab. 3) differ from those evaluated from the density-removed parameters. To check the observed discrepancy, new MCNP simulations were made especially for the two polyethylene cubes. The resulting λ values (Tab. 3) are in a very good agreement with the results calculated using the density-removed diffusion parameters obtained from the former simulations (for the spherical geometry). This confirms an existence of a certain disagreement between the MCNP simulation and the experiment. In order to verify the hypothesis that the difference can come from differences between real physical parameters of the material and the cross-section values used by the code, the decay constants for the two polyethylene cubes were calculated using the thermal neutron diffusion parameters obtained from a synthetic scattering model.

Table 3. Comparison of the decay constants λ of two cubic samples obtained in different ways

	λ (s ⁻¹) cube a=5.94 cm	λ (s ⁻¹) cube a=8.90 cm
Experiment	23684 ± 49	14523 ± 33
MCNP simulation for the cubes	24676 ± 32	14968 ± 21
Evaluation using data from Tab. 2	24517	14948
Calculation using the diffusion parameters from the Synthetic Model	23163	14373

Granada's [6] model for slow-neutron scattering in molecular gases has been used. The model is applicable in particular to hydrogenous media. The thermal neutron diffusion constant D_0 and the diffusion cooling coefficient C were

**Fig. 1.** Comparison of the experimental, theoretical and MCNP-simulated decay constants of the thermal neutron flux in polyethylene

calculated in the way summarized by Drozdowicz [7]. The values determined at the density $\rho=0.92\text{ g cm}^{-3}$ were: $D_0=26553\text{ cm}^2\text{ s}^{-1}$ [7], $C=2916\text{ cm}^4\text{ s}^{-1}$ [8]. The corresponding generalized parameters are $D_0^M=24429\text{ cm}^{-1}\text{ g s}^{-1}$ and $C^M=2271\text{ cm}^{-5}\text{ g}^3\text{ s}^{-1}$. The small correction F has been neglected in the present calculation. The average absorption rate has been obtained from the elemental composition using relevant microscopic absorption cross-sections: $\langle v\Sigma_a^M \rangle=6316\text{ cm}^3\text{ g}^{-1}\text{ s}^{-1}$ (code SIGSA [9]). The obtained decay constants (Tab. 3) are in a better agreement with the experimental data than the simulation results are, which is shown in Fig. 1. This might suggest that a new, higher-accuracy library of the thermal cross-sections for the MCNP is desired even for a such hydrogenous moderator as polyethylene.

In spite of the small discrepancy stated, the performed calculations have clearly shown a high usefulness of the MCNP code for simulations of the pulsed thermal neutron experiments. The possibility to investigate the time behaviour of the neutron flux and the access to the $S(\alpha, \beta)$ thermal treatment of scattering for low-energy neutrons is a big advantage. Unfortunately, the application for thermal neutrons is limited because the relevant cross-sections for hydrogenous media are available only for a few substances and temperatures. The $S(\alpha, \beta)$ model does not include the temperature adjustment of scattering cross-sections, and the free gas model is an inappropriate treatment for thermal neutron scattering in hydrogenous materials (in which the scattering kernel of hydrogen is always individual). In this respect we are undertaking an effort to generate and include necessary data for the thermal neutrons and to perform experiments to verify the used procedures.

References

1. M.M.R. Williams: *The Slowing Down and Thermalization of Neutrons* (North-Holland, Amsterdam, 1966) p.134
2. J.A. Czubek: Appl. Radiat. Isot. **48**, 237 (1997)
3. J.F. Briesmeister: *Monte Carlo N-Particle Code, Version 4B*, LA-12625-M (1997)
4. K. Drozdowicz, B. Gabańska, E. Krynicka: Rept. INP No.1635/AP (Kraków, 1993)
5. J. Dąbrowska, K. Drozdowicz: Nucl. Instr. Meth. **A443**, 416 (2000)
6. J.R. Granada: Phys. Rev. **B310**, 4167 (1985)
7. K. Drozdowicz: Rept. INP No. 1838/PN (Kraków, 1999)
8. K. Drozdowicz, V. H. Gillette: Ann. Nucl. Energy **26**, 1159 (1999)
9. K. Drozdowicz, E. Krynicka: Rept. INP No.1694/PN (Kraków, 1995)

Modelling Detector Responses to Neutrons Using MCNP

J. Tickner

CSIRO Minerals, PMB 5, Menai, NSW 2234, Australia

Abstract. This paper describes a method for modelling the neutron response of common gamma-ray detectors, such as sodium iodide (NaI), bismuth germanate (BGO) and hyperpure germanium (HPGe) devices. This response often constitutes an important source of background in neutron-gamma instruments.

The Monte Carlo code MCNP [1] is used to estimate the rate of capture and inelastic reactions in the detector as a function of neutron energy. Response functions for each of these reactions are then calculated, taking into account the production of multiple gamma-rays in a single neutron interaction. A response matrix is constructed which can be used to convert an energy dependent neutron flux into a pulse-height spectrum for a particular detector configuration.

Two of the commonly used gamma-ray detectors (HPGe and BGO) include the element germanium, which is not available in the standard MCNP data libraries. The production of suitable data files from the ENDF format JENDL-3.2 [2] libraries is described.

The method is used to determine the response function matrices of cylindrical 76 mm diameter by 76 mm length (3" \times 3") NaI, BGO and HPGe detectors. The pulse height spectrum for each of these detectors placed in a mixed neutron/gamma field is evaluated and compared with experiment.

1 Introduction

Commonly used gamma-ray detectors are also sensitive to both fast and thermal neutrons. In a PGNA instrument, the detector used to measure the gamma-ray spectrum will typically be situated in a mixed gamma-ray/neutron field. The detector's response to neutrons may constitute a significant background to the gamma-rays of interest, especially at high energies.

Experimental measurements of the response of certain detector configurations to neutrons have been performed [3]. Unfortunately, these only cover a limited range of neutron energies and detector geometries. On the other hand, directly modelling the response using a Monte Carlo code such as MCNP is not possible because of the importance of correlated emission of multiple particles following a neutron interaction. A non-analogue neutron transport code such as MCNP does not take these correlations into account.

This paper describes a method for simulating the response of an arbitrary detector to neutrons having any energy up to about 20 MeV, using a combination of Monte Carlo and deterministic methods. A response function matrix is derived that can be used to convert an energy dependent neutron flux into a pulse height spectrum.

2 Neutron Interactions in HPGe, BGO and NaI Detectors

Together, NaI, BGO and HPGe detectors consist primarily of the isotopes ^{23}Na , ^{127}I , ^{209}Bi , ^{16}O and the five isotopes of germanium (70, 72, 73, 74 and 76). For all of these isotopes, the cross-sections for neutrons from thermal energies up to about 20 MeV are dominated by the following reactions: elastic scattering; neutron capture; inelastic scattering to discrete final states; inelastic scattering to the continuum; the (n,2n) reaction; and simple charged particle production reactions, for example (n,p) and (n, α).

Elastic scattering does not generally lead to the deposition of substantial amounts of energy in the detector volume, even when the lightest nuclei are involved. For example, the maximum energy of a recoiling ^{16}O nucleus undergoing an elastic collision with a 14 MeV neutron is 3.1 MeV. However, in 90% of elastic collisions at this energy, the nucleus will recoil with an energy less than 1 MeV. For lower energy neutrons and heavier target nuclei, the energy deposition is even lower. Whilst elastic scattering can contribute substantially to the lowest part of the measured pulse height spectrum, the contribution at energies above 1 MeV is expected to be small and will not be further discussed.

The cross-sections for reactions producing charged particles are generally small for all of the isotopes considered here except at the very highest neutron energies. The largest contribution occurs with ^{16}O , where the (n, α) reaction accounts for 25% of the non-elastic cross-section at a neutron energy of 14 MeV. The contributions of charged particle production reactions to the measured pulse height spectrum is neglected in the following treatment.

For the remaining reactions listed above, the residual nucleus following the collision is left in an excited state. The excitation energy, U , is dissipated in the form of gamma-rays, conversion electrons and X-rays with the dominant contribution coming from gamma-ray emission. Ignoring target recoil, U equals the incident neutron energy plus/minus the binding energy of any particles captured/released during the interaction. Following the capture of a thermal neutron, U equals the neutron binding energy (typically in the range 4–10 MeV). At high energies, U values up to the incident neutron energy are possible for inelastic scattering reactions. Consequently, neutron induced gamma-ray reactions can contribute substantially to the measured pulse height spectrum up to energies of 10 MeV or more, which completely overlaps the energy range used for PGNA analysis.

The general purpose Monte Carlo code MCNP is used to estimate the rates of each reaction of interest for each isotope present in a cylindrical NaI, BGO or HPGe detector. A cylinder of the appropriate material and dimensions is surrounded by a spherical surface on which incident neutrons are started. The neutron flux is assumed to be homogeneous and isotropic. The rate of each reaction is measured as a function of neutron energy in 200 logarithmically spaced bins from 2×10^{-3} eV to 20 MeV. Standard data files (supplied with MCNP) derived from the ENDFB-VI [4] library are used for ^{16}O , ^{23}Na , ^{127}I and ^{209}Bi .

Unfortunately, the nuclear data libraries supplied with MCNP include no neutron data for germanium. Suitable files in the ACE format [1] (appendix F)

can be produced from standard ENDF format libraries using the nuclear processing code NJOY-97 [5].

Files for the 5 stable germanium isotopes were taken from the JENDL-3.2 library. By default, these files contain no gamma-ray production information. Data were added to the files describing discrete gamma-ray production via inelastic scattering and thermal capture reactions, using information taken from the NuDat library [6] and the compilation by Lone et al. [7]. No attempt was made to include continuum gamma-ray production, although it is hoped to include this information in a future version.

The modified ENDF files were then processed using NJOY-97 into the ACE format and the resulting files collected into a library suitable for use by MCNP.

3 Neutron Induced Gamma-ray Spectra

Once the rates of the relevant reactions are known, the next step is to calculate the energies of the gamma-rays produced in the decay of the excited nucleus. This process is straightforward for inelastic scattering reactions where the nucleus is left in a definite excited state, provided that the level diagram and decay probabilities are known for the isotope under consideration. Each level leads to one or more gamma-ray cascades, each of which consists of one or more gamma-rays. The NuDat library was used to obtain the level energies and decay probabilities for each of the isotopes used. It is assumed that all decays proceed via prompt gamma emission only, which is clearly an approximation for certain isotopes (for example, the lowest state of ^{72}Ge decays by internal conversion and the lowest state of ^{16}O by pair production).

The situation for the continuum reactions is more complicated as detailed information on the gamma-ray decay chain is not available. Instead, the following approximate approach is used. Firstly, the overall spectrum of individual photons from the gamma-ray cascade, $p(E_\gamma)$ is calculated as a function of the incident neutron energy. The photon multiplicity per neutron interaction can then be calculated simply as the ratio of the excitation energy U to the average photon energy. The sampling procedure described below is then used to randomly choose the energies of the cascade gamma-rays. The detector response to these gamma-rays is then calculated. The sampling procedure is repeated a large number of times to build up the average detector response for each type of neutron interaction.

3.1 Gamma-ray Spectra

Gamma-ray spectra are needed for capture, inelastic scattering to the continuum and (n,2n) reactions as a function of neutron energy. The continuum component of the gamma-ray spectrum is calculated using a simple evaporation model as described in [8]. The continuum contribution, $p^C(E_\gamma)$ is given over the gamma-ray energy range $0 < E_\gamma < U_{\text{max}}$ by

$$p^C(E_\gamma) \propto E_\gamma \exp(E_\gamma R) \cdot c_f \quad (1)$$

where $c_f = 1$ for $E_\gamma \leq U_{\text{mean}}$ and $c_f = (U_{\text{max}} - E_\gamma / U_{\text{max}} - U_{\text{mean}})$ for $E_\gamma > U_{\text{mean}}$. Here, U_{mean} is the mean excitation energy, given by

$$U_{\text{mean}} = \frac{A}{A+1} E_i + \text{BE} - \overline{E_n} \quad (2)$$

where A is the atomic number of the target nucleus, E_i is the incident neutron energy, BE is the binding energy associated with any absorbed/released neutrons and $\overline{E_n}$ is the average energy of any final state neutrons. The maximum possible excitation energy, U_{max} , occurs when the final state neutron(s) carries no energy. Note that for neutron capture, $U_{\text{mean}} = U_{\text{max}}$ as there are no neutrons in the final state. The empirical term R is approximately independent of the target nucleus and is taken to be

$$R \approx 0.95 + 4.5U_{\text{mean}}^{1.8}. \quad (3)$$

For the (n,2n) and inelastic scatter reactions, only the continuum contributions are considered. For the capture reaction, discrete gamma-rays lines [7] are added to the continuum contribution. The final gamma-ray spectrum is described as a histogram with 10 keV wide bins from 0 to 30 MeV. As the gamma-ray spectrum depends on the incident neutron energy, it is determined separately for each of the 200 neutron energy bins used for the reaction rate calculation where the reaction rate is non zero.

3.2 Correlated Sampling Procedure

Let the multiplicity of a gamma-ray cascade from a state with energy U be m . It is required to sample the energies of m^1 photons such that (i) the sum of the gamma-ray energies equals U and (ii) collectively, the gamma-rays have an energy spectrum given by $p(E_\gamma)$. The procedure used relies on being able to find a second probability distribution, $p'(E_\gamma)$ from which the gamma ray energies can be sampled using the following procedure:

- Sample the first energy, E_1 , from p' ;
- Sample subsequent energies E_n , ($2 \leq n < m$), from p' , discarding energies where $\sum_{j=1}^n E_j > U$;
- Set the energy of the m th photon to $U - \sum_{j=1}^{m-1} E_j$.

Initially, p' is chosen to equal p . The distribution p' is then improved iteratively by comparing the spectrum of sampled photons with the desired spectrum and updating p' appropriately. It is found that p' converges rapidly and for all the reactions and isotopes considered, a spectrum p' can be found which accurately reproduced the original spectrum p . The iteration procedure is terminated when the RMS difference between the true and sampled spectra stops decreasing.

A large number of photon sets can then be generated using the final spectrum p' . The detector response to these sets can then be calculated.

¹ For non-integral m , the value of m is randomly chosen for each cascade to be the nearest integer above or below m , with weights chosen to produce the correct mean multiplicity.

4 Gamma-ray Response Functions

The gamma-ray response of the detector to an internally generated photon of energy E_γ is calculated straightforwardly using the MCNP program. The starting photon position and direction are randomly sampled and the photon is tracked until it exits the detector volume, with the energy it deposits in the process being recorded. Two hundred thousand photons were generated for each 10 keV energy interval in the range 0 to 30 MeV (a total of 600M photons).

A similar method is used to calculate the response of the detector to external gamma-rays. A 1200×1200 response function matrix is calculated for external photons in the energy range 0–12 MeV. It is assumed that the flux of photons is homogeneous and isotropic.

The response of the detector to a cascade of photons produced in a single neutron interaction is calculated by convoluting the responses of the individual photons. Whilst computationally intensive, this process makes efficient use of the sampled photon sets and only a relatively small number of sets (20K) needs to be calculated for each neutron interaction and energy.

5 Results and Conclusions

Combining the results of the previous sections for neutron reaction rates, gamma-ray yields and detector responses yields a 1200×200 neutron response function matrix which converts an incident neutron flux (divided into 200 logarithmically spaced bins from 2×10^{-3} eV to 20 MeV) to a deposited energy spectrum. The deposited energy then needs to be smeared to account for detector resolution effects which are not included in the Monte Carlo model. For a typical HPGe detector, the energy resolution is better than the 10 keV bin width and no smearing is necessary. For NaI and BGO detectors, the smearing is assumed to be Gaussian, with an energy resolution proportional to the square root of the deposited energy.

To test the validity of the method for calculating neutron response functions, spectra were collected using a simple experimental arrangement. A 300 mCi ^{241}Am -Be neutron source producing approximately $6.6 \times 10^5 \text{ ns}^{-1}$ was placed above a 76 mm \times 76 mm HPGe, NaI and BGO detector in turn. A 12 cm thick tungsten block was used to shield the detector from the intense 4.4 MeV gamma-rays produced by the source and moderating blocks of paraffin were used to ensure that both fast and thermal neutrons passed through the detector. The neutron and gamma-ray fields at the detector were calculated using MCNP.

Figure 1(a) compares the experimentally measured detector response with that calculated using the MCNP fluxes and the response function matrices for gamma-rays and neutrons for a BGO detector. The dashed line shows the response that results if neutron interactions in the detector are ignored. The MC undershoots the data at low energies due to the omission of elastic scattering events in the model. Discrepancies around the H (2.23 MeV), C (4.44 MeV) and O (6.12 MeV) lines are thought to be due to the fact that the photon and neutron fluxes are not isotropic as assumed in the model. The H and C gamma-rays

are mainly incident on the side of the detector, whereas the O gamma-rays are produced inside the detector by fast neutrons incident on the front face. These discrepancies serve to illustrate the limits of the accuracy of the model.

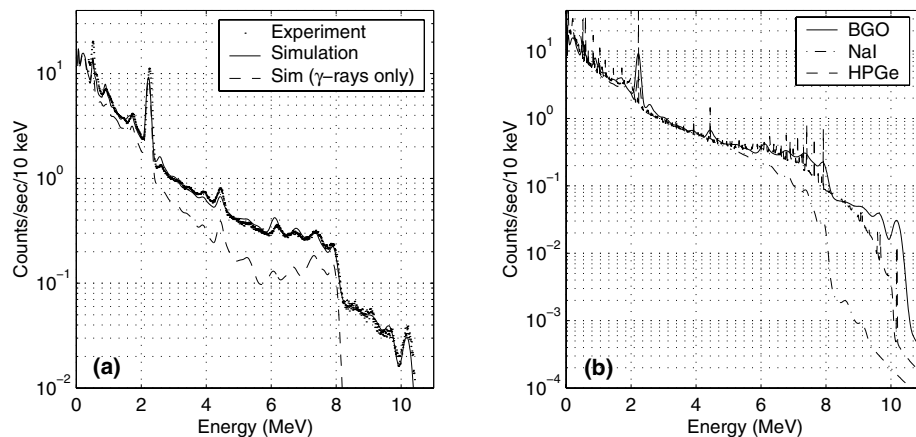


Fig. 1. (a) Comparison of measured and calculated BGO detector responses in a mixed neutron/gamma field. (b) Comparison of calculated responses of BGO, NaI and HPGe detectors

Similar agreement is found between experimental and model data for the NaI and HPGe detectors. For NaI, the model undershoots the data in the range 0-1.8 MeV, due to the beta-decay of ^{24}Na and ^{128}I nuclei, a reaction which is not included in the response functions. Figure 1(b) compares the model responses of BGO, NaI and HPGe detectors for the same experimental arrangement. At low energies, where the response is dominated by photons, the three detector spectra are fairly equal. At higher energies where neutron interactions become increasingly important, the responses of the three detectors differ considerably.

References

1. J. Briesmeister, Ed.: *Los Alamos National Laboratory Report LA-12625-M* (1997)
2. *The Japanese Evaluated Data Library version 3.2*, released by the Japan Atomic Energy Research Institute and the Japanese Nuclear Data Committee (1994)
3. O. Häusser et al: *Nucl. Inst. Meth.*, **213**, 309 (1983)
4. P.F. Rose, C.L. Dunfords, Eds.: *Brookhaven National Laboratory Report BNL-NCS-44945* (1990)
5. Oak Ridge National Laboratory PSR-368
6. C.L. Dunford, R.R. Kinset: *IAEA-NDS-205 (BNL-NCS-65687)* (1998)
7. M.A. Lone, R.A. Leavitt, D.A. Harrison: *Atom. Data and Nuc. Data Tab.* **260**, 511 (1981)
8. S.T. Perkins, R.C. Haight, R.J. Howerton: *Nucl. Sci. Eng.* **57**, 1 (1975)

Simulation of Thermal Neutron Transport Processes Directly from the Evaluated Nuclear Data Files

P.A. Androsenko¹, M.R. Malkov²

¹ Institute of Nuclear Power Engineering, Russia, Obninsk

² Institute of Physic and Power Engineering, Russia, Obninsk

Abstract. The main idea of the method proposed in this paper is to directly extract the required information for Monte-Carlo calculations from nuclear data files. The method being developed allows to directly utilize the data obtained from libraries and seems to be the most accurate technique. Direct simulation of neutron scattering in thermal energy range using file 7 ENDF-6 format in terms of code system BRAND has been achieved. Simulation algorithms have been verified using the criterion χ^2 .

1 Introduction

The most advanced information related to the accuracy of calculations is available in files of nuclear data libraries. It's common practice to use routines of Constant Unit to simulate the process of particles interaction with substances and to solve the neutron and photon transport problems. It is characteristics for the Constant Unit to derive parameters directly from data files without any simplification. The main idea of the method proposed by us is to directly extract the values required from data files. The usual practice so far applied is that data processing is followed by the Monte Carlo method application in calculational efforts. The method being developed allows to directly utilize the data obtained from libraries and seems to be the most accurate technique. Moreover, the method proposed doesn't introduce additional inaccuracy into the final results.

Three main types of neutron scattering are found to be possible in the thermal energy range, namely coherent elastic, incoherent elastic and incoherent inelastic.

2 Coherent Elastic Scattering

The coherent elastic scattering (no energy loss) from a material may be represented as follows:

$$\frac{d^2\sigma}{dE d\Omega}(E \rightarrow E', \mu, T) = \frac{1}{E} \sum_{i=1}^{E_i < E} s_i(T) \delta(\mu - \mu_i) \delta(E - E') / 2\pi \quad (1)$$

where

$$\mu_i = 1 - \frac{2E_i}{E} \quad (2)$$

E is the incident neutron energy (eV), E' is the secondary neutron energy (eV), μ is the cosine of the scattering angle, T is the moderator temperature (K), E_i are the energies of the Bragg edges (eV), s_i are proportional to the structure factors (eV-barns), and μ_i are the characteristic scattering cosines for each set of lattice planes. Equation (1) shows that in case of coherent elastic scattering $E' = E$, μ - is a random value. This random value takes a discrete meaning

$$P(\mu = \mu_i) = \frac{s_i(T)}{\sum_{i=1}^m s_i(T)} \quad (3)$$

where $m = \max\{i | E_i < E\}$ For modeling a standard algorithm of discrete random variable's simulation is used.

3 Incoherent Elastic Scattering

The differential cross section of the incoherent elastic scattering (no energy loss) is given by

$$\frac{d^2\sigma}{dE d\Omega}(E \rightarrow E', \mu, T) = \frac{\sigma_b}{4\pi} e^{-2EW'(T)(1-\mu)} \delta(E - E') \quad (4)$$

where σ_b is the characteristic bound cross section W' - is the Debye-Waller integral divided by the atomic mass (eV^{-1}), and all the other symbols have their previous meanings. From (4) it is visible, that at incoherent (Compton) elastic scattering $E' = E$, and μ is a continuous probability value. From (4) it is evident that random value μ distribution density is $f_\mu(x) = k e^{-2EW'(T)(1-x)}$ where the constant k is determined from a condition scale. The modeling of probability value is made by the method of inverse functions.

$$\mu = 1 + \frac{\ln(e^{-4EW'(T)} + \gamma(1 - e^{-4EW'(T)}))}{2EW'(T)} \quad (5)$$

where γ is a random variable uniformly distributed in the interval (0,1).

4 Incoherent Inelastic Scattering

Incoherent inelastic scattering is represented by the thermal neutron scattering law, $S(\alpha, \beta, T)$, and is defined for a moderating molecule or crystal by

$$\frac{d^2\sigma}{d\Omega dE'}(E \rightarrow E', \mu, T) = \sum_{n=0}^{NS} \frac{M_n \sigma_{bn}}{4\pi kT} \sqrt{\frac{E'}{E}} e^{-\beta/2} S_n(\alpha, \beta, T) \quad (6)$$

where (NS+1) types of atoms occur in the molecule or unit cell (i.e. for H_2O , NS=1) and M_n is the number of atoms of the n^{th} type in the molecule or unit cell. T is the moderator temperature (K), E is the incident neutron energy (eV), E' is

the secondary neutron energy (eV), β is the energy transfer, $\beta = (E' - E)/kT$, α is the momentum transfer, $\alpha = (E + E' - 2\mu\sqrt{EE'})/(A_0kT)$. The rest of the terms used here are commonly used terms. That is why they are described on detail. The data in File 7 for any particular material only contain the scattering law for the principal scatterer, $S_0(\alpha, \beta, T)$, i.e., the 0th atom in the molecule. These data are given as an arbitrary tabulated function. The scattering properties for the other atom types ($n=1, 2, \dots, NS$) are represented by analytic functions. In some cases, the scattering properties of other atom types in a molecule or crystal may be described by giving $S_0(\alpha, \beta, T)$ in another material. For some materials the scattering properties of all atoms in the molecule may be represented by analytic functions. In this case there is no principal scattering atom. The integrated cross section of incoherent inelastic scattering is calculated by formula

$$\sigma(E, T) = \int_0^\infty \int_0^{2\pi} \int_{-1}^1 \frac{d^2\sigma}{d\Omega dE'}(E \rightarrow E', \mu, T) d\mu d\varphi dE' \quad (7)$$

In this integral will make the following change of the variables $\alpha' = E' + E - 2\mu\sqrt{EE'}$, $\beta' = E' - E$. The Jacobian of transformation is equal to

$$\frac{1}{2\sqrt{E(E + \beta')}} \quad (8)$$

and we get the following formula

$$\sigma(E, T) = \frac{1}{E} \iint_{G(E)} F(\alpha', \beta', T) d\alpha' d\beta' \quad (9)$$

where

$$F(\alpha', \beta', T) = \sum_{n=0}^{NS} \frac{M_n \sigma_{bn}}{4kT} e^{-\beta/2} S_n(\alpha, \beta, T) \quad (10)$$

$$\alpha = \frac{\alpha'}{kT} \quad (11)$$

$$\beta = \frac{\beta'}{A_n kT} \quad (12)$$

The area $G(E)$ is $-E \leq \beta' < \infty$, $(\sqrt{E + \beta'} - \sqrt{E})^2 \leq \alpha' \leq (\sqrt{E + \beta'} + \sqrt{E})^2$. The calculation of the value $\sigma(E, T)$ is produced by the next algorithm. At the stage of preparing the values Q_i are calculated

$$Q_i = \iint_{G(E_i)} F(\alpha', \beta', T) d\alpha' d\beta' \quad (13)$$

for the set net of energies E_1, E_2, \dots, E_n . At the stage of the calculations for calculating the value $\sigma(E, T)$ we find which is close to E and calculate $\sigma(E, T)$ by the formula

$$\sigma(E, T) = \frac{1}{E} (Q_i + \iint_{G(E) \setminus G(E_i)} F(\alpha', \beta', T) d\alpha' d\beta' - \iint_{G(E_i) \setminus G(E)} F(\alpha', \beta', T) d\alpha' d\beta') \quad (14)$$

5 Simulating Algorithms of Incoherent Inelastic Scattering

We will shortly describe two algorithms of modeling incoherent inelastic scattering.

Algorithm 1 1. Get the full set of β_i , unifying the sets β_{in} for all atoms of the molecule for which the function $S(\alpha, \beta, T)$ in file 7 ENDF-6 is given in tables.
2. On the basis of the received set β_i get the set of energies E'_i .
3. Add the addition points in the intervals from 0 to the minimum value E_i and from maximum value E'_i to some value E'_{\max} in the set.
4. For all E'_i in addition to all n those added in a previous get the full set α_i^j for each i , and for added in a previous point take the sets for the extreme values E_i .
5. According to this sets α_i^j find the sets μ_i^j for the given i .
6. Add the addition points from -1 to the minimal value μ_i^j and from maximum value μ_i^j to 1 to the sets μ_i^j .
7. Get the function set in tables $f_{E,T}(E'_i, \mu_i^j)$. We determine the function $\tilde{f}(E', \mu)$ in the following way: in the nodes E_i, μ_i^j $\tilde{f}(E_i, \mu_i^j) = f(E_i, \mu_i^j)$ and between nodes we have linear interpolation. Now we simulate the segmented-linear density $\tilde{f}_{E,T}(E', \mu)$ by the method described in the paper [3] with the weight

$$\frac{f_{E,T}(E', \mu)}{\tilde{f}_{E,T}(E', \mu)} \quad (15)$$

Algorithm 2 The main idea of this algorithm based on possibility of analytical calculation of integrals from table function $R(x)$ (here $x \in [x_i, x_{i+1}]$, $R_i = R(x_i)$, $R_{i+1} = R(x_{i+1})$) with LIN-LOG interpolation between points (INT=4, there is the same possibility for another INT values)

$$\int_{\alpha_j}^{\alpha_{j+1}} S(\beta, \alpha) d\alpha = (S(\beta, \alpha_{j+1}) - S(\beta, \alpha_j))(\alpha_{j+1} - \alpha_j) \ln^{-1} \left(\frac{S(\beta, \alpha_{j+1})}{S(\beta, \alpha_j)} \right) \quad (16)$$

and another integral

$$\int_{x_i}^{x_{i+1}} e^{-x/2} R(x) dx = \frac{R_2 e^{-\frac{x_{i+1}}{2}} - R_1 e^{-\frac{x_i}{2}}}{\frac{\ln(R_2/R_1)}{x_{i+1} - x_i} - \frac{1}{2}} \quad (17)$$

Let ξ - random value with probability density function $R(x)$. Inverse function method can be used for modeling ξ (after normalization of $R(x)$):

$$\xi = \ln \left(1 + \frac{\gamma \ln(R_2/R_1)}{R_2(x_{i+1} - x_i)} \right) \ln^{-1}(R_2/R_1) \quad (18)$$

Play out the atom where the scattering has occurred. If this atom is set as a model of free gas then the scattering is simulated by the method described in the paper [4]. If this atom is set in table of $S(\alpha, \beta)$ in file 7 ENDF-6 then modulate the scattering by the following way.

1. For each β_i analytically calculate

$$b(\beta_i, T) = \int_{\alpha_{\min}(\beta_i)}^{\alpha_{\max}(\beta_i)} F(\alpha, \beta, T) d\alpha \quad (19)$$

2. Suppose that the interpolation law of $b(\beta_i, T)$ is LIN-LOG to analytically calculate the B_i integrals from $e^{-\beta/2}b(\beta, T)$ by β .

3. Select the interval $[\beta_i, \beta_{i+1}]$ according to probabilities B_i and sampling β .

4. Select the intervals $[\alpha_j^{(i)}, \alpha_{j+1}^{(i)}]$ and $[\alpha_j^{(i+1)}, \alpha_{j+1}^{(i+1)}]$ according to probabilities $b(\beta_i, T)$ and $b(\beta_{i+1}, T)$ and sampling $\alpha^{(i)}$ and $\alpha^{(i+1)}$ using inverse function method.

5. Calculate $\alpha = (1 - \epsilon)\alpha^{(i)} + \epsilon\alpha^{(i+1)}$ where $\epsilon = (\beta - \beta_i)/(\beta_{i+1} - \beta_i)$.

Thermal movement of nuclei. The effective cross section for a material at temperature T is defined to be that cross section that gives the same reaction rate for stationary target nuclei as the real cross section gives for moving nuclei. We play out the velocity of the nucleus using the algorithm from [5] and calculate cross section for this velocity in each collision.

6 Calculations

The description of the task. We calculate the spectrum of the neutrons which penetrate through the infinite slab H_2O which is 3 cm thick and we calculate the spectrum of the albedo. The neutrons have the energy 1 eV and are directed perpendicularly to the slab. Then we compare the results of MCNP calculations with our results using files h(h2o).ga and h(h2o).lan ENDF/B-VI. In the Fig. 1, 2 we present these comparisons. As we can see our results have the similar but not the same energy structure as MCNP results. The source of this differences require detailed comparison of BRAND and NJOY+MCNP algorithms. Please, note that the sums of probabilities are the following: albedo - $p(\text{MCNP})=0.4074$, $p(\text{BRAND-lan})=0.3916$, $p(\text{BRAND-ga})=0.3977$; penetration - $p(\text{MCNP})=0.4917$, $p(\text{BRAND-lan})=0.4872$, $p(\text{BRAND-ga})=0.4929$.

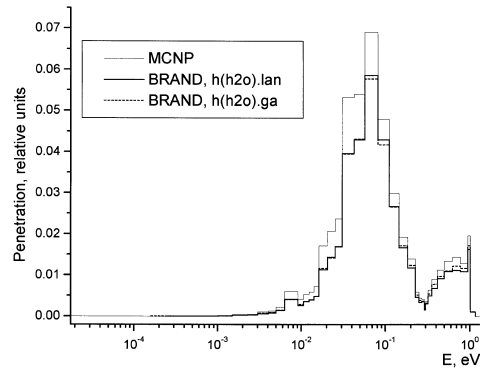


Fig. 1. Penetration neutron spectra for H in H₂O for incident energy 1 eV at a temperature 296 K

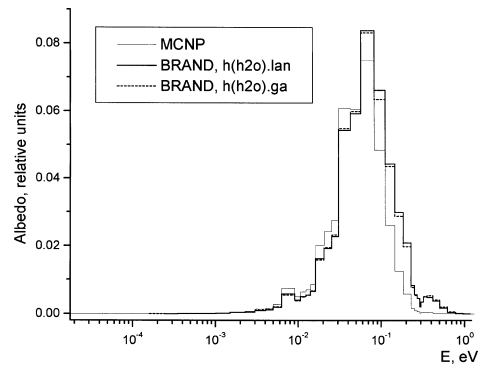


Fig. 2. Albedo neutron spectra for H in H₂O for incident energy 1 eV at a temperature 296 K

7 Conclusion

The tool for calculating of the neutron transport in the thermal energy range directly on Evaluated Nuclear Data Files has been developed.

Our gratitude to Mr. N.A. Soloviev for making the calculation on MCNP.

References

1. A.A. Androsenko, P.A. Androsenko et. al.: *Monte Carlo Simulation of Neutron Transport Process, Photons and Charged Particles*. Preprint FEI-2205, Obninsk, 1991
2. R.F. Rose, C.L. Dunford: ENDF-6 Format Manual, IAEA-NDS-76, 1991
3. P.A. Androsenko, G.V. Popova: *Journal of Computational Mathematics and Mathematical Physics* **21**, No.4 (1981), *in Russian*)
4. J.R. Eriksson: *Nucl. Sci. and Eng.* **41**, 307 (1970)
5. J.F. Briesmeister (Ed.): *MCNP - Version 4A*, LA-12625-M, November 1996

Influence of the Photoneutrons on the Kinetics of the Beryllium Reflected Core of the Budapest Research Reactor

G. Hordósy, A. Keresztúri, P. Vértes, and Cs. Hegedűs

KFKI Atomic Energy Research Institute H-1525 Budapest 114, POB 49, Hungary

1 Introduction

The disintegration of nuclei and the production of neutrons from photon-induced reactions may take different forms, for example the (γ, n) , $(\gamma, 2n)$ and $(\gamma, \text{fission})$ reactions. The nuclides of the beryllium and deuterium have particularly low threshold energies of 1.667 MeV and 2.225 MeV for the (γ, n) reactions. These two materials are efficient moderator and reflector materials in fission reactors. Although their (γ, n) cross sections are quite low, this process may have an essential influence on the reactor dynamics because of the relatively long delay time of the photons emitted by the fission products. In this paper the neutrons emerging from the (γ, n) reactions will be referred as photoneutrons.

The Budapest Research Reactor contains beryllium in the reflector, accordingly this phenomenon is presumably smaller than that in the cores where photoneutrons emerge in the moderator. On the other hand, the space dependence of the kinetic processes is stronger. The dynamics of this core has been investigated by the code KIKO3D [1] developed in KFKI Atomic Energy Research Institute. It is a nodal, three-dimensional coupled neutron physical - thermohydraulic code. The nodes in the fuel are represented by generalized response matrices while the absorbers and the reflector are described by precalculated albedo matrices depending on some parameters. The time - dependent equations are solved by the improved quasi - static method. The effect of the photoneutrons was neglected in the original form of KIKO3D . In the last years a more sophisticated version of the code was developed to include the effect of the photoneutrons with the help of modified albedo matrices for the reflector and with additional delayed neutron groups due to the (γ, n) reaction. The photoneutrons were treated by a modified form of the Monte Carlo code MCNP.

2 Inclusion of the Photon-Induced Neutrons into MCNP

A modification to MCNP4A including photoneutron treatment was developed by Gallmeier in 1995 [2]. He introduced a new option into MCNP4A [3] to turn on and off the production of the photoneutrons. The photoneutron cross sections had to be user-supplied data in MCNP cross section format given in separate tables. A new card was introduced to provide cross section identifiers for the corresponding isotopes. An approximate formula was derived for the

photoneutron energy from the conservation principles. The photoneutrons were created by the code according to isotropic or quadratically anisotropic angular distributions. This version of MCNP was used in our earlier investigation of photoneutrons of the beryllium reflected core [4].

This treatment was further modified by Vértés [5]. He modified MCNP to include the (γ, n) , $(\gamma, 2n)$ and $(\gamma, \text{fission})$ processes as well. In his modification of MCNP no special table for photon-induced neutrons was defined, instead the unused element of NXS and JXS arrays of the photon table were used to specify the required information. The code was modified so that each isotopes of an element could have its own photon table. No new input option was introduced, the appropriate photon table was associated with the neutron table of the isotopes. An auxiliary program ACEMOD was developed for generating photon tables with photon induced neutron data. The data to be added should be in ENDF/B-VI format. This program merged the photon induced neutron data into the original MCNP photon table. When photon-induced neutron data are taken into account for a particular isotope of a material, all of the other isotopes of this material must have the modified photon tables. These can easily be obtained by ACEMOD. The photoneutron energy is calculated by the formula given by Gallmeier. The measured data are used for sampling of the angle distribution if available, otherwise isotropic distribution is assumed. These modifications were patched to MCNP4B.

3 Description of the Calculations

3.1 Calculation of the Time-Dependent Photon Source, the Photoneutron Yield and the Number of Fissions

For taking into account the influence of the photoneutrons in the calculations the core was approximated by a cylinder which contained the homogeneous mixture of the fuel, moderator and absorber. This cylinder was surrounded by a cylindrical shell consisting of a mixture of beryllium and water and by an outer cylindrical shell of beryllium.

The calculation for the photoneutrons can be outlined as follows:

- Delayed γ particles due to the decay of fission products are born in the fuel region. The spatial dependence of γ source is proportional to the fission density taken from a criticality calculation. The intensity and the spectra of the delayed photons from the fission products are calculated as the function of time elapsed after a fission.
- γ radiation is attenuated by the fuel and reflector regions.
- γ particles reaching the reflector region induce photoneutrons.
- The photoneutrons reaching the fuel region contribute to the fission rate in the fuel. The time shift between a fission caused by a photoneutron and the creation of that photoneutron is neglected.

The time-dependence of the fission rate caused by the photoneutrons and the time dependence of the incoming photoneutron current at the core boundary can be determined by these calculations for a series of times elapsed after a fission. These quantities can then be fitted by a sum of exponential functions. The additional delayed neutron groups are identified by determining the coefficients and decay constants of these functions.

The calculations involving photoneutrons were performed by the modified form of MCNP [5]. The calculations of the intensity and spectra of the delayed photons emitted by the fission products were done by the TIBSO code developed by Vértés [6]. The code takes into account 1265 isotopes, where the production rates and decay constants were compiled from the NEA Data Bank, the Los Alamos National Library, the IAEA Nuclear Data Section and from the Brookhaven National Laboratory.

In the TIBSO and MCNP calculations eight photon energy groups were used with boundaries in MeV : 1.67 (threshold energy in beryllium for photoneutron production), 2.0, 2.4, 3.0, 3.5, 4.0, 4.5 and 5.0. Photons below the (γ, n) threshold of Be are omitted. About 12 percent of the photons have energy over thresholds at any time. The total number of photons in the first 100 sec is 6.84 and in the next 900 sec is 4.0. The angular dependence of photon source is assumed to be isotropic. The strong dependence of the delayed photon spectra on time should be mentioned.

Treating the photon transport, the secondary photons produced by electrons were neglected and the simple physics options of the MCNP4A was used. This means that

- at photoelectric events the fluorescent photons are neglected and the event is treated as pure absorption by implicit capture (the photon weight is reduced and the history of the photon with reduced weight is followed)
- at Compton scattering free electron approximation is used because the threshold energy for photons of interest is 1.67 MeV
- at pair production, the original photon disappears, the created positron is assumed to be annihilated immediately and thus two photons are created with energy 0.511 MeV and with opposite directions.

Due to the large number of computations to be performed, to achieve the desired statistical accuracy within reasonable computer time the weight-window methods was used for variance reduction with the built-in weight-window generator of MCNP4A. The efficiency of the calculations was improved essentially after a few iteration of the weight-windows. Introducing the quality factor by $q=1/(R^2T)$ for the efficiency of the calculation, it was found that the initial q value of 4–6 increased up to about 1200. (In the previous expression R is the relative error and T is the computer time required.) This generation of the weight windows was performed only once for a particular photon energy spectrum and the same weight windows were used in all subsequent calculations with different spectra. Despite of the fact that the spectra were quite different the calculational efficiency did not change essentially. All of the calculations were made

with 400.000 starting photons and the relative errors of the calculated quantities were about 0.008 - 0.01.

3.2 Calculation of the New Kinetic Parameters

It is well known in fission events that the emission of some neutrons are delayed by times ranging from less than a second to about a minute. These delayed neutrons result from beta decay of fission products. The time dependent behavior of a fission reactor is determined by the delayed neutrons. Several fission products are precursors of the delayed neutron emitters, but generally for practical purposes they are divided into six groups. In each groups the precursors decay exponentially with a characteristic decay constant λ_i , which determines the rate of the delayed neutrons in the group. Denote by ν the total number of neutrons from one fission and by β the total fraction of the delayed neutrons, then the number of prompt neutrons is $\nu(1-\beta)$ and the number of delayed neutron is $\nu\beta$ per fission. If the fraction of the delayed neutrons in a group is denoted by β_i then one has

$$\beta = \sum_{i=1}^6 \beta_i \quad (1)$$

This division accounts for all neutrons arising directly from fission. However, if materials having non-negligible (γ, n) cross-sections are present, the photoneutrons resulted by delayed photons from the fission products can act as additional delayed neutrons and can influence the kinetic behavior of the reactor core.

Using the time dependent fission rate due to the photoneutrons originating from the products of one previous fission, the parameters of additional delayed neutron groups can be evaluated using the following approximations

- The shape of the fission source is fixed (not depending on time).
- The worth of the neutrons originating from the fission caused by the photoneutrons is the same as the worth of neutrons originating from normal fission.

The introduction of new delayed neutron groups are based on the time-dependence of the number of fissions caused by photoneutrons originating from one fission. If this function is denoted by $H(t)$, then the integral of this curve - denoted by β^* - gives the total number of fission caused by the delayed photoneutrons originated from one fission. This value is equal to the total fraction of the additional delayed neutron groups because the number of neutrons resulting from the photoneutron effect due to one fission is $\nu\beta^*(1-\beta) \approx \nu\beta^*$. The additional delayed neutron groups can then be identified by fitting this function with a sum of exponentials:

$$H(t) = \sum_{j=1}^N \lambda_j^* C_j^*(t) = \sum_{j=1}^N \lambda_j^* \beta_j^* \exp\{-\lambda_j^* t\} \quad (2)$$

Table 1. The additional delayed neutron group parameters

j	1	2	3	4
λ_j^*	1.8379E+00	1.2875E-01	1.4104E-02	1.8349E-03
β_j^{p*}	2.9453E-06	4.0896E-05	3.2409E-05	3.6929E-05
β_j^{s*}	1.3227E-06	1.8366E-05	1.4555E-05	1.6585E-05

Here N is the number of the delayed neutron groups introduced for the description of the photoneutrons. Using this formula the condition for the total number of fissions and the decay equations are satisfied:

$$\int_0^\infty H(t)dt = \sum_{j=1}^N \beta_j^* = \beta^* \quad (3)$$

$$\frac{d}{dt} C_j^*(t) = -\lambda_j C_j^*(t) \quad (4)$$

Performing the fitting described above the best result was achieved by N=4. The fitted values of the decay constants λ_j^* and the partial fractions β_j^* of these exponentials corresponds to the point kinetical parameters of the new groups because up to this point no space dependence was taken into account in the procedure. The dependence may be essential because most of the fissions caused by photoneutrons take place next to the boundary of the core. The β values reflecting the space dependence can be calculated by KIKO3D. The new albedo matrix introduced into KIKO3D due to the photoneutrons can be evaluated by the flux and current calculated at the core boundary. The values of the new the kinetic parameters are summarised in Tab. 1. The upper indices p and s refer to the point kinetics or to the account the space dependence.

4 Evaluations of the Control Rod Worth Measurements

The kinetic parameters given above have been used to estimate the influence of the additional delayed neutron groups on the result of the doubling time measurement of control rod worth performed at the Budapest Research Reactor. The selected control rod was withdrawn from the core step by step and the $T_{1/2}$ doubling time of the flux change was measured. The reactivity was evaluated by using the in-hour equation [7]

$$\rho = \alpha \left(\Lambda + \sum_{j=1}^N \frac{\beta_j}{\lambda_j + \alpha} \right), \quad (5)$$

where Λ is the prompt neutron lifetime and $\alpha = \ln 2/T_{1/2}$.

The evaluation of the reactivity was performed according to this formula with the six original delayed neutron groups (ρ_6), including the four new groups but using the point kinetic values for the partial fraction (ρ_{10}^p), and using the partial fractions from a space dependent calculations by KIKO3D (ρ_{10}^s). The correspondingly obtained reactivity values, in units of cent (i.e. in units of β) are summarised in Tab. 2. In the Table h_1 and h_2 denote the control rod positions before and after a rod withdrawal.

Table 2. Reactivity change measurements using the doubling time method

h_1 [cm]	h_2 [cm]	$T_{1/2}$ [s]	ρ_6 [cent]	ρ_{10}^p [cent]	ρ_{10}^s [cent]
3.0	13.0	229.0	3.08	3.38	3.22
13.0	20.0	141.0	4.74	5.11	4.91
20.0	27.0	109.0	5.91	6.31	6.09
27.0	35.0	79.0	7.71	8.15	7.91
35.0	42.0	113.0	5.74	6.13	5.92
42.0	52.0	104.0	6.15	6.56	6.34
52.0	70.0	300.0	2.40	2.67	2.52

As can be seen from the sums of the last three columns of Tab. 2. the total rod worths are 35.73 cents, 36.30 cents and 38.32 cents, using three different sets of the parameters. The neglecting of the photoneutrons underestimates the rod worth by 3.2 percent compared to the value calculated by using the β_j^{s*} -s while the use of β_j^{p*} -s would give a value higher with 7.25 percent. It is seen that the effect of the photoneutrons can be essential but the use of simple point kinetics lead to overestimation of the effect. It should be pointed out that this effect becomes stronger for cores with high burnup.

References

1. A. Keresztúri: *KIKO3D - A 3D Kinetics Code for VVER-440*, Transactions of the American Nuclear Society, 1994 Winter Meeting, Washington DC, 1994.
2. F.X. Gallmeier: *General Purpose Photoneutron Production in MCNP4A*, ORNL/TM-13073, 1995
3. J.F. Briesmeister, Ed.: *MCNP - A General Monte Carlo N-Particle Transport Code, Ver. 4A*, LA-12625-M
4. G. Hordósy, A. Keresztúri, Cs. Hegedűs, P. Vértés: Monte Carlo Methods and Applications **444**, 163 (1998)
5. P. Vértés: <http://judit.aeki.kfki.hu/vertes/mcnp-photo/aeph.htm>
6. P. Vértés: Nuclear Technology **128**, 124 (1999)
7. G.I. Bell, S. Glasstone: *Nuclear Reactor Theory* (Van Nostrand Reinhold Company 1970)

Variance Reduction with Multiple Responses

K.W. Burn¹, G. Gualdrini², and E. Nava¹

¹ ENEA-SIEC v. Martiri di Monte Sole 4 I-40129 Bologna, Italy

² ENEA-IRP v. Dei Colli 16 I-40136 Bologna, Italy

1 Introduction

Radiation transport problems that involve high attenuation require non-analogue Monte Carlo. Non-analogue techniques [i.e. employing variance reduction (V.R.)] conserve the first moment whilst reducing the second and consequently the variance. However, because V.R. methods employ in one form or another an estimate of the importance (adjoint flux) which is strictly linked to a particular response, they are directed at a single response. V.R. parameters appropriate to one response (in that they significantly reduce the statistical error) may not necessarily be appropriate to another; they may even raise the errors of other responses compared with their analogue values. Thus Monte Carlo may treat problems involving a high attenuation only if a single response (or a set of responses with similar importances) is of interest. Monte Carlo tends to run into trouble when more differential information is required (flux distributions in many energy groups for example).

The technique presented here to optimize V.R. parameters to more than one response is based on the DSA (Direct Statistical Approach) [1–5] which is of general application in that it is based on V.R. techniques that are themselves of general use: population or weight control through splitting and Russian roulette. MCNP (ver. 4B) [6] is employed as a vehicle. The extension of the DSA to multiple responses is straightforward as it expresses the population second moment, S^2 , and the time per source history, τ , in terms of the unknown V.R. parameters and problem-dependent coefficients. In the case of population control, under normal conditions, both S^2 and τ are separable into a coefficient part and a parameter dependence part, the parameters being the phase space cell importances [3]. In the case of weight control, and with the parameters being the cell starting weights or “weight lines” [5], an approximation must be made to render S^2 separable [5]. Then, standard minimization routines are employed to find the set of V.R. parameters that renders the quality factor, q , minimum, where:

$$q = S^2 \cdot \tau \tag{1}$$

The justification for minimizing q is found in [1]: a reasonable measure of the inverse of the efficiency of a Monte Carlo calculation is:

$$q' = V_S \cdot T_S \tag{2}$$

where V_S is the variance of a sample of N independent histories, and T_S is the computing time required for the sample. With the assumption: $S^2 \gg D^2$ (where D is the first moment), justified in problems that require a non-analogue treatment, it is easy to show that q' can be approximated by q . For M responses, we rewrite expression (1) as:

$$q_{fc} = \sum_{i=1}^M \frac{q_i}{D_i^2} = \sum_{i=1}^M \frac{S_i^2}{D_i^2} \cdot \tau \quad (3)$$

where the subscript “fc” stands for “fractional and compound”. The well-known quantity the “figure of merit” (fom) used in such codes as MCNP to give a measure of the quality of a calculation on a given machine is defined as:

$$fom = (fsd^2 \cdot T_S)^{-1} \quad (4)$$

where fsd is the fractional standard deviation. If we define a “compound figure of merit” (fom_c) for a number of responses i , $i=1, M$ as:

$$fom_c = \left(\sum_{i=1}^M fsd_i^2 \cdot T_S \right)^{-1} \quad (5)$$

then $(q_{fc})^{-1}$ and fom_c are equivalent within the approximation of employing the second moment instead of the variance. Thus our objective is to maximize fom_c , through the estimation using the DSA model of S_i^2 and τ (and of D_i). The form of S_i^2 and τ may be found in [4] and [5]. The technique is illustrated through three examples: a reactor-based BNCT facility [7] for treatment of brain tumours via an epithermal neutron flux; a sub-critical assembly driven by a spallation source (ADS); a thermal neutron calibration facility [8,9].

2 BNCT Facility

TAPIRO at ENEA Casaccia is a fast assembly with a small, highly enriched, core. In one sector, the concrete biological shield and the outer part of the copper reflector have been removed and replaced by a structure whose role is to “shift” the neutron spectrum towards epithermal energies (see Fig. 1). At the irradiation position at the collimator exit, the neutron spectrum is of interest over the whole energy range: thermal (< 1 eV), epithermal (1 eV – 10 keV) and fast (> 10 keV). The γ dose is also required. It is desired to produce the maximum epithermal flux whilst minimizing the thermal and fast components as well as the γ dose. Using the DSA Cell Importance model [3], three optimizations were carried out, varying the number of neutron energy groups as responses of interest at the collimator exit: the first with one group - the total neutron flux, the second with three groups - thermal (< 1 eV), epithermal (1 eV – 10 keV), fast (> 10 keV); the third with five groups - low thermal (< 0.32 eV), high thermal (0.32 – 1 eV), epithermal (1 eV – 10 keV), low fast (10 keV – 1 MeV), high

fast ($> 1 \text{ MeV}$). The three sets of V.R. parameters thus generated were used in equal length calculations of the neutron spectrum, shown in Fig. 2 (where the neutron spectra in the 1 and 3 group optimization have been divided by factors of 100 and 10 respectively). We see an improvement in the quality of the neutron spectrum over the whole energy range in going from 1 to 3 to 5 groups. This is particularly evident in the fast part of the spectrum.

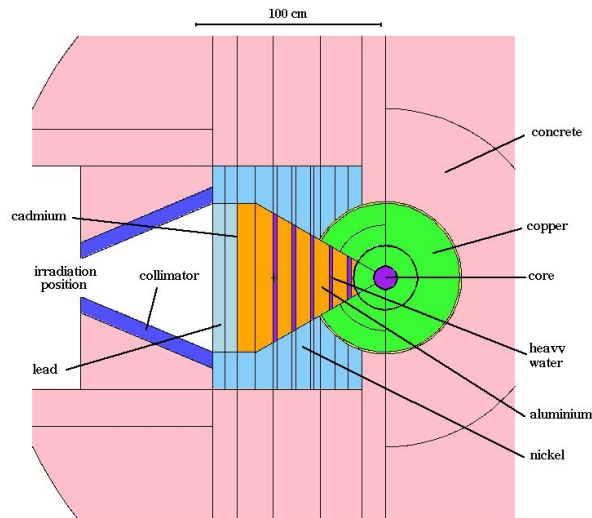


Fig. 1. TAPIRO; geometry; horizontal section

Possible savings in an M-response optimization compared with M single optimizations are in: 1) the CPU time and 2) the 'human' time and in the phase of: a) generation of the V.R. parameters and b) running with the optimum V.R. parameters. As far as the CPU time is concerned, phase a) is difficult to quantify as it depends on the user's experience. For what it is worth in the case of 3 energy groups, a saving of about 30% in CPU time was observed in the generation phase (this with a DSA version which was later improved to greatly reduce the time lost in book-keeping). Phase b) is quantifiable and in the same problem showed a saving of nearly 40% in CPU time. Such CPU time savings are of course due to correlations between the responses, with the same tracks contributing to a number of responses. We will not attempt to quantify the human time here apart from observing that each optimization requires a certain fixed time to execute plus a variable time dependent on the statistical difficulty. The saving function in human time looks to depend quite strongly on the number of responses, a result that users of optimizing methods will be familiar with. If pressed, the authors would regard this saving as potentially large.

A fourth multi-response optimization was carried out employing the three energy group neutron fluxes at the collimator exit ($< 1 \text{ eV}$, $1 \text{ eV} - 10 \text{ keV}$, $> 10 \text{ keV}$), together with the γ tissue dose, also at the collimator exit. The following results ensued (Φ_n in $n \cdot \text{cm}^{-2} \cdot \text{s}^{-1}$, the units of the γ dose in $\mu\text{Sv} \cdot \text{hr}^{-1}$):

	result	fsd
$(\Phi_n) < 1\text{eV}$	$1.41 \cdot 10^8$.0348
$1\text{eV} < (\Phi_n) < 10\text{keV}$	$5.44 \cdot 10^8$.0287
$(\Phi_n) > 10\text{keV}$	$2.65 \cdot 10^7$.0369
γdose	$2.71 \cdot 10^5$.0833

We note that the statistical error on the γ dose is appreciably higher than that on the neutron fluxes, possibly an unexpected result given the least squares minimization. In this problem the gamma rays are produced from absorption in the boron in the concrete of neutrons that have already passed through the collimator and contributed to the neutron flux. Thus it is clear that the optimum in this problem in the sense given in Sec. 1 will involve lower statistical errors on the neutron responses compared to the γ response. In this case the multi-response optimization provided somewhat larger savings in CPU time.

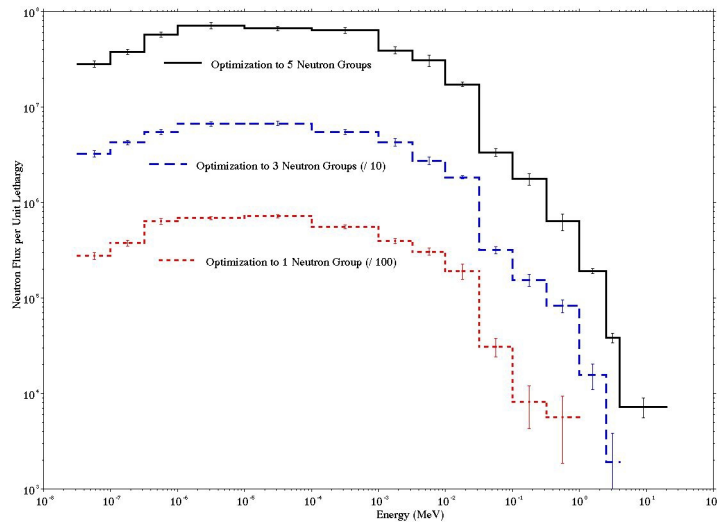


Fig. 2. TAPIRO neutron spectrum; three optimizations with different scale

3 Sub-Critical Assembly Driven by a Spallation Source

Sub-critical fissile assemblies driven by an external neutron source have aroused recent interest as a possible means to close the fuel cycle. This example deals

with a neutron spallation source deriving from 600 MeV protons bombarding a lead/bismuth target. The fuel is MOX and the primary coolant is also lead/bismuth. Interesting aspects of the Monte Carlo modeling of the radiation transport are the medium energy (some hundreds of MeV) transport of protons and neutrons, usually treated with intranuclear cascade models, followed by the subsequent transport of neutrons below 20 MeV in the sub-critical assembly. The latter feature gives rise to high variances when the level of sub-criticality is low (as is discussed in other papers at this meeting). These high variances arise mainly from the natural variance associated with the number of fission neutrons created per spallation neutron. (This particular model had a k_{eff} of 0.9724 and a k_s of 0.9715.) MCNPX (ver. 2.1.5) [10] was employed as the transport vehicle and, as an intermediate stage before being applied to all particles and energy ranges, the DSA was assigned to the same particles and energy ranges as MCNP4B. Although not actually designed to improve variances like the aforementioned ones, the DSA was firstly used to calculate the fission neutron source and as expected gave an improvement of just 15-20% in the *fom* over an analogue run. (This gain derived from the Russian rouletting of neutrons outside the fissile zone.) The DSA was then employed to optimize the V.R. parameters to a number of damage and flux responses throughout the reactor vessel. The spatial locations are shown in Fig. 3: ‘A’ is the lower part of the vessel below the target, ‘B’ is the radial part of the vessel, ‘C’ is a radial core retention ring, ‘D’ and ‘E’ are the lower and upper core support plates respectively and ‘F’ is the approximate position of the intermediate heat exchanger. All but ‘F’ are dpa responses; ‘F’ is the total neutron flux below 20 MeV. Here we will not enter into the details of the calculation but simply summarize the final results and discuss some interesting features. The results in Tab. 1 are presented for a running time of 10 y.

Table 1. First Moments and fsd’s (Sub-Critical-Assembly)

“A”(dpa)	“B”(dpa)	“C”(dpa)	“D”(dpa)	“E”(dpa)	“F”(n cm ⁻²)
7.92E-6	5.76E-3	8.80E-1	1.15E-1	1.71E+0	4.26E+21
(0.1050)	(0.0596)	(0.0584)	(0.1012)	(0.0574)	(0.0559)

The value of $(q_{fc})^{-1}$ at the optimum was about 5 times the value at the starting parameters which were a ‘good guess’. This is not a large gain and the reason for this is the aforementioned natural variance associated with the creation of fission neutrons. Approximately the same number of source protons (about 3500) that produced the results in Tab. 1 gave an error of 0.0469 on the fission source in a separate, quasi-analogue, calculation. Clearly a substantial fraction of the variance is associated with the fission source. Furthermore the very high natural correlation between the various responses, even in spatially distant parts of the core (due to a number of very high multiplication histories) also accounts for the inability to equalize the errors on the above six responses.

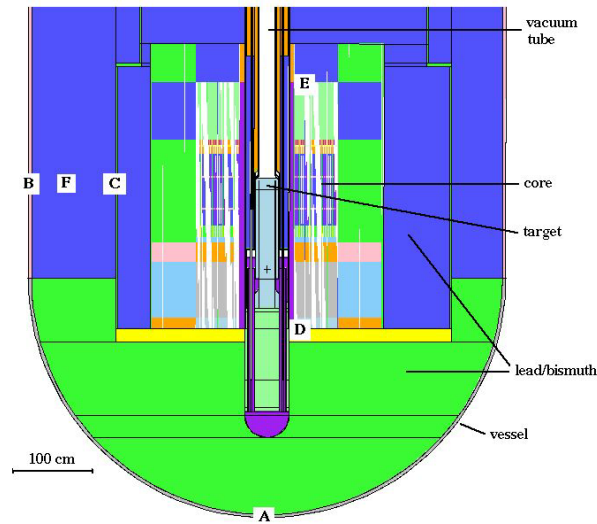


Fig. 3. Sub-Critical Assembly driven by Spallation Source

4 Thermal Neutron Calibration Assembly

The third example [8] concerns the characterization of a thermal neutron calibration facility. The facility consists of a $1 \times 1 \times 1 \text{ m}^3$ polyethylene cube containing three cavities of different dimensions where instruments to be calibrated are introduced and three $^{241}\text{Am} - \text{Be}$ neutron sources (see Fig. 4-a). TLD and CR39 detectors were employed to reconstruct the neutron flux over the whole spectrum and these detectors were sufficiently small to be modeled with point detectors. The spectrum, in 29 energy groups [9], was required at 14 points in line, 2 cm from the bottom of each cavity (five in cavities 1 and 3, four in cavity 2). Thus the Monte Carlo modeling was required to calculate $29 \times 14 = 406$ responses, each with an accuracy of $< 2\%$ (1 *fsd*). To reduce the problem to more manageable proportions, for the optimization the 29 energy groups were merged into a broad 6 energy group structure ($< 0.225 \text{ eV}$; $0.225 - 1 \text{ eV}$; $1 - 1.3 \text{ eV}$; $1.3 - 10 \text{ eV}$; $10 \text{ eV} - 1 \text{ MeV}$; $> 1 \text{ MeV}$) so as to produce a total of 84 responses (14 point detectors \times 6 broad energy groups). A total of 13 spatial cells were defined so as to transport neutrons from the sources to the vicinity of the detectors, to save time by not following unimportant tracks in the outer part of the assembly and to sample adequately the collisions near each detector. The latter point is extremely important: notwithstanding the fact that the point detectors were located in the cavity voids, the minimum distance to the cavity wall was just 2 cm and collisions near the detector strongly affect the variance. The above 6 energy group structure for the responses was expanded by adding 2 extra groups in the range $10 \text{ eV} - 1 \text{ MeV}$. The optimum variance

reduction parameters were generated in these 8 groups. Thus the DSA problem consisted of finding the optimum importances in 13×8 phase space cells and in the presence of 84 responses. The multi-response technique successfully generated a spectrum with a roughly constant noise level over the whole energy range at each of the detector positions. The maximum error was 2.06% (detector farthest from the sources in cavity 1, between 0.8 and 1 eV). A typical spectrum at one of the detector positions is shown in Fig. 4-b. Predicted gains in fom_c (us-

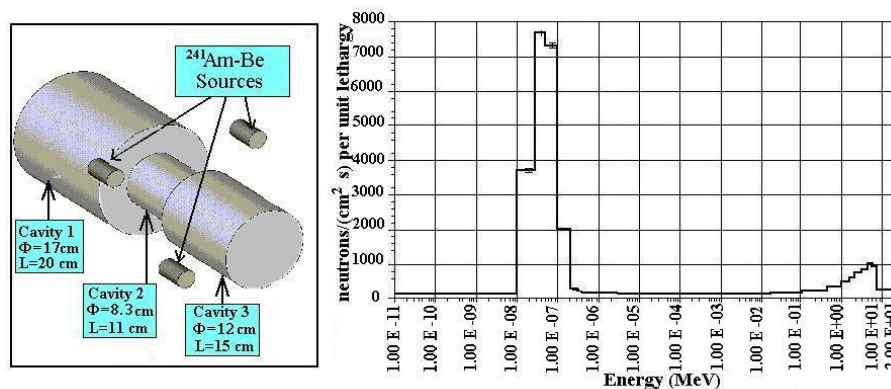


Fig. 4. a)(left) Thermal Neutron Calibration Facility: the Three Cavities. b)(right) Typical Spectrum at one of the Detector Positions

ing the DSA functions) were: 141 over analogue and 109 over the starting V.R. parameter guess ('quasi-analogue': analogue with some Russian roulette in the outer part of the assembly). The 406 figures of merit obtained were compared with those from the quasi-analogue run and from two series of calculations with the standard MCNP weight window generator [6]. The first of these employed the total flux averaged throughout the volume of the three cavities as the response of interest. The second attempted to account for the different width of the energy groups by weighting with the inverse of the lethargy width of each group. The comparison in the resulting fom's is shown in Figs. 5 and 6 for two representative detector points: that farthest from the sources in cavity 1 and in the centre of cavity 2 respectively. We note the tendency of the DSA to equalize the fom's as expected. We note also a substantial advantage in the quality of the DSA results: between a factor of 30 and 100 improvement over the other results.

5 Conclusions

This paper illustrates through three examples a technique that finds the set of variance reduction parameters that calculates the minimum error, in a least

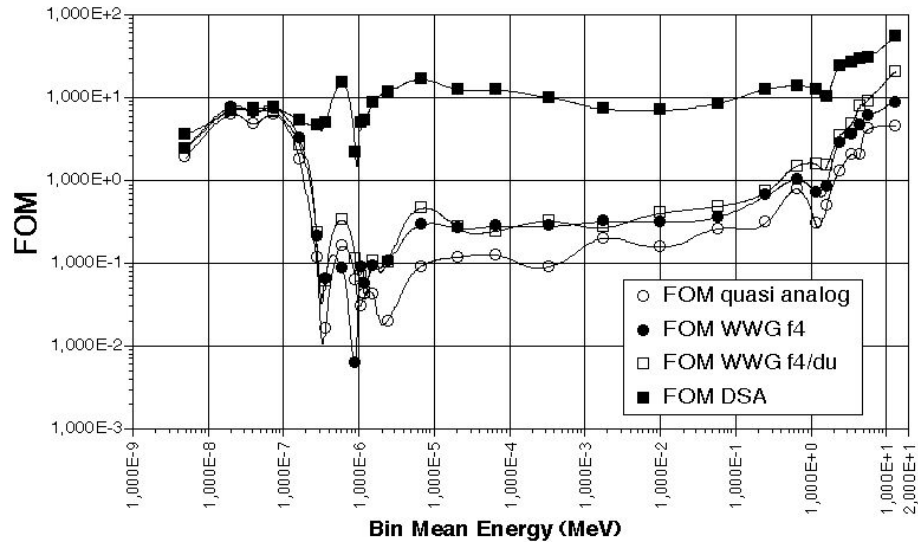


Fig. 5. Comparison of Figure of Merits for Position 1 Cavity 1

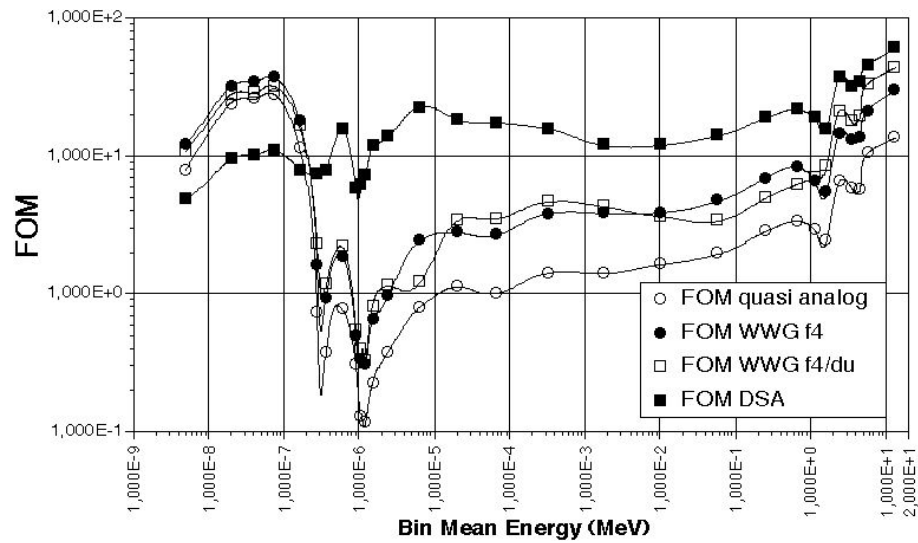


Fig. 6. Comparison of Figure of Merits for Position 2 Cavity 2

squared sense, of a set of radiation responses in a Monte Carlo calculation. The technique is based on the well-documented DSA and is of general application. The number of responses is unlimited and in the examples ranges from 3 to 84. Gain in CPU time is achieved over single optimizations directed at each response, through correlations in the histories. Some comparisons are made with

other approaches. Although less easily measurable, substantial gains in ‘human’ time are evident.

References

1. A. Dubi, T. Elperin, D.J. Dudzik: Nucl. Sci. Eng. **80**, 139 (1982)
2. A. Dubi: Trans. Theory and Stat. Phys. **14**, 167 and 195 (1985)
3. K.W. Burn: Ann. Nucl. Energy **19**, 65 (1992)
4. K.W. Burn: Nucl. Sci. Eng. **119**, 44 (1995)
5. K.W. Burn: Nucl. Sci. Eng. **125**, 128 (1997)
6. J.F. Briesmeister, Ed.: Group XTM, Los Alamos National Laboratory: *MCNP - A General Monte Carlo N-Particle Transport Code, Version 4B*, LA-12625-M, Version 4B, (1997)
7. K.W. Burn, E. Nava: ‘Optimization of Variance Reduction Parameters in Monte Carlo Radiation Transport Calculations to a Number of Responses of Interest’. In *Proc. Int. Conf. Nuclear Data for Science and Technology, Trieste, Italy, May 1997 (p. 260) (Italian Physical Society)*
8. K.W. Burn, G.F. Gualdrini, F. Monteventi, B. Morelli, E. Vilela: ‘Experimental and Monte Carlo Evaluation of the Dosimetric Characteristics of a Thermal Neutron Calibration Assembly’. *Int. Conf. on Solid State Dosimetry, Burgos, Spain, July 1998*
9. E. Vilela, B. Morelli, G. Gualdrini, K.W. Burn, F. Monteventi, E. Fantuzzi: ‘Characterizing a Thermal Neutron Calibration Assembly by Solid State, Nuclear Track Dosimeters and Monte Carlo Technique’, *ENEA RT/AMB/98/36 (1998)*
10. H.G. Hughes et al: ‘Status of the $MCNP^{TM}$ / LCS^{TM} Merger Project’. *Proc. of the Radiation Protection and Shielding Topical Conference, Nashville, Tennessee, April, 1998*

Use of a Hybrid Monte Carlo Technique for Power Shape Calculations

L. Hutton and N.R. Smith

The ANSWERS Software Service, AEA Technology plc, Winfrith Technology Centre, Dorchester, Dorset DT2 8ZE, United Kingdom

Abstract. There are many modelling situations in nuclear power reactors where a full three-dimensional solution of the transport equation would be of benefit. For example, in UK gas reactors there are significant three-dimensional effects associated with axial gaps in the fuel element, which cause significant perturbations to the flux and hence power. Other reactors also exhibit 3D effects, for example grids, partially inserted control rods and axial reflectors. To date these effects have been evaluated by approximate synthesis methods. There is a further requirement to accurately predict the effect of perturbations to parameters such as temperature and material density, an area where conventional Monte Carlo methods can be inefficient. Recent work has led to the development of an accurate and efficient 3D method, based on a hybrid Monte Carlo approach, to model the three-dimensional situations and provide accurate estimates of perturbed states. This paper outlines the approaches used for this method and demonstrates its application to practical situations.

1 Background

The WIMS [1] code suite has been established as a world-standard reactor physics package for more than thirty years. During that time, WIMS has been successfully applied to solve practical problems associated with a wide range of commercial power reactors and experimental and test facilities. The latest version of the code is WIMS8, which provides established calculation routes for LWR, heavy water moderated and gas cooled reactors. A range of solution methods exists, including diffusion theory, discrete ordinates, collision probabilities, characteristics and Monte Carlo.

WIMS also has an option that allows users to employ a hybrid Monte Carlo method to solve three-dimensional problems. This option has efficiency gains over conventional Monte Carlo approaches and accuracy benefits when compared with traditional reactor physics deterministic methods. This paper summarises the hybrid method and provides examples of its application to solve practical problems.

2 The Hybrid Monte Carlo Method MAX

2.1 Overview

MAX is a module of the WIMS reactor physics suite that solves the multigroup neutron transport equations by a hybrid deterministic/Monte Carlo method

based on exact perturbation theory. The calculation consists of a series of perturbations from a simple homogeneous geometry, each one being an incremental approach to the three-dimensional final model. The simple model is calculated (deterministically) using one of the other WIMS modules. This is then augmented by a series of Monte Carlo calculations for the perturbed flux and eigenvalue, as each perturbation to the simple model is performed. Thus the final perturbed flux solution is obtained from a hybrid of the deterministic and Monte Carlo fluxes.

2.2 Outline of MAX Theory

Using operator notation, the time independent Boltzmann Equation can be written as:

$$(\tilde{T} - \tilde{S} - \lambda\tilde{F})\phi = 0 \quad (1)$$

where the transport, scatter and fission yield operators are defined as:

$$\tilde{T}\phi(r, E, \Omega) = \Omega \cdot \nabla \phi(r, E, \Omega) + \Sigma_T(r, E)\phi(r, E, \Omega) \quad (2)$$

$$\tilde{S}\phi(r, E, \Omega) = \int \Sigma_S(r, E' \rightarrow \Omega)\phi(r, E', \Omega')dE'd\Omega' \quad (3)$$

$$\tilde{F}\phi(r, E, \Omega) = \chi(E) \int \nu \Sigma_f(r, E')\phi(r, E', \Omega')dE'd\Omega' \quad (4)$$

Now consider the unperturbed problem and let suffix 0 denote the operators and solution:

$$(\tilde{T}_0 - \tilde{S}_0 - \lambda_0\tilde{F}_0)\phi_0 = 0 \quad (5)$$

Now let this problem be perturbed with operators perturbed by the change in the cross sections between the problems as follows:

$$\tilde{T} = \tilde{T}_0 + \Delta\tilde{T}, \quad \tilde{S} = \tilde{S}_0 + \Delta\tilde{S}, \quad \tilde{F} = \tilde{F}_0 + \Delta\tilde{F} \quad (6)$$

The angular flux and eigenvalue will change due to the change in the operators:

$$\phi = \phi_0 + \Delta\phi, \quad \lambda = \lambda_0 + \Delta\lambda \quad (7)$$

and hence we have, for the change in the angular flux:

$$(\tilde{T} - \tilde{S} - \lambda\tilde{F})(\phi_0 + \Delta\phi) = 0 \quad (8)$$

Taking the initial angular flux to the right hand side, expanding the operators and eigenvalue in terms of the initial solution and remembering that the unperturbed problem satisfies the 'suffix 0' equation gives:

$$(\tilde{T} - \tilde{S} - \lambda\tilde{F})\Delta\phi = \left(\lambda_0\Delta\tilde{F} + \Delta\tilde{S} - \Delta\tilde{T}\right)\phi_0 + \Delta\lambda\tilde{F}\phi_0 \quad (9)$$

The change in the eigenvalue may be estimated by considering the adjoint equation. Multiplying by the adjoint flux and integrating over all space, angles and energy ranges, expanding the left hand side and re-arranging gives:

$$\begin{aligned} \int \phi_0^* (\tilde{T}_0 - \tilde{S}_0 - \lambda_0\tilde{F}_0) \Delta\phi dV dEd\Omega = \\ \int \phi_0^* (\lambda_0\Delta\tilde{F} + \Delta\tilde{S} - \Delta\tilde{T}) (\phi_0 + \Delta\phi) dV dEd\Omega + \Delta\lambda \int \phi_0^* \tilde{F} (\phi_0 + \Delta\phi) dV dEd\Omega \end{aligned} \quad (10)$$

By virtue of the adjoint solution, the left hand side is zero, thereby defining the change in the eigenvalue. Using this, (9) can then be written:

$$\begin{aligned} (\tilde{T} - \tilde{S} - \lambda\tilde{F})\Delta\phi = \left(\lambda_0\Delta\tilde{F} + \Delta\tilde{S} - \Delta\tilde{T}\right)\phi_0 \\ + \frac{\int \phi_0^* (\Delta\tilde{T} - \Delta\tilde{S} - \lambda_0\Delta\tilde{F}) \phi dV dEd\Omega}{\int \phi_0^* \tilde{F} \phi dV dEd\Omega} \tilde{F}\phi_0 \end{aligned} \quad (11)$$

3 Implementation Overview

During the development of the MAX method, several implementation issues were successfully addressed. The following sections discuss some of these issues.

3.1 Source Particles

The final equation from the above MAX theoretical section can be thought of as a fixed source equation with the source term defined by the right hand side. The source expression depends on the values of the perturbation operators, which in turn depend on the geometry of the perturbed problem. The source will also depend on the unperturbed flux, which can be any analytic function of space, energy and angle, and the eigenvalue. However, the current implementation of MAX assumes that the unperturbed case is a homogeneous cell with reflective boundary conditions.

The above source term will thus be an analytic function that is continuous in zones which have the same materials, with discontinuities at material boundaries. Also the source will have zones in space and energy where the value is negative as well as zones where it is positive (the operators in the source contain differences between the material cross sections). This approach leads to the concept of a negative weight particle tracking through space as well as the conventional positive weight particles. Both types of particles are tracked in the normal way, but throughout the tracking these particles can annihilate each other.

3.2 Sequences of Perturbations

It is possible using the MAX technique to break the complexity of realistic perturbations into several incremental stages. This improves both the efficiency of the calculation and the analysis and hence understanding of the problem. For example (which is discussed below), an AGR (Advanced Gas Reactor, a UK graphite moderated reactor design) lattice cell calculation can be generated from a homogeneous calculation in three or more stages:

- Separate the fuel zone into a 36 pin cluster and introduce voids into the moderator zone;
- Introduce axial variation in the fuel due to the presence of end gaps, aluminium pellets and fuel end caps;
- Introduce burnable poison toroids.

Each of these changes can be represented by a perturbation to the immediate lower level of complexity. In this way, the effect of each perturbation can be assessed separately. In addition, the uncertainties associated with each change can be separately controlled by optimising the Monte Carlo sampling for each perturbation individually.

3.3 Treatment of Absorbers

The source term for a perturbation that involves the introduction of a material with high absorption (e.g. gadolinium) can be very significant due to the change in the transport operator. This will lead to a markedly higher weight for neutrons tracked from the perturbation source, due to neutrons being started in all zones of the absorber; in fact, many of these particles have a negligible probability of escape from the absorber. The MAX implementation avoids this potential inefficiency by tracking source neutrons from a boundary enclosing the absorber.

4 Application of MAX

4.1 Comparison with MONK Calculations

The MAX method has been recently used to calculate reactivity and power profiles for a 3D model of a poisoned AGR fuel element. In particular the method has been applied to AGR problems with axial gaps in the fuel and toroids of burnable poisons. The geometry is an idealised AGR fuel element, with reflective boundaries at the mid-point of the fuel and the mid-point in the gap between fuel elements. Comparison calculations have been performed with MONK [2]. The relative power results from the MAX and MONK calculations are shown in Tab. 1, with efficiency comparisons given in Tab. 2.

These results show excellent agreement between MAX and MONK, with the fine power structure results (the two pellets at each end of the element) consistent within two standard deviations in all cases. In terms of efficiency, there is a general increase of at least an order of magnitude for the end of pin locations. For the results in the centre of the fuel, the efficiency gain is smaller due to the better sampling possible from a 'standard' Monte Carlo calculation.

Table 1. Comparison of MAX and MONK for AGR Relative Power

	Inner Ring (MAX-MONK)		Middle Ring (MAX-MONK)		Outer Ring (MAX-MONK)	
Position	Difference	St Dev	Difference	St Dev	Difference	St Dev
Bottom pellet	-1.21	1.79	0.62	1.10	1.42	1.19
2nd bottom pellet	2.35	1.39	1.83	1.03	1.75	1.04
Mid-element pellet	0.13	0.06	0.15	0.04	0.32	0.05
2nd top pellet	-0.65	1.63	-0.26	1.22	0.65	0.75
Top pellet	0.30	2.34	1.51	1.55	0.66	1.00

Table 2. Comparison of MAX and MONK Calculation Times for AGR Relative Power

Position	MONK/MAX time ratio	MONK/MAX time ratio	MONK/MAX time ratio
Bottom pellet	13.0	14.2	45.2
2nd bottom pellet	14.0	27.1	59.1
Mid-element pellet	1.8	1.4	2.0
2nd top pellet	12.9	22.4	19.9
Top pellet	21.8	27.2	29.0

4.2 Comparison with Experiment

As part of an on-going monitoring programme, a series of PIE (post irradiation examination) measurements have been carried out to examine the axial variation in power in an AGR fuel element. The measurements considered a range of fuel enrichment from 1.16 w/o to 2.5 w/o; the irradiation at which measurements were taken varied from 0 to 20GWd/Te. These situations have been calculated by WIMS using the MAX method. Table 3 shows the mean differences between experiment (E) and MAX calculations (C) for a range of enrichments and irradiations. In general the agreement with MAX is very good and shows that MAX reproduces the variation with both enrichment and irradiation.

Table 3. Mean (C-E)/E % for AGR Stage 1 Fuel

	Irradiation (GWd/te)				
Position	0	5	10	15	20
End Fuel Pellets - Mean	0.87	0.65	2.04	1.50	1.01
<i>Standard Deviation</i>	<i>1.38</i>	<i>0.89</i>	<i>1.56</i>	<i>0.80</i>	<i>0.81</i>
Next-to-end Fuel Pellets - Mean	1.21	0.55	0.28	-0.07	-0.09
<i>Standard Deviation</i>	<i>1.17</i>	<i>0.65</i>	<i>1.17</i>	<i>0.71</i>	<i>0.92</i>
Overall Mean	0.94				
<i>Standard Deviation</i>	<i>0.68</i>				

5 Benefits of MAX Approach

The above sections have outlined the method and application of a hybrid Monte Carlo approach to solving three-dimensional reactor analysis problems. This technique fits into the gap that exists between deterministic methods and full Monte Carlo approaches. The major benefits of this hybrid approach are:

- The method allows for improved geometry modelling capabilities compared with those that are present in conventional deterministic methods. In principle, full Monte Carlo modelling is available for the perturbation calculations, such that geometrical approximations required by lattice codes can be removed.
- The calculation time is much reduced compared with a full Monte Carlo analysis. For the example used here, the improvement in calculation time is of the order of at least a factor of ten in favour of MAX when calculating fine power profiles or poison worth.
- The efficiency of the MAX calculation is related to the sequences of perturbations employed. To date, MAX has started from a homogeneous calculation, with incremental perturbations thereafter to produce the 3D model. It has been shown that the first step in the perturbation sequence (from one-dimensional model to cluster geometry) is the largest source of uncertainty in the calculation. Further work is now in progress aimed at removing this source of uncertainty by enabling the starting process to be a CACTUS model, the main characteristics deterministic solution method in WIMS.

6 Conclusions

Recent work has led to the development of an accurate and efficient 3D method in the WIMS reactor physics code suite, based on a hybrid Monte Carlo approach. This paper has outlined the approaches used for the method and demonstrated its application to practical situations, where agreement with full Monte Carlo calculations and experiment has shown to be good. The major benefits of this approach are improved modelling accuracy compared with deterministic methods and improved efficiency over full Monte Carlo approaches, particularly for the calculation of fine details such as power profiles. Work is now in progress to improve the efficiency of the approach further, which will also lead to an extension in the range of calculations that is possible.

References

1. J.L. Hutton: 'New Capabilities of the WIMS Code'. In *Proceedings of PHYSOR'2000, Pittsburg (May 2000)*
2. N.R. Smith et al: 'The Current Status and Future Plans for the Monte Carlo Codes MONK and MCBEND'. These Proceedings p. 637

Eigenvalue Uncertainty Evaluation in MC Calculations, Using Time Series Methodologies

O. Jacquet¹, R. Chajari¹, X. Bay², A. Nouri³, and L. Carraro²

¹ Institut de Protection et de Sûreté Nucléaire, F-92265 Fontenay-aux-Roses, France

² Ecole des Mines de Saint-Etienne, Département 3MI, F-42023 Saint-Etienne, France

³ OECD NEA Data Bank, Issy-les-Moulineaux, F-92130 Issy-les-Moulineaux, France

1 Introduction

The accurate determination of confidence intervals is one of the outstanding problems of the standard Monte Carlo algorithm used for solving the homogeneous neutrons transport equation. If we denote k_i the k-effective estimate corresponding to generation i , the best estimate of the eigenvalue after N generations is the average of k_i within the N generations. Two usual hypotheses are made to calculate the standard deviation of the eigenvalue:

- The source distribution has converged to the fundamental mode, i.e. the successive estimates k_i are realization of the **same random variable**.
- The successive estimates k_i are **independent realisations** of this random variable.

These two assumptions simplify the standard deviation estimation, but Demaret et al. [1] have shown that these approximations are not valid because:

- The source convergence can require a large number of generations. Consequently, the first generations do not give reliable estimates of k-effective, and the (k_i) series contains an initial transient.
- The successive estimates k_i are correlated due to the sampling of starting neutrons for generation i among the fission sites of generation $i - 1$. The correlations can be excessively large especially in the settling process of source convergence.

Consequently it is crucial to control the **convergence** of the source distribution before starting the estimation of k-effective and its statistical error. Moreover, the **correlations** between generations should not be neglected even in the stationary phase, otherwise **the variance can be underestimated**. Some statistical methods which may be used for the elimination of the initial transient are presented in Part 2. Then in Part 3, three methods aiming at improving the variance estimation, already studied by Demaret et al. [1], are briefly described. They all three assume the stationarity of the (k_i) series. Part 4 is devoted to a comparison of the three methods on a real case. Statistics background can be found in [2] and was summarized in [1].

2 Stationarity Detection and Initial Transient Suppression

The initial transient observed in the k-effective series (k_i) is obviously a consequence of the process of the source distribution (or eigenvector) convergence from the initial guess to the fundamental mode. However, it is much easier to study the convergence in a series of scalar values than in a series of vectors. It could of course be argued that apparent convergence of eigenvalue does not strictly imply the convergence of the source distribution. Nevertheless, the statistical nature of Monte Carlo results makes it difficult to distinguish, near the equilibrium, between the variability of results due to randomness and the variability due to non strict convergence. It is then intended to roughly truncate the (k_i) series in order to skip the main part of the initial transient, with the risk of retaining few non strictly converged generations or skipping few converged generation. It should be noticed that the transient suppression aims only at obtaining a stationary series. As a consequence, it is necessary to run a sufficient number of generations to ensure that the powering algorithm has converged to the true eigenvalue, or to use an improved powering method which guarantees that the most reactive parts of the system are correctly sampled after the transient (see a discussion on this subject by Miss et al. in this conference).

Methods recently developed in the area of statistics were investigated to detect the stationarity. Let us define for $1 \leq j \leq N$:

$$B_N(j) = \frac{j(\bar{k}_j - \bar{k}_N)}{\tau\sqrt{N}} \quad (1)$$

with

$$\bar{k}_j = \frac{1}{j} \sum_{i=1}^j k_i \quad (2)$$

and

$$\tau^2 = \lim_{N \rightarrow \infty} N \times \text{Var}(\bar{k}_N). \quad (3)$$

According to the work of Schruben [3] and of Heidelberger and Welch [4], if the (k_i) series is close to ‘good’ stationarity, then $(B_N(j))_{j=1,\dots,N}$ converges in distribution to a Brownian bridge as N tends to infinity. Different methods were designed to test whether B_N looks like a Brownian bridge. Basically, the appropriate tests (Cramer–von Mises, Anderson–Darling, Kolmogorov–Smirnov, Schruben) are performed at first on the entire series. If the expected properties are verified, the (k_i) series is considered as stationary, otherwise the series is truncated (5 % of first generations skipped) and the tests are performed again. The procedure is repeated as long as the test is negative and the number of remaining generations is statistically sufficient.

The feasibility was tested with theoretical cases where an analytical model was designed, representing a stationary (k_i) series, and where various kinds of transients (different shapes and lengths) were added to the beginning of the

series. The investigations performed so far [5] show that the method using the Schruben statistic seems to be the most robust one. However these methods are efficient only if the variance of the mean estimator, τ^2 , is correctly estimated.

Non-parametric methods have been proposed to avoid the estimation of τ^2 [6]. The development and the evaluation of these methods with theoretical cases is still in progress but they seem to give promising results. The final step will consist in validating the transient suppression on real k-effective series but this point is delicate since the end of the transient is never known in the practical cases.

3 Review of Methods Improving the Variance Estimation

This part is devoted to the **calculation of the variance, taking into account the correlations between the k_i , once the initial transient has been truncated**. Let (k_i) be a stationary series of N observations of average \bar{k} . Three methods have been proposed to give a better estimation than the (underestimating) **classical variance estimator**: $\hat{\sigma}^2 = \frac{1}{N(N-1)} \sum_{i=1}^N (k_i - \bar{k})^2$.

3.1 The Batching Method

To reduce the effect of the correlations between successive generations in the variance estimation, Gelbard and Prael [7] suggested to cluster the N step estimators k_i into p batches of size n . The new estimator is then simply:

$$\sigma_g^2 = \frac{1}{p(p-1)} \sum_{i=1}^p (Y_i - \bar{Y})^2 \quad (4)$$

with

$$Y_i = \frac{1}{n} \sum_{j=1}^n k_{n(i-1)+j}. \quad (5)$$

3.2 Method by Ueki et al.

Having established the expression for the bias of the classical variance estimator as well as the expression for the bias of the standard estimator $\hat{c}(i)$ of autocovariances, Ueki et al. [8] suggested an iterative procedure allowing for the computation of the variance (denoted as σ_u^2 in the following):

$$\sigma_u^2 = \hat{\sigma}^2 + \frac{2}{N(N-1)} \sum_{i=1}^{N-1} (N-i) c(i) \quad (6)$$

and

$$c(i) = \hat{c}(i) + \sigma_u^2. \quad (7)$$

The autocovariances are considered as null for $i > 10$. As positive correlations between generations are expected in eigenvalue calculations, Ueki et al. suggested to set the negative estimates $\hat{c}(i)$ to zero. In the following, the results referred as Ueki in the tables are obtained by setting the negative autocorrelations to zero. Calculations have also been performed without setting the negative autocorrelations to zero to see the effect of that point. Our experience with this method shows that the iterative process converges at the first stage.

3.3 Use of Time Series Methodology

A more generic method proposed by Demaret et al. [1], using time series methodology [2], consists in representing the (k_i) by means of an autoregressive model.

The autoregressive models of order p , denoted as $AR(p)$, are defined as follows: $X_t = \sum_{i=1}^p \varphi_i X_{t-i} + \varepsilon_t$ where (ε_t) is a white Gaussian noise with a variance σ_ε^2 . The procedure used for the modelisation of the stationarised (k_i) series can be divided into three steps: 1) estimation of the $AR(p)$ parameters $\hat{\varphi}_i$ and of the residual $\hat{\varepsilon}_t$ for various orders p , 2) choice of the best order p using the criteria AIC or BIC aimed at reducing both the variance of the residual $\hat{\sigma}_\varepsilon^2$ and the number of parameters, 3) check that the residual is a white Gaussian noise.

The autocovariances are derived from the parameters of the AR model:

$$c(0) - \hat{\varphi}_1 c(-1) - \dots - \hat{\varphi}_p c(-p) = \hat{\sigma}_\varepsilon^2 \quad (8)$$

$$c(k) - \hat{\varphi}_1 c(k-1) - \dots - \hat{\varphi}_p c(k-p) = 0 \text{ for } 1 \leq k \leq N-1. \quad (9)$$

The variance is then:

$$\sigma^2 = \frac{1}{N} \left[c(0) + 2 \sum_{i=1}^{N-1} \left(1 - \frac{i}{N} \right) c(i) \right]. \quad (10)$$

4 Comparison of the Variance Estimators on a Special Case

Like in [1], the three methods described above were applied on k-effective series obtained with the Monte Carlo code MORET4 [9] on a particular case. The configuration is a lattice of $5 \times 5 \times 1$ highly enriched uranium metal spheres of radius 8.71 cm, with exception of the central one, which has a radius of 10 cm. The spheres are in interaction in air with a distance of 80 cm from centre to centre. The number densities of atoms for metal uranium are $0.04549 \cdot 10^{24} \text{ cm}^{-3}$ and $0.00256 \cdot 10^{24} \text{ cm}^{-3}$ for ^{235}U and ^{238}U respectively.

5 000 independent replicas were run (using different random number sequences), each of them consisting of 1 000 generations of 1 000 neutrons. To obtain stationary series, Demaret et al. [1] have determined the proportion of starters to be emitted in each sphere: 932 neutrons in the central sphere, 9 in

each of the 4 closest volumes to the central sphere, 4 in each of the 4 volumes in the diagonal position relative to the central sphere and 1 in each of the other 16 peripheral spheres.

The **external variance**, taken as the reference value, characterises the spread of the 5 000 average k-effective values. As the 5 000 values appear to follow a Gaussian distribution, the uncertainty on the variance estimate is about ± 4 % with a level of confidence of 95 %. 200 independent replicas, like in [1], allow estimating the variance with an uncertainty of ± 20 %, which is not sufficiently precise to compare the methods.

For each k-effective series, the variance of the mean (called the **internal variance**) was calculated using different methods (classical, batching, Ueki et al., fitting to $AR(p)$ model). The batching method was used with different batch sizes: 2, 5, 10 or 20 generations per batch. The variance based on time series methodologies has been calculated by fitting systematically to an $AR(p)$ with p fixed between 1 and 5, or by selecting the best order p according to AIC or BIC. The variance has been estimated even if the residual of the model was not a white noise. Thus, a certain proportion of the 5 000 estimates of the variance could be not valid.

Results with 1 000 (resp. 200) generations per replica are given in Tabs. 1 and 2 (resp. Tabs. 3 and 4). The bias of each estimator is estimated as the difference between the average of the 5 000 internal variance estimates and the external variance. The **mean quadratic error** (MQE) of an estimator, sum of the square of the bias and the variance of the estimates, should be as low as possible. At last, for each variance estimator, the level of confidence of a ' $\pm 3\sigma$ interval' is estimated as the rate of replicas such that the ' $\pm 3\sigma$ interval', around the estimated k-effective, contains the 'true k-effective' (5 000 results average).

Table 1. Classical, batching and Ueki et al. estimators.
5 000 replicas of 1 000 generations. External variance = $1.01 \cdot 10^{-6} \pm 4$ %

	Classical	batch-2	batch-5	batch-10	batch-20	Ueki
Average of intern. variances	$5.99 \cdot 10^{-7}$	$6.81 \cdot 10^{-7}$	$7.96 \cdot 10^{-7}$	$8.69 \cdot 10^{-7}$	$9.22 \cdot 10^{-7}$	$1.05 \cdot 10^{-6}$
Bias	-40.9 %	-32.8 %	-21.4 %	-14.2 %	-9.02 %	3.50 %
Variance of intern. variances	$7.62 \cdot 10^{-16}$	$1.94 \cdot 10^{-15}$	$6.23 \cdot 10^{-15}$	$1.50 \cdot 10^{-14}$	$3.30 \cdot 10^{-14}$	$2.21 \cdot 10^{-14}$
MQE	$1.72 \cdot 10^{-13}$	$1.12 \cdot 10^{-13}$	$5.34 \cdot 10^{-14}$	$3.58 \cdot 10^{-14}$	$4.14 \cdot 10^{-14}$	$2.33 \cdot 10^{-14}$
Conf. level of $\pm 3\sigma$ interval	98.0 %	98.7 %	99.3 %	99.6 %	99.5 %	99.8 %

From these results, the first observation is that the bias of the classical estimator is about -40 %, whatever the number of generations is.

The results obtained with the batching method show a systematic decrease of the bias with the number of generations per batch. However, results indicate that as much as 20 generations per batch are not sufficient (the bias is about -9 % (resp. -7 %) with 1 000 (resp. 200) generations per replica, compared to the

Table 2. Fitting to $AR(p)$ with a fixed order or with AIC or BIC criteria.
5 000 replicas of 1 000 generations. External variance = $1.01.10^{-6} \pm 4 \%$

	AR(1)	AR(2)	AR(3)	AR(4)	AR(5)	AIC	BIC
Average of intern. vari.	$8.17.10^{-7}$	$9.22.10^{-7}$	$9.81.10^{-7}$	$1.01.10^{-6}$	$1.04.10^{-6}$	$8.13.10^{-7}$	$8.15.10^{-7}$
Bias	-19.3 %	-8.95 %	-3.16 %	+0.14%	+3.15 %	-19.8 %	-19.5 %
Variance of intern. vari.	$7.12.10^{-15}$	$1.67.10^{-14}$	$2.85.10^{-14}$	$4.19.10^{-14}$	$5.63.10^{-14}$	$7.15.10^{-15}$	$7.09.10^{-15}$
MQE	$4.54.10^{-14}$	$2.49.10^{-14}$	$2.95.10^{-14}$	$4.19.10^{-14}$	$5.73.10^{-14}$	$4.73.10^{-14}$	$4.61.10^{-14}$
Conf. level of $\pm 3\sigma$ interval	99.4 %	99.7 %	99.8 %	99.7 %	99.7 %	99.3 %	99.3 %

Table 3. Classical, batching and Ueki et al. estimators.
5 000 replicas of 200 generations. External variance = $4.89.10^{-6} \pm 4 \%$

	Classical	batch-2	batch-5	batch-10	batch-20	Ueki
Average of intern. vari.	$2.98.10^{-6}$	$3.40.10^{-6}$	$3.96.10^{-6}$	$4.32.10^{-6}$	$4.55.10^{-6}$	$6.24.10^{-6}$
Bias	-39.0 %	-30.4 %	-18.9 %	-11.6 %	-6.90 %	+27.6 %
Variance of intern. vari.	$9.58.10^{-14}$	$2.48.10^{-13}$	$8.06.10^{-13}$	$1.98.10^{-12}$	$4.78.10^{-12}$	$2.64.10^{-12}$
MQE	$3.72.10^{-12}$	$2.45.10^{-12}$	$1.66.10^{-12}$	$2.30.10^{-12}$	$4.89.10^{-12}$	$4.47.10^{-12}$
Conf. level of $\pm 3\sigma$ interval	98.4 %	98.7 %	99.0 %	99.0 %	98.4 %	99.7 %

Table 4. Fitting to $AR(p)$ with a fixed order or with AIC or BIC criteria.
5 000 replicas of 200 generations. External variance = $4.89.10^{-6} \pm 4 \%$

	AR(1)	AR(2)	AR(3)	AR(4)	AR(5)	AIC	BIC
Average of intern. vari.	$4.91.10^{-6}$	$6.36.10^{-6}$	$7.64.10^{-6}$	$8.69.10^{-6}$	$1.01.10^{-5}$	$4.69.10^{-6}$	$4.73.10^{-6}$
Bias	+0.51 %	+30.2 %	+56.3 %	+77.8 %	+107 %	-4.09 %	-3.26 %
Variance of intern. vari.	$3.33.10^{-12}$	$1.24.10^{-11}$	$2.85.10^{-11}$	$5.22.10^{-11}$	$9.34.10^{-11}$	$2.82.10^{-12}$	$2.88.10^{-12}$
MQE	$3.33.10^{-12}$	$1.46.10^{-11}$	$3.60.10^{-11}$	$6.66.10^{-11}$	$1.21.10^{-10}$	$2.86.10^{-12}$	$2.90.10^{-12}$
Conf. level of $\pm 3\sigma$ interval	99.4 %	99.5 %	99.6 %	99.6 %	99.7 %	99.3 %	99.4 %

2 sigma relative uncertainty of the external variance of 4 %). The optimal size of batch, minimizing the MQE, depends on the number of generations available.

The method by Ueki et al. (either using all correlations or setting to zero negative ones) gives satisfactory results when the number of generations is important. However, with 200 generations only, if negative autocorrelations are not set to zero, negative variances are obtained in some cases. When negative autocorrelations are set to zero, a positive bias (+28 %) is obtained.

The performances of autoregressive model also depend on the number of generations. When this number is sufficient, high order AR models have better performances (very small bias in the case of AR(4) and minimum MQE for AR(2)). First order AR as well as AIC and BIC criteria have a strong negative bias (-19 %). When the number of observations is rather small, first order AR

seems adequate while high order AR strongly overestimate the variance (+107 % for $p = 5$). AIC and BIC criteria follow closely AR(1) model.

In fact, the general observation is that when the number of observations is sufficient, evidence of high order correlations in the k-effective series is clearly highlighted. In this case, an accurate calculation of the variance requires methods using a sufficient number of autocorrelations (high order AR models or Ueki et al.'s estimator) or defining large batches. When the number of observations in the series is too low, the correlation is unchanged (still high) but difficult to estimate. Thus, methods using high order autocorrelations fail when the number of generations is not sufficient: the variance of Ueki's method becomes negative if ten autocorrelations are used and the bias becomes important if the negative ones are set to zero. The method would probably improve if the number of autocorrelations was reduced. AR(p) methods with high orders also fail and an AR(1) model is sufficient.

As a conclusion, if a criterion to select the order of AR could be defined to take into account the number of generations available, the time series methodology would be the preferred one. AIC and BIC are clearly not the right criteria.

5 Conclusion

As far as stationarity detection is concerned, various methods using Brownian bridge theory exist in the literature. Most of them need the estimation of the asymptotic variance of the mean, which is all the more complicated when an initial transient exists. Non-parametric methods could be more robust because none parameter estimation is required.

As far as the estimation of variance is considered, it seems that the fitting to an autoregressive model is a complementary method to the method by Ueki et al. Indeed, when the number of generations is important, the two methods give comparable estimations (for an AR order of 3 or 4). When the number of generations is low (200), either Ueki et al.'s estimator overestimates the variance if the negative estimates of autocorrelations are set to zero, or it can give negative estimates otherwise. On the contrary, the fitting to an AR with a low order allows the computation of improved confidence intervals, without the tendency to overestimate the variance. In fact, the method by Ueki et al. systematically takes ten autocorrelations into account and requires an important number of generations to obtain a good estimation of all these autocorrelations. As a consequence, the interest of the method based on the fitting to an AR lies in the fact that it does not fix in advance the number of autocorrelations to consider. It is clear that the number of autocorrelations to take into account (which corresponds to the order of AR) should depend on the number of generations. An appropriate criterion to determine the suitable order of AR will have to be found in order to use the fitting to an AR. Indeed AIC and BIC criteria are not the good one because they systematically favour low orders. The prospect for a non-linear model, as an alternative to the fitting to an AR, is also considered to better take into account the dynamics of the k-effective series.

References

1. L. Demaret, A. Nouri, L. Carraro, O. Jacquet: ‘Accurate Determination of Confidence Intervals in Monte Carlo Eigenvalue Calculations’. In *ICNC’99 Proceedings, Versailles, France, Sept 1999*, vol. I pp. 66–80
2. P. Brockwell, R. Davis: *Time Series: Theory and Methods*. (Springer, 1987)
3. L. Schruben: ‘Detecting Initialization Bias in Simulation Output’. In *Operations Research*, vol. 30 (May–June 1982)
4. P. Heidelberger, P. Welch: ‘Simulation Run Length Control in the Presence of an Initial Transient’. In *Operations Research*, vol. 31 (Nov–Dec 1983)
5. S. Damoiseau: *Détection et suppression de la partie non stationnaire dans les calculs du facteur de multiplication effectif par Monte Carlo*. IPSN report SEC/T/99.306
6. G. Vassilacopoulos: ‘Testing for Initialization Bias in Simulation Output’. *Simulation Councils* (1989)
7. E. Gelbard, R. Prael: Prog. Nucl. Energy **24**, 237 (1990)
8. T. Ueki, T. Mori, M. Nakagawa: Nucl. Sci. Eng., **125**, 1 (1997)
9. A. Nouri, A. Le Cocq, J. Dupas, O. Jacquet, I. Vortisch: *MORET4: a versatile and accurate Monte Carlo code for criticality calculations*. IPSN report SEC/T/00.061

Development and Comparison of Monte Carlo Techniques Implemented in the MORET4 Code for the Calculation of Loosely Coupled Systems

J. Miss¹, O. Jacquet¹, and A. Nouri²

¹ Institut de Protection et de Sûreté Nucléaire, BP 6, 92265 Fontenay-aux-Roses, France

² OECD/NEA Data Bank, 12 Boulevard des Îles, 92130 Issy-les-Moulineaux, France

Abstract. The performances of the Monte Carlo method and the easiness of its use enable to calculate more and more complex configurations. In some cases, when there is little coupling of neutrons between the different fissile media of the system, a careful check of neutron simulation is needed. Within the framework of nuclear criticality, the use of the current codes and the reliability of their results suffer restrictions. In fact, as was stressed by Whitesides in a famous article [1], the calculated k_{eff} becomes erroneous under certain circumstances (often under-estimating the reactivity of the system). In this paper, one shows some aspects of the difficulty encountered when calculating weakly coupled systems. New developments have been performed in the MORET4 code [2] to improve the calculation of k_{eff} in geometries including such weakly coupled fissile units.

1 Introduction

Consider in a criticality study, a system composed of units which are very loosely coupled: for example, all objects have the same eigenvalue except one which has an higher eigenvalue. The correct sources distribution can be, in such a case, very difficult to achieve. So an erroneous estimation (underprediction) of k_{eff} can be obtained by conventional Monte Carlo calculations [3]. The main origins of this problem are:

1. the slowness of sources convergence: this difficulty is usually connected with the choice of the first generation source, i.e. the total number of neutrons per generation and the fraction of neutrons in each fissile unit,
2. the “desertification” of important fissile units; this problem is caused by the finite size of each stage and the procedure used to produce the source for next generation.

Three methods (superhistory powering, fission matrix method, and stratified sampling) were developed by different Monte Carlo teams and each of them was introduced in known codes and applied for the study of specific problems. Nevertheless, there is no clear consensus on these methods since: 1) they were not compared on the same set of problems, 2) other aspects of Monte Carlo implementation may be the origin of differences between the results obtained with different codes. The implementation of the three methods in the same Monte Carlo code MORET4 [4] enables to carry out reliable comparisons. The

paper aims at assessing the efficiency of these methods to solve the problems of slow convergence and undersampling.

2 Monte Carlo Strategies

A brief description of the different simulation techniques are given below:

- **Stratified sampling:** when the neutron population is relatively small in a system with several fissile units, the number of neutron sources in certain volumes can be less than one. The conventional sampling can miss generating sources in these volumes. Then these volumes can be definitely lost from the point of view of the simulation, if the units are weakly coupled. To avoid this, Mohamed and Gelbard [5] proposed a method of stratified sampling, introducing weights. Every fissile zone will always contain at least one neutron, possibly with a weight inferior to one. This method requires that the user places at least one starter in each fissile unit at the first stage.

- **Superhistory powering:** in conventional simulations the neutron population is renormalized at every generation in order to keep artificially a stable chain reaction. Brissenden and Garlick [6] showed that this leads to a bias on the k_{eff} value and proposed a method which renormalizes the neutron population every L generations (L is equal to 10 in this study). In order to stabilize the situation, the superpowering algorithm modifies the ν value for fission throughout the system by dividing the actual value by the best current estimate of k_{eff} .

- **Fission matrix method (or Green's function method):** Kadotani et al. [7] have proposed a method to speed up the convergence based on the use of the k -matrix, customarily called the fission matrix. Each element of the matrix represent the number of neutrons produced in the unit i as result of a neutron emitted by fission in the unit j . The highest eigenvalue of the matrix is the k_{eff} of the system, and the normalize eigenvector gives the fraction of the neutron-source in each fissile unit. They proposed to calculate the elements of the matrix only by considering the neutrons of the last generation. In order to reduce the uncertainty on the terms of the matrix, and to get an adequate eigenvector, Nouri [8] proposed to calculate the terms of the matrix for generation g using all the simulated histories during the generations $1, 2, \dots, g$. By using the eigenvector every F generations (F is equal to 10 in this study) to recalibrate the sources, the convergence of the fission distribution is expected to be satisfactory accelerated. This method requires that the user places at least one starter in each fissile unit at the first stage.

3 MORET4 code

MORET4 is a multigroup Monte Carlo code developed at IPSN and used by French nuclear companies for criticality safety studies. It is an important part of the standard route of the French criticality package CRISTAL [9]. The geometry is described by means of elementary volumes (spheres, cylinders, boxes, half-spaces, etc.) and of topological operations such as intersection and reunion. The

cross-sections are taken from its own 16 group Hansen-Roach library, or from external libraries (172 groups processed from JEF2.2) resulting of preliminary calculations performed with the assembly code APOLLO2.

4 Studied Configurations

The difficulty of calculating loosely coupled system is closely related to the geometry and to the material composition. The methods have been tested by several authors on various geometries where the most reactive unit is either of small dimension compared to the other units (Smith [10]), or located among a large number of other less reactive fissile units (Kadotani [7], and Whitesides [1]). As the comparison requires numerous replicas of the same calculation, the configuration enabling the lowest computation time has been chosen. This is why the paper is focused on a geometry inspired by Kadotani (Fig. 1). The system is a lattice of $5 \times 5 \times 1$ (highly enriched) critical uranium metal spheres of radius 8.71 cm, with exception of the central sphere, which has a radius of 10 cm. The spheres are considered to be in interaction in air with a distance of 80 cm from center to center. There is no reflector. The atom densities of ^{235}U and ^{238}U are $0.04549 \cdot 10^{24} \text{ atoms.cm}^{-3}$ and $0.00256 \cdot 10^{24} \text{ atoms.cm}^{-3}$. The true k_{eff} of the system is equal to 1.114. The k_{eff} of the array without considering the central sphere is equal to 1.007. In the following, a wrong convergence corresponds to the “loss” of the central sphere and has a consequence to a convergence to 1.007.

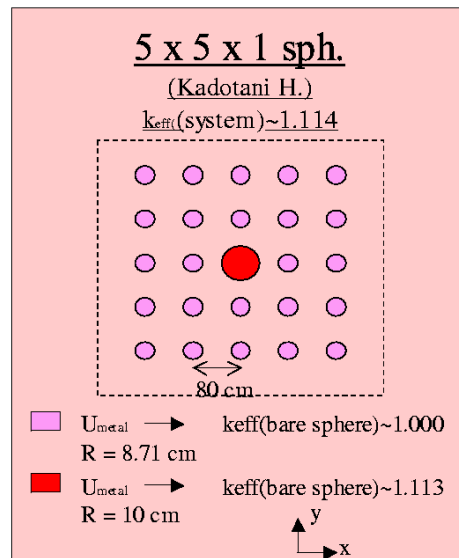


Fig. 1. geometry

Increasing the number of neutrons per generation usually improves the prediction; but it is not always easy to guess the appropriate number of starters. Concentrating the starters in the most reactive units usually leads to a safe convergence (avoiding the risk of underprediction). However, the subtlety of configurations (difference of reflector compositions for instance) can make difficult the choice of the most reactive parts. In the case of the geometry studied (Fig. 1), there is obviously no difficulty to place correctly the starters, and 500 neutrons are enough to avoid the risk of wrong convergence with the conventional method. In order to put at fault the conventional strategy, we voluntarily unskillfully placed a few number of starters: 100 neutrons have been positioned in one of the most distant sphere from the central sphere. Moreover, as some strategies like stratified or matrix sampling need at least one starter by fissile unit, one neutron has been added in each of the 25 spheres.

This configuration has been calculated 100 times for each method with different pseudorandom number sequences. Conventional, stratified, and matrix calculations have been performed using 1000 stages each consisting of one neutron generation of 125 starters, and the first 100 stages have been skipped. With the superhistory powering, calculations have been performed using 100 stages each consisting of 10 neutron generations of 125 starters and skipping the first 10 stages. This is the best way to compare the superhistory method to the others.

5 Results and Analyses

The results can be summarized as follow (Tabs. 1 and 2):

- With the stratified sampling method, none of the calculations converge to the solution of the array with only critical spheres ($k_{\text{eff}} = 1.007$). In fact, the central sphere, although not containing many neutrons remains active (Fig. 2). The fraction of neutrons in this sphere is thus increasing (slowly) after each iteration. One may not expect an important acceleration of source convergence with this method but the important feature is that the risk of neutrons ignoring the presence of the most reactive part of the system is minimised, or even cancelled if additional precautions are taken (use of track-length estimator rather than the collision estimator to tally fissions or even more elaborate estimators as delta-scattering). It could thus be considered that with this method, the source distribution converges to the right solution after a reasonable number of generations (few hundred generations in our case) even with a limited number of starters and a completely wrong distribution of starters.
- With the k-matrix method, the convergence acceleration can, in principle, be more spectacular. In fact, with all the other methods, the fraction of neutron which will be emitted in a given volume V , at the beginning of generation $i+1$, is directly connected to the ratio of the number of neutrons produced in generation i by fission in volume V to the total number of neutrons produced in the whole system during the same generation. Consequently, if the number of starters in V is small, this ratio will remain small even if the volume is very reactive. Many generations would be necessary to increase significantly the pro-

portion of neutrons in the most reactive parts of the system. To estimate k_{vv} with the matrix method, the own production in a volume V is divided by the number of starters in the same volume, thus normalising the productions in all volumes to one emitted neutron per volume. It can easily be understood that in principle, if volume $V1$ (in which $P1$ neutrons were produced starting with $S1$ neutrons) is more reactive than $V2$ (in which $P2$ neutrons were produced starting with $S2$ neutrons) then $P1/S1$ will be greater than $P2/S2$ even if $S2$ is larger than $S1$. If the difference between $P1/S1$ and $P2/S2$ is sensitive, the eigenvector obtained will largely favour volume 1. The reason why this simple rule does not apply is that the estimations of reaction rates ($P1$ and $P2$ for instance) during a simulation are not accurate enough to be reliable. The less a volume is sampled, the less reliable is the estimation of reaction rate. Consequently, an high ratio of production over sources can be obtained in a volume because of bad sampling. The consequence of that will be dramatic if the volume is not the most reactive one, since this volume will receive the majority of starters during the following generations and that until a new recalibration of sources using the matrix k is operated (ten generations later). It is interesting to notice that, although the matrix powering results to the highest number of wrong convergence (5% of replicas in Tab. 1), it leads in the mean time to a higher rate (67 %) of replicas for which the average value is close to the converged solution. This is a proof of convergence speed-up since it reflects the fact that a lower number of generations are needed to reach the equilibrium.

- The analysis of calculation time was also carried out. Tab. 2 gives the figure of merit (inverse of the product of the variance by the calculation time). One can observe that the expected precision is more rapidly achieved with the superhistory powering, but the method does not ensure the calculations always converge to the true value (Fig. 3).

Table 1. keff results comparison

	Strategy			
	Conventional	Stratified	Matrix	Superhistory
Stages	1000	1000	1000	100
Generations/stage	1	1	1	10
Stages \times Gen.	1000	1000	1000	1000
σ ; standard deviation	~ 0.00250	~ 0.00250	~ 0.00240	~ 0.00450
wrong convergence keff=1.007	3% of replicas	0% of replicas	5% of replicas	1% of replicas
keff- 3σ <keff(true)< keff+ 3σ	45% of replicas	50% of replicas	67% of replicas	54% of replicas

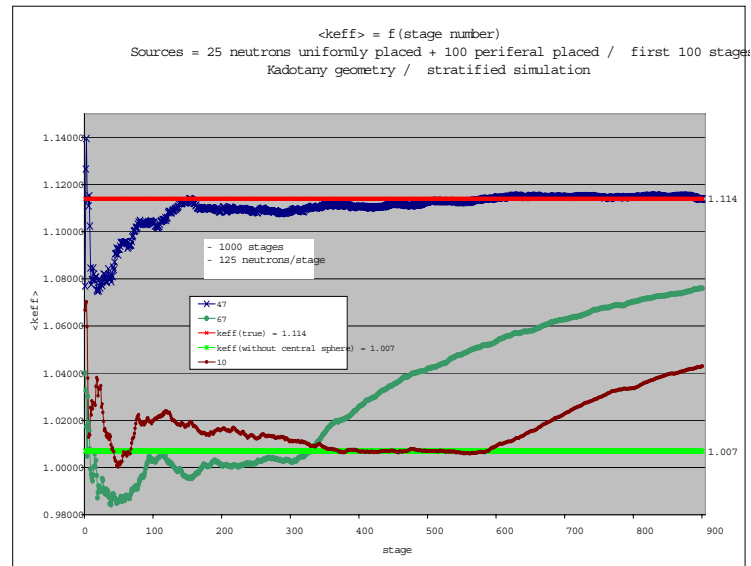


Fig. 2. Stratified sampling for 3 random number seeds (10, 47, 67)

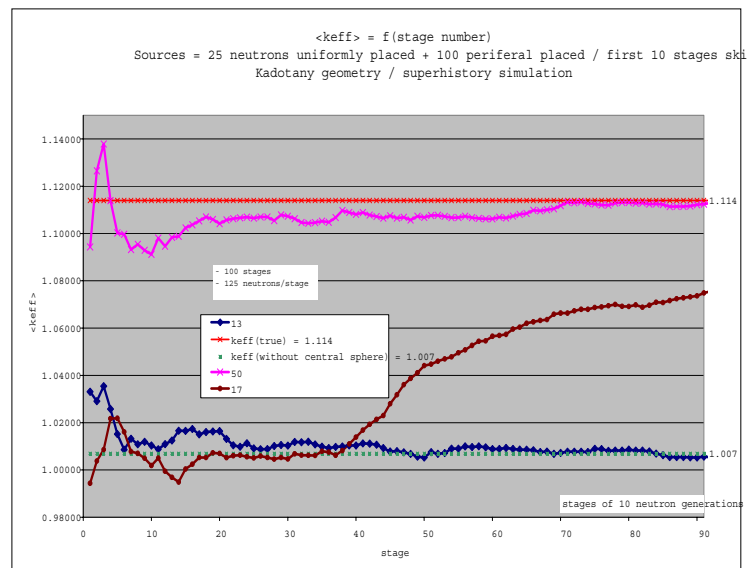


Fig. 3. Superhistory powering for 3 random number seeds (13, 17, 50)

Table 2. Calculation times comparison: figure of merit

Strategy	σ : standard deviation achieved					
	0.00030	0.00100	0.00150	0.00200	0.00250	0.00300
Conventional	33417	26455	21368	19231	17978	17921
Stratified	33855	25840	20964	15924	16162	14065
Matrix	34711	26178	22222	19841	17021	14815
Superhistory	67668	42553	28860	24038	19753	20202

6 Conclusions

Before drawing any conclusion, it must be recalled that we intentionally tried to make the standard powering algorithm fail in this case. In fact, a usual way of solving this problem would be by:

- running much more neutrons per history (thousands of neutrons per generation is a typical figure),
- choosing an appropriate starting source distribution to allow correct sampling of the whole system.

Nevertheless, situations do exist where these two conditions may not be easily satisfied and our aim was to imitate such situations. It must also be noted that our conclusions are preliminary and that more results should be accumulated on the comparison of the methods. Our limited investigations has shown that, none of the methods is able to drastically speed up the convergence, thus significantly reducing the extend of the transient. Consequently, if the transient is not automatically and adequately truncated, the k_{eff} obtained at the end of the simulation will always be biased. This is why we consider that a parallel area of investigation should be the implementation of methods which enable to automatically skip the appropriate number of initial non converged generations. Nevertheless, for such method to be feasible, it must be ensured that the convergence has occurred before the end of the simulation. The stratified sampling method seems to present this important advantage compared to the other methods. Our analysis has revealed too that the superhistory powering is appeared as the most efficient strategy concerning time cost. Therefore, a combination of these two methods seems to be of great interest to assess loosely coupled problems. Such developments and reflexions are currently investigated by IPSN and discussed during task force meetings organized regularly by OECD/NEA.

References

1. G.E. Whitesides: ANS Transactions **14**, 680 (1971)
2. I. de la Rive Box: *Accelerating the convergence of Monte Carlo calculations of k_{eff} in systems with weakly coupled fissile units*. Graduation report for the faculty of Applied Physics of the Delft University of Technology, RF-96, November 1996
3. R.N. Blomquist: *Monte Carlo Source Convergence and the Whitesides Problem*, OECD/NEA WPNCs Task Force on Monte Carlo Source Convergence (Sept. 2000)

4. A. Nouri, A. Le Cocq, J. Dupas, O. Jacquet, I. Vortisch: *MORET4: a versatile and accurate Monte Carlo code for criticality calculations*, IPSN report SEC/T/00.061 (2000)
5. A. Mohamed, E.M. Gelbard: 'Stratified Source-Sampling Techniques for Monte-Carlo Eigenvalue Analysis'. In *Proc. Int. Conf. On the Physics of Nuclear Science and Technology, Log Island NY October 98*, pp. 152–159
6. R.J. Brissenden, A.R. Garlick: *Ann. Nucl. Energy*: **13**, 63 (1986)
7. H. Kadotani, Y. Hariyama, M. Shiota, T. Takada: 'Acceleration of fission distribution convergence using eigenvectors from matrix K calculations in the KENO code'. In *Proc. ICNC'91, paper II-1, Oxford, September 1991*
8. A. Nouri: *Contributions à la qualification du code Monte Carlo Tripoli sur des expériences critiques et à l'étude de l'interaction neutronique entre unités fissiles*. PhD-thesis of the université Paris-XI - centre d'Orsay, January 1994
9. J.M. Gomit and al.: *The New French Criticality-Safety Package CRISTAL*. ICNC'99 Versailles (20-24 Sept 1999)
10. N.R. Smith: *The MONK superhistory powering algorithm*, Winfrith: AEA Technology, 1996

Sensitivity Analysis and Uncertainty Assessment in Applied Monte Carlo Particle Transport

B.R.L. Siebert

Physikalisch-Technische Bundesanstalt, Bundesallee 100, 38116 Braunschweig,
Germany

Abstract. Physical and numerical experiments yield estimates of true values of measurands. The uncertainties associated with those estimates need to be stated as a measure of the reliability of these estimates. The paper discusses the use of sensitivities of a model with respect to its input variables for the propagation of uncertainties associated with these input variables and summarizes some methods used in modern Monte Carlo transport codes to assess sensitivities.

1 Introduction

An experiment yields an estimate of the true value of the measurand. The ISO Guide to the expression of uncertainty in measurement (GUM) [1] defines uncertainty of measurement as a parameter, associated with the result of a measurement, that characterizes the dispersion of the values that could reasonably be attributed to the measurand. The uncertainty associated with an estimated value is therefore a measure of the reliability of the measurement.

Monte Carlo particle transport (MCPT) calculations are *numerical experiments* and the results are estimates, too. Many papers on transport simulations report stochastic uncertainties but neglect the propagation of uncertainties associated with input data. However, this propagation can be computed from the sensitivities of the underlying computational model with respect to its input data [1] with little extra effort. Several modern codes [2] and especially MCNP [3] provide ready to use tools for sensitivity assessment.

The interrelation among *Model*, *Sensitivity* and *Uncertainty* and their role in validation procedures are discussed in the next section. The third section summarizes some methods to assess sensitivities in MCPT and provides some guidance for application. Conclusions are drawn in the last section.

2 Model, Sensitivities and Uncertainties

The user of a MCPT code needs to formulate a computational model which includes both, the modeling of the experiment (including measurement procedures and input data such cross sections) and the algorithm used [4]. Computational models of complex measurements are inevitably never complete and need to be validated. Validation requires a comparison with experiments, theory or already validated calculations (benchmarks). The right hand side of Fig. 1 illustrates

a situation where only estimated values are given: one would have to conclude that x_{exp} and x_{sim} are inconsistent. This demonstrates the need to describe the reliability of estimated values.

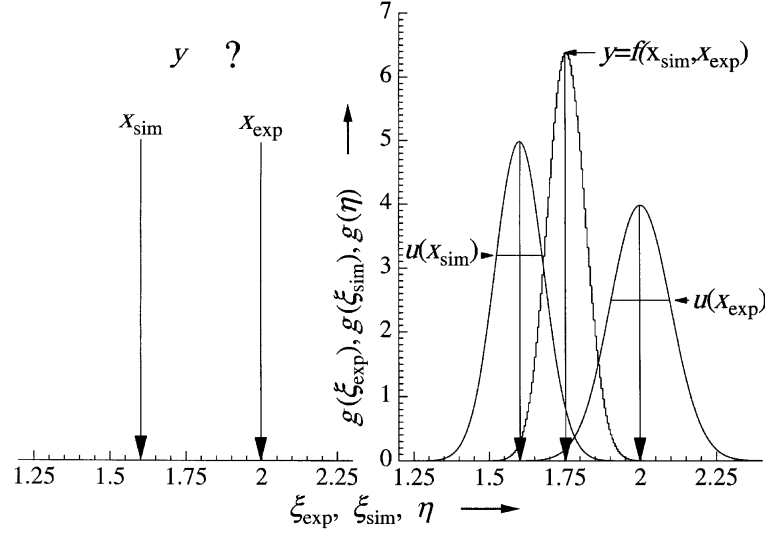


Fig. 1. Illustration of validation procedures for *incomplete* (LHS) and *complete* (RHS) measurements and simulations, details see main text

In the framework of Bayesian statistics, see *e.g.* [5] as introductory textbook, one can express *reliability* as the degree of belief in an estimated value, x , of a measurand, X , by a probability. For instance, if one only knew that the best estimate falls into an interval one would associate a uniform, *i.e.* rectangular, probability distribution density (PDD), $g(\xi)$, of the estimated value. The mean value of that distribution is then taken as the value (best estimate) of the measurement and its standard deviation as standard uncertainty. The uncertainty associated with x is termed $u(x)$ and $u_r(x) = u(x)/x$ is the relative uncertainty.

Figure 1 illustrates also a situation where the PDD of measured and simulated estimates of the measurand, $g(\xi_{\text{exp}}, \xi_{\text{sim}})$, is given by $g(\xi_{\text{sim}})g(\xi_{\text{sim}})$ upon assuming no correlation. The mean values and the uncertainties can be computed from the PDD. Now, “believing” experiment and simulation alike, one can formulate a model, *e.g.* $y = f(x_{\text{exp}}, x_{\text{sim}}) \equiv (u^2(x_{\text{sim}})x_{\text{exp}} + u^2(x_{\text{exp}})x_{\text{sim}})/(u^2(x_{\text{exp}}) + u^2(x_{\text{sim}}))$, and compute the PDD pertaining to y :

$$g(\eta) = \int \int g(\xi_{\text{exp}}, \xi_{\text{sim}}) \delta(\eta - f(\xi_{\text{exp}}, \xi_{\text{sim}})) d\xi_{\text{exp}} d\xi_{\text{sim}} \quad (1)$$

In praxis one encounters small uncertainties and does not need to solve this integral since it is justified to linearize the model by a first order Taylor expan-

sion. Upon generalizing to N input quantities one obtains [1]:

$$y = f(x_1, \dots, x_n) \text{ and } u^2(y) = \sum_{i=1}^{i=N} \sum_{j=1}^{j=N} \frac{\partial f}{\partial x_i} \frac{\partial f}{\partial x_j} u(x_i) r(x_i, x_j) u(x_j) \quad (2)$$

where $\frac{\partial f}{\partial x_i}$ is the sensitivity of Y with respect to X_i evaluated at x_i , $r(x_i, x_j)$ is the corresponding correlation coefficient, *i.e.* $\frac{u(x_i, x_j)}{u(x_i)u(x_j)}$, and $u(y)$ is the resulting (combined) uncertainty. In (2) one sees the contribution of the uncertainty of any input quantity, x_i , to the combined uncertainty, $u(y)$, if the sensitivities of the computational model and the underlying experiment are known. This may help to optimize the underlying experiment and to select appropriate variance reduction schemes.

3 Determination of Sensitivities in Monte Carlo Transport

Valuable general information on uncertainty analysis is found in [6] which also contains an article by H. Rief on Monte Carlo uncertainty analysis and sensitivity assessment based on the *differential operator technique* (DOT), which is predominantly used in modern codes. The theory of DOT and its use in MCNP [3] is thoroughly described and exemplified in [7,8]. This section will therefore not present extensive formalisms but rather describe basic ideas.

The transmission through and albedo (back scatter) from a wall consisting of hydrogen (H) or deuterium D with small admixtures is used as an extremely simple but realistic example, see right hand side of Fig. 2. The atomic fraction of D, n_D , in the wall is associated with an uncertainty $u(n_D)$. The transmitted fluence Φ is now calculated in two runs, both with N histories, however using $n_D + \Delta n_D/2$ in the first and $n_D - \Delta n_D/2$ in the second one. The results are Φ_+ and Φ_- and $\Delta\Phi = \Phi_+ - \Phi_-$ is used to approximate the sensitivity $\frac{\partial\Phi}{\partial n_D}$ by $\frac{\Delta\Phi}{\Delta n_D}$. If, as aimed at, $\Phi_+ \approx \Phi_-$ one expects $u(\Phi_+) \approx u(\Phi_-)$. The relative stochastic uncertainty of the sensitivity, $\frac{\partial\Phi}{\partial n_D}$, is then given by $u_r(\Phi) \frac{\Phi}{\Delta\Phi} \sqrt{2(1 - r(\Phi_+, \Phi_-))}$. In practice one indicates two significant digits for uncertainties. This requires that $u_r(\Delta\Phi) \approx 0.1$. In general, $\frac{\Phi}{\Delta\Phi} \gg 1$ and two long runs with a large number of histories are required. Therefore, this method, termed *brute force*, is not useful. It has been suggested, *e.g.* [9], to use the same sequence of random numbers in either calculation such that $r(\Phi_+, \Phi_+) \rightarrow 1$ and $u^2(\frac{\Delta\Phi}{\Delta n_D}) \rightarrow 0$. In general, this cannot be achieved since the same sequence of random numbers may cause significant different walks through phase space, see Fig. 2. But even if convergence is reached, additional calculations were necessary to check the quality of approximating $\frac{\partial\Phi}{\partial n_D}$ by $\frac{\Delta\Phi}{\Delta n_D}$.

The DOT avoids these problems. Assume a particle, *e.g.* a neutron, arrives at an interaction site with an energy, E_ν . For determining the next interaction site and the energy, $E_{\nu+1}$, the Monte Carlo code has to select a specific nucleus,

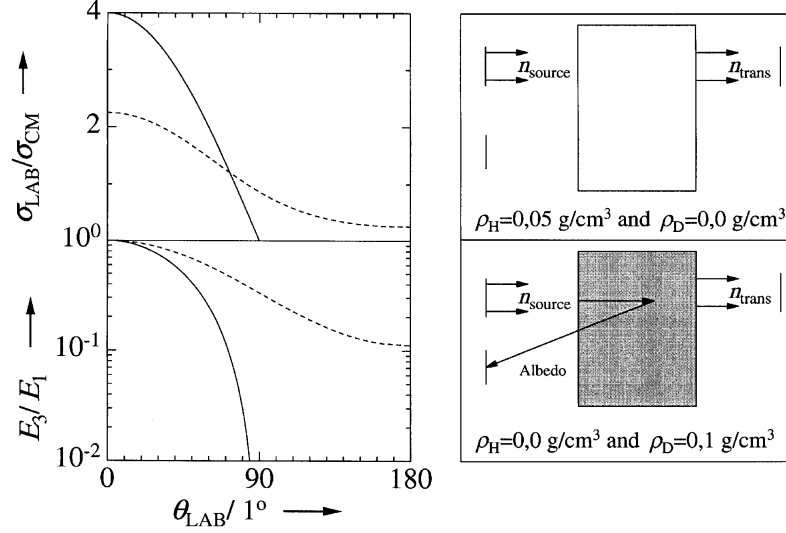


Fig. 2. Illustration of kinematical differences between the reactions $H(n,n')p$ (solid) and $D(n,n')d$ (dashes). LHS: Jacobian for center of mass (CM) to laboratory (LAB) co-ordinates system (top) and ratio of energies of incoming and scattered neutron (bottom), both as a function of the (elastic) scattering angle in the LAB system. RHS: In pure H (top) there is no 1st collision contribution to albedo and 1st collision neutrons are peaked in forward directions. This situation is reversed in pure D (bottom)

e.g. H or D, a possible reaction, a new direction of flight and a path length. Irrespective of the algorithm used, one can compute the probability for this event as a function of known input quantities, *e.g.* atomic fractions, partial, and angular cross sections and cross section densities. This probability, termed c in [7,8], would change if the values of one or several of these quantities are *perturbed*. This change is approximated by a Taylor series in up to 2nd order and for our example one obtains:

$$\Delta c \approx \frac{\partial c}{\partial n_D} \Delta n_D + \frac{1}{2} \frac{\partial^2 c}{\partial n_D^2} \Delta n_D^2 \quad (3)$$

The expectation values of $\frac{\partial c}{\partial n_D} \Delta n_D$ and $\frac{1}{2} \frac{\partial^2 c}{\partial n_D^2} \Delta n_D^2$ are termed 1st and 2nd order perturbations. If a particle scores, *i.e.* contributes to a bin in a tally, a parallel score for the perturbed particle is made in an additional tally; MCNP allows to choose separate tallies for each order. The method requires only one Monte Carlo calculation and allows several perturbations to be reliably computed in one calculation. In MCNP, one 1st order perturbation increases computing times by 10 to 20 %. The ratio of perturbed and not-perturbed fluence is an estimate of $\frac{\partial \Phi}{\partial n_D}$ and, in general, due to correlation $u_r(\frac{\partial \Phi}{\partial n_D}) \approx u_r(\Phi)$. Furthermore, a small ratio of 2nd to 1st order perturbation indicates that $\frac{\Delta \Phi}{\Delta n_D} \rightarrow \frac{\partial \Phi}{\partial n_D}$. In MCNP, the DOT allows to assess sensitivity with respect to cross sections and material den-

sities and to propagate the associated uncertainties. Figure 3 shows some results for the above discussed example. One sees clearly that the relative uncertainty for removing a small admixture of H in D is large for energies only accessed via scattering on hydrogen. More realistic problems of uncertainty assessment, however studied with the brute force method, may be found in [10]. Even geometry changes are accessible by DOT. *E.g.*, a hollow cylindrical scattering sample causes less multiple scattering than a solid one but worsens the resolution in angle and energy. This may be studied by use of three concentric cylinders and voiding the outer and the inner ones via perturbation.

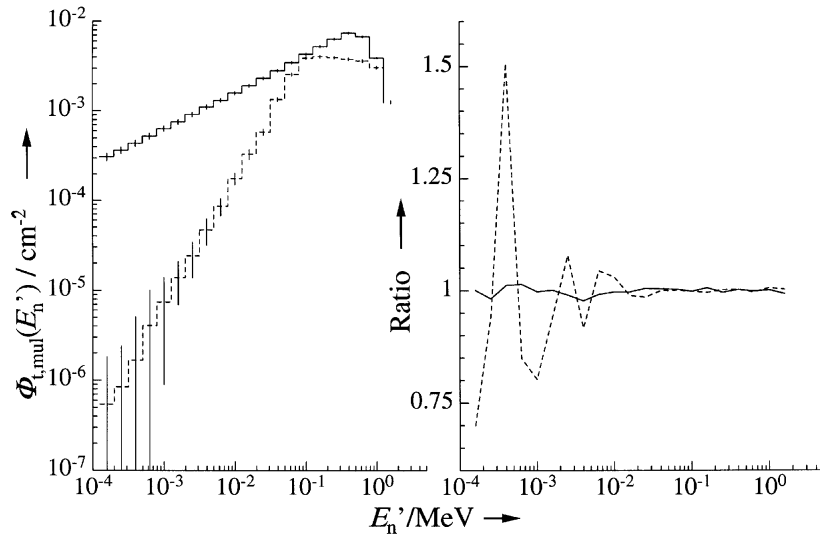


Fig. 3. LHS: More than once scattered transmitted fluence through a wall of deuterium (dashes) and hydrogen (solid) as sketched in Fig. 3, but with 1% admixtures of H in D and D in H as perturbation. RHS: ratios of corrected fluences to fluences for pure H or D. “Corrected” means that the 1% admixture was removed by DOT. The same number of histories was used for all four runs

An alternative to DOT is based on correlated importance sampling, *e.g.* [11]. One transports the main and one or several companion particles simultaneously. After each track (path segment in a history) of the main particle the companion particles are forced to move along the same track. They “see” a different physics and the statistical weight of the companion particles is corrected appropriately such as it is done in importance sampling. Companions score in identical points in phase space with an adjusted statistical weight. This method is straightforward and easily implemented in home made codes and can be used to compute sensitivities and determine propagated uncertainties and also to study different model variants simultaneously. However, similar to DOT, its use is limited to

changes in physics for which the main particle accesses the phase space of the companion particles sufficiently well.

4 Conclusions

Sensitivity and uncertainty assessment for results obtained from Monte Carlo particle transport calculations should be performed in order to assure and document the quality of the results and to provide a sound basis for validation. The differential operator technique used in some modern codes [2] and especially in MCNP [3] allows to assess the sensitivities of the computational model with respect to its input data without undue effort. The differential operator technique is based on sound and well understood perturbation theory [6–8].

The propagation of the uncertainties associated with input data is accomplished in accordance with the ISO-recommendations [1] in first order. Sensitivity assessment is necessary in this procedure and may in addition support the optimization of the computational model and the selection of appropriate variance reduction schemes in Monte Carlo particle transport problems.

References

1. International Organization for Standardization: *Guide to the Expression of Uncertainty in Measurement*. (ISO, Case postale 56, 1211 Geneva 20, Switzerland, ISBN 92-67-10188-9 1993)
2. H. Tagziria (editor): *Review of Monte Carlo and Deterministic Codes in Radiation Protection and Dosimetry*. NPL-Report (London (UK), 1999, ISBN number 0 946754 32 2)
3. J. Briesmeister (editor): *MCNP - A General Monte Carlo Code N-Particle Transport - Version 4B*. Report: LA 12625-M (Los Alamos (USA) 1997)
4. B.R.L. Siebert, R.H. Thomas: *Radiat. Prot. Dosim.* **70**, 371 (1997)
5. S.J. Press: *Bayesian statistics: principles, models and applications*. (John Wiley, New York, N.Y (USA), 1989)
6. Y. Ronen (editor): *Uncertainty Analysis*. (CRC Press Boca Raton, Florida (USA) 1988), ISBN number 0 8493 6714 X
7. G.W. McKinney, J.L. Iverson: *Verification of the Monte Carlo Differential Operator Technique for MCNPTM*. Report: LA 13098 (Los Alamos (USA) 1996)
8. A.K. Hess, J.S. Hendriks, G.W. McKinney, L.L. Carter: *Verification of the MCNPTM Perturbation Correction Feature for Cross-Section Dependent Tallies*. Report: LA 13520 (Los Alamos (USA) 1998)
9. K. Weise, H. Zhang: *J. Phys. A: Math. Gen.* **30**, 5971 (1997)
10. D. Schmidt, B.R.L. Siebert: *Fast neutron Spectrometry and Monte Carlo Simulation - the Codes SINENA and STREUER*. PTB-Report N-40 (Braunschweig (D), 2000, ISBN number 3-89701-531-5)
11. B.R.L. Siebert: 'Discussion of Methods for the Assessment of Uncertainties in Monte Carlo Particle Transport Calculations'. In *Advanced Mathematical and Computational Tools IV* ed. by P. Ciarlini et al. (World Scientific, Singapore, 2000), pp. 220–229

Sensitivity and Uncertainty Analysis for Nuclear Criticality Safety Using KENO in the SCALE Code System

B.T. Rearden

Oak Ridge National Laboratory, MS-6370, Oak Ridge, TN 37831-6370, USA

Abstract. Sensitivity and uncertainty methods have been developed to aid in the establishment of areas of applicability and validation of computer codes and nuclear data for nuclear criticality safety studies. A key component in this work is the generation of sensitivity and uncertainty parameters for typically several hundred benchmarks experiments used in validation exercises. Previously, only one-dimensional sensitivity tools were available for this task, which necessitated the remodeling of multidimensional inputs in order for such an analysis to be performed. This paper describes the development of the SEN3 Monte Carlo based sensitivity analysis sequence for SCALE.

Two options in the SEN3 package for the reconstruction of angular-dependent forward and adjoint fluxes are described and contrasted. These options are the direct calculation of flux moments versus the calculation of angular fluxes, with subsequent conversion to flux moments prior to sensitivity coefficient generation. The latter technique is found to be significantly more efficient.

1 Introduction

Extensive work has been conducted recently to demonstrate that sensitivity and uncertainty (S/U) analysis methodologies can be used to help establish areas of applicability and the related validation of computational codes and data for nuclear criticality safety [1]. In that work, three methodologies were demonstrated to quantitatively establish areas of applicability and to establish code and data biases. The methodologies are based on integral parameter applications, uncertainty analysis theory and generalized linear-least-squares methodology (GLLSM). In each of the three methodologies, energy-dependent sensitivity profiles for multiple nuclides and reactions are required to perform the analyses. These sensitivities predict the relative change in the system k_{eff} due to a perturbation in a constituent cross section.

Recently, the differential approach to perturbation theory as implemented in the FORSS [2] system in the 1970s was updated and applied to the industry-standard SCALE [3] code system for one-dimensional (1-D) and three-dimensional (3-D) criticality safety analyses. The perturbation techniques have been implemented in two prototypic analysis sequences, which execute a series of SCALE's functional modules in a specified order. The SEN1 sequence uses 1-D deterministic neutron transport to calculate the forward and adjoint neutron fluxes necessary for the sensitivity coefficient generation [4]. The prototypic SEN35 sequence utilizes 3-D Monte Carlo techniques from an enhanced version

of the KENO V.a code to generate the necessary forward and adjoint fluxes and computes sensitivity coefficients and their associated uncertainties. Recent enhancements in the SEN3 analysis sequence are the focus of this paper.

2 Methods

The SEN3 sequence implements an enhanced version of the KENO V.a Monte Carlo code, as well as the neutron cross-section processing modules of SCALE and the newly created Sensitivity Analysis Module for SCALE (SAMS). The enhanced version of KENO V.a, which was specifically developed for use in sensitivity analyses, is used to generate the forward and adjoint angular neutron fluxes, as well as flux moments, which are necessary for the generation of sensitivity coefficients. A novel approach to the calculation of the appropriate neutron flux moments was designed specifically for this project.

2.1 Calculation of Flux Moments

In previous publications on this topic, the techniques whereby the flux moments were calculated directly in KENO V.a were presented [5,6]. Recently, these techniques have been updated to improve the efficiency of the calculation by calculating the angular neutron flux in KENO V.a and, subsequently, by performing a spherical harmonics expansion within the SAMS module to produce the flux moments.

Using the track length estimator method, the group-wise scalar flux within a single region for a single generation of particles is calculated as follows: [7–9]

$$\phi_{g,z}^n = \frac{\sum_{j=1}^J wt_{j,z}/l_{j,z}}{V_z \sum_{j=1}^J wt_{j,0}} \quad (1)$$

where $l_{j,z}$ = distance traversed by particle j while within region z and energy group g ; $wt_{j,z}$ = weight of particle j while traversing region z ; $wt_{j,0}$ = initial weight of particle j ; J = total number of histories in the generation.

This method is easily modified to calculate the group-wise angular flux in a region as

$$\phi_{g,k}^n = \frac{\sum_{j=1}^J wt_{j,z}/l_{j,z,n}}{V_z \sum_{j=1}^J wt_{j,0}} \quad (2)$$

where $l_{j,z,n}$ = the distance traversed by particle j while within region z and energy group g within the solid angle $d\hat{\Omega}_n$ about the quadrature direction $d\hat{\Omega}_n$.

In (2) the direction of travel for each history is calculated using a transformed coordinate system based on a polar, rather than Cartesian, position vector. When combined with the spherical harmonics expansion, which is performed after the Monte Carlo calculations are complete, this is a 3-D extension of the 1-D method

for calculating the flux moments in terms of Legendre polynomials based only on μ the direction cosine with respect to the spatial coordinate.

For the angular flux tally, the direction of travel of the particle is calculated in a transformed coordinate system such that the transformed polar, or \hat{k}' axis, is co-linear with the position vector \mathbf{r}_c directed from the centroid of the system to the point at which the flux tally occurs. The centroid must be used because KENO V.a geometry can be input relative to any reference point. By using the centroid as a reference point, the consistency of the moment calculation is ensured with differing models of the same system. The actual position and direction of travel of the particle remain unchanged, but the angular fluxes are tallied using this transformed coordinate system. This coordinate transform is illustrated in Fig. 1. Here \hat{i} , \hat{j} , and \hat{k} represent the directional coordinate system axes; μ , η , and ξ represent the direction cosines; and θ and ρ represent the polar and azimuthal angles of the "normal" coordinate system. The same symbols "primed" represent the transformed coordinate system. With the direction cosines consistently transformed for each history, the new polar and azimuthal angles can be computed and each history can be appropriately tallied for the flux moment calculation by spherical harmonics expansion. The enhanced KENO V.a code

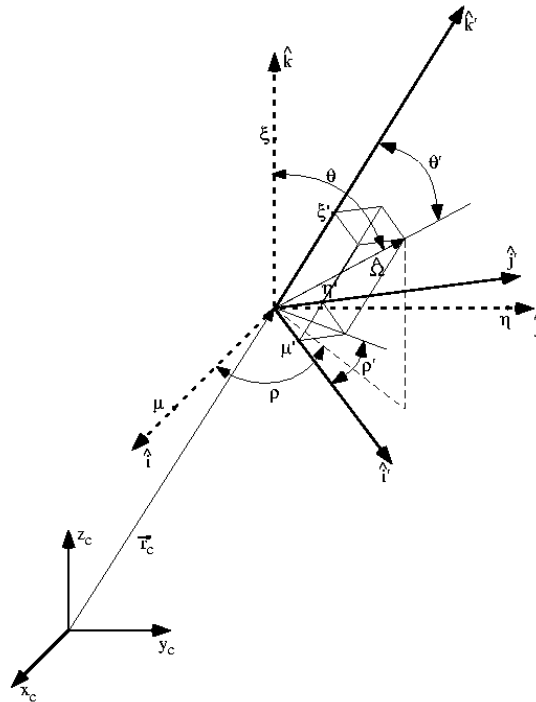


Fig. 1. Coordinate system transform for angular flux tally

uses symmetric-level quadrature sets up to an order of S_{16} . The SAMS module will perform a spherical harmonics expansion up to third-order.

2.2 Sensitivity Coefficient Generation

Once the fluxes have been calculated, the SAMS module, which is executed within the SEN3 sequence, automatically selects all of the sensitivity parameters that can be calculated for each nuclide in each region of the system based on available cross-section data. Sensitivity parameters for a given nuclide may be generated for a number of parameters, including total, scatter, capture, and fission cross sections, as well as $\bar{\nu}$ and χ . The sensitivities for any nuclide-reaction pair calculated with SEN3 are output on three bases: group-wise-region-dependent, energy-integrated-region-dependent, and energy- and region-integrated. This method gives the user the ability to interpret the data with varying levels of detail. SEN3 produces sensitivities in a number of convenient formats for further analysis, either manually or with other automated techniques. SEN3 produces the data necessary for evaluations with the integral parameter applications and cross-section covariance theory as well as GLLSM. Energy-dependent sensitivity profiles and their associated Monte Carlo uncertainties generated by SAMS can be visually displayed using the SAMSPLOT program. The sensitivity coefficient generation is fully explained in [5] and [6].

3 Results

The SEN3 sequence has been applied to hundreds of critical benchmark experiments and several practical design applications. This work has been documented elsewhere [10] and will not be repeated here. Instead, the results of the new angular flux method for calculating the flux moments are presented. To verify the accuracy and efficiency of this method, an early test case for this code was repeated. The selected sample problem is based on an unreflected rectangular parallelepiped containing a homogeneous mixture UF_4 and paraffin with an enrichment of 2% in ^{235}U . The H/ ^{235}U atomic ratio is 293.9:1. The dimensions of the experiment were 56.22 cm \times 56.22 cm \times 122.47 cm [11]. This critical experiment is designated as CAS14. For the purposes of an accurate comparison with the SEN1 code, this experiment was modeled as a sphere of the mixture material with a critical radius of 38.50 cm.

Two executions of SEN3 were conducted for this experiment: The first used the original flux moment tally method conducted during the Monte Carlo execution. The second used the new angular flux tally within KENO V.a and the subsequent flux moment calculation within the SAMS module. The parameters for the SEN3 executions are shown in Tab. 1. The sensitivity results for SEN1 and the two cases from SEN3 are shown in Tab. 2. The parameters shown in Tab. 1 demonstrate that the problem executes in nearly half the time using the new methodology, and the results shown in Tab. 2 demonstrate that virtually identical results are produced by all methods.

Table 1. Parameters from SEN3 executions for CAS14

Parameter	Flux moments (forward)	Flux moments (adjoint)	Angular fluxes (forward)	Angular fluxes (adjoint)
Neutrons per generation	1500	4500	1500	4500
Generations	400	400	400	400
Legendre order for flux moments	P_3	P_3	P_3	P_3
Angular quadrature			S_{10}	S_{10}
Execution time (CPU minutes)	5.40	11.54	2.82	5.85

Table 2. Energy-integrated sensitivities for spherical models of CAS14

Isotope	Reaction	SEN1	SEN3	SEN3
		$k_{\text{eff}} = 1.0045$	$k_{\text{eff}} = 1.0045 \pm 0.0010$	$k_{\text{eff}} = 1.0045 \pm 0.0010$
^1H	Total	2.89E-01	$2.85\text{E-}01 \pm 1.91\text{E-}02$	$2.86\text{E-}01 \pm 1.91\text{E-}02$
^1H	Scatter	3.91E-01	$3.86\text{E-}01 \pm 1.90\text{E-}02$	$3.88\text{E-}01 \pm 1.90\text{E-}02$
^1H	Elastic	3.91E-01	$3.86\text{E-}01 \pm 1.90\text{E-}02$	$3.88\text{E-}01 \pm 1.90\text{E-}02$
^1H	Capture	-1.01E-01	$-1.01\text{E-}01 \pm 9.69\text{E-}05$	$-1.01\text{E-}01 \pm 9.68\text{E-}05$
^1H	n, γ	-1.01E-01	$-1.01\text{E-}01 \pm 9.69\text{E-}05$	$-1.01\text{E-}01 \pm 9.68\text{E-}05$
^{12}C	Total	3.20E-02	$3.14\text{E-}02 \pm 1.10\text{E-}03$	$3.17\text{E-}02 \pm 1.10\text{E-}03$
^{12}C	Scatter	3.27E-02	$3.21\text{E-}02 \pm 1.10\text{E-}03$	$3.24\text{E-}02 \pm 1.10\text{E-}03$
^{12}C	Elastic	3.24E-02	$3.19\text{E-}02 \pm 1.10\text{E-}03$	$3.21\text{E-}02 \pm 1.10\text{E-}03$
^{12}C	n, n'	2.48E-04	$2.35\text{E-}04 \pm 1.31\text{E-}05$	$2.45\text{E-}04 \pm 1.30\text{E-}05$
^{12}C	Capture	-6.70E-04	$-6.70\text{E-}04 \pm 3.78\text{E-}06$	$-6.69\text{E-}04 \pm 3.77\text{E-}06$
^{12}C	n, γ	-4.98E-04	$-4.98\text{E-}04 \pm 4.74\text{E-}07$	$-4.98\text{E-}04 \pm 4.74\text{E-}07$
^{12}C	n, p	-3.10E-08	$-3.12\text{E-}08 \pm 1.03\text{E-}09$	$-3.09\text{E-}08 \pm 1.03\text{E-}09$
^{12}C	n, d	-7.84E-08	$-7.89\text{E-}08 \pm 2.61\text{E-}09$	$-7.81\text{E-}08 \pm 2.60\text{E-}09$
^{12}C	n, γ	-1.72E-04	$-1.73\text{E-}04 \pm 3.74\text{E-}06$	$-1.71\text{E-}04 \pm 3.73\text{E-}06$
^{235}U	Total	2.53E-01	$2.54\text{E-}01 \pm 1.18\text{E-}03$	$2.54\text{E-}01 \pm 1.18\text{E-}03$
^{235}U	Scatter	4.52E-04	$4.45\text{E-}04 \pm 7.14\text{E-}06$	$4.50\text{E-}04 \pm 7.09\text{E-}06$
^{235}U	Elastic	2.87E-04	$2.80\text{E-}04 \pm 5.55\text{E-}06$	$2.82\text{E-}04 \pm 5.50\text{E-}06$
^{235}U	n, n'	1.57E-04	$1.57\text{E-}04 \pm 4.26\text{E-}06$	$1.59\text{E-}04 \pm 4.25\text{E-}06$
^{235}U	$n, 2n$	1.10E-05	$2.96\text{E-}05 \pm 2.00\text{E-}07$	$2.97\text{E-}05 \pm 2.00\text{E-}07$
^{235}U	Fission	3.65E-01	$3.65\text{E-}01 \pm 1.04\text{E-}03$	$3.65\text{E-}01 \pm 1.04\text{E-}03$
^{235}U	Capture	-1.12E-01	$-1.12\text{E-}01 \pm 9.89\text{E-}05$	$-1.12\text{E-}01 \pm 9.88\text{E-}05$
^{235}U	n, γ	-1.12E-01	$-1.12\text{E-}01 \pm 9.89\text{E-}05$	$-1.12\text{E-}01 \pm 9.88\text{E-}05$
^{235}U	$\bar{\nu}$	9.50E-01	$9.50\text{E-}01 \pm 2.40\text{E-}04$	$9.50\text{E-}01 \pm 2.40\text{E-}04$
^{235}U	χ	9.50E-01	$9.50\text{E-}01 \pm 2.69\text{E-}04$	$9.50\text{E-}01 \pm 2.69\text{E-}04$

4 Conclusions

With the development of SEN3, a valuable tool has been added to those previously available at ORNL for determining the range of applicability of critical experiments. The calculation of sensitivity parameters from existing 3-D CSAS25

experiment models permits the use of the range-of-applicability techniques for a broader range of critical experiments and proposed criticality applications. However, further development is necessary before these techniques are available in a production-level code. Although the new methodology for the calculation of the flux moments produces a considerable speed enhancement over the previous methodology, shortcomings to the sensitivity methods in general, as noted in previous publications [6,7], have not yet been fully addressed.

References

1. B.L. Broadhead, C.M. Hopper, R.L. Childs, C.V. Parks: *Sensitivity and Uncertainty Analyses Applied to Criticality Validation, Volume 1: Methods Development*, NUREG/CR-5593, Vol. 1 (ORNL/TM-13692/V1), U.S. Nuclear Regulatory Commission, Oak Ridge National Laboratory (1999)
2. J.L. Lucius et al.: *A Users Manual for the FORSS Sensitivity and Uncertainty Analysis Code System*, ORNL-5316, Union Carbide Corp., Oak Ridge National Laboratory (1981)
3. *SCALE: A Modular Code System for Performing Standardized Computer Analyses for Licensing Evaluation*, NUREG/CR-0200, Rev. 6 (ORNL/NUREG/CSD-2R6), Vols. I, II, and III, May 2000. Available from Radiation Safety Information Computational Center at Oak Ridge National Laboratory as CCC-545
4. R.L. Childs: *SEN1: A One Dimensional Cross-Section Sensitivity and Uncertainty Module for Criticality Safety Analysis*, NUREG/CR-5719 (ORNL/TM-13738), U.S. Nuclear Regulatory Commission, Oak Ridge National Laboratory (1999)
5. B.T. Rearden: *Development of SAMS: A Sensitivity Analysis Module for the SCALE Code System Using KENO V.a in the CSAS25 Sequence*. Ph.D. Dissertation (Texas A & M University, College Station 1999)
6. B.T. Rearden: 'SAMS: A Sensitivity Analysis Module for Criticality Safety Analysis Using Monte Carlo Techniques'. In *Proc. of PHYSOR 2000, ANS Int. Topical Meeting on Advances in Reactor Physics and Mathematics and Computation into the Next Millennium*, CD-ROM, May 7-12, 2000, Pittsburgh, Pennsylvania, ANS
7. E.E. Lewis, W. F. Miller, Jr.: *Computational Methods of Neutron Transport*, American Nuclear Society, La Grange Park, Illinois (1993)
8. L.L. Carter, E.D. Cashwell: *Particle-Transport Simulation with the Monte Carlo Method*, TID-26607, U.S. Energy Research and Development Administration (1975)
9. E.L. Redmond II: *Multigroup Cross Sections Generation Via Monte Carlo Methods*. Ph.D. Dissertation (Massachusetts Institute of Technology, Cambridge, Massachusetts, June 1997)
10. B.T. Rearden, C.M. Hopper, K.R. Elam, B.L. Broadhead, P.B. Fox: 'Prototypic Applications of Sensitivity and Uncertainty Analysis for Experiment Needs'. In *Proc. of ANS/ENS 2000 International Winter Meeting and Embedded Topical Meetings*, CD-ROM, November 12-16, 2000, Washington, D.C.
11. W.C. Jordan, N.F. Landers, L.M. Petrie: *Validation of KENO V.a Comparison with Critical Experiments*, ORNL/CSD/TM-238, Martin Marietta Energy Systems, Oak Ridge National Laboratory (December 1986)

Monte Carlo Characterisation of the Radiation Field in the Thermal Column of the Portuguese Research Reactor

A. Fernandes, A. Vieira, I.C. Gonçalves, and A. Ramalho

Instituto Tecnológico e Nuclear, Estrada Nacional 10, 2686-953 Sacavém, Portugal

Abstract. The Monte Carlo program MCNP-4B was used to simulate the vertical access of the thermal column of the Portuguese Research Reactor. The reactor core was included in the simulations and two models for the neutron source were studied. Measurements were done with activation detectors. The order of magnitude of the thermal flux and gamma dose at the vertical access were predicted by using a neutron source obtained with a criticality calculation. A better agreement between experimental and measured values depends on a better description of the fuel burn-up and the geometry of the vertical access, where some arbitrary assumptions were made.

1 Introduction

The thermal column of the Portuguese Research Reactor (RPI) is being used on radiobiological experiments in the area of Boron Neutron Capture Therapy [1]. The establishment of dose-effect curves requires the knowledge of the gamma and neutron doses delivered to the cells. Usually, the neutron spectrum determination is the adjustment of a theoretical spectra to measurements done with activation detectors [2]. The fiability of the final result depends on the representativity of the input spectra. The present work aims to determine the neutron and photon spectra and doses at the irradiation place, using Monte Carlo code MCNP-4B [3].

2 Description of Reactor Core and Thermal Column

The RPI is a 1 MW, open-pool nuclear reactor, schematized in Fig. 1. The fuel elements are approximately $(8 \times 8 \times 60)$ cm, made of thin slices containing 93% enriched Uranium and are placed on a grid with (6×9) positions. The thermal column is a stacking of graphite blocks. The vertical access is a cylindrical region that accesses the upper part of a central graphite region. The positioning of the central graphite blocks is not documented. It was assumed that the distance between them and the pool wall is 110 cm.

In the biological experiments, the cell cultures are placed in a polymethyl-metachrylate (PMMA) box, at the base of the vertical access of the thermal column, shielded by Lead. It is experimentally known that the neutron spectrum and flux are constant along lines parallel to the core, changing in the perpendicular direction.

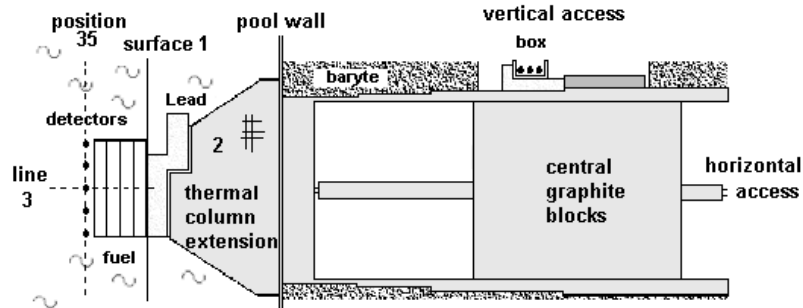


Fig. 1. Schematic representation of the RPI core and thermal column. Position 35 is at 4 cm from the fuel elements. The detectors are Gold foils, bare and covered with 1mm Cadmium. Surface 1 is used as surface source in the simulation of the thermal column. The cells created for variance reduction purposes are represented in 2. Line 3 is at mid-height of the fuel elements. Blank regions are filled with air

3 Simulations

3.1 Reactor Core

The simulation of the vertical access requires a model of the neutron source, which is related to the reactor core. The choice of a core model is based on the comparison of measured and calculated values. Part of the present work was devoted to the area inside the pool, where neutron flux measurements can be easily performed. The geometric model has included the thermal column extension, the control and standard fuel elements and the reflectors. Detailed models of the fuel elements were used. Burn-up was not included.

For the neutron source, two models were studied. In the first model, the fissions are not considered. Instead, a fission spectrum is imposed in every Uranium slices, with uniform intensity. The fission spectrum was described by the Watt formula $\exp(-E/0.965) \times \sinh(2.29 E)^{1/2}$ (E in MeV). The second model consists of a criticality calculation. Neutrons with an energy distribution described by the Watt formula are created in the fissionable material and the fissions they produce are taken into account. It is implicit that the flux distribution will not be uniform along the fuel elements.

The neutron spectrum was calculated in all the grid positions for which experimental data was available, at mid-height of the fuel elements. This data consists of neutron fluxes in three energy regions, calculated by code CITATION and smoothed to activation foil measurements in some grid positions [4]. As the vertical access of the thermal column is at a higher level than the fuel elements, the vertical profile of the thermal neutron flux at position 35 was calculated and compared to Gold foil measurements, as shown in Fig. 1. The neutron spectrum calculation was done for the BUGLE group structure [5].

For the subsequent simulations of the thermal column, a surface source was written at the interface between the fuel elements and the thermal column extension, by recording the positions and velocities of particles crossing the surface.

3.2 Vertical Access of the Thermal Column

Neutrons at the vertical access of the thermal column will have crossed more than 100 cm of graphite. The Weight Window Generator of code MCNP was used for variance reduction. The graphite region was divided in cells transversal to the reactor core, with square section of (6×6) cm, as shown in Fig. 1.

Two groups of weight windows were used for the neutron tallies - below and above 0.5 eV. Energy-independent weight windows were used for photon simulations.

The neutron spectrum along the base of the PMMA box was determined and compared with measurements done with Gold foils, bare and covered with 1 mm Cadmium.

4 Determination of Absolute Values

The calculation of the neutron flux and gamma dose at the nominal reactor power was based on the measured saturation activity of Gold foils placed on position 35, along the height of the fuel element. The neutron spectrum and the saturation activity it would produce in the detectors were calculated. To calibrate the theoretical values, the saturation activities considered are averaged over the height of the fuel element.

Two factors were calculated. One relates the calculated and experimental thermal neutron flux at position 35. The other relates the calculated thermal neutron flux at the PMMA box and at position 35. The thermal neutron flux at the PMMA box is the product of the previous calibration factors and the measured thermal neutron flux at position 35. The same method is used to determine the photon dose. The flux-to-dose conversion factors are those of ICRP 21 [6].

5 Results and Discussion

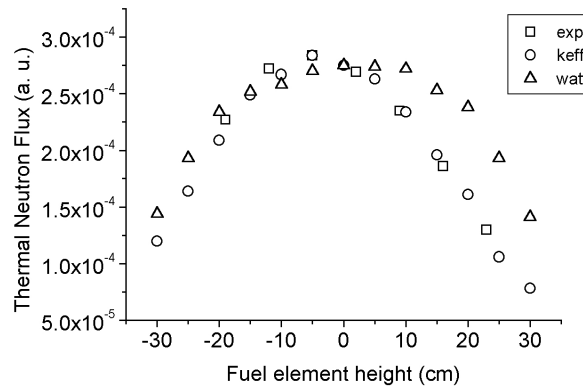
5.1 Reactor Core

Table 1 contains results of the comparison of theoretical fluxes, normalized to the thermal flux at position 35, and experimental fluxes. The calibration curves are of the type $\log(y)=A+B \times \log(x)$, where A and B are adjustment parameters and y and x are, respectively, the measured and calculated neutron fluxes. Also shown is the deviation between the calculated values, smoothed by the corresponding calibration curves, and the measurements. The results show that the relation between calculated and measured results is not strictly linear, as the parameter B is not equal to 1, and the lack of linearity increases for lower neutron energies.

Table 1. Adjustment parameters of calculated and measured neutron fluxes, in the positions of the core grid

Energy Region	Energy	A	B	Deviation
Thermal	$E \leq 625 \text{ meV}$	1.0 ± 0.1	1.35 ± 0.02	4 %
Epithermal	$625 \text{ meV} < E \leq 5.53 \text{ keV}$	0.9 ± 0.2	1.18 ± 0.03	6 %
Fast	$821 \text{ keV} < E \leq 10 \text{ MeV}$	0.9 ± 0.1	1.02 ± 0.02	3 %

In what regards the vertical profile of the thermal neutron flux, along the fuel height, Fig. 2 shows that the criticality calculation is able to reproduce the measured profile at position 35, while the Watt source predicts a flatter profile and higher neutron flux above the mid-height of the fuel elements. Concerning the neutron spectrum, there are no significant differences between the two models, at mid-height of the fuel elements, line 3 in Fig. 1. Above this line, the criticality calculation predicts a harder spectrum, as compared to the Watt source, reflecting the effect of the steeper flux profile. Measurements of the fast neutron profile along a fuel element were done with Nickel wire. The measured profile is flatter than calculated with the criticality code, probably because of burn-up effects, most important at the central area of the fuel.

**Fig. 2.** Vertical profile of the thermal neutron flux at position 35. Values are normalized to the thermal neutron flux at the mid-height of the fuel element. Exp, keff and watt are the thermal neutron fluxes - measured, calculated with the criticality code, and calculated with the Watt source, respectively

5.2 Vertical Access of the Thermal Column

Figure 3 presents the calculated neutron spectrum at the vertical access of the thermal column, with the Watt source and the criticality calculation. Table 2

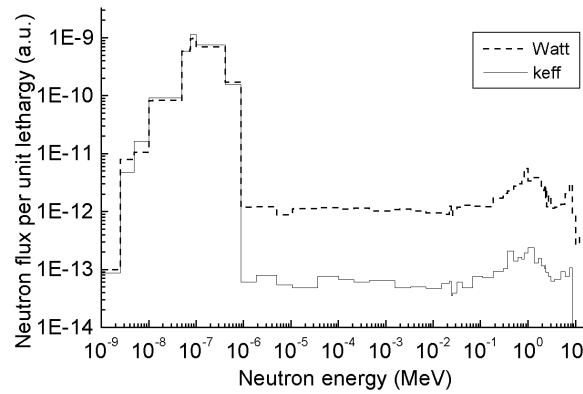


Fig. 3. Calculated neutron spectrum at the vertical access of the thermal column, for the two source models. Values are normalized to the thermal neutron flux. Watt and keff represent the Watt source and the criticality calculation, respectively. In this figure, the BUGLE group structure was refined in the thermal region

presents some of the relevant dosimetric data at the vertical access of the thermal column.

The results show that the Watt source predicts an epithermal neutron flux ten times higher than the criticality calculation and than is measured. Although the criticality calculation gives a better agreement with measurements, the present model is overestimating the neutron thermalization. The measured values of the thermal flux, photon dose and cadmium ratio of Gold foils differ from calculated by a factor of approximately two.

Table 2. The thermal and epithermal neutron fluxes, gamma-ray dose and cadmium ratio of Gold foils at the vertical access of the thermal column

	Watt source	Criticality calculation	Measured
Φ_{th}	$5.4 \times 10^7 \text{ cm}^{-2} \text{ s}^{-1}$	$1.3 \times 10^7 \text{ cm}^{-2} \text{ s}^{-1}$	$3.0 \times 10^7 \text{ cm}^{-2} \text{ s}^{-1}$
Φ_{epi} / Φ_{th}	3.7×10^{-3}	2.4×10^{-4}	4.0×10^{-4}
$R_{Cd} \text{ (Au)}$	130	775	443
$D_{\gamma,air}$	-	0.1 Gy/h	0.2 Gy/h

In what regards the relative profile of the thermal flux across the PMMA box, the calculations predict a steeper profile than is measured. The agreement between theoretical and experimental values is around 20%. The higher thermalization of neutrons that cross more graphite is shown on the increase of the cadmium ratio at larger distances from the core. Some of the discrepancy between experimental and theoretical results may be explained by a wrong assumption on the central graphite blocks position.

6 Conclusions

In the present work, the criticality code of MCNP was able to predict the order of magnitude of the thermal and epithermal neutron flux and gamma-ray dose at the vertical access of the thermal column. At the present stage, the calculated thermal neutron flux and gamma-ray dose are two times lower and the cadmium ratio of Gold foils is two times higher than measured. A better agreement between experimental and calculated results depends on knowing more precisely the location of the central graphite blocks. Some improvements must be done in the reactor core simulation. These include taking into account the burn-up of the fuel elements and its vertical profile.

Systematization of experimental measurements in the reactor core area is desirable. Most of the experimental data were obtained by a smoothing of two-dimensional calculations to some experimental measurements, done in the present reactor configuration and in previous ones. Next measurements shall be performed in the fuel elements, besides the remaining grid positions. As the vertical access is at a higher level than the fuel, it is important to obtain the agreement between measured and calculated results above the mid-height of the fuel elements.

References

1. I.C. Gonçalves, A. Ramalho, I.F. Gonçalves, J. Salgado, A. Fernandes, M. Castro, N. Oliveira, J. Rueff: 'BNCT Activities at the Portuguese Research Reactor'. In: *Proceedings of the International Symposium on Research Reactor Utilization, Safety and Management - Lisbon, September 1999*, (in press)
2. F. Stallmann: *LSL-M2-A Computer Program for Least-Squares Logarithmic Adjustment of Neutron Spectra*, Report ORNL/TM-9933, (Oak Ridge National Laboratory, 1986)
3. J.F. Briesmeister: *MCNP-A General Monte Carlo N-Particle Transport Code, Version 4B* Report LA-12625-M, (Los Alamos National Laboratory, 1997)
4. N. Barradas, F. Cardeira, A. Fernandes, I.C. Gonçalves, J.G. Marques, A. Ramalho: *Neutronics study of Core 2 of the Portuguese Research Reactor* Report ITN/RPI-R-00/57, (Instituto Tecnológico e Nuclear, Sacavém, 2000)
5. R. Roussin: *BUGLE-80 Coupled 47-Neutron 20 Gamma Ray P3 Cross Section Library*, Report DLC-75, (Oak Ridge National Laboratory, 1980)
6. ICRP-21, International Commission on Radiological Protection, Pergamon Press, April 1991

Fission Rate Analysis of a Fast Reactor Fuel Performance Test Using MCNP

T. Sekine and T. Aoyama

Experimental Reactor Division, Irradiation Center, O-arai Engineering Center, Japan
Nuclear Cycle Development Institute 4002, Narita-cho, O-arai-machi, Ibaraki-ken
311-1393, Japan

Abstract. The MCNP Monte Carlo code was applied to accurately calculate the fission rate of mixed oxide (MOX) fuel used in a fast reactor. The test fuel pins to be analyzed were irradiated in the experimental fast reactor JOYO. The heterogeneous structure of the irradiation test subassembly was modeled in the MCNP calculation. The neutron flux distribution in the subassembly was calculated with the neutron source distribution based on diffusion calculation by the JOYO core management code system MAGI. The fission rates of each fuel pin were then obtained by neutron flux and fuel composition. The calculation accuracy was verified by comparing the measured fission rate from the Post Irradiation Examination (PIE). The average ratios of calculations to the experimental values were 0.955 ± 0.020 , indicating MCNP can precisely calculate the fission rates.

1 Introduction

The experimental fast reactor JOYO at JNC's Oarai Engineering Center, has operated since 1983 as an irradiation test bed (MK-II core) to develop the fuels and materials for future fast breeder reactors.

A fuel performance test, in which fuel pellets were irradiated at high linear heat rate so that the center of each pellet could be melted, was conducted to optimize the thermal analysis method in the MOX fuel pin design. The test fuel pins were located inside the irradiation test subassembly (B5D-2). Due to the complexity of the B5D-2's internal structure, the precise fission rate could not be evaluated by a homogeneous model diffusion calculation.

In order to improve the calculation accuracy of fission rate inside the irradiation test subassembly, a three-dimensional, continuous energy Monte Carlo calculation code MCNP [1] was used. To verify the calculation accuracy of MCNP, calculated fission rates were compared with measured values from the PIE.

2 Description of Irradiation Test

The JOYO core configuration for the test and B5D-2 test subassembly structure are shown in Fig. 1. The B5D-2 test subassembly was loaded at the core center position. 24 irradiation test fuel pins were loaded in the cylindrical compartment

tubes of the B5D-2 test subassembly. A tie rod fixed the compartment tubes at the center of B5D-2 test subassembly. Table 1 lists the test fuel specifications and irradiation conditions. A fresh MOX fuel with Pu content of about 19wt% and ^{235}U enrichment of about 22wt% was used in this test.

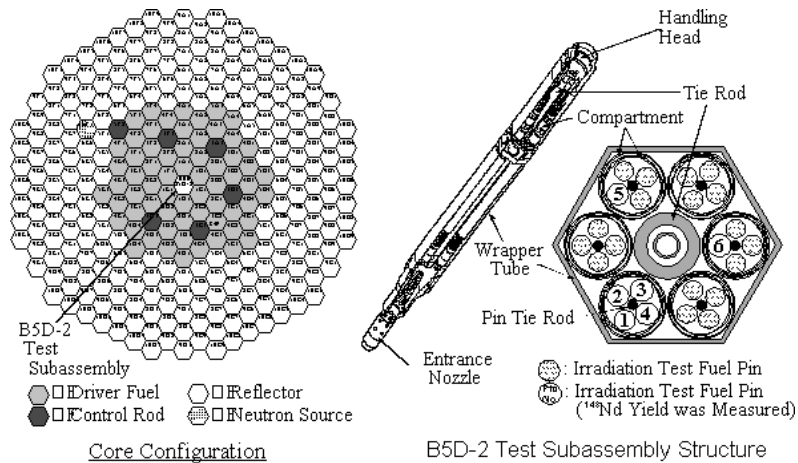


Fig. 1. Core configuration and structure of B5D-2 test subassembly

Table 1. Fuel specification and irradiation condition of B5D-2 test subassembly

Number of Fuel Pins	24
Fuel Type	Mixed Oxide
Pu Content	19 wt. %
Pu Isotope Ratio (Pu-238/239/240/241/242)	1 / 66 / 23 / 6 / 4
^{235}U Enrichment	22 wt. %
O/M Ratio	1.98
Theoretical Density	91–95% TD
Pellet Diameter	6.5 mm
Loaded Position	Core Center
Linear Heat Rate	620–685 W/cm
Neutron Flux (Total)	$4.6 \times 10^{15} \text{ n/cm}^2/\text{s}$
Neutron Fluence (Total)	$6.6 \times 10^{19} \text{ n/cm}^2$
Burn-up fraction	< 0.004 atom %

The irradiation time in Effective Full Power Days (EFPD) was determined by the reactor power history which was measured every 15 seconds using the JOYO Data Acquisition System (JOYDAS), and the result was 0.1596 EFPDs.

3 Calculation Method of MCNP

3.1 Geometry and Neutron Source

The MCNP calculation was conducted in the fixed source mode. Figure 2 shows the geometry model of B5D-2 test subassembly and the driver fuel. To accurately evaluate the neutron flux distribution within the B5D-2 test subassembly, its heterogeneous internal structure was modeled in a three-dimensional configuration. Neutron multiplication by fission reaction was considered as the neutron source in the B5D-2 test subassembly.

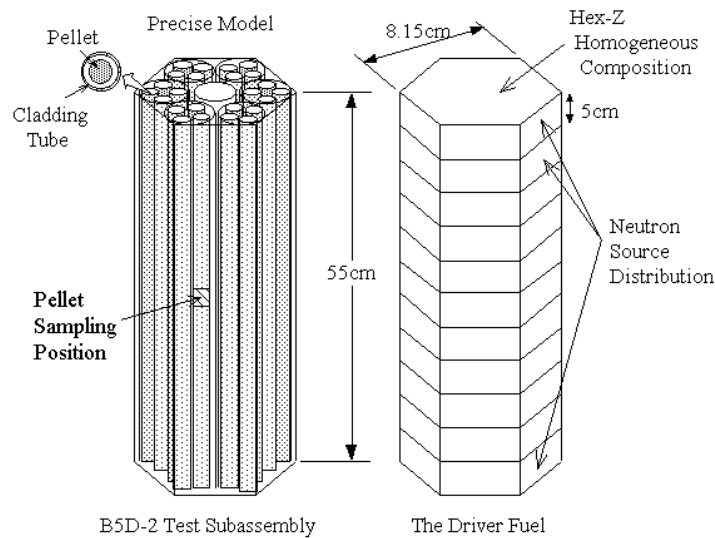


Fig. 2. Geometry model of B5D-2 test subassembly and the driver fuel

The fuel composition and the neutron source distribution of each driver fuel were calculated using the JOYO MK- II core management code system MAGI [2] and were inputted into MCNP. In the MCNP calculation, the homogeneous driver fuel was modeled in Hex-Z as it was in MAGI.

The system schematic of MAGI is shown in Fig. 3. The nuclear calculation used in MAGI is based on three-dimensional diffusion theory with seven neutron energy groups. The neutron cross section was collapsed from the 70 group JFS-3-J2 cross section set processed from the JENDL-2 library [3]. The absolute value of neutron flux by MAGI was normalized with the thermal output of reactor power obtained from the heat balance in the primary cooling system. Regarding the calculation accuracy of MAGI, the burn-up fraction of the driver fuel by MAGI agreed with the measured values within 5%.

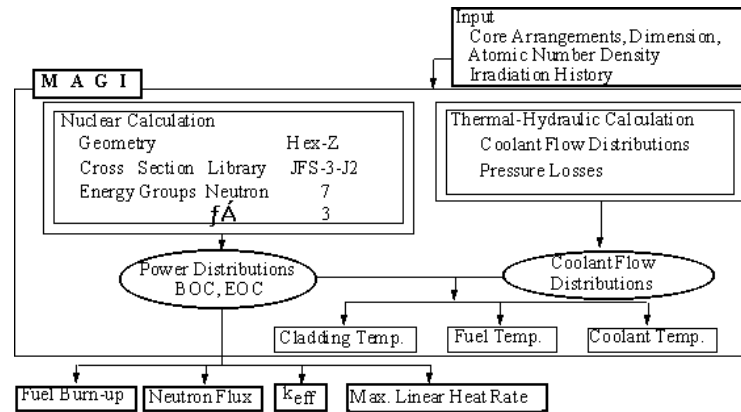


Fig. 3. JOYO core management code system MAGI

3.2 Neutron Flux and Fission Rate

Using precise three-dimensional modeling of the B5D-2 test subassembly, the neutron flux of each fuel pin was calculated. The detailed calculation method is described in Tab. 2. The FSXLIB-J3R2 cross section library [4], which was processed from JENDL-3.2, was used. The ^{239}Pu Watt type fission spectrum was used as an energy distribution representing the MOX fuel content.

Table 2. Calculation Method of MCNP

Geometry	B5D-2: Precise Configuration Other Subassembly: Hex-Z (Homogeneous)
Neutron Source Distribution	B5D-2: Fission Neutron by MCNP Other Subassembly: Calculated by MAGI
Neutron Cross Section	FSXLIB (Based on JENDL-3.2)
Fission Spectrum	Watt Type Fission Spectrum (induced fission spectrum of ^{239}Pu , in case incident neutron energy is 1 MeV)
Number of Histories	2×10^6

Neutron flux were calculated using track length estimation tally (F4 tally). Fission rate of each fuel nuclide were calculated using tally multiplier card (FM card) which multiplied neutron flux and fission cross section.

In the PIE, fission rates were measured in 6 fuel pins at the core center height. Diameters of the sampling pellets were approximately 6.5mm and heights were approximately 5mm. In the MCNP calculation, the pellet sampling positions were modeled precisely. Fuel compositions of sampling pellets were also measured in the PIE. The burn-up fraction of the B5D-2 test fuel pin was below 0.004 atom% and the changes of the fuel compositions during the irradiation can be

considered negligible. Therefore B5D-2's fuel compositions from the PIE were inputted into MCNP.

The calculated fission rates of each nuclide are listed in Tab. 3. In order to achieve sufficient precision, approximately 1% at 1σ error at the pellet sampling positions in the PIE, 20 million histories of particles were needed for this simulation case.

Table 3. Fission rate calculated by MCNP

Nuclide	Pin No.					
	1	2	3	4	5	6
^{235}U	3.04E+13	3.04E+13	3.25E+13	3.02E+13	3.25E+13	3.28E+13
^{238}U	3.47E+12	3.46E+12	3.60E+12	3.39E+12	3.51E+12	3.60E+12
^{238}Pu	2.52E+11	1.11E+11	1.44E+11	3.16E+11	3.09E+11	3.19E+11
^{239}Pu	2.29E+13	2.30E+13	2.43E+13	2.35E+13	2.35E+13	2.42E+13
^{240}Pu	2.24E+12	2.22E+12	2.34E+12	2.26E+12	2.24E+12	2.30E+12
^{241}Pu	2.65E+12	2.66E+12	2.83E+12	2.72E+12	2.72E+12	2.80E+12
^{242}Pu	2.72E+11	2.69E+11	2.85E+11	2.73E+11	2.70E+11	2.77E+11
Sum	6.22E+13	6.21E+13	6.60E+13	6.27E+13	6.50E+13	6.62E+13

4 Confirmation of the MCNP Calculation Accuracy

The calculation accuracy was confirmed using fission rate based on ^{148}Nd production measurement. ^{148}Nd is one of the stable fission products and its fission yield which is used from JNDC-V2 [5] is highly reliable, therefore the ^{148}Nd production obtained by the destructive examination has been commonly used as a burn-up index. In the PIE, ^{148}Nd production was measured by means of isotopic dilution mass spectrometry [6] which has an accuracy of approximately 1%.

Comparison of measured fission rates and MCNP calculations is shown in Fig. 4. The average ratio of the calculated to experimental (C/E) values was 0.955 ± 0.020 . This result indicated that MCNP calculates the fission rates precisely.

5 Conclusion

In order to improve the calculation accuracy of the fission rate of the MOX fuel in the fast reactor fuel performance test in JOYO, the Monte Carlo code MCNP was applied. The geometry of the irradiation test subassembly which had a heterogeneous internal structure was simulated using three-dimensional modeling. The neutron flux calculation was conducted with a fixed source mode and neutron sources of the driver fuels were generated based on three-dimensional diffusion theory.

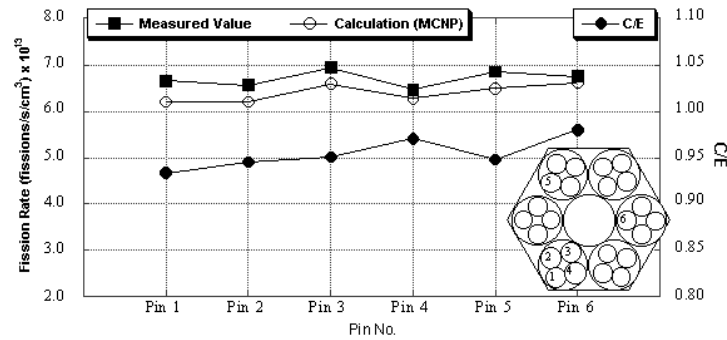


Fig. 4. Comparison of MCNP calculations with measurements

To confirm the calculation accuracy, calculated fission rate were compared with the measured values from PIE. The average ratio of the calculated to experimental values was 0.955 ± 0.020 . This result indicates that MCNP can accurately calculate the fission rate of the fast reactor MOX fuel.

Acknowledgement

The authors would like to note the contribution of Mr. Y. Kato of Information Technologies Japan Inc. for the neutron flux calculation by MAGI. We also greatly appreciate the cooperation and valuable comments by Dr. O. Sato of Mitsubishi Research Institute Inc. on the calculation method using MCNP.

References

1. J. F. Briesmeister et al.: *MCNP - A General Monte Carlo N-Particle Transport Code, Version 4A*, LA-12625 (1993)
2. T. Sekine et al.: *Characterization of Fast Neutron Field in the Experimental Fast Reactor "JOYO" -Current Status on the Evaluation of Irradiation Test Conditions and Its Upgrade-*, JNC Technical Review No.6 (2000) (in Japanese)
3. H. Takano, K. Kaneko: *Revision of Fast Reactor Group Constant Set JFS-3- J2*, JAERI-M 89-141, Japan Atomic Energy Research Institute (1989)
4. K. Kosako et al.: *A Continuous Energy Cross Section Library for MCNP Based on JENDL-3.2*, JAERI-Data-Code-94-20 (1994)
5. K. Tasaka et al.: *JNDC Nuclear Data Library of Fission Products -Second Version-*, JAERI 1320, Japan Atomic Energy Research Institute (1990)
6. *Atom Percent Fission in Uranium and Plutonium Fuel (Neodymium)*, Annual Books of ASTM Standard, E321-79 (1971)

Benchmarking Monte Carlo Codes for Criticality Safety Using Subcritical Measurements

T. Valentine

Oak Ridge National Laboratory, USA, P. O. Box 2008 Oak Ridge, TN 37831, USA

Abstract. Monte Carlo codes that are used for criticality safety evaluations are typically validated using critical experiments in which the neutron multiplication factor is unity. However, the conditions for most fissile material operations do not coincide to those of the critical experiments. This paper demonstrates that Monte Carlo methods and nuclear data can be validated using subcritical measurements whose conditions may coincide more closely to actual configurations of fissile material.

1 Introduction

The subcriticality of fissile assemblies is essential for safe processing, transportation, and storage operations. The assurance of the subcriticality of various fissile material operations is commonly obtained by criticality safety evaluations for the specific operation. The criticality safety evaluations are performed using detailed computations that have been validated using critical experiments in which the neutron multiplication factor is unity. In most cases, the actual fissile material operation does not coincide to the conditions that exist for the critical experiment, i.e. the geometry and neutron spectrum may both differ significantly between the subcritical operation and the critical experiment. These differences require that additional safety margins be included in the criticality safety evaluations [1]. Subcritical measurements can be used to address the use of additional safety margins by providing supplementary benchmark data for validating computation methods or by providing an in-situ measurement of the degree of subcriticality. The use of subcritical measurements would actually enhance the safety of operations with fissile materials.

This paper provides a brief review of subcritical noise analysis measurements followed by a description of the simulation of this measurement method. A brief description of a noise analysis measurement and the results of the simulation of this measurement are provided. Finally, the results of the analysis are summarized.

2 Source-Driven Noise Analysis Measurements

Subcritical source-driven noise measurements [2] are simultaneous Rossi- α and randomly pulsed neutron measurements that provide measured quantities that can be related to the subcritical neutron multiplication factor, k_{eff} . The source-driven noise analysis measurement requires the use of a timed neutron source

such as a ^{252}Cf source ionization chamber (detector 1) and two or more neutron detectors (detectors 2 and 3, respectively). The time-dependent response of the source and detectors are correlated with themselves and each other in the frequency domain to obtain auto and cross spectra. The source-detector cross spectra are designated as $G_{12}(\omega)$ and $G_{13}(\omega)$ and are the frequency domain equivalent of the randomly pulsed neutron measurement. The detector-detector cross spectra are designated as $G_{23}(\omega)$ and are the frequency domain equivalent of the two-detector Rossi- α measurement. The auto spectra of the source is designated as $G_{11}(\omega)$ and is related to the spontaneous fission rate of the source. The detector auto spectra are designated as $G_{22}(\omega)$ and $G_{33}(\omega)$ and are the frequency domain equivalent to the single-detector Rossi- α measurement. A certain ratio (R) of the frequency spectra is independent of detection efficiency and can be directly computed using Monte Carlo codes. The spectral ratio is defined as:

$$R(\omega) = (G_{12}^*(\omega)G_{13}(\omega))/(G_{11}(\omega)G_{23}(\omega)) \quad (1)$$

The spectral ratio is directly dependent on the subcritical neutron multiplication factor and thus can be used to ascertain changes in reactivity.

3 Monte Carlo Code MCNP-DSP

Subcritical measurements were developed to study the dynamic behavior of neutrons in a fissile system. One common aspect of this was to determine the neutron multiplication factor. Interpretation of measurements requires some model to relate what is measured to the neutron multiplication factor. In the past, the subcritical measurements were interpreted using equations developed from point kinetics models for the time-dependent behavior of neutrons in the subcritical configuration. This limited the application of the measurement to situations in which point kinetics was applicable. The most general model to relate the measured quantities to k_{eff} would involve the use of the generalized stochastic model developed by Muñoz-Cobo et al. [3]. Although an analytical solution of subcritical measurements in terms of the stochastic model is not practical, the Monte Carlo method provides a means to simulate the subcritical measurements and to also calculate the neutron multiplication factor. In fact, the same Monte Carlo code and nuclear data can be used for both calculations.

The Monte Carlo code MCNP-DSP [4] was developed from the MCNP [5] Monte Carlo code to simulate a variety of subcritical measurements. In MCNP-DSP, the variance reduction features were disabled to obtain a strictly analog particle tracking to follow the fluctuating processes more accurately. Because typical biasing techniques are employed to reduce the variance of estimates of first moment quantities, they do not preserve the higher moments; therefore, analog Monte Carlo calculations must be performed when analyzing subcritical measurements whose measured quantities are directly related to the higher moments of the neutron production. Because the use of average quantities reduces

the statistical fluctuations of the neutron population, average quantities such as the average number of neutrons from fission are not used; instead, appropriate probability distribution functions are sampled. The prompt particle tracking begins with the source event and the subsequent fission chains are followed to extinction. Time series of pulses are obtained at the detectors for each fission chain. These sequences are sampled into blocks of 512 or 1024 data points. The blocks of data are then processed according to the type of measurement being simulated. The auto and cross spectra are computed directly from the Fourier transform of the source and detector time series for each data block. The auto and cross spectra are then averaged over many blocks to obtain the final estimates of the auto and cross spectra. The spectral ratio can then be computed from the auto and cross spectra as is done in the noise analysis measurement.

4 Comparison of Measurements and Simulations

4.1 Measured Spectral Ratio Values

Source-driven noise analysis measurements were performed with varying amounts of a highly enriched uranyl nitrate solution in an acrylic tank (25.0825-cm ID, 53.34-cm height) to obtain the spectral ratio as a function of the solution height in the tank [6]. A 0.635-cm stainless steel plate was located at the bottom of the solution tank. A ^{252}Cf source was placed at the axial center of the tank at the mid-height of the solution. ^3He neutron detectors (5.08-cm OD, 38.1-cm long) were placed adjacent to the radial surface of the tank and were separated 180 degrees apart. The aqueous uranyl nitrate solution contained 0.29330 gram of uranium per gram of solution. The solution density was 1.64320 g/cm^3 and had a free acid content $<0.1\text{ wt\% HNO}_3$. The uranium isotopic content was 93.2 wt% ^{235}U , 5.37 wt% ^{238}U , 1.02 wt% ^{234}U , and 0.41 wt% ^{236}U . A detailed sensitivity study was performed for this measurement to determine the benchmark spectral ratio values and uncertainties that are presented in Tab. 1.

Table 1. Benchmark Spectral Ratio Values

H (cm)	R (10^{-3})
30.48	98.0 ± 12.0
27.94	139.0 ± 9.7
25.40	187.7 ± 10.6
22.86	248.0 ± 9.7
20.32	303.5 ± 9.7

4.2 MCNP-DSP Spectral Ratio Values

MCNP-DSP calculations were performed to simulate these measurements using ENDF/B-V and ENDF/B-VI neutron cross section data files. The computed spectral ratio values and k_{eff} values are provided in Tabs. 2 and 3. The statistical uncertainty in the k_{eff} calculations is 0.0003 for both cross section data libraries. The spectral ratio values computed with the ENDF/B-VI cross section data set are in better agreement with the measurements for the 30.48- and 27.94-cm solution heights and are very similar to those obtained using the ENDF/B-V cross section data for the other four solution heights. The computed spectral ratio values are in better agreement for the more reactive systems than for the less reactive systems. As the solution height decreases the reactivity of the system decreases and greater differences are observed between the measured and computed spectral ratio values.

The spectral ratio is a more sensitive parameter than k_{eff} as evident from the results presented in Tabs. 2 and 3. For example, the computed spectral ratio values change approximately 40% for a change in solution height from 30.48-cm to 27.94-cm whereas the computed k_{eff} values only change approximately 2%. The sensitivity of the computed spectral ratio to solution height decreases as the solution height decreases whereas the sensitivity of the computed k_{eff} increases as the solution height decreases. However, the computed spectral ratio is still a factor of three more sensitive to the change in solution height than k_{eff} .

Table 2. MCNP-DSP Spectral Ratio Values

	<i>ENDF/B – V ENDF/B – VI</i>	
<i>H</i>	<i>R</i>	<i>R</i>
(<i>cm</i>)	(10^{-3})	(10^{-3})
30.48	105.5 ± 0.1	102.7 ± 0.1
27.94	151.3 ± 0.1	149.4 ± 0.1
25.40	202.9 ± 0.1	201.6 ± 0.2
22.86	259.5 ± 0.3	268.1 ± 0.3
20.32	328.4 ± 0.3	327.0 ± 0.8

5 Summary

These calculations have demonstrated that subcritical source-driven noise analysis measurements can be simulated directly using Monte Carlo codes. The sensitivity of the computations has been demonstrated using ENDF/B-V and ENDF/B-VI cross section data libraries. Furthermore, these calculations have

Table 3. MCNP-DSP Spectral Ratio Values

H (cm)	$ENDFB - V$ k_{eff}	$ENDFB - VI$ k_{eff}
30.48	0.9599	0.9582
27.94	0.9391	0.9381
25.40	0.9141	0.9137
22.86	0.8829	0.8820
20.32	0.8445	0.8435

demonstrated that the bias between the measurement and calculations (difference between the measured and calculated spectral ratio values) increases as the system reactivity decreases. The bias is smaller for highly reactive systems. This result might be expected because the evaluated nuclear data is typically tested using critical experiments in which the neutron multiplication factor is one. The increased sensitivity of the spectral ratio as a function of the degree of reactivity makes this quantity useful for benchmarking Monte Carlo methods and nuclear data.

References

1. ANSI (American National Standards Institute): *Nuclear Criticality Safety in Operations with Fissionable Materials Outside Reactors*, ANSI/ANS-8.1-1998, American Nuclear Society, 1998
2. V.K. Paré, J.T. Mihalcz: Nucl. Sci. Eng. **56**, 213 (1975)
3. 18. J.L. Muñoz-Cobo, R.B. Perez, G. Verdu: Nucl. Sci. Eng. **95**, 83 (1987)
4. T.E. Valentine: *MCNP-DSP Users Manual*, ORNL/TM-13334, Oak Ridge Nat. Lab (January 1997)
5. J.F. Briesmeister Ed.: *MCNP4A - A General Monte Carlo N-Particle Transport Code*, LA-12625-M, Los Alamos National Laboratory (1993)
6. J.T. Mihalcz, E.D. Blakeman, G.F. Ragan, E.B. Johnson, Y. Hachiya: *Dynamic Subcriticality Measurements Using the ^{252}Cf -Source-Driven Noise Analysis Method*, Oak Ridge National Laboratory, ORNL/TM-10122 (1988)

Review of Industrial and Medical Applications that Utilize Coupled Neutron–Photon Monte Carlo Transport

T. Goorley

Nuclear Reactor Laboratory, Massachusetts Institute of Technology, Cambridge, USA

Abstract. The civilian uses of coupled neutron-photon Monte Carlo radiation transport programs are primarily source design and neutron applications. In the first case, these codes are used to simulate neutron and photon transport in different arrangements of shields, filters and moderators to design neutron sources. In the second case, these codes model the energy distribution, angular distribution and spatially dependent neutron and photon spectra from these sources to simulate radiation transport for imaging and quantification techniques, and radiation health physics applications. Coupled neutron and photon calculations are crucial in design and analysis for a number of diverse applications, which are summarized in this paper, along with descriptions of the computer programs used for these calculations.

1 Introduction

As the application of neutrons for industrial and medical techniques is quite diverse, so is the use of Monte Carlo (MC) calculations to support these efforts. MC neutron and photon transport calculations are used to help design neutron sources and aid in the development and usage of industrial neutron applications. In medical radiation physics applications, MC codes are used to calculate doses for therapies and accidents, as well radiation health physics efforts.

Monte Carlo codes are used extensively in the design of almost all varieties of neutron sources. The design of research, power and space nuclear reactors incorporates criticality calculations with size, location, density, and composition differences in fuel, moderators, reflectors, absorbers or other reactor components. In the case of accelerator neutron sources, optimal target thickness and neutron production may be calculated with a different code than is used for the coupled neutron photon transport, or a single comprehensive code can be used for charged particle, neutron and photon transport. For both of these sources, as well as sources based on spontaneous fission radioisotopes, photo-neutrons, alpha decay and (α, n) reactions, and even fusion devices, coupled n - γ transport is utilized to calculate activation in surrounding materials, penetration of shielding and dose to surrounding personnel. Often, when an optimal angular, spectral or spatial distribution of neutrons or accompanying gammas is desired for a specific application, MC codes simulate variations in filters, delimiters or collimators to investigate n or γ flux, dose, reaction rate, or heating rate in the target.

Monte Carlo codes are further used in the development of applications for these neutron sources. Industrial applications, which typically use neutrons for

imaging and quantification of isotopes, are usually based on elastic and inelastic neutron scattering, and prompt or delayed photon production. These nuclear processes are the basis for oil-well-logging units, contraband detectors, neutron activation analysis devices, and neutron radiography facilities, for example. MC transport codes are used in the design of these devices to calculate dose to operating personnel or sensitive electronics for various physical configurations, and to simulate instrument response for a variety of sample conditions.

Medical radiation physics includes the therapeutic application neutron sources, for which MC codes calculate radiation interactions with the human body. Neutron interactions with tissue are usually divided into thermal (below 0.5 eV) neutron dose, which results from the $^{14}\text{N}(\text{n,p})^{14}\text{C}$ reaction, and fast neutron dose. Below 10 MeV, fast neutron dose is mostly from elastic scattering with hydrogen ($^1\text{H}(\text{n,n}')^1\text{H}$). Since dose from the accompanying prompt gammas from $^1\text{H}(\text{n},\gamma)^2\text{H}$ neutron capture can be higher than the thermal neutron dose, depending on the neutron beam energy and physiological target, coupled n- γ transport is important in these MC calculations. Aside from therapy, MC codes are used to determine organ doses from whole body exposures [1], albedo effects on personal dosimetry, and the responses of tissue-equivalent neutron detectors [2].

This paper briefly reviews the MC software codes used for coupled n- γ transport below 20 MeV. Example cases of MC codes aiding in the development and design of neutron sources and applications are given.

2 Neutron Gamma Transport Codes

There are a number of general purpose coupled n- γ Monte Carlo transport codes available to the public, listed in Tab. 1, but all share a number of common characteristics. All support three dimensional modeling and transport, continuous energy cross section treatment, particle tallies with time, angle, location, and/or energy dependent bins, and energy dependent response functions, such as flux-to-kerma factors. Most of these codes also support multigroup cross sections, adjoint calculation modes, and variance reduction techniques, such as phase space or source biasing, all of which speed tally convergence. Many of these codes also have associated visualization software to help develop geometric models and view resulting tracks or tally values.

While the above codes are used for industrial, medical and health physics applications, there are also a few program which have been developed for neutron therapy treatment planning and dosimetry calculations. PERIGRINE [11], developed by Lawrence Livermore National Laboratory, and used for conventional X-ray and electron therapy treatment planning, has also been used for fast neutron therapy dose calculations. MacNCTPlan [12], developed by Harvard/MIT, and BNCT_rtpe [13], developed by Idaho National Environmental and Engineering Laboratory, have been used in Boron Neutron Capture Therapy (BNCT) clinical trials [14]. Modern treatment planning codes allow visualization of calculate dose rate distributions by superimposing the isodose-rate contours over the

Table 1. Monte Carlo N- γ Codes

MC Code	Developer	MC Code	Developer
COG [3]	LLNL,USA	MCBEND [4]	UKAEA,UK
MCNP4C [5]	LANL,USA	MCU [6]	Kurchatov Inst.,Russia
MORSE-CGA [7]	ORNL,USA	MVP [8]	JAERI,Japan
TART98 [9]	LLNL,USA	TRIPOLI [10]	CEA/CEN/LEPF,France

patient's CT or MRI images, allowing the medical physicist and radiation oncologist to compare combinations of radiation beam orientations and weights. They also allow 3-D manipulation of the images to visualize irradiation beam entry and exit locations and calculated isodose contours. The neutron transport codes used for treatment planning use the ENDF/B-VI [15] cross sections and apply $S(\alpha,\beta)$ thermal scattering models during neutron transport. The ENDF/B-VI evaluation is also the basis for the ICRU 63 [16] elemental neutron kermas, the most up to date as of this conference. Photon kermas, based on Hubble's (μ_{en}/ρ) data [17], and human tissue compositions, are available in ICRU 46 [18].

3 Example Applications

The above coupled n- γ Monte Carlo codes have been applied to a number of engineering design problems. The follow paragraphs give examples of how Monte Carlo codes were used in the design of specific facilities or devices.

3.1 Epithermal Neutron Beam Design

MCNP was used extensively in the recent design of an epithermal neutron beam for neutron capture therapy at the Massachusetts Institute of Technology Nuclear Reactor Laboratory. The premise of the beam design was to use a fission converter, a subcritical configuration of ^{235}U fuel placed outside the MITR-II core and reflector, but adjacent to a high intensity source of thermal neutrons, the thermal column. The fission neutrons produced in the converter pass through moderator and filter materials, resulting in an a high quality, high intensity epithermal neutron beam.

Kiger et al. [19] present a comprehensive analysis of the different components of the beam design, outlined in Tab. 2, to investigate the effects on neutron and γ flux and dose in air or in a water phantom at the patient position. Proposed designs were evaluated according to three criteria: high epithermal beam intensity ($\geq 10^{10}$ n/cm 2 s) at the patient position for short irradiation times, minimization ($\leq 2 \times 10^{-13}$ Gy cm 2 /n) of fast neutron and γ dose components to increase the therapeutic ratio, and adequate collimation to result in a penetrating beam to treat deep-seated brain tumors.

Their detailed model of the reactor core, fission converter, moderator and filter materials, and collimator also aided their understanding of the resulting beam. By selectively allowing photon production in individual components or from different isotopes in the model, the contribution to photon dose in the phantom from gammas produced in the filter, moderator and fission converter were evaluated. Photons from ^{28}Al decay and delayed gammas from fission products, not simulated by MCNP, were added in separate simulations as fixed sources, to determine their effects on photon dose. Photon dose from the $^1\text{H}(\text{n},\gamma)^2\text{H}$ reaction in the phantom was evaluated by terminating all photons from the mixed field beam impinging on the phantom.

Table 2. Variables changed in MITR-II fission converter beam MCNP calculations

Design Variable	Investigated	Design Variable	Investigated
Fuel Coolant	D ₂ O, H ₂ O	Fuel Enrichment	20%, 93%
Fuel Burnup	new, spent	Collimator Material	Bi, Pb, Graphite, Ni
Photon Shield	Bi, Pb	Reflector Material	Ni, Al, AlF ₃
Filter & Moderator Order	Al/AlF ₃ , AlF ₃ /Al, homogeneous mix	Filter & Moderator Material	AlF ₃ ,Al,Al ₂ O ₃ ,D ₂ O, PTFE,Ti,S,Graphite

3.2 Fast Neutron Radiography Facility

Ambrosi et al. [20], used MCNP to calculate neutron scintillator response from scattered (background) neutrons and neutrons unscattered from a beam, to determine signal to noise ratio in an accelerator-based fast neutron radiographic facility. The angular-dependent neutron yield for the two neutron production reactions, $\text{D}(\text{d},\text{n})^3\text{He}$ and $^7\text{Li}(\text{p},\text{n})^7\text{Be}$, was modeled by weighting neutron beams pointing various directions, located at the accelerator target. Their calculations showed that scattering off the camera housing, electronic shielding, and irradiation room walls were a much more significant problem for the $^7\text{Li}(\text{p},\text{n})^7\text{Be}$ reaction. Subsequently, scattering properties of 5 cm thick samples of U, W, Fe, Pb and polyethylene were calculated to determine their usefulness as electronic shielding in the radiographic facility.

3.3 National Ignition Facility Construction Materials

In a benchmark experiment by Belian, et al. [21], boronated and non-boronated cement, to be used for structural support at the National Ignition Facility Target Chamber (NIFTC), was irradiated by 14 MeV neutrons. For several hours after the irradiation was complete, photon dose from the decay of beta emitters ^{27}Mg ,

^{56}Mn and ^{24}Na , which were produced from neutron reactions with the cement, was measured by a nearby ion chamber. The dose rates agreed well with predictions by TART calculations, validating the coupled n- γ transport for similar situations. Further TART calculations showed that thermal neutron absorption in the NIFTC cement does not contribute significantly to dose rate, which led to the decision not to add boron to the cement, saving an estimated 800,000 USD in construction costs.

3.4 Land Mine Detector System

While there are numerous examples of MC codes used for shielding analysis, an interesting example is presented by Cousins et al. [23]. The Canadian Department of National Defense used MCNP in the design of their vehicle mounted land mine detection system. The ^{252}Cf neutron source emits deeply penetrating fast neutrons which become thermalized in the ground and are absorbed by nitrogen in the mine's explosive material. A 10.83 MeV prompt gamma is frequently emitted and detected by NaI(Tl) detectors on the vehicle. MCNP was used in the shielding design for personnel and electronics from the ^{252}Cf source. The transport code could have also been used to simulate detector response for a variety of land mine depths, nitrogen contents, and soil compositions.

3.5 Nuclear Oil Well Logging Measurements

The use of several nuclear techniques has become popular in oil well logging to determine hydrocarbon quantities in various earth formations. These techniques measure gamma ray backscatter, neutron slowing-down time, natural radioactive decay gamma emissions, and neutron induced prompt gamma emissions to determine earth formation average density, liquid porosity, water saturation and other properties. MCBEND and MCNP have been used to calculate neutron and photon detector responses for various nuclear well logging experiments [24]. Gardner and Liu have also tailored variance reduction techniques, including adjoint calculations, specifically for Monte Carlo well-logging simulations [25].

3.6 Neutron Therapy

Currently, therapeutic uses of neutron sources are based on fast neutron radiotherapy, neutron brachytherapy or BNCT [14]. Fast neutron radiotherapy [26] and brachytherapy [27], which have shown better clinical response than standard photon radiation therapy for some tumours, rely on the high-LET neutrons to kill anaerobic tumour cells, which are relatively insensitive to Low-LET radiation. BNCT, currently in clinical trials, combines neutron irradiation with a high capture cross section isotope, ^{10}B . Preferential loading in the target and short range of the reaction product nuclei from $^{10}\text{B}(\text{n},\alpha)^7\text{Li}$ add to the therapeutic advantage. Neutron therapies use MC codes to calculate peak and average doses to organs and tumours, to determine optimal neutron beam irradiation orientations or seed locations. MC codes have been used to study proposed neutron therapies, such as boron dose enhancement from ^{252}Cf seed sources [28].

4 Conclusions

General purpose coupled neutron photon Monte Carlo codes are exploited in the design of diverse industrial applications and medical techniques, and have lead to significant advances in science, engineering and medicine.

References

1. N. Yoshizawa, O. Sato, S. Takagi: J. Nucl. Sci. Tech. **35**, 928 (1998)
2. J. Chen, H.H. Hsu, W.H. Casson: Health Phys. **70**, 22 (1996)
3. R. Buck, et al: *COG Users Manual* (Lawrence Livermore National Lab., Livermore 1994)
4. S. Chukas, I. Curl, T. Shuttleworth, G. Morrell: In: *Proc. 8th Int. Conf. Rad. Shield., Arlington*, p. 1126 (1994)
5. J.F. Briesmeister, Ed.: LA-13709-M (April 2000)
6. <http://www.aeat.co.uk/answers/>
7. M.B. Emmett: ORNL-6174 (April 1985)
8. T. Mori, K. Okumura, Y. Nagaya: 'Status of JAERI's Monte Carlo Code MVP for Neutron and Photon Transport Problems'. These proceedings p. 625
9. D.E. Cullen: UCRL-ID-126455 Rev. 2 (November 1998)
10. J.P. Both, H. Derriennic, B. Morillon, J.C. Nimal: In: *Proc. 8th Int. Conf. Rad. Shield., Arlington*, p. 373 (1994)
11. C.L.H. Siantar, W.P. Chandler, J.A. Rathkopf, M.M. Svatos, R.M. White: In: *Proc.Int. Conf. Math. Computat. React. Phys. Envir. Ana., Portland*, p. 857-65 (1995)
12. R.G. Zamenhof, E. Redmond II, G.R. Solares, D. Katz, W.S. Kiger III, O.K. Harling: Int. J. Rad. Oncol. Biol. Phys. **35**, 383 (1996)
13. D.W. Nigg, F.J. Wheeler, D.E. Wessol, J. Capala, M. Chadha: J. Neuro-Oncol. **33**, 93 (1997)
14. R.G. Zamenhof, P.M. Busse, O.K. Harling, T. Goorley: In: *The Modern Technology of Radiation Oncology* (Medical Physics Publishing, Madison, WI 1999)
15. ENDF/BVI Summary Documentation, Brookhaven National Laboratory (1991)
16. ICRU Report 63. ICRU Publications, Bethesda, MD. 2000
17. J.H. Hubbell: Intl. J. Appl. Radiat. Isot. **33**, 1269 (1987)
18. ICRU 46 reference: ICRU Report 46. ICRU Publications, Washington, DC. (1992)
19. W.S. Kiger III, S. Sakamoto, O.K. Harling: Nucl. Sci. Eng. **131**, 1 (1999)
20. R.M. Ambrosi, J.I.W. Watterson, B.R.K. Kala: Nucl. Instr. Meth **B139**, 286 (1998)
21. A.P. Belian, J.F. Latkowski, E.C. Morse: Fusion Tech. **34**, 1028 (1998)
22. L. Zhao, E. Johnson, L. Robinson: J. Radioanal. Nucl. Chem. **240**, 531 (1999)
23. T. Cousins, et al.: J. Radioanal. Nucl. Chem. **235**, 53 (1998)
24. R.P. Gardner, K. Verghese: Nucl. Geophys. **4**, 4 (1991)
25. R.P. Gardner, L. Liu: Nucl. Sci. Eng. **133**, 80 (1999)
26. J.G. Douglas, et al.: J. Rad. Oncol. Biol. Phys. **46**, 551 (2000)
27. T. Tacev, J. Zaloudik, L. Janakova, V. Vagunda: Neoplasma. **45**, 96 (1998)
28. J.C. Yanch, R.G. Zamenhof: Rad. Res. **131**, 249 (1992)

MCNP Calculations for the Shielding Design of a Beam Tube to Be Installed at the Portuguese Research Reactor

I.F. Gonçalves, A.G. Ramalho, I.C. Gonçalves, J. Salgado

Instituto Tecnológico e Nuclear Est. Nacional 10, 2686-953 Sacavém, Portugal

Abstract. The work presented concerns the calculation of the external biological shielding for a neutron beam tube that will be installed at the Portuguese Research Reactor, RPI. This tube will have enough versatility to be used in fields so different as the analysis of the composition of samples or research work in Boron Neutron Capture Therapy, BNCT. The calculation was made by using the MCNP code. This code is a well validated and widely used code, and has therefore become an important tool in the design and optimisation work of experiences related to neutrons and gamma radiation.

1 Introduction

One of the most significant utilisations of nuclear research reactors is achieved through the use of neutron beams, which may be used in a variety of applications. The multipurpose beam considered in this work will be implemented at one of the irradiation tube of the Portuguese Research Reactor, RPI.

The RPI is a 1 MW swimming pool type reactor similar to various others designed by AMF Atomics using, at present, 93% enriched uranium. It is provided with seven beam tubes and a thermal column with two access ports. The reactor core is Be reflected in three sides.

The tube will be very versatile and at present is planned to use it to the analysis of the composition of samples and on research work in Boron Neutron Capture Therapy, BNCT. It will have the possibility of choosing from two different beam openings (1 or 2.5 cm radius), and to use neutron beams with or without thermal component, (eliminating the thermal component is achieved with a Cd filter).

The beam tube and the external shielding arrangement, are shown in Fig. 1. The external shielding is a hollowed parallelepiped, with an inner part of a hydrogenous material followed by a concrete enclosure.

2 Calculation Method

The calculation of the external biological shielding for the tube was made by using the MCNP code [1], developed at Los Alamos National Laboratory. This code is a well validated and widely used code, and has therefore become an important tool in the design and optimisation of experimental conditions using neutrons and gamma radiation.

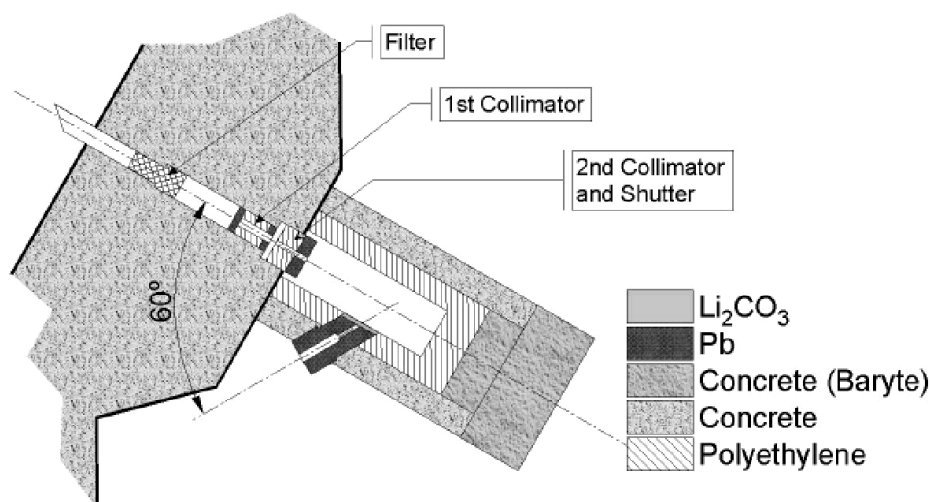


Fig. 1. Layout of the beam tube and the external shielding arrangement

The code was run either on a Pentium PC or an Alfa Station, and the nuclear cross sections used were those from the ENDF/B-VI data files. The typical running time to achieve a statistical error less than 10% was approximately 70 hours.

The input source to the program was obtained from previous calculations [2]. It consists of a plan source with the size of the cross section of the beam located at the point where the beam emerges from the reactor shielding. The intensity was obtained without neutron filters (this is the case for the maximum intensity of the source). The energy spectrum of the source was assumed consisting of 7 neutron groups, the thermal group with a cut-off at 0.625 eV and 6 other neutron groups.

The radiation dose was calculated at the end of the shielding (front surface), and at lateral sides. As the code calculates the average flux over a given surface the front surface was divided into annulus with different radii and the dose was calculated for each of them. The average over the total surface was also calculated. As the shielding is symmetrical with respect to the beam it was assumed that the dose is the same for all lateral surfaces, therefore, the calculation was made only for one of them. The surface was divided by vertical plans perpendicular to the base, 5 cm apart from each other and the dose was calculated for each slice. Further calculations were made dividing the full surface into squares (10 cm side) and the dose calculated at each of these squares.

To simulate the experimental set up calculations were made with and without spheres of Pb and polyethylene (2.5 and 5 cm radius) placed at 10 cm from the tube aperture, to simulate an experience, and without scatter. With this procedure the area of high doses was identified and further calculations were

made for detailed analysis. The calculations were repeated for scatterers placed at 86 cm from the beam exit.

The results were obtained for the 3 energy groups of neutrons that are frequently used for BNCT studies. It is recalled that such energy groups are as follows: thermal $E_n < 0.625$ eV, epithermal $0.625 \text{ eV} < E_n < 10 \text{ keV}$ and fast $E_n > 10 \text{ keV}$.

3 Results

Figure 2 shows the obtained gamma radiation dose rate, at the lateral wall of the shielding, with and without a polyethylene sphere of 2.5 cm radius, placed 10 cm from the tube aperture, for the case where the wall was divided into 5 cm slices. Similar results for fast neutron dose rate are shown in Fig. 3.

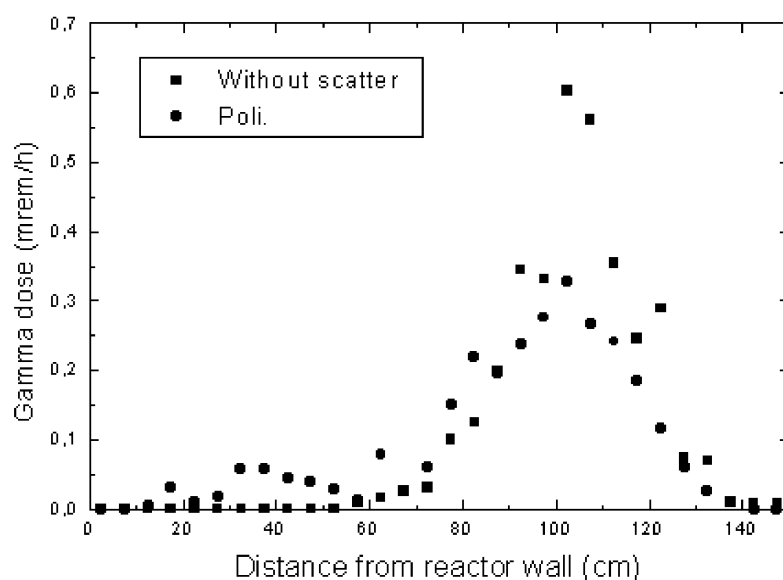


Fig. 2. Gamma dose calculated at the lateral wall of the shielding

The spheres have the effect of displacing the maximum dose towards the reactor wall, and to decrease the dose at the front surface as can be seen in Tab. 1, that summarises the maximum neutron dose obtained for the first calculations.

As can be seen the doses were too high which led to modifications of the shielding design particularly its thickness. Also a detector geometry configuration was selected where the sample was located 86 cm far from the tube aperture. Calculations were performed for this new situation; in this case the lateral surface was divided into squares (10 cm side) and the dose calculated at the squares. Figure 4 shows the fast neutron dose rate obtained for the case where Pb spheres

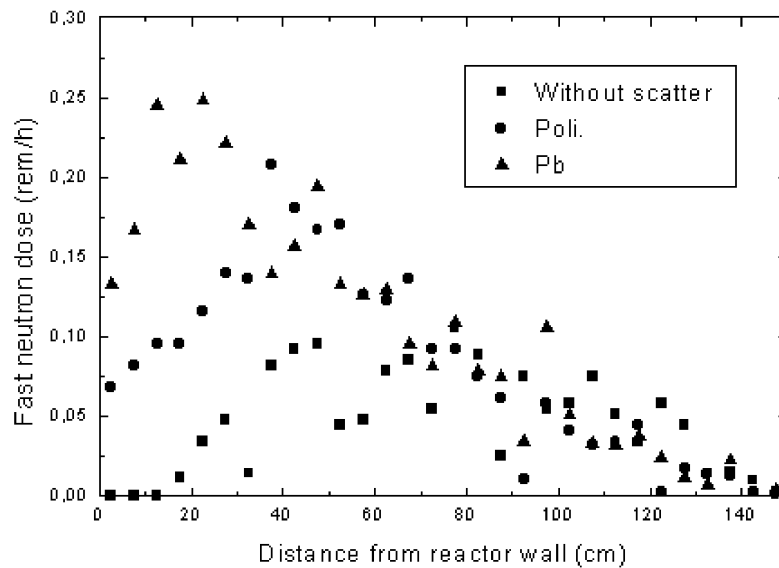


Fig. 3. Calculated fast neutron dose at the lateral wall of the shielding

Table 1. Maximum neutron dose (rem/h)

		Neutron energy	
		Thermal	Fast
Front	Without scatter	0.003	0.37
	With poliet.	0.002	0.18
	With Pb	0.002	0.15
Lateral	Without scatter	0.015	0.11
	With poliet.	0.023	0.2
	With Pb	0.026	0.26

were used to simulate the experiment. For this new configuration of shielding materials the gamma dose was reduced to approximately 30% .

4 Conclusions

The neutron dose is still too high, meaning that it is necessary to reinforce the shielding specially near the sample location. Calculations are still in progress in

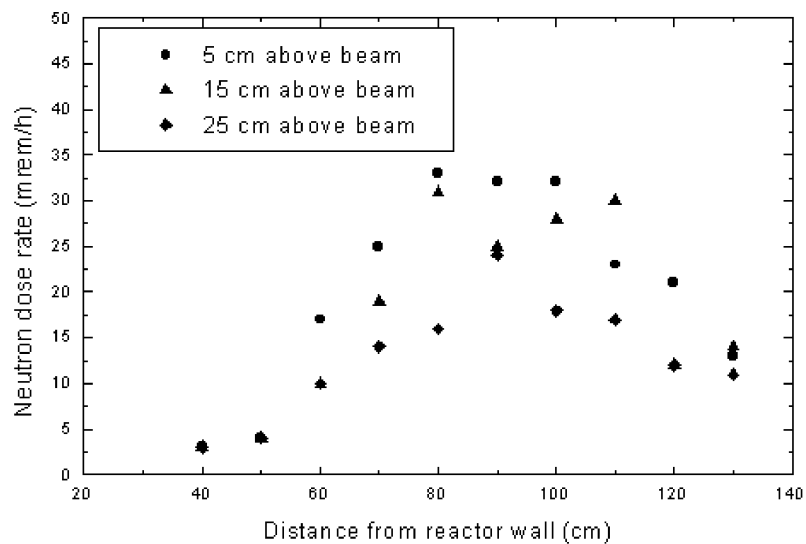


Fig. 4. Calculated fast neutron dose at the shielding lateral wall

order to study the best arrangement of shielding materials. To cut the thermal neutrons a 1 mm thick Cd foil will be tested. It is expected that the use of Cd will increase the gamma dose due to (n,γ) reactions, but the concrete shielding will absorb it.

References

1. J.F. Briesmeister (ed.): *MCNP-A general Monte Carlo N-Particle Transport Code*, version 4A, LA-12625-M, 1997
2. I.F. Gonçalves, A.G. Ramalho, I.C. Gonçalves, J.F. Salgado, V. Alcobr Bosch: 'Establishment of new irradiation facilities at the Portuguese Research Reactor'. In: *Proc. 9th Int. Symp. on Reactor Dosimetry*, ed. by H. Abderrahim, P. D'hondt, B. Osmera, pp. 118-123, 1996

Monte Carlo Applications in Fusion Neutronics^{*}

U. Fischer

Forschungszentrum Karlsruhe, Institut für Reaktorsicherheit, P.O. Box 3640, 76021
Karlsruhe, Germany

Abstract. An overview is given of Monte Carlo applications in fusion neutronics as being addressed at Forschungszentrum Karlsruhe in the framework of the European Fusion Technology Programme. Main applications are in the area of design and development of components for future fusion reactors such as ITER, the International Thermonuclear Experimental Reactor, and a Demo-type European tokamak reactor, further in the development of intense neutron sources for material research, and, finally, in the conduction and analyses of integral 14 MeV neutron experiments. The overview includes a short review of methods, tools and data and addresses key issues of Monte Carlo applications in fusion neutronics.

1 Introduction

Neutron and photon radiation transport in fusion reactors and related systems is the subject of fusion neutronics. The Monte Carlo method has proven to be the most suitable computational technique for these applications mainly because of its ability in representing the complex problem geometry typical of fusion tokamak reactors. Monte Carlo applications in fusion neutronics include design calculations to support the development of reactor components and facilities as well as computational analyses of integral experiments for nuclear data testing and design validation. In this paper, an overview is given of Monte Carlo applications in fusion neutronics as being addressed at Forschungszentrum Karlsruhe in the framework of the European Fusion Technology Programme.

2 Fusion Neutronics: Methods, Tools and Data

The design of future (d,t) fusion reactors relies to a large extent on the data provided by nuclear design calculations. Appropriate and qualified computational simulations are required for the nuclear design calculations to assure that their results are reliable. The Monte Carlo method has proven to be the most suitable computational techniques in this regard and is, therefore, the preferred method in fusion neutronics. It allows a very flexible geometry representation such that the reactor can be modelled in three-dimensional geometry very close to reality. In the Monte Carlo approach, neutron transport is described on the microscopic level by simulating individual neutron histories from birth in the (d,t)-reaction

^{*} This work has been performed in the framework of the nuclear fusion programme of Forschungszentrum Karlsruhe and is supported by the European Union within the European Fusion Technology Programme.

to death by absorption or leakage. There is, in principle, no numerical approximation included in the Monte Carlo calculation as no transport equation need to be solved. This enables the use of the cross-section data in a continuous energy representation in the same way they are given on the nuclear data file. The accuracy of the calculation is only affected by the statistical uncertainty of the calculation itself and the uncertainties involved in the nuclear cross-section data. For fusion neutronics applications, the Monte Carlo code MCNP [1] has become the main computational tool because of its ease and flexibility in modelling complicated fusion reactor components and its capability for a proper simulation of neutron and photon transport.

Fusion neutronics applications require specific nuclear data requests to be fulfilled. Accordingly, various projects are being conducted on the development of fusion nuclear data libraries, notably in the European Union (European Fusion File, EFF) and in Japan (JENDL-FF, Japanese Evaluated Nuclear Data Library - Fusion File). A major international effort was initiated by the International Atomic Energy Agency (IAEA) when launching the FENDL (Fusion Evaluated Nuclear Data Library) project [2]. A first version, FENDL-1, was adopted as reference library for design calculations of the ITER project and has been extensively benchmarked in an international effort [3]. A further update based on recent data evaluations from the present state-of-the-art nuclear data libraries has led to the improved FENDL-2 library that currently is considered the best available and validated nuclear data library for fusion applications [4,5].

3 Monte Carlo Applications in Fusion Neutronics

At Forschungszentrum Karlsruhe, the main areas are in the development of blanket concepts for a Demo fusion reactor and, on this basis, the design of a blanket module for test irradiation in a ITER-like next-step tokamak; testing and validation of fusion nuclear data by means of integral experiments and their analyses, and, finally, the development of an intense neutron source for fusion material test irradiations.

3.1 Blanket and Shield Design

A Helium-Cooled Pebble Bed (HCPB) blanket has been developed with the main objective to design a Demo-relevant solid breeder blanket [6]. The HCPB blanket is characterised by the use of ceramic Lithium compound pebbles as breeder material (Li_4SiO_4 , Li_2ZrO_3 , Li_2TiO_3), Beryllium pebbles as neutron multiplier and helium gas as coolant. The blanket structure consists of an heterogeneous array of alternating Beryllium and ceramics pebble bed layers separated by cooling plates arranged in toroidal-radial planes. The primary neutronic task is to optimise the design with regard to its breeding performance and to ensure, finally, Tritium self-sufficiency. To this end, a three-dimensional torus sector model of the EU Demo reactor has been developed (Fig. 1). The target value for the global Tritium Breeding Ratio (TBR) is at 1.13 which is necessary to arrive at a final TBR=1.05 when taking into account losses due to blanket ports.

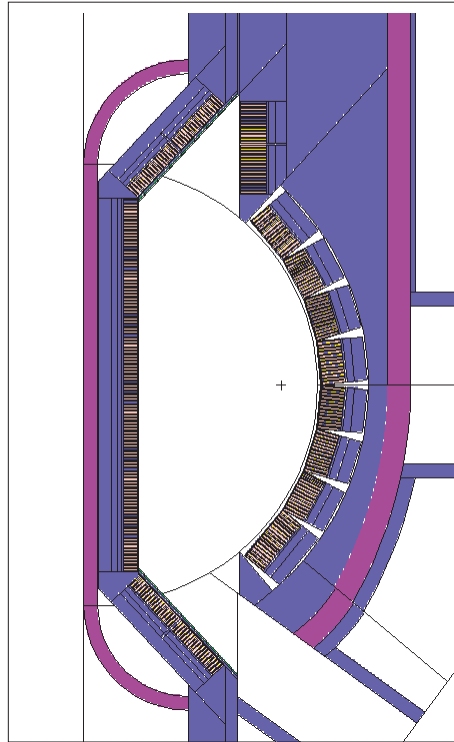


Fig. 1. MCNP model of EU Demo-type reactor with HCPB blanket modules (vertical cross-section)

The required ${}^6\text{Li}$ -enrichment is at 40 at% for Li_4SiO_4 , 75 at% for Li_2ZrO_3 and 65 at% for Li_2TiO_3 at a breeder pebble height of 10 mm. The pebble height is crucial due to the low heat conductivity of the breeder pebbles [7]. An accurate calculation of the nuclear power generation and its spatial distribution is therefore mandatory. This requires to base the nuclear heating calculation on the full 3d reactor model including a detailed representation of the pebble bed arrays. As part of the ITER test blanket programme, a HCPB test blanket test module (TBM) has been designed for insertion into a horizontal test blanket port. One of the objectives of the test blanket irradiation is to check the capability of neutronics codes and data to predict the nuclear responses in the TBM. The Monte Carlo method allows to deal with both the large sized ITER torus and the small sized TBM at the same time with both high accuracy and good calculational efficiency. A suitable model of the HCPB TBM was integrated into a torus sector model of ITER with a test blanket port to per-

form a nuclear analysis for assessing the Tritium and the power generation in the TBM and for proving shielding efficiency of the test blanket system [8].

3.2 Nuclear Data Testing and Integral Experiments

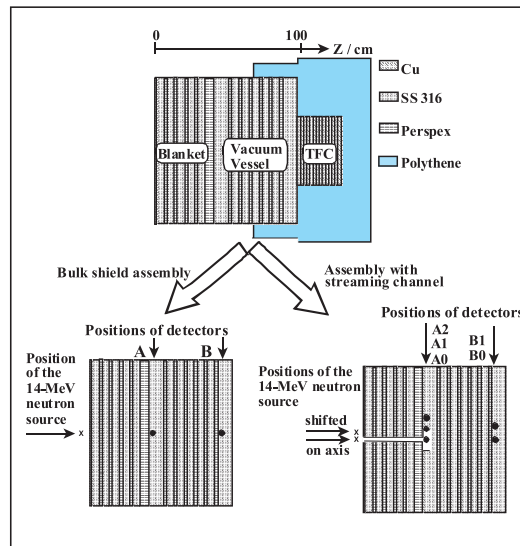
Computational tools and data need to be validated to assure that they give reliable results when applied in design calculations. This can be achieved through suitable integral benchmark experiments and their computational analyses. In such experiments, suitable material assemblies are irradiated with 14 MeV neutrons and nuclear responses of interest are measured and compared to calculations where the experiment has to be simulated by modelling the experimental set-up as close as possible.

The objective of benchmark experiments is to provide the data required for nuclear data testing. A typical example is the 14 MeV neutron transmission experiment on a 30 cm thick iron slab [9] conducted by the Technical University of Dresden (TUD) in the framework of the European Fusion File (EFF) project. In this experiment, neutron and photon leakage flux spectra have been measured at

Table 1. Neutron flux integrals [$\text{n}/(\text{cm}^2(\text{source neutron}))$] measured in the TUD iron transmission experiment and calculation-to-experiment (C/E) ratios

Energy range [MeV]	Experiment [$\text{n cm}^{-2}\text{sn}^{-1}$]	C/E			
		EFF-3	EFF-1	FENDL-1	JENDL-FF
0.1 - 1	$(2.56 \pm 0.28)10^{-7}$	1.04	0.94	0.99	1.03
1 - 5	$(4.51 \pm 0.21)10^{-8}$	0.99	0.83	0.94	0.92
5 - 10	$(3.42 \pm 0.19)10^{-9}$	0.74	0.64	0.95	0.88
> 10	$(1.59 \pm 0.07)10^{-8}$	0.87	0.72	0.83	0.79

a distance of 349 cm from the target. A full three-dimensional MCNP model of the experimental set-up including the collimator, the floor, the wall, the air, the assembly rack, the cooling and the target holder was used to calculate the neutron and photon leakage spectra for comparison with the measured data using the point detector tally. Sensitivity and uncertainty calculations were included making use of the Monte Carlo point detector technique for calculating sensitivity profiles [10]. A C/E (calculation/experiment) comparison is displayed in Tab. 1 for neutron flux integrals. It is noted that there is generally good agreement for the “state-of-the-art” data files except for the high energy component ($E > 10$ MeV) which is underestimated by 10 to 20 %.

**Fig. 2.** ITER shielding blanket mock-up assemblies with measurement positions indicated

straight streaming duct through the blanket mock-up [12]. Measurements of neutron and photon flux spectra have been performed inside the mock-up at penetration depths of 41.4 and 87.6 cm, respectively. Figure 2 shows the ITER

The objective of design-oriented experiments is to validate the nuclear performance of the considered reactor subsystem and thereby provide uncertainty margins of specific nuclear responses. The ITER shielding experiments performed at the Frascati Neutron Generator (FNG) aimed at validating the shielding performance of the ITER inboard shield system. To this end a mock-up has been assembled consisting of first wall, shielding blanket, vacuum vessel and a simulated TF-coil. Two kind of experiments have been performed in this framework, one on a bulk shield assembly [11]

and one on an assembly with a

shield mock-up assemblies with the measurement positions indicated. Figure 3 displays a comparison of calculated and measured photon flux spectra. Good agreement has been obtained even for the deep location at the back of the vacuum vessel mock-up. The same applies for the neutron flux spectrum except for the high energy ($E > 10$ MeV) part. It is thus concluded that the neutron and gamma flux attenuation in a design relevant bulk shield system can be satisfactorily described by MCNP based calculations using the state-of-the-art fusion nuclear data libraries.

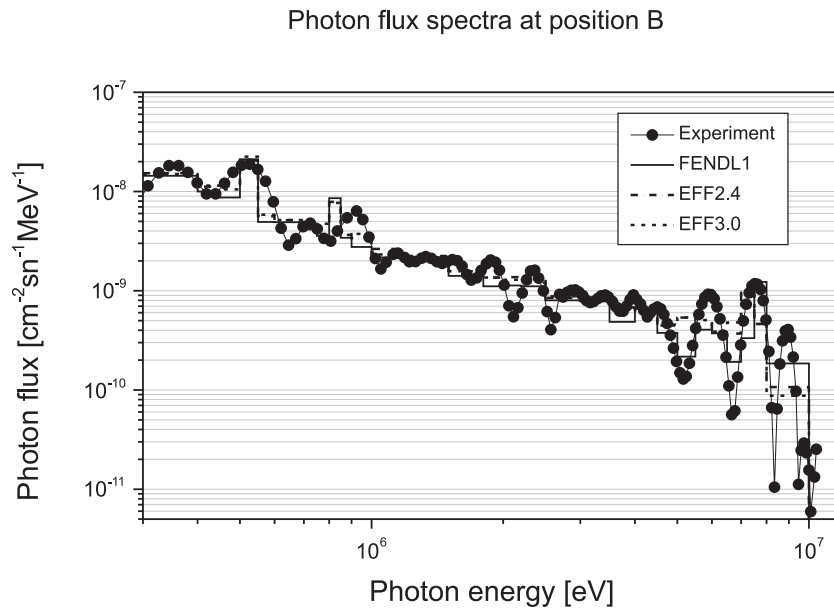


Fig. 3. Photon flux spectra at the back of the ITER shielding blanket mock-up

3.3 Intense Neutron Source for Fusion Material Test Irradiation

An accelerator-driven neutron source based on the $d(\text{Li}, \text{xn})$ reaction has been selected as preferred solution for a fusion material test irradiation facility. A corresponding project for an International Fusion Material Irradiation Facility (IFMIF) is currently being conducted in the framework of an IEA (International Energy Agency) task agreement [13]. IFMIF employs two continuous-wave linear accelerators each generating 125 mA of 40 MeV deuterons striking a flowing liquid Lithium target. Neutrons with energies up to 50 MeV are produced at a rate of 0.07 per incident proton resulting in a total neutron production of some 10^{17} s^{-1} and a maximum neutron flux density of $10^{15} \text{ cm}^{-2}\text{s}^{-1}$. A major neutronic task is to prove, by means of calculations, that (1) the primary goal to produce damage rates at least as high as in a Demo- type fusion reactor (some 20 dpa/fpy in iron) can be achieved in a volume of at least 0.5 liters, and (2) that the damage relevant nuclear responses are representative for fusion reactor conditions.

Extensive development work has been performed to provide the required nuclear data above 20 MeV neutron energy, to develop a Li(d,xn) source function model for MCNP, and to conduct the neutronic design analysis. Work on the Li(d,xn) source function has led to a new MCNP source function module, McDeLi [14], which is based on nuclear reaction models and capable of accurate and flexible modelling of the IFMIF neutron source term. A comprehensive characterisation of the high flux test region has finally demonstrated the facility's suitability as a fusion simulation environment [15].

4 Conclusions and Outlook

An overview has been given of Monte Carlo applications in fusion neutronics as being addressed at Forschungszentrum Karlsruhe. It has been pointed out that the Monte Carlo technique is best suited to meet the required objectives in these applications. In particular this is true for blanket and shield design of future fusion reactors which require computational methods and models that allow to accurately describe neutron transport both in global and local dimensions for representing at the same time both the reactor and small-sized details of the blanket structure. This can be accomplished by the Monte Carlo technique as available with state-of-the-art codes like MCNP. Numerous fusion relevant benchmarks have been shown the reliability of Monte Carlo based neutronic calculations when using modern high quality fusion nuclear data. A major task ahead is to further develop the capabilities of the Monte Carlo codes to allow three-dimensional sensitivity and uncertainty calculation of any response of interest in the full reactor geometry.

References

1. F. Briesmeister (ed.): Los Alamos National Laboratory, Report LA-12625-M (1993)
2. D. Muir, S. Ganesan, A. B. Pashchenko: In: *Int. Conf. on Nucl. Data for Sci. and Techn., Juelich, Germany, May 13-17, 1991*
3. U. Fischer et al., *Fusion Technology* **30**, No. 3, Part 2B (Dec. 1996), 1093-1100
4. M. Herman, A.B. Pashchenko: IAEA, Report INDC(NDS)-373 (1997)
5. U. Fischer et al: In: *5th Int. Symp. Fus. Nucl. Tec., Rome, Italy, Sept. 19-24, 1999*
6. M. Dalle Donne et al.: *Fus. Eng. Des.* **39-40**, 825 (1998)
7. U. Fischer et al.: In: *Proc. 20th Symp. Fus. Tech., Marseille, France, 7-11 Sept. 1998* p. 1149
8. U. Fischer, M. Dalle Donne: *Fusion Engineering and Design*, **39-40**, 835 (1998)
9. H. Freiesleben et al: *Tech. Universitaet Dresden, Report TUD-PHY-94/2*, 1995
10. U. Fischer et al.: In: *Proc. 20th Symp. Fus. Tec., Marseille, France, 7-11 Sept. 1998*, p. 1153
11. P. Batistoni et al: *Fusion Engineering and Design* **47**, 25 (1999)
12. K. Seidel et al: In: *5th Int. Symp. Fusion Nucl. Tech., Rome, Italy, Sept. 19-24, 1999*
13. M. Martone (ed.): ENEA Frascati, Report RT/ERG/FUS/96/11 (1996)
14. P. Wilson: Forschungszentrum Karlsruhe, Bericht FZKA 6218 (1999)
15. P. Wilson et al.: *Fusion Technology* **33**, 136 (1998)

MCNP Simulation of Void Reactivity in a Simplified CANDU Core Sub-region

F. Rahnema¹, S. Mosher¹, M. Pitts¹, P. Akhtar², and D. Serghiuta²

¹ Georgia Institute of Technology, Nuclear Engineering and Health Physics Programs,
Woodruff School of Mechanical Engineering, Atlanta GA 30332-0405, USA

² Canadian Nuclear Safety Commission, P.O. Box 1046, Station B, 280 Slater Street,
Ottawa Ontario K1P 5S9, Canada

Abstract. The Monte Carlo code MCNP with a continuous-energy ENDF/B-VI cross section library at the hot operating condition was used to determine the impact of the core environment on void reactivity in a sub-region of a simplified CANDU-6 core of 4 x 3 x 6 cell-size. The net (combined) impact of the adjuster rods, axial leakage and cell-to-cell radial leakage (due to fuel burnup variation in the core) was estimated to be between 1.44 ± 0.37 and 1.96 ± 0.39 mk ($10^{-3}k$).

1 Introduction

A distinctive characteristic of CANDU reactors is a positive void coefficient of reactivity. All safety analyses are required to account for this effect in a conservative manner. Hence, it is important to understand and quantify the uncertainties that are associated with the analysis methods. In the current three-dimensional (3-D) transport-diffusion methodology employed to evaluate static (e.g. void reactivity coefficient) or dynamic (e.g. power excursion) reactor behavior the main sources of uncertainties are related to lattice cell calculations and core simulations.

Monte Carlo methods, such as those in the MCNP [1] code, are used as the basis for developing adequately accurate lattice physics models, which in turn are used in generating the data needed for reactor core analysis. In recent years, it has become a common practice to use the continuous-energy MCNP code as a benchmarking tool to either supplement or replace experimental results when they are not available. Recently, a set of void reactivity calculations was performed [2] for a typical CANDU lattice cell by using MCNP and the lattice depletion code HELIOS [3]. However, that study did not address the three-dimensional (core environment) effects, such as the cell-to-cell neutron leakage and local absorbers, on void reactivity.

In this paper, three-dimensional Monte Carlo simulations of a selected sub-region of a simplified CANDU-6 core are performed to determine the 3-D core effects on void reactivity. Currently, coupled 3-D transport-diffusion codes are used for CANDU core analysis. The MCNP code is used to develop a set of numerical void reactivity results for benchmarking these diffusion codes. These results are also used to explore the importance of 3-D effects under conditions specific to reactor cores.

2 MCNP Model Description

The model configuration is representative of a central sub-region of a CANDU-6 core. Twelve channels were modeled in three rows (J, K, and L) and four columns (13, 14, 15, and 16). Each channel contains six bundles and spans half of the core axially. Each bundle contains all 37 fuel pins (both fuel and clad modeled), coolant, pressure and calandria tubes, and moderator. Four stainless steel adjuster rods were inserted perpendicular to and between the pressure tubes (see Fig. 1). The two type B rods were positioned between columns 13 and 14. One rod is located 80 cm from the mid-plane and the other is centered at the mid-plane, and so is modeled as a half rod. The two type C-inner rods were modeled similarly between columns 15 and 16. The guide tubes are not modeled. Each cell is 28.575 cm in the x and y (transverse) directions and 49.53 cm in the z (axial) direction. The model was designed so that no gap exists between cells. A specular reflective boundary condition was imposed on the outside surfaces of the rows and columns as well as at the core mid-plane.

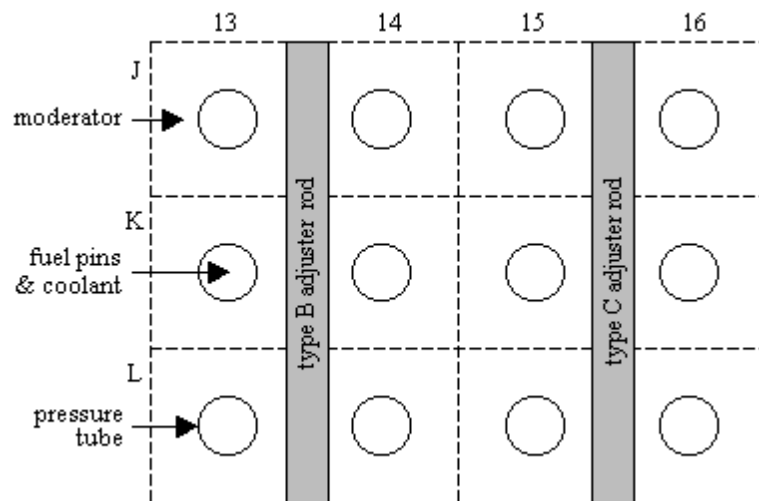


Fig. 1. Channel Numbering and Adjuster Rod Positions in the Sub-region

The average fuel burnup in each of the 72 bundles in the sub-region was taken from a diffusion theory code that is used for the core simulation. The lattice depletion code HELIOS was used to determine the isotopic number densities of the fuel material. To make the benchmark model manageable, the total number of fission products in each fuel region was reduced from 136 to 51, while increasing the concentration of Pm-149 to replace this loss of absorption. It was shown that the reactivity results are not affected by this simplification.

Using the cross section generator NJOY [4], an ENDF/B-VI [5] based continuous energy cross section library at the hot operating reactor temperature was developed for MCNP. A fractional tolerance of 0.001 was used in NJOY.

3 Results

The MCNP simulations used 5,000,000 active neutron histories out of a total of 5,500,000 (5.5M/5M). A converged fission source, generated by a corresponding initial case with 5.5M/5M histories, was used in each simulation. Some cases used 250 active and 25 inactive cycles with 20,000 histories per cycle. Others were run using 100 active and 10 inactive cycles with 50,000 histories per cycle.

The main objective of this paper was to study the effect of the adjuster rods and axial and radial neutron leakage on void reactivity. This is done by inserting the adjuster rods, changing the axial boundary condition from vacuum to specular reflection, and changing the core burnup pattern from a non-uniform to a uniform distribution. The k_{eff} results for the selected configurations are shown in Tab. 1. The 1σ Monte Carlo uncertainty follows the result in parentheses in all tables.

The configurations considered in this study are with and without adjuster rods for the cooled (operating condition), checkerboard-voided and fully-voided cases. In the checkerboard-voided configuration, the coolant is voided in every other channel which is typical of a loss of coolant accident (LOCA). The cases labeled “uniform burnup” have a burnup of 4 GWd/TU everywhere in the core. The volume and power weighted burnup averages over the voided channels in the checkerboard pattern are from 2209 to 2487 MWd/TU, depending on the weighting method. The maximum effect of this burnup difference on void reactivity would be about 0.4 mk, based on the HELIOS results in [2].

Table 1. MCNP Eigenvalue (k_{eff}) Results

Case ^a		k_{eff}			Void Reactivity ρ_v ^b	
		Cooled	CB ^c	Voided	CB ^c	Voided
ARW ^d	U ^e	1.04483 (.18) ^f	1.05276 (.21)	1.06103 (.20)	7.21 (.25)	14.61 (.24)
	D ^e	1.03456 (.19)	1.04371 (.20)		8.47 (.26)	
ARW	U	1.03496 (.21)	1.04303 (.21)		7.48 (.28)	
	D	1.03001 (.20)	1.03817 (.21)	1.04539 (.21)	7.63 (.27)	14.28 (.27)
ARI	D	0.99568 (.20)	1.00485 (.22)	1.01185 (.20)	9.17 (.30)	16.05 (.28)
	g→	0.99833 (.12)	1.00745 (.13)	1.01488 (.13)	9.07 (.17)	16.33 (.17)

^a The abbreviations ARW/ARI are for “all adjuster rods withdrawn/inserted”

^b See sec. 4 for the formula, units are mk

^c The checkerboard voiding pattern

^d The axial boundary condition for this case is specular reflection

^e U and D correspond to a uniform and distributed bundle exposures in the sub-region

^f The standard deviations in parentheses are in units of mk

We note that the MCNP calculations were performed with the $S_{\alpha\beta}$ temperature of hydrogen in the coolant and moderator at 300 K and 600 K, respectively. The operating temperatures are 341 K and 562 K. However, for the ARI configurations, results for the operating temperatures are also shown in Tab. 1 (see the row labeled “g→”).

4 Discussion of Results

4.1 Void Reactivity

Using the k_{eff} results, the calculated void reactivity (ρ_v), adjuster rod worth (Δk_{rod}), and axial leakage worth ($\Delta k_{\text{leakage}}$) are shown in Tab. 1. These quantities and the corresponding Monte Carlo uncertainties are defined as follows:

$$\begin{aligned}\rho_v &= 1000 (1/k_{\text{cooled}} - 1/k_{\text{voided}}), \quad \sigma_v = [\sigma_{\text{voided}}^2/k_{\text{voided}}^4 + \sigma_{\text{cooled}}^2/k_{\text{cooled}}^4]^{1/2} \\ \Delta k_{\text{rod}} &= 1000 (k_{\text{no rod}} - k_{\text{rod}}), \quad \sigma_{\text{rod}} = [\sigma_{\text{no rod}}^2 + \sigma_{\text{rod}}^2]^{1/2} \\ \Delta k_{\text{leakage}} &= 1000 (k_{\text{full refl}} - k_{\text{axial leakage}}), \quad \sigma_{\text{leakage}} = [\sigma_{\text{full refl}}^2 + \sigma_{\text{axial leakage}}^2]^{1/2}\end{aligned}$$

The change from a uniform to a non-uniform burnup distribution increases the void reactivity by 1.26 (0.36) mk and 0.15¹ (0.39) mk in the “no axial leakage” and “with axial leakage” cases, respectively. By accounting for the possible discrepancy in the definition of the equivalent average burnup, the burnup effects would be reduced by 0.4 mk resulting in 0.89 (.36) mk and -0.25 (0.39) mk, respectively. The Monte Carlo uncertainty must be reduced to ensure that this effect is statistically significant. The axial leakage seems to diminish the burnup effect.

The presence of the axial leakage does not seem to affect void reactivity for the uniform-burnup case. This effect however is more pronounced in the case of the distributed-burnup. Here, the “no axial leakage” case leads to a conservative void reactivity result (larger by 0.84 (0.37) mk). We note that the 0.84 difference is slightly larger than 2σ . The Monte Carlo uncertainty must be reduced to ensure that this difference is statistically significant.

The effect of the adjuster rods on void reactivity is determined by comparing the distributed-burnup case with and without the adjuster rods. Insertion of the rods increases void reactivity by $(9.17 - 7.63 =) 1.54 (0.40)$ mk.

For the distributed burnup configuration, the effect of the core environment on void reactivity is summarized as follows. The leakage effect is $(7.63 - 8.47 =) -0.84 (0.37)$ mk and the adjuster rods affect void reactivity by $(9.17 - 7.63 =) 1.54 (0.40)$ mk. Therefore, it seems that the adjuster rods and axial leakage each affect void reactivity in the opposite direction with a net effect of 0.70 (0.40) mk. The impact of the adjuster rods on void reactivity is almost twice as large as that of the axial leakage.

The combined impact of the adjuster rods, the axial leakage and the distributed burnup on the void reactivity worth can be determined by comparing the ARW configuration with uniform burnup and no axial leakage (7.21 ± 0.25) to the ARI configuration with distributed burnup and axial leakage (9.17 ± 0.30). The worth of the combined perturbations is 1.96 ± 0.39 mk. A similar comparison for the fully-voided configuration results in a void reactivity difference of $1.44 \pm 0.37 (= 16.05 - 14.61)$ mk. This difference ($1.96 - 1.44 = 0.52$ mk), if statistically significant, might be due to the discrepancy in the equivalent burnup. That is, for the fully-voided case, the average burnup discrepancy is about

¹ Statistically insignificant

400 MWd/TU whereas for the checkerboard-voided case, the average discrepancy can be as large as 1791 MWd/TU ($= 4000 - 2209$). The impact of the adjuster rods alone on void reactivity is slightly larger in the fully-voided configuration than in the checkerboard-voided case. However, the difference is within one standard deviation of the calculational uncertainty.

4.2 Fission Density

In the MCNP simulations, the fuel pin fission density distribution for channel K14 was tallied in six cases; namely, the configurations with and without adjuster rods for the cooled, checkerboard-voided and fully-voided cases. This data can be used for benchmarking deterministic codes. Caution must be exercised in using the data that have warnings generated by the MCNP statistical analysis. Substantially more computational effort is required to remove these warnings. The effect of the $S_{\alpha\beta}$ approximation noted earlier, on parameters such as the fission density was not evaluated but is conjectured to be small.

Table 2. MCNP Bundle Local Peaking-factors (LPF) for Channel K14

Case	Bundle Distance from Periphery ($z = 0$) in cm					
	0-50	50-100	100-150	150-200	200-250	250-300
Cooled, ^a	1.21 (2.6) ^d	1.16 (1.5)	1.15 (1.5)	1.15 (1.0)	1.17 (0.8)	1.17 (0.8)
ARW ^b	1.06 (2.7)	1.11 (1.6)	1.12 (1.2)	1.11 (1.0)	1.11 (0.9)	1.12 (0.8)
^c	12.20 (3.3)	3.88 (2.1)	2.82 (1.6)	3.49 (1.3)	4.42 (1.2)	4.18 (1.2)
Cooled,	1.16 (2.0)	1.14 (1.3)	1.16 (1.0)	1.16 (0.9)	1.21 (1.0)	1.18 (1.0)
ARI	1.07 (2.1)	1.10 (1.3)	1.11 (1.0)	1.10 (1.0)	1.10 (1.0)	1.12 (1.0)
	7.44 (2.7)	3.21 (1.7)	3.77 (1.4)	4.98 (1.3)	8.54 (1.3)	5.31 (1.3)
CB,	1.16 (2.5)	1.16 (1.5)	1.15 (1.2)	1.16 (1.0)	1.16 (0.9)	1.16 (0.8)
ARW	1.10 (2.6)	1.11 (1.5)	1.12 (1.2)	1.11 (1.0)	1.13 (0.9)	1.13 (0.8)
	5.52 (3.4)	4.36 (2.1)	2.68 (1.6)	3.59 (1.3)	2.25 (1.2)	2.05 (1.1)
CB,	1.17 (2.0)	1.16 (1.3)	1.16 (1.0)	1.16 (1.0)	1.18 (1.0)	1.18 (1.0)
ARI	1.09 (2.0)	1.09 (1.2)	1.11 (1.0)	1.12 (1.0)	1.08 (1.0)	1.11 (1.0)
	7.08 (2.6)	5.87 (1.7)	4.18 (1.4)	3.06 (1.3)	8.45 (1.3)	5.72 (1.3)
Voided,	1.12 (2.5)	1.11 (1.5)	1.11 (1.1)	1.12 (0.9)	1.12 (0.8)	1.13 (0.8)
ARW	1.05 (2.5)	1.08 (1.5)	1.08 (1.1)	1.08 (0.9)	1.10 (0.8)	1.09 (0.8)
	5.63 (3.4)	3.26 (2.0)	2.70 (1.6)	3.8 (1.3)	2.50 (1.2)	3.50 (1.1)
Voided,	1.13 (1.9)	1.12 (1.2)	1.11 (1.0)	1.12 (0.9)	1.16 (0.9)	1.14 (0.9)
ARI	1.06 (1.9)	1.06 (1.2)	1.07 (1.0)	1.08 (0.9)	1.07 (0.9)	1.09 (0.9)
	5.68 (2.6)	5.22 (1.6)	3.52 (1.3)	3.50 (1.3)	7.53 (1.2)	5.00 (1.2)

^a First row: Local peaking factor (LPF) $\equiv 37f_{\max}/\sum_1^{37} f_i$ (maximum to bundle-averaged fission density)

^b Second row: Minimum fission density in ring 4 (M)

^c Third row: Maximum % difference in pin fission density in ring 4 = $100(\text{LPF} - \text{M})/\text{LPF}$, $\sigma_{\text{difference}} = (\text{M}/\text{LPF})(R_{\text{LPF}}^2 + R_{\text{M}}^2)^{1/2}$

^d % fractional error (R) = $100\sigma_{\text{value}}/\text{value}$

The local peaking-factor and the minimum value in the outermost ring (number 4) for channel K14 are given in Tab. 2. Also shown is the maximum % difference in fission density in ring 4. This difference is calculated as an indication of the asymmetry in pin power caused by the core environment. It can be seen from Tab. 2 that the LPF ranges from approximately 1.11 to 1.21 and the 1σ uncertainty ranges from 0.8% to 2.6%. As expected, the location of the maximum rod fission density is in fuel ring 4. The maximum peaking factor of 1.212 occurs in a bundle at the periphery ($z = 0$) with low power. However, in high power bundles such as the ones in the range $z = 150 - 300$ cm (the three bundles closest to the mid-plane) the value of the LPF is still relatively high. For example, for the ARI configuration, the LPF is 1.207 (0.96%) and 1.179 (0.96%) for the bundle at 200-250 cm from the periphery, where the adjuster rods are inserted, for the cooled and checkerboard-voided cases, respectively.

5 Concluding Remarks

Three-dimensional core effects related to the presence of adjuster rods, axial and radial leakage due to the non-reflective external boundaries and non-uniform fuel burnup distribution in the core may impact the accuracy of the void reactivity calculations. The net impact of the combined (simultaneous) perturbations was found to be in the range of 1.44 ± 0.37 to 1.96 ± 0.39 mk.

6 Acknowledgements

The authors would like to acknowledge M. Scott McKinley for developing the continuous-energy MCNP cross section library. StudsvikScandpower is acknowledged for the permission to use HELIOS and Rudi Stamm'ler for the stimulating discussions in this project. We would like to thank Jim Donnelly of AECL for his clarification of our interpretation of the adjuster rod specification and Ken Kozier of AECL for his review and helpful comments. The work by the Georgia Tech authors was performed under a consulting agreement with the Canadian Nuclear Safety Commission.

References

1. J.F. Briesmeister, Ed.: *MCNP - A General Monte Carlo N-Particle Transport Code, Version 4B*. Los Alamos National Laboratory, LA-12625-M (1997)
2. F. Rahnema, S. Mosher, P. Akhtar, D. Serghiuta and R.J.J. Stamm'ler: 'Void Reactivity Calculations in a Typical CANDU Cell Using MCNP and HELIOS'. In: *International Conference on the Physics of Nuclear Science and Technology, Long Island, New York, USA, October 5-8, 1998*, **1**, p.356, Am. Nucl. Soc. (1998)
3. E.A. Villarino, R.J.J. Stamm'ler, A.A. Ferri, and J.J. Casal: Nucl. Sci. & Eng. **112**, 16 (1992)
4. R.E. McFarlane, D.W. Muir: *NJOY94.61: Code System for Producing Pointwise and Multigroup Neutron and Photon Cross Sections from ENDF/B Data*. Los Alamos National Laboratory, ORNL PSR-355 (1996)
5. P.G. Young, L. Weston, W. Poenitz (Evaluators): 'ENDF/B-VI'. File 1, MT 451, Revised (MOD 3) - August 1997, Distributed - September (1998)

Monte Carlo Simulation of Natural Gamma Ray Spectrometry for Underwater Surfaces

M. Maučec, P.H.G.M. Hendriks and R.J. de Meijer

Nuclear Geophysics Division, Kernfysisch Versneller Instituut, Zernikelaan 25, 9747 AA Groningen, The Netherlands

1 Introduction

In geological applications the development of nuclear-detection techniques has been strongly stimulated by the quests for determination of lithology via natural or induced gamma radiation. In the interactions between photons and matter, the cross-sections for absorption and scattering of γ -rays depend strongly on density ρ and atomic number Z . Hence the shape of the γ -ray spectra reflects the density (see [1]) and the composition of the geological matrix. For natural γ -rays, the dominant processes are Compton scattering and photo-electric absorption. The complexity of the photon transport is so high that one has to rely on numerical calculations. However, the use of Monte-Carlo simulation techniques for modelling measurements with predominantly natural radioactive sources has been very limited, mainly for two reasons.

The first reason is the rather complicated and comprehensive description of the source of natural radionuclides, particularly when heterogeneous formation layers with different activity concentrations are modelled. The second reason is much more profound and restrictive. Modelling of pulse-height detectors by most Monte-Carlo computational tools forbid the use of any standard variance reduction (VR) techniques. Some attempts to overcome this deficiency have evolved by Booth in [2] but the restrictions are so severe that many calculations are not even attempted.

The progress of modelling the natural radionuclides and photon detectors by Monte Carlo simulation tools has mainly been obtained in the borehole geometry by Hendriks et *al.* in [1]. Alternatively, this paper brings up the formulation of a sensitive γ -ray detector system MEDUSA [3], developed by the Nuclear Geophysics Division of Kernfysisch Versneller Instituut (NL), to map underwater bottom. The MCNP4B [4] code has been used for modelling of the BGO ($\text{B}_4\text{Ge}_3\text{O}_{12}$) detector with the adjacent formations and determination of the influence of various matrix configurations on γ -ray spectra.

2 Source Modelling Aspects

In Fig. 1 the geometry, as modelled with MCNP, is depicted. A cylindrical detector, surrounded by water, is placed on a (a) homogeneous and (b) heterogeneous SiO_2 seabed, respectively. Dimensions and compositions of applied materials are given in Tab. 1: dimensions of formation and water are related to optimised values (see chapter 3). The position and thickness of formation 2 are parameters in the calculations.

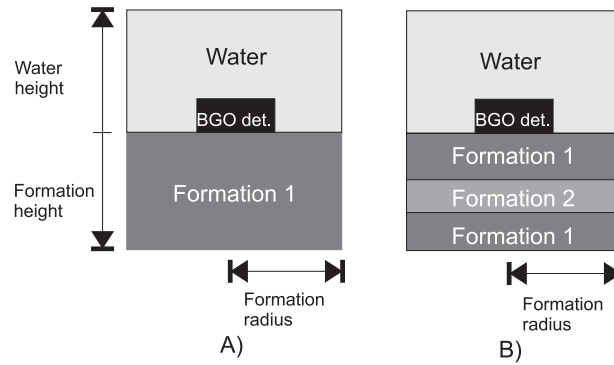


Fig. 1. Side view of the MCNP model of waterbed geometry measurements: A) homogeneous and B) heterogeneous formation. Dimensions are not to scale

Table 1. Dimensions and compositions of underwater surface geometry, as modelled with MCNP. The formation bulk density (2.65 g/cm^3) was reduced with a factor of 0.35 to correct for porosity of 0.35 %

Material	Density (g/cm^3)	Dimensions (cm)	
		Radius	Height
BGO detector ($\text{B}_4\text{Ge}_3\text{O}_{12}$)	7.13	2.5	15
Formation (SiO_2)	1.69	60	50
Water (H_2O)	1.00	60	50

The natural radionuclide source, with ^{40}K , ^{232}Th and ^{238}U isotopes defined through γ -ray energies and abundance of the γ -ray emissions, provided in [5] has been followed. Only γ -rays with energies between 100 keV and 3 MeV and a branching ratio greater than 1% have been implemented. Pulse-height estimates have been used to mimic the response of a physical detector in MCNP. The calculated response spectra are usually returned in counts per energy bin (channel) and have to be appropriately re-scaled (e.g. divided by the product of source mass and the cumulative probabilities for emission of γ -rays per specific decaying nuclide) to represent calibrated detector responses. Standard spectra represent the detector response to activity concentration of 1 Bq/kg of specific radionuclide derived from γ -ray spectra measured from a set of calibration materials. The comparison of MCNP calculated pulse-height spectra to measured standard spectra for towed waterbed experiments are presented in Fig. 2. The calculated spectra have been smoothed with the averaging of the adjacent data points.

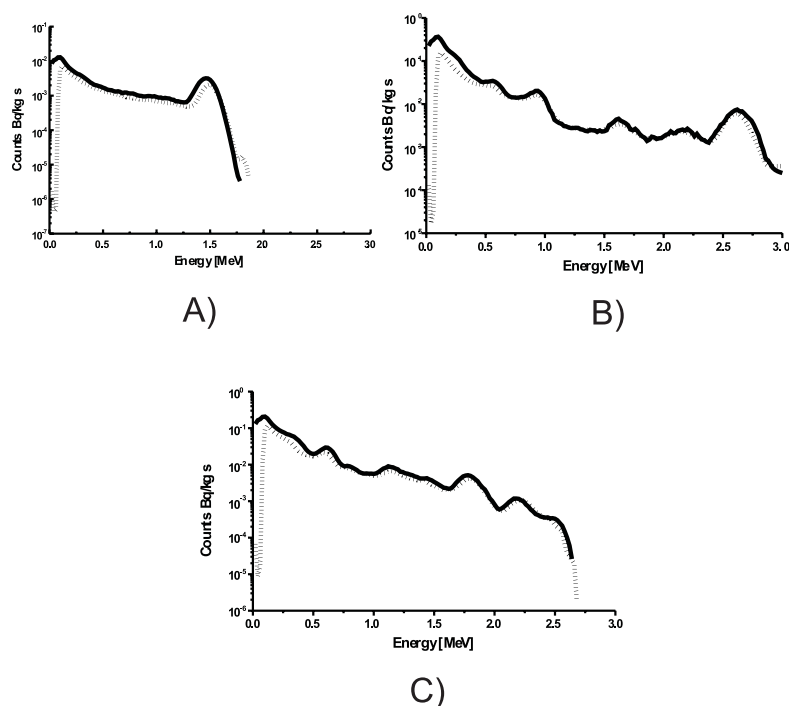


Fig. 2. Comparison between the MCNP calculated pulse-height spectra and measured standard spectra for A) ^{40}K , B) ^{232}Th and C) ^{238}U . Experimental results are depicted by dotted and MCNP calculated by solid lines, respectively

Initially, the energy resolution of 10% at 1.3 MeV has been assumed constant over the entire energy range for the simulated BGO detector. In general, a better match with the experimental spectra was observed for the higher energies, except for the ^{40}K . Hereby, a slight anomaly in the ^{40}K standard spectra was observed: the initial 1.47 MeV γ -line peak is horizontally shifted to the energy bin of 1.49 MeV. This peak off-set might emerge from superposition effects of nearby peaks from ^{232}Th and ^{238}U isotopes in the same calibration drum or from temperature gain-drift stabilisation of detector system. The statistical bin uncertainties remain acceptably low (approx. 5%) up to the energies of approx. 1.5 MeV and increase (up to 50%) with higher energy. To obtain spectra with this bin statistics, a CPU time of 600 min on a 450 MHz Pentium II processor was needed. The total number of processed particles was about 4.5 million. Calculated MCNP pulse-height spectra have been qualitatively compared to measured standard spectra with a simple weighted least square (χ^2) fit. The weighting factor was defined as the ratio between total detector responses (number of counts, integrated over the entire energy range) for experiment and MCNP calculated spectra. The weighted χ^2 value, averaged over all spectra was 7.97 thus proving good overall matching of calculated and measured spectra.

3 Geometry Modelling Aspects

The bulk dimensions (radius and height) of the source formation and the thickness of the water layer on top of detector have been optimised with respect to relevant source sampling and acceptable computation times. For the simulations the ^{232}Th source definition was applied because of its decay chain includes γ -rays over a wide range of energies (up to 2.62 MeV). For the cylindrical source (as described in Tab. 1) the regions beyond 60 cm in radius and below 50 cm of seabed formation, contribute less than 1.5% to the total photon flux. Furthermore, only $\sim 0.25\%$ of backscattered photon radiation contributes to detector response from above 20 cm. The MCNP model with these dimensions thus represents a radially and axially infinite geometry for Monte Carlo calculations, with the estimated systematic error introduced in total photon flux less than 6%.

4 Compound Radionuclide Seabed Calculations

The final step of this analysis was the simulation of a case with a compound radionuclide source composition. Two different soil formations were considered: the *homogeneous case*, with source geometry definition identical to that in Tab. 1 and the *heterogeneous case*, where 2 cm thick layer of soil, with activity concentrations of 1000 Bq/kg of ^{40}K , 100 Bq/kg of ^{232}Th and 100 Bq/kg of ^{238}U (hereafter referred to as 1000/100/100) was embedded in the bulk formation, with activity concentrations of 300 Bq/kg of ^{40}K , 10 Bq/kg of ^{232}Th and 10 Bq/kg of ^{238}U (hereafter referred to as 300/10/10). The geometry of the heterogeneous MCNP model is schematically depicted in Fig. 1b. Contrary to the previous calculations, the effect of background radiation from radionuclides present in the detector itself and a cosmic radiation part has now been taken into account.

4.1 Homogeneous Seabed Case

In the case of a homogeneous formation, the probabilities of sampling energy distributions have to be proportional to the total activity concentrations of specific radionuclides. The MCNP pulse-height spectra ($S^{MC}(E)$) have to be converted in calculated spectra ($S^{calc}(E)$) and in the final stage, take into account the background effects ($Bgd(E)$):

$$S^{calc}(E) = \left[\sum_{j=1}^M m_j \sum_{i=1}^N AC_i \cdot p_i \right] \cdot S^{MC}(E) + Bgd(E) \quad (1)$$

where m_j is a mass of source cell j , and AC_i is activity concentration of nuclide i .

The converted MCNP pulse height-spectrum for a cylindrical homogeneous seabed with concentration 300/10/10 is presented in Fig. 3. The calculated ^{40}K

1.47 MeV peak-to-2.62 MeV ^{232}Th peak ratio corresponds to the relative difference in total activity concentration within statistical uncertainty, thus proving that the source intensities of the nuclei have been sampled correctly within MCNP.

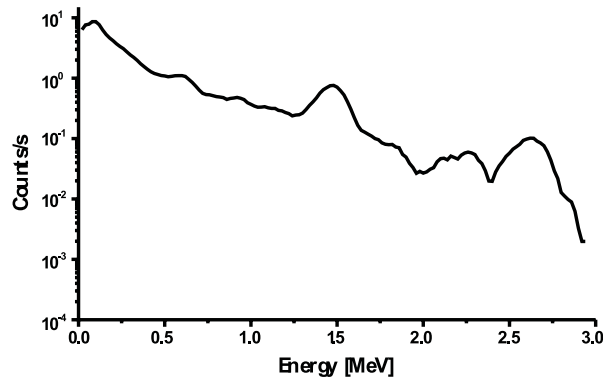


Fig. 3. MCNP calculated pulse-height spectra for a compound radionuclide homogeneous waterbed configuration

4.2 Heterogeneous Seabed Case

The parametric study was carried out where the depth of heterogeneity layer was varied in the steps of 0, 2, 4, 6, 10, 20 and 40 cm below the seabed top surface. The layer thickness was kept constant at 2 cm. In the case of heterogeneous seabed formations, sampling of the source energy distributions becomes cell-dependent and the source cells have to be sampled proportionally to their total activities. The final spectra are presented in Fig. 4.

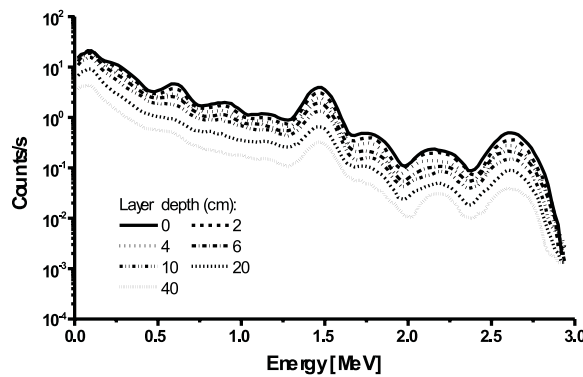


Fig. 4. MCNP calculated pulse-height spectra for a compound radionuclide heterogeneous waterbed configuration

When compared to the homogeneous waterbed model, the additional heterogeneity layer with activity concentration 1000/100/100 (in depths down to 6 cm) enhances the shape of the spectra particularly through γ -ray lines from thorium and uranium decay series with abundances higher than 15%. With heterogeneity layer placed on the waterbed surface the integral counts activity increases for approx. 3.5-times (the ratio between total activities of formations 1 and 2 is 3.75).

Figure 4 shows that expected photo-peak smearing effects are observed in the low-energy part of the simulated spectra as the depth of the heterogeneity layer increases. The intensity of γ -ray spectra exhibits almost perfect linear anti-correlation with the heterogeneity layer depth: for a 2 cm increase in depth, a energy-independent decrease of 10% in intensity is observed. It can be seen that for the layer depths beyond the estimated photon mean free path in soil (~ 10 cm), the shape of the spectra converge to the homogeneous-seabed case (Fig. 3). However, for heterogeneity layer depth up to 10 cm, the vertical location can be well extracted from the low-energy spectra shape.

As in the case of homogeneous seabed case, the acceptably low bin uncertainties (below 10%) have been obtained in the count-intense energy region (below 1.5 MeV) but they increase up to 60% with higher energies.

5 Conclusions

Presented calculation results prove that the Monte Carlo particle transport code MCNP can be successfully used as a tool for natural γ -ray spectrometry simulations of underwater measurements. The relatively simplified MCNP geometry model presented in this paper, will be enhanced by applying more detailed description of the detector (housing, photo-multiplier etc.) and formation, considering the presence of pore water. According to the results for borehole simulations, presented in [1], the presence of the water may considerably affect the scattering properties through the change of the average atomic number Z of the media.

To evaluate the results of compound radionuclide source simulations in absolute manner the comparison to experimental data is required. The presented layer-depth parametric study served as the first step to Monte Carlo based sensitivity analysis, where development of the inverse algorithm for determination of heterogeneous soil matrices, is anticipated as the goal.

References

1. P.H.G.M. Hendriks, M. Maučec, R.J. de Meijer: *Sediment–density dependency of Natural Gamma Ray Spectra in a Borehole Geometry*. These Proceedings p. 893
2. T.E. Booth: Nucl. Sci. Eng. **116**, 113 (1994)
3. R.J. De Meijer: Journal of Geochemical Exploration, **62**, 81 (1998)
4. J.F. Briesmeister, Ed.: *MCNP, A General Purpose Monte Carlo N-Particle Transport Code*, Version 4B, LA-12625-M, Los Alamos National Laboratory, (1997)
5. R.B. Firestone, Ed.: *Table of Isotopes, 8th edition* (John Wiley & Sons, Inc. 1996)

Monte Carlo Modelling of the Belgian Materials Testing Reactor BR2: Present Status

B. Verboomen¹, A. Beeckmans de West-Meerbeeck², Th. Aoust¹, and Ch. De Raedt¹

¹ Reactor Physics & Myrrha Dept., SCK•CEN, Boeretang 200, 2400-Mol, Belgium

² BR2 Reactor Dept., SCK•CEN

Abstract. A very detailed 3-D *MCNP-4B* model of the BR2 reactor was developed to perform all neutron and gamma calculations needed for the design of new experimental irradiation rigs. The Monte Carlo model of BR2 includes the nearly exact geometrical representation of fuel elements (now with their axially varying burn-up), of partially inserted control and regulating rods, of experimental devices and of radioisotope production rigs. The multiple level-geometry possibilities of *MCNP-4B* are fully exploited to obtain sufficiently flexible tools to cope with the very changing core loading.

1 Introduction

While the traditional 2-scale calculation scheme (cell homogenisation with transport theory, macroscopic evaluation of the flux with multigroup diffusion/transport theory, de-homogenisation for microscopic evaluations) used extensively for commercial reactors is theoretically well founded [1], it is not applicable for research reactors. Indeed, for e.g. BR2 : (i) the core configuration is far from a periodic array of nearly identical fuel cells (the average burn-up of the fuel elements varies between 0% and 50% and the fuel channel environment depends strongly on the channel location), (ii) the fuel channels do not possess cylindrical rotational symmetry (the fuel element orientation is thus of importance), (iii) the control rods distort the mid-plane symmetry of the axial flux distribution (practically all experiments have, at least, one control rod as first neighbour). Only the Monte Carlo methodology can cope rigorously with all these difficulties.

2 Description of the BR2 Reactor

The BR2 reactor is a heterogeneous thermal high flux engineering test reactor cooled and moderated by pressurised (1.2 MPa) light water. The compact core of highly enriched uranium fuel elements (the U-235/U-tot ratio is 93 % for fresh fuel) is positioned in, and reflected by, a beryllium matrix with outer diameter 110.04 cm. The light water flows downwards in the beryllium matrix under a constant pressure drop of about 0.3 MPa and maintains the water temperature between 40 and 50°C. The maximum thermal flux approaches 10^{15} n/cm² s and the ultimate cooling capacity is 125 MW. The aluminium reactor vessel, of hyperboloidal form, has an inner diameter of 110.70 cm at the mid-plane, a

thickness of 2.14 cm and a height of 749.5 cm. A very complex core geometry and versatile loading possibilities characterise the BR2 reactor (see Fig. 1(a)). The core is composed of long hexagonal skew beryllium prisms with central cylindrical channels parallel to the prism generatrices (the maximum inclination is $10^{\circ}42'$ for the outer channels). These channels (64 with a diameter of 84.2 mm and 10 with a diameter of 50 mm) form a twisted hyperboloidal bundle and can be loaded with fuel elements, control/regulating rods, experimental devices or beryllium plugs. Five channels with a diameter of 200 mm allow the loading of larger experimental devices. The standard fuel elements loaded in the 84.2 mm channels are assemblies of 6 x 3 concentric plates, each having a 76.2 cm active length and a thickness of 1.27 mm (see Fig. 1(b)). Three radial stiffeners in aluminium maintain the fuel plates in position. The distance between two concentric plates is 3 mm. A fuel plate consists of a cermet mixture of highly enriched UAl_x (400 g of U-235 per fuel element, for a total U content of 430 g) and burnable poisons (B_4C and Sm_2O_3), clad with aluminium. The uranium density is 1.4 g/cm^3 for a meat thickness of 0.51 mm. A standard fuel element allows for an experimental space having a diameter of 25.4 mm. Less fuel plates per element permit larger experimental spaces.

3 Modelling of the BR2 Reactor

3.1 Geometry

The *MCNP-4B* [2] core model of the BR2 reactor is enclosed in a straight cylinder of 140 cm diameter and 150 cm height. The only simplifying assumption used is to consider all beryllium prisms as vertical. With this assumption, the BR2 core may be considered as a hexagonal lattice of 9.644 cm pitch with five 200 mm holes (Fig. 1(a)). The model is structured by the *multiple level geometry* concept of *MCNP-4B*, which operates like a “zoom”. Each level can be considered, at least locally, as a description on a specified scale, the finer details appearing only on a higher level (i.e. on a larger scale). The *level zero* or “coarse grained” structure of BR2 is called *real world* in MCNP jargon and contains virtually all higher geometry levels, called *universes*, which “fill” the *real world* cells. Each geometric level can also be considered as the *real world* for the next higher level allowing the building of very complex structures. The BR2 *real world* is composed of only 11 volumes: 5 cells for the five 200 mm channels, 1 cell for the region inside the outer surface of the beryllium matrix (i.e. the BR2 core and beryllium reflector without the 200 mm channels) and 5 cells for the domain outside the beryllium matrix (i.e. the outer reflector). Level one describes the overall loading of BR2 and is composed of 6 universes, 5 for the five 200 mm channels and 1 for the hexagonal lattice. The next higher levels describe individually each fuel element (Fig. 1(b)), control/regulating rod, experiment and beryllium plug. All modifications of the core loading are straightforward: only the *universes* concerned must be modified. This constitutes an enormous advantage over the deterministic methods: no new mesh generation (a highly non-trivial operation!) is required.

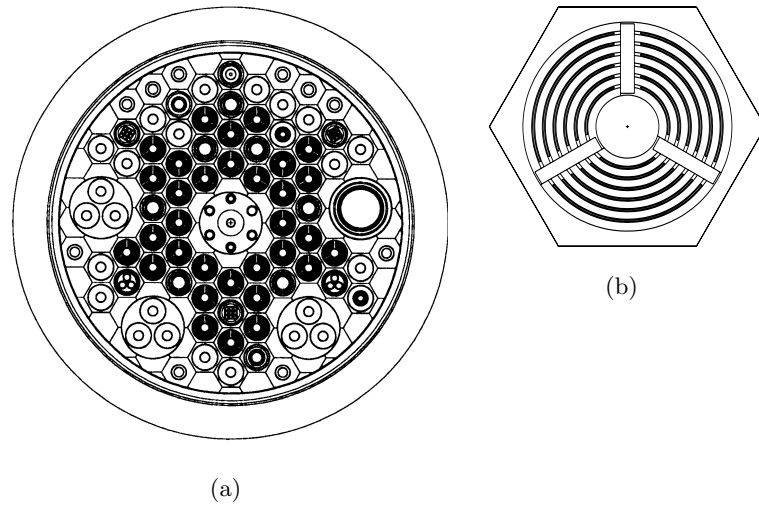


Fig. 1. (a) *MCNP-4B* model of BR2 with characteristic experimental loading (b) standard fuel element details

Figure 2 illustrates some consequences of the BR2 geometry on neutron distributions. Figure 2(a) compares the azimuthal external plate power density distribution of a fresh fuel element located in channel C 101 of the configuration seen on Fig. 1(a) with the power density distribution in the same fuel element but in a 2-D infinite lattice. Figure 2(b) makes the same comparison for the axial power density distribution.

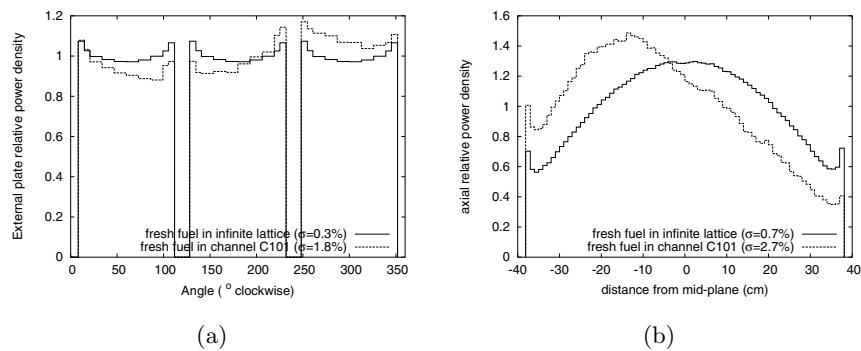


Fig. 2. (a) external plate azimuthal power density profile (external plate average power density = 1) (b) fuel element axial power density profile (fuel element average power density = 1)

3.2 Fuel Burn-Up

Each BR2 loading contains 30 to 40 fuel elements, not all fresh. The fissile content of the fuel elements at discharge is about 50% of the initial value. Each fuel element is used during two or three reactor cycles (BR2 operates on a year basis of 5 cycles of 21 days, each at a power of about 60 MW, leading to an average decrease of fissile content of 1% per day). The high burn-up rate attained in BR2 (about 15 times higher than in a PWR) is compensated by a continuous control rod retreat with an average speed of 2 cm per day. A rigorous account of the fuel burn-up requires the full knowledge of each fuel element history, necessitating the modelling and the calculation of a huge number of BR2 configurations.

In the BR2 modelling performed in the past only homogeneous burn-up over whole individual fuel elements was considered. A model was recently implemented to take into account also the spatial burn-up distribution. The model is based on the following assumptions: (i) we consider only the axial variation of the burn-up, (ii) the axially averaged burn-up of each element is supposed known, (iii) the concentrations of all actinides, burnable poisons and fission products depend only and univocally on the % disappearance of U-235, (iv) the axial power density distribution is constant during a reactor cycle, and (v) each fuel element has the same relative burn-up profile, equal to the core-averaged U-235 absorption rate profile of a characteristic BR2 configuration. Assumption (i) is admissible because axial variations constitute the most important contribution to the total burn-up variation (the ratio between the maximum microscopic absorption rate and the minimum microscopic absorption rate is about 1.3 for azimuthal and radial variations, and about 5 for axial variations). The determination of the fuel-element-averaged burn-up (ii) is a difficult task. The method used combines 2-D integral transport methods and experimental results. Assumption (iii) is not so restrictive because of the very low U-238 content. The compositions are calculated with the *BURN1D* homecode (coupling of a 1-D 40-group neutron transport routine and a depletion routine using pseudo fission products) and tabulated for burn-up values varying in steps of 5%. Assumption (iv) is reasonably well verified over the whole range of control rod heights (BR2 operates at constant power) and implies that the ratio between the axially varying absorption rate and the average absorption rate is a constant for a reactor cycle. Assumption (v) assumes that the relative burn-up profile of a particular fuel element, whatever its burn-up, follows the “overall” average relative burn-up profile.

The relative burn-up profile is calculated in an iterative manner. A typical BR2 configuration is chosen. A first MCNP calculation is made for this configuration, adopting for each fuel element the compositions corresponding to the average burn-up values of the fuel elements, as always done in the past. A typical axial position of the control rods is adopted and an adequate amount of Xe-135 is introduced in the fuel elements. A first burn-up profile is deduced from the MCNP calculation and an adequate subdivision (we actually consider 8 intervals) of the 76.2 cm active height of a BR2 fuel element is determined. The burn-up profile is therefore given by a histogram characterised by 8 factors A_1, A_2, \dots ,

A_8 . With these factors A_i , interpolations are carried out in the tables obtained with the *BURN1D* calculation (see assumption (iii)) to determine, for each of the 10 axially averaged burn-up values 5%, 10%, ..., 50%, the corresponding burn-up values in each of the 8 axial sections. A first complete set of 8 axially varying concentrations for the 10 average burn-up values is thus easily obtained. A new MCNP calculation is then made, similar to the first one, but now with the axially varying concentrations determined above. Again, a new set of 8 factors B_1, B_2, \dots, B_8 is determined and a second complete set of concentrations is obtained. A third set C_1, C_2, \dots, C_8 was calculated to ensure that convergence is reached (see Tab. 1).

Table 1. A, B and C factors

interval	length (cm)	A	B	C
1 (top)	15.1	0.44	0.40	0.40
2	11	0.79	0.76	0.76
3	7	1.04	1.05	1.05
4	6	1.27	1.31	1.34
5 (hot plane)	18	1.44	1.53	1.55
6	6	1.29	1.29	1.29
7	6	1.07	1.01	0.97
8 (bottom)	7.1	0.83	0.74	0.71

Figure 3 illustrates the effect of axial burn-up modelling on neutron distributions. Figure 3(a) shows relative U-235 concentration profiles for various U-235 fuel-element-averaged burn-up fractions. Figure 3(b) compares calculated U-235 fission rate measurements performed in the centre of a 50% burned fuel element in channel F 46 for homogeneous and heterogeneous burn-up.

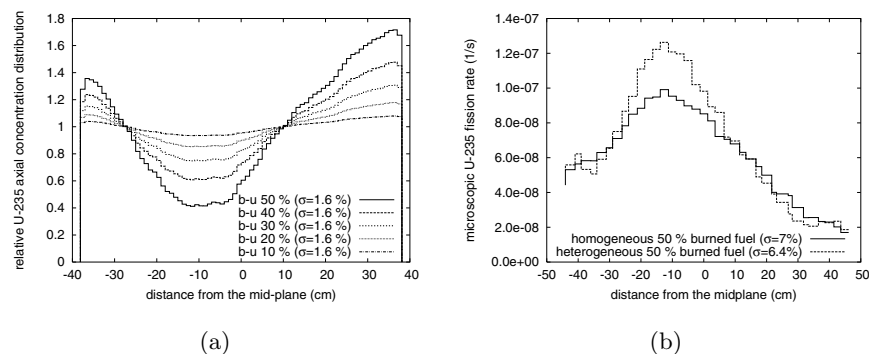


Fig. 3. (a) relative U-235 axial concentration distribution (average concentration = 1)
(b) axial microscopic U-235 fission rate distribution (fuel power = 1 MW)

4 Calculation Details

A typical 48 hour *MCNP-4B* mono-processor run, for neutron transport in k_{eff} mode, on a *SUN ULTRA ENTERPRISE 4000*, makes use of 500 neutron generations with 10 000 neutron histories per generation. The precision (σ) is 0.03% for k_{eff} , 1.5% for the total power of a fuel element, and 6% for the local power density in a fuel plate (i.e. a volume element with $\Delta R = 0.051$ cm, $\Delta\theta = 10^\circ$, and $\Delta Z = 18$ cm). *MCNP-4B* continuous energy cross-sections and $S(\alpha, \beta)$ tables for thermal neutron scattering were used throughout. The calculated k_{eff} is 0.994 for a typical BR2 configuration, which is acceptable.

5 Conclusions

The Monte Carlo *MCNP-4B* detailed model of the BR2 reactor is an invaluable tool for the design of experiments and core loading. For the first time, (i) the azimuthal and axial flux and fission power distributions inside BR2 channels were calculated, (ii) all BR2 experiments and control rods, were modelled accurately, (iii) more traditional calculation schemes used for experiment design, core loading and safety applications were evaluated [3,4], and (iv) the axial burn-up was modelled. The model was successfully utilised for the optimisation of the irradiation of novel high density MTR fuel plates [5]. Comparison between calculated and measured values is in progress: calorimetric measurements of the relative axial profiles confirm the calculated profiles [5], and calculated k_{eff} values are in good agreement with the experimental ones. Future activities will concentrate on burn-up modelling (comparisons with the Monte Carlo Burnup code *MCB* [6] will be made), and on coupled neutron/photon calculations.

References

1. J. Planchard: *Méthodes Mathématiques en Neutronique* (Collection de la Direction des Etudes et Recherches d'Electricité de France, Editions Eyrolles 1995)
2. J.F. Briesmeister, Ed.: *A General Monte Carlo N-Particle Transport Code, LA-12625-M, Version 4B*. (LA-12625-M, Version 4B March 1997)
3. Ch. De Raedt, E. Malambu, B. Verboomen, Th. Aoust: 'Increasing Complexity in the Modelling of BR2 Irradiations'. In: *PHYSOR 2000 International Topical Meeting: Advances in Reactor Physics and Mathematics and Computation into the Next Millennium, Pittsburgh, PA, May 7-11, 2000*, ANS, USA, 2000)
4. A. Makarenko, T. Petrova: 'BR2 Reactor Core Steady State and Transient Modelling'. In: *4th International Topical Meeting "Research Reactor Fuel Management (RRFM)", Colmar, France, March 19-21, 2000*, ENS, CH, 2000 pp. 111-115
5. B. Verboomen, Th. Aoust, A. Beeckmans de West-Meerbeeck, Ch. De Raedt: 'Irradiation of New MTR Fuel Plates in BR2'. In: *4th International Topical Meeting "Research Reactor Fuel Management (RRFM)", Colmar, France, March 19-21, 2000*, ENS, CH, 2000 pp. 135-139
6. J. Cetnar, J. Wallenius and W. Gudowski: 'MCB: A continuous energy Monte Carlo Burnup simulation code'. In: *Actinide and Fission Products Partitioning and Transmutation*, EUR 18898 EN, (OECD/NEA 1999)

Benchmark for a 3D Monte Carlo Boiling Water Reactor Fluence Computational Package – MF3D

S. Sitaraman¹, R-T. Chiang¹, K. Asano², and K. Koyabu²

¹ GE Nuclear Energy, San Jose, CA 95125, USA

² The Tokyo Electric Power Company, Yokohama, 230-8510, Japan

Abstract. A detailed three dimensional model of a quadrant of an operating BWR has been developed using MCNP to calculate flux spectrum and fluence levels at various locations in the reactor system. The calculational package, MF3D, was benchmarked against test data obtained over a complete fuel cycle of the host BWR. The test package included activation wires sensitive in both the fast and thermal ranges. Comparisons between the calculational results and test data are good to within ten percent, making the MF3D package an accurate tool for neutron and gamma fluence computation in BWR pressure vessel internals.

1 Introduction

A three dimensional model of a quadrant of an operating Boiling Water Reactor 4 (BWR4), the Kernkraftwerk Muehleberg (KKM) plant in Switzerland, was generated to calculate the flux spectrum and fluence at various locations inside the reactor system. The computational model development is part of a program which also included benchmark measurements conducted at KKM during Cycle 25 [1]. The test program consisted of placing dosimetry packages at various axial, radial, and azimuthal locations in the annular region between the shroud and reactor pressure vessel (RPV). The dosimetry package included sapphire crystals for the purpose of measuring radiation damage at these locations. In addition, helium deposition in the stainless steel (principally due to the boron impurities in the material) was also measured. The overall aim of the program is to benchmark a Monte Carlo-based computational package, called MF3D, against the test data. Comparisons of activation data to calculations have been done in the past, principally in the PWR area [2,3]. Preliminary results for the fast responses obtained were presented in 1999 [4]. This paper will present the final set of results comparing measurement and calculations for both thermal and fast responses. The results from the MF3D radiation damage model are discussed in another paper [5].

The fluence and flux spectrum information obtained from these calculations would find application in a diverse set of fields. These include better estimates of radiation damage in materials, better models for radiolysis and electrochemical potential estimations for hydrogen water chemistry applications, and determination of component weldability, particularly in the shroud. All of these are

important to understand from the point of view of mitigating the effects of radiation damage to aging reactor components, thus increasing the life of the plant.

2 Description of the Test

The test consisted of placing nine cylindrical dosimetry holders at three azimuths in the annular region between the shroud and the RPV: 4, 20, and 71 degrees with a holder placed at each of three axial locations: 0.548, 1.64, and 2.73 m above the bottom of the active fuel. The near end of each holder was in contact with the shroud wall and three pairs of dosimetry capsules were present in each holder: at the shroud, at approximately 0.185 m from the shroud, and at approximately 0.05 m from the RPV wall. The aluminum dosimeter capsules were each about 0.01 m in length and contained seven dosimetry wires and a sapphire crystal. At each radial location there was a bare capsule that principally contained wires sensitive in the thermal region, and a thermally shielded capsule that contained fast response wires. Thus, there was a total of fifty four capsules located in the annular region that underwent irradiation over a period of eleven months.

3 Computational Model

The computational model is based on the code, MCNP [6] used in conjunction with ENDF/B-V and -VI cross section data. The model was developed in two stages. In the first stage, a quadrant of the core was modeled with full geometric and material details in the core. This included rod-by-rod description in each of 25 axial nodes (15.24 cm) for all 60 bundles in the quadrant. The important structural components inside the RPV were also included and detailed water density distributions inside and outside the core were modeled. Four exposure points during the cycle were studied. At each point, a criticality run was performed and fast flux profiles, particularly in peripheral bundles, were compared with plant data. When these results compared within 10% at the periphery [7], the second stage of the calculations was performed using sources saved at the core periphery. These fixed source calculations, one at each of the four exposure points, were used to obtain activation rates at the various wires. The fixed source model included details of the dosimetry packages present in the downcomer region. A time integration with appropriate decay terms was performed to properly add the results of the four separate runs to obtain the final specific activity of each wire at the end of cycle (EOC) at every location. The test data specific activities were also obtained at EOC. Figure 1 shows an r - θ view of the fixed source model with dosimetry holders and other structural hardware.

4 Results

Results for three axial and radial locations for the three azimuths are shown in Tabs. 1a, 1b, 1c and 2a, 2b, 2c. The detector identification is as follows:

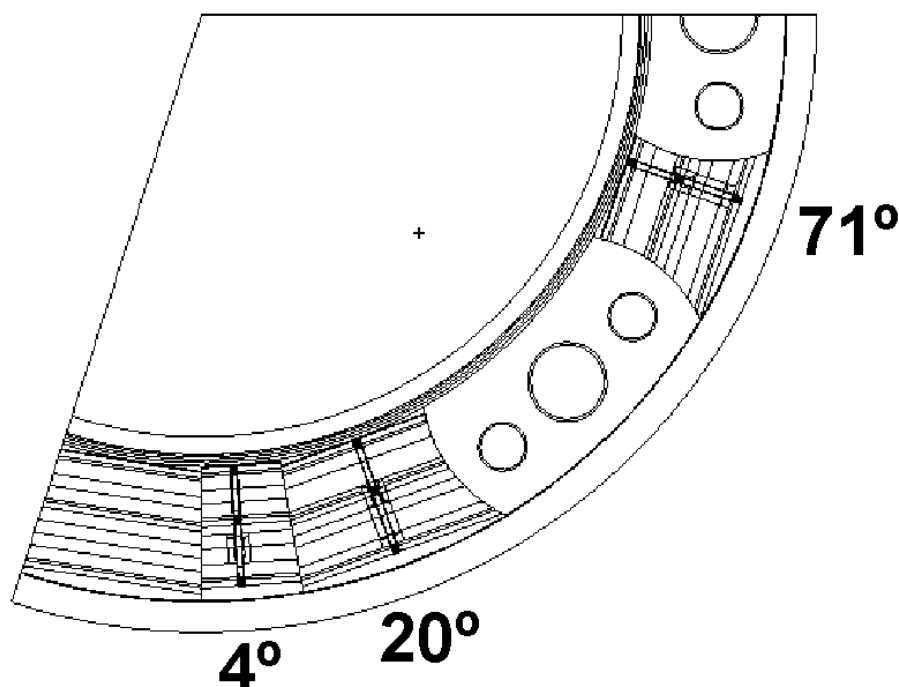


Fig. 1. R- Θ view of the model with the capsule holders

“A”, “B”, and “C” represent the low, middle, and high axial locations. The first numeral “1”, “2”, and “3” represent the shroud, mid-annulus, and RPV locations. The second numeral represents the azimuth, 1 representing 20° (next to a jet pump), 2 representing 4° (away from jet pumps), and 3 representing 71° (between jet pumps) (see Fig. 1). Table 1 shows the fast response comparisons as C/M (calculation to measurement) ratios. The uncertainties associated with each C/M ratio is of the order of 10% including statistical uncertainties. The actinide responses agree well with test data at the shroud and tend to be under predicted at the RPV. This is principally due to the fact that the neutron-to-gamma ratios fall rapidly when moving radially outward and the gamma induced fission becomes important. The calculations have ignored this contribution, thus under-predicting the activities. The remaining wires are consistent and are in good agreement with the test data. Table 2 presents the thermal response comparisons, including those obtained from the helium measurements. The agreement between test data and calculational results is good everywhere, especially at the shroud location. The exceptions are at the high axial locations where the center location has a C/M ratio of 1.3 and the RPV location has a C/M ratio of 0.7. This trend was consistent for all the azimuths leading to the conclusion that the attachment hardware was not at the nominal position used in the model, thus perturbing the local thermal field.

Table 1a. Fast C/M Ratios at 4 degrees

Det.	²³⁸ U			²³² Th		²³⁷ Np			⁵⁸ Ni	⁹³ Nb	⁵⁴ Fe	⁹³ Nb	Mean*	σ^*
ID	Cs	Zr	Ru	Cs	Zr	Cs	Zr	Ru		shield		bare		
A12	1.02	1.02	0.99	1.00	0.98	1.04	1.07	1.02	1.12	1.28	1.10	1.09	1.15	0.09
B12	0.95	0.94	0.98	0.99	0.93	0.96	1.01	1.01	0.96	1.13	0.95	1.03	1.04	0.10
C12	0.88	0.86	0.89	0.82	0.82	0.87	0.89	0.90	1.00	1.05	0.93	0.98	1.00	0.06
A22	0.77	0.74	0.75	0.79	0.71	0.86	0.86	0.84	0.96	1.05	1.07	1.06	1.03	0.05
B22	0.76	0.75	0.79	0.73	0.74	0.78	0.84	0.84	0.99	0.99	1.15	1.11	1.05	0.08
C22	0.74	0.71	0.76	0.70	0.72	0.75	0.78	0.80	0.98	0.95	0.99	0.95	0.96	0.03
A32	0.54	0.54	0.58	0.49	0.50	0.66	0.67	0.68	0.92	0.91	0.89	0.92	0.92	0.02
B32	0.56	0.55	0.60	0.50	0.51	0.65	0.70	0.74	0.97	0.95	0.88	0.89	0.93	0.04
C32	0.59	0.54	0.60	0.49	0.50	0.66	0.69	0.73	0.98	0.98	0.88	0.90	0.94	0.05

*Mean and σ for non-actinides only**Table 1b.** Fast C/M Ratios at 20 degrees

Det.	²³⁸ U			²³² Th		²³⁷ Np			⁵⁸ Ni	⁹³ Nb	⁵⁴ Fe	⁹³ Nb	Mean*	σ^*
ID	Cs	Zr	Ru	Cs	Zr	Cs	Zr	Ru		shield		bare		
A11	0.89	0.98	1.02	0.93	1.04	0.97	1.04	1.03	1.09	1.14	0.95	1.03	1.05	0.09
B11	0.91	0.97	1.02	0.97	1.08	0.97	1.03	1.05	1.15	1.18	1.21	1.22	1.19	0.04
C11	0.91	0.88	0.89	0.85	0.96	0.94	0.96	0.95	1.10	1.14	1.05	1.11	1.10	0.04
A21	0.75	0.73	0.74	0.76	0.74	0.85	0.84	0.82	0.90	1.03	0.98	1.00	0.98	0.14
B21	0.82	0.86	0.90	0.80	0.93	0.88	0.92	0.91	1.15	1.07	1.06	1.03	1.08	0.05
C21	0.82	0.78	0.80	0.83	0.84	0.85	0.85	0.84	1.02	1.09	1.07	1.05	1.06	0.10
A31	0.61	0.63	0.64	0.52	0.56	0.66	0.67	0.66	0.92	0.86	0.92	0.84	0.88	0.05
B31	0.56	0.57	0.63	0.48	0.57	0.68	0.71	0.72	0.90	0.89	0.93	0.90	0.91	0.09
C31	0.57	0.55	0.60	0.53	0.60	0.63	0.66	0.68	0.92	0.88	0.90	0.86	0.89	0.03

*Mean and σ for non-actinides only**Table 1c.** Fast C/M Ratios at 71 degrees

Det.	²³⁸ U			²³² Th		²³⁷ Np			⁵⁸ Ni	⁹³ Nb	⁵⁴ Fe	⁹³ Nb	Mean*	σ^*
ID	Cs	Zr	Ru	Cs	Zr	Cs	Zr	Ru		shield		bare		
A13	0.82	0.80	0.79	0.81	1.11	0.89	0.98	0.85	0.79	1.05	0.90	1.03	0.94	0.12
B13	0.94	0.98	1.01	0.95	1.11	0.95	1.04	1.02	1.04	1.18	1.14	1.21	1.14	0.07
C13	0.90	0.93	0.96	0.88	0.89	1.01	1.01	1.03	1.07	1.16	1.18	1.23	1.16	0.06
A23	0.82	0.85	0.86	0.83	1.11	0.88	1.03	0.91	1.10	1.09	1.03	1.01	1.06	0.05
B23	0.83	0.81	0.82	0.85	0.97	0.88	0.91	0.87	0.99	1.07	1.04	1.05	1.04	0.04
C23	0.88	0.88	0.92	0.86	0.84	0.88	0.86	0.91	1.14	1.15	1.12	1.08	1.12	0.03
A33	0.59	0.60	0.61	0.57	0.77	0.61	0.72	0.64	0.84	0.83	0.87	0.81	0.84	0.03
B33	0.63	0.64	0.68	0.57	0.69	0.70	0.72	0.71	0.98	0.96	0.89	0.91	0.93	0.04
C33	0.58	0.56	0.62	0.56	0.56	0.71	0.66	0.72	0.93	0.94	0.93	0.90	0.93	0.02

*Mean and σ for non-actinides only

Table 2a. Thermal C/M Ratios at 4 degrees

Det.	²³⁵ U			⁴⁵ Sc	He	Mean	σ
ID	Cs	Zr	Ru				
A12	1.11	1.12	1.10	1.11	0.96	1.08	0.07
B12	1.02	1.02	1.18	0.98	1.01	1.04	0.08
C12	1.10	1.10	1.29	0.90		1.10	0.16
A22	0.92	0.94	0.99	0.82	0.85	0.91	0.07
B22	1.00	1.05	1.16	0.81	0.94	0.99	0.13
C22	1.38	1.38	1.59	1.12		1.37	0.20
A32	0.89	0.91	0.97	0.81		0.89	0.07
B32	0.87	0.88	1.00	0.73		0.87	0.11
C32	0.79	0.79	0.94	0.63		0.79	0.12

Table 2b. Thermal C/M Ratios at 20 degrees

Det.	²³⁵ U			⁴⁵ Sc	⁶⁰ Co	He	Mean	σ
ID	Cs	Zr	Ru					
A11	1.02	1.02	0.98	0.97	1.20		1.05	0.09
B11	1.00	1.06	1.20	0.83	1.09		1.04	0.13
C11	0.93	0.96	1.13	0.81	0.99	No He	0.96	0.11
A21	0.81	0.82	0.87	0.73	0.78		0.80	0.05
B21	1.04	1.15	1.33	0.89	1.28		1.14	0.18
C21	1.39	1.38	1.54	1.12	1.38		1.36	0.15
A31	1.21	1.27	1.36	1.04	1.28		1.23	0.12
B31	0.91	0.92	1.06	0.75	1.03		0.94	0.12
C31	0.70	0.70	0.83	0.55	0.68		0.69	0.10

Table 2c. Thermal C/M Ratios at 71 degrees

Det.	²³⁵ U			⁴⁵ Sc	⁶⁰ Co	He	Mean	σ
ID	Cs	Zr	Ru					
A13	0.98	1.00	1.00	1.01	1.30		1.06	0.13
B13	0.99	1.08	1.10	1.01	1.15	1.08	1.07	0.06
C13	1.00	1.03	1.04	0.84	1.14	0.92	1.00	0.10
A23	0.86	0.89	0.88	0.78	0.87		0.86	0.04
B23	1.19	1.29	1.29	0.97	1.15	1.25	1.19	0.12
C23	1.33	1.36	1.36	1.08	1.37	1.38	1.31	0.12
A33	1.23	1.26	1.26	1.06	1.39		1.24	0.12
B33	0.96	0.99	0.99	0.84	1.05		0.96	0.08
C33	0.74	0.72	0.72	0.57	0.84		0.72	0.10

5 Conclusions

The three-dimensional Monte Carlo-based computational package, MF3D, has been benchmarked against an extensive set of test data and shown to be for the most part accurate to the order of 10%. In contrast, conventional methods used in BWR fluence estimations compare within 20-25% in the fast range and are usually unable to provide thermal neutron information. Thus, this effort represents a major improvement in the ability to reliably provide neutron fluence estimates over the whole spectrum and also gamma fluence at desired locations.

References

1. J.H. Terhune, S. Sitaraman, J.P. Higgins, R-T. Chiang, K. Asano: 'Neutron and Gamma Spectra in the BWR- Phase 1 Experimental and Computational Methods'. In: *Proceedings of the 5th International Conference on Nuclear Engineering*, Nice, France, ICONE5-2020, May 26-30, 1997
2. J.C. Wagner, A. Haghighat, B.G. Petrovic: *Nuclear Technology* **114**, 373 (1996)
3. P.G. Laky, N. Tsoulfanidis: *Nuclear Science and Engineering*, **121**, 433 (1995)
4. S. Sitaraman, R-T. Chiang, R.L. Kruger, A.L. Jenkins, K. Asano, K. Koyabu: 'BWR Neutron Fluence Computations Using MF3D'. In: *Reactor Dosimetry, ASTM STP 1398*, John G. Williams, David W. Vehar, Frank H. Ruddy and David M. Gilliam, Eds., American Society for Testing and Materials, West Conshohocken, PA 2000
5. R-T. Chiang, S. Sitaraman, K. Asano, K. Koyabu: 'Application of MCNP-based Software Package for BWR Radiation Damage Computations'. These Proceedings p. 877
6. J. Briesmeister, Ed.: *MCNP - A Monte Carlo N-Particle Transport Code- Version 4A*, LA12625, March 1994
7. R-T. Chiang, S. Sitaraman: 'Development of 3D MCNP-Based BWR Fluence Computational Software Package: MF3D'. In: *Reactor Dosimetry, ASTM STP 1398*, John G. Williams, David W. Vehar, Frank H. Ruddy and David M. Gilliam, Eds., American Society for Testing and Materials, West Conshohocken, PA 2000

Intercomparison of Monte Carlo and S_N Sensitivity Calculations for a 14 MeV Neutron Benchmark [★]

U. Fischer¹, I. Kodeli², C. Konno³, and R.L. Perel⁴

¹ Forschungszentrum Karlsruhe, P.O. Box 3640, 76021 Karlsruhe, Germany

² Institut “Jozef Stefan”, Jamova 39, 1000 Ljubljana, Slovenia

³ Centre for Neutron Science, JAERI, Tokai-mura, Ibaraki-ken 319-1195, Japan

⁴ Racah Institute of Physics, Hebrew University of Jerusalem, 91904 Jerusalem, Israel

Abstract. An inter-comparison has been performed of probabilistic and deterministic sensitivity calculations with the objective to check and validate the Monte Carlo technique for calculating point detector sensitivities as being implemented in MCSSEN, a local version of the MCNP4A code. A suitable 14 MeV neutron benchmark problem on an iron assembly has been considered to this end. Good agreement has been achieved for the calculated individual sensitivity profiles, the uncertainties and the neutron flux spectra as well. It is concluded that the Monte Carlo technique for calculating point detector sensitivities and related uncertainties as being implemented in MCSSEN is well qualified for sensitivity and uncertainty analyses of fusion neutronics integral experiments.

1 Introduction

Sensitivity and uncertainty analysis is a powerful means to assess uncertainties of nuclear responses in neutron transport calculations and trace down these uncertainties to specific nuclides, reaction cross-sections and energy ranges. When applied to the analysis of integral experiments, it enables to assess the calculational accuracy and provide information for improving the cross-section data evaluations.

The differential operator method developed originally by Hall [1] is a suitable method to calculate sensitivities with the Monte Carlo technique. Based on this method an algorithm has been developed for calculating point detector sensitivities with MCSSEN [2], a local update to the MCNP4A Monte Carlo code [3]. The point detector method is best suited for analysing integral benchmark experiments when leakage spectra are measured by detectors located far from the irradiated material assembly. Experiments of this kind are in frequent use for testing and validating fusion nuclear data evaluations and for assessing their uncertainty margins as well. This work is devoted to the benchmarking of the Monte Carlo technique for calculating point detector sensitivities on the basis of a suitable fusion neutronics benchmark problem.

[★] This work has been performed in the framework of the nuclear fusion programme of Forschungszentrum Karlsruhe and is supported by the European Union within the European Fusion Technology Programme.

2 Benchmark Problem

The benchmark problem consists of a spherical iron shell assembly with a 14 MeV neutron point source in the centre. The task is to calculate, first of all, the neutron flux spectra at a detector location of 6.8 m, second, the sensitivities profiles for specified neutron flux integrals and, on this basis, the related uncertainties due to cross-section uncertainties. Two different iron shell assemblies with wall thicknesses of 7.5 and 28 cm, respectively, are considered. Nuclear data are taken from the European Fusion File EFF-3.1 for ^{56}Fe [4] and FENDL-1 [5] for the other iron isotopes. The data were processed with NJOY [6] in pointwise energy representation for use with MCNP and in the 175 VITAMIN-J group structure for use with the discrete ordinates codes.

3 Methodological Approach

First, the neutron flux spectra are calculated and compared at the location of the detector. Two different discrete ordinates codes, ANISN [7] and ONEDANT [8], are employed in spherical geometry. Second, the sensitivities of the specified flux integrals are calculated. In the Monte Carlo approach, this requires one calculational run including the related point detector sensitivity estimator in the proper energy bin segmentation. With the deterministic approach, this step requires a direct and several adjoint ANISN/ONEDANT calculations followed by SUS3D [9] calculations to provide the sensitivity profiles. The next step consists of calculating the uncertainties, using the calculated sensitivity profiles and the processed covariance matrices. Finally, a detailed comparison of the sensitivity profiles, the integrated sensitivities and uncertainties is performed.

4 Computational Techniques

In the deterministic approach, the sensitivities of specified nuclear responses to the involved cross-section data are calculated on the basis of perturbation theory using direct and adjoint fluxes provided by discrete ordinates calculations. The fluxes are routed to the sensitivity/uncertainty code via interface files. Sensitivity and uncertainty calculations are performed with two variants of the SUS3D code, namely SUS3D [10] and SUS3D-FNS [11]. The SUS3D sensitivity and uncertainty code package is suitable for one-, two-, and three- dimensional cross section sensitivity and uncertainty analysis. Direct and adjoint fluxes generated by the transport codes of the DOORS or the DANTSYS packages can be used. The sensitivity/uncertainty with regard to the excitation functions and to the secondary energy and angular distributions (SAD/SED) can be studied. The system is fully compatible with the ENDF-6 format. The SUS3D-FNS code package was developed from the SUS3D code at FNS and can also use flux interface files from the ANISN, DORT and TORT code series. NJOY-SD, a modified NJOY-version is used for processing the nuclear data in ENDF-6 format for SUS3D-FNS. NJOY-SD generates self- shielded group cross-sections with one

single background cross-section σ_0 for the whole energy range. In this work, a background cross-section of $\sigma_0 = 0.2$ was used for ^{56}Fe .

The Monte Carlo method provides an alternative way to determine sensitivities, avoiding some inherent drawbacks of the S_N method: complex geometries can be handled without severe constraints, there are no numerical convergence problems, and, in addition, the energy dependence of the cross-sections can be accurately described by using the pointwise representation. For calculating point detector sensitivities based on the differential operator method, an algorithm has been developed previously [2] and implemented into a local update to the MCNP4A Monte Carlo code. With this approach, point detector sensitivities for all responses can be calculated in one single run. Sensitivity profiles can be calculated in an arbitrary group structure for calculating the uncertainties when multiplied with the covariance matrices.

5 Inter-comparison of Benchmark Results

The calculated neutron leakage flux spectra are inter-compared in Fig. 1 for the iron spherical shells with 7.5 and the 28 cm wall thickness, respectively. For both cases good agreement is obtained between the MCNP calculation with continuous energy cross-sections and the S_N -calculations with ANISN/ONEDANT and multi-group cross-section data. Thus it is concluded that both the deterministic and the probabilistic approaches are well suited to properly describe neutron problems of the considered kind.

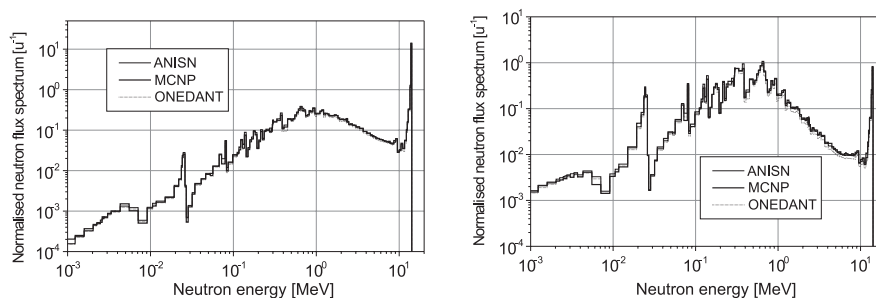


Fig. 1. Neutron flux spectra for the 7.5 cm and the 28 cm thick spherical iron shells

The relative sensitivities of neutron flux integrals as calculated for the 28 cm thick shell assembly (in terms of % per % change of the cross-section data) at the specified detector location are shown in Tab. 1¹.

The good agreement between the Monte Carlo and the deterministic approaches has been achieved only after removing some minor bugs in MCSN.

¹ MT=2: elastic scattering, MT=16: (n,2n)-reaction, MT=51 and 91: inelastic scattering to the first excitation level and the continuum, respectively.

The calculated sensitivities have also been tested against a direct calculation with modified cross-section data by introducing changes of 5 % in the cross-sections for elastic and inelastic scattering. The resulting sensitivities, based on ANISN-calculations with the modified cross-section data, agree again with the sensitivities as calculated by MCSEN, ANISN/SUSD-FNS and ONEDANT/SUSD3D.

Table 1. Relative sensitivities [%/%] for neutron fluxes in 28 cm thick shell assembly

E [MeV]	E < 0.098	0.098 - 1.003	1.003 - 4.966	4.966 - 7.408	7.408 - 10.0	10.0 - 13.84	E > 13.84	Total
		1.003	4.966	7.408	10.0	13.84		
MCSEN								
Total	1.248	0.290	-1.929	-2.955	-2.841	-2.764	-3.620	0.003
MT=2	0.739	0.001	-0.643	-0.356	-0.346	0.308	-0.556	-0.012
MT=16	0.345	0.259	-0.046	-0.455	-0.440	-0.788	-0.878	0.196
MT=51	0.284	0.102	-0.918	-0.157	-0.095	0.077	-0.157	-0.003
MT=91	-0.028	0.009	0.005	-0.735	-1.615	-1.849	-1.466	-0.049
ANISN/SUSD-FNS								
Total	1.255	0.277	-2.220	-3.025	-2.854	-2.864	-3.605	-0.013
MT=2	0.731	0.003	-0.785	-0.383	-0.304	0.226	-0.497	-0.0225
MT=16	0.332	0.253	-0.053	-0.475	-0.456	-0.813	-0.891	0.194
MT=51	0.325	0.100	-1.026	-0.157	-0.098	0.102	-0.159	-0.004
MT=91	-0.028	0.002	-0.018	-0.750	-1.615	-1.628	-1.859	-0.053
ONEDANT/SUSD3D								
Total	1.389	0.280	-2.251	-3.037	-2.869	-2.848	-3.630	0.007
MT=2	0.862	-0.003	-0.794	-0.382	-0.303	0.253	-0.513	-0.011
MT=16	0.333	0.257	-0.056	-0.472	-0.454	-0.797	-0.893	0.198
MT=51	0.320	0.101	-1.040	-0.158	-0.098	0.102	-0.160	-0.001
MT=91	-0.023	0.006	-0.017	-0.760	-1.648	-1.888	-1.491	-0.049

The total flux is rather insensitive to cross-section changes due to the fact that the sensitivities above and below several MeV neutron energy are negatively correlated. Neutrons with higher energies are down scattered by elastic and inelastic scattering collisions, and appear directly or through multiple collisions in the low energy part of the spectrum. Major contributors to the negative sensitivities in the source energy range ($E > 13.84$ MeV) are the (n,2n) and the inelastic scattering (MT=91, 51) reactions. Likewise, these reactions form the main contribution to the positive sensitivity in the lower part of the spectrum. In general, the sensitivity to elastic scattering is negative in the high energy range except for the window below the source peak (10–13.84 MeV). Below some

1 MeV this sensitivity is again positive as it is populated by down scattered neutrons through multiple collisions. Sensitivity profiles of a specified response to a given nuclear reaction have been calculated in the VITAMIN-J 175 group structure. Figure 2 shows the profiles as provided by MCSEN and ANISN/SUSD-FNS for the 28 thick spherical shell. There is an overall good agreement for the sensitivity profile as calculated by MCSEN and ANISN/SUSD-FNS except for minor deviations in the source energy group ($E > 13.84$ MeV) in the case of elastic scattering.

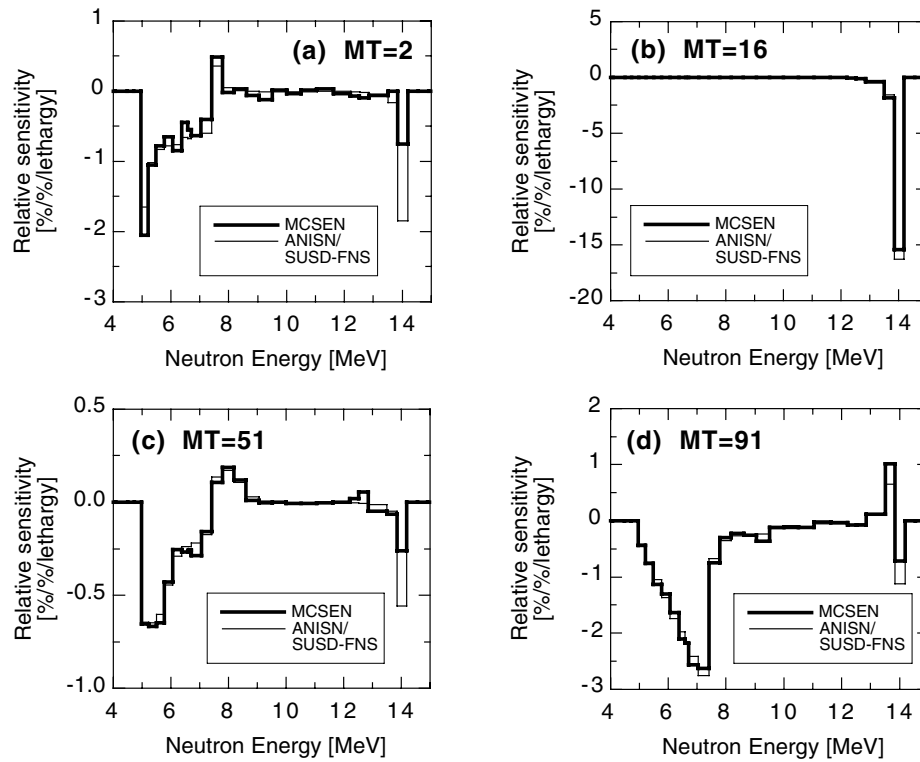


Fig. 2. Sensitivity profiles of the neutron flux in the energy range 5 - 7 MeV for the 28 cm thick iron shell

Uncertainties of the calculated neutron flux integrals due to uncertainties of the cross-section data have been assessed on the basis of the EFF-3.1 ^{56}Fe co-variance data processed with NJOY. The calculated uncertainties are displayed in Tab. 2 for the 7.5 and 28 cm thick iron spherical shells. Again there is good agreement between the Monte Carlo and the discrete ordinates based calculations.

Table 2. Uncertainties [%] of neutron flux integrals as calculated with ^{56}Fe EFF-3.1 co-variance data

E [MeV]	E < 0.098	0.098 - 1.003	1.003 - 4.966	4.966 - 7.408	7.408 - 10.0	10.0 - 13.84	E > 13.84	Total
		1.003	4.966	7.408	10.0	13.84		
7.5 cm shell								
MCSEN	2.47	1.90	1.18	4.64	4.77	2.63	1.20	0.48
ONEDANT/SUSD3D	2.46	1.90	1.18	4.76	4.64	2.67	1.22	0.49
ANISN/SUSD-FNS	2.41	1.90	1.17	4.00	3.15	2.62	1.22	0.49
28.0 cm shell								
MCSEN	3.64	1.00	1.43	12.1	7.46	5.73	4.35	0.72
ONEDANT/SUSD3D	4.10	1.04	1.59	12.4	7.45	5.74	4.54	0.72
ANISN/SUSD-FNS	3.60	0.99	1.54	9.94	5.76	5.68	4.53	0.74

6 Conclusions

An inter-comparison has been performed of sensitivity calculations with probabilistic and deterministic computational procedures with the main objective to check and validate the novel Monte Carlo technique for calculating point detector sensitivities. On the basis of a 14 MeV neutron benchmark problem, good agreement has been achieved for the individual sensitivity profiles, the uncertainties and the neutron flux spectra. In addition, the calculated sensitivities were shown to be consistent with the results of direct transport calculations using modified cross-sections. It is thus concluded that the Monte Carlo technique for calculating point detector sensitivities and related uncertainties as being implemented MCSEN is well qualified for sensitivity and uncertainty analyses of integral experiments.

References

1. M.C.G. Hall: Nucl. Sci. Eng. **81**, 423 (1982)
2. R.L. Perel, J.J. Wagschal, Y. Yeivin: Nucl. Sci. Eng. **124**, 197 (1996)
3. F. Briesmeister (ed.): Los Alamos National Laboratory, Report LA-12625-M (1993)
4. A. Trkov, M. Herman: personal communication
5. S. Ganesan, P.K. McLaughlin: IAEA Report IAEA-NSD-128, Rev. 1, Vienna (June) 1995
6. R.E. MacFarlane: Los Alamos National Laboratory, Report LA-12740-M (1994)
7. W.W. Engle: Union Carbide Corporation, Report K-1693(1967)
8. R.E. Alcouffe et al.: Los Alamos National Laboratory, Report LA-12969-M (1995)
9. K. Furuta, Y. Oka, S. Kondo: Report UTNL-R-0185 (1986)
10. K. Kosako, C. Konno, H. Takeuchi: In: *4th Int. Conference on Supercomputing in Nuclear Applications*, Tokyo, Japan (Sep. 2000)
11. I. Kodeli: Proc. In: *ANS Int. Topical Meeting on Advances in Reactor Phys, Math. and Comput. (PHYSOR-2000)*, Pittsburgh, PA (May 2000)

Comparison of Snyder Head Phantom Models Used for Neutron Capture Therapy Benchmark Monte Carlo Dosimetry Calculations

T. Goorley¹, W.S. Kiger III¹, and R. Zamenhof²

¹ Nuclear Reactor Laboratory, Massachusetts Institute of Technology, Cambridge MA, USA

² Department of Radiology, Beth Israel Deaconess Medical Center, Boston MA, USA

Abstract. As Boron Neutron Capture Therapy (BNCT) clinical trials are initiated in more countries, new treatment planning software programs are being developed to calculate dose distributions in patient specific models. A reference suite of test problems, i.e., head phantom irradiations and resulting depth-dose curves, would allow quantitative comparison of the treatment planning software. This paper presents sets of central axis depth vs. dose curves calculated with the Monte Carlo radiation transport code MCNP4B for five different representations of the Snyder head phantom. The first is a multi-shell analytic ellipsoidal representation, and the remaining four are voxelized representations with cube edge lengths of 16, 10, 8 and 4 mm. For these calculations, 10 cm diameter monoenergetic and monodirectional neutron and photon beams were incident along the central axes of the models. Individual beams of 0.0253 eV, 1, 2, 10, 100 and 1000 keV neutrons, and 0.2, 0.5, 1, 2, 5, and 10 MeV photons were simulated to high statistical convergence, with statistical error less than 1% in the center of the model. A “generic” epithermal neutron beam, with 1% fast flux contamination and 10% thermal flux contamination, similar to those proposed for BNCT treatments, was also simulated with all five models. Computations for both of the smaller sized voxel models produced thermal neutron, fast neutron, and gamma dose rates within 4% of those from the analytical representation. It is proposed that these data sets be used by the BNCT community for the verification of existing and new BNCT treatment planning software.

1 Introduction

Neutron Capture Therapy (NCT) is a bi-modal cancer therapy which combines neutron irradiation with an isotope with a high neutron capture cross section [1]. Boron-10 is the isotope of choice for clinical trials because it has a large thermal neutron capture cross section (3840 barns) and high energy release (2.79 MeV), emits high-LET, short range alpha particle and lithium ion on neutron capture, and has been bound to compounds which accumulate preferentially in tumors. Therapeutic advantage in BNCT is attained by preferentially loading the tumor with ¹⁰B compared to surrounding healthy tissue.

The radiation delivered in BNCT is a mixed field of high and low LET radiation that depends on the spatial, spectral, and angular characteristics of the incident neutron beam as well as the geometry and composition of the target

itself. For treatment planning and dosimetry purposes, the radiation field is generally divided into 4 dose components: thermal neutron, fast neutron, photon, and boron dose. The thermal neutron dose primarily arises from the $^{14}\text{N}(\text{n},\text{p})^{14}\text{C}$ capture reaction which comprises 97% of the adult brain neutron kerma below the 0.5 eV energy cut-off for thermal neutrons. Fast neutron dose is primarily due to elastic neutron collisions with hydrogen ($^1\text{H}(\text{n},\text{n}')^1\text{H}$), which represents 90% of the adult brain kerma between the energies of 600 eV and 3.0 MeV. Other neutron reactions with the isotopes ^{12}C , ^{16}O , and ^{31}P , generally contribute between 4% and 8% to brain kerma between 40 eV and 5 MeV, but at certain resonance energies comprise 15% of the neutron brain kerma. The photon dose component originates from two sources, contaminating photons in the neutron beam and prompt gammas produced by neutron capture in the target, principally by the $^1\text{H}(\text{n},\gamma)^2\text{H}$ reaction. For high quality neutron beams, the incident photon component is small compared to the photon component induced in the target. Boron dose, of course, arises from the $^{10}\text{B}(\text{n},\alpha)^7\text{Li}$ reaction.

During treatment planning for BNCT clinical irradiations, all 4 dose components are calculated throughout the target regions, e.g., the patient's head. These dose distributions are used to determine the optimum field orientation and often the delivered patient dose, so their accurate calculation is important. While different BNCT investigators may use different transport codes, dose calculations based on the same problem description should produce the same results. Evaluation and comparison of treatment planning software is a critical step in the standardization of dosimetry for the comparison of clinical results. As more BNCT clinical trials progress, the benefits of standardized dosimetry and calculations include the ability to compare patient dosimetry and the resulting clinical responses.

This paper presents high confidence thermal neutron, fast neutron, induced photon, and incident photon component dose rate profiles for comparison of treatment planning software. Dose rate profiles were calculated for a variety of photon and neutron beam energies in both analytical and voxel models to evaluate the effects of voxelizing patient image data, which is a technique for constructing customized patient models for radiation transport calculations used in the Harvard-MIT clinical trials of BNCT [2]. Issues regarding the most recently published ICRU kerma data and their impact on dose calculations are also discussed.

2 Methods and Materials

In-phantom dose profiles were calculated using the general purpose Monte Carlo radiation transport code MCNP4B [3], developed by Los Alamos National Laboratory, with both analytical and voxel model representations of the Snyder head phantom (SHP) [4]. The SHP consists of two ellipsoids, which divide the head into regions of cranium and adult brain. Material compositions from ICRU 46 [5] were used for adult brain and cranium. A third 5 mm thick shell of ICRU 46 adult skin has also been added [6]. The four voxel models were derived from

a 3D TIFF format image stack with 1 mm in-plane resolution representing the SHP in the same way that a CT image stack represents patient geometry in a BNCT treatment planning calculation. For the 16, 8 or 4 mm voxel models, the material for each voxel was assigned based on the most abundant pixel type (air/scalp/bone/brain) in the volume (i.e., no material mixtures were used). For the 10 mm voxel model, however, the BNCT treatment planning program MacNCTPlan [2] was used to construct a voxel model based on mixtures of air, bone and soft tissue (which was specified as brain) in 20% increments. Figure 1 shows the superposition of the 16, 8, and 4 mm models over the bounding ellipsoids from the analytical version in the central yz plane, and the axial tally regions.

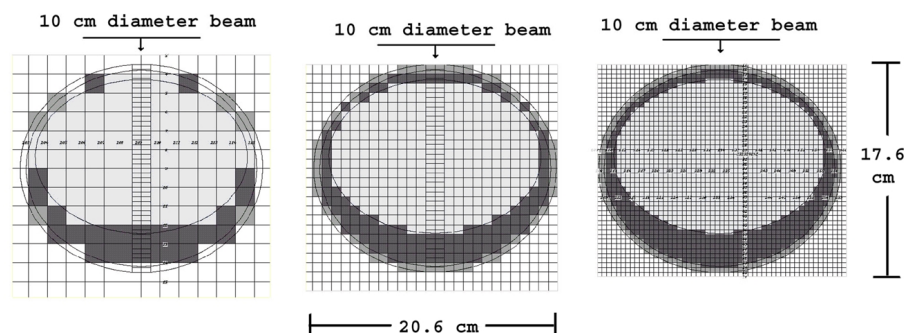


Fig. 1. Superposition of voxel and analytical models. The yz planes of the 16, 8 and 4 mm voxel models (left, center and right, respectively), are shown superimposed over the analytical model. ICRU 46 adult brain is colored in light gray, ICRU 46 cranium in dark gray, and ICRU 46 adult skin in medium gray. Dimensions shown are for the analytical model

The kerma factors applied in the models were calculated for ICRU 46 adult brain composition and are based on the recently published H, ^{12}C , ^{14}N , ^{16}O and ^{31}P total elemental neutron kermas in ICRU 63 [7]. To properly treat low energy thermal neutrons, the neutron kerma factors were log-log extrapolated from 0.0253 eV down to 0.0001 eV. These kermas, as well as the cross sections used for transport, are based on the ENDF/B-VI nuclear data library [8]. The contribution to adult brain kerma from Na, S, Cl, and K has been neglected, and they are not available in ICRU 63. Photon kermas were taken from ICRU 46 and are based on the mass energy absorption coefficients (μ_{en}/ρ) derived from Hubbell's elemental data [9].

3 Results

Different neutron beam energies resulted in significantly different dose rates. Varying the neutron beam energy from 1 keV to 1 MeV increased the fast neutron surface dose rate by a factor of 285. The 0.0253 eV beam produced thermal neutron and induced gamma peak doses a factor of 6.3 and 3.2, respectively, larger than the 1 MeV neutron beam. These differences can be seen in the separate dose component plots for the analytical model in Figs. 2a-c. Figure 2d shows the dose profile differences associated with incident photon beams. Calculated dose rates for the 2 keV neutron beam are also shown in Fig. 3. Other energies have been omitted for brevity.

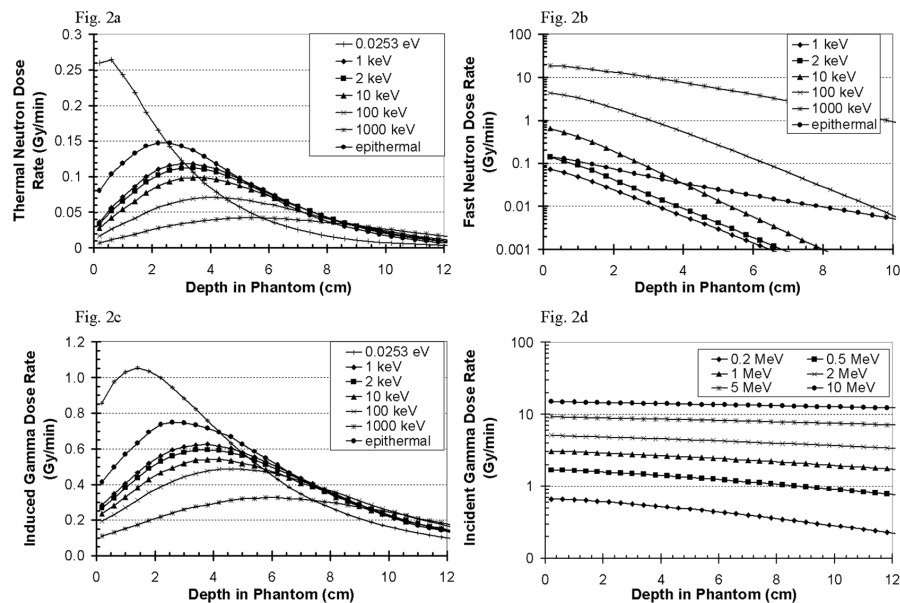


Fig. 2. Individual component dose rate profiles for monodirectional, 10 cm diameter, monoenergetic neutron beams (2a-c) of 10^{10} n/cm²s, and photon beams (2d) of 10^{10} γ /cm² s

Differences between doses calculated with the analytical and voxel models increased with voxel size for all dose components. The 4 mm voxel model closely approximated the analytical model, with thermal neutron and fast neutron doses 1% higher and 3% lower, respectively, in the voxel model at a depth of 2 cm where the thermal neutron flux (and the total biologically effective dose) peaks. The 8 mm voxel model produced 4% higher thermal and 2% higher fast neutron dose at 2 cm than in the analytical model. Within the 6 or 7 cm closest to the entrance, where the discrepancy between the two models is statistically significant, the largest differences occur between 2 and 3 cm for all three components. The

2 keV n beam	Analytical SHP Model				0.8 cm Voxel SHP Model			
	Thermal Neutron Dose Rate	Fast Neutron Dose Rate		Induced Gamma Dose Rate	Thermal Neutron Dose Rate	Fast Neutron Dose Rate		Induced Gamma Dose Rate
Depth (cm)	Gy/min	Gy/min	$\pm 1\sigma$	Gy/min	Gy/min	Gy/min	$\pm 1\sigma$	Gy/min
0.4	0.043	0.127	0.000202	0.296	0.043	0.124	0.000124	0.291
1.2	0.072	0.080	0.000617	0.409	0.071	0.077	0.000092	0.396
2.0	0.097	0.043	0.000095	0.510	0.094	0.042	0.000059	0.491
2.8	0.110	0.0228	0.000062	0.570	0.107	0.022	0.000039	0.553
3.6	0.111	0.0122	0.000041	0.594	0.108	0.012	0.000026	0.579
4.4	0.104	0.0066	0.000027	0.584	0.101	0.006	0.000017	0.572
5.2	0.091	0.00354	0.000018	0.550	0.089	0.00350	0.000011	0.539
6.0	0.076	0.00192	0.000012	0.499	0.075	0.00193	0.000008	0.490
6.8	0.062	0.00104	0.000007	0.442	0.061	0.00105	0.000005	0.435
7.6	0.048	0.000554	0.000004	0.379	0.048	0.000564	0.0000036	0.377
8.4	0.037	0.000289	0.000003	0.326	0.037	0.000298	0.0000025	0.322
9.2	0.028	0.000149	0.000002	0.274	0.028	0.000156	0.0000017	0.270
10.0	0.021	0.000076	0.0000020	0.228	0.021	0.000079	0.0000012	0.225
10.8	0.016	0.000039	0.0000014	0.188	0.015	0.000040	0.0000008	0.186
11.6	0.011	0.000019	0.0000010	0.155	0.011	0.000020	0.0000006	0.153
12.4	0.008	0.000009	0.0000007	0.128	0.008	0.000010	0.0000004	0.126
13.2	0.006	0.000005	0.0000005	0.105	0.006	0.000005	0.0000003	0.104

Fig. 3. Dose rate profiles for the 2 keV 10^{10} n/cm²s neutron beam calculated with the analytical and 8 mm voxel SHP models. Statistical error for the thermal neutron and induced gamma dose is less than 2% throughout the entire model

16 mm voxel model was a poor approximation of the analytical; it overestimated thermal neutron and gamma dose at the entrance voxel by more than 10% and underestimated both neutron dose components by 10% for depths more than 5 cm. The 10 mm model constructed with MacNCTPlan and used with an epithermal beam had thermal neutron, fast neutron and gamma dose components within 4% of the analytical model results at a depth of 2 cm.

4 Discussion

During the calculation of the dose rate profiles, a number of significant dosimetry issues were encountered. Thermal neutron dose rates 15% lower were encountered when the extrapolation of the kerma data to low neutron energies (below 0.0253 eV) was not used. Using kerma factors from ICRU 46 produced thermal neutron dose rates 2% lower than those computed using kerma factors based on ICRU 63 data. This difference arises from differences in cross sections and energy deposition between ENDF/B-V and ENDF/B-VI. Thermal neutron dose also shows a directly proportional change with the nitrogen concentration in the brain. Using a nitrogen weight concentration of 1.84% [6], which was used at Harvard-MIT prior to adoption of the ICRU 46 concentration of 2.2%, resulted in thermal doses 16% lower. Using the $S(\alpha, \beta)$ thermal neutron scattering treatment for hydrogen in 300 K light water significantly affected transport as well as

dose rates, resulting in 27% higher peak thermal neutron dose and 24% higher peak gamma dose when the epithermal beam was simulated. Some of these differences are more than a factor of three larger than the difference between the analytical model and the single materials 8 mm voxel model or mixed materials 10 mm voxel model, indicating other modeling considerations such as composition and the thermal neutron scattering law can have a larger impact than voxel size. Furthermore, the similarity between the dose profiles based on single material 8 mm voxels and mixed material 10 mm voxels shows that materials averaging (mixing) can mitigate the loss of accuracy due to larger voxel sizes.

While these calculations are not compared against experiments, their accuracy is based on the ability of the well-benchmarked MCNP4B code. MCNP4B has also compared well to other codes in similar circumstances. A comparison of BNCT treatment planning software showed close agreement in doses for clinical test cases [10], between the two predominant codes used in clinical trials, MacNCTPlan [2], developed at Harvard-MIT, which uses MCNP4B, and BNCT_rtp [11], developed by Idaho National Engineering and Environmental Laboratory.

References

1. R.G. Zamenhof, P.M. Busse, O.K. Harling, T. Goorley: 'Boron Neutron Capture Therapy.' In: *The Modern Technology of Radiation Oncology: A Compendium for Medical Physicists and Radiation Oncologists* (Medical Physics Publishing, Madison, WI 1999)
2. R.G. Zamenhof, E. Redmond II, G.R. Solares, D. Katz, W.S. Kiger III, O.K. Harling: *Int. J. Rad. Oncol. Biol. Phys.* **35**, 383 (1996)
3. J.F. Briesmeister, ed.: *MCNP - A General Monte Carlo N-Particle Transport Code, Version 4B*. LA-12625-M Los Alamos National Laboratory (1997)
4. W.S. Snyder, H. L. Fisher, Jr., Mary R. Ford, G. G. Warner: *MIRD. J. Nucl. Med. Suppl. 3. Phamplet 5*, **47** (1969)
5. ICRU Report 46, Washington, DC. 1992
6. R.G. Zamenhof, S.D. Clement, O.K. Harling, J.F. Brenner, D.E. Wazer, H. Madoc-Jones, J.C. Yanch: In: *Neutron Beam Design, Development, and Performance for Neutron Capture Therapy*, ed. by O.K. Harling, J.A. Bernard, and R.G. Zamenhof (Plenum Press, New York 1990) pp. 283-305
7. ICRU Report 63, Bethesda, MD. 2000.
8. Cross Section Evaluation Working Group, ENDF/B-VI Summary Documentation, BNL-NCS-17541 (ENDF-201), National Nuclear Data Center, Brookhaven National Laboratory, Upton, NY, 1991
9. J.H. Hubbell: *Intl. J. Appl. Radiat. Isot.* **33**, 1269 (1986)
10. T. Goorley, F. Wheeler, J. Capala, W.S. Kiger III, M. Palmer, R. Zamenhof: *Proc. 8th Int. Symp. Neutron Capture Therapy for Cancer*, La Jolla, California, Sept. 13-18, 1998
11. D.W. Nigg, F.J. Wheeler, D.E. Wessol, J. Capala, M. Chadha: *J. Neuro-Oncol.* **33**, 93 (1997)

Monte Carlo Modeling of Fast Sub-critical Assembly with MOX Fuel for Research of Accelerator-Driven Systems

A. Polanski¹, V. Barashenkov², I. Puzynin², I. Rakhno³, and A. Sissakian²

¹ Soltan Institute for Nuclear Studies, 05-400 Swierk, Poland

² Joint Institute for Nuclear Research, 141980 Dubna, Moscow region, Russia

³ Radiation Physics and Chemistry Problems Institute, 220109 Sosny, Minsk, Belarus

Abstract. It is considered a sub-critical assembly driven with existing 660 MeV JINR proton accelerator. The assembly consists of a central cylindrical lead target surrounded with a mixed-oxide (MOX) fuel ($\text{PuO}_2 + \text{UO}_2$) and with reflector made of beryllium. Dependence of the energetic gain on the proton energy, the neutron multiplication coefficient, and the neutron energetic spectra have been calculated. It is shown that for subcritical assembly with a mixed-oxide (MOX) BN-600 fuel ($28\%\text{PuO}_2 + 72\%\text{UO}_2$) with effective density of fuel material equal to 9 g/cm^3 , the multiplication coefficient k_{eff} is equal to 0.945, the energetic gain is equal to 27, and the neutron flux density is $10^{12} \text{ cm}^{-2} \text{ s}^{-1}$ for the protons with energy of 660 MeV and accelerator beam current of $1 \mu\text{A}$.

1 Introduction

As the first step in the studies of characteristics of the experimental set up the MOX fuel subcritical assembly with lead and concrete reflectors was proposed [1]. But, the results of calculations have shown that a beryllium reflector allows one to decrease significantly the used amount of the MOX fuel. The proposed ADS facility consists of: a 660 MeV proton accelerator, beam bending magnets, a spallation target with different materials, a subcritical core based on MOX fuel elements, beryllium reflectors, lead and concrete shielding, control and auxiliary systems.

2 Main Characteristics of the Fast Sub-critical Assembly with MOX fuel

The schematic model of the subcritical assembly is presented in Fig. 1.

The assembly is driven by the $1 \mu\text{A}$ proton current from the 660 MeV phasotron. Main parameters of the ADS facility are given in Tab. 1.

The proton beam is transported to the target through a vacuum duct going through a concrete and lead shielding. The proton beam interacts with the target placed in a steel tube. The lead with radius $r=4.5 \text{ cm}$ has been used as a target material. The target is surrounded by a blanket containing MOX fuel. The 127 fuel elements are located in a six hexagonal stainless steel cassettes. We

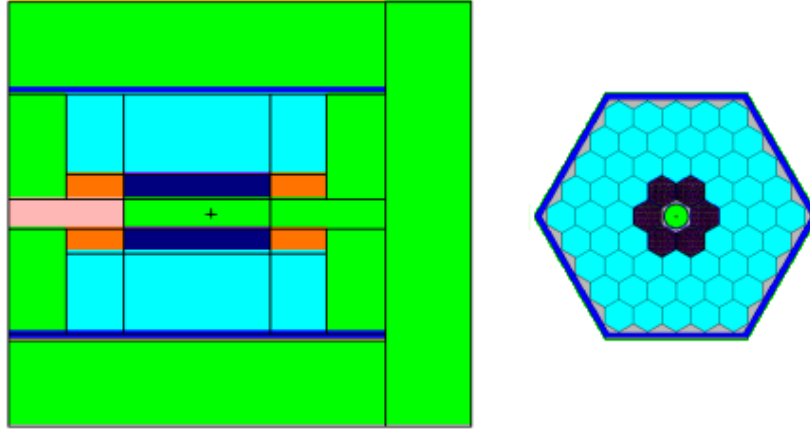


Fig. 1. Subcritical assembly scheme (black-fuel elements and stainless steel walls, grey-beryllium reflector, dark gray-lead target and lead shielding)

Table 1. Main parameters of the ADS facility:

Max. proton beam energy	660 MeV
Beam current	1 μA
Beam intensity	$6.25 \cdot 10^{12}$ p/s
k_{eff}	0.945
Energetic gain	27
Neutron flux density	$10^{12} \text{ cm}^{-2} \text{ s}^{-1}$
The full length of a fuel element	70 cm
Core length of a fuel element	50 cm
Number of a fuel elements	762
BN-600 MOX fuel	(27 – 29% of PuO_2)
Mass of the MOX material	100 kg
Effective density of the MOX fuel	8.6-9.5 g/cm ³

have considered a standard cassettes used in BN-600 fast reactor. The distance between centers of cassettes have been 96 mm. The fuel designed for the fast breeder BN-600 reactor will be adopted for the core of the assembly. The fuel elements with external diameter equal to 6.9 mm consists of a stainless steel tube 0.4 mm thick with the plutonium and uranium oxides mixture. The diameter of a fuel pellet is equal to 5.8 mm. The full length of a fuel element with its end details is about 70 cm, while the core length is 50 cm. The blanket is surrounded by a beryllium reflector and steel vessel. Around steel vessel there is lead shielding 30 cm thick. The target and fuel elements are cooled by air. The total length of the assembly is equal to 160 cm and high is equal to 140 cm.

3 Results of Monte Carlo Modeling

Properties of the experimental facility have been investigated by using the following particle transport codes: Dubna CASCADE, LCS [2], MCNP4B [3]. The calculated quantities were: dependence of the energetic gain G on the proton energy, the neutron multiplication coefficient and the neutron energy distribution for different places inside subcritical assembly.

The fuel has been considered with a composition of plutonium dioxide and uranium dioxide. The content of isotopes plutonium in plutonium was following: 95% ^{239}Pu , 4.5% ^{240}Pu , 0.5% ^{238}Pu . Uranium was natural one. Taken into account the split between fuel element wall and tablet the effective density of the fuel in the range from 8.6 to 9.5 g/cm^3 . Calculations have been done for different percentage of PuO_2 in the MOX fuel and for different density of the fuel.

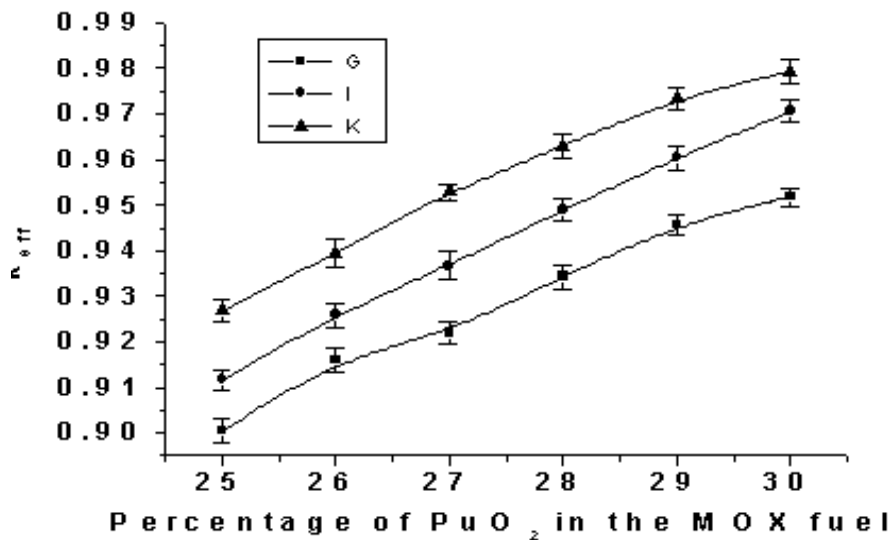


Fig. 2. The dependence of neutron multiplication coefficient k_{eff} on percentage of PuO_2 in the MOX fuel for effective density: 8.6 (line G), 9.0 (line I) and 9.5 (line K) g/cm^3

The dependence of neutron multiplication coefficient k_{eff} on percentage of PuO_2 for MOX fuel fabricated in Research Institute of Atomic Reactors in Dimitrovgrad in Russia is shown in Fig. 2. The calculations have been done by using MCNP4B neutron transport code for cells geometry presented at Fig. 1. According to Fig. 2, we have found that for $k_{\text{eff}} = 0.945$ the percentage of PuO_2 in MOX fuel is adequately 29, 28, 27 for effective density: 8.6 (line G), 9.0 (line I) and 9.5 (line K) g/cm^3 . Figure 3 presents neutron spectra averaged over small volumes (1cm^3) calculated along radius ($r=6 \text{ cm}, 12 \text{ cm}$ and 30 cm) of the subcritical assembly with $k_{\text{eff}} = 0.945$. Neutron flux $1.15 \cdot 10^{12} \text{ cm}^{-2} \text{ s}^{-1}$, $1.07 \cdot 10^{12}$

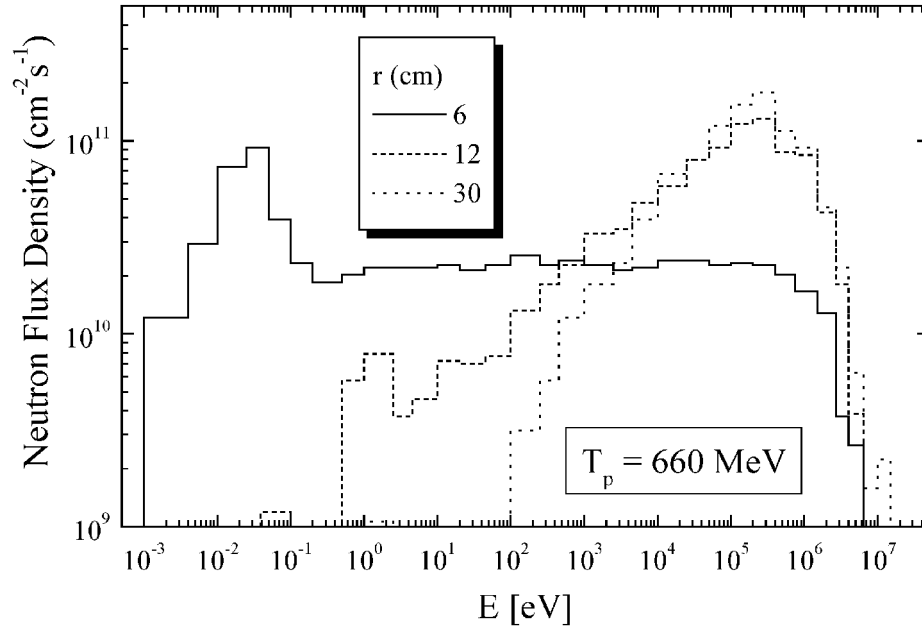


Fig. 3. Neutron spectrum calculated along radius ($r=6$ cm, 12 cm and 30 cm) of the subcritical assembly with $k_{\text{eff}} = 0.945$

$\text{cm}^{-2} \text{s}^{-1}$ and $0.815 \cdot 10^{12} \text{ cm}^{-2} \text{s}^{-1}$ respectively was obtained inside the core. Calculations were performed for protons with energy 660 MeV and 1 μA current. LCS computer code was used. Several conclusions follow from the presented results: (i) different neutron spectra can be formed inside the assembly - from hard up in blanket to thermal ones in beryllium reflector; (ii) fast neutron flux about $10^{12} \text{ cm}^{-2} \text{s}^{-1}$ can be obtained inside the core; (iii) neutron flux will be enough for study of reaction rates of actinides and fission products inside the reactor. The dependence of the energetic gain in the system with the lead target at various proton beam energies is presented in Fig. 4. It has been calculated by using Dubna CASCADE code.

The energetic gain G is a ratio of the heat produced in the device to the beam energy. A decrease in the energy gain (see Fig. 4) at low energies range is caused by ionization losses of primary protons. As we can see from Fig. 4 for 660 MeV proton energy the energetic gain is $G = 27$ and for 1.5 GeV proton energy $G = 32$.

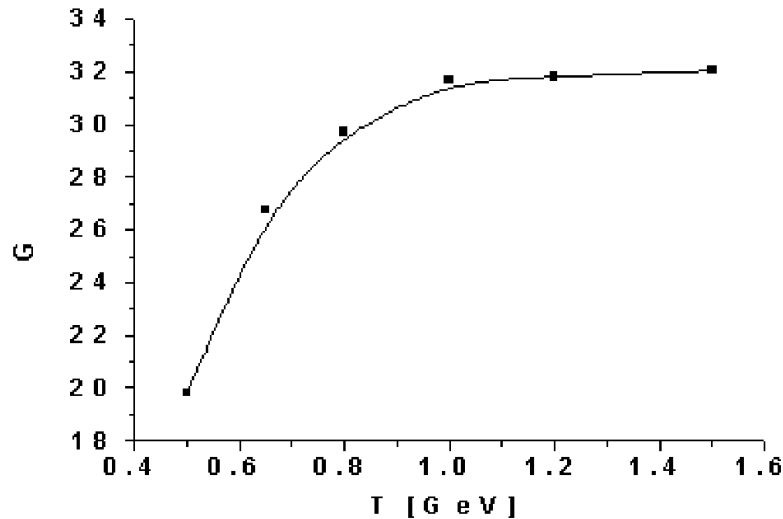


Fig. 4. Energetic gain G vs. incident proton energy T for $k_{\text{eff}} = 0.945 \pm 0.003$

4 Research Program for Subcritical Assembly with MOX Fuel

One horizontal experimental channel, not far from the target is planned as well as the three vertical channels: two of them on the ends of the core and one on the middle length of the core. The main aim of the experiment is to study physics of ADS. In order to explore that we propose to realize the following research tasks:

- Investigations of the heat distribution and neutron spectrum for different materials and sizes of target
 - Creation and development of the neutron spectrum measuring system and a technique for measurement of the heat distribution.
 - Installation of measuring system on an existing phasotron for measurements of the characteristics of the targets.
 - Investigation of spatial heat distribution.
 - Carrying out of energy and angle neutrons distribution.
 - Studying angle distribution of hadrons.
- Study transmutation rates for long lived nuclides and study of time-dependence of spallation product yields in the target.
 - Development and creation of spectroscopy system for measurements of transmutation rates and spallation products.
 - Preparing of samples.
 - Measuring the neutron spectrum using threshold detectors.
 - Examining transmutation cross sections and transmutation rate of fission products and minor actinides in varies neutron spectrum.

- Studying the time evolution of the nuclides concentration in the target.
- Investigations of the multiplication coefficient of subcritical assembly.
 - Installation of measuring system for measurements of the k_{eff} of the subcritical assembly.
 - Developing the monitoring on-line of the multiplication coefficient k_{eff} by correlation methods.
 - Investigation the dependence of the k_{eff} of subcritical assembly on the intensity and duration of the individual proton pulse at different levels of multiplication coefficient values of the zone. Measuring of the multiplication coefficient k_{eff} using infra-red method.
- Investigations of the energetic gain and neutron characteristics of subcritical assembly.
 - Installation of measuring system for measurements of the characteristics of the subcritical assembly.
 - Studying the energetic gain and neutrons production for different target materials, different target size, different shapes of the target, different position of the target in the subcritical assembly, different beam size and protons energy.
 - Investigation of neutron spectrum in subcritical assembly
 - Carrying out shielding for high-energy spallation neutrons by energy and angle neutron distribution measurements behind the shield area.
 - Studying the time evolution of the nuclides concentration in target and fuel elements after long-term irradiation.

The results of the measurements will be compared with the results of the Monte Carlo modeling of the corresponding processes to improve the computation methods.

5 Conclusion

It is shown that the proposed project allows one to obtain the data for designing a full-scale set up for the energy production, incinerating of plutonium and actinides, and transmutation of fission products.

References

1. A. Polanski: 'Monte Carlo Modeling of Electronuclear Processes in Experimental Accelerator Driven Systems'. In: *XXVI Mazurian Lakes School of Physics 1-11 September 1999, Krzyż, Poland. A NATO Advanced Research Workshop 2-4 September 1999*. Acta Physica Polonica, January 2000, Vol. B31 - Number 1
2. R.E. Prael, H. Lichtenstein: *User Guide to LCS: The LAHET Code System*. Report LA-UR- 89-3014, Los-Alamos National Laboratory, New-Mexico, USA
3. J.F. Briesmeister (Ed.): *MCNP - A General Monte Carlo N-Particle Transport Code*. Report LA-12625-M, Los-Alamos National Laboratory, New-Mexico, USA

Evaluation of CRISTO II Storage Arrays Benchmark with TRIPOLI-4.2 Criticality Calculations

Y.K. Lee

CEA-Saclay, DRN/DMT/SERMA/LEPP, 91191 Gif sur Yvette Cedex, France

Abstract. The new lattice feature of TRIPOLI-4.2 geometry package was applied to model the CRISTO II storage arrays of PWR fuels with various kinds of neutron absorber plates. The new ‘Kcoll’ collision estimator of TRIPOLI-4.2 code was utilized to evaluate the infinite multiplication factors, K_{inf} . Comparing with the published ICSBEP benchmark results of CRISTO II experiments and of three different continuous-energy Monte Carlo codes – TRIPOLI-4.1 (JEF2.2), MCNP4B2 (ENDF/B-V) and MCNP4XS (ENDF/B-VI.r4), the present study using cost-effective modeling, JEF2.2 and ENDF/B-VI.r4 libraries obtained satisfactory results.

1 Introduction

One of the new features of TRIPOLI-4 Monte Carlo code is the lattice geometry that makes easy to describe storage arrays and small research reactor core by pin-by-pin model [1,2]. Recently the lattice feature is improved in TRIPOLI-4.2 by introducing new operators so that the heterogeneous fuel pin arrays and various kinds of fuel assemblies in large research reactor or in power reactor could be also exactly modelled by several overlapped and repeated lattices [3].

The purpose of this study is firstly to investigate the performance of the new lattice feature and the new ‘Kcoll’ multiplication factor estimator in TRIPOLI-4.2, and secondly to evaluate the recently published CRISTO II criticality safety benchmark experiments [4]. Two continuous-energy cross section libraries JEF2.2 and ENDF/B-VI.r4 were independently utilized in TRIPOLI-4.2 calculations so as to compare with results computed by different Monte Carlo codes.

2 CRISTO II Storage Arrays Benchmark

The CRISTO II experiment was performed in the EOLE reactor (CEA-Cadarache, France) in 1980-1981. The aim of this experiment was to study the high density storage for PWR assemblies. Various kinds of neutron absorber plates were utilized in the water gap of the storage grid to investigate the negative reactivity introduced and the absorber efficiency.

Recently five configurations of the CRISTO II experiment corresponding to four different absorber plates and one without absorber are considered acceptable for use as ICSBEP benchmark experiments and published with identification number: LEU-COMP-THERM-041 [4].

The accepted benchmark model is an infinite storage array based on one 14×14 fuel assembly (180 fuel pins and 16 guide tubes) immersed in water. The characteristics of absorber plates introduced in water gap are presented in following five cases:

- / . Case A : 4.5 cm water gap without absorber plate
- / . Case B : 0.2 cm stainless steel plates
- / . Case C : 0.157 cm borated steel plates, ^{10}B : 2.6 mg/cm²
- / . Case D : 0.550 cm borated steel plates, ^{10}B : 9.6 mg/cm²
- / . Case E : 0.07 cm thick Cd sandwiched between 0.05 cm thick stainless steel.

The sample calculations are demonstrated in the ICSBEP Handbook by three different continuous-energy Monte Carlo codes: TRIPOLI-4.1 (JEF2.2), MCNP4B2 (ENDF/B-V) and MCNP4XS (ENDF/B-VI.r4). The tedious input listings, 18 pages for TRIPOLI-4.1 code and 4 pages for MCNP4 codes, and the benchmark results of these sample calculations are also provided in the handbook.

3 TRIPOLI-4.2 Modeling and Calculation

In reactor physics, criticality safety and radiation shielding calculations, there are many repeated structures to model and to compute. Thanks to the introduction of lattice geometry, continuous-energy cross sections and parallel calculation into TRIPOLI-4 code [5,6], the application of TRIPOLI-4 on heterogeneous storage arrays becomes practical.

In fact the lattice mode makes easy to realize the description of fuel assembly by pin-by-pin model, the continuous-energy cross sections allows to free from the self-shielding calculations of fuel and absorber, and the parallel calculation helps to reduce the waiting time for user in this kind calculations.

In present study the new lattice feature of TRIPOLI-4.2 were utilized to simplify the geometry modeling of heterogeneous fuel pin arrays. Three new introduced operators 'EXCEPT', 'REPLACE' and 'GARDE' were applied on lattice geometry so as to reduce the computer running time as well as to avoid the previous solution in TRIPOLI-4.1 of repeated usage of 'ECRASE' operator on specific fuel pin locations [1].

To describe the 14×14 fuel assembly of CRISTO II storage arrays, two lattices were overlapped. The first lattice using 'EXCEPT' operator was applied to model the 180 fuel pins in the 14×14 arrays and the second one using 'GARDE' operator to retouch the first one so as to introduce the 16 guide tubes with water into the 14×14 fuel pin arrays.

The typical input of TRIPOLI-4.2 for case A of CRISTO II storage arrays benchmark prepared for this study is presented here.

```
//NEA/NSC/DOC(95)03/IV LEU-COMP-THERM-041 Case A
//The CRISTO II Experiment in the EOLE Reactor - Storage Array of 3% Enriched LWR Assemblies
//Code: TRIPOLI-4.2 (JEF2.2) 20/04/2000

GEOMETRIE TITRE LEU-COMP-THERM-041 Case A TYPE 1 BOITE 22.12
```

```

22.12 10000 TYPE 2 B0ITE 1.26 1.26 10000 TYPE 3 CYLZ
0.47 5000 TYPE 4 CYLZ 0.4015 5000 TYPE
5 CYLZ 0.41 5000

VOLUME 1 COMBI 1 0 0 0 FINV // assembly +
water gap VOLUME 2 COMBI 2 -8.19 -8.19 0. ECRA 1 1 FINV // water
VOLUME 3 COMBI 3 0 0 0 V_ORIGIN 2 ECRA 1 2 FINV // cladding VOLUME 4
COMBI 4 0 0 0 V_ORIGIN 2 ECRA 1 3 FINV // fuel

VOLUME 40 RESC VOLUME 2 14 14 1 EXCEPT 15
3 6 1 3 9 1 4 11 1
6 3 1 6 6 1 6 9 1 6 12 1
9 3 1 9 6 1 9 9 1 9 12 1
11 4 1 11 11 1 12 6 1 12 9 1 FINV // fuel lattice

VOLUME 5 MAILLE 4 4 1 RESEAU 40 REMPLACE 2
ECRA 1 1 FINV // water
VOLUME 6 COMBI 3 0 0 0 V_ORIGIN 5 ECRA 1 5 FINV // guide tube VOLUME
7 COMBI 5 0 0 0 V_ORIGIN 5 ECRA 1 6 FINV // water

VOLUME 50 RESC VOLUME 5 14 14 1 BASE 4 4 1
GARDE 16
3 6 1 3 9 1 4 4 1 4 11 1
6 3 1 6 6 1 6 9 1 6 12 1
9 3 1 9 6 1 9 9 1 9 12 1
11 4 1 11 11 1 12 6 1 12 9 1 FINV // tube lattice

GRAF -12. -12. 0. 1 0 0 0 1 0 24. 24. 1 FING

LIMITE 6 1 REFL 1 1 REFL 2 1 REFL 3 1 REFL 4 1 REFL 5 1 REFL 6

COMPOSITION 4
PUNCTUAL 300 FUEL 5
U234 4.5568E-6 U235 6.9241E-4 U236 5.4681E-6 U238 2.2082E-2
O16 4.5568E-2
PUNCTUAL 300 CLAD 12
CR50 3.4108E-6 CR52 6.5775E-5 CR53 7.4575E-6 CR54 1.8565E-6
FE54 7.8470E-6 FE56 1.2199E-4 FE57 2.7930E-6 FE58 3.7240E-7
SN116 8.08E-5 SN118 1.36E-4 SN120 1.86E-4 ZR 3.678E-2
PUNCTUAL 300 TUBE 12
CR50 3.8584E-6 CR52 7.4406E-5 CR53 8.4360E-6 CR54 2.1001E-6
FE54 8.8500E-6 FE56 1.3758E-4 FE57 3.1500E-6 FE58 4.2000E-7
SN116 9.14E-5 SN118 1.54E-4 SN120 2.10E-4 ZR 4.158E-2
PUNCTUAL 300 WATER 2
H1_H2O 6.6734E-02 O16 3.3367E-02
FIN_COMPOSITION

GEOMCOMP WATER 4 1 2 5 7
FUEL 1 4
CLAD 1 3
TUBE 1 6
FIN_GEOMCOMP

LIST_SOURCE 1
SOURCE NORME 1. NEUTRON PUNCTUAL 0. 0. 0.
ANGULAR_DISTRIBUTION ISOTROPIC
ENERGETIC_DISTRIBUTION SPECTRE WATT_SPECTRE
TIME_DISTRIBUTION DIRAC 0.
FIN_SOURCE
FIN_LIST_SOURCE

SIMULATION CRITICITE BATCH 1000 SIZE 10000 EDITION 100
PARTICULES 1 NEUTRON
FIN_SIMULATION

```

It is clear that the length of this new modeling is largely reduced comparing with those input listings published in ICSBEP Handbook. Moreover the new lattice modeling is not only useful to reduce the modeling time but also helpful to lighten the verification work. With geometry plotting operator ‘GRAF’, it is useful to check for overdefined or underdefined zones by two-dimensional plots of cuts through the fuel assembly.

The boundary conditions ‘LIMITE’ were utilized to describe the infinite storage arrays based on unit storage cell (22.12 cm × 22.12 cm) containing one complete fuel assembly, water gap and absorber plates. The axial dimensions were set to a very large value so as to avoid the axial reflection simulation and to bring down the calculation time about 20%.

The compositions of TRIPOLI-4.2 calculations were taken directly from the benchmark. For case A there are only 4 compositions (fuel, fuel clad, water and water hole tube) but $3 \times 14 \times 14 + 1$ real volumes. Due to usage the new lattice geometry, the mixture of volume and composition was simplified and the total number of volumes in TRIPOLI-4.2 simulation is reduced to 7 for case A.

For the neutron source distribution an initial punctual source was placed in the center of the geometry. To optimise the statistics of neutron histories and to build up the user independent rejection process, the spatially optimal fission source distribution was automatically obtained from TRIPOLI-4.2 code [6] after the calculation was run about 20 cycles of 10000 neutron histories.

4 Calculation Results and Discussions

The results of this study are presented in Tab. 1. The upper part of the Tab. 1 shows the sample calculation results from ICSBEP Handbook. The TRIPOLI-4.2 calculation results are presented in the lower part of the table.

Table 1. The Infinite Multiplication Factors of CRISTO II Storage Arrays Benchmark

Case	Experiment Kinf (std. dev.)	TRIPOLI-4.1 (JEF2.2)	MCNP4B2 (ENDF/B-V)	MCNP4XS (ENDF/B-VI.r4)
A	1.1990 (0.0062)	1.2010 (0.0005)	1.2022 (0.0006)	1.2028 (0.0005)
B	1.1060 (0.0062)	1.1016 (0.0005)	1.1026 (0.0007)	1.1035 (0.0006)
C	0.8820 (0.0079)	0.8774 (0.0005)	0.8751 (0.0008)	0.8740 (0.0007)
D	0.8360 (0.0091)	0.8300 (0.0005)	0.8276 (0.0007)	0.8266 (0.0008)
E	0.8140 (0.0103)	0.8039 (0.0005)	0.8007 (0.0008)	0.8001 (0.0007)
Case				
		TRIPOLI-4.2 (JEF2.2) (Input: ICSBEP)	TRIPOLI-4.2 (JEF2.2) (Input: this study)	TRIPOLI-4.2 (ENDF/B-VI.r4) (Input: this study)
A		1.2001 (0.0003)	1.2008 (0.0003)	1.2018 (0.0003)
B		1.1025 (0.0003)	1.1026 (0.0003)	1.1029 (0.0003)
C		0.8753 (0.0003)	0.8762 (0.0003)	0.8743 (0.0003)
D		0.8290 (0.0003)	0.8307 (0.0003)	0.8286 (0.0003)
E		0.8023 (0.0003)	0.8027 (0.0003)	0.8001 (0.0003)

Generally a good agreement between experiments and calculations has been obtained as considering the experimental uncertainty (0.62 to 1.03%). Compar-

ing the results of TRIPOLI with those of MCNP, the largest difference of 0.59% in reactivity has been found for case E.

To examine the impact of the geometry modeling in TRIPOLI-4.2 code, two input files, one from published ICSBEP Handbook using old and tedious pin-by-pin description and another from this study using new lattice feature, were calculated. The results of TRIPOLI-4.2 (JEF2.2) using two different geometry modeling are in good agreement.

The results of TRIPOLI-4.1 (JEF2.2) and TRIPOLI-4.2 (JEF2.2) calculations are satisfactory and the old pin-by-pin input listings utilized in TRIPOLI-4.1 can be run perfectly with TRIPOLI-4.2. Using ENDF/B-VI.r4 library the results of TRIPOLI-4.2 and MCNP4XS codes are also in good agreement.

The impact of cross section libraries, JEF2.2 and ENDF/B-VI.r4, to results is very limited in TRIPOLI-4.2 calculations. Only in case E, a larger difference of 0.4% in reactivity was observed, probably due to cross sections of cadmium.

To evaluate the impact of the new lattice modeling and of the new 'Kcoll' collision estimator on the computer running time, three different TRIPOLI simulations using JEF2.2 library were run to compare the figure of merit (FOM), defined as $1/\sigma^2 t$, where σ is the relative error and t is the computer running time in seconds. The results of this study on FOMs are presented in Tab. 2.

Comparing with 'Kcoll' estimator utilized in TRIPOLI-4.1, the new one with regression on disparities of results was applied on TRIPOLI-4.2 calculations. The performance of the new 'Kcoll' estimator depends on the configurations of benchmark as comparing the FOMs presented on the first two columns of Tab. 2.

For cases A and B without absorber plate the FOMs using the new estimator are improved by three and two. For cases C, D and E with absorber plates the FOMs in TRIPOLI-4.2 calculations are only improved by 20% to 30%.

In fact the neutron coupling between storage arrays depends on the absorber plates introduced. In the water gap zone, the neutron spectra deform strongly and the gradient of thermal neutron flux is important as the absorber plate is introduced. That is why it is important to obtain the spatially converged fission source before to treat the statistics of neutron histories.

The impact of the new lattice modeling on FOM depends also on the configurations of benchmark as we compare the last two columns of Tab. 2. The degraded FOMs, from 22% in case B to 62% in case D, were obtained in all five cases when using the new lattice feature presented in this study. But comparing with the FOMs of TRIPOLI-4.1, this degradation of FOM due to new lattice modeling in TRIPOLI-4.2 was evidently compensated by using the new 'Kcoll' estimator.

Finally, it should be noted that the 1/4 fuel assembly model and 45 initial sources were applied in TRIPOLI-4.1 input which is taken from ICSBEP Handbook but one complete fuel assembly modeling and single punctual initial source were prepared in this study.

Table 2. The Comparison of FOM ($1/\sigma^2t$) between three TRIPOLI-4 calculations

Case	TRIPOLI-4.1 (Input: ICSBEP)	TRIPOLI-4.2 (Input: ICSBEP)	TRIPOLI-4.2 (Input: this study)
A	129	369	259
B	123	263	214
C	134	176	127
D	147	181	112
E	113	142	111

5 Conclusions

New lattice feature of TRIPOLI-4.2 code was successfully utilized to model the CRISTO II storage arrays of PWR UOX fuels. Comparing with TRIPOLI-4.1 calculations published in ICSBEP Handbook, the new lattice modeling and the improved criticality estimator 'Kcoll' in TRIPOLI-4.2 allow to shorten the length of input data from 18 pages to one page, to reduce the modeling-verification time and to improve the FOM of simulation.

The present study demonstrates the advantages of the new introduced features in TRIPOLI-4.2 on the criticality calculations of storage arrays. In the future investigation, it is interesting to evaluate the FOM of the pin power distribution in reactor whole core calculations with UOX and MOX fuels when practicing the new lattice modeling and the new lattice-flux-estimator in TRIPOLI-4.2.

References

1. Y. K. Lee et al.: 'Validation of Monte Carlo Code TRIPOLI-4 with PWR Critical Lattices by Using JEF2.2 and ENDF/B-VI Evaluations', In: *SNA1997, Saratoga Springs, NY, USA, Oct. 1997* pp. 253
2. Y. K. Lee et al.: 'CRISTAL, Criticality Safety Package Validation : TRIPOLI-4 Monte Carlo Code, JEF2.2 Library and ICSBEP Experiments', In: *ICNC'1999, Versailles, France, Sep. 20-24, 1999* pp. 1157
3. Y. K. Lee et al.: 'Application TRIPOLI-4 Monte Carlo Code on Nuclear Reactor Whole Core Calculations', to be published
4. A. Santamarina et al.: 'Storage Arrays of 3% Enriched LWR Assemblies: The CRISTO II Experiments in the EOLE Reactor' In: *Int. Handbook of Evaluated Criticality Safety Benchmark Experiments, NEA/NSC/DOC/(95)03/IV, Volume IV, LEU-COMP-THERM-041* Sep. 1999
5. J. P. Both et al.: 'A Survey of TRIPOLI-4'. In: *ICRS-8, Arlington, TX, USA, April 24-28, 1994*, pp. 373
6. Y. Penelieu et al.: 'Parallelization of the Monte Carlo Code TRIPOLI-4'. In: *M&C'99, Madrid, Spain, Sep. 27-30, 1999*, pp. 411

Current State of Monte Carlo Visualization Tools

R. Schwarz¹ and L. Carter²

¹ Pacific Northwest National Laboratory, Richland WA 99352, USA

² Carter M. C. Analysis, Inc., 6636 Hogan Dr. N., Keizer, Oregon 97303, USA

Abstract. The purpose of a Monte Carlo visualization tool is to aid in the generation of the input file while enabling the user to efficiently debug the input file and to optionally allow the user to display output information including random walks. This paper will provide an overview of three different aspects of Monte Carlo code visualization: 1) input file creation; 2) geometry visualization; and 3) output visualization. A brief description of some of the tools available in each area will be presented. However, the focus will be on the capabilities of the MCNP Visual Editor because it is the code most familiar to the authors.

1 Introduction

The most important aspect of a graphical user interface is how it aids the user in the creation of a Monte Carlo geometry along with the associated data cards. Several graphical user interfaces currently exist, including the MCNP Visual Editor [1,2] and SABRINA [3] (for MCNP) and the Criticality Safety Input Processor for Analysis (CSPAN) [4] (for KENO). Because input files are so complex, the tools used to help generate the input files need to be diverse enough to treat the complexities involved in the geometry. The tools also must address the most important input data.

A second important feature of a visualization tool for Monte Carlo codes is its ability to provide visual information about the geometry of the model. This can be done with two-dimensional plot views, such as in the KENO and MCNP codes themselves or VISAGE [5] (for MCBEND and MONK). Alternatively, advanced three-dimensional rendering tools exist such as KENO3D [6] (for KENO), SABRINA (for MCNP, MCNPX, and ITS ACCEPT), and VISTA-RAY [5] (for MCBEND and MONK). Two-dimensional visualization is better for interacting with the geometry, such as getting dimensional information. Three-dimensional visualization is better for gaining an appreciation of the complete model and may show errors not readily visible in a two-dimensional slice.

The third area of interest is the visualization of output data. This area probably has the fewest number of tools available, because output visualization is problem-dependent. The MCNP code package has a tally-viewing application interface, and MONK and MCBEND have VISTA-GRAPH [5] available for viewing results. Some tools available for displaying particle tracks are the MCNP Visual Editor and SABRINA (for MCNP, MCNPX, and ITS ACCEPT), and VISTA-TRACK [5] (for MCBEND and MONK).

2 Input File Creation Tools

Graphical user interfaces for Monte Carlo codes often focus on two-dimensional or three-dimensional rendering of the geometry after it has been created. However, most of the time required in generating a Monte Carlo input file is spent creating and debugging the input file. Currently only a few graphical user interface tools help in creating and debugging the input file.

For KENO, the CSPAN graphical user interface is available to aid in creation of the geometry and input data. Two new features of this code are the two-dimensional graphical depiction of the array input and the option to save the image to a bitmap file or copy to the clipboard to paste into another application.

For MCNP, two tools currently are in use for creating geometries – SABRINA and the MCNP Visual Editor. SABRINA uses body logic in the generation of a model. Thus, the user can define a cube by setting the origin and the distance to the sides of the cube instead of having to define the six surfaces of the cube.

The MCNP Visual Editor enables the user to create surfaces using two-dimensional views of the geometry and then define cells by indicating the surfaces that bound the cell. The Visual Editor provides complete support for MCNP geometries including universes and lattices. The Visual Editor also provides support for the most important data cards including transformations, importances, and materials.

A good graphical user interface will do more than just provide text boxes for data to be entered. It will provide helpful tools to aid in generating of the input file. One example of this in the Visual Editor is a lattice-creation feature that allows the user to create a hexagonal or rectangular lattice by specifying the pitch of the lattice and the number of rows in the lattice. The Visual Editor then will generate the surfaces for the lattice and the fill matrix.

Most graphical user interfaces are stand-alone codes. However, the MCNP Visual Editor is unique because it uses the Los Alamos National Laboratory (LANL) Fortran source code [7] for MCNP as the tool for reading the input file and generating the geometry plots and then adds C code to provide a graphical user interface. Currently, the Visual Editor consists of the LANL source code along with a 4,000-line Fortran patch code and 24,000 lines of C code for generating the graphical user interface. The interface can read any input file that can be read by the Monte Carlo code because they both use the same Fortran source code to read the input file. Also, support for universes and lattices in the MCNP Visual Editor was simplified by the availability of the Fortran source code to manipulate and display these more complex geometry features.

Another advantage of using the MCNP source code for the graphical user interface is that it is easier to upgrade the graphical user interface when the MCNP source code is modified or upgraded. For example, the addition of macro bodies to the Visual Editor was easier with the Fortran source code available than would have been possible if the Visual Editor had been a stand-alone C code.

MORITZ is a new program under development by White Rock Science [8] that will implement many of these features. The user can interactively create

surfaces, define cells, and assign materials and importances in several orthogonal 2D windows. Surfaces can be positioned with the mouse and/or exact coefficients typed in a dialog. In addition to supplying an absolute value for a coefficient, the user can supply an offset from another surface. Several choices of units are available. The 3D window displays the model and particle tracks using OpenGL, thereby taking advantage of hardware acceleration found in modern video cards. 3D window features include rotating, panning, and zooming with the mouse, persistent rotation, and cut planes.

3 Geometry Visualization Tools

A number of geometry visualization tools are available for Monte Carlo codes. Most codes have at least a two-dimensional plotter that can show cuts of the geometry. For MONK and MCBEND, VISAGE and VISTA-WIRE [5] can be used to generate two-dimensional views of the geometry. Both KENO and MCNP have a two-dimensional plotter included in the executable. Sabrina also offers a 2D plotting option for MCNP and solid body geometries. The MCNP Visual Editor uses the same MCNP two-dimensional plot mechanism to provide an interface between the user and the code. This method enables the user to easily modify the input file using the graphical user interface.

Advanced three-dimensional visualization tools are also available, such as KENO3D (for the KENO code), SABRINA (for MCNP, MCNPX, and ITS ACCEPT), and VISTA-RAY (for the MONK and MCBEND codes). All three of these packages have the capability to generate impressive three-dimensional images of the Monte Carlo geometry and provide tools to cut away pieces of the geometry for cut-away views.

The greatest advantage to the user is when the geometry visualization package has been linked to the input generation package so that the user is provided immediate feedback when generating a Monte Carlo geometry. Currently, most of the advanced three-dimensional rendering codes are capable of displaying partial Monte Carlo geometries and have a method to display geometry errors to provide useful information for debugging complex geometries. However, the user typically must make modifications to the input file and then execute the geometry visualization package to display the geometry, which can be cumbersome if many changes are required.

For MCNP input files, the MCNP Visual Editor is available to create or modify input files. The user can select cells or surfaces directly from the plot on the screen and can modify them, and the plot will be updated immediately to show the modifications.

Monte Carlo geometry visualization tools are helpful in the independent verification of input files. In the MCNP Visual Editor, dimensions can be obtained directly from the plot and the user can display dimensions in either centimeters or inches and has a tool to display the distance between two surfaces. A significant amount of information can be obtained directly from the plot to determine if dimensions and material compositions are correct.

4 Output Visualization Tools

Currently, very few applications exist for output visualization, because the type of output visualization required is dependent on the problem. In terms of general output data, MCNP has a tally-display option, and MONK and MCBEND have the VISTA-GRAPH application to display output data. MCNPX offers tallies of various quantities on a grid (a grid tally patch is available for MCNP); a postprocessor shipped with MCNPX converts the grid tallies to input files for PAWS, IDL, and TEKPLOT.

Some of the more advanced Monte Carlo graphical user interfaces such as VISTA-TRACK for MCBEND and the Visual Editor and SABRINA for MCNP can display particle track information. SABRINA can display the tracks superimposed over a three-dimensional geometry. Sabrina has numerous filters and options for selecting which tracks to display. A pruning option deletes branches of a history that do not reach selected cells or surfaces. Sabrina can write filtered and pruned particle track files. Both VISTA-TRACK and the Visual Editor display the tracks superimposed over a two-dimensional geometry.

Because the MCNP Visual Editor has access to the MCNP source code, it can run particles in exactly the same manner as the code itself runs the particles. Instead of drawing tracks, the MCNP Visual Editor draws points to indicate user-defined events that occur in the transport process. Thus, the user can choose to display the source, collision points, surface crossings, or tally crossings. Additional options allow the display of only those tracks that contribute to a tally, which allows the user to visualize the effectiveness of the biasing used in the input file.

For KCODE calculations, the source points for specified cycles can be displayed to show how the source is propagating between different cycles. In addition, the user can choose to run the KCODE calculation and show collision points or other transport data.

Other output visualization capabilities for Monte Carlo codes have been built for specific applications. One example [9] is a dose rate calculation tool that displays contour plots of MCNP-calculated dose rates for a changing source and geometry configuration. A user interface was then developed to allow the engineer to identify locations in the application where people will be present and then run the animation to calculate their accumulated dose rates to ensure that they are as low as reasonably achievable (ALARA). Most of these problem-specific applications rely on advanced graphical tools to display data generated by the Monte Carlo code.

5 Conclusions

The ideal visualization tool of the future should combine all three aspects of visualization: the creation of the input file; the display of the geometry and interaction with the geometry; and the display of output information. It should aid in the generation of the input file, providing debugging information as the

file is created so that errors can be fixed as they occur. It should allow the user to optionally display a three-dimensional plot of the geometry for an overview of the model, and it should be able to display particle tracks and output tally data. Current development efforts on the MCNP Visual Editor and other Monte Carlo tools are directed toward this goal.

In general, the visualization capabilities available for nuclear Monte Carlo codes lag behind the industry standard for visualization available for other disciplines. Much more advanced tools are available to mechanical, aeronautics, and chemical engineers. Part of the problem is that the nuclear community is very small, and most of the visualization development is done as an independent effort. In addition, little funding is available for the development of visualization tools, so developers must either sell their visualization tools or find a dedicated funding source.

Because the MCNP Visual Editor uses the LANL source code, it is available through the same distribution centers (Radiation Safety Information Computational Center (RSICC) in Oak Ridge and the Nuclear Energy Agency in France) as the MCNP computer code. KENO3D and CSPAN are also available from RSICC. The MONK and MCBEND codes are available from AEA Technology. Sabrina is available from White Rock Science.

References

1. Oak Ridge National Laboratory: *A Visual Editor for Creating MCNP4A Input Files* (Radiation Safety Information Computational Center, PSR-358, Oak Ridge National Laboratory, Oak Ridge Tennessee)
2. Pacific Northwest National Laboratory: *Visual Editor for MCNP* (Available URL: <http://www.pnl.gov/eshs/software/ved.html>)
3. K.A. Van Riper: *Sabrina: Visualization in Support of MCNP* (available URL: <http://www.rt66.com/kvr/sabrina/sabrina.html>)
4. Oak Ridge National Laboratory: *CSPAN Preview* (available URL http://www.cped.ornl.gov/scale/cspan_screens.html)
5. AEA Technology: *The ANSWERS Software Service* (available URL <http://www.aeat.co.uk/answers/>)
6. Oak Ridge National Laboratory: *A Visualization Tool for KENO V.A Geometry Models, Version 1.0* (Radiation Safety Information Computational Center, PSR 450, Oak Ridge National Laboratory, Oak Ridge Tennessee)
7. J.F. Briesmeister: *MCNP - A General Monte Carlo N-Particle Transport Code* (Los Alamos National Laboratory, LA-12625-M, Version 4B, March 1997)
8. K.A. Van Riper: *White Rock Science* (available URL <http://www.rt66.com/kvr>)
9. R.A. Schwarz, D.E. Bullock, J. Greenborg: 'ALARA Calculations Using Interactive Visualization Tools'. In: *Proceedings of the 1996 Topical on Radiation Protection and Shielding*, (American Nuclear Society, La Grange Park, Illinois 1996) Vol. 2, pp. 1004-1011

Conceptual Designing of a Reduced Moderation Pressurized Water Reactor by Use of MVP and MVP-BURN

T. Kugo

Department of Nuclear Energy System, Japan Atomic Energy Research Institute,
Tokai-mura, Ibaraki-ken, 319-1195, Japan

Abstract. A conceptual design of a seed-blanket assembly PWR core with a complicated geometry and a strong heterogeneity has been carried forward by use of the continuous-energy Monte Carlo method. Through parametric survey calculations by repeated use of MVP and a lattice burn-up calculation by MVP-BURN, a seed-blanket assembly configuration suitable for a concept of RMWR has been established, by evaluating precisely reactivity, a conversion ratio and a coolant void reactivity coefficient in a realistic computation time on a super computer.

1 Introduction

Concepts of advanced water-cooled reactors suitable for the future have been investigated at JAERI [1–3]. They are named RMWR with the high conversion ratio around 1.0 by using MOX fuel. Such a high conversion ratio can be attained by reducing the core water volume in general. Another design goal is the negative void reactivity coefficients for an inherent safety. In general, there is a trade-off relation between achievement of a high conversion ratio and a negative void coefficient. Therefore, it is required to estimate precisely core characteristics in core designs of RMWRs.

As one of RMWRs, we have investigated a seed-blanket assembly core concept [4]. It has a seed fuel pin bundle surrounded by a blanket fuel as shown in Fig. 1 (see also Fig. 4). In the present design, to improve the conversion ratio, we adopt a more tight lattice for the blanket fuel than that of the seed fuel. To reduce effectively the void reactivity coefficient, some surrounding blanket fuel rods are replaced by $\text{ZrH}_{1.7}$ rods. A blanket fuel region called the internal blanket is axially inserted and divides a seed core region into an upper and a lower seed core regions. Thus, the present core has a complicated geometry and a variety of neutron spectra. So, it seems difficult to evaluate precisely core characteristics by conventional deterministic transport codes.

In these days, lattice burn-up calculations based on the continuous-energy Monte Carlo method has become possible within a realistic computation time [5]. The continuous-energy Monte Carlo method is very useful for the special burn-up problems in which we have few experiences or the problems which are difficult to be treated by conventional deterministic neutron transport codes.

In the present work, we used MVP [6,7] and MVP-BURN [5] as design tools for a conceptual design of the seed-blanket assembly core. First, parametric

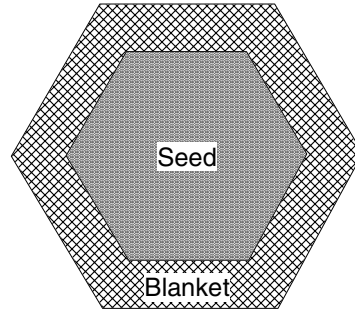


Fig. 1. Schematic view of seed-blanket assembly configuration

survey calculations with MVP have been done to establish an assembly configuration, that is, the numbers of layers of seed fuel and blanket fuel rods, the enrichment of the seed fuel and the number of the $\text{ZrH}_{1.7}$ rods. Then, a lattice burn-up calculation with MVP-BURN for a promising assembly configuration decided from the result of the survey calculations has been done.

2 Analysis Method

The MVP [6,7] code is employing a fast computation algorithm suitable for recent vector and/or parallel computers. The speed-up factor of ten or more is realized on such super-computers by MVP as compared with other scalar Monte Carlo codes. Therefore, MVP mitigates the large computation time required for the repeated use of a Monte Carlo code. The cross section libraries have been prepared from JENDL-3.2 [8]. Those at arbitrary temperature points are immediately produced from the existing libraries by a utility program or MVP itself. A simplified burn-up chain model has been used for MVP-BURN analyses. It treats 19 heavy nuclides and 30 fission products including 4 pseudo ones. This chain model was validated in typical burn-up analyses for light water reactors.

3 Specification of Seed-Blanket Assembly

This investigation has employed a seed fuel rod specification as follows; the outer diameter of 9.5 mm, SS-316 as a cladding materials, the cladding thickness of 0.4 mm, the pellet diameter of 8.6 mm and the gap width of 1.0 mm between rods. As for the surrounding blanket fuel rod, the outer diameter of the blanket fuel rod and pellet are approximately 15.0 mm and 13.0 mm, respectively. The assembly has a wrapper tube with the thickness of 1.0 mm at the border between seed and blanket fuel regions.

4 Parametric Survey Calculations by MVP

Parameter surveys have been performed with the initial fuel condition for (1) the assembly configuration, that is, the number of layers of seed fuel rods and blanket fuel rods, and the seed fuel enrichment and (2) the number of $\text{ZrH}_{1.7}$ rods. We have employed an infinite lattice of the assemblies as a calculation model. Survey calculations have been done by MVP with 500,000 histories (10,000 particles \times 50 batches; plus initial 10 batches skipped from tally). The standard deviations for the reactivity and void reactivity coefficient are within $0.1\% \Delta k$ and 2 pcm/%-void, respectively. Required computation time is about a quarter and a half hour for an un-voided or voided condition, respectively, on the FACOM VPP-500.

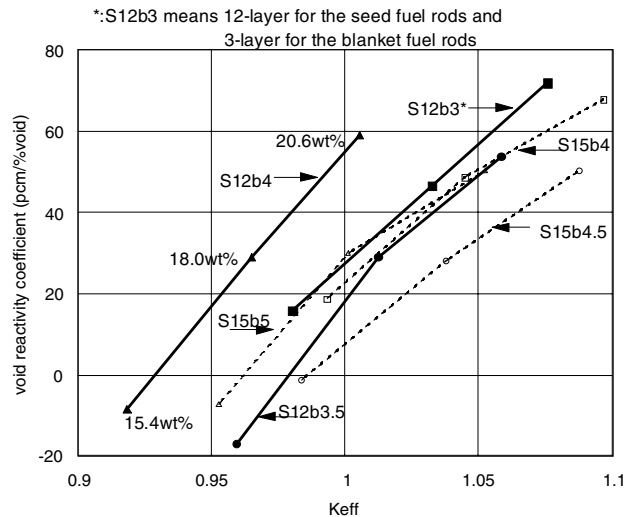


Fig. 2. Relation of initial k-effs and void reactivity coefficient of various seed-blanket assembly configurations

First, the result of survey calculations on the assembly configuration and the seed fuel enrichment, i.e. the Pu fissile enrichment, is presented. The number of layers of the seed fuel rods is considered as 12 or 15. The number of layers of the surrounding blanket fuel rods is three, three and a half or four for the assemblies of 12-layer seed fuel rods. For the assemblies of 15-layer seed fuel rods, it is four, four and a half or five. The seed fuel enrichment ranges from 15.4 wt% to 20.6 wt%. The total core height and the number of $\text{ZrH}_{1.7}$ rods are fixed as 200 cm (2×100 cm) and zero, respectively. Figure 2 shows a relation of k-eff and void reactivity coefficient at the initial fuel condition. From the figure, the best combination of layers is 15 and 4.5-layers for the seed and blanket fuel rods, respectively.

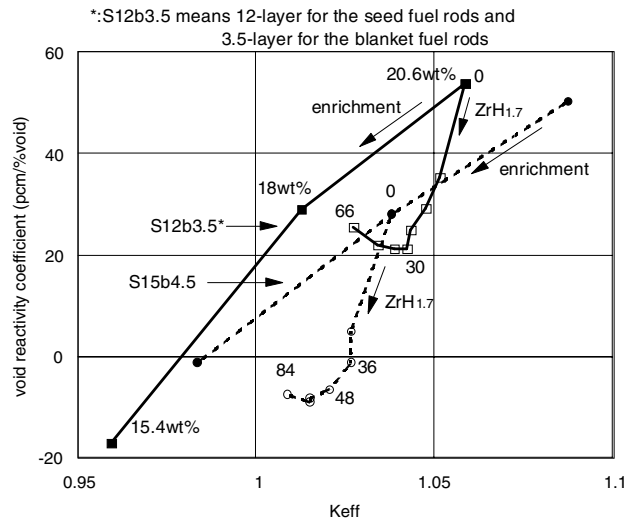


Fig. 3. Relation of initial k-effs and void reactivity coefficient of various number of $\text{ZrH}_{1.7}$ rods

Second, the result of survey calculations on the number of $\text{ZrH}_{1.7}$ rods in the surrounding blanket region is presented. The number of $\text{ZrH}_{1.7}$ rods ranges from zero to 84. The assembly configurations considered are of 12 and 3.5-layers and 15 and 4.5-layers for the seed and blanket fuel rods, respectively. The seed fuel enrichment is 20.6 wt% and 18.0 wt% for the configurations of 12 and 3.5-layers and 15 and 4.5-layers, respectively. The total core height is fixed as 200 cm (2×100 cm). Figure 3 shows a relation of k-eff and void reactivity coefficient on the number of $\text{ZrH}_{1.7}$ rods at the initial fuel condition together with that on the seed fuel enrichment. From the figure, introduction of $\text{ZrH}_{1.7}$ rods in the blanket region is more advantageous than reduction of the seed fuel enrichment to reduce the void reactivity coefficient. However, the void coefficient will not be reduced any more over 30 and 48 $\text{ZrH}_{1.7}$ rods for the assembly configurations of 12 and 3.5-layers and 15 and 4.5-layers, respectively. These numbers of $\text{ZrH}_{1.7}$ rods correspond to approximately 15% of that of the blanket fuel rods.

5 Burn-up Characteristics by MVP-BURN

From the result of the above survey calculations, we have tentatively established an assembly specification. Figure 4 shows a horizontal structure of the seed-blanket assembly. We choose a 15-layer for the seed fuel rods and a 4.5-layer for the blanket rods. This combination is most preferable from the viewpoint of the reactivity coefficient. The most outer blanket fuel rods commonly belong to neighboring assemblies. The Pu fissile enrichment of the seed fuel is 18 wt%. The 36 $\text{ZrH}_{1.7}$ rods per the assembly are scattered in the surrounding blanket

region. The axial blankets of 25 cm height are set on and beneath the seed core regions. The fuel loading length is a 3-cycle. A thermal power per assembly is defined so as to generate 1,200 MWe with an equivalent core diameter of 5.0 m.

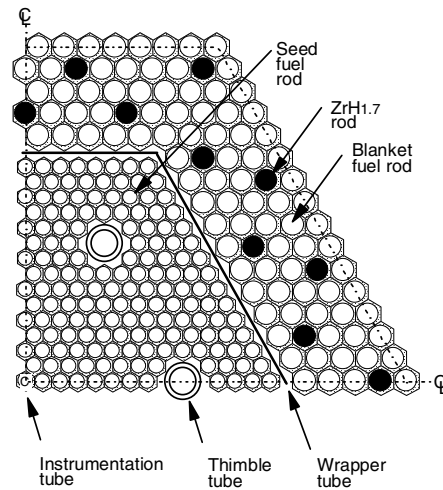


Fig. 4. Configuration of seed-blanket assembly

The burn-up characteristics have been evaluated with the infinite lattice of assemblies by MVP-BURN; the burn-up calculation version of MVP. The burn-up calculation was carried out with about 10 burn-up zones in the whole assembly. The history has been taken as 500,000 per burn-up step (10,000 particles \times 50 batches; plus initial 10 batches skipped from tally). The standard deviations for the reactivity, void reactivity coefficient and conversion ratio are within $0.1\% \Delta k$, 2 pcm/%-void and 0.01, respectively. Computation time is about a half or one hour for an un-voided or voided condition per burn-up step. Figure 5 shows the main burn-up characteristics. In this evaluation, we assume the reactivity loss of $2\% \Delta k$ for a whole core being supposed to employ an out-in fuel shuffling pattern compared with the infinite lattice of assemblies. From the figure, it is found that the k_{eff} value is 1.02 at 36 EFPDs. We assume a 3-cycle for the fuel loading length in the present work. Therefore, this core will achieve 18 EFPDs as the cycle length and 54 EFPDs for the fuel loading length. Integrated conversion ratio is about 0.98 after 54 EFPDs. The reactivity increases $2\% \Delta k$ at the early burn-up. This burn-up behavior is preferable to the reactivity control. In addition, the void reactivity coefficient oppositely decreases 15 pcm/%-void at the early burn-up. It is expected that void reactivity coefficient will be kept negative through the whole operation cycle under the 3-batch refueling scheme, although the void reactivity coefficient is positive at the beginning and end of life. Thus, the seed-blanket assembly shows very preferable characteristics.

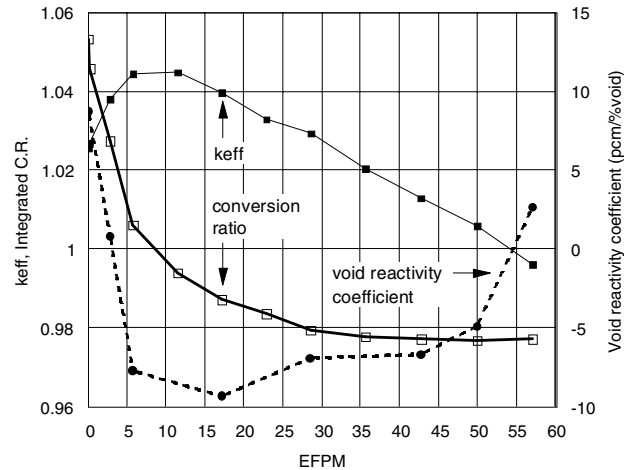


Fig. 5. Burn-up characteristics of seed-blanket assembly

6 Conclusion

A conceptual designing of the seed-blanket assembly core has been carried forward by use of the continuous-energy Monte Carlo method. Through parametric survey calculations by repeated use of MVP and a lattice burn-up calculation by MVP-BURN, a seed-blanket assembly configuration suitable for a concept of RMWR has been established, by evaluating precisely reactivity, a conversion ratio and a coolant void reactivity coefficient in a realistic computation time. More detailed investigation is necessary for the feasibility of the concept of the seed-blanket assembly PWR core. In the future, we will carry out optimization of a seed fuel enrichment distribution in the assembly and a fuel-shuffling pattern to flatten a power peaking, and a control rod arrangement to ensure a cold shutdown, by evaluating a power distribution and a control rod worth in an assembly and a whole core calculations by use of MVP and MVP-BURN.

References

1. T. Iwamura, et al.: JAERI-Research 99-058 (1999)
2. T. Okubo, et al.: *Proceedings of ICONE 8*, #8422 (2000)
3. K. Hibi, et al.: *Proceedings of ICONE 8*, #8423 (2000)
4. EPRI: EPRI NP-2176, Project 712-1 Final Report (1981)
5. K. Okumura, et al.: *J. Nucl. Sci. Technol.* **37**, 128 (2000)
6. T. Mori, M. Nakagawa, M. Sasaki: *J. Nucl. Sci. Technol.* **29**, 325 (1992)
7. M. Nakagawa, T. Mori: *J. Nucl. Sci. Technol.* **30**, 692 (1993)
8. T. Nakagawa, et al.: *J. Nucl. Sci. Technol.* **32**, 1259 (1995)

The Role of Graphical Supporting Tools for Monte Carlo Analysis

M. Armishaw, A. Bird, H. Crofts, and N. Smith

The ANSWERS Software Service, AEA Technology plc, Winfrith Technology Centre, Dorchester, Dorset DT2 8ZE, United Kingdom

Abstract. The increasing power of computer systems continues to give users of the Monte Carlo method the ability to model complex three-dimensional systems in ever greater detail. In support of this more exacting use of the Monte Carlo method, three requirements have been identified:

- The need to demonstrate the validity of the geometry models employed;
- The need to easily interpret large volumes of calculation output;
- The need to prepare calculation data from a range of available options.

The graphical tools summarised in this paper have been developed to address these requirements and are designed for use with the MONK and MCBEND Monte Carlo codes [1] for criticality/reactor physics and radiation shielding/dosimetry/general radiation transport applications respectively. All codes described in this paper are licensed and actively supported in use by the ANSWERS Software Service of AEA Technology, with the development of several of the codes continuing within a partnership between AEA Technology and BNFL.

1 Background

The Monte Carlo method is ideally suited to analysing complex three-dimensional systems. This capability has been exploited in many codes and the increasing power and availability of desktop computer systems over the last decade has enabled the user to model ever more complex systems in greater detail. An unfortunate side-effect is the rise in the likelihood that errors are introduced into a model, some that cause the code to fail and others that do not. A typical example of an error that causes the code to fail is when the content of a region of the model remains undefined by the user (i.e. there is no material allocated to it). The opposite effect is when the content of a region is ambiguous, such that two or more materials have been allocated to the same volume; these are referred to as multiply defined regions. An error that does not cause the code to fail is when components are legitimately entered but misplaced within the model (i.e. the model is acceptable to the code but not as the user intended). Other examples of potential problems that need to be checked include ensuring that the specified source geometry is located correctly, and, where the user has overlaid an independent three-dimensional splitting/roulette mesh (as used in MONK and MCBEND), that it also is correctly positioned. These requirements for model verification have led to the development of a range of graphical tools: VISAGE, VISTA-RAY, VISTA-MOVIE and VISTA-WIRE.

The increasing range of options available within a typical Monte Carlo code for scoring results can mean that the user can be inundated with tables of numbers to be analysed (e.g. flux or dose-rates in many regions, in many energy groups). An option exists in MONK and MCBEND to enable the user to control the quantity and order of these data, principally for aiding their transfer to a spreadsheet. In addition, VISTA-GRAPH has been developed to provide a linked graphical facility for MONK and MCBEND to view selected results graphically. A further consideration in output analysis is to verify the adequacy of the Monte Carlo sampling performed. In-built sampling analysis exists in both MONK and MCBEND to assist with the identification of such problems. In addition, use can be made of VISTA-TRACK for displaying and selectively analysing the location of selected tracks overlaid on an image of the geometry model.

Turning to the selection of calculation requirements, increasing emphasis is now placed on cross-checking, for example by the use of alternative nuclear data libraries. In the case of MONK and MCBEND, a range of nuclear data libraries are available (UKNDL, JEF2.2, JENDL3.2, ENDF/B-VI) and the task of selecting and assigning appropriate versions of these files can be a source of error. Correct matching of physics code and graphical tool is clearly a further pre-calculation requirement, as is the assignment of additional files needed for the particular calculation. These problems have been addressed by the development of LAUNCHPAD, an intelligent graphical tool that searches through the user's input and identifies all the files required. Where two or more valid choices are available these will be put into a list for user selection.

This paper reviews the role of these supporting tools for use with MONK and MCBEND to address the three requirements of geometry verification, output analysis and calculation preparation.

2 VISAGE

VISAGE provides the user with the capability for interactively viewing two-dimensional slices through a geometry model (see Fig. 1). The images are produced using the same tracking processes that are used in the corresponding Monte Carlo codes and ensures VISAGE displays exactly what the code will track through. This use of the Monte Carlo tracking processes allows VISAGE to identify multiply defined or undefined regions in the model (see Fig. 2) as they would be processed during a MONK/MCBEND calculation. The facility to display the material or zone at any point on the image allows the user to identify quickly the offending components and rectify their model.

When the geometry model is complete it is useful to check the placement of the components in the model. VISAGE provides the user with the capability to use the mouse pointer both to identify the co-ordinates of any point on the image, and to measure the distance between two selected points. These features allow the user to check their model for inaccuracies. Where there is fine detail to be inspected, the option to zoom in on selected parts of the image prior to measuring the component placement is available. To check the model thoroughly

it is necessary to draw several slices through the model perpendicular to each of the axes to ensure that all the components are positioned correctly. VISAGE provides a range of options to simplify the process of generating multiple slices, easing the task of checking the model.

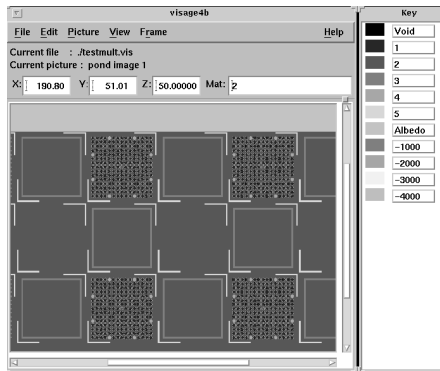


Fig. 1. Main VISAGE screen and colour map

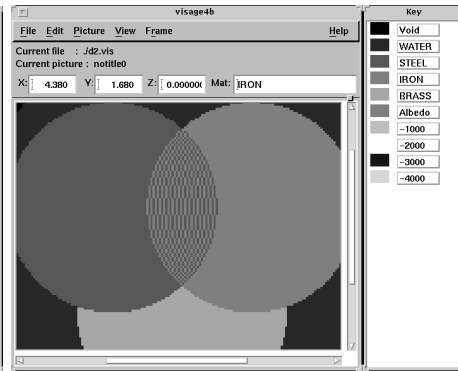


Fig. 2. Multiply defined region (dithered area)

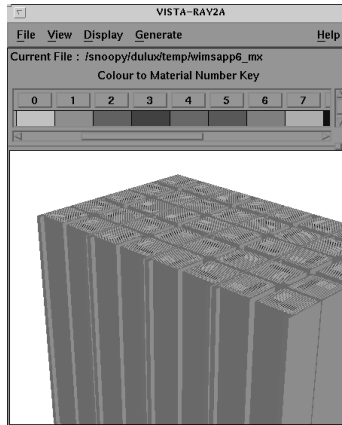
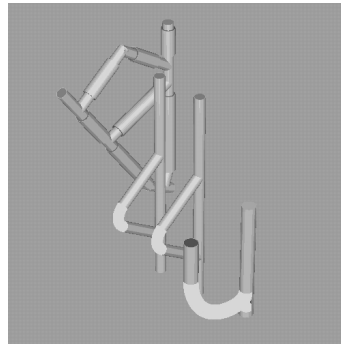
Both MONK and MCBEND allow the source locations to be defined independently of the geometry definition. Similarly an independently defined splitting/roulette mesh can be overlaid on the geometry. The need to check the location of both of these components has led to the requirement for an option to enable them to be overlaid on the image from the geometry data so their placement can be verified.

The above range of options make VISAGE the front-line visualisation and verification tool used with MONK and MCBEND. Through its use the user can increase their confidence in the model and can rapidly provide verification data for Quality Assessment purposes.

3 VISTA-RAY

The two-dimensional slices produced by VISAGE do have some limitations. The main ones are that many slices can be required to image enough of the model before the user can be confident it is correct, and that it can sometimes be difficult in a two-dimensional slice to check the relative position of arbitrarily placed components. The development of VISTA-RAY (Fig. 3) overcomes these limitations by providing the user with the capability to interactively view three-dimensional images of the geometry model.

As in VISAGE, the images are produced using the same tracking processes as are used in the Monte Carlo codes, but in this case they provide a three dimensional ray-tracing capability. The ray-tracing process tracks a series of lines, one for each point on the image, from the user's viewpoint to the image. The

**Fig. 3.** VISTA-RAY Main window**Fig. 4.** Arrangement of pipes

angle between the track and the surface normal is used to apply shading to the surface, thus highlighting its angle or curvature. By changing the user's viewpoint the image can easily be manipulated and the component placements checked. The option to zoom in (Fig. 4) on small components is available. Selected materials can be made transparent if it is necessary to allow inspection of components buried within the model. An alternative to transparent materials is the cutaway, that allows the user to selectively remove sections of their model and inspect the internal arrangement of the components.

The three-dimensional images produced by VISTA-RAY have proved useful in increasing the confidence that components are correctly positioned within the model.

4 VISTA-MOVIE

Experience has shown that most users view their models from several different viewpoints when using VISTA-RAY. This led to the development of VISTA-MOVIE which provides the capability for automatically generating a series of three-dimensional images from a moving viewpoint through the model (animated GIFs). These images are then displayed sequentially (using either a web browser or GIF-viewer) to give the impression of moving either through or around the model.

The input required from the user to generate these images can be as little as giving the start and end co-ordinates of a track. For a more complex animation several intermediate points can be specified to give a complete journey through and around the model. The viewpoint is not the only item that can be varied between images. Any co-ordinate used by VISTA-RAY can be changed from image to image, such as the location of cutaway planes. By changing the cutaway plane position from image to image it is possible to slice through the model in consecutive images and view the models interior.

5 VISTA-WIRE

VISAGE and VISTA-RAY both use the Monte Carlo tracking processes to determine what should be displayed and where. This can sometimes be time-consuming if fine detail is required. In many cases a wire frame representation of the geometry is adequate to check the component positions. This led to the development of VISTA-WIRE, which displays a wire frame representation of the geometry model. The speed of VISTA-WIRE enables component location and orientation to be quickly verified and can provide a convenient starting point for more detailed visualisation using the other VISTA package components.

6 VISTA-TRACK

There are occasions where a calculation has been done but there is some question about the results, perhaps they do not agree with the expected values. In these cases it is useful to be able to inspect the Monte Carlo tracking process itself. This might be to ensure that the splitting/roulette mesh is not inappropriate and caused over splitting, or that many sources of different strengths and source spectra have been used and the user wishes to ensure that they have been sampled correctly in space and energy. These requirements led to the development of an interactive graphical tool for displaying particle histories, VISTA-TRACK, which overlays the selected particle tracks on a background image generated by VISAGE.

7 VISTA-GRAPH

The output from a MONK or MCBEND case is text based and often comprises several large tables of values such as flux or dose-rate by region and energy group. The default format for these tables is not always appropriate for the user so VISTA-GRAPH was developed to provide a rapid interactive tool for displaying selected results graphically. VISTA-GRAPH itself enables the creation of custom output suitable for pasting directly into reports.

8 LAUNCHPAD

The minimum data required to run a typical Monte Carlo calculation comprises a nuclear data library, the user's input file and an output file for the results. More typically there will be additional thermal data, gamma production data, and perhaps a dump file for continuing the run later if necessary. For both MONK and MCBEND there is a range of neutron data libraries to choose from, each with its corresponding thermal library. A further need is to ensure that matching graphics and Monte Carlo code versions are employed. These requirements have led to the development of a graphical tool to aid the user in assembling the files required for their Monte Carlo calculation.

The tool is called LAUNCHPAD and provides a graphical user interface through which all of the analysis and graphical tools can be launched. The first step is to select the Monte Carlo code and input file to be used. LAUNCHPAD scans the input file and determines which data library type (e.g. neutron or gamma) and other channel connections are required for the selected code. When the scan is complete the required files are displayed on the main screen of LAUNCHPAD (see Fig. 5).

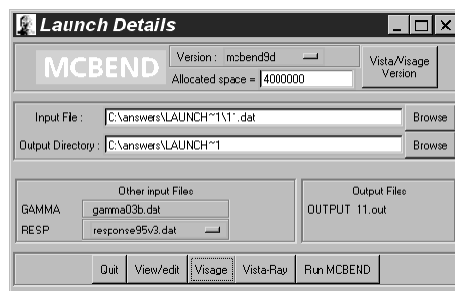


Fig. 5. LAUNCHPAD main window with MCBEND selected

Where appropriate, a list of possibilities will be presented to the user from which to select (e.g. neutron data library from JEF2.2, UKNDL, ENDF/B-VI, JENDL3). On completion of the calculation, the output can be viewed in a browser or the results processed using one of the VISTA post-processing packages, also started from within LAUNCHPAD.

9 Summary

This paper has reviewed a range of supporting graphical tools for the Monte Carlo codes MONK and MCBEND that have been developed and refined over a number of years. These tools enable Monte Carlo models to be verified, executed and analysed with significantly increased confidence. This not only increases the efficiency of the analysis but also reduces the scope for error, a major consideration in all nuclear operators.

References

1. N.R. Smith et al: 'The Current Status and Future Plans for the Monte Carlo Codes MONK and MCBEND'. These Proceedings p. 637

Simulating Variable Source Problems via Post Processing of Individual Particle Tallies^{*}

D.L. Bleuel^{1,2}, R.J. Donahue¹, B.A. Ludewigt¹, and J. Vujic²

¹ Lawrence Berkeley National Laboratory, Berkeley CA, 94720, USA

² University of California at Berkeley, Berkeley CA, USA

Abstract. Monte Carlo is an extremely powerful method of simulating complex, three dimensional environments without excessive problem simplification. However, it is often time consuming to simulate models in which the source can be highly varied. Similarly difficult are optimization studies involving sources in which many input parameters are variable, such as particle energy, angle, and spatial distribution. Such studies are often approached using “brute force” methods or intelligent guesswork. One field in which these problems are often encountered is accelerator-driven Boron Neutron Capture Therapy (BNCT) for the treatment of cancers.

Solving the reverse problem of determining the best neutron source for optimal BNCT treatment can be accomplished by separating the time-consuming particle-tracking process of a full Monte Carlo simulation from the calculation of the source weighting factors which is typically performed at the beginning of a Monte Carlo simulation. By post-processing these weighting factors on a recorded file of individual particle tally information, the effect of changing source variables can be realized in a matter of seconds, instead of requiring hours or days for additional complete simulations. By intelligent source biasing, any number of different source distributions can be calculated quickly from a single Monte Carlo simulation. The source description can be treated as variable and the effect of changing multiple interdependent source variables on the problem’s solution can be determined. Though the focus of this study is on BNCT applications, this procedure may be applicable to any problem that involves a variable source.

1 Introduction to BNCT

BNCT is a cancer treatment modality primarily aimed at *glioblastoma multiforme* (GBM), a non-localized malignant tumor growth in the brain. Because GBM is not confined to a single tumor mass, it is impossible to remove completely by surgery, and conventional radiation treatments and chemotherapy are highly ineffective.

To treat GBM or other cancers, BNCT utilizes a binary method. The first step involves administering a cancer-seeking pharmaceutical that has been loaded with ^{10}B . An ideal drug is harmless to the patient and is absorbed in cancerous cells far more selectively than in normal tissue cells. The second step is irradiation of the patient by a soft neutron beam. ^{10}B has a very high thermal

^{*} Supported by the U.S. Department of Energy under Contract No. DE-AC03-76SF00098.

neutron capture cross section of 3830 barns and decays immediately into high LET particles via a $^{10}\text{B}(n, \alpha)^7\text{Li}$ reaction, as well as a 480 keV γ ray in 93% of the reactions. The energy of the combined high LET particles is largely confined within the diameter of a single cell, about 10 μm , thus targeting a large radiation dose preferentially to malignant cells without significantly irradiating healthy tissue. Because BNCT is a binary therapy, advances in both boron delivery and in neutron beam shaping are important to improving the quality of treatment.

Many different neutron sources have been proposed or used for BNCT. Two primary sources considered have been reactor sources and accelerator sources. Feasibility of an accelerator-based BNCT facility has been studied at Lawrence Berkeley National Laboratory and extensively compared to several existing reactor sources [1]. The accelerator would produce neutrons via the $^7\text{Li}(p, n)^7\text{Be}$ reaction at proton energies at about 2.5 MeV, which produces a high neutron yield as well as a low maximum neutron energy. Epithermal neutrons in the range of about 2 keV - 20 keV are most desirable [2] for BNCT. Slower neutrons do not penetrate far into the brain, where treatment is most difficult, and faster neutrons are largely absorbed in hydrogen at shallow depths.

2 Neutron Beams

The spectra of several different neutron beams that have been evaluated are seen in Fig. 1, demonstrating that there can be large differences in energy distribution for different beams, each of which leads to a different dose distribution in the brain. A wide variety of different spectra can be produced by various neutron sources (eg: reactors, accelerators tuned to different proton energies or utilizing different target materials) and various moderator assemblies. The clinical efficacy of each spectra must be evaluated by extensive Monte Carlo modelling with a program such as MCNP [3]. Generally, this is done in a two-step process. The first step involves modelling the neutron beam through a filter assembly [4] to determine the spectrum that will be applied to the patient, such as depicted in Fig. 1. The second step models this neutron beam emerging from the filter through an assumed patient phantom geometry to determine radiation dose distributions in the brain.

When modelling neutron beams in a head phantom, four primary reactions must be considered: Thermal neutrons produce the so-called nitrogen dose (D_N) through the $^{14}\text{N}(n, p)^{14}\text{C}$ reaction and the very important boron dose (D_B). Thermal neutrons are also the main contributor to the γ dose (D_γ) via the $^1\text{H}(n, \gamma)^2\text{H}$ reaction, though external γ contamination is also important to consider. For higher neutron energies (> 1 keV), recoil protons dominate the tissue dose. The hydrogen dose (D_H), primarily due to proton-recoil reactions, is strongly dependent on the energy spectrum of the neutron beam. Optimizing neutron beams for treatment is primarily a matter of designing neutron sources, moderators, and filters to produce a spectrum which limits the unwanted “background” doses (primarily D_H , but also D_N and D_γ) while maximizing the pen-

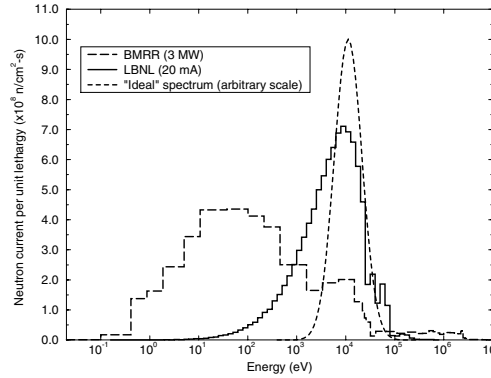


Fig. 1. Neutron energy spectra for the BMRR beam, an LBNL accelerator-based design, and an “ideal” spectrum which produces the greatest tumor dose at the brain midpoint as determined from extensive Monte Carlo optimization

etration of the beam and maintaining a high enough dose rate to treat in a reasonable amount of time.

3 Dose Calculation

The total effective dose to either tumor or healthy tissue is calculated by adding these different dose components, multiplied by appropriate weighting factors to obtain the total photon equivalent dose (D_{tot}) in Gray-equivalent (Gy-eq) units:

$$D_{tot}(x) = CF \cdot D_B(x) + RBE_N \cdot D_N(x) + RBE_H \cdot D_r(x) + RBE_\gamma \cdot D_\gamma(x) \quad (1)$$

Doses, which vary with depth (x) in the phantom, are multiplied by relative biological effectiveness (RBE) factors or, in the case of the boron dose, a compound factor (CF) which reflects both the boron RBE and compound specific properties. In LBNL optimization studies, the dose calculation protocol [5] developed for BNCT clinical trials at the Brookhaven Medical Research Reactor has been applied, with boron concentrations and compound factors for the boron compound boronphenylalanine (BPA) used.

These doses are calculated in small cylindrical tally volume cells (0.4 cm x 0.25 cm radius) along the neutron beam centerline in a modified Synder head phantom [2,6], after a lithiated polyethylene delimiter as shown in Fig. 2.

4 The “Ubertally” Method

Previous optimization studies have involved hundreds of Monte Carlo simulations to compare properties of different neutron beams. Some studies [2,7,8]

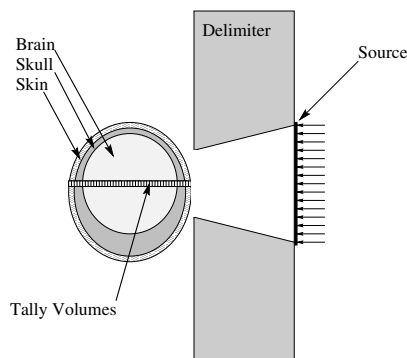


Fig. 2. Simulation geometry

have analyzed beam optimization on a more fundamental level, examining the effects of different energies, beam sizes, and angular distributions. While such studies offer insight into desirable beam properties, the results are often unwieldy and too specific to a particular set of treatment parameters. Small changes in phantom geometry or RBE values, for instance, can produce drastic changes in the performance of different neutron beams. Usually, the only way to determine the effect of changing one or several of the many different variables involved in a BNCT treatment is to rerun many Monte Carlo processes, each of which can take hours or days.

To accelerate the process of performing a great number of Monte Carlo simulations with the same geometry but different sources, the “Ubertally” method was devised. Instead of simulating many different sources, a single simulation is performed and source weighting factors are applied *after* the simulation. Several steps are involved.

4.1 The Master Monte Carlo Run

The first step is the MCNP input file which creates the “ubertally.” In most respects, this input file is like any other MCNP input file, with a few exceptions. First, the particle source distribution is completely isotropic, uniformly distributed over a circular plane, and isoenergetic – a flat spectrum that covers the range of interest. For BNCT sources, the range of 0.001 eV to 15.84893 MeV was chosen for neutrons. To produce adequate sampling across the entire spectrum, this source is then biased by equal sampling probability in bins of equal lethargy, ten bins per decade. While the spectrum remains linearly flat for calculations, any energy bin of equal lethargy will produce the same sample frequency.

Second, the MCNP “FILES” card is used to produce two output files for the “ubertally,” sequential, unformatted files named UBERTALE and UBERTALF. Source particle information will be stored in UBERTALE and cell tally information will be stored in UBERTALF, as described in the TALLYX subroutine.

Third, the FU card is used to call a customized TALLYX subroutine on all tally volumes.

4.2 TALLYX

A new tally is designed via the TALLYX subroutine in MCNP. This tally records particle information into the UBERTALE and UBERTALF files, to be processed later. These two files are obviously quite large (on order of a gigabyte), since information on every tallied particle is recorded. To save space, floating point variables are first converted to 4-byte REAL numbers and certain integers (particle type and cell number) are converted to single bytes.

When a particle track first encounters a tally volume, source information is saved into UBERTALE. The variables recorded are particle number, source position (Y and Z), source energy, and source angle. This information is only recorded once, even if the particle encounters several different tally volumes. Every particle track in the tally cells causes tally information to be saved into UBERTALF. The variables recorded in this file are particle number (for cross-referencing with the source information in UBERTALE), tally cell, particle type, tally energy, and flux (track length divided by cell volume).

4.3 Post-processing

With this information collected and saved, different source weights can be applied on a particle-by-particle basis, obtaining problem solutions to any number of different source distributions with the same simulation. For BNCT, doses in small cylindrical tally volumes along the beam centerline in the head phantom are calculated:

$$D_X = \frac{\Psi}{N} \sum_{i=1}^N \Phi_i \cdot K_X(E_i) \cdot \left[\frac{W}{W_o} \right]_i \quad (2)$$

where X represents each dose component in (1), N is the number of particle simulations, Ψ is the beam flux, Φ_i is the flux contribution of particle i in the tally region, $K_X(E_i)$ is the energy-dependent kerma factor for each dose component, and W and W_o respectively are the new source weight and old source weight. The new source weight is the probability of the particle's energy, position, and angle in the source bin of interest. The old source weight is the probability of an equivalent bin in the original MCNP run, based on the original isoenergetic, isotropic, uniform distribution:

$$W_o = \frac{\Delta E_i}{E_{\max} - E_{\min}} \cdot \frac{\Delta \mu_i}{\mu_{\max} - \mu_{\min}} \cdot \frac{\Delta A_i}{A_{\text{tot}}} \quad (3)$$

in which ΔE_i , $\Delta \mu_i$, and ΔA_i are respectively the bin widths of the new source's energy, angle, and area corresponding to the original values of particle

i , and the *max* and *min* values are the maximum and minimum energies of the original master Monte Carlo simulation.

These new doses are calculated and summed to produce the final result. Values of $K_X(E_i)$ can be calculated to reflect different tissue compositions as desired to determine the effect of different phantom models, though it must be understood that the material modelled for particle transport is fixed. For photon flux tallies, an effective kerma factor is calculated from mass energy absorption coefficients for average soft tissue [9]:

$$K_X(E_i) = \frac{\mu_{en}}{\rho} \cdot E_i. \quad (4)$$

5 Results

The calculations performed in this method are exactly the same that would be performed if the source distributions were input initially into MCNP and biased by equal lethargy bins as described above. The order of the calculations has simply been altered. Instead of source weighting occurring at the beginning of each particle history, weighting is applied after the simulation has been completed. Therefore, benchmarking is straightforward. In equivalent simulations with different sources, biased as described, results are identical to the number of significant digits reported by MCNP. Figure 3 shows the differences in the “ubertally” method compared to non-biased full MCNP simulations for several different neutron beams.

In most cases, comparison between a straight-forward MCNP simulation and the “ubertally” method is as expected. Percentage differences between the two methods is low. Since the error bars represent a single standard deviation, approximately 63% of the data points should have error bars that overlap. This appears to be the case, with the exception of one dose component. For the LBNL beam, discrepancies are apparent only in the proton-recoil dose, D_H and only at large depths, where the dose contribution nears zero. For the BMRR beam, these proton-recoil discrepancies are more pronounced at all depths, affecting the agreement in the total dose as well. The difference in the total doses, though notable, is still low. However, this indicates that the “ubertally” method might benefit from altering the biasing of the master MCNP run to give greater emphasis to modelling higher energy particles.

These comparisons have assumed no gamma contamination is present in the neutron beam. In actual treatment planning, the gamma component is important and should be included. The post-processing “ubertally” algorithm can combine the results of a neutron and external gamma source for a true mixed beam analysis.

6 Error Analysis

Care must be taken when using the “ubertally” method that sources of error are considered. It is best if a much greater number of particles are simulated

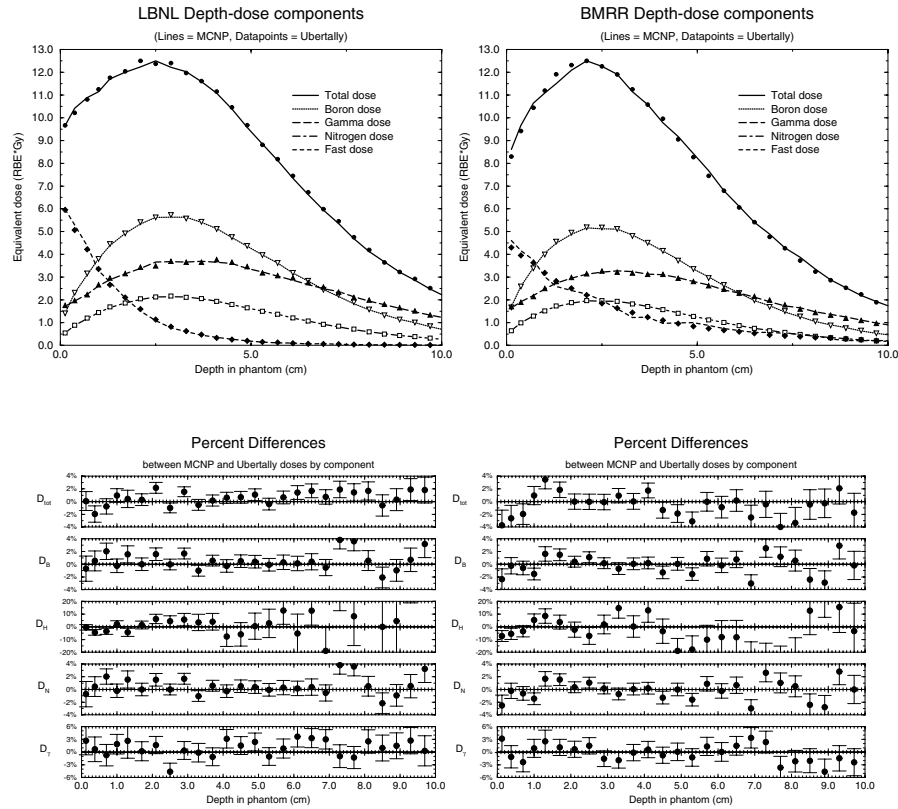


Fig. 3. Comparison of depth-dose components for healthy tissue in two different neutron beams. The data points on the top graphs represent “ubertally” values while the lines represent values of a normal MCNP run. The bottom graphs show the percentage variations of these values, with error bars representing one standard deviation statistical error, added in quadrature from each simulation

in the master run than are normally required, as many simulated particles may be wasted in the final calculation, especially if the source applied is narrow in energy, angle, and/or spatial distribution. Fifty million particles were sufficient to produce low statistical errors, though additional particles, especially biased to higher energies, may be needed.

It should also be noted that because a single Monte Carlo simulation can be applied to many different sources, any source of error in the original run will be applied to all results. Thus, comparison between “ubertally” results can be misleading and the ten statistical checks MCNP normally make are not necessarily applicable. Only the relative error is calculated by the “ubertally.”

7 Conclusions

The “ubertally” method of applying source weighting factors to readjust a Monte Carlo simulation for different variable sources is quite powerful. It can eliminate the need for many lengthy simulations when the source can change, but the environment geometry does not. A simulation that normally takes up to a full day of computation can be accomplished in 10–15 minutes. More error analysis studies are needed to ensure that results are accurate and not misleading. Future study will utilize the “ubertally” to produce high-resolution response functions of dose vs. neutron energy, angle, beam size, phantom size, and RBEs.

References

1. D.L. Bleuel, R.J. Donahue, B.A. Ludewigt, J. Vujic: Medical Physics **25**, 1725 (1998)
2. D.L. Bleuel, R.J. Donahue, B.A. Ludewigt, J. Vujic: ‘Development of a Neutron Energy-Biased In-Air Figure of Merit for Predicting In-Phantom BNCT Neutron Beam Characteristics’, presented at the Eighth International Symposium on Neutron Capture Therapy for Cancer in La Jolla, CA, Sep. 13-18, 1998
3. J.F. Briesmeister: *MCNP - A General Monte Carlo N-Particle Transport Code, Version 4B*, Los Alamos National Lab (1997)
4. D.L. Bleuel, W.T. Chu, R.J. Donahue, B.A. Ludewigt, R.J. McDonald, A.R. Smith, N.A. Stone, J. Vujic: ‘Initial Experimental Verification of the Neutron Beam Modeling for the LBNL BNCT Facility’. In: *Applications of Accelerators in Research and Industry, Proceedings of the Fifteenth International Conference*, November 4-7, 1998, Denton, Texas, AIP Conference Proceedings **475** Vol. 2, pp. 1050 (1999)
5. J.A. Coderre, R. Bergland, J. Capala, M. Chadha, A.J. Chanana, E. Elowitz, D.D. Joel, H.B. Liu, D. Slatkin: J. Neuro. Oncol. **33**, 93 (1997)
6. W.S. Snyder, H.L. Fisher Jr., M.R. Ford, G.G. Warner: ‘Estimates for Absorbed Fractions for Monoenergetic Photon Sources Uniformly Distributed in Various Organs of a Heterogeneous Phantom (Appendix B)’, *J. Nucl. Medicine*, MIRD Supplement No. 3, Pamphlet 5 (1969)
7. J.C. Yanch, O.K. Harling: Radiation Research **135**, 131 (1993)
8. J.M. Verbeke, J. Vujic, K. N. Leung: Nucl. Techn. **129**, 257 (2000)
9. *Photon, Electron, Proton and Neutron Interaction Data for Body Tissues*, ICRU Report 46, February 28, (1992)

MCNP Modelling of HTGR Pebble-Type Fuel

Z. Karriem, C. Stoker, and F. Reitsma

South African Nuclear Energy Corporation, PO Box 582, Pretoria, 0001, South Africa

1 Introduction

Criticality calculations for systems (reactor, critical assembly or storage tank) in which pebble-type fuel is used or stored, presents itself as an interesting problem. This is due to the heterogeneous nature of the fuel itself, as well as the heterogeneity that occurs in an arrangement of such pebbles. An example of this heterogeneity at the pebble level, is found in the ASTRA Critical Facility [1] where fuel pebbles are mixed with non-fuel (moderator and absorber) pebbles that are identical in size, but different in material composition.

Figure 1 shows the composition of a typical spherical fuel element (hence pebble). The pebble has a diameter of 6 cm and consists of an inner fuel region (diameter 5 cm) that is encased in a graphite shell. The fuel region contains micro-particles (diameter 0.106 cm) that are stochastically distributed in a graphite matrix. Each of these micro-particles consists of a UO_2 -kernel, that is coated with four carbon- and silicon based layers. Each pebble contains about 15000 micro-particles.

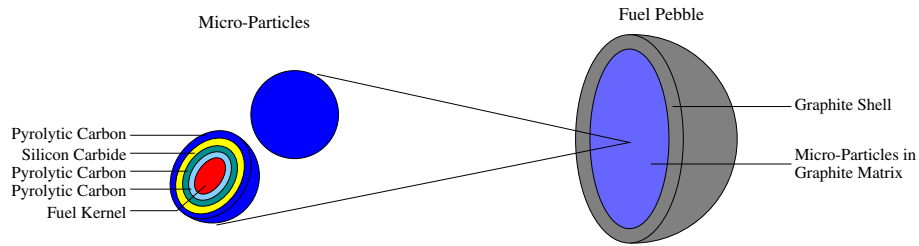


Fig. 1. HTGR Fuel Pebble Composition

The purpose of this study was to establish appropriate geometric models with which pebble-type systems may be modelled with MCNP4B2 [2]. In Sect. 2 the geometric modelling at a micro-particle level is considered, while the modelling at a pebble level is presented in Sect. 3. The models developed in Sect. 2 and 3 are applied in calculating the k_{eff} for the ASTRA facility.

2 Micro-Particle Modelling

MCNP is well known for the geometric capabilities it has to offer. It is also accepted that the more detail included in the geometric model, the more accurate the results. The micro-particles are however stochastically distributed and this randomness cannot be modelled with MCNP. It does, however, allow the packing of individual particles (15000) by means of its cubic (square pitch) and hexagonal (triangular pitch) repeated structures. The question of which micro-particle packing arrangement to use in the fuel region, is considered in this section.

Criticality calculations were performed for both square- and triangular micro-particle arrangements. In both cases the fuel elements contained a total heavy metal mass of 9 g (8.5% enriched in ^{235}U) and were packed on a triangular pitch (packing ratio 0.61) in an infinite array, without any moderation between the pebbles.

In order to determine the importance of the explicit specification of the micro-particle coatings, criticality calculations were also performed for various geometric representations of these coatings, namely:

- exact geometric modelling of the four coatings,
- the coatings modelled as a single homogenised region, and
- with the coatings homogenised into the graphite matrix.

In all cases the UO_2 -kernel was modelled exactly.

Table 1. Effect of Micro-Particle Arrangement and Specification on k_{eff}

Case	Pitch	Coatings	k_{eff}	σ	Difference (%)	Rel. CPU time
A	Triangular	4	1.52001	0.00061	-	1
B	Triangular	1	1.51941	0.00059	0.04	0.69
C	Triangular	none	1.51704	0.00060	0.20	0.57
D	Square	4	1.52006	0.00061	-	1
E	Square	1	1.51975	0.00060	0.02	0.71
F	Square	none	1.51759	0.00060	0.16	0.58

The results for the criticality calculations performed are shown in Tab. 1. It is immediately apparent that there is no significant difference in the k_{eff} values for the two types of repeated structures. The reason for this is that the particles are spaced relatively far from each other and hence the specific arrangement is irrelevant. Thus for the micro-particle packing ratio considered (0.04), either arrangement for micro-particle distribution in the matrix will suffice.

The k_{eff} values for both the triangular- and square arrangements decrease between the explicit four-coating model and the models with homogenised coatings. The effect is greatest when the silicon carbide (SiC) is homogenised over

the entire matrix volume, i.e. cases C and F respectively. The reduction in k_{eff} is due to the smearing of the SiC layer, since the other carbon coatings differ only in density from the surrounding carbon matrix.

A considerable reduction in computing time can be achieved if the particle coatings are smeared. For example, the use of the simplified one-coating model could save 30% computing time, while the difference in k_{eff} values (relative to the four-coating model) is only 0.04% for the triangular and 0.02% for the square arrangement. This falls within the uncertainty of the explicit four-coating k_{eff} values. The one-coating representation of the micro-particle coatings could thus be used when computing power is limited or when initial design calculations are being performed. However, the differences in k_{eff} for the kernel-only models (Cases C and F) compared to the corresponding four-layer values are significant.

Since the fully explicit model (4-coating) consumes a considerable amount of computing time, the one-coating model was adopted for subsequent calculations in this paper. The micro-particles were specified (an arbitrary choice) on a triangular pitch (hexagonal prism lattice).

3 Fuel Pebble Modelling

As in the case for the micro-particles, the packing arrangement of the fuel pebbles and its effect on criticality was studied. First, the effect on criticality due to neutron streaming in a finite system was addressed, followed by the effect of the packing arrangement on the criticality of infinite water moderated systems. Again, the MCNP repeated structures were used to approximate the irregular packing of the pebbles. Criticality calculations for body centered tetragonal (bct) and hexagonal close packing (hcp) arrangements, were performed.

The finite system considered was that of a sphere (radius 140 cm) and was filled with pebbles packed in bct and hcp packing arrangements with a packing ratio of 0.625 (as in the ASTRA facility) and void between the pebbles. Criticality under non-reflected and reflected (100 cm thick graphite shell) conditions were determined for each packing arrangement. The results for these calculations are shown in Tab. 2.

Table 2. Effect of Pebble Arrangement on Criticality

Case	System	Packing	k_{eff}	σ	Difference (%)
A	Unreflected Sphere	bct	0.91610	0.00051	
		hcp	0.91766	0.00050	0.17
B	Reflected Sphere	bct	1.31046	0.00040	
		hcp	1.30936	0.00041	0.08

The effect of the packing is significant in case A, with the k_{eff} value for the hcp arrangement 0.17% higher than that of the bct arrangement. In the reflected system, case B, the difference is much smaller (0.08%) indicating that in reflected systems the k_{eff} is less sensitive to the specific pebble arrangement. Only in unreflected geometries (i.e. large leakage systems) the packing arrangement of pebbles seems to be important.

Under conditions where the thermalisation length of neutrons is shortened as a result of more moderation, the geometric arrangement of pebbles was found to play an important role. An example of such a case, is the determination of criticality safety of a pebble storage facility, under the upset condition of water ingress. Table 3 shows the results for a series of infinite lattice calculations similar to that in Sect. 2, but with water (density 1 g.cm^{-3}) between the pebbles.

Table 3. Effect of Pebble Arrangement and Moderation on Criticality

Packing Ratio	Body Centered Tetragonal $k_{\text{eff}} (\sigma)$	Hexagonal Close Packing $k_{\text{eff}} (\sigma)$	Difference (%)
0.52	0.68501 (0.00051)	0.67834 (0.00051)	0.97
0.61	0.84958 (0.00051)	0.84391 (0.00049)	0.67
0.74	1.11345 (0.00055)	1.10794 (0.00055)	0.49

The percentage differences clearly show the effect of packing arrangement on k_{eff} . Since the thermalisation length under the additional water moderation is much shorter, the local arrangement of the pebbles is important. Thus the appropriate packing arrangement of pebbles should thus be determined for a specific application.

4 Modelling the Criticality of the ASTRA Facility

The ASTRA facility is depicted in Fig. 2. The facility has an annular octagon-shaped core, with graphite reflectors at the sides and bottom. The side reflector outer radius is 190 cm and has a total height of 460 cm. The core of the facility is divided into three regions. The central region contains only moderator pebbles and is surrounded by a mixed zone that is filled with fuel-, moderator- and absorber pebbles in the ratio of 19/20/1. The outer fuel region of the core is filled with fuel- and absorber pebbles with the fuel-absorber ratio of 19/1.

The fuel pebbles each have a total heavy metal mass of 2.44 g (21% enriched in ^{235}U). The moderator pebbles consist of graphite. The absorber pebbles consist of an inner absorber region (diameter 4 cm) and an outer graphite shell (thickness 1 cm). The absorber region contains B_4C micro-particles (diameter 6×10^{-3} cm) with a total natural boron mass of 0.1 g.

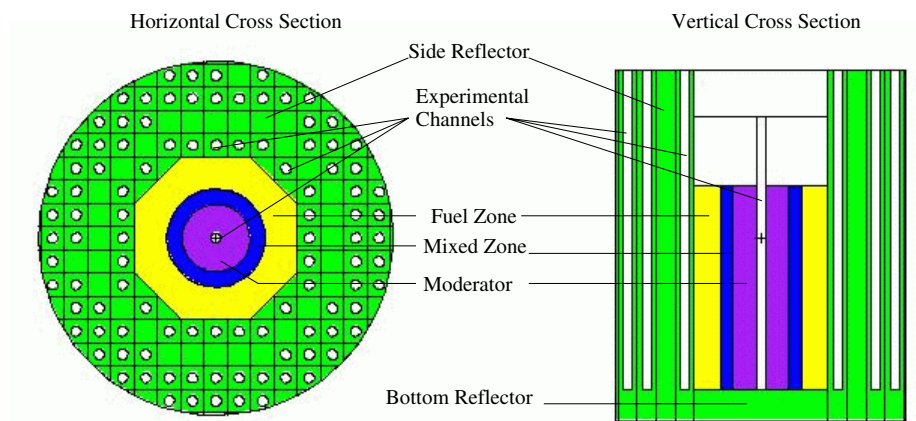


Fig. 2. Schematic of the ASTRA Critical Facility

The crucial part in calculating the k_{eff} for the ASTRA facility, is to ensure that the pebble ratios for the mixed- and fuel zone are modelled as accurately as possible. This was achieved using cells containing 40 pebbles and with a bct arrangement of pebbles. The 40 pebbles are made up by 19 fuel, 20 moderator and 1 absorber pebble for the mixed zone and 38 fuel and 2 absorber pebbles for the fuel zone. The bct arrangement was selected since it allows easy construction of lattice cells that contain the appropriate pebble ratios and since it is closer to the physical packing in ASTRA. Furthermore, since ASTRA is reflected in all but one side the relative leakage is not expected to be so large that the selection of the pebble arrangement will be important (see results in Sect. 3).

Another complexity is introduced when MCNP truncates lattice cells beyond the region being filled. Care has to be taken to ensure that the relative pebble ratios are still maintained in each region. By adjusting the dimensions of an asymmetric unit cell, the effect of truncation on pebble ratios can be minimized.

Three MCNP criticality calculations, with varying absorber pebble representation, were performed for the ASTRA facility. These cases are depicted in Tab. 4 along with the k_{eff} results. The experimental value of $k_{\text{eff}} = 1$ was obtained at a core height of 269 cm, with a stochastic distribution of pebbles in the mixed- and fuel zones. Among these cases, case A is the most accurate geometrical representation of the facility and the result compares well with experiment. The difference in k_{eff} between case A and B is 0.2 %. This is the same effect that was noted due to homogenisation of the SiC in Sect. 2, i.e. higher absorption when the B_4C is smeared into matrix. Within the forty pebble cell the absorber spheres were uniformly distributed (cases A and B), while the absorber spheres were less evenly distributed (positioned closer to each other in fewer axial layers) in case C. The difference in k_{eff} between cases B and C is 0.2 %, indicating that the absorber pebble arrangement in the fuel zone plays an important role

Table 4. MCNP Criticality Results for ASTRA

Case	Absorber Pebble Distribution	B ₄ C Kernel Specificat.	k_{eff} (σ)
A	Pebbles approximately randomly distributed	Kernels explicitly modelled	0.99928 (0.00055)
B	Pebbles approximately randomly distributed	Kernels Homogenised into matrix	0.99751 (0.00053)
C	Pebbles on same plane at various heights in assembly	Kernels Homogenised into matrix	0.99967 (0.00048)

on criticality and is most likely the greatest source of uncertainty between the calculated and the experimental results.

5 Conclusion

In this work appropriate models for MCNP modelling of pebble-type fuel (and absorber pebbles) were investigated. It is evident from this study that the specific micro-particle arrangement is irrelevant due to the high neutron scattering properties of graphite and the small packing ratio (0.04) of the particles. The packing arrangement of the pebbles (as in a reactor or critical assembly) is relatively unimportant, except for small unreflected critical experiments. For a system of pebbles with different moderation conditions (e.g. water ingress) the packing arrangement could be important and should be determined in accordance to the specific application. Packing of non-identical pebbles should be done with great care, especially when strong neutron absorber pebbles are present.

Given the results of this study, in particular that of the ASTRA facility, it is clear that pebble-type systems (reactor, critical facilities or storage tanks) can be modelled with confidence using MCNP, despite the fact that the stochastic nature of these systems cannot be modelled exactly.

References

1. ASTRA Critical Assembly, Kurchatov Institute, Moscow; D. Naidoo: *ASTRA Critical Facility Configuration Report*, Internal report 3402-165, August 2000, PBMR, South Africa
2. Judith F. Briesmeister, Editor: *MCNPTM – A General Monte Carlo N-Particle Transport Code*, Los Alamos National Laboratory, Report LA-12625-M, Version 4B2 (March 1997)

Universal Approach for ADS Blanket Calculations Using the Monte Carlo Method

V.V. Korobeinikov

Institute of Physics and Power Engineering, Obninsk, Russia

Abstract. The universal scheme of Monte Carlo method has been developed for neutronic calculations of ADS blanket.

The new approach can be successfully used for calculations of ADS in a wide range of subcriticality levels. The theoretical substantiation and the results of test problem calculation are given.

1 Introduction

The interest in Accelerator Driven System (ADS) has grown rapidly in the last years. These systems offer solutions to several apparently problematic issues related to energy production in conventional fission reactors, such as

- Disposal of long lived actinides and fission products.
- Hazards involved in maintaining criticality margins.
- Exhausting supplies of uranium fuels.
- Proliferation of plutonium for weapon production.

In order to investigate scientific expectations the development of cods are demanded.

It is known that the efficiency of Monte Carlo calculation for subcritical systems with external source depends on subcriticality level. The lower subcriticality level the worse efficiency of Monte Carlo calculation.

The new scheme has been suggested for efficiency increasing of subcritical systems calculation. The efficiency of calculations by Monte Carlo method with new scheme does not depend on level of subcriticality.

2 Theory

The main points of our approach are given below. The equation for neutron transport in a system with external source is:

$$\hat{L}\Phi(x) = \hat{B}\Phi(x) + Q(x), \quad (1)$$

where:

\hat{L} - neutron consumption operator (neutron absorption and leakage);

\hat{B} - neutron production operator;

Q - external neutron source.

The source multiplication factor is defined as:

$$M = \frac{\langle \hat{L}\Phi \rangle}{\langle Q \rangle}, \quad (2)$$

where $\langle \dots \rangle$ means an integration over all variables. Many authors (see, for example [1]) use instead of factor M another value which is defined as:

$$k_s = \frac{\langle \hat{B}\Phi \rangle}{\langle \hat{L}\Phi \rangle}, \quad (3)$$

Factor k_s is more convenient for subcritical system analysis. It is interpreted as the part of fission neutrons in all neutron balance of ADS blanket. k_s must be smaller than 1 for all subcritical systems with external source. Using (1) we may connect k_s and M:

$$M = \frac{1}{1 - k_s}, \quad (4)$$

$$k_s = \frac{M - 1}{M} \quad (5)$$

At the same time for the system with fission materials can be defined the k_{eff} factor.

It should be noted that k_{eff} may be differed from k_s significantly. Really, for example, k_s depends on source position, source energy structure and so on. k_{eff} does not depend on source characteristics.

The calculation of subcritical system by Monte Carlo method is not simple problem if k_s near one. To improve this situation the new scheme of calculation was developed and realized in a Monte Carlo code. The idea of our approach is based on a new formulation of (1). Using (3) equation (1) may be written in the form:

$$\hat{L}\varphi = \hat{B}\varphi + \frac{\langle \hat{B}\varphi \rangle}{\langle Q \rangle} \frac{1 - k_s}{k_s} Q. \quad (6)$$

Equation (6) is converted into (1) if $\varphi = \Phi$, but (6) has another solutions too. All functions:

$$\varphi(x) = \Phi(x) \cdot C, \quad (7)$$

where C - arbitrary constant are solutions of (6). Transform (7) to the next form:

$$\hat{L}\varphi = \frac{\langle \hat{B}\varphi \rangle}{k_s} \left[k_s \frac{\hat{B}\varphi}{\langle \hat{B}\varphi \rangle} + (1 - k_s) \frac{Q}{\langle Q \rangle} \right]. \quad (8)$$

Since C is arbitrary constant we may choose it so that

$$\langle \hat{L}\varphi \rangle = 1. \quad (9)$$

Using last equation we may write:

$$\hat{L}\varphi = k_s \frac{\hat{B}\varphi}{\langle \hat{B}\varphi \rangle} + (1 - k_s) \frac{Q}{\langle Q \rangle}. \quad (10)$$

The right part of (10) is the superposition of two normalized distributions. With probability k_s neutron is distributed on fission spectrum and with probability $(1-k_s)$ neutron is distributed on external source spectrum. The last equation gives the way of the subcritical problem solution. This way is similar to the criticality problem solving.

The calculation procedure consists of two stages:

- Simulation of some preliminary generations to set up the initial distribution of fission neutrons.
- Simulation of basic generations. Estimations of flux functionals and k_s value.

The constant number N of neutrons is maintained in every generation. k_s fission neutrons are chosen from total N neutrons. $(1-k_s) \cdot N$ are the external source neutrons. So, the total number of neutrons is kept and equal N . The connection between ϕ and Φ is very simple:

$$\Phi(x) = \frac{\langle Q \rangle}{1 - k_s} \varphi(x) \quad (11)$$

Only light modifications of Monte Carlo Code MMKFK (k_{ef} option) was made for realization of this scheme.

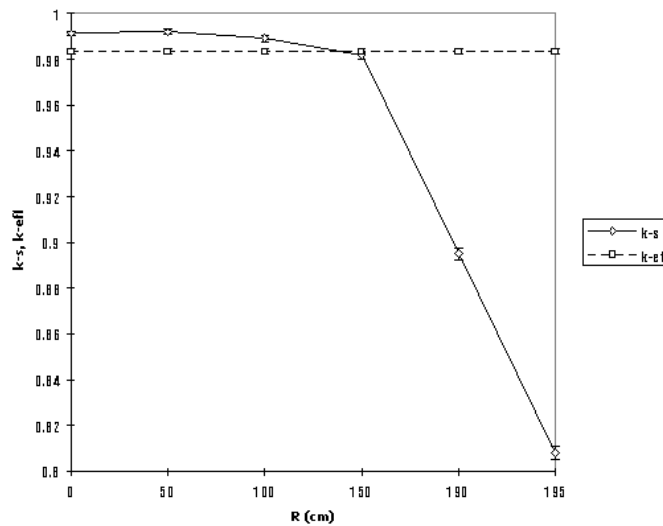


Fig. 1. k_s as a function of source location

3 Numerical Results

Results of k_s calculations for different source positions in ADS blanket are given on Fig. 1. k_{ef} is given on Fig. 1 too (for comparison). We see that statistic errors depend on k_s value very weakly. In case if $k_s > 1$ the neutrons emit from fission source only and subcritical problem transfers to quasicritical one. Instead of k_s value we get k_{ef} automatically.

4 Conclusions

- The new scheme for subcritical system calculation was developed.
- The new approach has been tested on ADS blanket model. The efficiency of new scheme depends on k_s (k_{ef}) value very weakly.
- The new approach is universal and transfers to quasicritical problem if $k_s = 1$.

References

1. I. Slessarev: *Accelerator Driven Systems (ADS): A Principal neutronics and transmutation potential. Accelerator Driven Systems: Energy Generation and Transmutation of Nuclear Waste. Status Report.* IAEA. Vienna, 1997. IAEA-TECDOC-985

Monte Carlo Depletion Analysis of a PWR Integral Fuel Burnable Absorber by MCNAP

H.J. Shim, C.S. Jang, and C.H. Kim

Nuclear Engineering Department, Seoul National University, Seoul, Korea

Abstract. The MCNAP is a personal computer-based continuous energy Monte Carlo (MC) neutronics analysis program written on C++ language. For the purpose of examining its qualification, a comparison of the depletion analysis of three integral burnable fuel assemblies of the pressurized water reactor(PWR) by the MCNAP and deterministic fuel assembly(FA) design vendor codes is presented. It is demonstrated that the continuous energy MC calculation by the MCNAP can provide a very accurate neutronics analysis method for the burnable absorber FA's. It is also demonstrated that the parallel MC computation by adoption of multiple PC's enables one to complete the lifetime depletion analysis of the FA's within the order of hours instead of order of days otherwise.

1 Introduction

The MCNAP is a Monte Carlo code designed exclusively for neutronics analysis of power reactors. Like many existing *Monte Carlo depletion codes* [1–7] where a Monte Carlo code is combined with an isotope depletion code, it is capable of depletion analysis of fuel pins, fuel assemblies, and power reactor cores. To establish its qualification, we previously examined its prediction accuracy on the criticality and pin power measurements of Venus critical facilities and the beginning-of-life(BOL) core neutronics of the Younggang unit 3(YGN 3) pressurized water reactor(PWR) [8]. For the further examinations, we herein present a comparison of the depletion analysis of integral burnable absorber fuel assemblies of PWR by the MCNAP and deterministic FA design vendor codes and to demonstrate that the continuous energy MC calculation provides a very accurate neutronics analysis method for the burnable absorber FA's. We also demonstrate that the parallel MC calculation by the use of multiple personal computers enables one to complete the lifetime depletion analysis of the FA's within the order of hours instead of the order of days otherwise.

The longer cycle operation and low-leakage fuel management of the current PWR make it necessary to adopt the burnable absorbers(BA's). The gadolinia, zirconium diboride, and erbia are three major types of integral burnable absorbers(BA's) [9,10]. They are utilized in the form of the gadolinia- and erbia-bearing UO_2 pellets and UO_2 pellets coated with zirconium diboride. Because of exceptionally strong thermal absorption of the gadolinium isotopes, the low-lying resonance of Erbium-157, and the thin layer of ZrB_2 , the three BA's pose an interesting lattice physics analysis problem. In particular, because the burnout rate of the BA isotopes affect the pin power peaking behavior during depletion

as well as the residual reactivity at the end of the intended fuel cycle, the accurate prediction on the burnup behavior of these BA's is essential for ensuring the economic and safe fuel management scheme of the BA-shimmed PWR cores. In this paper the prediction accuracy of the MCNAP against the deterministic fuel design codes is assessed in terms of the depletion analysis of the three BA's.

2 Description of the MCNAP

The MCNAP code is a personal computer(PC)-based continuous energy Monte Carlo(MC) neutronics analysis program written on the C++ language. It adopts standard MC simulation techniques for neutron flux and criticality estimation [11–13]. The code estimates neutron flux based on the track length estimator and the multiplication factor by taking the weighted average of collision, absorption, and track length estimators. It uses only the Russian roulette kill as variance reduction methodology and ENDF/B-VI version 3 as the nuclear data. For the MCNAP depletion, the MC neutron flux determined for each computation cell at the beginning of each burnup step is utilized in solving the isotopic depletion chain equations. All the isotopes in the decay library of the ORIGEN2 code are included in the depletion chain equation [14]. The MCNAP can perform the parallel calculations by networking multiple personal computers with the help of the message passing interface(MPI) libraries.

3 Depletion Analysis of Burnable Absorber Fuel Assemblies

Erbia burnable absorber has been developed by ABB CE. Figure 1 depicts erbia burnable absorber benchmark test problems for 16×16 and 17×17 lattices that ABB-CE presented for fuel management studies with erbia burnable absorbers [15]. The two fuel assemblies contain 60 erbia-bearing fuel pins consisting of 2.1 w/o erbia(Er_2O_3) in 4.2 % enriched UO_2 . They have the enrichment zoning of the typical ABB CE FA design. The 16×16 FA has a large waterhole while the 17×17 FA a small water hole. Other details including dimensions of the fuel rods are available in [15]. We performed the MCNAP calculations using 300,000 particles, namely, 3,000 particles per cycle on 120 cycles with the first 20 cycles dedicated for the fission source distribution. Table 2 compares the MCNAP prediction with DIT calculations [16] on the depletion characteristics of the assembly k-infinity values over the burnup range from 0 to 74,000 MWd/MTU. The differences between the DIT calculations and the mean values of the MCNAP on k-infinity are mostly within 1σ (the standard deviation) of the MCNAP predictions except for several burnup steps where differences of more than 500 pcm are observed. Considering that prediction accuracy of the DIT code has been benchmarked against experiments on the erbia-shimmed FA's, it can be safely said that the MCNAP can predict the depletion behavior of the erbia as accurately as the DIT code.

The ZrB_2 -coated integral fuel burnable absorber(IFBA) has been developed by the Westinghouse to improve low-leakage cores and to offer other advantages as well. Figure 2 shows the IFBA fuel assembly which has been designed for the 18 month cycle operation of the YGN 2 PWR by Korea Nuclear Fuel Company. The fuel assembly contains 48 ZrB_2 -coated fuel rods with the 4.2 % U-235 enrichment. The ZrB_2 coating is 0.02 mm thick, which correspond to 1.52 mg ZrB2 per inch. Because of thinness of ZrB2 coating in its explicit geometrical representation in the Monte Carlo calculations, we first imagined it might be necessary to sample more particles than the erbia case to ensure the acceptable variance. But it turns out that sampling of the 300,000 particles as we did in the erbia case is enough to predict the assembly k-infinity and the pin power distribution with acceptable variances. Table 3 show a comparison of the MCNAP and the PHOENIX [17] calculations on the k-infinity versus burnup. As noted in these results, the MCNAP can predict the depletion characteristics of the k-infinity of the ZrB_2 -coated IFBA acceptably well in comparison with the PHOENIX code, which is the design basis of the Westinghouse FA's. We observe k-infinity predictions are in good agreement with each other.

The gadolinia-bearing fuel rods have been utilized as a major burnable absorber of the YGN 3 PWR. Figure 3 shows the two types of gadolinia-shimmed fuel assemblies of YGN 3. The two FA's contain 4 and 8 gadolinia rods consisting of 4 w/o Gd_2O_3 in natural UO_2 pellet, respectively. Because of strong thermal absorption characteristics of Gd isotopes, the progressive change of the self-shielding effects in the gadolinia rod with burnup usually is modeled by dividing the gadolinia rod into 10 to 20 radial zones in the deterministic codes. For the MCNAP analysis, here, we sliced the individual gadolinia fuel rod into five radial zones. Table 4 shows a comparison of the MCNAP and CASMO-3 [18] prediction on the variation of k-infinity with assembly burnup. As in the cases of the erbia and ZrB_2 , we observe fairly good agreement between two calculations.

4 Performance of Parallel Computing MCNAP

The MCNAP depletion computation takes a very lengthy computational time even for the FA analysis. For example, the burnup analysis of the erbia BA from 0 to 74,000 MWd/MTU conducted on 27 burnup steps took the CPU time of 83.3 hours on the Alpha-workstation. This means that one has to wait for so many hours of elapse time to get the computational results. Because of this, the routine application of the MCNAP even to the FA analysis can not be justified even with the PC's at present. In order to shorten the turnaround time, we networked multiple alpha workstations and performed parallel MC calculations with the help of the MPI software.

Table 1 shows the elapse time for the macro-parallel MCNAP depletion analysis of the 16×16 erbia FA as a function of the number of the employed alpha workstations. We note that the more the number of workstations is, the less the elapse time. It is shown that the several days' work on the single processor reduced to 22.0 hours' with the six processors, which is rather tolerable. But we

note that the idle time is increasing with the number of the employed workstations. This is attributable to the weakness of the macro-parallel scheme. In this scheme, each processor is assigned to sampling of the equal number of particle histories every batch. No matter how fast any one processor completes its assigned sampling, therefore, it has to wait till all the other processors finish their assigned samplings before it starts sampling again for the next batch. Because of this, the idle time tends to increase with the number of the employed processors. The micro-parallel computation in Tab. 1 is designed to take the full advantage of the parallel MC computation by reducing the idle time as little as possible. In this scheme, one host processor divides the total number of particle histories into small pieces and assigns one piece to an available slave processor every time it complete its assigned samplings. In this case, the elapse time with the six processor is 15.6 hours and the loss of efficiency is shown to be less than 20%.

Table 1. Parallel Computing Time with 16×16 Erbia Assembly

Parallel Type	Single CPU	Macro	Tasks	Micro	Tasks
	1 CPU	4 CPU	6 CPU	4 CPU	6 CPU
Elapsed Time (hour)	83.3	26.7	22.0	22.28	15.6
Idle Fraction (%)	-	36.2	67.4	13.6	19.3

5 Discussions and Conclusion

We reconfirmed the good computational accuracy of the continuous MC neutronics computation. We showed that the continuous energy MCNAP depletion calculation can predict the burnup characteristics of the three major integral burnable absorbers of the current PWR as accurately as the deterministic FA design codes of fuel vendors. We also showed that, unlike the cases of deterministic FA design codes, its prediction accuracy is consistently good regardless of the types of the burnable absorber FA's.

The long computational time required for the MC depletion calculation poses major hindrance to the routine application of the method. But we demonstrated that the adoption of the parallel computing MC scheme can reduce the prohibitively long turn around time of the order of several days to the reasonably acceptable turn around time less than one day in terms of six processor depletion analysis of the erbia-shimmed FA. Considering the PC-affluent working environment and ever-increasing computational speed of the PC's, therefore, the parallel computing MCNAP can be conducted without too much extra expense and within acceptable time.

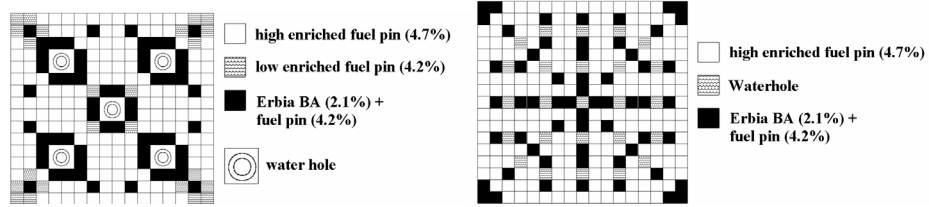


Fig. 1. Erbium BA assembly configuration for 16×16 and 17×17 assemblies

Table 2. Comparison of k-infinity calculated by MCNAP and DIT for Erbium BA Assembly

Burnup (MWd/mtU)	16x16 DIT	Assembly MCNAP (σ)	17x17 DIT	Assembly MCNAP (σ)
0	1.18082	1.18162 (0.00117)	1.19968	1.20202 (0.00128)
50	1.15050	1.15267 (0.00112)	1.16848	1.17023 (0.00119)
500	1.14362	1.14265 (0.00106)	1.16008	1.16541 (0.00122)
1000	1.14191	1.14412 (0.00115)	1.15778	1.16614 (0.00112)
2000	1.14079	1.14115 (0.00107)	1.15574	1.16030 (0.00135)
3000	1.13891	1.14139 (0.00133)	1.15301	1.15786 (0.00106)
5000	1.13278	1.13465 (0.00127)	1.14529	1.15075 (0.00111)
7000	1.12489	1.12609 (0.00119)	1.13596	1.14126 (0.00110)
9000	1.11609	1.11562 (0.00110)	1.12592	1.13030 (0.00128)
11000	1.10666	1.10715 (0.00133)	1.11544	1.11994 (0.00132)
14000	1.09180	1.09453 (0.00118)	1.09933	1.10317 (0.00122)
17000	1.07597	1.07575 (0.00115)	1.08271	1.08760 (0.00118)
20000	1.05924	1.05897 (0.00103)	1.06553	1.06680 (0.00115)
23000	1.04175	1.04269 (0.00117)	1.04791	1.04937 (0.00119)
26000	1.02382	1.02382 (0.00103)	1.03000	1.02783 (0.00111)
30000	0.99971	0.99802 (0.00125)	1.00615	1.00629 (0.00110)
34000	0.97539	0.97481 (0.00089)	0.98226	0.97938 (0.00111)
38000	0.95118	0.94828 (0.00113)	0.95857	0.95699 (0.00125)
42000	0.92734	0.92434 (0.00112)	0.93529	0.93349 (0.00103)
46000	0.90409	0.90081 (0.00125)	0.91261	0.91106 (0.00112)
50000	0.88161	0.88077 (0.00105)	0.89067	0.88784 (0.00104)
54000	0.86015	0.85963 (0.00110)	0.86972	0.86453 (0.00106)
58000	0.83975	0.84006 (0.00105)	0.84978	0.84406 (0.00103)
62000	0.82053	0.82202 (0.00109)	0.83093	0.82940 (0.00108)
66000	0.80258	0.80598 (0.00106)	0.81327	0.81280 (0.00117)
70000	0.78600	0.79175 (0.00103)	0.79688	0.79867 (0.00117)
74000	0.77083	0.77474 (0.00125)	0.78180	0.78327 (0.00095)

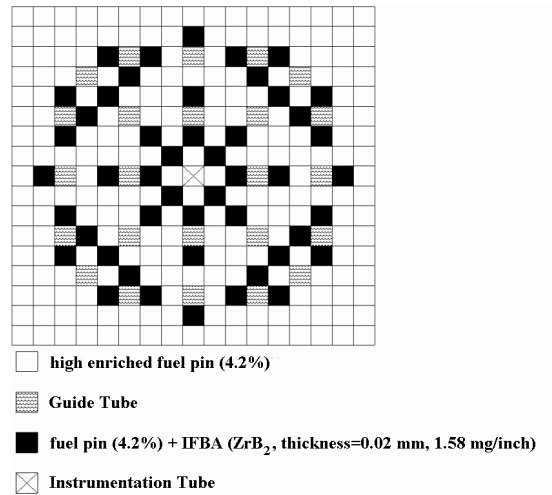


Fig. 2. IFBA BA assembly configuration with 48 IFBA BA rods

Table 3. Comparison of k-infinity calculated by MCNAP, PHONIX, CASMO for IFBA BA Assembly

Burnup (MWd/mtU)	PHEONIX	CASMO	MCNAP (σ)
0	1.26210	1.26600	1.26946 (0.00140)
150	1.22399	1.22777	1.22718 (0.00112)
1000	1.21748	1.22186	1.22446 (0.00116)
2000	1.21559	1.21999	1.22568 (0.00120)
4000	1.20899	1.21232	1.21526 (0.00117)
6000	1.19722	1.20077	1.20297 (0.00102)
8000	1.18347	1.18721	1.18784 (0.00115)
10000	1.16870	1.17260	1.17180 (0.00128)
12000	1.15359	1.15740	1.15729 (0.00106)
16000	1.12357	1.12677	1.12484 (0.00119)
20000	1.09362	1.09615	1.09231 (0.00111)
24000	1.06436	1.06610	1.06266 (0.00107)
28000	1.03606	1.03679	1.03398 (0.00123)
32000	1.00866	1.00825	1.00657 (0.00118)

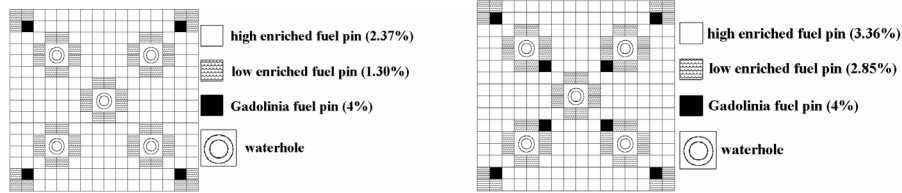


Fig. 3. Gadolinia BA assembly configuration for 4Gd and 8Gd assemblies

Table 4. Comparison of k-infinity calculated by MCNAP, CASMO for Gadolinia BA Assembly

Burnup (MWd/mtU)	16x16 CASMO	Assembly MCNAP (σ)	17x17 CASMO	Assembly MCNAP (σ)
0	1.07209	1.07270 (0.00107)	1.11297	1.11640 (0.00124)
150	1.03822	1.04024 (0.00109)	1.07981	1.08124 (0.00121)
500	1.03469	1.03630 (0.00120)	1.07618	1.07915 (0.00121)
1000	1.03436	1.03735 (0.00112)	1.07571	1.07901 (0.00110)
1500	1.03399	1.03480 (0.00118)	1.07607	1.07958 (0.00122)
2000	1.03322	1.03401 (0.00116)	1.07647	1.07839 (0.00105)
2500	1.03232	1.03333 (0.00105)	1.07691	1.07866 (0.00123)
3000	1.03143	1.03500 (0.00118)	1.07761	1.07815 (0.00103)
3500	1.03075	1.03182 (0.00102)	1.07864	1.07977 (0.00106)
4000	1.03029	1.03129 (0.00107)	1.07993	1.08221 (0.00116)
4500	1.03010	1.03143 (0.00104)	1.08165	1.08662 (0.00112)
5000	1.02975	1.03125 (0.00099)	1.08370	1.08899 (0.00111)
5500	1.02848	1.03109 (0.00110)	1.08586	1.08832 (0.00116)
6000	1.02591	1.02794 (0.00125)	1.08749	1.08942 (0.00108)
6500	1.02219	1.02549 (0.00111)	1.08792	1.08897 (0.00108)
7000	1.01786	1.01973 (0.00110)	1.08690	1.09337 (0.00118)
7500	1.01329	1.01613 (0.00116)	1.08452	1.08806 (0.00120)
8000	1.00864	1.01072 (0.00121)	1.08106	1.08570 (0.00117)
9000	0.99943	1.00356 (0.00115)	1.07274	1.07589 (0.00109)
10000	0.99034	0.99449 (0.00092)	1.06344	1.06582 (0.00114)
12000	0.97303	0.97387 (0.00119)	1.04526	1.04900 (0.00120)
14000	0.95640	0.95869 (0.00118)	1.02775	1.02947 (0.00114)
17000	0.93307	0.93770 (0.00104)	1.00297	1.00725 (0.00119)
20000	0.91112	0.91337 (0.00113)	0.97933	0.98406 (0.00123)

References

1. MONK5W9A USER Guide, AEA Technology (1994)
2. K. Okumura, M. Nakagawa, K. Kaneko: 'Development of Burnup Calculation Code System MVP-BURN Based on Continuous Energy Monte Carlo and Its Validation'. In: *Proc. Joint Int. Conf. on Math. Methods and Supercomputing for Nuclear Applications, Saratoga Springs, N.Y., Vol. I pp.495-509. (Oct. 1997)*
3. T. Mori, K. Okumura, Y. Nagaya, M. Nagagawa: 'Application of Continuous Energy Monte Carlo Code MVP to burnup and Whole Core Calculations, Using Cross Sections at Arbitrary Temperature'. In: *Proc. Math. Comp., Reactor Physics and Environmental Analysis in Nuclear Applications, Madrid, Spain, Vol II, pp987-1015. (Sep. 1999)*
4. D.I. Poston, H.R. Trellue: *User's Manual, Version 1.00, for Monteburns, Version 3.01*, LA-UR-98-2718, Los Alamos National Lab. (June 1998)
5. O.W. Hermann: *COUPLE: Scale System Module to Process Problem-Dependent Cross Sections and Neutron Spectral Data for ORIGEN-S Analysis*, NUREG/CR-0200, Rev. 5, Vol. 2, Sec. F6, Oak Ridge National Lab./U.S. Nuclear Regulatory Commission (Sep. 1995)
6. R.L. Moore, B.G. Schnitzler, C.A. Wemple, R.S. Babcock, D.E. Wessol: *MOCUP: MCNP/ORIGEN Coupling Utility Programs*, INEL-95/0523 RSICC Code PSR-365, Idaho National Engineering and Environmental Lab. (Oct. 1997)
7. D. Bowen, R.D. Busch: *Trans. Am. Nucl. Soc.* **77**, 223 (1997)
8. Hyung Jin Shim, Chang Hyo Kim, Won Seok Park, Hyung Kook Joo: 'Monte Carlo Depletion Analysis of a PWR with the MCNAP', M & C'99, Madrid, Spain, (Sep. 1999)
9. A. Jonsson et al.: 'CE Reactor Physics Experience with Gadolinia', *Proc. Int. Reactor Phys. Conf. Jackson Hole, Wyoming I-135 (Sep. 1988)*
10. A. Jonsson, J.E. Gunn: 'Application of Erbium Burnable Absorbers in the Design and Operation of 18- and 24-month Fuel Cycles', *Trans. Am. Nucl. Soc.* (winter 1995)
11. J.E. Pritchett, D.E. Mueller: *Trans. Am. Nucl. Soc.* **56**, 117 (1987)
12. L.L. Carter, E.D. Cashwell: *Particle-Transport Simulation with the Monte Carlo Method*, TID-26607, Los Alamos Scientific Laboratory (1975)
13. T.J. Urbatsch, R.A. Forster: *Estimation and Interpretation of Keff Confidence Intervals in MCNP*, LA-12458-MS, Los Alamos National Lab. (1995)
14. A.G. Croff: *A User's Manual for ORIGEN2 Computer Code*, ORNL/TM-7175, Oak Ridge National Lab. (July 1980)
15. Private Communication with Dr. David J. Dixon, ABB Combustion Engineering Nuclear Power on "Erbium Burnable Absorber Benchmark Test Problems For 16x16 and 17x17 Lattices"
16. *DIT, Discreet Integral Transport Assembly Design Code*, CE-CES-11, Rev. 4-P (1994)
17. *PHOENIX-P'', Users' Manual*, Westinghouse Electric Corporation
18. M. Edenius, E.H. Forssen: *CASMO-3 User Manual*, STUDSVIK/NFA-89/3, Studsvik (1989)

Application of Biasing Optimization Techniques to Monte Carlo Shielding Analysis of a Transport Cask

S. Mitake¹, O. Sato², and H. Tsunoda²

¹ Institute of Nuclear Safety, NUPEC, Japan

² Mitsubishi Research Institute Inc., Japan

1 Introduction

Three-dimensional calculations are often required for the shielding analysis of spent fuel casks, particularly for the evaluations of radiation leakage through some area of cask such as trunnion structure. Because of thick shielding materials and radiation sources distributed in a relatively large source region, effective and practicable variance reduction techniques are required for efficient calculations. The weight window and the source biasing have been generally applied in the dose rate distribution calculations around the cask. However, it is not easy to apply the weight window and the source biasing in the best suited conditions since these parameters are significantly dependent on problems to be analyzed. Use of the importance distribution for radiation analysis, which is easily calculated from adjoint flux distribution, has been widely recognized as one of the best methods for finding the optimized parameters.

In this study, the adjoint flux distribution calculated with discrete ordinate methods was applied to accelerate the Monte Carlo simulations for the cask shielding analysis. This kind of acceleration technique has been applied to the Monte Carlo calculations on nuclear-well logging [1] and reactor cavity dosimetry [2].

An analytical tool to generate automatically the weight windows for MCNP-4B [3], named ECBO (Efficient Cask shielding calculation with Biasing Optimization), was developed for precise shielding calculations of spent fuel transport casks. With this tool, the parameters for weight windows or cell importance and for source biasing are determined from the adjoint flux distributions calculated with one-dimensional discrete-ordinate code ANISN [4] or two-dimensional code DORT [5]. The ECBO system and modified MCNP-4B were applied to the radiation shielding analysis of spent fuel casks, and calculated results and their performance are presented in this paper.

2 ECBO System

Schematic flow of the ECBO system is shown in Fig. 1. Using the adjoint fluxes calculated with ANISN or DORT, the MKWW program calculates the weight window parameters (lowest weight bounds) and energy and spatial distributions

of the source biasing. MKWW outputs the weight window parameters to interim binary file and the source biasing to text file which can be used in MCNP input file (SI, SP, and SB cards). The Monte Carlo calculations are performed with the MCNP-4B code modified to read the weight window parameters from the file prepared by MKWW. The weight window parameters are defined for the regions independent from the cells assigned for MCNP.

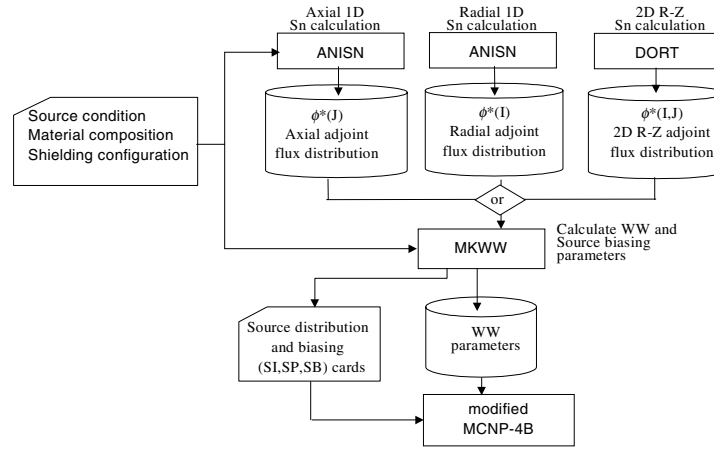


Fig. 1. Schematic flow of the ECBO system

The lowest weight bounds W_L for spatial mesh i and energy group g are calculated from adjoint flux by following formula.

$$W_L(i, g) = \frac{C}{\int_{V_i} \int_{E_g} \{\phi^+(r, E)\} x dr dE} \quad (1)$$

where, $\phi^+(r, E)$ is adjoint flux at point r and energy E , V_i and E_g represents the volume of spatial mesh i and energy of group g , and C is a constant for normalization, making W_L in the source regions to be a half of the biased weight of source particle. With finite weight window mesh sizes, significant increase of the particle numbers at the boundary of weight window meshes is generally caused by the large attenuation of adjoint flux (e.g. gamma-rays in lead). In this case, lowered efficiency of calculations is resulted with increase of CPU time per history. Then, “relaxation factor”, χ is employed to improve the calculation efficiency for these cases. In the case of ^{60}Co gamma-rays penetrating 20cm-thick lead plate, $\chi = 0.7 - 0.8$ shows best efficiency for the calculation of dose equivalent.

The source biasing is applied both for spatial distribution and energy spectrum of source particles. The biases are calculated from source distribution, source energy spectrum and adjoint flux in source regions.

The angular flux is read from a scalar flux file written by ANISN or DORT. ANISN is used for radial penetration calculation in cylindrical geometry, and for axial calculation in slab geometry. Only R-Z geometry can be used in DORT.

The original MCNP-4B requires to define the weight window parameters for each material cell. The thick material cells must be divided to a number of smaller cells to adjust the weight window parameters adequately, and it makes preparation of input data to be more complex. To simplify the input data preparation, MCNP-4B was modified to assign the weight window parameters to the mesh structures in R-Z (cylindrical) geometry. MCNP-4B was modified to read the weight window parameters from binary file, and to set the spatial boundaries for weight windows independent to material boundaries. This modification is based on MCNP-CEAR [6], and extension to R-Z- θ geometry from its original for X-Y-Z geometry has been made in this study.

MCNP-4B was also modified to calculate flux or dose rate distributions on specified plane or cylindrical surface, assigning two-dimensionally allocated meshes, named “scoring mesh tally”. Modification to the TALLYX subroutine of MCNP-4B was made to monitor multiple tallies allocated two-dimensionally on a cylindrical or a plane surface with scoring meshes. The surface is equally divided in height and azimuth angle directions for cylindrical surface, and in radial and azimuth angle directions for plane geometry with the scoring mesh.

3 Test Problems

The ECBO system is tested by applying to an analytical model of a cask, shown in Fig. 2, used in shielding experiment [7]. This cask was designed to contain 3-PWR or 7-BWR spent fuel assemblies. The thickness of shields are 14.6cm for lead and 10cm for resin. The shielding experiment was made with a 50cm ϕ x 50cmH ^{252}Cf source placed at the center of cavity.

In the present calculations, ^{239}Pu neutron induced fission source and gamma-rays from fission products in spent fuel, with burnup of 44,000MWD/ton and uniformly distributed in active fuel length of 364cm, were assumed to model actual cask condition. The dose equivalent rate distributions at side, top, and bottom surfaces were calculated by modified MCNP-4B with scoring meshes. The source biasing and weight window parameters were obtained from the adjoint flux in R-Z geometry calculated with DORT. To find the best adjoint source model which will result most effective dose distribution calculation, four different source were tested in the adjoint calculation: the whole surface, one of the side, top, or bottom surface. DLC-23E/Cask cross section library [8] was used for all adjoint flux calculations. The weight window parameters and source energy biasing were given in the energy group structure of DLC-23E/Cask library: neutron 22 groups and photon 18 groups.

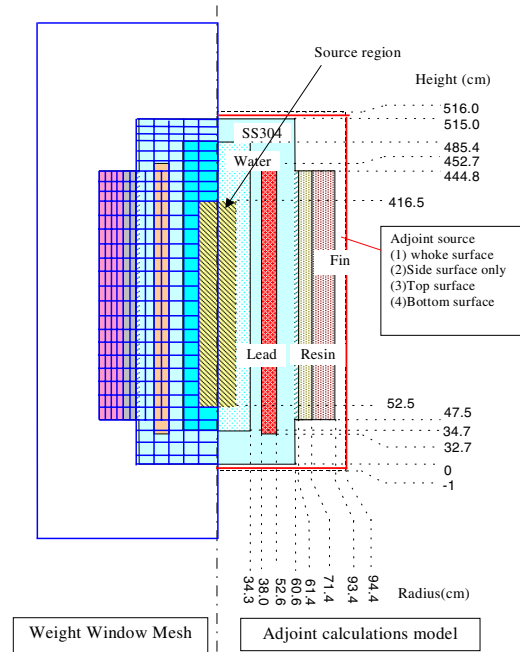


Fig. 2. Calculation model for two-dimensional test problem

4 Results and Discussions

Distribution of FOM (Figure of Merit) is plotted in Fig. 3 (side surface) and Fig. 4 (bottom surface) in the neutron dose equivalent calculations. The FOM is defined as $1/R^2T$, where R is relative statistical error and T is CPU time.

The FOM for the side surface dose is significantly improved by the weight window parameters calculated with the adjoint fluxes from adjoint sources, both for the side and whole surface sources. The acceleration compared to the case without variance reduction is up to the order of several hundreds. Application of the source energy biasing for neutrons does not show significant improvement of the efficiency since the energy spectrum of fission neutron is hard and the fast neutrons, which mainly contribute to the surface dose, are massively generated from the source. For bottom surface dose, the weight window parameters calculated from the adjoint flux with the adjoint source on bottom surface significantly improve the calculation efficiency, however the adjoint source on whole surface improve the efficiency for the surface not near the bottom center, by the order of a few hundreds. For the secondary gamma-ray dose, as shown in Fig. 5, the efficiency was slightly improved but its improvement ratio was limited up to ten times, compared to the neutron doses mentioned above.

The results of fission product (FP) gamma-rays are shown in Fig. 6. Effect of the source energy biasing was very large for this case: no particle comes to almost all scoring meshes when the source energy was not biased even if the weight window variance reduction was applied. The optimum relaxation factor was 0.7 for this case, and FOM was multiplied about several thousands compared to the case only with source energy biasing.

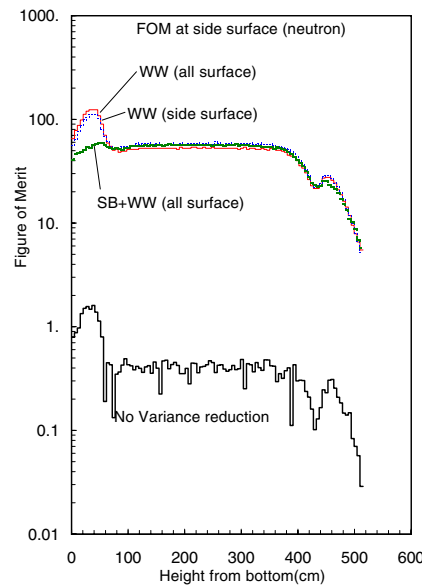


Fig. 3. FOM (Figure of Merit) for the neutron dose distribution at side surface of cask calculated with weight window (WW) and source energy biasing (SB). The adjoint source was placed on the whole surface ('all surface') or side surface ('side surface') of cask

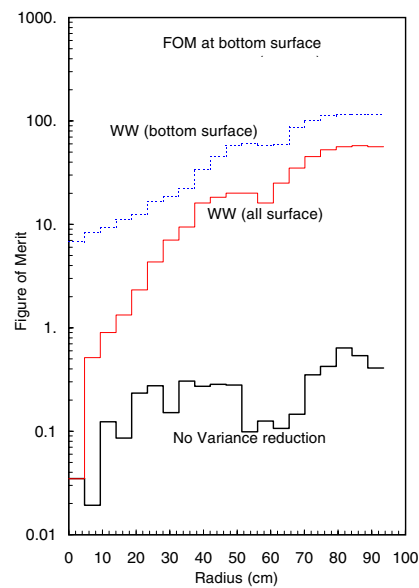


Fig. 4. FOM for the neutron dose distribution at bottom surface of cask calculated with weight window (WW). The adjoint source was placed on the whole surface ('all surface') or bottom surface ('bottom surface') of cask

5 Conclusion

Usefulness of the variance reduction with the adjoint flux calculated by one- or two-dimensional discrete ordinate method was demonstrated for the Monte Carlo shielding calculations of spent fuel transport cask. The ECBO system was developed for automatically calculating the parameters of weight window and source biasing, and man-hours and CPU-hours for precise shielding calculations will be greatly reduced with the systems.

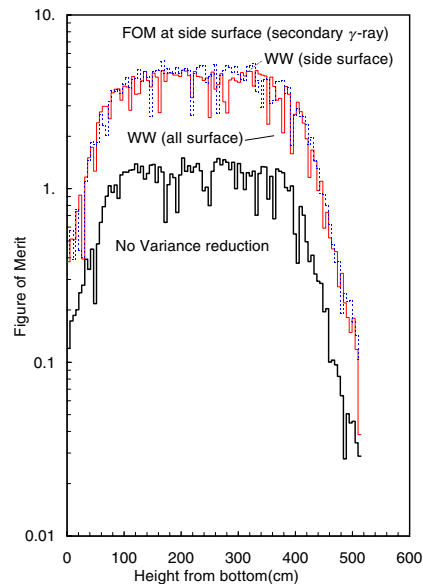


Fig. 5. FOM for the secondary γ ray dose distribution at side surface of cask calculated with weight window (WW). The adjoint source was placed on the whole surface ('all surface') or side surface ('side surface') of cask

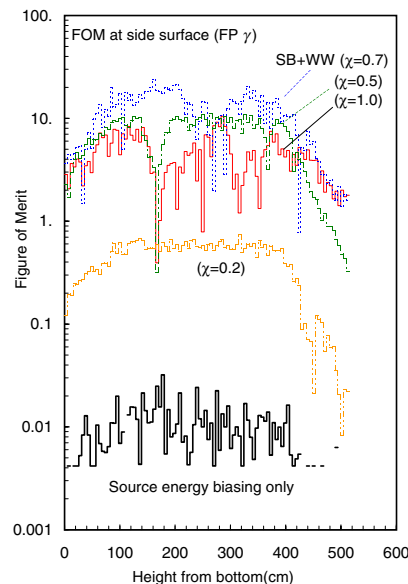


Fig. 6. FOM for the FP γ ray dose distribution at side surface of cask calculated with weight window (WW) and source energy biasing (SB). The weight window parameters are calculated with relaxation factors(χ) of 1, 0.7, 0.5 and 0.2.

References

1. K.A.V. Ripper et al.: 'AVATAR - Automatic Variance Reduction in Monte Carlo Calculations'. In: *Proc. of the 1998 ANS Radiation Protection and Shielding Division Topical Conference*, p.661, Nashville Tenn. (April 1998)
2. J.C. Wagner, A. Hagighat: 'Automatic Variance Reduction for Monte Carlo Shielding Calculations with the Discrete Ordinate Adjoint Functions'. In: *Proc. of the 1998 ANS Radiation Protection and Shielding Division Topical Conference*, p.671, Nashville Tenn. (April 1998)
3. J.F. Briesmeister Ed.: *MCNP - A General Monte Carlo N-Particle Transport Code - Version 4B*, LA-12625-M Version 4B (1997)
4. W.W. Engle, Jr.: *ANISN, A One-Dimensional Discrete Ordinates Transport Code with Anisotropic Scattering*, K-1693, Union Carbide Corporation (1967)
5. M.B. Emmett, W.A. Rhoades, R.L. Childs, J.O. Johnson: the DORT section of *A User's Manual for MASH 1.0 - A Monte Carlo Adjoint Shielding Code System*, ORNL/TM-11778 (March 1992)
6. L.L. Liu, R.P. Gardner: *Nucl. Sci. Eng.* **125**, 188 (1997)
7. K. Ueki, M. Inoue, Y. Maki: *Nucl. Sci. Eng.* **84** 271 (1983)
8. *CASK - 40 Group Coupled Neutrons and Gamma-Ray Cross-section Data*, RSIC Data Library Collection, DLC-23 (1973)

Improvement and Benchmarking of the New Shutdown Dose Estimation Method by Monte Carlo Code

L. Petrizzi¹, H. Iida², D. Valenza³, P. Batistoni¹

¹ Associazione Euratom - ENEA sulla fusione, C.R. Frascati, via E. Fermi 27 00044 Frascati Roma Italy

² ITER Garching Joint Work Site c/o Max Planck Institut für Plasmaphysik Boltzmannstraße 2 D-85748 Garching, Germany

³ temporary at the Material Forschung Bereich, Max Planck Institut für Plasmaphysik Boltzmannstraße 2 D-85748 Garching, Germany

Abstract. In the ITER (International Thermonuclear Experimental Reactor, [1]) project calculations of the dose rate after shutdown are very important and their results are critical for the machine design. A new method has been proposed [2] which makes use of MCNP [3] also for decay gamma-ray transport calculations. The objective is to have an easy tool giving results affected by low uncertainty due to the modeling or simplifications in the flux shape assumptions. Further improvements to this method are here presented.

This methodology has been developed, in the ITER frame, in a limited case in which the radioactivity comes only from the Vacuum Vessel (made of stainless steel) till a time around few days after ITER shutdown. Further improvement is required to make it applicable to more general cases (at different times and/or with different materials).

Some benchmark results are shown. Discrepancies between the different methods are due mainly to the different cross section used. Agreement with available *ad hoc* experiment is very good.

1 Introduction

Reliable estimation of the dose equivalent rate levels around the ITER machine after reactor shutdown is essential for determining machine operation and maintenance strategies. Fully comprehensive estimation of biological dose rate requires, generally, the following three step calculations:

a) a neutron transport calculation to obtain the spatial distributions and energy spectrum of the neutron flux during reactor operation inside and outside the machine

b) an activation calculation for every component using the neutron flux distribution including energy spectrum obtained in step a) in order to obtain distributed gamma-ray sources after shutdown and, finally

c) a gamma ray transport calculation using the gamma ray source obtained in step b).

The best way is to perform full 3-D calculations for each of the above steps, due to the complexity of the ITER system. A part from the fact that it is not

possible to have an integrated tool able to handle the three steps procedure in a semiautomatic way, that procedure give intrinsic unpredictable approximations. First: the activation codes want the flux to be given in energy bins. The score calculated by Monte Carlo method is accurate if the value is integrated over all the energy range. The statistical error increases when energy bins are asked, less precise thinner the bins are. Deterministic Sn codes give exact solution for multigroup fluxes, apart for resonance problems, but they cannot be used to treat complex geometries. Second: the Monte Carlo codes give score as volume average; the volume can be thick few mean free paths. Especially in strong absorbing media, information on the flux gradient inside the cell is lost. Average value can under or overestimate the emission of the gamma ray by the radioactive isotopes in thin layers of the cell.

A simpler approach is the usage of a flux-to-dose conversion factor. This method has been extensively applied in the ITER frame itself [4]. Results have shown that such a factor is not a definite value, dependent on the assumed scenario, the component around which the dose is calculated, and also on the calculation tools. The flux-to-dose conversion factor can give a rule of thumb value, but its uncertainty is very large: it can be a factor between 2 and 5.

To have fewer approximations, also without having the problem of the interface of the three steps methodology, a different approach has been developed [2]. The new methodology, called single step procedure, uses the MCNP [3] Monte Carlo code to transport neutrons and the gamma ray, emitted by the radioactive isotopes, in the same run. In this article the improvements to that innovative method are presented. In the following paragraphs an illustration of the new methodology, the improvements added and the results of the benchmarks, even with the available experiments will be shown.

2 Coupling the Decay Gamma-ray to the Neutrons

According to the new methodology the gamma rays emitted by the radioactive isotopes are coupled to the neutrons as they were promptly emitted. At the purpose a special ACE [3] format cross-section library is needed. The neutron part is like a normal transport library. For the photon generation, only the cross sections generating radioisotopes are included. Absolute and relative intensities, energy spectra of the gamma can be taken from every ENDF library in file 8 or 9 [5]. This trick allows the decay gamma rays to be transported, as they were prompt. The eventual energy release is scored in a given cell.

A second trick is introduced to distinguish the different gamma rays coming from the different isotopes. A delay time, expressed in shakes ($1 \text{ shake} = 10^{-8} \text{ sec}$ [3]), is given to each different gamma. A proper time binning of the gamma related tallies in MCNP, shares the contributions of the different isotopes. That time delay is artificial, it has nothing to do with the decay time of the radioactive isotope; the purpose is only to distinguish the different gamma rays.

For dose calculations the user has to couple the contributions of the different isotopes by a factor, which is function essentially of the time. This factor takes

into account the build up of the isotope during irradiation and its decay at shut down. It can be derived in an analytical way or derived using properly the outcome of the inventory codes. THIDA-2 [6] or FISPACT [7] have been used so far. More details can be found in [2].

The single step approach has the advantage to divide the time dependency of the radioactive decay from its spatial dependency. The time dependency is calculated by any inventory codes. Isotopes production rates, gamma decay transport, space dependent, are calculated with MCNP.

3 Improvements to the New Method

The first single step version of MCNP [2], soon at the beginning showed some features capable of improvement.

The first used ACE transport library including the decay gamma rays was done by editing data line by line. This procedure was too slow and risky; an automatic procedure is preferable. A software has been written that modifies an already existing transport data in ACE format for MCNP, replacing the prompt gamma part with a new gamma decay cross section data according to the instructions given by the user. The software partially uses already existing routines of NJOY code [8].

The software works in this way: the original *classic* transport library is read; in the first part there is the neutron transport and in the second the prompt gamma generation data. The first part is kept as it is, the reaction rates generating radioactive isotopes are picked and added together to give the total new total gamma generation cross section. The gamma part is then built up introducing those partial cross sections and the gamma spectra with intensities. The decay gamma data can be from any library in ENDF format; both FENDL 2A and EAF99 [9,10] were used. The user drives all the process by an input file, in which selections of the reactions and decay data are done.

The first single step version of MCNP is not able to use the PIKMT card. This is a powerful tool to control and bias the photon generation in the system. PIKMT can be used to pick only a small subset of isotopes and reactions. The computer time can be reduced cutting all the photons that have no interest. An improvement gave back the use of the PIKMT card.

The “time delay”, used like a label for the emitted gamma rays, is assigned in ACEGAM the main routine managing the gamma generation. An improvement has been introduced. An external file is created, a *time* matrix, divided in rows according to the target nucleus and reaction identifiers (MT). The *time* matrix file is read once at the beginning of the MCNP run, during the set-up.

More details of the introduced improvement are in [11].

4 Benchmarks

The first benchmark has been conducted in a simple spherical model, comparing the two single step MCNP versions the one in [2] and the here proposed. A

general good agreement is found, differences can be ascribed to the difference in nuclear data used in the two versions. The use of PIKMT card can speed up the time by a factor between 3 and 10 depending on the isotopes.

A first list of nuclides prepared is in Tab. 1. This limited set can tackle the dose rate calculations for the structural material used normally in the ITER frame.

Table 1. List of the parent nuclides, reactions and daughters

Parent isotope	Reaction	Radioactive isotope
Fe ⁵⁸	(n,γ)	Fe ⁵⁹
Co ⁵⁹	(n,2n)	Co ⁵⁸
	(n,γ)	Co ⁶⁰
	(n,p)	Fe ⁵⁹
Ni ⁵⁸	(n,p)	Co ⁵⁸
Ni ⁶⁰	(n,p)	Co ⁶⁰
Ni ⁶¹	(n,np)	Co ⁶⁰
Ni ⁶²	(n,α)	Fe ⁵⁹
Cu ⁶³	(n,α)	Co ⁶⁰
Mn ⁵⁵	(n,2n)	Mn ⁵⁴
Fe ⁵⁴	(n,p)	Mn ⁵⁴
	(n,α)	Cr ⁵¹
Fe ⁵⁶	(n,t)	Mn ⁵⁴
Cr ⁵⁰	(n,γ)	Cr ⁵¹
Cr ⁵²	(n,2n)	Cr ⁵¹

The first benchmark assures us that the new proposed version is consistent with the previous one. A second benchmark has been done. In this case the comparison is conducted towards calculations performed by THIDA-2 in a cylindrical geometry. This compares the single step approach with the *classical* three step approach. A comparison of the two results shows that the differences in the two kinds of calculations can be ascribed again to differences in the nuclear data libraries used. In that benchmark the single step MCNP uses data from FENDL/MC-2.0, decay gamma spectra and yields are taken from EAF-99. THIDA 2 uses FENDL/A-2.0 cross sections [12]. A recent work [13] has shown that, for example, Co⁵⁸ production can be different by 25% if FENDL/MC-2.0 or FENDL/A-2.0 cross section is used.

A third even more and interesting benchmark is the one performed with experimental data (Fig. 1). In the frame of an ITER Task 426: “Experimental

validation of shut down dose rates calculations inside ITER cryostat”, the new tool is used to calculate dose rates. More insights are in [14]. The new one step method is in good agreement with the classical three steps procedure method when using the same cross section file (i.e. FENDL/A-2.0, see Fig. 2). The difference obtained using data from FENDL/A-2.0 or FENDL/MC-2.0 is mainly due to the $\text{Ni}^{58}(\text{n,p})\text{Co}^{58}$ cross section, at the times considered, which results in about 16% difference in Co^{58} production in the two cases. The agreement with experimental measurements is in any case very good.

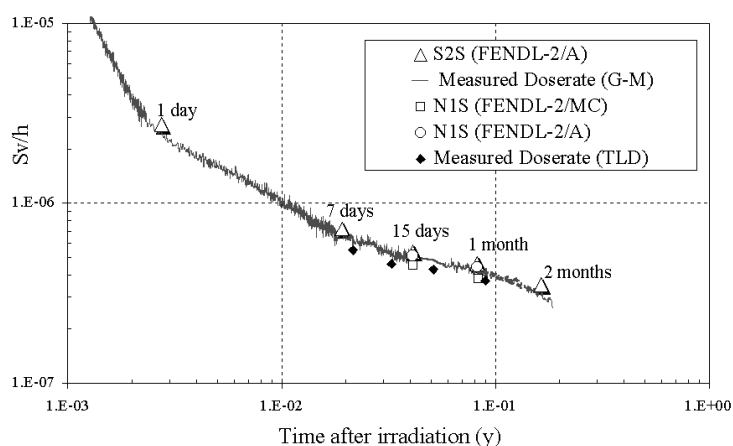


Fig. 1. Comparison of experimental data with calculated ones. N1S is the single step method, S2S is the three step method

5 Conclusions

The modified version of MCNP for dose rate calculation looks to be a very attractive tool. The so-called one step method goes towards a major accuracy in that kind of calculations, even if the benefit is not easily quantified. In this work a new more powerful software has been prepared. A user-friendly program able to prepare ad hoc ACE transport library has been written. A complete library of isotopes, able to treat ITER related problems, has been prepared. In the new modified MCNP the use of the PIKMT card is back again, with a control of the photon generation achieving higher computational efficiency.

Benchmarking give satisfying results. Discrepancies with previous versions or other methods are due mainly to differences on the cross sections data used. Unexpected large discrepancies are found in cross section data that have the same origin. This fact suggests the evaluators to carefully check the available data, and to give more consistency among the different library versions even if they are released for different purposes, in different frames.

The new proposed method, at the moment, has some limits. For example multi-step isotopes formation or calculations in which there is a strong high burn-up cannot be handled. Fortunately this does not give any significant problem, at least in low fluence machines like ITER.

References

1. P.H. Rebut: Fus. Eng. Des. **30**, 85 (1995)
2. D. Valenza, H. Iida, R. Plenteda: 'Proposal of Shutdown Dose Estimation Method by Monte Carlo Code', submitted to the journal of Fusion Engineering and Design in Sept. '99
3. J.F. Briesmeister, Editor: *MCNP – A General Monte Carlo N-Particle Transport Code, Version 4b*, Los Alamos National Laboratory (March 1997)
4. H. Iida, R.T. Santoro, et al: *Analysis of Flux-To-Dose Conversion Factor*, NAG 89-10-06-98, inserted in the ITER Final Design Report
5. Cross Section Evaluation Group: *Endf 102: Data Formats and Procedures for ENDF 6* BNL-NCS-44945 Rev. 2/97 Brookhaven National Laboratory Upton, N.Y.
6. Y. Seki, H. Iida, H. Kawasaki, K. Yamada: *THIDA-2: An advanced Code System for Transmutation, Activation, Decay Heat and Dose Rate*, Japan Atomic Energy Research Institute, JAERI 1301 (March 1986)
7. R.A. Forrest, J.-Ch. Sublet: *FISPACT-99: User Manual*, UKAEA FUS 407 (Dec. 1998)
8. R. Mc Farlane: *NJOY94.105: User Manual*, Los Alamos National Laboratory (July 1997)
9. A.B. Pashchenko, H. Wienke, J. Kopecky, J.-Ch. Sublet, R.A. Forrest: *FENDL/A-2.0 Neutron Activation Cross Section Data Library for Fusion Applications*, IAEA report IAEA-NDS-173, Rev. 1 (October 1998)
10. R.A. Forrest, J.-Ch. Sublet: *The European Activation File: EAF-99 decay data library*, UKAEA FUS 409, EASY Documentation Series (Dec. 1998)
11. L. Petrizzi, H. Iida, D. Valenza: *Further development of a method for calculating the dose rate by means of MCNP*, NAG-143-13-12-99
12. H. Wienke, M. Herman: *FENDL/MG-2.0 and FENDL/MC-2.0 The processed cross-section libraries for neutron photon transport calculations*, IAEA-NDS-176 Rev. 1 (October 1998)
13. L. Petrizzi: *Library Tape Modification for the Dose Rate Calculations by MCNP*, Progress Meeting on Neutronics Tasks, July 2000, ITER Garching JWS
14. P. Batistoni, M. Angelone, L. Petrizzi, M. Pillon: 'Experimental Validation of Shutdown dose rates calculations inside ITER cryostat', presented at the 21th SOFT Madrid, September 2000, to be published

Monte Carlo Simulation of Neutron and Photon Transport with Direct Utilization of Information from Evaluated Nuclear Data Files

P.A. Androsenko, D.L. Joloudov, and A.V. Kompaniyets

Institute of Nuclear Power Engineering, Obninsk, Russia

Abstract. The most advanced constant information related to the accuracy of calculations is available in files of nuclear data libraries. It is common practice in Monte Carlo to use routines of Constant Unit to simulate the process of particles interaction with substances and to solve neutrons and photons transport problem. It is a characteristic of Constant Unit to derive parameters directly from data files without any simplification. The main idea of the method proposed by us is to directly extract the values required from data files. The usual practice so far applied is that data processing is followed by the Monte Carlo method application in calculational efforts. The method being developed allows to directly utilize the data obtained from libraries and seems to be the most accurate technique. Moreover, the method proposed doesn't introduce additional inaccuracy into the final results.

1 Methods and Comparison

This paper presents a special option of the code system BRAND [1]. This option directly uses the continuous-energy neutron and photon data libraries in ENDF-6 format [2]. All phase coordinates of particles are modeled according to the laws described in the evaluated nuclear data files. In particular we calculate the values of cross section during each Monte Carlo neutron trajectory in the resonance energy range. Algorithms and results of this approach were published [1,3]. Hence, as an example we consider the only computational experiment.

This computational experiment sampling neutron and secondary photon leakage spectra from *Pb*-sphere. Experiment was performed in one-dimensional spherical geometry. Nuclide ^{252}Cf was used as a neutron source with output flow 10^9 sec^{-1} and was considered as a point isotropic source.

Pb-sphere (isotope concentrations $\rho_{206 \text{ Pb}} = 0,00792 \times 10^{24}$, $\rho_{207 \text{ Pb}} = 0,00759 \times 10^{24}$, $\rho_{208 \text{ Pb}} = 0,01749 \times 10^{24}$) was considered as a calculation model. External radius of the sphere is $R = 20$ cm. The neutron point isotropic source in the center of *Pb*-sphere is surrounded by vacuum sphere with $r_0 = 1,3$ cm. Calculational results are presented of Figs. 1, 2.

As we can see there are no sufficient differences between MCNP-results with NJOY and BRAND calculations with using direct information from data files.

Below we consider the simulation of neutron cross section values in the unresolved resonance energy region and photon coherent/incoherent scattering simulation.

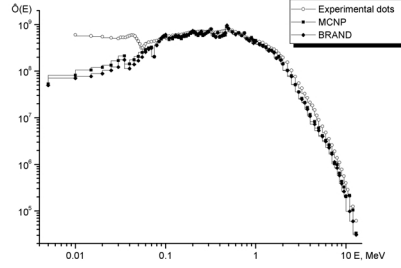


Fig. 1. Neutron leakage spectra for the Pb sphere

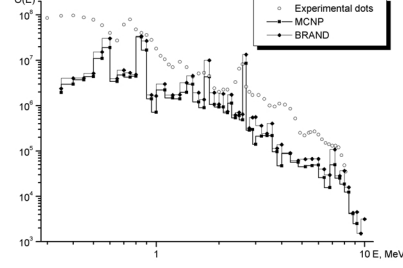


Fig. 2. Photon leakage spectra for the Pb sphere

2 Simulating Unresolved Resonance Widths

Each unresolved resonance parameter width is distributed according to χ_n^2 distribution with a certain number (n) of degrees of freedom. It is assumed that distributions of parameter values are described by a δ -function at $n < 1$ (in particular at $n = 0$) and at $n > 4$. Thus, from the point of view of sampling resonance widths only the cases $n = 1, 2, 3$ and 4 are of interest. By definition, the random value χ_n^2 is defined as:

$$\chi_n^2 = \sum_{k=1}^n \eta_k^2 \quad (1)$$

where η_k are the normalized independent Gauss distributed random values. Probability density function for χ_n^2 at non-negative values of argument is:

$$f_n(x) = C_n x^{\frac{n}{2}-1} e^{-\frac{x}{2}} \quad (2)$$

and at $n = 2$ agrees with the density of the exponential distribution with parameter $\frac{1}{2}$. Let us denote pseudo-random number to symbol γ with various indexes independently uniform distributed at interval $[0, 1)$. Then, applying a method of inverse functions, we receive simulating formula for this case:

$$\chi_2^2 = -2 \ln(\gamma) \quad (3)$$

It is easy to see, that the sum of two independent random values distributed exponentially is distributed by the χ^2 law with four degrees of freedom. Therefore for $n = 4$ the simulating formula looks as follows:

$$\chi_4^2 = -2 \ln(\gamma_1 \gamma_2) \quad (4)$$

For cases $n = 1, 3$ let us take the definition of χ^2 distribution and the known way of normal distribution modeling based on properties of isotropic vector. Then for $n = 1$:

$$\chi_1^2 = -2S \ln(\gamma) \quad (5)$$

And, accordingly, for $n = 3$:

$$\chi_3^2 = -2 (\ln(\gamma_1) + S \ln(\gamma_2)) \quad (6)$$

where: S - square of an angle sine between a $2D$ -isotropic vector and coordinate axis. Value of S is calculated using rejective method by following algorithm:

$$\alpha_i = (1 - 2\gamma_i)^2, \quad (7)$$

$$\alpha_{i+1} = (1 - 2\gamma_{i+1})^2, \quad (8)$$

$$S = \frac{\alpha_i}{(\alpha_i + \alpha_{i+1})} \quad (9)$$

provided that $\alpha_i + \alpha_{i+1} < 1$. Otherwise pair (α_i, α_{i+1}) is rejected and the new values (γ_i, γ_{i+1}) are generated.

As an example here we compare cross sections in unresolved energy region for two materials: isotope ^{232}Th and natural Mo consisted of 7 isotopes.

In Tabs. 1, 2 three values are represented for BRAND: minimal sampled cross section value, maximal sampled cross section value and average value of 10000 sampled cross section values. It should be noted that maximal difference between NJOY values and BRAND's average values is not greater than 5,9% for natural Mo and 1,7% for ^{232}Th .

Table 1. Comparison of unresolved cross sections for natural Mo

E, eV	Program	σ_t	σ_{nn}	$\sigma_{n\gamma}$
60000	NJOY	8.842	8.735	1.077E-1
	BRAND average	9.297	9.187	1.100E-1
	BRAND min	6.326	6.233	7.287E-2
	BRAND max	16.808	16.693	1.363E-1
80000	NJOY	9.019	8.931	8.839E-2
	BRAND average	9.547	9.456	9.051E-2
	BRAND min	6.300	6.223	5.934E-2
	BRAND max	18.172	18.076	1.120E-1
97500	NJOY	9.140	9.062	7.849E-2
	BRAND average	9.611	9.531	8.013E-2
	BRAND min	6.606	6.538	5.516E-2
	BRAND max	17.078	16.994	9.814E-2

Table 2. Comparison of unresolved cross sections for ^{232}Th

E, eV	Program	σ_t	σ_{nn}	$\sigma_{n\gamma}$
5000	NJOY	17.158	16.174	9.836E-1
	BRAND average	17.211	16.230	9.810E-1
	BRAND min	11.764	11.760	3.162E-3
	BRAND max	92.363	91.115	3.286
15000	NJOY	14.893	14.273	6.193E-1
	BRAND average	14.916	14.297	6.189E-1
	BRAND min	11.603	11.598	3.390E-3
	BRAND max	54.204	53.476	1.832
49500	NJOY	13.609	13.216	3.932E-1
	BRAND average	13.603	13.210	3.935E-1
	BRAND min	11.245	11.149	8.025E-2
	BRAND max	24.295	23.671	6.947E-1

Two computational experiments were performed to calculate neutron leakage spectra in unresolved energy regions from spherical samples using code system BRAND and MCNP. Experiments were performed in one-dimensional spherical geometry. As a calculated model a *Mo*-sphere (nuclear concentration $\rho_{Mo} = 0,0640344 \times 10^{24}$) and a *Th*-sphere (nuclear concentration $\rho_{Th} = 0,03039558 \times 10^{24}$) were considered. The external radius of the *Mo*-sphere is $R = 7$ cm, the external radius of the *Th*-sphere is $R = 10$ cm. A point isotropic monoenergetic neutron source ($E_0 = 100$ keV for *Mo* and $E_0 = 50$ keV for *Th*) is located in the center of both spheres. Results of calculations are shown in Figs. 3 and 4.

Figures show that the difference between BRAND calculation with random cross section values differ from results obtained by using another cross section models (point-wise, probability tables). This fact was predictable since it is well known that average value of random function is not usually equal to average value of random argument function.

According to our approach we have to select the results of BRAND calculation with random cross section values as mostly correct results.

3 Photon Coherent and Incoherent Scattering Simulation

Most programs based on Monte-Carlo method use the Klein-Nishina distribution to describe the energy and angle of scattered photons. It is assumed that this distribution describes the effect of both coherent and incoherent scattering. Since the energy of the photon does not change when coherent scattering occurs but the Klein-Nishina law implies an energy decrease, we can say that part of the photons

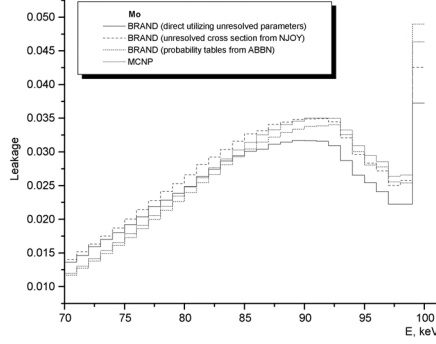


Fig. 3. Neutron leakage from Pb sphere

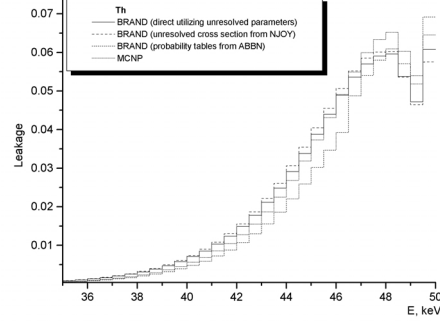


Fig. 4. Neutron leakage from Pb sphere

scattered at small angles is underestimated. Besides, additional falsification is introduced into scattered photon spectra at the energy range, where incoherent scattering is dominating. Actually, the Klein-Nishina density is not equal to zero at zero scattering angle, but the incoherent scattering density in this case is null. A special algorithm, based on optimal linear votes construction and further line-segment density simulation using the rejective method, have been developed to simulate the incoherent scattering density. We use the following optimal algorithm [4] for the simulation of the random value with the linear probability density function. Let us denote the left and right value of interval x_L and x_R and the values of density f_L and f_R in the respective points. Then let us calculate

$$\xi = x_L + \gamma_1(x_R - x_L) \quad (10)$$

$$\eta = \gamma_2(f_L + f_R) \quad (11)$$

If $\eta < f_L + \frac{f_R - f_L}{x_R - x_L}(\xi - x_L)$ then ξ is the required random value, otherwise $\xi = x_L + x_R - \xi$. Since the form-factor for the coherent scattering is tabulated we can represent distribution function as follows:

$$\int \frac{d\sigma_{coh}(E, \mu)}{d\mu} d\mu = \sigma_{coh}(E) \sum_i p_i \quad (12)$$

where p_i is the probability of i -th range check which is defined by the table of impulse q_i (MT=502) in file 27. We achieve the μ partition formula

$$\mu_i = 1 - \frac{q_i^2}{2k^2} \quad (13)$$

where k is the initial energy in mc^2 units. Because of the log-log interpolation (INT = 5) is used for representation of the form factor in ENDF-6 format, we may present the form factor as follows:

$$FF_i(q) = e^{b_i q^{a_i}} \quad (14)$$

and calculate p_i analytically.

The coherent scattering function is such, that for $\mu \cong 1$ it sufficiently grows at small angle interval, hence it is not efficient to use the rejective method in the whole interval $\mu \in [-1, 1]$. However, for $\mu \cong 1$ only the two first summands ($C_1\mu$ and $C_2\mu^3$) are sufficient and this fact allow us to find the inverse function and to use the inverse function method. Tests of the developed methods have shown their correctness with χ^2 criteria for high enough computer speed.

The calculational comparison was made for the following model problem: *Pb*-sphere ($R = 10$ cm) with point monoenergetic ($E_0 = 6$ MeV) isotropic source in the centre of sphere. Leakage spectra was estimated by:

- 1) previous option of BRAND with Storm, Israel cross sections [5] using Klein-Nishina distribution;
- 2) using Klein-Nishina distribution and cross sections from file 23 of ENDF-6 format;
- 3) using files 23,27 of ENDF-6 format;
- 4) using MCNP.

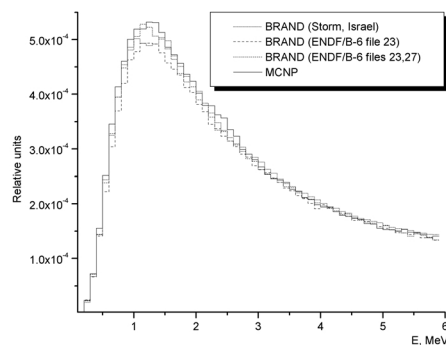


Fig. 5. Photon leakage from Pb sphere

Calculated results are represented in Fig. 5.

We do not take into account photons produced by electrons. In this way we can estimate pure effect from replacing the Klein-Nishina law by coherent and incoherent distributions. As we can see from Fig. 5 there are no sufficient differences in the energy spectra. The same results can be applied to other materials.

4 Conclusion

A benchmark code for calculating the neutron and photon transport directly using Evaluated Nuclear Data Files has been developed. This tool is used for testing other codes. Our gratitude to Mr. N.A. Soloviev for making the calculation on MCNP.

References

1. A.A. Androsenko, P.A. Androsenko et. al.: *Monte Carlo Simulation of Neutron Transport Process, Photons and Charged Particles*. (Preprint FEI-2205, Obninsk, 1991)
2. R.F. Rose, C.L. Dunford: *ENDF-6 Format Manual*, IAEA-NDS-76, 1991
3. P.A. Androsenko, A.V. Kompaniyets: *Nuclear Energy* **3**, 46 (1998)
4. P.A. Androsenko, G.V. Popova, *J. of Computational Math. and Math. Phys.* **21** (1981)
5. J.R. Eriksson: *Nucl. Sci. Eng.* **41**, 307 (1970)

Application of MCNP-Based Software Package MF3D for BWR Radiation Damage Computations

R-T. Chiang¹, S. Sitaraman¹, K. Asano², and K. Koyabu²

¹ GE Nuclear Energy, San Jose, CA 95125, USA

² The Tokyo Electric Power Co., Yokohama, 230-8510, Japan

Abstract. The steel and sapphire damage doses and their ratios are computed using the MCNP-based MF3D computed neutron fluence. The computed steel dpa are reliable and the computed dpa ratios between sapphire and steel are useful to convert the measured sapphire dpa to the corresponding steel dpa. The effective spectrum-average displacement cross sections of steel and sapphire above 0.1 or 1 MeV are very useful for evaluating the steel and sapphire dpa by multiplying them with the fast neutron fluence.

1 Introduction

A MCNP Monte Carlo-based software package [1–3], MF3D, was utilized to compute BWR (Boiling Water Reactor) radiation damage in addition to the fluence computations in the reactor shroud and pressure vessel. The primary reactor vessel steel damage from neutrons and associated capture gamma rays bombardment is the displacement of atoms from their normal lattice sites. The amount of displacement damage to reactor steel due to neutron and gamma irradiation depends on their spectra and the duration of irradiation.

Iron (Fe) nuclei in BWR shrouds and reactor vessel steels recoil after collisions with fast neutrons. The recoiled steel atoms are likely to be displaced from their normal positions in the solid lattice if the recoil energies exceed 25 eV, which is the minimum energy required to displace an atom in metal [4]. The displacement damage due to Compton scattering is dominant for gamma energies above 1 MeV and the displacement damage due to pair production becomes important only for gamma energies above 5 MeV [5].

High purity, single crystal sapphire (α -alumina, Al_2O_3) has been widely employed as an integrating, fast neutron (energy greater than 10 keV), displacement damage monitor for neutron fluences in the range 10^{16} – 10^{20} n/cm² and for a temperature range of 200–320°C, within which aluminum vacancies and interstitials in sapphire are stable. The measured damage dose of sapphire can then be converted to that of Fe in stainless steel using a calculated sapphire-to-steel dpa (displacement per atom) ratio. Consequently, both the steel and sapphire damage doses and their ratios were computed in this application.

2 Radiation Damage Model

The reactor vessel steel displacement damage dose is calculated by summing the product of neutron flux and the steel displacement cross section over the entire energy range and over the irradiated time period at a given location as

$$Dpa = \sum_g \sigma_{d,g} \sum_i \varphi_{g,i} \Delta t_i \quad (1)$$

where $\sigma_{d,g}$ is the g -th group steel displacement cross section and $\varphi_{g,i}$ is the average g -th group neutron flux in the i -th time interval Δt_i .

Since the majority of the displacement damage is caused by fast neutrons, a practical reactor vessel steel displacement damage dose correlation can be constructed by first creating an effective spectrum-average displacement cross section ($\sigma_{d,eff}$) above 0.1 or 1 MeV, which is the average of the steel displacement damage dose per unit fast fluence above 0.1 or 1 MeV:

$$\sigma_{d,eff} = Dpa / \sum_{g,i} \varphi_{g,i}(> 0.1 \text{ or } 1 \text{ MeV}) \Delta t_i \quad (2)$$

Then, the estimated steel dpa damage dose is simply the product of the effective spectrum-average displacement cross section and the fast fluence above 0.1 or 1 MeV at a given location in or near the reactor shroud and reactor vessel.

3 Results

The neutron fluences of a fuel cycle at three (lower, middle, and upper) axial locations of a typical line outside the shroud of a typical BWR were computed using the MCNP-based MF3D [3]. The steel and sapphire displacement cross sections are available in the SPECTER 100 groups format [6]. The steel and sapphire dpa in the three locations outside the shroud were calculated by summing the neutron fluence and the displacement cross-sections and are listed in Tab. 1. The dpa is the highest in the upper location because the void fraction is the largest among the three in the upper portion of the core, resulting in the highest fast fluence in the annulus.

Table 1. Computed steel and sapphire dpa outside the shroud

Location	Sapphire	Steel	Steel/Sap
upper	2.75E-02	2.13E-02	0.776
middle	2.01E-02	1.51E-02	0.751
lower	1.77E-02	1.30E-02	0.733

The mean effective spectrum-average displacement cross sections of steel and sapphire above 0.1 or 1 MeV outside the shroud were also computed and they

are listed in Tab. 2. These effective displacement cross sections can be utilized to estimate the steel and sapphire dpa by multiplying them with the fast neutron fluence at a given location in or near the shroud. The estimated steel and sapphire dpa, calculated using the mean effective spectrum-average displacement cross sections in Tab. 2, and their ratios with respect to directly computed steel and sapphire dpa for the KKM samples are shown in Tab. 3. Note that the estimated to directly computed dpa ratios (E/C) are within 5%, which is quite good, and the deviation variations result from the difference in the dpa cross section distribution and neutron energy spectrum.

Table 2. Mean effective spectrum-average displacement cross sections for steel and sapphire outside the shroud

$\sigma_{d,eff}$ (barns)	Steel	Sapphire
E > 0.1 MeV	709.9	941.5
E > 1 MeV	1371	1819

Table 3. Estimated steel and sapphire dpa and their ratios with respect to directly computed steel and sapphire dpa outside the shroud

Location	Neutron Energy > 0.1 MeV				Neutron Energy > 1 MeV			
	Sapphire	Fe	S E/C	Fe E/C	Sapphire	Fe	S E/C	Fe E/C
upper	2.72E-02	2.05E-02	0.99	0.96	2.90E-02	2.19E-02	1.05	1.02
middle	2.00E-02	1.51E-02	1.00	1.00	1.97E-02	1.48E-02	0.98	0.99
lower	1.80E-02	1.35E-02	1.01	1.04	1.73E-02	1.31E-02	0.98	1.01

Similar computations can be done for locations in or near the reactor vessel.

4 Conclusion

The steel and sapphire damage doses and their ratios have been computed using the MCNP-based MF3D computed neutron fluence. The computed steel dpa are reliable, because the steel displacement cross section was obtained from the ASTM standards and the neutron fluence was computed by the benchmarked MF3D [3]. The computed dpa ratios between sapphire and steel are useful to convert the measured sapphire dpa to the corresponding steel dpa. The effective spectrum-average displacement cross sections of steel and sapphire above 0.1 or 1 MeV are very useful for evaluating the steel and sapphire dpa by multiplying them with the fast neutron fluence at a given location in or near the shroud and reactor vessel.

References

1. R-T. Chiang, S. Sitaraman: 'Development of 3D MCNP-Based BWR Fluence Computational Software Package: MF3D'. In: *Reactor Dosimetry*, ASTM STP 1398 (2000)
2. S. Sitaraman, R-T. Chiang, R.L. Kruger, A.L. Jenkins, K. Asano, K. Koyabu: 'BWR Neutron Fluence Computations Using MF3D'. In: *Reactor Dosimetry*, ASTM STP 1398 (2000)
3. S. Sitaraman, R-T. Chiang, K. Asano, K. Koyabu: 'Benchmark for a 3D Monte Carlo Boiling Water Reactor Fluence Computational Package - MF3D'. These Proceedings p. 785
4. G.J. Dienes, G. H. Vineyard: *Radiation Effects in Solids*, (Interscience Publishers, Inc, New York 1957)
5. J. Kwon, A.T. Motta: 'Role of Radiation in BWR Core Shroud Cracking'. In: *Reactor Dosimetry*, ASTM STP 1398 (2000)
6. L.R. Greenwood, R.K. Smither: *SPECTER: Neutron Damage Calculations for Materials Irradiations*, Argonne National Laboratory, ANL/FPP/TM-197 (1985).

Why Do We Need TARGET?

D. Schlegel and S. Guldbakke

Physikalisch-Technische Bundesanstalt Braunschweig Section 6.41, Bundesallee 100,
D-38116 Braunschweig, Germany

Abstract. Powerful transport codes such as MCNP are generally available and very useful for simulating experimental arrangements for the calculation of the expectation values of physical quantities. Nevertheless, there are many problems which cannot at all, or cannot be satisfactorily, simulated with these codes. In these cases special home-made codes are still an efficient way of modelling specific physical problems.

TARGET is such an example. For a given ion beam and a solid neutron-producing target design this Monte Carlo code calculates the neutron fluence in the position of a detector. It has been an essential tool in the Neutron Metrology Laboratory of the PTB for many years. The useful application of the TARGET code will be demonstrated by practical examples and comparisons with measurements.

1 Introduction

The PTB provides standard neutron fields for the calibration of neutron detectors. The energy and angularly distributed neutron fluence is the basic quantity describing a neutron field. Proton recoil counters (proportional counter, telescope) are used as standard instruments for measuring the neutron fluence in the energy range from 0.01 MeV to 20 MeV. To derive the measurand 'neutron fluence' from the measured response of a detector, its response function or efficiency as a function of the energy of the incoming neutrons must be known. Other important influences, e.g. the geometrical configuration and the interaction of neutrons with the detector itself, have also to be considered.

The first version of the TARGET Monte Carlo code was written in 1983 by Lesiecki [1,2] to calculate the neutron fluence as a function of neutron energy or time of flight (TOF) in any angular position of a detector for various neutron production processes in the energy range from 1 keV to 20 MeV. The TARGET code calculates the uncollided and target-scattered neutron distributions separately. In the meantime the code has been developed and extended to cover new additional features [3]: energy and angle straggling of the impinging ions in the reactive target layer, impregnation of the target backing material with reactive nuclides, a routine to calculate stopping power and range distributions of ions in any material, and variance calculations for the expectation values of various quantities.

By practical examples and comparisons with measurements the useful application of the TARGET code with its new options is demonstrated. The measurements presented here were performed in the low scattering area of the accelerator facility at the PTB in Braunschweig [4].

2 Measurements in a 1.2 MeV Neutron Field

Below 2 MeV the calculated neutron energy distribution is used to calculate the response of a cylindrical proportional counter filled with hydrogen or propane. Corrections for attenuation and in-scattering due to the component parts of the counter have been estimated by means of MCNP calculations.

A pulsed neutron beam was produced using the T(p,n) reaction. The tritiated titanium target consisted of a 1.87 mg/cm^2 thick titanium layer on a 0.05 cm thick silver backing. The impinging protons had a Gaussian energy distribution with a mean energy of 2.1 MeV (fwhm=2 keV). Their mean energy loss is about 98 keV in the tritiated titanium layer. An NE-213 detector (1"x1") was positioned under zero degrees about 302 cm in front of the neutron source. Fig. 1 shows the measured time-of-flight (TOF) distribution compared with the TOF distribution calculated with the TARGET code. The energy straggling of the protons in the reactive target layer was taken into account. The shape of the neutron spectrum of scattered neutrons is mainly influenced by the different materials from which the target is constructed

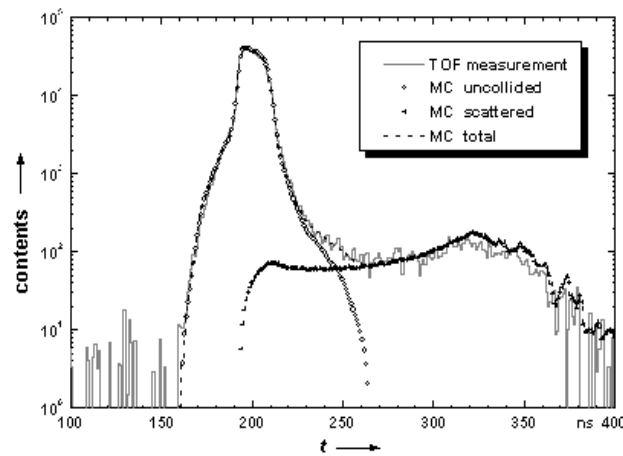


Fig. 1. Comparison of calculated TOF spectrum with measurement in the 1.2 MeV neutron field

The neutron fluence was determined in the unpulsed neutron beam with a cylindrical recoil-proton proportional counter (RPPC) with a 60 kPa propane gas filling positioned at 116 cm in front of the neutron source. The energy-distributed neutron fluence calculated with the TARGET code (see Fig. 2) was folded with the energy response matrix of the RPPC which was calculated with another home-made code. The comparison between measured and calculated pulse-height distribution is shown in Fig. 3. The recoil carbon and photon-

induced events below 0.3 MeV are not taken into account in the calculation of the RPPC response.

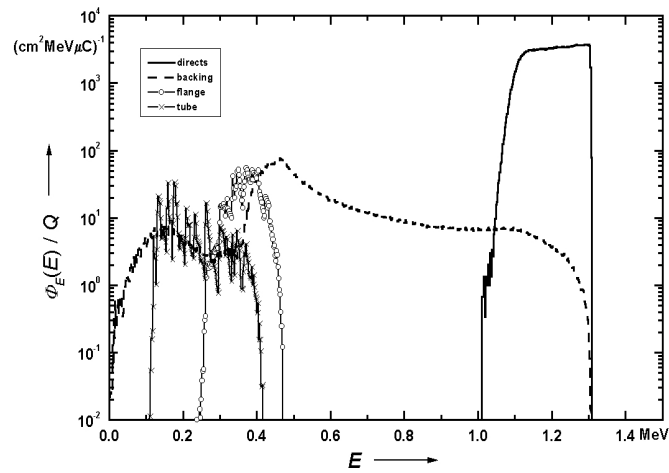


Fig. 2. TARGET-calculated energy-distributed fluence per beam charge (uncollided and scattered separately) for the 1.2 MeV neutron field showing the contribution of different constructive parts of the target

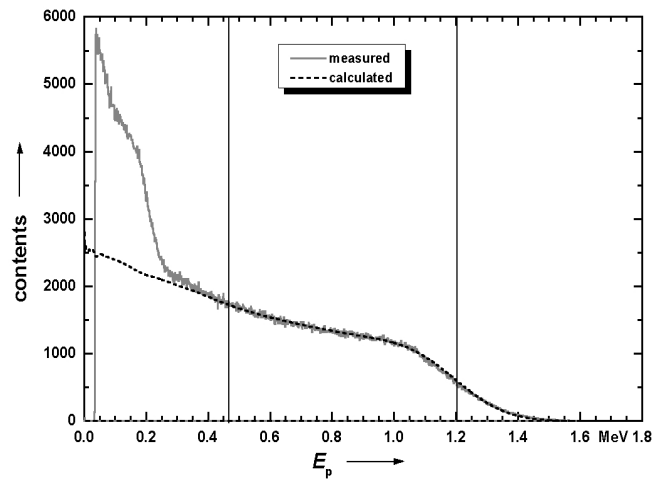


Fig. 3. Calculated and measured response function of a recoil-proton proportional counter and photon-induced events below 0.3 MeV are not taken into account in the calculation of the RPPC response

3 Measurements in a 2.5 MeV Neutron Field

Above 2 MeV a proton recoil telescope is regularly used at the PTB for neutron fluence measurements. For quasi-monoenergetic neutron fields in the energy range from 5 MeV to 15 MeV, a gas target has often been applied. The SINENA [5] Monte Carlo code offers a full simulation of this measuring arrangement, from the neutron production in the gas target to the detection of the recoil protons generated via an n-p reaction in the radiator of the telescope. A new feature in the TARGET code now also allows the response and efficiency function of the telescope for solid targets to be calculated.

With the same experimental arrangement measurements were carried out in a 2.5 MeV neutron field. The proton energy was 3.36 MeV with a mean energy loss in the target layer of 72 keV. The measured and calculated TOF distribution are compared in Fig. 4, and Fig. 5 shows the energy distribution of the uncollided and target-scattered neutrons. The neutron fluence was determined with a recoil-proton telescope (RPT) with its entrance window 20 cm in front of the target. The new TARGET code option allows to calculate the pulse-height distribution. The neutron-proton scattering in the homogeneous radiator and the proton transport through the counter gas, wires and diaphragms to the semiconductor detector in the telescope are simulated. The measured and calculated pulse-height distributions are compared in Fig. 6.

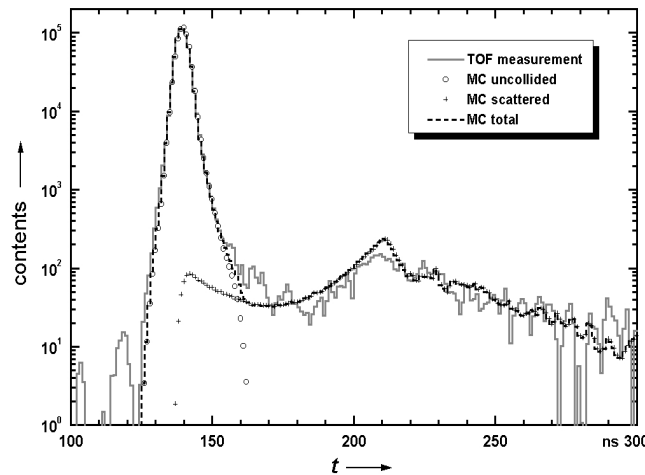


Fig. 4. Comparison of calculated TOF spectrum with measurement in the 2.5 MeV neutron field

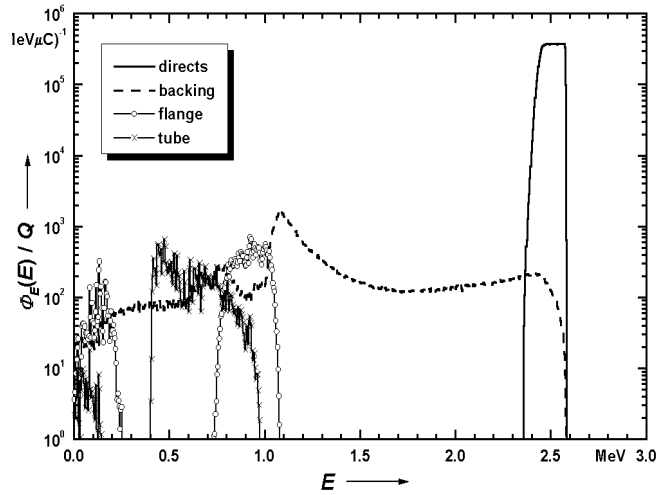


Fig. 5. TARGET-calculated energy-distributed fluence per beam charge (uncollided and scattered separately) for the 2.5 MeV neutron field showing the contribution of different constructive parts of the target

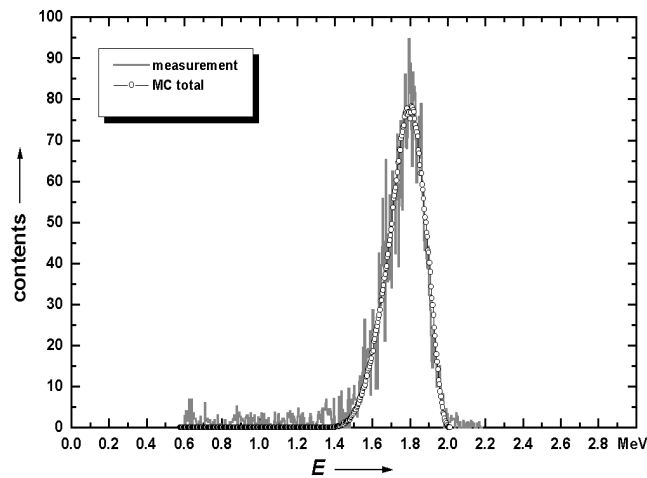


Fig. 6. Calculated and measured response function of a recoil-proton telescope

4 Discussion

These two practical examples are intended to demonstrate the applicability of a problem-oriented Monte Carlo code that allows coupled ion-neutron-ion transport to be simulated. While the presented 1.2 MeV measurements could – with some restrictions – also be simulated with MCNP using the external source option also for the ion transport and neutron generation process, the second

problem cannot yet be simulated – even not with the new version MCNPX. Another advantage of the TARGET code is that each history contributes to the uncollided and scattered neutron fluence tally independently of the angular position of an extended detector. In MCNP this is valid only for point detectors (F5 tally). But for a realistic simulation the angular dependence of the neutron fluence averaged over the finite solid angle spanned by the detector is often important, e.g. when the detector is not positioned under zero degrees and the angular straggling [6] of the ions within the target influences mean energy and energy width of the emitted neutrons. This can be done in MCNP with the cell F4 tally which is, however, the result of an analog Monte Carlo simulation.

5 Conclusion

High-quality calibration fields require precise knowledge of the energy- or time-distributed neutron fluence in the measuring position free in air. All disturbing quantities should be quantitatively known. Most of the neutron detectors use the (n,p) reaction for monitoring the neutrons. Their response as a function of energy or time must be known. The ‘entirety model’ is the best way to study in detail the behavior of a detector, i.e. the simulation of the neutron source and the neutron-ion transport including scattering processes in the detector itself. An extended MCNPX code including light ion transport with joint production of neutrons and photons would be a great help for neutron standard laboratories all over the world. But as long as this has not been realized, we must rely on codes like TARGET and SINENA for the simulation of the neutron production in solid or gas targets.

References

1. H. Lesiecki, M. Cosack, B.R.L. Siebert: ‘Influence of Target-Scattered Neutrons on Cross Section Measurements’. In: *Nuclear Standard Reference Data IAEA-TECDOC-335*, IAEA, Vienna (1985), pp. 144–147
2. H. Lesiecki, M. Cosack, B.R.L. Siebert: ‘Target Scattering in the Production of Monoenergetic Neutrons at Accelerators’. In: *Proc. IAEA Advisory Group Meeting on “Properties of Neutron Sources”, Leningrad, USSR, 1986*, IAEA-TECDOC-410, IAEA, Vienna (1987), pp. 274–278
3. D. Schlegel: *TARGET User’s Manual*. PTB Laboratory Report PTB-6.41-1998-1, April 1998
4. H.J. Brede, M. Cosack, G. Dietze, H. Gumpert, S. Guldbakke, R. Jahr, M. Kutscha, D. Schlegel, H. Schölermann: Nucl. Instr. Meth. **169**, 349 (1980)
5. B.R.L. Siebert, H. Brede, H. Lesiecki: Nucl. Instr. Meth. A **235**, 542 (1985)
6. H. Klein, H.J. Brede, B.R.L. Siebert: Nucl. Instr. Meth. **193**, 635 (1982)

Noise Method for Monitoring the Subcriticality in Accelerator-Driven Systems

Y. Rugama¹, J.L. Muñoz-Cobo², T.E. Valentine³

¹ Universidad Politecnica de Valencia Chemical and Nuclear Engineering
Department, 46071-Valencia, Spain

² Instrumentation and Controls Division, Oak Ridge National Laboratory, Oak
Ridge, TN 37831-6004 USA

Abstract. In this paper, an absolute measurement technique for the subcriticality determination is presented. The development of A.D.S., requires of methods to monitor and control the subcriticality of this kind of systems, without interfering its normal operation mode. This method is based on the Stochastic Neutron and Photon Transport Theory developed by Muñoz-Cobo et al, and which can be implemented in presently available neutron transport codes. As a by-product of the methodology a monitoring measurement technique has been developed and verified using two coupled Monte Carlo programs. The first one LAHET simulates the spallation collisions and the high energy transport and the other MCNP-DSP is used to estimate the counting statistics from neutron ray counter in fissile system, and the transport for neutrons with energies less than 20 MeV. With the coupling LAHET+MCNP-DSP has been checked that a subcriticality monitoring system, is feasible. Through the analysis of the counter detectors is possible to get the kinetics parameters and the Keff value.

1 ADS Description

A conceptual design of the fast energy amplifier has been proposed by Rubia et al (1995) at CERN. The prototype design used in this paper consists of a fast neutron subcriticality facility fueled with U_{233} and Th_{232} and which is cooled with liquid lead-bismuth under natural convection. The driving neutron source are spallation neutrons produced by an intense beam (about 11mA and 380 MeV) proton pulse from a cyclotron. The proton beam is injected in the lead-bismuth coolant slightly above the core centre, which is used as a spallation target for the neutron generation, that will be used as source for the ADS system.

The kinetics parameters and the subcriticality of the system are only known from core calculations, and therefore require experimental verification and a subsequent monitoring. The envisaged Keff values are ranging between 0.945 and 0.985.

2 Stochastic Theory

The behavior of neutrons and gamma rays in a nuclear reactor or configuration of fissile materials can be represented as a stochastic process. Measurements of the fluctuations of the neutrons and also of gamma rays in a system are typically

used to characterize the fissile material. The representation of the statistical descriptor by Muñoz-Cobo et al (1987) for neutrons and Muñoz-Cobo et al (2000) for coupled neutron and photon, is applicable for many neutron noise analysis measurements.

In this paper we have used fission detectors sensitive to neutrons so the formalism used to determine the cross correlation function was the stochastic transport theory of neutrons which was developed by Verdu et al (1987) and Muñoz-Cobo et al (1987).

The objective of this paper was to apply this formalism to develop a noise methodology for monitoring the subcriticality of the ADS.

The aim to use MCNP-DSP is the possibility to obtain 3 detector responses in the system getting the following autopower and cross power spectral densities: CPSD₁₁, CPSD₂₂, CPSD₃₃, CPSD₁₂, CPSD₁₃, CPSD₂₃ of the three detectors (1,2 and 3). It means that it will be used to determine the kinetics parameters and also the subcritical reactivity. The coupled codes LAHET+MCNPDSP provide us a tool to use the CPSD as a descriptor of the noise analysis, and which is obtained using Monte Carlo statistics in the simulation experiments.

The cross-power spectral density CPSD₁₂(w) between one source detector and system detector will give us the possibility to know the Keff value from the position of the first pole in the phase and Bode diagrams. Since the source-detector CPSD₁₂ correlates events in the detector with events in the source, its magnitude changes with the induced fission rate. This pole or α eigenvalue is related to the subcriticality by:

$$\alpha_0 = \frac{\rho}{\Lambda} \quad \text{with} \quad \rho = \frac{1-k}{k} \quad (1)$$

$$\alpha_0 \Rightarrow \text{eigenvalue for the fundamental mode} \quad (2)$$

In this methodology only the fundamental mode and prompt neutrons will be considered, because higher modes are not very important above 0.95 and delayed neutrons contribution are important only near critical.

The α_0 value will be obtained from the CPSD₁₂(w) phase and the Bode diagram. One approximation that we consider is getting the Λ value as a constant independently of the changes in the multiplication constant. The Keff value changes on a small range when the ADS is working, and although there are small changes of Λ with the variations of Keff, these will be so small that we can consider it almost constant in the operational range.

The method developed to obtain α_0 , from the CPSD₁₂ phase and amplitude plots versus frequency will be justified in the next discussion.

The source for the ADS is a proton pulsed beam defined as a periodic array of Dirac Deltas with period, T .

$$S(t) = S_0 \sum_{n=0}^{N-1} \delta(t - nT) \quad (3)$$

Using Stochastic Transport Theory and the adjoint transport equation, we can get the cross power spectral density $CPSD_{12}(w)$ expression, given by:

$$CPSD_{12}(w) = \frac{1}{2\pi} \int_{-\infty}^{\infty} dw_2 S(w + w_2) \exp(i(w + w_2)tf_1) h(w_2) g_{n/p} I^{D_2}(w) \quad (4)$$

where the average importance for source neutrons is given by:

$$I^{D_2}(w) = \int dr^3 \rho_s(r) \int dv' \int d\Omega f_{sp}(v', \Omega) n_c^{D_2}(r', v', \Omega, w) \quad (5)$$

$n_c^{D_2}(r', v', \Omega, w)$ is the average number of counts produced in detector D2, per injected neutron at the phase space point and frequency (r', v', Ω, w) and $S(w + w_2)$ is the Fourier transform of the proton pulse source, $h(w_2)$ is the Fourier transform of the response function for detector 1, ρ_s is the spatial distribution of source neutrons and f_{sp} is the energetic and directional distribution for the source neutron from spallation, $g_{n/p}$ is the neutron proton gain expressed as the number of neutrons obtained per each source proton.

If (3) is the general equation for an arbitrary source then, the cross power spectral density for the proton pulsed beam, as described by (2), is:

$$CPSD_{12}(w) = S_0 \sum_{n=0}^{N-1} \exp(-iwnT) \int dw_2 \exp(-iw_2nT) \exp(i(w + w_2)tf_1) h(w_2) g_{n/p} I^{D_2}(w) \quad (6)$$

Fourier Transforming the adjoint Boltzmann equation, it is obtained:

$$\left(-\frac{iw}{v} + L^+\right) n_c^{D_2}(1, w) = \Sigma_D(r, v) \quad (7)$$

Where we can expand $n_c^{D_2}(1, w)$, in α modes as follows

$$n_c^{D_2}(1, w) = \sum_m T_m^{D_2}(w) \Phi_m^+(1) \quad (8)$$

Where $\Phi_m^+(1)$ is solution of the eigenvalue equation

$$L^+ \Phi_m^+(1) = -\frac{\alpha}{v} \Phi_m^+(1) \quad (9)$$

And satisfying the biorthogonality condition

$$\left(\frac{\Phi_p^+}{v}, \Phi_m\right) = \delta_{mp} N_m \quad (10)$$

substitution of (7) into (6), and use of (8) yields:

$$n_c^{D_2}(1, w) = \sum_m -\frac{(\Sigma_D^{(2)} \Phi_m)}{iw + \alpha_m} \Phi_m^+(1) \quad (11)$$

Using the fundamental mode approximation, we obtain:

$$n_{c0}^{D2} = -\frac{(\Sigma_D^{(2)}\Phi_0)}{iw + \alpha_0}\Phi_0^+(1) \quad (12)$$

Considering (11) the CPD₁₂(w) will be

$$CPD_{12}(w) = S_o \left(\sum_{n=0}^{N-1} \exp(-iw(tf_1 - nT)) W_n^{D1} g_{n/p} \left[\frac{C(D2)}{(\alpha_0 + iw)} \right] \right) \quad (13)$$

Where W_n^{D1} , is a weight factor that depends on the transfer function of the detector 1 (source detector).

$$W_n^{D1} = \int dw_2 \exp(-iw_2(tf_1 - nT)) h^{D1}(w_2) = h^{D1}(tf_1 - nT) \quad (14)$$

We note that $h^{D1}(tf_1 - nT)$ becomes zero by the causality condition when $nT > tf_1$.

And C(D2) depends of the system detector D2:

$$C(D2) = \int d^3r \int \rho_s(r) \int dv' \int d\Omega f_{sp}(v', \Omega) \sum_D^{(2)} \Phi_0(1) \Phi_0^+(1) \quad (15)$$

Being detector 2 one of the system detectors and C(D2) is a function of the location of this detector, the source neutron distribution ρ_s , inside the target, and the direct and adjoint fluxes $\Phi_0(1)$ and $\Phi_0^+(1)$. From the phase and amplitude diagram of CPD₁₂(w), we can get the α_0 value and from this value and the previous calculated Λ value the Keff. From this methodology we can know the pole (α_0) location independently of the source, it means that can be used for all subcritical systems, always with Keff values ranging from 0.94 to 1.

3 LAHET+MCNP-DSP

The Monte Carlo code LAHET simulate the interactions of the protons within the target region to produce high-energy neutrons but also to produce another particles as:pion, neutron, ... the LAHET code also simulates the slowing-down of the high-energy neutrons to energies below 20MeV.

MCNP-DSP is an ORNL modification of the code MCNP-4A; the modification is an analog Monte Carlo code to simulate source-driven measurements and it is required to simulate the interactions for neutrons with energies less than 20MeV, this code is also used to estimate the counting statistics for neutrons and/or gamma rays counters in fissile systems.

The coupling of both Monte Carlo codes provide an estimator of the time-dependent response, that can be used to design a subcriticality monitoring system. The LAHET code provides a neutron or/and gamma source to the MCNP-DSP and the final output contains the correlated detector responses in the time or frequency domains.

4 Methodology Applications with LAHET+MCNPDSP

Using LAHET+MCNP-DSP we can obtain the CPSD_{12} function between two detectors. The detectors location will be given by the users and the CPSD_{12} will be dependent on the detectors location. This dependence is related with the higher subcritical modes and will be more important when the system becomes more subcritical.

The proton pulse frequency will be limited by the measurement set-up frequency given by the maximum frequency and the number of bins per block. The maximum frequency value on the plot is taking in such a way that includes all the information that we need to get the break frequency. It must be enough big to differentiate the pole, it means that it will change system to system as the changing on Λ and ρ as is giving on (1).

The α_0 value is the eigenvalue of the system for the fundamental mode, so it will be independent of the number of proton pulses per block. In this study the data will be given using one pulse per block because as we can observe in Fig. 1., the pole location using 1 pulse or 5 pulses per block is at the same frequency. But if we want to know exactly the data for α_0 , only for one pulse, the frequency at a phase equal to $\frac{\pi}{4}$ will give us the exactly value for the break frequency (f_{bc}) and from that we will know the prompt neutron decay doing ($\alpha_0 = 2\pi f_{bc}$). It is only possible to calculate this frequency value for the one pulse phase because when we have more than one pulse the phase graphic has information of the pulse frequency, so that we will use the one pulse frequency in ours simulations.

The next two plots represents the results obtained with LAHET+MCNP-DSP for $\text{CPSD}_{12}(w)$, where we have used a source that has one pulse per block of the data acquisition system.

These plots display the phase and amplitude $\text{CPSD}_{12}(w)$ versus frequency. We note that the pole α_0 of (12) is obtained at the frequency where the phase is equal to $\frac{\pi}{4}$. Therefore from this method is possible to get α_0 at any given time, and assuming a previous knowledge of the Λ from a previous calibration or calculation, it is possible also to determine from CPSD_{12} phase and amplitude

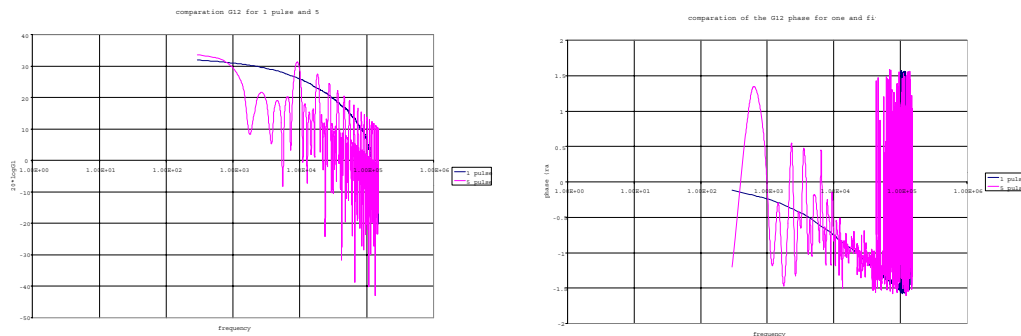


Fig. 1. Amplitude and Phase versus frequency for one pulse and five pulses per block respectively

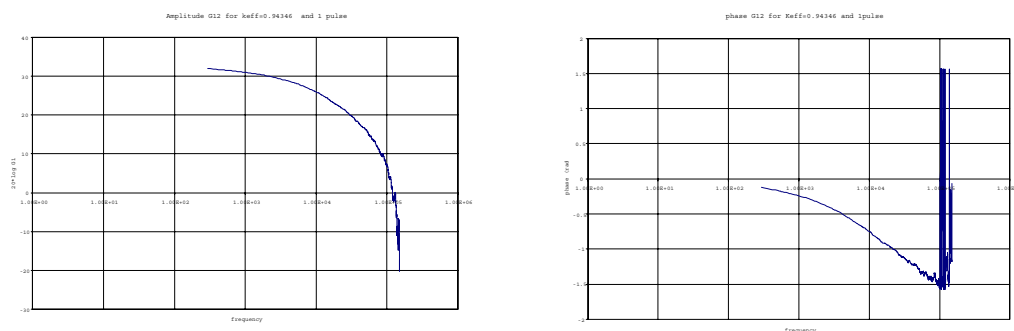


Fig. 2. Amplitude and Phase versus frequency for one pulse respectively

diagrams the K_{eff} value for different enrichments. Proceeding in this way is possible to monitor the subcriticality control.

The proton pulse frequency limitation will disappear if a perturbation of the source is performed, and it is periodic with a frequency less than the decay constant, and with an amplitude about 1% of the original proton pulse amplitude. It can allow us to consider this methodology as general, speaking about frequency.

5 Conclusions

A methods to monitor and control the subcriticality of ADS has been developed in this paper using the stochastic transport theory and it has been simulated using two coupled Monte-Carlo codes, LAHET and MCNP-DSP. A LAHET+MCNP-DSP calculation of a source-driven measurement essentially follows the natural chain of events. Source particle histories are initiated by a proton beam and the neutrons obtained from the injection of this proton beam on a spallation target are tracked to their extinction by absorption or escape. In practice to apply this methodology will be necessary to perform a previous calibration.

In conclusion from the $CPSD_{12}$ phase diagram versus frequency, we can obtain the frequency value that correspond to a phase of $\frac{\pi}{4}$, and from this value is possible to get the α_0 value for the fundamental mode and the reactivity from this eigenvalue.

References

1. J.L. Muñoz-Cobo, R.B. Perez, G. Verdu: Nucl. Sci. Eng. **95** 83 (1987)
2. J.L. Muñoz-Cobo, R.B. Perez, T.E. Valentine, Y. Rugama, J.T. Mihalcz: Ann. Nucl. Energy **270**, 1087 (2000)
3. T.E. Valentine, J.T. Mihalcz: Ann. Nucl. Energy **23**, 1271 (1996)
4. R.E. Prael, H. Lichtenstein: *Users Guide to LCS* LA-UR-97-4981 (1997)
5. J.F. Briesmeister (Ed.): *MCNP-a General Monte Carlo N-Particle Transport Code, Version 4A*, LA-12625, Los Alamos National Laboratory (1993)

Sediment-Density Dependency of Natural Gamma Ray Spectra in a Borehole Geometry

P.H.G.M. Hendriks, M. Maučec and R.J. de Meijer

Nuclear Geophysics Division, Kernfysisch Versneller Instituut, Zernikelaan 25, 9747 AA Groningen, The Netherlands

1 Introduction

The Nuclear Geophysics Division of the Kernfysisch Versneller Instituut (NL) is developing and applying tools based on nuclear principles for *in-situ* measurements such as towed waterbed, airborne and borehole measurements. One of these tools, the MEDUSA system, is tailored for *in-situ* high-efficiency measurements of natural gamma ray spectra [1]. The concentrations of the natural radionuclides ^{40}K , ^{232}Th and ^{238}U present in the sediment are extracted from the (nearly) full natural gamma-ray spectrum utilizing so-called “standard spectra” [2]. Via a “radiometric fingerprint”, the radiometry maps can be converted to sediment composition maps [1]. This new system has been successfully applied in e.g., mapping underwater bottoms, see [3]. These measurements showed a good agreement between the activity concentrations of *in-situ* data and of collected samples.

For the radiometric fingerprint-method to be successful, an *absolute* calculation of the radioactivity levels is a prerequisite. However, because the system is used for continuous, *in-situ* measurements, changes in experimental conditions may mask, or be mistaken for, changes in sediment composition. This paper addresses the influence of changes in the density of the matrix on the shape and intensity of the measured natural γ -ray spectra. It is our aim to extract the density of the matrix from the natural gamma ray spectrum using an enhanced multi-channel analysis. In a sense this is similar to the experiments carried out by Minty et al. to estimate the altitude in airborne surveys [4]. Due to experimental limitations such calibrations are probably best done via Monte Carlo simulations, as was already pointed out by Minty. Thus far simulations of the density dependence of γ -ray transport through a matrix have always focused on γ -radiation induced by a source [5]. As far as the authors are aware, the data presented in this contribution is the first Monte Carlo-based study concerning the sediment-density effects on natural γ ray spectra. For all simulations the general transport code MCNP4b was used [6].

2 Simulation Description and Experimental Verification

The energies and relative intensities of the γ -rays emitted in the decay of ^{40}K and the decay series of ^{232}Th and ^{238}U are based on data provided by the well-known

Table of Isotopes, [7]. All γ -rays with energies between 100 keV and 3 MeV which have a branching ratio greater than 1% are included in the simulations. In this manner ^{40}K is characterized by 1 γ -ray emission; ^{232}Th and ^{238}U by 26 and 25 γ -rays, respectively. The source is contained in cylindrical symmetric quartz sand (SiO_2), see Fig. 1. The density of the sand is calculated from the porosity. In the laboratory experiments the pore space is filled with air, which corroborates with the void space in the simulations. For the density-dependent simulations, which are discussed in the next chapter, the pore space is saturated with water (H_2O , $\rho_{\text{water}} = 1.00 \text{ g/cm}^3$). The density and composition of the matrix are assumed to be homogeneously distributed both in radial as in z -direction. A cylindrical BGO detector ($\text{Bi}_4\text{Ge}_3\text{O}_{12}$, $\rho_{\text{BGO}} = 7.13 \text{ g/cm}^3$) of 5 cm diameter and 15 cm length is placed in the borehole which has a 5 cm diameter. The remainder of the borehole is filled with water. In this simplified model elements such as detector casing and Photomultiplier Tube are omitted.

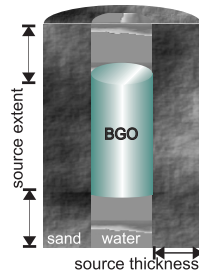


Fig. 1. Cross-view of the geometry used to simulate the response of a BGO detector in a borehole geometry

It is found that a source with a 50 cm diameter and 50 cm extent in both directions mimics an infinite source with an accuracy of more than 98.4%. These dimensions are used for all subsequent simulations. All MCNP pulse height spectra are converted to Bq/kg to enable comparison with experimental results. An example of this is given in Fig. 2, which shows simulated and measured standard spectra for all three natural radionuclides. The simulated spectra have been modified to emulate the energy resolution of the detector, which is quoted at 9% for 1.332 MeV γ -rays. The number of bins and the bin widths are chosen equal to that of the experiments: 300 bins, each of 10 keV width. The sediment densities of the simulations have been adapted to match those of the experiments and are 1.44 g/cm^3 for ^{40}K and ^{232}Th , and 1.65 g/cm^3 for ^{238}U , respectively. Each simulation tracked 40 million source particles and had to run for nearly 24 hours on four 450 MHz RISC CPU's in PVM mode. The relative uncertainty in the simulated spectra varies from less than 10% for the count-rate intense part below 1 MeV, to approximately 25% for the bins at Compton energies of the high energy γ -rays. Afterwards, data have been smoothed via averaging of the data points. The derivation of the experimental data is described by [2]. The energy threshold for data acquisition in the experiments is set to 200 keV.

All dominant structures reproduce well, both in shape and intensity. The deficiency in simulating the photopeak of ^{40}K is possibly caused by incomplete removal in the experimental data of background potassium present in the concrete surrounding the calibration set-up and in the photomultiplier tube of the BGO detector. For thorium, deviations from experimental results occur in the continuum parts of the spectrum for energies roughly between 500 keV and 2.2 MeV. This may be caused by cascade-summing. This effect can occur in cases with a close detector-source geometry, when multiple γ -rays are emitted simultaneously in a time interval shorter than the combined time resolution of detector and electronics. Summing effects in a detector mainly lead to a decrease in peak-to-background ratio. For ^{208}Tl , a member of the ^{232}Th decay series, many decay channels exist, several (e.g., 510 keV, 583 keV and 860 keV) having a high-probability of feeding the 2.614 MeV level. In our simulations it was not yet possible to include summing effects; in fact it remains questionable if any of the present Monte Carlo transport codes at hand can provide this functionality. Despite this shortcoming, in general a good agreement is reached between simulations and experiments. When the uncertainty in the simulated spectra can be further reduced, the possibility for simulated calibrations of the probe becomes an option.

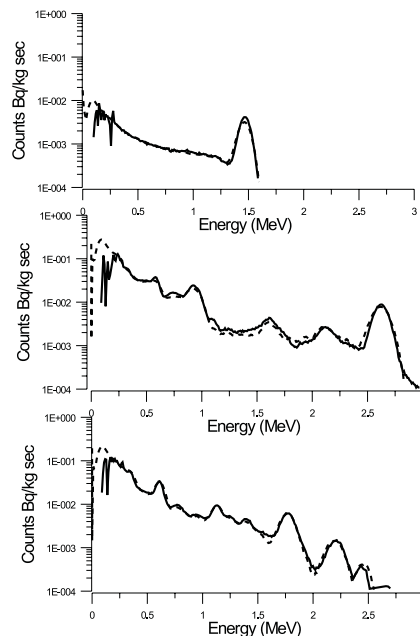


Fig. 2. Comparison between standard spectra from simulations (dashed line) and experiment (solid line). From top to bottom the spectra for ^{40}K , ^{232}Th and ^{238}U are shown

3 Density Dependence Simulations

The density of a matrix is determined by the bulk density of the material corrected for the porosity and for the type of fluid that has filled up the pore space. Thus when speaking of density, in fact a bulk property is meant that is a function of porosity ε and average atomic number Z . In Tab. 1, the densities and total mass fractions of Si, O and H are listed for SiO_2 with water-filled pores, for various porosities.

Table 1. Sediment densities and mass fractions for various porosities. Pore space is assumed to be saturated with water

sediment porosity (Vol. %)	sediment density (g/cm ³)	mass fractions fractions (%)		
		Si	O	H
0	2.65	46.7	53.3	0.0
15	2.40	43.8	55.6	0.7
25	2.24	41.5	57.3	1.2
40	1.99	37.3	60.5	2.2
55	1.74	31.9	64.6	3.5

The response of the γ -ray detector system is determined for various densities. The top panel of Fig. 3 shows the simulated pulse-height spectrum in a detector irradiated with a pure ^{232}Th source for $\rho_{\text{matrix}}=2.65 \text{ g/cm}^3$. The lower panel shows selected data of the intensity variations relative to $\rho_{\text{matrix}}=2.65 \text{ g/cm}^3$ as a function of γ -ray energy. The data have been smoothed to filter out noise at energies above 1.5 MeV.

At this point only a qualitative analysis of the data is presented, because the first topic of interest is whether or not the density-inferred fluctuations in the γ -ray spectra are sufficiently large that they influence the standard data analysis of the natural γ -ray logs. Figure 3 shows that the intensity of the γ -ray spectra exhibits a definite anti-correlation with the sediment density, a more or less linear off-set that increases with decreasing sediment density and superimposed on this are variations related to photopeak structures in the spectrum. To understand this dependency one has to consider the interaction processes responsible for the shape of the natural γ -ray spectra, namely the photo-electric absorption, with its cross section $\sigma_p \propto Z^{3.6}$, and Compton scattering, cross section σ_e linear with Z [8]. Therefore, the relation between sediment density (determined by sediment composition) and γ -ray spectra is perhaps better illustrated by the dependence of the Total Counts, i.e., counts integrated over all energy channels, with the average Z of the matrix. The left panel of Fig. 4 shows a linear decrease in the Total Counts for increasing Z (and density), indicating that Compton scattered γ -rays are the dominant contribution to the energy spectra of natural γ -rays in SiO_2 . An important consequence of this is that the density in simulations should

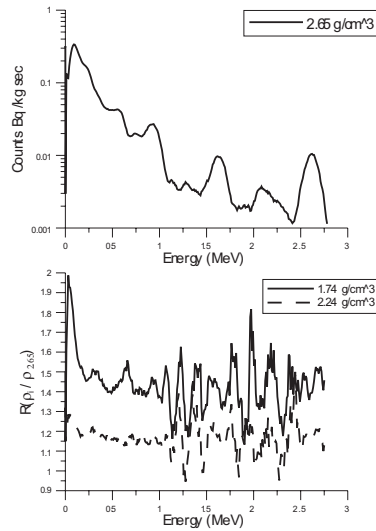


Fig. 3. Simulated BGO pulse height spectrum in a borehole geometry for $\rho_{\text{matrix}}=2.65\text{g/cm}^3$ (top panel) and relative intensity variations as a function of γ -ray energy (bottom panel)

not be changed as a parameter itself, but only in combination with sediment composition.

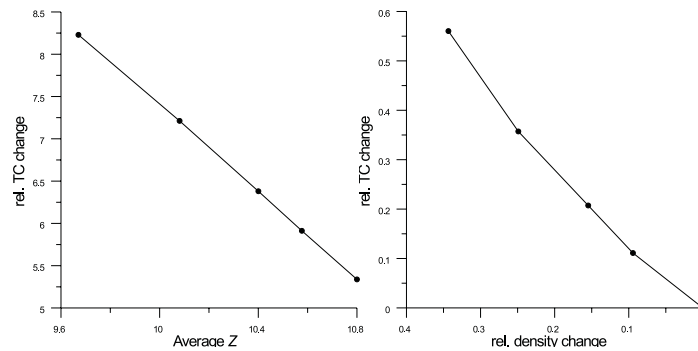


Fig. 4. Total Counts variation in the simulated pulse height spectra as a function of the average Z-value of the sediment (left panel). Relative Total counts changes as a function of the relative density variation. The relative uncertainty in Total Counts is less than 0.5%

The dependence between relative change in total intensity of the simulated γ -ray spectra and relative density is shown in the right panel of Fig. 4. For

a 15% decrease in density, an increase of approximately 20% in intensity is observed. Generally, the statistics in the high-energy part of *in-situ* measured spectra are not sufficient to detect changes in density. The low-energy part of the spectrum, below 500keV, is most affected by changes in sediment density. Since this part is also the most count intense part of the spectrum it is emphasized in the current – least squares – data analysis of the MEDUSA system. This means that for field experiments in which variations in matrix density are expected it is necessary to correct for density effects in the data analysis of spectral logs. Alternatively, density changes can be monitored from the fit of the full spectrum analysis in the low energy part of the spectrum.

4 Conclusions

It is shown that it is possible to model the measurements of the decay of the natural radionuclide ^{40}K and the complicated decay schemes of ^{232}Th and ^{238}U in borehole measurements. Even though we have not yet been able to include cascade summing effects in our simulations a good agreement with experimental data has been achieved, both in spectral shape and in absolute intensities. The variations of the γ -ray dependence with the sediment density are investigated, based on a density that is determined by a combination of porosity and sediment composition. The intensity variations induced by density changes are in the order of 20% for a 15% change in density and thus the need arises to compensate the analysis of spectral γ -logs for density variations. Currently a principal component analysis of the simulated γ -ray spectra is underway to identify the main variations with densities. This must lead to an improved data-analysis of natural γ -ray spectra measured in boreholes in which the sediment density will be an additional parameter. Before the inverse problem can be solved however, a further sensitivity analysis will be necessary to determine the vertical and depth response of the system, in combination with inhomogeneity of the matrix and the stand off of the detector of the borehole wall.

References

1. R.J. de Meijer: *Journal of Geochemical Exploration* **81** (1998)
2. P.H.G.M. Hendriks, J. Limburg, R.J. De Meijer: 'Full spectrum analysis of natural gamma ray spectra', *Journal for Environmental Radioactivity* (accepted) (2000)
3. L.B. Venema, J. Limburg, R.J. de Meijer: 'Natural radionuclides as tracers for dispersal of dredge spoil dumped at sea', *Journal of Environmental Radioactivity* (submitted) (2000)
4. B.R.S. Minty, P. McFadden, B.L.N Kennet: *Geophysics* **63**, 1971 (1998)
5. W. Bertozzi, D.V. Ellis, J.S. Wahl: **46** (1981)
6. J. Briesmeister, Ed.: *MCNP, A General Purpose Monte Carlo N-Particle Transport Code*, Version 4B, LA-12625-M, Los Alamos National Laboratory (1997)
7. R.B. Firestone, Ed.: *Table of Isotopes*, 8th edition (John Wiley & Sons, Inc. 1996)
8. G.F. Knoll: *Radiation detection and measurement*, (John Wiley & Sons 1987)

Some Experimental and Monte Carlo Investigations of the Plastic Scintillators for the Current Mode Measurements at Pulsed Neutron Sources

A. Rogov¹, Yu. Pepyolyshev¹, M. Carta², and A. d'Angelo²

¹ Frank Laboratory of Neutron Physics, Joint Institute for Nuclear Research, Dubna, Moscow region, 141980, Russia

² ENEA, C.R. Casaccia, via Anguillaraese, 301, 0060 S. Maria di Galeria (ROMA) Italy

1 Introduction

Scintillation detector (SD) is widely used in neutron and gamma-spectrometry in a count mode. The organic scintillators for the count mode of the detector operation are investigated rather well. Usually, they are applied for measurement of amplitude and time distributions of pulses caused by single interaction events of neutrons or gamma's with scintillator material. But in a large area of scientific research scintillation detectors can alternatively be used on a current mode by recording the average current from the detector. For example, the measurements of the neutron pulse shape at the pulsed reactors or another pulsed neutron sources. So as to get a rather large volume of experimental data at pulsed neutron sources, it is necessary to use the current mode detector for registration of fast neutrons. Many parameters of the SD are changed with a transition from an accounting mode to current one. For example, the detector efficiency is different in counting and current modes. Many effects connected with time accuracy become substantial. Besides, for the registration of solely fast neutrons, as must be in many measurements, in the mixed radiation field of the pulsed neutron sources, SD efficiency has to be determined with a gamma-radiation shield present. Here is no calculations or experimental data on SD current mode operation up to now. The response functions of the detectors can be either measured in high-precision reference fields or calculated by a computer simulation. We have used the MCNP code [1] and carried out some experiments for investigation of the plastic performances in a current mode. There are numerous programs performing simulating similar to the MCNP code. For example, for neutrons there are [2–4], for photons - [5–8]. However, all known codes to use (SCINFUL, NRESP4, SANDYL, EGS49) have more stringent restrictions on the source, geometry and detector characteristics. In MCNP code a lot of these restrictions are absent and you need only to write special additions for proton and electron recoil and transfer energy to light output. These code modifications allow taking into account all processes in organic scintillator influence the light yield.

2 Model of the Detector and Calculation Conditions

It is necessary to construct a model of the scintillator and its components, which approximates to the real detector construction in the current mode operation as closely as possible within the limitations of the calculation method. Fast neutron scintillation detector in a current mode (SDCM) is constructed on the base of photomultiplier (PMP) with polystirol plastic scintillator ($C_9H_{10} + 2\%$ PPP + 0.2 % POPOP). Gamma shielding with variable thickness surrounds scintillator with photomultiplier. The neutron beam is made by a collimator system with output window of 50 mm in diameter (X). We consider here only lead shielding. The lead shielding was used in experimental measurements needed for comparison with the calculations. For the same purpose, it is used in the simulation the exact experimental conditions, such as the exact geometry of the core, biological shielding, neutron collimator of 5 cm in diameter and strictly detector. The detector is situated on neutron guide of the IBR-30 at a distance of 10 meters from the reactor core. In this case we could use the real neutron and gamma spectra from the IBR-30 in simulation.

3 SDCM Detector Efficiency

Because of the efficiency of the detector to neutrons and gamma's in wide range of energies is practically can not be determined experimentally, we used the calculated results in general. An approximation of narrow neutron and gamma beam geometry in the calculations is applied. Diameter of the scintillator is chosen as a parameter. Neutron and gamma flow 5 cm in diameter is directed transversely to the scintillator axis. The numerical data are shown in the Tab. 1. They may be used for further sophisticated treatment of the scintillator performances, for example for evaluation of sensitivity.

Table 1. Energy dependence of light output. No Shield, L = 5 cm, E.cut for Neutrons, Photons and Electrons = 0.01 MeV. D is a scintillator diameter. Monoenergy Neutron Source, Average Light/Incident Neutron

E_n, MeV	D=0.5cm	D=1cm	D=2cm	D=3cm	D=4cm	D=5cm	D=7cm
0.1	$9.33 \cdot 10^{-5}$	$3.44 \cdot 10^{-4}$	$1.15 \cdot 10^{-3}$	$2.11 \cdot 10^{-3}$	$3.03 \cdot 10^{-3}$	$3.70 \cdot 10^{-3}$	$4.04 \cdot 10^{-3}$
0.3	$2.18 \cdot 10^{-4}$	$8.33 \cdot 10^{-4}$	$2.97 \cdot 10^{-3}$	$5.83 \cdot 10^{-3}$	$8.79 \cdot 10^{-3}$	$1.13 \cdot 10^{-2}$	$1.32 \cdot 10^{-2}$
0.5	$3.35 \cdot 10^{-4}$	$1.29 \cdot 10^{-3}$	$4.71 \cdot 10^{-3}$	$9.43 \cdot 10^{-3}$	$1.45 \cdot 10^{-2}$	$1.91 \cdot 10^{-2}$	$2.31 \cdot 10^{-2}$
0.7	$4.60 \cdot 10^{-4}$	$1.78 \cdot 10^{-3}$	$6.59 \cdot 10^{-3}$	$1.34 \cdot 10^{-2}$	$2.09 \cdot 10^{-2}$	$2.77 \cdot 10^{-2}$	$3.44 \cdot 10^{-2}$
1.0	$6.69 \cdot 10^{-4}$	$2.60 \cdot 10^{-3}$	$9.73 \cdot 10^{-3}$	$1.99 \cdot 10^{-2}$	$3.16 \cdot 10^{-2}$	$4.23 \cdot 10^{-2}$	$5.41 \cdot 10^{-2}$
3.0	$2.07 \cdot 10^{-3}$	$8.24 \cdot 10^{-3}$	$3.16 \cdot 10^{-2}$	$6.71 \cdot 10^{-2}$	$1.09 \cdot 10^{-1}$	$1.53 \cdot 10^{-1}$	$2.12 \cdot 10^{-1}$
5.0	$3.15 \cdot 10^{-3}$	$1.27 \cdot 10^{-2}$	$4.94 \cdot 10^{-2}$	$1.05 \cdot 10^{-1}$	$1.75 \cdot 10^{-1}$	$2.47 \cdot 10^{-1}$	$3.50 \cdot 10^{-1}$
7.0	$3.90 \cdot 10^{-3}$	$1.58 \cdot 10^{-2}$	$6.23 \cdot 10^{-2}$	$1.34 \cdot 10^{-1}$	$2.24 \cdot 10^{-1}$	$3.18 \cdot 10^{-1}$	$4.60 \cdot 10^{-1}$
10.	$4.60 \cdot 10^{-3}$	$1.90 \cdot 10^{-2}$	$7.54 \cdot 10^{-2}$	$1.64 \cdot 10^{-1}$	$2.75 \cdot 10^{-1}$	$3.91 \cdot 10^{-1}$	$5.72 \cdot 10^{-1}$
15.	$5.03 \cdot 10^{-3}$	$2.17 \cdot 10^{-2}$	$8.73 \cdot 10^{-2}$	$1.92 \cdot 10^{-1}$	$3.23 \cdot 10^{-1}$	$4.63 \cdot 10^{-1}$	$6.81 \cdot 10^{-1}$
20.	$4.99 \cdot 10^{-3}$	$3.03 \cdot 10^{-2}$	$9.23 \cdot 10^{-2}$	$2.05 \cdot 10^{-1}$	$3.49 \cdot 10^{-1}$	$5.04 \cdot 10^{-1}$	$7.48 \cdot 10^{-1}$

Monoenergy Photon Source, Average Light/Incident Photon

E_γ, MeV	D=0.5 cm	D=1 cm	D=2 cm	D=3 cm	D=4cm	D=5 cm	D=7 cm
0.1	$1.22 \cdot 10^{-4}$	$4.91 \cdot 10^{-4}$	$1.89 \cdot 10^{-3}$	$4.08 \cdot 10^{-3}$	$6.78 \cdot 10^{-3}$	$9.58 \cdot 10^{-3}$	$1.36 \cdot 10^{-2}$
0.3	$4.83 \cdot 10^{-4}$	$1.94 \cdot 10^{-3}$	$7.53 \cdot 10^{-3}$	$1.62 \cdot 10^{-2}$	$2.70 \cdot 10^{-2}$	$3.84 \cdot 10^{-2}$	$5.54 \cdot 10^{-2}$
0.5	$7.93 \cdot 10^{-4}$	$3.24 \cdot 10^{-3}$	$1.28 \cdot 10^{-2}$	$2.77 \cdot 10^{-2}$	$4.65 \cdot 10^{-2}$	$6.64 \cdot 10^{-2}$	$9.68 \cdot 10^{-2}$
0.7	$1.01 \cdot 10^{-3}$	$4.29 \cdot 10^{-3}$	$1.72 \cdot 10^{-2}$	$3.78 \cdot 10^{-2}$	$6.38 \cdot 10^{-2}$	$9.16 \cdot 10^{-2}$	$1.35 \cdot 10^{-1}$
1.0	$1.19 \cdot 10^{-3}$	$5.43 \cdot 10^{-3}$	$2.29 \cdot 10^{-2}$	$5.05 \cdot 10^{-2}$	$8.64 \cdot 10^{-2}$	$1.25 \cdot 10^{-1}$	$1.84 \cdot 10^{-1}$
3.0	$8.76 \cdot 10^{-4}$	$6.30 \cdot 10^{-3}$	$3.76 \cdot 10^{-2}$	$9.25 \cdot 10^{-2}$	$1.67 \cdot 10^{-1}$	$2.52 \cdot 10^{-1}$	$3.96 \cdot 10^{-1}$
5.0	$6.85 \cdot 10^{-4}$	$5.19 \cdot 10^{-3}$	$3.68 \cdot 10^{-2}$	$1.04 \cdot 10^{-1}$	$1.98 \cdot 10^{-1}$	$3.15 \cdot 10^{-1}$	$5.10 \cdot 10^{-1}$
7.0	$6.01 \cdot 10^{-4}$	$4.53 \cdot 10^{-3}$	$3.37 \cdot 10^{-2}$	$1.02 \cdot 10^{-1}$	$2.10 \cdot 10^{-1}$	$3.43 \cdot 10^{-1}$	$5.85 \cdot 10^{-1}$
10.	$5.50 \cdot 10^{-4}$	$4.20 \cdot 10^{-3}$	$3.16 \cdot 10^{-2}$	$9.55 \cdot 10^{-2}$	$2.13 \cdot 10^{-1}$	$3.71 \cdot 10^{-1}$	$6.75 \cdot 10^{-1}$
15.	$5.08 \cdot 10^{-4}$	$3.81 \cdot 10^{-3}$	$2.95 \cdot 10^{-2}$	$9.52 \cdot 10^{-2}$	$2.11 \cdot 10^{-1}$	$3.77 \cdot 10^{-1}$	$7.50 \cdot 10^{-1}$
20.	$4.91 \cdot 10^{-4}$	$3.82 \cdot 10^{-3}$	$2.96 \cdot 10^{-2}$	$9.64 \cdot 10^{-2}$	$2.14 \cdot 10^{-1}$	$3.87 \cdot 10^{-1}$	$7.96 \cdot 10^{-1}$

We can see from the tables that the light output saturation for neutrons actually does not depend on neutron energy or the diameter of scintillator. On the contrary, for gamma's, saturation curves essentially depend on the latters. However, behaviour of light saturation has a similar character in region of mean neutron or gamma energy for nuclear reactor ($E \approx 1 \text{ MeV}$). Because of this the choose of a scintillator diameter is not important for gamma's elimination in neutron measurements. In the previous case we should use a gamma shielding.

Table 2. Light output with lead Shield. Source is neutron & gamma from IBR-30 Average Light/Incident Neutron

Scint.,d,cm	Pb=0 cm	Pb=2 cm	Pb=5 cm	Pb=10 cm	Pb=15 cm
0.5	$1.51 \cdot 10^{-3}$	$1.10 \cdot 10^{-3}$	$7.00 \cdot 10^{-4}$	$3.32 \cdot 10^{-4}$	$1.07 \cdot 10^{-4}$
1.0	$5.98 \cdot 10^{-3}$	$4.51 \cdot 10^{-3}$	$2.84 \cdot 10^{-3}$	$1.18 \cdot 10^{-3}$	$4.68 \cdot 10^{-4}$
2.0	$2.28 \cdot 10^{-2}$	$1.78 \cdot 10^{-2}$	$1.08 \cdot 10^{-2}$	$4.64 \cdot 10^{-3}$	$2.01 \cdot 10^{-3}$
3.0	$4.87 \cdot 10^{-2}$	$3.80 \cdot 10^{-2}$	$2.32 \cdot 10^{-2}$	$1.00 \cdot 10^{-2}$	$4.37 \cdot 10^{-3}$
4.0	$8.01 \cdot 10^{-2}$	$6.19 \cdot 10^{-2}$	$3.82 \cdot 10^{-2}$	$1.66 \cdot 10^{-2}$	$7.32 \cdot 10^{-3}$
5.0	$1.11 \cdot 10^{-1}$	$8.64 \cdot 10^{-2}$	$5.38 \cdot 10^{-2}$	$2.37 \cdot 10^{-2}$	$1.03 \cdot 10^{-2}$
7.0	$1.55 \cdot 10^{-1}$	$1.24 \cdot 10^{-1}$	$7.99 \cdot 10^{-2}$	$3.57 \cdot 10^{-2}$	$1.60 \cdot 10^{-2}$

Average Light/Incident Photons

Scint.,d,cm	Pb=0 cm	Pb=2 cm	Pb=5 cm	Pb=10 cm	Pb=15 cm
0.5	$7.60 \cdot 10^{-4}$	$2.00 \cdot 10^{-4}$	$5.90 \cdot 10^{-5}$	$4.40 \cdot 10^{-6}$	$1.25 \cdot 10^{-6}$
1.0	$4.05 \cdot 10^{-3}$	$1.24 \cdot 10^{-3}$	$3.05 \cdot 10^{-4}$	$1.91 \cdot 10^{-5}$	$5.90 \cdot 10^{-6}$
2.0	$2.05 \cdot 10^{-2}$	$6.92 \cdot 10^{-3}$	$1.73 \cdot 10^{-3}$	$1.19 \cdot 10^{-4}$	$1.68 \cdot 10^{-5}$
3.0	$4.88 \cdot 10^{-2}$	$1.70 \cdot 10^{-2}$	$4.35 \cdot 10^{-3}$	$3.75 \cdot 10^{-4}$	$5.03 \cdot 10^{-5}$
4.0	$8.42 \cdot 10^{-2}$	$3.00 \cdot 10^{-2}$	$1.18 \cdot 10^{-3}$	$7.23 \cdot 10^{-4}$	$8.49 \cdot 10^{-5}$
5.0	$1.24 \cdot 10^{-1}$	$4.39 \cdot 10^{-2}$	$7.84 \cdot 10^{-3}$	$1.13 \cdot 10^{-3}$	$1.25 \cdot 10^{-4}$
7.0	$1.95 \cdot 10^{-1}$	$7.10 \cdot 10^{-2}$	$1.94 \cdot 10^{-2}$	$1.97 \cdot 10^{-3}$	$1.86 \cdot 10^{-4}$

4 Experimental Checking of the Calculations

The detector response is usually simulated and then checked against measurements in particular well-known reference fields to be sure that the computer simulation is sufficient. A number of experimental works on scintillator light output with lead shield for checking of possibility of application code have been performed. As irradiation sources, it was used the following: IBR-30, Co⁶⁰, Pu²³⁸-Be and Cf²⁵². The main comparative results are presented in the Tabs. 3 and 4. Data obtained for IBR-30 is presented in Tab. 3. The flux unit in Tab. 4 is taken without lead shield in all cases.

Table 3. The IBR-30. Relative change of the plastic scintillator light yield (S_0/S_i) in the mixed flux of neutron and gamma irradiation, neutron flux (F_o/F_{ni}) and ratio of the gamma flux to neutron one ($F_{\gamma i}/F_{ni}$) on the scintillator in the site of the detector installation at 10 meters from the core via a thickness of lead shielding (X_{pb}). The basis values (S_0, F_o) by lead thickness of 15 cm are taken. Diameter of scintillator is 4 cm

$X_{pb}, \text{ cm}$	S_0/S_i		F_{no}/F_{ni}	$F_{\gamma i}/F_{ni}$
	Experiment	Calculation		
15	1	1	1	$3.43 \cdot 10^{-3}$
10	2.26	2.31	2.39	$6.90 \cdot 10^{-3}$
5	5.31	5.27	4.63	$1.19 \cdot 10^{-1}$
0	17.24	17.52	13.88	$2.8 \cdot 10^{-1}$

Remarks: 1) The experimental value S_i is determined as a total charge from the detector in reactor pulse. This value was averaged over 1024 neutron pulses to eliminate the pulse energy fluctuations. The values F_{ni} and $F_{\gamma i}$ are calculated by MCNP code

Table 4. Neutron and gamma sources Co⁶⁰, Pu²³⁸ - Be and Cf²⁵². Relative change of the plastic scintillator light yield via a thickness of lead shielding (X_{pb})

$X_{pb}, \text{ sm}$	Co ⁶⁰		Pu ²³⁸ - Be		Cf ²⁵²	
	Exper.	Calcul.	Exper.	Calcul.	Exper.	Calcul.
0	1	1	1	1	1	1
4.7	0.11	0.091	0.5	0.39	0.3	0.29
9.2	0.018	0.0127	0.33	0.2	0.17	0.16

The results presented in the Tab. 3 for the IBR-30 show a good agreement between the experiments and calculations. The data presented on the Tab. 4 are obtained in order to get an additional checking of the simulations against measurements in well-known reference fields. However, all calculated relative fluxes in Tab. 4 are less than experimental ones. This odds is attributable to not exact simulation of the experiment geometry. Anyway, from the efficiency point of view for fast neutrons registration with plastic scintillator in a current

mode, it is sufficient to use 10-15 cm lead shielding. Neutron flux in this case is decrease by 8-17 times, and gamma's contribution is less, than 0.7-0.4 %.

5 Influence of the Lead Thickness on the Accuracy of the Neutron Pulse Shape Measurement

There are two main components of an inaccuracy of neutron pulse shape measurement connected with plastic scintillator. They are as follows:

1. Distortions connected with an influence of gamma's. Gamma pulse shape may be differs on neutron one. It depends from gamma's energy. The difference is coursed by gamma leakage from the shielding of the reactor and experimental equipment.

2. Distortions defined by time response of the scintillator light output on neutrons impact.

The amplitude of the registered pulse changes in accordance with the change of the detector sensitivity (see Tab. 3). The influence of the gamma irradiation on the pulse shape accuracy is negligible small when the lead thickness is more than 5 cm.

Time response of the plastic scintillator is investigated by calculation and only for neutrons.

Table 5. Time decay constant of plastic scintillator (nanosec) caused by neutron δ - pulse with and without lead shielding via initial neutron energy for some values of the scintillator diameter

Pb thickn.cm	Scint dia,cm	Neutron energy			IBR-30 n. sp.
		0.1 MeV	1.0 MeV	5.0 MeV	
0	1	2.2	1.8	1.0	–
0	5	6.0	2.5	1.5	19.7
5	5	6.2*	5.6*	6.8*	15.9
10	5	8.7*	6.2*	10.6*	–

*) The second component of the total decay. The main first component is practically the same as without lead shielding.

As the analysis of the obtained data is shown, there is a rangerous correlation of time decay constant with neutron energy and the diameter of the scintillator. It is to be notified that response function of the plastic scintillator essentially varies with lead shielding. In addition, it becomes more complicated with increasing of neutron energy. The main decay constant is being determined without shielding. Lead shielding inserts some number of more slow components. The weight of these components depends on initial neutron energy. This explains, for example, why under the impact of the IBR-30 neutron spectrum, the average time decay constant with lead shielding is less, than without one. Anyway, lead shielding increases the time constant of the plastic scintillator for monoenergy neutrons.

6 Conclusions

The investigations have confirmed that the scintillation detector with plastic scintillator can be used in a current mode for fast neutron registration in vast area of experiments at pulsed neutron sources. In order to eliminate the influence of gamma's on the detector indications, the latter must be surrounded by 10–15 cm thick gamma shielding. Naturally, there are others suitable gamma shielding, for example, tungsten, or uranium-238. In author's opinion, the latter may be better for such a kind of detectors, because of their higher density and lower neutron cross section. This is a subject of the next step of research. Even by using of lead shielding with above mentioned thickness, neutron flux on the scintillator is being decreased by 8–17 times, and gamma's contribution is no more than 0.7–0.4 %. A time response function of plastic scintillator to neutrons essentially depends on the diameter of the scintillator and neutron energy, And in mixed neutron flux with neutron spectrum from the reactor, behaviour of the response function in time does not essentially depend on lead thickness. A peculiar value of time constant under an impact of neutrons from reactors with plutonium fuels is approximately 16–20 nsec. Thus, this type of the detector may successfully be used for the measurements of the transients or pulse shape at pulsed reactors or other subcritical facilities within time interval more, than 20 nsec without any corrections.

The work was carried out under the ISTC N°682-97 project.

References

1. MCNP - A General Monte Carlo N-Particle Transport Code, Version 4B, LA-12625, J.F. Briesmeister, Ed., Los Alamos National Laboratory Report (1997)
2. G. Dietze, H. Klein: *NRESP4 and NEFF4 Monte Carlo Codes for the Calculation of Neutron Response Functions and Detection Efficiencies for NE-213 Scintillation Detectors*, Report PTB-ND-22, Braunschweig (1982)
3. R.E. Textor, V.V. Verbinski: *O5S: A Monte Carlo Code for Calculating Pulse Height Distributions due to Monoenergetic Neutrons Incident on Organic Scintillators*, ORNL-4160 (1968)
4. J.K. Dickens: *SCINFUL - A Monte Carlo Based Computer Program to Determine a Scintillator Full Energy Response to Neutron Detection for En Between 0.1 and 80 MeV*, ORNL-6462, 6463 (1988)
5. C. Chen, J.A. Lockwood, L. Hsieh: Nucl. Instr. and Meth. **138**, 363 (1976)
6. K. Shin, Y. Hayashida, S. Shiroya, T. Hyodo: J. of Nucl. Sci. and Technol. **16**, 390 (1979)
7. T. Novotny: *Photon Spectrometry in Mixed Neutron-Photon Fields using NE-213 Liquid Scintillation Detectors*, Report PTB-N-28, Braunschweig (1997)
8. R.L. Ford, W.R. Nelson: *The EGS Code System: Computer Program for the Monte Carlo Simulation of Electromagnetic Cascade Showers*, SLAC-210, Stanford Linear Accelerator Center (1978)

Feasibility Study of Non-Radioactive Tracers for Monitoring Injected Water in Oil Reservoirs

H. Sawamura¹, K. Nishimura¹, H. Mituishi², T. Muta¹, and J.S. Schweitzer³

¹ Computer Software Development Co., Ltd, Mitubishi-juko Shinjyuku Bldg.(4F)
15-1 Tomihisa-cho, Shinjyuku-ku, Tokyo 162-0067 Japan

² Japan National Oil Corporation, 2.2, Hamada, 1-chpme, Mihama-ku, chiba-shi,
chiba 261 Japan

³ University of Connecticut, Department of Physics, 2152 Hillside Road, U-46 Storrs,
Connecticut 06269-3046, U.S.A.

Abstract. This paper discusses the results of analyses conducted on non-radioactive tracers that can be used in combination with the sea water injected into a well for monitoring the water permeating through the oil reservoir by a nuclear logging tool utilizing a pulsed neutron generator. The model of the pulsed neutron tool is constructed to permit Monte Carlo Simulations to be performed of the tool response to the presence of non-radioactive tracers to achieve a desirable level of the neutron absorbing cross sections in the sea water injected into and permeating through the oil reservoirs. Sensitivity analyses of the tool response of the nuclear logging tool were performed for two types of non-radioactive tracers, ammonium tetraborate and gadolinium chloride.

1 Introduction

As a technique for clarifying the geological structure in the oilfield producing zone, an investigation of the underground hydraulics by injecting water soluble non-radioactive tracer has been studied. In the oil field, tracers including radioactive isotopes such as iodine, cesium and cobalt have been utilized. However, obtaining the detection signal in a producing oil well requires injecting a considerable amount of radioactive material. With regard to the environment and safety, it is necessary to protect the oil reservoir and underground water against radioactive contamination.

This paper discusses the results of the analysis conducted on tracers that can be used with injected water, for monitoring the water penetrating through the reservoir with a nuclear logging tool utilizing a Pulsed Neutron Generator(PNG). The most useful technique available today for monitoring in situ water flow, possibly behind a casing, is a Nuclear Logging Technique which uses a PNG to measure the macroscopic Thermal Neutron absorption cross section. The most likely candidates are compounds containing boron as borate, or those containing gadolinium as chloride. Recently, the latter has been used to measure water flow in a horizontal well [1,2].

2 Principle of Pulsed Neutron Capture Logs

A logging tool [3] to measure the macroscopic thermal neutron capture cross section (Σ) of the formation, requires a sealed D-T pulsed accelerator and γ -ray detectors, as shown in Fig. 1. The 14 MeV neutron source is pulsed for a brief period, forming a cloud of high energy neutron in the borehole and the formation which become thermalized through repeated collisions. The neutron are captured at rate which depends on the thermal neutron absorption properties of the formation and the borehole, as shown in Fig. 2. The decay of the capture γ -ray counting rate reflects the decay of the thermal neutron population. The reaction rate for thermal neutron absorption is given by the product of Σ and the velocity of neutron, v . The number of neutrons remaining at time t is:

$$N(t) = N(0)e^{-\Sigma vt} \quad (1)$$

If capture were the only process by which neutrons disappear, the measured decay time would be equal to the intrinsic decay time, τ_{int} . The τ_{int} of a formation is related to its capture property by:

$$\tau_{\text{int}} = 4.545/\Sigma \quad (2)$$

However, neutron capture is not the only process occurring. At any observation point, the local thermal neutron density decreases, because the neutrons are diffusing as well as being captured. The apparent decay time of the local neutron population in an infinite medium has two components:

$$\tau_a = 1/\tau_{\text{int}} + 1/\tau_{\text{diff}} \quad (3)$$

where τ_{int} is the intrinsic formation decay time and τ_{diff} is the diffusion time, which depends on the distance from the neutron source and the thermal diffusion coefficient. As in most logging situations, the measurement includes both borehole and formation signals. Since the borehole component is of little interest for determining formation properties, techniques which decompose the capture γ -ray time decay into formation and borehole components and correct for diffusion effects have been developed [4,5]. The model used as the pulsed neutron tool to be used in the MC simulations of the tool response to non-radioactive tracers in the injected water is based on, the dual-burst PNC tool [6,7]. The dual burst neutron generator provides a short neutron burst and a long neutron burst to optimize the counting rate of capture γ -rays. The count rate after the short burst is low enough to permit counting gates to be placed very near to the burst in order to obtain a maximum borehole-to-formation-signal contrast. The count rate from the long burst remains high long afterwards so there is good statistical precision for the long formation decay component. The dual-burst timing is shown in Fig. 3.

3 Tracer Sensitivity Analysis

On the basis of the results obtained in chemical tests using various types of tracers previously mentioned, gadolinium chloride and ammonium tetra borate

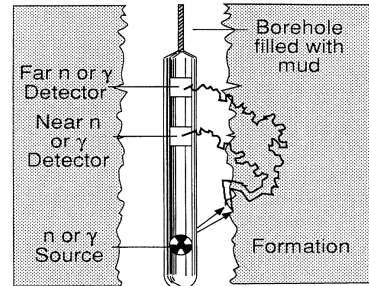


Fig. 1. Schematic representation of a generic logging tool in the borehole

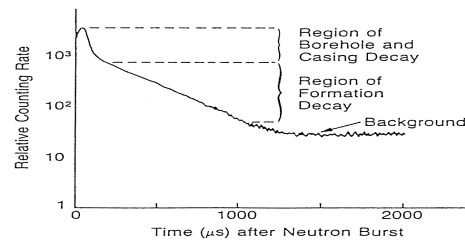


Fig. 2. Decay of capture gamma ray counting rate

were selected as the candidates tracers. For each of these tracers, the PNC tool response, which was explained in chemical solubility test, chemical stability test and absorption test, was calculated by MC simulation, and the tracer detection limit was studied. The analysis code used was the MC simulation code MCNP-4A [8]. ENDF/B-VI was used as the nuclear data library.

3.1 Gadolinium Chloride

The analysis was conducted by varying the tracer concentration in the solution and the water saturation in the geologic formation as parameters. A typical PNC tool and a model of the casing of an oil well, cementing, and the geologic formation are shown in Fig. 4. The γ -ray decay time was calculated by the moment method for each of the time gates shown in Tab. 1. The γ -rays due to the short burst of neutrons were detected by the Near detector, while the γ -rays due to the long burst were detected by the Far detector. The γ -ray decay time in the Near detector and that in the Far detector, both obtained by MC

Table 1. Time gate for γ -ray decay time (μ s)

Near detector	39 ~ 250 (3 μ s intervals)
Far detector	560 ~ 1790 (30 μ s intervals)

Neutron short burst: 8~30 μ s, Neutron long burst: 250~500 μ s

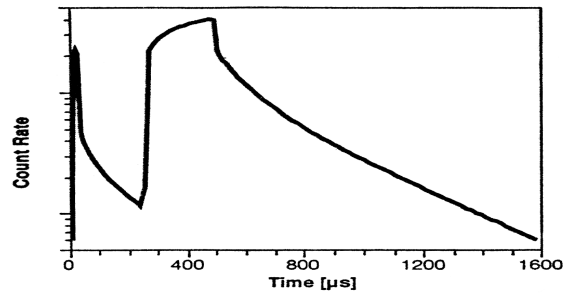


Fig. 3. Typical Dual-Burst spectrum measured with PNC tool

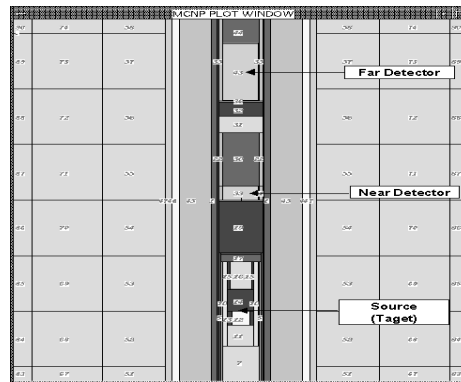


Fig. 4. Analyzed model of Monte Carlo simulation

simulations, are shown in Fig. 5 (Far detector). The Gd index, defined as the weight of Gd in the unit volume of the geologic formation, is shown in Fig. 6. Figure 5 shows that the γ -ray decay time stays almost constant for a tracer concentration of 10 g/l or higher.

3.2 Ammonium Tetraborate

Analysis was conducted by varying the tracer concentration in the solution and the water saturation in the geologic formation as parameters. As with detection of gadolinium chloride, the γ -ray decay time in the Near detector and that in the Far detector were obtained, as shown in Fig. 7. As can be seen the γ -ray decay time does not show any change until the tracer concentration rises to 0.1 g/l or higher. This means that, although the tracer is not adsorbed on the rock so that the tracer solution injected at the injection well readily reaches the test well, the PNC tool cannot detect the tracer unless the tracer concentration is high. The B-index, defined as the weight of boron in the unit volume of the geologic formation, is shown in Fig. 8.

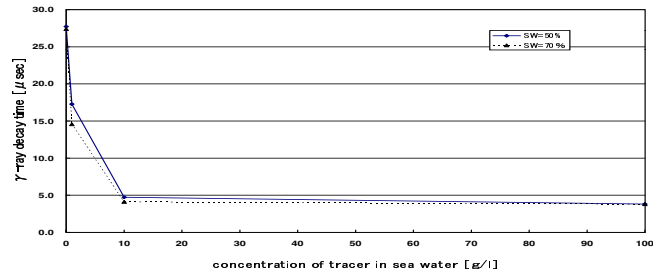


Fig. 5. γ -ray decay time of Gadolinium chlorid

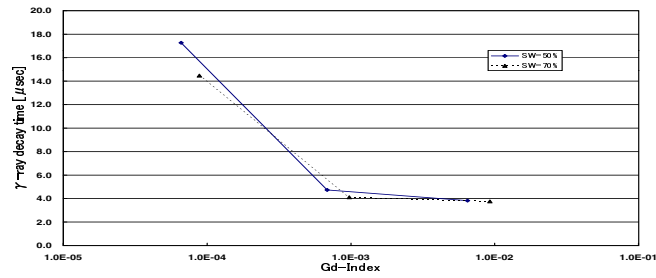


Fig. 6. Relation between γ -ray decay time and Gd-index

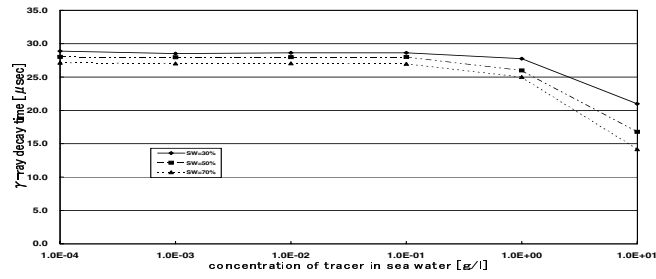


Fig. 7. γ -ray decay time of Ammonium Tetra Borate

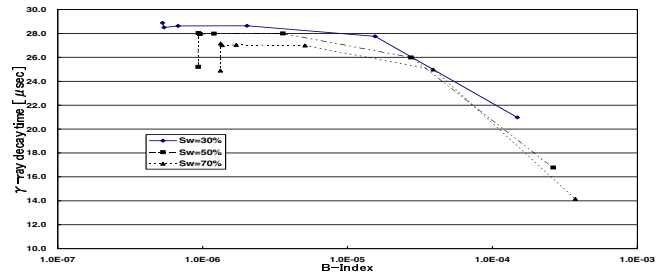


Fig. 8. Relation between γ -ray decay time and B-index

4 Conclusion

As candidates for non-radioactive tracers, chlorides that contain gadolinium and compounds that contain boron were selected, because the thermal neutron absorption cross sections of these substances are greater than the cross section of Cl which is naturally contained in oil reservoirs. For gadolinium chloride, it was shown that the γ -ray decay time stays almost at a level for tracer concentrations of 10 g/l or higher. This shows that the PNC tool can be used for detection even if the tracer concentration is quite low, and that, due to adsorption of the tracer on rock, it is difficult for the tracer solution injected at the injection well to reach the test well. Consequently, chelate complexes of low adsorption on oil formation or rock, such as meglumine gadopentetate, gadoteridol, gadodiamide hydrate, and Crown Ether Complex could be used as tracer candidates; however use of these substances proved to be impractical because of their high cost, and the development of inexpensive gadolinium complexes is needed. For ammonium tetraborate, the γ -ray decay time shows no change until the tracer concentration rises to 0.1 g/l or higher. This means that, although the tracer is not adsorbed on the rock so that the solution with the tracer injected at the injection well readily reaches the test well, the PNC tool cannot detect the tracer unless the tracer concentration gets high. Since formation water frequently contains Cl at high concentration, it is necessary to use a solution containing enough boron tracer, that its thermal neutron absorption cross section is higher than that of Cl.

References

1. B.A. Roscoe et al.: 'Oil and Water Flow Rate Logging in Horizontal Wells Using Chemical Markers and a Pulsed-Neutron Tool'. In: *The 7th Abu Dhabi International Petroleum Exhibition and Conference, Abu Dhabi, U.A.E., 13-16 October, 1996*, Paper SPE36230
2. B.A. Roscoe et al.: 'Measurement of the oil and Water Flow Rates in a horizontal well using Chemical Markers and a Pulsed-Neutron Tool'. In: *The 1996 SPE Annual Technical Conference and Exhibition, Denver, Colorado, U.S.A., 6-9 October 1996*, Paper SPE36563
3. J.S. Schweitzer: Nucl. Geophys. **5**, 65 (1991)
4. W.E. Schultz et al.: 'Experimental basis for a new borehole corrected pulsed neutron capture logging system', CWLS-SPLA Symp., Calgary, Paper CC, 1983
5. D.K. Steinman et al.: 'Dual-burst thermal decay time logging principles', Tech. Symp. Soc. Pet. Eng., New Orleans, Paper SPE15437, 1986
6. B.A. Roscoe et al.: 'A New Through-Tubing Oil Saturation Measurement System'. In: *The SPE Middle East Oil Show, Bahrain, November 16-19, 1991*, Paper SPE21413
7. R.E. Plasek et al.: 'Improved Pulsed Neutron Capture Logging with Slim Carbon-Oxygen Tools: Methodology'. In: *The SPE Annual Technical Conference & Exhibition, Dallas, U.S.A., 22-25, October, 1995*, Paper SPE30598
8. J.F. Briesmeister, Ed.: *MCNPTM - A General Monte Carlo N-particle transport code Version 4A*, LA-12625-M (1993)

Neutronics and Shielding Analysis of an Ignitor

S. Rollet and M. Rapisarda

ENEA, C.R.E. Frascati, C.P. 65 - I-00044 - Frascati, Rome, Italy

Abstract. This paper presents the Monte Carlo calculations made to test the effectiveness of the shields required to allow hands-on maintenance in the Ignitor tokamak.

The Ignitor experiment is designed to reach ignition in a magnetically confined plasma and to address the fundamental physics issues of a burning plasma. During deuterium-tritium (D-T) operation, at the maximum of neutron production, the plasma is expected to emit about 3×10^{19} n/s with an energy of 14 MeV during pulses lasting 4 s. Such a strong emission requires a high Z shield around the device assembly to shield the gamma flux emitted from the inner activated parts, plus a low Z shield around the horizontal ports to reduce the activation, due to neutron streaming, of the cryostat, the diagnostics and the auxiliary systems.

Here we report the neutron and the gamma fluxes (calculated with the MCNP-4B code) in the cryostat at various heights above the equatorial plane, either in absence or in presence of the shield. Then, for the farthest part of the cryostat, we report the neutron and the gamma spectra and the dose rates (calculated with FISPACT-99) as a function of the shield characteristics. Finally, we present the dose rate in the most exposed portion of the cryostat in function of time after irradiation reaching the conclusion that the proposed shield is properly designed to allow machine maintenance.

1 Introduction

Ignitor [1] will be a compact tokamak operating at high toroidal field (13T) generated by a copper toroidal magnet, strengthened by steel C-clamps and cooled in a cryostat at liquid helium temperature (Fig. 1). Its aim is to reach ignition and to study the fundamental physics of a burning plasma.

During the D-T operation its energetic neutron emission will induce a wide spread activation in every piece of hardware surrounding the plasma. Although the safety of normal operations can be easily assured by the insertion of an appropriate screen between the tokamak and the personnel, intervention for maintenance and repair on the machine will pose severe limits to the activation of the structures. Thus an internal shield, surrounding the C-clamps and the horizontal ports, has been proposed [2] to limit the activation inside the cryostat.

A previous article [3] calculated the neutron fluxes and the doses in the C-clamps and inside the cryostat at the equatorial plane; the present paper extends the calculations to the full length of the cryostat, checking the efficacy of the shield in other critical parts of the assembly.

Like every tokamak, Ignitor will be a rather complex machine and the path followed by neutrons in their way out from the plasma is not easily predictable.

The unavoidable presence of ports will cause neutron streaming processes, thus Monte Carlo transport calculations, performed in three dimensions, are the most suitable way to reach exhaustive results.

2 Computational Tools

The complex geometry of Ignitor has been described in the 3-D input model for the MCNP-4B Monte Carlo neutron transport code [4]. A 30° sector of the machine, including a horizontal port, has been detailed in about 400 cells. Reflective boundary conditions at the symmetry planes have been applied to describe the whole assembly. Figure 2 shows the cross section at the equatorial plane (a) and the vertical cut through the toroidal magnet, the C-clamps and the ports (b) of the model.

The main portion of the shield, aimed to absorb the gamma rays, has been modeled by a vertical wall of Pb, 10 cm thick, placed against the C-clamps. A reinforcing sleeve is added around the horizontal port, to shield the neutrons streaming through the port itself. The sleeve, 25 cm thick, is made of a mixture of low Z materials (CH_2 and B) to moderate and absorb the neutrons.

The geometrical model is given in input to MCNP-4B, which calculates the neutron fluxes and spectra in all the cells of interest, using as cross section libraries the latest version of the European Fusion Files [5]. Fluxes and spectra are then given to FISPACT-99 activation code [6] for the evaluation of the induced radioactivity.

In order to increase the efficiency of the calculations, variance reduction techniques are used applying the splitting and Russian Roulette both in geometry

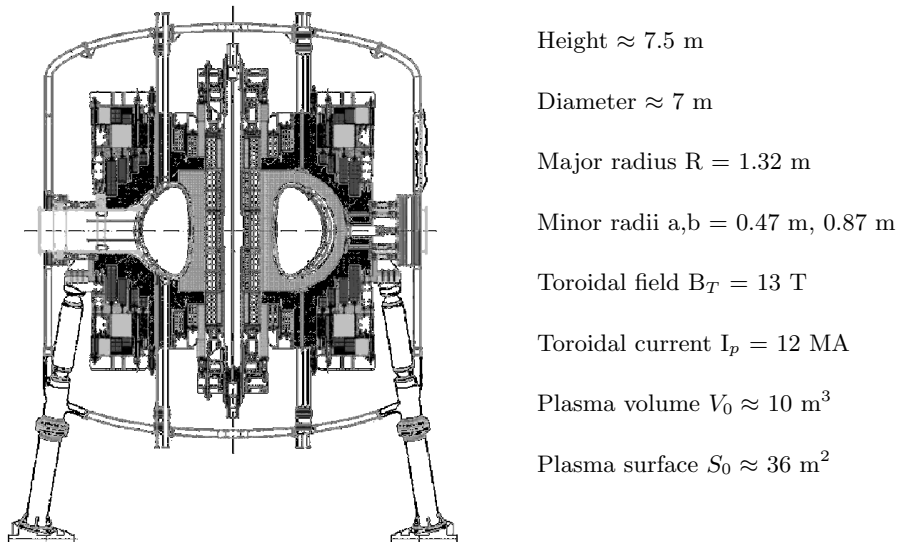


Fig. 1. The Ignitor experiment layout

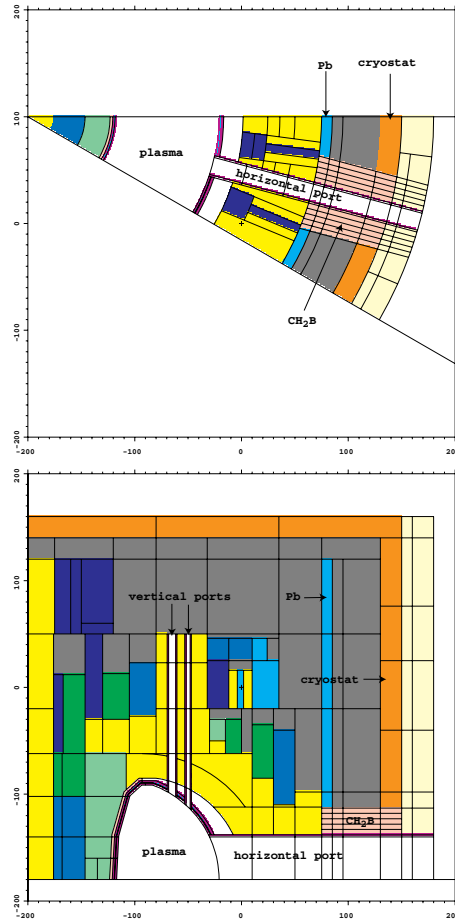


Fig. 2. Ignitor geometry simulated in the MCNP code: (a) horizontal cut at the equatorial plane; (b) vertical cut through the vertical and horizontal port

and energy domain. The running time is greatly reduced thanks to the use of the parallelized version of MCNP-4B on a IBM-SP2 multiprocessor machine.

3 Results

The neutron and the gamma fluxes have been calculated inside the cryostat at various heights above the mid-plane, with or without shield, for unit neutron source, and shown in Fig. 3.

For neutrons the effect of the shield is to reduce at least an order of magnitude the value of the flux inside the cryostat. For gamma rays the decrease is lower (a factor 2). The bump in the dashed curve close to the mid-plane is due to the gamma rays produced in the low-Z shield itself (when present).

The neutron and gamma spectra have been calculated in the inner part of the cryostat at various heights in order to compute the activation of hardware lying inside. The spectra show similar shapes and decrease with height, although, as expected, the neutrons near the equatorial plane are significantly harder and more abundant.

In Fig. 4 are shown the neutron spectra inside the upper part of the cryostat without any shielding, with the Pb only and with Pb and CH₂B together. Adding the CH₂B sleeve around the port causes a great difference especially in the high energy region of the spectrum, as shown in the Fig. 4 b.

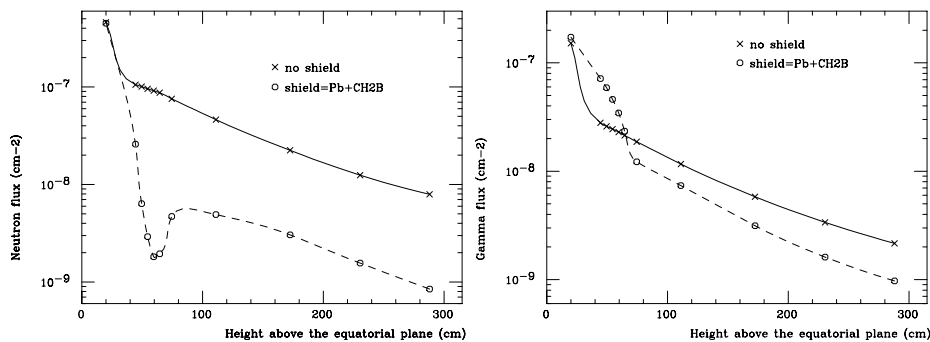


Fig. 3. The neutron (a) and gamma (b) fluxes inside the cryostat, at different height above the equatorial plane. In both cases are reported the curves without any shielding (solid line) and with the complete shielding (dashed line)

In the same upper part of the cryostat (the least exposed to activation) the contact dose rate in absence of shield results larger than the threshold of 100 $\mu\text{Sv/h}$ (Fig. 5) for months after the end of operations. Such threshold is derived from the ICRP limit of 100 mSv in 5 years, never exceeding 50 mSv per year [7], with an average exposure of 200 h/year per person. In presence of the shield, the threshold of 100 $\mu\text{Sv/h}$ is reached in a much shorter time, allowing a rapid intervention on the machine. Nevertheless, it must be kept in mind that the value of 200 hours per year could be a rather short limit in case of complex operations to be done on the machine. Thus, when the Ignitor design will specify the details of the maintenance operations expected during its lifetime, it will be wise to reconsider the practical adequacy of these numbers, taking into account, moreover, that the real screen could have holes or interstices not foreseeable today, that could weaken its overall shielding capability. The effect of the sleeve on the cryostat dose rate is shown in the same figure, where it can be seen that the cooling time needed to the dose rate to fall below the allowed limit, at the end-of-life, is reduced from about 2 month to few days only.

This lag is not very important at the end of the machine lifetime, but is substantial during operations. We have then calculated the dose rate after 1 day, 1 week, 1 month and 1 year of intense operations, at different heights in

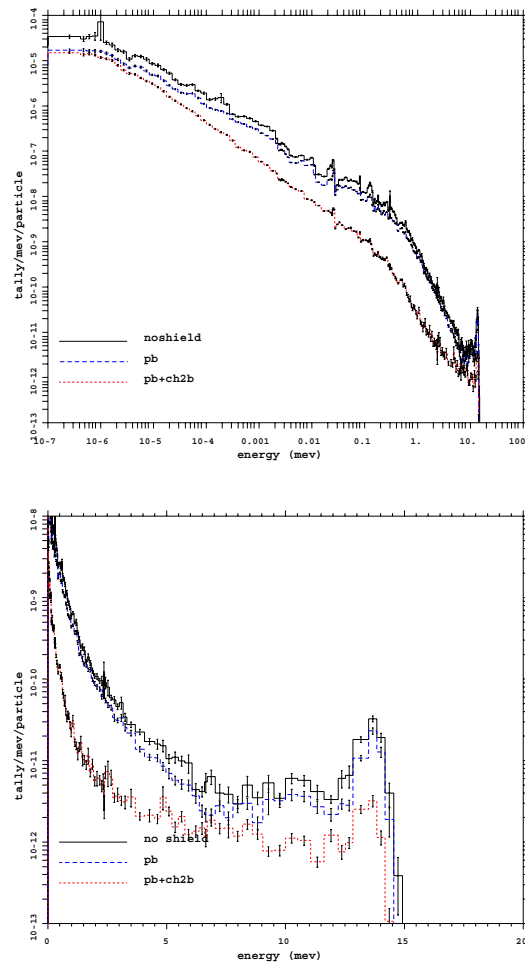


Fig. 4. The neutron spectra inside the upper region of the cryostat, (a) down to thermal energies and (b), enlargement of the high energy region

the cryostat, and verified that in presence of the complete shielding the dose level falls below the limit in a reasonable span of time. This is true even for the most exposed part of the cryostat, just above the port, as shown in Fig. 6, for which we report the dose levels versus cooling time. It can be noticed that, even following one year of D-T operation it will be possible to act one week after the last shot making the maintenance of Ignitor a feasible duty.

Finally, the dependence of the fluxes versus height suggests that a reduction of the Pb wall dimension should be possible with increasing height. A calculation with a one dimensional code should be able to optimize the thickness in detail.

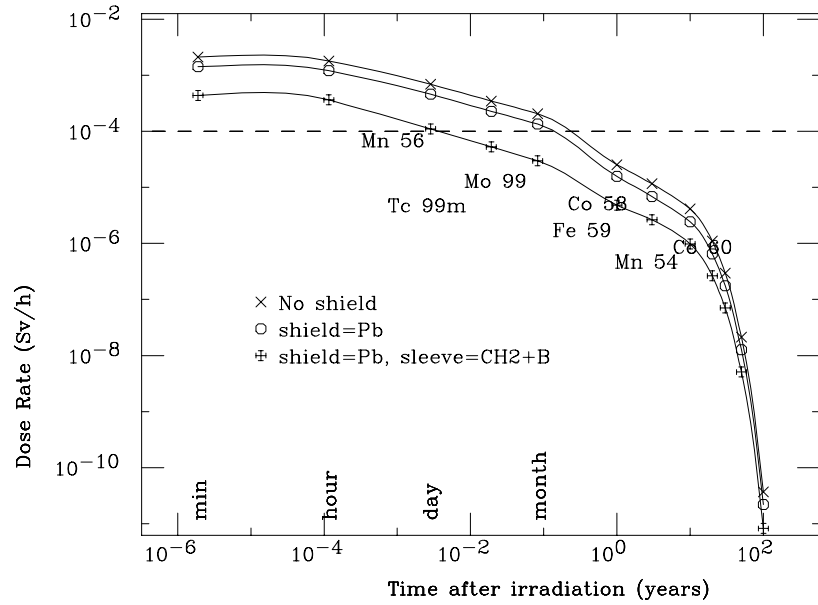


Fig. 5. Contact dose rate versus cooling time in the upper part of the cryostat, without any shielding, with the Pb only and with Pb and CH₂B together

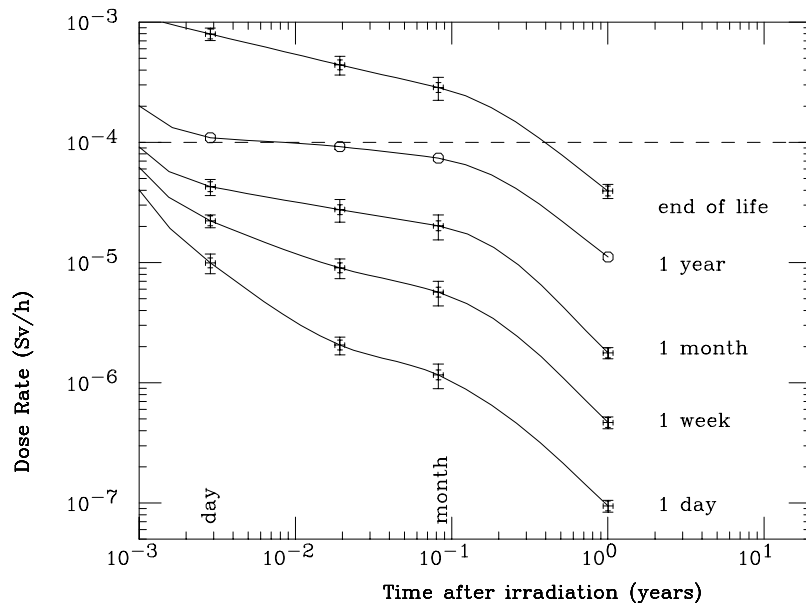


Fig. 6. Contact dose rate versus cooling time in the region of the cryostat above the horizontal port, after 1 day, 1 week, 1 month, 1 year and at end-of-life of DT operation

Conclusions

The problem of maintenance and repair of hardware inside the cryostat of Ignitor can be solved with the insertion of a composite screen (Pb, CH₂, B) around the C-clamps and the horizontal ports of the machine. Calculations show that a relatively thin (10 cm vertically and 25 cm around the port) screen is enough to keep the activation inside the cryostat at an acceptable level. Out of the equatorial plane, the insertion of such screen, provided that it is not weakened by holes and interstices, will allow intervention on the cryostat, diagnostics and auxiliary systems within one day in most cases and one week in the worst conditions, making the maintenance of Ignitor a feasible task.

References

1. B. Coppi et al.: *Ignitor Program: Engineering Design Description*, Vol. II, RLE Report PTP 96/03(1996)
2. S. Rollet, P. Batistoni, R. Forrest: 'Activation Analysis For The Ignitor Tokamak', Accepted for publ. in *Fus. Eng. and Des.* (2000)
3. S. Rollet, P. Batistoni: 'Shielding aspects of a tokamak reaching ignition'. In: *Shielding Aspect of Accelerators, Target and Irradiation Facilities*, 5th Int. Conf. at Paris, France July 17-21, 2000
4. J. Briesmeister (Ed.): *MCNP: A General Purpose Monte Carlo N-Particle Transport Code (Version 4B)*, LA-12625-M, Los Alamos Nat. Lab. Rep. (1997)
5. J. Kopecky, H. Gruppelaar, A. Hogenbirk, H. Van Der Kamp, D. Nierop: *European Fusion File EFF-2.4*, EFF-DOC-347, 1994
6. R.A. Forrest, J-Ch. Sublet: *FISPACT-99 User Manual*, UKAEA-FUS-407 Report 1998
7. ICRP Recommendation, ICRP publication N. 60, *Annals of ICRP* Vol. 21, N. 1-3 (1990)

Monte Carlo Calculations for Neutron and Gamma Radiation Fields on a Fast Neutron Irradiation Device

A. Vieira, A. Ramalho, I.C. Gonçalves, A. Fernandes, N. Barradas, J.G. Marques, J. Prata, and Ch. Chaussy

Instituto Tecnológico e Nuclear, Estrada Nacional 10, 2685 Sacavém, Portugal

Abstract. We used the Monte Carlo program MCNP to calculate the neutron and gamma fluxes on a fast neutron irradiation facility being installed on the Portuguese Research Reactor (RPI). The purpose of this facility is to provide a fast neutron beam for irradiation of electronic circuits. The gamma dose should be minimized. This is achieved by placing a lead shield preceded by a thin layer of boral. A fast neutron flux of the order of 10^9 n/cm²s is expected at the exit of the tube, while the gamma radiation is kept below 20 Gy/h. We will present results of the neutron and gamma doses for several locations along the tube and different thickness of the lead shield. We found that the neutron beam is very collimated at the end of the tube with a dominant component on the fast region.

1 Tube Description

This work describes a Monte Carlo simulation for a new irradiation facility to be installed in a beam tube of the Portuguese Research Reactor - RPI. The RPI is a swimming pool type nuclear reactor with a maximum power of 1 MW and a neutron flux at the core of about 2×10^{13} n/cm²s. The facility was designed to maximize the fast neutron component of the neutron beam and minimize the gamma dose.

The tube is described schematically in Fig. 1. It is roughly a cylinder with 275 cm of length and 16 cm of diameter. The entrance of the tube is located close to the center of the South hall of the reactor core in an oblique direction. To eliminate the thermal neutrons a 0.8 cm disk of boral is placed at about 160 cm from the entrance of the tube (marked in Fig. 1 as “filter”). It is followed by a 4 cm disk of lead designed to attenuate the gamma radiation with minimum interference with fast neutrons. At the exit we introduced a lead collimator to prevent scattering of gamma rays.

2 Monte Carlo Simulation

To simulate the transport problem of gamma photons and neutrons on the tube we used the Monte Carlo code MCNP version 4b [1]. This is a widely used code to solve the transport problem for neutrons and photons using the Monte Carlo method. To run this program we have to specify the geometry of the problem

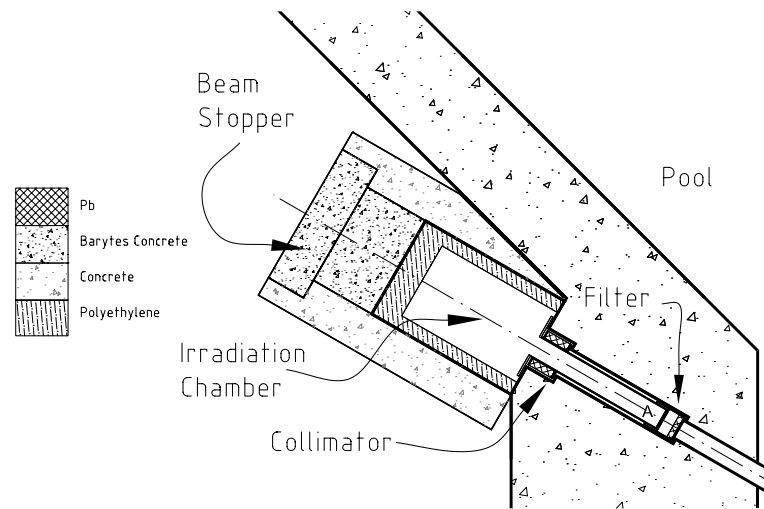


Fig. 1. Schematic representation of the irradiation facility. The region designated A marks the inner irradiation position

(size, location and composition of materials), an adequate particle source that simulates the real source (size, configuration and particle emission probabilities in energy and direction), and finally the desired particle statistics (fluxes at a given surface, doses, etc). The program uses nuclear data tables libraries containing tabulated values of nuclear cross sections for most materials. The advantage of this method is that it is very general and have the possibility to deal with complicated geometries. The drawback is that it is a statistical approach to the transport problem, hence time consuming and the results may carry considerable errors.

2.1 Neutrons

For this problem we considered a circular isotropic neutron source with an emission probability given by the fission spectrum. The choice of a correct source location is difficult given the position of the tube with respect to the reactor core. To avoid this difficulty, the source was made larger than the tube diameter and was placed 5 cm behind the entrance, well inside the reactor water pool.

To calibrate the neutron source we used experimental measurements at several positions along the tube entrance. The fast neutron fluxes were determined by the activation method using nickel detectors. For the reactor core configuration N2-P1/5 the fast neutron flux measured at the entrance of the tube was measured 1.9×10^{11} n/cm²s (all values refers to the reactor at a nominal power of 1 MW). For positions very close to the entrance of the tube we noted that the source considered in MCNP does not describe properly the real neutron source - MCNP source showing a steeper decrease with distance. This discrepancy may

be explained by the proximity of our source to the entrance of the tube. However, for distances greater than 20 cm the behaviour of the neutron flux to the distance is very similar with the predicted by MCNP. We then choose the experimental flux on this position to calibrate our neutron source. To increase the fast neutron flux, the reactor core was updated to the current configuration N2-P1/6. For this new configuration the code CITATION was used to determine the fast neutron flux at a position near the entrance of the tube. It has calculated to be about 3 times higher than previously.

2.2 Gamma Radiation

For gamma radiation we used the same source but with a different energy distribution. We simulated the reactor core and run the MCNP in the criticality mode for neutrons and photons. While the calculated neutron spectrum at the entrance of the tube is very similar to the theoretical Watt fission spectra (apart from the thermal neutrons), the gamma spectrum deviates considerably from the prompt gammas spectrum resulting from fission. The major modification was a dominant contribution in the group between 2 and 3 MeV due to the 2.1 MeV gammas resulting from thermal neutron capture reactions in hydrogen.

To calibrate the gamma source we used the same method as for neutrons, using the experimental measurements obtained at the entrance of the tube, where we measured a gamma dose rate of about 150 Gy/h.

3 Results

Table 1 presents the calculated and measured values for the neutron fluxes in the thermal, fast and epithermal range, as well as the gamma dose rates. The experimental values were measured at the centerline of the tube. The calculated values refer to averages over cross section surfaces on the tube. All errors are below 5%. For the fast neutron we found an excellent agreement at the irradiation positions A and A+50cm. For the thermal neutrons we found a significant discrepancy.

Table 1. Neutron fluxes ($\times 10^8$ n/cm²s) and gamma dose rate (Gy/h) in the irradiation tube. The lower line refers to values obtained by MCNP and the upper line are experimental values

Config	Position A				Position A + 50cm				Exit of tube			
	ϕ_{th}	ϕ_{ep}	ϕ_{fast}	D_γ	ϕ_{th}	ϕ_{ep}	ϕ_{fast}	D_γ	ϕ_{th}	ϕ_{ep}	ϕ_{fast}	D_γ
Empty exp	30.8	0.91	22.21	245					5.81	0.04	30.1	81
cal												
Filter exp	1.69	0.49	12.9	18	0.25	0.34	4.65	13	0.03	0.05	1.05	4.5
cal	0.88	0.59	14.0	23	0.09	0.15	5.30	10				

We can see that the fast neutron component is dominant in the irradiation positions - see Fig. 2 that shows the neutron spectrum at several positions. The measured ratio $\phi_{fast}/\phi_{thermal}$ is respectively 15.9 and 58.8 at the irradiation position A and 50 cm after. The further position is thus preferred if we want a neutron beam less contaminated of thermal neutrons. The relative intense flux of thermal neutrons predicted by MCNP in the irradiation position is mainly due to neutrons that are thermalized in the concrete hall, thus not being absorbed by the boron screen. The ratio of fast neutrons flux to gamma dose rate is almost the same in the irradiation position A and A+50 cm, thus if contamination from thermal neutrons is not important, there is advantage in using irradiation position A of the tube, The only disadvantage being a lower ratio of $\phi_{fast}/\phi_{thermal}$.

This tube was designed to be a flexible irradiation device due to its capability to select a specific neutron to gamma dose ratio originated in a mixed radiation field. This can be achieved by increasing the thickness of the lead shield in order to reduce the gamma radiation. Figure 3 shows the neutron and gamma flux as a function of the thickness of the lead disk. Depending on the circumstances we may place a specific width. If we want a lower contamination of gamma radiation, we should increase the thickness of lead.

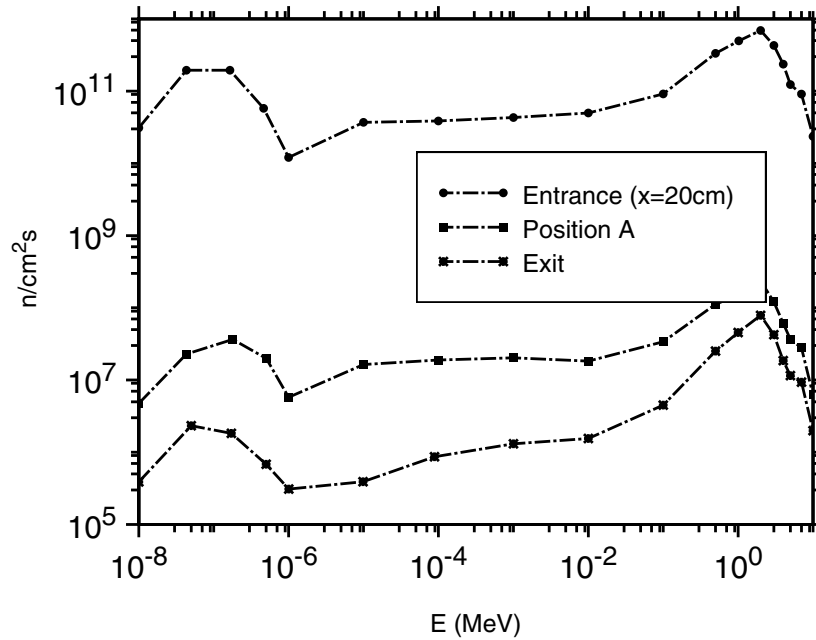


Fig. 2. Neutron spectra at several positions along the tube

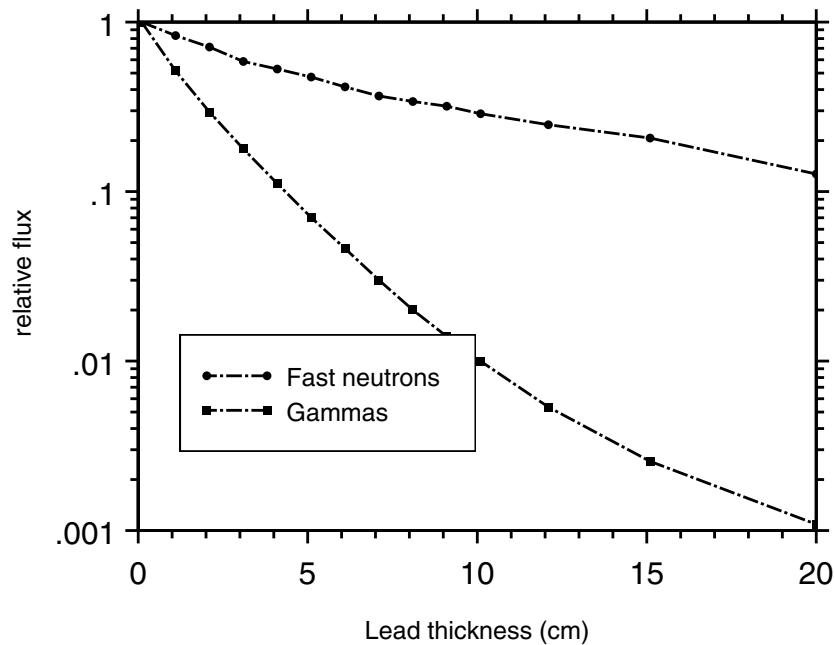


Fig. 3. Relative neutron and gamma flux as a function of the lead width

4 Conclusions

A Monte Carlo simulation of a fast neutron beam was performed. A intense fast neutron flux of 10^9 n/cm²s is obtained at the irradiation position with a gamma dose rate of about 20 Gy/h. The agreement between Monte Carlo calculations and experiments is very good and allows us to simulate any modifications in the tube in order to create different irradiation conditions. The tube is very flexible allowing a variable fast neutron to gamma dose ratio.

References

1. J. F. Briesmeister ed.: *MCNP - A General Monte Carlo n-particle Transport Code - Version 4B*, LA-12626-M (1990)
2. A. Ramalho, J. Marques, I.C. Goncalves, I.F. Goncalves, A. Fernandes, J. Prata, A. Vieira: 'Use of RPI to test the behaviour under irradiation of electronic circuits and components for CERN'. In: *Proceedings of IAEA International Symposium on Research Reactor Utilization, Safety and Management, IAEA-SM-360, Lisboa (1999)*

Shielding Assessment of the MYRRHA Accelerator-Driven System Using the MCNP Code

M. Coeck, Th. Aoust, F. Vermeersch, and A. Abderrahim

SCK•CEN, Boeretang 200, 2400 Mol, Belgium

Abstract. The MYRRHA project includes the design and the development of an accelerator driven system (ADS) aimed at providing protons and neutrons for various R&D applications. With regard to the safety aspects, the assessment of the shielding and of the dose rates around the installation is an important task. In a first approach standard semi-empirical equations and attenuation factors found in the literature were applied. A more detailed determination of the neutron flux around the reactor is made here by Monte Carlo simulation with the code MCNP4B. The results of the shielding assessment give an estimate of the neutron flux at several positions around the core vessel and along the beam tube. Dose rates will be determined by applying the ICRP74 conversion factor.

1 Introduction

The MYRRHA project aims at the design and development of an accelerator driven system for R&D applications. At the end of 1994 the SCK•CEN, started in collaboration with IBA, to study the feasibility of coupling a proton accelerator to a liquid Pb-Bi windowless spallation target surrounded by a sub-critical neutron multiplying medium, as a new neutron source for the production of radioisotopes. In 1997 this project evolved to MYRRHA aiming at various research topics, namely: ADS technological demonstration, waste transmutation studies of minor actinides and long lived fission products, structural material and nuclear fuel behaviour studies, and radioisotope production.

Conceiving an adequate shielding for this system is an important task with regard to safety aspects. In a first step, preliminary ideas for the shielding are deduced from semi-empirical equations and attenuation factors found in the literature. A second step involves the confirmation of the proposed shielding through a thorough MC simulation with the code MCNP4B [1].

2 Modelling of MYRRHA

Figure 1 shows a two-dimensional view of the MYRRHA ADS. The model consists of a vessel of HT-9 steel filled with Pb-Bi. The beam channel is modelled by a vacuum duct in HT-9 steel. The free surface (windowless design) between the liquid Pb-Bi target and the beam channel is at 7 cm above the center of

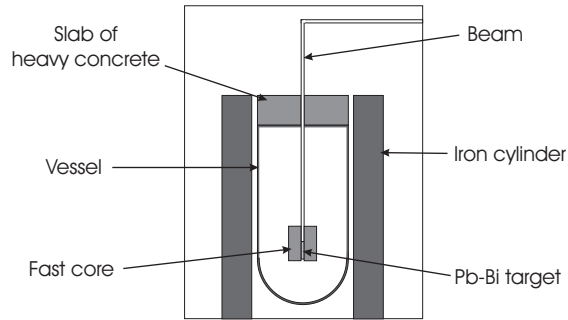


Fig. 1. Two-dimensional view of MYRRHA

the source, positioned at $z=0$. The shielding consists laterally of a 1 m pure iron cylinder, and above the vessel of a 1 m heavy concrete slab.

The fast core consists of two rings of hexagonal assemblies of MOX fuel pins of respectively 30% and 15% Pu content. Each assembly contains 127 fuel pins arranged in a triangular lattice with a pitch of 1 cm. The fuel pins have an active fuel length of 60 cm and their cladding consists of martensitic steel.

Two sources are considered (see Fig. 2): a point source with a Watt fission spectrum and a spallation source given by the High Energy Transport Code HETC. The main difference in the spectra of both sources is the additional high energy part inherent to the spallation source. Comparing the results of both simulations will give an idea of the relative importance of this high energy part of the spectrum and its influence on the dosimetric values around the system.

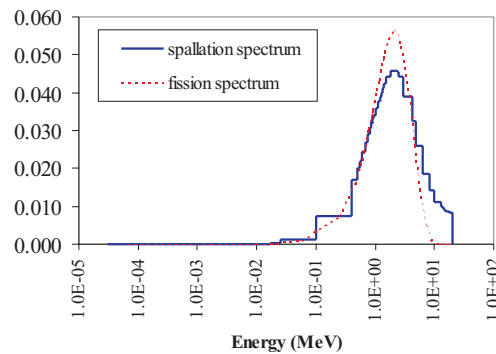


Fig. 2. Spectrum of the sources used

The point source energy spectrum is the built-in Watt fission spectrum:

$$f(E) = \exp(-E/a) \sinh(bE)^{1/2}. \quad (1)$$

with $a = 0.799$ and $b = 4.903$.

The spallation source is obtained by simulating, with the code HETC, the bombardment of Pb-Bi by a beam of protons of 350 MeV and 5 mA, leading to a source strength of $1.23\text{E}+17$ n.s-1 [2]. The spatial and energetic distributions of the neutrons obtained are input as fixed source to the code MCNP4B. The simulations are performed with a PC Pentium III 450 MHz and with a Sun Ultra Enterprise 4000. These simulations run for one to three weeks depending on the number of histories ($1.0\text{E}+5$ - $1.0\text{E}+7$)

3 Results and Discussion

3.1 Calculation of the Lateral Shielding

In order to assess the attenuation of the neutron source through the different materials we first made calculations without the fast core. This gives the opportunity to compare the shielding dimensions with those estimated by the Moyer theory [3] used in shielding accelerator targets.

Flux Outside the Vessel: Figure 3 represents the flux outside the vessel per unit source strength for both the fission and the spallation spectrum up to 20 MeV. A good agreement at the level of the source ($z = 0$ cm) is found between both calculations, however near the top of the vessel ($z = 400$ cm) a difference of a factor 100 is found. The spatial distribution or the spectral difference between the spallation and the fission spectrum used in the calculation could cause this difference. Further work is being done to investigate this divergence.

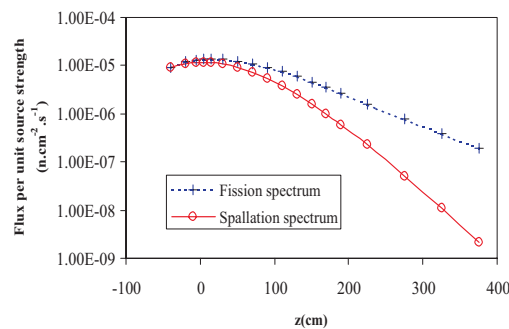


Fig. 3. Flux per unit source strength outside the vessel

Flux Rate behind a 1 m Fe Shield: In order to shield the high-energy neutrons above 8 MeV an iron shield of 1 m is introduced at a distance of 0.2 m from the vessel surface. The effect of this shield is represented in Fig. 4.

The flux reduces by an average factor of 450 for the spallation spectrum. The reduction for the fission spectrum is about 370.

Neutron Dose Rates: Taking into account the source strength and the neutron spectrum we derive the neutron dose rates at $z=0$ cm near the vessel and beyond the 1 m Fe shielding. The conversion from the neutron spectra to the dose is based on the ICRP74 conversion factors for $H^*(10)$ [4]. The results are given in Tab. 1.

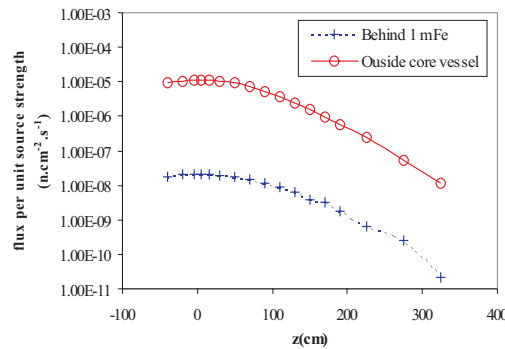


Fig. 4. Flux per unit source strength for a spallation spectrum

Table 1. Neutron dose rates at $z=0$ cm for different source spectra near the vessel and beyond the 1 m Fe shielding

Source spectrum	Fission		Spallation		Spallation with core	
Position	Sv/h per unit source strength	Sv/h $I_p=5$ mA $E_p=350$ MeV	Sv/h per unit source strength	Sv/h $I_p=5$ mA $E_p=350$ MeV	Sv/h per unit source strength	Sv/h $I_p=5$ mA $E_p=350$ MeV
outside the vessel	2.76E-12	3.64E+05	1.45E-12	1.91E+05	1.45E-11	1.91E+06
outside 1 m Fe shield	1.15E-14	1.52E+03	3.00E-15	3.96E+02	1.75E-14	2.31E+03

The dose reduction factor due to the Fe shield is 480 for the spallation spectrum and 240 for the fission spectrum. The fact that the dose reduction factors are of the same order as the flux reduction factors indicates that the spectrum remains a hard spectrum. In order to reduce the neutron dose rate a shield with low Z-elements is needed to thermalise the neutrons. A concrete shield is proposed of 1.5 m thickness. Using the dose attenuation curves of Clark et al. [5], we find that this shield should reduce the dose rate to the order of $20 \mu\text{Sv/h}$. Shielding thicknesses of the same order of magnitude were found using the Moyer method for the assessment of accelerator shielding. Monte Carlo calculations are planned to further assess the concrete shielding.

Calculations Including the Subcritical Core: Calculations including the subcritical core were performed in order to assess the contribution of neutrons

from the core to the dose rate. The calculations were performed with the spallation spectrum as driving source. As can be seen in Fig. 5, the presence of the core increases the flux by a factor 10 in the region $z=0$ cm and by a factor 4 at the top of the vessel ($z=400$ cm).

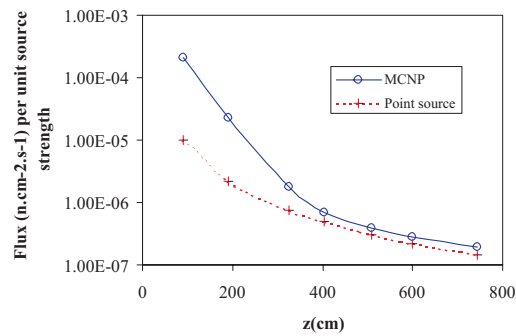


Fig. 5. Flux per unit source strength outside the vessel for a driver source with a spallation spectrum

The neutron doses near the vessel and behind the 1 m Fe shielding were also calculated and are included in Tab. 1. A neutron dose reduction of the order of 800, due to the iron shield, is found.

3.2 Flux Calculations in the Beam Tube

The beam line is a potential way for neutrons to stream from the core. The flux variation in the beam tube was calculated for a fission source spectrum and is represented in Fig. 6. This figure also includes the flux variation for a free point source, i.e. not surrounded by the beam tube and Pb-Bi vessel.

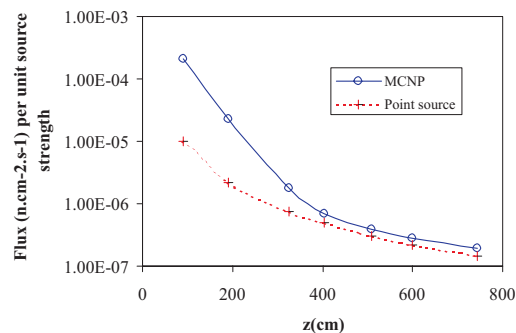


Fig. 6. Flux per unit source strength as a function of the distance in the beam tube

The flux values at a distance of 100 cm to 400 cm from the source position are higher than the ones predicted with a free source. This can be explained by the backscattering of neutrons on the Pb-Bi reflector.

Neutron dose rates were evaluated at the top the vertical beam tube (at 2.45 m above the concrete shield) and in a ring of 10 cm outside the beam tube positioned 1 m above the concrete shield. They are given in Tab. 2.

Table 2. Dose rates in and near the beam tube above the concrete shield

	Sv/h per unit source strength	Sv/h $I_p=5$ mA $E_p=350$ MeV
at the top and inside of the vertical beam tube	2.70E-13	3.32E+04
around the beam tube 150 cm from the top	2.20E-15	2.71E+02
average above the concrete slab	1.60E-16	1.97E+01

The average neutron dose rate above the concrete slab is 20 Sv/h. Dose rates near to the beam tube increase by one order of magnitude due to neutrons escaping the beam tube. An appropriate local shielding should be provided to reduce these dose rates to acceptable levels.

4 Conclusions

In this work the results obtained from MCNP calculations are discussed with a view to the shielding assessment of an ADS with PbBi coolant and target. Both fission and spallation spectra were introduced in the simulations. The distribution of the flux outside the vessel was calculated for both spectra. A good agreement was found near the source height, however, a divergence for larger distances was observed. This result will be studied in more detail. Taking into account an iron shielding of 1 m thickness, positioned at 20 cm from the vessel, it could be seen that the total flux (calculated up to 20 MeV) is decreased 450 to 370 times, depending on the spectrum introduced. Also the dose equivalent $H^*(10)$ values are decreased by a comparable factor, indicating that the iron shield does not have any significant spectrum degradation effect. To further reduce the dose equivalent values at the side of the vessel, the introduction of a heavy concrete shielding is suggested. We intend to use in the near future MCNPX to take into account the effect of the high energy neutrons on the shielding.

References

1. J.F. Briesmeister, Ed.: *A General Monte Carlo N-Particle Transport Code, LA-12625-M, Version 4B*. (LA-12625-M, Version 4B March 1997)
2. E. Malambu: *Neutronic Performance Assessment of the MYRRHA ADS Facility*, SCK•CEN internal report R3438-B, April 20, 2000
3. K. Tesch: *Rad. Prot. Dosim.* **11**, 166 (1985)
4. ICRP 74 report
5. F.H. Clark et al.: *Monte Carlo calculations of the penetration of normally incident neutron beams through concrete*, ORNL-3926, 2000

Numerical Tests for the Problem of U–Pu Fuel Burnup in Fuel Rod and Polycell Models Using the MCNP Code

V.G. Muratov and A.V. Lopatkin

RDIFE, Russia

An important aspect in the verification of the engineering techniques used in the safety analysis of MOX-fuelled reactors, is the preparation of test calculations to determine nuclide composition variations under irradiation and analysis of burnup problem errors resulting from various factors, such as, for instance, the effect of nuclear data uncertainties on nuclide concentration calculations. So far, no universally recognized tests have been devised. A calculation technique has been developed for solving the problem using the up-to-date calculation tools and the latest versions of nuclear libraries. Initially, in 1997, a code was drawn up in an effort under ISTC Project No.116 to calculate the burnup in one VVER-1000 fuel rod, using the MCNP Code. Later on, the authors developed a computation technique which allows calculating fuel burnup in models of a fuel rod, or a fuel assembly, or the whole reactor. It became possible to apply it to fuel burnup in all types of nuclear reactors and subcritical blankets.

The computation technique involves a traditional stepwise procedure within one code:

Step 1. Spatial and energy neutron flux distribution in the system is calculated. One-group cross-sections are prepared for the nuclear reactions of actinides and the main fission products. In this step, the MCNP-4B code [1] featuring point-by-point representation of nuclear data, is used. The MCNP code has been provided with an additional module which allows correctly calculating the transfer of delayed fission neutrons. The MCNP relies on the nuclear data library ML45, version 3 [2] based on the estimated data files ENDF/B-6, JEF-2.2, BROND-2.2, and JENDL 3.2.

Step 2. The neutron flux and nuclear data obtained in step 1 are used to calculate nuclide concentration variations over a certain period of time. The CEFA Code [3] and nuclei decay library prepared by the authors, are involved in integrating the set of isotope kinetics equations. Both steps are managed by the CEFA Code which provides data exchange, prepares input data for MCNP, and processes the output.

Steps 1 and 2 are repeated as many times as may be necessary to solve the burnup problem for the specified time interval.

To avoid errors in going from Step 1 to Step 2, the calculation of neutron flux distribution and the preparation of cross-sections for all nuclides covered by burnup calculations, are performed in one calculation run. Considering that MCNP provides the most adequate description of the geometrical model of the fuel rod, fuel assembly, fuel channel, etc., that no group cross-sections are involved in neu-

tron transport calculations, and that there are no intermediate steps to prepare one-group cross-sections for nuclide kinetics calculations, it would be reasonable to expect that the final calculation error will depend only on nuclear data errors. The relative error of nuclide concentration calculations in the CEFA Code does not exceed 10^{-6} and has practically no influence on the calculation results. Therefore we consider the burnup calculations by CEFA code as precision numerical tests for the problem of fuel burnup.

The CEFA Code involves actinides ranging from actinium to fermium for the problem of fuel burnup. The list of fission products (81 nuclides) covers all fission products whose concentrations are calculated by the WIMS-D4 Code: Kr^{83} , Mo^{95} , Tc^{99} , Ru^{101} , Ru^{103} , Rh^{103} , Rh^{105} , Pd^{105} , Pd^{108} , Ag^{109} , Cd^{113} , In^{115} , I^{127} , Xe^{131} , Xe^{135} , Cs^{133} , Cs^{134} , Cs^{135} , Nd^{143} , Nd^{145} , Pm^{147} , Pm^{148} , Pm^{148m} , Sm^{147} , Sm^{149} , Sm^{150} , Sm^{151} , Sm^{152} , Eu^{153} , Eu^{154} , Eu^{155} , Gd^{157} , with their associated nuclides. Besides, a procedure has been developed to make allowance for all other fission products in the MCNP calculations. With regard to fuel burnup in the fast reactor spectrum, another procedure has been drawn up which treats fission products as combined fragments. Isotope transition chains have been generated based on the preliminary analysis. The CEFA matrix of nuclide transmutations takes into account the reactions of fission and radiative capture, threshold reactions (n,p), (n,2n), (n,3n), etc., and all kinds of nuclear disintegration. In regard to fission products, it also incorporates their output in fission of the actinides under consideration.

The CEFA Code includes a module to perform computations on the conjugated burnup problem and to calculate coefficients of nuclide concentration sensitivity to nuclear data uncertainties. The sensitivity coefficients make possible comparative analysis of various nuclide formation pathways and – given covariance matrices – allow numerically assessing the effect of accuracy in the knowledge of cross-sections of some nuclides on the calculated accumulation of others.

Besides, it is possible to specify the boron absorber burnup in the CEFA Code. In calculating the neutron flux density in a cell, allowance is also made for the energy given off by photons arising from fission and capture of neutrons in structural materials. The delayed fission gamma-quanta are also properly accounted for.

Modular arrangement of the computation technique – MCNP Code, nuclear data library ML45, CEFA Code – allows using it for any fuel burnup problems. The number of zones where fuel or boron absorber burnup is calculated and the number of nuclides involved are limited only by the MCNP and computer capabilities, by the nuclear data library content, and by the computation time. At the same time, the computation technique combines all the best features of the MCNP Code.

The developed technique was used to perform burnup calculations on the mixed fuel containing plutonium of complex composition [4,5]. Besides Pu, the fuel contained also a small amount of Am. The geometrical characteristics of the fuel rod cell and polycell are close to standard parameters of PWR. The

calculations were run assuming that the fuel heat rate remains constant over the whole fuel life. The results of the calculations are presented in tabulated sets for each time step, including concentrations of all nuclides considered in the calculations, neutron flux density spectrum, variations in K_{∞} , fission energy, flux density, photon component of the fission energy (prompt fission photons and capture gamma-quanta, fission and actinide capture rate during the fuel life, and integral characteristics of a cell. The resultant data can be used to verify engineering techniques of burnup calculations. The findings of verification of TRIFON Code computations, are given by way of an example. In view of the restricted publication size, only input data are given in full and the calculation results are presented only as figures. Additional information will be provided in a panel presentation. Reference 5 contains detailed description of input data and numerical results.

Figures 1 and 2 and Tabs. 1 and 2 present the input data for calculation of the MOX fuel burnup in models of a fuel cell and a polycell.

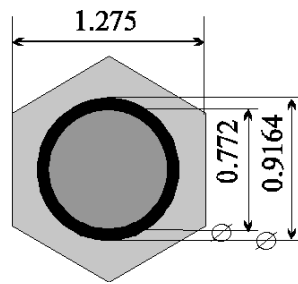


Fig. 1. Calculated model of the fuel rod

Table 1. Atom Densities and Temperatures

	Atom Densities, atoms/cm ³	Temp. K
1-Fuel	Pu ²³⁹ : 1.16e21 Pu ²⁴⁰ : 4.9e20 Pu ²⁴¹ : 1.9e20 Pu ²⁴² : 1.05e20 Pu ²³⁸ : 3.0e19 Am ²⁴¹ : 2.5e19 U ²³⁵ : 5.0e19 U ²³⁸ : 2.21e22 O: 4.63e22	1027
2-Cladding (w/ air gap)	Zr: 4.23e22	579
3 Water	H: 4.783e22 O: 2.391e22 B ¹⁰ : 4.7344e18 B ¹¹ : 1.9177e19	579

Table 2. Atom Densities and Temperatures

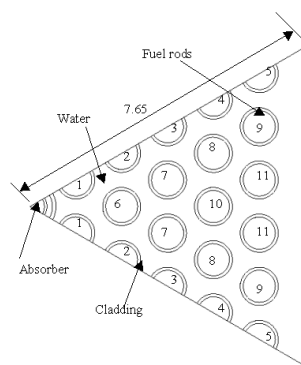


Fig. 2. Calculated model of the polycell

	Atom Densities $\times 10^{24}$ atoms/cm ³	Temp. K
1. Boron absorber	B ¹⁰ 0.01557 B ¹¹ 0.06306 C 0.01966	579
2. Cladding (with air gap)	Zr: 0.0423	579
3. Water	H 0.04783 O ¹⁶ 0.02391 B ¹⁰ : 4.7344×10^{-6} B ¹¹ : 1.9177×10^{-5}	579
4. Fuel	U ²³⁵ 3.8393×10^{-5} U ²³⁸ 1.8917×10^{-2} Pu ²³⁹ 6.5875×10^{-4} Pu ²⁴⁰ 4.2323×10^{-5} Pu ²⁴¹ 7.0246×10^{-6} O 4.1707×10^{-2}	1027

The main results are presented below as figures: Figs. 3, 4 showing variation of k_{∞} as a function of irradiation time for one fuel rod and polycell modeled; Figs. 5–8 showing variations in nuclear concentrations of the main isotopes of plutonium, americium, uranium and some fission products as a function of irradiation time for one fuel rod modeled.

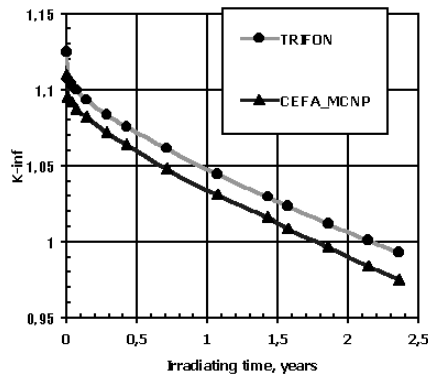


Fig. 3. The changing of K_{inf} during irradiating for fuel cell

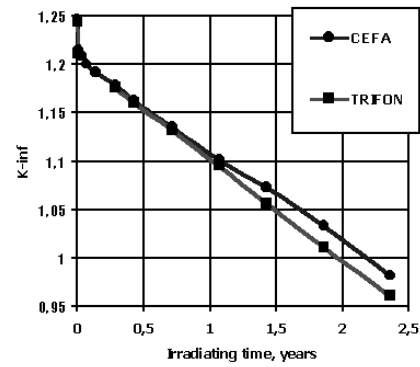


Fig. 4. The changing of K_{inf} during irradiating for polycell.

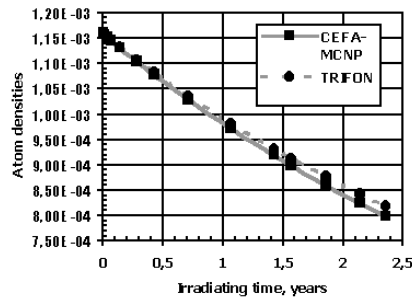


Fig. 5. The changing of K_{inf} during irradiating for fuel cell.

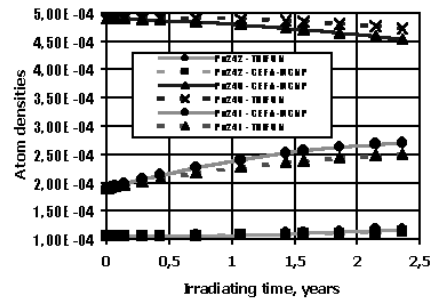


Fig. 6. The changing of K_{inf} during irradiating for polycell.

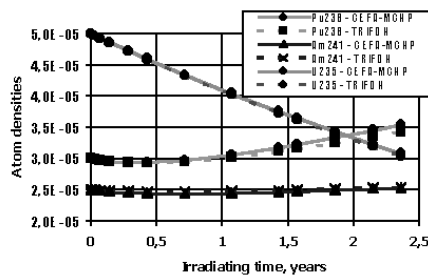


Fig. 7. The changing atom density Pu^{239} during irradiating

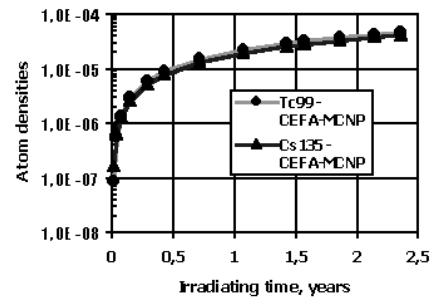


Fig. 8. The changing atom densities Pu^{240} , Pu^{241} , Pu^{242} during irradiating

Figures 9–12 showing the distribution of nuclear concentrations of the main isotopes of plutonium, americium, uranium and some fission products in the polycell fuel rods at the end of irradiation. The figures provide comparison of results against the data of the TRIFON Code involving micro-cross-sections, which was verified in the tests discussed.

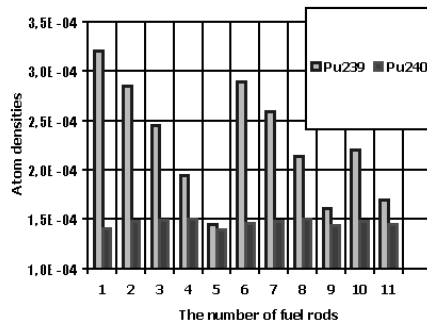


Fig. 9. Allocation atom densities Pu^{239} and Pu^{240} on fuel rods for the end of irradiating.

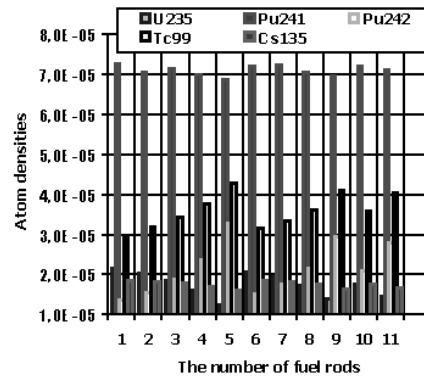


Fig. 10. Allocation atom densities U^{235} , Pu^{241} , Pu^{242} , Tc^{99} , Cs^{135} on fuel rods for the end of irradiating.

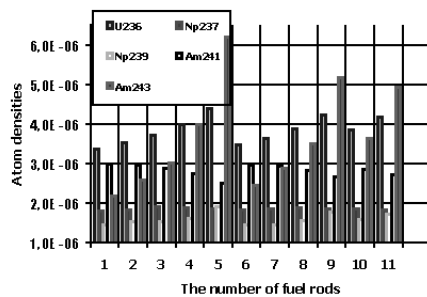


Fig. 11. Allocation atom densities U^{236} , Np^{237} , Np^{239} , Am^{241} , Am^{243} on fuel rods for the end of irradiating

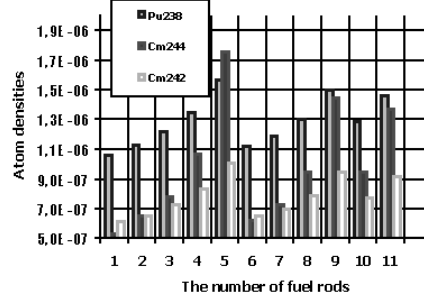


Fig. 12. Allocation atom densities Pu^{238} , Cm^{242} , Cm^{244} on fuel rods for the end of irradiating

Conclusions

1. A technique for numerical analysis of fuel burnup has been prepared. The technique includes the MCNP Code (with an added module for calculating the transfer of delayed fission neutrons), CEFA Code (integration of forward and conjugate fuel burnup equations and calculation of coefficients of sensitivity of estimated nuclide concentrations to nuclear data uncertainties), and the nuclear data library. The serviceability of the library was proved by calculations made for experimental critical assemblies. Modular arrangement allows expanding, within reasonable time, the capabilities of the technique

both in terms of complexity of the fuel system geometry described and in the number of nuclides covered in the fuel burnup calculations.

2. Considering that MCNP provides the most adequate description of the geometrical model of the fuel rod, fuel assembly, fuel channel, etc., that no group cross-sections are involved in neutron transport calculations, and that there are no intermediate steps to prepare one-group cross-sections for nuclide kinetics calculations, it would be reasonable to expect that the final calculation error will depend only on nuclear data errors. This constitutes the principal advantage over the engineering codes containing a fuel burnup calculation module. As regards disadvantages, the only real shortcoming is the computation time which, however, is easily offset by rapid development of the computation technology.
3. The technique has been employed to calculate fuel burnup in one fuel rod cell and in a modeled PWR polycell. The fuel examined is MOX containing small quantities of americium. References [4,5] provide detailed description of the input data and numerical results. The results are presented in tabulated form for each time step, including concentrations of all nuclides considered, the neutron flux density spectrum, the rates of actinide fission and capture, and integral characteristics of the cell. The data produced may be used for verifying the engineering fuel burnup calculation techniques.
4. The developed technique has been also employed to calculate the burnup in fuel assemblies of the RBMK reactor and pulse reactor IBR-2.
5. The software package will be further developed to cover delayed fission gamma-quanta and photonuclear reactions in the MCNP Code and to allow for use of various burnable absorbers in the CEFA Code.
6. By and large, it may be suggested that the computation technique elaborated has the lowest possible degree of procedural errors (at the current development level of codes and nuclear data libraries) and is acceptable for use in studies on nuclear safety of reactors. At the current stage, the technique has been used for preparing numerical tests of fuel burnup, which may find application in verification of engineering techniques, as it was done, for example, with the TRIFON software package.

References

1. J.F. Briesmeister (ed.): *MCNP-4B Manual*, LA-12625M, 1997
2. A.V. Lopatkin, V.G. Muratov, I.V. Zayko: *ML45 ver. 2: Neutron cross-section and photon interaction cross section library for the MCNP*. RDIPE Report. Ref. 450-413-5507, (2000) (in Russian)
3. A.V. Lopatkin, V.G. Muratov: *CEFA Code for burnup calculations and error analysis*. RDIPE Report. Ref. 050-085-5070 (1997) (in Russian)
4. A.V. Lopatkin, V.G. Muratov: *Burnup of mixed uranium-plutonium fuel containing Pu of complex composition using one fuel rod cell as an example*. RDIPE Report (1999) (in Russian)
5. A.V. Lopatkin, V.G. Muratov: *Burnup of mixed uranium-plutonium fuel containing Pu of complex composition using polycell as an example*. RDIPE Report (2000) (in Russian)

The HERMES Monte Carlo Program System: a Versatile Tool for Spallation Physics and Detector Applications

D. Filges, R.-D. Neef, H. Schaal, and G. Sterzenbach

Institut für Kernphysik, Forschungszentrum Jülich, Germany

Abstract. The code system HERMES [1] (High Energy Radiation Monte Carlo Elaboration System), which we use for the assessment of high intensity spallation neutron sources and detector simulations, is a collection of Monte Carlo codes and auxiliary programs to simulate the different physics of radiation transport and interaction with matter. Latest developments of the code based on recent validation experiments will be presented: Two additional collision kernels have been implemented, parts of existing models have been revised, the databases and codes for radioactivity estimates have been updated. Furthermore important sample applications like particle multiplicity distributions in comparison with experiments, predictions of materials- damage and high energy source shielding will be shown.

1 Introduction

Spallation sources and high energy detectors which are subject to high or medium energetic radiation experience a large variety of physical processes. In order to cover these requirements HERMES consists of a set of independent Monte Carlo Programs for the simulation of hadronic and electro-magnetic showers at different energies and auxiliary programs used to compute physical and technical quantities derived from the observed particle cascades. The development of HERMES was started in 1987 for design studies for the ZEUS [2] detector system at DESY. For ZEUS event-wise correlated results from the different parts of particle showers were needed. Therefore we designed a communication structure between the MC programs providing common geometry description, comprehensive analysis, and controlling the particle flow between the different main modules. The MC modules themselves were kept separate in order to keep the statistical behaviour, and systematic errors accessible for each module. The STATIST module is used to gather the results of different parts of HERMES from submission files.

Throughout the history of the program system the fields of applications and requirements have changed. We designed detector systems for few particle reactions. In these applications we focused on the acceptance and resolution of the detector system. This effort resulted in the new Monte Carlo program MC4 [3]. MC4 provides a wide interface for user programming. It was intended to work as a test bed for reconstruction programs working on experimental data. Therefore beside the other needs of any particle transport code it needed features to encode the output of technical equipment responding to physical processes. It was also helpful to run the code with different levels of physics simulation. Therefore we

designed it in a modular way where physical models can be easily implemented and turned on or off. This makes MC4 a appropriate tool to test MC model features and finally a candidate inheritor of HETC.

2 Features of the HERMES System

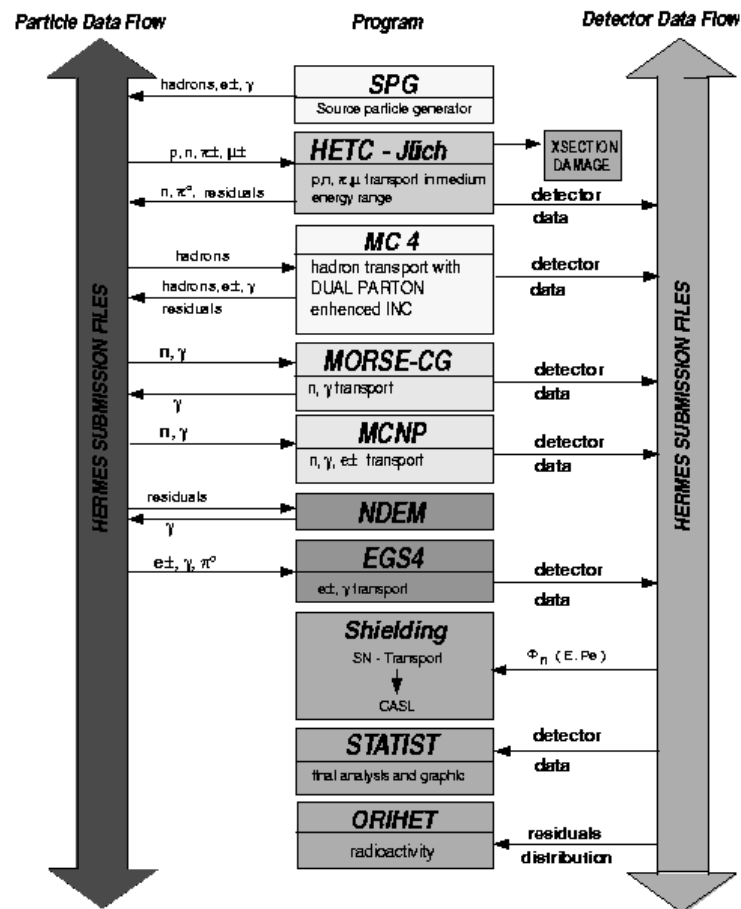


Fig. 1. Schematic view of the modular structure of HERMES

The most important physical models in HERMES simulate in-elastic collisions. In the following the implemented models and some subsequent packages are summarized. For detailed information refer to the HERMES web-page: <http://ikp332.ikp.kfa-juelich.de/hermes>

High Energy: In MC4, we implemented a dual parton dual chain decay model to provide a description of high energetic hadronic collisions. The implementation was done within a revised version of the Bertini model [3,4]. This kind of implementation allows feedback of final state particles into INC within the nucleus.

Medium Energy: The medium energy region is of special interest for spallation physics. In addition to the standard HETC collision kernel which includes the Bertini-INC model [4], the Lindenbaum-Sternheimer-model [5] for pion production, and a scaling model [6] for high energy reactions), we have implemented three models into MC4: a revised HETC model [3], the ISABEL [7,8] model and the INCL Model [9] INC and INCL both handle the nucleon-nucleus collision, but the model assumptions differ in some principal points:

INC uses the Hofstaedter distribution for the nucleon density in the nucleus.

$$\rho(r) = \rho_0 / (1 + e^{(r-c)/\alpha})$$

with $c = 1.07 fm A^{1/3}$, and $\alpha = 0.545 fm$ The nucleus is then divided into 3 spherical shells where $\rho(r_1) = 0.9\rho(0)$, $\rho(r_2) = 0.2\rho(0)$, and $\rho(r_3) = 0.01\rho(0)$ whereas INCL uses constant nucleon density in the whole nucleus. This implies differences in the description of the collisions with large impact parameter, where the INC model predicts a much less dense nucleus, where one can see the quasi-elastic and quasi-inelastic scattering (cascades, with only 1 intra nuclear collisions).

INCL uses newer compilations of intra nuclear cross-sections for $N - N$, $\pi - N$, and (in contrast to INC) also $\Delta - N$, and $\Delta - \Delta$ reaction. Also the angular distributions are parameterized in a new way.

In INCL the cascade evolves in a time dependent scheme and terminates the cascade when distribution of intra nuclear momenta becomes isotropic. INC assumes that there is no change in the nucleus structure (nucleon density, potential, Pauli blocking) during the INC stage of the collision and therefore neglects the time structure of the collision.

Any of these models leave an excited nucleus which then emits particles in the evaporation process and finally gamma rays to return to ground state. In HET, we have the EVAP-model [10] (Dressner et. al.), and the RAL Fission model [11]. In MC4 we included a combined and revised version of both.

Low Energy: The low energy part is the domain of MC-Programs running under the control of X-section datasets rather than analog MC models.

In HERMES the MORSE-CG code is fully implemented. It uses grouped X-sections like MATXS11, which are generally based on ENDFB files for neutron and gamma transport. Because of the limited resolution of a given group structure and because of the generalized handling of different reaction channels MORSE needs rather sophisticated cross-section files.

Beside MORSE-CG we also use MCNP [12]. MCNP uses point X-sections which are compiled with NJOY or similar programs from ENDF, ENDL and

other sources. They are tabulated on energy grids fine enough to use linear interpolation schemes. Different reaction types described on ENDF etc. are kept separate. So different inelastic collision channels can be used with different secondary particle angular distributions. In MCNP thermal and even subthermal scattering can be treated by means of special scattering datasets. MCNP contains photon and electron transport. Biasing features in MCNP are even more elaborate than in MORSE.

Electro-magnetic Cascades: We implemented EGS4 which provides a widely used standard for the simulation of electro-magnetic showers. The EGS4 “user code” used in HERMES connects the EGS4 to the HERMES geometry packages and the SIM analysis package.

SID: The code for spallation induced damage is a special analysis feature of HETC. Materials damage is due essentially to two phenomena: the implementation of hydrogen and helium isotopes inside a material as the outcome of evaporation, and displacements of atoms in the materials lattice. SID produces cross-sections for the damage energy and displacements based on the theory of Lindhard et. al. The Lindhard theory defines a fraction of kinetic charged particle energy going into the creation of PKA (primary knock-on atoms) during slow down. Is this energy \hat{T} greater than a displacement threshold E_d which is material dependent the number of displacements per PKA may be estimated as $\nu_d \sim \hat{T}/2E_d$.

NDEM: NDEM computes the gamma emission from excited residual nuclei when the evaporation of particles is no longer possible. NDEM uses a gamma library containing over 50000 nuclear excitation levels together with a set of models describing the transition probabilities in the continuum and from continuum to discrete levels.

Shielding: [13] Three methods are available for shielding design. The straight forward method is using HERMES. There are some biasing techniques implemented into HETC (but not available through standard input methods) and of course in MORSE and MCNP. These methods extend the deep penetration capabilities of the MC method.

A better approach for bulk shields is the coupling of MC methods used in the inner inhomogeneous part of the assembly with deterministic methods like the ANSIN code for the essentially one dimensional outer part of a shield.

The third method treats geometry exactly, the source term for penetrating high energy neutron flux is taken from a database computed with HETC and the attenuation parameter from a database computed with ANISN. The fast neutron flux and the resulting dose is then computed along rays from the source to points on the shield surface by the semi-empirical formula:

$$D = k(r) * S * B(r)e^{-r/\lambda(r)}/r_2$$

where k, S, B, r are the flux to dose conversion factor, the angular dependent source strength, the buildup factor, and the distance from the source respectively.

OriHet3: [14] ORIHET has been added to the HERMES suite as an auxiliary program to study the build-up and decay of activity after the primary cascades. It is derived from ORIGEN and essentially solves the Bateman Equation:

$$dN_i/dt = -\tau_i N_i + \sum_k f_{ik} \tau_k N_k + B_i$$

where B_i, N_i, τ_i are the production rate, the concentration and the mean life time of nuclide i , N_k, τ_k the concentration and mean life time for nuclide k and f_{ik} the branching ratio of nuclide k decaying into nuclide i .

The initial concentrations N and / or the production rates B may be input from HET or MC4 results. Version OriHet3 (released in 2000 by F. Atchinson and H. Schaal) has an improved database and new treatment of spontaneous fission. The database consists of the old ORIHET decay library (used in ASCII format) which is a compilation of the data of Lederer et. al. [15] with many updates from different sources, and the NUBASEX database by Audi et. al. completed by O. Bersillon [16]. The ORIHET file has data for 2456 nuclides and recognizes 7 decay modes, the NUBASEX include 3738 nuclides with more than 40 decay modes.

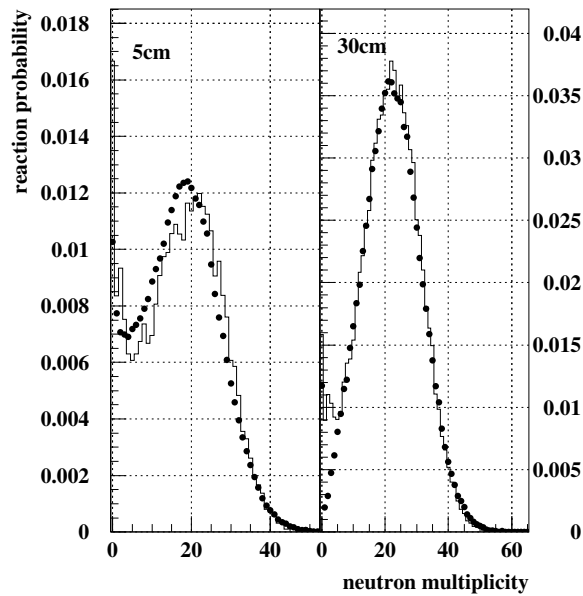


Fig. 2. 1.2 GeV p on Hg-target of 15cm diameter

3 Sample Applications and Outlook

Besides detector simulation an important field of application for HERMES is the nuclear assessment of the high intensity pulsed European Spallation Neutron Source (ESS) [17]. Here the central optimization goal is to get the maximum neutron flux for the utilization of neutron scattering. Validation experiments recently carried out by the NESSI collaboration at COSY Juelich over a broad range of incident proton energies, targets and geometries demonstrate the capability to predict the correct neutron leakage distributions thick targets as shown in Fig. 2.

Also detector simulations and reconstruction by event-wise correlations cover the field of the HERMES system. The prediction of cross-sections implies closer view into the physics of the models. The production of charged particles in contrast to neutron production differs significantly [18] comparing the different INC-Models used HERMES. Here further development is needed.

References

1. P. Cloth et. al: *HERMES, A Monte Carlo System for Beam Materials Interaction Studies*, KFA-Report Jül-2203(1988)
2. B. Anders et. al: Nucl. Instr. Meth. A **277**, 56 (1989)
3. G. Sterzenbach et. al: 'MC4 A New Hadronic Monte Carlo Code for High to Medium Energies'. In: *Proc. of SARE4, Sept.1998, Knoxville, TN, USA*
4. H.W. Bertini: Phys. Rev. C **188**, 1711 (1969)
5. R. Sternheimer, S. Lindenbaum: Phys. Rev. C **123**, 333 (1961)
6. T. Gabriel et al.: *An Extrapolation Method for Predicting Nucleon and Pion Differential Production Cross Sections from High-Energy Nucleon-Nucleus Collisions*, ORNL-4542 (1970)
7. Y. Yariv, Z.Fraenkel: Phys. Rev. C **20**, 2227 (1997)
8. Y. Yariv, Z. Fraenkel: Phys. Rev. C **24**, 448 (1981)
9. J. Cugnon et al.: Nucl. Phys. A **620**, 475 (1997)
10. L. Dresner: *EVAP A Fortran Program for Calculating the Evaporation of Various Particles from Excited Compound Nuclei* ORNL-TM-196, (1961)
11. F. Atchinson: In: *Proc. of Specialists' Meeting on Intermediate Energy Nuclear Data, May 1994, Issy-les-Moulineaux (France)*
12. Group x-6,LANL: *MCNP* Report LA-7396M (1981)
13. D. Filges et al.: 'Radiation Shielding and Protection of the European Spallation Neutron Source'. 9th Int. Conf. on radiation shielding Oct 17-22nd 2000, Tsukuba, Japan
14. F. Atchinson, H. Schaal: *OriHet3 Users Guide*, to be published
15. C.M. Lederer et al.: *Table of Isotopes*, 6th ed. (Wiley, New York 1967)
16. G. Audi et al.: Nucl. Phys. A **624**, 1 (1997)
17. G. Bauer et al. (eds.): *The European Spallation Source Study ESS, Vol III, The ESS Technical Study*, Report ESS-96-53-M, ISBN 0902376659 (1996)
18. M. Enke et al.: Nucl. Phys. A **657**, 317 (1999)

MARS Code Status

N.V. Mokhov and O.E. Krivosheev

Fermilab, P.O. Box 500, Batavia, IL 60510, USA

Abstract. Recent developments of the MARS Monte Carlo code system for simulation of hadronic and electromagnetic cascades in shielding, accelerator and detector components in the energy range from a fraction of an electronvolt up to 100 TeV are described. These include hadron production model, unified treatment of heavy particle electromagnetic interactions and absorption, interface to MCNP for low-energy neutrons, and newly created electromagnetic shower module (down to 1 keV), *MAD-MARS Beam Line Builder* and Graphical-User Interface.

1 Introduction

The MARS Monte Carlo code system [1], which has been developed over 26 years, allows fast and reliable inclusive and exclusive simulation of 3-D hadronic and electromagnetic cascades, and the transport of muon, neutrino and low-energy neutron/photon particles, through shielding, accelerator and detector components, with energies ranging from a fraction of an electron-volt up to about 100 TeV. The performance of the previous version of the code, MARS13 [2,3], has been demonstrated in numerous applications at Fermilab, CERN, KEK and other centers as well as in special benchmarking studies. The most recent developments to the current version MARS14 [4] further increase the code reliability, applicability and user friendliness, and are briefly described here.

2 Physics Model

Hadron Production. New compilations, parameterizations and integration algorithms for total and partial cross sections σ_{hN} , σ_{hA} and $\sigma_{\gamma A}$ are implemented covering a hadron kinetic energy range $1 \text{ MeV} < E < 100 \text{ TeV}$ [3]. Hadron-nucleus elastic scattering at $10 \text{ MeV} < E < 5 \text{ GeV}$ is improved and further work is underway. The hadron production model is improved, especially for pions and kaons in the 2 to 50 GeV energy region, and also for photonuclear interactions. The full exclusive production simulation at 1 MeV–5 GeV is now the default, using the latest cascade-exciton model CEM97 [5]. At higher energies, an inclusive approach is a default, with an optional use of the (time-consuming) DPMJET [6] exclusive event-generator, although currently only for the very first nuclear collision in the cascade. By default, deuteron-nucleus interactions are described within a model developed in [3]. In the exclusive mode, information on the nuclides generated

in nuclear collisions is now scored, or tallied and reported in the results of the simulation.

Neutrino Interactions. A special weighted neutrino interaction generator has been developed [3,7] and incorporated into MARS. This model permits the selection of the energy and angle of each particle (ν, e, μ and hadrons) emanating from a simulated interaction. These particles, and the showers initiated by them, are then further processed in the code in the usual way. Four types of neutrinos are distinguished throughout ($\nu_\mu, \bar{\nu}_\mu, \nu_e, \bar{\nu}_e$) and the model identifies all possible types of neutrino interactions with nuclei. The corresponding formulas for these processes as well as results of Monte Carlo simulations for muon colliders and storage rings are described in [7].

Interface to MCNP. Once the energy of neutrons falls below 14 MeV, all subsequent neutron interactions are described using the appropriate MCNP4 [8] subroutine modules. Recent implementation in MARS of the accurate treatment of MCNP4 generated recoil protons, as well as heavier recoils and photons from the thermal neutron capture on ${}^6\text{Li}$ and ${}^{10}\text{B}$, allows the detailed description of corresponding effects in hydrogenous, borated and lithium-loaded materials [9].

Electromagnetic Interactions of Heavy Particles. Electromagnetic interactions of muons and charged hadrons in arbitrary composite materials are simulated down to several tens of keV. Radiative processes and atomic excitation and ionization with energy transfer ϵ greater than a cutoff ϵ_c are considered as discrete events involving production of δ -electrons, e^+e^- -pairs, and bremsstrahlung photons which are followed explicitly [10]. Energy losses with $\epsilon < \epsilon_c$ (so-called restricted losses) are considered as continuous. Their distribution is described by Vavilov function—with redefined parameters—which approaches a Gaussian with decreasing ϵ_c . Independent of energy, material or thickness traversed, the quality of the Gaussian approximation is governed by the average number of events (κ_n) one chooses to evaluate individually and becomes acceptable for most purposes when $\kappa_n > 10$. Bremsstrahlung and direct e^+e^- production differential cross-sections used in the code are as given in [11]. Multiple Coulomb scattering is modeled from the Moliere distribution with nuclear form-factors included [12]. A very careful treatment is done in MARS of processes near and below the Coulomb barrier in hadron and muon transport (ionization absorption *vs* nuclear interaction *vs* decay) as is further described in [3].

Electromagnetic Showers. New modules for simulating electromagnetic showers based on current knowledge of physics of electromagnetic interactions were recently developed and have been implemented into the code [13]. The main focus is given to electron and photon interactions in arbitrary composite solid, liquid and gaseous materials at low energies (1 keV to a few MeV). The entire shower, and such processes as emission of synchrotron photons, photohadron production, $\gamma Z \rightarrow \mu^+\mu^-$ and $e^+e^- \rightarrow \mu^+\mu^-$, can be treated – in the spirit of the MARS framework – either analogously or inclusively with corresponding statistical weights. The choice of method is left for the user to decide, via the input settings.

3 Materials, Tracking and Histograming

The precise treatment of individual elements in mixtures and compounds defined through the weight or atomic fractions, is done for all the electromagnetic and nuclear elastic and inelastic processes. Homogenization (averaging) of materials thus becomes obsolete and is strongly discouraged. Up to 50 composite materials may be present in a run. Material-dependent energy cutoffs, boundary localization precision and pilot steps can now be defined by the user region by region or material by material; this feature allows noticeable improvement of both a CPU performance and physics description accuracy in the regions of interest. The appropriate parameters for particle transport in arbitrary magnetic fields are chosen automatically, providing extremely high accuracy of tracking. The user can now choose between sampling and forcing π -, K - and μ -decays. Algorithms for splitting and Russian roulette at hA vertices and in particle transport are also further improved. For ‘deep penetration’ problems in complex highly non-uniform geometries, algorithms for scoring probabilities, rather than real particle crossings or interactions, take into account all possible processes for both stable and unstable particles and charged as well as neutral hadrons. Use of accelerating field (RF-cavities) is now optional in the code. The I/O sequence as well as the histograming for surface and volume detectors is substantially improved and extended. Interfaces to the ANSYS code for thermal and stress analyses and to the STRUCT code for multi-turn particle tracking in accelerators have also been improved.

4 MAD-MARS Beam Line Builder

The MAD [14] lattice description language has become the *lingua franca* of computational accelerator physics. Any new developments in accelerator physics computational codes and libraries should have the requirements to read and understand lattice descriptions written in MAD. The ideas and modules of [15] are used in a new interface, which is able to read, parse, and store in memory MAD lattice descriptions, with the ability to generate an output file which translates those descriptions for input to MARS, and can also be used as input to other tracking and CAD applications.

The created interface system—*MAD-MARS Beam Line Builder* (MMBLB)—reads a MAD lattice file and puts the elements in the same order into MARS geometry. Each element is assigned six functions which provide information about the element type/name, geometry, materials, field, volume and initialization. The user specifies the element type and an optional element name. If no name is specified, the element is considered to be a generic one. A building algorithm first tries to match the type/name pair and then substitute a generic element if needed. Once an element is described, it is registered with the system and its name is binded with the respective geometry, materials, volume and field descriptions. For each region search during tracking, MMBLB finds the corresponding type/name pair and calls its appropriate functions. MMBLB calculates

a local rotation matrix \mathcal{R}_i and a local translation vector \mathcal{L}_i . Then a global rotation matrix \mathcal{M}_i and a position \mathcal{P}_i are calculated and stored for each element

$$\begin{aligned}\mathcal{M}_i &= \mathcal{M}_{i-1} \times \mathcal{R}_i, & \mathcal{M}_0 &= \mathcal{U} \\ \mathcal{P}_i &= \mathcal{M}_{i-1} \times \mathcal{L}_i + \mathcal{P}_{i-1}\end{aligned}$$

where \mathcal{U} is the unit matrix. $\mathcal{R}_i = \mathcal{U}$ for all elements, except RBEND and SBEND.

5 Graphical-User Interface

A Graphical-User Interface, MARS-GUI-SLICE, has been developed. It is based on *Tcl/Tk* and is linked in to the user's executable, however it is active only when specific flags are set in the input file. When the interface is active, no events are generated, but the user's encoded geometry is probed and visually displayed. The interface displays all the details of the encoded geometry, showing the encoded zone numbers, materials and magnetic fields; it is a valuable tool for checking complex geometries before executing event generation. During event generation runs, the user can specify output files holding histograms and particle tracks; these output files can be opened by the *GUI* interface, post-run, and projected onto the visual display of the geometry. The main MARS-GUI-SLICE features are:

- Two-dimensional geometry slice and magnetic field view on a graphical display panel (GDP). Maximum and minimum coordinates along each axis and maximum field components are provided for the given view in corresponding entry fields (EF). They are changed automatically by grabbing a desirable view box on the GDP holding a *CTRL* key and clicking with the mouse left button at the two diagonal box corners. Alternatively, the lower and upper view boundaries can be typed in the EF along with a binning of the magnetic field grid seen on the GDP. There is a *1:1 scale* check field (CF) to return to a *natural* scale.
- A slice plane is chosen by a corresponding radio-button. A magnetic field view can be interactively turned ON and OFF in a corresponding CF.
- Materials distribution in a given view is represented in a color or black and white *wire-frame (contour) mode* or in a *color region-filled mode*, with the mode chosen by a corresponding radio-button. By clicking a corresponding button, a *Materials* window is created, with the CF displaying material index and name and select boxes (SB) showing color of each material in the given view on the GDP. The pre-set materials colors can arbitrary be modified in the corresponding SB individually for each material. The colors can be reset individually or globally. Changing the view automatically adjusts the material info in this window.
- By clicking a left mouse button at any point of the GDP, a *Point Info* window is created with information display fields (IDF) containing coordinates, region number, material name and index, magnetic field module and a value of histogram (see below) for this point. This window keeps the position intact.

- Particle tracks in the given view can be displayed on the GDP by loading a *.PLOT file generated by MARS. Similar to materials, by clicking a corresponding button, a *Particles* window is created, with information similar to the *Materials* window: particle ID, name, color and SB displaying color of each particle and allowing color modification. A corresponding CFs allow turning ON and OFF any ID and global track visibility. One can examine tracks by clicking a middle mouse button at any track point on the GDP. A *Track Info* window is created with IDF containing the particle ID, name, as well as the current energy, statistical weight and coordinates at the point.
- After the run, a variety of calculated 2-D histograms can be loaded and overlapped with the geometry view on the GDP. A *.HBOOK file is loaded in the *Load Hist* window and a desirable histogram is selected there from the IDF list by its ID or name. The geometry/histogram view is now handled as a whole. The *Point Info* window allows now for a detailed examination of the histogram values even within the same decade (color).
- The view can be inverted both vertically and horizontally.
- One can add arbitrary texts all over the GDP with a *Text* window activated by the mouse right button. Variety of fonts can be chosen there. Fonts, subscripts and superscripts are handled as in the XMGR plotting tool. Text can be modified, moved around the GDP or deleted.
- Up to 20 of the GDP views can be stored and restored back and then viewed by clicking << or >> buttons.
- The GDP can be saved as an Encapsulated Postscript file by clicking the *Print* button. The entire window or its arbitrary fraction can be xv-grabbed by clicking the *Grab* button.
- A version exists for a 3-D solid body representation [16].

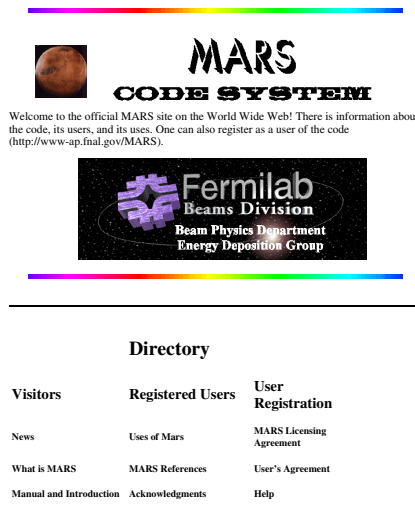


Fig. 1. MARS web page

6 Benchmarking and Worldwide Support

The code's reliability is confirmed by numerous benchmarkings shown at several SATIF/SARE meetings and demonstrated in many applications at Fermilab and other centers (see, e. g., recent [3,4,9,13]). The code is distributed and supported worldwide for the Unix and Linux operating systems. The official MARS Web site is <http://www-ap.fnal.gov/MARS/> which contains information about the code, its users, and its uses (see Fig. 1).

This work was supported by the U.S. Department of Energy. We thank C.C. James for useful comments.

References

1. <http://www-ap.fnal.gov/MARS/>
2. N.V. Mokhov: 'The MARS Code System User's Guide', Fermilab-FN-628 (1995); O.E. Krivosheev, N.V. Mokhov: 'New MARS and its Applications'. In: *Proc. of the Third Workshop on Simulating Accelerator Radiation Environments (SARE3)*, Tsukuba, Japan, May 7-9, 1997, KEK Proceedings 97-5, pp. 12-20 (1997), Fermilab-Conf-98/043 (1998)
3. N.V. Mokhov, S.I. Striganov, A. Van Ginneken, S.G. Mashnik, A.J. Sierk, J. Ranft: In: *Proc. of the Fourth Workshop on Simulating Accelerator Radiation Environments (SARE-4)*, Knoxville, TN, September 14-16, 1998, pp. 87-99, Fermilab-Conf-98/379 (1998), nucl-th/9812038-v2-16-Dec-1998
4. N.V. Mokhov: In *Proc. of ICRS-9 International Conference on Radiation Shielding*, Tsukuba, Ibaraki, Japan, October 17-22, 1999, J. Nucl. Sci. Tech. **1**, 167 (2000); Fermilab-Conf-00/066 (2000)
5. S.G. Mashnik, A.J. Sierk: In *Proc. of the Fourth Workshop on Simulating Accelerator Radiation Environments*, Knoxville, TN, Sept. 14-16, 1998, pp. 29-51
6. J. Ranft: Phys. Rev. D **51**, 64 (1995); Gran Sasso Report INFN/AE-97/45 (1997)
7. N.V. Mokhov, A. Van Ginneken: In *Proc. of ICRS-9 International Conference on Radiation Shielding*, Tsukuba, Ibaraki, Japan, October 17-22, 1999, J. Nucl. Sci. Tech. **1**, 172 (2000); Fermilab-Conf-00/065 (2000)
8. J.F. Briesmeister, editor: *MCNP - A General Monte Carlo N-Particle Transport Code, Version 4A*. Pub. LA-12625-M, LANL (1993)
9. M. Huhtinen, N.V. Mokhov: *A Cross-comparison of MARS and FLUKA Simulation Codes*, Fermilab-FN-697 (2000)
10. N.V. Mokhov, S.I. Striganov: in *Handbook of Accelerator Physics and Engineering*. Ed. by A.W. Chao, M. Tigner (World Scientific, Singapore 1999) pp. 234-240
11. D.E. Groom, N.V. Mokhov, S.I. Striganov: Atomic Data and Nuclear Data Tables (2000), LBNL-44742 (2000)
12. I.S. Baishev, N.V. Mokhov, S.I. Striganov: Sov. J. Nucl. Phys. **42**, 745 (1985)
13. O.E. Krivosheev, N.V. Mokhov: 'Status of MARS Electromagnetic Physics'. These Proceedings p. 141
14. F.C. Iselin: *The MAD Program (Methodical Accelerator Design)*, Version 8/13/8, CERN/SL/92 (1992)
15. D.N. Mokhov et al.: *MAD Parsing and Conversion Code*, Fermilab-TM-2115 (2000)
16. O.E. Krivosheev, N.V. Mokhov: *OO Geometry Engine for Monte-Carlo Simulation*, Fermilab-Conf-96/077 (1996)

Present Status of Nucleon–Meson Transport Code NMTC/JAERI

H. Takada¹, S. Meigo¹, and K. Niita²

¹ Center for Neutron Science, Japan Atomic Energy Research Institute, Japan,

² Research Organization for Information Science & Technology, Japan

Abstract. The nucleon-meson transport code NMTC/JAM has been developed for the neutronics design study of the joint project for high-intensity proton accelerators with a power of mega-watts. The applicable energy range is extended by the inclusion of the Jet AA Microscopic transport model (JAM). The nucleon-nucleus cross sections are also updated for accurate transport calculation. The applicability of NMTC/JAM is studied through the analyses of thick target experiments such as neutron transmission through shield and activation reaction rate measurements.

1 Introduction

Recently, significant progress has been achieved in the upgrading of the nucleon-meson transport code NMTC/JAERI [1,2]. This work is motivated and accelerated by the proposal of the joint project of JAERI and KEK [3] for the proton accelerators and experimental facilities using proton beams with energies from 600 MeV to 50 GeV and a power of 1 MW. As already reported last year [2], the available energy range of the code was extended from 3.5 GeV to 200 GeV for nucleon and pions by implementing the high-energy nuclear reaction code JAM (Jet AA Microscopic transport model) [4] for the intra-nuclear cascade calculation. The neutron differential elastic cross sections were modified from the approximation with first-order Bessel function to the data calculated with optical model potentials so that the accuracy of neutron transport calculation could be improved at tens of MeV region. This extended version is denoted as NMTC/JAM in this paper.

Further upgrade has been successively carried out in a view of optimization of the specifications of various facilities planned in the joint project. For example, number of different kind of particles treated in the transport process have been increased so that most of mesons and baryons could be taken into account. Nucleon-nucleon cross sections have been modified using systematics. In particular, proton-nucleon cross sections have been changed from the default data. The function such as displacement cross section calculation has been also implemented.

With this upgrading work, benchmark calculation has been also carried out to study the validity of NMTC/JAM. This paper describes the features of the present NMTC/JAM and some comparisons of the calculation with the experiments for thick target experiments.

2 Features of the Code

2.1 Nuclear Reaction Calculation

The nuclear reactions are simulated with the intra-nuclear cascade models i.e. JAM [4] for incident energy region above 3.5 GeV and Bertini model for the energy region below 3.5 GeV, respectively, followed by the particle evaporation model including high energy fission process. JAM is the hadronic cascade model and designed to simulate ultra-relativistic nuclear collisions from initial stage of nuclear collision to final state interaction in hadronic gas stage. As incident energy increases, the inelastic hadron-hadron collisions are modeled by the resonance picture, string picture and hard parton-parton scattering, respectively. Hadrons, their excited states and on-shell partons, which are produced from hard parton-parton scattering, are explicitly propagated in space-time by the cascade method. The production of all particles listed in the particle table is taken into account. The total and elastic hadron-hadron cross sections were parameterized to the experimental data. Since JAM can simulate the nuclear reactions irrespective of the mass number of target nucleus, the restriction of the original NMTC/JAERI [1] that cannot treat the light nuclei with mass number less than 6 was removed.

2.2 Particle Transport Calculation

Inter-nuclear transport processes of nucleons in medium are simulated using the O5R algorithm for neutron and a continuous slowing down model for charged particles. The importance sampling technique is available to trace the particle transport phenomena in thick medium efficiently. The transport of the other mesons and baryons such as η , Λ , Σ , Ξ , etc., and their anti-particles have been newly taken into account in addition to nucleons, pions, and kaons. Some leptons of muons and neutrinos are also treated in the present version. The transport cross sections of these mesons, baryons and leptons are based upon the geometric cross section of a target nucleus. These particles collide with the nucleus in medium and decay into the other particles.

The nucleon-nucleus cross section has been slightly changed so as to take account of their energy dependence as accurately as possible. For neutron, the systematics of Pearlstein [5] was modified to take the values obtained optical model parameters (OMPs) at energy region below 40 MeV. For proton, on the other hand, a new systematics was developed on the basis of the experimental data and the database of LA-150 [6]. Resultant non-elastic cross section for proton incidence on Pb is shown in Fig. 1 by the thick solid line. It is observed that the cross section data are improved to agree with the experimental data in the energy region below 30MeV.

The angular distribution data for elastic scattering were also modified by the systematics based on the experimental data and the OMPs to treat the scattering to wide angles properly. The resultant differential cross sections are shown in Fig. 2 for neutron incidence on C, Fe and Pb at 55 MeV.

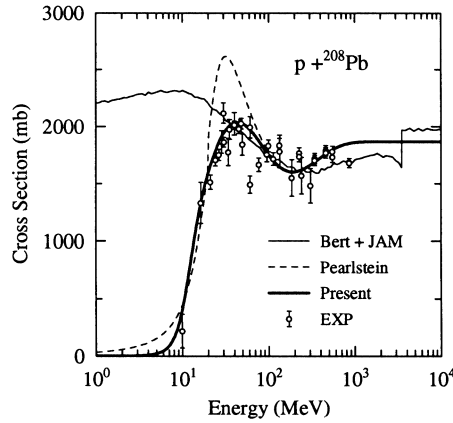


Fig. 1. Non-elastic cross section for proton incidence on Pb

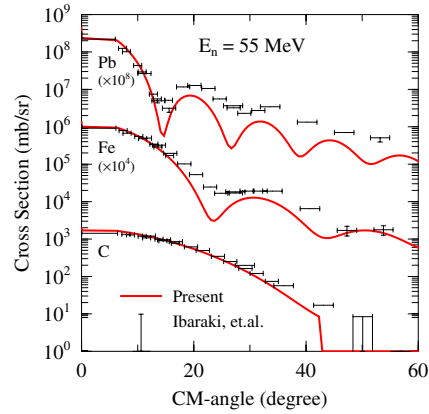


Fig. 2. Differential elastic cross sections for 55-MeV neutron incidence on C, Fe and Pb

2.3 Other New Function

For the feasibility in radiation registivity the structural component such as the beam window, the container of spallation neutron target will be critical issue in the joint project. In order to estimate the radiation damage of structural materials, Lindhard-Robinson model [7,8] was implemented in NMTC/JAM to calculate the displacement per atom (DPA). According to the model, the DPA is obtained by the threshold displacement energy, the energy of primary knock-on-atom, mass and atomic number of the recoiled nuclei. The threshold displacement energy depends upon the target element and the value is assumed to be 27 to 90 eV. The other quantities are obtained by the Monte Carlo simulation in NMTC/JAM.

3 Code Validation

The present NMTC/JAM was validated though the analyses of neutron transmission experiments and activation reaction rates measurements using thick mercury target. Figure 3 compares the NMTC/JAM calculation with the experiments for the 68-MeV quasi-monoenergetic neutrons transmitted through 40-cm thick iron shield [9]. For comparison, the result calculated with the angular distribution approximated by the first-order Bessel function is also shown. It is observed that the NMTC/JAM calculation agrees with the experiment quite well both on the axis and 40-cm off axis. Due to the lack of the scattering component to wide angles, however, the calculation with first-order Bessel function can not estimate the elastic scattering to 40-cm off axis and overestimates the experiment on the axis by about factor of 5. As a result of the analyses [10] of the other shielding materials of iron, concrete and polyethylene, it has been also

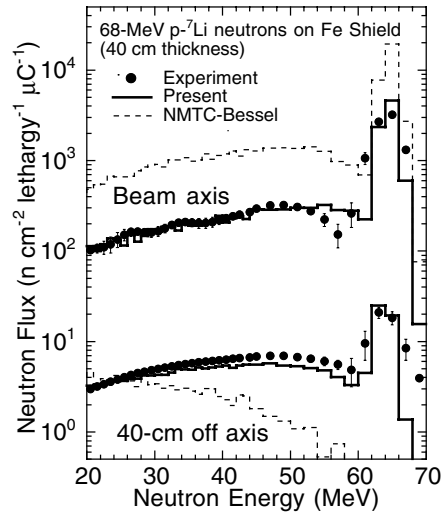


Fig. 3. Energy Spectra of 68 MeV quasi-monoenergetic neutrons transmitted through 40 cm thick iron shield

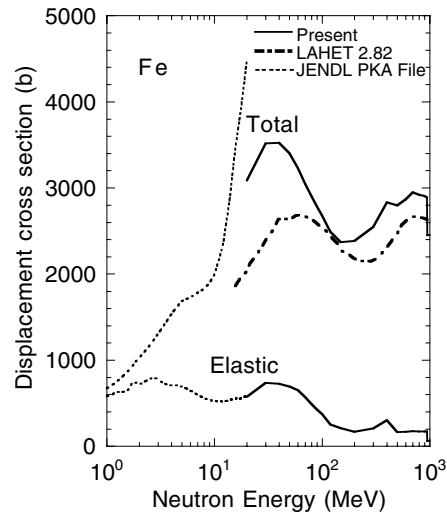


Fig. 4. Displacement cross section for neutron incidence on Fe

confirmed that the NMTC/JAM calculation agrees with the experiments by the difference of 0.9 to 1.4 in C/E ratio.

Figure 4 shows the displacement cross section calculated with NMTC/JAM for neutron incidence on Fe. NMTC/JAM gives higher values than LAHET [11] above 20 MeV. It is difficult to discuss about validity of the calculation because of lack of experimental data. Judging from the data of JENDL-PKA file [12], the elastic component of the displacement cross section value calculated with NMTC/JAM keeps the trend of the database as a function of incident energy. On the contrary, significant gap appears at 20 MeV between the data and the NMTC/JAM calculation.

Figure 5(a) and 5(b) show the results of the reaction rate distribution measurements of various reactions such as $^{209}\text{Bi}(n,4n)^{206}\text{Bi}$, $^{27}\text{Al}(n,\alpha)^{24}\text{Na}$, and so on along the cylindrical mercury target of 20-cm diameter and 130-cm length bombarded with high-energy protons at AGS [13]. It is found from Fig. 5 (a) that the present NMTC/JAM gives higher reaction rates than ever for the $^{209}\text{Bi}(n,4n)^{206}\text{Bi}$ and $^{209}\text{Bi}(n,5n)^{205}\text{Bi}$ reactions at proton energy of 24 GeV. This is because of the increase of the neutrons produced via the transport of various secondary mesons and baryons. For both reactions, the calculation agrees well with the experiment at the positions far from 30 cm in the longitudinal distance. As the foil position becomes closer to beam incident point, the agreement becomes worse. Since the $^{209}\text{Bi}(n,4n)^{206}\text{Bi}$ and $^{209}\text{Bi}(n,5n)^{205}\text{Bi}$ reactions are sensitive to the neutrons with energies 30 to 40 MeV, these neutron yield may be underestimated by the NMTC/JAM calculation. As shown in Fig. 5(b), good agreement is obtained between the present NMTC/JAM calculation and

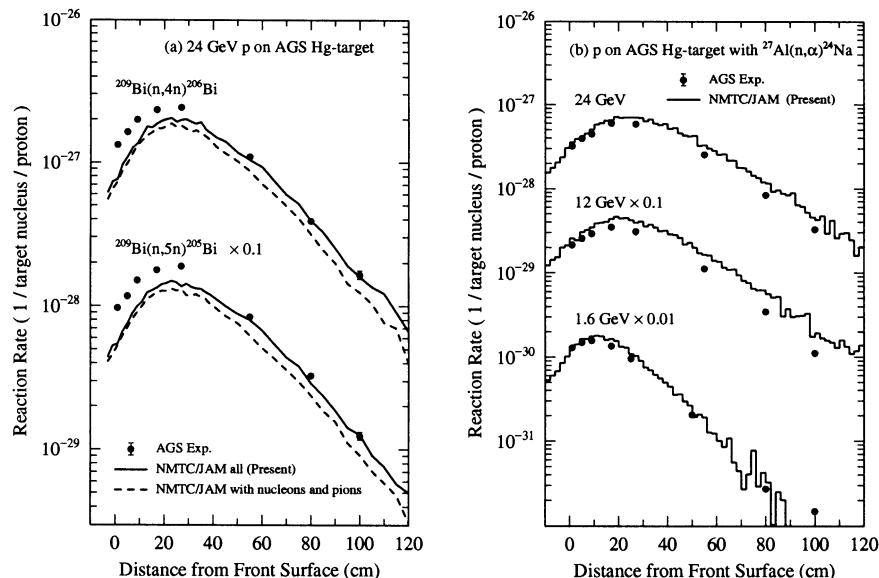


Fig. 5. Reaction rates along the cylindrical surface of 20-cm diameter and 130-cm long mercury target bombarded high-energy protons. (a) $^{209}\text{Bi}(n,4n)^{206}\text{Bi}$ and $^{209}\text{Bi}(n,5n)^{205}\text{Bi}$ reactions for 24 GeV proton incidence. (b) $^{27}\text{Al}(n,\alpha)^{24}\text{Na}$ reaction for 1.6, 12 and 24 GeV proton incidence

the experimental data for the $^{27}\text{Al}(n,\alpha)^{24}\text{Na}$ reaction at proton energies of 1.6, 12 and 24 GeV, respectively. Here, the MCNP-4A code was employed for the transport calculation of neutrons with energies below 20 MeV.

4 Summary

Nucleon-meson transport code NMTC/JAM has been successively upgraded by revising both the nuclear reaction calculation part and the transport calculation one so that its applicable energy range is extended to 200 GeV. The updated NMTC/JAM was validated through the analyses of the transmission experiment of neutrons with tens of MeV and the activation reaction rate measurements on the thick mercury target bombarded with 1.6, 12 and 24 GeV protons. It is confirmed that NMTC/JAM estimates very well not only the transmission component on the beam axis but also the scattering one to the off axis. NMTC/JAM is also in a reasonable agreement with the experimental reaction rates on the thick mercury target although some underestimation remains.

Based on the reliability confirmed through these code validation, the neutronics design study of the joint project for high-intensity proton accelerator is under progress by the use of NMTC/JAM in combination with other related codes.

References

1. H. Takada et al.: *An upgraded version of the nucleon-meson transport code*, NMTC-JAERI97, JAERI-Data/Code 98-005 (1998)
2. H. Takada: 'Recent Progress of Nucleon-meson Transport Code Development at JAERI'. In: *Proc. of Int. Conf. on Mathematics and Computation, Reactor Physics and Environmental Analysis in Nuclear Applications*, J. M. Aragoes (Ed.), Madrid, Spain, September 27-30, 1999, pp. 929-938, (1999)
3. S. Nagamiya: 'JAERI-KEK Joint Project on High Intensity Proton Accelerators', J. of Nucl. Sci. Technol., Supplement 1, p40-48, (2000)
4. Y. Nara et. al.: Phys. Rev. C **16**, 1 (2000), <http://hadron31.tokai.jaeri.go.jp/jam/>
5. S. Pearlstein: Nucl. Sci. Eng. **49**, 162 (1972); Nucl. Sci. Eng. **95**, 116 (1987); Astrophys. J. **346**, 1049 (1989)
6. M.B. Chadwick et al.: Nucl. Sci. Eng. **131**, 293 (1993)
7. J. Lindhard, V. Nielsen, M. Scharff: Mat. Fys. Medd. Dan. Vid. Selsk. **360**, No.10 (1963)
8. M.J. Norgett, M.T. Robinson, I.T. Torrens: Nucl. Eng. Des. **33**, 50 (1974)
9. H. Nakashima. et al.: Nucl. Sci. Eng. **124**, 243 (1996)
10. H. Takada, S. Meigo, K. Iga: J. Nucl. Sci. Technol. **37**, 307 (2000)
11. E.J. Pitcher et al.: 'The Effect of the New Nucleon-Nucleus Elastic Scattering Data in LAHET version 2.8 on Neutron Displacement Cross Section Calculations', private communication.
12. M. Kawai et al.: 'PKA, KERMA, and DPA Files of JENDL'. In: *Proc. of Int. Conf. on Nucl. Data for Sci. Technol., May 19-24, 1997, Trieste*, p.1110 (1997)
13. H. Takada et al.: *Measurements of Activation Reaction Rate Distributions on A Mercury Target Bombarded with High-Energy Protons at AGS*, JAERI-Data/Code 2000-008 (2000)

FLUKA: Status and Prospects for Hadronic Applications

A. Fassò¹, A. Ferrari², P.R. Sala², and J. Ranft³

¹ SLAC, Radiation Phys. Dept., ms 48, P.O. Box 4349, Stanford CA94309, USA

² CERN CH-1211 Geneva 23, Switzerland (on leave from INFN-Milan)

³ Phys. Dept., Universität Siegen, D-57068 Siegen, Germany

1 General Description

The standalone FLUKA code [1] is capable of handling transport and interactions of hadronic and electromagnetic particles in any material over a wide energy range, from thermal neutrons to cosmic rays. It is intrinsically an analogue code, but can be run in biased mode for a variety of deep penetration applications.

Interactions are treated in a theory-driven approach, and models and model implementations are always guided and checked against experimental data. Hadron-nucleon interaction models are based on resonance production and decay below a few GeV, and on the Dual Parton Model(DPM) above. Two models are used also in hadron-nucleus interactions. At momenta below 3-5 GeV/c the so-called PEANUT includes a very detailed Generalized IntraNuclearCascade (GINC) and a preequilibrium stage, while at high energies the Gribov-Glauber multiple collision mechanism is included in a less refined GINC. Both modules are followed by equilibrium processes: evaporation, fission, Fermi break-up, γ deexcitation. A specialized multigroup transport, based on a dedicated neutron library, is implemented for low energy (<20 MeV) neutrons. Details can be found in [1], only the latest developments in the hadronic models are described here.

2 The Hadronization Model and Neutrino Beams

FLUKA is a continuously evolving code. Several aspects of the implementation of the Glauber-Gribov cascade and of the following hadronisation have been improved along the years, leading to very satisfactory performances already in 1995. The latest refinements [2] were mainly triggered by the needs of neutrino beam calculations, and by the new data from the SPY collaboration [3]. A global revision of the hadronization model has been performed, strongly constrained by low energy data for what concerns the finite mass and threshold effects, and by a variety of h-A and h-N data for the fragmentation functions and the transverse momentum distribution. Representative results are shown in Fig. 1.

Differences in the hadronic models reflect on the predicted ν fluxes in ν beams. For instance, there is a difference of about 15% in the CERN West Area ν_μ calculated intensity between the new FLUKA and the very old FLUKA92 models, the one included in the GEANT-FLUKA package.

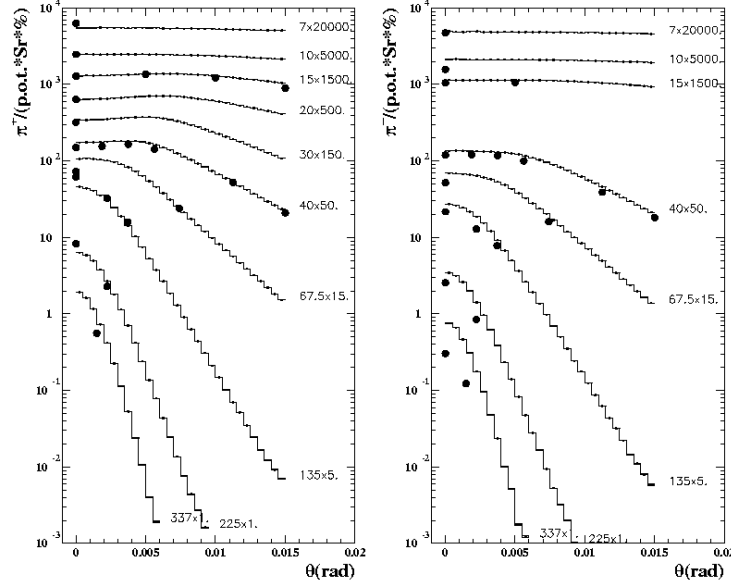


Fig. 1. Double differential cross section for π^+ (left) and π^- (right) production for 450 GeV/c protons on a 10 cm thick Be target (dots: data from [3,4])

The nice agreement with experimental data on exclusive particle distributions add reliability to the FLUKA predictions for the new Cern Neutrino to Gran Sasso (CNGS) beam. All calculations relative to CNGS make use of the FLUKA particle production in the target. Besides this, FLUKA is also used to simulate energy deposition, radiation levels, background components etc.

Charm production is a very recent development triggered again by neutrino beam issues. First simulations of charm production in proton proton collisions follow the data within the experimental errors (see Fig. 2)

3 Kaon Interactions

Kaon Interactions at medium-low energies are relevant for several topics, such as proton decay, penetrating background at LHC, B physics. The FLUKA implementation exploits all the nuclear effects already present in PEANUT. All Kaon-nucleus interactions are described through phase shift analysis [7,8]. Isospin relations are used to link different charge states and mass differences are taken into account. K^+ and K^0 interact weakly with nucleons, only the elastic and charge exchange channels are open up to ≈ 800 MeV/c (π prod. threshold), thus their interactions are easily described and they are a good probe for the nuclear medium, in particular for the Fermi distribution. Examples of quasi-elastic K^+ scattering off nuclei are shown in Fig. 3 Conversely, a variety of hyperons can be produced in K^- and \bar{K}^0 -N interactions, with the $\Sigma\pi$ and $\Lambda\pi$ channels already

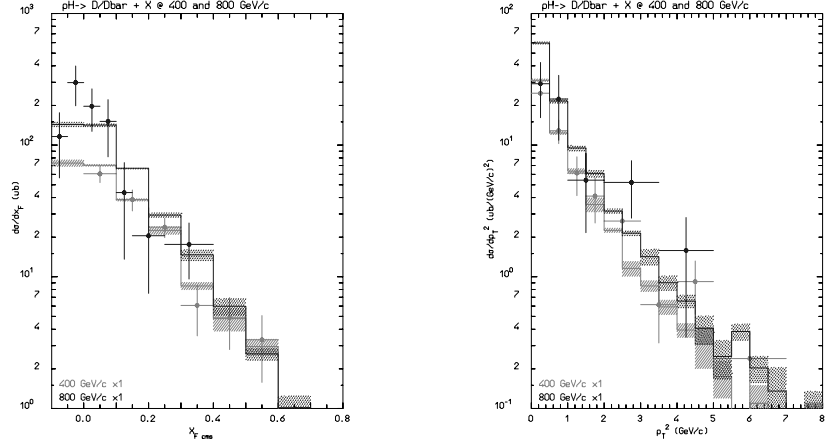


Fig. 2. Charm x_F (left) and p_T (right) distributions in p-p at 400 (light grey) and 800 (dark grey) GeV/c. Dots: data from [5]

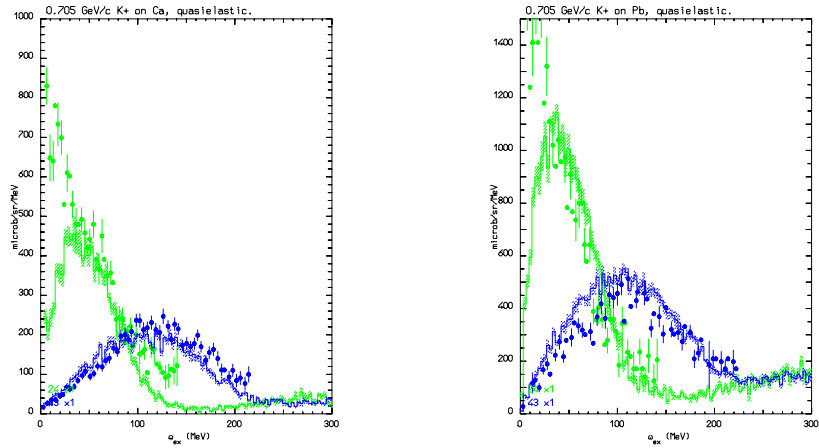


Fig. 3. $(K^+, K^{+'})$ on Ca(left) and Pb(right) vs residual excitation, 705 MeV/c, at 24° and 43° . Histo: FLUKA, dots: data[6]. Elastic scattering is not included in the calculations

open at rest. A complex multichannel phase shift analysis is needed, and specific nuclear effects must be accounted for: a significant kaon nuclear potential, and the creation of bound hypernuclei. Details are still under definition in FLUKA.

4 Evaporation

Evaporation is based on the standard Weisskopf-Ewing formalism. Improvements [1] with respect to the 1995 version [9] can be summarized as:

- Improved state density $\rho \propto \exp(2\sqrt{aU})/U^{\frac{5}{4}}$

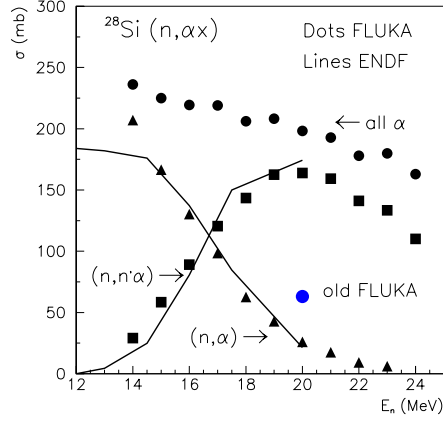


Fig. 4. Excitation function for neutron induced α production on ^{28}Si

- No Maxwellian approximation for energy sampling
- γ competition in progress
- Sub-barrier: $\sigma_{inv}^x = (R + \bar{\lambda})^2 (\hbar\omega_x/2E) \ln [1 + \exp \{2\pi(E - V_c)/(\hbar\omega_x)\}]$

Neutron and proton production are marginally affected, while residual nuclei production and alpha emission are nicely improved. Since it is relevant for damage to detectors, the excitation function of α emission in Silicon across the threshold for low energy neutron transport is presented in Fig. 4, compared with ENDFB-VI data and with an old (1995) FLUKA version, still used by the CMS collaboration [10]. While the present FLUKA reproduces the data, the old one was underestimating the total α yields at 20 MeV by a factor 4.

5 Neutrino Interactions

Neutrinos are not hadrons, however to describe their interaction nuclear effects are critical. The NUX-FLUKA event generator exploits all sophisticated nuclear physics of PEANUT. The quasielastic event generator is built-in. For Resonance and DIS the ν -nucleon interaction is described via the NUX code from A. Rubbia, target nucleons and all secondaries are treated by PEANUT. The results agree very well with experimental observables as measured in NOMAD [11].

6 Atmospheric Neutrino Calculations

Although the evidence for neutrino oscillation is considered robust after the SK results, a precise understanding of asymmetries, absolute fluxes, angular distributions, is essential to investigate oscillation parameters and/or new physics. The FLUKA-based calculations aim to exploit the precision of the interaction and transport models and the full three-dimensionality of the geometry. The

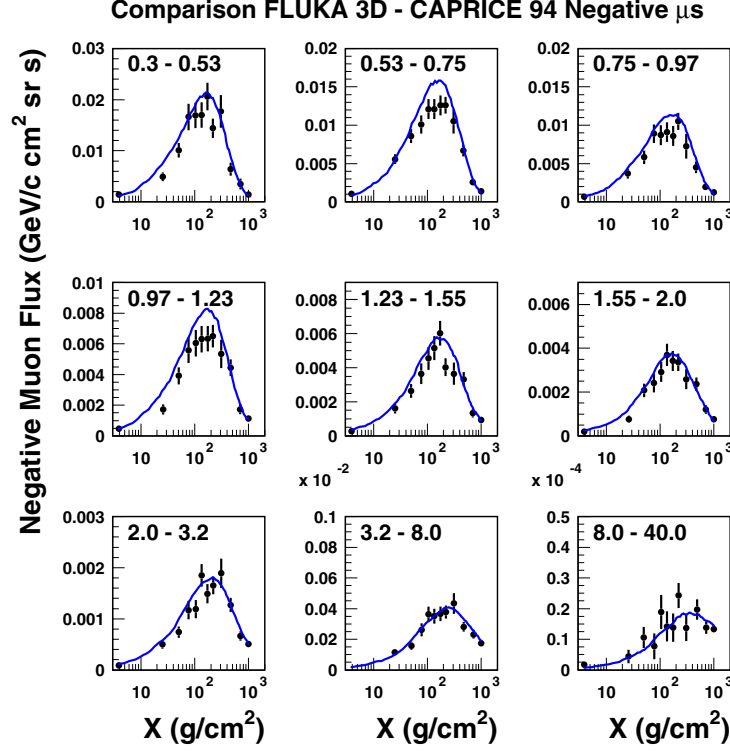


Fig. 5. μ^- Flux in the atmosphere, in different momentum bins as a function of height. Histograms: FLUKA, dots: exp. data[15]

3D/1D comparison can be found in [12]. The effects of the hadronic interaction models are under investigation in collaboration with the Bartol [14] group, preliminary results show differences of the order of 20% for sub-GeV ν fluxes [13]. Checks of the FLUKA simulations against experimental measurements of μ at different heights in the atmosphere show remarkable agreement (Fig. 5).

7 FLUGG: the Geant4 Geometry Interface

FLUGG [16] (FLuka with Geant4 Geometry) Is an extension of FLUKA that uses the GEANT4 geometry package to build the geometry, find the particle locations and boundary interceptions. It provides a more flexible geometry than the default one and allows to run FLUKA using geometry inputs in the GEANT4 format (or GEANT3 via the ALICE translator, with some limitations). It has been tested on HP and Linux platforms for single level and multi-level geometries, for neutral and charged particles, including biasing options and magnetic field. An input user interface has been developed, while the output is in FLUKA format.

8 Heavy Ions

Heavy Ions transport and interactions are of utmost importance for the assessment of dose rate and radiation damage during space flights. Multiple scattering and ionization are already implemented in FLUKA, with accurate treatment of effective charge and straggling of energy losses. The high energy nucleus-nucleus interactions will be available soon through an interface to the DPMJET code (see this conference). For the low energy A-A interactions, an extension of PEANUT is planned for the next future.

9 Conclusions and Future Work

There are still many areas of ongoing work, despite the smallness of the collaboration and the richness of the results:

- Heavy Ions : In collaboration with the Huston University, NASA contract
- input/output: interface to ROOT (NASA, R.Brun, F.Carminati)
- PEANUT: extension to high energy
- Neutrons : new low energy library.....never find the time to do it
- Residual dose rate: almost implemented, from decay database

References

1. A. Fassò et al.: 'New developments in FLUKA modelling of hadronic and EM interactions'. In: *SARE-3, KEK-Tsukuba, May 7-9 1997*, ed. by H. Hiramaya, KEK report Proceedings 97-5, p. 32; A. Ferrari, P.R.Sala: 'Intermediate and High Energy Models in FLUKA: Improvements, Benchmarks and Applications'. In: *International Conference on Nuclear Data for Science and Technology, Miramare-Trieste, Italy, May 19-24 1997*, ed. by G. Reffo, A. Ventura and C. Grandi, pp. 247-253
2. G. Collazuol et al.: Nucl. Instr. Meth. A **449**, 609 (2000)
3. G. Ambrosini et al.: Phys. Lett. B **425**, 208 (1988)
4. H.W. Atherton et al.: CERN 80-07 (1980)
5. R. Ammar et al.: Phys. Rev. Lett. **61**, 2185 (1988); M. Aguilar-Benitez et al.: Z. Phys. C **41**, 191 (1988)
6. C.M.Kormanyos et al.: Phys. Rev. C **51**, 669 (1995)
7. G. Giacomelli et al.: Nucl. Phys. B **71**, 138 (1974)
8. A.D. Martin: Nucl. Phys. B **179**, 33 (1981); G.P. Gopal et al.: Nucl. Phys. B **119**, 362 (1977)
9. A. Ferrari et al.: Z. Phys. C **70**, 413 (1996)
10. M. Huhtinen, F. Faccio: Nucl. Instr. Meth. A **450**, 155 (2000)
11. A. Bueno, A. Rubbia: private communication; The ICANOE Collaboration, CERN/SPSC 99-15
12. G. Battistoni et al.: Astropart. Phys. **12**, 315 (2000)
13. G. Battistoni et al.: In: *NOW2000, Otranto, Italy, Sep 10-16 2000*
14. V. Agrawal et al.: Phys Rev. D **53**, 1314 (1996)
15. M. Boezio et al.: Phys. Rev. Lett. **82**, 4757 (1999)
16. M. Campanella et al.: ATL-SOFT-98-039 (1998), ATL-SOFT-99-004 (1999)

Status of the MCNPX Transport Code

H.G. Hughes¹, M.B. Chadwick¹, R.K. Corzine², H.W. Egdorf¹,
F.X. Gallmeier³, R.C. Little¹, R.E. MacFarlane¹, S.G. Mashnik¹, E.J. Pitcher¹,
R.E. Prael¹, A.J. Sierk¹, E.C. Snow⁴, L.S. Waters¹, M.C. White¹, and
P.G. Young¹

¹ Los Alamos National Laboratory, Los Alamos NM 87545 USA

² Georgia Institute of Technology, Atlanta GA 30332-0405 USA

³ Oak Ridge National Laboratory, Oak Ridge TN 37831 USA

⁴ TechSource, Inc., Santa Fe NM 87594-1057 USA

1 Introduction

The Monte Carlo particle transport code MCNPX and its associated data have been the focus of a major development effort at Los Alamos for several years [1]. The system has reached a mature state, and has become a significant tool for many intermediate- and high-energy particle transport applications. A recent version has been released to the Radiation Safety Information Computational Center (RSICC). A recent report [2] provides an overview of the code and an extensive set of references for the component physics modules used in the code.

In this paper we review the status of the developmental version of MCNPX, and describe some important new enhancements, including the use of evaluated nuclear data files for proton transport; the use of photonuclear reaction data; improved elastic and inelastic reaction cross sections for nucleons, antinucleons, pions, and kaons; and two new modes of operation of the code. We also illustrate the use of the new proton and photonuclear data in two representative applications.

2 Table-Based Proton Transport

Table-based charged-particle transport is a new feature of MCNPX and has been implemented for protons in the developmental version. Proton evaluations for energies up to 150 MeV have been completed for 42 isotopes [3]. All evaluations include production cross sections for light particles, gamma rays, and heavy recoil particles, energy-angle correlated spectra for secondary light particles, and energy spectra for gamma rays and heavy recoil nuclei. The NJOY system [4] is used to process evaluated proton data into a tabular form appropriate for MCNPX. The MCNPX implementation uses tabular proton data to model nuclear reactions and large-angle scattering; continuous slowing down and multiple scattering models traditionally used in MCNPX for proton transport are used to model small-angle scattering.

Initial benchmarking of table-based MCNPX proton transport [5,6] concentrated on neutron production from thick targets. MCNPX calculations, both

with tables and with physics models, were compared to experiment for 30-MeV protons on Fe, 68-MeV protons on C and Al, and 113-MeV protons on C, Al, Fe, and Pb.

We have recently performed similar studies for a thin proton target. We have modeled the 43-MeV proton source from JAERI's TIARA AVF cyclotron. Protons impinge on a 3.6-mm thick ^7Li target. Resulting neutrons are constrained by an iron collimator 10.9 cm in diameter and 225 cm long. We have modeled this target, assuming a monoenergetic point proton source. The neutron flux is tallied on the surface exiting the collimator. In a report of the experimental results [7], the neutron flux is normalized to unity in an energy band between 36.3 and 45.5 MeV. We have normalized our calculated results in the same manner. Two MCNPX calculations were performed, one using proton tables and the other using the Bertini intranuclear cascade model in conjunction with a pre-equilibrium model.

Results for the experiment and the two calculations are shown in Fig. 1. Overall, neither calculation is in completely satisfactory agreement with the experiment. However, we observe that the width of the neutron peak more closely matches the experiment when proton tables are used. The Bertini model predicts a neutron peak that is lower in energy and much broader than observed.

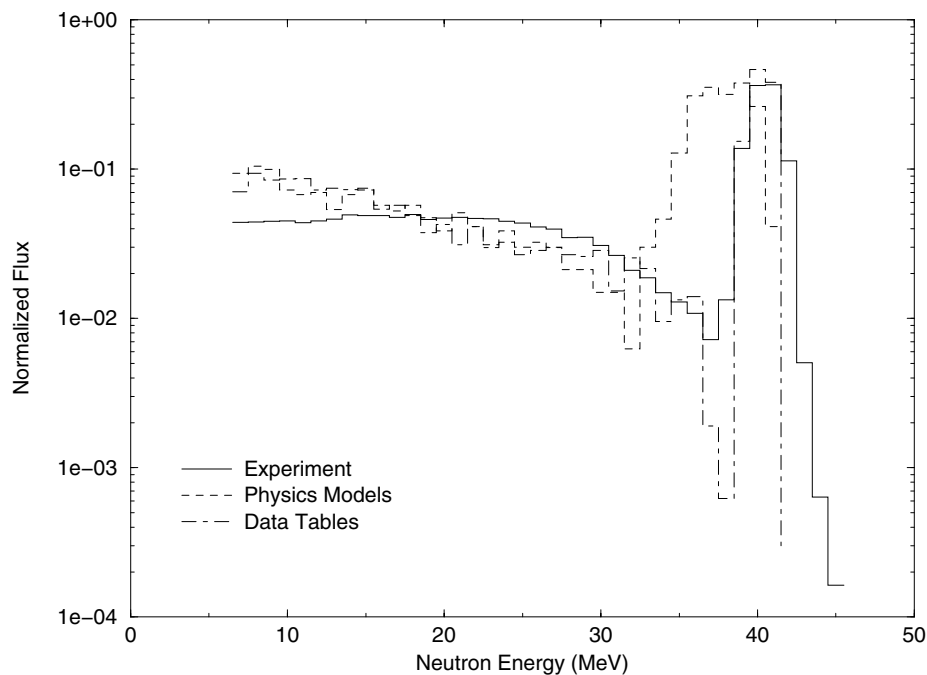


Fig. 1. Neutron Spectrum from 43-MeV Protons on ^7Li

3 Photonuclear Interactions

Evaluated photonuclear data have recently become available for the first time [8]. These data include the doubly-differential cross sections necessary for Monte Carlo transport. MCNPX has been extended to use the newly available tabular data. Specifically, the distance to the next photon collision reflects the possibility of a photonuclear collision, and such collisions will produce a combination of neutrons, photons or light ions ($A \leq 4$) for further transport. Thus, photonuclear events are fully integrated within a simulation. The implementation has been subjected to verification and validation testing [9]. Related work is in progress to enable the use of the Cascade-Exciton Model [10,11] physics module to handle photonuclear events outside the tabular region.

The need for photonuclear physics in a Monte Carlo n-particle transport code has been generally accepted for some time. An interesting example of this need was the design of an electron beam stop for the Dual Axis Radiographic Hydrotest Facility (DARHT) at Los Alamos National Laboratory [12,13]. DARHT produces a 20-MeV electron beam for use in photon radiography. The beamstop is designed to allow pulsing the accelerator while personnel are in the experimental area. The original design was a 20 cm diameter cylindrical plug with 7 cm of graphite backed by 25 cm of tungsten. The length of the tungsten backing was optimized to reduce the photon dose in the experimental area to acceptable levels. However, as seen in Fig. 2, this ignored a significant contribution to the

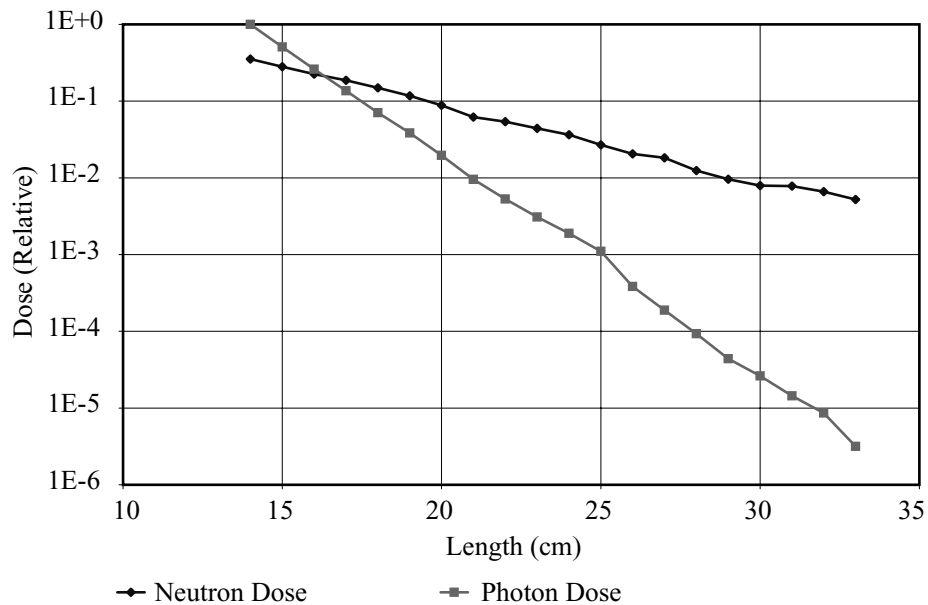


Fig. 2. Relative dose contribution from neutrons (diamonds) and photons (squares) for increasing thickness of tungsten in an electron beam stop

dose from neutrons. Further calculations were performed using a multi-step approach to estimate the neutron contribution. Based on these calculations, the tungsten in the beam stop was extended to bring the dose from neutrons to an acceptable level. Figure 2 illustrates the new capability of MCNPX to calculate the contribution to the dose from neutrons and photons in a single simulation.

4 Defined Elastic and Reaction Cross Sections

Previously the concept of a reaction cross section for use with the intranuclear cascade model has been implicit in the model and not explicitly defined for use in the transport process. The new cross-section treatment [14] provides a defined (explicit) reaction cross section as well as a defined nuclear elastic cross section (previously utilized) in the absence of data libraries; these defined cross sections determine the transport process and constrain the corresponding reaction rates.

The new cross-section treatment has been implemented including an interpolation table for neutron elastic and reaction cross sections derived from the new 150-MeV MCNPX neutron libraries [3] (and some older 100-MeV libraries). Elastic scattering for protons is as implemented in LAHET2.8 [15]. Proton reaction cross sections are obtained by the methods of Barashenkov and Polanski [16], with Madland's optical model calculations [17] used where available, augmented by the coding of Tripathi [18,19] below 1 GeV and by the methods from FLUKA89 (Moehring formulation [20]) above 1 GeV. Beyond the range of the new tabular data, neutron reaction cross sections are similarly obtained. Elastic and reaction cross sections for pions are derived from the methods of Barashenkov and Polanski and of FLUKA89. For antinucleons and kaons, there are no elastic cross sections available, and the reaction cross sections are obtained only from the FLUKA89 methods.

5 Other Enhancements

With the implementation of the defined elastic and reaction cross sections in MCNPX, it becomes possible to treat primary beam transport [21] without nonelastic interactions or secondary particle production, determining attenuation by weight reduction using the prescribed reaction cross sections. This provides a relatively efficient method for examining small-angle dispersion of the primary beam and for testing methods for treating nuclear elastic scattering, multiple Coulomb scattering, and energy straggling. It also provides a necessary feature for the development of next-event estimators for higher energy neutron flux above the energies where standard MCNP methods, using evaluated data libraries, are commonly used.

A cross-section generation option has been adapted from LAHET [22] and implemented in MCNPX. Using this option, the interaction models are accessed directly for any source particle, and the interaction products are recorded to a history file. This history file may be subsequently processed by a postprocessing

code (called XSEX3) to create double differential cross sections for any of the interaction models included in MCNPX.

Finally, the developmental version of MCNPX includes a new atomic mass data base [23] and the code to access it; in the current version it is used by all the physics packages shared by LAHET and MCNPX.

References

1. H.G. Hughes, K.J. Adams, M.B. Chadwick, J.C. Comly, S.C. Frankle, J.S. Hendricks, R.C. Little, R.E. Prael, L.S. Waters, P.G. Young: 'MCNPX — The LAHET/MCNP Code Merger'. In: *Proceedings of the Third Workshop On Simulating Accelerator Radiation Environments (SARE3)*, May 7–9, 1997, Tsukuba, Japan (KEK Proceedings 97–5, June 1997) pp. 44–51
2. H.G. Hughes, K.J. Adams, M.B. Chadwick, J.C. Comly, L.J. Cox, H.W. Egendorf, S.C. Frankle, J.S. Hendricks, R.C. Little, R.E. MacFarlane, S.G. Mashnik, R.E. Prael, A.J. Sierk, L.S. Waters, M.C. White, P.G. Young, F.X. Gallmeier, E.C. Snow: 'MCNPX for Neutron-Proton Transport'. In: *Mathematics and Computation, Reactor Physics and Environmental Analysis in Nuclear Applications*, September 27–30, 1999, Madrid, Spain, ed. by J. M. Aragones, C. Ahnert, and O. Cabellos (Senda Editorial, Spain, 1999) pp. 939–948
3. M.B. Chadwick, P.G. Young, S. Chiba, S. Frankle, G.M. Hale, H.G. Hughes, A.J. Koning, R.C. Little, R.E. MacFarlane, R.E. Prael, L.S. Waters: Nucl. Sci. Eng. **131**, 293 (1999)
4. R.E. MacFarlane, D.W. Muir: *The NJOY Nuclear Data Processing System, Version 91*. Los Alamos National Laboratory report LA-12740-M (1994)
5. M.B. Chadwick, H.G. Hughes, R.C. Little, E.J. Pitcher, P.G. Young: 'Nuclear Data for Accelerator-Driven Systems'. Los Alamos National Laboratory report LA-UR-00-30 (2000), to be published in Progress in Nuclear Energy
6. M.B. Chadwick, H.G. Hughes, R.C. Little, E.J. Pitcher, P.G. Young: 'Physics Models and Nuclear Data Evaluations for Enhanced Monte-Carlo Transport'. These Proceedings p. 967
7. N. Nakao, H. Nakashima, T. Nakamura, S. Tanaka, S. Tanaka, K. Shin, M. Baba, Y. Sakamoto, Y. Nakane: Nucl. Sci. Eng. **124**, 228 (1996)
8. P. Oblozinsky, M.B. Chadwick, A.I. Blokhin, T. Fukahori, Y.-O. Lee, M.N. Martins, V.V. Varlamov, B. Yu, Y. Han, S.F. Mughabghab, J. Zhang: *Handbook on Photonuclear Data for Applications: Cross Sections and Spectra*. International Atomic Energy Agency TEC-DOC In Press (To be published in 2000; see <http://iaeaand.iaea.org/photonuclear> for draft)
9. M.C. White: *Development and Implementation of Photonuclear Cross-Section Data for Mutually Coupled Neutron-Photon Transport Calculations in the Monte Carlo N-Particle (MCNP) Radiation Transport Code*. Los Alamos National Laboratory report LA-13744-T (July 2000)
10. S.G. Mashnik, A.J. Sierk, O. Bersillon, T.A. Gabriel: 'Cascade-Exciton Model Detailed Analysis of Proton Spallation at Energies From 10 MeV to 5 GeV', (Los Alamos National Laboratory Report LA-UR-97-2905), Nucl. Instr. Meth. A **414**, 68 (1998)
11. F.X. Gallmeier: 'Implementation of the CEM-Code into the MCNPX-Code'. In: *Proceedings of the Fourth Workshop on Simulating Accelerator Radiation Environments (SARE4)*, September 14–16, 1998, Knoxville, Tennessee, ed. by Tony A. Gabriel, Oak Ridge National Laboratory (1998) pp. 131–139

12. T.H. Brown: 'Shielding Design of the Electron Beam Stop for the Dual-Axis Radiographic Hydrotest Facility (DARHT)'. In: *Proceedings of the 1996 Topical Meeting on Radiation Protection and Shielding*, April 21–25, 1996, No. Falmouth, Massachusetts (American Nuclear Society, 1996) pp. 102–109
13. M.B. Chadwick, T.H. Brown, R.C. Little: 'Photoneutron Production in the Electron Beam Stop for the Dual Axis Radiographic Hydrotest Facility (DARHT)'. In: *Proceedings of the ANS Radiation Protection and Shielding Topical Conference*, April 19–23, 1998, Nashville, Tennessee (American Nuclear Society, 1998) Vol. II, pp. 356–363
14. R.E. Prael, A. Ferrari, R.K. Tripathi, A. Polanski: 'Comparison of Nucleon Cross Section Parameterization Methods for Medium and High Energies'. In: *Proceedings of the Fourth Workshop on Simulating Accelerator Radiation Environments (SARE4)*, September 14–16, 1998, Knoxville, Tennessee, ed. by Tony A Gabriel, Oak Ridge National Laboratory (1998) pp. 171–181
15. R.E. Prael, D.G. Madland: 'A Nucleon-Nucleus Elastic Scattering Model for LAHET'. In: *Proceedings of the 1996 Topical Meeting on Radiation Protection and Shielding*, April 21–25, 1996, No. Falmouth, Massachusetts (American Nuclear Society, 1996) pp. 251–257
16. V.S. Barashenkov, A. Polanski: 'Electronic Guide for Nuclear Cross Sections'. Comm. JINR E2–94–417, Dubna (1994)
17. D.G. Madland: 'Recent Results in the Development of a Global Medium-Energy Nucleon-Nucleus Optical-Model Potential,' In: *Proceedings of a Specialist's Meeting on Preequilibrium Reactions*, Semmering, Austria, February 10–12, 1988, ed. by Brigitte Strohmaier (OECD, Paris, 1988) pp. 103–116
18. R.K. Tripathi, F.A. Cucinotta, J.W. Wilson: 'Universal Parameterization of Absorption Cross Sections'. NASA Technical Paper 3621 (January 1997)
19. R.K. Tripathi, J.W. Wilson, F.A. Cucinotta: 'New Parameterization of Neutron Absorption Cross Sections'. NASA Technical Paper 3656 (June 1997)
20. H.J. Moehring: 'Hadron-nucleus Inelastic Cross-sections for Use in Hadron-cascade Calculations at High Energies'. CERN report TIS-RP/116 (October 1983)
21. R.E. Prael: 'Primary Beam Transport Methods in LAHET'. In: *Transactions of the 1999 Annual Meeting*, June 6–10, 1999, Boston, Massachusetts (American Nuclear Society, 1999) pp. 325–326
22. R.E. Prael, H. Lichtenstein: 'User Guide to LCS: The LAHET Code System'. Los Alamos National Laboratory report LA-UR-89-3014 (September 1989)
23. R.E. Prael: 'Upgrading Physics Packages for LAHET/MCNPX'. In: *Proceedings of the 2nd International Topical Meeting on Nuclear Applications of Accelerator Technology*, September 20–23, 1998, Gatlinburg, Tennessee (American Nuclear Society, 1998) pp. 276–280

Physics Models and Nuclear Data Evaluations for Enhanced Monte Carlo Transport

M.B. Chadwick, H.G. Hughes, R.C. Little, E.J. Pitcher, and P.G. Young

University of California, Los Alamos National Laboratory, Los Alamos, New Mexico 87545, USA

Abstract. We describe recent evaluations of neutron and proton interaction cross sections up to 150 MeV in the LA150 Data Library, for use in MCNPX computer code simulations of accelerator-driven systems (ADS). An overview is provided of the nuclear theory used. A number of benchmark comparisons against experiments are described, for thin and thick-target neutron production, neutron transmission through macroscopic slabs, and neutron heating and damage. Future data needs for waste transmutation are also briefly described.

1 Model Calculations for the LA150 Databases

A suite of evaluated reaction cross section files collectively known as the LA150 Library has been developed [1,2] in support of accelerator-driven systems design. These evaluations are in ENDF-6 format, and have recently been accepted into the U.S.-standard ENDF/B-VI Library as Release-6. For incident neutrons, they extend the previously-existing ENDF/B-VI information from 20 MeV up to 150 MeV. For incident protons, the files extend from 1–150 MeV. To date, evaluations have been completed for isotopes of the following structural, shielding, and target-blanket materials: H, Li, C, N, O, Al, Si, P, Ca, Fe, Ni, Cr, Cu, Nb, W, Hg, Pb, and Bi.

These LA150 evaluated cross sections are designed for use in radiation transport codes, such as the MCNPX code [3]. The primary motivation for using these evaluated data is the accuracy improvements that one can expect to obtain in the below-150 MeV energy region. In most previous transport simulations, intranuclear-cascade methods have been used for neutrons above 20 MeV and for protons at all energies, even though the semiclassical assumptions inherent within such models do not hold at lower energies. By developing evaluated cross section libraries up to 150 MeV, using state-of-the-art nuclear reaction models in the GNASH code as well as experimental data, one can expect to have the most accurate possible representation of the nuclear cross sections.

The nuclear models used are based on theoretical approaches that are appropriate for the energies in the few-MeV to 150 MeV range: the Hauser-Feshbach compound nucleus theory; preequilibrium calculations based on the Feshbach-Kerman-Koonin theory or the exciton model; direct reactions calculated from the optical model using collective excitation form factors; and elastic scattering from the optical model. The GNASH code was demonstrated to be one of the

most accurate codes available for model calculations below 150 MeV in a Nuclear Energy Agency code intercomparison [4].

The optical model is used for predictions of the total, reaction, and elastic scattering cross sections, making use of nucleon potentials at higher energies developed by Madland [5], Chiba, and Koning. It is particularly useful for accurately representing the angular distributions in elastic scattering, allowing more accurate neutron transport simulations. (Many previous intranuclear cascade transport codes instead represent elastic scattering using a black-disc diffraction formula or use even simpler approaches, which poorly approximate reality below a few hundred MeV.)

2 Results

2.1 Neutron Multiplication in (n, xn) and (p, xn) Reactions

Neutron multiplication reactions play an important role in spallation targets, and when the nucleon energies fall below 150 MeV much of the neutron production comes from (n, xn) rather than (p, xn) reactions. This is simply because the probability that protons below 150 MeV stop before having a nuclear reaction is significant. Because of this, we have placed a large emphasis on accurately modeling the (n, xn) reactions.

An example is shown in Fig. 1 (left-hand-side) for the 26 MeV $^{209}\text{Bi}(n, xn)$ angle-integrated secondary neutron spectrum, where measurements exist [6]. The figure shows the components of the calculated spectrum due to compound nucleus emission, preequilibrium emission, and direct reactions. The direct reactions were calculated using Distorted-Wave Born Approximation theory. Collective excitations of excited vibrational states were treated using the weak-coupling model, with a $h_{9/2}$ proton coupled to a ^{208}Pb core. This allows extensive deformation-length information from direct reactions on ^{208}Pb to be used in the bismuth calculations.

Figure 1 (right-hand-side) shows the calculated 113 MeV $\text{Pb}(p, xn)$ neutron energy spectra at various angles, compared with data [7]. Agreement is good except at the backward angle where the calculations underpredict the experiment in the preequilibrium region. At low energies the large evaporation peak from sequentially-emitted compound nucleus neutrons is evident. Above about 10 MeV, the spectra have a hard preequilibrium tail that extends up to the incident energy minus the Q-value. These preequilibrium neutrons are seen to be strongly forward-peaked, whereas the evaporation neutrons are approximately isotropic.

2.2 Proton-Induced Thick-Target Neutron Production

It is important for nuclear simulation codes to adequately predict secondary neutron production from protons as they traverse target, blanket, and shielding materials. Secondary neutron production is central to spallation neutron target design, beam-stop design, and shielding considerations. Thick-target neutron

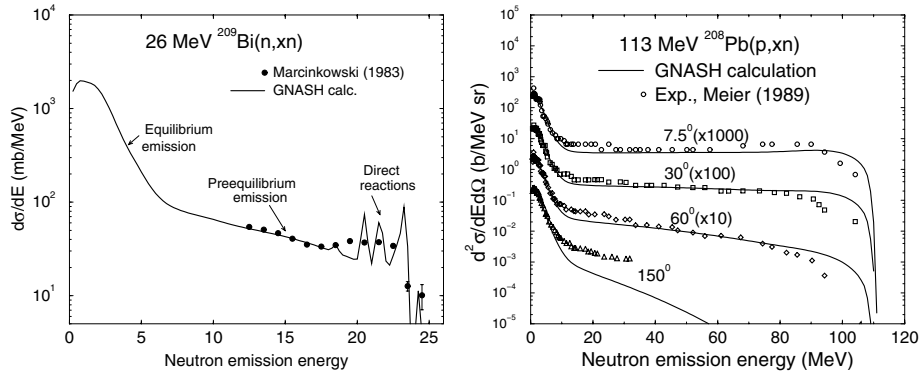


Fig. 1. (a) *l.h.s.*: Measured secondary angle-integrated neutron spectrum for 26 MeV neutrons on bismuth compared with GNASH calculations used in the LA150 Library; (b) *r.h.s.*: Evaluated $^{208}\text{Pb}(p,xn)$ double-differential neutron emission spectra compared with experimental data [7] at 113 MeV incident energy

production measurements provide an ideal way to test the microscopic nuclear data, in this case the LA150 proton data library, and test the proton transport algorithms used within MCNPX. Such measurements are usually made for targets that are sufficiently thick to stop the incident protons, though the targets are generally “thin” as far as the secondary neutrons are concerned. Thus, the probability that a secondary neutron produced has a subsequent nuclear interaction within the target is small. The protons slow down from their maximum energy, and for the maximum energy and all lower energies they have a probability of undergoing nuclear collisions leading to neutron production. Thick-target measurements therefore represent an integral over all incident energies up to the maximum of the differential “thin-target” cross sections, weighted by the stopping power function.

At 68 MeV and 113 MeV, proton-induced thick-target neutron production has been measured [7,8]. These data are compared with our MCNPX calculations in Fig. 2. The MCNPX with LA150 data simulation appears to more accurately describe the emitted neutron spectra compared to use of LAHET physics.

2.3 Neutron Transmission and Shielding Design

Japanese measurements [9] have been particularly useful for assessing the capabilities of a simulation code for shielding studies. A quasi-monoenergetic neutron source was generated by bombarding a Li target with 68 MeV protons, using the $\text{Li}(p,n)$ reaction. These neutrons subsequently impinged upon macroscopic slabs of iron and concrete, of various thicknesses. The transmitted neutrons were then measured at locations both on and off the beam’s axis. We demonstrated [1] that, compared to LAHET simulations, significant gains can be obtained when modeling neutron transmission through iron by use of the LA150 data in

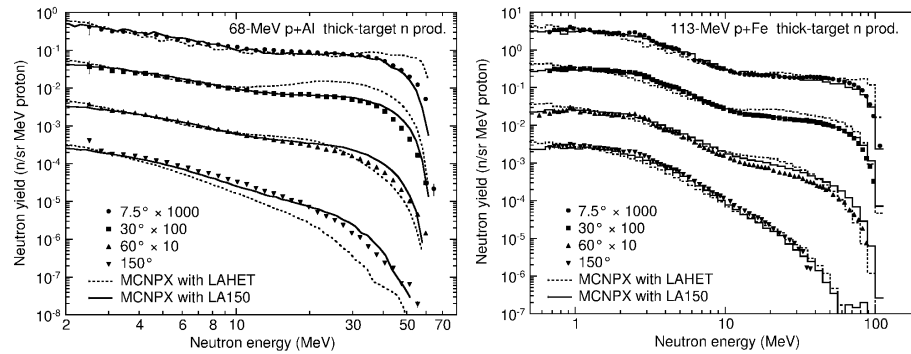


Fig. 2. Thick target neutron production spectra for: (a) *l.h.s.*: 68 MeV protons incident on aluminum [8] compared with calculations; (b) *r.h.s.*: 113 MeV protons incident on iron [7]. The solid lines show MCNPX using the LA150 data, the dashed lines show MCNPX using LAHET physics

MCNPX. Similar conclusions were also obtained by Sweezy *et al.* [10] who used MCNPX with LA150 data to simulate broad-spectrum neutron transmission through shields of iron, lead, concrete, and graphite.

2.4 Radiation Heating and Damage

The LA150 cross section data were developed with an emphasis on providing an accurate description of energy deposition, for radiation heating calculations. One of the reasons for this was their use in medical applications for calculations of absorbed dose in fast neutron and proton radiotherapy [11,12]. Radiation heating is also important in accelerator-driven systems. Comparisons between our evaluated neutron kerma coefficients and measured values are given in [11,12].

The NJOY Nuclear Data Processing System has, since 1979, been capable of calculating the neutron damage energy cross section. A description of the theory of damage energy and the computation of damage energy are described in the NJOY Manual, Chapter 4 [13]. This cross section is used to calculate lattice defect production rates in materials, which are an important measure of radiation damage. The LA150 Library is the first Los Alamos release of a continuous-energy MCNPX library to include the damage energy cross section. For accelerator applications, this cross section is a welcomed addition as radiation damage effects are particularly severe in accelerator-driven neutron sources.

At energies above nuclear data evaluations, the LAHET code [14] may be used to generate the damage energy cross section. The LAHET code relies on physics models of the intranuclear cascade in calculating the damage energy cross section, and again these are known to be less reliable at energies below approximately 150 MeV. The community that uses damage energy cross section data has noted a substantial discrepancy between evaluated damage energy cross sections and those generated by LAHET at the traditional transition energy of 20 MeV. The extension of this transition energy to 150 MeV brought about by

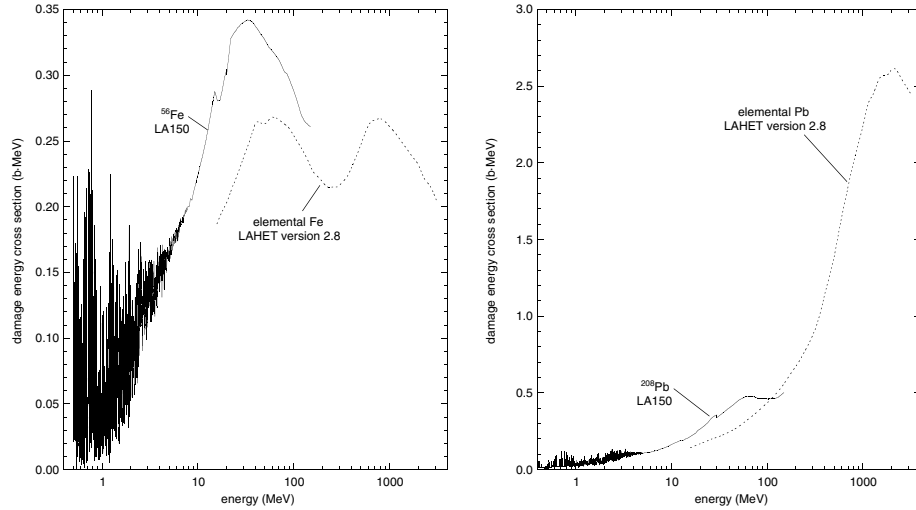


Fig. 3. The neutron damage energy cross section [13] from the LA150 Library over the energy range 400 keV to 150 MeV for ^{56}Fe and ^{208}Pb . Also plotted is the damage energy cross section as calculated using LAHET version 2.8 over the energy range 16 MeV to 3.1 GeV

the advent of the LA150 Library reduces the observed discrepancy. In Fig. 3 we plot the damage energy cross section from the LA150 Library over the energy range 400 keV to 150 MeV for ^{56}Fe and ^{208}Pb . Also plotted is the damage energy cross section as calculated using LAHET version 2.8 over the energy range 16 MeV to 3.1 GeV for the elements corresponding to the isotopes [15]. For the representative isotopes considered here, the agreement between the evaluated data and the LAHET-generated data is generally better at 150 MeV than at 20 MeV. This is consistent with expectations since LAHET should be less reliable at the lower energy.

3 Future Work and ATW

In order to build upon the work described here for use in the accelerator-transmutation of waste (ATW) program, a number of advances will be needed. First and foremost is a focus on nuclear cross section data for minor actinides and fission products, as well as for nuclides used in the spallation target and coolant (e.g. Bi, Pb, and possibly W or depleted U). Although some higher energy particles from the spallation target will enter the transmuter (subcritical reactor), the main focus for the transmuter will be on cross section data below 20 MeV at fast neutron energies. We anticipate that experimental work will also be needed to guide the calculations and evaluations, particularly for fission and capture processes.

4 Acknowledgments

We would like to thank Dr. Laurie Waters in the Accelerator Production of Tritium Technical Project Office for many useful discussions and for supporting the work described here. Dr. Robert MacFarlane played an important role in this project by developing the NJOY code to process LA150 data, and by processing the library for use by MCNPX. This research is supported by the Department of Energy under contract W-7405-ENG-36.

References

1. M.B. Chadwick et al.: Nucl. Sci. Eng. **131**, 293 (1999)
2. A.J. Koning, T. Fukahori, and A. Hasegawa: Technical Report No. NEA/WPEC-13, Nuclear Energy Agency, Paris
3. H.G. Hughes et al.: In *Proc. of the Mathematics and Computation, Reactor Physics and Environmental Analysis in Nuclear Applications*, Madrid, Spain, September 27-30, 1999, edited by J. M. Aragonés (Senda Editorial, S. A., Madrid, Spain, 1999), p. 939
4. M. Blann, H. Gruppelaar, P. Nagel, J. Rodens: *International Code Comparison for Intermediate Energy Nuclear Data* (Organization for Economic Cooperation and Development Nuclear Energy Agency, Paris, 1994), pp. 1–206
5. D.G. Madland: in *Proc. of a Specialists Meeting on Preequilibrium Reactions*, Semmering, Austria, 1988, ed. B. Strohmaier (OECD Nuclear Energy Agency, Paris, France, 1988), No. NEANDC-245, pp. 103–116
6. A. Marcinkowski et al.: Nucl. Phys. A **402**, 220 (1983)
7. M.M. Meier et al.: Nucl. Sci. **102**, 310 (1989)
8. S. Meigo et al.: In *Proc. of the International Conference on Nuclear Data for Science and Technology*, Trieste, Italy, May 18-24, 1997, edited by G. Reffo (Società Italiana di Fisica, Bologna, Italy, 1997), pp. 413–415
9. H. Nakashima et al. Nucl. Sci. Eng. **124**, 243 (1996)
10. J.E. Sweezy, N. Hertel, L.S. Waters, H.G. Hughes: In *Proc. of the International Topical Meeting on Nuclear Applications of Accelerator Technology*, Long Beach, California, November 14-18, 1999, edited by G. Van Tuyle (American Nuclear Society, La Grange Park, IL, 1999), pp. 391–398
11. M.B. Chadwick et al.: Med. Phys. **26**, 974 (1999)
12. ICRU Report 63, *Nuclear Data for Neutron and Proton Radiotherapy and for Radiation Protection* (International Commission on Radiation Units and Measurements, Bethesda, MD, 2000)
13. R.E. MacFarlane, D.W. Muir: Technical Report No. LA-12740-M (1994), Los Alamos National Laboratory, Los Alamos, NM
14. R.E. Prael, H. Lichtenstein: Technical Report No. LA-UR-89-3014, Los Alamos National Laboratory, Los Alamos, NM
15. E.J. Pitcher: In *Proceedings of the Symposium on Materials for Spallation Neutron Sources*, Orlando, Florida, February 10-12, 1997, edited by M.S. Wechsler, L.K. Mansur, C.L. Snead, and W.F. Sommer (1997)

Development of Heavy Ion Transport Monte Carlo Code

H. Iwase¹, T. Kurosawa¹, T. Nakamura¹, N. Yoshizawa², and J. Funabiki²

¹ Department of Quantum Science and Energy Engineering, Tohoku University,
Aoba, Aramaki, Aoba-ku, Sendai, Japan

² Mitsubishi Research Institute, 3-6, Otemachi 2-Chyome, Chiyoda-ku, Tokyo, Japan

Abstract. We developed a heavy ion transport Monte Carlo code HETC-CYRIC which can treat the fragments produced by heavy ion reactions. The HETC-CYRIC code is made by incorporating a heavy ion reaction calculation routine, which consists of the HIC, the SPAR, and the Shen's formula, into the hadron transport Monte Carlo code HETC-3STEP. The results calculated with the HETC-CYRIC were compared with the experimental data, and the HETC-CYRIC gave rather good agreement with the experiment.

1 Introduction

Recently, high-energy heavy ions have been used in various fields of nuclear physics, material physics and medical application, especially cancer therapy, and several heavy ion accelerator facilities are now operating or planned for construction. The high-energy heavy ions are also important constituents of cosmic radiation for space utilization, such as the international space station project including the JEM (Japanese Experimental Module). In this circumference, the interaction and transport of heavy ions in a medium including human body are indispensable basic informations to estimate the absorbed dose of the patients during the cancer treatment, to design the shielding of the accelerator facility and to estimate the exposure of the astronauts and the space scientists in space. There exists however only one heavy-ion transport code, HZTRAN [1], developed by NASA in the world, but this code is one-dimensional discrete ordinates calculation code. It is therefore needed to develop the three dimensional heavy-ion transport code. Here in this study, we tried to develop the three-dimensional Monte Carlo code for heavy ion transport calculation.

2 Basic Method of the Code Development

We developed a heavy ion transport Monte Carlo code by incorporating a newly-developed heavy ion routine (HIR) into the HETC-3STEP [2].

The heavy ion transport routine HIR can treat the transport and reaction of incident heavy ion and fragments produced by a chain of heavy ion reactions. For this heavy ion reaction calculation, we used the two existing Monte Carlo code, HIC [3] and ISABEL [4]. First, we compared these two codes with the

experimental data in order to investigate the calculational accuracy and to decide which is suitable for the heavy ion routine. The comparisons were made for double-differential neutron production cross sections (DDX) in angle and energy by heavy ions, as shown in Fig. 1.

The HIC code is the Heavy Ion Code which can treat the heavy ion reaction of energy higher than 50 MeV/nucleon which is based on the intranuclear cascade model and the evaporation model. The ISABEL code includes only intranuclear cascade model but this model treats a nucleus by dividing into 16 segments which is more precise than 3 segments in the HIC code, and the ISABEL code also considers the reflection at a boundary of a nucleus, which can be the same effect as considering the preequilibrium process. As the results of comparisons shown in Fig. 1, the ISABEL code showed good agreement with the experimental data at angles of larger than 30 degrees, while on the other hand, the ISABEL underestimated the experimental data terribly from 0 degree to 15 degrees. The HIC results rather well with the experimental data at all angles. So, we decided to use the HIC code in heavy ion reaction calculation for the heavy ion transport routine.

We then developed the heavy ion transport routine HIR by combining the HIC code, SPAR [6] code, and Shen's formula [7]. The SPAR code can calculate the heavy ion stopping powers and ranges, and the Shen's formula can calculate the heavy ion total reaction cross sections.

The HETC-3STEP is a high energy hadron transport Monte Carlo code developed by Yoshizawa et al. This code is revised from the original HETC code [8] which includes the intranuclear-cascade evaporation process (2-step model) based on a Fermi free gas model, by adding the pre-equilibrium emission based on the exciton model (3-step model). The HETC-3STEP can also treat the heavy ion (atomic mass less than 20) transport and reaction, but the treatment is restricted to incident particles and the accuracy of heavy ion calculation is poor.

3 Procedure of the Code Development

The heavy ion transport calculation code is composed of the following steps,

1. A distance D in which a heavy ion projectile collides with a target nucleus in a medium is decided as follows,

$$D = -\frac{\ln(r)}{\Sigma_t},$$

where Σ_t is a total reaction cross section of a projectile in a medium calculated by the Shen's formula and r is a uniform random number.

2. A range R of a projectile in a medium can be calculated by the SPAR code.
3. It is decided whether a projectile collides or stops. If $D < R$, a projectile collides with a target nucleus after flying straight-forward to a distance of D and losing its energy. This energy loss can also be calculated by the SPAR code. If $D > R$, a projectile loses its energy completely without collision in a medium,

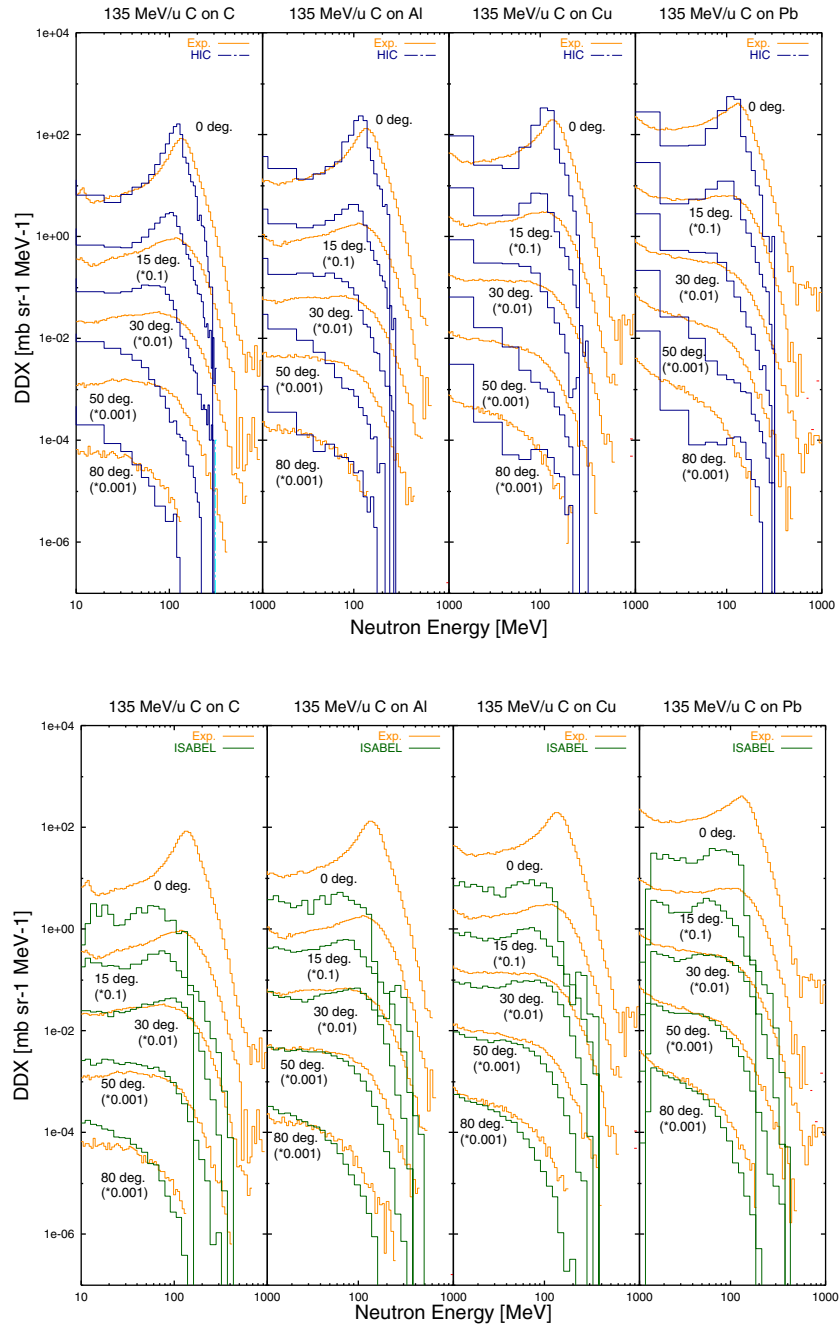


Fig. 1. Comparison of HIC and ISABEL calculation; [Upper] Neutron DDX calculated by HIC compared with our experimental data of 135 MeV/nucleon C ion on C, Al, Cu, and Pb targets [5]. [Lower] The same results between ISABEL and the experiment

and the transport of this projectile does not follow any more.

4. The heavy ion reaction calculation is performed using the HIC code. The HIC code gives the output results of many heavy ions and hadrons as fragment products. These heavy ion outputs are stored and used as an incident heavy ion for continuing the extranuclear cascade reactions. The hadron outputs on their particle types (neutron, proton and pion), energies, positions, directions and weights are stored in a file during the heavy ion calculations. This file is used as hadron sources produced by heavy ions for the hadron transport calculation using the HETC-3STEP code.

Figure 2 shows the thus-obtained HETC-CYRIC code structure.

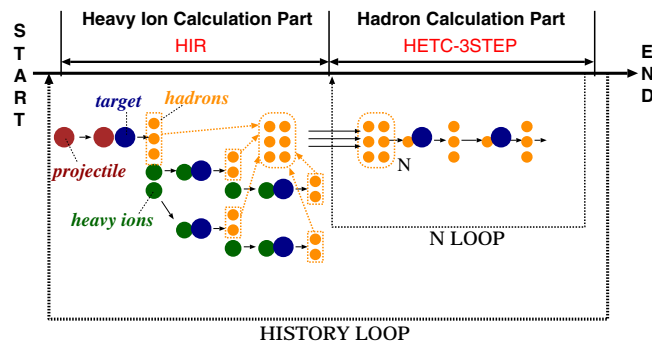


Fig. 2. Structure of HETC-CYRIC

4 Comparison of HETC-CYRIC and Experimental Data

In order to investigate the accuracy of the HETC-CYRIC code, we compared the results calculated by the HETC-CYRIC with the data measured by Kurosawa et al. [9]. Figures 3 and 4 show the comparison of the HETC-CYRIC results with the measured neutron spectra for 400 MeV/nucleon carbon and iron ions on stopping-length carbon and lead targets.

In Fig. 3 of C ion, the HETC-CYRIC gives good agreement with the experiment from 7.5 to 30 degrees, but gives underestimation at 0 degree and gives overestimation from 60 to 90 degrees comparing with the experiment for carbon target. In the case of lead target, the HETC-CYRIC gives good agreement as a whole excluding an overestimation in the low energy region at all angles.

In Fig. 4 of Fe ion, the HETC-3STEP gives good agreement as a whole, excluding an underestimation in the forward direction comparing with the experiment for carbon target, and an overestimation in the low energy region for lead target as well as in the case of carbon ion.

This underestimation in the forward direction and overestimation at large angle and in the low energy region for heavier target material in the HETC-CYRIC code may come from the inaccurate heavy ion model of the HIC code.

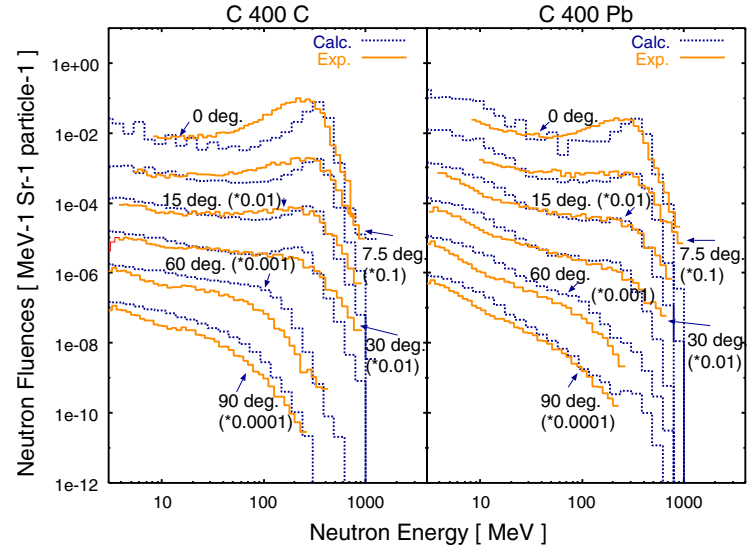


Fig. 3. Comparison of the neutron spectra calculated with the HETC-CYRIC and the measured data for 400 MeV/nucleon C ion on C and Pb targets [9]

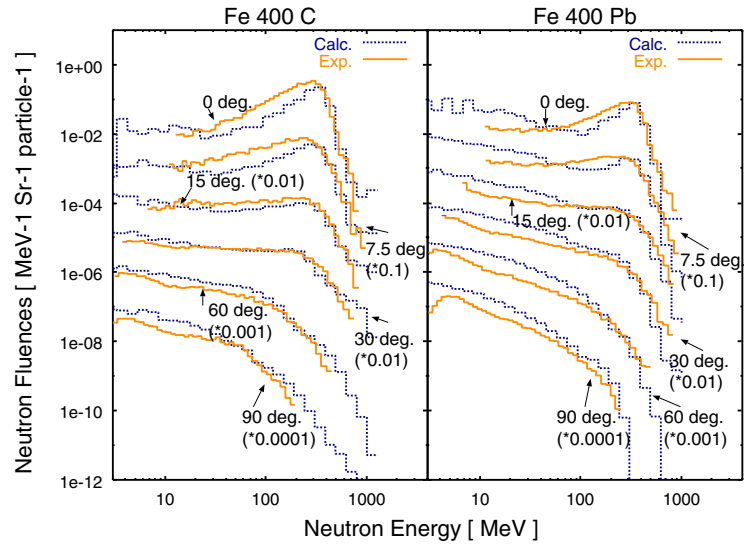


Fig. 4. Comparison of the neutron spectra calculated with the HETC-CYRIC and the measured data for 400 MeV/nucleon Fe ion on C and Pb targets [9]

We are now investigating the way to improve the present code more accurately by revising the HIC code or using the different heavy ion reaction calculation code such as the QMD code [10] based on the quantum molecular dynamics model.

5 Conclusion

We developed a heavy ion transport Monte Carlo code, HETC-CYRIC by combining the newly-developed heavy ion transport routine HIR including the HIC code and the hadron transport Monte Carlo code HETC-3STEP. The HETC-CYRIC can treat the heavy ion and hadron transport calculations. This code is still under developing and the first general-purpose heavy ion transport Monte Carlo code in the world.

References

1. W. John. Wilson et al.: NASA Tech. Paper 3146, (1991)
2. N. Yoshizawa et al.: J. Nucl. Sci. Tech. **32**, 601 (1995)
3. H.W. Bertini: ORNL-TM-4134 (1996)
4. Y. Yariv et al.: Phys. Rev. **188**, 1711 (1969)
5. H. Sato et al.: JAERI-Conf. **261**, 5 (2000)
6. T.W. Armstrong et al.: ORNL-4869, (1973)
7. Shen Wen-quinf et al.: Nucl. Phys. A **491**, 130 (1989)
8. P. Cloth et al.: KFA-IRE-E, AN/12/88 (1988)
9. T. Kurosawa et al.: Nucl. Sci. and Engin. **132**, 30 (1999)
10. J. Aichelin. et al.: Phys. Rep. **202**, 233 (1991)

Baryon Stopping in High-Energy Collisions in the DPMJET-III Model

J. Ranft¹, R. Engel², and S. Roesler³

¹ Physics Dept. Universität Siegen, D-57068 Siegen, Germany

² University of Delaware, BRI, Newark DE 19716, USA

³ SLAC, P.O. Box 4349, Stanford CA 94309, USA

A recently discovered feature of hadron production in nuclear collisions is the large stopping of the participating nucleons in hadron-nucleus and nucleus-nucleus collisions. Experimental data demonstrating this effect have been presented in [1,2].

Multistring fragmentation models like the Dual Parton Model or similar models did originally not show this enhanced stopping in nuclear collisions. Therefore, in order to incorporate the effect into multistring fragmentation models new diquark breaking DPM-diagrams acting in hadron-nucleus and nucleus-nucleus collisions were proposed by Kharzeev [3] and Capella and Kopeliovich [4] and investigated in detail by Capella and Collaborators [5,6]. Similar ideas were discussed by Vance and Gyulassy [7] and by Casado [8].

The Monte Carlo implementation into DPMJET-II.5 of the new diquark breaking diagrams of Kharzeev [3] and Capella and Kopeliovich [6] was first discussed by Ranft [9]. The implementation into DPMJET-III [10] of these diagrams differs somewhat from [9] and is described here.

There are two possibilities for the first fragmentation step of a diquark. Either we get in the first step a baryon, which contains both quarks of the diquark and the string junction or in the first step a meson is produced containing only one of the two quarks and the baryon is produced in one of the following fragmentation steps. This mechanism was implemented under the name *popcorn* fragmentation in the Lund chain fragmentation model JETSET [11,12] which is presently used in DPMJET. The popcorn mechanism alone is not enough to explain the baryon stopping observed experimentally in hadron-nucleus and nucleus-nucleus collisions [1,2].

In [9] we describe these new diquark breaking DPM-diagrams in detail, this will not be repeated here. The two important diagrams are (i)GSQBS, the Glauber sea quark mechanism of baryon stopping, this diagram acts in nuclear collisions already at low energy. (ii)USQBS, the unitary sea quark mechanism of baryon stopping, this mechanism leads to baryon stopping also in proton-proton collisions at collider and cosmic ray energies.

In DPMJET-III we first construct the system of parton chains according to the model without the diquark breaking diagrams. Having this we search for situations (i) as plotted on the left hand side of Fig. 1 or situations (ii) (not plotted), where the left lower diquark is replaced by an antiquark. On the left hand side in Fig. 1 we have a diquark-quark chain and a seaquark-

diquark chain with the (upper) diquark and seaquark belonging to the same projectile hadron and also the (lower) diquark and valence-quark belonging to the same target-nucleon. In situation (ii) we have a diquark-quark chain and a seaquark-anti-seaquark chain with the (upper) diquark and seaquark belonging to the same projectile hadron and also the (lower) anti-seaquark and valence-quark belonging to the same target-nucleon. The left hand chain system are transformed as plotted on the right hand side of Figs. 1. The projectile diquark is split and the two resulting quarks come to the upper ends of both chains and the projectile seaquark goes into the middle of the second chain and determines the position where the baryon is produced. The sea quarks in Figs. 1 might be Glauber sea quarks or unitary sea quarks.

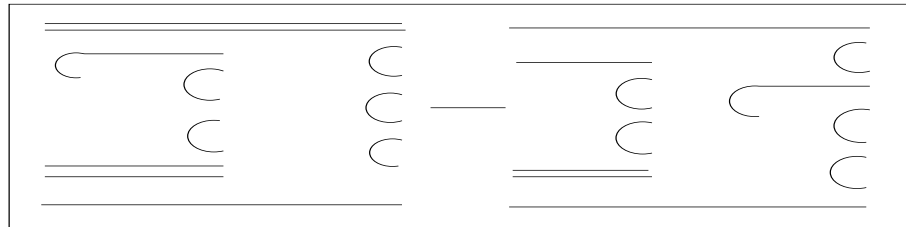


Fig. 1. Diquark breaking in an original diquark-quark and seaquark-diquark chain system

Besides the situations already discussed we consider also the ones where projectile and target are exchanged as well as situations with anti-diquarks.

For each of the new diquark breaking diagrams (GSQBS and USQBS) we have to introduce a new parameter. These parameters give the probability for the diquark breaking mechanisms to occur, given a suitable sea quark is available and given that the diquark breaking mechanism is kinematically allowed. For an original diquark-quark chain of small invariant mass, which originally just fragments into two hadrons, the diquark breaking is often not allowed. The optimum values of the new parameters are determined by comparing DPMJET-III with experimental data on net-baryon distributions. We obtain for the GSQBS parameters the value 0.6 and use the same value for the USQBS parameter.

Introducing the new baryon stopping mechanisms into DPMJET we get an significant modification of the model in different sectors: (i) The Feynman- x distributions of leading protons in proton-proton and proton-nucleus collisions. The leading particle production is especially important for the cosmic ray cascade simulation. (ii) The net- p ($p - \bar{p}$) and net- Λ ($\Lambda - \bar{\Lambda}$) rapidity distributions in hadron-nucleus and nucleus-nucleus collisions. These are the data on the enhanced baryon stopping mentioned already above. (iii) The production of Hyperons and anti-Hyperons in nuclear collisions. We present here examples for (i) and (ii).

In Fig. 2 we compare the distribution in the energy fraction x_{lab} carried by the leading proton. The data are photoproduction and DIS measurements from the HERA collider at $\sqrt{s} \approx 200$ GeV [13]. We compare to DPMJET-III for p-p collisions at $\sqrt{s} = 200$ GeV. The forward production of leading protons is not expected to depend strongly on the reaction channel. We present the DPMJET-III distributions for the models with and without the diquark breaking diagrams (No Sto in the plot). Unfortunately the x_{lab} region of the measurements is outside the region, where the diquark breaking changes the x_{lab} distribution strongly. So we have to wait for measurements in the full x_{lab} region before we can claim an improvement of the agreement due to the diquark breaking diagrams.

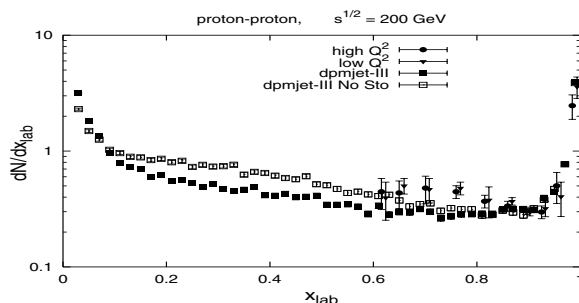


Fig. 2. Energy fraction x_{lab} carried by the leading proton. The data are photoproduction and DIS measurements at $\sqrt{s} \approx 200$ GeV [13] compared to DPMJET-III with and without (No Sto) the diquark breaking diagrams for p-p collisions at $\sqrt{s} = 200$ GeV

In Fig. 3 we compare the net-proton distributions according to the models with and without the diquark breaking diagrams with data in p-Au collisions [2]. Now the dip at central rapidity, which occurs in the model without the baryon stopping diagrams is filled. We observe in the full model like in the data at central rapidity a flat net-proton rapidity distribution.

In Fig. 4 we compare the DPMJET-III model with and without the diquark breaking diagrams with data on net-proton production in central S-S collisions. Also here the big dip at central rapidity in the model without the new diagrams has disappeared largely in the full model, however, the agreement to the data [2] is not perfect.

The presence of the new baryon stopping diagrams modifies also the extrapolation of multistring models to cosmic ray energies. The energy fractions carried by baryons decrease against those predicted by models without the new diagrams. The energy fractions carried by mesons and the spectrum weighted moments of mesons increase against models without the new diagrams. We present as function of the energy for two important variables the predictions of DPMJET-III with and without the new baryon stopping diagrams. All our plots are for p-p collisions, the model behaves in a rather similar way also for

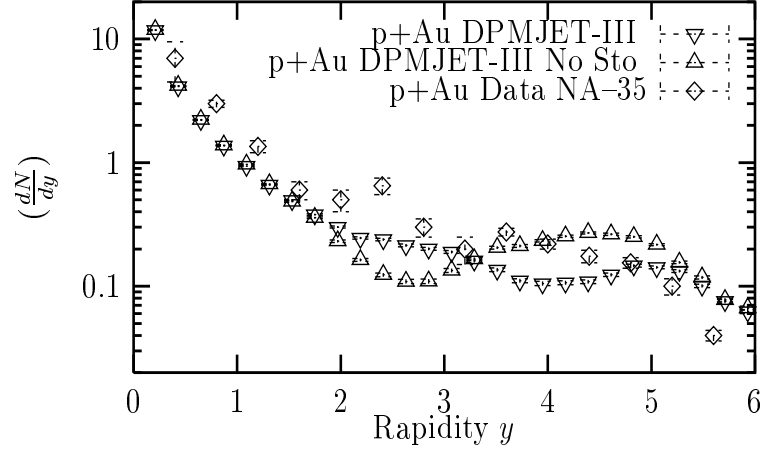


Fig. 3. Net proton ($p - \bar{p}$) rapidity distribution in p–Au collisions. The DPMJET–III results with and without (No Sto) the diquark breaking diagrams are compared with data [2]

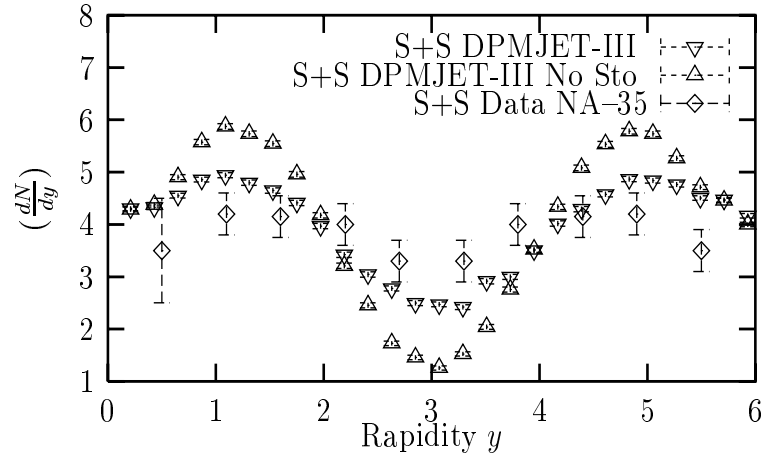


Fig. 4. Net proton ($p - \bar{p}$) rapidity distribution in central S–S collisions. The DPMJET–III results with and without (No Sto) the diquark breaking diagrams are compared with data [2]

p–Air collisions. We first discuss plots, where the baryon stopping mechanism causes significant differences.

The cosmic ray spectrum–weighted moments are defined as moments of x_{lab} distribution for the production of secondary particles i in hadron–hadron and hadron–nucleus collisions

$$F_i(x_{lab}) = x_{lab} \frac{dN_i}{dx_{lab}} \quad (1)$$

as follows

$$f_i = \int_0^1 (x_{lab})^{\gamma-1} F_i(x_{lab}) dx_{lab}. \quad (2)$$

Here $-\gamma \simeq -1.7$ is the power of the integral cosmic ray energy spectrum. The spectrum-weighted moments for nucleon-air collisions, as discussed in [14], determine the uncorrelated fluxes of energetic particles in the atmosphere.

We also introduce the energy fraction K_i :

$$K_i = \int_0^1 F_i(x_{lab}) dx_{lab} \quad (3)$$

As for x_{lab} , the upper limit for K is 1 in h-nucleus collisions.

In Figs. 5 we present the spectrum weighted moments for charged pions in p-p collisions as function of the cms energy \sqrt{s} .

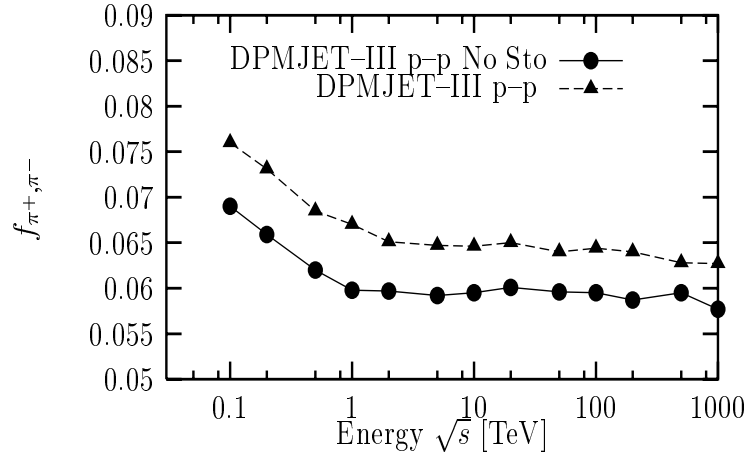


Fig. 5. Spectrum weighted moments for charged pion production in p-p collisions as function of the cms energy \sqrt{s}

In Fig. 6 we present again for pp collisions the energy fraction K for net baryons $B - \bar{B}$ (baryon minus antibaryon). The difference between $K_{B-\bar{B}}$ and K_B is the energy fraction going into antibaryons $K_{\bar{B}}$ which is equal to the energy fraction carried by the baryons which are newly produced in baryon-antibaryon pairs.

There are also observables where the difference between the two versions of the model are rather insignificant. Examples are the average transverse momentum of charged hadrons as function of the energy and the average charged multiplicity $\langle n_{ch} \rangle$ as function of the collision energy.

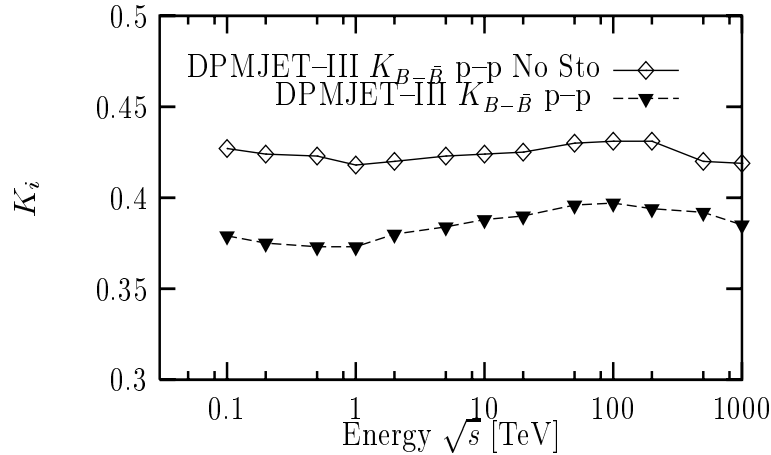


Fig. 6. Laboratory energy fractions for net baryons (baryon minus antibaryon) $B - \bar{B}$ production in p-p collisions as function of the cms energy \sqrt{s}

Acknowledgements

R.E. is supported in part by the US Department of Energy contract DE-FG02 91ER 40626

References

1. NA35 Collaboration, T. Alber et al.: Z. Phys. C **64**, 195 (1994)
2. NA35 Collaboration, T. Alber et al.: Eur. Phys. J. C **2**, 643 (1998)
3. D. Kharzeev: Phys. Lett. B **378**, 238 (1996)
4. A. Capella, B. Kopeliovich: Phys. Lett. B **381**, 325 (1996)
5. A. Capella, E.G. Ferreira, C.A. Salgado: Phys. Lett. B **459**, 27 (1999)
6. A. Capella, C.A. Salgado: *Baryon stopping and hyperon enhancement in the improved dual parton model*, hep-ph/9903414, preprint LPT Orsay 99-20 (1999)
7. S.E. Vance, M. Gyulassy: *Anti-hyperon enhancement through baryon junction loops*, Preprint Cu-YP-929, nucl-th/9901009, unpublished 1999
8. J.A. Casado: hep-ph/9810357v3, Manchester preprint MC-TH-98-17 (1999)
9. J. Ranft: *Baryon stopping in high energy collisions and the extrapolation of hadron production models to cosmic ray energies*, Preprint hep-ph/0002137, 2000
10. S. Roesler, R. Engel, J. Ranft: 'The Monte Carlo Event Generator DPMJET-III'. These proceedings p. 1033
11. T. Sjöstrand: Comp. Phys. Comm. **82**, 74 (1994)
12. B. Andersson, G. Gustafson, T. Sjöstrand: Physica Scripta **32**, 574 (1985)
13. A. Solano: Nucl. Phys. Proc. Suppl. **82**, 26 (2000)
14. T.K. Gaisser: *Cosmic Rays and Particle Physics* (Cambridge University Press, Cambridge 1990)

Muons and Neutrinos at High-Energy Accelerators

N. Mokhov¹, S. Striganov², and A. Van Ginneken¹

¹ Fermilab, P.O. Box 500, Batavia, IL 60510, USA

² Institute for High Energy Physics, Protvino, Russia

Abstract. Background levels in detectors and radiation problems at future colliders – whether pp , e^+e^- or $\mu^+\mu^-$ – are in large part determined by the presence of muons. Neutrinos from muon decay at muon colliders or storage rings are highly collimated and propagate outward within a narrow disk in which significant radiation doses persist out to very large distances. This paper highlights physics models and Monte Carlo algorithms developed mainly for studying these problems as well as some typical results.

1 Introduction

High Energy Physics codes do an excellent job of simulating interactions of elementary particles with nuclei and electrons which occur in a detector and its immediate environment. HEP experiments demand that the detector geometry be represented in great detail and require events to be simulated in analog fashion. This is necessary to discriminate against spurious signals as well as to study fluctuations and correlations. But the same reasons make such codes less suited for studying a host of problems which need only *averaged* results for their resolution, e.g., radiation environment and generic detector backgrounds. Although there is a lot of common ground between these two approaches, radiation oriented codes can take advantage of weighted Monte Carlo (MC) algorithms – based on inclusive reaction cross sections *vis-a-vis* full event generators – and of simplified descriptions of the geometry and magnetic environment. This results in great savings in programing effort and execution times. Note, however, not all fluctuations can be ignored in radiation type problems, e.g., fluctuations in energy loss and multiple scattering of muons traversing soil largely determine the spatial distribution of radiation dose. At high energy hadron and lepton colliders muons often determine background and radiation levels. With new proposals for muon colliders ($\mu\mu C$) and storage rings (μSR) actively under study, muons and – surprisingly – neutrinos play an increasingly important role in radiation physics problems. This paper briefly summarizes our recent work in this area.

2 Muon Production

Muons are produced in *hadronic* cascades mainly via decay of pions and kaons. If space is present to allow mesons to decay before interacting, this decay will tend to dominate all other muon production. In a solid target ‘prompt’ muons

may play a more important role. The physical model [1] for the prompt component includes muons from D -mesons, vector mesons ($\rho, \phi, \omega, J/\psi$), η, η' -mesons along with production via Drell-Yan and low mass continuum annihilation. Muons are less plentiful in *electromagnetic* showers (EMS): Bethe-Heitler $\mu\bar{\mu}$ pairs with lesser contributions from vector mesons produced by γA interactions and positron annihilation. There is coupling between both types of cascades: generation of EMS via decay of π^0 produced in hadronic cascades and conversely – but to a much lesser extent – from hadrons produced in γA interactions. At lepton machines muons from EMS obviously dominate.

3 Muon Interactions

Ionization Energy Loss. The conventional approach to muon energy loss due to atomic excitation and ionization assumes it occurs continuously at a rate equal to the mean stopping power for charged particles in the material traversed. In certain situations fluctuations may be important since they affect the energy subtracted from the muon, the number of energetic electrons (δ -rays) produced in the material, or muon energy-angle correlations introduced by close μe^- encounters. To include these fluctuations and correlations in the MC an energy-transfer cut-off, ϵ_c , is introduced. Events below ϵ_c are treated collectively as a continuous, ‘restricted’ energy loss, above it events are treated by simulating individual μe (Bhabha) scattering with full energy-angle correlation [2,3]. Even the restricted energy loss is subject to fluctuations, which depends on ϵ_c , and follows a Vavilov-type distribution [2]. The latter is difficult to evaluate and to sample from in the MC but it approaches a Gaussian with decreasing ϵ_c . Independent of energy, material or thickness traversed, the quality of the Gaussian approximation is governed by the average number of events (κ_n) one chooses to evaluate individually and becomes acceptable for most purposes when $\kappa_n > 10$ [3]. A modified Gaussian (Edgeworth series) provides a better fit at all values of $\kappa_n \geq 1$ and retains ease of MC sampling [4]. The number of events simulated is chosen from a Poisson distribution with mean of κ_n .

Coulomb Scattering. The conventional approach to multiple Coulomb scattering assumes a Gaussian distribution in projected angle with zero mean and standard deviation dependent on muon momentum and material traversed. It can be shown that the Gaussian increasingly underestimates the tails of the distribution beginning at about 2σ [5]. A more accurate treatment is provided by the Moliere distribution. However, nuclear form factors must be included [6] to describe the correct angular distribution. These objections may be overcome by an approach similar to that of muon energy loss: below cut-off, θ_c treat all events collectively while those with $\theta > \theta_c$ are treated individually. With decreasing θ_c the collective distribution approaches a Gaussian while selection of individual events (Rutherford scattering with form factor) is easily adapted to MC selection. Here also using the Edgeworth series instead of the Gaussian significantly improves accuracy and/or reduces the number of events to be treated individually [4]. The Edgeworth series is considerably simplified here by the symmetry

of the underlying distribution about zero. In both collective and event-by-event treatments, scattering of muons with atomic electrons must be included in a manner consistent with the ionization loss algorithms. The difference between electron and nuclear mass strongly affects the kinematics of individual collisions.

Radiative Processes. For muons with energies above a few hundred GeV, bremsstrahlung and direct e^+e^- production dominate ionization losses especially in heavy materials. Differential cross sections presented in the literature for these processes are too complicated to serve in MC selection routines. Instead these formulae are approximated by parameterizations for which selection is more easily performed [3,7,8]. The model [9] used in MARS [10], agrees with experimental data [11] within a few %. In many applications one requires only the cross-section with respect to energy loss and angular deflection of the muon. Where detailed energy deposition is important one also needs approximations to the angle of the emitted photon in bremsstrahlung and of the angles and energy division of e^+ and e^- in pair production [7]. Thereafter these produced particles are traced using MARS. Radiative processes of muons on atomic electrons are also included.

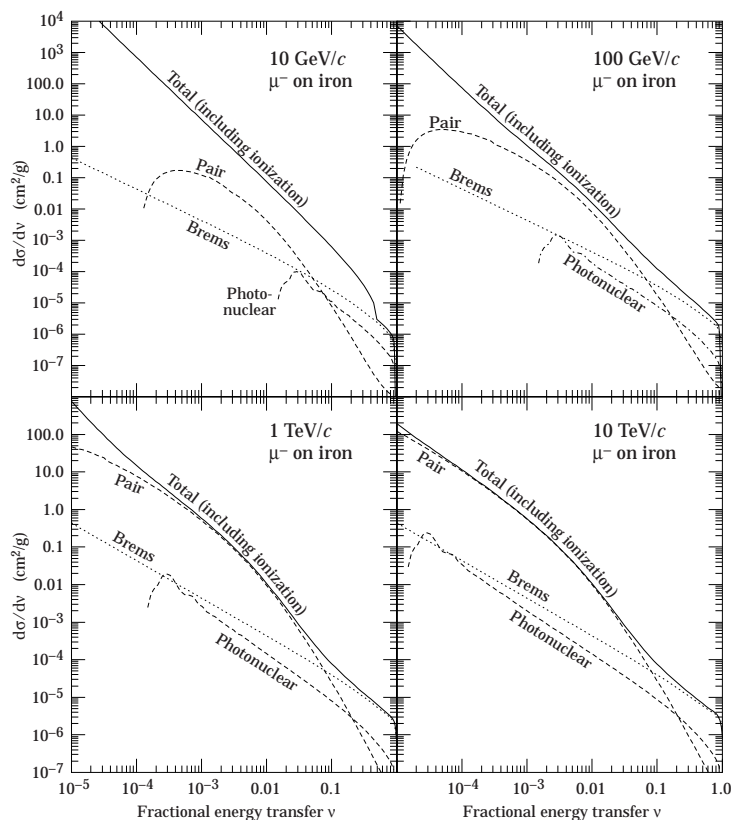


Fig. 1. Fractional energy loss probabilities of muons in iron [12]

Deep Inelastic Interactions. As with the radiative processes, simulation of deep inelastic (photonuclear) muon interactions relies on parameterizations of more accurate descriptions. Existing models for this process are consistent only at the 30% accuracy level while the corresponding mean energy loss is at most 10% of the total. Fig. 1 shows the probability of fractional energy loss for high energy muons in iron due to the various mechanisms as calculated with MARS.

4 Muon Radiation

The MARS code serves well to estimate generic backgrounds due to muons in HEP detectors [13] and to study for multi-TeV radiation shielding [14]. To illustrate the latter, Fig. 2(left) shows transversely integrated fluxes in rock downstream of the 7 TeV LHC beam dump of muons and particles produced in their interactions. Hadrons accompanying the muons can be a source of rock and ground-water activation far from the proton beam dump though the rate is rather low. In the LHC arcs – both for operational and accidental beam loss – muons are generated and traced through the lattice elements over about 350 m length. The magnet geometries and the influence of the field in the aperture as well as in the magnet structure results in an interesting pattern of dose contours in the surrounding rock (Fig. 3(right)). Muons are observed as far as 1.5 km outside the ring in the orbit plane where they contribute – along with the accompanying particles – to both dose and radioactivation.

At $\mu\mu C$ secondary muons determine radiation shielding in the first tens of meters outward of the tunnel. Where beam is dumped the muons cause a significant dose up to 3.5 km downstream [15]. Hadrons from interactions along the muon tracks produce radionuclides in the soil. For 2 TeV muon extracted beam a cylinder 2.5 km long and 2 m in radius must be isolated to keep 3H and ^{22}Na concentration below legal limits.

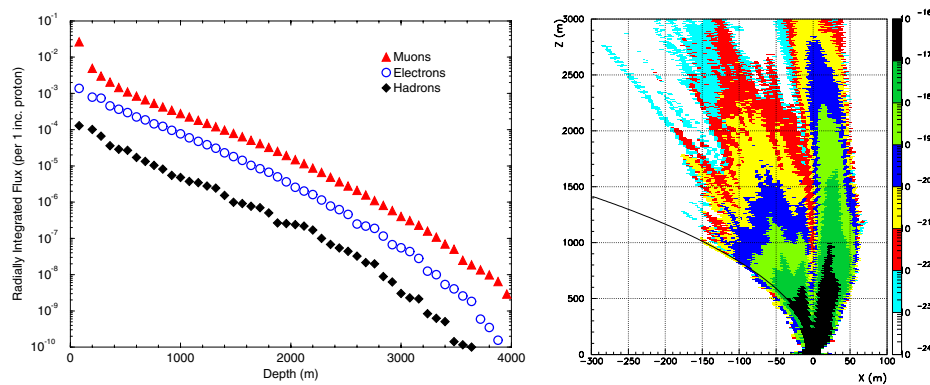


Fig. 2. Transversely integrated flux of muons, e^+e^- , and hadrons in rock downstream of LHC beam dump (left) and isodose contours (Sv/proton) in horizontal plane for a 7 TeV beam accident in LHC arc starting at $X=Z=0$; solid line represents arc

5 Neutrino Interactions

Neutrinos interacting in the human body or its immediate surroundings produce charged particles which may cause biological harm. In simulating these interactions, a neutrino interaction model is called upon which permits selection of energy and angle of each particle: ν, e, μ and hadrons involved in the interaction [16] on an inclusive basis. These particles are then further processed by MARS. The interaction model distinguishes four types of neutrinos ($\nu_\mu, \bar{\nu}_\mu, \nu_e, \bar{\nu}_e$) and identifies a number of interactions for each type of neutrino: deep inelastic interactions via both charged and neutral currents, neutrino-nucleon elastic and quasi-elastic scattering where proton and neutron targets (within a nucleus) are distinguished, neutrino interactions with atomic electrons, and coherent elastic scattering off a nuclear target. All these interactions produce a lepton (ν, e , or μ) in the final state. To first approximation, the formulae for the energy and angle of the lepton are simple enough for use in MC selection. Once selection of the lepton is made, (vectorial) momentum is balanced by imparting the missing momentum to the target nucleon, nucleus or electron. For deep inelastic scattering momentum is balanced by a single π which is then forced to interact in the target nucleus after which the reaction products are followed by MARS.

6 Neutrino-Induced Radiation

So far, in all cases studied where neutrino induced radiation may be a problem, the ‘source’ of the neutrinos is a $\mu\mu C$ or μSR so that energy and direction of the decay ν are readily obtained. These neutrinos propagate almost tangentially to the muon direction in a relatively narrow disk with negligible attenuation. Dose at a given location grows with muon energy roughly as E^3 due to three factors: increase with E of the neutrino interaction cross section and of total energy deposited while the decay angle decreases roughly as m_μ/E . Transverse dimensions of the neutrino disk may be smaller than human dimensions and one must distinguish between *maximum* and *whole body dose* which has legal as well computational ramifications. A useful concept is that of *equilibrium* dose, i.e. dose is proportional to neutrino fluence in the vicinity of its maximum. This applies when a minimal thickness of material (a few meters of soil or equivalent) is present immediately upstream of the ‘phantom’ to which dose is delivered so as to allow the ν -induced cascades to develop fully in the material. The ‘non-equilibrium’ dose, calculated for a bare phantom, is much less than the equilibrium dose – a factor of three at 1 GeV and up to three orders of magnitude for 10 TeV neutrinos. Neutrino doses become surprisingly large for some of the more ambitious muon devices contemplated. For proposed μSR located underground, the off-site dose limit of 0.1 mSv/yr is met 50 m outward from the arc tunnel, but downstream of a 600-m long straight section only at 1.8 and 4.2 km for the 30 and 50 GeV μSR , respectively (Fig. 3(left)). Figure 3(right) shows the large distances (up to 60 km) required to reduce neutrino dose to acceptable levels around a high energy $\mu\mu C$ if no other precautions are taken.

This work was supported by the U.S. Department of Energy.

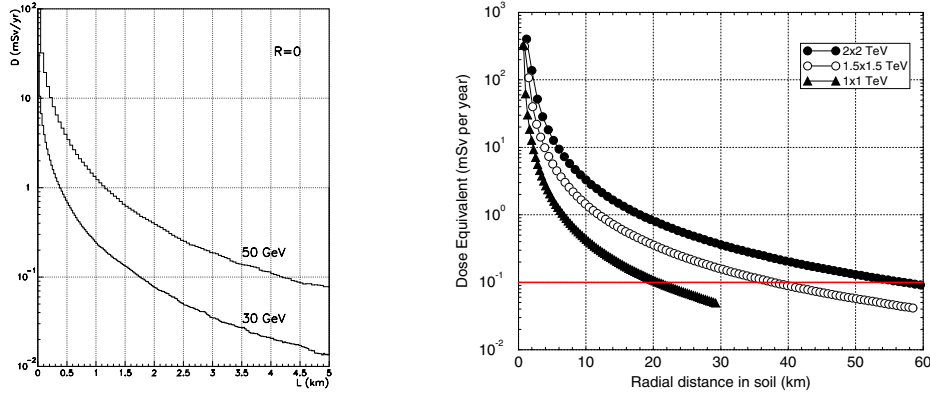


Fig. 3. Annual maximum dose equivalent (mSv/yr) in a phantom embedded in soil *vs* distance downstream of 30 and 50 GeV μ SR straight sections (left) and in a μ C orbit plane with 1.2×10^{21} decays per year *vs* distance from ring center (right)

References

1. A. Van Ginneken: *MUSIM. Program to Simulate Production and Transport of Muons in Bulk Matter*, Fermilab-FN-594 (1992) and FN-610 (1993)
2. A. Van Ginneken: Nucl. Instr. Meth. A **362**, 313 (1995)
3. N.V. Mokhov, S.I. Striganov: In *Handbook of Accelerator Physics and Engineering*. Ed. by A.W. Chao, M. Tigner (World Scientific, Singapore 1999) pp. 234–240
4. A. Van Ginneken: Nucl. Instr. Meth. B **160**, 460 (2000)
5. J.D. Jackson: *Classical Electrodynamics*, 2nd edn. (Wiley 1975)
6. I.S. Baishev, N.V. Mokhov, S.I. Striganov: Sov. J. Nucl. Phys. **42**, 745 (1985)
7. A. Van Ginneken: Nucl. Instr. Meth. A **251**, 21 (1986)
8. N.V. Mokhov, S.I. Striganov: In: *Proc. 9th Advanced ICFA Beam Dynamics Workshop, Montauk, NY, October 15–20, 1995* (AIP, Woodbury 1996) pp. 234–256
9. S.R. Kelner, R.P. Kokoulin, A.A. Petrukhin: Phys. Atom. Nucl. **60**, 576 (1997); A.I. Nikishov: Sov. J. Nucl. Phys. **27**, 677 (1978)
10. N.V. Mokhov: *The MARS Code System User's Guide*, Fermilab-FN-628 (1995); N.V. Mokhov, S.I. Striganov, A. Van Ginneken, S.G. Mashnik, A.J. Sierk, J. Ranft: *MARS Code Developments*, Fermilab-Conf-98/379 (1998); <http://www-ap.fnl.gov/MARS/>
11. E. Berger et al: Z. Phys. C **73**, 455 (1997)
12. D.E. Groom, N.V. Mokhov, S.I. Striganov: Atomic Data and Nuclear Data Tables (2000), LBNL-44742 (2000)
13. N.V. Mokhov: Nucl. Phys. B (Proc. Suppl.) **51A**, 210 (1996)
14. N.V. Mokhov: *Muons at LHC. Part 1: Beam Dumps*, CERN/TIS-RP/TM/95-27 (1995), *Part 2: Arcs and Interaction Regions*, CERN/TIS-RP/TM/96-11 (1996), CERN CMS TN/96-089 (1996)
15. N.V. Mokhov: *Radiation Issues at $\mu^+\mu^-$ Colliders*, Fermilab-Conf-96/367 (1996)
16. N.V. Mokhov, A. Van Ginneken: In *Proc. of ICRS-9 International Conference on Radiation Shielding, Tsukuba, Ibaraki, Japan, October 17–22, 1999*, J. Nucl. Sci. Tech. **1**, pp. 172–179 (March 2000); Fermilab-Conf-00/065 (2000)

Utilization of Monte Carlo Calculations in Radiation Transport Analyses to Support the Design of the U.S. Spallation Neutron Source (SNS)

J.O. Johnson

Oak Ridge National Laboratory, P. O. Box 2008, MS-6363, Oak Ridge, Tennessee
37831-6363, USA

Abstract. The Department of Energy (DOE) has given the Spallation Neutron Source (SNS) project approval to begin Title I design of the proposed facility to be built at Oak Ridge National Laboratory (ORNL) and construction is scheduled to commence in FY01. The SNS initially will consist of an accelerator system capable of delivering an approximately 0.5 microsecond pulse of 1 GeV protons, at a 60 Hz frequency, with 1 MW of beam power, into a single target station. The SNS will eventually be upgraded to a 2 MW facility with two target stations (a 60 Hz station and a 10 Hz station). The radiation transport analysis, which includes the neutronic, shielding, activation, and safety analyses, is critical to the design of an intense high-energy accelerator facility like the proposed SNS, and the Monte Carlo method is the cornerstone of the radiation transport analyses.

1 Introduction

The use of neutrons in science and industry has increased continuously during the past fifty years with applications now widely used in physics, chemistry, biology, engineering, and medicine. Within this history, the relative merits of using pulsed accelerator spallation sources versus reactors for neutron sources have been debated. A consensus from the neutron scattering experiment community has finally emerged endorsing short pulse spallation sources as a high priority option for the future. To address this future need, the Department of Energy (DOE) has initiated the design of the Spallation Neutron Source (SNS) and given approval for the proposed facility to be constructed at Oak Ridge National Laboratory (ORNL). The DOE directive is to design and build a short pulse spallation source in the 1 MW power range with sufficient design flexibility that it can be upgraded and operated at a higher power at a later stage.

A diverse representation of scientific and technical disciplines are required to produce a successful spallation neutron source design, including accelerator and target station physics and engineering, remote handling, neutronics, materials, thermal hydraulics, and instrumentation. Within each of these disciplines, there are multiple layouts and designs that must be eventually integrated into a reference design. The radiation transport analysis, which includes the neutronic, shielding, activation, and safety analyses, is critical to almost all operations

important to the design and construction of an intense high-energy accelerator facility like the proposed SNS. These analyses are fundamentally important because of the impact on conventional facility design, maintenance operations, and because the costs associated with incorporating the results of the radiation transport analysis comprise a significant part of the total facility costs. Towards the goal of producing the most optimum design, traditional concepts utilized in current facilities are being re-examined, and new concepts are being considered to meet the higher power challenge of the SNS. Since target stations are vital components of spallation neutron sources, the design of the target stations is critical to determining the overall performance of the facility as a neutron source. A brief overview of the Title I SNS design is presented in Section 2. The general philosophy adopted for the radiation transport analysis of the SNS facility is presented in Section 3, and a brief summary of the calculational methodology is discussed in Section 4.

2 The Proposed U.S. Spallation Neutron Source

The U.S. SNS proton accelerator system consists of a front-end ion source, linac, high-energy beam transport system, and accumulator ring. The ion source produces negative hydrogen ions that are formed into a pulsed beam and accelerated to a energy of 2.5 MeV. This beam is delivered to a large linear accelerator that accelerates the H^- beam from 2.5 MeV to 1 GeV. Three different types of accelerators are used in the SNS design. The first two, the drift tube linac and the coupled-cavity linac are made of copper, operate at room temperature, and accelerate the beam to about 200 MeV. The remainder of the acceleration is accomplished by super-conducting niobium cavities, cooled with liquid helium to an operating temperature of 2 K, which accelerate the beam to 1 GeV. The proton beam is then transported to an accumulator ring structure, which bunches and intensifies the ion beam for delivery onto the mercury target to produce the pulsed neutron beams. The intense H^- beam from the linac is wrapped into the ring through a stripper foil that strips the electrons to produce the protons that circulate in the ring. Approximately 1200 turns are accumulated, and then all the protons are extracted at once, producing a pulse of approximately 0.5 microseconds that is delivered to the target at a rate of 60 times a second.

The basic function of the SNS target system is to produce 18 to 24 lower-energy (<1 eV), short-pulsed (approximately tens of microseconds) neutron beams optimized for neutron scattering instruments from the short pulsed (<1 microsecond, 60 Hz, 17 kJ/pulse), high-average power (1 MW), 1 GeV proton beam. The proton beam target is liquid mercury flowing inside a stainless steel container. The target is positioned within a layered iron, and high-density concrete shielding monolith approximately 12 meters in diameter. An ambient water moderator and a composite ambient water/supercritical hydrogen cryogenic moderator are positioned under the target and two supercritical hydrogen cryogenic moderators are positioned above the target. Moderator poisoning and decoupling are used to manipulate the time width and magnitude of the neutron

pulses. The moderators also utilize ambient water pre-moderators on some sides and are surrounded by a heavy water cooled beryllium inner reflector region and lead outer reflector region. The core region, which includes the target, moderators, and beryllium/lead reflector, is contained inside a 3.5-meter diameter vessel. The target is to be installed and removed horizontally into an adjacent service cell using a target cart assembly. The target service cell is located behind the target cart assembly and measures 6 meters wide by 31 meters long by 12 meters high. Work will normally be performed via remote handling techniques behind a one-meter thick high-density concrete wall. The other core components (e.g. moderators, reflector plug assemblies, etc.) are designed for vertical removal and are serviced in the target service cell. There are 18 to 24 neutron beam lines viewing the moderators, 9 to 12 on each side, and approximately equally spaced in angle. Each beam line has an independently operable shielding shutter controlled by the experimentalists. The beam lines are located at two levels; 9 to 12 lines directed at the ambient water and composite moderators under the target, and 9 to 12 directed at the cryogenic hydrogen moderators above the target. The shielding extends to a radius of approximately 8 meters at the beam line level to provide a region for the neutron beam T0 choppers.

3 Radiation Transport Analysis Philosophy

The radiation transport analysis of the SNS can be subdivided into four categories: (1) neutronic performance; (2) energy deposition distribution; (3) material damage and activation; and (4) shielding design and analysis. A strategy utilizing Monte Carlo calculations and coupled Monte Carlo and multi-dimensional discrete-ordinates calculations is being implemented to perform the radiation transport analysis. Within each of these four areas, there is an optimization procedure to follow which will yield the best design allowing for the interdependent relationships the four categories have with respect to each other and the implications associated with the overall facility design. Collaborative efforts interfacing the radiation transport analysis with the neutron and proton beam transport systems design, thermal hydraulic analysis, structural materials selection, remote handling/target maintenance requirements, and general facility layout are being implemented.

The determination of the neutronic performance involves characterizing the target station and accelerator radiation environments. Calculations are being performed to determine the neutron, proton, heavy ion, and gamma-ray flux spectra as a function of time, energy, and space for all components of the target station (target, moderators, reflectors, etc.) and accelerator (linac, ring, beam dumps, etc.). These calculations optimize (maximize or minimize) these distributions depending on the target station or accelerator component in question and desired design criteria. Within this analysis, the target/moderator/reflector configurations and material selections are being determined to yield the optimum neutron source for the experiment stations. The energy deposition distribution analysis is directly tied to the neutronic performance and interfaces with the

thermal hydraulic analyses to determine the optimum accelerator and target station design with respect to heat transfer and fluid flow requirements. Energy deposition profiles are also being determined for the beam dumps associated with the accelerator design. These calculations are being performed for all components of the SNS requiring heat removal and/or subjected to thermal shock phenomena.

Material damage and activation analyses are being performed to assess facility component lifetime estimates and aid in the structural materials selection process. In particular, gas production, displacement damage, and primary knock-on atom (pka) spectra are being determined for target station and selected accelerator components. Material selections are being determined utilizing this information in conjunction with additional material issues (compatibility, machinability, costs, etc.). Activation analyses are being performed to determine facility radioactive waste streams, on-line material reprocessing requirements (mercury, liquid hydrogen, cooling water, etc.) and remote handling/maintenance requirements. Analyses are also being performed to determine background radiation levels within all parts of the facility for normal operation, shutdown, and postulated accident scenarios (single-failure/anticipated events and unlikely design basis accidents).

Shielding a spallation neutron source is more difficult than shielding a reactor neutron source because spallation neutrons have higher energies than fission neutrons. For a spallation neutron source, the highest-energy cascade neutrons approach the energy of the incident proton beam. These high-energy neutrons are extremely penetrating, and well-designed shielding is needed to prevent them from causing excessive biological dose rates. Shielding design calculations have been performed for all sections of the SNS facility. Biological shields are being designed and assessed for the proton beam transport system and associated beam dumps, the target station, the target service cell, and utility vault. Calculations are being performed for normal operation, catastrophic accident scenarios, and shutdown activation sources. Shield designs are being integrated into the overall facility design and optimized to achieve as low as reasonably achievable dose to the facility personnel, visiting experimentalists, and sensitive electronic equipment. The SNS design, consistent with other DOE accelerators, includes very rapidly-acting and highly-reliable automatic systems that cut off the beam when it is not in its desired path (or if personnel access to the tunnel is attempted during operation of the beam). The automatic beam cutoff would function to limit personnel exposures to a small number of micro-Sieverts even for worst-case beam-control accidents.

All four of these principal categories effect the environmental impact and safety design of the SNS facility. The SNS facility safety (personnel, public, environment, equipment, etc.) will be assured through reliance on both instrumentation-based active safety systems and passive shielding.

4 Radiation Transport Computational Methodology

The accuracy of the radiation transport analysis is dependent on the utilization of state-of-the-art cross-section data and computer codes. The MCNPX [1] code system has become the cornerstone computational tool used for the radiation transport analyses now that it has been officially released. MCNPX is the resulting code system from the merger, advancement, and enhancement of the LAHET [2] and MCNP4B [3] codes. The three-dimensional, multimedia, high-energy nucleon-meson transport portion (LAHET) of MCNPX is being used to obtain a detailed description of the nucleon-meson cascade. This Monte Carlo code takes into account the slowing down of charged particles via the continuous slowing-down approximation; the decay of charged pions and muons; and inelastic nucleon-nucleus and charged-pion-nucleus (excluding hydrogen) collisions through the use of a multitude of high energy physics models. The MCNP4B portion of MCNPX is being used to perform the transport of the low energy ($E < 20$ MeV) neutrons and gamma rays. For the shielding design of high power spallation targets and hadron accelerators with energies up to 2 GeV, it is beneficial to use deterministic methods for the shielding calculations instead of Monte Carlo methods because deep penetration problems and/or shield streaming problems require very high particle numbers to obtain good statistics, and high particle numbers typically lead to high computational times. Typically, in the Title I design phase of a facility like SNS, the project schedule will not accommodate Monte Carlo calculations requiring long running times. For the SNS shielding analyses, two approaches are being implemented. One approach is to couple MCNPX with the ANISN [4] one-dimensional, DORT [5] two-dimensional, or TORT [6] three-dimensional discrete ordinates deterministic transport codes to analyze the deep penetration shielding requirements. In these analyses, the newly developed Monte Carlo to discrete ordinates coupling codes (MTA, MTD, and MTT) [7], and the new HILO2k coupled 83-neutron, 22- gamma-ray cross-section library [8] are being used. HILO2k is a new high-energy neutron and photon transport cross-section library containing neutron cross sections to 2 GeV and photon cross sections to 20 MeV. To address the shielding for shutdown activation sources, the MCNPX code provides the required input data for the isotope generation and depletion code, ORIHET95 [9], which utilizes a matrix-exponential method to study the buildup and decay of activity for any system in which the nuclide production rates are known. The combination of the MCNPX(LAHET) generated high-energy spallation product source and the MCNPX(MCNP4B) low energy neutron activation source yields the radionuclide concentrations, radioactivity, and time dependent decay gamma source spectra, as a function of buildup and decay time.

5 Conclusions

Radiation transport analyses of the SNS design indicates that a very attractive short-pulse neutron source can be constructed using liquid mercury as the

target material. Within this effort, critical path research and development activities have been identified to validate design concepts and allow future upgrades to higher power levels. A radiation transport design strategy utilizing coupled low and high energy Monte Carlo calculations and multi-dimensional discrete ordinates calculations has been devised and implemented to characterize the neutronic performance of the proposed SNS and perform the requisite radiation transport design analyses. The radiation transport analyses are being interfaced with the neutron and proton beam transport systems design, thermal hydraulic analysis, structural materials selection, remote handling/target maintenance requirements, and general facility layout design. Lessons learned from existing facility experience are being utilized in the design. Design modifications are constantly being addressed to ascertain the impact the modifications have on the neutronic performance or radiological safety of the SNS. Future analyses will continue to refine the models to account for the details of the advanced Title I and Title II designs that effect the neutronic performance, radiological safety, or impact environmental concerns.

References

1. H.G. Hughes et.al.: 'MCNPX for Neutron-Photon Transport'. In: *International Conference on Mathematics and Computation, Reactor Physics & Environmental Analysis in Nuclear Applications*, American Nuclear Society, Madrid, Spain, September 27-30, 1999
2. R.E. Prael, H. Lichtenstein: *User Guide to LCS: The LAHET Code System*. LA-UR-89-3014, Los Alamos National Laboratory, (September 1989)
3. J.F. Briesmeister, Ed.: *MCNP - A General Monte Carlo Code for Neutron and Photon Transport: Version 4B*. LA-12625-M, Los Alamos National Laboratory (March 1997)
4. W.W. Engle Jr.: *A User's Manual for ANISN: A One-Dimensional Discrete Ordinates Transport Code with Anisotropic Scattering*. Union Carbide Nuclear Division Report K-1693 (1967)
5. W.A. Rhoades, R.L. Childs: *Nuclear Science & Engineering* **99**, 88 (1988)
6. W.A. Rhoades, R.L. Childs: *Nuclear Science & Engineering* **107**, 397 (1991)
7. F.X. Gallmeier, R.E. Pevey: 'Creation of a Set of Interface Utilities to Allow Coupled Monte Carlo/Discrete Ordinates Shielding Analysis'. In: *AccApp'99, The Third American Nuclear Society Topical Meeting on Nuclear Applications of Accelerator Technology*, Long Beach CA., November 14-18, 1999
8. R.A. Lillie, F.X. Gallmeier: 'HILO2k: A Coupled Neutron-Photon Transport Cross-Section Library for Neutron Energies Up To 2000 MeV'. To be published in: *AccApp'00 - The Fourth American Nuclear Society Topical Meeting on Nuclear Applications of Accelerator Technology*, Washington D.C., November 12-16, 2000
9. P. Cloth et al.: *HERMES, A Monte Carlo Program System for Beam Material Interaction Studies*, KFA Juelich, Report Jul-2203 (1988)

Deep Penetration Monte Carlo Calculations for the European Spallation Source ESS

I. Koprivnikar and E. Schachinger

Technische Universität Graz, Institut für Theoretische Physik, Petersgasse 16, A-8010
Graz, Austria

Abstract. The design of high intensity spallation sources, like the European Spallation Source (ESS) [1] with a proton beam energy of 1334 MeV and a beam power of 5 MW, requires best possible estimates for the biological shield. The use of Monte Carlo simulation techniques in the shielding design calculations represents an increasingly important alternative to the traditional semi-empirical calculations and multi-dimensional discrete ordinates calculations. In this paper, a Monte Carlo shielding design calculational strategy which utilizes a large body of variance reduction techniques is described. This strategy was implemented to perform a rough evaluation of the proposed conceptual design of the ESS target station shield.

1 Introduction

Shielding design is important for the construction of high-energy accelerator and spallation source facilities, since the cost for the radiation shielding contributes a considerable part of the total cost. Moreover, a shield that is too thick reduces the particle fluxes needed by increasing the distance to the detector. On the contrary, the shield that is too thin results in an unwanted additional radiation exposure to personnel.

Intrinsic to shielding calculations are problems with accuracy as large flux attenuations of several orders of magnitude are to be traced through thick shields. Spallation sources produce neutrons covering about 14 decades in energy. The presence of high-energy deeply penetrating neutrons as a result of nucleon-nucleon spallation reactions complicates the design of the biological shield. The high-energy neutrons have a strong angular dependence and they can, particularly in the extreme forward direction of the proton beam, reach energies up to the energy of the incident protons. Neutrons are attenuated by elastic and inelastic scattering, and especially, below the lowest energy threshold for inelastic scattering (the pion production threshold is about 290 MeV) they can build up and penetrate the shield in large numbers since elastic scattering is not an effective means of absorbing high-energy neutrons. Thus, forward-going neutrons constitute the most significant shielding problem. Moreover, the attenuation of the high-energy neutrons generates (i) secondary evaporation neutrons, which are emitted isotropically and have energies down to the thermal region, and (ii) additional secondary gamma rays. Thus, deeply penetrating neutrons together with their progeny determine the local dose rate inside the shield and on the outer shield's surface.

The biological shield of a neutron spallation source can be designed by employing different computational approaches like the classical methods, as for instance discrete ordinate methods or semi-empirical calculations based on the Moyer model, and, nowadays, Monte Carlo (MC) based methods. The increasing speed and memory capacity of modern computers together with the implementation of variance reduction techniques turned the application of MC codes in the design of biological shields into an alternative of growing importance. Advantages of the MC shielding simulation are: (i) the particle distributions in the complicated geometry around the target assembly can be precisely evaluated, (ii) charged particles and photons can be treated, (iii) the shield with its beam ducts and holes, where the narrow gaps provide paths for radiation streaming, can be modeled by a detailed description, and (iv) no high energy material-dependent cross-section library is required.

By applying different variance reduction techniques in the MC simulations, a proper convergence of the tally scores within reasonable computing time (most importantly, for the tallies near and at the outer boundaries of the shield) can be achieved. Therefore, the chosen random walk sampling amounts to preferentially sampling “important” particles at expense of “unimportant” particles. However, by use of proper variance reduction techniques the efficiency of MC calculations can be increased dramatically.

We present in this paper some deep penetration MC calculations in an attempt to verify the preliminary conceptional design of the target station shield of the ESS made by Forschungszentrum Jülich.

2 Calculational Strategy and Geometry Models

The new LAHET [2] /MCNP [3] code merger MCNPX [4] was the main calculational tool used in our deep penetration study. The simulations were performed in a two-step process.

2.1 MC Calculations of the Particle Flux Spectra from the Target Vicinity

In a first step MCNPX was employed to obtain the high energy, angular dependent neutron and proton leakage from the target-moderator-reflector (TMR) system. This required the development of an exact geometrical TMR model which is based on the one used for the simulation of the JESSICA experiment [5]. JESSICA [6] is a 1:1 sized ESS TMR mock-up and test facility for advanced cold moderators for high-power spallation neutron sources. A cutaway view of the TMR geometry model used is shown in Fig. 1.

In all these calculations the pre-equilibrium model which describes the situation after the intranuclear cascade was active. This step is an analog simulation of the multiple particle transport, where a detailed description of the nucleon-meson cascade is obtained. Because primary low-energy neutrons in the lead-reflected-target vicinity contribute negligibly to the dose at the target station

shield surface, it was able to set the neutron low energy cutoff to 10 MeV for all the calculations in the first step. The transport parameters of all neutrons and protons leaving the cylindrical reflector of the TMR region were saved on file to obtain the proper source for the deep penetration transport in the next stage of the calculations.

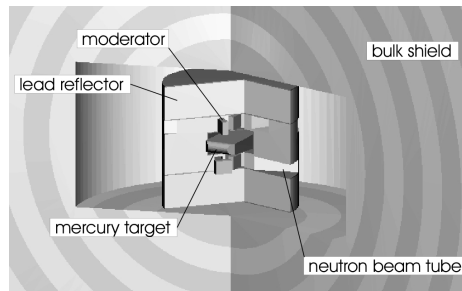


Fig. 1. Cutaway view of the MC geometry used to obtain the proper source for the bulk shielding calculations

2.2 Bulk Shielding Calculations

In the second stage the particle penetration through the target station shield is simulated. The new expanded MCNPX nuclear data tables (proton and neutron libraries to 150 MeV) were used in our simulations. These enable a detailed description of the nuclear structure effects up to an energy of 150 MeV, where the simpler INC physics can model reaction probabilities adequately. Thus, also secondary neutrons from high energy protons are included in the problem. A simplified cylindrical model of the target station shield was constructed to determine the radiation flux spectra and the bulk shielding requirements. The starting-point for the construction were the preliminary geometric parameters of the ESS ([7], Section 4.6.5). An effective modeling within the MCNPX framework required a subdivision of the iron-concrete shield into concentric spherical shells. An incremental radius of 25 cm proved to be most successful. A model of the ESS target shield divided into concentric spheres is presented in Fig. 2.

We analyzed the influence of different biasing techniques and their combinations on the efficiency of calculations. A combination of two techniques proved to be most efficient, namely, energy dependent weight windows and an exponential transform technique. The weight window is a space-energy-dependent splitting and Russian roulette technique, and the exponential transform technique stretches distances between collisions in a defined direction. The spatial weight windows (only one energy range) are obtained from previously optimized cell importances from the geometry-splitting technique. On the basis of these, the parameters for the energy dependent weight windows were obtained empirically

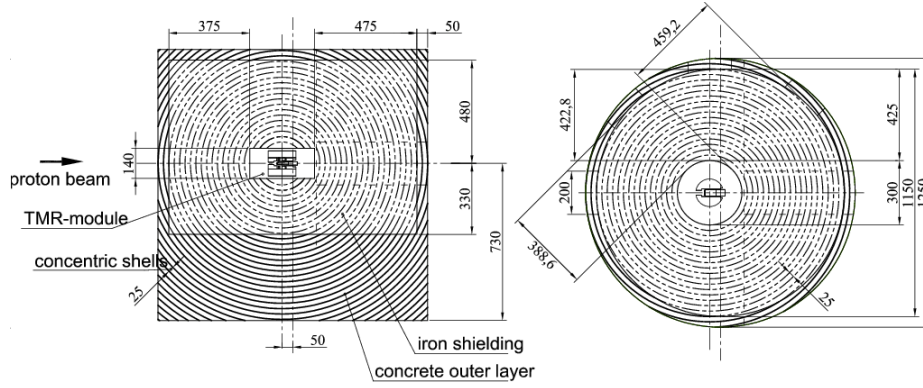


Fig. 2. Schematic view of the ESS target station shield. All dimensions in cm

by making a careful statistical analysis of history distributions. As an example, Fig. 3 demonstrates neutron weight windows used for the computation of the radiation flux spectra in the proton beam direction. In all calculations, special care was taken to match the space-energy weight windows at the boundaries at which the equilibrium neutron spectrum is disturbed by a change in the shielding material. To additionally increase the calculational efficiency, space-dependent

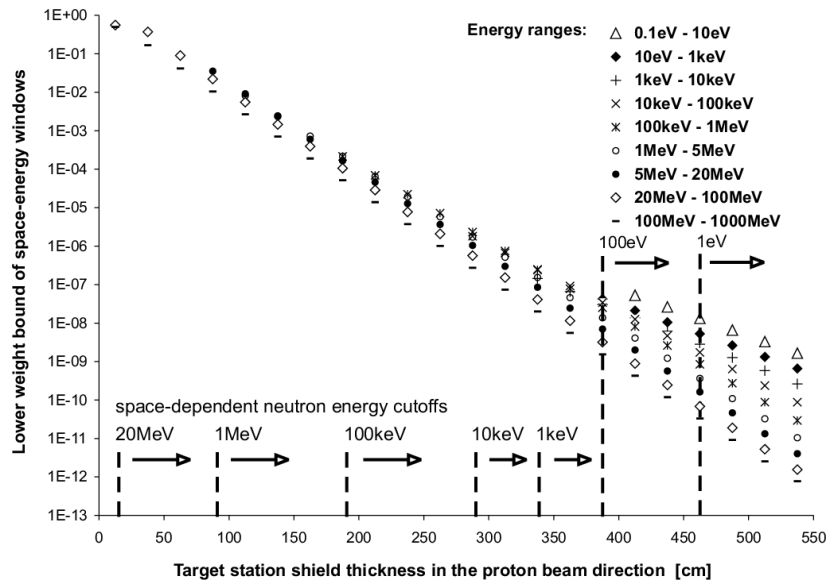


Fig. 3. Weight windows assigned to the spherical shells on the thicker shield side in the proton beam direction

neutron energy cutoffs were employed to terminate particle tracks of negligible importance for the dose rate on outside shield surfaces (see Fig. 3).

3 Shielding Analysis

The described calculational strategy allows to determine the neutron fluence spectra at different locations within the shield and makes it possible to calculate the neutron ambient dose equivalent rates on the outer surface of the biological shield. These rates were found by folding the corresponding fluence to dose conversion factors with the local neutron fluences. For this reason, the ambient dose conversion coefficients included in MCNPX, which are based on the ICRP74 Recommendations [8], were extended to the high energy region [9]. In Tab. 1 the neutron dose values at the outer perimeter of the shield are compared to those of the preliminary study of the target station shielding for different angles relative to the incident proton beam direction. The preliminary shielding design was scaled by FZ-Jülich using a semiempirical code CASL [10] as well as a method of coupling HETC with ANISN [11]. The results obtained using MCNPX indicate lower dose values than the results of the preliminary study calculated with the HETC-ANISN method. The comparison indicates also, particularly in the backward direction of the proton beam, that the CASL dose rates have been overestimated.

Table 1. Comparison of neutron dose rates outside the bulk shield calculated with MCNPX and values of the preliminary study performed by FZ-Jülich.

MCNPX deep penetration calculations				ESS shield design calculations made by FZ-Jülich				
Angle to the beam (degree)	Shield thickness		Neutron dose rate (μSv/h)	Angle to the beam (degree)	Shield thickness		CASL (μSv/h)	HETC ANISN (μSv/h)
	(cm)				(cm)			
	iron	concrete			iron	concrete		LESS THAN
0	475	50	0.7 (9%)	0 - 20	520	40	1 - 10	7.5
45	460	50	0.6 (11%)	20 - 40	470	40		7.5
90	423	50	0.3 (13%)	80 - 100	460	30	1 – 10	7.5
135	389	50	0.5 (18%)	100 - 150	420	30		7.5
180	375	50	0.8 (20%)	150 - 180	390	30	10 - 100	7.5

Furthermore, shielding design calculations have been performed in order to get a neutron dose rate less than $1 \mu\text{Sv/h}$ at the shield surface. These results indicate that an iron shield of 475 cm thickness and an outer concrete layer of 50 cm thickness in the proton beam direction seem to be reasonable. Namely, during normal operation the shielding should be designed in such a way that dose rate on accessible surfaces of the shield is less than $5 \mu\text{Sv/h}$.

Moreover, the photon dose equivalent rates as a result of the prompt decay can also be determined within and outside of the shield. Our preliminary results prove that in the case of an iron-concrete shield prompt photons are an important component of the total dose rate.

4 Conclusions

A calculation strategy utilizing the MCNPX code, suitable for performing shielding design analyses, is described. It was used in an attempt to verify the preliminary conceptional design of the target station shield of the ESS. The results obtained using this strategy show partly lower values than those from the preliminary study calculated with the HETC-ANISN method. In a future analysis, the shielding models need to be refined to account for beam ducts and holes in the target station shield.

References

1. <http://www.fz-juelich.de/ess/ess.html>
2. R.E. Prael, H. Lichtenstein: *User Guide to LCS: The LAHET Code System*, Los Alamos National Laboratory, September 1989
3. J.F. Briesmeister, Ed.: *MCNPTM - A General Monte Carlo N-Particle Transport Code, Version 4B*, Los Alamos National Laboratory, LA-12625-M, March 1997
4. L.S. Waters, Ed.: *MCNPXTM User's Manual, Version 2.1.5*, Los Alamos National Laboratory, November 1999
5. <http://www.fz-juelich.de/ess/INT/JESSICA/JESSICA.html>
6. H. Tietze-Jaensch: *Physica B* **276-278**, 102 (2000)
7. G. Bauer et al.: *The ESS Target Station Concept*, Offprint from The ESS Feasibility Study, ESS-96-60-T, December 96
8. *Conversion Coefficients for use in Radiological Protection against External Radiation*, ICRP Publication 74, September 1995
9. A.V. Sannikov, E.N. Savitskaya: *Radiation Protection Dosimetry* **70**, 383 (1997)
10. H. Schaal, D. Filges et al.: *Shielding Calculations for ESS using the CASL Computer Codes (Computer Aided Shield Layout)*, Forschungszentrum Juelich GmbH, ESS 96-43-T, July 1996
11. H. Schaal, D. Filges, G. Sterzenbach: *Methods to Calculate Spallation Source Shields, Comparison with Experiments and Application to ESS*, SATIF 4, Workshop Proceedings, Knoxville, Tennessee, USA, September 1998

Validation of MC Models of Spallation Reactions in Thin and Thick Targets in the GeV Range

F. Goldenbaum¹, M. Enke², D. Filges¹, J. Galin³, C.-M. Herbach²,
D. Hilscher², U. Jahnke², A. Letourneau³, B. Lott³, R.-D. Neef¹,
K. Nünighoff¹, N. Paul¹, A. Péghaire³, L. Pienkowski⁴, H. Schaal¹,
U. Schröder⁵, G. Sterzenbach¹, A. Tietze¹, V. Tishchenko², J. Toke⁵, and
M. Wohlmuther¹

¹ Forschungszentrum Jülich GmbH, Institut für Kernphysik, 52425 Jülich, Germany

² Hahn-Meitner Institut Berlin GmbH, Glienickerstr.100, 14109 Berlin, Germany

³ GANIL-Caen BP5027, 14076 Caen cedex 05, France

⁴ Heavy Ion Laboratory Warsaw University, Pasteura 5a, 02-093 Warszawa, Poland

⁵ University of Rochester, Rochester, New York 14627, USA

Abstract. In the framework of new projects of intense spallation neutron sources an extensive experimental and theoretical effort is devoted to the precise prediction and optimization of the targets and shielding in terms of reaction cross sections, hadronic interaction lengths and usable neutrons produced in proton induced spallation reactions. Strong constraints on Monte-Carlo high energy transport codes are put by a measurement campaign of the NESSI (*NEutron Scintillator and Silicon detector*) collaboration. While the predictive power of inter- and intra-nuclear cascade models coupled to evaporation codes and transport systems is excellent as far as neutron production in thick targets is concerned, there are considerable discrepancies not only between experiments and models, but also among the different codes themselves when regarding charged particle production in thin targets. In the current contribution a representative validation will be executed and possible deficiencies within the codes are elaborated.

1 Introduction

A renaissance of interest for energetic proton induced production of neutrons originates recently by the inception of new projects for target stations of intense neutron spallation sources [1], accelerator-driven nuclear reactors nuclear waste transmutation and also the application for radioactive beams or the production of tritium (APT project in the US).

In this framework the most important question is to determine the most efficient way to convert the primary beam energy into neutron production. Although the task has been quite successfully investigated experimentally by varying the incident proton energy for various target materials and a huge collection of different target geometries – providing an exhaustive matrix of benchmark data – the ultimate ambition is to increase the predictive power of transport codes currently on the market. Reaction cross sections, hadronic interaction lengths, averaged neutron multiplicities, neutron multiplicity and energy distributions of neutrons are investigated in order to validate codes considered in the present contribution.

Unlike older measurements providing only average neutron multiplicities the NESSI collaboration has very successfully extended experimentally the available information by the eventwise measurement of the neutron multiplicity (dM_n/dN) [2] (and references therein) for different incident proton energies, various target materials and a large number of different cylindrical target geometries using a high efficient 4π gadolinium loaded scintillator detector [3].

In the present contribution the accent is put on the theoretical predictions obtained by the application of different high energy program suites such as the HERMES, MC4 [4,5], LCS [6] or MCNPX [7]. The description of the essential constituents and concatenations of the various program packages will be subject of another contribution within the MC2000 conference.

2 Comparison Between Experiment and MC-Approach

A study was performed in order to investigate the predictive power of the combination of various codes by intercomparing theoretical models and confronting the different approaches with experimental results [2,8]. We will outline the influence of important parameters optionally chosen in the models and finally point out some possible deficiencies in the models which shall be amended. While the production of neutrons is generally well described over a broad range of incident energies and different target geometries, there are big discrepancies with experimental data and among the different codes themselves when looking at the charged particle production cross sections in thin targets. Due to the multitude of possible interlinkings of these models and the plurality of adjustable options and parameter within these codes here only a representative selection is executed. This repertoire however convinces already of the bodacious describability of the complex circumstances regarding neutron production in thick targets. In the following for LCS/MCNPX and HERMES a “standard” set of parameters was applied. The RAL evaporation-fission model [9] and the HETC level density have been selected. In addition the cutoff parameter for particles escaping during INC phase was set to 7 MeV. If not differently specified in the following all calculated observables will include the correction for the precise detector response, respectively. The details of the experimental setup can be found elsewhere [2,8].

2.1 Reaction Cross Section and Hadronic Interaction Length

For measurements using the 4π neutron detector BNB [2,3] and thick targets of the order of several cm in diameter and length the key observables are the neutron multiplicity M_n (measured eventwise!) and the reaction probability P_{reac} .

The hadronic interaction length for 1.2 GeV p induced reaction on W, Hg and Pb following the MC-approach correspond with the experimental values [2] of 10.84 ± 0.2 , 15.06 ± 0.3 and 18.00 ± 0.3 cm, respectively. Incident energy dependence is weak. The experimental reaction cross section σ_{reac} as deduced from $1-P_{\text{reac}}$ amounts to $\sigma_{\text{reac}} = 1.69 \pm 0.03$, 1.64 ± 0.05 and 1.46 ± 0.03 barn as compared to calculated values (HERMES) of 1.73, 1.71 and 1.62 barn for W, Hg and Pb, respectively. This eminent conformity is confirmed also by the LCS2.70 or MCNPX code and shows that the observable σ_{reac} is well under control.

2.2 Neutron Multiplicities

The average number of neutrons produced per incident proton M_n/p can be derived from the independently measured product of the reaction probability P_{reac} and the mean number of neutrons per inelastic reaction $\langle M_n \rangle$. Representative as a function of target length and for the two energies 1.2 and 2.5 GeV Fig. 1 shows M_n/p for Hg, Pb and W. The solid line presents the HETC+MORSE calculation using the RAL evaporation model, $B_0 = 10$ for Pb, $B_0 = 8$ for Hg and W, option fission and elastic scattering switched on. After considering the detector response the theoretical prediction (dashed line) agrees completely with the experimental data (symbols) over a broad range of geometries, target materials and incident energies. The observed shift towards higher M_n/p for thicker targets is related to the increase of $\langle M_n \rangle$ due to secondary reactions and the increase of P_{reac} with target thickness.

In contrast to previous measurements the event-wise character of the experiment NESSI allowed to gain access even to the distributions dM_n/dN rather than average values only. As a general tendency for all incident proton energies and target geometries the model predictions are in good agreement not only as far as the absolute values, but also the shape of the M_n -distributions is concerned as demonstrated in Fig. 2. For all codes under consideration the deviation between experiment and model for P_{reac} and $\langle M_n \rangle$ is well below 8% except for peripheral reactions (low neutron multiplicity) on thin targets, where large deviations are obvious. The decrease of the latter deviations are due a compensation effect to be discussed below.

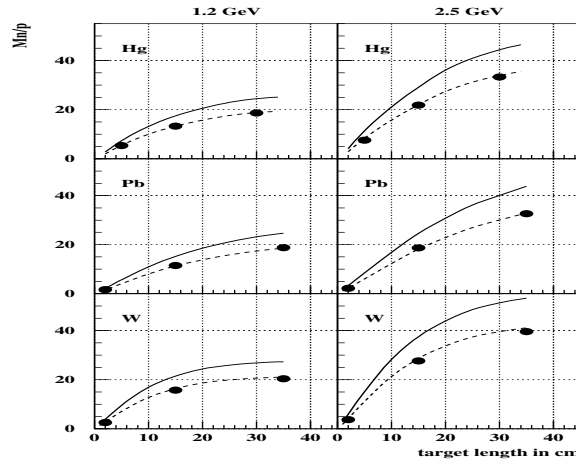


Fig. 1. Average neutron multiplicity produced per incident proton M_n/p as a function of target thickness (diameter 15cm) for 1.2 and 2.5 GeV p+Hg, Pb and W. Solid line: HETC+MORSE, dashed line: HETC+MORSE with detector efficiency taken into account, ●: NESSI exp. data

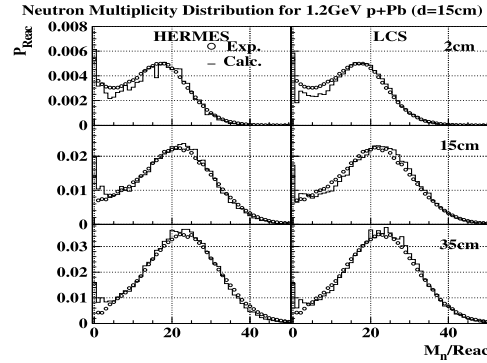


Fig. 2. Neutron multiplicity distributions following the reaction 1.2 GeV p+Pb for different target thicknesses (diameter 15cm). Histograms: HETC+MORSE(left) and LCS2.70(right), \bullet : NESSI exp. data

3 Deficiencies and Particular Variations Within the Codes

The previous section documented a very good general agreement between experimental and calculated neutron multiplicities and reaction cross sections for thick targets. If one decouples however the entire transport of the whole particle ensemble within thick targets and regards the primary reaction (one single nuclear reaction in thin targets) and specific decay channels (protons, neutrons, π ,...) separately, then serious inconsistencies not only between experiment and simulation, but also among the codes themselves show up. This already indicates a kind of compensatory effect or redistribution of the total available energy in thick as compared to thin targets.

More specifically it is obvious e.g. that using BERTINI-like intra-nuclear cascade codes [10] we observe thermal excitation energy distributions *in thin targets* which are extending to larger values than the distributions of the INCL2.0 [11] calculations do for the same incident proton energy – as demonstrated in Fig. 3.

For the cut-off conditions determining equilibration standard parameters have been taken, respectively. ISABEL [12] and INCL2.0 calculations have been normalized to the reaction cross section of 1688 mbarn which is widely independent on incident proton kinetic energy.

Confronting $d\sigma/dE^*$ with experimental distributions [8] an almost perfect agreement can be obtained only with the INCL2.0 and ISABEL approaches. The BERTINI based codes fail to predict $d\sigma/dE^*$. On the average for large incident proton energies the BERTINI codes predict almost a factor of two higher E^* values than INCL2.0 does.

The considerable deviant between BERTINI on one hand and INCL2.0/ISABEL on the other hand for higher E^* is all the more pronounced the larger the energy of the incident proton is. One assertion which could explain the disagreement is the way the originally transferred energy is being exhausted. While the INCL2.0 code predicts many relatively high energetic particles during the INC,

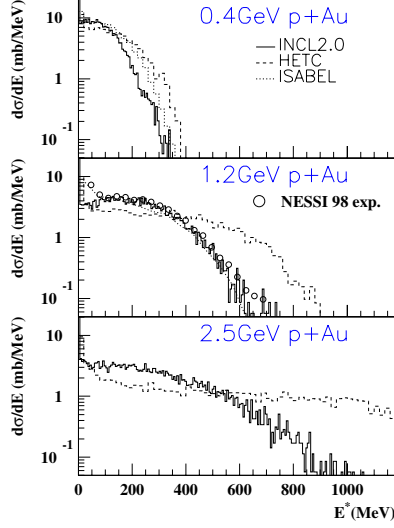


Fig. 3. E^* -differential cross-sections for 0.4, 1.2 and 2.5 GeV p+Au reaction following HETC, INCL2.0 and the ISABEL code

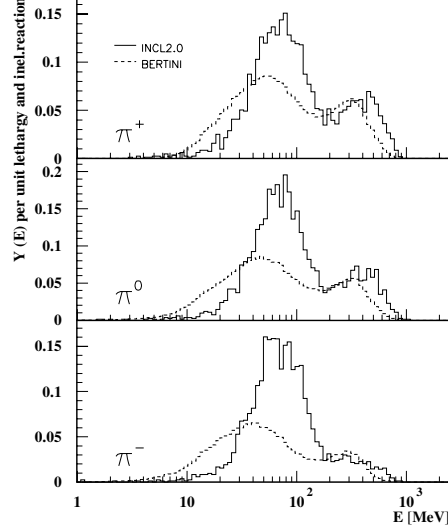


Fig. 4. Kinetic energy spectra of π^\pm and π^0 per unit lethargy following an inelastic reaction of 1.2 GeV p on Au for INCL2.0 and HETC codes

the HETC codes (LAHET or HERMES) produce not only fewer, but also less energetic particles as shown representatively in Fig. 4 for π^\pm and π^0 production following the reaction 1.2 GeV p+Au. All pion kinetic energy distributions shown in Fig. 4 are based on the same inelastic reaction cross sections of 1688mb. While conserving the total incident energy in all codes, it is obvious that during the INC the originally transferred energy is partitioned differently between E^* and the sum of kinetic energies and multiplicities of emitted particles or $\sum_{\pi^0, \pi^\pm, p, n} E_{\text{kin}} + \sum_{\pi^0, \pi^\pm} m_\pi \cdot c^2$. As a matter of energy balance for BERTINI at the expense of larger E^* the quantity $\sum_{\pi^0, \pi^\pm, p, n} E_{\text{kin}} + \sum_{\pi^0, \pi^\pm} m_\pi \cdot c^2$ is smaller than for the INCL2.0 approach. Since the pion model implemented in HERMES and LAHET is essentially the same, the kinetic energy spectra and pion multiplicities predicted by these codes coincide perfectly.

As a consequence of the extremely high thermal excitation energy E^* in the BERTINI based codes (in addition to deficiencies in the evaporation codes) also the particle production cross sections are overestimated. This applies especially to charged particles p, d, t and α , because they are subject to the Coulomb barrier and therefore preferentially emitted from high excitation energies. As shown by [8] for 1.2 and 1.8 GeV proton induced reactions on a variety of thin targets (mg/cm^2) ranging from Fe to U the production cross sections for H (all targets) and He (for heavy targets) isotopes are overestimated by a factor of two for BERTINI based codes, while the INCL2.0 code coupled to the statistical evaporation model GEMINI [13] gives reasonable agreement with the NESSI experiment as representatively demonstrated in Fig. 5 for 1.2 GeV proton induced reactions.

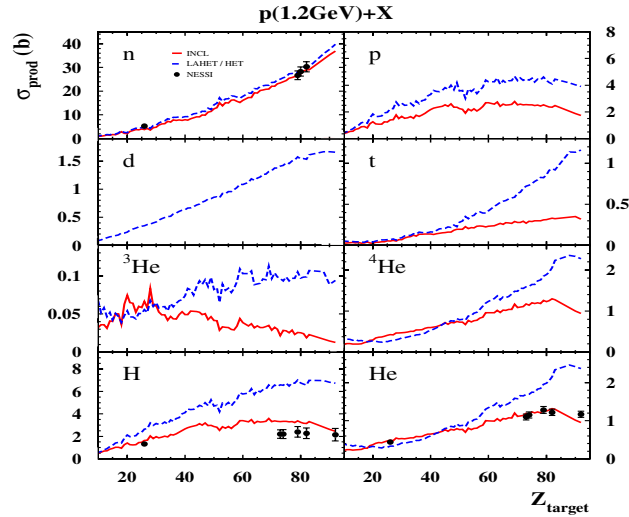


Fig. 5. Production cross sections of neutrons H- and He isotopes as a function of the atomic number Z following the bombardment of 1.2 GeV protons

Due to the shortage of space the details could not be discussed completely, but we intend to submit a major contribution to Phys. Rev. C soon.

References

1. *The European Spallation Source Study ESS, vol III, The ESS Technical Study*, report ESS-96-53-M, ISBN 090 237 6659 Nov.96, (1996)
2. A. Letourneau et al.: Nucl. Inst. & Meth. B, in press (2000)
3. J. Galin, U. Jahnke: Nucl. Part. Phys. **20**, 1105 (1994)
4. G. Sterzenbach et al.: In: *2nd International Topical meeting on nuclear App. of Acc. Technology, AccApp98, Getlinburg, Sep. 20-23, 1998*, ISBN 0-89448-633-0
5. P. Cloth et al.: *HERMES*, Report Juel 2203, ISSN 0366-0885, May 1988
6. R.E. Prael et al.: *User Guide to LCS: The LAHET Code System*, Los Alamos National Laboratory, Report LA-UR-89-3014, Sep. 1989
7. H.G. Hughes et al.: *MCNPX-The LAHET/MCNP Code Merger*, Research Note XTM-RN(U)97-012, LA-UR-97-4891, Los Alamos National Laboratory (1997)
8. M. Enke et al.: Nucl. Phys. A **657**, 317 (1999)
9. F. Atchison et al.: In: *Proc. of a specialists' meeting, Intermediate Energy Nuclear Data: Models and Codes, Issy-les-Moulineaux (France), May 30-June 1 (1994)*
10. H.W. Bertini et al.: Phys. Rev. **134**, 1801 (1963)
11. J. Cugnon et al.: Nucl. Phys. A **470**, 558 (1987)
12. Y. Yariv et al.: Phys. Rev. C **20**, 2227 (1979)
13. R.J. Charity et al.: Nucl. Phys. A **483**, 371 (1988)

Design and Effects of the Proton Window of the Spallation Neutron Source

F.C. Difilippo

Oak Ridge National Laboratory, P. O. Box 2008, Oak Ridge, TN 37831-6363, U.S.A.

Abstract. Design parameters for the target region of the Spallation Neutron Source were calculated by following histories of 1 GeV protons and their shower of particles with the Monte Carlo code MCNPX. In particular, neutron currents, radiation damages, doses and heat distributions for the target region of the facility along the path of the proton beam are presented from the point of view of the perturbation effects of the proton beam window.

1 Introduction

The Spallation Neutron Source project [1] is a national effort, within the United States, to build a powerful pulsed neutron source at the Oak Ridge National Laboratory. The multidisciplinary endeavor requires the coordination of the research and development of several national laboratories that follows, more or less, a natural progression: ion source, acceleration, storage of the proton beam,

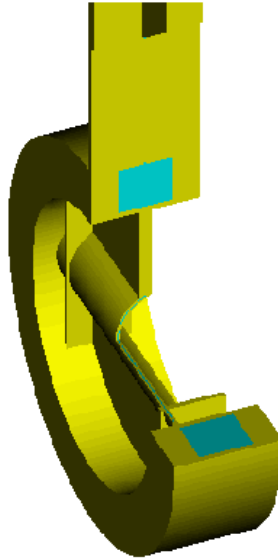


Fig. 1. Cut of the inconel proton beam window of the Spallation Neutron Source showing the coolant

target station and experimental area. Present parameters of the design are for a 2 mA current of 1 GeV protons.

The target area is the part of the facility built around the Hg target that converts the proton beam into 18 neutron beams via the spallation reaction. It includes, beside the Hg target, ambient and cryogenic temperature moderators, beam tubes, shielding materials and associated coolant systems. Some key radiation transport parameters of the design are: neutron production, heating rates, radiation damage, doses and neutron currents in the experimental areas.

The physical boundary between the incoming proton beam and the target station is a semicircular inconel window, cooled with water, of approximately 8 cm height, 30 cm extent and 4 mm width (two 2 mm sections separated by 1.6 mm of cooling water). See Fig. 1 for details.

Although the width is very narrow, it affects the proton beam distribution and consequently the neutron, radiation damage and heat distributions in the vicinity of the direction of the beam. Since this is also the region of the Hg converter and its container that is subject to the most intense heat, it is important to know, not only the condition at the window region, but also the effects along the path of the beam. Figure 2 shows a view of the target station model along the path of the proton beam and in the vicinity of the window. Detailed calculations of the design parameters are presented in the following sections. They were done by tracking the protons and their shower of particles with the Monte Carlo code MCNPX [2], a synthesis of the hadronic code LAHET [3,4] and MCNP [5].

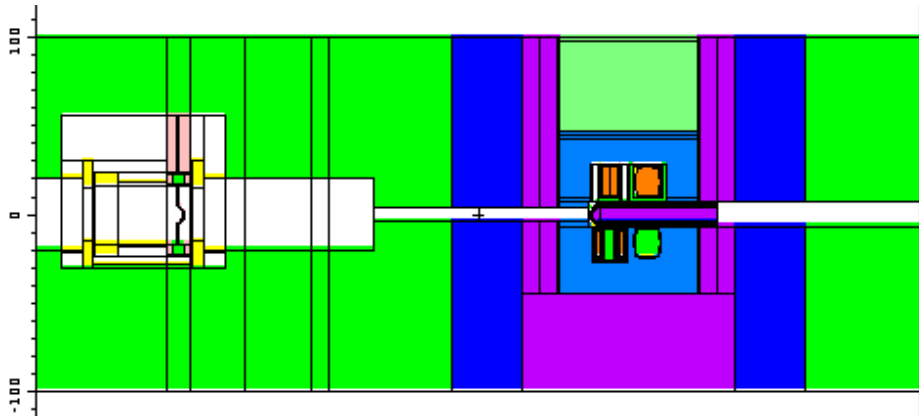


Fig. 2. Cross section of the Spallation Neutron Source target station model along the proton beam. The left of the figure shows the location of the proton beam window and the box for beam diagnostics

2 Interactions of the Proton Current with the Proton Window

The boundary of the model is the Ring to Target Building Transport (RTBT) tunnel, thus the proton current coming through the beam path and colliding with the proton window is used as the external source of the model [6]. Particularly relevant for the design is the beam profile over the Hg target, shown in Fig. 3 together with the profile of the unperturbed beam. The distributions, normalized to an incoming proton current of 2 mA, show some spread with a substantial part (94.4 %) of the beam impacting the Hg target. There is a shift of about 5 MeV, not shown here, in the proton spectra.

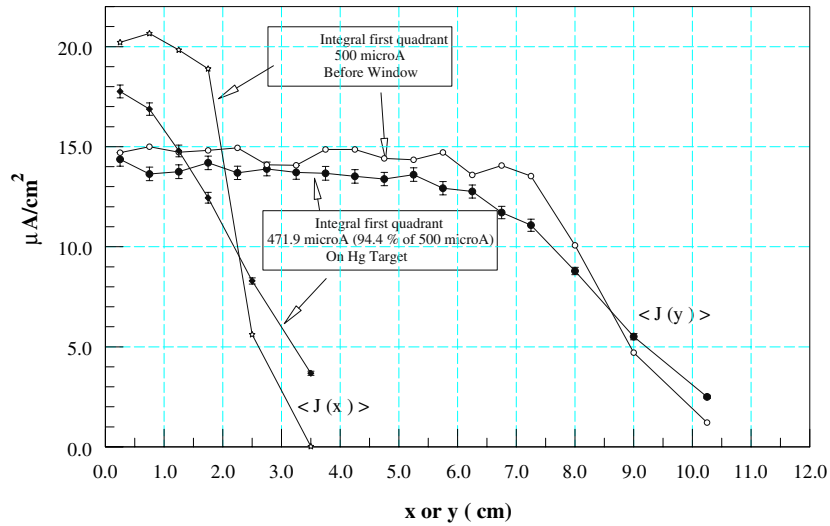


Fig. 3. Proton current densities in front of the proton beam window and on the Hg target; average distributions in x (vertical) and y (horizontal)

The window itself is the subject of intense heating and radiation damage. Detailed maps of these magnitudes are thus very important for the engineering details of the design. Our window is composed of two Inconel walls (2 mm each) separated by water coolant 1.6 mm thick. Two dimensional total heat distributions for the walls were computed for a total current of 2 mA. There is a strong correlation of the heat density with the proton current density: $H(w/g) = 2.185 J(A/cm^2)$. Displacements per atom (dpa) of stainless steel atoms due to the protons were calculated with the proton flux and cross sections from [7] and are shown in Fig. 4.

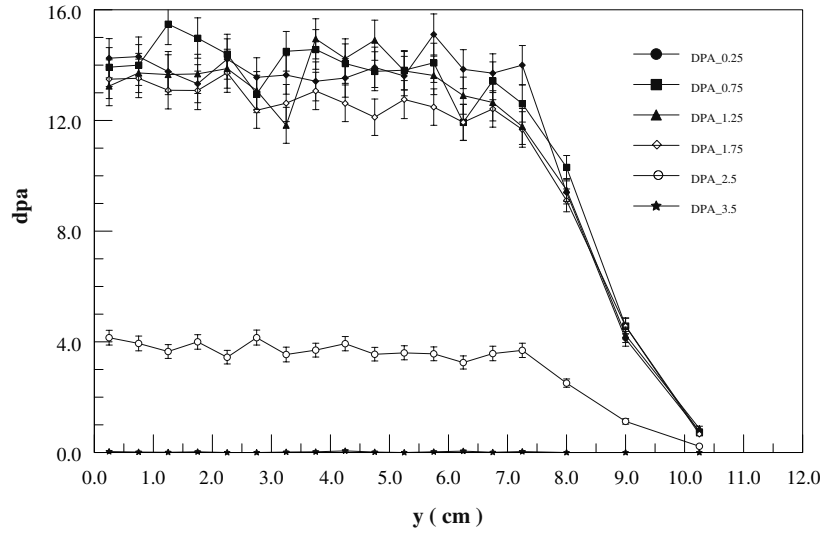


Fig. 4. dpa (due to protons) for stainless steel in the proton beam window for 1 full year operation at 2 mA

3 Heating and Radiation Damage Along the Beam Path

Table 1 summarizes the geometry of the beam path and the media around it. Tallies were defined for the material regions in rings along and around the beam path.

Table 1. Geometry and Material Regions Along the Beam Path

z (cm from center)	Geometry	Materials Around
22.5 to 144.4	Rectangular duct 8x22 cm	Target and Inner(Be), Mid(Pb) and Outer(SS) shielding plugs
144.4 to 228.6	Circular Duct (16")	SS shielding plugs
228.6 to 312.2	Rectangular duct 86.36x60.96 cm for beam diagnostic box and proton beam window	SS shielding plugs
312.2 to 506	Circular Duct (16")	SS shielding plugs

Figure 5 shows the heating rates in 2 cm thick rings of material regions along the path of the beam. Neutron contributions are important only near the target and the local maximum of the heat occurs at the contractions of the material media along the beam path.

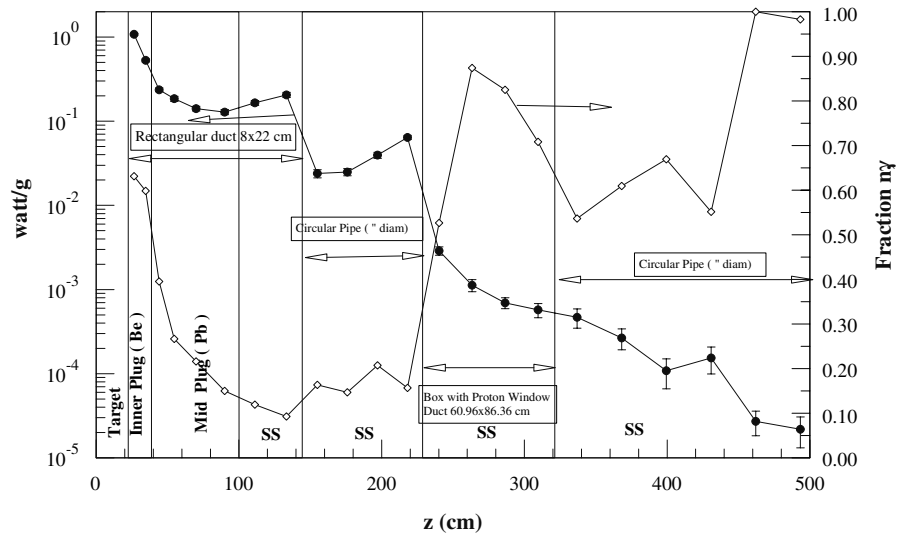


Fig. 5. Total heating rate and n plus gamma heating fractions for 2 cm thick rings along the path of the beam

Total (neutron plus proton) dpa and the proton fraction are shown in Fig. 6 for stainless steel (1 year at 2 mA) located in 2 cm rings along the path of the beam, the proton contributions also have a local maximum at the contractions of the media along the path.

4 Conclusions

Detailed maps of the heating rates and the radiation damage were prepared to describe the conditions along the path of the proton beam of the Spallation Neutron Source project. The scattering of the protons by the window and the changes of the cross sections of the media along the path affect the distributions via the appearance of local maximums. About 94.4 per cent of the protons arrive to the Hg target.

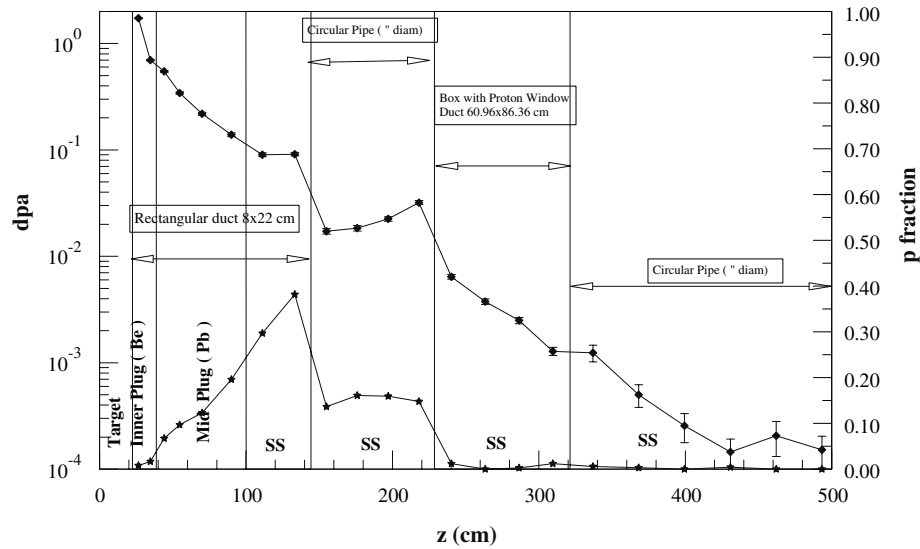


Fig. 6. Total dpa and proton fractions (in stainless steel for 1 year at 2 mA) for 2 cm thick rings along the path of the beam

References

1. J. Johnson: 'Target Neutronics for the Spallation Neutron Source' in <http://nas.cped.ornl.gov/pgm-sns.html>
2. H.G. Hughes et.al: 'MCNPX for Neutron-Proton Transport', Mathematical and Computation Topical Meeting, American Nuclear Society, Sept 27-30, Madrid, Spain
3. R.E. Prael, H. Lichtenstein : *User guide to LCS: The Lahet System*, Los Alamos National Laboratory, LA-UR-89-3014 (Sept 1989)
4. T.A. Gabriel et al: *CALOR98: A Monte Carlo Program Package for the Design and Analysis of Calorimetric System* , Oak Ridge National Laboratory, ORNL-TM-11185,
5. J.F. Briemeister, Editor: *MCNP: A General Monte Carlo N-Particle Transport Code*, Los Alamos National Laboratory, LA-12625-M (March 1997)
6. F. Gallmeir: Private Communication, ORNL, April 20, 2000
7. M.H. Barnett, L.K. Mansur, L.A. Charlton: *Radiation Damage Analysis of the Spallation Neutron Source Target Vessel*, Private Communication, ORNL, August 13, 1999

Application of the EA-MC Code Package to the Design of Accelerator-Driven Systems

Y. Kadi

CERN, CH-1211 Geneva 23, Switzerland

1 Introduction

The Monte Carlo method (MC) is currently used to simulate the real time behaviour of a sub-critical system [1,2] like for instance the Energy Amplifier Demonstration Facility (EADF). The advantage of this method is that it can be made intrinsically free of unwanted approximations, provided that (i) the relevant cross sections are well known – a necessity of any method of computation – and (ii) the actual geometry is sufficiently well modeled. For instance a variety of processes with many different particles in the final state as well as detailed angular distributions can be taken correctly into account and there is no real limit to the complexity of the geometry and the number of separate components. This technique also ensures continuity between the simulation of the high energy, proton induced initial cascade, for which MC is the only formalism [3,4], and the subsequent sub-critical, fission dominated nuclear cascade. Therefore MC constitutes a superb tool to simulate realistically both the ordinary operation and a variety of transients in sub-critical or critical systems.

2 The EA-MC Code Package

EA-MC is a general geometry, “point-energy”, Monte Carlo code which stochastically calculates the distribution of neutrons in three-dimensional space as a function of energy and time. The neutron data are derived from the latest nuclear data libraries [5]: ENDF/B-VI 6 (USA), JENDL-3.2 (Japan), JEF-2.2 (Europe), EAF-4.2 (Europe), CENDL-2.1 (China), EFF-2.4 (Europe) and BROND-2 (Russia).

The general architecture of the EA-MC code is shown in Fig. 1. The geometrical description is first automatically translated into FLUKA’s combinatorial geometry, and the FLUKA simulation is carried out [3,4]. Neutrons are transported down to 20 MeV and then handed over to EA-MC which continues the transport.

The EA-MC code is designed to run both on parallel and scalar computer hardware. Having used standard language elements, the code can be implemented on different systems. A common initialization section is followed by a parallel phase where every CPU runs an independent simulation with the same initialization data. A parallel analysis program collects the results and calculates the standard deviation among the different CPUs. This gives an estimate of the statistical fluctuations [6].

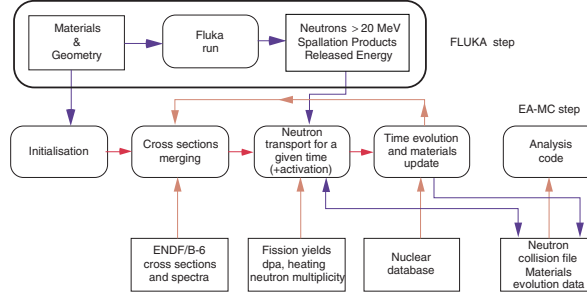


Fig. 1. General architecture of the EA-MC simulation of neutron transport and element evolution

3 Neutronic Analysis of the EADF

As in the case of the Energy Amplifier's conceptual design [1], the EADF core consists of an annular structure immersed in molten lead/bismuth eutectic which serves as primary coolant and spallation target. The central annulus contains the spallation target unit which couples the proton accelerator to the sub-critical core. The core is arranged in a honeycomb-like array forming an annulus with four coaxial hexagonal rings of fuel sub-assemblies. The fuel core is itself surrounded by an annular honeycomb-like array of four rings of dummy sub-assemblies, which are essentially empty ducts. The detailed description of the EADF reference configuration can be found in [2].

The present version of the EA Monte Carlo code package enables a rather complete and detailed modelling of the EADF reference configuration at the level of individual fuel pins or heat exchanger tubes (presently arranged in square lattices).

The main global results for the Beginning-Of-Life performance of the EADF reference configuration are summarized in Tab. 1.

Table 1. Main parameters of the EADF reference configuration

<i>Global parameters</i>	<i>Symbol</i>	<i>EADF</i>	<i>Units</i>
Initial fuel mixture	MOX	(U-Pu)O ₂	
Initial fuel mass	m _{fuel}	3.793	ton
Initial Pu concentration	m _{Pu} /m _{fuel}	18.1	wt%
Initial fissile enrichment	Pu ^{239,241} /U ²³⁸	18.6	wt%
Thermal power output	P _{th}	80	MW
Proton beam energy	E _p	600	MeV
Spallation neutron yield	N _(n/p)	14.51 ± 0.10	n/p
Net neutron multiplication	M	27.80 ± 0.56	
Multiplication coefficient	k=(M-1)/M	0.9640 ± 0.0007	
Energetic gain	G	42.73 ± 0.88	
Gain coefficient	G ₀	1.54	
Accelerator current	I _p	3.20 ± 0.07	mA

Table 1 reports a source multiplication coefficient (k_{src} , depending on the external spallation source which is different, having in general a slightly higher numerical value, from the $k_{eff} \approx 0.962$, an intrinsic core feature) of 0.964 at Beginning-Of-Life. This value has been chosen in such a way that criticality conditions are prevented, with adequate margins, under all normal conditions as well as following transient and accident conditions. A proton beam current of approximately 3.2 mA, at Beginning-Of-Life, is thus required to drive the 80 MW_{th} sub-critical core. Despite the large sub-criticality margin (see Tab. 1), the radial and axial power profiles have a moderate peaking factor, mostly as a result of the diffusivity of lead/bismuth eutectic coolant.

The heat deposition of the proton beam in the lead/bismuth eutectic target of the EADF, has been accurately calculated using FLUKA. The beam profile was considered as Gaussian with a FWHM in both the x - and y - direction of ~ 7.615 cm. A contour map of the power deposited in the spallation target unit and the surrounding core structures is given in Fig. 2. To give an idea about the cooling capabilities required for such a target, we plot the power deposited by the 600 MeV, 3.2 mA proton beam in W/cm³.

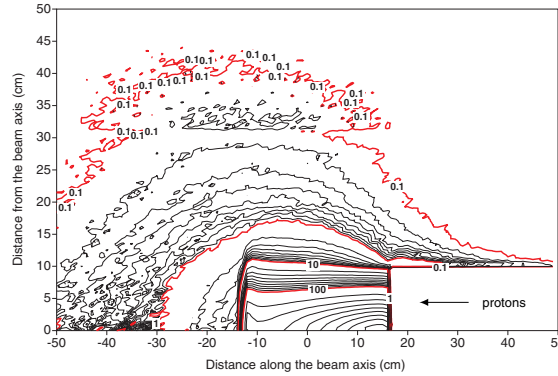


Fig. 2. Power deposited (W/cm³) by the 600 MeV, 3.2 mA proton beam impinging on the lead/bismuth eutectic spallation target

The total heat released in the lead/bismuth eutectic target amounts to ~ 1.45 MW, i.e. 75% of the proton beam power. This occurs mostly as a result of ionization losses of charged particles (83.4%), electro-magnetic cascade (4.4%), nuclear recoils and heavy fragments (2.9%), and finally in the form of kinetic energy of low-energy neutrons (9.3%). 600 MeV protons deposit most of their energy locally through ionization processes, very few produce stars (only 30%). This explains the very high power densities observed close to the beam-target interaction point (up to 900 W/cm³, 5 cm away from the impact point). These power densities are a factor two larger than the maximum observed in the hottest fuel sub-assemblies.

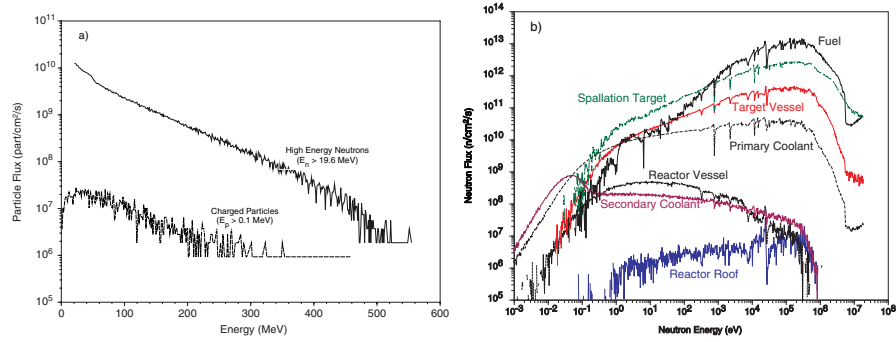


Fig. 3. a) High-energy particle flux spectra at the exit of the spallation target unit; b) Low-energy neutron flux spectra in different parts of the EADF

The EA-MC code package (including FLUKA) allows for the straightforward production of neutron flux spectra at selected locations. Figure 3 shows some spectra, which allow further insight into the neutronic characteristics of the device. Note in particular the flat neutron spectrum in the primary coolant, where the dominating process is elastic scattering with very small lethargy variation.

The neutron flux spectra generated by the EA-MC code can be used to estimate the heating and damage to structural materials by neutrons with energy above and below 20 MeV. Indeed, in the EADF one can consider separately the high energy portion of the spectrum, due to the primary proton shower, with its intensity proportional to the beam current, and a lower energy region associated with the fission multiplying medium, proportional to the reactor power.

Table 2 reports results of damage and heating calculations concerning both effects. An accurate calculation is made by using the detailed geometric model of the device and by computing the neutron induced damage self-consistently in each geometrical element (made by a given material) for each interacting nuclide [7]. The heating and damage-energy cross sections are extracted from the latest nuclear data libraries [5].

Table 2. Integrated flux, heating and damage of the spallation target unit internal structures, due to low-energy neutrons (LE) and high-energy particles (HE)

Region	Flux (part/cm²s)		Heat (W/cm³)		DPA/year	
	HE	LE	HE	LE	HE	LE
Proton beam tube	$2.0 \cdot 10^{13}$	$2.2 \cdot 10^{13}$	$2.7 \cdot 10^{-1}$	$9.4 \cdot 10^{-2}$	$9.5 \cdot 10^{-1}$	$5.5 \cdot 10^{-2}$
Spallation target	$1.7 \cdot 10^{14}$	$5.9 \cdot 10^{14}$	26	$5.2 \cdot 10^{-1}$	8.0	1.6
Spall. target vessel	$4.1 \cdot 10^{12}$	$1.3 \cdot 10^{14}$	2.1	$4.9 \cdot 10^{-1}$	$1.9 \cdot 10^{-1}$	$4.3 \cdot 10^{-1}$
Target unit vessel	$4.8 \cdot 10^{11}$	$8.2 \cdot 10^{13}$	$1.6 \cdot 10^{-2}$	$2.6 \cdot 10^{-1}$	$2.3 \cdot 10^{-2}$	$2.3 \cdot 10^{-1}$

The lead/bismuth eutectic target, in spite of its low absorbing characteristics, allows an important attenuation of the neutron flux and energy, so that the spallation target internal structures and the reactor core fixed structures (located at a distance of only 40 cm from the spallation target) experience acceptable dose damage of a few dpa's over the reactor lifetime.

The evolution of the EADF fuel core composition in terms of the initial loading of fissile materials, minor actinides breed, and accumulated fission products and poisons is simulated with the EA-MC code. It gives a measure of the transmutation/incineration capability of the EADF for plutonium and minor actinides which may be both relevant for the depletion/denaturation studies for plutonium elimination and for the assessment of the total radiotoxicity eventually left in the environment. The time dependence of the generic parameters and neutronic characteristics of the EADF after one burnup cycle is summarized in Tab. 3.

Table 3. Main parameters of the EADF after one burnup cycle

<i>Global parameters</i>	<i>BOC</i>	<i>EOC</i>	<i>Units</i>
Fuel mixture	(U-Pu)O ₂	(U-Pu)O ₂	
Fuel mass	3.793	3.723	ton
Pu concentration	18.1	16.7	wt%
Fissile enrichment	18.6	18.1	wt%
Fuel burnup	–	20	GWd/ton
Cycle length	–	900	EFPD
Thermal power output	80	80	MW
Proton beam energy	600	600	MeV
Spallation neutron yield	14.51 ± 0.10	14.51 ± 0.10	n/p
Net neutron multiplication	27.80 ± 0.56	15.29 ± 0.65	
Multiplication coefficient	0.9640 ± 0.0007	0.9346 ± 0.0009	
Energetic gain	42.73 ± 0.88	23.55 ± 1.00	
Gain coefficient	1.54	1.54	
Accelerator current	3.20 ± 0.07	6.00 ± 0.09	mA

Table 3 reports the variation in the neutron multiplication coefficient after a fuel burnup of 20 GWd/ton, that is 900 days of operation at 80 MW_{th}. During this period of operation, the reactivity of the EADF drops by 2.94% in Δk , which is compensated by a factor two increase in the accelerator current in order to

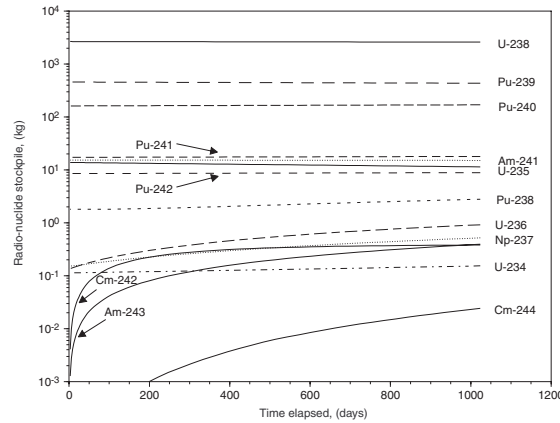


Fig. 4. Evolution of the actinide fuel concentration as a function of time

maintain a constant power output. In Fig. 4 the variation of the UPu MOX fuel composition is plotted as a function of time.

The rate of plutonium incineration rapidly settles to approximately 7 kg/TWh, at the expense of long-lived minor actinides, namely Np^{237} , $\text{Am}^{241,243}$ and Cm^{244} , which are produced at a constant rate of 0.23, 0.17 and 0.01 kg/TWh respectively. This is compared with the production rates of 11 kg/TWh for plutonium, 0.6 kg/TWh for Np^{237} and $\text{Am}^{241,243}$, and 0.05 kg/TWh for Cm^{244} , in a standard PWR.

4 Conclusions

By means of 3-D Monte Carlo simulations we have analyzed a number of neutronic features of the proposed Energy Amplifier Demonstration Facility reference configuration. Realistic models of the spallation target unit in-vessel structures which may affect the overall neutronics have been included in the simulations.

The results show that the desired sub-criticality level and power distributions can be achieved, and that low-energy neutron and high-energy particle induced damage of the structures can be kept at tolerable values. Detailed information on power distribution, neutron spectra, transmutation rates and material damage has been generated, which may be useful for the thermal-hydraulic and mechanical designs of the spallation target unit.

Acknowledgements

This work is part of the activity on the Energy Amplifier, promoted by prof. C. Rubbia. We also thank L. Cinotti, who is coordinating the engineering design of the prototype at Ansaldo Nucleare, for many discussions on the subject.

References

1. C. Rubbia et al.: *Conceptual Design of a Fast Neutron Operated High Power Energy Amplifier*, CERN report CERN/AT/95-44 (EET), Geneva, September 29, 1995
2. Ansaldo: *Energy Amplifier Demonstration Facility Reference Configuration: Summary Report*, ANASALDO Nucleare, EA-B0.00-1-1200 – Rev. 0, January, 1999
3. A. Fassó et al.: In *Intermediate Energy Nuclear Data: Models and Codes*, Proceedings of a Specialists' Meeting, Issy les Moulineaux (France) May 30 – June 1, 1994, p.271, published by OECD, 1994 and references therein
4. A. Fassó et al.: Nucl. Instr. and Meth A **332**, 459 (1993), also, CERN report CERN/TIS-RP/93-2/PP (1993)
5. ENDF/B-VI, JENDL-3.2, JEF-2.2, EAF-4.2, BROND-2, OECD/NEA Data Bank, Issy-Les-Moulineaux, Paris, France, 1994
6. A. Atzeni et al.: *Statistical Fluctuations in Monte Carlo Simulations of the Energy Amplifier*, CERN report CERN/LHC/97-12 (EET), Geneva, December 7, 1997
7. F. Carminati, Y. Kadi: *Implementation of a new Routine for Damage Calculations for the EA Monte Carlo*, CERN report CERN/LHC/EET 98-004, Geneva, April 20, 1998

Hadronic Collisions: Physics, Models and Event Generators

J. Ranft

Physics Dept. Universität Siegen, D-57068 Siegen, Germany

Models and event generators for hadronic collisions belong to the basic building blocks of hadron cascade calculations to simulate radiation problems around high energy accelerators and to simulate the Cosmic Ray cascade in the atmosphere, within the earth or within space stations. The models for hadronic collisions have to provide the produced hadrons preferably in the form of Monte Carlo events as well as the inelastic cross sections of the collisions considered. The event generators of interest for our applications have to provide minimum bias events, not only events for selected (hard) collisions. Let me first mention some important models, which I will not discuss:

- (i) There are dedicated event generators inside hadronic codes like FLUKA, HERMES, MARS, MCNPX, NMTC or GEANT. The event generators inside all of these codes will be covered by contributions to this Meeting.
- (ii) PHOJET [1,2] is a minimum bias Dual Parton Model event generator with a very broad applicability for hadrons, photons and electrons as projectiles and targets. PHOJET is contained in the new DPMJET-III [3] event generator, which adds nuclei as targets and projectiles to the above PHOJET list.

Nearly all event generators for hadronic or nuclear collisions in the energy range of say 5 to 10^{11} GeV are constructed out of the following ingredients:

- (i) In hadron-hadron collisions or in elementary nucleon-nucleon collisions of nuclear collisions multiple soft color singlet chains with quarks, diquarks and antiquarks at their ends are formed according to Gribov-Regge theory.
- (ii) In collisions involving nuclei one starts with the construction of multiple interactions according to the Gribov-Glauber theory. In simple models each collision leads just to the formation of one pair of colorless chains. In evolved models there is the full multi-chain system according to (i) and (iii) in each elementary collision. There are simplified models (using the superposition model), which do not treat the full Gribov-Glauber theory for nucleus-nucleus collisions.
- (iii) At sufficiently large energy besides the soft chains according to (i) and (ii) we have a system of multiple minijets. At high collision energies hard and semihard parton-parton collisions occur and become more and more important with rising collision energy. The produced jets and minijets become important features of most models, they determine the transverse momentum or transverse energy properties of the models at high energy. Now after the HERA measurements of structure functions at small Bjorken x_{bj} it is very essential to use for these calculations modern structure functions, which agree to the HERA data.
- (iv) After forming all partonic chains according to (i) to (iii) the next step is initial state and final state QCD evolution of all hard chains, after this all chains

are hadronized using the Lund codes JETSET or PYTHIA or in some codes private dedicated codes for string hadronization.

(v) There are diffractive interactions (or interactions with rapidity gaps between the produced particles). Diffractive hadron production is usually treated in special routines. Since the discovery of hard processes also in diffractive interactions at HERA and at the TEVATRON this has become more complicated.

(vi) After steps (i) to (v) we have events consisting out of produced hadrons (from string fragmentation) and spectators (these are nucleons from the original projectile and target nuclei, which have not taken part in the interaction). In the next step the codes treat secondary interactions. This is in simple cases just a formation zone intranuclear cascade, where the produced hadrons interact with the spectators, a more complete treatment is the full secondary hadron cascade, where the produced hadrons interact with the spectators as well as with other produced co-moving hadrons.

(vii) Now we have the produced hadrons and the remains of the projectile and target nucleus. These remains are considered as excited residual nuclei, which in a following evaporation step deexcite by the emission of evaporation particles. Finally the excited nuclei, which no longer are able to emit evaporation particles emit deexcitation photons to form finally a residual nucleus.

Let us summarize important aspects of some event generators used in calculating the Cosmic Ray cascade:

The DPMJET-II.5 event generator based on the two-component Dual Parton Model (DPM) was described in detail [4–7]. DPMJET-II.5 describes well minimum bias hadron and hadron jet production up to present collider energies.

The SIBYLL model [8] is a minijet model and has been reported to be applicable up to $E_{\text{lab}} = 10^{20}$ eV. However, the EHQL [9] parton structure functions used for the calculation of the minijet component might, after the HERA experiments, no longer be adequate. It is known, that a significant updating of SIBYLL is on the way, but the new code is not yet available.

VENUS [10], a model applied originally mainly for describing heavy ion experiments, is has become the leading event generator within the Corsika Cosmic Ray cascade code [11]. VENUS is applicable up to $E_{\text{lab}} = 5 \times 10^{16}$ eV. A new version of VENUS called *neXus* seems not yet to be available for distribution.

QGSJET [12] is based on the Quark Gluon String (QGS) model, this model is largely equivalent to the DPM. QGSJET also contains a minijet component and is reported to be applicable up to $E_{\text{lab}} = 10^{20}$ eV.

There is certainly the need to understand the systematic errors of the hadronic models and event generators. This is more easy in all the region, where experimental data exist. Here it is useful to compare the models to as many experimental data as possible. We can assume, that most published models agree to most of the available data. Systematic errors of models are more difficult to estimate in regions, where no experimental data are available. This might be collisions at energies beyond the energies of existing accelerators or in regions of the phase space, where no experimental data are available. A very prominent example for the latter is the fragmentation region at large Feynman- x , which

was never studied in hadron production experiments at the CERN and Fermilab colliders. The systematic comparison of Monte Carlo models in such regions is very useful to understand how certain the extrapolations of the models into such regions might be. The Karlsruhe code comparison [13] was a first extensive comparison of Monte Carlo models, which are available as event generators within the CORSIKA Cosmic Ray cascade code [11,14]. The energies, mainly in the 10^{14} and 10^{15} eV range in this comparison were motivated by the interest of the KASCADE [15] experiment. Here I will present some code comparisons up to the highest energies, for which the models are able to run. The first idea was just to use the event generators implemented in the last distributed version CORSIKA-5.61 [14]. But there is only the version DPMJET-II.4 implemented and even this is not correct. So I use for DPMJET my stand-alone version of DPMJET-II.5 [7,8]. With SIBYLL-1.6 as implemented in CORSIKA-5.61 I got funny results at high energy (above 10^{18} eV). Using the stand-alone code SIBYLL-1.7, the last SIBYLL version distributed by the authors, these anomalies disappeared. My conclusion: also the implementation of SIBYLL in CORSIKA is not without problems. With QGSJET in CORSIKA, I did not find any problems, so I use it in the form as implemented in CORSIKA-5.61.

In all the following plots I present and compare the result of the three event generators in the implementations as mentioned. The first comparisons are for p-N (proton-Nitrogen) collisions, p-N collisions are a good approximation to p-Air collisions which are important for the Cosmic Ray cascade.

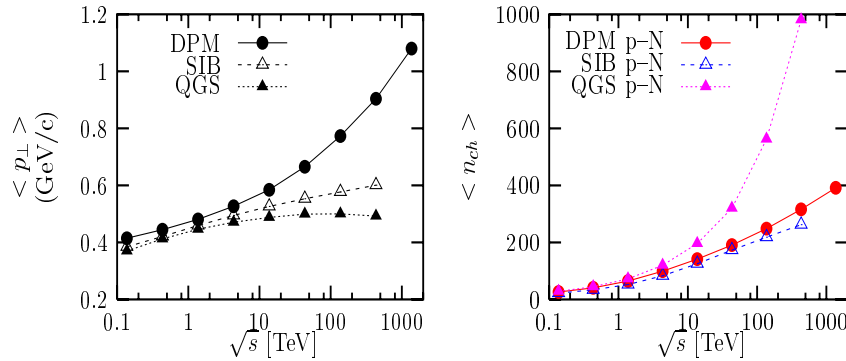


Fig. 1. (a) Average transverse momenta for charged hadron production in p-N (proton-Nitrogen) collisions as function of the (nucleon-nucleon) cms energy \sqrt{s} . (b) The average multiplicity of charged hadron production in p-N (proton-Nitrogen) collisions as function of the (nucleon-nucleon) cms energy \sqrt{s}

In Fig. 1.a we present average transverse momenta of charged hadrons as obtained from DPMJET-II.5, QGSJET and SIBYLL for p-N collisions as function of the cms energy \sqrt{s} . At energies where data (in p-p or p- \bar{p} collisions) exist all models agree rather well with each other and with the data. However, we find completely different extrapolations to higher energies. We should note, all three

models have a minijet component. But it seems, that in spite of the minijets the average transverse momentum in QGSJET becomes constant at high energies, while it continues to rise in DPMJET. There are even bigger differences in the models, if we consider the average transverse momenta of secondary protons.

Fig. 1.b presents the rise of the total charged multiplicity with the cms energy \sqrt{s} according to DPMJET, QGSJET and SIBYLL. we find again, at low energies, where data are available, the models agree rather well. DPMJET and SIBYLL agree in all the energy range shown. However, QGSJET above the energy of the TEVATRON extrapolates to higher energies in a completely different way.

In Fig. 2.a we present for p-N collisions the energy fractions K charged pion production. In the case of K_{π^+, π^-} we find DPMJET and QGSJET to agree largely, but SIBYLL behaves quite differently.

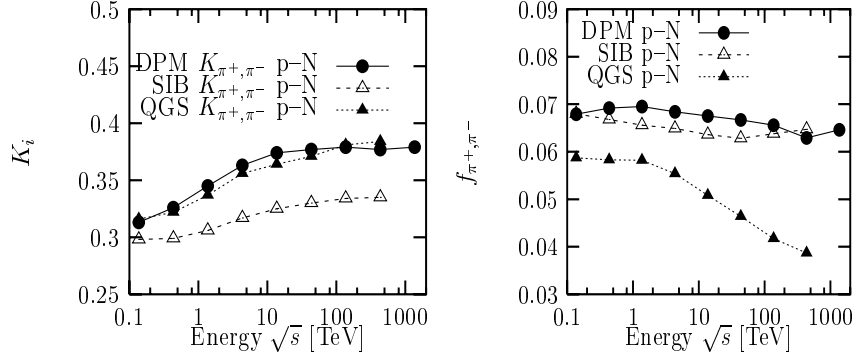


Fig. 2. (a) Average energy fraction for charged pion π^+, π^- production K_{π^+, π^-} in p-N collisions as function of the (nucleon-nucleon) cms energy \sqrt{s} . (b) Spectrum weighted moments for charged pion production f_{π^+, π^-} in p-N collisions as function of the (nucleon-nucleon) cms energy \sqrt{s}

In Fig. 2.b we present the spectrum weighted moments for pion production in p-N collisions as function of the cms energy \sqrt{s} per nucleon. In contrast to Fig. 2.a we find this time DPMJET and SIBYLL to agree approximately, but QGSJET behaves completely different.

In Figs. 3.a and 3.b we present the extrapolations to high energy E_{lab} of the x_{lab} distributions dN/dx_{lab} for secondary protons produced according to the two models DPMJET-II.5 and QGSJET. The distributions are plotted for $E_{\text{lab}} = 10^{13}, 10^{16}$ and 10^{20} eV. At the lowest energy all three models agree roughly, but there are considerable differences in the extrapolations to 10^{16} and 10^{20} eV. The differences between DPMJET-II.5 and SIBYLL-1.7 are mainly due to the baryon stopping diagrams implemented in DPMJET-II.5 [7,16] but not present in SIBYLL-1.7. The scaling behaviour of the distributions according to DPMJET-II.5 and SIBYLL-1.7 is nearly perfect in the x_{lab} region from 0.1 to 0.6, but this is just the region where the non-scaling appears in QGSJET. The behaviour of the models in p-p and p- \bar{p} is rather similar to the one in p-N colli-

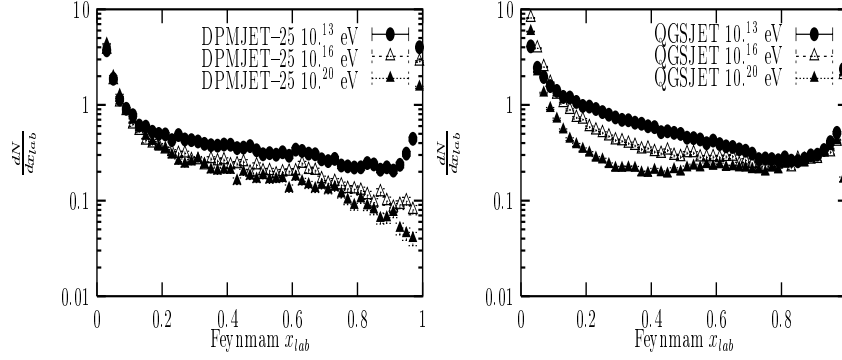


Fig. 3. (a) x_{lab} -distributions of secondary protons produced in p-N collisions at $E_{\text{lab}} = 10^{13}$, 10^{16} and 10^{20} eV according to the DPMJET-II.5 model. (b) x_{lab} -distributions of secondary protons produced in p-N collisions at $E_{\text{lab}} = 10^{13}$, 10^{16} and 10^{20} eV according to the QGSJET model

sions. Clearly, measurements of leading baryon distributions at the TEVATRON and/or at the LHC will resolve the conflict between the three models.

The differences in the extrapolations to high energy in Fe-N collisions are at least as large as in p-p or p-N collisions.

There were in the past and there are at present some activities to standardize some features of the Monte Carlo codes. Examples are:

- (i) Universal code numbers for particles and nuclei in the computer codes. The Particle Data Group proposed such a Monte Carlo particle numbering scheme, see for instance [17]. This scheme is used for the output of events by many event generators (examples are PYTHIA, JETSET and other Lund codes and the DPM event generators DPMJET and PHOJET), but the scheme is not suitable for the internal running of the codes, therefore each event generator uses a second (internal) particle numbering scheme. It would certainly be of advantage to standardize also these internal particle codes.
- (ii) A standard COMMON block for the presentation of the Monte Carlo events was proposed by working groups for the LEP and LHC colliders. The structure of this common block has been suggested in [18,19]. This standard COMMON follows closely a scheme first used in Monte Carlo codes of the Lund group. This COMMON contains not only the final particles produced in the collisions, it also documents all the internal features of the model.
- (iii) A similar effort has been started by the community of heavy ion experiments for the event generators for heavy ion collisions [20].

Most hadronic event generators which can be used for simulating hadronic and nuclear collisions up to the highest energies are quite similar in their construction and in the underlying theoretical concepts. At energies, where data from accelerator and collider experiments are available the models agree rather well with each other and with the most important features of the data. As soon as we compare the extrapolations of the models at higher energy we find in spite

of the similarities in the underlying theoretical concepts quite often striking differences between the predictions of the models. We conclude: (i) Measurements of inclusive hadron production at the TEVATRON Collider and in the future at the LHC collider are very important to guide the models. (ii) More theoretical efforts to improve the hadronic and nuclear collision models are needed to get better extrapolations.

References

1. R. Engel: Z. Phys. C **66**, 203 (1995)
2. R. Engel, J. Ranft: Phys. Rev. D **54**, 4244 (1996)
3. S. Roesler, R. Engel, J. Ranft: 'The Monte Carlo Event Generator DPMJET-III'. These proceedings p. 1033
4. J. Ranft: Phys. Rev. D **51**, 64 (1995)
5. J. Ranft: *Dpmjet version ii.3 and ii.4*, Preprint INFN/AE-97/45, Gran Sasso report 1997
6. J. Ranft: *New features in dpmjet version ii.5*, Preprint, Siegen preprint Si-99-5, hep-ph/9911213, 1999
7. J. Ranft: *Baryon stopping in high energy collisions and the extrapolation of hadron production models to cosmic ray energies*, Preprint hep-ph/0002137, 2000
8. R.S. Fletcher, T.K. Gaisser, P. Lipari, T. Stanev: Phys. Rev. D **50**, 5710 (1994)
9. E. Eichten et al.: Rev. Mod. Phys. **56**, 579 (1984)
10. K. Werner: Phys. Rep. **232**, 87 (1993)
11. J. Knapp, D. Heck: *Extensive air shower simulation with corsika*, Preprint KFK 5196 B, Karlsruhe report 1993
12. N. Kalmykov et al.: Physics of Atomic Nuclei **58**, 1728 (1995)
13. J. Knapp, D. Heck, G. Schatz: *Comparison of hadronic interaction models used in air shower simulations and their influence on shower development and observables*, Preprint FZKA 5828, Karlsruhe report 1996
14. J. Knapp, D. Heck: *Extensive air shower simulation with corsika, a users guide*, Preprint, Karlsruhe report 1998
15. P. Doll et al.: *The Karlsruhe cosmic ray project kaskade*, Preprint KFK 4686, Karlsruhe report 1990
16. J. Ranft, R. Engel, S. Roesler: 'Baryon stopping in high energy collisions in the dpmjet-iii model'. These Proceedings p. 979
17. C. Caso et al.: European Phys. Journ. C **3**, 1 (1998)
18. G. Altarelli, R. Kleiss, C. Verzegnassi (Eds.): *Z Physics at LEP 1, Vol. 3: Event generators and software*, CERN 89-08 v.3 pp.327 1989
19. F. Carminati, O. DiRosa, B. van Eijk, I. Zacharov, D. Hatzifotiadou: 'Standard interfaces between modules of event generators using dynamical common structures'. In *Proc. Large Hadron Collider workshop*, CERN 90-10 vol. III (1990) pp. 52 1990
20. OSCAR: See details on OSCAR home page <http://rhic.phys.columbia.edu/oscar/>

Modelling Hadronic Interactions

J.P. Wellisch

CERN, 1211 Geneva 23, Switzerland

Abstract. Optimal exploitation of hadronic final states played a key role in successes of all recent collider experiments in HEP, and the ability to use hadronic final states will continue to be one of the decisive issues during the analysis phase of the LHC experiments. Monte Carlo techniques facilitate the use of hadronic final states, and have been developed for many years. We will give a brief overview of the physics models underlying hadronic shower simulation, discussing the three basic types of modelling used in the geant4 tool-kit; data driven, parameterisation driven, and theory driven modelling, and provide comparisons with experimental data for selected models.

1 Model Overview

The physics modelling provided by a tool-kit for hadronic shower simulation has to cover an energy range starting at thermal energies for neutron cross-sections and interactions, going up to 7 TeV laboratory energy for interactions of all hadrons that traverse macroscopic distances in the case of the two large LHC experiments, and extending to even higher energies for the case of cosmic ray physics.

It will have to include the cross-sections for scattering any meson or baryon with macroscopic path length off any stable or long lived nuclear isotope. A complete hadronic shower simulation tool-kit will in addition offer lepton nuclear interactions, and alternative models with varying CPU performance and predictive power for the individual physics processes pertaining to hadronic shower simulation. Extendibility of the provided set of models by the expert user is an additional requirement.

The number of model currently provided with or in development in the context of GEANT4 is growing continuously. We give an enumeration of the current status, focussing on final state production.

Data driven models: When experimental or evaluated data are available with sufficient coverage, the data driven approach is considered to be the optimal way of modelling. Data driven modelling is used in the context of neutron transport, photon evaporation, absorption at rest, calculation of inclusive cross-sections and isotope production, and in the calculation of the inclusive scattering cross-sections for hadron nuclear scattering.

The main data driven models in GEANT4 deal with neutron and proton induced isotope production, and with the detailed transport of neutrons at low energies. The codes for neutron interactions are generic sampling codes, based

on the ENDF/B-VI data format, and evaluated neutron data libraries such as ENDF/B-VI, JENDL3.2, and FENDL2.2. Note that any combination of these can be used with the sampling codes. The approach is limited by the available data to neutron kinetic energies up to 20 MeV, with extensions to 150 MeV for some isotopes. The isotope production models that run in parasitic mode to the transport codes are based on the MENDL data libraries for proton and neutron induced production. They complement the transport evaluations in the sense that reaction cross-sections and final state information from the transport codes define the interaction rate and particle fluxes, and the isotope production model is used only to predict activation.

The data driven approach is also used to simulate photon evaporation at moderate and low excitation energies, and for simulating radioactive decay, based on the ENSDF data. In the case of photon evaporation the data are supplemented by a simple theoretical model (giant dipole resonance) at high excitation energies.

Finally, data driven modelling is used in the simulation of the absorption of particles coming to a rest, mainly for μ^- , π^- , K^- , and \bar{p} , in order to describe the fast, direct part of the spectrum of secondaries, and in the low energy part of the modelling of elastic scattering final states in scattering off Hydrogen.

Parameterized models: Parameterisations and extrapolations of cross-sections and interactions are widely used in the full range of hadronic shower energies, and for all kinds of reactions. In GEANT4, models based on this paradigm are available for low and high particle energies respectively, and for stopping particles. They are exclusively the result of re-writes of models available from GEANT3.21, predominantly GEISHA. They include induced fission, capture, and elastic scattering, as well as inelastic final state production.

Theory based models: Theory based modelling is the basic approach in many models that are provided by or in development for GEANT4. It includes a set of different theoretical approaches to describing hadronic interactions, depending on the addressed energy range and CPU constraints.

Parton string models for the simulation of high energy final states ($E_{\text{CMS}} > O(5 \text{ GeV})$) are provided and in further development. Both diffractive string excitation, and dual parton model or quark gluon string model are used. String decay is generally modelled using well established fragmentation functions. The possibility to use quark molecular dynamic is currently in preparation.

Below 5 GeV centre of mass energy, intra-nuclear transport models are prepared. A re-write of HETC [1] and INUCL [2] is in preparation, as well as a time-like cascade [3]. For quantum molecular dynamics models, an enhanced version of UrQMD [4] is being written. The QMD model calculates the interaction Hamiltonian from two- and three-body interactions of all particles, and solve the Newtonian equations of motion with this time-dependent Hamiltonian numerically. Scattering is done, using smeared resonance cross-sections, taking Pauli's principle into account by investigating local phase-space. The approach promises to give all correlations in the final state correctly, and has no principle limitations in its applicability at low energies. It is very CPU expensive.

At energies below $O(100 \text{ MeV})$ we provide the possibility to use exciton based pre-compound models to describe the energy and angular distributions of the fast particles, and to soften the otherwise too steep behaviour of the quasi-elastic peaks. In this area one model is released, and one more is in preparation.

The last phase of a nuclear interaction is nuclear evaporation. In order to model the behaviour of excited, thermalised nuclei, variants of the classical Weisskopf-Ewing model are used. Specialised improvements such as Fermi's break-up model for light nuclei, and multi-fragmentation for very high excitation energies are employed. Fission, and photon evaporation can be treated as competitive channels in the evaporation model.

As an alternative for, among others, intra-nuclear transport, the chiral invariant phase-space decay model CHIPS is in development. It is a quark-level 3-dimensional event generator for fragmentation of excited hadronic systems into hadrons, and is expected to find applicability in a wide range of hadron and lepton nuclear interactions, once fully explored.

For lepton nuclear interactions, muon nuclear interactions are provided. Neutrino nuclear interactions will be added in due course.

2 Sample Data Driven Models

As an example of a data driven model, we display in Fig. 1 sample results for neutron induced isotope production. This model allows for detailed isotope production studies, covering most of the spallation energy range. For a complete description and a more comparisons, see [5].

The evaluated data libraries that are the basis of the GEANT4 neutron transport and activation library G4NDL are Brond-2.1 [6], CENDL2.2 [7], EFF-3 [8], ENDF/B-VI.0 [9], ENDF/B-VI.1, ENDF/B-VI.5, FENDL/E2.0 [10], JEF2.2 [11], JENDL-FF [12], JENDL-3.1, JENDL-3.2, and MENDL-2 [13]. The G4NDL selection was guided in large parts by the FENDL2.0 selection. The inclusion of the MENDL data sets is fundamental, though.

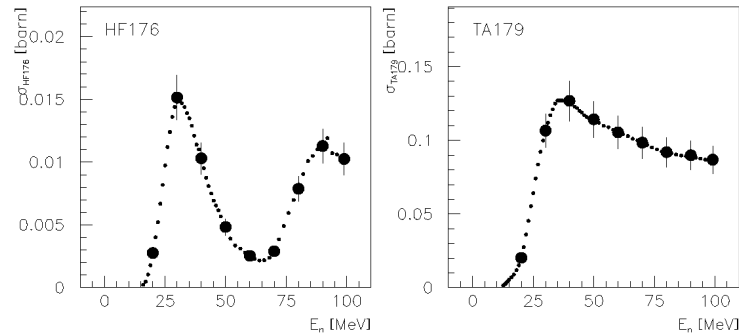


Fig. 1. Isotope production for neutron induced production on ^{180}W . Large points are simulation results, small points are evaluated data from the MENDL2 data library

3 Sample Parameterized Models

Parameterization based models have been found to be very powerful in the case of calorimeter simulation. Without giving a detailed description of these models, we want to illustrate the predictive power for the case of the GEANT4 high energy models in Fig. 3 for production of neutral pions in interactions of kaons and pions with Gold and Aluminum.

4 Sample Theory Driven Models

Given that the chiral invariant phase-space decay model CHIPS is a rather new development and is developed only within GEANT4, we choose this as an example for a theory based model. CHIPS is a quark-level 3-dimensional event generator for fragmentation of excited hadronic systems into hadrons. An important feature is the universal thermodynamic approach to different types of excited hadronic systems including nucleon excitations, hadron systems produced in e^+e^- interactions, high energy nuclear excitations, etc.. Exclusive event generation, which models hadron production conserving energy, momentum, and charge, generally results in a good description of particle multiplicities and spectra in multi-hadron fragmentation processes. To illustrate the predictive possibilities of this ansatz, we show a comparison between CHIPS predictions and measurement in the case of proton anti-proton annihilation in Fig. 2. For details of the model please see [14] and [15].

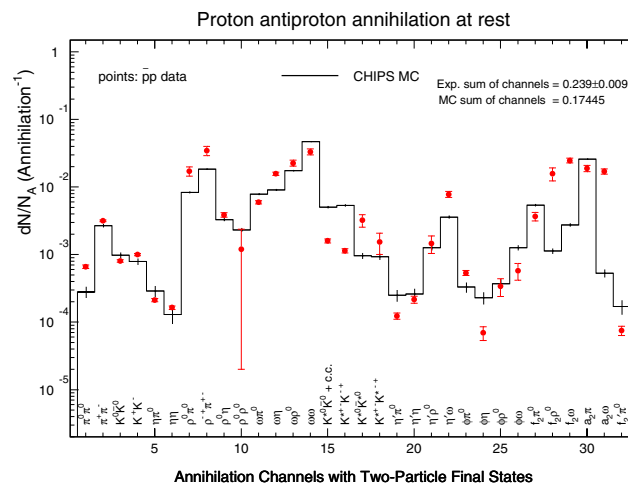


Fig. 2. Comparison of the branchings in two particle final states in proton anti-proton annihilation with the predictions of CHIPS

5 Conclusions

Taking the view of the LHC experiments, it has become evident that all modeling techniques - data driven, parameterisation driven, and theory driven - are need to satisfy LHC needs in an optimal manner. Data driven modeling is known to provide the best, if not only, approach to low energy neutron transport for radiation studies in large detectors. Parametrisation driven modeling has proven to allow for tuning of the hadronic shower Monte Carlo for particle energies accessible to test-beam studies, and is widely used for calorimeter simulation. Theory driven modeling is the approach that promises safe extrapolation of results toward energies beyond the test-beam region, and allows for maximal extendibility and customizability of the underlying physics.

The use of state of the art software technology is the key that allows for distributed development of the physics base of a hadronic shower simulation tool-kit in the GEANT4 context. It allows the work of many experts in the field to be combined in a coherent manner, and offers the user the possibility to unify their knowledge in a single executable program in a manner that he deems optimal for his particular problem. This is a completely new situation. In a very short time it has lead to an unexpectedly wide range of modelling possibilities in GEANT4, and an unprecedented ease of flexibility of usage of models and cross-sections.

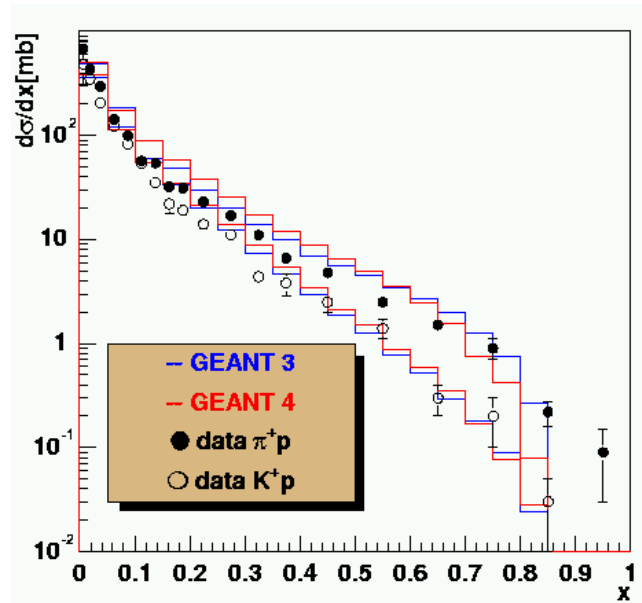


Fig. 3. Comparison of production cross-sections of neutral pions in kaon and pion induced reactions with measurement

References

1. R.G. Alsmiller, F.S. Alsmiller, O.W. Hermann: Nuclear Instruments and Methods in Physics Research A, **295**, 337 (1990)
2. Yu.E. Titarenko et al.: *Experimental and computer simulations study of radionuclide production in heavy materials irradiated by intermediate energy protons*, nucl-ex/9908012
3. M.G. Pia: 'Object oriented design and implementation of an intra-nuclear transport model', CHEP 2000, Padova
4. S.A. Bass et al.: URQMD: 'A new molecular dynamics model from GANIL to CERN energies', Wilderness 1996, Structure of vacuum and elementary matter, 399-405
5. J.P. Wellisch: *Neutron Induced Isotope Production On Selected CMS Elements Using GEANT4*, CMS-Note 1999/07
6. A.I. Blokhin et al.: 'Brond-2.2: 'Current status of Russian Nuclear Data Libraries''. In: *Nuclear Data for Science and Technology*, Volume 2, p.695. edited by J. K. Dickens (American Nuclear Society, LaGrange, IL, 1994)
7. CENDL-2: Chinese Nuclear Data Center: *CENDL-2, The Chinese Evaluated Nuclear Data Library for Neutron Reaction Data*, Report IAEA-NDS-61, Rev. 3 (1996), International Atomic Energy Agency, Vienna, Austria
8. H.D. Lemmel (IAEA): *EFF-2.4, 'The European Fusion File 1994, including revisions up to May 1995'*, Summary Documentation, IAEA-NDS-170, June 1995
9. ENDF/B-VI: Cross Section Evaluation Working Group: *ENDF/B-VI Summary Document*, Report BNL-NCS-17541 (ENDF-201) (1991), edited by P.F. Rose, National Nuclear Data Center, Brookhaven National Laboratory, Upton, NY, USA
10. H. Wienke, M. Herman: *FENDL/E2.0, The processed cross-section libraries for neutron-photon transport calculations, version 1 of February 1998*. Summary documentation, report IAEA-NDS-176 Rev. 0 (IAEA, April 1998)
11. C. Nordborg, M. Salvatores: 'JEF-2.2: Status of the JEF Evaluated Data Library'. In: *Nuclear Data for Science and Technology*, edited by J. K. Dickens (American Nuclear Society, LaGrange, IL, 1994)
12. T. Nakagawa et al.: JENDL-3: J. Nucl. Sci. Technol. **32**, 1259 (1995)
13. Yu.N. Shubin, V.P. Lunev, A.Yu. Konobeyev, A.I. Ditjuk: *Cross section data library MENDL-2 to study activation as transmutation of materials irradiated by nucleons of intermediate energies*, report INDC(CCP)-385 (IAEA, May 1995)
14. P.V. Degtyarenko, M. Kossov, J.P. Wellisch: 'Chiral Invariant Phase Space Event Generator, CHIPS-I, EPJA', accepted for publication
15. P.V. Degtyarenko, M. Kossov, J.P. Wellisch: 'Chiral Invariant Phase Space Event Generator, CHIPS-II, EPJA', submitted for publication
16. J.P. Wellisch: 'Hadronic shower models in geant4 - the frameworks', CHEP 2000, Padova
17. R. Brun et al.: CERN Data Handling Division, DD/EE/84-1, 1987
18. J.P. Wellisch, D. Axen: Phys. Rev. C **54**, 1329 (1996)
19. M. Laidlaw, J.P. Wellisch: private communication
20. A. Tripathi et al.: NASA technical paper 3621
21. The GEANT4 Collaboration: CERN/DRDC/94-29, DRDC/P58 1994
22. C. Nordborg, M. Salvatores: 'Jef-2: Status of the JEF Evaluated Data Library', *Nuclear Data for Science and Technology*, edited by J. K. Dickens (American Nuclear Society, LaGrange, IL, 1994)

The Monte Carlo Event Generator DPMJET-III

S. Roesler¹, R. Engel², and J. Ranft³

¹ SLAC, P.O. Box 4349, Stanford CA 94309, USA

² University of Delaware, Bartol Res. Inst., Newark DE 19716, USA

³ University of Siegen, D-57068 Siegen, Germany

Abstract. A new version of the Monte Carlo event generator DPMJET is presented. It is a code system based on the Dual Parton Model and unifies all features of the DTUNUC-2, DPMJET-II and PHOJET1.12 event generators. DPMJET-III allows the simulation of hadron-hadron, hadron-nucleus, nucleus-nucleus, photon-hadron, photon-photon and photon-nucleus interactions from a few GeV up to the highest cosmic ray energies.

1 Introduction

Hadronic collisions at high energies involve the production of particles with low transverse momenta, the so-called *soft* multiparticle production. The theoretical tools available at present are not sufficient to understand this feature from QCD and phenomenological models are typically applied instead. The Dual Parton Model (DPM) [1] is such a model and its fundamental ideas are presently the basis of many of the Monte Carlo (MC) implementations of soft interactions in codes used for Radiation Physics simulations.

Many of these implementations are however limited in their application by, for example, the collision energy range which they are able to describe or by the collision partners (hadrons, nuclei, photons) which the model can be used for. With respect to modern *multi-purpose* codes for particle interaction and transport these limitations at high energy are clearly often a disadvantage.

In this paper we present the DPMJET-III code system, a MC event generator based on the DPM which is unique in its wide range of application. DPMJET-III is capable of simulating hadron-hadron, hadron-nucleus, nucleus-nucleus, photon-hadron, photon-photon and photon-nucleus interactions from a few GeV up to the highest cosmic ray energies.

In the present paper we give an overview over the different components and models of DPMJET-III and present a few examples for comparisons of model results with experimental data.

2 The Concept of the Program

DPMJET-III is the result of merging all features of the event generators DPMJET-II [2,3] and DTUNUC-2 [4,5] into one single code system. The latter two codes are similar in their underlying concepts, however they differ in the Monte Carlo realization of these concepts, in particular, of the DPM.

Whereas individual nucleon-nucleon collisions in DPMJET-II are simulated based on the DTUJET model [3], DTUNUC-2 is using PHOJET1.12 [6,7]. Since PHOJET describes not only hadron-hadron interactions but also hadronic interactions involving photons, DTUNUC-2 allows also the simulation of photoproduction off nuclei. Therefore, the strength of DTUNUC-2 is in the description of photoproduction and nuclear collisions up to TeV-energies. On the other hand, DPMJET-II is widely used to simulate cosmic-ray interactions up to the highest observed energies [3].

However, many program modules in DPMJET-II and DTUNUC-2 are also identical. Examples are the Glauber-Gribov formalism for the calculation of nuclear cross sections [8], the formation-zone intranuclear cascade, the treatment of excited nuclei [9,10] and the HADRIN-model for the description of interactions below 5 GeV [11].

The core of DPMJET-III consists of DTUNUC-2 and PHOJET1.12. In addition all those features of DPMJET-II were added which were not part of DTUNUC-2 so far. This includes, for example, quasi-elastic neutrino interactions [12] and certain baryon-stopping diagrams [13].

3 Models Implemented in DPMJET-III

3.1 The Realization of the Dual Parton Model

The DPM combines predictions of the large N_c, N_f expansion of QCD [14] and assumptions of duality [15] with Gribov's reggeon field theory [16]. PHOJET, being used for the simulation of elementary hadron-hadron, photon-hadron and photon-photon interactions with energies greater than 5 GeV, implements the DPM as a two-component model using Reggeon theory for soft and perturbative QCD for hard interactions. In addition to the model features as described in detail in [17], the version 1.12 incorporates a model for high-mass diffraction dissociation including multiple jet production and recursive insertions of enhanced pomeron graphs (triple-, loop- and double-pomeron graphs). In the following only the new features are briefly discussed.

High-mass diffraction dissociation is simulated as pomeron-hadron or pomeron-pomeron scattering, including multiple soft and hard interactions [18]. To account for the nature of the pomeron being a quasi-particle, the CKMT pomeron structure function [19] with a hard gluonic component is used. These considerations refer to pomeron exchange reactions with small pomeron-momentum transfer, $|t^2|$. For large $|t^2|$ the rapidity gap production (e.g. jet-gap-jet events) is implemented on the basis the color evaporation model [20].

Extrapolating the two-channel eikonal-unitarization of a hadron-hadron amplitude as used in PHOJET to very high energies raises the question of the treatment of enhanced graphs which become more and more important at high energy and lead to large multiplicity fluctuations. A full amplitude calculation including enhanced graphs is very involved and not suited for a Monte Carlo implementation. Therefore, based on the results of [21], we use the simpler approach of interpreting each soft pomeron as the sum of a series of a bare soft pomeron

and enhanced graphs (Froissaron). In practice, this results in the simulation of possibly recursive subdivisions of a single Froissaron cut into various other configurations such as, for example, two cut pomerons or a single cut pomeron and a diffractive scattering. However, the current implementation should only be considered as a first step toward a consistent treatment of enhanced graphs at very high energy because of its limitation to soft interactions.

3.2 Hadronic Interactions Involving Photons

The photon is assumed to be a superposition of a *bare* photon interacting in direct processes and a *hadronic* photon interacting in resolved processes.

The description of interactions of the hadronic photon with nuclei is based on the Generalized Vector Dominance Model (GVDM) [22]. Photons are assumed to fluctuate into quark-antiquark states V of a certain mass M and the interaction is described as scattering of the hadronic fluctuation on the nucleus. Correspondingly, the scattering amplitude a_{VA} reads [4]

$$a_{VA}(s, Q^2, M^2, \mathbf{B}) = \int \prod_{j=1}^A d^3 r_j \psi_A^* a_{VA}(s, Q^2, M^2, \mathbf{B}_1, \dots, \mathbf{B}_A) \psi_A \quad (1)$$

$$a_{VA}(s, Q^2, M^2, \mathbf{B}_1, \dots, \mathbf{B}_A) = \frac{i}{2} \left(1 - \prod_{\nu=1}^A [1 + 2ia_{VN}(s, Q^2, M^2, \mathbf{B}_\nu)] \right) \quad (2)$$

where a_{VA} is expressed in terms of interactions on individual nucleons N according to the Gribov-Glauber picture (see below). The model is limited to low photon-virtualities Q^2 satisfying the relation $Q^2 \ll 2m_N \nu$ (ν and $2m_N$ being the photon energy and nucleon mass). For individual $q\bar{q}$ -nucleon interactions it is sufficient to consider only two generic $q\bar{q}$ -states, the first one grouping ρ^0 , ω and ϕ and $\pi^+\pi^-$ -states up to the ϕ -mass together and the second one including all $q\bar{q}$ -states with higher masses [6].

Direct photon interactions are treated as either gluon-Compton scattering or photon-gluon fusion processes on a single nucleon. The consideration of so-called anomalous interactions allows a steady transition between direct and resolved interactions [4].

Finally, an interface to LEPTO6.5 [23] allows to simulate deep-inelastic scattering off nuclei.

3.3 The Gribov-Glauber Multiple Scattering Formalism

The Monte Carlo realization of the Gribov-Glauber multiple scattering formalism follows the algorithms of [8] and allows the calculation of total, elastic, quasi-elastic and production cross sections for any high-energy nuclear collision. Parameters entering the hadron-nucleon scattering amplitude (total cross section and slope) are calculated within PHOJET.

For photon-projectiles ideas of the GVDM have been incorporated in order to correctly treat the mass of the hadronic fluctuation and its coherence length

as well as pointlike photon interactions [4]. Realistic nuclear densities and radii are used for light nuclei and Woods-Saxon densities otherwise.

During the simulation of an inelastic collision the above formalism samples the number of “wounded” nucleons, the impact parameter of the collision and the interaction configurations of the wounded nucleons. Individual hadron(photon,nucleon)-nucleon interactions are then described by PHOJET including multiple hard and soft pomeron exchanges, initial and final state radiation as well as diffraction.

As a new feature, DPMJET-III allows the simulation of enhanced graph cuts in non-diffractive inelastic hadron-nucleus and nucleus-nucleus interactions. For example, in an event with two wounded nucleons, the first nucleon might take part in a non-diffractive interaction whereas the second one scatters diffractively producing only very few secondaries. Such graphs are predicted by the Gribov-Glauber theory of nuclear scattering but are usually neglected.

Finally, all color neutral strings are hadronized according to the Lund model as implemented in PYTHIA [24,25].

3.4 The Intranuclear Cascade and Break-up of Excited Nuclei

The treatment of intranuclear cascades in spectator prefragments and their subsequent fragmentation is largely identical to the one described in [9,10].

Particles created in string fragmentation processes are followed on straight trajectories in space and time. A certain formation time is required before newly created particles can re-interact in the spectator nuclei. These re-interactions are of low energy and are described by HADRIN based on parameterized exclusive interaction channels. In nucleus-nucleus collisions the intranuclear cascade is calculated in both the projectile and target spectators.

Excitation energies of prefragments are calculated by summing up the recoil momenta transferred to the respective prefragment by the hadrons leaving the nuclear potential (a constant average potential is assumed). The prefragments are assumed to be in an equilibrium state and excitation energy is dissipated by the evaporation of nucleons and light nuclei and by the emission of photons.

4 Comparison to Experimental Data

Since DPMJET-III is the result of merging DPMJET-II and DTUNUC-2 its predictions have to be in agreement to experimental data where there was agreement for the two latter codes before. However, this has to be proven again. Here, only a few examples are given which should represent the large amount of comparisons of DPMJET-III results with experimental data which exist.

Figure 1a shows the transverse momentum distribution of negative hadrons from p-W collisions together with data [26]. The rapidity distributions of negative hadrons in central S-S and S-Ag collisions are compared to data [27] in Fig. 1b.

Two examples for interactions involving photons are given in Fig. 2. Hadronic interactions of muons are described by the radiation off the muon of a quasi-real

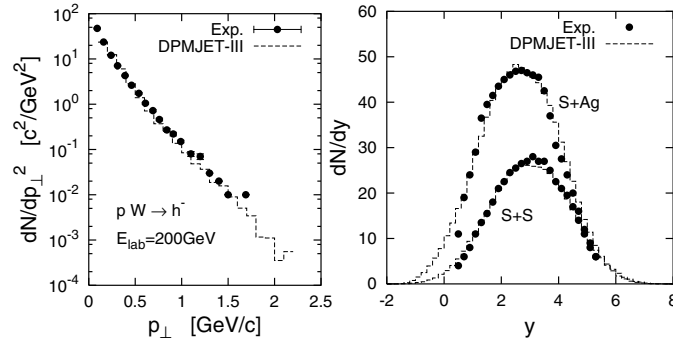


Fig. 1. Negatively charged hadron production in nuclear collisions at 200 GeV/nucleon

photon and the subsequent interaction of the photon. Figure 2a shows average multiplicities of charged hadrons from μ -Xe interactions at 490 GeV compared to data [28]. In Fig. 2b the calculated inclusive transverse momentum cross section of charged particles produced in two-photon collisions at LEP is compared to the combined data set of the ALEPH, L3, and OPAL Collaborations for low- Q^2 deep inelastic scattering [29].

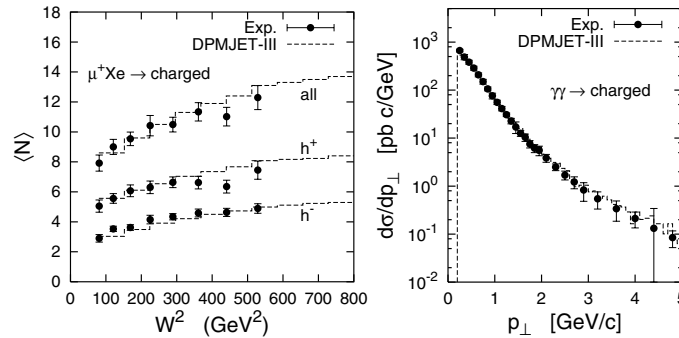


Fig. 2. Comparison of DPMJET-III results to data on interactions involving photons

5 Conclusions

A new version of the DPMJET event generator is presented. DPMJET-III is based on DPMJET-II, DTUNUC-2 and PHOJET1.12 and unifies all features of these three event generators in one single code system. It has been thoroughly tested and, in due time, will largely supersede the older DPMJET and DTUNUC versions.

It is presently not advisable to use the code for very low-energy nucleus-nucleus collisions (below ≈ 10 – 20 GeV). This requires further testing and tuning of parameters. Furthermore deficiencies exist in the description of some effects observed in heavy ion collisions at AGS- and SPS-energies (e.g. strangeness suppression, transverse energy flow).

The code is available on request from the authors (Stefan.Roesler@cern.ch, Johannes.Ranft@cern.ch) and further information can be found on the World Wide Web (<http://home.cern.ch/sroesler/dpmjet3.html>).

6 Acknowledgements

The work of S.R. and R.E. was supported by the Department of Energy under contracts DE-AC03-76SF00515 and DE-FG02-91ER40626, respectively.

References

1. A. Capella et al.: Phys. Rept. **236**, 225 (1994)
2. J. Ranft: Phys. Rev. D **51**, 64 (1995)
3. J. Ranft: *DPMJET version II.5: Sampling of hadron-hadron, hadron-nucleus and nucleus-nucleus interactions at accelerator and cosmic ray energies according to the two-component dual parton model: Code manual*, hep-ph/9911232, Preprint University of Siegen SI-99-6 (1999)
4. R. Engel, J. Ranft, S. Roesler: Phys. Rev. D **55**, 6957 (1997)
5. S. Roesler, R. Engel, J. Ranft: Phys. Rev. D **57**, 2889 (1998)
6. R. Engel: Z. Phys. C **66**, 203 (1995)
7. R. Engel, J. Ranft: Phys. Rev. D **54**, 4244 (1996)
8. S.Y. Shmakov, V.V. Uzhinskii, A.M. Zadorozhny: Comput. Phys. Commun. **54**, 125 (1989)
9. A. Ferrari, J. Ranft, S. Roesler, P.R. Sala: Z. Phys. C **70**, 413 (1996)
10. A. Ferrari, J. Ranft, S. Roesler, P.R. Sala: Z. Phys. C **71**, 75 (1996)
11. K. Hänßgen, J. Ranft: Comput. Phys. Commun. **39**, 37 (1986)
12. G. Battistoni, P. Lipari, J. Ranft, E. Scapparone: *Simulation of nuclear effects in quasielastic and resonant neutrino interactions*, hep-ph/9801426, Preprint INFN-AE-03-98 (1998)
13. J. Ranft, R. Engel, S. Roesler: 'Baryon stopping in high energy collisions in the DPMJET-III model'. These Proceedings p. 979
14. G. Veneziano: Nucl. Phys. B **74**, 365 (1974)
15. G.F. Chew, C. Rosenzweig: Phys. Rept. **41**, 263 (1978)
16. V.N. Gribov: Sov. Phys. JETP **26**, 414 (1968)
17. R. Engel: *Hadronic interactions of photons at high energies*. Ph.D. thesis (Universität Siegen 1997) <http://lepton.bartol.udel.edu/~eng/phojet.html>
18. F.W. Bopp, R. Engel, J. Ranft: 'Rapidity gaps and the PHOJET Monte Carlo', hep-ph/9803437, in: *Proceedings of LAFEX Int. School on High-Energy Physics (LISHEP98), Session C: Workshop on Diffractive Physics, Rio de Janeiro, Brazil, February 16-20, 1998*
19. A. Capella et al.: Phys. Rev. D **53**, 2309 (1996)
20. O.J.P. Eboli, E.M. Gregores, F. Halzen: Phys. Rev. D **58**, 114005 (1998)
21. A.B. Kaidalov, L.A. Ponomarev, K.A. Ter-Martirosyan: Sov. J. Nucl. Phys. **44**, 468 (1986)
22. A. Donnachie, G. Shaw: *Generalized Vector Dominance*, in *Electromagnetic Interactions of Hadrons*, Volume 2, ed. by A. Donnachie and G. Shaw (Plenum Press, New York 1978)
23. G. Ingelman, A. Edin, J. Rathsman: Comput. Phys. Commun. **101**, 108 (1997)
24. T. Sjöstrand: Comput. Phys. Commun. **82**, 74 (1994)
25. T. Sjöstrand: *Recent progress in PYTHIA*, hep-ph/0001032, Preprint Lund University LU TP 99-42 (1999)
26. The HELIOS Collaboration: T. Åkesson et al.: Z. Phys. C **46**, 361 (1990)
27. The NA35 Collaboration: T. Alber et al.: Eur. Phys. J. **2**, 643 (1998)
28. The E665 Collaboration: M.R. Adams et al.: Z. Phys. C **61**, 179 (1994)
29. A.J. Finch: Nucl. Phys. B (Proc. Suppl.) **82** 156 (2000)

Object-Oriented Approach to Preequilibrium and Equilibrium Decays in Geant4

V. Lara

CERN, Geneva, Switzerland

Abstract. The Geant4 simulation toolkit [1] provides a set of parameterized models that allow to model hadronic showers. However, in order to allow extrapolation beyond the experimental data and to offer an alternative set of models at conventional energies, Geant4 also provides a set of theory based hadronic shower models. We present the Object Oriented Design of a semiclassical exciton model for preequilibrium decays and a set of statistical models for deexcitation of compound nuclei. Our design follows the philosophy of hadronic models in Geant4, allowing for maximum of extendibility and customizability of the underlying physics by means of the use of abstract interfaces. We exploit advanced Software Engineering techniques and Object Oriented technology to achieve those goals. We present also a series of comparisons against experimental data being made in order to test the model.

1 Introduction

Spallation reactions dominate the interactions of high energy hadrons or light nuclei with nuclear targets in the GeV range (from $O(100\text{ MeV})$ to $O(10\text{ GeV})$). It corresponds to the reaction mechanism by which this projectile pulls out of the target some nucleons and/or light particles, leaving a residual nucleus. In the GeV range this is by far the dominant interaction pattern. This kind of interactions are interesting from several points of view, for instance, they are the basic mechanism in hadronic showers at intermediate energies.

The most common theoretical approach to model this kind of reactions is by means of an Intra-Nuclear Cascade model plus an deexcitation model. The importance of the deexcitation stage is crucial because of its contribution to the yields. The separation between Intra-Nuclear Cascade and deexcitation is somewhat artificial and model dependent. But the necessity to flip to deexcitation models is dictated by the fact that the deexcitation process involves structure effects that are not taken into account by the cascade. To fill the gap between the arbitrary cutoff of the Intra-Nuclear Cascade and equilibrium evaporation decays and to model the high energy continuum region of ejectile spectrum, it is sometimes used the precompound model.

2 Preequilibrium Decays

Precompound model is a mechanism of particle emission during the attainment of statistical equilibrium in an excited nuclear system. It can be used to link

smoothly Intra-Nuclear Cascade models and deexcitation models or can be, also, applied directly for incoming particles energies below $O(100 \text{ MeV})$. We use Griffin's semiclassical Exciton model [2] to implement such mechanism. The essential feature is the description of the time dependent excitation energy of the nucleus by a evolving population of excitons (particle-hole pairs). Successive two-body interactions give rise to an Intra-Nuclear Cascade which eventually leads to a fully equilibrated residual nucleus. At each stage of this equilibrium process there is a competition between two decays modes: the decay by exciton-exciton interactions to more complex configurations or the decay by emission of particles into the continuum that can be used by geometrical tracking.

The class `G4VPreCompoundModel` has a two-folded interface because there two use-cases: as a hadronic interaction model and as a back-end to models that work at higher energies. `G4VPreCompoundModel` inherits the public interface to the processes as defined in `G4HadronicInteraction`. As an example, detailed design of preequilibrium design is shown in Fig. 1

The decay by exciton-exciton interactions to more complex configurations is managed by `G4PreCompoundTransitions`. This class calculates the rate at which a nucleus in a given state makes transitions to other states respecting the restrictions imposed by the selection rules.

The decay by emission of particles into the continuum is split into a set of six channels which are managed by `G4PreCompoundFragmentVector` in such

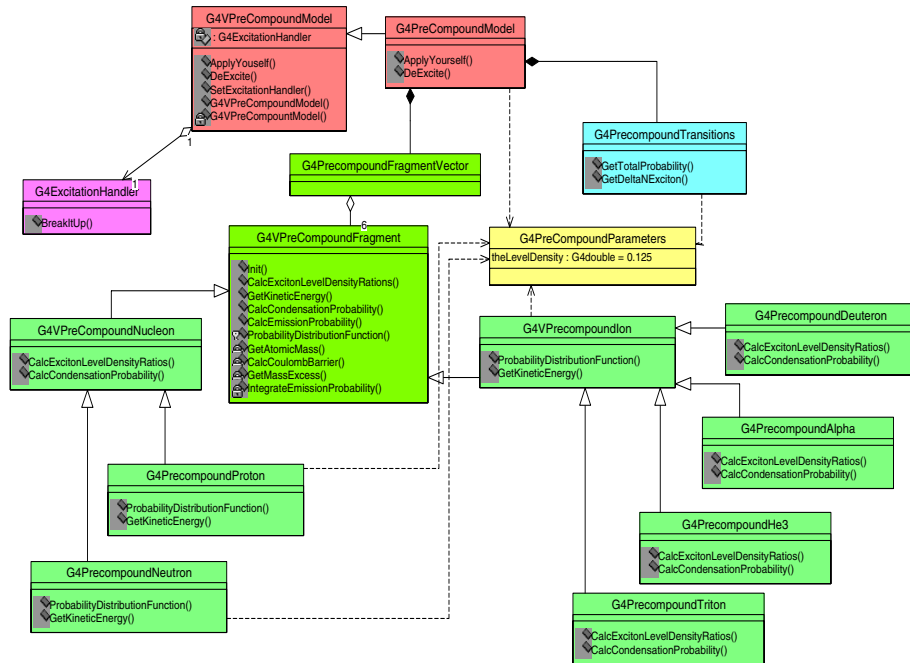


Fig. 1. Detailed Object Oriented Design of preequilibrium category

a way that this is transparent for `G4PreCompoundModel`. Each channel have to be able to calculate its decay rate and to sample its kinetic energy. The channels are treated polymorphically through `G4VPreCompoundFragment`. We can distinguish between two kind of fragments. `G4VPreCompoundNucleon` is a specialization of `G4VPreCompoundFragment` that implements commonality between `G4PreCompoundProton` and `G4PreCompoundNeutron`. By the other hand, for more complex fragments, represented by `G4VPreCompoundIon`, we have to take into account the probability of formation of such fragments.

3 Equilibrium Decays

Compound nuclei are nuclear fragments produced in an interaction that have excitation energies and have reached a state of statistical equilibrium. The decay process of these fragments is managed by the `G4ExcitationHandler` class. Its responsibility is to dispatch individual fragments to the models that perform the actual break up of the nucleus, based on ranges of applicability of the models and to return a list of nuclear fragments without excitation energy and macroscopic path length. `G4ExcitationHandler` manages five deexcitation models: `G4VEvaporation`, `G4VFission`, `G4VFermiBreakUp`, `G4VMultiFragmentation` and `G4VPhotonEvaporation`. These are abstract classes, so that the user can register alternative implementations. The statistical deexcitation classes are used as a default.

3.1 Evaporation Phase

Evaporation model is the basic deexcitation mechanism. It is applicable to excited nuclei with $A > 16$ and excitations energies less than ~ 3 MeV/nucleon. At such excitation energies, the nucleon density stays very close to the saturation density of cold nuclear matter and the global nuclear properties are well described by the standard liquid-drop model. The time between successive emissions is enough for the relaxation of the compound nucleus to a new equilibrium state.

`G4Evaporation` implements the statistical Weiskopf-Ewing's model [3] and inherit from the interface expected by the excitation handler class. `G4Evaporation` has a default set of eight competitive evaporation channels that are treated polymorphically through `G4VEvaporationChannel`. The number of evaporation channels can be changed at initialization time by the user. Those evaporation channels that always result in evaporation of nucleons or light ions are modelled in the `G4EvaporationChannel` class. Here the evaporation probability, the Coulomb barrier and the level density parameter are abstracted out for code re-use and to provide the user with the possibility to implement separate strategies. `G4VLevelDensityParameter` is the abstract interface and it is implemented in `G4EvaporationLevelDensityParameter` allowing the user to implement his own model. With respect to the Coulomb barrier, the abstract interface is defined in `G4VCoulombBarrier` while `G4CoulombBarrier` implements commonality

for Coulomb barriers calculation. There exist specific classes for each kind of default fragments (n, p, ^2H , ^3H , ^3He and ^4He) that implement particularities for Coulomb barriers calculation like barrier penetration factors and serves to initialize properly the particular channel moving out of **G4Evaporation** the knowledge needed to instantiate the channels. The same schema is followed in the probability calculation. Here **G4VEmissionProbability** is the abstract interface and the implementation of that interface is done in the **G4EvaporationProbability** class. Particular classes are also responsible for the right initialization and storing all the data needed in the probability classes. Finally, a set of subclasses, for instance **G4DeuteronEvaporationChannel** for ^2H , instantiate the channels mentioned above.

An important channel of deexcitation of heavy nuclei is fission. This process competes with evaporation particle emission and therefore it is implemented like a evaporation channel by using the abstract interface **G4VEvaporationChannel**. The implementation is done following the Bohr–Wheeler statistical approach in the **G4CompetitiveFission** class. Again we have abstracted out the probability, level density parameter and fission barrier calculations re-using the already defined **G4VLevelDensityParameter** and **G4VEmissionProbability** abstract classes. The probability calculation is implemented now by means of the class **G4FissionProbability** and calculation of level density parameter is done in **G4FissionLevelDensityParameter** class which uses **G4EvaporationLevelDensityParameter**. The new abstract interface defined is **G4VFissionBarrier** and the height of the fission barrier is worked out in the **G4FissionBarrier** class.

3.2 Explosive Decays

At very high excitation energies (> 3 MeV/nucleon) the sequential decays like the evaporation process are not valid any more. In this case we should expect a continuous flux of nucleons and light clusters from the decaying nucleus or even an explosion-like process leading to the total disintegration of the nucleus and the multiple emission of nuclear fragments of different masses for excitation energies comparable with the total binding energy. This fast process is the so called multifragmentation [5].

The **G4StatMF** implements the interface expected by excitation handler. We have implemented two ensembles defined by the common interface **G4VStatMFEnsemble**. In the microcanonical ensemble (**G4StatMFMicroCanonical**) all microscopic states obey strictly the conservation laws. All such states are considered to be equally probable and the statistical weights of a break-up partition, implemented in the **G4StatMFMicroPartition** class, are determined by their entropy. The probability of each partition is calculated by **G4StatMFMicroManager**. In the macrocanonical ensemble **G4StatMFMacroCanonical** we have only constraints on the average mass and charge of the system. The distribution of partitions probabilities is given by a thermodynamical potential which depends on two chemical potentials and the free energy of the system. The temperature is fixed by the energy balance equation. All these quantities and some other like the mean

multiplicity are calculated by solving a set of coupled equations through the classes `G4StatMFMacroTemperature`, `G4StatMFMacroChemicalPotential` and `G4StatMFMacroMultiplicity`. In order to re-used the zero finding algorithm the parenthesis operator of those classes has been overloaded and the `G4Solver` template class is responsible to solve equations. Due to the fact that liquid-drop description is meaningless for the lightest clusters, we have created an interface `G4VStatMFMacroCluster` for clusters implementing in `G4StatMFMacroMultiNucleon` the characteristics of clusters with more than four nucleons and particular classes for clusters with one to four nucleons.

When a partition has been selected the excitation energy of each fragment is calculated. The fragment momenta the chaotic thermal motion is generated and the collective flow included. The kinetics energies obey the Boltzmann–Maxwell distribution with the common temperature. After the break up fragments fly away from each other under the influence of the mutual Coulomb field leading to redistribution of fragment energies. All those processes are achieved with the help of `G4StatMFChannel` which, of course, manages a set of `G4StatMF Fragments`.

For light fragments (with $A < 17$) even a relatively small excitation energy may be comparable with their total binding energy. In this case we assume that the main mechanism of deexcitation is the explosive decay of the excited nucleus into several smaller clusters. To describe this process we use the Fermi model [6].

Fermi’s model is analogous to the statistical multifragmentation model, but final states are assumed to be in their ground state. Due to the limitation to deal with light nuclei, we use only the microcanonical approach because the number of available channels is smaller. `G4FermiBreakUp` has a configuration list. `G4FermiConfigurationList` creates all possible configurations for a given nucleus. Each `G4FermiConfiguration` contains a list of fragments chosen between 100 available fragments. The interface `G4VFermiFragment` is implemented for two kinds of fragments: `G4StableFermiFragment` and `G4UnStableFermiFragment` that will decay into stable fragments. The last class has four specialised classes for ${}^5\text{He}$, ${}^5\text{Li}$, ${}^8\text{Be}$ and ${}^9\text{Be}$ which know how to decay those unstable ions. When a configuration has been chosen it is given to `G4FermiFragment` and the momenta distribution is obtained by random generation over the whole accessible phase space instead of consider explicitly the Coulomb expansion.

4 Results

In order to evaluate the code a series of comparisons with evaluated data are done. Emphasis has been placed on thin target double differential cross sections. The experimental data used comes from NEA [7]. It includes single and double differential cross sections at incident proton energies of 25, 45, 80, 160, 256 and 800 MeV for (p,xn) reactions with ${}^{90}\text{Zr}$ and ${}^{208}\text{Pb}$.

Figure 2 shows an example of the simulated double differential cross section (stars) in comparison with evaluated data (dots) for the reaction ${}^{90}\text{Zr}(\text{p},\text{xn})$ at 80 MeV.

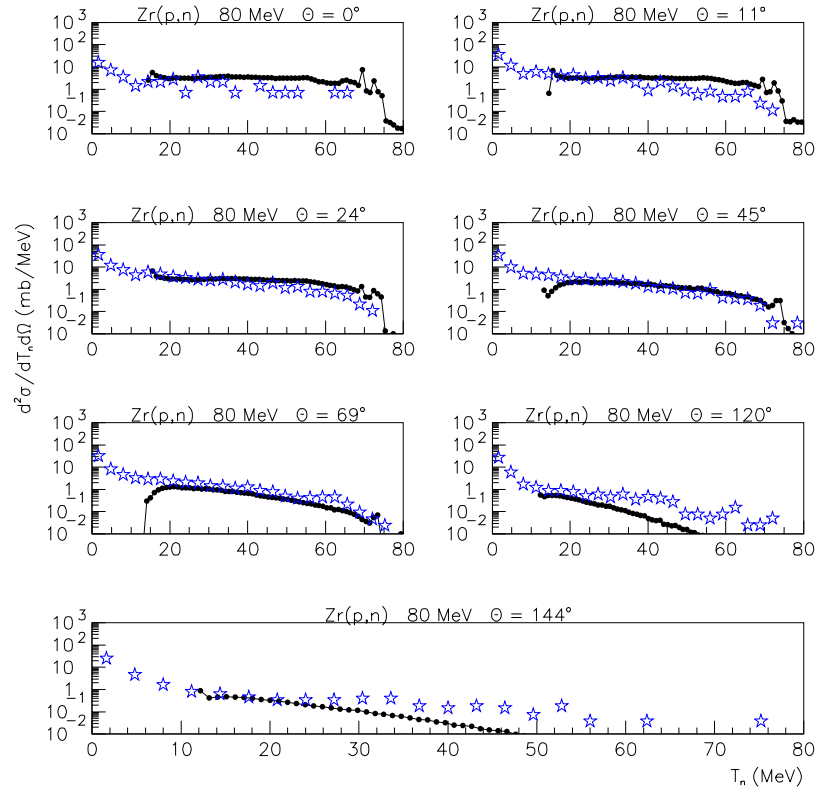


Fig. 2. Comparison between simulated (stars) and experimental (dots) angular distributions for Zr(p,xn) at 80 MeV

References

1. <http://wwwinfo.cern.ch/asd/geant4/geant4.html>
2. J.J. Griffin: Phys. Rev. Lett **17**, 478 (1966); K.K. Gudima, S.G. Mashnik, V.D. Toneev: Nuclear Physics **A401** 329 (1983)
3. I. Dostrovsky, Z. Fraenkel, G. Friedlander: Physical Review **116**, 683 (1959)
4. N. Bohr, J.A. Wheeler: Physical Review **56**, 426 (1939)
5. J.P. Bonford, A.S. Botvina, A.S. Iljinov, I.N. Mishustin, K. Sneppen: Physics Reports **257**, 133 (1995)
6. E. Fermi: Progr. Theor. Phys. **5**, 570 (1950)
7. M. Blann, H. Gruppelaar, P. Nagel, J. Rodens: *International Code Comparison for Intermediate Energy Nuclear Data*. Nuclear Energy Agency. Organization for Economic Co-operation and Development. Paris 1993

The GEM Code – the Generalized Evaporation Model and the Fission Model

S. Furihata

Mitsubishi Research Institution INC., 2-3-6 Otemachi, Chiyoda-ku, Tokyo, 100-8141, Japan

Abstract. We have developed the GEM code based on the generalized evaporation model proposed by Furihata and the RAL fission model. The parameters for the fission model, which determine the mass, charge, and kinetic energy distributions of fission fragments are reevaluated in this study. The cross sections for nuclide produced from protons incident on ^{208}Pb and ^{198}Au are estimated by using a combination of the intranuclear cascade model (INC) implemented in the LAHET code and the GEM code. INC/GEM reproduces successfully the cross sections for fission fragment production as well as light particle productions.

1 Introduction

A knowledge of cross sections of nuclide production is essential and important for nuclear physics, astrophysics and nuclear engineering. Since a wide range of nuclear data is needed and not all cross sections have been measured by experiments, theoretical calculations are often used for applications. The combination of an intranuclear cascade model (INC) and an evaporation model is useful because it can simulate reactions in a wide range of targets bombarded by nucleons with incident energies from a few tens of MeV to a few GeV. However, there is no code that is fully reliable to predict production cross sections for all target-product combination [1]. One of the problems is a fission model. A model for a complex particle and a fragment emission is also needed.

To improve a prediction, we develop the GEM code, which is based on the **Generalized Evaporation Model** proposed by Furihata [2] and the RAL fission model [3]. A combination of the Bertini INC model implemented in LAHET [4] and the generalized model successfully reproduces excitation functions of ^7Be production [5]. In this study, we also reevaluate the parameters for a symmetrical fission model, which determine the kinetic energy, the mass, and the charge distributions of fission products.

By using a combination of INC and GEM, we analyze fragments and residual nuclei produced from proton-induced reactions. Mass A_i , charge Z_i , excitation energy E , recoil energy, and the direction of the recoil motion of the excited nuclei produced after the initial non-equilibrium stage are extracted from the INC calculation done by LAHET. Then the de-excitation process of these excited nuclei is calculated by using the GEM code instead of by using the evaporation-fission model employed in LAHET. The INC/GEM results are compared with experimental data as well as the results calculated by using LAHET. For the

LAHET calculations, all the default options (i.e. the Bertini INC model without the preequilibrium model, the RAL fission model [3], and the Dostrovsky's evaporation model [5,6] with the Gilbert-Cameron-Cook-Ignatyuk level density parameter [4]) are used in this study.

2 The Generalized Evaporation Model

The generalized evaporation model proposed by Furihata [2] is based on the Weisskopf-Ewing model [7]. In the model, 66 ejectiles up to Mg, not only in their ground state but also in their excited states, are taken into account. Also, the accurate level density function ρ is used in the model for deriving the decay width of particle emission, instead of the approximate form of $\rho \propto \exp(2\sqrt{aE})$. In this study, we use the Gilbert-Cameron-Cook-Ignatyuk (GCC) level density parameter a [4] in GEM. For the cross sections of inverse reaction, the parameters determined by Dostrovsky *et al.* [6] are used for light ejectiles, and those determined by Matsuse *et al.* [8] are used for heavy ejectiles.

The results of light particle productions calculated by INC/GEM are shown in Figs. 1 and 2. INC/GEM reproduces both neutron evaporation spectra and the excitation function of ^7Be production.

3 Reevaluation of Parameters in a Fission Model

The RAL fission model [3] is employed in the GEM code for fission of nuclei with $Z_i > 70$. In the RAL model, the masses, the charges, and the kinetic energies of fission fragments are selected according to the Gaussian distribution functions. In this study, we reevaluate the parameters for these distribution functions.

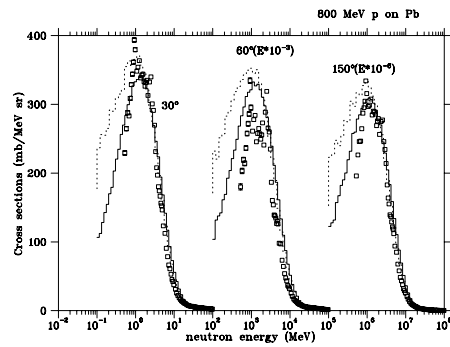


Fig. 1. Double differential cross sections of neutron emission from 800 MeV proton induced Pb reactions: experimental data (the squares) [9], the INC/GEM results (the solid lines), and the LAHET results (the dashed lines) are shown.

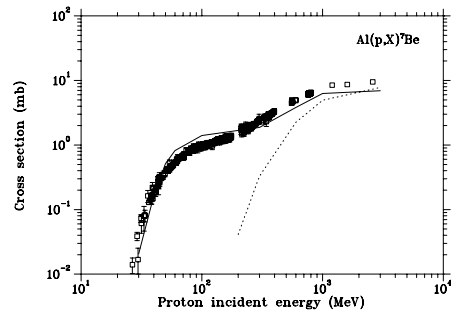


Fig. 2. The excitation function of ^7Be produced from proton induced ^{27}Al reactions: experimental data (the squares) [1], the INC/GEM result (the solid line), and the LAHET result (the dashed line) are shown

1. Mass distribution

The mass distribution of fission fragments produced by symmetric fission has Gaussian shape of mean $A_i/2$ and width σ_M . From the experimental data collected in [10] and [11], we assume that σ_M is expressed as

$$\sigma_M = C_1(Z_i^2/A_i)^2 + C_2(Z_i^2/A_i) + C_3(E - B_f) + C_4, \quad (1)$$

where the fission barrier B_f is given by the expression of Myers and Swiatecki [12]. By fitting the above expression to the experimental data, we determine the parameters as $C_1 = 0.122$, $C_2 = -7.77$, $C_3 = 3.32 \times 10^{-2}$ and $C_4 = 134.0$ where σ_M is assumed to be constant for $E - B_f > 450$ [MeV]. The Z^2/A dependency of σ_M are shown in Fig. 3. The original expression of σ_M used in the RAL model, i.e., $\sigma_M = 3.97 + 0.425(E - B_f) - 0.00212(E - B_f)^2$ (constant for $E - B_f > 100$ MeV), is replace with (1) in GEM.

2. Charge distribution

Furihata [13] shows that using the Gaussian distribution with width $\sigma_Z = 0.75$ instead of original value $\sigma_Z = 2.0$ improves predictions of isotopic distribution of fission fragments produced from ^{238}U . Therefore, $\sigma_Z = 0.75$ is used in the GEM code.

3. Kinetic energy

The kinetic energy of a fission fragment is determined by the Gaussian distribution with mean ϵ_f and width σ_{ϵ_f} . Instead of $\epsilon_f = 0.133Z_i^2/A_i^{1/3} - 11.4$ originally used in the RAL model, ϵ_f determined by Rusanov *et al.* [10] is used in GEM, which is given by

$$\epsilon_f = \begin{cases} 0.131Z_i^2/A_i^{1/3} & \text{for } Z_i^2/A_i^{1/3} \leq 900, \\ 0.104Z_i^2/A_i^{1/3} + 24.3 & \text{for } 900 < Z_i^2/A_i^{1/3} \leq 1800. \end{cases} \quad (2)$$

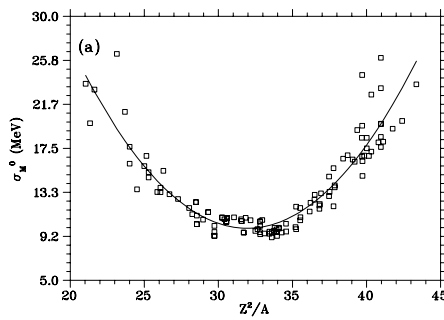


Fig. 3. The Z^2/A dependency of σ_M which is adjusted to $E - B_f = 0$ (i.e. $\sigma_M^0 \equiv \sigma_M - C_3(E - B_f)$). The squares represent the experimental data collected in [10,11], and the solid lines show the values given by (1).

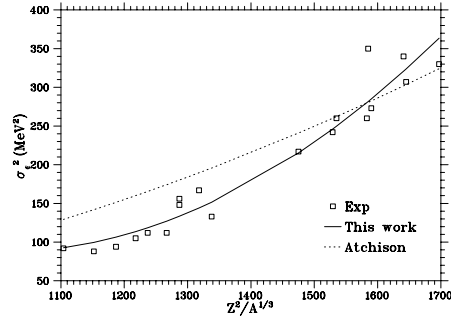


Fig. 4. The $Z_i^2/A_i^{1/3}$ dependency of $\sigma_{\epsilon_f}^2$: The fitted values given by (3) (the solid line) and those calculated by using the expression in the RAL model (the dotted line) are compared with the experimental values [14] (the open squares)

For σ_{ϵ_f} , we assume the following expression instead of original $\sigma_{\epsilon_f} = 0.084\epsilon_f$:

$$\sigma_{\epsilon_f}^2 = C_5 \left(Z_i^2/A_i^{1/3} - 1000 \right)^2 + C_6 \quad \text{for } Z_i^2/A_i^{1/3} > 1000. \quad (3)$$

By fitting (3) to the experimental data collected by Itkis *et al.* [14]¹, $C_5 = 5.70 \times 10^{-4}$ and $C_6 = 86.5$ are obtained. From the experimental data [14], $\sigma_{\epsilon_f}^2$ is assumed to be constant ($= C_6$) below $Z_i^2/A_i^{1/3} = 1000$. The fitted results and the experimental data are shown in Fig. 4 as well as the values originally used in the RAL model.

4 Results

The mass distributions of the nuclei produced from the bombardment of ^{208}Pb with 1 GeV protons are shown in Fig. 5. INC/GEM produces a sharper distribution for the fission products with $20 < A < 140$ than LAHET. The difference in the width is due to the mass distribution parameter σ_M used in the fission model. INC/GEM produces less spallation products with $A < 160$ than LAHET. However, INC/GEM still overestimates these spallation residues compared to the experimental data [15].

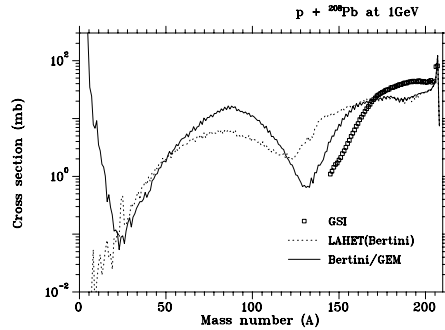


Fig. 5. The mass distributions of nuclei produced by the bombardment of ^{208}Pb with protons at 1 GeV: experimental data (the squares) [15], the INC/GEM result (the solid line), and the LAHET result (the dashed line) are shown.

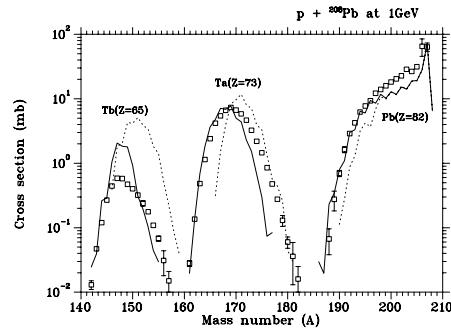


Fig. 6. Isotopic distribution of nuclei produced by the bombardment of ^{208}Pb with protons at 1 GeV: The marks and lines are the same as in Fig. 5

Figure 6 shows the isotopic distributions of spallation residues produced from the bombardment of ^{208}Pb with protons at 1 GeV. INC/GEM reproduces Pb isotopes, however, it underestimates neutron-rich isotopes of lighter residues. The

¹ The extrapolated values to the nuclear temperature 1.5 MeV in Tab. 1 of [14] are used for fitting.

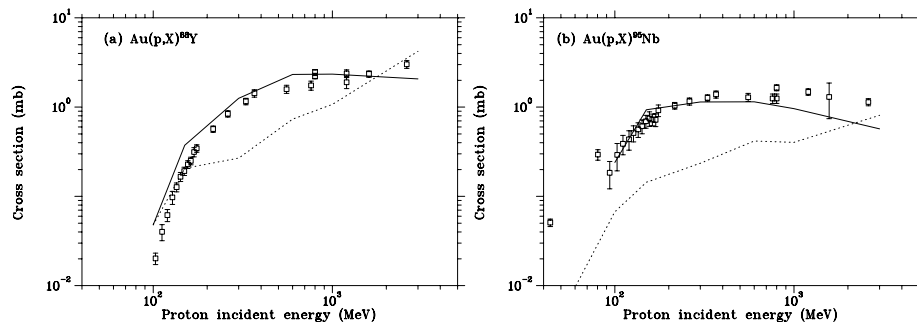


Fig. 7. The excitation functions for the nuclei produced from the $^{198}\text{Au}(p,X)$ reactions (both independent yields): (a) ^{88}Y ; and (b) ^{95}Zr . The estimates by INC/GEM (the solid line) as well as those calculated by the LAHET code (the dotted line) are compared with the experimental values [16] (the open squares)

differences of the calculated results are mainly caused by the Coulomb potential reduction in the evaporation models. In LAHET, the Coulomb potential for inverse reactions are multiplied by $1/(1 + 0.005E/Z_j)$, where Z_j is the charge of an ejectile, to correct an excitation dependency of the Coulomb barrier. With this correction, more charged particles are emitted from an excited nucleus. As a result, the neutron emission is suppressed. Since this correction is not included in GEM, the isotopic distributions calculated by using INC/GEM are shifted to proton-rich side compared to the results by LAHET. Both the calculated widths of the isotopic distributions of Ta are narrower than the experimental ones.

The excitation functions for the production of ^{88}Y and ^{95}Nb , produced from ^{198}Au are shown in Fig. 7. We focus on the nuclides with their masses around $A = 90$, which is at the maximum of the mass distribution of fission products from Au. The calculated results are compared with the experimental data measured by Michel *et al.* [16]. The estimates by INC/GEM agree with most of the experimental data to within 50%. INC/GEM successfully reproduces the shapes of the excitation functions, whereas LAHET fails to reproduce them.

The result calculated by INC/GEM shows that the excitation function for the production of ^{88}Y monotonically increases with increasing proton energy up to 600 MeV, whereas that for ^{95}Nb reaches a plateau after a steep increase above the threshold energy and then decreases slightly above 1 GeV. The former shape is specific to the excitation function of a proton-rich nucleus produced from Au, and the latter shape is typical for the excitation function of a neutron-rich product. Since highly excited nuclei emit many neutrons before and after fission, proton-rich nuclei are produced more from higher energy reactions. Besides, proton-rich nuclei are produced as spallation residues from high energy reactions as well as fission fragments. According to the INC/GEM calculations, about a half of ^{88}Y are produced as spallation residues at 3 GeV proton induced reactions. On the other hand, nuclei at low excitation energy produce neutron-rich fission fragments. While the probability of producing neutron-rich isotopes

decreases with increasing excitation energy, the fission cross section increases up to 1 GeV and decreases above 1 GeV. For the ^{95}Nb production in the energy region between 150 MeV and 1 GeV, the effects of the decreasing probability and the increasing fission cross sections are canceled. Thus the resulting production cross sections of ^{95}Nb become almost constant.

5 Conclusion

The combination of INC and GEM successfully predicts cross sections of light fragment and fission fragment productions. The use of the reevaluated parameters in the RAL fission model improves the predictions of fission fragments produced by low to medium energy fission. However, since INC/GEM does not perfectly predict isotopic distribution of spallation residues, the parameters for the cross sections of inverse reactions and the Coulomb potential reduction for a excited nucleus are still need to be investigated. Although INC/GEM successfully reproduces the excitation function of ^{88}Y and ^{95}Nb produced from Au, it is still too early to conclude the RAL fission model with new parameter set is perfect. GSI is now measuring the isotopic distributions of fission fragments from the bombardment of ^{208}Pb , Au, and ^{238}U with protons. A comparison of calculations with these experimental data will give more detailed information on the accuracy of the models.

Acknowledgements

The author is grateful to Dr. L. Moritz for support on this study, and also appreciates Dr. R. E. Prael for supplying the LAHET code.

References

1. R. Michel, P. Nagel: OECD/NEA, NSC/DOC(97)-1 (1997)
2. S. Furihata: Nucl. Inst. Meth. in Phys. Res. B **171**, 251 (2000)
3. F. Atchison: Jül-conf-34, KFA-Jülich, 1980
4. R.E. Prael, H. Lichtenstein: LA-UR-89-3014, (Los Alamos National Laboratory 1989)
5. L. Dresner: ORNL-TM-196, Oak Ridge National Laboratory, 1962
6. I. Dostrovsky et al.: Phys. Rev. **116**, 683 (1959)
7. V.F. Weisskopf: Phys. Rev. **52**, 295 (1937)
8. T. Matsuse et al.: Phys. Rev. C **26**, 2338 (1982)
9. W.B. Amian et al.: Nucl. Sci. Eng. **112**, 78 (1992)
10. A.Y. Rusanov et al.: Phys. Atom. Nucl. **60**, 683 (1997)
11. M.G. Itkis et al.: Phys. Atom. Nucl. **58**, 2026 (1995)
12. W.D. Myers, W.J. Swiatecki: Phys. Rev. C. **60**, 14606 (1999)
13. S. Furihata, L. Moritz: TRI-DN-I7-3-14, TRIUMF (1998)
14. M.G. Itkis et. al: Sov. J. Nuc. Phys. **52**, 15 (1990)
15. W. Wlazlo et al.: Phys. Rev. Lett. **84**, 5736 (2000)
16. R. Michel et al.: Nucl. Inst. Meth. in Phys. Res. B **129**, 153 (1997)

Application of Monte Carlo to Proton Beam Radiation Therapy

J.V. Siebers

Medical College of Virginia, Virginia Commonwealth University, USA

Abstract. As with photon and electron radiotherapy, the future of dose calculation for hadron beams will be based upon Monte Carlo algorithms. Benchmark calculations of the LAHET Monte Carlo code with respect to measured in-phantom dose distributions show that the proton physics modules in LAHET accurately reproduce measured results. Since MCNP-X incorporates the proton and high energy neutron physics modules from LAHET, similar agreement with MCNP-X is expected. In addition to beam-line simulations, MCNP-X has the ability to input the lattice geometry required for simulating patient treatments based on CT data sets. The ability of MCNP-X to perform patient dose calculation simulations for proton radiotherapy was demonstrated by simulating a two-beam prostate treatment plan. While MCNP-X is fully capable to perform patient-planning calculations, currently, it is too time consuming to be used for routine patient planning.

1 Introduction

The highly conformal dose distributions achieved using proton beams has resulted in a worldwide increase in the number of new and planned proton beam therapy facilities. Monte Carlo has, and will continue to play a major role in the assessment of these facilities. Applications include evaluation of radiation shielding parameters [1–4], pre-fabrication design, testing, and optimization of the therapy beam-lines [5], evaluation of dosimetric parameters and detector response [6], and assessment of beam-line component and patient activation [7]. Due to the fact that Monte Carlo fully accounts for energy-loss, straggling, scattering, and production of secondary particles in the heterogeneous patient material, it should provide the most accurate method of computing patient dose.

Several groups have applied Monte Carlo techniques to radiation therapy treatment planning for photon and electron beams with accurate results [8–15] (See also the photon/electron sessions of this conference). This paper will demonstrate the benchmarking of the LAHET Monte Carlo code with respect to measurements for a proton therapy treatment beam-line, and using the MCNP-X Monte Carlo code to compute patient dose distributions for proton beam radiation therapy.

2 Materials and Methods

LAHET [16] version 2.8 and MCNP-X [17] version 2.1.5 were used to model proton therapy beam-lines from the Loma Linda University Medical Centers’

proton therapy facility. Details of the physics in LAHET and MCNP-X are given elsewhere. The proton physics incorporated in the two codes is the same, as are the neutron interaction modules above the upper limit of the MCNP-X cross-section table (currently 20 MeV for most elements.) The same combinatorial geometry input files are used to specify the beam-line for the two codes. A schematic layout of the proton therapy beam-line modeled is shown in Fig. 1. The devices included in the therapy beam-line simulation include the secondary emission monitor, the multi-wire ionization chamber, three transmission ionization chambers, the dual scattering system and beam collimators. Monte Carlo models for the beam-line devices were based upon the machinist drawings used to manufacture the devices.

The range modulator wheel, used to spread the dose from mono-energetic Bragg peaks into clinically useful flat dose distributions, was modeled as a sequence of pie-shaped sections centered on the beam center-line. The thickness and fractional area covered by each section corresponded to the actual thickness and fractional area of the beam intersected by the rotating modulator wheel. The rotation of the range modulator wheel was simulated by rotating particles by a random angle about the beam-centerline immediately downstream of the range modulator wheel [5].

The energy of protons incident upon the beam-line was derived from the known synchrotron radius and frequency for each nominal beam energy (155-250 MeV beam energies were modeled). Energy cut-offs were selected to be 1 MeV for protons, and 20 MeV and 5 MeV for neutrons in LAHET and MCNP-X simulations respectively.

In-phantom dose distributions were compared with ionization chamber measurements made in a water phantom to investigate the accuracy of the Monte Carlo codes for the beam-line simulation. Non-modulated (mono-energetic) and range modulated beams were modeled. For the Monte-Carlo simulations, the total energy deposited was scored in 35 mm radius, 1 mm thick disks centered in a 500 mm radius cylindrical phantom. Ionization measurements were performed with a parallel plate ionization chamber. Ionization results were not corrected for depth/energy dependence of the water-to-air stopping power ratio. A 140 mm diameter circular field was used for the calculations and the measurements.

To demonstrate the ability of MCNP-X to perform patient calculations, a sample prostate treatment plan was calculated. The patient plan consisted of opposing lateral fields. Patient calculations required geometric modeling of the patient apertures and the range compensating bolus which is used to shape the distal portion of the dose distribution to match the target tissue contour. The patient aperture was modeled exactly and the bolus was modeled as a hexagonal prism lattice that closely matches the drill pattern used in making the bolus. The patient CT dataset was converted into the MCNP-X lattice geometry as follows. Using CTCREATE [8] from the BEAM/EGS [18] distribution, the patient CT dataset ($0.1 \times 0.1 \times 0.2$ cm³ voxels) was transformed onto the dose calculation grid ($0.4 \times 0.4 \times 0.4$ cm³ voxels). Each dose calculation grid voxel was assigned to be either air, tissue, soft-bone, or cortical bone depending upon the average CT

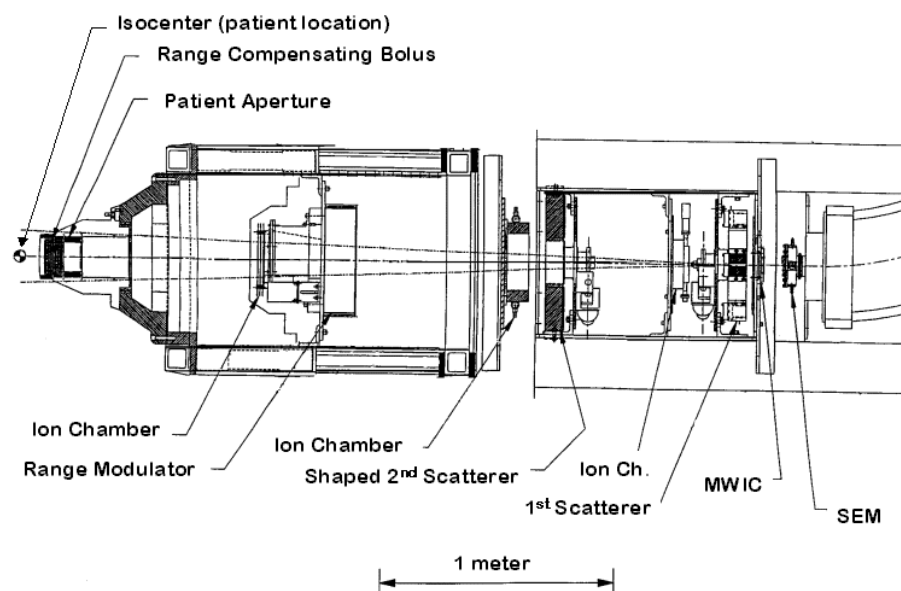


Fig. 1. Schematic layout of the proton therapy beam-line modeled

number in the voxel. CTCREATE output was converted to MCNP-X lattice geometry input using an in-house developed program. MCNP-X does not allow a material to be used at more than one density. To account for the material density variations, in MCNP-X, the filling cells for the lattice contained one of >900 different “materials”. Each of these materials was a duplicate of one of the four EGS materials, but with the density specified to the nearest $0.02 \text{ g}\cdot\text{cm}^{-3}$. Scoring for the patient calculation was done using the MCNP-X mesh tally. The scoring mesh was specified to exactly overlay the lattice used to specify the patient materials. Use of the mesh tally resulted in a decrease in the execution time when compared to using the lattice scoring tally.

The patient test calculations proceeded in three stages. The first stage transported from before the beam-line vacuum exit window to the exit of the final beam-line ionization chamber where particles were written to a phase space file (wssa). Following this stage, particles were rotated by a random angle about the beam centerline to account for the stationary model of the rotating range modulator wheel. As a variance reduction technique, individual particles from the original phase space file were randomly rotated to N different angles about the beam centerline and had their weight reduced by $1/N$ ($N=10$ was used for results shown). The rotated phase space file was used as input for the second stage calculation in which particles were transported through the patient field-specific aperture and range compensating bolus, then written to a phase space file at the exit of the bolus. The patient calculation followed as a third stage. The

beam entry angle into the patient was accounted by transforming the patient lattice into the beam-line coordinate system.

3 Results

LAHET and MCNP-X computed mono-energetic and range-modulated depth-dose results are compared with measured depth-ionization curves in Fig. 2. The nominal modulation for the range-modulated beam is 110 mm. The results agree with the statistical uncertainty of the calculations. For the cases studied, no adjustment of beam-line parameters was required to match calculated dose profiles with measurements.

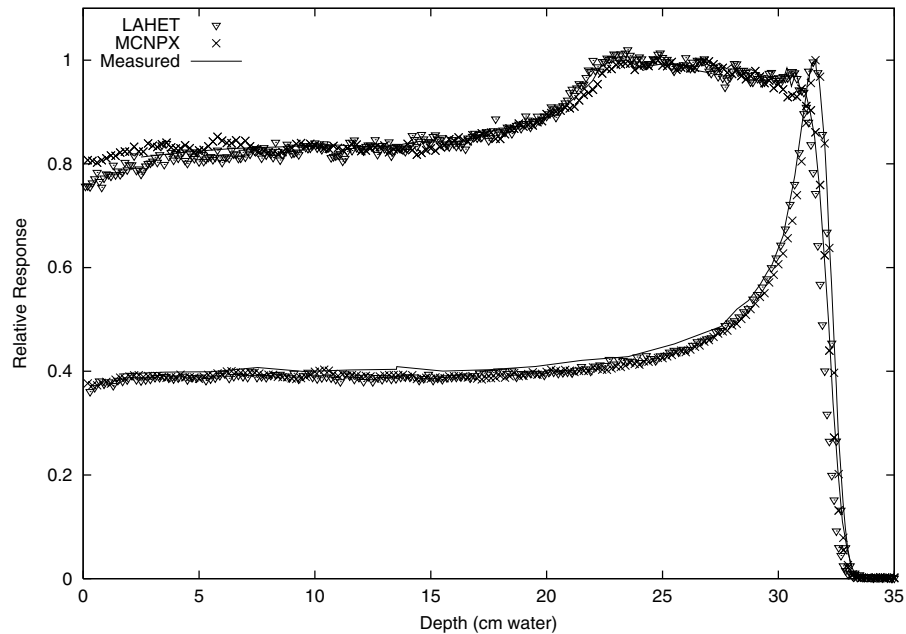


Fig. 2. Mono-energetic and range modulated central axis measured depth-ionization and LAHET computed depth-dose profiles

The dose distribution computed using MCNP-X for the prostate patient test case is shown in Fig. 3. This calculation was from 8.8×10^6 source particles incident upon the beam-line, with particles exiting the range-modulator being rotated 10 times about the central axis. In total, the plan took 445 CPU hours to compute on 500 Mhz Intel Pentium processors running LINUX. Of that, 3% of the time was transporting protons through the beamline, 82% of the time was transporting protons through the patient specific aperture and range-compensating bolus, and 15% of the time was transporting and scoring dose

deposition in the patient geometry. The statistical uncertainty in the dose at the patient isocenter is 2%. It is anticipated that substantial speed improvements can be achieved by increasing energy cut-offs in the patient aperture and by applying other variance reduction techniques.

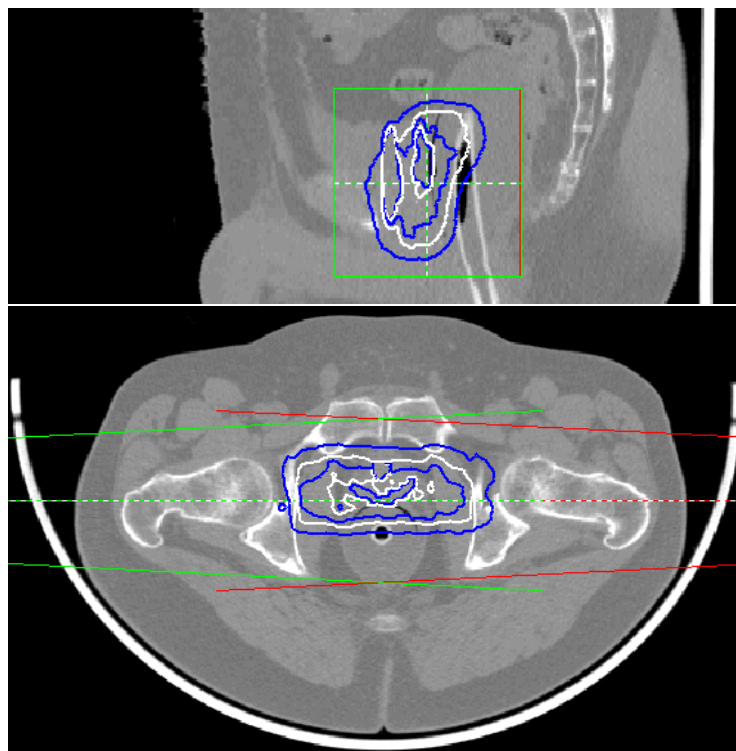


Fig. 3. Sagittal and transverse isodose plots for the two-field prostate test case computed with MCNP-X. The 95%, 90%, 80%, 70% and 50% isodose lines are displayed

4 Summary

LAHET accurately reproduced measured depth-dose profiles for a actual proton therapy beam-line. Use of MCNP-X for patient dose calculations has been demonstrated, although, currently MCNP-X is too time consuming for routine clinical proton-therapy dose calculations.

References

1. T.H. Braid, R.F. Rapids, R.H. Siemssen, J.W. Tippie, K. O'Brien: IEEE Trans. Nucl. Science **NS-18** (1971)

2. Jr. R.G. Alsmiller, R.T. Santoro, J. Barish: *Accelerators* **7**(1) (1975); also ORNL-TM-4754, February 1975
3. W.K. Hagen, B.L. Colborn, T.W. Armstrong, M. Allen: *Nucl. Sci. Eng.* **98**(172) (1988)
4. J.V. Siebers, P.M. DeLuca, Jr., D.W. Pearson, G. Coutrakon: *Nucl. Sci. Eng.* **115**(1) (1993)
5. J.V. Siebers, M. Traynor: *J. of Brachy. Int.*: **13**(1) (1997)
6. J. Medin, P. Andreo: *hys. Med. Biol.*: **42**, 89 (1997)
7. A. Del Guerra, G.D. Di Domonico, M. Gambaccini: *Nucl. Inst. Meth. A* **345** (1994)
8. C.-M. Ma, P. Reckwerdt, M. Holmes, D.W.O. Rogers, B. Geiser, B. Walters: *DOSXYZ users manual*. Technical Report Report No. PIRS-0509b, National Research Council of Canada, 1995
9. A.F. Bielajew: EGS4 timing benchmark results: 'Why Monte Carlo is a viable option for radiotherapy treatment planning'. In: *Presented at the International Conference on Mathematics and Computations, Reactor Physics, and Environmental Analyses, Portland, Oregon*, 1995
10. I. Kawrakow, M. Fippel, L. Friedrich: *Med. Phys.* **23** (1996)
11. C.L. Hartmann-Siantar, P.M. Bergstrom, W.P. Chandler, L. Chase, L.J. Cox, T.P. Daly, D. Garrett, S.M. Hornstein, R.K. House, E.I. Moses, R.W. Patterson, J.A. Rathkopf, A. Schach von Wittenau: *Peregrine project report*. Technical Report UCRL-JC-126732, Lawrence Livermore National Laboratory, 1997
12. J.J. DeMarco, T.D. Solberg, J.B. Smathers: *Med. Phys.* **25**(1) (1998)
13. L. Wang, C.-S. Chui, M. Lovelock: *Med. Phys.* **25**(6) (1998)
14. M. Fippel: *Med. Phys.* **26**(8) (1999)
15. C.M. Ma, E. Mok, A. Kapur, T. Pawlicki, D. Findley, S. Brain, K. Forster, A.L. Boyer: *Med. Phys.* **26**(10) (1999)
16. R.E. Prael, H. Lichtenstein: *Users guide to LCS: The LAHET Code System*. Technical Report LA-UR-89-3014, Los Alamos National Laboratory, 1989.
17. G.H. Hughes, R.E. Prael, R.C. Little: *MCNPX - the LAHET/MCNP code merger*. Technical Report LA-UR-97-4891, Los Alamos National Laboratory, 1997
18. D.W.O. Rogers, B.A. Faddegon, G.X. Ding, C.M. Ma, J. We, T.R. Mackie: *Med. Phys.* **22**, 503 (1995)

Monte Carlo Analysis of Correlation of Displacement Damage Due to Neutrons, Protons, Electrons and Gamma Ray in Microelectronic Devices

Huang Liu Xing, Chen Shi Bin, and Chen Yu Sheng

Northwest Institute of Nuclear Technology, P. O. Box 69, Section No.15, 710024,
Xi'an, China

Abstract. In this paper, the correlation of displacement damage produced by neutrons, protons, electrons and gamma ray in microelectronic devices is studied quantitatively by Monte Carlo method on basis of NIEL concept. The physical model and processes of NIEL caused by different particles with different energies are discussed and the computer programs have been set up to calculate the NIEL of neutrons, protons, electrons and gamma ray in silicon. The calculated results agree well with the typical values reported in literatures.

1 Introduction

Energetic particles such as neutrons, protons, electrons, and heavy ions can cause damage in semiconductor materials by displacing atoms as the particles transverse the materials. The secondary electrons produced by high energy gamma ray can also cause this type of damage. This displacement damage can reduce minority carrier lifetime, change majority carrier charge density, and reduce carrier mobility, all of which lead to degradation in device properties. The displacement damage factor K , which links directly the variation in particular electrical parameter to the incident particle fluence, was introduced to characterize the damage effects [1]. The value of K depends on many factors including the material type and carrier concentration. And it has been demonstrated that the displacement damage effects from different particles on several different devices can be correlated on the basis of the nonionizing energy loss (NIEL) [2–5]. Although the displacement damage effect has been studied extensively and systematically in past 30 years [6], however, the need for displacement damage data of devices in space applications has triggered a renewed interest in theoretical aspects of displacement because it would allow usage of data from ground experiment (with neutron, electron or gamma ray) to predict the behavior of devices in space radiation environment (high energy protons and electrons with different energy and different fluence).

In this paper, correlation of displacement damage produced by neutrons, protons, electrons and gamma ray in microelectronic devices is studied quantitatively by Monte Carlo method on basis of NIEL concept. The physical model and processes of NIEL caused by different particles with different energy will be discussed in section 2 and section 3.

2 Damage Model Based on NIEL

When a high energy particle passes through a matter, the normalized energy loss (stopping power) can be expressed as

$$S = \frac{1}{\rho} \frac{dE}{dR} = NIEL + IEL \quad (1)$$

where ρ is the density of the matter and dE/dR is the rate of energy loss along the path. NIEL and IEL stand for energy loss per unit mass due to atomic displacements and ionizing effects, respectively. Thus NIEL does not include any energy loss to ionizing effects.

According to what has been learned about displaced damage in past 30 years, a direct proportionality has been found between damage factor and NIEL of the particle [7,8]. Because of the importance and usage of the NIEL concept, it will be taken as the basis for correlation of displacement damage by different particles.

The NIEL of a particle of a given energy in a given material can be simply expressed as [8]

$$NIEL = \frac{N}{A} (\sigma_e T_e + \sigma_i T_i) \quad (2)$$

where N is Avogadro number, A is the gram atomic weight. σ are cross sections and T are energy transferred to recoil atoms for elastic collision and inelastic collision with nucleus, respectively.

Considering the angular dependence involved in collisions, the NIEL is then calculated by [8,9]

$$NIEL = \frac{N}{A} \int L[T(\theta)] T(\theta) \frac{d\sigma}{d\Omega} d\Omega \quad (3)$$

where $\frac{d\sigma}{d\Omega}$ is the differential cross section for a recoil in direction θ , $T(\theta)$ is the recoil energy, and $L[T(\theta)]$ is the fraction of the recoil energy that goes into displacements. The lower limit in the integral in (3) is determined by the displacement threshold energy and the upper limit occurs when a direct hit between the incident particle and the target takes place. The recoil energy $T(\theta)$ will contribute to secondary recoils, ionization and lattice vibration (phonons) process, and the partitioning of the recoil energy is simulated with a convenient approximation to Lindhard model given by Ziegler [10].

3 Simulation of Recoil Energy Spectrum Produced by Different Particles

The energy spectrum of primary knock-on atoms (PKAs) produced by different particles can be simulated by Monte Carlo method and the physical process for neutrons, protons, electrons or gamma ray is discussed in this section.

3.1 Neutrons

An incident neutron will probably undergo at most only one interaction in the active regions of device because of the mean free path of neutron is much longer than the dimension of a device. The first forced collision is used in Monte Carlo simulation. Both elastic and inelastic interaction are considered. The standard neutron data library for MCNP4b2 [11] is used in calculations.

As mentioned above, incident energetic neutrons can cause elastic nuclear or inelastic nuclear interactions with atoms in material. What kind of interaction will take place depends on its cross-sections by sampling. In elastic event, the amount of energy transferred to the recoil atom $T(\theta)$ can be obtained by following equation

$$T(\theta) = \frac{4M_1M_2E_{in}}{(M_1 + M_2)^2} \sin^2 \frac{\theta}{2} \quad (4)$$

where E_{in} is incident neutron energy, M_1 and M_2 are mass of neutron and target atom respectively, and θ is the scattering angle in center-of-mass coordinate system. The scattering angle is sampled as the same method with that used in MCNP4b2 code.

For an inelastic scattering, the treatment depends upon the particular inelastic scattering chosen and can refer to [11].

3.2 Protons

The basic interactions considered for protons include Coulombic elastic collision, nuclear elastic scattering and inelastic collisions. All of these processes generate energetic PKAs which are capable of displacing many silicon atoms from their normal positions. These can be simulated using the approach presented by Burke [8].

3.3 Electrons

Electrons interact with matter mostly through ionization processes and thus contribute little to displace damage. In order to simulate the creation of recoils by electrons, the single scattering Monte Carlo method is used. It involves calculating a cross section and a recoil energy, which are outlined in Seitz and Koehler [12].

3.4 Gamma ray

Gamma ray can not create displacement in matter, however, the secondary electrons produced by gamma ray can cause this type of damage. The generated electron energy spectrum on the active region of devices is obtained through calculating the initial generated electron spectrum from photoelectric and Compton scattering processes and then calculating the slowed electron energy spectrum (the spectrum of electrons arrives at the region of interest).

4 Results and Discussion

Based on the physical model considered above, the computer program NIEL_N, NIEL_P, NIEL_E and NIEL_G have been set up to calculate the NIEL of neutrons, protons, electrons and gamma ray in silicon. Figures 1 and 2 show the calculated energy spectrum of recoil atoms produced by 1 MeV neutron and 1 MeV electron, respectively.

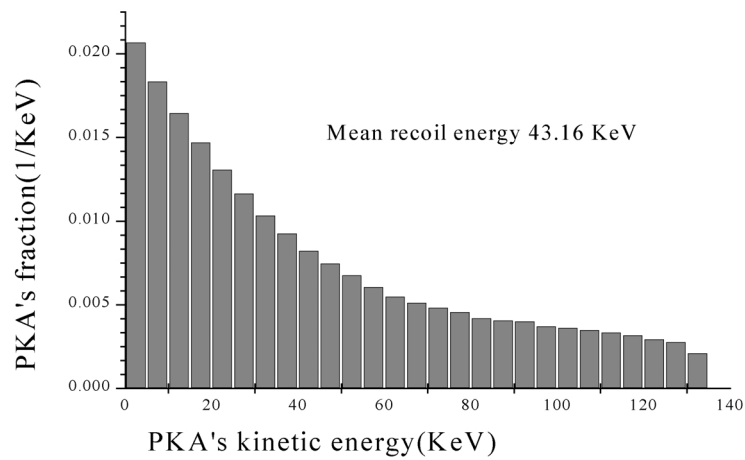


Fig. 1.

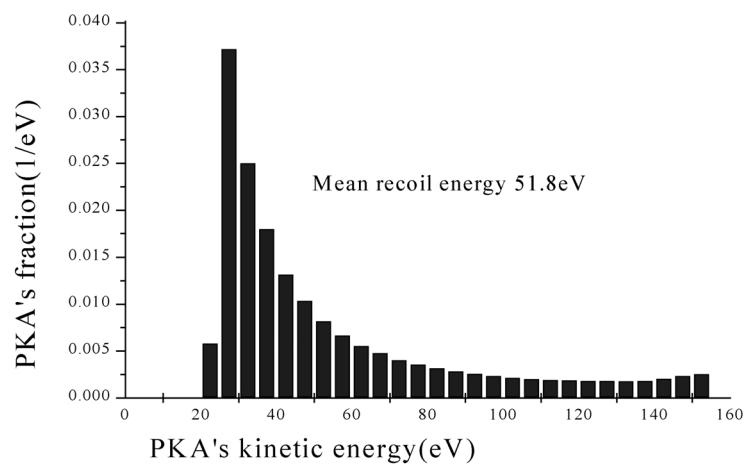


Fig. 2.

The calculated values of NIEL of 1 MeV neutron, 20 MeV proton, 1MeV electron and 1.25 MeV gamma ray in silicon agree well with the typical values reported in literatures.

These two figures are normalized, i.e., the area in each of the figures equals unity. These two figures show that the PKA with the lower energy has the bigger fraction. The mean energy of PKA induced by 1 MeV neutron is much higher than that induced by 1MeV electron. It implies that 1MeV neutrons can produce more severe displacement damage.

The calculated stopping powers of displacement for 1 MeV neutron, 1MeV electron and ^{60}Co gamma ray in silicon are illustrated and compared with the typical values reported in some literatures in Fig. 3. They agree very well with each other. The calculated stopping powers of NIEL and IEL in silicon irradiated by protons are shown in Fig. 4. From Figs. 3 and 4, we can obtain the following verdicts: the amount of NIEL to Si orderly decreases by several orders in rank of 1MeV neutrons, protons, electrons and ^{60}Co gamma rays. Owing to the PKA's energy produced by 1MeV neutrons and protons higher than 20keV and the PKA's energy produced by 1MeV electrons and ^{60}Co gamma rays lower than 2keV, according to Wood et al. [13], the damage to silicon irradiated by 1MeV electrons and gamma rays can only appear point defects, and that 1MeV neutrons and protons produce tree-like defect structure.

Therefore, by computing the NIEL of neutrons, protons, electrons and gamma ray with different energy spectrum, we may make quantitative predictions for particle-induced device degradation in complicated practical environment from one or more ground facility (for example, ^{60}Co gamma ray sources, neutron reactors and electron accelerators etc.) test results.

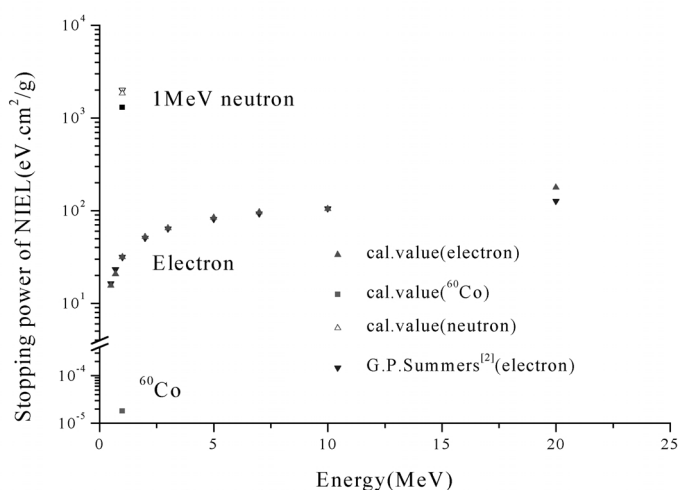
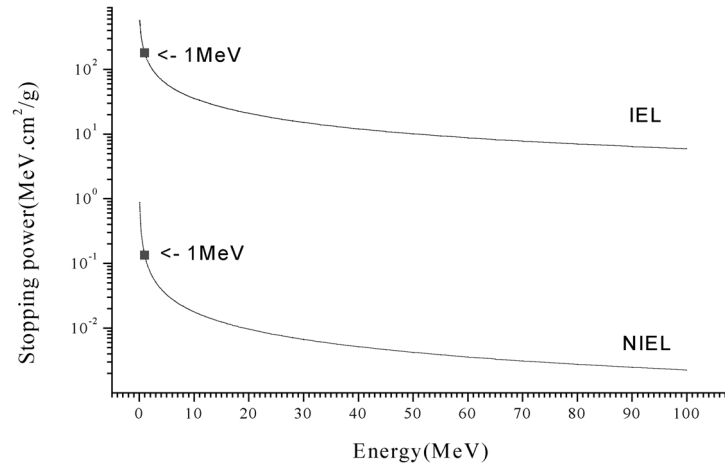


Fig. 3.

**Fig. 4.**

References

1. D. Brautig, F. Wulf: 'Radiation Effects in Electronic Components'. In *Instabilities in Silicon Devices, Volume 3*, ed. by G.Barbottin, A. Vapaille (North-Holland, 1999) pp.639-722
2. G.P. Summers et al.: IEEE Trans. Nucl. Sci. **34**, 1134 (1987)
3. E.A. Burke et al.: IEEE Trans. Nucl. Sci. **35**, 1220 (1988)
4. P.W. Marshall et al.: IEEE Trans. Nucl. Sci. **36**, 1882 (1989)
5. G.P. Summers et al.: IEEE Trans. Nucl. Sci. **40**, 1372 (1993)
6. G.P. Summers: 'Displacement Damage: Mechanisms and Measurements'. In: *IEEE NSREC Short Course*, 1992
7. C.J. Dale et al.: IEEE Trans. Nucl. Sci. **35**, 1208 (1988)
8. E.A. Burke et al.: IEEE Trans. Nucl. Sci. **33**, 1276 (1986)
9. G.P. Summers et al.: IEEE Trans. Nucl. Sci. **35**, 1221 (1988)
10. J.F. Ziegler et al: *The Stopping and Range of Ions in Solids*, Vol.1, (Pergammon Press, New York, 1985)
11. *MCNPXS: Standard neutron, photon, and electron data library for MCNP4b2*, DLC-189, Los Alamos National Laboratory, 1997
12. F. Seitz, J.S. Koehler: *Displacement of Atoms during irradiation*'. In *Solid State Physics*, Vol.2, ed. by F. Seitz and D. Turnbull. (Academic Press Inc., New York, 1956)
13. S. Wood et al.: IEEE Trans. Nucl. Sci. **28**, 4107 (1981)

Monte Carlo Simulations of Neutral Gas and Fast Ion Dynamics in GDT Experiments

K. Noack

Forschungszentrum Rossendorf, Postfach 51 01 19, 01314 Dresden, Germany

1 Introduction

The Budker Institute of Nuclear Physics (BINP) Novosibirsk proposed a highly intense 14 MeV neutron source based on a gas dynamic trap (GDT) [1]. The GDT is an axisymmetric mirror plasma device. In case of the complete effectiveness at the necessary parameters this type of neutron source promises several advantages in comparison to other proposals [2]. Its actual disadvantage is the incomplete data base which does not yet allow a reliable interpolation of its feasibility. To close this gap is the goal of the experimental and computational research presently being under way.

Figure 1 shows a schematic drawing of the GDT experimental facility. The scheme is similar to that of the proposed steady state neutron source. The experiments are performed in a shot type regime over a total time of about 5 milliseconds. After putting up the magnetic field the so-called *target plasma* composed of protons and electrons is fed into the system by a plasma gun. In this stage the density of the plasma reaches the range of $5\text{--}15 \times 10^{13} \text{ cm}^{-3}$ and its electron temperature is about 5–10 eV. After 2–3 milliseconds six hydrogen neutral beams of an energy between 13–17 keV are injected under an angle of 45 degrees to the axis. This injection pulse takes 1.1 milliseconds and reaches its maximum total power around 4 MW. 50–60 per cent of the injected hydrogen atoms are ionised by the interaction with the target plasma. The protons start their gyrating motion in the magnetic field and shuttle back and forth somewhere between the mirror coils. They represent the population of the so-called

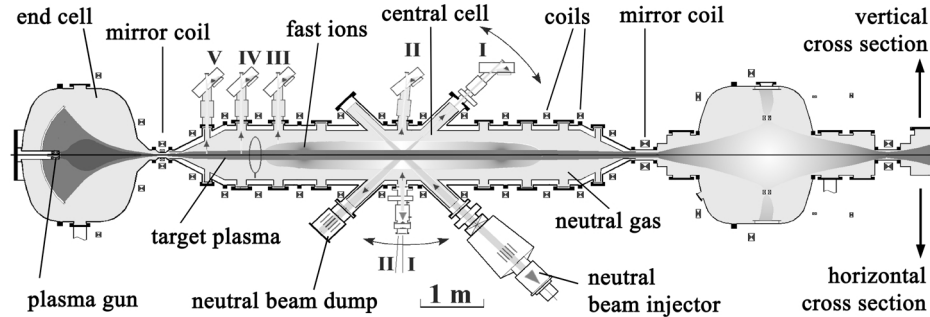


Fig. 1. GDT experimental facility

fast ions. Usually, the measurements of various functionals of their distribution function are performed up to 2 milliseconds after the start of the injection. The axial positions of their turning points depend only on the pitch angle between the flight directions and the system axis when crossing the midplane. Therefore, the density of the fast ions is well peaked in the regions of their turning points on both sides of the system provided that their pitch angle distribution is a pretty narrow one. In case of the neutron source when the fast ions are a mixture of deuterons and tritons just these density peaks are to be the intense source regions of D-T fusion neutrons. This fact makes clear that the behaviour of the fast ions is a key issue of the project. Especially, intense particle losses, a great pitch angle spreading and a fast energy loss have to be avoided. The project assumes that the behaviour of both plasma components is completely determined by classical transport phenomena basing on two-body collisions between the particles and no anomalous effects will occur. Only in this case the projected source parameters can be achieved.

Angular scattering and energy moderation of the fast ions are caused by the interaction with the target plasma resulting in its heating up to about 100 eV, whereas, the main part of the particle losses result from the interaction with the *neutral gas* contained in the chamber. Measurements have shown that during the shots the gas predominantly consists of hydrogen atoms and molecules. Besides a central gas cloud appearing around the centre where the neutral beams hit the target plasma the gas is mainly located outside the plasma but infiltrates its edge up to a certain depth. With respect to the fast ions the neutral gas takes the part of an absorber because the possible charge exchange (cx) between a fast ion and a hydrogen atom/molecule transforms a fast ion into a fast neutral which may leave the plasma and hit the chamber wall.

To interpret measured quantities of the fast ions and to decide whether they correspond to classical behaviour or whether non-classical effects are involved demands the comparison with results of numerical codes simulating the classical particle fields. The Monte Carlo codes TUBE for the hydrogen gas and MCFIT for the fast ions which have been developed by Forschungszentrum Rossendorf in collaboration with BINP take just this important part. A short description of the TUBE code and comparisons of calculated and measured results are given in [3]. Therefore, in section 2 only the MCFIT code is shortly described. Section 3 compares some numerical with measured results and draws certain conclusions.

2 Monte Carlo Fast Ion Transport Code MCFIT

The general scheme of the code is of standard Monte Carlo type. The history of a particle within the phase space (\mathbf{r}, \mathbf{v}) is randomly generated by a sequence of certain events. Each fast ion starts as an energetic atom which is emitted from the neutral beam injection system. After its ionisation by the target plasma the random walk of a fast ion follows. It consists of an alternate sequence of an interaction-free flight under the Lorentz-force of a given, may be time dependent magnetic field $\mathbf{B}(r, z, t)$ – r, z are cylindrical coordinates – and an interaction

process with both the target plasma and the neutral gas. The target plasma is assumed to be given by a discrete density $p(r, z, t)$ and its electron temperature $T_e(r, z, t)$. The hydrogen gas g may consist of three components: g_{fast} – fast atoms with energies corresponding to that of the fast ions, usually defined above 1 keV, g_{slow} – slow atoms with energies of the target plasma ions and moderated by reflections from the container wall and g_{mol} – molecules with energies corresponding to the wall temperature. These gas densities must be given as discrete radial, axial and time dependent distributions. During its life the particle ages. Its age is measured relatively to the start of the injection. The particle history may terminate in various ways: either by radial or longitudinal leakage from the system or by killing the particle when its energy, age or statistical weight is going beyond a user-defined limit. The main components of the random walk may be briefly described as follows.

Source: Each source particle starts from the emitter surface of one of the six neutral beam injectors. The particles are distributed among the individual injectors according to their portions of the total injected energy. The point of emission is homogeneously selected on the surface. The energy of the starting neutral is put equal to that value E_{inj}^i specified for the injector i and the flight direction is selected from a two-dimensional Gauss-distribution for the tangents of the angle between the flight direction and the lateral and transversal axis of the local coordinate system. These distributions for each injector have the widths α^i and β^i . The age of the starting particle is selected in accordance to the time course of the injection power $P_{inj}^i(t)$ of the selected injector and its statistical weight is set equal to one.

Ionisation of the neutral beam atoms and generation of slow atoms: Flight and collision of an injected atom are analogously simulated. At the collision point the fast ion history begins. The atom could be ionised by ion impact, electron impact or charge exchange. The corresponding cross sections are taken from [4]. Without resolving the type of collision occurred a slow atom is born at the same point and its data are written on a special file which may be used as a source by the neutral gas codes TUBE and NEUSI [5].

Interaction-free flight in the given magnetic field: For the step by step simulation of the gyrating motion a modified version of the predictor-corrector algorithm has been developed. It is used with a sufficiently small time step Δt so that the constants of motion – the energy, the generalised moment and the adiabatic invariant magnetic moment – are kept nearly constant over the lifetime of the ion within an acceptable accuracy. The time step Δt varies with the magnetic field strength $B^{-1}(\mathbf{r})$ in dependence on the location \mathbf{r} of the ion, so that the angle of the larmor rotation remains constant.

Interaction with the target plasma: The interaction with the target plasma and with the neutral gas during the time Δt at the new ion location completes the transition in the phase space. The simulation of the interaction with the target plasma bases on the classical theory of two-body coulomb interactions with a maxwellised plasma. The energy loss ΔE of the ion, which is mainly caused by electron-drag, is determined by $\Delta E = E * \Delta t / \tau_E$ where τ_E is the “total

energy relaxation time". The scattering of the flight direction is simulated on the base of the "total deflection time" τ_d : the cosine of the scattering angle θ is determined by $\cos(\theta) = 1 - \Delta t/(2\tau_d)$ and then the new flight direction vector is uniformly selected around the old flight direction. All quantities involved in the time constants are calculated taking into account their dependencies on the plasma density $p(r, z, t)$, on the electron temperature $T_e(r, z, t)$ and on the energy E of the fast ion to maximum extent. The only approximation is the assumption that the plasma ion temperature T_i is equal to T_e which is made because no other information is available from the experiment so far.

Interaction with the neutral gas and generation of fast hydrogen atoms: The only interaction of the fast ion with the slow atoms and with the molecules is the charge exchange process resulting in its loss and in the simultaneous birth of a fast neutral. The absorption is implicitly taken into account, i.e. by an appropriate weight reduction. This weight reduction is also the contribution to the estimator of the charge exchange loss power P_{cx} . In contrast to this procedure fast atoms are born by an analogous simulation, though, here an optical age takes the part of the optical path length in stationary problems. The birth data of fast neutrals are written on a special file which may be used by the TUBE and NEUSI codes to simulate their transport inside the GDT. MCFIT also offers the possibility to consider the interaction with fast atoms. Ion impact and charge exchange with these atoms would give a multiplication and angular scattering of the fast ion. All cross sections necessary for the simulations of the various interactions with the gas components are taken from [4].

MCFIT offers a great spectrum of physical quantities that may be estimated. The results represent the quantities of interest as discrete distributions over a phase space grid for a sequence of time intervals. In space an axisymmetric mesh-grid $[r(z), \phi, z]$ is used where the radius coordinate $r(z)$ scales proportional to $B^{-1/2}(r=0, z)$ in accordance with the magnetic flux tube and ϕ is the azimuth angle. In order of growing degree of differentiation the code estimates the following quantities together with their standard errors:

- *Global quantities:* several averaged fast ion characteristics.
- *Time functions:* quantities which are phase space integrated and averaged over the time intervals. The main functions are: energy content $W_f(t)$, power of the neutral beams which is deposited as fast ions $P_{tr}(t)$, cx-loss power $P_{cx}(t)$ and the drag-loss power $P_{drag}(t)$.
- *Energy distributions:* $f(E)|_{r,t}$ – for various time intervals Δt the mean number of fast ions per energy interval integrated over magnetic flux tubes defined by radial intervals Δr .
- *Pitch angle distributions at the midplane of the GDT:* $f(\theta)|_{E,r,t}$ – mean number of fast ions per pitch angle interval for user-defined energy intervals, radial volumes and time intervals.
- *Densities of linear and non-linear functionals of the fast ion field:* $F(r, \phi, z)|_t$ – several energy and flight direction integrated quantities averaged over volume cells of the space mesh-grid and over time intervals. Via input the user may specify the degree of discretisation. Examples of linear functionals

are the particle density f itself, the energy density w_f and the densities of the various loss powers mentioned above. An example of a non-linear functional is the neutron density produced in D-D fusion reactions which occur in experiments with deuterium injection instead of hydrogen. At present, a non-linear quantity must be calculated in two steps: in a MCFIT pre-calculation information on the fast ion distribution in dependence on space, energy, flight direction and time is collected and then put into the second calculation which actually estimates the non-linear functional. The user may determine the output of the wanted quantities in several partially integrated dependencies.

The tallies are scored at the midplane crossings in case of the angle distributions and at the interaction points for the other quantities.

MCFIT realises the particle transport in a cycle of transport simulations. In each cycle a batch of particles is transported from their emissions up to their deaths. This is carried out in a vectorised manner. In the version for parallel computers the code simply simulates the same number of cycles of particle batches on each processor. In general, the time diffusion of the processors is negligible in comparison to the total CPU-time of a calculation. At present, the code runs under Message Passing Interface (MPI) on a Hewlett Packard parallel computer HP V2250/V-Class with sixteen PA-RISC 8200 processors. It is written in FORTRAN 77.

3 Results and Conclusions

For the GDT regime with high-power injection up to 4 MW the fast ion population was experimentally investigated in great detail [6]. Corresponding calculations were performed by means of MCFIT with measured target plasma data and with the calculated neutral gas field as input. Figure 2 shows some of the measured and calculated *time functions*. The only remarkable difference appears in the cx-loss power P_{cx} . Since this loss is low compared to the drag-power P_{drag} the influence of the discrepancy on the particle and on the energy content re-

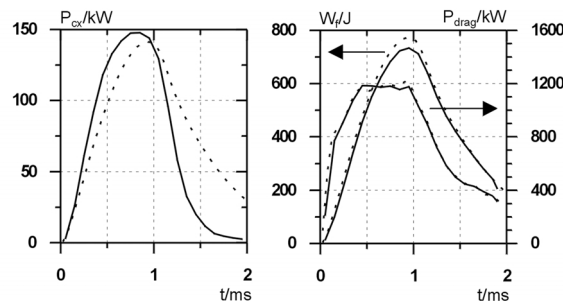


Fig. 2. Absolute values of measured (dashed lines) and calculated *time functions*

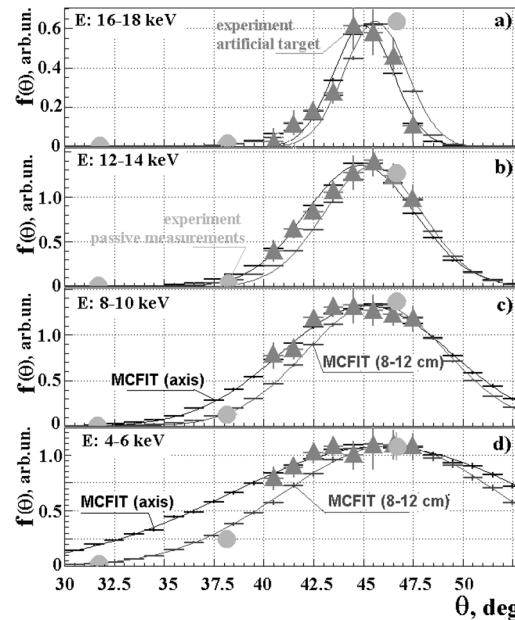


Fig. 3. Measured and calculated pitch angle distributions (normalised)

mains moderate. There are no statistical difficulties for the estimation of those quantities.

Figure 3 presents the comparison between normalised measured and calculated pitch angle distributions of the fast ions for several intervals of energy and radius averaged over the time interval 0.6–0.9 ms. An excellent agreement may be stated. A great computation time is necessary to get these distributions with sufficient statistical accuracy.

Concerning the fast ion study the general conclusion may be drawn that – up to the present plasma parameters of the GDT – they really behave classically. This conclusion which is of extraordinary importance for the project of a GDT based neutron source can be drawn with high reliability because it rests on the solid foundation of the two Monte Carlo codes TUBE and MCFIT.

References

1. A.A. Ivanov, D.D. Ryutov: Nucl. Sci. Eng. **106**, 235 (1990)
2. E.P. Kruglyakov: Trans. Fusion Technol. **35**, 20 (1999)
3. P.A. Bagryansky et al.: J. Nucl. Mater. **265**, 124 (1999)
4. R.K. Janev et al.: *Elementary Processes in Hydrogen-Helium Plasmas - Cross Sections and Reaction Rate Coefficients*, Springer Series on Atoms and Plasmas, vol. 4 (Springer, New York 1987)
5. S. Collatz, K. Noack: Trans. Fusion Technol. **35**, 375 (1999)
6. A.V. Anikeev et al.: Nuclear Fusion **40**, 753 (2000)

Treatment Planning for Carbon Ion Radiotherapy

M. Krämer¹, O. Jäkel², T. Haberer¹, G. Kraft¹, D. Schardt¹, D. Scholz¹, and U. Weber¹

¹ GSI, Planckstr. 1, D-64291 Darmstadt, Germany

² DKFZ, INF 280, D-69120 Heidelberg, Germany

1 Introduction

One of the main objectives in radiotherapy is the conformal delivery of the prescribed dose to the target volume, whereas the surrounding healthy tissue and critical structures should be spared as much as possible. In comparison with conventional photon beams, therapeutic ion beams in general offer the advantage of a depth dose distribution with a pronounced maximum (Bragg maximum) and a sharp dose fall-off at large penetration depth, in contrast to the exponential dose deposition of photons or neutrons, or the broad maximum generated by electrons. This is also known as *inverted dose profile* and it allows a higher degree of dose conformation to the target volume. Heavier ions like ^{12}C offer further advantages over protons or other lighter charged particles: First, the lateral scattering in tissue is reduced roughly by a factor of 3. Second, carbon ions have an increased relative biological effectiveness (RBE), especially in the stopping region at the Bragg peak. These particular properties make carbon ion beams an ideal candidate to be combined with the evolving techniques of intensity modulated radiotherapy (IMRT).

In December 1997 an experimental heavy ion radiotherapy facility became operational at the German heavy ion research center GSI (Gesellschaft für Schwerionenforschung, Darmstadt). The aim is to investigate the clinical impact of the unique properties of heavy ions and to show which patients can benefit from such a therapy.

The GSI facility realizes for the first time a combination of an active field shaping, using a scanned beam [1], with an active energy variation of the beam, thus making full use of the advantages of heavy charged particles for therapy. This novel irradiation technique requires a method for dose calculation and optimization which is radically different from conventional approaches used for example in photon and even proton therapy, due to the strong dependence of the RBE on particle charge, energy and absorbed dose. A prerequisite is the development of a physical beam model as well as a radiobiological model to describe the interactions of ion beams with biological material.

2 Beam Delivery System

The general design idea is to use completely active volume scanning in three dimensions. This can be achieved by magnetic deflection of the ^{12}C beam in

lateral direction (intensity-controlled raster scan [1]) and by energy variation of the GSI synchrotron to cover different depths in order to spread out the dose across the target volume. Figure 1 shows a schematic overview. In order to match the needs of radiotherapy the accelerator control system was modified to allow selection of the energy, beam spot size and intensity level of the ^{12}C beam from one synchrotron cycle to the next [2]. A list of 253 energies has been setup in order to achieve a constant spacing of the corresponding ranges in water. This is important to obtain a homogenous depth dose distribution. The energy range is between 80 MeV/u and 430 MeV/u corresponding to a range in tissue between 20 mm and 330 mm, respectively. The ion energy can be switched within ≈ 5 seconds and thus different depths can be reached without the need of additional absorbers. This way the target region is divided into subsequent slices corresponding to beams of different energies. A large tumour may require up to 50000 different beam positions.

3 Requirements for Treatment Planning

For photon beams numerous commercial and research prototype software packages exist. For heavy ions commercial treatment planning systems do not exist. We thus decided to couple an existing conventional radiotherapy planning system (Voxelplan, developed at the German Cancer Research Center, DKFZ, [3]) with a code developed newly at GSI (TRiP, **T**reatment planning for **P**articles, [4]). Voxelplan covers the conventional tasks of graphics rendering and user interface, whereas TRiP handles all physical and radiobiological aspects of heavy ions, including dose optimization.

Treatment planning for scanned heavy ion beams starts just like conventional planning, that is, imaging devices such as magnetic resonance (MR) and computer tomography (CT) are used to generate a digital model of the irradiation region. While MR images deliver high resolution information on tumour location

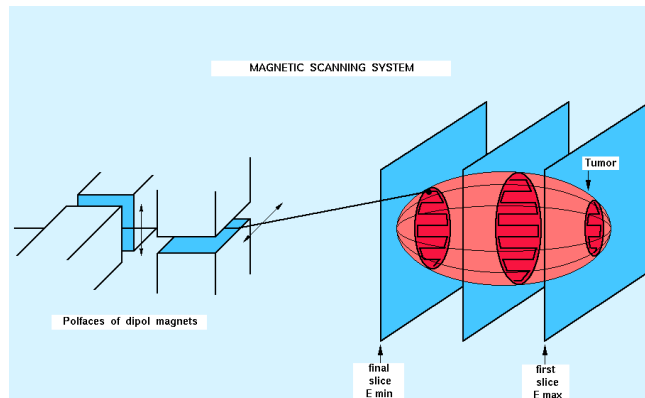


Fig. 1. Schematic view of the magnetic scanning system

and critical structures, the CT data are mandatory for dose computation and optimization.

The main task of treatment planning for scanned ion beams is to determine the different particle fluence values for all beam energy slices and beam positions. This is best achieved by applying a pencil model (rather than Monte Carlo) for the individual beams and by using inverse planning methods to obtain the desired values automatically from the prescribed dose distribution.

4 Physical Beam Model

The beam model we use so far is based on the fact that for ion beams as heavy as ^{12}C the multiple elastic scattering plays only a minor role. The light fragments, which are generated while a heavy ion traverses matter, will experience larger deflections. However, since they contribute only a small amount to the overall dose, their multiple scattering is neglected as well in first order.

Under these assumptions the (partial) dose generated by a single heavy ion beam with energy E_{beam} can be described as

$$D(E_{\text{beam}}, \mathbf{x})[\text{Gy}] = 1.6 \times 10^{-8} \times d(E_{\text{beam}}, z) \left[\frac{\text{MeV}}{\text{gcm}^{-2}} \right] \times \frac{N}{2\pi\sigma^2[\text{mm}^2]} \exp\left(-\frac{1}{2} \frac{r^2}{\sigma^2}\right) \quad (1)$$

where r is the distance from the beam centre, σ is the actual width (variance) of the Gaussian beam profile and N is the total number of particles. The most important quantity, however, is the energy loss distribution $d(E_{\text{beam}}, z)$, for a given initial beam energy, E_{beam} , as a function of penetration depth, z , which has to be described by an appropriate model. Such a model has to include not only the single particle energy loss, but also the energy loss straggling and the process of projectile fragmentation in order to reproduce experimentally determined dose profiles with sufficient accuracy [5]. For the sake of brevity we will not describe the model in detail, we refer to [4] instead.

For practical use in therapy planning it is sufficient to calculate the depth dose profiles in steps of 10 MeV/u initial beam energy from 50 to 500 MeV/u. The profiles are calculated only once and then stored as tables. The fragment spectra $dN(E_{\text{beam}}, z, T, E)/dE$ for each depth are stored as well, to be used in algorithms where the fragment and energy distribution is required, such as calculation of RBE or response of solid state detectors. When beam energies are required which are not represented in the pre-calculated database, linear interpolation between the next neighbours is performed.

5 Radiobiological Beam Model

A main advantage of heavy charged particles in radiotherapy is their increased RBE which is due to increased local ionization density on the level of the cell nucleus. Many attempts have been made in the past to describe charged particle radiation action on biological systems [6]. For the GSI radiotherapy we chose the

local effect model (LEM) of Scholz [7,8] which is based on the x-ray sensitivity of cells, the structure of a heavy ion track and the size of the cell nucleus. This model is the best choice for a number of reasons:

- it clearly separates the physical properties of the radiation from the biological properties of the irradiated object;
- the relevant biological properties can be measured or estimated, like the radiation sensitivity represented by the α/β -ratios of x-ray dose-effect curves for single cells and by the known response of tumors and normal tissue to x-rays;
- the physical properties of the radiation, that is the radial dose distribution around a heavy ion track can be described with reasonable accuracy by various models, either analytical [9] or by Monte Carlo simulations [10].

LEM essentially allows to predict the response of biological systems irradiated with particles of a particular type and energy from the knowledge of the x-ray response. This is an important advantage because few experimental data for tissue response to ion radiation are available.

In the context of treatment planning we apply this model to replace the physically absorbed dose by the biologically effective dose [11]

$$D_{\text{biol}} = D_{\text{abs}} \times RBE(\mathbf{x}, D_{\text{abs}}) \quad (2)$$

where the RBE depends on the location within the irradiated volume as well as on the absorbed dose level.

6 Dose Optimization

For the dose optimization it is sufficient in first order to use one-dimensional dose distributions $d(E_{\text{beam}}, z)$ because the lateral beam scattering is negligible compared to the initial beam width as delivered by the beam optics. In this case the dose computation (1) can be simplified to

$$D(E_{\text{beam}}, \mathbf{x})[\text{Gy}] = 1.6 \times 10^{-8} \times d(E_{\text{beam}}, z) \left[\frac{\text{MeV}}{\text{gcm}^{-2}} \right] \times F(E_{\text{beam}}, x, y) [\text{mm}^{-2}] \quad (3)$$

with the fluence

$$F(E_{\text{beam}}, x, y) = \frac{N(E_{\text{beam}}, x, y)}{\Delta x \Delta y} \quad (4)$$

where the Δx and Δy are the scanner step sizes in x and y, respectively. Within the target volume the lateral overlapping of neighbouring beam positions compensates for this crude approximation of a gaussian profile by a delta function.

The task of particle fluence optimization with respect to dose represents a least squares minimization with respect to the fluence values $F(E_{\text{beam}}, x, y)$:

$$\chi^2 = \sum_z w(\mathbf{x}) (D_{\text{prescribed}} - D(\mathbf{x}))^2, \quad \frac{\partial \chi^2}{\partial F} = 0. \quad (5)$$

with appropriately chosen weight factors $w(\mathbf{x})$ and the dose $D(\mathbf{x})$ as given by (3).

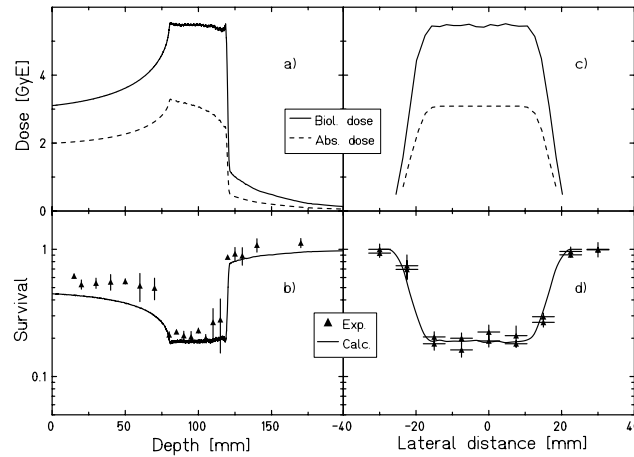


Fig. 2. Biologically effective dose equivalent optimization for CHO cells. The prescribed dose was 5.5 GyE in a single fraction, corresponding to a 20% survival level. The target region was between 80 and 120 mm depth, field size $40 \times 100 \text{ mm}^2$. Experimental data from [12]. Part a: Calculated absorbed and biologically effective dose profile as a function of depth. Part b: Measured (symbols) and calculated survival as a function of depth. Part c: Calculated absorbed and biologically effective lateral dose profile. Part d: Measured (symbols) and calculated survival in lateral direction

The task is solved by iteration in two major steps, as described in [4]. First a simple dose matching procedure is applied, proceeding from the distal to the proximal slices of the target volume. With the resulting fluences as start values, text book minimization algorithms like Conjugate Gradients or Marquardt's algorithm are used in a second step to yield satisfactory dose conformation. The method works for absorbed as well as for biologically effective dose provided the RBE is correctly calculated as a function of the absorbed dose level and the location within the irradiated volume.

Figure 2 illustrates a biologically effective dose optimization including experimental verification performed for CHO cells. The target region was a cuboid with a volume $40 \times 100 \times 40 \text{ mm}^3$. For a description of the experimental procedure we refer to [12]. As expected the absorbed dose decreases in the distal part of the target volume due to the increasing RBE of stopping particles. The lower left part of the figure compares measured and calculated survival profiles as a function of depth. While there is good agreement in the target region and beyond, the calculated cell response in the entrance channel is larger than the measured one due to experimental dose rate effects. In any case we are on the safe side, however, since the biologically effective dose is overestimated rather than underestimated. The lower right part finally shows the lateral survival profile on a line through the center of the target volume. Here good agreement could be

achieved between measurement and calculation, which includes the finite beam width.

7 Summary and Conclusion

We have developed and described the first ion therapy planning system based on the concept of biologically effective dose which is able to generate a strictly tumor conformal irradiation using intensity modulated fields of scanned heavy ions. These features make it a unique tool for the cancer treatment with heavy ions. The algorithms and procedures presented in this contribution are in regular use since 1995 for the planning of numerous irradiation experiments including cell and animal experiments such as mini-pig lungs and skin, and the central nervous system of rats, where they have proven to be correct. Finally, the methods have been transferred unchanged to patient treatment planning. More than 60 patients have been planned and treated with this software. Good tumour response and almost no acute side effects have been observed.

Future developments will be directed towards further exploitation of the high RBE, for example simultaneous multiport optimization in order to take full advantage of the high RBE of stopping ^{12}C in a larger part of the target volume.

Monte Carlo simulations may improve dose calculation in cases of sharp density gradients because here the effects of multiple scattering might be significant. We plan, however, to implement MC directly into our code rather than relying on external packages.

References

1. Th. Haberer et al.: Nucl. Inst. Meth. A **330**, 296 (1993)
2. T. Eickhoff, B. Franczak, U. Krause, C. Riedel, W. Rösch, R. Steiner: *Accelerator development for the GSI therapy project*. GSI-report 96-01
3. G. Gademann, W. Schlegel, J. Bürkelbach, C. Laier, S. Behrens, S. Brieger, M. Wannenmacher: *Strahlentherapie und Onkologie* **169**, 159 (1993)
4. M. Krämer, O. Jäkel, T. Haberer, G. Kraft, D. Schardt, U. Weber: *Phys. Med. Biol.* **45**, 3299 (2000)
5. Th. Haberer: *Entwicklung eines magnetischen Strahlführungssystems zur tumorkonformen Strahlentherapie mit schweren geladenen Teilchen*, GSI-report 94-09
6. K.H. Chadwick, G. Moschini, M.N. Varma: *Biophysical Modelling of Radiation Effects*, (Adam Hilger, Bristol 1992)
7. M. Scholz, G. Kraft: *Adv. Space Res.* **18**, 5 (1996)
8. M. Scholz, A.M. Kellerer, W. Kraft-Weyrather, G. Kraft: *Rad. Environ. Biophysics* **36**, 59 (1997)
9. C.X. Zhang, D.K. Dunn, R. Katz: *Radiat. Prot. Dosim.* **13**, 215 (1985)
10. M. Krämer, G. Kraft: *Rad. Environ. Biophysics* **33**, 91 (1994)
11. M. Krämer, M. Scholz: *Phys. Med. Biol.* **45**, 3319 (2000)
12. A. Mitaroff, W. Kraft-Weyrather, O. B.Geiß, G. Kraft: *Rad. Environ. Biophysics* **37**, 47 (1998)

Neutron Shielding Calculations for a 230-MeV Proton Therapy Facility

U. Titt¹, W.D. Newhauser¹, X. Yan^{1,2}, and D.T. Dexheimer³

¹ Massachusetts General Hospital, 55 Fruit Street, NPT-100, Boston, MA, USA

² Harvard Cyclotron Laboratory, 44 Oxford Street, Cambridge, MA, USA

³ Bechtel National Inc., 50 Beale Street, San Francisco, CA, USA

Abstract. Proton radiation therapy is of increasing interest in the treatment of cancer because of its superior outcome in several clinical trials. High energy protons produce unwanted neutrons, which in turn necessitates the protection of patients, staff and the public from neutron exposures. A Monte Carlo method to model the neutron production and shielding at a proton therapy facility is described here. This method can be used to study existing facilities and optimize neutron shielding for future proton centers.

1 Introduction

The Northeast Proton Therapy Center (NPTC) at the Massachusetts General Hospital consists of a cyclotron producing 230 MeV protons, an energy degrader and magnetic momentum-analysis system, and a beam transport system feeding two isocentric gantries and two horizontal beam treatment stations [1]. Proton-induced nuclear reactions produce neutrons in beam production and delivery components, as well as in the patient. Massive shielding barriers are present in order to reduce personnel neutron exposures to acceptable levels. The shielding design task is complicated by multiple neutron sources and shielding barriers. In the past, this complexity has lead shielding designers to adopt simplifications and approximations in order to render the problem soluble with the available computational resources. Furthermore, the uncertainties are large and difficult to estimate for shielding calculations of this type, *e.g.* due to errors introduced by overly simplistic models, or due to large uncertainties in the anticipated facility usage patterns and in fast-neutron interaction data [2].

This work aims to reduce the uncertainties in neutron shielding predictions with the aid of Monte Carlo (MC) simulations. The distinguishing features of these simulations are the realism and completeness of models for the the sources, shielding barriers, and radiation transport physics. The MC results are compared with analytical-model predictions and with measurements.

2 Methods and Materials

The neutron shielding was simulated with the MCNPX Monte Carlo program from Hughes *et al.* [3]. This code includes flexible source-specification options,

radiation cross-section libraries and models, and allows the specification of an arbitrarily complex combinatorial geometry for radiation transport simulations. A separate MC simulation for each discrete neutron source provided a track-length estimate of the neutron spectral fluence (per proton incident on that source), Φ_E/p , at each of 206 receptor locations throughout the NPTC. Once all of the MC simulations were complete, the dose equivalent per proton at a given receptor location, denoted as H/p_i where the index i corresponds to the neutron source, was calculated from the spectral fluences and fluence-to-dose equivalent conversion coefficients, h_ϕ , from [4]. Then, for each receptor location, the total dose equivalent per proton delivered to isocenter was estimated as the weighted sum

$$\frac{H}{p_{\text{iso}}} = \sum_i w_i \frac{H}{p_i} \quad (1)$$

where w_i denotes the relative weight of the i^{th} source, *i.e.*, the number of protons stopping in the i^{th} source divided by the number stopping at isocenter. Finally, the dose equivalent values (including all predicted and measured values) were normalized to proton absorbed dose to water at isocenter by multiplying by $5 \cdot 10^{11}$ protons per Gy.

Neutron Sources Proton losses during acceleration, energy degrading, beam transport, and protons stopping in tissue during treatment lead to neutron production at various locations throughout the facility (see Fig. 1). In this work, we considered 12 discrete sources. Proton losses in the cyclotron were approximated with eight equally-weighted 235-MeV proton pencil beams, each tangential to a circle of the cyclotron's extraction radius (120 cm) and evenly spaced at $\pi/4$ intervals, in the cyclotron's medial plane.

Upon extraction from the cyclotron, the proton beam enters an energy selection system (ESS) that controls the beam energy and momentum spread with a variable-thickness carbon absorber and a magnetic momentum analyzer, respectively. For the 235-MeV beam considered here, no degrading occurs, but approximately 70% of the beam incident on the collimator of the ESS is lost there. The remaining sources and loss rates are the energy-selection slit (0.5%), a fixed-emittance-slit (5%), and the patient aperture located near the isocenter of the gantry (100%). For simplicity, each of the 12 proton sources is approximated as monoenergetic and monodirectional, and many of the proton beamline components, *i.e.*, neutron sources, are approximated as stopping length spheres.

Shielding Geometry A detailed three-dimensional model of the building and the beam delivery system was assembled in the MCNPX combinatorial geometry format. The development was greatly facilitated by the SABRINA geometry visualization code [5]. The setup comprises concrete shielding walls, labyrinths, shields mounted on the rotational gantries, and the self-shielding of the cyclotron's mechanical support structure. Figure 2 shows an isometric cutaway view of the treatment level. The vast majority of shielding material is ordinary poured concrete with an assumed density of 2.35 g/cm³. In total, the facility model includes 420 geometric cells, 15 materials, and 27 elements. The neutron

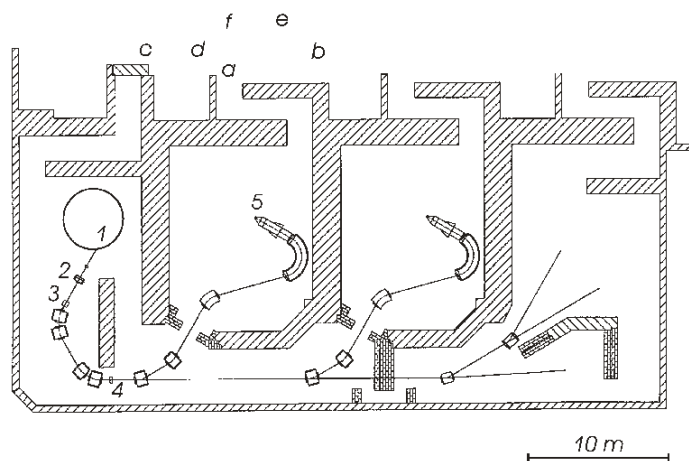


Fig. 1. Locations of receptors used in MC calculations, analytical calculations and measurements at NPTC. One location (a) is on the treatment level, all others (b-f) are on the level above. The numbers label the following neutron sources: (1) cyclotron, (2) energy degrader, (3) momentum analyzing magnets, (4) slits, (5) brass aperture at isocenter

spectral fluences were tallied at various receptor locations throughout the facility, corresponding to those of analytical-model predictions and measurements of neutron dose equivalent rates (see Fig. 1).

MCNPX Physics Models The Monte Carlo simulations include proton transport and neutron production and transport. Monoenergetic protons were directed toward stopping length targets of various materials. The details of the proton energy loss by coulombic interactions, *e.g.*, multiple coulomb scattering and energy straggling, are not particularly important in these shielding calculations. On the other hand, elastic and non-elastic nuclear reactions are of great importance.

The neutron production is based on the intranuclear cascade (INC) model (cf. Bertini [7,8]). In essence, this model describes proton-nucleus interactions in several stages: including so-called direct reactions in which the projectile interacts with one or a few of the nucleons, resulting in the emission of single hadrons. If the projectile and the nucleus form a compound nucleus, its energy is distributed among the nucleons. The nucleus may de-excite by the evaporation of neutrons or other particles.

Below 15 MeV, neutron elastic scattering cross-sections are from evaluated libraries. Above that energy, the cross sections are from model predictions made within the MCNPX code.

Program Flow A single simulation input file is automatically generated by combining one of the 12 proton sources with a predefined facility geometry and various physics and tally options. Simulations were executed in parallel with a

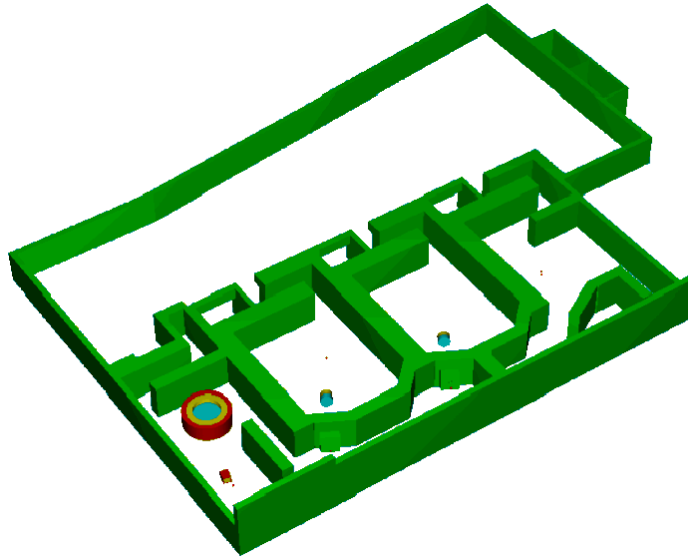


Fig. 2. An isometric cutaway view of the geometric model of the proton center's treatment level, rendered with the SABRINA visualization code [5]. The model includes the concrete floor, the ground and roof levels and the soil and airspace outside the building (not shown)

17-node LINUX cluster using static load balancing, where each new simulation is assigned to the node with the shortest queue. Upon completion of $5 \cdot 10^6$ proton histories, the simulation results (neutron spectral fluences at each receptor location) are converted to neutron dose equivalent and the statistical uncertainties are assessed. This assessment involves subjective judgement. Additional histories are accumulated (in increments of $5 \cdot 10^6$ protons) until the statistical fluctuations are acceptably small, typically requiring $5 \cdot 10^7$ protons to achieve 30% statistical uncertainties.

Measurements and Analytical Calculations The Monte Carlo simulations were benchmarked with measurements at the locations shown in Fig. 1. Commercial meters (Model 42-30/2241, Ludlum Instruments, Sweetwater, Texas) measured neutron dose equivalent rates while a 230-MeV proton beam was delivered to a brass beam stop located near the isocenter of the gantry. The measurement uncertainties were typically 30% and range from 20% to 80%, with the statistical counting fluctuations predominating the largest values.

The NPTC shielding design is based on semi-empirical analytical models for slab and maze shielding geometries. The models rely on two basic assumptions: the neutron dose equivalent behind a thick shield is determined by high energy neutrons; and low-energy neutrons and high-energy neutrons are in radiation equilibrium deep in the shield. The uncertainties for this method are large and

Table 1. Analytical model predictions, H_a , measurements, H_m , and Monte Carlo simulations, H_{MC} , of neutron dose equivalent per proton dose at isocenter (in units of Sv/Gy). The locations are shown in Fig. 1. The angles describe the nozzle position, *e.g.*, at 207° the beam is pointed towards the main control room (like drawn in Fig. 1). H_a/H_m and H_{MC}/H_m correspond to the ratios of the average neutron dose equivalent per proton (column 7)

Pos		0°	90°	180°	270°	Average	$\frac{H_a}{H_m}$	$\frac{H_{MC}}{H_m}$
a	H_a	$1.2 \cdot 10^{-8}$	$6.2 \cdot 10^{-9}$	$1.2 \cdot 10^{-8}$	$1.0 \cdot 10^{-7}$	$3.2 \cdot 10^{-8}$	1.28	0.88
	H_m	$2.2 \cdot 10^{-8}$	$2.8 \cdot 10^{-8}$	$2.2 \cdot 10^{-8}$	$2.6 \cdot 10^{-8}$	$2.5 \cdot 10^{-8}$		
	H_{MC}	$2.6 \cdot 10^{-8}$	$1.7 \cdot 10^{-8}$	$2.0 \cdot 10^{-8}$	$2.4 \cdot 10^{-8}$	$2.2 \cdot 10^{-8}$		
b	H_a	$1.9 \cdot 10^{-9}$	$1.9 \cdot 10^{-9}$	$1.5 \cdot 10^{-8}$	$1.9 \cdot 10^{-9}$	$5.2 \cdot 10^{-9}$	62.6	1.1
	H_m	$1.0 \cdot 10^{-11}$	$3.3 \cdot 10^{-11}$	$2.5 \cdot 10^{-10}$	$3.7 \cdot 10^{-11}$	$8.3 \cdot 10^{-11}$		
	H_{MC}	$1.6 \cdot 10^{-10}$	$5.6 \cdot 10^{-12}$	$1.3 \cdot 10^{-8}$	$6.3 \cdot 10^{-11}$	$9.0 \cdot 10^{-11}$		
c	H_a	$9.5 \cdot 10^{-9}$	$8.6 \cdot 10^{-9}$	$1.7 \cdot 10^{-8}$	$5.0 \cdot 10^{-8}$	$2.1 \cdot 10^{-8}$	100	7.1
	H_m	$3.8 \cdot 10^{-11}$	$2.6 \cdot 10^{-11}$	$1.7 \cdot 10^{-10}$	$6.0 \cdot 10^{-10}$	$2.1 \cdot 10^{-10}$		
	H_{MC}	$1.2 \cdot 10^{-10}$	$1.3 \cdot 10^{-10}$	$2.8 \cdot 10^{-10}$	$5.3 \cdot 10^{-9}$	$1.5 \cdot 10^{-9}$		
d	H_a	$1.0 \cdot 10^{-8}$	$6.2 \cdot 10^{-9}$	$3.5 \cdot 10^{-8}$	$7.3 \cdot 10^{-8}$	$3.1 \cdot 10^{-8}$	124	44
	H_m	$9.3 \cdot 10^{-11}$	$6.7 \cdot 10^{-11}$	$2.2 \cdot 10^{-10}$	$6.3 \cdot 10^{-10}$	$2.5 \cdot 10^{-10}$		
	H_{MC}	$4.9 \cdot 10^{-9}$	$5.5 \cdot 10^{-9}$	$2.5 \cdot 10^{-8}$	$1.0 \cdot 10^{-8}$	$1.1 \cdot 10^{-8}$		
e	H_a	$3.1 \cdot 10^{-9}$	$2.9 \cdot 10^{-9}$	$4.6 \cdot 10^{-9}$	$4.6 \cdot 10^{-9}$	$3.8 \cdot 10^{-9}$	10.5	5.3
	H_m	$5.0 \cdot 10^{-11}$	$4.1 \cdot 10^{-11}$	$4.1 \cdot 10^{-10}$	$9.6 \cdot 10^{-10}$	$3.6 \cdot 10^{-10}$		
	H_{MC}	$4.9 \cdot 10^{-10}$	$5.9 \cdot 10^{-11}$	$1.7 \cdot 10^{-10}$	$2.8 \cdot 10^{-11}$	$1.1 \cdot 10^{-10}$		
f	H_a	$8.7 \cdot 10^{-9}$	$4.0 \cdot 10^{-9}$	$3.9 \cdot 10^{-8}$	$3.9 \cdot 10^{-8}$	$2.2 \cdot 10^{-8}$	88	0.72
	H_m	$1.1 \cdot 10^{-10}$	$6.4 \cdot 10^{-11}$	$2.2 \cdot 10^{-10}$	$5.9 \cdot 10^{-10}$	$2.5 \cdot 10^{-10}$		
	H_{MC}	$4.4 \cdot 10^{-10}$	$5.4 \cdot 10^{-10}$	$6.3 \cdot 10^{-9}$	$1.0 \cdot 10^{-10}$	$1.8 \cdot 10^{-10}$		

difficult to estimate. These methods are described by Newhauser *et al.* [2] and in references therein.

3 Results and Discussion

Table 1 summarizes the dose equivalent values per proton absorbed dose in water at isocenter, as calculated with (1), for the receptor locations in Fig. 1. In addition, the corresponding analytical-model predictions and measurements are given for comparison. The predicted values are for 235-MeV proton beams, whereas the beam energy obtained for the measurements was 230 MeV. A comparison of the ratios of the MC to measured values, H_{MC}/H_m , (averaged over

four gantry angles) ranges from 0.7 to 7. The ratios of the analytical predictions to measurements, H_a/H_m , range from 11 to 124. These findings suggest that the MC simulations are more accurate than the analytical-model predictions. This is the expected result, since these MC simulations include more detailed treatments of the neutron production and transport physics as well as a very complex shielding geometry. However, these encouraging results might also mask the possible presence of compensating errors. For example, an underestimation of the concrete shield density may be cancelled by a corresponding underestimate of proton losses. Hence, these results should be considered as preliminary. To reduce the possibility of systematic errors, additional measurements are planned, including the proton loss rates, neutron dose equivalent rates, and absorbed dose to water at isocenter per proton-beam charge. The simulations described here comprise part of a comprehensive study including a total of 147 source locations and 206 receptor locations at 100 MeV, 150 MeV, 200 MeV, and 235 MeV proton energies.

4 Conclusion

Detailed neutron shielding simulations of a 230-MeV proton therapy center provide estimates of neutron dose equivalent that are in good agreement with measurements and analytical calculations. These preliminary results provide convincing evidence that the simulation techniques described here are well-suited to solve practical shielding problems for high-energy proton accelerator facilities.

References

1. Y. Jongen: 'The Proton Therapy System for MGH's NPTC: Equipment Description and Progress Report', In: *Proceedings of NIRS International Seminar on the Application of Heavy Ion Accelerators to Radiation Therapy of Cancer in Connection with XXI PTCOG, Nov. 14-16, 1994*, ed. by Tatsuaki Kanai and Eiichi Takada, pp.59
2. W.D. Newhauser, U. Titt, D. Dexheimer, X. Yan, S. Nill: 'Neutron Shielding Verification Measurements and Simulations for a 235-MeV proton Therapy Center', submitted to Nucl. Instr. Meth. (July 2000)
3. H.G. Hughes, H.W. Egdorf, F. Gallmeier, R.C. Little, R.E. Prael, E. Snow, L.S. Waters, M. White: *MCNPX User's Manual*, TPO-E83-G-UG-X-00001, Revision 0 (1999)
4. NCRP Report 38, *Protection Against Neutron Radiation*, National Council on Radiation Protection and Measurements, Bethesda (1971)
5. K.A. van Riper: *SABRINA User's Guide*, Los Alamos National Laboratory, LA-UR-93-3696 (October 1993)
6. M.B. Chadwick, P.G. Young, S. Chiba, S.C. Frankle, G.M. Hale, H.G. Hughes, A.J. Koning, R.C. Little, R. MacFarlane, R.E. Prael, L.S. Waters: Nucl. Sci. Eng. **131**, 293 (1999)
7. H.W. Bertini: Phys. Rev. **131**, 1801 (1963)
8. H.W. Bertini: Phys. Rev. **188**, 1711 (1969)

Coupling MCNP-DSP and LAHET Monte Carlo Codes for Designing Subcriticality Monitors for Accelerator-Driven Systems

T. Valentine¹, Y. Rugama², J.L. Muñoz-Cobo², and R. Perez¹

¹ Oak Ridge National Laboratory P. O. Box 2008 Oak Ridge, TN 37831, USA

² Poly. Tech. Univ. of Valencia, Chemical and Nuclear Engineering Department
APDO. 22012, Valencia, 46071, Spain

Abstract. The design of reactivity monitoring systems for accelerator-driven systems must be investigated to ensure that such systems remain subcritical during operation. The Monte Carlo codes LAHET and MCNP-DSP were combined together to facilitate the design of reactivity monitoring systems. The coupling of LAHET and MCNP-DSP provides a tool that can be used to simulate a variety of subcritical measurements such as the pulsed neutron, Rossi- α , or noise analysis measurements.

1 Introduction

Accelerator-driven spallation neutron sources are an attractive and safe option for waste transmutation of material from commercial power reactors. The cost effectiveness of accelerator-driven fissile systems is highly dependent on the degree of subcriticality of the system core and hence dependent on the ability to control and maintain the system core at a specific subcritical state. Conventional control of commercial nuclear reactors is made possible by the presence of negative reactivity feedback mechanisms and delayed neutrons, which slow down the reactor dynamic response to easily manageable levels and the fact that the neutron flux or power is directly related to the reactivity of the system. For waste transmutation and fissile material disposition, however, it is often desirable to harden the neutron spectrum, which could make control a difficult problem because the inherent natural feedback mechanisms that are common in thermal reactors are reduced. Control of accelerator-driven fissile targets is made possible by operating the system in a subcritical state and controlling the reactor power by adjusting the beam current. For these and other reasons, significant research efforts are ongoing in both Europe and the U. S. to address issues related to accelerator-based actinide waste burners.

Concerns about the degree of subcriticality of an accelerator-driven fissile system have mandated that methodologies be developed to measure the subcriticality of the system. The Polytechnic University of Valencia and Oak Ridge National Laboratory undertook an effort to develop a computational tool to investigate the time-dependent response of neutron detectors in an accelerator-driven system. This is the first step necessary to develop a measurement methodology. This paper provides a brief description of the research performed to develop a time-dependent Monte Carlo calculation for accelerator-driven systems.

2 Monte Carlo Methods

The computation of the time-dependent detector responses in an accelerator-driven system is best accomplished using Monte Carlo programs. Monte Carlo codes preserve the exact nature of particle interactions within a fissile system and are only limited by the ability to describe the geometry of the fissile system and by the nuclear data to describe the particle interaction probabilities.

The accelerator-driven system of interest injects protons into a target assembly to produce high-energy neutrons. These high-energy neutrons slow down in the target assembly and transmute the nuclear waste. The Monte Carlo code LAHET [1] is used to simulate the interactions of the protons within the target region to produce high-energy neutrons. The LAHET code also simulates the slowing-down of the high-energy neutrons. The Monte Carlo program MCNP-DSP [2] is required to simulate the interactions for neutrons with energies less than 20 MeV. This code is used to estimate the counting statistics for neutron and/or gamma ray counters in fissile systems. Therefore, the coupling of LAHET and MCNP-DSP provides a means to estimate the time-dependent response of neutron and/or gamma ray detectors that may be used in the design of a sub-criticality monitoring system for an accelerator-driven system.

3 Monte Carlo Code MCNP-DSP

The Monte Carlo code MCNP-DSP was developed from the MCNP [3] Monte Carlo code to simulate a variety of subcritical measurements. In MCNP-DSP, the variance reduction features were disabled to obtain a strictly analog particle tracking to follow the fluctuating processes more accurately. Because typical biasing techniques are employed to reduce the variance of estimates of first moment quantities, they do not preserve the higher moments; therefore, analog Monte Carlo calculations must be performed when analyzing subcritical measurements whose measured quantities are directly related to the higher moments of the neutron populations. Because the use of average quantities reduces the statistical fluctuation of the neutron population, average quantities such as the average number of neutrons from fission are not used; instead, appropriate probability distribution functions are sampled. The prompt particle tracking begins with the source event. The source particles and their progeny are tracked to their extinction by either absorption or escape. During the particles' histories, appropriate interactions within the detectors produce detection events, and the time of the detection events are tracked to produce time-dependent detector responses. These time sequences are sampled into blocks of 512 or 1024 data points. The blocks of data are then processed according to the type of measurement being simulated. Each data block can be Fourier transformed and a complex multiplication performed to obtain estimates of auto and cross spectra from the detector responses. The auto and cross spectra are then averaged with previous estimates until the desired number of data blocks have been accumulated.

4 LAHET

The Monte Carlo code LAHET was developed by Los Alamos as a general tool for simulating the transport of nucleons, pions, and muons. In the simulation of accelerator-driven systems, the LAHET code is used to track the interaction of protons within a target and to track the subsequent neutrons produced from the spallation events. Neutrons with energies greater than 20 MeV are tracked using LAHET. The data for neutrons with energies less than 20 MeV are written to a file to be tracked using MCNP-DSP. The neutron's position, direction, energy, and time are provided in the output file produced by LAHET. The data in LAHET are broken down into batches. A given number of protons are produced in each batch with varying numbers of neutrons produced for each batch.

5 Use of LAHET Data in MCNP-DSP

MCNP-DSP treats each batch from the LAHET file as a pulse from the proton injector. The number of source particles per pulse (per batch) is specified in the LAHET calculation. Likewise, the initial time distribution of the proton pulse is specified in LAHET. There are additional inputs required in the MCNP-DSP input file and in the extra MCNP-DSP input file. The user must supply the frequency of the proton injector. The simulation assumes that the injector behaves as a pulsed source with a fixed period between the pulses. The time of the pulse depends on the number of proton pulses that occur in each data block. The data block is the time over which the detector responses are accumulated and is equal to the number of detector time bins divided by the sampling rate as specified in the MCNP-DSP extra input file. If there is only one proton pulse per block the starting time of the injector signal is sampled uniformly in the data block. This simulates the use of an internal clock on a processor to start the data accumulation. If more than one proton pulse occurs per block, then the starting time (t_s) of the pulse is sampled uniformly between 0 and T_{pp} where T_{pp} is the period between pulses and is equal to the inverse of the proton pulse frequency. The time of the subsequent pulses is determined by $t_s + i \cdot T_{pp}$ where i is the i^{th} pulse after the first. An option is included in MCNP-DSP to allow the proton injector to serve as a trigger resulting in only one pulse per block occurring at time zero.

The number of data blocks that are acquired are determined by the number of pulses per block and the total number of batches in the LAHET input file. The energy, position, direction, weight, time, and particle type are provided in the LAHET output file. This information is used to determine the location of the particle in the MCNP-DSP model. If the particle cannot be found anywhere in the geometry the particle will be skipped. If the source particle time is greater than the period of the data block, then the particle is also skipped. These are the only factors that will result in the omission of a particle from being tracked.

A simulation of an accelerator-driven system [4] was performed using the LAHET source file with MCNP-DSP. This simulation was performed to determine

the cross spectra between the proton injector and a detector in the system. The cross spectra can then be used to determine the prompt neutron decay constant for the system. The prompt neutron decay constant is directly related to the subcriticality of the system. An example of the cross spectra between the proton injector and the system detector for a single pulse per data block is provided in Fig. 1.

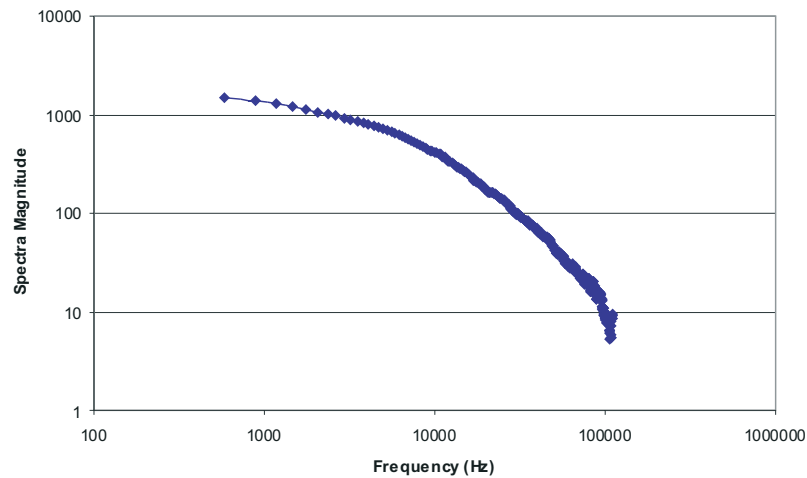


Fig. 1. Source-detector cross spectra for accelerator-driven system

6 Summary

The coupling of LAHET with MCNP-DSP provides a general tool for the calculation of the time dependent detector response for an accelerator-driven system. The coupling is achieved by reading a binary LAHET file that describes the particle's energy, position, direction, weight, time, and type of particle. MCNP-DSP uses this information to determine the location of the particle in the MCNP-DSP model. MCNP-DSP models the accelerator-driven system with the proton injector signal as one of the measured quantities. MCNP-DSP allows for two possible computation modes depending on the use of the proton injector signal.

References

1. R.E. Prael, H. Lichtenstein: *User Guide to LCS: The LAHET Code System*, LA-UR-89-3014, Los Alamos National Laboratory (1989)
2. T.E. Valentine: *MCNP-DSP Users Manual*, ORNL/TM-13334, Oak Ridge Nat. Lab (January 1997)
3. J.F. Briesmeister, Ed.: *MCNP4A-A General Monte Carlo N-Particle Transport Code*, LA-12625-M, Los Alamos National Laboratory (1993)
4. Y. Rugama, J.L. Muñoz-Cobo, T.E. Valentine: "Noise Method for Monitoring the Subcriticality in Accelerator Driven Systems", *These Proceedings* p. 887

Shielding Benchmark Experiments Through Concrete and Iron with High-Energy Proton and Heavy Ion Accelerators

T. Nakamura¹, M. Sasaki¹, T. Nunomiya¹, N. Nakao², E. Kim³, T. Kurosawa⁴,
S. Taniguchi⁵, H. Iwase¹, Y. Uwamino⁶, T. Shibata², S. Ito⁶, A. Fukumura⁷,
D.R. Perry⁸, and P. Wright⁸

¹ Department of Quantum Science and Energy Engineering, Tohoku University,
Aoba, Aramaki, Aoba-ku, Sendai, 980-8579, Japan

² High Energy Accelerator Research Organization(KEK), Oho 1-1, Tsukuba, Ibaraki
305-0801, Japan

³ Tokai Establishment, Japan Atomic Energy Research Institute (JAERI), Tokai,
Ibaraki, 319-1195, Japan

⁴ Japan Synchrotron Radiation Research Institute (JASRI), Hyogo, 679-5198, Japan

⁵ Electrotechnical Laboratory (ETL), Tsukuba, Ibaraki, 305-8568, Japan

⁶ The Institute of Physical and Chemical Research (RIKEN), Hirosawa 2-1, Wako,
Saitama, 351-0198, Japan

⁷ National Institute of Radiological Sciences (NIRS), Anagawa, Inage-ku, Chiba,
263-8555, Japan

⁸ Health and Safety Group, Rutherford Appleton Laboratory (RAL), Chilton,
Didcot, Oxfordshire, OX11 0QX, UK

Abstract. The deep penetration of neutrons through thick shield has become a very serious problem in the shielding design of high-energy, high-intensity accelerator facility. In the design calculation, the Monte Carlo transport calculation through thick shields has large statistical errors and the basic nuclear data and model used in the existing Monte Carlo codes are not well evaluated because of very few experimental data. It is therefore strongly needed to do the deep penetration experiment as shielding benchmark for investigating the calculation accuracy.

Under this circumstance, we performed the following two shielding experiments through concrete and iron, one with a 800 MeV proton accelerator of the Rutherford Appleton Laboratory (RAL), England and the other with a high energy heavy iron accelerator of the National Institute of Radiological Sciences (NIRS), Japan. Here these two shielding benchmark experiments are outlined.

1 Introduction

In high-intensity and high-energy hadron accelerator facilities, massive shields are required to reduce the leakage of high-energy neutron having strong penetrability. In order to estimate the deeply penetrating neutrons for shielding design of such facilities, the point kernel method, the Monte Carlo calculation and the discrete-ordinate Sn calculation are usually used for shielding calculations. The calculations for such a large attenuation through a very thick shield generally give large statistical errors of the neutron flux. In the Monte Carlo

calculation, a variance reduction method and a step-by-step calculation using multi-layer slabs are usually used for statistically good estimation of neutron flux outside a very thick shield. The accuracies of the calculated results are, however, not well evaluated because the experimental data are very scarce. On the other hand, most of conceptual shielding design for high-energy accelerator facilities have been generally performed by using a point kernel method, that is the Moyer model, which is based on single exponential attenuation of neutron dose equivalent behind a thick shield to be in a spectral equilibrium state. In this deep penetration problem, the dose attenuation length, which is ruled by high-energy neutrons above about 100 MeV, is an essentially important parameter of the Moyer model. Neutron shielding experiments at several accelerator facilities have ever been performed to get the attenuation length, but the reliable experimental data behind a very thick shield are still very scarce and dispersed [1–3].

Under this circumstance, we performed the following two shielding experiments through concrete and iron, one with a 800 MeV proton accelerator of the Rutherford Appleton Laboratory (RAL), England and the other with a high energy heavy ion accelerator of the National Institute of Radiological Sciences (NIRS), Japan. Here these two shielding benchmark experiments are outlined.

Since 1992 the shielding experiments of deep penetration have been performed at an intense spallation neutron source facility, ISIS, of the Rutherford Appleton Laboratory [4,5]. A series of the experiments were performed at the top surface of the bulk shield (shield top) just above the spallation target to measure deeply penetrated neutrons through the transverse shield of 284-cm thick iron and 97-cm thick concrete. In the latest experiment in 1998, the C, Bi and Al activation detectors using the $^{12}\text{C}(\text{n},2\text{n})^{11}\text{C}$, $^{209}\text{Bi}(\text{n},\text{xn})^{210-\text{x}}\text{Bi}(\text{x}=4\sim 10)$ and $^{27}\text{Al}(\text{n},\alpha)^{24}\text{Na}$ reactions together with the In-loaded multi-moderator spectrometer [6] were used to get the reaction rate and neutron energy spectra outside the additionally equipped concrete and iron shields and attenuation profiles of high energy neutrons produced by 800 MeV protons were obtained [7]. This benchmark shielding experiment at an intense high-energy accelerator facility will give useful informations for estimating the accuracy of the transport calculation for deep penetration.

The second shielding experiment was performed using a high energy heavy ion accelerator, HIMAC of the National Institute of Radiological Sciences (NIRS), Japan. In this experiment, a 400 MeV/nucleon C ion beam was stopped completely in a Cu target to produce secondary neutrons. The neutrons produced in the forward direction were penetrated through concrete and iron shields up to 200- and 100-cm thickness, respectively. The neutrons were measured with the Self-TOF spectrometer [8], the NE-213 scintillation counter and the Bi activation detector. This benchmark experiment gives the very valuable data of neutron spectra and flux attenuation through the shield at 0 degree which ever scarcely exists in high energy region above about 100 MeV.

2 Experiment at ISIS

2.1 ISIS Facility

The experiment was performed at the ISIS spallation neutron source facility, RAL. The ISIS facility consists of 70 MeV H-linear accelerator, 800 MeV proton synchrotron and a spallation neutron target station. The beam intensity was about $170\text{ }\mu\text{A}$ at the target with 50 Hz repetition rate.

A cross sectional view around the target station along the 800 MeV proton beam axis is shown in Fig. 1. The tantalum target is placed at the center of the helium-filled stainless-steel vessel. The moderators and reflectors to produce thermal and cold neutrons are placed around the target.

The spallation target is shielded with 284-cm thick iron and 97-cm thick ordinary concrete toward the upper direction. This experiment was performed at the top of the shield just above the target station which corresponded to the 90 degree to the incident proton beam. As seen in Fig. 1, a big bent duct in which the helium gas flows for target cooling reaches the shield top through the bulk shield downstream from the target. Neutrons that leaked from the duct exit became large background components on our measurement. Therefore, as shown in Fig. 2 an iron-igloo (120-cm inner diameter, 60-cm thick and 196-cm high) was equipped upon the top center of the bulk shield just above the target to reduce the background.

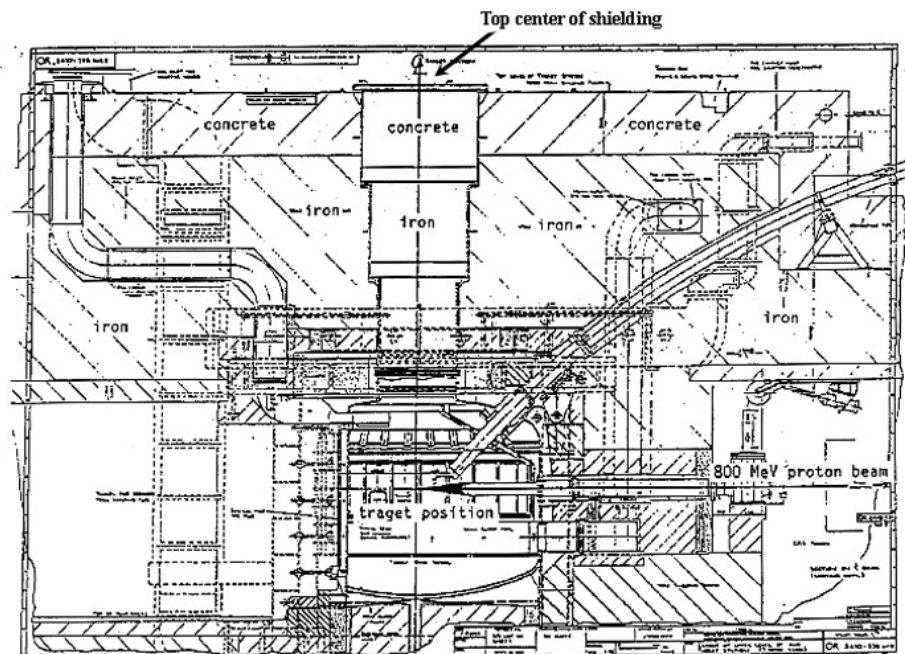


Fig. 1. Cross sectional view along the beam axis of the ISIS target station

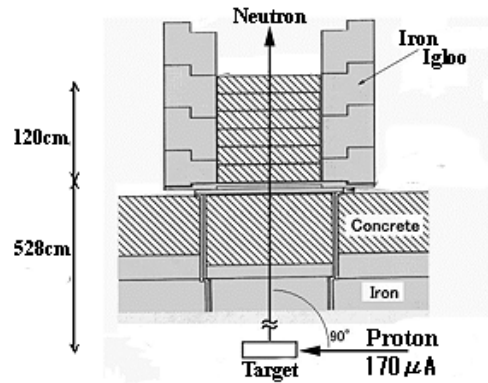


Fig. 2. Experiment geometry with iron-igloo to reduce the background neutrons

2.2 Shielding Materials

In this shielding experiment, the additional shielding blocks of ordinary concrete and iron were piled inside the igloo as shown in Fig. 2. Concrete shields of 20-, 40-, 60-, 80-, 100-, and 120-cm thicknesses were assembled by using the 119-cm diam by 20-cm thick blocks of 2.36 g/cm^3 , and iron shields of 10-, 20-, 30-, 40-, 50- and 60-cm thicknesses were assembled by using the 119-cm diam by 10-cm thick blocks of 7.8 g/cm^3 .

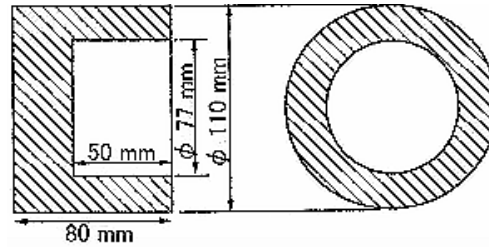
2.3 Detectors

The neutrons were produced from the target as the burst pulses corresponding to the 50Hz synchrotron operation, and the pulse counters could not be used here because of the pulse pile-up problem. We therefore used the C, Al and Bi activation detectors using $^{12}\text{C}(\text{n},2\text{n})$, $^{27}\text{Al}(\text{n},\alpha)$ and $^{209}\text{Bi}(\text{n},\text{xn})$ reactions and the In-loaded multi-moderator spectrometer, that is Bonner ball, using $^{115}\text{In}(\text{n},\gamma)$ reaction. Their sizes, threshold energies and the cross section references [9,10] are listed in Tab. 1. The disk type and Marinellii type (shown in Fig. 3) detectors were used. The γ rays from the activation detectors after irradiation in this experiment were measured with two HP Ge detectors (GC-1818 and GC-2020, Canberra Industries, Inc.). For the Bonner ball, the In_2O_3 powder of 2.875 g is sealed in a spherical cavity of a small Lucite cylinder which is placed in the center of a spherical polyethylene moderator [6]. Five different moderators of 9.8-, 5.5-, 3.2-, 2.0- and 0-cm radius were used. The response functions of the five detectors calculated up to 400 MeV using the MCNPX-2.1.5 [11] are shown in Fig. 4.

We also used the ionization-type neutron (Rem Ion Monitor by Harwell Co. Ltd.) and γ ray (R02 by Eberline Co. Ltd.) survey meters to measure the dose equivalent data behind the shield.

Table 1. Comparison of measured and calculated neutron fluences and attenuation lengths in the energy region of 100 MeV and 400 MeV

Reaction	Detector Type	Detector Size (Diam-Thick) [mm]	Average Mass [g]	Half life	Threshold energy [MeV]	Cross section data [ref]
$^{12}\text{C}(\text{n},2\text{n})^{11}\text{C}$	Disk	80-30	265.6	20.4 min	20.40	[9]
$^{27}\text{Al}(\text{n},\alpha)^{24}\text{Na}$	Marinelli	See Fig. 3	901.7	20.4 min	20.40	[9]
$^{209}\text{Bi}(\text{n},10\text{n})^{200}\text{Bi}$	Marinelli	See Fig. 3	1425	15.02 hr	3.25	[10]
$^{209}\text{Bi}(\text{n},9\text{n})^{201}\text{Bi}$	Disk	80-11	529.6	36.4 min	70.79	[9]
$^{209}\text{Bi}(\text{n},8\text{n})^{202}\text{Bi}$	Disk	80-11	529.6	1.77 hr	61.73	[9]
$^{209}\text{Bi}(\text{n},7\text{n})^{203}\text{Bi}$	Disk	80-11	529.6	1.67 hr	53.98	[9]
$^{209}\text{Bi}(\text{n},6\text{n})^{204}\text{Bi}$	Disk	80-11	529.6	11.76 hr	45.31	[9]
$^{209}\text{Bi}(\text{n},5\text{n})^{205}\text{Bi}$	Disk	80-11	529.6	11.30 hr	37.99	[9]
$^{209}\text{Bi}(\text{n},4\text{n})^{206}\text{Bi}$	Disk	80-11	529.6	15.31 day	29.63	[9]
$^{155}\text{In}(\text{n},\gamma)^{116\text{m}}\text{In}$	Disk	80-11	529.6	6.243 day	22.56	[9]
	Sphere	ϕ 14.7	2.875	54.15 min	Thermal	[6]

**Fig. 3.** Cross sectional view of the Marinelli-type detector

2.4 Experimental Procedure

This experiment was performed by changing the thickness of iron and concrete shields. The activation detectors were set upon the shield for irradiation. In order to get good statistics of photo-peak counts measured with two HP Ge detectors, repeated irradiations and activity measurements were performed for each shielding material and thickness several times a day, and the photo-peak counts in the same condition were summed up to get the reaction rates.

The peak efficiencies of the Ge detectors including the self-absorption effect were estimated by using the EGS4 Monte Carlo code [12]. The thus-obtained reaction rates of $^{115}\text{In}(\text{n},\gamma)^{116\text{m}}\text{In}$ for five detectors of the Bonner sphere and $^{27}\text{Al}(\text{n},\alpha)$, $^{12}\text{C}(\text{n},2\text{n})$ and $^{209}\text{Bi}(\text{n},\text{xn})$ ($\text{x}=4\sim 10$) were unfolded by the SAND-II code [13] with the response functions and the cross section data, and the neutron energy spectra in the energy range down to thermal energy were analyzed. Neutron energy spectra calculated in an approximate spherical shield geometry by the ANISN code [14] with the DLC119/HILO86 multi-group cross section data library [15] were used as initial guess spectra for the unfolding.

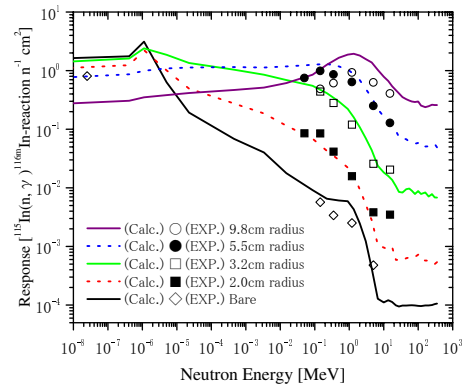


Fig. 4. Response functions of indium activation Bonner sphere

The relative proton beam current was monitored by the electromagnetic coil voltage at the muon target during the experiment. These data were converted to the beam current (Coulomb) and used in the analysis of the activation detectors.

3 Results and Discussions of the ISIS Experiment

Figure 5 shows the attenuation profiles of the $^{12}\text{C}(n,2n)^{11}\text{C}$ reaction rates with the iron and concrete thicknesses. The errors of the results are the statistical errors of the photo-peak counts of the 511 keV γ rays. This figure also gives the spatial distribution in the air along the vertical axis of the bulk shield upward from the tantalum target without any additional shield on the shield top. These three curves are the results on the center of this vertical axis. It is found that the data without additional shield (No shield) decrease with the square of the distance from the tantalum target. The attenuation lengths of this reaction rates correspond to those for neutron flux above 20 MeV, and are 161.1 ± 2.1 g/cm² for iron (7.8 g/cm³) and 125.4 ± 5.1 g/cm² for concrete (2.36 g/cm³). This iron attenuation length of 161.1 g/cm² for 800 MeV proton accelerator is a little larger than that of 148 g/cm² obtained by Jeffrey et al. using a 800 MeV proton accelerator at LANL [16].

Figure 6 shows the attenuation profiles of the $^{209}\text{Bi}(n,xn)^{210-x}\text{Bi}$ ($x=4\sim 10$) reaction rates in the concrete shield. All experimental data are well fitted to a solid line of the same slope as that fitted to the $^{12}\text{C}(n,2n)$ reaction data, in spite of different threshold energies of these reactions. This clarifies that the neutron energy spectrum behind this thick shield is in an equilibrium state.

Figure 7 shows the neutron energy spectra on the shield top floor, and on the additional concrete and iron shields, which were obtained with the activation detectors and the indium-loaded Bonner ball through the SAND-II unfolding. These three spectra have two components; high energy components above 10 MeV having a broad peak around 100 MeV and lower energy widespread components having a broad peak around 500 keV. The neutron spectrum through

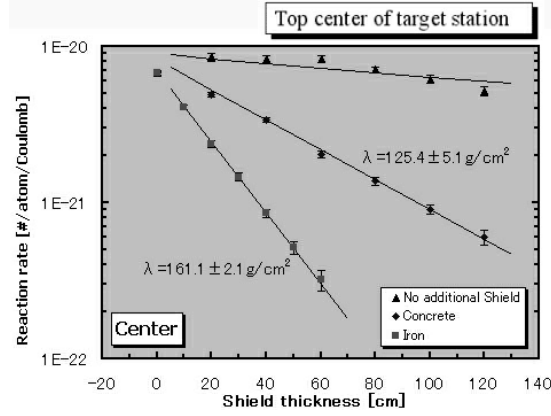


Fig. 5. Attenuation profiles of $^{12}\text{C}(\text{n},2\text{n})^{11}\text{C}$ reaction

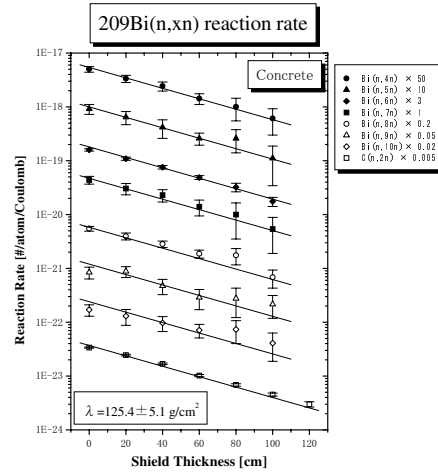


Fig. 6. Attenuation profiles of $^{209}\text{Bi}(\text{n},\text{xn})$ reaction for concrete

60-cm thick concrete shield shows rather flattened lethargy spectrum down to thermal energy and that through 30-cm thick iron shield shows less peak in high-energy component.

4 Experiment at HIMAC

4.1 Materials and Methods

The concrete and iron shielding experiments were also done at HIMAC. For this experiment, a new type detector, called 'Self-TOF detector' has been de-

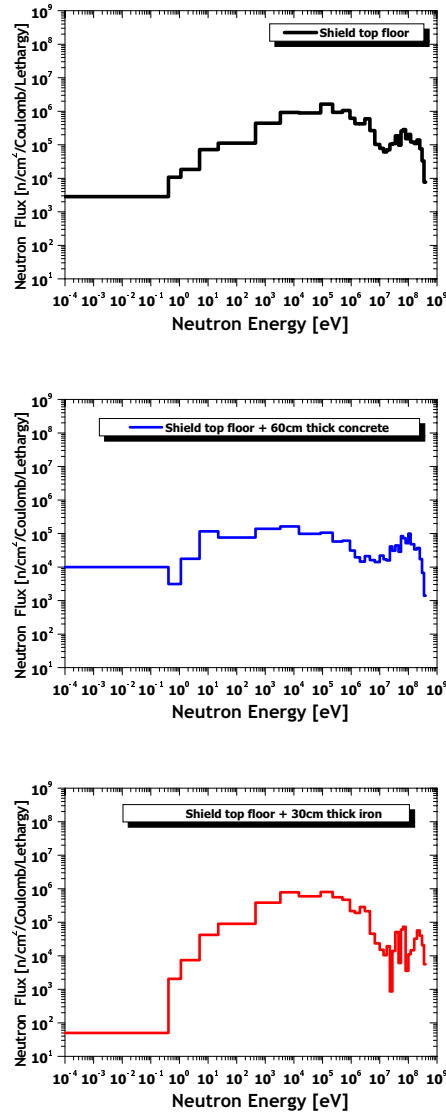


Fig. 7. Comparisons of neutron energy spectra on the shield top floor, 60-cm thick additional concrete and 30-cm thick additional iron shield

veloped [17] for high-energy neutron spectrometry, especially above about 100 MeV behind a shield.

Figure 8 shows the experimental arrangement at HIMAC. The neutrons were produced by bombarding 400 MeV/nucleon ^{12}C ion on 5-cm thick (stopping-length) copper target. The Self-TOF detector was placed at 516.5-cm downstream the target and the distance between the start and the stop counters was

1.2 m. It is already known that this radiation field has a lot of charged particles generated by fragmentation reactions [18]. The iron collimator of $60\text{ cm} \times 60\text{ cm} \times 40\text{ cm}$ thickness with a hole of $10\text{ cm} \times 10\text{ cm}$ was set in front of the Self-TOF detector to decrease the contribution of charged particles incident to the Self-TOF detector and also to put neutrons almost normally into the detector. The veto counter was placed in front of the radiator (RAD) to discriminate charged particles from neutrons.

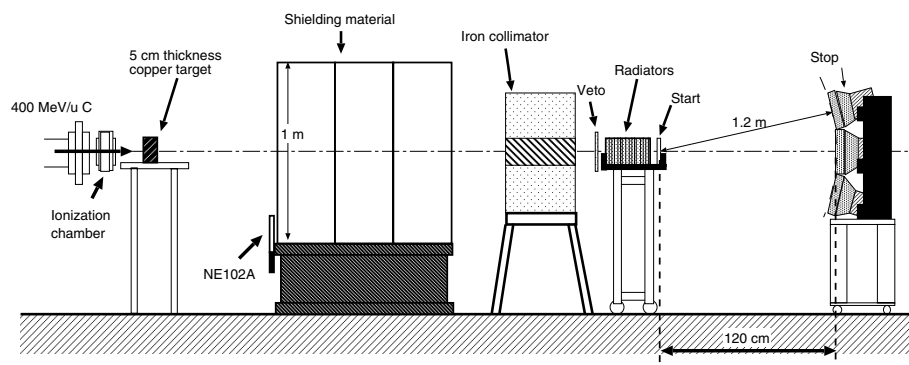


Fig. 8. Experimental arrangement at HIMAC

In the experiment, a 12.7-cm diam by 12.7-cm long NE-213 scintillation detector were also used to get the neutron energy spectrum mainly below 100 MeV, where the iron collimator was removed and the detector was set just on the rear surface of the shield. The response functions of this NE-213 detector are now being obtained by the experiment at HIMAC and the neutron spectrum can be obtained by unfolding with the FERDO-U code [19].

The concrete shield of 100-cm by 100-cm and 25-cm thickness and iron shield of 100-cm by 100-cm and 10-cm thickness were set between the target and the detector. The shield thickness was increased up to 200-cm for concrete and 100-cm for iron. The transmission-type ionization chamber was placed behind the end window of a beam line as a beam monitor.

4.2 Self-TOF detector

Figure 9 shows the schematic view of the detector. The detector consists of a veto counter ($150\text{ mm} \times 150\text{ mm} \times 5\text{ mm}$ thickness), a set of radiators with 20 thin detectors ($100\text{ mm} \times 100\text{ mm} \times 6\text{ mm}$ thickness), a start counter ($100\text{ mm} \times 100\text{ mm} \times 6\text{ mm}$ thickness), and a stop counter of nine segments ($200\text{ mm} \times 200\text{ mm} \times 20\text{ mm}$ thickness each), which is set on a plane perpendicular to the neutron beam. These detectors are all NE102A plastic scintillators. An in-coming neutron produces charged particles in the radiator, then the charged particles emitted in the forward direction reach the stop counter through the start counter. The

energy of a charged particle is determined by using the time-of-flight method between the start and stop counters. In this detector, we selected only proton events from $H(n,p)$ and $C(n,p)$ reactions and the proton energy spectrum was converted into the neutron energy spectrum by unfolding using the FERDO-U code, coupled with the detector response function which has also been obtained up to 800 MeV neutron energy by the experiment at HIMAC [8]. Since in this Self-TOF detector the proton energy spectra data were used instead of the usual light output data, we could measure higher energy protons which were produced by higher energy neutrons beyond the uppermost energy coming from the finite detector length.

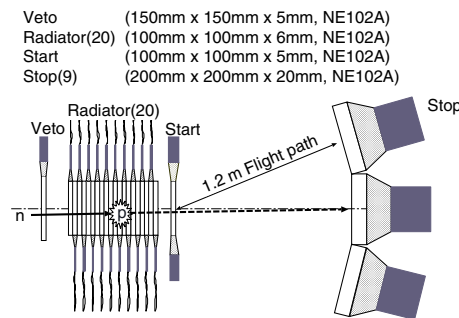


Fig. 9. Schematic view of the Self-TOF detector

5 Results and Discussions of the HIMAC Experiment

Figures 10 and 11 show the experimental results for concrete and iron shields obtained by the Self-TOF detector, respectively. Neutron spectra behind the shielding were also compared with the LCS calculation (LAHET Code System) [20]. The measured data by Kurosawa et al. [18] was used for the source neutron spectra in this calculation. The neutron spectra on the front surface of the radiator were obtained. The calculated results are shown in these figures. In Figs. 10 and 11, the neutron spectra cannot be seen below 100 MeV and above 600 MeV, except for the cases of 80-cm and 100-cm thick iron shields. This may be caused by the incomplete response function for high-energy (above 600 MeV) neutrons. For neutrons below 100 MeV, the detection efficiency decreased steeply because a proton which was generated from the upstream radiator stopped in the following radiators.

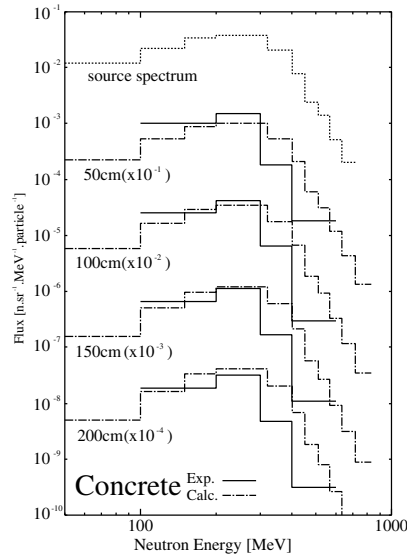


Fig. 10. Neutron energy spectra penetrated through concrete

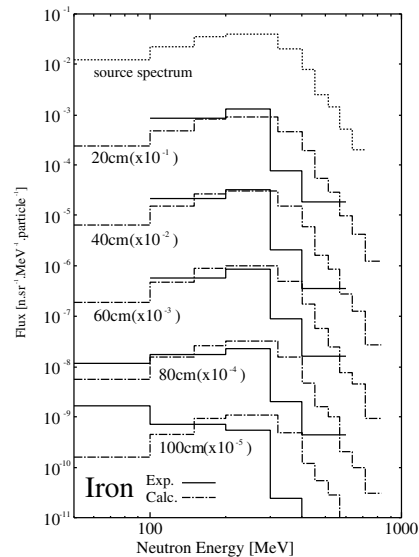


Fig. 11. Neutron energy spectra penetrated through iron

As seen in Figs. 10 and 11, both neutron spectra penetrated through concrete and iron shields have nearly constant values between 100 and 300 MeV, and rapidly decrease above 300 MeV, and for 80-cm and 100-cm thick iron shields, the neutrons below 100 MeV increase. The LCS calculation gives good agreement of the experimental spectra between 100 and 300 MeV, but gives the large overestimation between 300 and 600 MeV. The LCS calculated spectrum behind 100-cm thick iron is much harder than the measured spectrum. This discrepancy must be further investigated both from the experimental and calculational accuracies.

We are now analyzing the neutron spectra below 100 MeV measured with the NE-213 detector.

6 Conclusion

We performed two shielding experiments of high-energy (above 100 MeV) neutrons penetrated through concrete and iron, using high-energy (800 MeV) proton and high energy (400 MeV/nucleon) heavy ion accelerators. The former experiment at the ISIS is a deep penetration experiment of neutrons produced at 90 degree to the incident projectile beam, where the attenuation lengths of concrete and iron are obtained in a spectrum equilibrium state after about 3m thick iron and 1m thick concrete. The latter experiment at the HIMAC is the shielding experiment of neutrons produced at 0 degree to the incident projectile beam, where the experimental geometry is very simple and source neutron spectrum is given with good accuracy. Both experiments give neutron energy spectra and

are good shielding benchmark data for investigating the accuracy of the Monte Carlo neutron transport code in high-energy region.

References

1. G.R. Stevenson, K.L. Liu, R.H. Thomas: Health Phys. **43**, 13 (1982)
2. S. Ban et al.: Nucl. Instr. and Meth. **174**, 271 (1980)
3. S. Ban, H. Hirayama, K. Katoh.: Nucl. Instr. and Meth. **184**, 409 (1981)
4. Y. Uwamino, T. Shibata, T. Ohkubo, S. Sato, D.R. Perry: 'Study on Bulk Shielding of an 800-MeV Proton Accelerator'. In: *Proc. of OECD/NEA Specialists' Meeting on Shielding Aspects of Accelerator Target and Irradiation Facilities (SATIF-1), Arlington, Texas (1994)*
5. N. Nakao, T. Shibata, T. Ohkubo, S. Sato, Y. Uwamino, Y. Sakamoto, D.R. Perry: 'Shielding Experiment at 800 MeV Proton Accelerator Facility'. In: *Proc. 1998 ANS Radiation Protection and Shielding Division Topical Conference, Nashville, Tennessee 2*, pp. 192–199 (1998)
6. Y. Uwamino, T. Nakamura, A. Hara: Nucl. Instr. and Meth. A **239**, 229 (1985)
7. T. Nunomiya, N. Nakao, E. Kim, T. Kurosawa, S. Taniguchi, M. Sasaki, H. Iwase, T. Nakamura, Y. Uwamino, T. Shibata, S. Ito, D.R. Perry, P. Wright: 'Measurements of Neutron Attenuation through Iron and Concrete at ISIS', J. Nucl. Sci. Technol. Supplement 1, pp. 158–161 (2000)
8. M. Sasaki, N. Nakao, T. Nunomiya, M. Nakao, T. Nakamura, T. Shibata: 'Development of Self-TOF neutron detector and its application to shielding experiment at HIMAC', J. Nucl. Sci. Technol. Supplement 1, pp. 794–797 (2000)
9. E. Kim, T. Nakamura, A. Konno: Nucl. Sci. Eng. **129**, 209 (1998)
10. ENDF-B/VI: *Evaluated Nuclear Data File, ENDF-B/VI* National Neutron Cross Section Center, Brookhaven National Laboratory (1990)
11. L.S. Waters, ed.: *MCNPX User's Manual, ver 2.1.5* LA-UR 99-6058, Los Alamos National Laboratory, Los Alamos, New Mexico
12. W.R. Nelson, H. Hirayama, D.W.O. Rogers, *The EGS4 Code System*, SLAC-265, Stanford Linear Accelerator Center (1985)
13. W.N. McElroy, S. Berg, T. Crockett, R.G. Hawkins: *A computer automated iterative method for neutron flux spectra determination by foil activation*, AFWL-TR-67-41, Air Force Weapons Laboratory, Kirtland Air Force Base (1967)
14. W.W. Engle, Jr.: *A User's Manual for ANISN, A One-Dimensional Discrete Ordinates Transport Code With Anisotropic Scattering* USAEC Report K-1693, Oak Ridge Gaseous Diffusion Plant (1967)
15. R.G. Alsmiller Jr. et al.: *Neutron-Photon Multigroup Cross Sections for Neutron Energies up to 400 MeV (Revision 1)* ORNL/TM-9801, Oak Ridge National Laboratory (1986)
16. J.S. Bull, J.B. Donahue, R.L. Burman: *Measurement of Neutron Attenuation Through Thick Shields and Comparison with Calculation* Los Alamos National Laboratory (1999)
17. M. Sasaki, M. Nakao, T. Shibata, N. Nakao, T. Nakamura: Nucl. Instr. Meth. A **446**, 553 (2000)
18. T. Kurosawa, N. Nakao, T. Nakamura, Y. Uwamino, T. Shibata, N. Nakanishi, A. Hukumura, K. Murakami: Nucl. Sci. Eng. **132**, 30 (1999)
19. K. Shin et al.: Nucl. Technol. **53**, 78 (1981)
20. R.E. Prael et al.: *User Guide to LCS: The LAHET Code System* MS B226, LANL (1989)

New Method and Data on Residue Production in Spallation by ^{208}Pb on Protons for the Design of Spallation Sources

T. Enqvist¹, W. Wlazole², J. Benlliure³, F. Rejmund⁴, P. Armbruster¹, M. Bernas⁴, A. Boudard², S. Czajkowski⁵, R. Legrain², S. Leray², B. Mustapha⁴, M. Pravikoff⁵, K.-H. Schmidt¹, C. Stéphan⁴, J. Taieb⁴, L. Tassan-Got⁴, and C. Volant²

¹ GSI, Planckstraße 1, D-64291 Darmstadt, Germany

² DAPNIA/SPhN CEA/Saclay, F-91191 Gif-sur-Yvette, France

³ University of Santiago de Compostela, E-15706 Santiago de Compostela, Spain

⁴ IPN Orsay, IN2P3, F-91406 Orsay, France

⁵ CENBG, IN2P3, F-33175 Gradignan, France

1 Introduction

The design of an accelerator-driven system (ADS) requires precise knowledge of nuclide production cross sections in order to be able to predict the amount of radioactive isotopes produced inside the spallation target. Short-lived isotopes may be responsible for maintenance problems, and long-lived ones will increase the long-term radiotoxicity of the system. Recoil kinetic energies of the fragments are important for studies of radiation damages in the structural materials. Spallation of lead is particularly important since in most of the ADS concepts actually discussed, lead or lead-bismuth alloy is considered as the preferred material of the spallation target.

The accuracy of existing spallation models to estimate residual production cross sections is still far from the performance required for technical applications. This is shown, for example in the intercomparison in [1]. These difficulties can mostly be ascribed to the lack of complete distributions of all isotopes produced which would be needed to constrain the models. Therefore, experimental data are urgently needed.

We report here on the complete isotopic production cross sections of all elements from titanium to lead, measured in the inverse-kinematics spallation reaction of 1 GeV protons with lead. In addition, the velocity distributions of all the produced isotopes were measured, giving crucial information on the reaction mechanisms involved. A detailed description of this experiment is given in [2,3].

2 Experiment and Data Analysis

The experimental method and the analysis procedure have been developed and applied in previous experiments [4–6]. The primary beam of 1 A GeV ^{208}Pb was delivered by the heavy-ion synchrotron SIS at GSI, Darmstadt. The dedicated

experimental set up is shown in Fig. 1. The proton target was composed of 87.3 mg/cm² liquid hydrogen [7] enclosed between thin titanium foils of a total thickness of 36 mg/cm². The primary-beam intensity was continuously monitored by a beam-intensity monitor based on secondary-electron emission [8]. In order to subtract the contribution of the target windows from the measured reaction rate, measurements were repeated with the empty target. Heavy residues produced in the target were all strongly forward focused due to the inverse kinematics. They were identified using the Fragment Separator (FRS) [9].

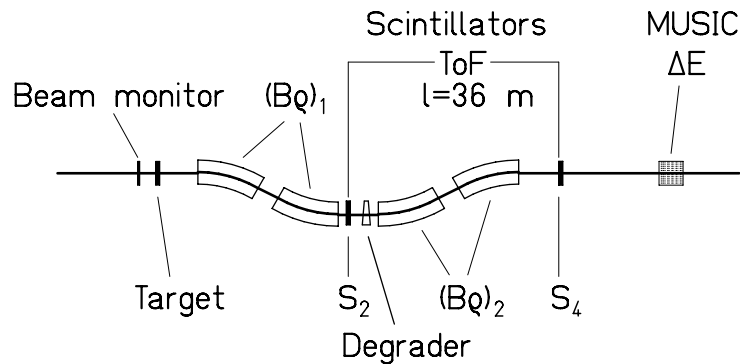


Fig. 1. Schematic drawing of the fragment separator FRS with the detector equipment. For details see text

The FRS is a two-stage magnetic spectrometer with a dispersive intermediate image plane (S_2) and an achromatic final image plane (S_4) with a momentum acceptance of 3% and an angular acceptance of about 15 mrad around the beam axis. Two position-sensitive plastic scintillators placed at S_2 and S_4 , respectively, provided the magnetic-rigidity ($B\rho$) and time-of-flight measurements, which allowed to determine the mass-over-charge ratio of the particles.

For an unambiguous isotopic identification of the reaction products, the analysis was restricted to ions which passed both stages of the fragment separator fully stripped. The losses in counting rate due to the fraction of incompletely stripped ions and the losses due to secondary reactions in the layers of matter in the beam line were corrected for.

To separate all residues with nuclear charges from 22 to 82, it was necessary to use two independent methods in the analysis. The nuclear charges of the lighter elements, mainly produced by fission, were deduced from the energy loss in an ionisation chamber (MUSIC). The nuclear-charge resolution obtained is $Z/\Delta Z = 170$ for the primary beam. Combining this information with the mass-over-charge ratio, a complete isotopic identification is performed. A mass resolution of $A/\Delta A = 480$ was achieved in the present work.

Since part of the heavier reaction products was not completely stripped, the MUSIC signal was not sufficient for an unambiguous Z identification. Therefore, the identification of reaction products of elements from terbium to lead was performed with the help of an achromatic energy degrader [10] placed at the intermediate image plane of the FRS. Two degrader thicknesses, 5.8 g/cm² and 5.2 g/cm² of aluminium were used for the lighter and for the heavier part of the elements. The nuclear charge of the products was deduced from the reduction in magnetic rigidity by the slowing down in the energy degrader. The MUSIC signal was still essential for suppressing events of incompletely stripped ions and from nuclei destroyed by secondary reactions in the degrader.

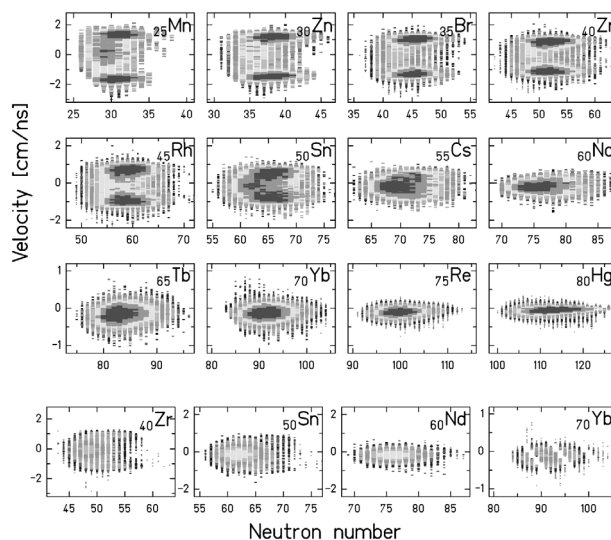


Fig. 2. Two-dimensional cluster plots of velocity versus neutron number for 12 selected elements. The three uppermost rows show the reaction rate with the full target and the lowest row with the empty target (target windows). The velocity is given in the centre-of-mass system of the primary beam in the middle of the target. The intensity scale is logarithmic and different for each element, the full and empty target contributions can directly be compared. The distribution of the ytterbium isotopes produced in the empty target was incompletely measured. Note also the different scales in velocity in different rows

The velocity of the identified residue was determined at S_2 from the $B\rho$ value and transformed into the frame of the beam in the middle of the target, taking into account the appropriate energy loss. More than 100 different values of the magnetic fields were used in steps of about 2% in order to cover all the produced residues and to construct the full velocity distribution of each residue.

The re-construction of the full velocity distribution allows to disentangle reaction products formed in fragmentation and fission reactions due to their different

kinematical properties. The velocity distributions as a function of neutron number for 12 selected elements are shown in Fig. 2 as cluster plots. It can be seen from the distributions that the reaction products can be attributed to different reaction mechanisms, i.e. fission and fragmentation. The production of lighter elements from fragmentation ($Z < 60$, and mean velocity centred close to the primary-beam velocity) seen in Fig. 2, does not result from primary reactions in the liquid-hydrogen target, but from secondary reactions or from reactions in the titanium target windows.

For heavy residues (Tb, Yb, Re, Hg), only contributions from fragmentation reactions can be seen as centred closely below the velocity of the projectiles. For lighter elements, also contributions of fission can be observed at backward and forward velocities due to the Coulomb repulsion of the two fission products. The averaged velocities of backward- and forward-emitted fission fragments differ from zero in Fig. 2, because the velocity of the fissioning nucleus is lower than that of the projectile due to a slowing-down process in the intra-nuclear cascade phase of the reaction.

The data are normalised to the number of projectiles recorded by the beam-intensity monitor. Corrections for dead time, for the contribution from incompletely stripped ions and for counting losses due to secondary reactions in the degrader and the scintillation detector at S_2 have already been performed. The distributions shown in Fig. 2 still contain a contribution of reaction rates in the titanium windows of the target. Additional corrections account for the angular transmission of the FRS and secondary reactions inside the liquid-hydrogen target, before the production cross sections are deduced.

Table 1. Incineration experiments performed at GSI. For the published and accepted papers, electronic files of the preprints and the data are accessible via the WEB address: <http://www-wnt/kschmidt/publica.htm>

Exp.	Reaction	Time	Ref.
test	^{238}U (1 A GeV) + ^{208}Pb	(Nov. 1996)	[5]
1.	^{197}Au (800 A MeV) + H_2	(Feb. 1997)	[14,15]
2.	^{238}U (1 A GeV) + H_2 , D_2	(July 1997)	Data analysis
3.	^{208}Pb (1 A GeV) + H_2 , D_2	(Oct. 1997)	[2,3]
4.	^{208}Pb (500 A MeV) + H_2 , D_2	(Apr. 1999)	Data analysis
5.	^{56}Fe + H_2 , D_2	(Oct. 2000)	Measured

3 Results

Table 1 gives the incineration experiments performed at GSI. The measured total fission cross section from Pb+p at 1 A GeV for elements from titanium to tellurium amounts to $\sigma_f = (157 \pm 7)$ mb in the present work. Only the statistical uncertainty is given here. The total fission cross section can be compared with previously measured values of $\sigma_f = (132 \pm 13)$ mb and $\sigma_f = (142 \pm 14)$ mb [11] obtained in direct kinematics with 1 GeV p+Pb. In view of the 15% systematic uncertainty of our value, all the high-accuracy measurements are in reasonable agreement. The total fragmentation cross section amounts to $\sigma_{\text{frag}} = (1.67 \pm 0.22)$ b. The total reaction cross section measured in the present experiment for ^{208}Pb at 1 A GeV on protons amounts to $\sigma_{\text{tot}} = (1.82 \pm 0.18)$ b. The model of Karol [12] with the modifications of Brohm [13] gives $\sigma_{\text{tot}} = 1.80$ b.

The measured production cross sections for fission and fragmentation of ^{208}Pb at 1 A GeV on protons have been summarised in Fig. 3 on a chart of the nuclides. It shows the production of about 900 isotopes.

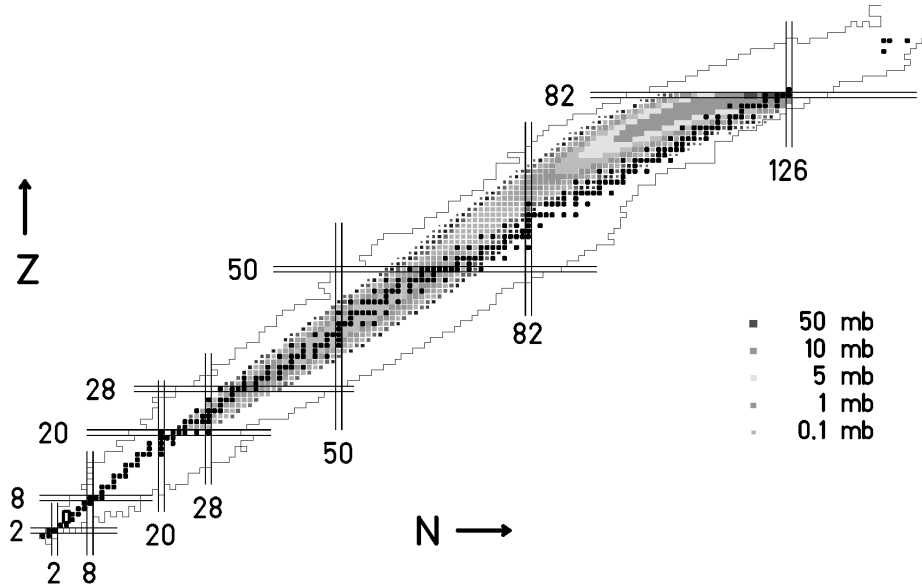


Fig. 3. Two-dimensional cluster plot of the nuclide production cross sections obtained in the present work shown as chart of the nuclides. Full black squares correspond to stable isotopes. Fragmentation-evaporation residues and fragmentation-fission residues are separated by a minimum of cross sections at $Z = (53 \pm 3)$

The average kinetic energy of the recoil product formed by fragmentation can be determined using the measured velocity distribution, see Fig. 4. From these distributions, an average velocity \bar{v}_{cm} and width $\bar{\sigma}_{\text{cm}}$ of the velocity component parallel to the beam axis are extracted for all isotopes. The velocity components

perpendicular to the beam axis have an average velocity equal to zero and, in accordance with available systematics [16] we assume that they have the same width as the parallel component. The average kinetic energy of a spallation recoil product can then be written as

$$\bar{E}_{\text{kin}} = \frac{1}{2} \cdot Am_0 \cdot (\bar{v}_{\text{cm}}^2 + 3\bar{\sigma}_{\text{cm}}^2)$$

The kinetic energy of a spallation recoil product as a function of the proton and mass numbers, determined as the weighted average, is shown in Fig. 4(a).

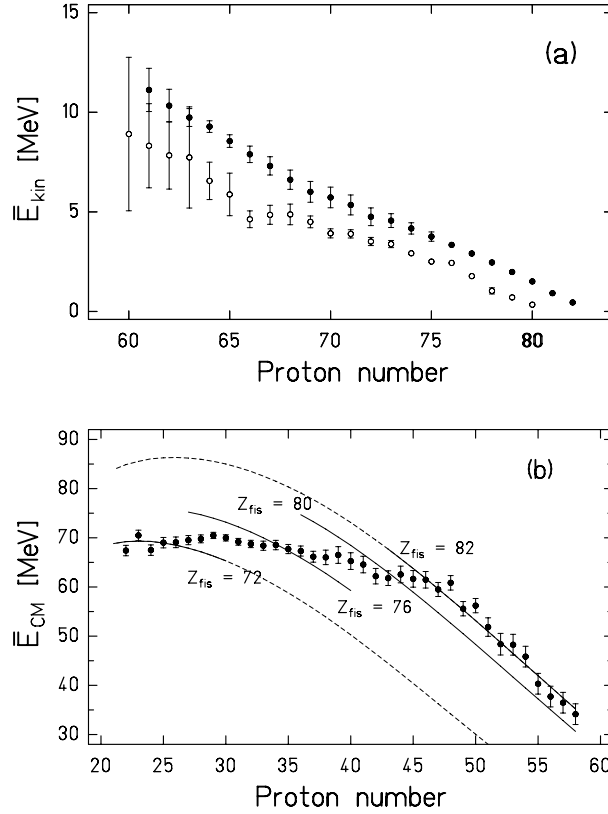


Fig. 4. (a) Measured spallation-residue mean kinetic-energy as a function of the mass number. The data of the present work (full symbols) are compared to the data of ^{197}Au (0.8 A GeV) + p from [14] (open symbols). (b) Measured fission-fragment mean kinetic energies as a function of the proton number. Error bars include only statistical uncertainties. The lines show calculated values when different fissioning elements are assumed (see [3] for details)

The average kinetic energy of a fission fragment can be calculated by the equation

$$\bar{E}_{\text{cm}} = \frac{1}{2} \cdot Am_0 \cdot (\bar{v}_{\text{fis}}^2 + \bar{v}_{\text{cm}}^2)$$

when a uniform isotropic velocity distribution is assumed; m_0 is the atomic mass unit, \bar{v}_{fis} the average velocity of the fission fragment with respect to the fissioning nucleus. Finally, \bar{v}_{cm}^2 is the velocity of the fissioning nucleus in the frame of the projectile, determined as the average fission-fragment velocity. The kinetic energy of one fission fragment as a function of its proton number, determined as the weighted average, is shown in Fig. 4(b).

4 Conclusions

The production cross sections and the energies of about 900 nuclear species produced in the reaction of 1 A GeV ^{208}Pb on proton have been determined in detail. They cover elements from titanium to lead. The reaction products were fully identified in atomic number Z and mass number A using the magnetic spectrometer FRS. Moreover, the velocity of each individual nucleus was measured.

The data, production cross sections and energies, are of highest interest for the design of accelerator-driven systems. Using the measured production cross sections, combined with the known decay properties, the short- and long-term radioactivities in the target material can be calculated. The number of atomic displacements being the reason for radiation damages in the structural materials can now be estimated from the measured kinetic-energy distributions. Most of the radiation damages are caused by spallation residues because of their higher production cross sections. The data also allow to estimate the admixtures of specific chemical elements in the liquid lead target, accumulated in long-term operation of the reactor, which enhance corrosion of the walls or any material in the container.

References

1. R. Michel, P. Nagel: *International Codes and Model Intercomparison for Intermediate Energy Activation Yields*, OECD, 1997
2. W. Wlazlo, T. Enqvist et al.: Phys. Rev. Lett. **84**, 5736 (2000)
3. T. Enqvist, W. Wlazlo et al.: accepted by Nucl. Phys. A.
4. M. de Jong, K.-H. Schmidt et al.: Nucl. Phys. A **628**, 479 (1998)
5. T. Enqvist, J. Benlliure et al.: Nucl. Phys. A **658**, 47 (1999)
6. J. Benlliure, K.-H. Schmidt et al.: Nucl. Phys. A **660**, 87 (1999)
7. P. Chesny et al.: *GSI Ann. Rep. (1996)* p. 190
8. A. Junghans, H.-G. Clerc et al.: Nucl. Instrum. Methods A **370**, 312 (1996)
9. H. Geissel, P. Armbruster et al.: Nucl. Instrum. Methods B **70**, 286 (1992)
10. K.-H. Schmidt, E. Hanelt et al.: Nucl. Instrum. Methods A **260**, 297 (1987)
11. L.A. Vaishnane, L.N. Andronenko et al., Z. Phys. A **302**, 143 (1981)
12. P.J. Karol: Phys. Rev. C **11**, 1203 (1975)

13. T. Brohm: PhD thesis (IKDA, TH Darmstadt 1994)
14. F. Rejmund, B. Mustapha et al.: accepted by Nucl. Phys. A
15. J. Benlliure, P. Armbruster et al.: accepted by Nucl. Phys. A
16. D.J. Morrissey: Phys. Rev. C **39**, 460 (1989)

Determination of Stopping Power of Ions in Matter

N.P. Barradas^{1,2}, C. Jaynes³, R.P. Webb³, and E. Wendler³

¹ Instituto Tecnológico e Nuclear, Reactor, E.N. 10, 2686-953 Sacavém, Portugal

² Centro de Física Nuclear da Universidade de Lisboa, Av. Prof. Gama Pinto 2, 1643-003 Lisboa, Portugal

³ University of Surrey, Ion Beam Centre, Guildford, Surrey GU2 5XH, England

Abstract. Knowledge of the energy loss of ions in matter is fundamental to many applications dependent on the transport of ions in matter, particularly ion implantation and ion beam analysis techniques such as Rutherford backscattering (RBS). We have devised a new method for the experimental determination of these stopping powers: we extract both the stopping powers and their uncertainties from RBS measurements with a Markov chain Monte Carlo method based on Bayesian inference. We have validated the method on a technologically important system in which the stopping powers are already known to a good accuracy: namely backscattering of ^4He off Si. We collected spectra with incident beam energy between 1 and 3 MeV, and determined the stopping power of ^4He in Si in an energy range 0.5–3 MeV.

1 Introduction

Knowledge of the energy loss of ions in matter, commonly described as stopping power, is fundamental to many applications dependent on the transport of ions in matter, particularly ion implantation (a hugely important process in the silicon industry) and ion beam analysis (an enabling scientific technique for thin film technology).

Ion beam analysis is a cluster of complementary techniques for characterising thin films, particularly determining their elemental depth profiles. The simplest of these techniques is Rutherford backscattering (RBS) [1]. An RBS analysis involves directing a beam of fast ions, such as 2 MeV $^4\text{He}^+$, at a target, such as a silicon wafer, and detecting and energy analysing the ions scattered in a backward direction from the nuclei of the target atoms. Because the ions in the incident beam lose energy rapidly as they penetrate the target, the energy of the backscattered ions carries depth information about the target. Therefore, knowledge of the stopping power of the target for the ions is central to determining the depth profile.

The accuracy with which the stopping powers are known is currently rather poor. As an example, there were 10% errors even for the technologically important element silicon until very recently [2]. The main reason for this poor accuracy is that the experimental determination of stopping powers by traditional methods is difficult, involving preparation of pure thin targets and accurate measurements of their thicknesses [3]. For a recent evaluation of the current stopping power database see [4].

We have devised a new method for the experimental determination of stopping powers which avoids all the previous difficulties related to thin target preparation. It involves simply measuring the RBS spectra from known target, which is experimentally trivial. We can then simulate a theoretical spectrum for the known experimental parameters since the physics is well known, apart from the stopping power. Since the experimental parameters are known with well-defined errors, we can fit the stopping powers to obtain a match between the simulated spectrum and the data.

We have developed a code based on Bayesian Inference (BI) with the Markov chain Monte Carlo (MCMC) algorithm to determine both the stopping powers and the confidence limits on the values calculated.

2 Rutherford Backscattering

The algorithms for calculating RBS spectra are well covered in the literature (see [1] for example). Briefly, the energy loss to the incident ion is calculated by determining the energy loss at the collision from the kinematics, and then integrating the energy loss on the pathlengths to the collision and from the collision to the detector. Since the RBS cross-section is given analytically by the Coulomb law the scattering probability is well known and the whole spectrum can be calculated. However, we make the assumption in this work that no incident ion reaching the detector suffers more than one scattering event, that is, we ignore plural and multiple scattering. We point out the effect this has on the calculated spectrum below.

The energy loss per unit path length dE/dx is known as the stopping $S[E(x)]$. Many measurements of these energy loss values have been made, for many incident beams and targets, leading to a spread of values up to 10%. A database for the periodic table has long been available [5].

Different parameterisations and calculations of stopping powers have been presented. Parametrisations are based on fitting empirical or semi-empirical formulas to the data available. The most widely used have been those presented by Ziegler and co-workers [5,6]. Other parameterisations have been presented [3,7–10], which include different amounts of theoretical input and ad-hoc formulas. Theoretical calculations of stopping power have also been formulated [11–14]. In this work we will use the parameterisation of [5] for the electronic stopping, also used in the well-known code RUMP [15], which has a functional form based on 8 parameters to be fitted:

$$S(E) \propto (SL \cdot SH)/(SL + SH) \quad (1)$$

$$SL = a_1 V^{a_2} + a_3 V^{a_4} \quad (2)$$

$$SH = a_5/V^{a_6} \ln(a_7/V + a_8 V) \quad (3)$$

$$V = E/m. \quad (4)$$

3 Experimental Details

Amorphous Si samples were produced by multiple implantations of Si into (100) crystalline Si [16]. The RBS experiments were conducted in Jena at normal incidence using a $^4\text{He}^+$ beam at energies 1 to 3 MeV. The scattering angle was 170.2° . It should be noted that the data we analysed were measured for the round robin exercise by Bianconi et al. [17].

The precision of the beam fluence measurement was 0.3%. The correct working of the system for suppression of secondary electrons was validated by measuring the same beam current for both He^+ and He^{++} beams at 2 MeV. The error in the solid angle of the detector depends on the determination of the physical dimensions of the system, and was 0.4%. The energy calibration of the electronics gain was determined from the surface edge positions of Au, In, Si, O, and C, with an error of around 1%. All these sources of error influence the error with which the stopping powers are determined, and were taken into account in the MCMC analysis.

4 Methodology

Suppose that the result of an RBS analysis of a sample gives a spectrum $\mathbf{X}=(X_1, \dots, X_k)$ where k is the number of channels in the spectrum. This spectrum can be viewed as a stochastic vector, in the sense that it has been contaminated with noise and/or modelling errors. However we assume an underlying deterministic model which depends on a set of quantities $\Theta=(\theta_1, \dots, \theta_n)$. These include some over which we have some degree of control, such as the beam energy, incident angle, and detector solid angle. It contains known elements such as the sample composition (pure Si). It also contains parameters about which we would like to learn, in this case the stopping power curve. By combining the standard theory of RBS and statistical models of the error mechanisms we can connect \mathbf{X} and Θ into a single statistical model.

We then use Bayesian inference [18] to infer information about the parameters Θ given a statistical model and the observed \mathbf{X} . We assume for simplicity independent Poisson noise on the RBS yield. The prior distribution is obtained by conditioning the stopping power curve shape on the parametrisation given by (1)–(4), with a uniform distribution on the a_i parameters.

Computation is done with a Markov Chain Monte Carlo (MCMC) algorithm, according to the Metropolis-Hastings criterion [19]. We calculate the mean solution $\langle\Theta\rangle$ as well as confidence intervals given by the standard deviation $\sigma(\Theta)$. In this case we take the Θ_i to be the stopping power curve.

5 Results and Discussion

We have previously presented a code based on the simulated annealing (SA) algorithm [20], which can analyse automatically RBS [21] and other IBA data, determining depth profiles of the measured samples. It also implemented the

BI/MCMC formalism to determined confidence limits on the depth profiles obtained [22]. We now expanded the algorithm to apply BI/MCMC to stopping power values.

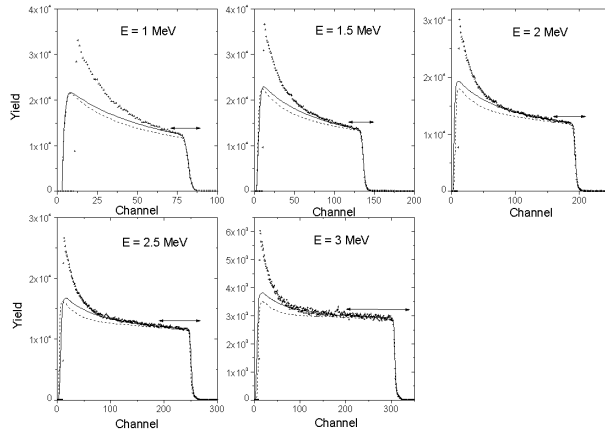


Fig. 1. Experimental data (dots) and simulations obtained with the nominal parameters and the tabulated stopping power values (dashed lines). Simulations obtained with the stopping power values of one of the accepted states are also shown (solid lines)

between the data and the simulated spectrum even in the high energy region where no plural and multiple scattering exists. The discrepancy is smaller for larger beam energy. It cannot be accounted for by the small errors in the beam fluence and solid angle of the detector, which are a normalisation factor on the simulation. It must then be due to the stopping power values.

We constructed a Markov chain with 112000 elements, that is, stopping power data sets up to 3 MeV. Each leads to RBS spectra that fit the five experimental spectra well, as defined by the χ^2 value. Hence the stopping power values determined are consistent with the entire energy range probed.

To test for convergence, plots of moving averages of sample moments against the number of accepted states were used. These plots converge to a constant as equilibrium is reached. To calculate the average and standard deviation of the a_i and of the stopping power curve, we used only the last 100000 elements of the Markov chain.

The results are shown in Fig. 2. The energy regions accessed with each initial beam energy are also shown. For each beam energy two discontinuous energy regions are accessed, corresponding to the energy lost by the beam on its way in, and on the way out. The discontinuity is due to the energy lost in the scattering process itself.

The confidence limits are narrower where the density of data available is larger, that is, in the energy range 1000–1700 keV. Above, there are fewer energy regions accessed, and the width of the error bars increases. Finally, the minimum

The data are shown in Fig. 1, together with the simulations obtained with the nominal experimental parameters and the tabulated stopping power values. The measured yield increases with decreasing energy (channel number) much faster than the simulation. This is due to plural and multiple scattering. We hence only used, for each spectrum, the higher energy portion that is unaffected by these effects.

For the data collected for the 1 MeV beam there is a large discrepancy between the data and the simulated spectrum even in the high energy region where

energy accessed is 482 keV. Energies below that value are not probed at all, and consequently the confidence limits are much broader.

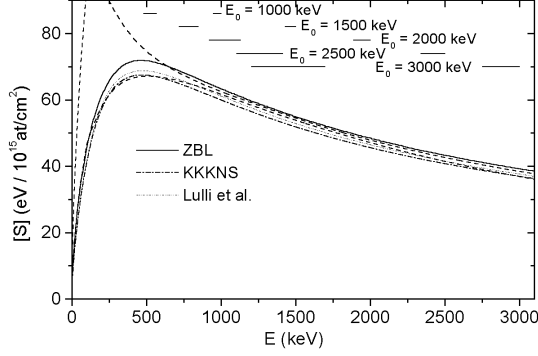


Fig. 2. Confidence limits ($\pm 1\sigma$) obtained for the stopping power values (dashed curves). The energy ranges probed with each beam energy are shown

Both the data of Lennard et al., who determined the stopping power values at 0.5, 1, 2 and 3 MeV [2], and those of Lulli et al., which have determined the stopping power values at 1.16, 1.5, 2, 3 and 3.7 MeV [23], agree with the data of Konac et al. [3] within 2%. Lulli et al. obtain a better agreement by scaling Konac's data up by a uniform factor of 2%, while Lennard et al. find a slightly different energy dependence, with values 1 to 1.5% larger than Konac's data in most of the energy range.

We show the ^4He in Si electronic stopping power values obtained by us and by Lulli et al in Tab. 1 (Lennard et al do not quote S_e values directly). We obtain values which are between 2 and 4.5% larger than those of Konac et al but point out that from all the participating labs in the Bianconi et al round robin [17] it was Jena (our present data) that obtained the smallest surface yields H_0 in the energy range 1.5-3 MeV, corresponding to the largest stopping power values. We suggest that, by analysing simultaneously the whole set of data collected by Bianconi et al as well as those collected by Lennard et al, we would obtain stopping power values closer to those cited by those groups, i.e. around 2% larger than the values given by Konac et al, together with larger error bars reflecting the dispersion in the different data sets.

Table 1. Electronic stopping powers at different beam energies

	S_e (eV/ 10^{15} at/cm 2)					
E_0 (MeV)	0.5	1	1.5	2	2.5	3
This work	70.9(3.9)	62.10(41)	54.20(34)	47.51(37)	42.03(58)	37.65(78)
Lulli et al.	68.76	61.15	52.88	46.48	41.55	37.66
RUMP	71.8	63.4	54.9	48.4	43.3	39.2
KKKNS	67.41	59.95	51.84	45.57	40.74	36.92

Several energy intervals (e.g. [2500, 2754] or [2000, 2341]) are not accessed in the experiment but the confidence limits are not significantly broader on these energy ranges because the parameterisation used effectively constrains the stopping power values in the whole energy range.

6 Summary

We have used a Monte Carlo method for the first time to determine both stopping powers of fast ions in solids and the confidence interval for this determination. We have shown that the results are as good as those obtained with a much more difficult experimental procedure. The values obtained are very important parameters for major technologies. We intend to use this method to make further accurate stopping power measurements.

References

1. J.R. Tesmer, M. Nastasi (eds.): *Handbook of Modern Ion Beam Materials Analysis*, (MRS, Pittsburgh, 1995)
2. W.N. Lennard, G.R. Massoumi, T.W. Simpson, I.V. Mitchell: Nucl. Instr. Meth. B **152**, 370 (1999)
3. G. Konac, S. Kalbitzer, C. Klatt, D. Niemann, R. Stoll: Nucl. Instr. Meth. B **136-138**, 159 (1998)
4. J.F. Ziegler: Nucl. Instr. Meth. B **136-138**, 141 (1998)
5. J.F. Ziegler, J.P. Biersack, U. Littmark: *Stopping and Ranges of Ions in Solids* (Pergamon, New York, 1985)
6. J.F. Ziegler, J.P. Biersack: SRIM2000 - The Stopping and Range of Ions in Matter, Version 0.06 (2000), code available from Ziegler@Watson.IBM.Com
7. G. Reiter, N. Kniest, E. Pfaff, G. Clausnitzer: Nucl. Instr. Meth. B **44** 399 (1990)
8. D. Niemann, P. Oberschachtsiek, S. Kalbitzer, H.P. Zeindl: Nucl. Instr. Meth. B **80-81**, 37 (1993)
9. F. Munnik, A.J.M. Plompen, J. Räisänen, U. Wätjen: Nucl. Instr. Meth. B **119**, 445 (1996)
10. A.J.M. Plompen, F. Munnik, J. Räisänen, U. Wätjen: J. Appl. Phys. **80** 3147 (1996)
11. H.A. Bethe: Ann. Phys. **5** 325 (1930)
12. J. Lindhard, A.H. Sørensen, Phys. Rev. A **53**, 2433 (1996)
13. P.L. Grande, G. Schiwietz: Phys. Rev. A **58**, 3796 (1998)
14. G. Schiwietz, P.L. Grande, Nucl. Instr. Meth. B **153**, 1 (1999)
15. L. Doolittle, Nucl. Instr. Meth. B **9**, 344 (1985)
16. G. Lulli, E. Albertazzi, M. Bianconi, R. Nipoti, M. Cervera, A. Carnera, C. Cellini: J. Appl. Phys. **82**, 5958 (1997)
17. M. Bianconi, F. Abel, J.C. Banks, A. Climent Font, C. Cohen, B.L. Doyle, R. Lotti, G. Lulli, R. Nipoti, I. Vickridge, D. Walsh, E. Wendler: Nucl. Instr. Meth. B **161-163**, 293 (2000)
18. P.M. Lee: *Bayesian Statistics*, 2nd edition (Arnold, London, 1997)
19. C.R. Smith, W.T. Grandy (Eds.): *Maximum Entropy and Bayesian Methods in Inverse Problems*, (Reidel Pub. Co. 1985)
20. S. Kirkpatrick, C.D. Gelatt, M.P. Vecchi: Science **220** 671 (1983)
21. N.P. Barradas, C. Jeynes, R.P. Webb: Appl. Phys. Lett. **71** 291 (1997)
22. N.P. Barradas, C. Jeynes, M. Jenkin, P.K. Marriott: Thin Sol. Films **343** 31 (1999)
23. G. Lulli, E. Albertazzi, M. Bianconi, G.G. Bentini, R. Nipoti, R. Lotti: Nucl. Instr. Meth. B **170** 1 (2000)

Comparison of Spallation Neutron and Residual Nuclide Production Data with Different Intra-Nuclear Cascade Models

S. Leray¹, A. Boudard¹, J. Cugnon², R. Legrain¹, and C. Volant¹

¹ CEA/Saclay, DAPNIA/SPhN, 91191 Gif-sur-Yvette Cedex, France

² University of Liège, 4000 Sart-Tilman Liège 1, Belgium

Abstract. Recent results on neutron production obtained at SATURNE and isotopic distributions of residual nuclides measured at GSI are compared to high-energy transport code calculations in which three different Intra-Nuclear cascade models, Bertini, Isabel and Cugnon, are used. It is shown that the Bertini INC model generally fails to reproduce the data while the Cugnon and Isabel models give a better agreement.

1 Introduction

In high energy transport codes, used in the various applications of spallation neutron sources, the elementary cross-sections are calculated by nuclear physics models. Generally, the interaction is modeled as a two step process: a first fast stage, the Intra-Nuclear Cascade (INC), leading to an excited residue, followed by a second slower stage of de-excitation by evaporation and, sometimes, fission. Some authors introduce a pre-equilibrium step between INC and decay. Although, most of the neutrons produced in spallation reactions are emitted during the evaporation process, the INC stage plays a major role since it determines the initial excitation energy of the decaying hot residue and, therefore, the number of evaporated particles. Also, the initial charge and mass of the nucleus prior to de-excitation, together with its excitation energy, are expected to condition the final distribution of residual nuclides.

In high energy transport codes, the most widely used INC model is the old Bertini [1] one. However, several other models are available, among which the Isabel [2] model which can be used in the LAHET [3] Code System from Los Alamos and the Cugnon [4] model, recently improved [5]. Although most of the data depend in an intricate way of both INC and evaporation-fission details, it is interesting to confront experimental results with calculations using different INC models in order to test their validity and understand their difference.

During the last years, a significant experimental effort has been undertaken in several places to collect new spallation data. In this paper, the results of two recent experiments regarding the production of neutrons at SATURNE and of residual nuclei at GSI in proton induced reactions are compared with calculations using different Intra-Nuclear Cascade models.

2 Neutron Production Measured at SATURNE

The experimental set-up ensured the measurement of angular distributions from 0° to 160° , either by time-of-flight with several neutron scintillators or with a magnetic spectrometer placed on a rotating platform. Measurements were performed with protons of 0.8, 1.2 and 1.6 GeV energy impinging on different targets [6]. Figure 1 presents neutron production double-differential cross-sections in 800 MeV proton reaction on a 2 cm thick Pb target. The histograms are numerical calculations, taking into account the actual geometry and composition of the target, performed with the TIERCE [7] code system developed at Bruyères-le-Châtel or with LAHET [3]. Within LAHET calculations either the Bertini (dotted line) or the Isabel (dashed line) Intra-Nuclear Cascade model (without pre-equilibrium) were used, while in TIERCE the Cugnon (solid line) INC model was chosen.

At 0° , an abnormal behaviour is obtained with the Bertini cascade at energies corresponding to the excitation of the Δ resonance. This is due to a bad parameterisation of the $NN \rightarrow N\Delta$ reaction angular distribution. In the Cugnon INC (and likely Isabel), a different parameterisation validated on experimental data was introduced [8] and solves the problem. The Bertini calculation overestimates

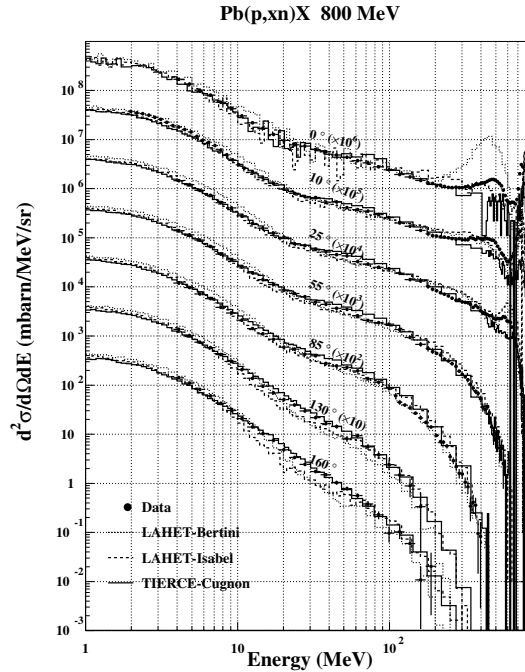


Fig. 1. Experimental p (800 MeV) + Pb neutron double-differential cross-sections [6] compared with calculations performed with LAHET using either Bertini (*dotted line*) or Isabel (*dashed line*) INC model and with the TIERCE - Cugnon code (*solid line*)

neutron production at low energies. Both Isabel and Cugnon INC give a similar good global agreement with the data, except that Isabel under-predicts backward angle results at intermediate energies but is a little better than Cugnon at very forward angles.

All the calculations above discussed were performed with the same evaporation-fission model from Dresner-Atchison [9,10], although the Dresner codes are slightly different in TIERCE and LAHET. It can therefore be presumed that the variations observed in the production of low energy (below 20 MeV) neutrons depending on the choice of the INC model are due to the difference in the initial conditions for the de-excitation of the residual nucleus after the INC stage. In fact, while the mass of the residue prior to evaporation is very similar in the three models, the excitation energy distribution is found to extend to much higher values in the case of Bertini than in the Cugnon or Isabel cases (see Fig. 2), leading to more evaporated neutrons. This could be ascribed partly to the more drastic Pauli blocking in Bertini compared to the two other models in which the actual phase space occupation rate is taken into account. Indeed, a too strict Pauli blocking inhibits the emission of low energy INC particles, preventing the decrease of the excitation energy.

The same experimental set-up also permitted the measurement of energy spectra of neutrons coming out from thick targets. Measurements with various lengths and diameters of cylindrical targets were conducted with 0.8, 1.2 and 1.6 GeV protons [11]. The results were compared with calculations [12] performed with the TIERCE code including either the Bertini or the Cugnon INC model. It was found that, in general, the production of low energy neutrons was over-

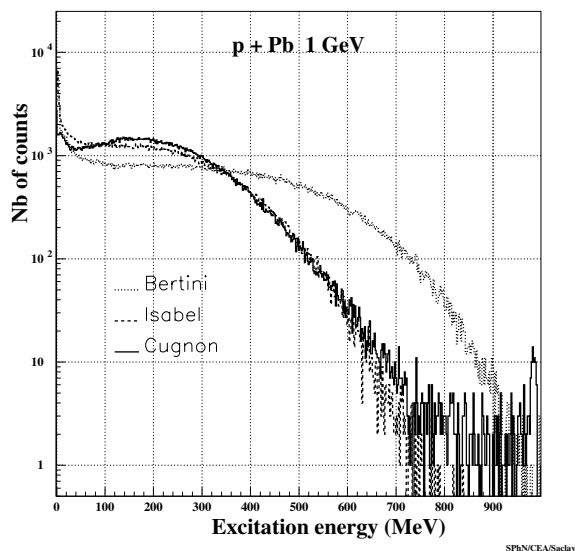


Fig. 2. Excitation energy distribution in the p (1 GeV) + Pb reaction found with the Bertini (dotted line), Isabel (dashed line) or Cugnon (solid line) INC models

predicted with the Bertini model but rather well estimated with the Cugnon one. This results from the larger number of evaporation neutrons emitted in the high energy primary interactions with Bertini, as above shown. In fact, the total number of neutrons per incident proton escaping the target is found to be 43.7 with Bertini and 34.8 with Cugnon model at 1600 MeV, and respectively 28.6 and 23.6 at 1200 MeV. This makes a 20% discrepancy, which is probably not acceptable in the design of spallation targets. Other simulations [13] were performed using the LAHET code system with the Bertini and Dresner models but adding the option of a pre-equilibrium stage between intra-nuclear cascade and evaporation-fission. In that case, the calculation agrees better with the experimental data but are still over-estimating a little the low energy neutron production. Actually, the decrease of E^* induced by the adding of a pre-equilibrium stage is not yet sufficient since E^* is still larger than in the Cugnon or Isabel case.

3 Residual Nuclide Isotopic Distributions Measured at GSI

The reverse kinematics technique, together with the fragment separator FRS is being used at SIS accelerator in Darmstadt to identify isotopically all spallation residues, with production cross-sections larger than 0.1 mb, ranging from fission fragments to beam isotopes (see the paper by P.Armbruster in this conference for details). So far, experiments with ^{197}Au [15], ^{238}U and ^{208}Pb [14] beams between 0.5 and 1 GeV/A on liquid hydrogen and deuterium targets have been carried out. The element distribution measured in the Pb (1 GeV/A) + p is compared in

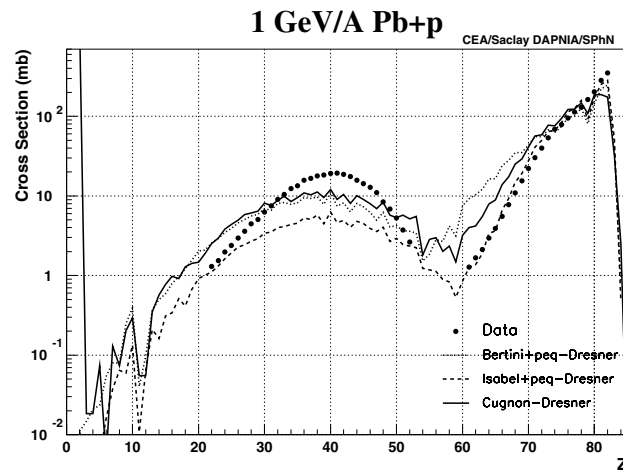


Fig. 3. Element distribution measured in the 1 GeV/A Pb on H2 reaction [14]. The solid, dashed and dotted curves were calculated with the Cugnon, Isabel and Bertini INC models, respectively, followed by the Dresner-Atchison evaporation-fission model. Pre-equilibrium was added in the case of Bertini and Isabel calculations

Fig. 3 with three models: Bertini and Isabel INC + pre-equilibrium and Cugnon INC followed by the same Dresner-Atchison evaporation-fission model. It can be seen that the slope of the Z-distribution for fragmentation residues ($Z > 65$) varies strongly with the model. In fact, it is related to the difference in excitation energy, the larger E^* , the steeper the slope. The calculation with Cugnon (solid line) and Isabel (not shown), which were giving good agreement with the neutron data, are not able to reproduce these data. Only, the adding of a pre-equilibrium stage to Isabel INC (dashed curve) lead to a fair agreement.

However, the same calculation (dashed line in Fig. 4) cannot reproduce the isotopic distributions of fragmentation residues measured in the same experiment. Actually, whatever the INC model, the shape of these distributions are exactly identical as far as the same evaporation-fission model is used. Only the height of the peak changes with INC, following the trends of Fig. 3. The solid line shows the results obtained with Cugnon model as an example. The distribution shapes differ significantly from the experimental ones: they are shifted with respect to the data towards the neutron-rich side. This is ascribed to the fact that the prediction of the neutron/proton/composite particle competition in the Dresner code is not satisfying, likely because the charged particle emission barriers are not correct as suggested by Enke et al. [16]. The use of a new

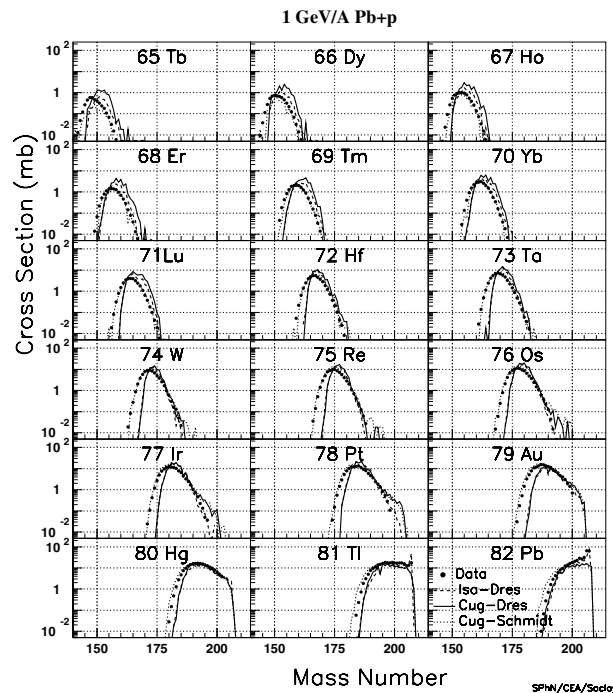


Fig. 4. Isotopic production cross-sections of elements between $Z=82$ and 65, in the 1 GeV/A Pb on H2 reaction, versus mass number. The data are from [14]

evaporation-fission model, presently being developed at GSI [17], together with the Cugnon INC leads a fairly good agreement with both the isotopic and Z experimental distributions.

4 Conclusions

Spallation neutron production on both thin and thick targets as well as isotope production have been compared with simulations using different Intra-Nuclear Cascade models. It was found that the Bertini code followed by the Dresner evaporation-fission models (the most commonly used in high-energy transport codes) generally fails in reproducing the data. On the contrary, the use of the Cugnon or Isabel INC models leads to a fairly good global agreement with neutron results. This has been ascribed to the too high excitation energy at the end of the cascade stage in the Bertini model. On the other hand, none of the calculation is able to reproduce the residue isotopic distributions, as far as it is coupled with the Dresner evaporation.

References

1. H.W. Bertini et al.: Phys. Rev. **131**, 1801 (1963)
2. Y. Yariv, Z. Fraenkel: Phys. Rev. C **20**, 2227 (1979)
3. R.E. Prael, H. Lichtenstein: Report LA-UR-89-3014 Los Alamos National Laboratory (1989)
4. J. Cugnon: Nucl. Phys. A **462**, 751 (1987)
5. J. Cugnon, C. Volant, S. Vuillier, Nucl. Phys. A **620**, 475 (1997)
6. X. Ledoux et al.: Phys. Rev. Lett. **82**, 4412 (1999); F. Borne et al.: Rapport CEA-R-5887 (2000)
7. O. Bersillon: *2nd Int. Conf. on Accelerator Driven Transmutation Technologies, Kalmar, Suède, 3-7 Juin (1996)*
8. J. Cugnon et al.: Phys. Rev. C **56**, 2431 (1997)
9. L.W. Dresner: Oak Ridge Report ORNL-TM-196 (1962)
10. F. Atchison: 'Intermediate Energy Nuclear Data: Models and Codes'. In: *Proc. of a Specialists' Meeting, OECD/NEA, Issy-les-Moulineaux, France, May 30-June 1 (1994)*
11. S. Ménard: PhD Thesis (Orsay, January 1998)
12. P. Casoli: Stage DEA, CEA/DAPNIA/SPhN (June 1999)
13. C. Varignon: PhD thesis (Caen University 1999)
14. W. Wlazlo et al.: Phys. Rev. Lett. **84**, 5740 (2000); T. Enqvist et al.: to appear in Nucl. Phys. A.
15. J. Benlliure et al.: to appear in Nucl. Phys. A; F.Rejmund et al.: to appear in Nucl. Phys. A.
16. M. Enke et al.: Nucl. Phys. A **657**, 317 (1999)
17. A.R. Junghans et al.: Nucl. Phys. A **629**, 635 (1998)

Design of Tracking and Generic Processes in Geant4

M. Asai^{1,5}, K. Amako^{2,3}, J. Apostolakis², H. Kurasige⁴, T. Sasaki³, J.-P. Wellisch²

¹ Hiroshima Institute of Technology, Japan

² CERN, Geneva, Switzerland

³ KEK, Tsukuba, Japan

⁴ Kobe University, Japan

⁵ on behalf of the Geant4 Collaboration

Abstract. Geant4 is one of the first successful products in HEP which fully takes the advantages of the modern software engineering technologies such as object-orientation. The design of a central part of Geant4, the tracking and generalised processes, is introduced. Emphasis is put on how physics processes are generalised, being treated in abstract manner by the tracking in Geant4.

1 Introduction

Geant4 [1] is the successor of GEANT3, the most widely used toolkit for HEP detector simulation. Geant4 is one of the first successful attempt to re-design a major package of HEP software for the next generation of experiments using an Object-Oriented environment. A variety of requirements also came from heavy ion physics, CP violation physics, cosmic ray physics, medical applications and space science applications. In order to meet such requirements, a large degree of functionality and flexibility are provided.

Development of Geant4 started in December 1994 as a CERN R&D project [2], with the goal of creating a simulation package with a long lifetime. The first public production version was released in December 1998. Since this release Geant4 is maintained and improved by an MoU-based collaboration. Currently it consists of about 100 physicists and computer scientists, that belong to many laboratories, institutes and HEP experiments around the globe, contribute to its development and testing. Key early choices were the adoption of the most recent software engineering methodologies, Object-orientation and C++.

Collaborating institutions provide contributions (defined in the MoU) and in return get guarantee of support from the Geant4 collaboration. Two public releases are made each year. Also monthly reference tag releases for collaboration users are provided.

Wide coverage of physics in Geant4 comes by allowing the mixture of theory-driven, cross-section tables, and empirical formulae. Thanks to polymorphism mechanism, cross-sections and models can be combined in an arbitrary way to create a particular process [3]. An event and a track are each a class object. In this way the treatment of overlap events and pile-up arises naturally. Also it is

the two volumes, boundary processes such as transition radiation or refraction can be simulated simply.

3 Design of Processes

3.1 Tracking and Processes

Geant4 tracking is general. It is independent of the particle type or the physics processes for a particle. It gives the chance to all processes

- To contribute to determining the step length
- To contribute any possible changes in physical quantities
- To generate secondary particles
- To suggest changes in the state of the track e.g. to suspend, postpone or kill.

In Geant4, particle transportation is a process as well, by which a particle interacts with geometrical volume boundaries. Because of this, shower parameterization process can take over from the ordinary transportation.

Each particle has its own list of applicable processes. At each step, all processes listed are invoked to get proposed physical interaction lengths. The process which requires the shortest interaction length (in space-time) limits the step.

In Geant4 tracking, each process can act at any of three space-time intervals

- In time, i.e. when it is at rest (e.g. decay at rest)
- Continuously along a step (e.g. Cherenkov radiation)
- At a point, i.e. at the end of the step (e.g. decay in flight)

“Along step actions” are applied cumulatively, while others are selectively applied. Figure 2 is the scenario diagram which illustrates how Geant4 tracking handles processes in general and generates simulated hits. A process can have more than one types of action according to its nature. For example, Ionization process has Along and End step actions.

Tracking handles each type of action in turn. It loops over all processes with such a type of action. The motivation for creating these categories of actions is to keep the Geant4 tracking independent of the physics processes. All seven combinations of actions are possible. The traditional Continuous, Continuous-Discrete, Discrete and AtRest are found in these cases. The ordering of processes is important in some cases, e.g. multiple scattering affects the step length seen by the transportation.

In Geant4, two kinds of methods of processes play important roles in tracking.

- The `GetPhysicalInteractionLength` (GPIL) method gives the step length from the current space-time position to the next space-time point where the `DoIt` method should be invoked.
- The `DoIt` method describes what happens in the interaction. It gives change of energy and momentum direction, change of position, and secondary tracks.

Each process can have a GPIL and a `DoIt` method for each type of its actions. Typical cases are further aided by an additional layer of substructure, that creates, for example, a `GetMeanFreePath` method for discrete processes.

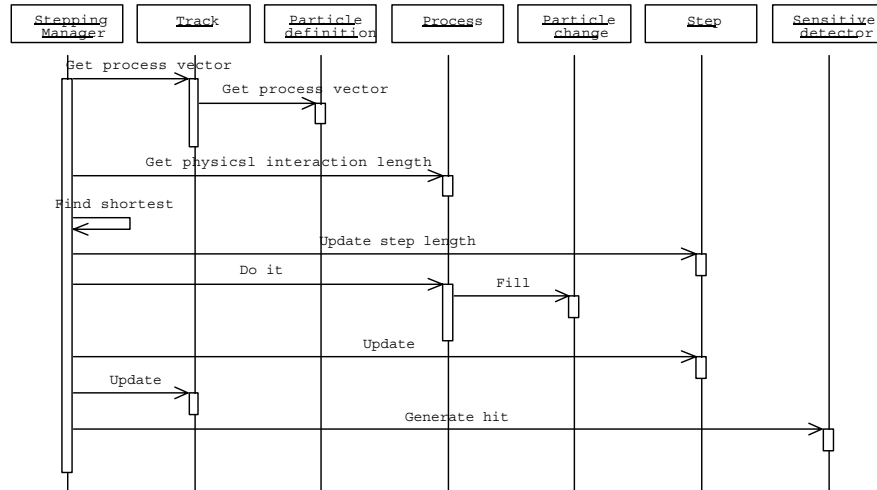


Fig. 2. Scenario diagram for one step

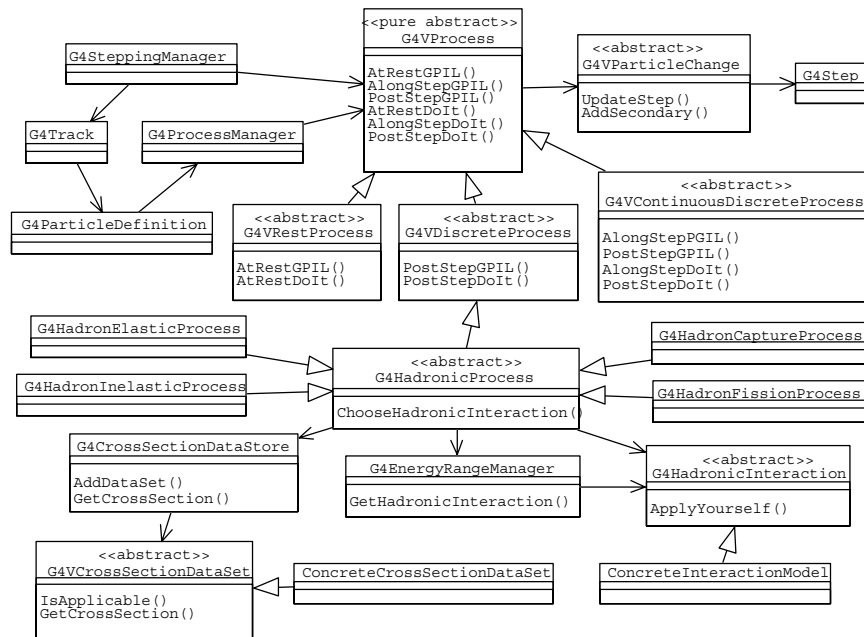


Fig. 3. Class diagram for tracking and processes

3.2 Physics Processes

In Geant4, one physics process can have more than one cross-section tables and physics models. Much wider coverage of physics comes from mixture of theory-driven, cross-section tables, and empirical formulae. Thanks to polymorphism mechanism, both cross-sections and models can be combined in arbitrary manners into one particular process. Each cross-section table or physics model has its own applicable energy range. Combining more than one tables/models, one physics process can have enough coverage of energy range for wide variety of simulation applications.

Figure 3 shows the major classes of tracking and processes in Geant4. Only a small number of classes are drawn in this figure, illustrating a general process and also showing some of the substructure of the design of a hadronic process.

3.3 Built-in Processes

Physics processes describe how particles interact with material or volume itself. There are 7 major process categories in Geant4.

- Electromagnetic [5–7]
- Hadronic [8]
- Photolepton-hadron
- Decay
- Optical
- Transportation
- Parameterization [9,10]

It is the user's responsibility to choose physics processes, models and/or cross-section tables and assemble them into a coherent set for each particle. Although Geant4 provides no default, it does provide examples to aid in this task.

For many energy ranges we offer alternative processes, cross-sections or models. These alternatives can have different strengths and trade-offs. Our examples offer a choice for some use cases, while we try to assist users to make appropriate choices for different uses.

We expect that some users will wish to try several different approaches. We accommodate this easily thanks to polymorphism, which lets them replace one process, model and/or cross-section with another. Finally an advanced user can create his/her own particular implementation of a process, a model and/or a cross-section. He/she can utilise it by plugging in without modifying any part of Geant4.

3.4 Parameterization

Geant4 includes a built-in framework for fast simulation. This can be used to do shower parameterization [9,10]. Currently users must create their own specific parameterizations. Then they assign one to a volume, which is then called as an "envelope". A parameterization can choose whether to happen, depending on

the particle type, its energy or other parameters. If it triggers a particle that comes into the envelope will fully treated by a parameterization, regardless of the existence of geometry substructure.

So the user can have a dynamic choice to take his/her parameterization or to follow the ordinary tracking in the granular geometry. A parameterization must then directly contact the sensitive detector associated with the volume to produce and distribute its multiple hits. By contrast the “ordinary” tracking sends information to the sensitive detector at every step.

4 Summary

Geant4 is a simulation toolkit built using Object-Orientation and Software Engineering to address requirements from HEP, heavy ion physics, CP violation physics, cosmic ray physics, and space science and medical applications.

By utilising Object-orientation, a flexible mechanism was create for integrating an open set of processes with a general mechanism for tracking. Thus wide coverage of physics processes is possible, and it realized. Also its extension by any user with a new model or process is achieved without changing Geant4. Intensive use of Geant4 in various fields has started.

5 Acknowledgements

The authors thank all Geant4 collaborators [1] for their contributions.

References

1. Principle Geant4 web site is at <http://cern.ch/geant4/>
2. S. Giani et. al.: *Geant4: An Object-Oriented toolkit for Simulation in HEP*, CERN/LHCC 98-44
3. J.P. Wellisch: *Hadronic shower models in geant4 - the frameworks*, Proceedings of CHEP 2000, Padova, Italy
4. K. Amako et. al.: *Geant4 Users requirements document*. The latest version cn be found at Ref. 1
5. V. Grichine: ‘Fast simulation of X-ray transition radiation in the Geant4 toolkit’. These Proceedings p. 117
6. M.G. Pia et. al.: ‘Geant4 electromagnetic physics’. These Proceedings p. 153
7. P. Arce et. al.: ‘Multiple scattering in Geant4, A comparison with Moliere theory and L3 detector data’. These Proceedings p. 503; S. Chauvie et al.: ‘Medical applications of the Geant4 toolkit’. These Proceedings p. 543
8. J.P. Wellisch: ‘On hadronic models in Geant4’. These Proceedings p. 1027
9. P. Mora de Freitas et. al.: ‘RD-44: Going Fast with GEANT4 Parameterization Mechanism’. In: *Proceedings of CHEP 1998, Chicago, U.S.A.*
10. P. Mora de Freitas et. al.: ‘Using parallel geometries in Geant4: the “Ghost Volumes”’. In: *Proceedings of CHEP 1998, Chicago, U.S.A.*

Multigroup Boltzmann–Fokker–Planck Approach for Ion Transport in Amorphous Media

N.D. Keen, A.K. Prinja, and G.D. Dunham

Chemical and Nuclear Engineering Department, The University of New Mexico,
Albuquerque, NM 87131, USA

1 Introduction

The interaction and transport of energetic ions in matter is of importance in applications as diverse as ion implantation in semiconductor materials [1], heavy ion radiotherapy [2] and galactic cosmic ray interactions with sensitive spacecraft components. Computational modeling and analyses of ion transport in the complex geometries typically encountered in these applications invariably rely on Monte Carlo (MC) simulation tools. While *continuous* energy MC codes such as LAHET [3] and TRIM [4] are extensively used (although TRIM is strictly a 1D planar geometry code), *multigroup* Monte Carlo (MGMC) methods, known from neutral particle transport to be accurate and computationally more efficient than continuous Monte Carlo, are lacking for ion transport.

Here we present a MGMC approach for the transport of arbitrary mass ions having energies up to a few MeV. Specifically, we consider interactions with target atoms through Coulomb mediated elastic nuclear and inelastic electronic collisions and restrict considerations to ion implantation and energy deposition of primary ions in amorphous media. That is, correlated events such as channeling associated with crystalline structure are ignored, as is recoil driven secondary atom transport. While the latter restriction can be readily relaxed, incorporating crystalline material effects in an approach based strictly on the random distribution of scattering centers presents a significant and unsolved challenge. A Boltzmann Fokker-Planck (BFP) transport model is introduced which accurately and efficiently treats the highly forward peaked charged particle scattering cross sections and incorporates a novel multigroup electronic energy-loss straggling formalism. This approach makes it feasible to simulate ion transport using the existing MCNP4B code [5], capable of handling continuous slowing down and Fokker-Planck angular scattering. A specially constructed cross section data code, consistent with the BFP transport model, provides multigroup data for the different collision processes.

2 Boltzmann–Fokker–Planck Transport Model

Ion transport in the regime of interest is accurately described by the classical linear Boltzmann or transport equation, which we express as

$$\boldsymbol{\Omega} \cdot \nabla \psi(\mathbf{r}, E, \boldsymbol{\Omega}) = J_{\text{nucl}}[\psi] + J_{\text{elec}}[\psi], \quad (1)$$

where $\psi(\mathbf{r}, E, \boldsymbol{\Omega})$ is the ion angular flux, and $J_{\text{nuc}}[\psi]$ and $J_{\text{elec}}[\psi]$ are collision integrals describing, respectively, nuclear and electronic interactions, (assumed independent processes over the energy range of interest here.) Explicitly, $J_{\text{nuc}}[\psi]$ may be written as

$$J_{\text{nuc}}[\psi] = \int dE' \int_{4\pi} d\boldsymbol{\Omega}' \sigma_s(E' \rightarrow E, \boldsymbol{\Omega}', \boldsymbol{\Omega}) \psi(\mathbf{r}, E', \boldsymbol{\Omega}') - \sigma_s(E) \psi(\mathbf{r}, E, \boldsymbol{\Omega}), \quad (2)$$

where $\sigma_s(E' \rightarrow E, \boldsymbol{\Omega}', \boldsymbol{\Omega})$ is the ion/target atom double differential scattering cross section and $\sigma_s(E)$ the total scattering cross section. The differential cross section describing elastic nuclear collisions is highly forward peaked about small deflection angles and small energy transfers but is slowly varying otherwise. This makes the standard Legendre moments expansion impractical to implement. However, a computationally tractable representation may be obtained by first decomposing the cross section into so-called smooth and singular components. The smooth or Boltzmann component, describing the large deflection angle, large energy transfer collisions, is then amenable to a truncated Legendre moments representation while the singular component, describing strictly the small deflection angles and small energy transfers, can be approximated using a Fokker-Planck expansion. Thus, formally (for now) decomposing the differential cross section as $\sigma_s(\dots) = \sigma_s^B(\dots) + \sigma_s^{FP}(\dots)$, we obtain the BFP representation of the nuclear collision integral

$$J_{\text{nuc}}[\psi] = \int dE' \int_{4\pi} d\boldsymbol{\Omega}' \sigma_s^B(E' \rightarrow E, \boldsymbol{\Omega}', \boldsymbol{\Omega}) \psi(\mathbf{r}, E', \boldsymbol{\Omega}') - \sigma_s^B(E) \psi(\mathbf{r}, E, \boldsymbol{\Omega}) + \frac{\partial}{\partial E} [S_N^R(E) \psi] + \frac{\sigma_{tr}^R(E)}{2} \left[\frac{\partial}{\partial \mu} (1 - \mu^2) \frac{\partial \psi}{\partial \mu} + \frac{1}{(1 - \mu^2)} \frac{\partial^2 \psi}{\partial \phi^2} \right], \quad (3)$$

where the restricted nuclear stopping power and restricted momentum transfer cross section are defined by $S_N^R(E) = 2\pi \int d\mu_0 \int dE' (E - E') \sigma_s^{FP}(E \rightarrow E', \mu_0)$ and $\sigma_{tr}^R(E) = 2\pi \int dE' \int d\mu_0 (1 - \mu_0) \sigma_s^{FP}(E \rightarrow E', \mu_0)$, respectively, both associated with the singular piece. Thus the energy transfer associated with the singular part of the cross section is modeled in the continuous slowing down (CSD) approximation while the corresponding angular deflections are represented as a diffusion process on the unit sphere. Given the extreme anisotropy of scattering these approximations are very accurate. A practical decomposition algorithm will be presented in the next section.

Electronic energy loss is usually handled in the CSD approximation [4], which preserves the mean energy loss per unit path length of travel but neglects fluctuations about this mean. For most ion implantation problems of interest, this approximation suffices because energy spreading is dominated by large energy transfer nuclear collisions. For high energy light ions, however, electronic energy-loss fluctuations dominate the spectral softening and lead to broader implantation profiles than would result from nuclear effects only. In such cases it is necessary to incorporate energy straggling effects. To lowest order, this can be accomplished by additionally preserving the mean-square energy loss per unit path

length which can be achieved with a Fokker-Planck approximation to $J_{\text{elec}}[\psi]$, i.e.,

$$J_{\text{elec}}[\psi] = \frac{\partial}{\partial E}[S_e(E)\psi] + \frac{1}{2} \frac{\partial^2 [T(E)\psi]}{\partial E^2} \quad (4)$$

where $S_e(E)$ is the electronic stopping power and $T(E)$ is the straggling coefficient. Very accurate representations of $S_e(E)$ and $T(E)$ are available in the literature [4,6].

Equations (1)–(4) define our BFP model of ion transport in amorphous media. However, to form the basis of a MC simulation algorithm the model must be complemented with a suitable data set. Furthermore, a method of dealing with the non-canonical Fokker-Planck terms must be devised. These issues are addressed in the next section.

3 Cross Section Data and Coupling to MCNP

All nuclear scattering data is generated from the highly forward peaked center of mass (CM) differential cross section $\sigma(E, \mu_{cm})$, $-1 \leq \mu_{cm} \leq 1$, which in turn can be obtained from the underlying interatomic potential through the classical scattering integral [4]. A computationally less demanding approach is to use Lindhard's single parameter universal approximation given by [4]

$$d\sigma \equiv 2\pi \sigma(E, \mu_{cm}) d\mu_{cm} = \left(\frac{\pi a_u^2}{2} \right) \frac{f(t^{\frac{1}{2}})}{t^{\frac{3}{2}}} dt, \quad (5)$$

where $t = (E/E_L)^2(1 - \mu_{cm})/2$, E_L is the Lindhard energy [4] and $f(t^{\frac{1}{2}})$ is a function that depends on the nuclear stopping power. Explicit representation of this function is given in [4] and is used to compute $\sigma(E, \mu_{cm})$. Details of the procedures as well as numerical comparisons against exact results obtained using the scattering integral may be found in [7] where it is shown that the Lindhard approximation is highly accurate except at extremely low energies, $E \ll 1$ keV. The decomposition into smooth and singular components can be summarized as follows (see [7] for details). An angular cut-off μ_{cut} is first selected such that $\sigma(E, \mu_{cm})$ is reasonably smooth over the partial range $-1 \leq \mu_{cm} \leq \mu_{cut}$. Using a least squares procedure an expansion in shifted Legendre polynomials is used to fit the cross section over this partial range, with the expectation that a relatively low order expansion suffices. The smooth or Boltzmann cross section $\sigma^B(E, \mu_{cm})$ is then obtained by simply extending the partial range cross section to the full angular range $-1 \leq \mu_{cm} \leq 1$. The singular component follows from the difference between the exact and the smooth cross sections and is used to define the Fokker-Planck coefficients $S_N^R(E)$ and $\sigma_{tr}^R(E)$ over the restricted angular interval $\mu_{cut} \leq \mu_{cm} \leq 1$. Although the choice of μ_{cut} is somewhat arbitrary, selected numerical values must be consistent with the use of the Fokker-Planck approximation. When supplemented with momentum and energy conservation laws, the above representations directly yield the Legendre moments of the lab system group

transfer cross sections in desired form for MCNP4B. The electronic stopping power model is adopted directly from TRIM [4], known to be accurate over a broad range of energies and ion/target atom masses.

The angular and energy diffusion terms in our BFP model must be transformed into effective discrete processes in order to be handled in a particle Monte Carlo algorithm. It has been shown [8] that the angular Fokker-Planck term can be accurately modeled by a Boltzmann collision integral with kernel

$$\sigma_{FP}(E' \rightarrow E, \mu_0) = \frac{\sigma_{tr}^R}{2\pi(1 - \mu_{FP})} \delta(\mu_0 - \mu_{FP}) \delta(E' - E), \quad (6)$$

where μ_{FP} is a preassigned constant. This discrete approximation preserves the restricted momentum transfer cross section and rigorously reproduces the Fokker-Planck limit as $\mu_{FP} \rightarrow 1$. For most computations it suffices to set $\mu_{FP} = 0.9$. This representation has been incorporated into MCNP4B [5,8] and it suffices to provide multigroup values of the restricted momentum transfer cross section.

We have recently developed a novel multigroup representation of energy-loss straggling [9]. Briefly, adjacent group downscatter and upscatter cross sections are defined such that the mean-square energy loss per unit path length is preserved, i.e.

$$\sigma_{g \rightarrow g'} = \begin{cases} 0, & g' \leq g - 2 \\ \frac{T_g}{2(E_g - E_{g-1})^2}, & g' = g - 1 \\ \frac{T_g}{2(E_g - E_{g+1})^2}, & g' = g + 1 \\ 0, & g' \geq g + 2, \end{cases} \quad (7)$$

where T_g is the straggling coefficient for group g . The justification is that energy transfers are small enough that scattering occurs only to adjacent groups. The model has been demonstrated to be very accurate for thick targets [9]. Furthermore, it may be readily shown that the resulting Boltzmann collision integral reproduces the Fokker-Planck model as the group width $\Delta E_g \rightarrow 0$. A strictly downscatter model has also been developed which eliminates the unphysical upscatter while preserving the mean and mean-square energy loss. Note that the straggling cross sections are simply added to the smooth component group transfer cross sections and hence no computational penalty is incurred.

A data code, YATC [7], has been developed employing the above methodology to generate all cross sections and stopping powers in multigroup format suitable for input to MCNP4B. It should be emphasized that CSD is handled exactly during simulation. That is, between collisions the ion energy is varied deterministically at a rate given by the group dependent total stopping power ($S_{e,g} + S_{N,g}^R$). Representative simulation results using MCNP/YATC are presented in the next section.

4 Numerical Results and Conclusions

Extensive convergence studies have been performed using MCNP/YATC with respect to: group refinement, Legendre expansion order of the smooth cross section, and μ_{cut} . Depending upon the incident ion energy and ion/target mass ratio, convergence for ion and energy deposition profiles is typically obtained with 100–200 logarithmic energy groups, $P_5 - P_7$ expansion order, and $\mu_{cut} \sim 0.9 - 0.95$. The Monte Carlo implementation of the BFP algorithm has also been compared with equivalent *deterministic* computations using a high order accurate discontinuous finite element discretization of the 1D S_N BFP equations [10].

Implantation profiles for 10 keV boron ions incident on a silicon substrate obtained using MCNP/YATC, TRIM and the finite element code (with quadratic discontinuous elements) are displayed in Fig. 1. The MCNP4B and deterministic predictions are practically identical, giving confidence in the implementation of the BFP algorithm. Agreement with TRIM results is also very good, with TRIM predicting a slightly more peaked distribution. Note that the MCNP4B results are fully converged with respect to the available parameters, while no optimization has been attempted with TRIM. Similar comparisons are realized for different mass ratios and energies while energy deposition profiles (electronic and nuclear) show even better agreement [7]. The significance of electronic energy-loss straggling is demonstrated in Fig. 2, showing MCNP/YATC deposition profiles of 100 MeV protons in tungsten with and without straggling, compared against TRIM results.

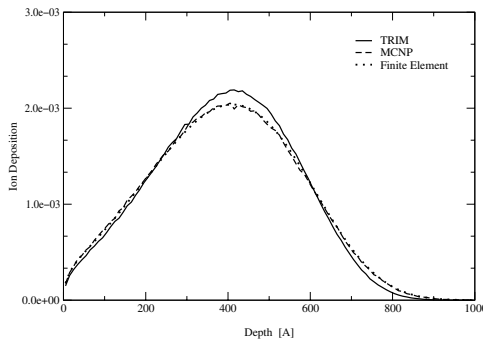


Fig. 1. Implantation of 10 keV B in Si

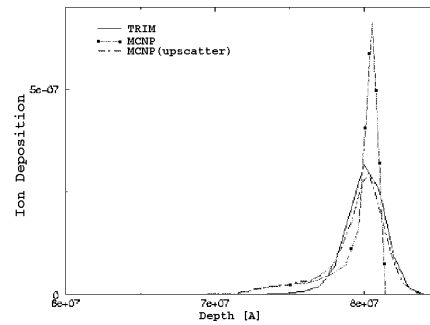


Fig. 2. Implantation of 100 MeV H in W

Finally we consider ion transport in the highly heterogeneous geometry shown in Fig. 3, representing a 30 keV B line source inclined at 7° and incident on a Si substrate through a mask. While the geometry is realistic we have arbitrarily modified the material densities to highlight the effects of lateral material heterogeneities on the implantation profile. Thus, $\rho = 1$ represents nominal density Si

while $\rho = 0.1$ represents 10% nominal density Si. The resulting deposition profile is shown in Fig. 4. The effects of the mask and the heterogeneous assembly is very clear in the plot.

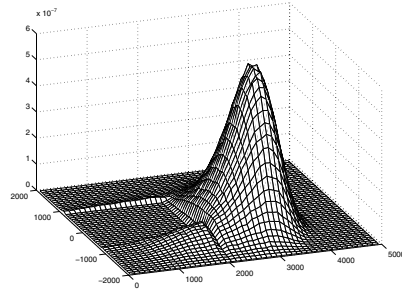
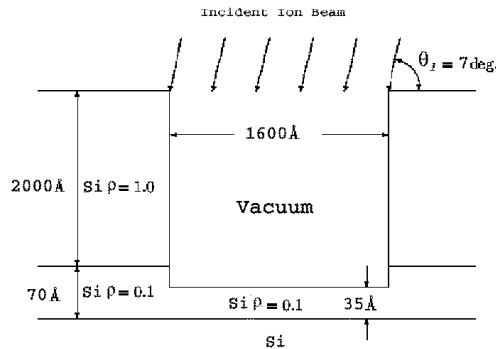


Fig. 3. Heterogeneous Geometry Specification **Fig. 4.** 3D Implantation Profile

In conclusion, we have demonstrated implementation of a multigroup Monte Carlo BFP algorithm for ion transport in amorphous media. A specially constructed ion cross section library, YATC, has been coupled with MCNP4B to perform ion transport simulations. Planar geometry results for implantation profiles compare well with TRIM predictions. Use of MCNP4B allows truly multi-dimensional simulation in highly heterogeneous geometries, making it possible to simulate realistic implantation conditions.

References

1. J.S. Williams, J.M. Poate (eds.): *Ion Implantation and Beam Processing* (Academic Press, 1984)
2. M.R. Raju: *Heavy Ion Radiotherapy* (Academic Press, New York 1990)
3. R. Prael, H. Lichtenstein: *User Guide to LCS: The LAHET Code System*. Los Alamos National Laboratory Report LA-UR-89-3014 (1989)
4. J.F. Ziegler, J.P. Biersack, U. Littmark: *The Stopping and Range of Ions in Solids* (Pergamon Press, New York 1985)
5. J.F. Briesmeister: *MCNPTM - A General Monte Carlo N-Particle Code, Version 4B*. Los Alamos National Laboratory Report LA-12625-M (1997)
6. Q. Yang, D.J. O'Conner: Nucl. Instr. Meth. B **61**, 149 (1991)
7. N.D. Keen: *Ion Cross Sections and Monte Carlo Simulations Using Multigroup Boltzmann Fokker-Planck Transport*. MS Thesis (The University of New Mexico, Albuquerque, New Mexico, USA 1999)
8. J.E. Morel et al.: Nucl. Sci. Eng. **124**, 369 (1996)
9. A.K. Prinja, F. Gleicher et al.: Trans. Amer. Nucl. Soc. **81**, 131 (1999)
10. F. Gleicher, A.K. Prinja: to be published

A Stochastic Model of Multiple Scattering of Charged Particles: Process, Transport Equation and Solutions

L. Papież¹, V. Tulovsky², and V. Moskvina¹

¹ Department of Radiation Oncology, Indiana University, USA

² Department of Mathematics, St. John's University, New York, NY, USA

Abstract. The process of angular-spatial evolution of multiple scattering of charged particles can be described by a special case of Boltzmann integro-differential equation called Lewis equation. The underlying stochastic process for this evolution is the compound Poisson process on the surface of the unit sphere. The significant portion of events that constitute compound Poisson process that describes multiple scattering have diffusional character. This property allows to analyze the process of angular-spatial evolution of multiple scattering of charged particles as combination of soft and hard collision processes and compute appropriately its transition densities. These computations provide a method of the approximate solution to the Lewis equation.

1 Introduction

Multiple scattering of high energy charged particles is a classical problem in statistical, non-equilibrium physics. Solutions of this problem are of critical importance in calculations of dose deposition in human tissue during its irradiation by beams of elementary particles. The transport problem that arises in multiple scattering is most often described by an integro-differential Boltzmann equation, called Lewis equation [1]. The general solution of the Lewis equation has not been advanced much beyond the original contribution of Lewis [1]. However, considerable insight into the solution of this equation can be gained from realization that process that underlies mathematical modelling of the multiple scattering phenomena has a characteristic of a compound Poisson process. This observation allows Lewis equation to be analyzed appropriately in the framework of stochastic processes theory. In particular, this insight allows to perceive the process describing the kinematics of the scattering particles as a combination of scatterings that have characteristics of soft and hard collisions. This method of the analysis has not been applied before to the problem of the solution of the general, angular-spatial Lewis equation.

2 Notation and the Interpretation of the Lewis Equation

A momentum of a moving particle is described in Cartesian coordinate system with $\hat{\mathbf{p}}_x$ and $\hat{\mathbf{p}}_y$ axes lying in a horizontal plane P' and $\hat{\mathbf{p}}_z$ axis pointing down. We use for the description of particle's momentum a radius-vector from the

origin \vec{O}_p of $(\hat{p}_x, \hat{p}_y, \hat{p}_z)$ axes to the point $\vec{p} = (p_x, p_y, p_z) \in \mathbf{R}^3$, and similarly, we use for the description of particle's position a radius-vector from the origin \vec{O} of $(\hat{x}, \hat{y}, \hat{z})$ axes to the point $\vec{r} = (x, y, z) \in \mathbf{R}^3$. Thus the evolution of a charged particle is described in phase space $\mathfrak{S} = (\vec{p}, \vec{r}) = \mathbf{R}^3 \times \mathbf{R}^3$ of momenta $\vec{p} = (p_x, p_y, p_z) \in \mathbf{R}^3$ and positions $\vec{r} = (x, y, z) \in \mathbf{R}^3$. Following Lewis we will consider here evolutions for which the loss of particle's energy during the scattering process is negligible. This means that during particle's evolution the value of $|\vec{p}| = \sqrt{p_x^2 + p_y^2 + p_z^2} = p$ is invariant. Thus momenta \vec{p} of the particle can be parameterized by the unit vector $\vec{\Omega}$ and constant, scalar parameter p . Specifically, we can write

$$\vec{p} = p(\theta_x, \theta_y, \theta_z) = p \vec{\Omega} \quad (1)$$

where $\vec{\Omega}$ is a unit vector (point on the unit sphere S that is centered on point O of the space of particle's momenta) with Cartesian coordinates θ_x, θ_y and θ_z that has an interpretation of the instantaneous direction of the particle motion. Thus in the case under consideration the phase space \mathfrak{S} of the charged particle can be represented by Cartesian product of \mathbf{R}^3 and unit sphere S , i.e. as $\mathfrak{S} = (\vec{\Omega}, \vec{r}) = S \times \mathbf{R}^3$. The above notation allows to express the infinitesimal change of position $d\vec{r}$ of the particle that moves over pathlength interval dt in the instantaneous direction $\vec{\Omega}$ as $d\vec{r} = \vec{\Omega} dt$. The evolution of point $\vec{\Omega}$ on the unit sphere S is represented by the stochastic process $\vec{\Omega}(t)$ trajectories of which are almost everywhere continuous (i.e. probabilistic measure of the set of points for which each trajectory is not continuous equals to 0 for this process). These trajectories are parameterized by pathlength t and so the change of position $\vec{r}(t)$ of the particle that moves over the pathlength interval $[0, t]$ is a stochastic process $\vec{r}(t)$ given by $\vec{r}(t) = \int_0^t \vec{\Omega}(t') dt'$. The integration in expression $\int_0^t \vec{\Omega}(t') dt'$ can be understood as Lebesgue integration over each (almost everywhere continuous) realization of the process $\vec{\Omega}(t')$.

Let us assume first that the scattering process starts at the point \vec{O} and that the direction of motion of the particle in the beginning of the scattering process coincides with the direction $\vec{\Omega}_0$ of \hat{p}_z axis. In other words we assume that $\vec{\Omega}(0) = \vec{\Omega}_0$ and $\vec{r}(0) = \vec{O}$. For these initial conditions it was shown before [2] that, provided the process $\vec{\Omega}(t)$ is a compound Poisson process on S (with appropriately defined addition of changes $\Delta\vec{\Omega}_i$ of directions of scattering particle [3]), then the angular-spatial transition probability density function $f(t, \vec{\Omega}, \vec{r} | 0, \vec{\Omega}_0, \vec{O})$ is the fundamental solution of the Lewis equation [1]

$$\frac{\partial f}{\partial t} + \vec{\Omega} \cdot \nabla f = \lambda \int_S [f(t, \vec{\Omega}', \vec{r}) - f(t, \vec{\Omega}, \vec{r})] p(\vec{\Omega} - \vec{\Omega}') d\vec{\Omega}' \quad (2)$$

$$f|_{t=0} = \delta(\vec{r} - \vec{O}) \delta(\vec{\Omega} - \vec{\Omega}_0) \quad (3)$$

Here λ is the average number of collisions per unit path length and $p(\vec{\Omega})$ is the normalized angular scattering cross-section for single interaction. For the

interpretation of addition and subtraction of directions, e.g. for the interpretation of expression $\vec{\Omega} - \vec{\Omega}$ in (2), we refer the reader to [3].

3 Soft and Hard Collisions in the Solution of Lewis Equation

The solution $f(t, \vec{\Omega}, \vec{r} \mid 0, \vec{\Omega}_0, \vec{O})$ of the Lewis equation (2),(3) can be constructed as follows.

First, let us divide the unit sphere S into two subsets $S^<$ and $S^>$. The subset $S^<$ consists of points $\vec{\Omega} \in S$ that are no further from point $\vec{\Omega}_0$ (i.e. point defining direction coincident with $\widehat{\mathbf{p}}_z$ axis) than θ_{sep} . Thus we can write

$$S^< = \{ \vec{\Omega} \in S : dist(\vec{\Omega}, \vec{\Omega}_0) < \theta_{sep}, \theta_{sep} > 0 \} \quad (4)$$

where $dist(\vec{\Omega}, \vec{\Omega}_0)$ denotes the distance on the sphere S between points $\vec{\Omega}$ and $\vec{\Omega}_0$ (the length of the shorter arc of the great circle on the sphere containing $\vec{\Omega}$ and $\vec{\Omega}_0$). The subset $S^>$ is a complement of $S^<$ in S i.e. $S^< \cup S^> = S$ and $S^< \cap S^> = \emptyset$.

Identifying current direction of motion of the charged particle with $\vec{\Omega}_0$ we can divide now the scattering events of the compound Poisson process $\vec{\Omega}(t)$ into those that are characterized by individual changes of direction of motion satisfying $\Delta\vec{\Omega}_i \in S^<$ and those satisfying $\Delta\vec{\Omega}_i \in S^>$ ($i = 1, 2, 3, \dots$). In other words the first group of events consists of scatterings that change direction of particle motion by angle *smaller* than θ_{sep} (we will call them soft scatterings) and the second group of events consists of scatterings that change direction of particle motion by angle *no smaller* than θ_{sep} (we will call them hard scatterings). Processes $N_{soft}(t)$ and $N_{hard}(t)$, counting respectively independent events of soft and hard collisions along particle's pathlength, are independent Poisson processes. Let us denote by $N(t)$ the Poisson process defined by $N(t) = N_{soft}(t) + N_{hard}(t)$. Poisson processes $N_{soft}(t)$ and $N_{hard}(t)$ are characterized by parameters λ_{soft} and λ_{hard} ($\lambda_{soft} \gg \lambda_{hard}$) that denote average number of soft and hard collisions per unit path length in each process, respectively. The parameter λ defined by $\lambda = \lambda_{soft} + \lambda_{hard}$ characterizes then process $N(t)$. As a consequence the space of elementary events of the process $(\vec{\Omega}(t), \vec{r}(t))$ can be decomposed into union of disjoint subsets each having the interpretation of an event characterized by zero, one, two etc. number of *hard* collisions on the interval $[0, t]$. This decomposition allows to express the transition probability density $f(t, \vec{\Omega}, \vec{r} \mid 0, \vec{\Omega}_0, O)$ (i.e. the solution of the Lewis equation (2),(3)) as

$$f(t, \vec{\Omega}, \vec{r} \mid 0, \vec{\Omega}_0, O) = e^{-\lambda_{hard}t} \sum_{n=0}^{\infty} \frac{(\lambda_{hard}t)^n}{n!} p^{(n)}(t, \vec{\Omega}, \vec{r} \mid 0, \vec{\Omega}_0, O, n_{hard} = n) \quad (5)$$

where $p^{(n)}(t, \vec{\Omega}, \vec{r} \mid 0, \vec{\Omega}_0, \vec{O}; n_{hard} = n)$ denotes the transition probability density of charged particle coming to a point $(\vec{\Omega}, \vec{r})$ at t conditional on starting

from point $\vec{\Omega}_0, \vec{O}$ at 0 and *provided that exactly n hard collisions occurred between 0 and t* . For typical multiple scattering of charged particles we have small number of hard collisions on a given pathlength interval $[0, t]$, even for small values of θ_{sep} , and large number of soft collisions. The condition $\lambda_{soft} \gg \lambda_{hard}$ means that we can model the physical process of multiple scattering by the stochastic process with the property that after each hard collision the sequence of numerous soft (small angle) collisions follows. Finally, when θ_{sep} is small enough, while at the same time λ_{soft} is large enough, the scattering process $\vec{\Omega}(t)$ between two hard collisions can be ultimately approximated by a diffusion on the sphere [4]. Assuming the availability of formulas for the diffusional limit approximation of the process $\vec{\Omega}(t)$ (that follows after each hard collision or after starting from any fixed pathlength \tilde{t}) allows to design the efficient method of calculations of transient probability densities $p^{(n)}(t, \vec{\Omega}, \vec{r} | 0, \vec{\Omega}_0, \vec{O}; n_{hard} = n)$. To this end we introduce first the quantity $\Pr((\vec{\Omega}(t), \vec{r}(t)) \in \Delta V | 0, \vec{\Omega}_0, \vec{O}; n_{hard}(t) = n)$ that denotes the probability of particle coming to domain ΔV of the state space $S \times \mathbf{R}^3$ at t conditional on starting from point $\vec{\Omega}_0, \vec{O}$ at 0 and *provided that exactly n hard collisions occurred between 0 and t* . Let us notice that this probability describes the evolution of the general process $(\vec{\Omega}(t), \vec{r}(t))$ but that it is conditioned *on the hard collision events*. It results from integration of $p^{(n)}(t, \vec{\Omega}, \vec{r} | 0, \vec{\Omega}_0, \vec{O}; n_{hard} = n)$ in variables $\vec{\Omega}, \vec{r}$ over $\Delta V \subset S \times \mathbf{R}^3$, i.e.

$$\Pr((\vec{\Omega}(t), \vec{r}(t)) \in \Delta V | 0, \vec{\Omega}_0, \vec{O}; n_{hard}(t) = n) = \int_{\Delta V} p^{(n)}(t, \vec{\Omega}, \vec{r} | 0, \vec{\Omega}_0, \vec{O}; n_{hard} = n) d\vec{\Omega} d\vec{r} \quad (6)$$

Let us divide now the interval $[0, t]$ into N equal, and disjoint, subintervals that we denote by $I_1 = [0, t/N]$, $I_2 = [t/N, 2t/N]$, ..., $I_N = [(N-1)t/N, t]$. The path lengths of a particle at moments of first, second ... and n -th hard collision we will denote by $t_1 < t_2 < \dots < t_n$. Then we can write

$$\begin{aligned} \Pr((\vec{\Omega}(t), \vec{r}(t)) \in \Delta V | 0, \vec{\Omega}_0, \vec{O}; n_{hard}(t) = n) &= \\ \sum_{k=1}^N \Pr((\vec{\Omega}(t), \vec{r}(t)) \in \Delta V; t_{n-1} < \frac{(k-1)t}{N}, t_n \in I_k | 0, \vec{\Omega}_0, \vec{O}; n_{hard}(t) = n) & \\ + o(1/N) = \sum_{k=1}^N \Pr(t_{n-1} < \frac{(k-1)t}{N}, t_n \in I_k | n_{hard}(t) = n) & \\ \Pr((\vec{\Omega}(t), \vec{r}(t)) \in \Delta V | 0, \vec{\Omega}_0, \vec{O}; t_{n-1} < \frac{(k-1)t}{N}, t_n \in I_k, n_{hard}(t) = n) & \\ + o(1/N) & \end{aligned} \quad (7)$$

The above equality holds as the space of elementary events was divided there into mutually disjoint subsets indexed by $k = 1, 2, \dots, N$ (except for $k = 1$ that

provides the term the probability of which is of the order of $O(1/N)$. Properties of the Poisson process (Karlin (1981)) allow us to find that

$$\Pr(t_{n-1} < (k-1)t/N, t_n \in I_k \mid n_{hard}(t) = n) = \frac{(k-1)^{n-1} \cdot n}{N^n} + O(1/N) \quad (8)$$

The second factor in the sum (7) express probabilities of coming to ΔV given that there are $(n-1)$ hard collisions on $[0, (k-1)t/N]$ and one hard collision on I_k (provided exactly n hard collisions happened on $[0, t]$). The elementary events that describe the process $\vec{\Omega}(t)$ (and thus also the process $(\vec{\Omega}(t), \vec{r}(t))$ on I_k (conditioned by the event $(t_{n-1} < (k-1)t/N, t_n \in I_k, n_{hard}(t) = n)$) consist of

- A set of all soft evolution trajectories between $(\vec{\Omega}_1, \vec{r}_1)$ and $(\vec{\Omega}', \vec{r}')$ on interval $[(k-1)t/N, t']$, $t' \in I_k$,
- A set of all points $(t', \vec{\Omega}'')$ $\in I_k \times S$ characterizing the hard collision at t' , and again of
- A set of all soft evolution trajectories between $(\vec{\Omega}' + \vec{\Omega}'', \vec{r}')$ and $(\vec{\Omega}, \vec{r})$ on interval $[t', kt/N]$ terminating at fixed state $(\vec{\Omega}, \vec{r})$

where t' denotes a path length at the moment of $n - th$ hard collision and $\vec{\Omega}''$ denotes a change of direction in this hard collision. Taking into account mutual independence of events before and after hard collision, independence of both of these classes of events from change of direction in hard collision $\vec{\Omega}''$, and finally independence of all the above events from the event defining pathlength instant of hard collision t' we can take as the minimal space describing the complete set of events defining the evolution of the process $(\vec{\Omega}(t), \vec{r}(t))$ on I_k as the set $G = S \times \mathbf{R}^3 \times S \times \mathbf{R}^3 \times [(k-1)t/N, kt/N] \times S$ with measure on G defined as

$$\begin{aligned} & f^{diff}(t', \vec{\Omega}', \vec{r}' \mid (k-1)t/N, \vec{\Omega}_1, \vec{r}_1) \cdot \frac{p_{hard}(\vec{\Omega}'') \cdot N}{t} \cdot \\ & f^{diff}(t, \vec{\Omega}, \vec{r} \mid t', \vec{\Omega}' + \vec{\Omega}'', \vec{r}') d\vec{r}_1 d\vec{\Omega}_1 d\vec{r}' d\vec{\Omega}' dt' d\vec{\Omega}'' \end{aligned} \quad (9)$$

where f^{diff} denotes transition densities for the process $(\vec{\Omega}(t), \vec{r}(t))$ in the diffusional limit approximation (i.e. in the limit when $\vec{\Omega}(t)$ is the diffusion on sphere). Then, we can write

$$\begin{aligned} & \Pr((\vec{\Omega}(t), \vec{r}(t)) \in \Delta V \mid 0, \vec{\Omega}_0, \vec{r}_0; t_{n-1} < \frac{(k-1)t}{N}, t_n \in I_k, n_{hard}(t) = n) = \\ & \int_{G \times \Delta V} p^{(n-1)}(\frac{(k-1)t}{N}, \vec{\Omega}_1, \vec{r}_1 \mid 0, \vec{\Omega}_0, \vec{r}_0, n_{hard} = n-1) \cdot \\ & f^{diff}(t', \vec{\Omega}', \vec{r}' \mid \frac{(k-1)t}{N}, \vec{\Omega}_1, \vec{r}_1) \cdot \\ & \frac{p_{hard}(\vec{\Omega}'') \cdot N}{t} \cdot f^{diff}(t, \vec{\Omega}, \vec{r} \mid t', \vec{\Omega}' + \vec{\Omega}'', \vec{r}') d\vec{r}_1 d\vec{\Omega}_1 d\vec{r}' d\vec{\Omega}' dt' d\vec{\Omega}'' d\vec{\Omega} d\vec{r} \end{aligned} \quad (10)$$

Applying the average theorem for integral with respect to t' allows us to rewrite the above expression as

$$\begin{aligned}
 & \Pr((\vec{\Omega}(t), \vec{r}(t)) \in \Delta V \mid 0, \vec{\Omega}_0, \vec{O}; t_{n-1} < (k-1)t/N, t_n \in I_k, n_{hard}(t) = n) = \\
 & \int_{S \times \mathbf{R}^3 \times S \times \mathbf{R}^3 \times \Delta V} p^{(n-1)}((k-1)t/N, \vec{\Omega}_1, \vec{r}_1 \mid 0, \vec{\Omega}_0, \vec{O}, n_{hard} = n-1) \cdot \\
 & f^{diff}(kt/N, \vec{\Omega}, \vec{r} \mid (k-1)t/N, \vec{\Omega}_1, \vec{r}_1) \cdot \\
 & \left[\int_S p_{hard}(\vec{\Omega}^n) f^{diff}(t, \vec{\Omega}, \vec{r} \mid \frac{kt}{N}, \vec{\Omega} + \vec{\Omega}^n, \vec{r}) d\vec{\Omega}^n \right] d\vec{\Omega}_1 d\vec{r}_1 d\vec{\Omega} d\vec{r} d\vec{\Omega} d\vec{r} \\
 & + O(\frac{\Delta V}{N})
 \end{aligned} \tag{11}$$

The expression

$$\int_S p_{hard}(\vec{\Omega}^n) f^{diff}(t, \vec{\Omega}, \vec{r} \mid kt/N, \vec{\Omega} + \vec{\Omega}^n, \vec{r}) d\vec{\Omega}^n$$

has a meaning of transition probability density for diffusional limit transport from $(kt/N, \vec{\Omega}, \vec{r})$ to $(t, \vec{\Omega}, \vec{r})$ averaged over initial angular distribution of directions imposed by to the hard collision at kt/N . This transition density can be precalculated (functions f^{diff} and p_{hard} are fixed for a given transport problem) and denoted by $\widetilde{f^{diff}}(t, \vec{\Omega}, \vec{r} \mid kt/N, \vec{\Omega}, \vec{r})$. Thus

$$\widetilde{f^{diff}}(t, \vec{\Omega}, \vec{r} \mid \frac{kt}{N}, \vec{\Omega}, \vec{r}) = \int_S p_{hard}(\vec{\Omega}^n) f^{diff}(t, \vec{\Omega}, \vec{r} \mid \frac{kt}{N}, \vec{\Omega} + \vec{\Omega}^n, \vec{r}) d\vec{\Omega}^n \tag{12}$$

Substituting now (8) and (11) into (7) and defining $\mathbf{H} = S \times \mathbf{R}^3 \times S \times \mathbf{R}^3$, we will get

$$\begin{aligned}
 & \Pr((\vec{\Omega}(t), \vec{r}(t)) \in \Delta V \mid 0, \vec{\Omega}_0, \vec{O}; n_{hard}(t) = n) = \\
 & \sum_{k=1}^N \frac{(k-1)^{n-1} \cdot n}{N^n} \int_{\mathbf{H} \times \Delta V} p^{(n-1)}((k-1)t/N, \vec{\Omega}_1, \vec{r}_1 \mid 0, \vec{\Omega}_0, \vec{O}, n_{hard} = n-1) \\
 & f^{diff}(kt/N, \vec{\Omega}, \vec{r} \mid (k-1)t/N, \vec{\Omega}_1, \vec{r}_1) \cdot \\
 & \widetilde{f^{diff}}(t, \vec{\Omega}, \vec{r} \mid kt/N, \vec{\Omega}, \vec{r}) d\vec{\Omega}_1 d\vec{r}_1 d\vec{\Omega} d\vec{r} d\vec{\Omega} d\vec{r} + O(\Delta V/N)
 \end{aligned} \tag{13}$$

Taking the limit $N \rightarrow \infty$ we notice that $f^{diff}(kt/N, \vec{\Omega}, \vec{r} | (k-1)t/N, \vec{\Omega}_1, \vec{r}_1)$ converges to the delta function in $\vec{\Omega} - \vec{\Omega}_1$ and $\vec{r} - \vec{r}_1$ and also that $\sum_{k=1}^N \frac{(k-1)^{n-1} \cdot n}{N^n}$ can be transformed into integration $\int_0^t \dots \tau^{n-1} d\tau$. Thus application of the limit of $N \rightarrow \infty$, integration with respect to variables $d\vec{\Omega} d\vec{r}$ over $S \times \mathbf{R}^3$, division of both sides of (13) by ΔV and finally taking a limit of $\Delta V \rightarrow 0$ transforms formula (13) into the following recurrence relation

$$p^{(n)}(t, \vec{\Omega}, \vec{r} | 0, \vec{\Omega}_0, \vec{O}, n_{hard} = n) = \frac{n}{t^n} \int_{S \times \mathbf{R}^3} \int_0^t p^{(n-1)}(\tau, \vec{\Omega}_1, \vec{r}_1 | 0, \vec{\Omega}_0, \vec{O}, n_{hard} = n-1) \widetilde{f^{diff}}(t, \vec{\Omega}, \vec{r} | \tau, \vec{\Omega}_1, \vec{r}_1) \tau^{n-1} d\tau d\vec{\Omega}_1 d\vec{r}_1 \quad (14)$$

The above expression for $p^{(n)}(t, \vec{\Omega}, \vec{r} | 0, \vec{\Omega}_0, \vec{O}, n_{hard} = n)$ allows to calculate the solution to the Lewis equation (2),(3) through formula (5) provided $f^{diff}(t, \vec{\Omega}, \vec{r} | t', \vec{\Omega}_1, \vec{r}_1)$ is known. As $f^{diff}(t, \vec{\Omega}, \vec{r} | t', \vec{\Omega}_1, \vec{r}_1)$ describes transition densities in the case when $\vec{\Omega}(t)$ is the diffusion on the sphere, this function is given as a fundamental solution of the equation given by [4]

$$\frac{\partial f}{\partial t} + \vec{\Omega} \cdot \nabla f = \frac{D}{2} \Delta_{sph} f \quad (15)$$

$$f|_{t=0} = \delta(\vec{r} - \vec{O}) \delta(\vec{\Omega} - \vec{\Omega}_0) \quad (16)$$

The symbol Δ_{sph} above denotes the Laplacian on the sphere S and D is an angular diffusion constant defined in [3]. The solution of the above equation (in approximation based on small angle change and small spatial detour from original straight line trajectory of the particle) has been derived in [5].

4 The Small Angle Approximation (saa) for Charged Particle Transport

Let points $\vec{\Omega}_1, \vec{\Omega}_2, \vec{\Omega}$ on the unit sphere S represent original direction of travel of the particle, change in the direction of travel of the particle, and the final direction of particle's travel resulting from the accumulation of original direction of travel $\vec{\Omega}_1$ and change in direction of travel $\vec{\Omega}_2$, respectively. In our previous works [3,2] we called direction $\vec{\Omega}$ the sum of $\vec{\Omega}_1$ and $\vec{\Omega}_2$ and used a symbolic notation of $\vec{\Omega}_1 + \vec{\Omega}_2$ for $\vec{\Omega}$ (even though $\vec{\Omega}$ is not a *sum of vectors* $\vec{\Omega}_1$ and $\vec{\Omega}_2$). Nevertheless, when $\vec{\Omega}_1$ and $\vec{\Omega}_2$ are given the unit vector $\vec{\Omega}$ is

unambiguously specified and formulas for its Cartesian (or spherical) coordinates can be specified [3]. Let us denote now by $\vec{\theta}$ the point on plane P' (see Section 2) that is an image of $\vec{\Omega} \in S$ onto P' through the transformation T_{sa} :

$$\begin{aligned} T_{sa} : S &\rightarrow P', \quad T_{sa}(\vec{\Omega}) = \vec{\theta} \\ \vec{\Omega} &= (\sin \theta \cos \varphi, \sin \theta \sin \varphi, \cos \theta) \\ \vec{\theta} &= (\theta \cos \varphi, \theta \sin \varphi) \end{aligned} \quad (17)$$

Thus according to these equations we have $T_{sa}(\vec{\Omega}_1) = \vec{\theta}_1 = (\theta_{1,x}, \theta_{1,y})$ and $T_{sa}(\vec{\Omega}_2) = \vec{\theta}_2 = (\theta_{2,x}, \theta_{2,y})$. Let us also denote by $\vec{\theta}^* = (\theta_x^*, \theta_y^*)$ the sum of vectors $\vec{\theta}_1$ and $\vec{\theta}_2$ on plane P i.e. $\vec{\theta}^* = \vec{\theta}_1 + \vec{\theta}_2 = (\theta_{1,x}, \theta_{1,y}) + (\theta_{2,x}, \theta_{2,y}) = (\theta_x^*, \theta_y^*)$. Now, we are ready to state the property of planar *saa* that has important consequences for the calculation of multiple scattering distributions. This statement can be formulated as follows:

*If $T_{sa}(\vec{\Omega}_1) = \vec{\theta}_1$ and $T_{sa}(\vec{\Omega}_2) = \vec{\theta}_2$ are vectors on plane P corresponding to directions $\vec{\Omega}_1 \in S$ and $\vec{\Omega}_2 \in S$ through *sa* transformation T_{sa} (17) then the vector $\vec{\theta}^* \in P'$ denoting the sum of vectors $\vec{\theta}_1$ and $\vec{\theta}_2$ on plane P ($\vec{\theta}^* = \vec{\theta}_1 + \vec{\theta}_2$) and the vector $T_{sa}(\vec{\Omega}) \in P'$ denoting the vector corresponding to direction $\vec{\Omega} = \vec{\Omega}_1 + \vec{\Omega}_2 \in S$ are equivalent in the sense of small angle approximation (i.e. the length of vector $\vec{\theta}^* - \vec{\theta} \in P'$ is of the order higher than one relative to small parameter determining the length of any vector describing the particle's direction on plane P').*

The above property allows to treat the *saa* of the process $\vec{\Omega}(t)$ as a classical, compound Poisson process $\vec{\theta}(t) = \sum_{i=1}^{N(t)} \vec{\theta}_i$ with the space of outcomes being the Euclidean plane P' [6]. Moreover, we may recall [3] that processes $\vec{\theta}^{soft}(t)$ and $\vec{\theta}^{hard}(t)$ are also compound Poisson processes that are mutually independent [6] and that their vectorial sum $\vec{\theta}^{soft}(t) + \vec{\theta}^{hard}(t)$ equals $\vec{\theta}(t)$. Under *saa* the spatial transport of a particle moving a pathlength dt in direction $\vec{\Omega}$ can be written as $\vec{\Omega} dt = (\vec{\theta}, 1) dt = (\theta \cos \varphi, \theta \sin \varphi, 1) dt = (\theta_x, \theta_y, 1) dt = (dx, dy, dz) \in \mathbf{R}^3$ (if one consistently omits terms of order higher than one for all coordinates). Therefore

$$\vec{r}(t) = \int_0^t \vec{\Omega}(t') dt' = \int_0^t (\vec{\theta}(t'), 1) dt' = \left(\int_0^t \theta_x(t') dt', \int_0^t \theta_y(t') dt', t \right) \in \mathbf{R}^3 \quad (18)$$

As z coordinate of vector $\vec{r}(t)$ is identical to pathlength t we can omit from now on this coordinate from explicit parameterization of particle's position. Thus $\vec{r}(t)$ will denote now a vector $\vec{r}(t) = (r_x(t), r_y(t))$ in a plane P . Taking into account properties of the compound Poisson process $\vec{\theta}(t) = \sum_{i=1}^{N(t)} \vec{\theta}_i$ we can

rewrite (18) as

$$\begin{aligned}\vec{r}(t) &= \int_0^t \vec{\theta}(t') dt' = \int_0^t [\vec{\theta}^{soft}(t') + \vec{\theta}^{hard}(t')] dt' \\ &= \int_0^t \vec{\theta}^{soft}(t') dt' + \int_0^t \vec{\theta}^{hard}(t') dt' = \vec{r}^{soft}(t) + \vec{r}^{hard}(t) \\ \vec{r}(0) &= (0, 0) \in P, \quad \vec{r}^{soft}(0) = (0, 0) \in P, \quad \vec{r}^{hard}(0) = (0, 0) \in P\end{aligned}\quad (19)$$

where $\vec{r}^{soft}(t)$ and $\vec{r}^{hard}(t)$ are mutually independent processes. Thus (19) leads, with parameter z substituted in place of t due to their identity in *saa*, to formula

$$(\vec{\theta}(z), \vec{r}(z)) = (\vec{\theta}^{soft}(z), \vec{r}^{soft}(z)) + (\vec{\theta}^{hard}(z), \vec{r}^{hard}(z)) \in P' \times P \quad (20)$$

that expresses the fact that random vector $(\vec{\theta}(z), \vec{r}(z))$ is the sum of independent, random vectors $(\vec{\theta}^{soft}(z), \vec{r}^{soft}(z))$ and $(\vec{\theta}^{hard}(z), \vec{r}^{hard}(z))$ in vector space $P' \times P$.

Considering that the processes $(\vec{\theta}^{soft}(z), \vec{r}^{soft}(z))$ and $(\vec{\theta}^{hard}(z), \vec{r}^{hard}(z))$ are independent, the transition density $f(z, \vec{\theta}, \vec{r} | 0, \vec{0}, \vec{O}) = f(z, \vec{\theta}, \vec{r})$ from the original point $(\vec{0}, \vec{O}) \in P' \times P$ can be represented in small angle approximation by the following equality

$$f(z, \vec{\theta}, \vec{r}) = \int_{P \times P'} f^{soft}(z, \vec{\theta} - \vec{\theta}', \vec{r} - \vec{r}') f^{hard}(z, \vec{\theta}', \vec{r}') d\vec{\theta}' d\vec{r}' \quad (21)$$

where $f^{soft}(z, \vec{\theta}, \vec{r})$ is given by diffusional limit of soft collision process in small angle approximation and the formula for $f^{hard}(z, \vec{\theta}, \vec{r})$ is given by the $P' \times P$ analog of formula (2.13) of [2] i.e.

$$f^{hard}(z, \vec{\theta}, \vec{r}) = e^{-\lambda_{hard} z} \sum_{n=0}^{\infty} \frac{(\lambda_{hard} z)^n}{n!} p_{hard}^{(n)}(z, \vec{\theta}, \vec{r} | 0, \vec{0}, \vec{O}) \quad (22)$$

with

$$\begin{aligned}p_{hard}^{(n)}(z, \vec{\theta}, \vec{r} | 0, \vec{0}, \vec{O}) = \\ \frac{n}{t^n} \int_P \int_0^t p_{hard}^{(n-1)}(\tau, \vec{\theta} - \vec{\theta}', \vec{r} - (z - \tau) \vec{\theta} | 0, \vec{0}, \vec{O}) p_{hard}(\vec{\theta}') \tau^{n-1} d\vec{\theta}' d\tau\end{aligned}\quad (23)$$

provided $p_{hard}(\vec{\theta}) = p(\vec{\theta}) \cdot \chi_{D>}(\vec{\theta})$ and λ_{hard} is the average number of hard collisions per unit pathlength (depth).

Finally, let us notice that in our considerations we have not been restricted in any way to initial conditions of the evolution given by any particular point

(like $(\vec{0}, \vec{O})$, for example). Due to homogeneity of the problem the fundamental solution $f(z, \vec{\theta}, \vec{r} \mid 0, \vec{0}, \vec{O})$ has obvious translational symmetries. If the initial condition (for both soft and hard collisions) is assumed to be point $(\vec{\theta}', \vec{r}')$ instead of standard initial point $(\vec{0}, \vec{O})$ then the following formula is valid

$$f(z, \vec{\theta}, \vec{r} \mid 0, \vec{\theta}', \vec{r}') = f(z, \vec{\theta} - \vec{\theta}', \vec{r} - \vec{r}' - z\vec{\theta}' \mid 0, \vec{0}, \vec{O}) \quad (24)$$

5 Conclusion

The above results demonstrate that solving the multiple scattering angular-spatial transport problem, equivalently finding a solution of the Lewis equation (2) and (3), can, in the case when diffusional limit for soft collisions is justified, be calculated through (5), (14) and any solution of (15) (see, for example, [5]). Moreover, under conditions of small angle approximation, applied to the global angular-spatial evolution, we obtain the solution of the Lewis equation through formula (21) based on calculations of functions $f^{soft}(z, \vec{\theta}, \vec{r})$ and $f^{hard}(z, \vec{\theta}, \vec{r})$. Numerical calculations of $f^{soft}(z, \vec{\theta}, \vec{r})$ and $f^{hard}(z, \vec{\theta}, \vec{r})$ are feasible due to analytic form of functions $f^{soft}(z, \vec{\theta}, \vec{r})$, low dimensionality of integration in calculations of $p_{hard}^{(n)}(z, \vec{\theta}, \vec{r} \mid 0, \vec{0}, \vec{O})$ and small number n of recurrence relations involved in calculations of $p_{hard}^{(n)}(z, \vec{\theta}, \vec{r} \mid 0, \vec{0}, \vec{O})$.

References

1. H. Lewis: Phys. Rev. **78**, 526 (1950)
2. L. Papież, V. Tulovsky: Rad. Phys. Chem. **53**, 257 (1998)
3. X. Ning, L. Papież, G. Sandison: Phys. Rev. E **52**, 5621 (1995)
4. K. Yosida: Ann. Math. Stat. **20**, 292 (1949)
5. V. Tulovsky, L. Papież: 'Closed form solution of the diffusion transport equation in multiple scattering', Appl. Math. Lett. (2001), in press
6. S. Karlin, H.M. Taylor, *A second course in stochastic processes* (Academic Press, San Diego 1981)
7. H.A. Bethe: Phys. Rev. **89**, 1256 (1953)
8. S. Goudsmit, J.L. Saunderson: Phys. Rev. **57**, 24 (1940)
9. L. Eyges: Phys. Rev. **79**, 1534 (1948)
10. G.Z. Molière: Z. Naturforsch. **3a**, 78 (1948)
11. L. Papież, G.A. Sandison: Adv. Appl. Prob. **22**, 533 (1990)
12. C.N. Yang: Phys. Rev. Lett. **84**, 599 (1951)

PICA3, an Updated Code of Photo-nuclear Cascade Evaporation Code PICA95, and Its Benchmark Experiments

T. Sato¹, K. Shin¹, S. Ban², T.A. Gabriel³, C.Y. Fu³, and H.S. Lee⁴

¹ Department of Nuclear Engineering, Kyoto University, Yoshida, Sakyo, Kyoto 606-8501, Japan

² High Energy Accelerator Research Organization (KEK), Japan

³ Oak Ridge National Laboratory, USA

⁴ Pohang Accelerator Laboratory, POSTECH, Korea

Abstract. PICA95, a calculation code for high-energy photo-nuclear reactions is updated as PICA3. PICA3 can predict experimental total photo-nuclear reaction cross section for incident photon energies from the reaction threshold to 3.5 GeV very well. It also can predict other experimental data such as yields of residual nuclides and emitted particle spectra from mono-energetic photo-nuclear reaction, but underestimates neutron yields produced from electron bombarded thick targets.

1 Introduction

Recently, high-energy electrons have been used rather widely for synchrotron orbital radiation and other purposes. Once the electrons hit a beam dump or an accelerator tube, they produce electro-magnetic cascades, as well as high-energy photons as bremsstrahlung. Therefore, calculation codes which are able to treat high-energy photo-nuclear reaction are required for shielding calculations of such high-energy electron accelerators. Several calculation codes (CEM95 [1], DINREG [2], FLUKA [3], MARS [4], PICA95 [5] etc.) have been developed for the purpose.

PICA95 is an update version of the original PICA [6] which works for incident photon energies from 30 MeV to 400 MeV. These energy limitations are due to ignorance of the giant resonance and the multiple-pion production, which are the dominant photo-nuclear reaction below 30 MeV and above 400 MeV, respectively. For the PICA95 case, the higher energy limit is extended up to 3.5 GeV by including multiple-pion (up to five pions) production channels.

Over the years, many experimental data for the total photo-nuclear reaction cross sections were reported by several authors. However, the total photo-nuclear reaction cross sections predicted by PICA95 usually do not agree with the experimental data very much. At the photon energies in the quasi-deuteron disintegration (QDD [7]) dominant region (below 150 MeV), the cross sections predicted by PICA95 are obviously larger than experimental data (see section 3). The main reason for the discrepancy is an overestimation of the QDD cross section due to using too large normalized parameter. At the photon energies in the pion production dominant region (above 150 MeV), the total cross sections

predicted by PICA95 do not agree with experimental data very much (see section 3). The main reason for the discrepancy is an ignorance of nuclear medium effect on the cross sections of the Δ and higher resonances.

From these consideration, we have improved the code to solve the discrepancies, and named the code as PICA3. The angular distribution of emitted particles adopted in the code have also been improved. As benchmark tests of the code, several experimental results concerning the photo-nuclear reaction are compared with calculated results by PICA3. The detail description for the modification process of the code are given in section 2, comparison between new calculated results and experimental data are shown in section 3. The final section is for conclusions.

2 Modification Process

We had modified PICA95 to calculate the QDD cross section without using the normalized parameter, and consider the giant resonance (GR) by using its cross section fitted by Lorentz curve. The lower limit of incident photon energy had been extended down to the reaction threshold by including the GR. The total cross sections predicted by PICA95 after these two modifications agreed with the experimental data very well. The detail of the modification processes and results are well described in [8]. The nucleon-nucleon scattering cross section used in the cascade calculation process, and the level density parameter and the mass formula used in the evaporation process had been updated at the time. The details are also described in the paper [8].

As well known, the QDD cross section can be evaluated by the photo-deuteron disintegration cross section. However, the photo-deuteron disintegration cross section data used in PICA95 is relatively old, and must be updated. Therefore, the cross section evaluated by Jenkins [9] is substituted for photon energies between 20 MeV and 440 MeV. His fitting result is also adopted for the angular distribution of protons produced by the disintegration in the calculation. For photon energies below 20 MeV, we assume that the angular distribution is the same as that for the 20 MeV incident case, and the disintegration cross section is determined by a fitting equation written in [10]. For photon energies above 440 MeV, we also assume that the angular distribution is the same as that for the 440 MeV incident case. The disintegration cross section at the energy region is derived from several experimental data [11–13]. These assumptions are not true for all cases, but the QDD reaction is not the dominant reaction, and the contribution from the reaction is not so large at the energy regions.

At the photon energies above 150 MeV, the photo-pion production reaction becomes the dominant reaction. Therefore, the main reason for the discrepancy of total cross sections at the energy region is substitution of the total photo-pion production cross section of nucleons in free space for the values in nuclear matter in PICA95 calculation. It is found out that the widths of the resonances for a nucleon in the nuclear matter are broaden, and their peaks are shifted to higher energy side. Furthermore, for very high energy photon (above 1 GeV),

the nuclear shadowing effect is not negligible, and the cross sections per nucleon in nuclear matter become smaller.

Therefore, we modified PICA95 to adopt calculated total photo-pion production cross section per nucleon with considering those effects. The calculation method of the cross section is basically the same as written in [14]. A sum of six Breit-Wigner resonances plus a smooth background, whose forms are written in (3) to (7) in [14], are used for evaluating the cross section. The fitting parameter used in the equations are the values for a proton evaluated in [14], except for parameters for the resonance widths and masses. As described before, those parameters must be determined with considering the nuclear medium effect. Therefore, those parameters are assumed to be expressed by linear functions of nucleon density, and their coefficients are deduced from Fig. 13 in [14].

To consider the nuclear shadowing effect, the calculated cross sections by (7) in [14] are multiplied by the shadowing parameter A_{eff}/A , where A_{eff} represents the effective number of nucleons seen by the incident photon, and A represents the real number of nucleons. The calculation method of the shadowing parameter is described in [15]. The obtained total photo-pion production cross sections per nucleon are distributed to each reaction channel, and the branching ratios are decided by input data of the code.

Not only the production cross section of pions, but also their angular distribution used in PICA95 must be updated. The emitted angle of produced pion is sampled from the isotropic distribution. However, the angular distributions are very complicated, and depends on the charge of pion and the photon energy very much. Therefore, we modified PICA95 to use the calculated angular distributions given by Metcalf [16] for the single pion production.

We named the calculation code of PICA95 with these modification as PICA3.

3 Comparisons with Experimental Data

In this section, we will show some calculated results by PICA3 together with corresponding experimental data. At first, the total photo-nuclear reaction cross section for several nuclei calculated by PICA3 are shown in Figs. 1 (a) - (c). The calculated results by PICA95 and some experimental data [14,17-19] are also shown in the figures. From the figures, it is found out that the calculated results given by PICA3 have much better agreement with the experimental data compared with those by PICA95 have. The cross section at the GR dominant region for the O target case does not agree with the experimental data very much, because the Lorentz parameters used in the calculation is not derived from the experimental data [18].

The ratios between calculated and experimental residual nuclide yields produced in 2.5 GeV electron bombarded thick targets are plotted as a function of residual nuclides' mass number in Figs. 2 (a) and (b). The detail calculation and experimental methods are described in [8] and [20]. From the figures, it is found out that the agreement between the calculation and the experimental data is very good, especially for the case of calculated values given by PICA3.

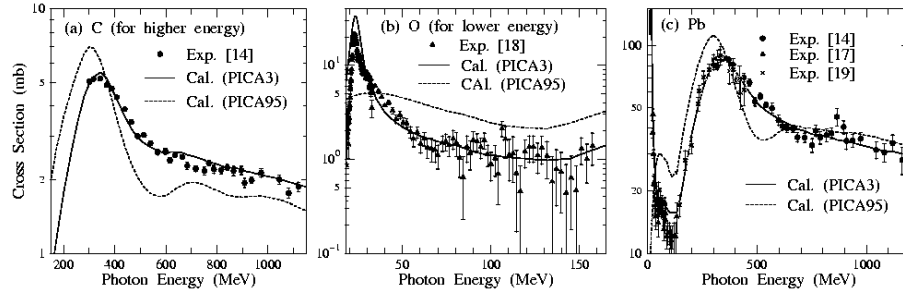


Fig. 1. The calculated total photo-nuclear reaction cross sections by PICA3 and PICA95 are compared with some experimental data for C (a), O (b), and Pb (c) targets. The full and broken lines are calculated by PICA3 and PICA95, respectively. The experimental points in (a) have been taken from [14]; in (b) from [18]; in (c) from [14,17], and [19]

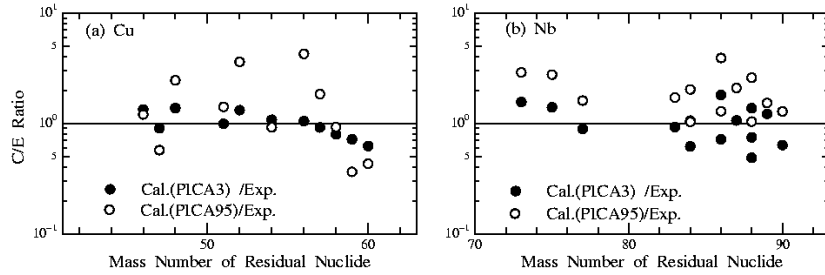


Fig. 2. The ratios between calculated and experimental residual nuclide yields produced in 2.5 GeV electron bombarded thick Cu (a) and Nb (b) targets are plotted as a function of residual nuclide's mass number. The detail calculation and experimental methods are described in [8] and [20]. The solid and open circles are the values calculated by PICA3 and PICA95, respectively

The calculated results of the double differential cross section for the photoemission of a proton and a π^+ from ^{12}C targets by photon energy 305 MeV are shown in Figs. 3 (a) and (b). The experimental data [21,22] are also shown in the figures. For the proton case (a), the calculation underestimates high energy proton emission cross section for forward direction. Such high energy protons are usually produced by the QDD reaction, and the reaction mechanism of the QDD for such a high incident photon energy is not well figured out. For the π^+ case (b), the agreement between the calculation and the experimental data is fairly well.

For more benchmark test of PICA3, we performed measurements of neutron spectra produced from 2.0 GeV electron beam bombarded thick targets [23]. The measured neutron spectra are compared with the corresponding calculated values evaluated by a combination of EGS4 [24], LAHET2.7 [25], and PICA3. As an example, a comparison result for the case of 10 radiation length (X_0) Pb target are shown in Fig. 4 (a). From the figure, it is found out the calculated spectra tended to underestimate the measured ones approximately by factor 3. A similar discrepancy can also be seen for the case of neutron spectra data mea-

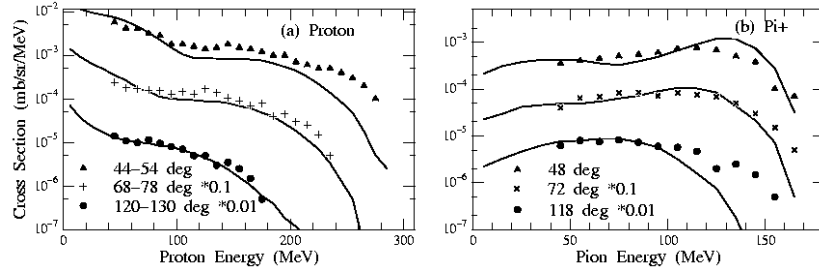


Fig. 3. The double differential cross sections for the photoemission of a proton (a) and a π^+ (b) off ^{12}C by photon energy 305 MeV. The solid lines are calculated by PICA3. The experimental points in (a) have been taken from [21], in (b) from [22]

sured by Eyss [26]. Their experimental procedure was basically the same as ours except for their lower incident electron energies. Therefore, the calculated values corresponding to the experimental data were evaluated by the same method, i.e. the combination of EGS4, LAHET2.7 and PICA3. As an example, a comparison result for the case of the incident electron energy 266 MeV, 4.3 radiation length Pb target are shown in Fig. 4 (b). From the figure, it is found out that the calculated yields are smaller than the experimental ones especially for lower energy neutrons. The reasons for these discrepancies are now under investigation, but one considerable reason is an ignorance about the pre-equilibrium process in the PICA3 calculation.

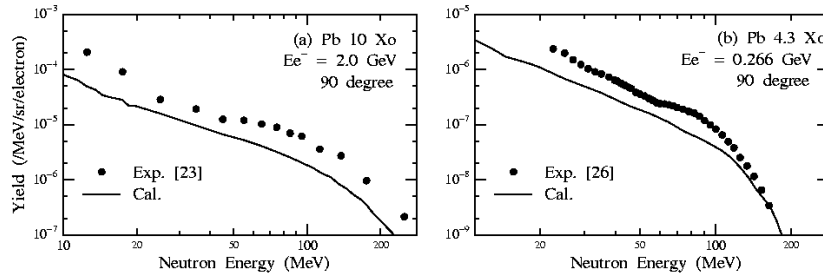


Fig. 4. The double differential photo-neutron yields per incident electron produced from electron bombarded thick Pb targets calculated by a combination of EGS4, LAHET2.7 and PICA3. The experimental points in (a) are for the 10 Xo Pb at electron energy 2.0 GeV [23], and in (b) are for the 4.3 Xo Pb at the energy 0.266 GeV [26]

4 Conclusions

PICA95 is updated as PICA3. The total photo-nuclear reaction cross sections predicted by PICA3 have better agreement with the experimental results compared with the values by PICA95 have. It also can predict other experimental data such as yields of residual nuclides and emitted particle spectra from mono-energetic photo-nuclear reaction, but underestimates neutron yields produced from electron bombarded thick targets. More experimental data are required for the systematic benchmark test of the code.

5 Acknowledgement

The authors wish to thank Dr. Ukai for his helpful advise on calculating the angular distribution of emitted pions.

References

1. S.G. Mashnik, A.J. Sierk, O. Bersillon, T.A. Gabriel: *Cascade-Exciton Model Detailed Analysis of Proton Spallation at Energies from 10 MeV to 5 GeV*, LA-UR-97-2905, Los Alamos National Laboratory (1997)
2. P. Degtyarenko: 'Application of the Photonuclear Fragmentation Model to Radiation Protection Problems'. In: *Proc. SATIF-2, Geneva, 12-13 October, 1995*, p.67
3. A. Fasso, A. Ferrari, J. Ranft, P.R. Sala: 'An Update about FLUKA', In: *Proc. SARE-2, Geneva, 9-11 October, 1995*, p.158
4. O.E. Krivosheev, N.V. Mokhov: 'New MARS and Its Applications', In: *Proc. of SARE-3, Tsukuba, 7-9 May, 1997*, p.12
5. C.Y. Fu: 'PICA95, An Intra-Nuclear Cascade Code for 25-MeV to 3.5-GeV Photon-Induced Nuclear Reactions', presented at *SATIF-3, Sendai, 12-13 May, 1997*
6. T.A. Gabriel, M.P. Guthrie, O.W. Hermann: *Instructions for the operation of the program PICA, an intra-nuclear-cascade calculation for high energy(30 to 400 MeV) photon-induced nuclear reactions*, ORNL-4687 (1971)
7. J.S. Levinger: *Phys. Rev.* **84**, 43 (1951)
8. T. Sato, K. Shin, S. Ban, Y. Namito, H. Nakamura, H. Hirayama: *Nucl. Inst. Meth. A* **437**, 471 (1999)
9. D.A. Jenkins, P.T. Debevec, P.D. Harty: *Phys. Rev. C* **50**, 74 (1994)
10. J.R. Wu, C.C. Chang: *Phys. Rev. C* **16**, 1812 (1977)
11. P. Dougan, T. Kivikas, K. Lugner, V. Ramsay, W. Stiefler: *Z. Phys. A* **276**, 55 (1976)
12. R. Ching, C. Schaerf: *Rhys. Rev.* **141**, 1320 (1966)
13. C. Bochna et al.: *Phys. Rev. Lett.* **81**, 4576 (1998)
14. N. Bianchi et al.: *Phys. Rev. C* **54**, 1688 (1996)
15. G. Piller, W. Ratzka, W. Weise: *Z. Phys. A* **352**, 427 (1995)
16. W.J. Metcalf, R.L. Walker: *Nucl. Phys. B* **76**, 253 (1974)
17. A. Lepretre, H. Beil, R. Bergere, P. Carlos, J. Fagot, A. De Miniac, A. Veyssiere: *Nucl. Phys. A* **367**, 237 (1981)
18. J. Ahrens et al.: *Nucl. Phys. A* **251**, 479 (1975)
19. P. Carlos et al.: *Nucl. Phys. A* **431**, 573 (1984)
20. T. Sato, K. Shin, S. Ban, Y. Namito, H. Nakamura, H. Hirayama: *Nucl. Inst. Meth. A* **401**, 476 (1997)
21. J. Arends et al.: *Z. Phys. A* **298**, 103 (1980)
22. J. Arends et al.: *Z. Phys. A* **305**, 205 (1982)
23. T. Sato, K. Shin, R. Yuasa, S. Ban, H. S. Lee: submitted
24. W.R. Nelson, H. Hirayama, D.W.O. Rogers: *The EGS4 code system*, SLAC-265 Stanford University, Stanford (1985)
25. R.E. Prael, H. Lichtenstein: *User's Guide to LCS: The LAHET Code System*, LA-UR-89-3014, Los Alamos National Laboratory (1989)
26. H.J. von Eyss, G. Luhrs: *Z. Phys.* **262**, 393 (1973)

Monte Carlo Simulation as an Aid to Alpha-Particle Spectrometry

A. Martín Sánchez¹, A. Fernández Timón¹, and C.J. Bland²

¹ Departamento de Física, Universidad de Extremadura, 06071 Badajoz, Spain

² Dept. of Physics and Astronomy, University of Calgary, Calgary Alberta, Canada
T2N 1N4

Abstract. The computer simulation code SRIM (stopping and range of ions in matter) developed by Ziegler and coworkers, has been applied previously to study the transport of α -particles within various materials. In particular, the detection of α -particles in silicon or gas detectors has been investigated. In this work, we apply the code to simulate the propagation through a common type of α -particle source used in spectrometry. The source consists of ^{226}Ra activity in secular equilibrium with its daughters distributed within a barium sulfate matrix. We have calculated the number and energy spectrum of those particles that reach the detector from the source, for several source thicknesses and for various detector distances. As these parameters are changed, the resulting energy resolution and the consequent accuracy of derived activities may be derived. Thus the optimum conditions for α -spectrometry can be determined given the accuracy desired.

1 Introduction

Alpha-particle spectrometry is used to find the activities of selected nuclides from which may be derived, in cases of interest, certain ratios of activities. Actual measurements are usually made with sources in which the activities are distributed within a matrix of finite mass e.g. within a precipitate. The source may be placed close to the detector to achieve adequate counting statistics. These two factors may combine to produce broader peaks with tailing to lower energies in the pulse-height spectrum. Thus counts from a nuclide emitted at a given energy may fall within the region of interest of another nuclide at lower energy. It is possible to deconvolute spectra from several nuclides to some degree, by means of curve fitting using special fitting functions [1,2]. More detailed insight into the processes leading to characteristic peak shapes at different energies can be achieved by the use of the SRIM program¹ developed by Ziegler et al. [3]. In an earlier publication [4], the authors made use of this program to investigate α -particle backscattering from different materials.

We present here a simple example of the spectrum from the decay of the nuclide ^{226}Ra in secular equilibrium with its prompt α -emitting daughters ^{222}Rn , ^{218}Po and ^{214}Po distributed within a BaSO_4 matrix uniformly deposited over a disc. Unless there are losses such as emanation of ^{222}Rn , the four activities should

¹ SRIM software and documentation is available from the web-site <http://www.research.ibm.com/ionbeams> courtesy of IBM Inc.

tend to equal values after several days have elapsed since source deposition. The nuclide ^{226}Ra was chosen because of its common occurrence in the environment wherever Uranium mining and ore processing has taken place.

In our simulations, a Monte-Carlo procedure selects the coordinates and the emission angles at the source for each particle emitted at the different initial energies. The SRIM program is run for many such simulations in order to compute the energy losses for those particles which are able to reach the detector after emerging from the source. The energy spectrum that would be recorded, can then be computed.

2 Physical Considerations

Self-absorption within the source is one of the important problems in α -particle counting. Another problem arises with detectors that provide energy spectra, because the tailing to lower energies causes some counts to fall in adjacent peaks. Both of these effects are present due to ionization losses and straggling within the material containing the source activity. The resultant peak broadening can almost be eliminated by using sources, which are extremely thin compared with the range of the α -particles being counted. As well the detector may be placed far away from the source so that it subtends a very small solid angle Ω , and then, the geometrical factor G , defined as $G = 4\pi/\Omega$, is large. The use of large G values greatly reduces the detection efficiency and may demand unreasonable counting times.

The preparation of very thin sources by electro-deposition or evaporation from organic solvents demands great skill to prepare very pure solutions of activity and may not be feasible in measurements of environmental radioactivity. It may not be possible to achieve very thin sources (equivalent to $< 10\%$ of the α -particle range) if nuclides of very low specific activity such as ^{232}Th or ^{238}U , are present.

Mann et al. [5] has described the earlier work on self-absorption and tailing. Other works have emphasized the role of tailing in high-resolution α -spectrometry caused by the response of solid-state detectors to almost mono-energetic helium ions [6–8].

In this work we shall revisit the problem of self-absorption and tailing which arises in practical α -activity measurements when the source may not be very thin and the activity level in the source may require rather small geometrical factors. Under these circumstances, the detector response plays a minor role in shaping the peaks in the energy spectrum. It is however, of interest to be able to determine the relative advantages of varying source thickness and source-detector geometry, in terms of counting efficiency, self-absorption losses and resolving power.

3 Details of the Example

Alpha-particle sources may be prepared from solutions of radium activity by adding barium as a carrier and precipitating barium/radium sulfate. Other activities such as polonium and lead are also present in the precipitate but can be removed by chelation purification [9]. The precipitate is usually filtered using sub-micron membrane filters of about 2.5 μm diameter. The membrane, after drying, can be attached to a support before counting. Since the range of 5 MeV α -particles in BaSO_4 is only about 16 μm , the source needs to contain very much lower quantities than 7.4 mg cm^{-2} equivalent of precipitate. Radium can be recovered from solution using a total precipitate of about 1 mg without too much difficulty. Sill [10] described a procedure using as little as 50 μg to yield high resolution in the recorded energy peaks.

In the simulations to be described, we have assumed that the source consists of a thin disc of BaSO_4 of 1.25 cm radius with various thicknesses between 0.1 to 0.8 μm (equivalent to about 0.05 to 0.4 mg cm^{-2}). Radium activity (^{226}Ra in secular equilibrium with daughters ^{222}Rn , ^{218}Po and ^{214}Po) is assumed to be uniformly distributed through the disc. Each nuclide contributes major α -particle emissions at 4.87, 5.59, 6.11 and 7.83 MeV respectively. A minor emission ($\approx 5\%$) at 4.68 MeV from ^{226}Ra has also been included. The detector is assumed to consist of another concentric and parallel disc of the same diameter located at various distances from 0 to $4R$ (where R is the radius of the discs). All of the parameters that were chosen for this sample calculation, can easily be altered to accommodate different geometries, energies etc.

4 Computational Details

All of the computations were performed on personal computers running Windows. The latest version, free from IBM for non-commercial applications, contains operating instructions and details of the physics involved in the computations. The program follows the path of charged particles through absorbers and computes by means of a Monte-Carlo procedure how the particle loses energy as well as scattering along its path. Rather than specifying identical starting parameters (energy, direction and location) for a number of particles entering the absorber, the authors wrote a program to specify different parameters for each individual event. Our program generates an input file to SRIM (TRIM.DAT) which randomly assigns position within the source (coordinates x , y , and z , where x is the direction perpendicular to the plane of the disc). Direction cosines are also randomly assigned. Each event is assigned an energy so that when all the events are generated, we have the correct proportions for each emission. Up to 99999 events can be generated (the limit being set by the SRIM program). The SRIM program then generates a file containing the parameters pertaining to particles, which emerge from the front of the source (the file TRANSMIT.TXT), or from the back (BACKSCAT.TXT). Given the symmetry it is possible to use both results, which is available from the output file TRIMOUT.TXT. The SRIM

program takes no more than a few minutes on a 266MHz Pentium II PC for each run for each source thickness.

The SRIM output provides the energy, position and direction of each α -particle emerging from the source. This information allows one to determine whether or not a given α -particle will intersect the detector. The lateral coordinates y_d and z_d are calculated at the detector distance $x = d$ to see whether this places the particle within the radius of the detector. We wrote a program, which picks out and records these events according to the specified geometrical parameters of the source and detector and their separation. This program also computes a histogram of the number of events, which hit the detector versus energy (i.e. a multi-channel spectrum). At this stage we have not taken into account the detector response although it would be relatively easy to generate a convolution of the incident spectrum with a simplified detector response (e.g. Gaussian with exponential tailing).

5 Results

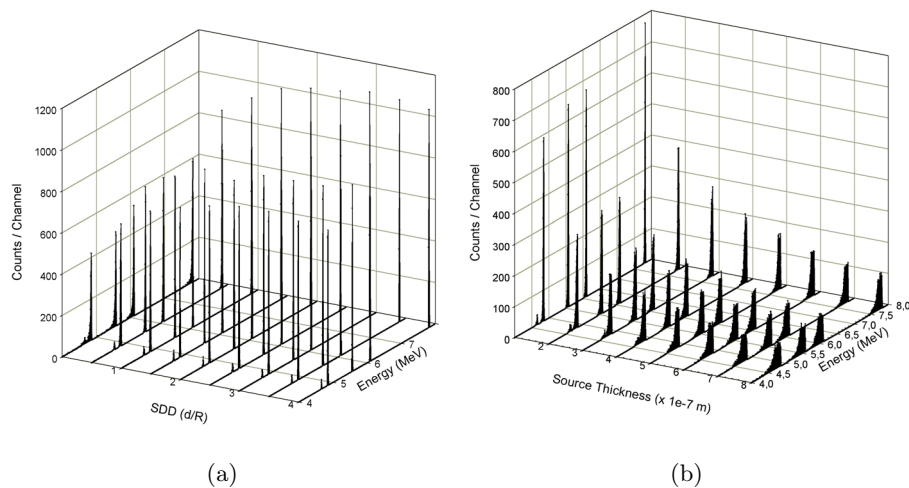


Fig. 1. The energy spectra generated by SRIM simulating an α -particle source of ^{226}Ra (and daughters) in a matrix of BaSO_4 (a) with a thickness of $0.1\ \mu\text{m}$, versus source to detector distance, (b) for a source-detector spacing of $0.4R$, versus source thickness

Figure 1(a) shows a composite view of several spectra from a source of $0.1\ \mu\text{m}$ thickness for various source-detector distances. Figure 1(b) shows the variation with the thickness, for a source to detector spacing of $5\ \text{mm}$. This spacing is typical of the values used for low-activity samples. Figure 2 shows ^{226}Ra peaks in more detail. One may note that there is more pronounced tailing when the source and detector are next to each other. The smaller peak cannot then be clearly distinguished, but can be when the separation is increased.

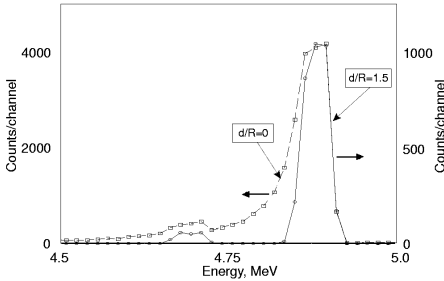


Fig. 2. The energy spectra given by a simulation of the ^{226}Ra line in a BaSO_4 source of $0.2\text{ }\mu\text{m}$ thickness, for source-to-detector distances of $d/R = 0$ and $1.5R$

Table 1. The resolution (FWHM) in keV for each nuclide, calculated from the simulated spectra for a source thickness of $0.1\text{ }\mu\text{m}$, with increasing source to detector distance (SDD in units of source/detector radius)

SDD (d/R)	^{226}Ra	^{222}Rn	^{218}Po	^{214}Po
0	31	30	27	24
0.2	29	29	27	22
0.4	27	27	27	23
0.8	27	23	25	20
1.6	23	22	21	17
2.4	23	21	19	16
3.2	22	20	19	16
4.0	22	21	19	16

Table 2. The resolution (FWHM) in keV for each nuclide, calculated from the simulated spectra with increasing source thickness. The source to detector distance was set to $0.4R$

Thickness (μm)	^{226}Ra	^{222}Rn	^{218}Po	^{214}Po
0.1	27	27	27	23
0.2	55	47	51	42
0.3	84	81	71	58
0.4	108	99	99	83
0.5	135	136	106	97
0.6	181	155	132	121
0.7	191	156	149	136
0.8	198	179	176	155

Tables 1 and 2 give the peak widths as FWHM, for the different peaks for several cases of source thickness and source-detector distance.

6 Conclusions

The Monte-Carlo simulation of the interactions of α -particles within the source may be used to predict the energy spectrum of those particles, which proceed to strike the detector. In this way the feasibility of measuring distinct emissions with certain accuracy may be predicted by examining the computed spectrum. The geometry factor is also provided by our modification of the SRIM program simulation. We note that Williams [11] described the use of Monte-Carlo calculations to calculate the geometry factor, much earlier. It may be possible to use the procedures described here to reconstruct the spectra that would be recorded from essentially mass-less sources. For example, in those cases where chemical procedures fail to isolate pure activities and yield a thicker source than expected. Alternatively one may be able to relate the fitting parameters, used in the analysis of energy spectra, to the physical parameters that are specified in SRIM. We conclude that the SRIM program provides an excellent method for dealing with the causes of uncertainty in α -particle spectrometry including, absorption in the source, energy losses resulting in peak broadening, as well as the effective geometry factor when the former effects are present.

References

1. C.J. Bland: Appl. Radiat. Isot. **49**, 1225 (1998)
2. A. Martín Sánchez, P. Rubio Montero, F. Vera Tomé: Nucl. Instrum. Methods Phys. Res. A **369**, 593 (1996)
3. J.F. Ziegler, J.P. Biersack, U. Littmark: The stopping and range of ions in solids. (Pergamon Press, New 1985 York)
4. A. Martín Sánchez, C.J. Bland, A. Fernández Timón: Appl. Radiat. Isot. **52**, 341 (2000)
5. W.B. Mann, A. Rytz, A. Spornol: Special Issue of Appl. Radiat. Isot. **39** (1998)
6. A. L'Hoir: Nucl. Instrum. Methods Phys. Res. **223**, 336 (1984)
7. E. Steinbauer, G. Bortels, P. Bauer, J.P. Biersack, P. Burger, I. Ahmad: Nucl. Instrum. Methods Phys. Res. A **339**, 102 (1994)
8. E. Steinbauer, P. Bauer, M. Geretschlager, G. Bortels, J.P. Biersack, P. Burger: Nucl. Instrum. Methods Phys. Res. B **85**, 642 (1994)
9. A.S. Goldin: Anal. Chem. **33**, 406 (1961)
10. C.W. Sill: Nucl. and Chem. Waste Management **7**, 239 (1987)
11. I.R. Williams: Nucl. Instrum. Methods **44**, 160 (1966)

Measurements and Calculations of Secondary Particle Yields from 100–to 800 MeV/Nucleon Heavy Ions

T. Kurosawa¹, T. Nakamura², H. Iwase², H. Sato², N. Nakao³, Y. Uwamino⁴, and A. Fukumura⁵

¹ Electrotechnical Laboratory, 1-1-4 Umezono, Tsukuba, 305-8568, Japan

² Tohoku University, Aoba, Aramaki, Sendai, 980-8578, Japan

³ High-Energy Accelerator Research Organization, 1-1 Oho, Tsukuba, 305-0801, Japan

⁴ The Institute of Physical and Chemical Research, 2-1 Hirosawa, Wako, 351-0198, Japan

⁵ National Institute of Radiological Sciences, 4-9-1 Anagawa, Inage-ku, Chiba, 263-8555, Japan

1 Introduction

Recently, high-energy heavy ions have been used in various fields of nuclear physics, material physics and medical application, especially cancer therapy. At the National Institute of Radiological Sciences (NIRS) in Chiba, Japan, the HIMAC (Heavy Ion Medical Accelerator in Chiba) has been used for the heavy ion cancer therapy for the last three years, and the GSI (Gesellschaft für Schwerionenforschung) in Germany has just started heavy ion cancer therapy. Several institutes in the world have started or planned to build the radioactive beam facility where high-energy radioactive heavy ions are used for investigating exotic nuclei, nuclear synthesis and so on.

To design these facilities, the radiation shielding is essential to protect workers and nearby inhabitants from an amount of penetrating neutrons produced by high-energy heavy ions. The data on the energy - angle distribution of secondary neutrons from a thick target which fully stops heavy ions, so called thick target neutron yield (TTY), are indispensable to estimate radiation source terms for accelerator shielding design [1]. For heavier ions, there is only one set of experimental data on TTY for 160 and 177.5 MeV/u helium ions [2]. Recently, Heilbronn et al. published two reports on TTY for 155 MeV/u He, 155 MeV/u C and 272, 435 MeV/u Np ions [3,4].

Our group also performed a systematic study on TTY using the HIMAC and published three papers on TTY for 100, 180 MeV/u He, 100, 180, 400 MeV/u C and 100, 180, 400 MeV/u Ne ions [5–7]. This work is a summary report of this systematic study on TTY including some newly obtained results for 400 MeV/u Ar, 400 MeV/u Fe, 400 MeV/u Xe and 800 MeV/u Si ions. The measured spectra are compared with those calculated with the HIC code [8] based on an intranuclear - cascade and evaporation model.

2 Experimental Procedure

The energy of neutrons produced in the target was measured by the time-of-flight (TOF) method. A thin NE102A plastic scintillator (30mm diam. by 0.5mm thick) was placed just behind the end window of the beam line as a beam pick-up scintillator. The output pulses from this scintillator were used as the start signal of the TOF measurement. These output pulses were also used to count the absolute number of projectiles incident on the target. A target was set on the beam line 10 cm behind the beam pick-up scintillator. The beam spot size incident on the target was about 1.5 cm diameter and the beam height was 1.25m above the concrete floor of the experimental area. The NE213 liquid scintillator (12.7cm diam. by 12.7cm thick), which is designed to expand the dynamic range of output pulses for high energy neutron measurements [9], was used for neutron detector (E counter), and the NE102A plastic scintillator (15 cm by 15cm square and 0.5cm thick) for ΔE counter was placed in front of the E counter to discriminate charged particles from noncharged particles, neutrons and photons. Three sets of E and ΔE counters were used for simultaneous angular distribution measurements at three different angles. The detectors were located 2 m at large angles to 5 m at small angles away from the target to provide better energy resolutions in the forward directions where there are larger yields of high energy neutrons. In order to minimize neutrons in-scattering, no local shielding was used near the detectors. By interposing an iron shadow bar 15cm by 15cm square and 60cm thick between the target and detector, the background neutron components from room scattering were measured.

The incident energies of heavy ions and the target materials with their thicknesses are given in Tab. 1. Target materials are C (1.77g/cm³), Al (2.7g/cm³), Cu (8.93g/cm³) and Pb (11.34g/cm³) and each target has a shape of 10cm by 10cm square and its thickness was determined to stop the incident particles completely. When the measurements were carried out at large angles, the target was set at 45 degree to the beam line to minimize the attenuation effect of neutrons through the target.

3 Data Analysis

As neutrons and gamma rays do not scintillate in the ΔE counter the neutron and gamma ray events could be selected from the charged particle events, by using two-dimensional ΔE -E graphical plots. After this discrimination, the neutron and the gamma ray events were clearly separated by using two-dimensional graphical plots of total-slow pulse height components of the E counter. After each experimental run, each E counter was calibrated with a ⁶⁰Co gamma-ray source, and the Compton edge in the gamma-ray spectrum was used as the energy calibration point. After obtaining the TOF spectrum of neutrons, it was converted into the energy spectrum of neutrons. For this conversion, the detection efficiency is essential. The experimental data of the detection efficiency for this scintillator has been published by Nakao et al. [9], but there is no data

Table 1. Projectile type with incident energy per nucleon and target thickness

Projectile type	Energy per nucleon (MeV/u)	Target material and thickness (cm)
He	100	C (5.0), Al (4.0), Cu (1.5), Pb (1.5)
He	180	C (16.0), Al (12.0), Cu (4.5), Pb (5.0)
C	100	C (2.0), Al (2.0), Cu (0.5), Pb (0.5)
C	180	C (6.0), Al (4.0), Cu (1.5), Pb (1.5)
C	400	C (20.0), Al (15.0), Cu (5.0), Pb (5.0)
Ne	100	C (1.0), Al (1.0), Cu (0.5), Pb (0.5)
Ne	180	C (4.0), Al (3.0), Cu (1.0), Pb (1.0)
Ne	400	C (11.0), Al (9.0), Cu (3.0), Pb (3.0)
Ar	400	C (7.0), Al (5.5), Cu (2.0), Pb (2.0)
Fe	400	C (6.0), Al (4.0), Cu (1.5), Pb (1.5)
Xe	400	C (3.0), Al (2.0), Cu (1.0), Pb (1.0)
Si	800	C (23.0), Al (17.0), Cu (6.5), Pb (6.5)

for neutrons of energy higher than 135MeV. Therefore, the neutron detection efficiency was calculated with the Monte Carlo code by Cecil et al. [10].

4 Calculation of the Neutron Spectra

These experimental results were compared with calculations. The neutron spectra were calculated by using the Heavy Ion Code, HIC [8]. The HIC code is a Monte Carlo code that calculates continuum state transitions between projectile and target in heavy ion reactions at energies above 50MeV/u. The assumption in the model is that the reaction can be represented by the interaction of two Fermi gases that pass through each other. In this code, an intranuclear-cascade and an evaporation model are used. As the HIC code only gives the double differential neutron production cross section, so called thin target yield, the calculations were performed for a series of thin target yield calculations, which were then summed to obtain the neutron yields from heavy ions stopping in a thick target, considering the projectile continuous energy loss and the projectile number attenuation in the target, as follows,

$$\frac{d^2\phi}{dEd\Omega} = \sum_{i=1}^m \sigma_i N P_i dE_i / \left(\frac{dE_i}{dx_i} \right) \quad (1)$$

$$P_i = P_{i-1} \exp(-\sigma_{\text{Tot}} N dx_i) \quad (2)$$

where σ_i is the double differential neutron production cross section calculated by HIC, N is the atomic density of target, P_i is the number of beam particles in the target ($P_0 = 1.0$), $\Delta E_i / \Delta x_i$ is the stopping power calculated by the SPAR code [11], σ_{Tot} is the total reaction cross section given as an experimental formula by Shen et al. [12], and Δx_i is the thickness of thin target divided. In (2), the neutron production from the extranuclear cascade is still neglected, and this approximation can hold in relatively lower energy region.

5 Results and Discussions

5.1 Measured Neutron Spectra

Measured neutron spectra for C target bombarded by 400MeV/nucleon C projectile are shown in Fig. 1, as example. Neutron spectra measured in the forward direction have a broad peak at high-energy end, especially a large bump at 0 degree and this peak becomes more prominent for lighter target and for higher projectile energy. The peak energy of this bump is about 60 to 70 % of the projectile energy per nucleon. This means that these high energy neutron components produced in the forward direction by a break-up process and the momentum transfer from projectile to target nuclei are both higher for lighter nucleus and higher projectile energy than for heavier nucleus and lower projectile energy. The energy of the neutrons in the forward direction extends to about twice that of the incident particle energy per nucleon. This can be explained in the following. When the Fermi energy is approximated to be 40MeV, the relative velocity of a nucleon in a nucleus, becomes 0.28. The relative velocities of 100MeV/u, 180MeV/u and 400MeV/u projectiles are 0.43, 0.54 and 0.71, respectively. Thus, the composite relative velocities of a nucleon in a projectile are 0.63, 0.71 and 0.83, and the resultant nucleon energies can be estimated as 270MeV, 400MeV and 730MeV for 100MeV/u, 180MeV/u and 400MeV/u projectiles, respectively.

5.2 Comparison with Calculations

The calculated spectra are also shown in Fig. 1 with the experimental results. These figures clarified that a broad high energy peak in the forward direction appears around the incident particle energy per nucleon, while on the other hand the measured peak appears about 60 to 70% of that as described before. This marked discrepancy may come from the fact that the HIC calculation which does not include the effects of neither the nuclear potential nor the viscosity of nuclear matter fails to express the break-up process. The superposition of thin target yields in the calculation pretty well gives the measured thick target yield at large neutron emission angle where the breakup process is negligibly small, although the extranuclear cascade reaction are neglected in this superposition.

5.3 Total Yields

The total neutron yields above 5MeV were integrated over a hemisphere from 0° to 90°, and they are shown in Fig. 2. The total neutron yields become slightly

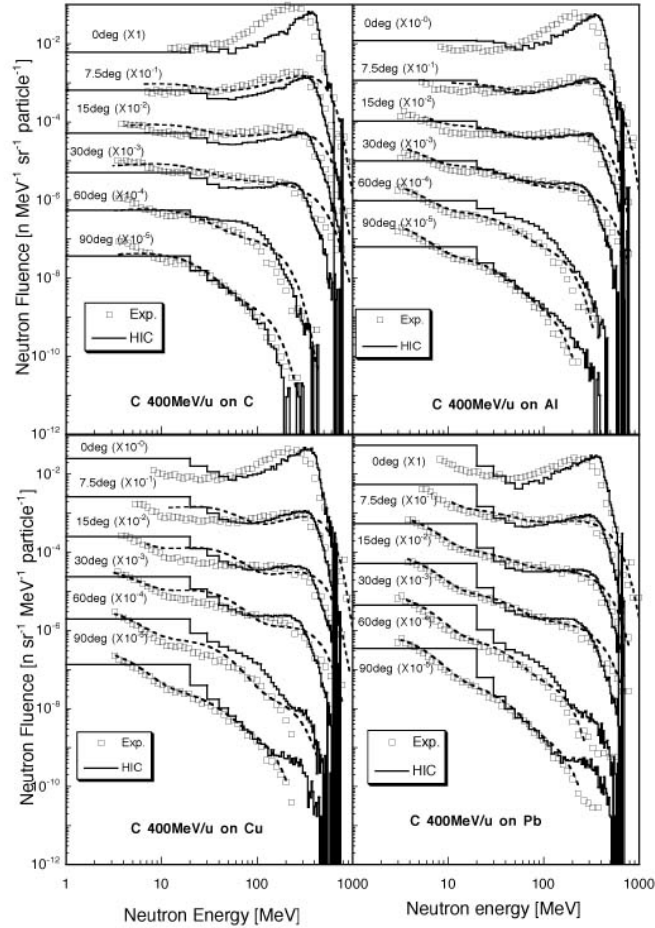


Fig. 1. Neutron spectra from 400 MeV/u C ions

larger with increase of the target mass, but their dependence on the target mass is very small compared with the difference of neutron numbers of the target. The difference in neutron yields between He, C and Ne ion projectiles is also very small, but the yields from Ar and Fe ion projectiles are larger than from the those lighter ions. These differences in neutron yields might be caused by the neutron production cross section, the thickness of the target and neutrons produced by secondary charged particles.

6 Conclusion

We measured angular and energy distributions of neutrons produced by 100 and 180 MeV/u He, 100, 180, 400 MeV/u C, 100, 180, 400MeV/u Ne, 400MeV/u

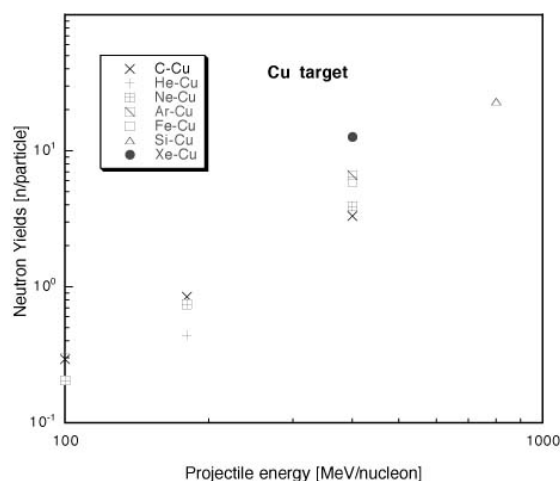


Fig. 2. Total neutron yields above 5MeV integrated for a hemisphere from 0 to 90 degrees

Ar, 400MeV/u Fe, 400MeV/u Xe and 800MeV/u Si ions stopping in carbon, aluminum, copper and lead targets. The neutron spectra in the forward direction have a broad peak at about 60 to 70 % of the incident particle energy per nucleon due to break-up process and extend up to almost twice the projectile energy per nucleon.

The experimental results were also compared with the calculations using the HIC code, and the calculated results agree with the measured results within a factor of 2 margin of accuracy. This is the first systematic study on neutron production from thick targets by heavy ions and will be useful for shielding design of high-energy heavy ion accelerator facilities.

References

1. T. Kato, T. Nakamura: Nucl. Instr. and Meth. A **311** 548 (1992)
2. R.A. Cecil et al.: Phys. Rev. C **210**, 2471 (1980)
3. L. Heilbronn et al.: Nucl. Sci. Eng. **132**, 1 (1999)
4. L. Heilbronn et al.: Phys. Rev., to be published
5. T. Kurosawa et al.: Nucl. Sci. Eng. **132**, 30 (1999)
6. T. Kurosawa et al.: J. Nucl. Sci. Technol. **36**, 41 (1999)
7. T. Kurosawa et al.: Nucl. Instr. and Meth, to be published
8. H.W. Bertini: ORNL-TM-4134, (1974)
9. N. Nakao et al.: Nucl. Instr. Meth. A **362**, 454 (1995)
10. R.A. Cecil, B.D. Anderson, R. Madey: Nucl. Instr. and Meth. **161**, 439 (1979)
11. T. Nakane et al.: JAERI-M 93-152 (1993)
12. Shen Wen-qing, et al.: Nucl. Phys. A **491** 130 (1989)

Development of an Extended Range Bonner Sphere Spectrometer

C. Birattari¹, P. Cappellaro², A. Mitaroff², and M. Silari²

¹ University of Milan, LASA, Via Fratelli Cervi 201, 20090 Segrate (Milano), Italy

² CERN, 1211 Geneva 23, Switzerland

Abstract. To improve the response to high-energy neutrons of a conventional Bonner Sphere Spectrometer, the response functions of several detector configurations of different sizes and materials were calculated with the Monte Carlo programme FLUKA. The two most promising configurations were selected, built and afterwards exposed to neutrons of an Am-Be source and to a broad high-energy neutron spectrum at CERN. The comparison between the measured and calculated detector responses of the new spheres in these radiation fields confirms their simulated response functions and justifies their implementation into the conventional Bonner Sphere Spectrometer.

1 Introduction

Stray radiation fields outside the shielding of hadron accelerators are of a complex nature. They consist of a multiplicity of radiation components (neutrons, photons, electrons, pions, muons, ...) which extend over a wide range of energies. Since the dose equivalent in these mixed fields is mainly due to neutrons, neutron dosimetry is a particularly important task. Also at commercial flight altitudes a large fraction of the exposure of aircraft personnel is due to neutrons with an energy spectrum comparable to that along hadron accelerators [1]. The neutron energy in these fields ranges from thermal up to several hundreds of MeV, thus making dosimetry difficult.

A well known instrument for measuring neutron energy distributions from thermal energies up to about 10 MeV is the Bonner Sphere Spectrometer (BSS) [2]. It consists of a set of moderating spheres of different radii made of polyethylene, with a thermal neutron counter (either an active or passive detector) in the centre. Each detector (sphere plus counter) has a maximum response at a certain energy value depending on its size, but the overall response of the BSS drops sharply above 10 MeV. To extend the overall response two new detectors with a good high-energy response were designed, built and tested in order to be added to a conventional BSS.

2 Monte Carlo Simulations

The design of two additional detectors was performed following the same approach adopted in the development of the extended range neutron rem counter LINUS [3-6] and recently applied to bubble detectors [2]. Monte Carlo simulations were carried out with the FLUKA code [8,9]. The present simulations

were based on an already existing and simulated set of detector spheres. This set consists of a spherical ^3He proportional counter placed inside five moderating spheres composed of 0.963 g/cm^3 polyethylene. The proportional counter has a diameter of 3.2 cm and is filled with 2 atm ^3He and 1 atm Krypton. The diameters of the five spheres are 233 mm, 178 mm, 133 mm, 108 mm and 83 mm. The sphere with a diameter of 83 mm is used both bare and wrapped with 1 mm of cadmium in order to absorb the thermal neutron component. Figure 1 shows the response functions of the five detectors as previously calculated [6].

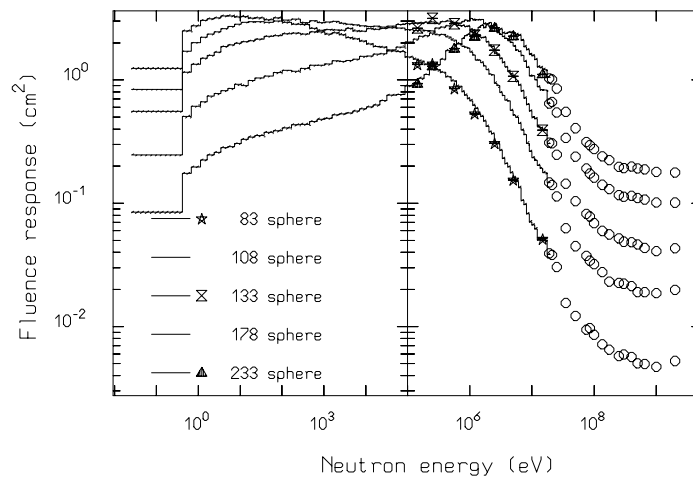


Fig. 1. Absolute neutron fluence response (counts per unit fluence) of the polyethylene spheres. The spheres are labelled with their diameter in millimetres

For the extended range BSS, nineteen configurations of different size and material composition were investigated, all with a spherical ^3He proportional counter in the centre. The response of each detector was calculated for energies between 10^{-14} GeV and 2 GeV. To extend the response of the BSS basically a high-Z material (lead, iron or copper) and cadmium was added into the polyethylene sphere. The effect of the high-Z material is to detect neutrons with energies greater than 10 MeV via the evaporation neutrons produced in inelastic scattering reactions while no significant effect is produced on neutrons with energies below 10 MeV. The cadmium has a very high cross section for thermal neutrons and placed inside the moderator it reduces the response to neutrons with energies lower than a few hundreds of keV. A description of all the configurations and their calculated responses can be found in [10].

Two configurations turned out to be most promising (see Fig. 2) and were chosen for construction. The first (called ‘ollio’) is a sphere with a diameter of 255 mm and consists of (from the ^3He proportional counter outwards) 3 cm polyethylene, 1 mm cadmium, 1 cm lead and 7 cm polyethylene. This configuration suppresses the response to incident neutrons with energies lower than

100 keV and increases it for energies above 10 MeV and up to 1 GeV, as compared to the 233 mm sphere of our conventional BSS. However it still shows the peak at about 10 MeV. The second detector (called 'stanlio'), with a diameter of 118.5 mm, consists of 2 cm polyethylene, 1 mm cadmium and 2 cm lead. It does not show the peak at 10 MeV. At low energies it behaves like a small Bonner Sphere, but at high energies the response is increased compared to the 233 mm sphere.

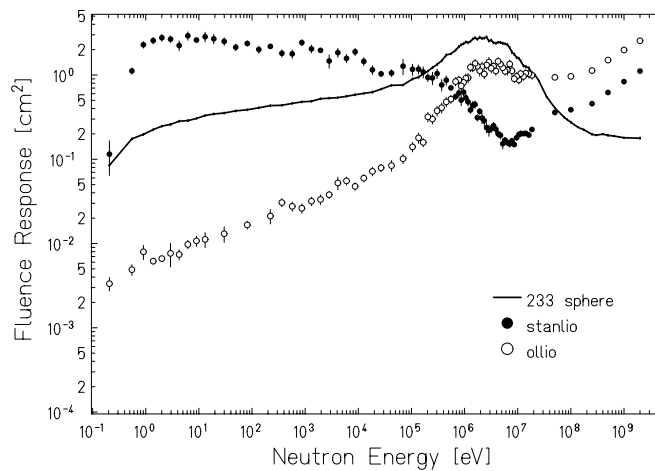


Fig. 2. Absolute neutron fluence response (counts per unit fluence) of the two extended range spheres, stanlio and ollio

3 Experimental

The first tests of the extended BSS were performed with an Am-Be source and a broad high-energy neutron spectrum at CERF.

3.1 Measurements with an Am-Be Source

The measurements were carried out in a calibration laboratory at CERN. An $^{241}\text{Am-Be}$ source was used with an emission of $6.94 \cdot 10^5$ neutrons per second, i. e. a fluence of $5.52 \text{ s}^{-1} \text{ cm}^{-2}$ at 1 m. In order to get the response of the BSS to the pure Am-Be field the reading had to be corrected for all extraneous effects, including consequences of the detector size and neutron scattering by the air and by the walls of the laboratory. This was done by applying the semi-empirical method of calibration procedures described in [11].

3.2 Measurements at CERF

CERF is a high-energy reference radiation facility [12,13] housed at CERN in the SPS North Experimental Hall and used for the intercomparison of active

and passive detectors in high-energy neutron fields [14]. A positive hadron beam (61 % pions, 35 % protons and 4 % kaons) with momentum of 120 GeV/c hits a copper target, 50 cm thick and 7 cm in diameter. The secondary particles produced in the interactions are filtered by a roof shielding made of 80 cm concrete. Above the shielding, the neutron spectrum has a pronounced maximum at about 1 MeV and another at about 70 MeV [13]. Several reference exposure positions are available where the particle fluence and their energy spectra are well known by both Monte Carlo calculations and experimental measurements [13]. In order to compare the experiment with the simulation, the tests of the extended BSS were carried out in the same position where the spectrum was calculated with FLUKA, i. e. 25 cm above the concrete roof shielding on top of the copper target. The beam intensity was tuned low enough to prevent dead time and pile up effects. Before each measurement the beam was switched off and a measurement of the background coming from other beam lines and experiments in the hall was performed.

4 Results and Discussion

To compare experimental and calculated detector responses the computed response functions of the extended BSS to monoenergetic neutrons were folded with the spectral fluences. For the measurements done in the calibration laboratory, the spectrum of the Am-Be source was taken from [15]. For the experiments at CERF the spectral fluence given in [13], calculated with FLUKA, was used. Table 1 and 2 summarise the results obtained. The quoted errors are only statistical but take already the correlation of the computed response functions and fluence spectra into account when summing up over the energy bins. However, they do not include systematic uncertainties in the detector efficiency and in the FLUKA code.

The agreement between the experiments and the calculations for the exposure to Am-Be neutrons is very good. Only the measurements with the two smallest spheres (83 mm and 83 mm with cadmium) show large deviations from the calculations. For these two detectors the corrections due to the backscattered neutrons were of the same order than the response to the direct neutrons, while for the stanlio it was 60 % and for all other detector spheres less than 6 %. This points out the limits of the semi empirical method [11] in correcting the influence of backscattered neutrons. Also for the CERF exposure the overall agreement between the two sets of data is very good taking into account the unknown systematic uncertainties described above.

5 Summary and Conclusion

Given the interest of measuring neutron spectra up to several hundreds of MeV, the aim of this work was to add to an existing Bonner Sphere Spectrometer two new detectors optimised for high energies. For this purpose the response functions of nineteen different detector configurations were calculated with FLUKA

Table 1. Experimental and calculated absolute response of the extended Bonner Sphere Spectrometer to neutrons from an Am-Be source

Sphere	Response (counts per incident neutron, cm ⁻²)		
	Experimental	Calculated	Ratio ($\frac{calc}{exp}$)
83+cadmium	0.280±0.006	0.34±0.02	1.21±0.09
83	0.274±0.008	0.36±0.03	1.31±0.10
108	0.835±0.022	0.91±0.06	1.09±0.08
133	1.502±0.029	1.48±0.10	0.98±0.07
178	2.180±0.043	2.14±0.15	0.98±0.07
233	2.241±0.045	2.26±0.16	1.01±0.07
stanlio	0.319±0.008	0.36±0.03	1.13±0.10
ollio	1.016±0.020	1.08±0.08	1.06±0.08

Table 2. Experimental and calculated absolute response of the extended Bonner Sphere Spectrometer to the broad neutron spectrum on the concrete roof of CERF

Sphere	Response (cm ²)		
	(counts per incident hadron on the copper target)		
	Experimental	Calculated	Ratio ($\frac{calc}{exp}$)
83+cadmium	(1.38±0.07)·10 ⁻⁵	(1.56±0.26)·10 ⁻⁵	1.13±0.19
83	(2.01±0.09)·10 ⁻⁵	(2.30±0.31)·10 ⁻⁵	1.14±0.16
108	(2.72±0.12)·10 ⁻⁵	(2.87±0.42)·10 ⁻⁵	1.06±0.16
133	(3.19±0.15)·10 ⁻⁵	(3.20±0.47)·10 ⁻⁵	1.00±0.15
178	(3.23±0.15)·10 ⁻⁵	(3.30±0.47)·10 ⁻⁵	1.02±0.15
233	(2.81±0.13)·10 ⁻⁵	(2.96±0.40)·10 ⁻⁵	1.05±0.15
stanlio	(1.58±0.07)·10 ⁻⁵	(1.93±0.29)·10 ⁻⁵	1.22±0.20
ollio	(1.93±0.09)·10 ⁻⁵	(2.36±0.32)·10 ⁻⁵	1.22±0.17

and intercompared. The two most promising were built and tested with an Am-Be source and with high-energy neutrons at CERF. The experimental responses of the various BSS detectors were found in good agreement with the calculated ones. These results confirm the simulated response functions of the two new detector spheres, which can be added to the existing Bonner Sphere Spectrometer.

6 Acknowledgements

The authors would like to thank A. Ferrari for supplying the FLUKA code and G.R. Stevenson, P.R. Sala and T. Otto from CERN and T. Rancati from the University of Milan for many useful discussions.

References

1. U.J. Schrewe, W.G. Alberts, A.V. Alevra, A. Ferrari, T. Otto, M. Silari: *Radiat. Prot. Dosim.* **86**, 289 (1999)
2. R.L. Bramblett, R.I. Ewing, T.W. Bonner: *Nucl. Instrum. Meth.* **9**, 1 (1960)
3. C. Birattari, A. Ferrari, C. Nuccetelli, M. Pelliccioni, M. Silari: *Nucl. Instrum. Meth. A* **297**, 250 (1990)
4. C. Birattari, A. Esposito, A. Ferrari, M. Pelliccioni, M. Silari: *Radiat. Prot. Dosim.* **44**, 193 (1992)
5. C. Birattari, A. Esposito, A. Ferrari, M. Pelliccioni, M. Silari: *Nucl. Instrum. Meth.* **324**, 232 (1993)
6. C. Birattari, A. Esposito, A. Ferrari, M. Pelliccioni, T. Rancati, M. Silari: *Radiat. Prot. Dosim.* **76**, 135 (1998)
7. S. Agosteo, M. Silari, L. Ulrici: *Radiat. Prot. Dosim.* **88**, 149 (2000)
8. A. Fassò, et al.: 'New Developments in Fluka Modelling of Hadronic and EM Interactions'. In: *Third Workshop on Simulating Accelerator Radiation Environments (SARE3) at KEK Tsukuba, Japan*, ed. by H. Hirayama, KEK Proceedings **97-5** (1997), pp. 32-43
9. A. Ferrari, T. Rancati, P.R. Sala: 'Fluka Applications in High Energy Problems: From LHC to ICARUS and Atmospheric Showers'. In: *Third Workshop on Simulating Accelerator Radiation Environments (SARE3) at KEK Tsukuba, Japan*, ed. by H. Hirayama, KEK Proceedings **97-5** (1997), pp. 165-175
10. A. Mitaroff, M. Silari: *Improving the High Energy Response of a Bonner Sphere Spectrometer*. CERN Internal Report, TIS-RP/IR/**99-27** (1999)
11. International Standard ISO/FDIS 8529-2:1999(E): *Reference neutron radiations- Part 2*. (1999)
12. M. Höfert, G.R. Stevenson: 'The CERN-CEC High Energy Reference Field Facility'. In: *8th International Conference on Radiation Shielding at Arlington, Texas, USA* (American Nuclear Society, Inc., Illinois, USA, 1994) pp. 635-642
13. C. Birattari, T. Rancati, A. Ferrari, M. Höfert, T. Otto, M. Silari: 'Recent Results at the CERN-EC High Energy Reference Field Facility'. In: *Third Specialists Meeting on Shielding Aspects of Accelerators, Targets and Irradiation Facilities (SATIF-3) at Tohoku University, Sendai, Japan*, ed. by OECD (1998), pp. 219-234
14. C. Birattari, A. Esposito, A. Fassò, A. Ferrari, J.G. Festag, M. Höfert, M. Nielsen, M. Pelliccioni, Ch. Raffnsøe, P. Schmidt, M. Silari: *Radiat. Prot. Dosim.* **51**, 87 (1994)
15. International Standard ISO/DIS 8529-1: *Reference neutron radiations- Part 1*. (2000)

Influence of the FLUKA Geometrical Model on the ADS Demonstration Facility Criticality Calculations

P. Neuhold

Ansaldo Nucleare, Divisione di ANSALDO ENERGIA, corso Perrone 25, 16161 -
Genova, ITALY

1 Scope

Criticality calculations for a typical ADS have been performed by means of the codes chain FLUKA-CMCS (formerly *FLUKA – MC²* [1]).

As it is well known [1] the FLUKA code calculates the neutron source for the subsequent neutron transport calculations performed by CMCS.

In this paper it will be investigated how the geometrical model used in FLUKA can impact the CMCS criticality calculations.

2 Introduction

FLUKA evaluates the behaviour of the spallation born neutrons in the high energy domain down to energies where spallation is not possible any more and the neutron energy is suitable for subsequent standard Monte Carlo calculations (that is in an energy range where sound cross-sections libraries exist. The lowest neutron energy here used in FLUKA is 20 MeV (the worldwide common cross-sections libraries energy upper bound). FLUKA writes a number of information on neutrons (such as coordinates, direction and energy) in a dedicated ASCII file.

It is well known that the innermost fuel bundles in an ADS core are missing to permit the introduction of the dedicated target where, generated by the accelerated protons, the spallation process occurs, for instance, in a lead-bismuth eutectic, as in the ANSALDO design.

Due to the strong scattering characteristics of lead and bismuth, which bring neutron energy below 20 MeV in a few centimeters from the proton beam impact point (actually the neutron density is decreasing exponentially as it approaches the core [2]), it seems not necessary, in order to have a good description of the neutron source for the Monte Carlo calculation, to model in the FLUKA calculations, at least in a detailed way, the whole core, but only the target region and a portion of the coolant outside it. This, if true, will save a lot of time and possible (probable ?) errors in the input preparation as only the target detailed description is requested. Not only: the same neutron source can be useful for a number of different core CMCS calculations.

In the following the impact of this approach for two alternative core (target) designs will be investigated.

Two different targets have been investigated the reference target and a smaller one. In Fig. 1 a sketch of the small target is shown.

AREA TOTALE = 1148 cm²
DELLA ZONA CENTRALE

AREA ACCIAIO DEI 3 TUBI = 0,49 cm²
AREA ACCIAIO = 67,4 cm²
AREA ACCIAIO = 38,5 cm²
AREA ACCIAIO = 24,3 cm²
AREA ACCIAIO = 68,6 cm²
AREA GAS= 40cm²
**AREA GAS
DEI 3 TUBI=5,7cm²**

Dimensions and radii shown:
R138.00
R130.00
R125.00
R120.00
R80.00
R75.00
R10.65
R7.85
322.40
317.77
72.44
79.44
383.36
137.60
253.20
263.20
275.20
133.60
77.13
397.22
4.00
5.00
5.00

3.2 Analysis of FLUKA Written Neutron Source File for CMCS

An analysis has been performed, by means of ad hoc programs, on the data written by FLUKA in the file which is the neutron source for the subsequent criticality calculations performed by CMCS. It has been investigated: a) how many neutrons were born in the core region; b) which is their average energy; c) how many neutrons with energy higher than 20 MeV were born; d) which is their

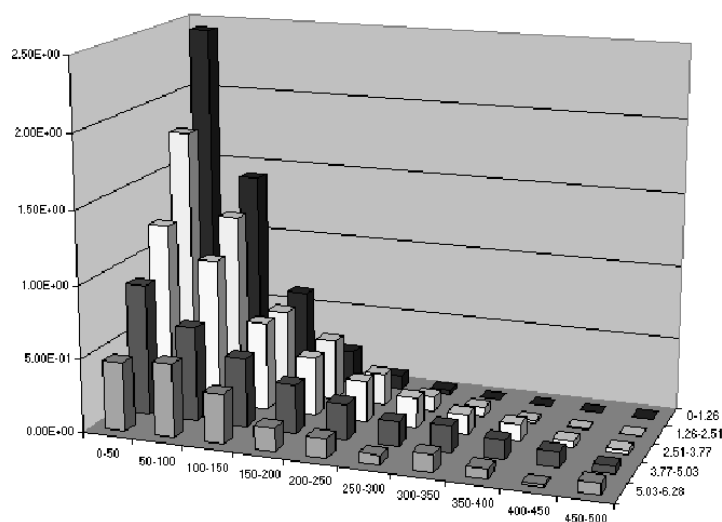


Fig. 2. Neutron flux through steel cladding between the 2 innermost regions; neutron energy range between 0 and 500 MeV, solid angle between 0 and 2π (reference target)

average energy. An explanation has to be given about statement c) above; this is not in contrast with what said before, that is FLUKA writes only information for neutrons with energy below 20 MeV: actually this is true unless neutrons escape the outermost border1. It is worth noting that CMCS, when dealing with a neutron having energy higher than 20 MeV, for which no cross-section data are available, assigns to it cross-sections related to 20 MeV anyway. An investigation on the FLUKA written files shows that all neutrons with energy higher than 20 MeV remain within the outermost target border and they all move towards the outside. In Tab. 1 data a), b), c), d) listed above are reported for the reference target (large target) and the small target configurations; data a) and b) can be roughly compared with Fig. 2.

New FLUKA calculations have been performed where the outermost border is substantially enlarged to permit more (hopefully all) neutrons to reach energies lower than 20 MeV. Actually the outermost border is doubled in the reference target and increased of the 50% in the small one. The new a), b), c), d) data are reported in Tab. 2. It can be seen that the percentage of neutrons with energy lower than 20 MeV is greatly decreased.

4 CMCS Criticality Calculations

FLUKA calculations with the approach outlined before produced neutron source files for the subsequent utilization by CMCS. To evaluate the influence on CMCS criticality calculations of such an approach, these calculations have been repeated

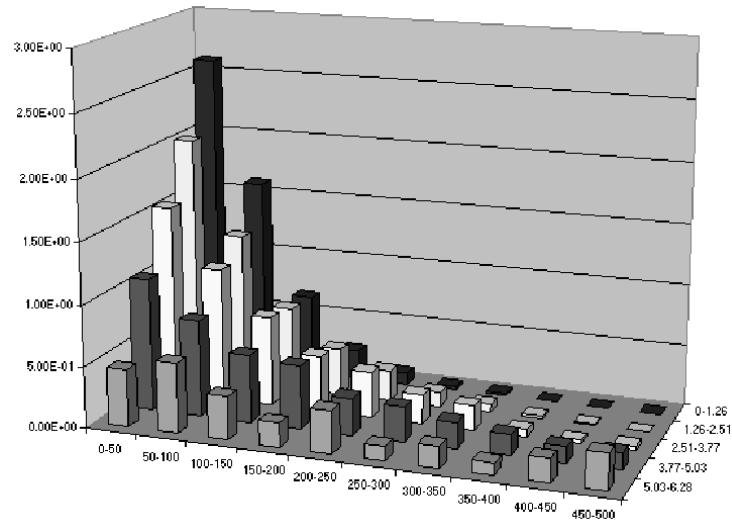


Fig. 3. Neutron flux through steel cladding between the 2 innermost regions; neutron energy range between 0 and 500 MeV, solid angle between 0 and 2π (smaller target)

Table 1. Neutrons behaviour from old FLUKA calculations

Items	Reference target configuration	Small target configuration
a ncore (%) ^a	4.70	5.58
b average E (MeV)	16.8	17.6
c total > 20 MeV (%)	1.09	1.42
d average E (MeV)	80.9	94.6

^a all neutrons produced outside a radius = 0.3 m and at elevation between +0.435 and -0.435 m (elevations of the active length).

with the input files of the neutron source coming from the new FLUKA calculations mentioned above. In Tab. 3 the neutron multiplication factor (k_{source} , which is in principle different from k_{eff} in presence of an external spallation source [3]) for both target configurations and with the two modelizations described before, that is the “old model” and the “new model”, is shown. A good overlapping in k_{source} ranges, due to the existing uncertainties, can be seen, even if a weak tendency to an increase can be envisaged.

Table 2. Neutrons behaviour from new (“enlarged”) FLUKA calculations

Items	Reference target configuration	Small target configuration
a ncore (%) ^a	7.48	8.22
b average E (MeV)	3.66	5.74
c total > 20 MeV (%)	0.14	0.45
d average E (MeV)	78.4	87.3

^a all neutrons produced outside a radius = 0.3 m and at elevation between +0.435 and -0.435 m (elevations of the active length).

Table 3. Neutrons behaviour from new (“enlarged”) FLUKA calculations

Cases	Reference target configuration k-source	Small target configuration k-source
old model	0.97600	0.97464
	+0.00142 -0.00161	+0.00151 -0.00172
new model	0.97786	0.97521
	+0.00200 -0.00244	+0.00115 -0.00127

5 Summary and Conclusions

The adequacy of the approach of modeling in the FLUKA ADS calculations only the target region and a portion of the coolant outside it in order to have a good description of the neutron source for the subsequent neutron transport calculations performed by CMCS is here discussed. In particular the impact on the CMCS criticality calculations has been investigated.

FLUKA-CMCS joint calculations show that there is a negligible effect (that is within the related standard deviation) on k_{source} , at least when the percentage of neutrons which escape the outermost border of the simulated geometrical domain (that is those ones with energy higher than 20 MeV) is of the order of 1% or less. Apparently two effects are counterbalancing. If the outermost border is enlarged we get more neutrons in the core region, but their average energy is reduced: so we gain more fissions because we have more neutrons but we loose fissions because the spectrum is softer. It has however to be underlined that the latter statement is true when the core fuel composition is such that a hard spectrum is effective, as it is the case in the ANSALDO ADS Demonstration Facility design; care has to be exercised if the fuel composition is such to be more effective for a thermal spectrum.

A warning can be anyway suggested by the above evaluations: at least in principle the neutron source calculated by FLUKA for CMCS calculations should not contain any neutron with energy higher than 20 MeV, unless the percentage of these neutrons is very little (say about 1%).

References

1. *Study of behaviour of neutrons produced by protons spallation by FLUKA – MC²: theory and experimental comparisons*, Ansaldo document 1EA 4000 TRIX 0005 000 Rev. 0
2. F. Carminati, Y. Kadi: *EA MonteCarlo benchmark*, CERN/AT/ET,19/3/97
3. C. Rubbia: *An analytical approach to the Energy Amplifier*, CERN/AT/ET 94-03

Simulation of Nucleus–Nucleus Interactions in the Framework of the FRITIOF Model

A. Polanski¹, A.S. Galoyan², and V.V. Uzhinskii²

¹ Soltan Institute for Nuclear Studies, 05-400 Swierk, Poland

² Joint Institute for Nuclear Research, 141980 Dubna, Moscow region, Russia

Abstract. The cascade-evaporation model overestimates the multiplicity of the produced mesons in nucleus-nucleus interactions. In order to overcome the problem, it is proposed to use the FRITIOF model adapted to low energies in a combination with the reggeon theory inspired model of nuclear destruction. It is shown that the combination allows one to reproduce satisfactory the meson and baryon yields in the nucleus-nucleus collisions.

There are many models for simulation of hadron-nucleus interactions at intermediate and high energies. Most of them are using the ideas of the cascade-evaporation model (CEM) (see [1–6]). First versions of the model considered only nucleons and mesons cascading, and reached a good description of the interactions. The best results in this direction were obtained by S. Mashnik [7]. Application of the models for simulation of nucleus-nucleus interactions shown that they gave satisfactory description of the nucleon yield, but overestimated the meson production. One of the possible solution is inclusion of meson and baryon resonances production.

Many authors tried to take the resonances into account, and had, as a rule, decreasing meson and **baryon** production. It is natural, because a reduction of the particle multiplicity leads to a weak cascading. So, the problem of a self-consistent description of the baryon and meson yields appeared.

Note, that in the models the nuclear destruction mechanism and the calculation procedure of the residual nucleus excitation energy have not been changed. Maybe, it is a reason of the difficulty. In our paper we consider a combination of the FRITIOF [8,9] model which take into account the resonance production, and the reggeon theory inspired model of the nuclear destruction [10,11].

The FRITIOF code [9] that is a program of Monte Carlo simulation of the inelastic hadron-hadron, hadron-nucleus and nucleus-nucleus interactions is very popular in high energy experimental physics. It is explained by its access, its easy of usage, its physical ideas simplicity and a defined beauty of the code by itself.

The model assumes that an excitation of hadrons into states with continuous mass spectra take place in inelastic hadron-hadron collisions

$$a + b \longrightarrow a' + b', \quad (1)$$

where a' and b' are the excited hadrons a and b . The excited hadrons can suffer additional collisions with intra-nuclear nucleons in the case of the hadron-nucleus

or nucleus-nucleus interactions, and go into more excited state, or de-excite. The probabilities of the multiple collisions are calculated within the framework of the Glauber approach [12–17]. Usually, the inelastic collisions are considered only [17]. In order to reproduce the baryon yield we introduce elastic re-scattering too.

The excited hadrons are characterized by masses. The algorithm for the sampling of the masses is given in [18]. The excited hadrons are considered as quark strings, and a corresponding quark model [19,20] is applied for simulation of its de-excitations or fragmentation.

It is assumed that the FRITIOF program can not be used at the relatively low energies because the picture about the creation and decay of the quark strings is not valid. An attempt to compel the program to operate at energies below 5-10 GeV/nucleon for AA-interactions is a failure as a rule. Though an analysis of the code operation shows that the program cycles due to too simple-hearted interpretation of the Fermi-motion of the nucleons. The change of the Fermi-motion simulation algorithm [18] allows one to decrease the lower limit of the model application region.

For application of the model at moderate energies it is needed to correct the algorithm of the fragmentation of the quark string with small masses, because the excited hadrons have small masses in this case. To do this, we turned to the experimental data on neutron-proton interactions at momentum 1.25 – 5.1 GeV/c [21].

In Fig. 1 the experimental and calculated rapidity distributions of π^- -mesons in np -interactions are presented. As seen, the distributions calculated according to the original version of the model (see dashed curves) have two-bump structure especially at lower energies. We have clarified that this is caused due to anisotropic fragmentation of the strings with small masses. Therefore, we have introduced an isotropic decay of strings with masses lower than 1.7 GeV. We have changed the minimal mass of the excited baryon state from 1.2 GeV to 1.1 GeV after analysis of the transverse momentum distributions of the π^- -mesons in np -interactions. All of these allowed us to describe quite well the meson and proton rapidity distributions (see Figs. 1 and 2).

One of the disadvantages of the FRITIOF code is an omission of the slow particle cascading into the nuclei. Usually under the “cascading” one understands what to be the standard intra-nuclear cascade scenario (see, e.g., [1]), which neglects the quantum mechanical effects. Quantum mechanical description of particles cascading in nuclei can be achieved within the framework of the Regge theory. According to Regge approach [22] a consideration of the cascade interactions necessitate a calculation of the yields of the so-called enhanced diagrams to the elastic scattering amplitude. Using the procedure for the calculation proposed in [23] and Abramovski-Gribov-Kancheli cutting rules [24] one can obtain the positive defined cross-section of the inelastic process. At first glance this returns one to the classical cascade picture of the interactions. There is, however, essential difference. The cascade model assumes that the cascade is developed in three-dimensional space of target nucleus. According to the Regge approach [10]

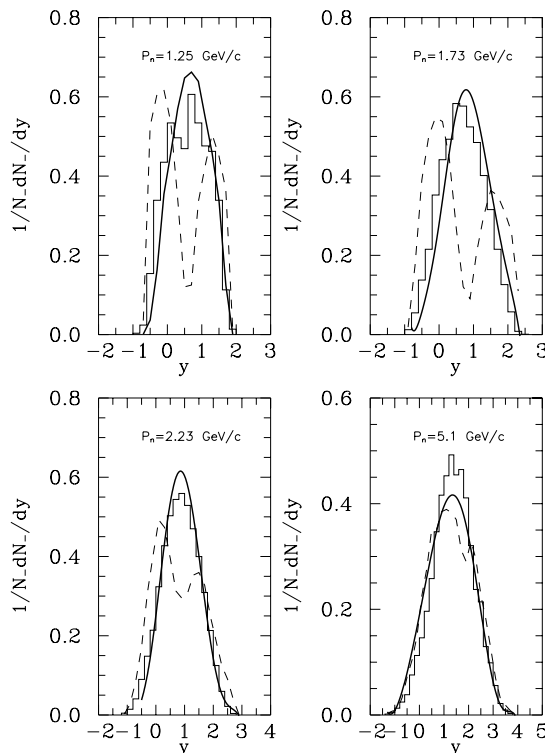


Fig. 1. π^- -meson rapidity distributions in np -interactions. Histograms are the experimental data. The solid and dashed curves are the standard and modified FRITIOF calculations, respectively

“cascade” of the Regge exchanges occurs in two-dimensional space of projected radius-vectors of nucleons on a plane perpendicular to momentum of projectile particle (on a plane of impact parameter), with a “cascade power” independent of multiplicity of produced particles and defined by the Regge vertex constants and the size of nucleus. The algorithm for the simulation of the nuclear destruction in this approach is presented in [10,11]. We have used the following values of the model parameters:

$$C_{nd} = 0.2, \quad r_{cnd}^2 = 1 \text{ (fm}^2\text{)}. \quad (2)$$

In Fig. 3 π^- -meson and proton rapidity distributions in different nucleus-nucleus interactions at the momentum 4.2 GeV/c/nucleon are presented. They were calculated with a help of the modified FRITIOF model and the cascade-evaporation model [25]. As seen, the models give the close results for the dd -interactions. Because in this case the effect of the cascading is small, we conclude that CEM describes well NN -collisions (the CEM code used by us does not allow one a direct simulation of NN -interactions).

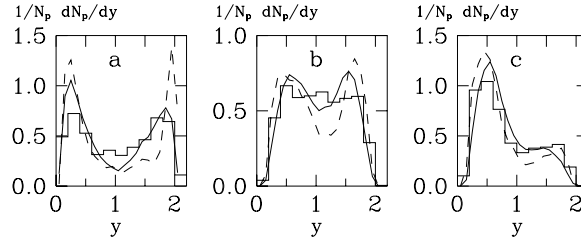


Fig. 2. Proton rapidity distributions in a) $np \rightarrow pp\pi^-$, b) $np \rightarrow pp\pi^-\pi^0$, c) $np \rightarrow np\pi^+\pi^-$ reactions. Histograms are the experimental data. The solid and dashed curves are the standard and modified FRITIOF calculations, respectively

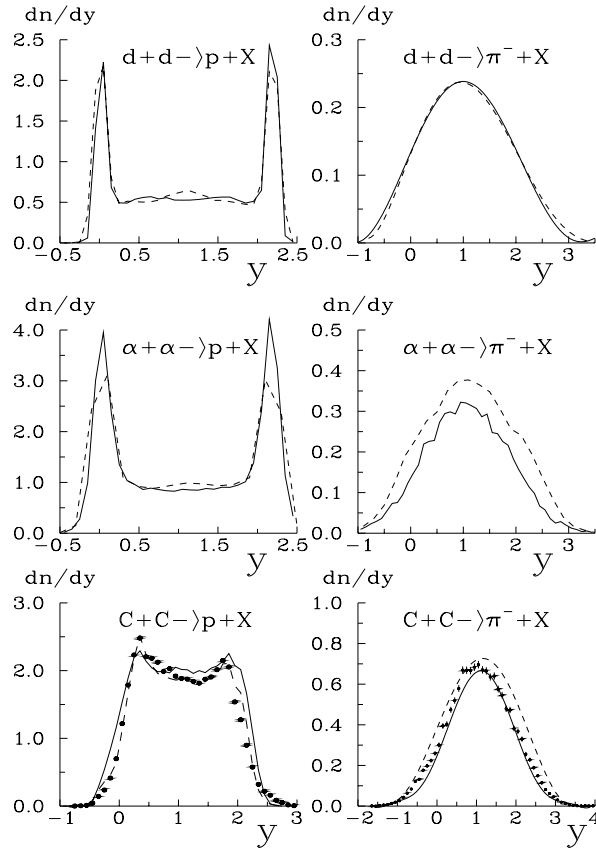


Fig. 3. Proton and π^- -meson rapidity distributions in nucleus-nucleus interactions. Points are the experimental data [26]. The solid and dashed curves are CEM and the modified FRITIOF calculations, respectively

The cascading plays essential role in $\alpha\alpha$ -interactions, and, as a results, we have the different predictions for π^- -meson distributions. As it was expected, the accounting of the resonances in the FRITIOF model leads to low multiplicity of the meson. The enhanced yield of the mesons in CEM becomes more pronounced in the CC -interactions. As it was said above, CEM overestimates the meson production.

As seen in Fig. 3, we have reached a coincidence of the model predictions for proton production due to tuning of the reggeon nuclear destruction model parameters. At the same time we have a good description of the meson yield.

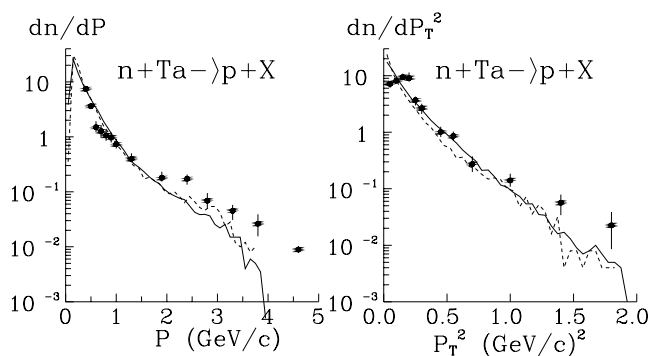


Fig. 4. Proton distributions in nTa interactions. Points are the experimental data [27]. The solid and dashed curves are CEM and the modified FRITIOF calculations, respectively

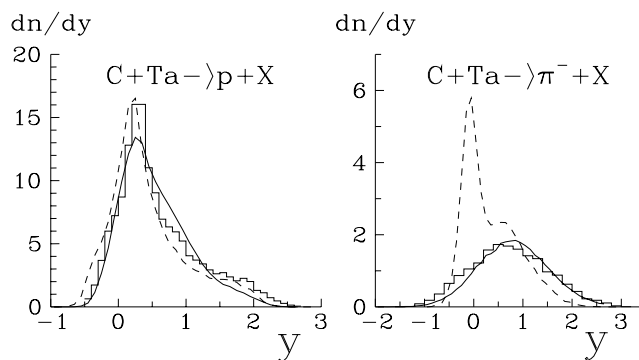


Fig. 5. Proton and π^- -meson rapidity distributions in CTa -interactions. Points are the experimental data [28]. The solid and dashed curves are CEM and the modified FRITIOF calculations, respectively

The same situation we have for heavy target nuclei. In Figs. 4 and 5 we present the modified FRITIOF model and CEM calculations for $n + Ta$ and $C + Ta$ interactions at the momentum 4.2 GeV/c/nucleon. As seen, the model

predictions on the proton production coincide. Though there are a big difference of the calculation results for the meson distributions. The results of the modified FRITIOF model are more close to the experimental data. The combined model can be used for a self-consistent description of the nucleus-nucleus interactions.

The authors are thankful to Prof. V.S. Barashenkov, Dr. Zh.Zh. Musulmanbekov, and Dr. B.F. Kostenko for useful discussions. One of the authors (V.V.U.) is thankful to Russian Foundation for Basic Research (project No. 00-01-00307) for the particular financial support.

References

1. V.S. Barashenkov, V.D. Toneev: *Interaction of high energy particles and atomic nuclei with nuclei*, Moscow, Atomizdat, 1972
2. N.W. Bertini et al.: Phys. Rev. C **9**, 522 (1974)
3. N.W. Bertini et al.: Phys. Rev. C **14**, 590 (1976)
4. J.P. Bondorf et al.: Phys. Lett. B **65**, 217 (1976)
5. J.P. Bondorf et al.: Zeit. Phys. A **279**, 385 (1976)
6. V.D. Toneev, K.K. Gudima: Nucl. Phys. A **400**, (1983) 173
7. S.G. Mashnik: In *Proceedings of a Specialists Meeting - Intermediate Energy Nuclear Data: Models and Codes*. Paris, 1994, P.107
8. B. Andersson et al.: Nucl. Phys. B **281**, 289 (1987)
9. B. Nilsson-Almqvist, E. Stenlund: Comp. Phys. Comm. **43**, 387 (1987)
10. Kh.El-Waged, V.V.Uzhinskii: Yad. Fiz. **60**, 925 (1997)
11. V.V. Uzhinskii, Kh.Abdel-Waged, A.S.Pak, A.Polanski: JINR commun., 1995, E2-95-296, Dubna
12. R.J. Glauber: In: *Lectures in Theoretical Physics*. Ed. by W.E.Brittin et al., v. **1** (Interscience Publishers, N.Y. 1959)
13. R.J. Glauber: In: *Proc. of the 2nd Int. Conf. on High Energy Physics and Nuclear structure, (Rehovoth, 1967)* Ed. G.A.Alexander, North-Holland, Amsterdam, 1967
14. V. Franco: Phys. Rev. **175**, 1376 (1968)
15. W. Czyz, L.C. Maximon: Ann. of Phys. (N.Y.) **52**, 59 (1969)
16. A. Bialas et al.: Nucl. Phys. B **111**, 461 (1976)
17. S.Yu. Shmakov, V.V. Uzhinski, A.M. Zadorojny: Comp. Phys. Commun. **54**, 125 (1989)
18. M.I. Adamovich et al. (EMU-01 Collaboration): Zeit. für Phys. A **358**, 337 (1997)
19. T. Sjöstrand: Comp. Phys. Comm. **39**, 347 (1986)
20. T. Sjöstrand, M. Bengtsson: Comp. Phys. Comm. **43**, 367 (1987)
21. A. Abdivaliev et al.: JINR preprint, P1-82-507, Dubna, 1982
22. K.G. Boreskov, A.B. Kaidalov, S.T. Kiselev, N.Ya. Smorodinskaya: Yad. Fiz. **53**, 569 (1991); Sov. J. Nucl. Phys. **53**, 569 (1991)
23. A.B. Kaidalov, L.A. Ponomarev, K.A. Ter-Martirosyan: Yad. Fiz. **44**, 722 (1986); Sov. J. Nucl. Phys. **44**, 722 (1986)
24. V.A. Abramovski, V.N. Gribov, O.V. Kancheli: Sov. J. Nucl. Phys. **18**, 308 (1974)
25. V.S. Barashenkov, F.G. Zhereg, Zh. Zh. Musulmanbekov: JINR preprint, P2-83-117, Dubna, 1983
26. Ts. Baatar et al.: JINR preprint, P1-99-45, Dubna, 1999 (will be published in Yad. Fiz.)
27. R.N. Bekmirzaev et al.: Yad. Fiz. **49**, 488 (1989)
28. R.N. Bekmirzaev et al.: Yad. Fiz. **58**, 1822 (1995)

Monte Carlo Simulation of the Neutron Time-of-Flight Facility at CERN

V. Vlachoudis¹, C. Borcea^{1,2}, S. Buono³, P. Cennini¹, A. Ferrari^{1,4}, Y. Kadi¹, V. Lacoste¹, and E. Radermacher¹

¹ CERN, Switzerland

² IFIN-HH, PO Box MG-6, Bucharest-Magurele, Romania

³ CRS4, Cagliari, Italy

⁴ INFN Milan, Italy

1 n_TOF Facility

The neutron Time of Flight (n_TOF) facility at CERN is a source of neutrons produced by spallation of 20 GeV/c protons onto a solid lead target. The outstanding characteristics of this facility (very high intensity, 200 m flight path, wide spectral function) make it an extremely useful tool that provides the necessary data for the design and understanding of Accelerator Driven Systems [1–3]. The proton beam is delivered by the CERN-PS [4] which is capable of providing one to four bunches with an intensity of $7 \cdot 10^{12}$ protons per bunch, within a 14.4 s supercycle, at a momentum of 20 GeV/c.

Following an overall optimisation [2], the spallation target resulted to be a lead block of 40 cm length and 80 cm diameter, followed by a 5 cm thick water moderator. The neutron emission takes place at an angle of 10° , with respect to the proton beam direction [5]. The actual target is a lead block of $80 \times 80 \times 60 \text{ cm}^3$, except in the spallation area where a volume of $30 \times 55 \times 20 \text{ cm}^3$ is removed to have the nominal design dimension of 40 cm.

Detailed calculations [5] have shown that the power dissipation of the incident beam increases the lead temperature and therefore requires cooling. In the extreme conditions (4 bunches per 14.4 s) the power deposited in the target is about 3 kW and after one month irradiation time, the lead activity will reach 3200 Ci. Correspondingly, the maximum dose rate in contact after one day cooling will be of the order of 25 Sv/h.

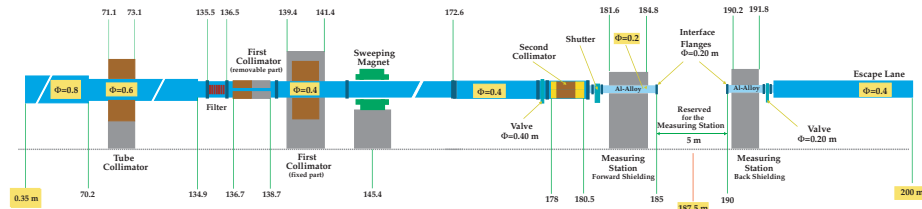


Fig. 1. TOF tube sections up to the end of the TT2A tunnel (200 m)

The TOF tube is separated from the water moderator by a 1.6 mm thick aluminum window and ends where it touches the sloped floor of the TT2A tunnel (1.18% gradient), allowing a time of flight length of 200 m. The vacuum inside the tube is about 1 mbar. The TOF tube is made up of four sectors, the first one, closest to the target is made of aluminum alloy whereas the others are made of stainless steel [5]. Two collimators will be installed to reduce the radius of the neutron beam. The first one, 1 m iron + 1 m concrete with an inner diameter of 11 cm, will be located at 136.7 m. The second one, consisting of 50 cm of 5% borated polyethylene, 125 cm of iron and 75 cm of borated polyethylene will be placed at 178 m; its inner diameter will be of 18 mm (Fig. 1).

In spite of the 10° angle between the neutron tube and the proton beam, some charged particles will remain and contaminate the neutron beam. A 2 m long dipole magnet of 1.5 Tm will be used to sweep away these unwanted secondary particles.

2 Monte Carlo Calculations

Simulating geometries like the n-TOF tunnel, where the flight path is as large as ~ 200 m, and the imposed background conditions are of the order of 10^{-6} in relative units, is a very difficult and time consuming task. The solid angle is so small that only one neutron out of $\sim 10^7$, emerging from the lead target, will finally reach the detector station at the end of the neutron tube. Moreover, the call for low background implies the use of heavy shielding.

For these reasons, it was decided to divide the problem into several small and discrete steps. The first step was the Monte Carlo simulation of the hadronic interactions of the proton beam with the lead target and the subsequent production of particle distributions entering the neutron tube. In this stage, only the geometry of the lead target, water moderator and the nearby materials were taken into account. The lead used for the target was of high purity (99.99%) with

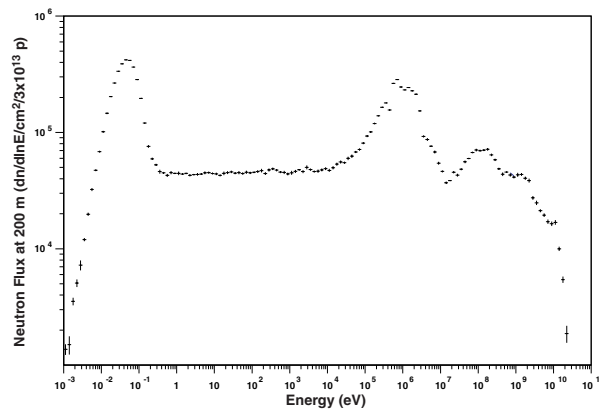


Fig. 2. Neutron flux spectrum at 200 m

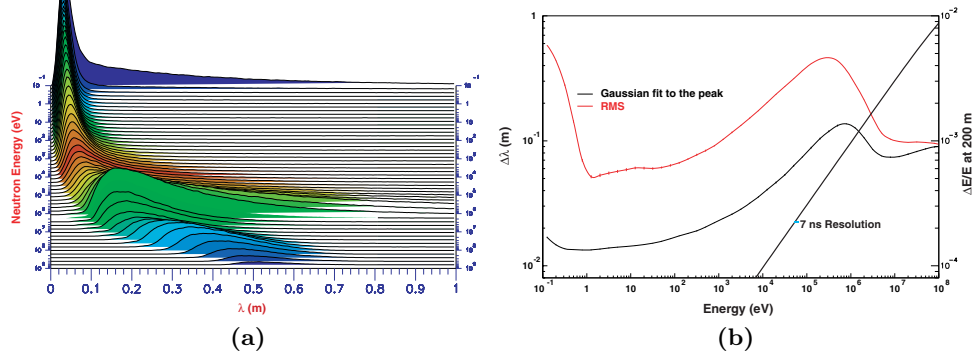


Fig. 3. **a)** Monte Carlo simulation of the equivalent neutron path inside the lead spallation target followed by a 5 cm hydrogen rich moderator (water), evaluated at the energy of observation; **b)** energy resolution at 200 m

known concentration levels of 60 elements. The hadronic interactions and the propagation of charged particles, prompt photons and neutrons down to 20 MeV were simulated with *FLUKA-99* [6]. *FLUKA* utilizes the multigroup approach for transporting neutrons with kinetic energies below 20 MeV, averaging the effect of resonances. Therefore, detailed Monte Carlo simulations using point-wise neutron cross sections [7] were carried out with the use of the *EA-MC* neutron transport code, that was created in the frame of the Energy Amplifier project [8]. This code was tested and validated in the *FEAT* [9] and *TARC* (PS-211) [10] experiments at CERN. The neutron flux expected at 200 m is shown in Fig. 2. The thermal neutrons will follow a parabolic trajectory due to the gravitational field and they will be eliminated by the neutron tube.

The energy resolution has been estimated using the relation between energy and the equivalent neutron path λ [1] $\Delta E/E = \frac{2\Delta\lambda}{\lambda+L}$, where $\lambda = v \times t$ is the equivalent neutron path evaluated when the neutron is entering the vacuum tube; v is the neutron velocity, t is the time elapsed since the impact of the proton beam on the lead target, and L is the length of the time of flight tube. Figure 3a shows the Monte Carlo distribution of the equivalent neutron path λ when entering the neutron tube, evaluated at the energy of observation. The distributions are rather narrow for energies $\leq 10^4$ eV, $\Delta\lambda \sim 1.7$ cm. For higher energies, the isoethargic model breaks down due to the onset of the inelastic channels. The $\Delta\lambda$ initially increases, and then decreases again, determining the behaviour of the energy resolution (Fig. 3b).

The 20 GeV/c proton beam interacting with the lead target is also a source of many other charged and neutral particles [11]. The momentum distribution of the charged particles is shown in Fig. 4a. All the particles with momentum below 10 GeV/c will be eliminated by the sweeping magnet.

The photons emerging from the target (Fig. 4b) can be clearly separated into two groups [11]. A “fast” component, which results from the spallation process,

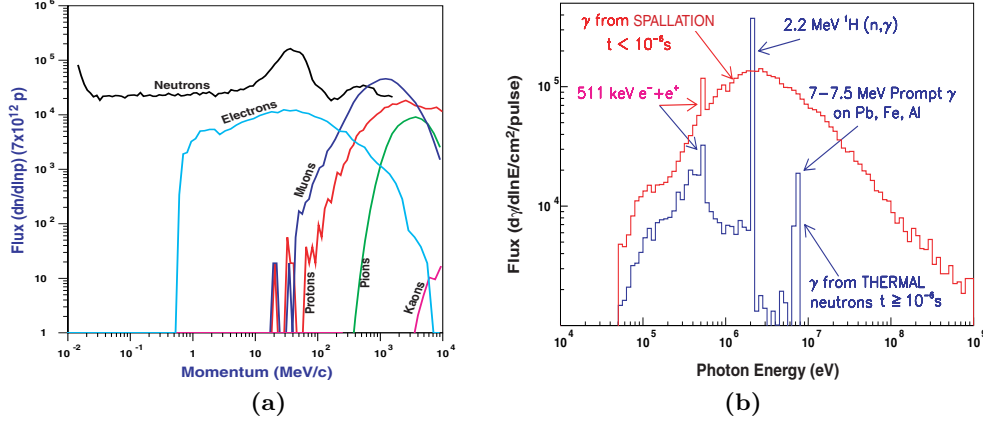


Fig. 4. **a)** Fluxes of charged and neutral particles as a function of their momentum; the neutron flux is also given for reference. **b)** Prompt photon distribution at 200 m, contribution of both spallation and neutron captures are included

arrives at the detector station at times $t < 1 \mu\text{s}$. The second group of photons arrives at times $t > 1 \mu\text{s}$ and are mainly due to the thermal neutron captures in the elements present in the moderator and the lead target. Considering the energy distribution of these photons, 40% of the contribution is due to neutron captures on hydrogen (2.2 MeV), another 5% comes from photons with energies around 7 MeV resulting from the captures on lead, the aluminum alloy container, and the iron support. The distributions of neutrons, photons and charged particles (Fig. 4a) were parameterized in terms of position, momentum and time at the moment of their entrance in the time of flight tube. This parameterization was used as the source routine in *FLUKA* for the subsequent simulations, generating random particles with the same distributions and correlations between the parameters, but with a preference in the direction towards the measuring station, biasing the simulation to an area close to the detector station. In these simulations *the full geometry of the tunnel and neutron tube was used, translating it directly from the civil engineering plans into FLUKA geometry* [12], along with all the elements, i.e. collimators, sweeping magnet, reductions etc. This enabled a detailed evaluation of the background and the neutron profile, in the detector room and in several areas of interest (Fig. 5).

To estimate the continuous γ background, resulting from radioactive decays, we have used the activity of all the residual nuclei produced in the lead target and the surrounding materials after some time of operation of the facility. The activity (Fig. 6a) was calculated using a program part of the *FLUKA* package. Using the ENSDF database of nuclei decay modes [13], the photon energy spectrum was reconstructed from the radioactive decays (Fig. 6b), weighting the activity of each isotope, with the photons emitted from it [14]. The photon spectrum was used as the source for generating all over the lead target random

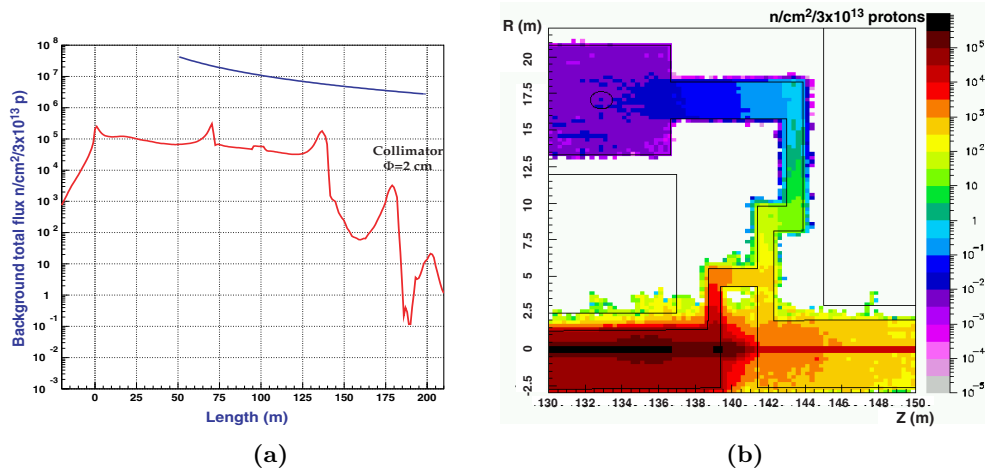


Fig. 5. **a)** Total neutron background flux in the tunnel (lower curve) and inside the neutron beam tube (upper curve) versus the flight distance, with a collimator of 2 cm in diameter (neutron capture cross-section measurements); **b)** Neutron flux in the tunnel, with the concrete labyrinth

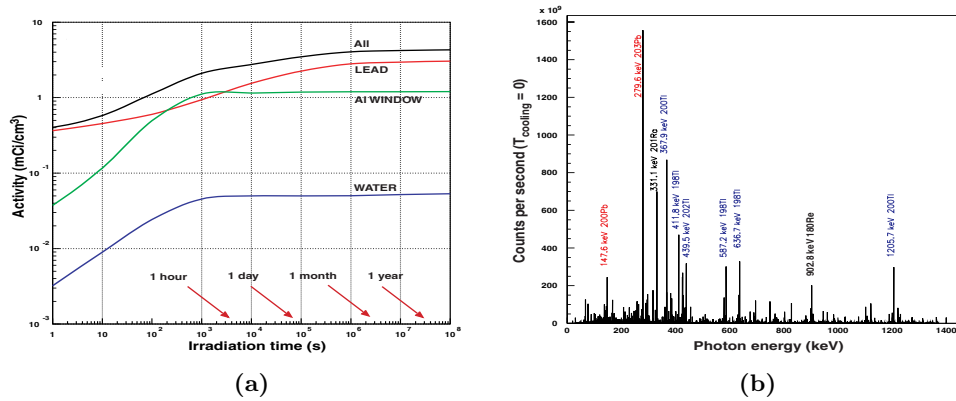


Fig. 6. **a)** Activation of the exit face of the target; **b)** Delayed photon distribution from the exit face of the target (5 cm of Pb, 5 cm of H_2O and 1.6 cm of Al)

and isotropic photons with the same energy distribution. These photons were propagated in the full detailed geometry of the tunnel using *FLUKA*, providing thus a good estimate of the background contamination at the detector station.

3 Conclusions

The n_TOF facility at the CERN-PS will offer unique features (high neutron flux and low background conditions) for precise and systematic study of neutron cross sections in a wide energy domain. Its design is the result of intensive simulation studies performed with different Monte Carlo codes and using advanced computing techniques. These studies helped us in optimising the physical parameters of the installation and calculating its safety characteristics.

References

1. C. Rubbia et al.: *A High Resolution Spallation Driven Facility at the CERN-PS to measure neutron cross sections in the interval from 1 eV to 250 MeV*, CERN/LHC/98-02 (EET), 30 May 2000
2. C. Rubbia et al.: *A High Resolution Spallation Driven Facility at the CERN-PS to measure neutron cross sections in the interval from 1 eV to 250 MeV. A relative performance assessment*, CERN/LHC/98-02 (EET)-Add. 1, 15 June 2000
3. The TOF collaboration: *Proposal for a Neutron Time of Flight Facility*, CERN/SPSC 99-8, 17 Mars 1999
4. R. Billinge: *The CERN PS Complex: A Multipurpose Particle Source*, Proc. of XIIth Intl. Conf. on High Energy Acc., 1983
5. S. Andriamonje et al.: *Neutron TOF Facility (PS 213) Technical Design Report*, CERN/INTC/2000-004, 11 Feb. 2000
6. A. Fassó et al.: in *Intermediate Energy Nuclear Data: Models and Codes, Proceedings of a Specialists Meeting, Issy les Moulineaux (France) 30 May – 1-June 1994*, p.271, published by OECD, 1994 and references therein.
7. ENDF/B-VI, JENDL-3.2, JEF-2.2, EAF-4.2, BROND-2, OECD/NEA Data Bank, Issy-Les-Moulineaux, Paris, France, 1994
8. C. Rubbia et al.: *Conceptual Design of a Fast Neutron Operated High Power Energy Amplifier*, CERN/AT/95-44 (ET), 29 Sept. 1995
9. S. Andriamonje et al: Physics Letters B **348**, 697 (1995)
10. H. Arnould et al.: Physics Letters B **458**, 167 (1999)
11. V. Vlachoudis et al.: *Particle distributions, entering the vacuum tube, from an $80 \times 80 \times 60 \text{ cm}^3$ lead target*, CERN/SL-Note-2000-029 EET, 30 Mars 2000
12. http://www.cern.ch/CERN/Divisions/SL/EET/TOF/Welcome/TOF_TB.welcome.html
13. J.K. Tuli: *Evaluated Nuclear Structure Data File - A Manual for Preparation of Data Sets*; T.W. Burrows: *The program RADLIST* National Nuclear Data Center, Brookhaven National Laboratory, Upton, NY 11973, 29 Feb. 1988
14. V. Lacoste et al.: *Activation Studies and Radiation Safety for the n_TOF Experiment* OECD/NEA SATIF-5, 18-21 Jul. 2000 Paris

Systematic Uncertainties on the Determination of the top Mass at the LHC from Soft Fragmentation Effects

M. David^{1,2}, A. Maio¹, A. de Angelis², and A. Gomes¹

¹ LIP and Faculty of Sciences Lisbon, Portugal

² University of Udine, Italy

Abstract. The mass of the *top* quark is one of the Standard Model fundamental parameters that will be measured with high accuracy at the LHC. About 8 million $t\bar{t}$ pairs per year are expected to be produced in the initial (low luminosity) phase; the error on the determination of M_{top} will thus be dominated by systematics.

In this report, the contribution to the systematic error from the Monte-Carlo modelling is evaluated by comparing the production and decay of $t\bar{t}$ pairs simulated using the Pythia, Herwig and Isajet generators.

1 Introduction

ATLAS is a general purpose experiment for the Large Hadron Collider (LHC). The LHC is a *proton – proton* collider with a centre of mass energy of 14 TeV and design luminosity of $10^{34} \text{ cm}^{-2}\text{s}^{-1}$. One of the goals of the experiments at the LHC is the precision measurement of the mass of the top quark (M_{top}), a fundamental parameter of the Standard Model (SM). Radiative corrections relate M_{top} and M_W to the mass of the SM Higgs boson. The present error on the direct measurement of the W mass is $38 \text{ MeV}/c^2$ and the error on the *top* mass is $5.1 \text{ GeV}/c^2$ [1]. Assuming that M_W can be measured at $\pm 15 \text{ MeV}/c^2$ [2] and from the current theoretical uncertainties, a determination of $\delta M_{top} \leq \pm 2 \text{ GeV}/c^2$ would be required not to impair on the determination of the Higgs mass. Assuming the Higgs discovery prior to LHC or in the first year of LHC running, those measurements would serve as consistency checks of the model. Moreover, models beyond the SM, such as top-bottom-tau Yukawa coupling unification in a super-symmetric SO(10) GUT [3], would profit from a precision of the order $\delta M_{top} \simeq \pm 1 \text{ GeV}/c^2$.

With the large rate of production of the top quark the LHC [4], the uncertainty in the measurement of M_{top} will be dominated by the systematic errors [2]. These studies resulted in an uncertainty of $2 \text{ GeV}/c^2$, for the case when the top mass is reconstructed in the semi-leptonic channel ($t\bar{t} \rightarrow W^+bW^-\bar{b} \rightarrow l^+\nu bj\bar{j}\bar{b}$).

The QCD Monte Carlo (MC) generators used in those analysis are based on a large number of model-dependent assumptions and parameters. Modifying one of those parameters, does not necessarily give a good estimate of the deviation between the simulated process and the real physics process. The direct comparison of different Monte Carlo generators can give additional hints on the contribution of the systematic uncertainties involved in the measurements.

The simulations were done as follows: the production and decay of $t\bar{t}$ pairs are generated with Pythia [5], Herwig [6] and Isajet [7]; the decay products are the input to the ATLFAST [8] package, a reconstruction code with a parameterization of the ATLAS detector based on detailed (full) simulation and test-beam results [2].

2 Study of M_{top} and M_W

2.1 Monte Carlo Samples and Event Selection

In this section, the results comparing three MC generators, Herwig 6.1, Pythia 6.115 and Isajet 7.49, are presented. The input values are $M_{top} = 175 \text{ GeV}/c^2$ and $M_W = 80.33 \text{ GeV}/c^2$ and the semi-leptonic final state is used:

$$t\bar{t} \rightarrow W^+ b W^- \bar{b} \rightarrow l^+ \nu b j j \bar{b}$$

This topology has four jets (two of which are b -jets), one lepton (μ in the present case) and missing transverse energy due to the ν . The CTEQ4 \overline{MS} parton distribution function set was used [9]. The jets are reconstructed with a fixed cone algorithm with $\Delta R = 0.4$. It is assumed that the detector is properly calibrated (see [2] for details). The same treatment and analysis procedure is used for the three physics generators.

Events are selected using the following topological and kinematical cuts:

- At least one μ with $P_T^\mu \geq 20 \text{ GeV}/c$ and $|\eta^\mu| \leq 2.5$.
- $\cancel{E}_T \geq 20 \text{ GeV}/c$.
- Four or more 4 jets with $P_T^j \geq 40 \text{ GeV}/c$ and $|\eta^j| \leq 2.5$, from which at least 2 b -tagged.

These cuts were optimised to reduce the physics background, and to achieve a S/B ratio of about 65 [2]. Four million events were generated with each MC. The fraction of events after selection is around 12% for the three MC's.

2.2 Comparison Between Simulations

Figure 1 shows the light-jet¹ multiplicity (N_{jet}) after the selection cuts, for the three generators. The shape of the histograms are similar for the three MC, but Isajet has a higher multiplicity than Pythia and Herwig for $N_{jet} \geq 5$, indicating that Isajet produces more gluon radiation than the other generators. No difference was observed between Pythia and Herwig in the spectra of several kinematic variables studied in the event, but the light-jets P_T spectrum in Isajet is slightly harder than in Pythia and Herwig.

The W and top masses were reconstructed using two algorithms:

¹ We call light-jets the jets originated from (u,d,s,c) quarks and from gluons.

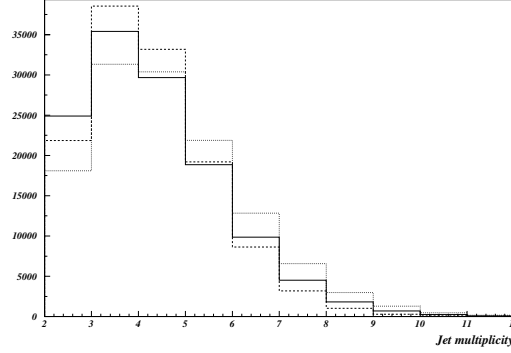


Fig. 1. Light-jet multiplicity after selection cuts. Pythia – full line. Herwig – dashed line. Isajet – dotted line

1. The $W \rightarrow jj$ is reconstructed from the pair of light-jets with an invariant mass closest to M_W . The top candidate is formed by adding to the W candidates within a window of $|M_{jj} - M_W| \leq 20 \text{ GeV}/c^2$, the b -tagged jet which results in the highest P_T^{top} [2].
2. The reconstruction of an invariant jj mass that best matches the W mass, biases M_{jj} towards M_W . So, an alternative method to reconstruct the W is proposed. The pair of highest P_T light-jets in the event, is used to reconstruct the W . The top is reconstructed with the b -jet which makes the highest P_T^{top} . Events still satisfy $|M_{jj} - M_W| \leq 20 \text{ GeV}/c^2$. The selection cuts are the same as in the previous section.

The P_T^W and P_T^{top} spectra for the first reconstruction algorithm are shown in Fig. 2. The W P_T spectrum is similar for the three generators; the P_T spectrum of the top is similar for Pythia and Herwig, while Isajet shows a slightly higher number of events in the P_T range of 100-200 GeV/c. Fig. 3 shows the invariant M_W spectrum and the invariant M_{top} spectrum for the three MC. No differences are observed between Pythia and Herwig, while Isajet shows larger high mass tails and the both peaks are displaced at lower values. Similar conclusions are drawn for the second reconstruction algorithm (Fig. 4).

A Gaussian fit was done to the W and top mass spectra, respectively in the ranges $\pm 7 \text{ GeV}/c^2$ and $\pm 12 \text{ GeV}/c^2$ around the mean Gaussian value. The values obtained for the mean and resolution (σ) are shown in Tab. 1 for the first reconstruction method, and in Tab. 2 for the second reconstruction method. The last two columns show the difference in the mean and resolution between Herwig and Pythia, and between Isajet and Pythia respectively (Pythia being taken as a reference).

It can be seen that, in the first algorithm, the position of the W mass peak in Isajet is $1.7 \text{ GeV}/c^2$ below Pythia and in Herwig. For these last two MC no difference in the mean nor in the resolution are observed.

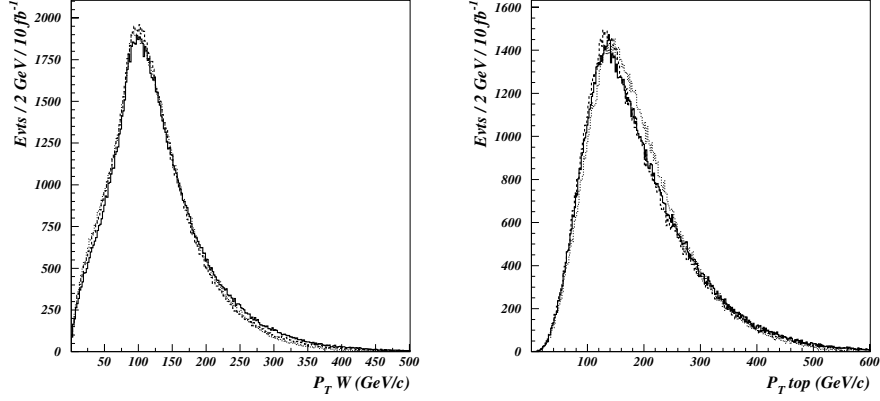


Fig. 2. P_T^W (left) and P_T^{top} (right) using the first reconstruction algorithm. Pythia – full line. Herwig – dashed line. Isajet – dotted line

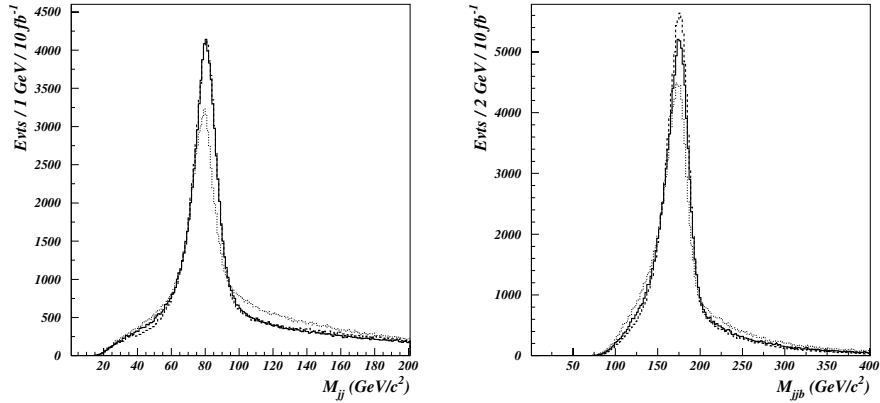


Fig. 3. Invariant mass spectra for M_{jj} (left) and $M_{j\bar{j}b}$ (right) using the first reconstruction method. Pythia – full line. Herwig – dashed line. Isajet – dotted line

A very good agreement is obtained between Pythia and Herwig also for the top mass and resolution, the difference being compatible with zero within 1σ of the statistical error from the fit. The values for the reconstructed top mass agree with the generated M_{top} value within 2σ of the statistical error from the fit, while the difference between Pythia/Herwig and Isajet is $2\text{ GeV}/c^2$.

For the second reconstruction algorithm, very good agreement (within 2σ of the statistical error) was also found between Pythia and Herwig, both in the W and top mass and resolution. The difference in the W and top mass, between Isajet and Pythia/Herwig is slightly enhanced with the second reconstruction

algorithm, ($2.5 \text{ GeV}/c^2$ for the W) compared with $1.7 \text{ GeV}/c^2$ obtained with the first algorithm.

The fact that the invariant mass reconstructed has a lower peak value in Isajet, can be partly explained by the generation of a higher amount of gluon radiation. In the high range of the W mass spectrum, the tails are larger in Isajet than in Pythia and Herwig. This is not so evident in the top mass spectrum, because events are selected only if $|M_{jj} - M_W| < 20 \text{ GeV}/c^2$, cutting a large fraction of the high mass tails.

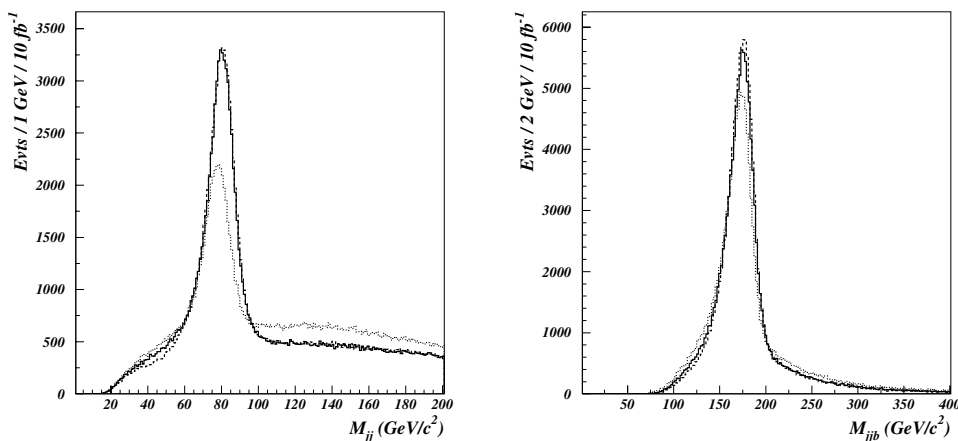


Fig. 4. Invariant mass spectrum for jj pairs (left), and for jjb (right) using the second reconstruction method. Pythia – full line. Herwig – dashed line. Isajet – dotted line

3 Conclusions

In this report, a comparison between three physics generators: Pythia 6.115, Herwig 6.1 and Isajet 7.49 all interfaced with ATLFast 2.22 was performed in the $t\bar{t}$ semi-leptonic channel $t\bar{t} \rightarrow W^+bW^-\bar{b} \rightarrow l^+\nu bj\bar{j}\bar{b}$.

The differences in the hadronization mechanisms of the three generators induce a systematic uncertainty in M_{top} of $200 \text{ MeV}/c^2$ without taking into account Isajet (see the next paragraph). This value is of the order of the expected statistical uncertainty ($100\text{--}200 \text{ MeV}/c^2$).

Taking into account the difference between Pythia (or Herwig) and Isajet, a systematic error of $1 \text{ GeV}/c^2$ or higher due to MC generators, would be obtained. This contribution alone would amount to half of the precision in the top mass ($2 \text{ GeV}/c^2$) expected from ATLAS. On the other hand, it is known from the CDF collaboration [10] that Isajet does not reproduce well the kinematics of $t\bar{t}$ events due to features of the models implemented in this generator, as the use of independent fragmentation and incoherent shower evolution.

Table 1. W and top mass and resolution obtained from different generators using the first reconstruction algorithm

	Pythia	Herwig	Isajet	Her - Pyt	Isa - Pyt
$\langle M_W \rangle$ (GeV/ c^2)	80.45 \pm 0.03	80.44 \pm 0.03	78.71 \pm 0.03	-0.01 \pm 0.04	-1.74 \pm 0.04
σ_W (GeV/ c^2)	6.56 \pm 0.05	6.65 \pm 0.05	7.14 \pm 0.07	0.09 \pm 0.07	0.58 \pm 0.09
$\langle M_{top} \rangle$ (GeV/ c^2)	174.8 \pm 0.1	174.9 \pm 0.1	172.8 \pm 0.1	0.1 \pm 0.1	-2.0 \pm 0.1
σ_{top} (GeV/ c^2)	12.4 \pm 0.1	12.2 \pm 0.1	12.8 \pm 0.2	-0.2 \pm 0.2	0.4 \pm 0.2

Table 2. W and top mass and resolution obtained from different generators using the second reconstruction algorithm.

	Pythia	Herwig	Isajet	Her - Pyt	Isa - Pyt
$\langle M_W \rangle$ (GeV/ c^2)	80.33 \pm 0.04	80.42 \pm 0.04	77.87 \pm 0.06	0.09 \pm 0.06	-2.46 \pm 0.07
σ_W (GeV/ c^2)	6.92 \pm 0.07	7.04 \pm 0.05	7.80 \pm 0.12	0.12 \pm 0.09	0.88 \pm 0.14
$\langle M_{top} \rangle$ (GeV/ c^2)	175.0 \pm 0.1	175.0 \pm 0.1	172.7 \pm 0.1	0.0 \pm 0.1	-2.3 \pm 0.1
σ_{top} (GeV/ c^2)	12.2 \pm 0.1	12.3 \pm 0.1	12.6 \pm 0.2	0.1 \pm 0.2	0.4 \pm 0.2

References

1. Preliminary report of the LEP Electro-Weak Working Group, Summer 2000, [http : //lepewwg.web.cern.ch/LEPEWWG/](http://lepewwg.web.cern.ch/LEPEWWG/)
2. 1999 CERN Workshop on Standard Model Physics (and more) at the LHC. Ed. G. Altarelli and M.L. Mangano, CERN-2000-004 25 - 26 May 1999; ATLAS Collaboration, Detector and Physics Performance Technical Design Report, CERN/LHCC/99-15
3. U. Sarid: *Precision top mass measurements vs. Yukawa unification predictions*, hep-ph/9610341
4. R. Bonciani et al.: Nucl. Phys. B **529**, 424 (1998)
5. T. Sjöstrand: Computer Physics Communications **82**, 74 (1994)
6. G. Marchesini, B.R. Webber, G. Abbiendi, I.G. Knowles, M.H. Seymour, L. Stanco: Computer Physics Communications **67**, 465 (1992)
7. F. Paige, S. Protopopescu: BNL report No. 38034, 1986 (unpublished)
8. E. Richter-Was, D. Froidevaux, L. Poggioli: *ATLFAST 2.0 a fast simulation package for ATLAS*, ATLAS Internal Note ATL-PHYS-98-131 (1998)
9. CTEQ Collaboration: MSUHEP-60426, CTEQ-604
10. F. Abe et al.: Phys. Rev. D **59**, 092001 (1999)

Author Index

- Abderrahim, A. 925
Acosta, E. 105, 147
Agostinelli, S. 543
Akhtar, P. 767
Alber, M. 217
Albers, D. 323, 395, 523
Alves, C. 311
Amako, K. 1117
Androsenko, P.A. 675, 871
Aoust, Th. 779, 925
Aoyama, T. 737
Apostolakis, J. 1117
Arce, P. 503
Armbruster, P. 1097
Armishaw, M. 637, 827
Arráns, R. 211, 329, 555, 561, 565
Artaud, J.-L. 413, 419
Arzamendi, S. 473
Asai, M. 1117
Asano, K. 785, 877
Asenjo, J. 147
Azeredo, A. 345

Ballesteros, L. 517
Ban, S. 1139
Baraldi, C. 75
Barashenkov, V. 803
Barradas, N.P. 919, 1105
Batistoni, P. 865
Battisti, P. 489
Bay, X. 703
Beeckmans de West-Meerbeeck, A. 779
Benassi, M. 455
Benedito, E. 105, 147
Benlliure, J. 1097
Berberan-Santos, M.N. 577
Bernal 211, 329
Bernas, M. 1097
Bielajew, A.F. 1

Birattari, C. 1157
Bird, A. 637, 827
Birkner, M. 217
Bland, C.J. 1145
Bleuel, D.L. 833
Booth, T.E. 609, 643
Borcea, C. 1175
Borisov, N.M. 181, 193, 443
Born, E. 223
Boudard, A. 1097, 1111
Briesmeister, J.F. 643
Bruzzaniti, V. 455
Bufacchi, A. 455
Buono, S. 1175
Burn, K.W. 687

Campbell, J.M. 657
Cappellaro, P. 1157
Caroli, E. 87
Carraro, L. 703
Carrasco, E. 211, 329, 555, 561, 565
Carta, M. 899
Carter, L. 815
Casnati, E. 75
Cennini, P. 1175
Cerullo, N. 449
Chabalier, B. 413, 419
Chadwick, M.B. 961, 967
Chajari, L. 703
Chany, P. 413
Chaussy, Ch. 919
Chauvie, S. 543
Chaves, A. 311
Chen, S.B. 1057
Chen, Y.S. 1057
Chiang, R.-T. 785, 877
Cirioni, L. 479
Cobut, V. 479
Coeck, M. 925

- Conde, C.A.N. 535
 Connolly, S. 637
 Corzine, R.K. 961
 Cox, L.J. 643
 Cremers, F. 323, 395, 523
 Cris, C. 223
 Crofts, H. 827
 Crotch, I. 357
 Cucinotta, F.A. 251
 Cugnon, J. 1111
 Curado da Silva, R.M. 87
 Curziom G. 449
 Czajkowski, S. 1097

 D'Andrea, M. 455
 d'Angelo, A. 899
 Díaz-Perches, R.D. 473
 Dąbrowska, J. 663
 da Silva, F.C. 345
 Daly, E. 401
 Dantas, B.M. 345
 Dapor, M. 43
 Daquino, G. 449
 Das, I.J. 199
 David, M. 1181
 de Angelis, A. 1181
 De Felice, P. 489
 de Meijer, R.J. 773, 893
 De Raedt, Ch. 779
 de Souza-Santos, D. 345
 Dexheimer, D.T. 1075
 Di Domenico, G. 75
 Dias, T.H.V.T. 535
 Difilippo, F.C. 1009
 Dilmanian, F.A. 93
 Dingfelder, M. 147, 267
 Donahue, R.J. 833
 Dragoun, O. 431
 Drozdowicz, K. 663
 Duane, S. 299
 Dunham, G.D. 1123
 Duverger, E. 407

 Egdorf, H.W. 961
 Eggers, I. 323
 Emfietzoglou, D. 273
 Emmett, M.B. 631
 Engel, R. 979, 1033
 Enghardt, W. 123
 Enke, M. 1003

 Enqvist, T. 1097
 Errazquin, L. 555, 561, 565
 Evans, H. 401

 Fassò, A. 159, 955
 Fernández Timón, A. 1145
 Fernández-Varea, J.M. 27, 33, 105, 147
 Fernandes, A. 731, 919
 Ferrari, A. 159, 955, 1175
 Ferrari, P. 489
 Ferreira, L. 497
 Filges, D. 21, 937, 1003
 Fippel, M. 217
 Fischer, U. 761, 791
 Fitting, H.-J. 39
 Foltanova, S. 345
 Foppiano, F. 543
 Forster, R.A. 643
 Frühwirth, R. 571
 France, N. 637
 Franck, D. 443
 Frankle, S.C. 657
 Frei, D. 223
 Friedland, W. 267
 Fu, C.Y. 1139
 Fukumura, A. 1085, 1151
 Funabiki, J. 973
 Furihata, S. 1045

 Gabriel, T.A. 1139
 Galin, J. 1003
 Gallmeier, F.X. 961
 Galoyan, A.S. 1169
 Gambaccini, M. 69, 351
 Garelli, S. 543
 Glière, A. 461
 Goldenbaum, F. 1003
 Gomes, A. 1181
 Gonçalves, I.C. 731, 755, 919
 Gonçalves, I.F. 755
 Goorley, T. 749, 797
 Gorodkov, S. 467
 Gouriou, J. 437
 Grichine, V.M. 117, 153
 Grimestone, M. 637
 Grosswendt, B. 237
 Gschwind, R.I. 407
 Gualdrini, G. 687
 Gudowska, I. 317
 Gudowski, W. 21

- Guladrini, G. 489
 Guldbakke, S. 881
 Gumplinger, P. 153
- Haberer, T. 1069
 Hage-Ali, M. 87
 Haghighat, A. 619
 Hegedűs 681
 Hendricks, J.S. 643
 Hendriks, P.H.G.M. 773, 893
 Henn, A. 93
 Herbach, C.-M. 1003
 Hilscher, D. 1003
 Hirayama, H. 63, 99
 Hollenbach, D.F. 631
 Hoogenboom, J.E. 597, 613
 Hordósy, G. 681
 Huang, L.-x. 483, 1057
 Hubbell, J.H. 55
 Hughes, H.G. 961, 967
 Hugtenburg, R.P. 583
 Hunt, J.G. 345
 Hutton, L. 637, 697
- Iida, H. 865
 Isakson, M. 345
 Ito, S. 1085
 Ivanchenko, V. 153
 Iwase, H. 973, 1085, 1151
- Jäkel, O. 1069
 Jacquet, O. 703, 711
 Jahnke, U. 1003
 Jang, C.S. 851
 Jeynes, C. 1105
 Johnson, J.O. 991
 Joloudov, D.L. 871
- Kadi, Y. 1015, 1175
 Karriem, Z. 841
 Kausch, C. 395
 Kawrakow, I. 135, 217, 229
 Keall, P.J. 205
 Keen, N.D. 1123
 Keresztúri, A. 681
 Khvostunov, I.K. 251
 Kiger III, W.S. 797
 Kim, C.H. 851
 Kim, E. 1085
 Kling, A. 529
- Kloosterman, J.L. 597
 Klusoň, J. 339
 Kodeli, I. 791
 Kokoulin, R. 153
 Kompaniyets, A.V. 871
 Konno, C. 791
 Koprivnikar, I. 997
 Korobeinikov, V.V. 847
 Koyabu, K. 785, 877
 Krämer, M. 1069
 Kraft, G. 1069
 Krivosheev, O.E. 141, 943
 Kugo, T. 821
 Kuhr, J.-Ch. 39
 Kurasige, H. 1117
 Kurosawa, T. 973, 1085, 1151
- López-Robles 377
 Lacoste, V. 1175
 Lara, V. 1039
 Larsen, E.W. 49
 Laub, W. 217
 Laval, L. 443
 Leal, A. 211, 329, 555, 561, 565
 Lee, H.S. 1139
 Lee, Y.K. 809
 Legrain, R. 1097, 1111
 Lehnert, U. 123
 Lei, F. 401
 Leray, S. 1097, 1111
 Letourneau, A. 1003
 Liljequist, D. 33
 Little, R.C. 657, 961, 967
 Llovet, X. 105, 147
 Longo, F. 401
 Lopatkin, A.V. 931
 Lopes, J.A.M. 535
 Lopes, M.C. 311
 Lott, B. 1003
 Ludewigt, B.A. 833
 Lux, I. 7
- Möslang, A. 467
 Müller, E. 123
 Ma, C.-M. 549
 MacFarlane, R.E. 657, 961
 Magni, S. 153, 401
 Maio, A. 549, 1181
 Maire, M. 153, 503
 Makovicka, L. 407

- Malatova, I. 345
 Malkov, M.R. 675
 Marchetto, F. 543
 Mariani, A. 449
 Marques, J.G. 529, 919
 Martínez-Dávalos, A. 377
 Martín Sánchez, A. 1145
 Martinavarro, A. 333
 Martinho, J.M.G. 577
 Marziani, M. 351
 Mashnik, S.G. 961
 Maučec, M. 772, 893
 McAlpin, S. 357
 McKinney, G.W. 643
 Medrano, J.C. 565
 Meigo, S. 949
 Merlet, C. 389
 Milgram, M.S. 175
 Mini, R. 223
 Miotello, A. 43
 Mishev, A. 407
 Misraki, J. 413
 Miss, J. 711
 Mitake, S. 859
 Mitaroff, A. 1157
 Mituishi, H. 905
 Mobit, P.N. 305
 Mohan, R. 205
 Mokhov, N. 985
 Mokhov, N.V. 141, 943
 Mora, G. 549
 Mori, T. 625
 Mosher, S. 767
 Moskvín, V. 199, 1129
 Mosteller, R.D. 643
 Muñoz-Cobo, J.L. 887, 1081
 Muratov, V.G. 931
 Mustapha, B. 1097
 Muta, T. 905

 Nünighoff, K. 1003
 Nüsslin, F. 217
 Núñez, L. 555, 561
 Nagaya, Y. 625
 Nakamura, T. 973, 1085, 1151
 Nakao, N. 1085, 1151
 Namito, Y. 63
 Nariyama, N. 81
 Nartallo, R. 401
 Naumann, B. 123

 Nava, E. 687
 Neef, R.-D. 937, 1003
 Neubert, W. 123
 Neuenschwander, H. 223
 Neuhold, P. 1163
 Newhauser, W.D. 1075
 Nieminen, P. 153, 401, 543
 Niita, K. 949
 Nikjoo, H. 251
 Nimal, J.C. 651
 Nishimura, K. 905
 Niu, S.-l. 483
 Noack, K. 1063
 Nouri, A. 703, 711
 Nunomiya, T. 1085
 Nutbrown, R. 299

 O'Malley, J. 357
 Okumura, K. 625
 Oliveira, A.D. 425
 Oliveira, C. 311, 497
 Orion, I. 93
 Ortiz, J. 517
 Oulad ben Tahar, H. 147

 Péghaire, A. 1003
 Panin, M.P. 181, 193
 Panteleeva, A. 123
 Papiež, L. 199, 1129
 Patau, J.P. 479
 Paul, N. 1003
 Pawelke, J. 123
 Pawlicki, T. 549
 Peña, L. 93
 Pedroso de Lima, J.J. 425
 Penelíau, Y. 129
 Pepyolyshev, Yu. 899
 Peralta, L. 311
 Perel, R.L. 791
 Perez, R. 1081
 Perot, B. 413, 419
 Perreira, E.J.N. 577
 Perry, D.R. 1085
 Perucha, M. 211, 329, 555, 561, 565
 Petrizzi, L. 865
 Pia, M.G. 153, 401, 543
 Pienkowski, L. 1003
 Pierotti, L. 489
 Pitcher, E.J. 961, 967
 Pitts, M. 767

- Polanski, A. 803, 1169
 Prael, R.E. 17, 643, 961
 Prata, J. 919
 Pravikoff, M. 1097
 Prinja, A.K. 1123
 Puzynin, I. 803

 Quillin, S. 357

 Ródenas, J. 333, 517
 Rachinhas, P.J.B.M. 535
 Radermacher, E. 1175
 Rahnema, F. 767
 Rakhno, I. 803
 Ramalho, A.J.G. 529, 731, 755, 919
 Ranft, J. 955, 979, 1021, 1033
 Rapisarda, M. 911
 Rearden, B.T. 725
 Regler, M. 571
 Reitsma, F. 841
 Rejmund, F. 1097
 Rincón, M. 211, 329, 555, 561, 565
 Rius, V. 333
 Rodríguez-Villafuerte, M. 473
 Rodrigues, P. 311
 Roesler, S. 979, 1033
 Rogers, D.W.O. 135, 291
 Rogov, A. 899
 Rolando, V. 543
 Rollet, S. 911
 Rosenberg, E. 389
 Rosenfeld, A.B. 93
 Rosetti, M. 455
 Rugama, Y. 887, 1081
 Rybin, A. 153

 Sánchez-Calzado, J.A. 555, 561, 565
 Sánchez-Doblado, F. 211, 329, 555, 561, 565
 Sánchez-Nieto, B. 561
 Sánchez-Reyes, A. 147
 Sagi, I. 93
 Sala, P.R. 159, 955
 Salgado, J. 497, 755
 Salvat, F. 27, 33, 105, 147
 Sandison, G.A. 305
 Santos, F.P. 535
 Sasaki, M. 1085
 Sasaki, T. 1117
 Sato, H. 1151
 Sato, O. 859
 Sato, T. 1139
 Sawamura, H. 905
 Sawchuk, S. 383
 Schaal, H. 937, 1003
 Schachinger, E. 997
 Schardt, D. 1069
 Schlegel, D. 881
 Schmidt, K.-H. 1097
 Schmidt, R. 323, 395, 523
 Scholz, D. 1069
 Schröder, U. 1003
 Schwarz, R. 815
 Schweitzer, J.S. 905
 Segui, S. 27
 Sekine, T. 737
 Selcow, E.C. 643
 Seltzer, S.M. 55
 Sempau, J. 147
 Serghiuta, D. 767
 Serradell, V. 517
 Sheikh-Bagheri, D. 187
 Shibata, T. 1085
 Shim, H.J. 851
 Shin, K. 1139
 Shipley, D. 299
 Shuttleworth, T. 603, 637
 Siebers, J.V. 205, 1051
 Siebert, B.R.L. 719
 Sierk, A.J. 961
 Siffert, P. 87
 Silari, M. 1157
 Sissakian, A. 803
 Sitaraman, S. 785, 877
 Smith, N. 637, 697, 827
 Snow, E.C. 961
 Solano, A. 543
 Sood, A. 643
 Sorbier, L. 389
 Sorcini, B. 317
 Spalek, A. 431
 Spanier, J. 165, 589
 Stéphan, C. 1097
 Stamenov, J. 407
 Starý, V. 369
 Stauffer, A.D. 535
 Stephen, J.B. 87
 Sterzenbach, G. 937, 1003
 Stewart, R.D. 285
 Stoker, C. 841

- Striganov, S. 985
Svensson, R. 317
- Távora, L.M.N. 351
Tabary, J. 461
Tabata, T. 199
Taibi, A. 69, 351
Taieb, J. 1097
Takada, H. 949
Taniguchi, S. 1085
Tartari, A. 69, 75
Tassan-Got, L. 1097
Terrissol, M. 261, 279
Thomas, R. 299
Tickner, J. 111, 669
Tietze, A. 1003
Tishchenko, V. 1003
Titt, U. 1075
Todorovic, M. 323, 395, 523
Toke, J. 1003
Tolar, D.R. 49
Toubon, H. 419
Traub, R.J. 285
Trindade, A. 311
Truscott, P.R. 401
Tsige-Tamirat, H. 511
Tsunoda, H. 859
Tulovsky, V. 1129
- Uehara, S. 251
Ueki, T. 597
Urbán, L. 153, 503
Uwamino, Y. 1085, 1151
Uzhinskii, V.V. 1169
- Vértes, P. 681
- Valentine, T.E. 743, 887, 1081
Valenza, D. 865
Van Ginneken, A. 985
Verboomen, B. 779
Vergnaud, T. 651
Vermeersch, F. 925
Vieira, A. 731, 919
Vlachoudis, V. 1175
Vladimirov, P. 467
Volant, C. 1097, 1111
Volken, W. 223
Vrigneaud, J.M. 261, 279
Vujic, J. 833
- Wadhwa, M. 503
Wagner, J.C. 619
Waters, L.S. 961
Webb, R.P. 1105
Weber, U. 1069
Wellisch, J.-P. 1027, 1117
Wendler, E. 1105
Werner, Ch.J. 657
White, M.C. 657, 961
White, S.W. 643
Wlazło, W. 1097
Woźnicka, U. 663
Wohlmuther, M. 1003
Wright, P. 1085
- Yan, X. 1075
Yoshizawa, N. 973
Young, P.G. 961, 967
- Zamenhof, R. 797
Zhang, D.-h. 483
Zhong, Z. 93